

Lecture Notes in Electrical Engineering 766

Ramesh C. Bansal
Anshul Agarwal
Vinay Kumar Jadoun *Editors*

Advances in Energy Technology

Select Proceedings of EMSME 2020

 Springer

Lecture Notes in Electrical Engineering

Volume 766

Series Editors

Leopoldo Angrisani, Department of Electrical and Information Technologies Engineering, University of Napoli Federico II, Naples, Italy

Marco Arteaga, Departament de Control y Robótica, Universidad Nacional Autónoma de México, Coyoacán, Mexico

Bijaya Ketan Panigrahi, Electrical Engineering, Indian Institute of Technology Delhi, New Delhi, Delhi, India
Samarjit Chakraborty, Fakultät für Elektrotechnik und Informationstechnik, TU München, Munich, Germany

Jiming Chen, Zhejiang University, Hangzhou, Zhejiang, China

Shanben Chen, Materials Science and Engineering, Shanghai Jiao Tong University, Shanghai, China

Tan Kay Chen, Department of Electrical and Computer Engineering, National University of Singapore, Singapore, Singapore

Rüdiger Dillmann, Humanoids and Intelligent Systems Laboratory, Karlsruhe Institute for Technology, Karlsruhe, Germany

Haibin Duan, Beijing University of Aeronautics and Astronautics, Beijing, China

Gianluigi Ferrari, Università di Parma, Parma, Italy

Manuel Ferre, Centre for Automation and Robotics CAR (UPM-CSIC), Universidad Politécnica de Madrid, Madrid, Spain

Sandra Hirche, Department of Electrical Engineering and Information Science, Technische Universität München, Munich, Germany

Faryar Jabbari, Department of Mechanical and Aerospace Engineering, University of California, Irvine, CA, USA

Limin Jia, State Key Laboratory of Rail Traffic Control and Safety, Beijing Jiaotong University, Beijing, China

Janusz Kacprzyk, Systems Research Institute, Polish Academy of Sciences, Warsaw, Poland

Alaa Khamis, German University in Egypt El Tagamoa El Khames, New Cairo City, Egypt

Torsten Kroeger, Stanford University, Stanford, CA, USA

Yong Li, Hunan University, Changsha, Hunan, China

Qilian Liang, Department of Electrical Engineering, University of Texas at Arlington, Arlington, TX, USA

Ferran Martín, Departament d'Enginyeria Electrònica, Universitat Autònoma de Barcelona, Bellaterra, Barcelona, Spain

Tan Cher Ming, College of Engineering, Nanyang Technological University, Singapore, Singapore

Wolfgang Minker, Institute of Information Technology, University of Ulm, Ulm, Germany

Pradeep Misra, Department of Electrical Engineering, Wright State University, Dayton, OH, USA

Sebastian Möller, Quality and Usability Laboratory, TU Berlin, Berlin, Germany

Subhas Mukhopadhyay, School of Engineering & Advanced Technology, Massey University, Palmerston North, Manawatu-Wanganui, New Zealand

Cun-Zheng Ning, Electrical Engineering, Arizona State University, Tempe, AZ, USA

Toyoaki Nishida, Graduate School of Informatics, Kyoto University, Kyoto, Japan

Federica Pascucci, Dipartimento di Ingegneria, Università degli Studi "Roma Tre", Rome, Italy

Yong Qin, State Key Laboratory of Rail Traffic Control and Safety, Beijing Jiaotong University, Beijing, China

Gan Woon Seng, School of Electrical & Electronic Engineering, Nanyang Technological University, Singapore, Singapore

Joachim Speidel, Institut of Telecommunications, Universität Stuttgart, Stuttgart, Germany

Germano Veiga, Campus da FEUP, INESC Porto, Porto, Portugal

Haitao Wu, Academy of Opto-electronics, Chinese Academy of Sciences, Beijing, China

Junjie James Zhang, Charlotte, NC, USA

The book series *Lecture Notes in Electrical Engineering* (LNEE) publishes the latest developments in Electrical Engineering - quickly, informally and in high quality. While original research reported in proceedings and monographs has traditionally formed the core of LNEE, we also encourage authors to submit books devoted to supporting student education and professional training in the various fields and applications areas of electrical engineering. The series cover classical and emerging topics concerning:

- Communication Engineering, Information Theory and Networks
- Electronics Engineering and Microelectronics
- Signal, Image and Speech Processing
- Wireless and Mobile Communication
- Circuits and Systems
- Energy Systems, Power Electronics and Electrical Machines
- Electro-optical Engineering
- Instrumentation Engineering
- Avionics Engineering
- Control Systems
- Internet-of-Things and Cybersecurity
- Biomedical Devices, MEMS and NEMS

For general information about this book series, comments or suggestions, please contact leontina.dicecco@springer.com.

To submit a proposal or request further information, please contact the Publishing Editor in your country:

China

Jasmine Dou, Editor (jasmine.dou@springer.com)

India, Japan, Rest of Asia

Swati Meherishi, Editorial Director (Swati.Meherishi@springer.com)

Southeast Asia, Australia, New Zealand

Ramesh Nath Premnath, Editor (ramesh.premnath@springernature.com)

USA, Canada:

Michael Luby, Senior Editor (michael.luby@springer.com)

All other Countries:

Leontina Di Cecco, Senior Editor (leontina.dicecco@springer.com)

**** This series is indexed by EI Compendex and Scopus databases. ****

More information about this series at <http://www.springer.com/series/7818>

Ramesh C. Bansal · Anshul Agarwal ·
Vinay Kumar Jadoun
Editors

Advances in Energy Technology

Select Proceedings of EMSME 2020

 Springer

Editors

Ramesh C. Bansal
Department of Electrical Engineering
University of Sharjah
Sharjah, United Arab Emirates

Anshul Agarwal
Department of Electrical and Electronics
Engineering
National Institute of Technology Delhi
New Delhi, India

Vinay Kumar Jadoun
Department of Electrical and Electronics
Engineering
Manipal Institute of Technology
Manipal Academy of Higher Education
Manipal, Karnataka, India

ISSN 1876-1100

ISSN 1876-1119 (electronic)

Lecture Notes in Electrical Engineering

ISBN 978-981-16-1475-0

ISBN 978-981-16-1476-7 (eBook)

<https://doi.org/10.1007/978-981-16-1476-7>

© The Editor(s) (if applicable) and The Author(s), under exclusive license to Springer Nature Singapore Pte Ltd. 2022

This work is subject to copyright. All rights are solely and exclusively licensed by the Publisher, whether the whole or part of the material is concerned, specifically the rights of translation, reprinting, reuse of illustrations, recitation, broadcasting, reproduction on microfilms or in any other physical way, and transmission or information storage and retrieval, electronic adaptation, computer software, or by similar or dissimilar methodology now known or hereafter developed.

The use of general descriptive names, registered names, trademarks, service marks, etc. in this publication does not imply, even in the absence of a specific statement, that such names are exempt from the relevant protective laws and regulations and therefore free for general use.

The publisher, the authors and the editors are safe to assume that the advice and information in this book are believed to be true and accurate at the date of publication. Neither the publisher nor the authors or the editors give a warranty, expressed or implied, with respect to the material contained herein or for any errors or omissions that may have been made. The publisher remains neutral with regard to jurisdictional claims in published maps and institutional affiliations.

This Springer imprint is published by the registered company Springer Nature Singapore Pte Ltd. The registered company address is: 152 Beach Road, #21-01/04 Gateway East, Singapore 189721, Singapore

Preface

This book presents the select proceedings of the 1st International Conference on Energy, Material Sciences and Mechanical Engineering 2020 (EMSME-2020), held at National Institute of Technology Delhi, India. The motive of this conference was of great importance. It was considered as a forum to bring together scientists, university professors, graduate students, and engineers, presenting new science, technology, and engineering ideas and achievements.

More than 160 papers were presented at EMSME-2020. Various topics covered in this book include clean materials, solar energy systems, wind energy systems, power optimization, grid integration of renewable energy, smart energy storage technologies, artificial intelligence in solar and wind system, analysis of clean energy material in environment, converter topology, modeling and simulation. However, for this book, only 70 peer-reviewed papers, authored by research groups representing various universities and institutes, were selected for inclusion. This book will be useful for researchers and professionals working in the areas of solar material science, electrical engineering, and energy technologies. Research papers (with starting page number in Table of contents) are broadly classified as follows:

- Solar Energy Systems
- Wind and Hybrid Energy Systems
- Microgrid, Distributed Generation, Smart Grid
- Electrical Vehicles
- Renewable Energy
- Power System
- Power Electronics and Power Quality
- Electronics & Communication Systems
- Optimization Techniques
- Miscellaneous Topics

Furthermore, we thank Padamshri Dr. Satish Kumar, Hon. Director, National Institute of Technology Delhi and all members of the program committee and the organizing committee for their work in preparing and organizing the conference. We also thank the staff and management of the institute for their cooperation and support.

Last but not least, we thank Springer for its professional assistance and particularly Swati Meherishi and Priya Vyas who supported this publication.

Sharjah, United Arab Emirates
New Delhi, India
Manipal, India

Ramesh C. Bansal
Anshul Agarwal
Vinay Kumar Jadoun

Contents

A New High Output Resistance Accurate CMOS Current Mirror	1
Bhawna Aggarwal, Maneesha Gupta, Himani Malik, Mahak Garg, and Gaurav Taneja	
Designing and Comparison of Geometric Mean Circuits Based on MOS Translinear Principle Using Different FVF Structures	13
Aakansha and Bhawna Aggarwal	
A New Linear CMOS CDTA with Improved Characteristics	23
Bhawna Aggarwal and Saurabh Kumar Sharma	
Design of Wind Energy Conversion System Utilizing Induction Generator with Pitch Angle Control	31
Subash Chandra Parida, V. K. Tayal, and S. K. Sinha	
Analysis of SPA Scheme for Massive MIMO	41
Manisha Bharti and Tanvika Garg	
Multiple Frequency Band Planar Antenna for Different Applications	49
Sakshi and Manisha Bharti	
Implementation of Attendance Management System Based on Text and Face Recognition	55
Vaithyanathan Dhandapani, Swathi Majji, Kishore Udata, and M. Manigandan	
Performance Analysis of Fuzzy Logic-Based MPPT Controller for Solar PV System Using Quadratic Boost Converter	69
Servavidya Kumar Manas and Bharat Bhushan	
An Analysis on Frequency Control of Microgrid Including Diverse Renewable Energy Sources	81
Ritwik Tripathi and Omveer Singh	

Islanding Detection Scheme for Single-Phase Grid-Connected Solar Photovoltaic System using Support Vector Machine	97
Jyoti Sagar, Omveer Singh, and Shabana Urooj	
Thermal Imaging-Based Fault Diagnosis of Electronics Circuit Boards	111
Laxmi and Rajesh Mehra	
Power-Efficient Bidirectional Shift Register Using Conditional Bidirectional Pulsed Latch Circuit	123
Karan Kumar and Vaithyanathan Dhandapani	
A State-of-the-Art Review on LVRT Enhancement Techniques for DFIG-Based Wind Turbines	131
Priyanka Paliwal	
Design of Traffic Sign Detection Using Hardware and Software Co-design	143
V. Muthu Ganesh and N. Janakiraman	
Electricity Generation Using Wind Tree	153
Yogesh Tomar, Ashutosh Kumar, Pradhan Singh Meena, Sunil Kumar Yadav, Anshul Agarwal, and Vinay Kumar Jadoun	
Reliability-Based Optimal Sizing for an Isolated Wind–Battery Hybrid Power System Using Butterfly PSO	163
Priyanka Paliwal	
Analyzation of Temperature Rise in Induction Motor for Electric Vehicles	173
Sohail Khazi, Anusha Vadde, Krishnan Manickavasagam, Govind R. Kadambi, Venkat Narayanan, B. M. Lokesh, Swapan Sarkar, and Jagadeesha	
Technical Review on Optimal Reactive Power Dispatch with FACTS Devices and Renewable Energy Sources	185
S. N. V. S. K. Chaitanya, R. Ashok Bakkiyaraj, and B. Venkateswara Rao	
A Deep Learning Approach to Recognize Faces After Plastic Surgery	195
Tanupreet Sabharwal and Rashmi Gupta	
IoT-Based Energy Monitoring and Controlling System for Home Automation	205
C. S. S. Barath and R. Nirmaladevi	
Power Transformer Summer Peak Load Prediction Using SCADA and Supervised Learning	215
Neeraj Kanwar, Divay Bargoti, and Vinay Kumar Jadoun	

Analysis of M-ary QAM-Based OFDM Systems in AWGN Channel 223
 Sarthak Pandey, Manisha Bharti, and Ayush Kumar Agrawal

Detection of Imagery Vowel Speech Using Deep Learning 237
 Jigar Patel and Syed Abudhagir Umar

Optimization of Process Parameters by Application of Adaptive Neuro-Fuzzy Inference System (ANFIS) Model of FFF Process 249
 Imran Siraj and Pushpendra S. Bharti

Skin Lesion Characterization with Ensembles of Machine Learning and Deep Learning Models 265
 D. Abhila, B. Priyanka, A. Aishwariya, S. Nihal Mathew, S. Suriya Kumar, and Kunaraj Kumarasamy

Auto Streetlight Control with Detecting Vehicle Movement 279
 Dinesh Kumar Saini, Sameer Meena, Kamlesh Choudhary, Sheetal Bedia, Anshul Agarwal, and Vinay Kumar Jadoun

Optimal Automatic Generation Control in Multi-Area Power Systems with Diverse Energy Sources 289
 Ashwini Kumar and Omveer Singh

BLDC Motor Torque Ripple Minimization Technique by Using Isolated Type DC–DC Buck–Boost Converter 301
 Arpit Satta, Jay Prakash Keshri, Harpal Tiwari, and Vishal Jain

High Gain Converter with Switched Coupled Inductors for Renewable Energy Systems 313
 Pankaj, Jay Prakash Keshri, Harpal Tiwari, and Arpit Satta

Five-Level Single-Phase Converter Using SiC with Reduced Switched Voltage Stress 327
 Vishal Jain, Jay Prakash Keshri, Harpal Tiwari, and Pankaj

Chassis Design with Integrated Battery Pack Space for Electric Motorcycle 339
 Mohammad Irfan Ahmad and Pankaj Dorlikar

Extraction of Maximum Electrical Power from Solar Photovoltaic-Based Grid-Tied System 351
 Dhairya Karna, Aditya Vikram, Astitva Kumar, and M. Rizwan

Power System Service Restoration Methods—A Study 363
 Prapti Rastogi, Neeraj Kanwar, and Samarendra Pratap Singh

A Study on Implementation of Various Approaches for Shop Floor Management 371
 Varun Tripathi, Suvandan Saraswat, and Girish Dutt Gautam

An Analysis on Cyber Security Issues in the Smart Grid	389
Shikha Kuchhal, Ikbal Ali, and Ibraheem	
Optimal Planning of EV Fast-Charging Station with DG in Distribution System Using PSO	397
Dhiraj Kumar Singh and Aashish Kumar Bohre	
Congestion Management of System with N-1 Contingency by Optimal Placement of TCSC Using PSO	409
Ashish Singh and Aashish Kumar Bohre	
Optimal Reactive Power Dispatch Under Load Uncertainty Incorporating Solar Power Using Firefly Algorithm	423
P. Ramkee, S. N. V. S. K. Chaitanya, B. Venkateswara Rao, and R. Ashok Bakkiyaraj	
Power Quality Improvement Using Harmonic Passive Filter in Distribution System	435
Arjun Baliyan, Majid Jamil, and M. Rizwan	
Implementation and Performance Measurement of Q-Varying and r-Varying IIR Notch Filter for Bio-medical Application	447
Kunal Kumar, Sandeep Kumar, and Upendra Kumar Acharya	
Advanced Optimization Scheme to Improve Photon Management to Increase Solar Cell Efficiency	463
Dilip Yadav and Nidhi Singh	
Music Generation Using Supervised Learning and LSTM	477
Suman Maria Tony and S. Sasikumar	
Controlling an SSB-SC Amplitude Modulator Using a Second-Order Control System	487
Manisha Bharti, Aditya Joshi, and Tanvika Garg	
Simultaneous Frequency and SSB Modulation for Ultrasonic Speakers	499
Manisha Bharti, Meghav Shukla, Aditya Joshi, and Tanvika Garg	
Opportunities and Challenges in Solar Photovoltaic-Based Electric Vehicles Charging Stations: A Step Toward Smart Cities Development	507
Mohammad Bilal and M. Rizwan	
Role of IoT in Industry 4.0	517
Ankita Sharma, Vibha Burman, and Shipra Aggarwal	
Three-Level Modified Capacitor-Assisted Extended Boost Z-Source Multilevel Inverter for Photovoltaic Applications	529
S. Nagaraja Rao, B. M. Kiran Kumar, and Swathy Nair	

An Overview on the Topologies and Control Strategies for Solar Photovoltaic Emulators 541
 K. R. Jeswanth Kumar, S. Kamatchi Rajeswari, S. Sridharan, and K. Sundararaman

An Enhanced Boost Z-Source Inverter Topology for Electrical Vehicle Applications 557
 S. Nagaraja Rao, V. Praveen Kumar, and Veerabhadra

Study of Human Body Temperature and Different Modes of Heat Transfer Using Steady-State Energy Balance Model 571
 Shashikant Das and Sudhakar Subudhi

Power Quality Analysis and Enhancement Using DSTATCOM for Three-Phase Variable Load 583
 Shamshad Ali, Majid Jamil, and M. A. Khan

A Dopingless Tunnel FET and MOSFET-Based Comparative Study of a Simple Current Mirror 597
 Harihar Nath, Suruchi Sharma, Abhishek Verma, and Baljit Kaur

Energy Harvesting Techniques for Self-sustainable Energy Systems 609
 Bishal Nahak, Yogesh Dewang, and Vipin Sharma

A Novel Color-Coded Light-Based Communication for Autonomous Swarm Robotics Research 621
 Abhishek Kaushal and Anuj Kumar Sharma

Recent Advancement of Weed Detection in Crops Using Artificial Intelligence and Deep Learning: A Review 631
 Puneet Saini

A Review of Performance of Solar Photovoltaic Refrigeration System 641
 Shailendra Kasera, Rajlakshmi Nayak, and Shishir Chandra Bhaduri

A New Design Based on Grid Integrated Solar PV Array Using Vector Control 653
 Jaya Singh and Vineet Kumar Tiwari

Performance-Based Study of HFC134A, HC600A, and HFO1234YF in a VCR System 663
 Sunil Kumar Gupta, B. B. Arora, and Akhilesh Arora

STT-MRAM A Universal Memory from Device to Circuit 673
 Jyoti Garg and Subodh Wairya

Designing and Analysis of Dynamic Model for Robotic Manipulator 683
 Aditi Saxena, Jitendra Kumar, Kamal Sharma, and Debanik Roy

Design and Implementation of Energy Efficiency Augmentation Using Renewable Energy Source for Small-Scaled Residential Micro-grid	693
Ikbal Ali and Swati Sharma	
Application of Modified Clonal PSO in Distributed Generator Placement for Enhancement of Efficiency and Voltage Stability in Distribution System	703
Vikas Singh Bhadoria, Shiva Pujan Jaiswal, Nidhi Singh Pal, and Vivek Shrivastava	
Performance of an L-shaped Duct Oscillating Water Column Wave Energy Converter Device Under Irregular Incident Waves	719
Kshma Trivedi and Santanu Koley	
Study of Human Behaviour During Lockdown Owing to Corona Epidemic	729
Brijesh Singh	
Numerical Investigation of Electro-osmotic Flow of Fluid in Tapered Microchannel	741
Ravinder Jhorar, Shashi Bhushan, RaviKumar Sharma, and Dharmendra Tripathi	
Optimal Placement of Distributed Generators in Power System Using Sensitivity Analysis	749
Anoop Arya, Swatantra Singh Verma, Shweta Mehroliya, Shilpi Tomar, and C. S. Rajeshwari	
A Review on Performance of Electric Motor Vehicle	761
Gagandeep Singh, Harshit Manchanda, and Sunny Bhatia	
Comparison of SVM and ARIMA Model in Time-Series Forecasting of Ambient Noise Levels	777
S. K. Tiwari, L. A. Kumaraswamidhas, and N. Garg	
Circuit Theory Base Loss Allocation Methods for Contemporary Distribution System: A Comparative Study	787
Pankaj Kumar, Nikhil Gupta, K. R. Niazi, and Anil Swarnkar	
A Comparative Study on the Performance of Energy Storage Systems for Hybrid Electric Vehicles	795
Kanchan Yadav and Sanjay Maurya	

About the Editors



Prof. Ramesh C. Bansal has more than 25 years of diversified experience of research, scholarship of teaching and learning, accreditation, industrial, and academic leadership in several countries. Currently he is a Professor in the Department of Electrical Engineering at University of Sharjah and extraordinary (Honorary) Professor at University of Pretoria. Previously he was Professor and Group Head (Power) in the ECE Department at University of Pretoria (UP), South Africa. Prior to his appointment at UP, he was employed by the University of Queensland, Australia; University of the South Pacific, Fiji; BITS Pilani, India; and Civil Construction Wing, All India Radio. Prof. Bansal has significant experience of collaborating with industry and Government organizations. He has made significant contribution to the development and delivery of BS and ME programmes for Utilities. He has extensive experience in the design and delivery of CPD programmes for professional engineers. He has carried out research and consultancy and attracted significant funding from Industry and Government Organizations. Prof. Bansal has published over 350 journal articles, presented papers at conferences, books, and chapters in books. He has Google citations of over 12000 and h-index of 50. He has supervised 25 PhD, 4 Post Docs and currently supervising 5 Ph.D. students. His diversified research interests are in the areas of Renewable Energy (wind, PV, micro grid), Power Systems, and Smart Grid. Professor Bansal is an Editor/Associate Editor of several highly regarded journals including IEEE Systems Journal, IET Renewable Power Generation, and Technology and Economics

of Smart Grids and Sustainable Energy. He is a Fellow and Chartered Engineer IET-UK, Fellow Institution of Engineers (India), and Senior Member of IEEE-USA.



Dr. Anshul Agarwal graduated from the Uttar Pradesh Technical University, Lucknow, India, with B.Tech. degree in Electrical and Electronics Engineering in 2007 and completed his M.Tech. (Gold Medalist) in Power Electronics and ASIC Design in July 2009 and Ph.D. in 2013 at MNNIT, Allahabad. He is currently the faculty in Electrical and Electronics Engineering Department at NIT Delhi. He has served as Assistant Professor in the National Institute of Technology Hamirpur, HP. His research interests include power electronic devices, modelling of converters/inverters, AC to AC power conversion, renewable energy, integration of grids, hybrid vehicles, FPGA based converters design, solar and wind energy integration. Dr. Anshul Agarwal has published more than 20 papers in reputed international journals, more than 40 papers in reputed IEEE international conferences. He has also published one book and eight book chapters in different Books. He has been awarded by POSOCO Power System (PPSA-2014) for the top Ph.D. research work. He has also served as guest editor in special issue for various journals. He is active reviewer of various international conferences and reputed journals.



Dr. Vinay Kumar Jadoun is currently Assistant Professor (Senior Scale) in the Department of Electrical and Electronics Engineering, Manipal Institute of Technology, MAHE, Manipal, India. He has obtained B.E. from SATI, Vidisha, M.P., India. He obtained M. Tech. and Ph.D. from the Department of Electrical Engineering, Malaviya National Institute of Technology (MNIT), Jaipur, India. Previously, he worked as a faculty in the National Institute of Technology, Delhi, and National Institute of Technology, Hamirpur, India. Dr. Vinay Kumar Jadoun has published 18 papers in reputed international journals, 25 papers in international and national conferences and 10 book chapters in different books. His areas of interest are economic operation of power system, hydrothermal scheduling,

multi-area economic dispatch, soft computing techniques, renewable power generation, micro grid, smart grid, electric vehicles, condition monitoring of electrical apparatus, DGA, health monitoring of power transformer and AI techniques. He is a senior member of IEEE, PES, and smart grid community. He has experience for organizing international conferences and short-term course. He has got 2016 Electric Power Systems Research (EPSR) Best Reviewer Certificate and Certificate of Outstanding Contribution in reviewing award from various reputed journals. He is also member of technical programme committee of different international and national conferences.

A New High Output Resistance Accurate CMOS Current Mirror



Bhawna Aggarwal, Maneesha Gupta, Himani Malik, Mahak Garg,
and Gaurav Taneja

1 Introduction

Current mirror (CM) is a widely used basic building block used for the development of analog and/or mixed mode integrated circuits (ICs). The performance of these ICs is very much affected by the characteristics of these CMs. Majorly, the characteristics determining the performance parameters of a CM are its input resistance, output resistance, and current matching accuracy. High output resistance and low input resistance help in avoiding loading effect at output and input sides, respectively, and thereby help in providing consistent and accurate output. Several crucial applications like biomedical circuits, low-power bioamplifiers, etc., demand ideally infinite output resistance and zero input resistance [1, 2]. Moreover, the use of accurate CM in differential amplifier improves its common mode and power supply rejection ratios [3, 4]. Furthermore, charge pump of phase-locked loops (PLLs) which are very extensively used as low-voltage clock generators is also in need of high-performance CMs [5, 6]. As CM plays vital role in designing high-performance circuits, consistent effort has been made for improving its various characteristics. The current trend is to use short-channel MOS devices as they provide compact circuits with low power consumption and higher bandwidth. However, these devices have inherent problem of low current transfer accuracy because of increased channel length modulation effect and low output resistance. Thereby, various configurations like Wilson, improved Wilson and cascode CMs were designed to increase accuracy and output resistance of a CM [7]. However, improvement in these configurations is achieved at the expense of increase in minimum required output voltage (output compliance voltage) and hence requires a higher supply voltage.

In the literature, various techniques like self-biased high-swing cascode CM [8, 9], regulated cascode CM [10], and active-input regulated cascode CM [10] have been reported that improve output resistance and accuracy without compromising

B. Aggarwal (✉) · M. Gupta · H. Malik · M. Garg · G. Taneja
Netaji Subhas University of Technology, Delhi, India

with the required supply voltage of original circuit. Conventionally, input resistance can be improved by increasing DC bias voltage or width of the input MOSFETS, however at the price of enhancement in power consumed and required silicon area. Several procedures like FVF and active CM based on negative series feedback have been reported in the literature that help in achieving lower input resistance for CM [7].

The objective of this paper has been to design a near-ideal CM that can be used for the development of integrated circuits having higher performance. Here, a high-performance Ramirez CM having FVF configuration at input and negative series feedback at output [11] is combined with super-cascode configuration [12] to improve accuracy and resistance offered at output terminal of CM. This proposed CM operates at a higher bandwidth and consumes less power. Presentation of this paper is as follows: Sect. 2 offers an insight into the previously reported high-performance CMs. Section 3 explains the proposed accurate CM having very high output resistance and provides its small-signal analysis for deriving output resistance. The simulation results obtained using standard SPICE 0.18 μm CMOS technology are presented in Sect. 4. Finally, the last section comprises of conclusion and future scope.

2 Current Mirrors with Enhanced Characteristics Reported in the Literature

In the literature, various topologies involving negative feedback with shunt-series configuration have been implemented to improve input and output resistances of a CM [13, 14]. These feedback schemes improve the resistances by feedback factor that is dependent on the gain of the amplifiers used. A few important architectures employing these techniques are discussed here. The self-biased high-swing cascode CM shown in Fig. 1a includes a CM and a cascode bias generator [8, 9]. This bias generator consists of a resistor ‘ R ’ whose value is chosen to obtain a voltage drop of $V_{\text{DS,sat}}$ across it, where $V_{\text{DS,sat}}$ denotes the minimum saturation voltage required by a MOSFET. The compliance voltages obtained at input and output sides are $V_{\text{T}} + 2V_{\text{DS,sat}}$ and $2V_{\text{DS,sat}}$, respectively. This reduces the required supply voltage by V_{T} as compared to cascode CM. This CM provides high voltage swing and high output resistance and consumes less power. However, its input resistance gets increased by ‘ R .’

Regulated cascode CM (Fig. 1b) provides high output resistance [10]. In this configuration, negative series feedback at the output side is provided by MOSFET M3 and amplifier A. The amplifier helps in stabilizing the output current when the output voltage is varied by providing an equivalent change in the gate voltage of MOSFET M3. Approximate output resistance (r_{out}) of this CM is given as $A(g_{\text{m3}}r_{\text{o3}})r_{\text{o2}}$, where A represents voltage gain of supplementary amplifier, r_{o} is small-signal output resistance, and g_{m} is transconductance of the corresponding MOSFET. In this circuit,

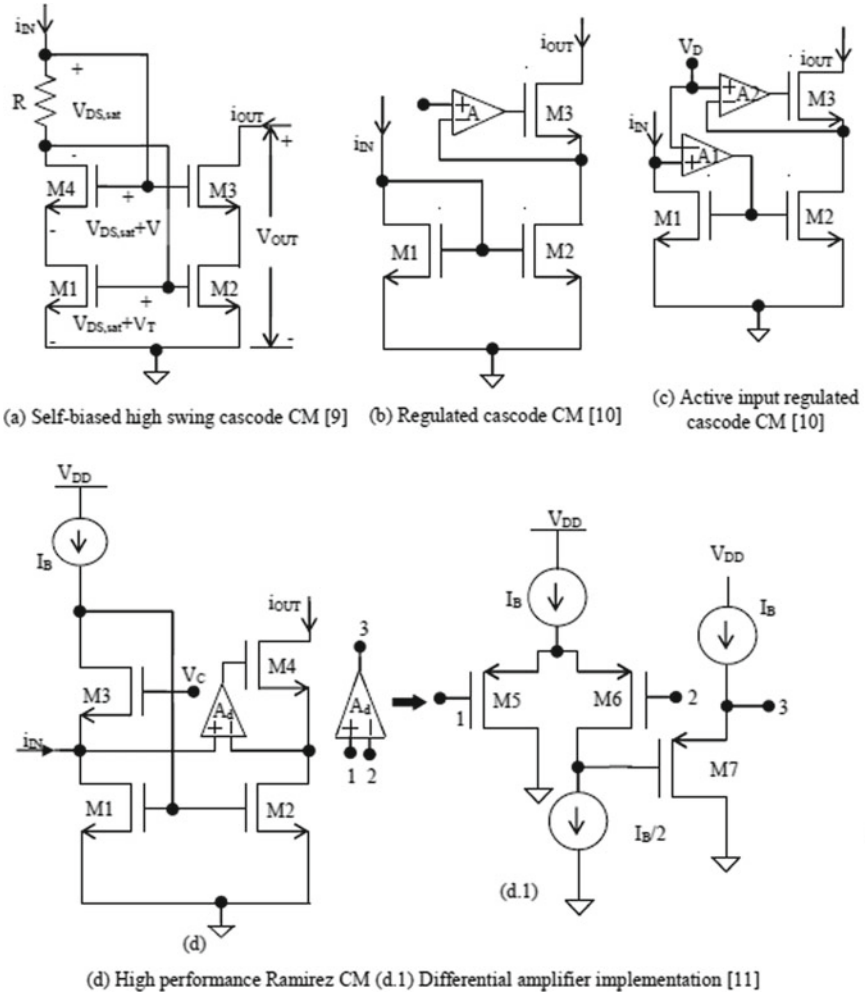


Fig. 1 Current mirrors with enhanced characteristics

output resistance of CM increases without affecting its input compliance voltage (which is same as that of a simple CM).

In active-input regulated cascode CM, Fig. 1c, two amplifiers having differential configuration are used. One of these amplifiers is used at input side and other one at output side [10]. Positive input terminals of the differential amplifiers are maintained at a reference voltage, V_D . This circuit has very high output resistance and very low input resistance. As this CM uses two amplifiers, its power consumption and chip area requirement are more. Moreover, the accuracy of the CM to some extent depends on the mismatch of the two amplifiers used.

Some high-performance CM topologies based on bulk-driven MOSFET, floating gate MOSFET (FGMOS), and quasi-floating gate MOSFET (QFGMOS) have been proposed time to time [15–18]. However, these CMs demand special type of MOSFETs and cannot be designed using standard CMOS technology.

3 Proposed Accurate Current Mirror with Very High Output Resistance

Negative feedback is a technique that has been used extensively by the circuit designers to improve the performance characteristics of an amplifier [4]. It has been observed that this technique can be used to improve the characteristics of a CM significantly [7]. Thereby, motivation for this work has been to design a CM that can be used as a basic building block in the development of high-performance circuits. For this, an existing high-performance CM topology has been chosen and combined with a negative feedback configuration to achieve a near-ideal CM.

Ramirez CM, Fig. 1d, proves to be a promising CM having very low input resistance (few $k\Omega$ s) and very high output resistance (100s of $M\Omega$). However, in this CM, the output current contains a DC offset current component equivalent to biasing current I_B . This offset term should be removed if accurate current matching is required at the output side. It can be eliminated by the help of super-cascode configuration [12]. Complete circuit of this high-performance proposed CM is shown in Fig. 2a. Here, amplifier A_d has been implemented by the circuit as shown in Fig. 1d.1. The super-cascode configuration is formed at the output side by MOSFETs M4, M5, and M6 and biasing currents I_B and I_{B1} . Here, M5 is controlled by drain terminal of M4. In this circuit, MOSFET M6 drives MOSFET M5 by controlling its gate voltage as

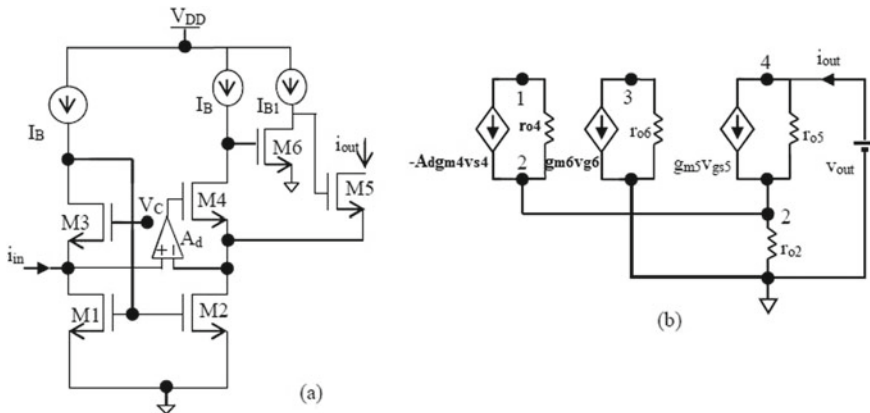


Fig. 2 a Proposed very high output resistance accurate CM. b Small-signal equivalent model for deriving output resistance of a

it acts as an inverting stage to reverse the polarity of the drain terminal of M4. This super-cascode configuration helps in eliminating the offset component appearing in output current by segregating biasing current I_B from the output current.

The inverting stage used in super-cascode configuration provides further enhancement in gain, thus increasing the output resistance significantly. Here, output resistance increases due to two nested feedback loops present at output side: differential amplifier 'A_d' and super-cascode configuration. Thus, in the proposed CM, super-cascode configuration employed at the output side not only helps in eliminating the offset term present at the output terminal, but also helps in enhancing output resistance of current mirror as well.

The use of nested feedback loops at output side further nullifies the channel length modulation effect and improves its accuracy with high load significantly. All these are achieved while maintaining similar supply voltage requirement as that of Ramirez CM (Fig. 1d). As the proposed CM uses negative series feedback at the output side, thus it operates at a higher bandwidth.

3.1 Small-Signal Analysis

Equivalent small-signal model of the proposed CM to derive output resistance is shown in Fig. 2b. Output resistance (r_{out}) is given by Eq. (1):

$$r_{out} = v_{out}/i_{out}|_{i_{IN}=0} \quad (1)$$

The equations obtained after routine analysis of this model are as follows:

$$i_{out} = g_{m5}(v_{G5} - v_{S4}) + (v_{out} - v_2)/r_{05} \quad (2)$$

$$v_2 = v_{S4} = i_{out}r_{02} \quad (3)$$

$$v_{G5} = -r_{06}g_{m6}v_{G6} \quad (4)$$

$$v_{S4} - v_{G6} = -A_d r_{04} g_{m4} v_{S4} \quad (5)$$

$$v_{G5} - v_{S4} = -r_{06}g_{m6}v_{G6} - i_{out}r_{02} \quad (6)$$

Simplifying Eqs. (1)–(6), we get:

$$i_{out}[1 + r_{02}/r_{05} + g_{m6}r_{02}r_{06}(1 + A_d r_{04} g_{m4}) + r_{02}g_{m5}] = v_{out}/r_{05} \quad (7)$$

Now, since $g_{m}r_0 \gg 1$ [19], Eq. (7) can be expressed in simplified form as:

$$r_{out} = v_{out}/i_{out} = A_d g_{m5} r_{05} g_{m6} r_{06} g_{m4} r_{04} r_{02} \quad (8)$$

From Eq. (8), it is observed that r_{out} of the proposed CM gets increased by a factor of $r_{05} g_{m5} r_{06} g_{m6}$. The proposed circuit has the same input resistance as that of Ramirez CM (Fig. 1d) as input configuration of the two circuits is similar.

4 Simulation Results and Discussions

The simulations of the CMs discussed in this paper have been performed in standard SPICE with 0.18 μm CMOS technology. A supply voltage of 1.5 V and input current of 0–100 μA has been used for simulations. To obtain a fair comparison, the circuits have been simulated on same platform under similar conditions. The component values used for simulation have been shown in Table 1.

Transfer characteristic showing variations of output current with input current of Ramirez and proposed CMs for a current range of 0–100 μA is shown in Fig. 3. From these results, Ramirez CM operating range is observed from 0 to 10 μA with an offset current of 1 μA that is equivalent to the biasing current, while proposed CM operating range is found to be 0–100 μA with almost negligible offset current. Figure 3 shows

Table 1 Component values used for simulation of CM configurations discussed in the paper

Component name	Values	Component name	Values	Component name	Values
M1–M4	150 μ /20 μ	Amplifier MOSFETs	100 μ /2 μ	V_{DD}	1.5 V
M5	2 μ /2 μ	I_B	1 μA	V_C	0.95 V
M6	10 μ /0.3 μ	I_{B1}	10 μA		

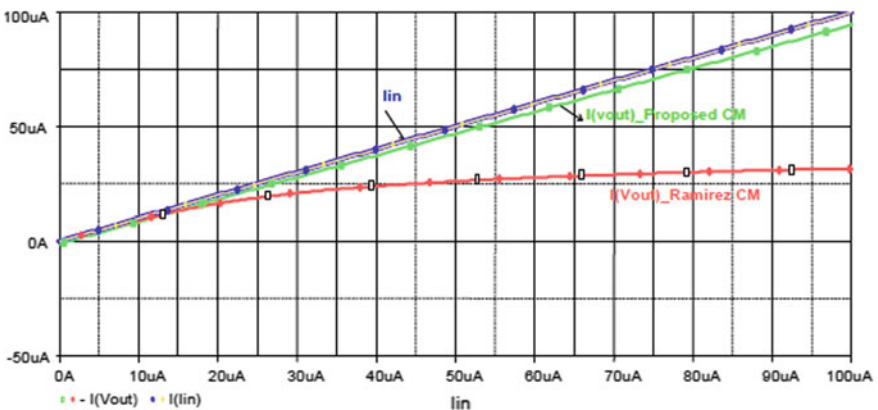


Fig. 3 Characteristics showing variations of output current with input current of Ramirez CM and proposed CM

that accuracy of the proposed CM is much higher than that of Ramirez structure. This is due to negative feedback used for implementing super-cascode configuration, which not only eliminates the offset biasing component but also increases output resistance and reduces channel length modulation effect as discussed in Sect. 3.

Frequency response in Fig. 4 shows that Ramirez CM has a BW of 1.9 MHz, whereas the proposed CM has 7.20 MHz BW. This shows an improvement of 5.3 MHz in BW, which is due to additional negative feedback loop at the output side as discussed in Sect. 3.

The variations in output resistance with frequency for Ramirez and proposed CMs are shown in Fig. 5 and Fig. 6, respectively. Output resistance of Ramirez CM is 385 MΩ till 1 kHz and reduces to approximately 100 MΩ after that. The expected value of output resistance (r_{out}) was in GΩ range but is obtained in MΩ range due to the presence of leakage current at drain terminal of output MOSFET. r_{out} for the proposed CM is 5.11 TΩ till 1 kHz and reduces to around 90 GΩ from 1 to 100 kHz. In Sect. 3, it has been mathematically derived that the proposed CM’s output resistance increases by a factor of ‘ $r_{o5}g_{m5}r_{o6}g_{m6}$.’ Figures 5 and 6 validate this result and show

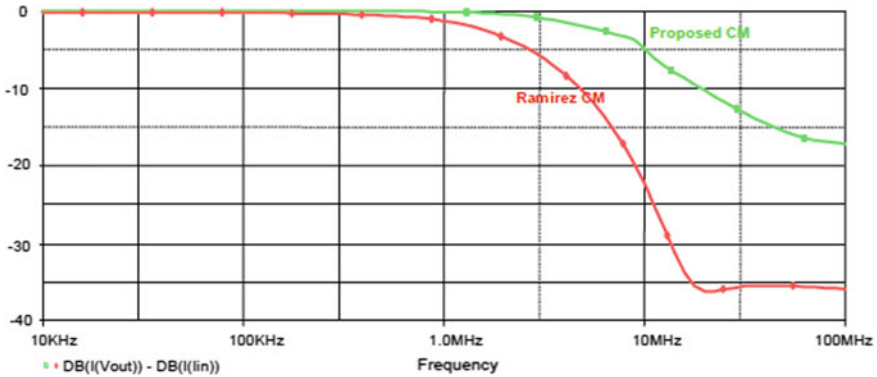


Fig. 4 Frequency plots for Ramirez CM and proposed CM

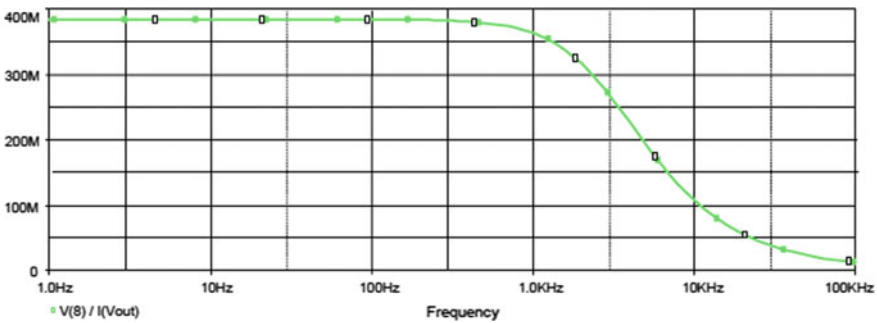


Fig. 5 Output resistance plot for Ramirez CM

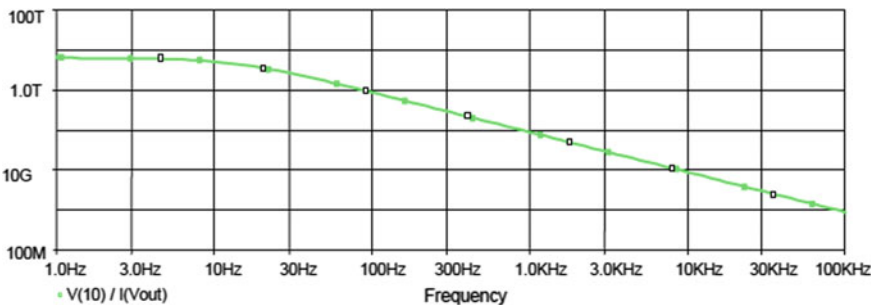


Fig. 6 Output resistance plot for proposed CM

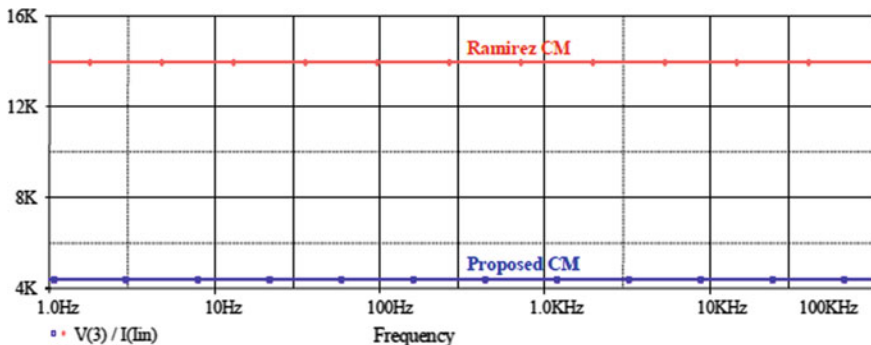


Fig. 7 Input resistance plots for Ramirez and proposed CMs

a significant improvement in the proposed CM's output resistance compared to that of Ramirez structure.

Figure 7 gives comparison for input resistance of Ramirez CM and proposed CM. Input resistance decreases from 13.93 K Ω in Ramirez CM to 4.16 K Ω in proposed CM. As discussed in Sect. 3, the input resistances of these circuits must be in same range. However, introduction of another negative feedback in proposed CM improves input resistance to a certain extent. The error in the current transfer characteristics of the proposed CM is shown in Fig. 8. The error in the plot has been shown for 0–10 μ A range only, as error has been maximum in this range, being very high till 0.5 μ A. This is due to the fact that expression for error is given as:

$$\% \text{ Error} = (i_{\text{out}} - i_{\text{in}}) / i_{\text{in}} \times 100 \quad (9)$$

Equation (9) clearly depicts that when i_{in} is very small the error has to be very high. It has been observed that the maximum error for i_{in} ranging from 0.5 to 100 μ A is approximately 5%.

Simulation results showing minimum input voltage requirement of the proposed CM have been plotted by observing the variations in voltage at the input terminal,

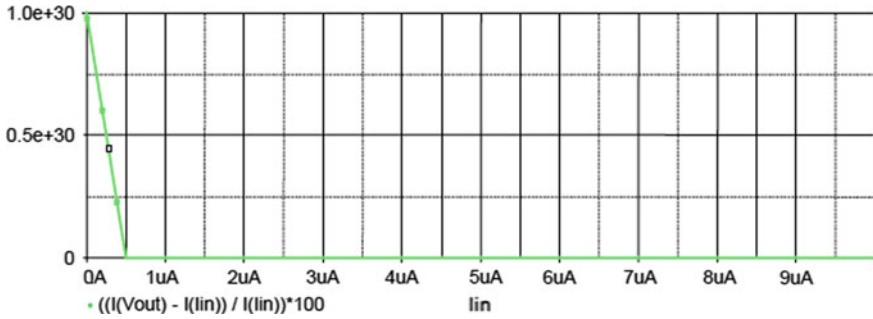


Fig. 8 Percentage error in the current matching accuracy for proposed CM

while current is swept for the complete operating range. The magnitude of this input compliance voltage is observed to be 0.5 V for input current range of 0–100 μA . Similarly, output compliance voltage has also been observed for the proposed CM and has been found to be 0.9 V for the complete range of operation.

All these values and comparative results of the proposed CM with Ramirez CM (simulated on same platform under similar conditions by authors) have been shown in Table 2. Along with these simulated results, comparative results for self-biased high-swing cascode CM and FVF CM (as given in [7]) have also been summarized in this table. All these results illustrate that proposed CM offers very high output resistance while maintaining low supply voltage requirement and hence is a good choice for circuit designers working in strict conditions for designing high-performance circuits.

Table 2 Comparative results

Characteristics	Self-biased high-swing cascode CM [8]	FVF CM [7]	Ramirez CM [11]	Proposed CM
Technology (μm CMOS)	0.18	0.18	0.18	0.18
Supply voltage (V)	1.8	1.8	1.5	1.5
Valid current Range (μA)	500	150	10	100
Output resistance (till 1kHz)	800 k	8.6 M Ω	385 M Ω	5.11 T Ω
Output resistance (1–100kHz)	–	–	100 M Ω	90 G Ω
Input resistance (till 100 kHz)	5 k	930 Ω	13.93 k Ω	4.36 k Ω
Bandwidth	–	–	1.9 MHz	7.20 MHz
Power consumed (μW)	26.86	99.86	5.53	30.7

5 Conclusion and Future Scope

An accurate very high output resistance CMOS CM has been proposed and verified in the paper. In the proposed CM, accuracy and resistance seen at the output terminal of Ramirez CM have been improved by using super-cascode configuration at this terminal. This configuration helps in nullifying the offset current component present in the output current. Moreover, gain of negative feedback helps in improving output resistance of the proposed CM significantly (in $T\Omega$ range). Furthermore, the negative feedback increases the operating range and bandwidth. The results have been validated with the help of standard SPICE 0.18 μm CMOS technology with 1.5 V supply voltage. The proposed CM operates for 0–100 μA with 7.2 MHz bandwidth. Due to the near-ideal features of proposed CM, it can be used as a basic building block for devising a large number of high-performance integrated circuits like operational transconductance amplifiers, operational amplifiers, current differencing transconductance amplifiers, etc.

References

1. Savaria Y (2008) A very-high output impedance current mirror for very-low voltage biomedical analog circuits. In: IEEE Asia Pacific conference on circuits and systems. Macao, pp 642–645
2. Ghovanloo (2008) VLSI circuits for biomedical applications, Chapter 10. Artech House, pp 191–205
3. You F, Embabi SHK, Duque-Carrillo JF, Sanchez-Sinencio E (1997) An improved tail current source for low voltage applications. IEEE J Solid-State Circ 32(8):1173–1180
4. Sedra AS, Smith KC (2011) Microelectronic circuits theory and applications, 6th edn. Oxford, New York
5. Gosselin B, Sawan M, Chapman CA (2007) A low-power integrated bioamplifier with active low-frequency suppression. IEEE Trans Biomed Circ Syst 1(3):184–192
6. Tanguay LF, Sawan M (2009) An ultra-low power ISM-band integer-N frequency synthesizer dedicated to implantable medical microsystems. Analog Integr Circ Sig Process 58(3):205–214
7. Aggarwal B, Gupta M, Gupta AK (2016) A comparative study of various current mirror configurations: topologies and characteristics. Microelectron J 53:134–155
8. Gupta M, Aggarwal B, Gupta AK (2013) A very high performance self-biased cascode current mirror for CMOS technology. Analog Integr Circ Sig Process 75(1):67–74
9. Brooks TL, Rybicki MA (1994) Self-biased cascode current mirror high voltage swing and low power consumption. United States Patent US5359296 A
10. Serrano T, Linares-Barranco B (1994) The active-input regulated cascode current-mirror. IEEE Trans Circ Syst I 41(6):464–467
11. Ramirez-Angulo J, Carvajal RG, Torralba A (2004) Low supply voltage high-performance CMOS current mirror with low input and output voltage requirements. IEEE Trans Circuits Syst II Express Briefs 51(3):124–129
12. Torralba A, Carvajal RG, Ramirez-Angulo J, Munoz E (2002) Output stage for low supply voltage, high performance CMOS current mirrors. Electron Lett 38(24):1528–1529
13. Sackinger E, Guggenbuhl W (1990) A high swing, high impedance MOS cascode circuit. IEEE J Solid-State Circ 25(1):289–298
14. Itakura T, Czarnul Z (1997) High output-resistance CMOS current mirrors for low-voltage applications. IEICE Transactions on Fundamentals of Electronics, Communications and Computer Science, vol E80-A(11), pp 230–232

15. Sharma S, Rajput SS, Magotra LK, Jamuar SS (2002) FGMOS based wide range low voltage current mirror and its applications. *Proc Asia-Pacific Conf Circ Syst* 2:331–334
16. Raj N, Singh AK, Gupta AK (2016) Low voltage high performance bulk driven quasi-floating gate based self-biased cascode current mirror. *Microelectron J* 52:124–133
17. Doreyatim M, Akbari M, Nazari M, Mahani S (2019) A low-voltage gain boosting-based current mirror with high input/output dynamic range. *Microelectron J* 90:88–95
18. Bchir M, Aloui I, Hassen N (2020) A bulk-driven quasi-floating gate FVF current mirror for low voltage, low power applications. *Integration* 74:45–54
19. Gregorian R, Temes GC (2008) *Analog MOS integrated circuits for signal processing*. Wiley, New Delhi (India), pp 126–156

Designing and Comparison of Geometric Mean Circuits Based on MOS Translinear Principle Using Different FVF Structures



Aakansha and Bhawna Aggarwal

1 Introduction

In today's time, as size of the devices is reducing, the circuits are forced to operate at low supply voltages. Portable devices require low power dissipation and low supply voltages. Due to downscaling of MOS and increased demand of portable devices, analog designer are forced to develop new circuits or techniques that can operate with continuously reducing supply voltage requirements [1–4].

Various methods have been proposed in the literature that help in reducing the supply voltage requirement in analog and mixed signal circuits. A few of them are—current mode processing, floating gate technique, quasi-floating gate technique, bulk-driven technique, subthreshold operation of MOS, etc. [1]. Circuits based on current mode processing have gained importance in recent years as it provides improved linearity, more accuracy, wider bandwidth, low supply voltage, low circuit complexity and reduces power consumption [1]. So, the analog designers are focusing more on current mode processing.

Flipped voltage follower (FVF) offers the advantages of current mode circuits. It is an improved version of voltage follower that provides low-voltage and low-power operations. FVF is extensively used in designing of analog circuits like current mirror, operational transconductance amplifier (OTA), current conveyors, multipliers, etc. [1].

Geometric mean circuit is a fundamental cell that is used to realize various analog processes. Geometric mean circuit has been implemented using various configuration: (i) stacked MTL topology (ii) up-down MTL topology, (iii) electronically simulated topology [3, 4]. Up-down MOS translinear loop topology offers several advantages over other configurations as it minimizes body effect and power dissipation and ensures low-voltage operation [4].

Aakansha (✉) · B. Aggarwal
Netaji Subhas University of Technology, Delhi, India

An up-down topology-based geometric mean circuit using different FVF structures is presented in the paper. The paper is classified as: Various FVF cells and their properties are explained in Sect. 2. MOS translinear loop (MTL) and proposed geometric mean circuit is presented in Sect. 3. Simulation results for the circuits are presented in Sect. 4. The conclusions drawn are presented in Sect. 5.

2 FVF and Its Important Characteristics

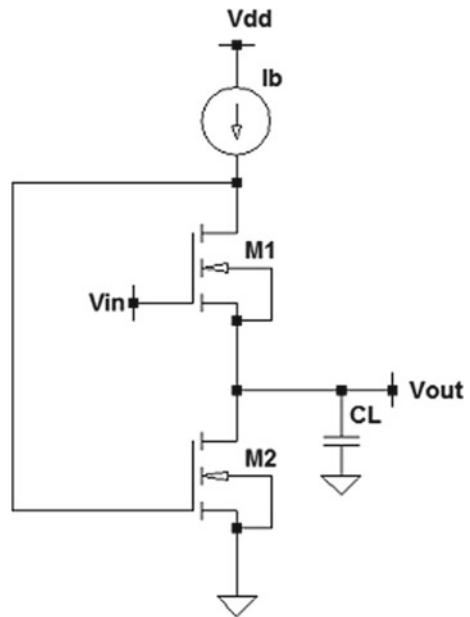
2.1 Flipped Voltage Follower

Flipped voltage follower (FVF) is a voltage follower with enhanced characteristics [5]. It is a cascode amplifier with shunt feedback. Circuit of NMOS-based FVF is shown in Fig. 1. Here, MOSFET M1 operates in common drain configuration and negative feedback is provided by MOS M2. The input is applied at the gate terminal of M1, and output is taken from its source terminal. The output voltage (V_{out}) is given as [5]:

$$V_{out} = V_{in} - V_{GS(M1)} \quad (1)$$

where V_{in} is the input voltage and $V_{GS(M1)}$ is the gate–source voltage of MOSFET M1.

Fig. 1 NMOS-based flipped voltage follower



In FVF, the bias current (I_b) is constant which makes the current through M1 constant. Also, M2 absorbs any variation in the output current that occurs due to loading. This leads to constant gate–source voltage of M1 ($V_{GS(M1)}$) [5]. Thus, V_{out} follows V_{in} leading to unity gain in FVF. Moreover, it can sink large currents and provide high bandwidth.

If V_{in} changes, V_{out} changes by the same amount which changes the current through MOSFET M2 thus varying $V_{GS(M2)}$. As the gate of M2 is connected to the drain of M1, the drain voltage of M1 also varies. Thus, the negative feedback present in FVF is in series-shunt configuration [5]. Due to this, in FVF, input resistance is increased and output resistance is decreased. The output resistance can be given as [5]:

$$r_{out} = \frac{1}{g_{M1} g_{M2} r_{0i}} \quad (2)$$

where g_{Mi} is transconductance of MOSFET M_i and r_{0i} is output resistance of M_i MOSFET. The supply voltage requirement of FVF is close to transistors threshold voltage.

The limitations of FVF are: (i) Its operating range is restricted and does not increase even by increasing the supply voltage. (ii) Sourcing capacity is limited. (iii) FVF allows very low input/output swing. This is because the swing of M1 is suppressed by the $V_{GS(M2)}$ of MOSFET M2 [5, 6].

2.2 Level Shifted and Cascaded Flipped Voltage Follower

The level shifted FVF (LSFVF) is shown in Fig. 2a. It is a modified version of conventional FVF. Here, a third MOSFET M3 is introduced between the drain terminal and gate terminal of MOS M1 and M2, respectively. M3 is a voltage follower which acts as DC level shifter. Due to this, input/output swing and operating range of LSFVF increase [6]. In LSFVF, factor by which operating range gets increased is given as [5]:

$$V_{T3} + \sqrt{\frac{2I_b}{K_N(W/L)_{M3}}} \quad (3)$$

Here, K_N is transconductance parameter, V_T represents threshold voltage, and $(W/L)_{M3}$ is aspect ratio of respective MOSFET M3. However, due to additional MOSFET M3, bandwidth degrades and quiescent power consumption increases.

Circuit of cascoded flipped voltage follower is shown in Fig. 2b. In CASFVF, a PMOS M3 is introduced in the drain of M1 and gate of M2 of FVF configuration. MOSFET M3 provides additional loop gain in the feedback path [6]. This leads to very small variations in voltage at node A. Also, the output resistance gets reduced.

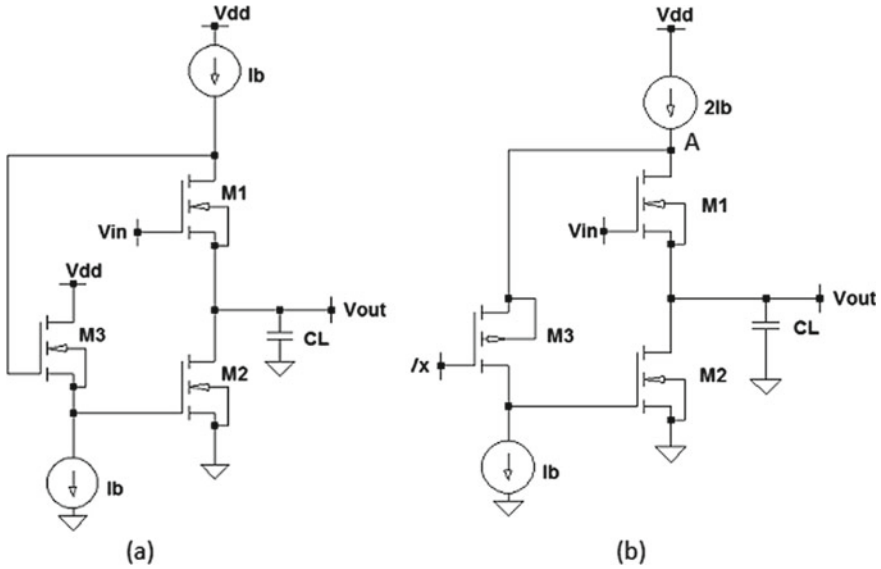


Fig. 2 a Level shifted flipped voltage follower b Cascoded flipped voltage follower

The output impedance of CASFVF is given as [6]:

$$r_{out} = \frac{1}{g_m(g_m r_{o1})^2} \quad (4)$$

The voltage at drain terminal of M1 (V_{D1}) is close to V_{DD} and can be given as [6]:

$$V_{D1} = V_{G3} + V_{SG3} \quad (5)$$

where V_{SG3} is gate-to-source voltage of M3.

3 Geometric Mean Circuits

Geometric mean circuit is the basic building block of various analog circuits such as multiplier/divider circuits, RMS–DC converter, phase synchronizer, fuzzy controller, defuzzification, and fuzzy neural network [5]. In analog domain, geometric mean circuit can be designed using methods like quadratic translinear principle, bulk-driven techniques, and/or MOS translinear loop principle.

3.1 MOS Translinear Loop

MOS translinear loop principle [7] is analogous to bipolar translinear principle given by Gilbert. As per MTL principle, it is applicable in loops that satisfy the following statement: “even the number of MOSFETs operating in strong inversion or saturation mode is present in closed loop such that gate–source voltage of half of these MOSFET appears in clockwise direction and for rest half it appears in anticlockwise direction.”

In [8], up-down topology, geometric mean circuit is presented. It uses alternate biasing of MTL loop instead of diode-connected MOS of the current mirror as used in [8–11]. Due to stacking, diode connected MOS prevents low-voltage operation of the geometric mean circuit. The biasing of the MTL loop is based on application of FVF. FVF sets adequate DC reference voltage at the loop nodes, thus reducing the supply voltage requirement of the geometric mean circuit [8]. The geometric mean circuit using conventional FVF is shown in Fig. 3. The MTL loop comprises of transistor M1, M2, M3, and M4. Using the translinear principle and MOS square law current equation and assuming all the transistors are matched, loop current can be represented as [8]:

$$\sqrt{I_1} + \sqrt{I_2} = \sqrt{I_3} + \sqrt{I_4} \tag{6}$$

The current in M3 and M4 is forced to be:

$$I_3 = I_4 = \frac{I_1 + I_2 + 2I_{out}}{4} \tag{7}$$

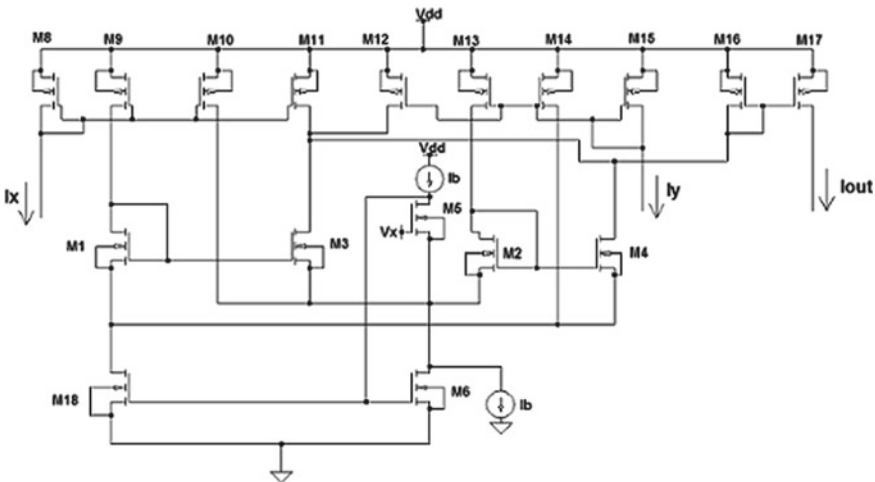


Fig. 3 Geometric mean circuit using conventional FVF [8]

On solving the above equations, I_{out} is obtained as:

$$I_{out} = \sqrt{I_1 I_2} \tag{8}$$

3.2 Proposed Geometric Mean Circuit Using Level Shifted FVF and Cascoded FVF

The proposed geometric mean circuit using level shifted FVF is given in Fig. 4. It uses level shifted FVF to bias the MOS translinear loop. MOSFET M5, M6, and M7 comprises of the level shifted FVF. A NMOS is inserted in the feedback path which sets proper reference voltage at the nodes of MTL loop.

Figure 5 shows the proposed geometric mean circuit using cascoded FVF. In the figure, MOSFET M5, M6, and M7 comprises of the cascoded FVF. In order to bias MTL loop, a PMOS is inserted in the feedback path of conventional FVF. MOSFETs M1–M4 forms the translinear loop. MOSFETs M8–M18 constitute of simple current mirror that are used to inject appropriate current in MTL loop. The input current of geometric mean circuits is I_x and I_y , where I_x is analogous to current across M1

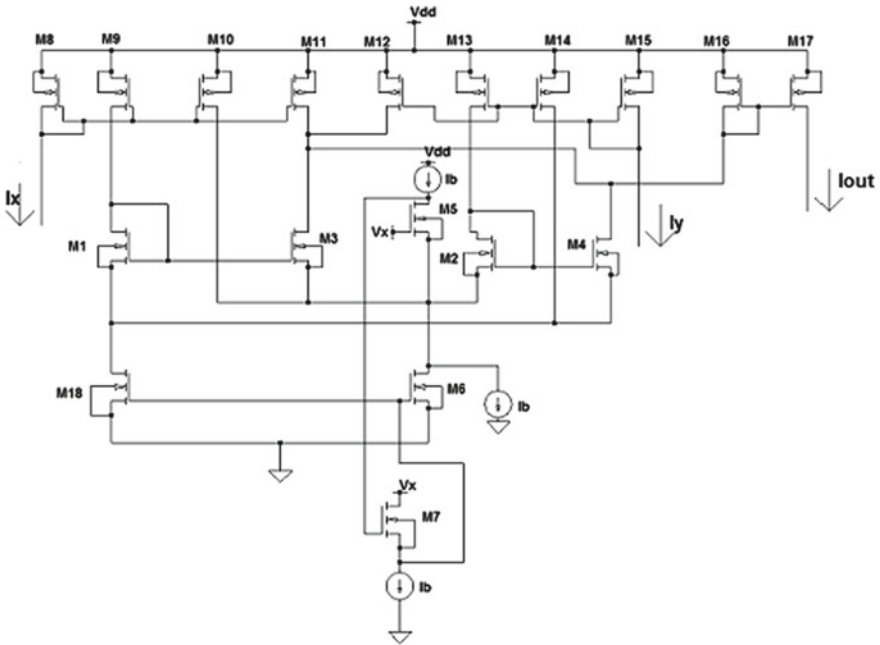


Fig. 4 Proposed geometric mean circuit using level shifted FVF

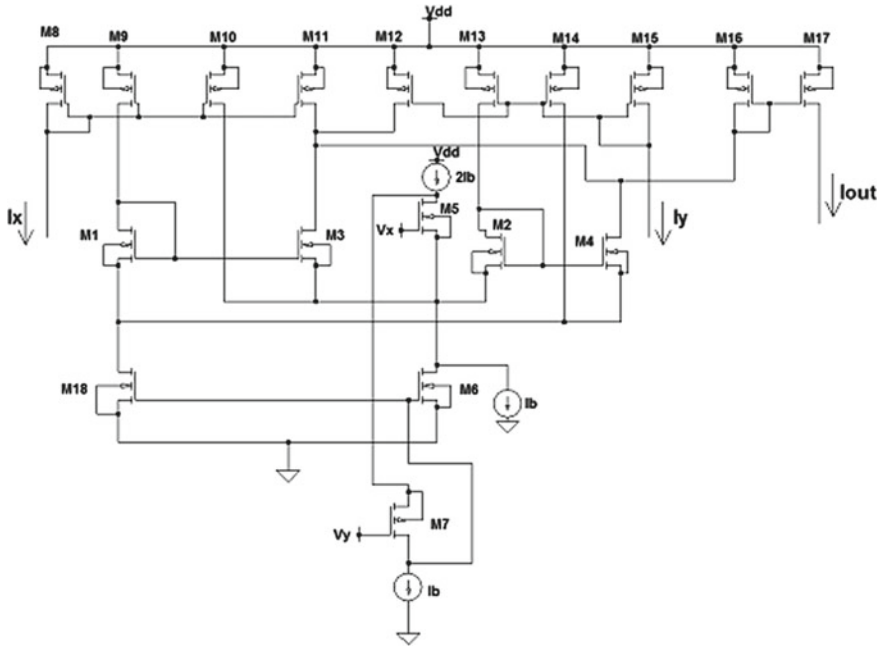


Fig. 5 Proposed geometric mean circuit using cascoded FVF

and I_y is analogous to current across M2. The output current (I_{out}) of the circuit is observed through MOSFET M17 and can be derived as follows:

Applying MTL principle in translinear loop,

$$V_{gs1} + V_{gs2} = V_{gs3} + V_{gs4} \tag{9}$$

The current of MOSFET in saturation region is given as:

$$I = K(V_{gs} - V_{th})^2 \tag{10}$$

where K is:

$$K = \frac{1}{2} \mu_n C_{ox} \frac{W}{L} \tag{11}$$

On rearranging Eq. (10),

$$V_{gs} = \sqrt{\frac{I}{K}} + V_{th} \tag{12}$$

Substituting the above equation in Eq. (9):

$$\sqrt{\frac{I_1}{K_1}} + V_{th1} + \sqrt{\frac{I_2}{K_2}} + V_{th2} = \sqrt{\frac{I_3}{K_3}} + V_{th3} + \sqrt{\frac{I_4}{K_4}} + V_{th4} \quad (13)$$

Since all the MOSFETs are matched, Eq. (13) reduces to:

$$\sqrt{I_1} + \sqrt{I_2} = \sqrt{I_3} + \sqrt{I_4} \quad (14)$$

Squaring Eq. (14) and assuming I_3 and I_4 to be equal,

$$I_3 = I_4 = \frac{I_1 + I_2 + 2\sqrt{I_1 I_2}}{4} \quad (15)$$

On comparing Eq. (15) with (7), it is observed that

$$I_{out} = \sqrt{I_1 I_2} \quad (16)$$

The above equation can also be written as,

$$I_{out} = \sqrt{I_x I_y} \quad (17)$$

Equation (17) shows that output current is geometric mean of input currents (I_x and I_y).

4 Simulation Results

The circuit is simulated by 180 nm CMOS technology with threshold voltage 0.37 V for NMOS and -0.38 V for PMOS. LTSpice XVII has been used for simulation of designed circuits. For biasing of LSFVF and CASFVF configuration bias current $I_b = 2 \mu\text{A}$, $V_x = 1$ V and $V_y = 0$ V have been used. The aspect ratio of all the MOSFETs except M11 and M12 is $6/0.36 \mu\text{m}$. The aspect ratio of MOSFETs M11 and M12 is $3/0.36 \mu\text{m}$. The current I_x is varied from 0 to $10 \mu\text{A}$, and the current I_y is stepped for $2-10 \mu\text{A}$ with a step size of $2 \mu\text{A}$. Figure 6a and b shows DC output of the proposed geometric mean (GM) circuits using level shifted FVF and cascaded FVF, respectively. The output of the circuits follows more closely to the mathematical value, thus reducing the error.

Percentage error in the output current has been plotted in Fig. 7. It shows percentage error, construed as $\{100*(I_{out} - I_{ideal})/I_{ideal}\}$. This figure shows that for high current values the percentage error is approximately same, but for small values of input current, significant reduction in error is obtained. In comparison to the conventional FVF-based geometric mean circuit, the error reduces by 35 and 20% in the proposed LSFVF- and CASFVF-based geometric mean circuit, respectively (Table 1).

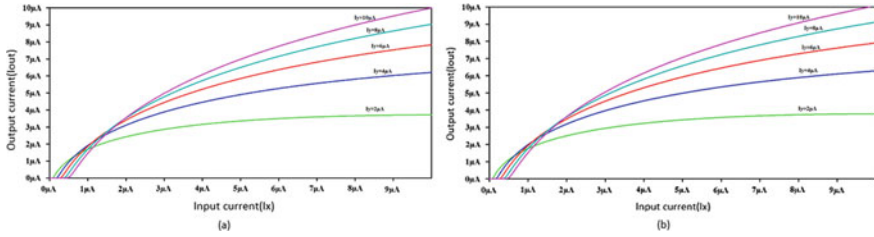


Fig. 6 **a** Output of LSFVF-based proposed geometric mean circuit. **b** Output of CASFVF-based proposed geometric mean circuit

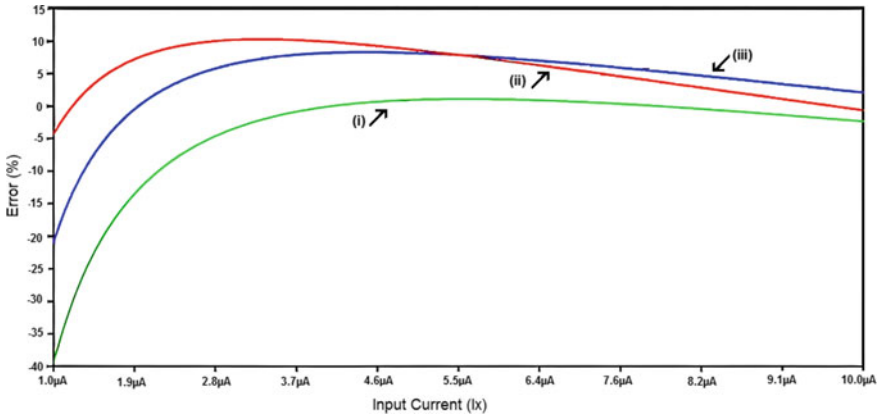


Fig. 7 Percentage error in output current corresponding to $I_y = 8 \mu A$. (i) FVF GM circuit. (ii) Proposed LSFVF GM circuit. (iii) Proposed CASFVF GM circuit

Table 1 Comparison table showing simulation results of different GM circuits

Parameter	Geometric mean circuit in [8]	Proposed geometric mean circuit using LSFVF	Proposed geometric mean circuit using CASFVF
Technology	2.4 μm DPDM CMOS technology	TSM 0.18 μm CMOS technology	TSM 0.18 μm CMOS technology
Supply voltage (V_{dd}) (V)	1.5	1.5	1.5
Bias voltage of FVF (V_x) (V)	1.5	1	1
Bias current (I_b) (μA)	2	2	2
W/L ratio (μ/μ)	80/4.8	6/0.36	6/0.36

5 Conclusions

In this paper, two new geometric mean circuits—one based on LSFVF and the other based on CASFVF—have been designed and proposed. These circuits have been designed by replacing conventional FVF by LSFVF and CASFVF, respectively. The simulations of all the circuits have been carried out in LTSpice XVII using 180 nm technology. The proposed circuits function with much lower error as compared to conventional FVF-based geometric mean circuit. For smaller values of current, the error reduces by approximately 35% in proposed LSFVF-based geometric mean circuit and by approximately 20% in proposed CASFVF-based geometric mean circuit. For larger values of current, this improvement in error is very small. Thereby, it can be inferred that the proposed LSFVF- and CASFVF-based circuits are a good choice for circuit designers working on low-voltage analog-based mixed signal processing circuits.

References

1. Ramírez-Angulo J, Carvajal RG, Torralba A, Galán J, Vega-Leal AP, Tombs J (2002) The flipped voltage follower: A useful cell for low-voltage low-power circuit design. In: Proceedings of International symposium on circuits and systems, ISCAS 3, pp 615–618
2. Maryan MM, Sajadinia H, Azhari SJ (2019) A high precision low distortion current squarer/divider circuit based on FGMOS translinear principle. In: 5th conference on knowledge-based engineering and innovation. Iran University of Science and Technology, Tehran, Iran
3. Kumar JV, Rao KR (2003) A low-voltage low power CMOS companding filter. In: 16th International conference on VLSI design
4. López-Martín AJ, Carlosena A (2001) Current-mode multiplier/divider circuits based on the MOS translinear principle. *Anal Int Signal Process* 28(3):265–278
5. Aggarwal B, Gupta M, Gupta AK (2013) A low voltage wide swing level shifted FVF based current mirror. In: International conference on advances in computing, communications and informatics (ICACCI)
6. Ramírez-Angulo J, Gupta S, Padilla I, Carvajal RG, Torralba A, Jimenez M, Munoz F (2005) Comparison of conventional and new flipped voltage structures with increased input/output signal swing and current sourcing/sinking capabilities. In: IEEE 48th Midwest symposium on circuits and systems, pp 1151–1154
7. Seevinck E, Wiegink RJ (1991) Generalized translinear circuit principle. *IEEE J Solid-State Circ* 26(8):1098–1102
8. Carvajal RG, Ramírez-Angulo J, López-Martín AJ, Torralba A, Gómez Galán JA, Carlosena A, Chavero FM (2005) The flipped voltage follower: a useful cell for low-voltage low-power circuit design. *IEEE Trans Circ Syst I: Regular Papers* 52(7):1276–1291
9. Wiegink RJ (1992) Analysis and synthesis of MOS translinear circuits. Ph.D. Thesis
10. De La Cruz-Blas CA, López-Martín A, Carlosena A (2003) 1.5-V MOS Translinear loops with improved dynamic range and their applications to current-mode signal processing. *IEEE Trans Circ Syst II Analog Digit Signal Process* 50(12):918–927
11. Seevinck E, Vittoz E, Plessis MD, Joubert TH, Beetge W (2000) CMOS translinear circuits for minimum supply voltage. *IEEE Trans Circ Syst II Analog Digit Signal Process* 47(12):1560–1564

A New Linear CMOS CDTA with Improved Characteristics



Bhawna Aggarwal and Saurabh Kumar Sharma

1 Introduction

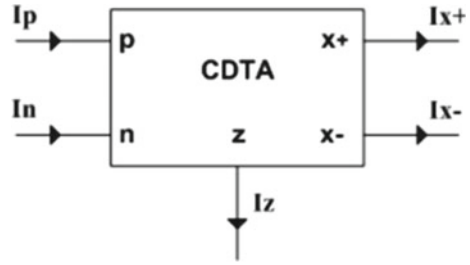
Current differencing transconductance amplifier (CDTA) circuit had been designed by Biolek in 2003 [1]. It behaves as a current mode device and amplifies the difference of the currents supplied at its input terminals. It offers large bandwidth and can be used efficiently as a basic building block in various applications like filters, current limiters, multipliers, oscillators, Schmitt trigger and rectifiers. [2–8]. Different papers with distinct advantages have been published in the literature proposing various structures of CDTA [9]. In this paper, a linear CDTA has been proposed, which has been designed using linear CMOS transconductance amplifier [10, 11]. This proposed CDTA offers higher linearity for a wide operating current range. Distribution of the paper is as follows: Sect. 2 consists of detailed discussion about the basic CDTA circuit and its characteristics. Linear OTA circuit has been presented in Sect. 3. Proposed improved CDTA circuit along with its elaborate analysis has been discussed in Sect. 4. Simulations of the circuits have been carried out using Mentor Graphics Eldo Spice in TSMC 180 nm technology and presented in Sect. 5. Finally, the advantages and further scope of work have been given in Sect. 6 under conclusion.

2 Current Differencing Transconductance Amplifier

CDTA is a differential current amplifier. It consists of two parts, one is current differencing unit (CDU), and second one is transconductance amplifier (TA). CDU provides the difference of input currents I_P (current at positive input terminal) and I_N (current at negative input terminal). The differential voltage developed at output

B. Aggarwal (✉) · S. K. Sharma
Netaji Subhas University of Technology, Delhi, India

Fig. 1 Schematic symbol of CDTA



terminal of CDU (Z) is applied as input to transconductance unit. This unit amplifies the voltage at Z terminal (V_Z), and proportional positive and negative currents are provided at terminals $X+$ and $X-$. The symbolic structure of CDTA is shown in Fig. 1.

The port equations of CDTA are summarized as follows:

$$\left. \begin{aligned} V_P &= V_N = 0 \\ I_Z &= I_P - I_N \\ I_{X+} &= g_m \cdot V_Z \\ I_{X-} &= -g_m \cdot V_Z \end{aligned} \right\} \quad (1)$$

where I_P and I_N are the input currents at terminals P , N , respectively, and I_Z , I_{X+} and I_{X-} are the output currents at output ports Z , $X+$ and $X-$, respectively, and g_m is transconductance of CDTA.

3 Linear Operational Transconductance Amplifier

Linear operational transconductance amplifier (LOTA) is an analog integrated circuit in which gain can be tuned linearly by a biasing voltage. In the circuit of LOTA, there are two cross-coupled differential amplifier pairs that operate in saturation mode. It offers offset-free operation with single-ended as well as differential input and provides a perfect linear transfer characteristic. The complete circuit diagram of LOTA is given in Fig. 2.

The equations involved are given as:

$$g_m = 2 \cdot k \cdot V_b \quad (2)$$

$$I_{\text{out}} = 2 \cdot k \cdot V_b \cdot (V_1 - V_2) \quad (3)$$

where k is a drain current constant, and V_b is biasing voltage that can be used to electronically tune the transconductance of LOTA. V_1 and V_2 are the input voltages

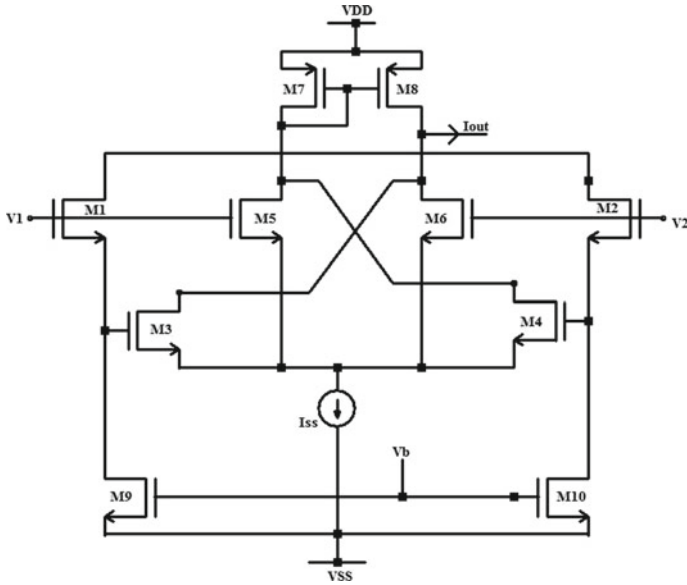


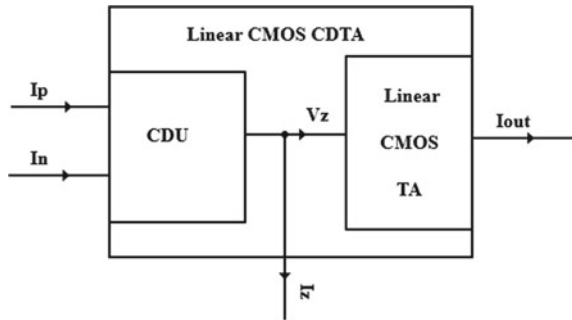
Fig. 2 Circuit diagram of CMOS linear operational transconductance amplifier (LOTA)

applied at differential inputs, I_{out} is the output current, and g_m is the transconductance of LOTA.

4 Proposed Linear CMOS CDTA

In this paper, a linear CMOS CDTA has been proposed. The circuit has been designed by replacing the TA unit of conventional CDTA circuit by a linear CMOS transconductance amplifier. The block layout of proposed linear CMOS CDTA circuit is given in Fig. 3, and its complete circuit diagram is presented in Fig. 4.

Fig. 3 Block layout of proposed linear CMOS CDTA



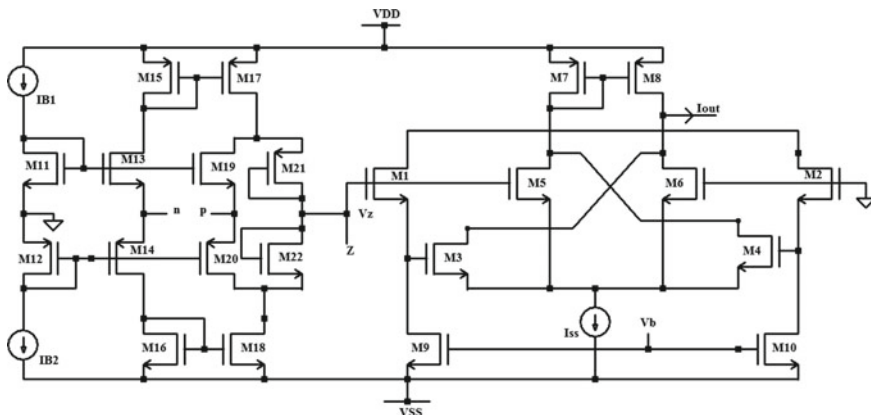


Fig. 4 Circuit diagram of proposed linear CDTA

Equations of the proposed improved linear CMOS CDTA are similar to that of conventional CDTA. However, in the proposed circuit, g_m varies linearly with biasing voltage, and modified equations are given as:

$$\left. \begin{aligned} V_P &= V_N = 0 \\ I_Z &= I_P - I_N \\ I_{out} &= 2 \cdot k \cdot V_B \cdot V_Z \\ g_m &= 2 \cdot k \cdot V_B \end{aligned} \right\} \quad (4)$$

where k is a drain current constant, and V_B is biasing voltage that can be used to electronically tune the transconductance of proposed amplifier.

Conventional CDTA circuits proposed in the literature behave linearly for a narrow range of input current. However, the linear transconductance amplifier used in Fig. 2 does not assume any approximation [10] and thereby offer much wider operating current range. Hence, the overall operating range of CDTA gets increased. Moreover, the transconductance parameter (g_m) of proposed CDTA is higher than conventional CDTA.

5 Simulation Results

The simulations of the proposed linear CDTA are carried out in Mentor Graphics Eldo Spice tool using 180 nm CMOS technology. The design parameters for the proposed circuit (Fig. 4) are summarized in Table 1.

DC response showing variation of output current with change in input differential current ($I_p - I_n$) is shown in Fig. 5.

Table 1 Design parameters

Parameter		Value
Technology		180 nm CMOS
Supply voltage		± 2 V
Power consumed		2.5656 mW
Aspect ratio (W/L in μm)	M1-M4	6/1
	M5, M6, M9, M10	2/1
	M7, M8	4/1
	M11-M14, M19, M20	8/1
	M15-M18	5/1
	M21, M22	20/2
Biasing current (I_{ss})		125 μA

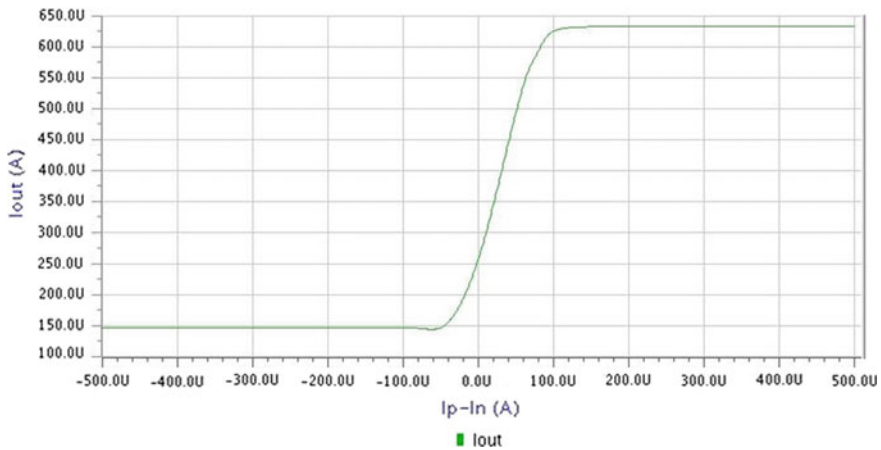


Fig. 5 DC response of the linear CDTA circuit

It depicts the linear relation of output current with variations in input current in the range of -50 to $+50 \mu\text{A}$. However, the response shows that the output current has an offset component; this offset component can be changed by varying biasing current I_{ss} . The corresponding DC response curves obtained by varying I_{ss} are shown in Fig. 6. Frequency response showing transconductance and current gain of linear CDTA is shown in Figs. 7 and 8, respectively. Bandwidth of proposed linear CDTA circuit is observed to be 139.9626 MHz (Fig. 8). All these results validate the functioning of the proposed circuit.

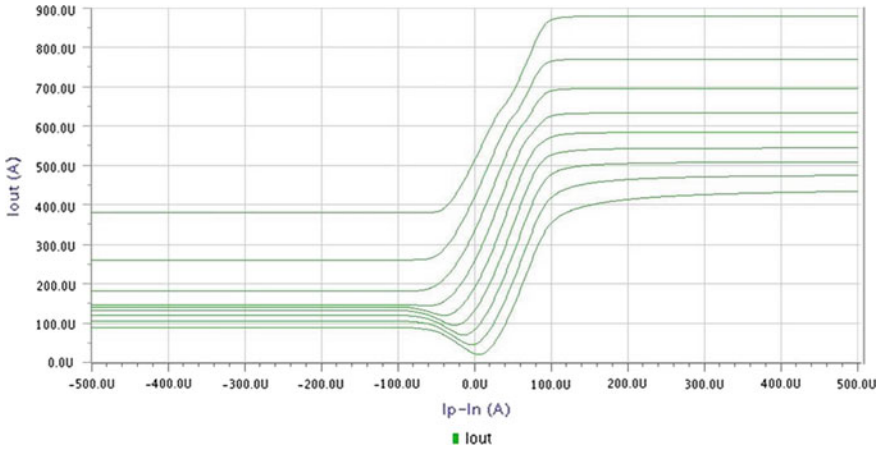


Fig. 6 DC response of linear CDTA circuit with different values of I_{ss}

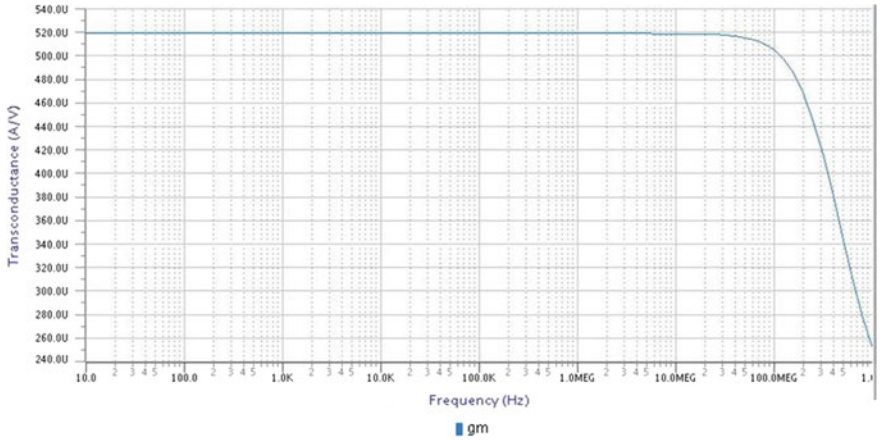


Fig. 7 Transconductance curve of proposed CDTA

6 Conclusion

In this paper, a new linear CDTA structure based on linear CMOS OTA has been designed and proposed. This circuit combines the linear behavior of linear CMOS OTA (LOTA) with conventional current differencing unit to realize the proposed structure. The functional behavior of the proposed structure has been validated in Eldo Spice using level 53 TSMC based 180 nm CMOS technology. The results depict the linear behavior of the proposed structure for a wide range of input differential current, and bandwidth of the proposed circuit is observed in hundreds of MHz range.

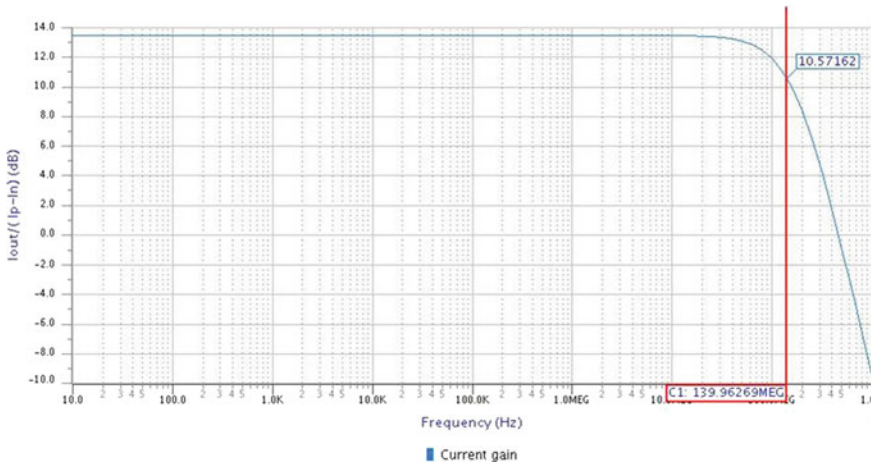


Fig. 8 Current gain of proposed CDTA

References

1. Biolek D (2003) CDTA-building block for current-mode analog signal processing. In: Proceedings of the European conference on circuit theory and design. Krakow, pp 397–400
2. Jaikla W, Siripruchyanun M, Bajer J, Biolek D (2008) A simple current mode quadrature oscillator using single CDTA. *Radioengineering* 17(4):33–40
3. Silapan P, Siripruchyanun M (2011) Fully and electronically controllable current mode schmitt triggers employing only single MO-CCCDTA and their applications. *Analog Integr Circ Sig Process* 68(1):111–128
4. Srivyshnavi T, Srinivasulu A (2015) A current mode schmitt trigger using current differencing transconductance amplifier. *VFSTR J STEM* 1(1):18–22
5. Calvo B, Celma S, Sanz MT (2003) High-frequency digitally programmable gain amplifier. *Electronic Letters* 39(15):1095–1096
6. Summart S, Thongsopa C, Jaikla W (2015) New current controlled current mode sinusoidal quadrature oscillators using CDTAs. *Int J Electron Commun* 69(1):62–68
7. Das R, Bhowmick B, Paul P, Karmakar S, Banerjee K (2019) Current differencing transconductance amplifier (CDTA) based current mode quadrature oscillator. In: Biswas U, Banerjee A, Pal S, Biswas A, Sarkar D, Haldar S (eds) *Advances in computer, communication and control. Lecture notes in networks and systems vol 41*. Springer, Singapore, pp 35–47
8. Rana C, Prasad D, Afzal N (2018) Low voltage floating gate MOSFET based current differencing transconductance amplifier and its applications. *J Semicond* 39(9):094002
9. Koton J, Herencsar N, Vrba K, Minei S (2011) Precision full wave current mode rectifier using current differencing transconductance amplifier. In: 3rd International conference on communication software and networks (ICCSN), pp 460–463
10. Wang Z, Guggenbuhl W (1990) A voltage-controllable linear MOS transistor using bias offset technique. *IEEE J* 25:315–317
11. Sengupta S (2005) Adaptively biased linear transistor. *IEEE Trans Circ Syst-I: Regular Papers* 52(11):2369–2375

Design of Wind Energy Conversion System Utilizing Induction Generator with Pitch Angle Control



Subash Chandra Parida, V. K. Tayal, and S. K. Sinha

1 Introduction

Energy is primary concern to enhance economic development, industrial development and to meet day-to-day human need. The World Energy Council in cooperation with the UN Intergovernmental Panel on Climate Change (IPCC) is continually monitoring world energy consequences to make energy endowment for network of global members. To meet the complexity and global energy transition, lots of opportunities are being introduced into the energy sector which is creating investment opportunities for global industry leaders. Developed countries mostly use fossil fuel-based nuclear power to meet the energy need. With respect to this, there is approximately 60% of worlds energy is from nuclear source [1]. Nuclear power plants have fallen its importance due to various serious concerns like waste management, nuclear radiation and other maintenance and operational complexity. Various conventional power plants based on gas, coal and fuel oil, etc. generate harmful toxic gases like nitric monoxide (NO_x), sulphuric dioxide (SO_2), ammonia (NH_3) and ozone (O_3) in their exhaust during combustion process. Global warming and ozone layer depletion are the major concerns for the humanity because of these toxic gasses [1]. To meet the day-to-day energy demand, researchers in the world are searching various alternative sources of renewable energy. The technological development of recent years is bringing more efficient and reliable sources of renewable energy.

The motivation of present-day WECS is to optimize operational efficiency for its most reliable operation. Comparing various available options, SCIG-based (Type-1) is best suited. With respect to DC motor, the performance of induction motor is better in prospect of fast torque response, simplified speed control and desired accuracy level. Application of PMSG motors into WECS is not abundant due to various constraints such as less availability of permanent magnet materials, initial cost involvement and complexities involved in control scheme. The manufacturing

S. C. Parida (✉) · V. K. Tayal · S. K. Sinha
Amity University, Noida Campus, Noida, Uttar Pradesh 201313, India

of PMSG machines requires special skill and equipment. Application of DFIG into WECS is comparatively less than SCIG-based systems due to various constraints such as complexity in power electronics involved, high maintenance involvement and complexity in control action. Also DFIG machines have high sensitivity to grid faults. Hence, regardless of various types of wind turbines are used to convert aerodynamic power to electrical power, fixed speed wind turbines are commonly used in application because of various reasons such as system economics, simplicity in control scheme, less maintenance involvement at generator side, its robustness and proven track record. The advancement of variable-speed induction motor and power electronics sector has encouraged research communities to enhance their desire because of simplicity attended with induction motors.

In WECS, various aerodynamic control strategies are implemented to extract maximum power from wind through its blade. These are pitch control (i.e. fixed pitch and variable pitch type) and yaw control. In fixed pitch wind turbine systems (suitable for small-size wind turbines), design of air foil is carried out taking considerations of various parameters like tip-speed ratio, angle of attack for aerodynamic blades, maximum and minimum wind speed of the area and rotor blade diameter. Inside variable pitch WECS, the air foil is of straight shape.

In the proposed scheme, wind turbine model has been simulated at different wind speeds. Power extraction at cut-in, rated and cut-out wind speed has been verified. Pitch angle control with the help of PID controller has been implemented in the WECS. Active power, reactive power, rotor angular velocity and mechanical torque requirement have been verified. The performance comparison between output of PI and PID controllers for pitch angle control has been carried out. PID control manages the pitch angle of blades with better operational flexibility, robustness of design, better stability and speed of operation than existing PI control scheme.

2 Literature Review

Active power control is one of the best methods to control aerodynamic power through pitch angle controller. They have used servo system, integrating rotor speed with power feedback signals. They have verified fatigue, turbulence and aerodynamics. This method has effectiveness on frequent action of pitch actuator while commanding to adequate dispatch of required amount of active power [2].

There are huge variation in wind speed when ambient parameter changes. Pitch angle controller has to synchronize with these variations. The results of PI controller, fuzzy logic controller and fractional-order PI controller have been compared. FLC-based controller has provided better result in comparison to the other methods [3].

To meet the key challenges of wind speed variation, fuzzy receding horizon pitch control has been implemented to verify the performance of variable-speed wind turbine. This controller has better effectiveness to control simple online quadratic optimization problem with minimum computational time [4]. To meet the dynamics of pitch angle controller and to optimize the controller set values, PI controllers

are generally used in the wind energy conversion system. It has been suggested to implement PI controller with grey wolf optimizer for tuning purpose. They have also implemented various AI techniques in combination with PI controller to optimize and compare the performance criteria. Result suggests that grey wolf optimizer has better influence for the particular application of pitch angle control [5].

To increase the efficiency of controller and enhance the stability criteria, it has been suggested to implement Nonlinear Autoregressive Moving Average (NLARMA-L2)-based PI controller. NLARMA-L2 furnishes better result than other methods in terms of steady-state error, ripple minimization and speed of response. This controller is more effective with load variation [6].

3 Different Energy Conversion System

Basically, there are two types of wind turbine with respect to installation point of view. These are mentioned below [7].

- (1) Horizontal axis wind turbine,
- (2) Vertical axis wind turbine.

With respect to type generators used, the wind turbines are segregated into following types [1, 7]:

Type-1: squirrel cage induction generator (SCIG) based, Type-2: wound rotor induction generator (WRIG) based, Type-3: doubly fed induction generator (DFIG) based, Type-4: permanent magnet induction generator (PMIG) based.

In this paper [1, 8], we purpose squirrel cage induction generator (SCIG)-based wind turbine with fixed speed rotor (Type-1) with pitch angle controller to control aerodynamic power of wind energy conversion system using PID controller.

The pitch angle control provides better control of mechanical power which is used mostly for fixed-speed wind turbine (Type-1) and limited variable-speed wind turbine (Type-2). As stall control uses mostly constant pitch angle of turbine rotor blades, pitch control and stall control combination provides operator the better control access whenever required. The wind as a source of energy has no consistency on the flow because of various technical criteria like change of temperature, pressure, air density, humidity, etc., which leads for third dynamics of energy conversion with first dynamics as input source variation and second dynamics as load demand variation.

By application of pitch angle control, optimization in power generation scheme is accomplished during low wind velocity—Case-1 [9]. Pitch angle controller helps wind turbine to speed up at faster speed when wind velocity is below rated value by changing pitch angle to maximum value. Hence, optimum pitch setting is required to extract rated aerodynamic power from wind—Case-2 [9]. At approximately fixed wind speed, turbine rotor rotates at constant value if pitch angle and other ambient predefined criteria held constant. At this duration, small change in pitch angle creates appreciable effect in power output—Case-3 [9]. WECS attains its maximum aerodynamic power extraction limit when wind velocity exceeds the rated limits and within

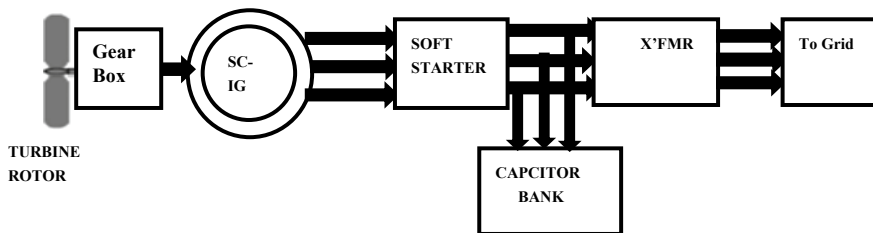


Fig. 1 Schematic of SCIG-based WECS (Type-1)

its dead zone. When wind velocity crosses the rated value, pitch angle control helps wind turbine to generate rated power by reducing pitch angle of blade—Case-4 [9]. When wind velocity crosses the maximum limit of designed data, turbine and generator decouple themselves from gear box mechanism by minimizing fatigue loads of various mechanical components (Fig. 1).

This pitch angle control is accomplished by coupling a servo motor at turbine blade. The pitch angle controller is designed with the help of various control mechanisms like PI, PID, etc. In this scheme, we have used PID-based controller taking various quality parameters into considerations such as complexity, speed of operation, stability limit and offset values. The control action of pitch angle controller has major influence on various so-changed ambient criteria discussed previously. Pitch angle controller provides better regulation for the management of power system stability by controlling aerodynamic power. Hence, pitch angle controller design plays vital importance to operate the WECS. The discussed model has been presented for reference [1, 10].

4 Modelling of Proposed System

Wind energy conversion system basically consists of wind turbine, gear box unit, generator unit and reactive power source and distribution power grid. In the process of energy conversion, WECS converts aerodynamic energy to mechanical energy in the turbine and through gear box mechanism. Mechanical energy is converted into electrical energy which is supplied to power grid by generator for distribution purpose. The power contained in the wind velocity is mathematically represented by Eq. (1) [11–14].

$$P_{\text{wind}} = \frac{1}{2} \rho A v^3 \quad (1)$$

where ρ is the density of air (kg/m^3) and v is the wind velocity (m/s) and A is swept area of rotor, (m^2). The air density is proportional to the air temperature and the air pressure, both of which are variable criteria and depend on height above sea level.

Hence, the converted power from aerodynamic to mechanical power is diminished by power coefficient (C_p) [10]. The power coefficient is mathematically represented by Eq. (2).

$$C_p = \frac{P_t}{P_{wind}} \quad (2)$$

The power coefficient C_p can be mathematically achieved by using power extracted Eq. (3).

$$P_t = (P_{in} - P_{out}) \quad (3)$$

where P_t is defined as power available at turbine. The power attained by the wind turbine is mathematically represented by Eq. (4) [13].

$$P_t = C_p \times (0.5\rho Av^3) \quad (4)$$

Maximum value of C_p detects max efficiency of wind turbine with reference to Betz limit. A maximum value of C_p is of 59.3%, and normal range is from 25–45% for HAWT system. The tip-speed ratio λ of the wind turbine is defined as the ratio of turbine blade speed to that of the wind. The tip-speed ratio, (λ) and the power coefficient, C_p , are dimensionless. Wind turbine performance is measured using tip-speed ratio (λ), which is mathematically represented by Eq. (5) [13].

$$\lambda = \frac{\omega R}{v} \quad (5)$$

Tip-speed ratio is dependent on various technical parameters such as blade mechanical design (airfoil shape and size), no. of blades available, etc.

Cut-in wind speed [9]—the lowest wind velocity which can be exploited to extract useful power (general range between 3.5 and 4 m/s for HAWT). Also varies with manufacturer to manufacturer depending on various criteria like length of blade, area of blade, blade construction material and shape of blade.

Rated wind speed [9]—the wind velocity which can be exploited to extract rated power (in this case, rated power is manufacturer's defined data on name plate that the generator can able to deliver) and general range between 12 and 14 m/s for HAWT).

Cut-out wind speed [9]—the wind velocity which can be exploited to extract maximum power, this velocity is the design limitation for turbine and generator unit (general range above 25 m/s for HAWT). This criterion is fixed by manufacturer with respect to statutory and regulatory recommendation given by consultants.

The following approximate model has been used to mathematically define the relation of C_p with TSR and pitch angle [6, 11, 14].

$$C_p(\lambda, \beta) = \left(\frac{C_2}{\lambda_i} - C_3\beta - C_4 \right) e^{\frac{C_5}{\lambda_i}} + C_6\lambda \quad (6)$$

Table 1 Variable identifications

Abbreviation	Description
1/S	Transfer function
y(s)	Output function
U(s)	Input function
E(S)	Error function
K_p	Proportional gain
K_i	Integral gain
K_D	Derivative gain
P_e	Active power generated
W_e	Angular velocity
P_m	Mechanical power extracted
V_w	Free wind velocity
λ	Tip-speed ratio
C_p	Power coefficient

$$\frac{1}{\lambda_i} = \frac{1}{\lambda_i + 0.08\beta} - \frac{0.035}{\beta 3 + 1} \quad (7)$$

The coefficients of given equations are mentioned as $C_1 = 0.5176$, $C_2 = 116$, $C_3 = 0.4$, $C_4 = 5$, $C_5 = 21$, and $C_6 = 0.0068$ [13].

The mechanical power produced by the WECS is mathematically given by [11, 14, 15].

$$P_{\text{mech}} = C_P(\lambda, \beta) \frac{\rho A}{2} + V 3 \quad (8)$$

Aerodynamic model of WECS [3] defines the magnitude and distribution of drag force. The direction of the drag force is parallel to the relative wind. The referred model defines conversion scheme with various unit controls like turbine control, generator control and protection. Inside wind turbine, aerodynamic power is controlled through pitch control and active stall control which delivers power to the shaft of turbine. Generator dynamics is controlled through converter control and protection scheme. The various variables used with abbreviations in the aerodynamic modelling and PID controller design are mentioned in Table 1 (Fig. 2; Tables 2 and 3).

5 Simulation Results

The above-mentioned WECS scheme has been used for simulation, results have obtained, and detailed analysis has been made. With respect to analysis, comparison

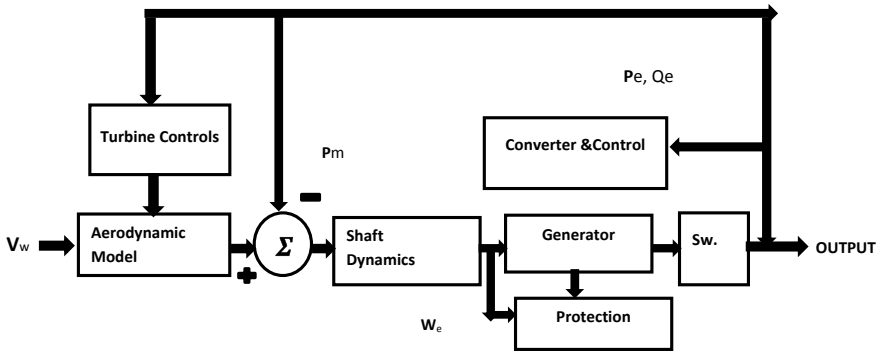


Fig. 2 Schematic of aerodynamic model of WECS

Table 2 Wind turbine specifications

<i>Generator specifications</i>	
Power rating	1.5 MW
Voltage rating	575 V
Frequency rating	60 Hz
Speed	3600 RPM
<i>Wind turbine specifications</i>	
Mechanical power	1.5 MW
No. of blades	3
Rotational speed	0–20 RPM
Gear box ratio	100:1
Pitch angle	0–90°

Table 3 Performance comparison

Criteria	Existing scheme	Purposed scheme
Complexity (operational)	Higher	Lower
Control action	Large disturbance and noise in the response	Comparatively low disturbance and noise in the response
Speed (operational)	Slower due to transportation delay	Better than previous
Rise time	Higher	Comparatively better
Max peak	Higher	Comparatively better
Stability time	Higher	Comparatively lower
Output variation w.r.t. wind speed variation	Higher	Better

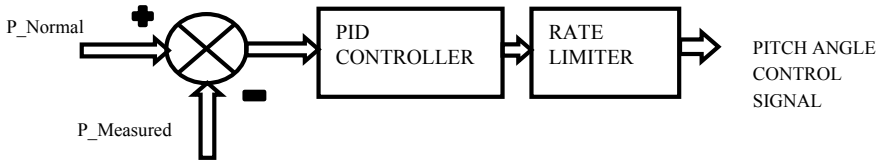


Fig. 3 PID control schematic for pitch angle control

has been established. Through PID controller during simulation, excellent performance has been attended by varying control gains such as proportional control gain, integral control gain and derivative control gain (K_p , K_i & K_d). During simulation in MATLAB, closed-loop step response of $t = 1$ s has been simulated. Fine tuning has yielded better response by changing gain variables K_p , K_i & K_d (Figs. 3 and 4).

Figure 5 depicts relation of active power with time when WECS was simulated with respect to rated wind speed. Figure 6 depicts relation of reactive power with

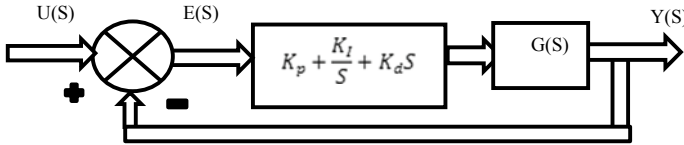


Fig. 4 PID controller block diagram

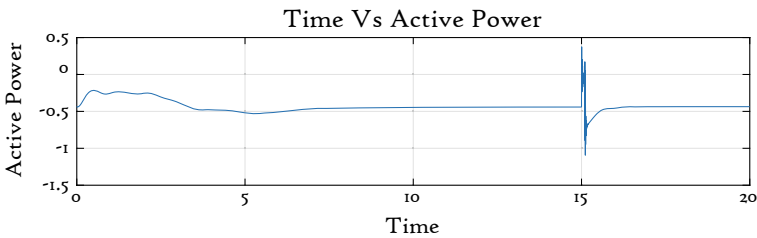


Fig. 5 Active power variation with time

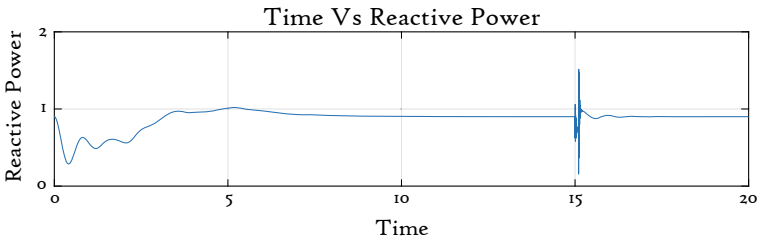


Fig. 6 Reactive power variation with time

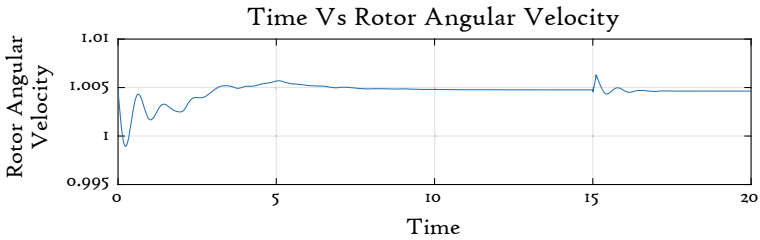


Fig. 7 Rotor angular velocity variation with time

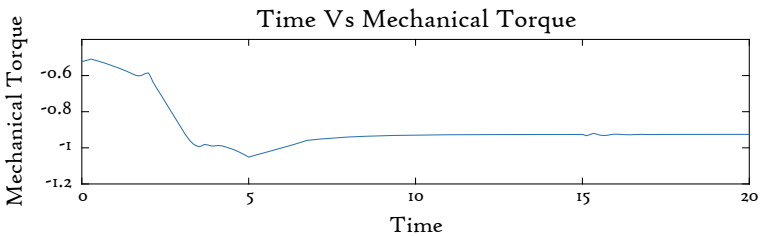


Fig. 8 Rotor mechanical torque variation with time

time under rated wind speed. Figure 7 depicts relation of rotor angular velocity with time, and Fig. 8 depicts rotor mechanical torque with time under rated wind speed.

6 Conclusion

As statutory and regulatory interventions are being implemented to reduce global warming effect, modern-day power industry is shifting towards renewable energy market. Technological modification and application of superior control scheme in wind turbine aerodynamics can convert it into low cost and optimal, reliable and outstanding supplementary energy source. In this work, various control schemes have been attempted to stabilize the WECS aerodynamic system and minimize noises. The study acknowledged the problem in existing aerodynamic control and implemented as guideline for purposed scheme. To overcome the limitations of low stability, noise and low efficiency, purposed scheme has established an advanced solution. This paper refers to validated MATLAB/Simulink mathematical model of WECS based on aerodynamic structure of the wind turbine. In proposed control scheme, the drift values and errors in rotational speed have been reduced in comparison with existing PI control scheme. The time for control action has also been improved to appreciable limit to maintain stability. Through the modified scheme, extraction of wind power limit has also been enhanced.

References

1. Bhutto DK, Ansari JA, Bukhari SSH (2019) Wind energy conversion systems (WECS) generators: a review. In: IEEE, international conference on computing, mathematics and engineering technologies, 1–6
2. Tang X, Yin M, Shen C, Xu Y, Dong ZY, Zou Y (2019) Active power control of wind turbine generator via coordinated rotor speed and pitch angle regulation. *IEEE Trans Sustain Energy* 10:822–832
3. Kumar A, Kumar B (2019) Pitch control of variable speed wind turbine using fuzzy logic. In: IEEE international conference on power electronics, (10). 1109-8897
4. Abdelbaky MA, Liu X, Kong X (2019) Wind turbine pitch controller using constrained fuzzy receding horizon control. In: IEEE Chinese control and decision conference, (10). 1109-8833
5. Sule AH, Mokhtar AS, Jamian JJB, Khidrani A, Masood R, Jogendra L, Thongam S, Ouhrouche M (2019) Optimal tuning of proportional integral controller for fixed-speed wind turbine using grey wolf optimizer. *Int J Electr Comput Eng (IJECE)* (10):5251–5261
6. Mustafa S, Ruhman A, Hawas MN (2017) Optimal pitch angle control for wind turbine using intelligent controller. In: The Fourth postgraduate engineering conference, (10). 1757-899X
7. Nelson V, Starcher K (2019). Wind energy, renewable energy and the environment, 3rd edn. Taylor & Francis Group, LLC, Turkey
8. Essam M, Harby M, Elmasry SE, El Samahy A (2014) Fault analysis and control of a grid connected wind turbine driving squirrel cage induction generator using genetic algorithm PID controller. *IEEE transaction, Nineteenth international Middle East power systems conference (MEPCON)*. Menoufia University, Egypt, (10) 10–2478
9. Demirtas M, Serefoglu S (2014) Design and implementation of a microcontroller-based wind energy conversion system. Department of Electrical and Electronics Engineering, Faculty of Technology, Gazi University, Turkey, pp 1582–1595
10. Mirecki A, Roboam X, Richardeau F (2007) Architecture complexity and energy efficiency of small wind turbines. *IEEE Trans Ind Electron* 54:660–670
11. Hammadi S, Hidouri H, Sabita L (2015) A DTC-induction-generator drive scheme for an isolated wind turbine system. *Int J Renew Energy Res* 5:5
12. Moussa I, Bouallegue A, Khedher A (2015) 3 kW wind turbine emulator implementation on FPGA using Matlab/Simulink. *Int J Renew Energy Res* 5:5
13. Sokolovs A, Grigans L, Kamolins E, Voitkans J (2014) Induction motor based wind turbine emulator. *Latevian J Phys Tech Sci* 51(12):11–21
14. Wu F, Zhang X-P, Ju P (2009) Small signal stability analysis and control of the wind turbine with the direct-drive permanent magnet generator integrated to the grid. *Electr Power Syst Res* 79:1661–1667
15. Gonzalez LG, Figueres E, Garcera G, Carranza O (2009) Modelling and control in wind energy systems (WECS). In: 13th European conference on power electronics and applications, (10). Barcelona, pp 1–9

Analysis of SPA Scheme for Massive MIMO



Manisha Bharti and Tanvika Garg

1 Introduction

Recently, the mobile traffic has increased exponentially in wireless systems. In order to satisfy this condition, massive MIMO is brought into the picture [1, 2]. In massive MIMO, there are many antennas in BS which provides service to many user terminals at the same time. The assignment of pilot sequences is done to the users of a cell. These sequences are limited hence in other cells too same sequences are assigned to the user terminals. Due to similar sequences, there is a possibility of inter-cell interference among adjacent cells. There is a conventional method in which the pilot sequences are assigned to user terminals randomly. This method is not efficient and does not reduce the inter-cell interference among adjacent cells. So, a smart pilot assignment (SPA) scheme has been given in this paper. In this proposed scheme, the assignment of pilot sequences is done in such a way that the minimum uplink SINR of every user is maximised in the target cell.

The proposed smart pilot assignment sequence does the assignment of pilot sequences in such a way that the user having the worst channel quality gets the smallest inter-cell interference. The simulation has been done, so that the SPA scheme's performance gain can be estimated in massive MIMO systems.

M. Bharti · T. Garg (✉)
National Institute of Technology Delhi, Delhi, India
e-mail: 192220010@nitdelhi.ac.in

M. Bharti
e-mail: manishabharti@nitdelhi.ac.in

2 System Model

Here is the scenario with multiple users and multiple cells. It consists of L hexagonal cells. Every cell consist a BS which has M number of antennas. There are K number of users with one antenna (here $K \ll M$) [1, 2]. $h_{ijk} \in C^{M \times 1}$ is the vector of channel from the j -th cell 's k -th user to the i -th cell's base station which is given as:

$$h_{ijk} = g_{ijk} \sqrt{\beta_{ijk}} \quad (1)$$

Here, β_{ijk} is a large-scale fading coefficient which does not vary rapidly. These coefficients are not very difficult to track. $g_{ijk} \sim CN(0, I_M)$ are the small-scale fading vectors [3–5] (Fig. 1).

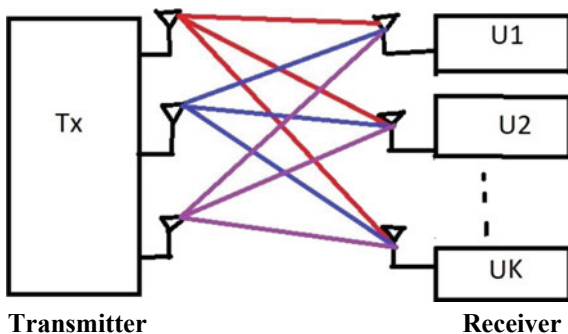
The pilot sequences have been assumed as $\phi = [\phi_1, \phi_2, \dots, \phi_K]^T \in C^{K \times \tau}$. These pilot sequences have length τ . They are orthogonal ($\phi \phi^H = I_K$). These pilot sequences are utilised in the cells other than the target cell as well because of the limitation [1]. In the conventional method, the k th user is assigned the pilot sequence ϕ_k . In this method the user terminals' channel qualities are not considered [1, 2]. In the i th cell, $Y_i^p \in C^{M \times \tau}$ is the pilot sequence received at the BS which are given as:

$$Y_i^p = \sqrt{\rho_p} \sum_{j=1}^L \sum_{k=1}^K h_{ijk} \phi_k^T + N_i^p \quad (2)$$

Here, the power of the transmitted pilot is given by ρ_p , and $N_i^p \in C^{M \times \tau}$ is the AWGN matrix. Entries in this matrix are independent and identically distributed. Similar to this, the user receives data $y_i^u \in C^{M \times 1}$ at the i th cell's base station which can be given as:

$$y_i^u = \sqrt{\rho_u} \sum_{j=1}^L \sum_{k=1}^K h_{ijk} x_{jk}^u + n_i^u \quad (3)$$

Fig. 1 Block diagram for massive MIMO



Here, x_{jk}^u is the j th cell's k th user, ρ_u is the transmission power of uplink data, and n_i^u is the AWGN vector. The channel estimate can be given as:

$$\widehat{h}_{ijk} = \frac{1}{\sqrt{\rho_p}} Y_i^p \phi_k^H = \sum_{j=1}^L h_{ijk} + v_{ik} \quad (4)$$

Here, v_{ik} is the equivalent noise which is equal to $\frac{1}{\sqrt{\rho_p}} N_i^p \phi_k^H$. The uplink SINR of the i -th cell's k -th user can be given as:

$$\text{SINR}_{ik}^u = \frac{|h_{iik}^H h_{iik}|}{\sum_{j \neq i} |h_{ijk}^H h_{ijk}|^2 + \frac{|\epsilon_{ik}^u|^2}{\rho_u}} \xrightarrow{M \rightarrow \infty} \frac{\beta_{iik}^2}{\sum_{j \neq i} \beta_{ijk}^2} \quad (5)$$

The average capacity can be given as:

$$C_{ik}^u = E\{\log_2(1 + \text{SINR}_{ik}^u)\} \quad (6)$$

The limitation of average uplink capacity is that there is no improvement if either of ρ_u or ρ_p is increased.

3 Proposed Scheme

The assignment of pilot sequences for a target cell is first done by using optimisation technique. After this, the SPA scheme is used to do the same in this section.

3.1 Problem Formulation

The assignment of pilots for a particular cell is considered. This cell is the target cell. The other base stations manage their corresponding pilot assignments independently. The assignment of pilots for this particular cell is huge that is $p(K, K) = K!$

The user terminals, which suffer from severe contamination of pilots, are the drawback in massive MIMO systems. The aim is to maximise the minimum uplink signal to SINR of K number of users. This is formulated in the optimisation problem as:

$$P : \max_{\{\mathcal{F}_s\}} \min_{\forall k} \frac{|h_{iik}^H h_{iik}|^2}{\sum_{j \neq i} |h_{ijk}^H h_{ijk}|^2 + \frac{|\epsilon_{ik}^u|^2}{\rho_u}} \quad (7)$$

Here, $\{\mathcal{F}_s : s = 1, \dots, K!\}$ gives all the possibilities, i.e. $K!$. These are the different pilot assignments, for example, $\mathcal{F}_s = [f_s^1, f_s^2 \dots f_s^K]$ is the s -th assignment. The large-scale fading coefficients β_{ijk} have slow variation [3–5]. The base stations can track them easily. Hence, the optimisation problem approaches to

$$P \xrightarrow{M \rightarrow \infty} P' : \max_{\{\mathcal{F}_s\}} \cdot \min_{\forall k} \cdot \frac{\beta_{iif_s^k}^2}{\sum_{j \neq i} \beta_{ijk}^2} \quad (8)$$

By using proposed SPA scheme, optimisation problem P' can be solved in greedy way. This will be illustrated later:

3.2 Pilot Assignment

The exhaustive search is the most direct method for solving the optimisation problem. In exhaustive search, all possible assignments are tried, and later, the best assignment is chosen. The assignments are huge in number, i.e. $K!$. This huge number results into a computational complexity which is high. In this paper, proposed scheme is used which has lower complexity.

A parameter series has been defined for the target cell $\{\alpha_k\}_{k=1}^K$. This is for the quantification of the K users' channel quality which is given as:

$$\alpha_k = \beta_{ijk}^2, \quad k = 1, 2, \dots, K \quad (9)$$

The definition of other parameter series $\{\gamma_k\}_{k=1}^K$ (for K pilots) is given for the quantification of the inter-cell interference of pilot sequences as:

$$\gamma_k = \sum_{j \neq i} \beta_{ijk}^2, \quad k = 1, 2, \dots, K \quad (10)$$

The decision of the uplink SINR that is $\text{SINR}_{ik}^u \rightarrow \alpha_{f_s^k} / \gamma_k$ is made by two factors:

- (1) The channel quality $\alpha_{f_s^k}$
- (2) The inter-cell interference γ_k .

To maximise the minimum uplink SINR, the assignment of pilots with high inter-cell interference is avoided for the user which has the worst channel quality which could lead to lower uplink SINR.

This has been used as a motivation for the proposal of the SPA scheme. The SPA assigns the pilot sequence with the lowest inter-cell interference to the user terminal having the worst channel quality. The K number of pilot sequences is arranged in descending order of their severity of inter-cell interference, i.e.

$$\mathcal{F}_p : [\emptyset_{f_p^1}, \emptyset_{f_p^2}, \dots, \emptyset_{f_p^K}], \quad (11)$$

The permutation \mathcal{F}_p satisfies $\gamma_{f_p^1} \geq \gamma_{f_p^2} \geq \dots \geq \gamma_{f_p^K} > 0$. In the similar fashion, the sorting of K users is done in descending order with respect to their channel qualities, i.e.

$$\mathcal{F}_q : [U_{f_q^1}, U_{f_q^2}, \dots, U_{f_q^K}], \quad (12)$$

The permutation \mathcal{F}_q satisfies $\alpha_{f_q^1} \geq \alpha_{f_q^2} \geq \dots \geq \alpha_{f_q^K} > 0$.

For the sorting process of pilots, merge sort is used, so the computational complexity of the proposed SPA scheme is $O(K \log K)$; whereas for exhaustive search, it is $O(K!)$.

4 Numerical Results

In simulation, the number of base stations used is 100, 200, 300 and 400. The graphs are plotted for capacity versus base stations using this number of antennas. The exhaustive search scheme is the ideal solution for assignment of pilots. Here, the attempt has been made to make the plot of proposed scheme as close as possible to that of exhaustive search. As the antenna number increases, the system capacity will increase (Fig. 2; Table 1).

In simulation, the number of base stations used is 100, 200, 300 and 400. The graphs are plotted for SINR versus base stations using this number of antennas. The exhaustive search scheme is the ideal solution for assignment of pilots. Here, the attempt has been made to make the plot of proposed scheme as close as possible to that of exhaustive search. As the number of antenna increases, the SINR will increase (Fig. 3; Table 2).

A pattern has been selected for the channel coefficients for every case.

Fig. 2 Capacity versus number of base stations

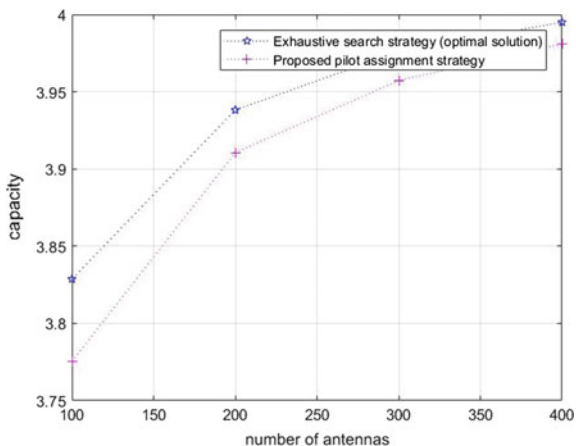


Table 1 Comparison of capacity for different pilot assignment strategies

Number of base station antennas	Capacity	
	Exhaustive search strategy	Proposed strategy
100	3.8286	3.7753
200	3.9382	3.9106
300	3.9759	3.9573
400	3.9950	3.9809

Fig. 3 SINR versus number of base stations

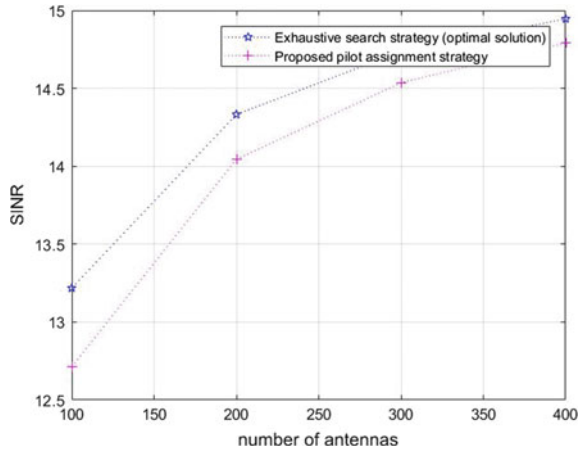


Table 2 Comparison of SINR for different pilot assignment strategies

Number of base station antennas	SINR	
	Exhaustive search strategy	Proposed strategy
100	13.2181	12.7126
200	14.3321	14.0441
300	14.7366	14.5359
400	14.9456	14.7917

5 Conclusion

In this paper, SPA scheme has been proposed for the improvement of the minimum uplink SINR of every user in massive MIMO systems. Here, the SPA scheme is proposed such that the user with the worst channel quality gets the pilot sequence with the smallest inter-cell interference. It has been proved theoretically that the SPA scheme generates the pilot assignment which solves the optimisation problem and hence approaches to original optimisation problem as M approaches towards infinity.

References

1. Marzetta T (2010) Noncooperative cellular wireless with unlimited numbers of base station antennas. *IEEE Trans Wirel Commun* 9(11):3590–3600
2. Rusek F, Persson D, Lau B, Larsson E, Marzetta T, Edfors O, Tufvesson F (2013) Scaling up MIMO: opportunities and challenges with very large arrays. *IEEE Signal Process Mag* 30(1):40–60
3. Li M, Jin S, Gao X (2013) Spatial orthogonality-based pilot reuse for multi-cell massive MIMO transmission. *IEEE International Conference on Wireless Communication Signal Processing (WCSP) 2013*, pp 1–6, 24–26 Oct. 2013
4. Ashikhmin A, Marzetta T (2012) Pilot contamination precoding in multicell large scale antenna systems. In: *IEEE international symposium on information theory (ISIT)*, pp 1137–1141
5. Muller R, Cottatellucci L, Vehkaperä M (2014) Blind pilot decontamination. *IEEE J Sel Top Signal Process* 8(5):773–786

Multiple Frequency Band Planar Antenna for Different Applications



Sakshi and Manisha Bharti

1 Introduction

Several band antennas are an antenna designed to act on different bands. These antennas also use structures in which one section of the antenna is working for one band, and an additional portion for a distinctive band is successful. A multiband antenna will gain less than the average or be physically greater in compensation [1]. Multiple band antennas are good for supporting more than one frequency while retaining ideal antenna characteristics throughout all frequencies such as gain, omnidirectional radiation pattern and return loss. Bluetooth and wireless area network work at 2.4 GHz in ISM band, i.e., industrial, scientific and medical bandwidth recurrence extend (2.4–2.5 GHz).

Mobile Worldwide Interoperability for Microwave (WiMAX) which belongs to the wireless networking protocol based on IEEE802.16 with high data rate and operating bands have frequency span 2.3–2.4 GHz and frequency span 3.4–3.6 GHz [2–7]. A multiband antenna for WiMAX, Wi-Fi and WLAN service is necessary for combined Web access to mobile phones. Numerous design structures of multiband antennas have been displayed in the most recent couple of years. A compact multiband antenna which can be applied to multiservice wireless application is proposed in this paper. The antenna is designed to cover both Wi-Fi and WiMAX. Microstrip line feeding is to be picked as a result of its effortlessness and simplicity of incorporation with other microwave segments on the equivalent.

Sakshi (✉) · M. Bharti

Department of Electronics and Communication Engineering, National Institute of Technology,
Delhi, India

e-mail: sakshi@nitdelhi.ac.in

M. Bharti

e-mail: manishabharti@nitdelhi.ac.in

There are certain advantages of microstrip line over strip line, coaxial line and waveguides. The fabrication cost of microstrip line is less as compared to the others due to complete conductor patterns may be deposited and processed on a single layer dielectric substrate which is supported by a single metal ground plane. The proposed modified antenna is developed on FR4 substrate.

2 Proposed Antenna Design

The demonstrated antenna is grown with a substrate thickness of 1.5 mm on FR4 (flame-resistant) with relative dielectric constant (ϵ_r) and loss tangent of 4.4 and 0.02, respectively. The overall antenna size ($W \times L$) $50 \times 90 \text{ mm}^2$. Proposed antenna design has a limited conducting ground (LG) as shown in Fig. 1 is 34.5 mm which is rear of the substrate. The suggested antenna contains triple monopole antennas. Each individual monopole antenna is working at different frequency bands. All printed monopole antenna is analyzed and simulated for a different antenna. The advanced patch parameters are as appeared in Table 1.

In the given Fig. 1, the proposed antenna has three monopole antennas. The first monopole antenna of length L_1 which is the largest antenna, L_2 and L_3 are second and third, respectively. Antenna of L_1 shaped is functioning at the smallest frequency, i.e., 800–900 MHz. L-shaped antenna of length L_2 and width W_2 resonant at frequency 2.4–2.5 GHz. Third monopole antenna of length L_3 and width W_3 is the smallest antenna whose resonant frequency 3.4–3.5 GHz. Each antenna is investigated and optimized each antenna parameters.

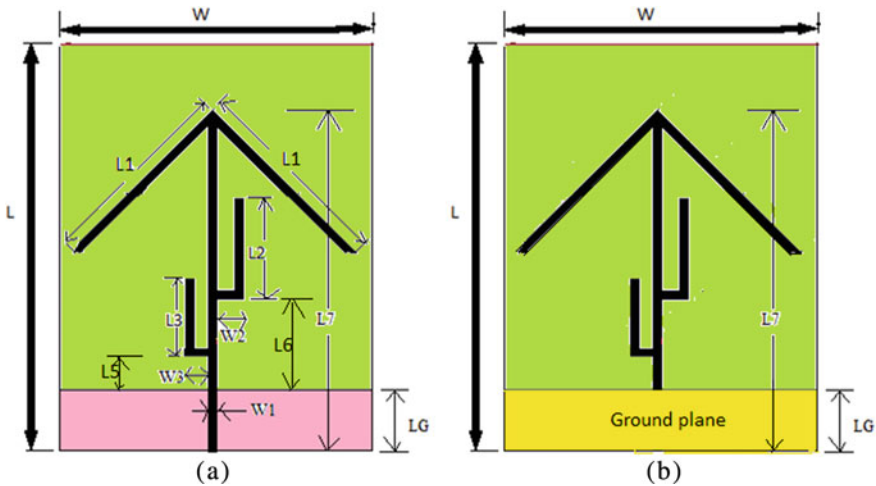


Fig. 1 Access proposed multiband antenna geometry, a front, b backside

Table 1 Optimized antenna specifications

S. No.	Parameters	Reference antenna (mm)	Proposed antenna (mm)
1	L1	37	30
2	L2	33	25
3	L3	19	14
4	L4	42	20
5	L5	12	5
6	L6	48.5	20
7	L7	70	70
8	W1	2.5	1.55
9	W2	5.7	8
10	W3	5.7	3

3 Simulation Result

All the simulations are done using high frequency structure simulator [8]. It is a popular commercial finite element method solver from ANSYS Corporation for electromagnetic structure in frequency domain. Distinct antenna characteristics are simulated, including 3D gain, return loss, etc. Figure 2 shows the simulation result of the demonstrated multiband antenna.

In Fig. 2, it can be noticeable that there are four distinct resonant frequency of the proposed antenna. These frequencies are 0.9, 1.8, 2.49 and 3.5 GHz. In the given

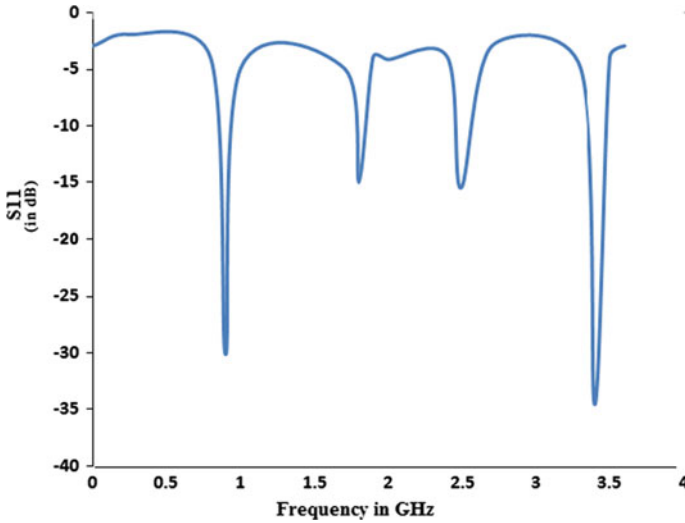


Fig. 2 Proposed antenna return loss at frequency 2.4 GHz

Fig. 2, lowest resonant frequency at 900 MHz which cover GSM band where the return loss value. The second resonant frequency at 1.8 GHz which is good for DCS application and the return loss is -15.01 dB. The third resonant frequency at 2.49 GHz which cover Bluetooth application. And the fourth resonant frequency is at 3.5 GHz and return loss at this frequency is -16 dB which covers WiMAX applications. Figure 3 shows the 3D radiation pattern at dissimilar resonance frequencies of the proposed antenna is 900 MHz, 1.8, 2.4 and 3.5 GHz.

In Fig. 3, it can be observed that 3D gain of the proposed antenna at distinct frequencies such as 0.9, 1.8, 2.5 and 3.5 GHz is 3.27 dB, 1.35 dB, 1.5 dB and 5.67 dB, respectively. It can be observed that antenna whose length is more works at lower frequency and the smallest length antenna resonant at higher frequency.

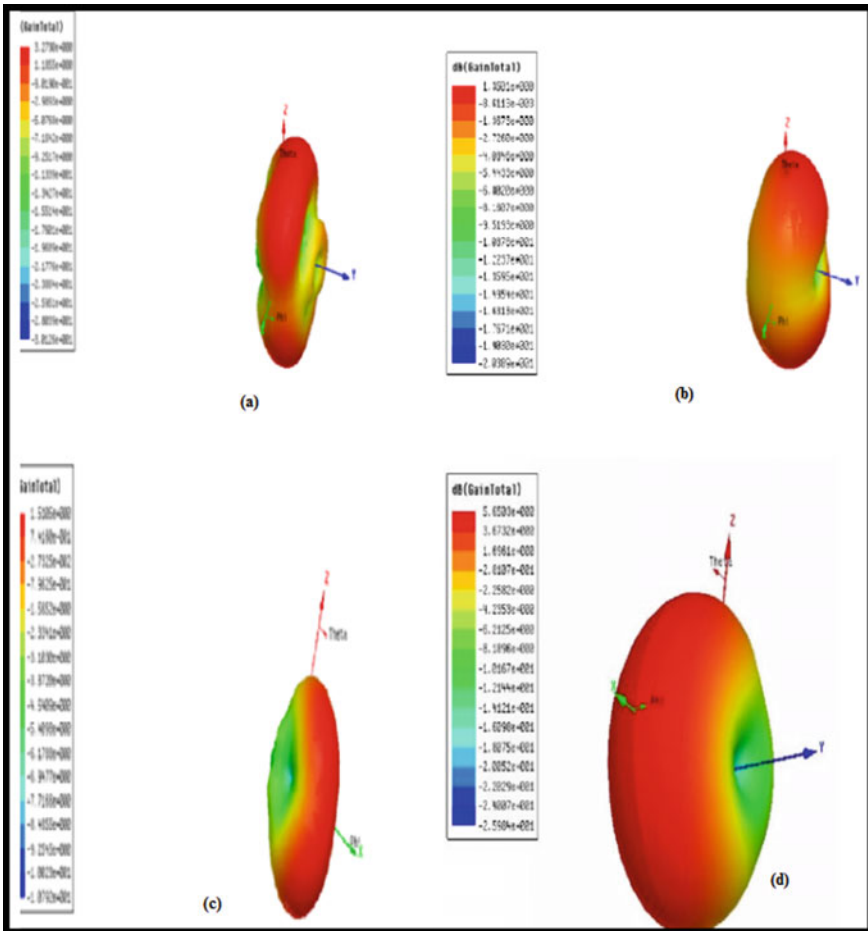


Fig. 3 3D radiation pattern of the demonstrated antenna **a** 2.5 GHz, **b** 1.8 GHz, **c** 2.5 GHz, **d** 3.5 GHz

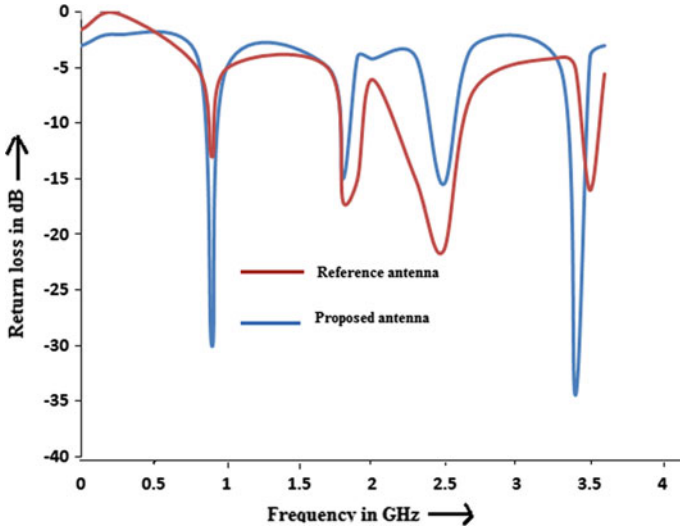


Fig. 4 Return loss graph between modified and proposed antenna

Figure 4 clearly shows that proposed antenna has four distinct resonance frequencies at 0.9, 1.8, 2.4 and 3.5 GHz.

4 Conclusion

In this paper, multiple band PCB antennas are proposed for various application like GSM, DCS, WLAN, Wi-Fi, and WiMAX application. All the simulation result of the demonstrated antenna shows that multiple band antenna suits multiple resonance frequency at 0.9, 1.8, 2.4 and 3.5 GHz. In Table 2, it can observe that the demonstrated antenna has better gain and return loss at different frequency and omni-directional radiation gain. The proposed antenna has good return loss at 0.9 and 3.5 GHz.

Table 2 Return loss and gain comparison between reference antenna and proposed antenna

1	Frequency (GHz)	0.9	1.8	2.49	3.5
2	Reference antenna gain (dB) [1]	1.73	1.04	2.83	5.01
3	Reference antenna return loss (dB) [1]	-13	-17	-21.5	-16
4	Proposed antenna gain (dB)	3.27	1.35	1.51	5.67
5	Proposed antenna return loss (dB)	-30.1	-15.01	-15.51	-34.5

References

1. Haraz OM, Sebak A (2011) Quadband planar PCB antenna for WLAN and mobile WiMAX applications. In: IEEE international symposium on antennas and propagation (APSURSI). Spokane, WA, pp 416–418
2. Wong K-L, Lai P-Y (2008) Wideband integrated monopole slot antenna for WLAN/WiMAX operation in the mobile phone. *Microw Opt Technol Lett* 50(8):2000–2005
3. Lin Y-D, Chi P-L (2005) Tapered bent folded monopole for dual band wireless local area network (WLAN) systems. *IEEE Antennas Wirel Propag Lett* 4:355–357
4. Chung KL, Mak TH, Tam WY (2009) A modified two-strip monopole antenna for Wi-Fi and WiMAX applications. *Microw Opt Technol Lett* 51(12):2884–2886
5. Wong K-L, Chou L-C, Su C-M (2005) Dual-band flat-plate antenna with a shorted parasitic element for laptop applications. *IEEE Trans Antennas Propag* 53(1):539–544
6. Wang Y-S, Lee M-C, Chung S-J (2007) Two PIFA related miniaturized dual-band antennas. *IEEE Trans Antennas Propag* 55(3):805–811
7. Balanis CA (1997) *Antenna theory analysis and design*, 2nd edn. Wiley
8. Ansoft HFSS V130.0

Implementation of Attendance Management System Based on Text and Face Recognition



Vaithiyanathan Dhandapani, Swathi Majji, Kishore Udata,
and M. Manigandan

1 Introduction

Attendance management system is nothing but having a count of the number of students present for the lecture. Nowadays, minimum attendance has become a must for students to appear for end-semester examinations. It is essential for both faculty and students. Conventional attendance marking system, i.e. attendance marking in sheets or books, is used when students are lesser in number. It is a tiresome and time-consuming task. If a class has a significant number of students, it becomes accessible to a proxy. This problem led to the use of automated systems such as biometrics. In the first step, they used fingerprint scanning as the fingerprint of an individual is unique. This issue is inefficient since students should stand in a queue. This process consumes precious individual time. Furthermore, in this pandemic situation, it is not encouraged to use biometrics since this may result in the spread of the virus. This reason can be stated as an added advantage of facial recognition over biometrics.

In recent days, many researchers reported various attendance managing systems based on different sensor techniques. Radio frequency identification (RFID)-based attendance management system was implemented in [1–4]. In paper [5], the author reviewed the fingerprint-based biometric attendance system. The implementations of a wireless iris recognition attendance system were discussed in [6, 7]. The authors in [8] implemented the automated attendance management system using face recognition algorithms. Attendance system with Bluetooth low energy beacon and android devices is presented in [9, 10]. The authors in [11] implemented the IoT-based system on Raspberry Pi 3B hardware. Feedback and complaint management functions were used to develop the attendance system in [12]. The author in [13] discussed the cloud-based system using near-field communication and face recognition. Biometric-based

V. Dhandapani (✉) · S. Majji · K. Udata · M. Manigandan
National Institute of Technology, Delhi, New Delhi 110040, India
e-mail: dvaithiyanathan@nitdelhi.ac.in

systems were presented in paper [14, 15]. In paper [16], authors implemented the face recognition-based attendance monitoring system using Python and OpenCV.

In this paper, our work comes with implementation of the attendance marking system using text recognition and face recognition [17]. Text recognition is done using optical character recognition (OCR). This process is done by scanning individual student ID cards. OCR scans the ID card and converts the data into a documented format. Facial recognition is highly recommended since facial parts of an individual are unique. These methods reduce the time of both faculty and students. Using either of the processes for attendance marking consumes more time, it results in the scanning of massive databases. Using both of the techniques, it reduces time and ends up with fruitful results.

2 Methodology Used in Implemented System

In this work, the attendance marking system implementation uses the scanner. This methodology will now be static where the student can verify his/her identity after the concerned lecturer allows it to do so by entering a passkey, thereby indicating the system to take attendance for the corresponding lecture/laboratory. In the future, the camera for face recognition will be the surveillance camera, a high-resolution one. Text recognition data on the ID card is documented. Facial identification detects a face on the ID card. Facial recognition identifies the unique patterns on the face. The results are verified against the database, and attendance is marked. The flow of the system is shown in Fig. 1. To develop the system, the following software and hardware components such as Nanonets, OpenCV, AWS recognition, Raspberry Pi and camera module are used.

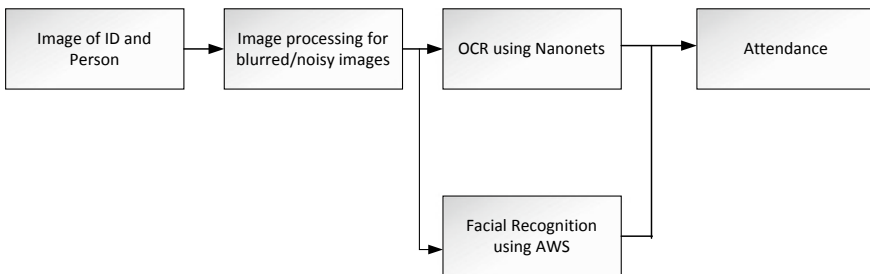


Fig. 1 Flow of the attendance marking system

2.1 Nanonets

It is a Python wrapper that provides an easy way to use the application program interface (API) to communicate with its servers. It is also used to build machine learning models for making predictions on image data. The models that can be built are classification of images, multi-label classification, detection of objects from images and optical character recognition. Nanonets have a cloud service where based on the application, training of the models is required. After creating a user account, the API key is generated and trains our models on respective official websites.

2.2 OpenCV

Open-source computer vision library is an open-source library offering various computer vision and machine learning algorithms. OpenCV is used to develop real-time computer vision technologies. It was developed in 1999, has over 47,000 community members and provides 2500 algorithms. The OpenCV is used to identify the presence of a face in an image.

2.3 AWS Rekognition

It is one of the Amazon web services that are cloud-based software as a service computer vision platform. It is not open source, and pricing depends on the services that the customer used. Users can also custom train a face recognition model, where a user needs to index the pre-labelled faces and to use this model as a service with an API. Then, the user can upload the new images to the API and receive information about the faces in the image. The model is trained by sending an image to Rekognition using an `index_face` API call. It sends us unique values for the image called image id and face ID. These face ID to recognize faces in later images and called as indexing. In order to recognize the face from a different image, the Rekognition using a `search_face` API call, if the previously indexed faces match, it sends us the matched face ID. The flow of API calls to AWS Rekognition is presented in Fig. 2.

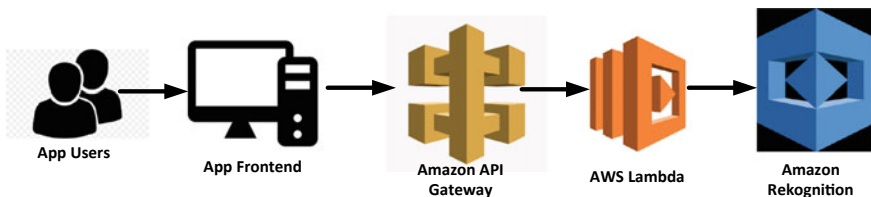


Fig. 2 API Call to AWS Rekognition [Internet source]

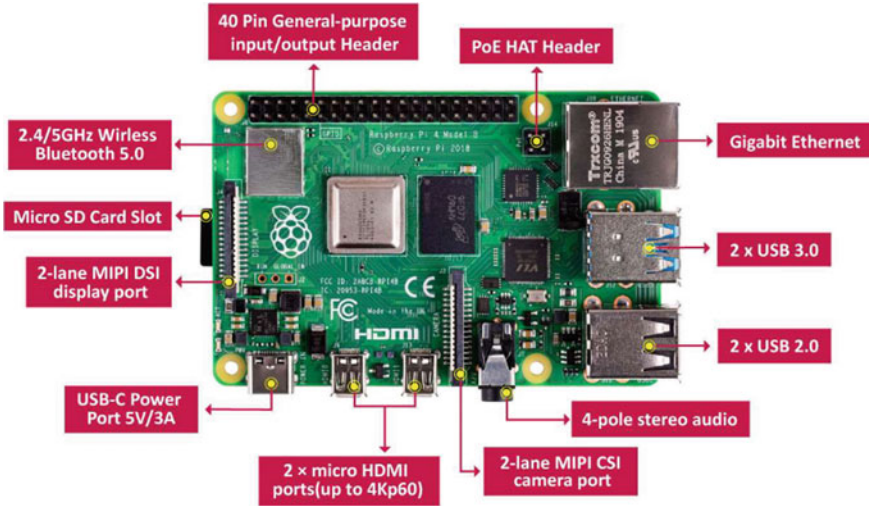


Fig. 3 Raspberry Pi 4 model B [18]

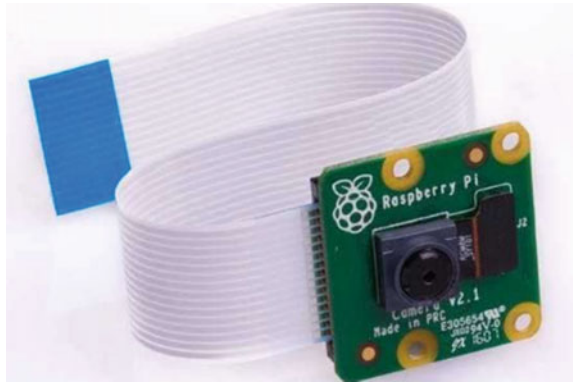
2.4 Raspberry Pi

Figure 3 is Raspberry Pi 4 models B, and it is similar to a micro-computer, compact-sized and mighty. In our work, the low-end devices such as ESP32 were used. It was created and developed by Espressif systems, a microcontroller with integrated wireless connectivity and very cheap compared to the Raspberry Pi. But it has I/O pins rather than interfacing ports such as USB, HDMI, LAN and some more features. The robustness and high flexibility of Raspberry Pi for high-end performance make us choose this hardware. Raspberry Pi 4 model has Broadcom BCM2711 as system-on-chip (SoC) with four Cortex-A72 processors with 1.5GHz. In our work, it is decided that the 4GB variant, although other options with 1GB, 2GB is also available. It has 2 USB2.0 ports and 2 USB3.0 ports, 1 LAN port with 1Gbps capability. It also has Bluetooth with dual-band Wi-Fi connectivity. It has GPIO pins that can be used for wired communications such as UART, SPI and I2C communications. It has a full HD 4K resolution capability. It also has a camera and stereo audio ports.

2.5 Camera Module

The camera used is the Raspberry Pi camera module version 2 is shown in Fig. 4, which is compatible with our chosen hardware. The camera module has a Sony IMX219 8MP sensor. These can be used for taking the still photographs as well as high-definition video. It is easy to use for beginners and also has plenty to offer

Fig. 4 Raspberry Pi camera module v2 [18]



advanced users. This can also be used for slow motion, time lapse and another video cleverness.

3 Optical Character Recognition

The flow of optical character recognition (OCR) in Fig. 5 is used to scan the printed documents or hand-written documents that contain numerals, letters or symbols. The scanned text is converted into computerized text in the form of word documents. Then, these converted documents can be formatted or reused in other documents. Documents therefore can be easily readable and reused. If a page is scanned using a scanner, it is generally stored as a bit-mapped file in tagged image format file (TIF/TIFF). Humans can view this image, but the computer stores it in the form of 0 and 1, the information is just a series of black and white dots.

OCR was initially developed to assist visually impaired people. Now, the same technique can be used to make the computer understand the text in an image. It is not only useful for visually impaired people but also for several applications, scanning a vast number of documents in search of some information which when done manually is tedious. Also, this work includes a considerable investment of time,

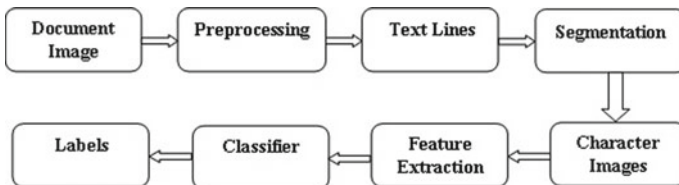


Fig. 5 Flow diagram of OCR

payrolls and may lead to several human errors. Recently, OCR finds many applications such as conversion of all offline documents to online by capturing images, business documents, number plate recognition for vehicles, translating the text of unknown language to known one and many other applications.

3.1 Training Nanonets OCR Model for ID Card Data Extraction

In this work, text recognition is a student ID card. The several labels are present in the ID card such as roll number, name, date of birth, branch, program, valid up to. The reason we need to go for another model different from the basic model is that this new model identifies the text in the image containing student ID cards. This text is extracted in the form of different labels where the output in the form of JavaScript object notation (JSON) response, which is then provided to the database. The process of identifying a student is easy. Thus, it makes sense of the data extracted while the basic model just extracts data from an image where the machine could not understand what type of information it is. In our experiment, fifty ID images of different students in our college were trained. In this, some images are uploaded in different angles, and upright positions so that the model can be trained well and could quickly identify the ID cards whose images are taken in real-time. The following are some of the ID images taken from the students that are uploaded on our own while training the data is shown in Fig. 6.



Fig. 6 Data sets for training the model

An application ID (model ID) is created after the model is trained, which is later used to access it during testing and usage. It is observed from our model was hosted and got an accuracy of 68.22%, which is quite acceptable one. This model is successful for the ID card images. It is observed for the experimental results, and it could identify the images which are currently uploaded from local storage due to lack of hardware components, which are in low lighting conditions and even when the ID is in an upright position.

4 Facial Recognition

The face of an individual plays a crucial role in the identification and emotion of the person. Each individual has a unique face that can be used for identification purposes. The facial recognition system is a part of biometrics. It can identify an individual from an image by scanning against the trained data. Billboards have been designed with software that recognizes the ethnicity, gender and estimated age of onlookers to deliver targeted marketing. The system involves three steps, namely pre-processing, face detection and face recognition.

4.1 Pre-processing

Before sending the image for face recognition, the images are entered into the initial process. So that the images with noise, blurred images, were taken in poor lighting conditions, and many other factors can be identified easily without misleading us to incorrect data. To achieve this, brightness and contrast of the image are adjusted, and by use of filters, the image enhancement is performed, edge detection techniques such as Laplacian of Gaussian, canny edge detector or any other techniques, and many noise removal techniques can be adopted.

4.2 Face Detection

Face detection is a major step in the facial recognition system. It is mainly locating the face of an individual in an image. After detecting the face, facial features are extracted. After identifying the face, facial recognition algorithms are applied. In general, detecting faces from an image is smooth, but when the image is a group image, detecting faces becomes difficult.

4.3 Face Recognition

Face recognition is the process of recognizing the distinctive patterns on an image of an individual face and stores the data as a trained set. When a face is scanned, then the system looks for patterns, verifies across the trained set and gives the information of the individual stored in the database.

5 Experimental Results and Discussion

5.1 Accomplishments

5.1.1 Output of Basic OCR Model

This is the output when a new image is uploaded to the basic OCR (text recognition model) is shown in Figs. 7 and 8.

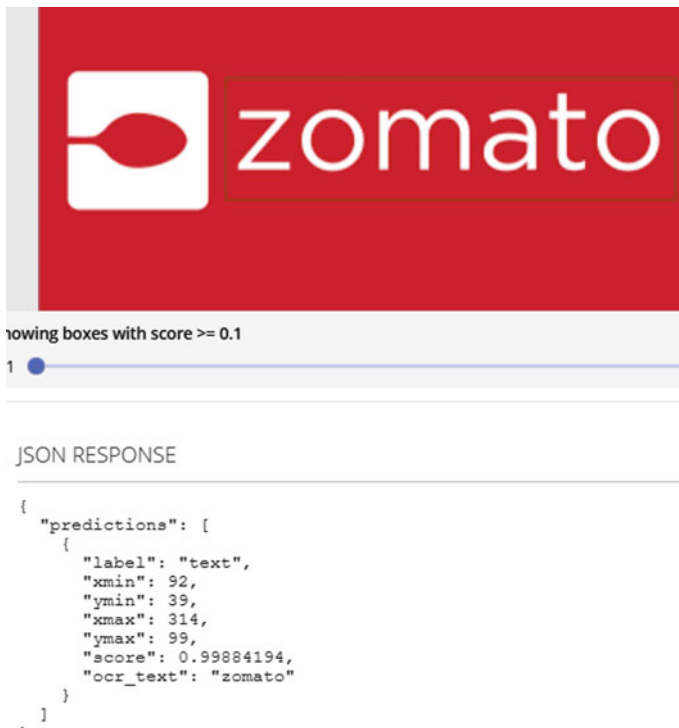
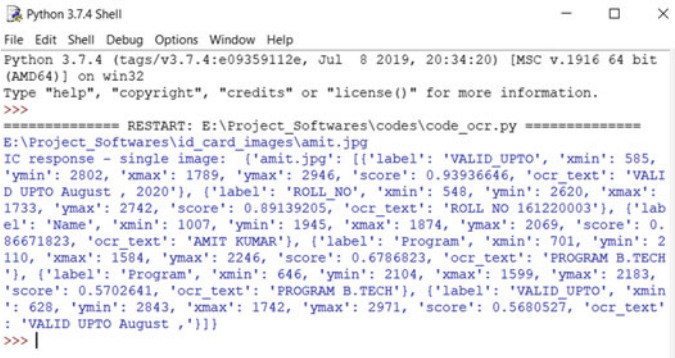


Fig. 7 OCR-based text extraction and its JSON response output



```
Python 3.7.4 Shell
File Edit Shell Debug Options Window Help
Python 3.7.4 (tags/v3.7.4:e09359112e, Jul 8 2019, 20:34:20) [MSC v.1916 64 bit
(AMD64)] on win32
Type "help", "copyright", "credits" or "license()" for more information.
>>>
===== RESTART: E:\Project_Softwares\codes\code_ocr.py =====
E:\Project_Softwares\id_card_images\amit.jpg
IC response - single image: [{'label': 'VALID UPTO', 'xmin': 585,
'ymin': 2802, 'xmax': 1789, 'ymax': 2946, 'score': 0.93936646, 'ocr_text': 'VALID
UPTO August , 2020'}, {'label': 'ROLL_NO', 'xmin': 548, 'ymin': 2620, 'xmax':
1733, 'ymax': 2742, 'score': 0.89139205, 'ocr_text': 'ROLL NO 161220003'}, {'lab
el': 'Name', 'xmin': 1007, 'ymin': 1945, 'xmax': 1874, 'ymax': 2069, 'score': 0.
86671823, 'ocr_text': 'AMIT KUMAR'}, {'label': 'Program', 'xmin': 701, 'ymin': 2
110, 'xmax': 1584, 'ymax': 2246, 'score': 0.6786823, 'ocr_text': 'PROGRAM B.TECH
'}, {'label': 'Program', 'xmin': 646, 'ymin': 2104, 'xmax': 1599, 'ymax': 2183,
'score': 0.5702641, 'ocr_text': 'PROGRAM B.TECH'}, {'label': 'VALID UPTO', 'xmin
': 628, 'ymin': 2843, 'xmax': 1742, 'ymax': 2971, 'score': 0.5680527, 'ocr_text'
: 'VALID UPTO August , '}]
>>> |
```

Fig. 8 JSON response output for student database

5.1.2 JSON Response for Image Uploaded from Local Storage to Nanonets

The response that it can identify the text in the image in the form of different labels that are predefined for which the model is trained, and its corresponding face identification using OpenCV is shown in Fig. 9, and OCR-based text extraction from the student ID card and its corresponding data values are stored in database for verification purpose as shown in Fig. 10.

5.1.3 Face Identification Using OpenCV

See Fig. 9.

5.1.4 Output for OCR

In the above images, as shown in Fig. 10a–d, it is clear that the model can identify the images even when given to the camera in inverted or different angles. Therefore, extracting the text from the images in the form of predefined labels is obtained. Further, Fig. 11 shows outputs for face recognition using OpenCV, AWS Rekognition with the help of API requests.

In the future, other applications of OCR/text recognition are invoice recognition to help visually impaired people, number plate recognition of a vehicle violating traffic rules, Aadhar/PAN card/other document detail extraction without manual process. Furthermore, the face recognition accuracy can be improved using several machine learning algorithms. It can further be extended to find the emotions of a student and how interested he/she is in a particular course. In the second step, iris recognition is recommended since individual eyeballs are unique, making this model a multimodal authentication system in need of highly secure systems.

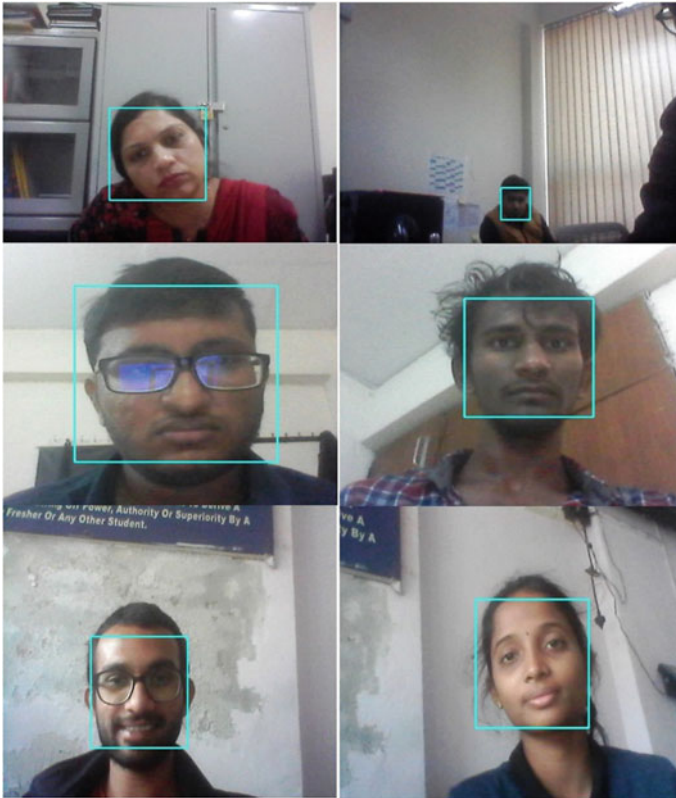


Fig. 9 Face identification using OpenCV

6 Conclusions

The use of this system provides automated data capture, which can save organizations considerable time and labour costs. The system thus provides automation, effective use of time and high adaptability to new data with only a few patterns to calculate. One has to notice a point that the model's accuracy depends on the resolution of the camera, clarity of the image and of course, the network equipment apart from algorithms. So, the cost estimation increases as quality improves. Thus, this work achieves text recognition and facial recognition of the input data.

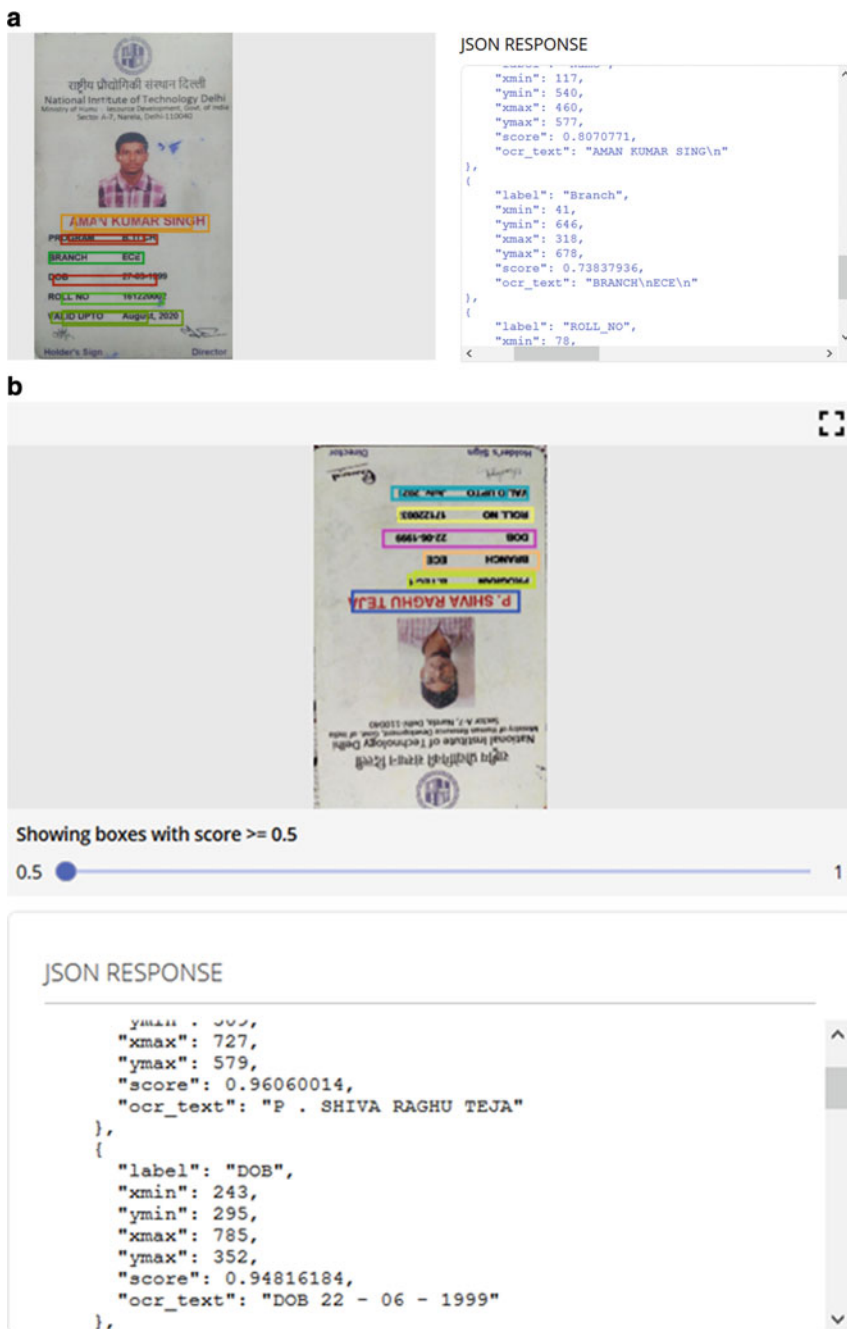


Fig. 10 a OCR-based text extraction from the student ID card-1, b OCR-based text extraction from the student ID card-2, c OCR-based text extraction from the student ID card-3 and d OCR-based text extraction from the student ID card-4

c



JSON RESPONSE

```

    "xmax": 666,
    "ymax": 1242,
    "score": 0.9834494,
    "ocr_text": "ROLL NO 161220022"
  },
  {
    "label": "Name",
    "xmin": 338,
    "ymin": 892,
    "xmax": 641,
    "ymax": 950,
    "score": 0.9823385,
    "ocr_text": "M. VIJAY RAJ"
  }

```

d



Fig. 10 (continued)

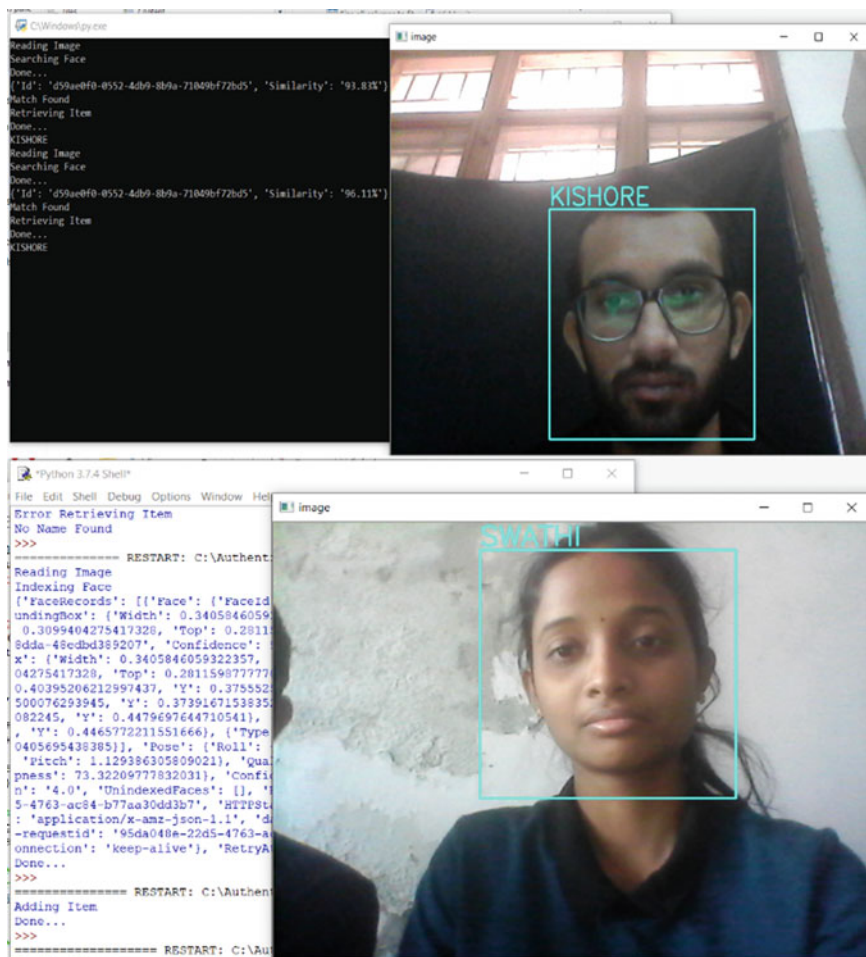


Fig. 11 Face recognition using Open CV, AWS Rekognition with the help of API requests

References

1. Agrawal A, Bansal A (2013) Online attendance management system using RFID with object counter. *Int J Inf Comput Technol* 3(3):131–138
2. Nainan S, Parekh R, Shah T (2013) RFID technology based attendance management system. *IJCSI Int J Comput Sci* 10(1):516–521
3. Patel UA, Priya RS (2014) Development of a student attendance management system using RFID and face recognition: a review. *Int J Adv Res Comput Sci Manage Stud* 2(8):109–119
4. Arulogun OT, Olatunbosun A, Fakolujo OA, Olaniyi OM (2013) RFID based students attendance management system. *Int J Sci Eng Res* 4(2):1–9
5. Sarkar A, Banerjee RK (2020) A review on fingerprint based biometric attendance system. *Prepare* 1(1), 1–8

6. Kadry S, Smaili K (2007) A design and implementation of a wireless iris recognition attendance management system. *Inf Technol Control* 36(3):323–329
7. Seifedine K, Smaili M (2010) Wireless attendance management system based on Iris recognition. *Sci. Res. Essays* 5(12):1428–1435
8. Chintalapati S, Raghunadh MV (2013) Automated attendance management system based on face recognition algorithms. In: 2013 IEEE International conference on computational intelligence and computing research. Enathi, pp 1–5
9. Noguchi S, Niibori M, Zhou E, Kamada M (2015) Student attendance management system with bluetooth low energy beacon and android devices. In: 2015 18th International conference on network-based information systems. Taipei, pp 710–713
10. Bhalla V, Singla T, Gahlot A, Gupta V (2013) Bluetooth based attendance management system. *Int J Innov Eng Technol (IJJET)* 3(1):227–233
11. Ruhitha V, Prudhvi Raj VN, Geetha G (2019) Implementation of IOT based attendance management system on Raspberry Pi. In: 2019 International conference on intelligent sustainable systems (ICISS). Palladam, Tamil Nadu, India, pp 584–587
12. Ahmed FYH, Aik KLT, Radzi AS, Salleh MD (2019) Develop attendance management system with feedback and complaint management function. In: 2019 IEEE 7th conference on systems, process and control (ICSPC). Melaka, Malaysia, pp 248–252
13. Rana A, Pugaokar V, Sawant A, Gore A (2019) Cloud based employee attendance management system using NFC and face recognition. *Int J Adv Res Ideas Innov Technol* 5(2):988–991
14. Gupta A, Kundu A, Das R (2019) Automated attendance system for efficient employee management: a biometry based approach. *Int J Recent Trends Bus Tourism* 3(3):117–121
15. Shoewu O, Idowu OA (2012) Development of attendance management system using biometrics. *Pacific J Sci Technol* 13(1):300–307
16. Kowsalya P, Pavithra J, Sowmiya G, Shankar CK (2019) Attendance monitoring system using face detection and face recognition. *Inter Res J Eng Technol (IRJET)* 06(03):6629–6632
17. Anith S, Vaithyanathan D, Seshasayanan R (2013) Face recognition system based on feature extraction. In: 2013 International conference on information communication and embedded systems (ICICES). Chennai
18. Raspberry-Pi, <https://www.element14.com/community/community/raspberry-pi/blog/2019/02/05/image-classification-using-nanonetsio-with-raspberry-pi>. Last accessed 05 Feb 2019

Performance Analysis of Fuzzy Logic-Based MPPT Controller for Solar PV System Using Quadratic Boost Converter



Servavidya Kumar Manas  and Bharat Bhushan

1 Introduction

Solar PV systems can be configured in different ways, depending on the type of load and control circuit. One of the configurations could be SPV system with DC load and electronic control circuit which comprises a DC–DC converter and a maximum power point tracker (MPPT) as shown in Fig. 1. A DC–DC converter transforms voltages and currents supplied from the PV module to the DC load from one DC level to another, and hence acts like a DC–DC transformer. The MPPT circuit harvests maximum power from the PV modules under all ambient conditions of irradiation and temperature [1].

DC–DC boost converter is one of the important components in solar photovoltaic system. However, it is pertinent to mention that a conventional boost converter may not meet the demand of high-voltage step-up ratio requirement of the system. Quadratic boost converter has high-voltage step-up ratio with lower duty cycle and shows a good converter efficiency. In [2, 3], design of conventional boost converter (CBC) and quadratic boost converter (QBC) is presented and a comparative analysis is done based on converter efficiency. In [4], an improved voltage lift technique-based QBC is presented. In [5], a novel quadratic boost switched capacitor converter (QBSCC) for PV system is compared with basic QBC which provides higher voltage step-up ratio for the same duty cycle and with the same objective [6] proposed a fifth-order quadratic following boost converter (QFBC).

In most PV power systems, maximum power point tracking (MPPT) control algorithm is used to harness the available solar energy. Several studies are going on to develop control algorithms to derive the maximum power from the solar panel. Review on widely used MPPT techniques for solar PV applications and their

S. K. Manas (✉) · B. Bhushan

Department of Electrical Engineering, Delhi Technological University, Delhi, India

B. Bhushan

e-mail: bharat@dce.ac.in

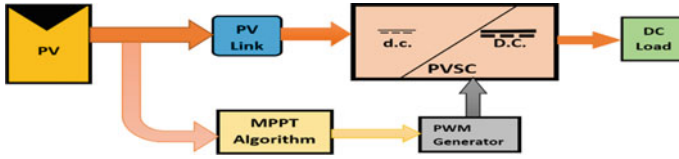


Fig. 1 Block diagram of a solar PV system with PVSC

comparative analysis is dealt in detail in [7–9], whereas a chronological sequence of evolution and modification of the old and new MPPT technique is presented in [10] where modern MPPT methods for PV system under partial shading conditions is taken into consideration. In [11], the author explains design approaches of fuzzy logic controllers (FLCs) in MATLAB/Simulink environment. Further quadratic boost converter and boost converter were compared for efficiency in [12], with fuzzy MPPT controller and QBC was found exhibiting high voltage gain.

2 DC–DC Converter

The DC–DC converter is also known as photovoltaic side converter (PVSC) as its input is coupled to the PV link as shown in Fig. 1. A high value capacitor C_{in} is used as DC-link and acts as a filter.

A basic quadratic boost converter is realized by the components of two boost converters by using single switch as shown in Fig. 2.

When IGBT is turned on, D_3 is forward biased, whereas D_1 and D_2 are reverse biased, and the currents are supplied to L_1 and L_2 by V_{in} and C_1 , respectively. During this mode of conduction, the inductor current i_{L1} gradually increases. When IGBT is turned off, D_3 is reverse biased, whereas D_1 and D_2 are forward biased. The energy stored in the inductors L_1 and L_2 reverses its polarity to charge the capacitor C_1 and C_2 through the diode D_1 and D_2 , respectively. During this mode of conduction, the inductor current gradually decreases gradually. These operation conditions are shown in Fig. 3a and Fig. 3b, respectively. Let f be the switching frequency.

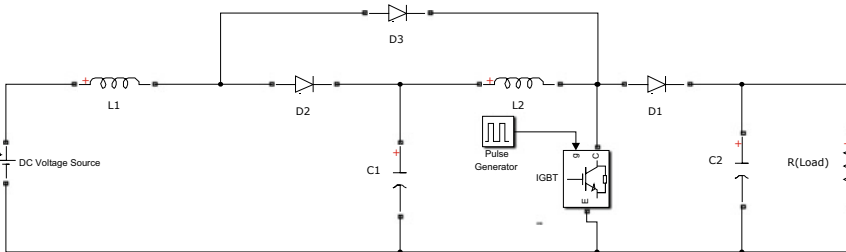


Fig. 2 A quadratic boost converter

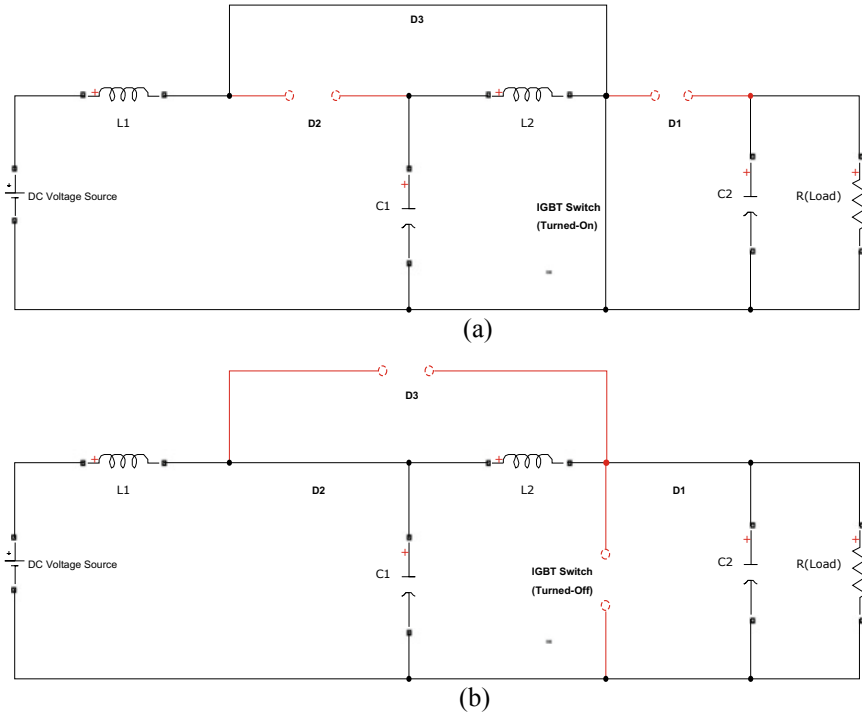


Fig. 3 a On-state, b Off-state

The duty cycle is given by:

$$D = 1 - \frac{\sqrt{V_{in}}}{\sqrt{V_{out}}} \tag{1}$$

The output and inductor currents are calculated as follows:

$$I_{out} = \frac{V_{out}}{R} \tag{2}$$

$$I_{L1} = \frac{I_{out}}{(1 - D)^2} \tag{3}$$

$$I_{L2} = \frac{I_{out}}{(1 - D)} \tag{4}$$

The inductors values are calculated as:

$$L_1 = \frac{DV_{in}}{f \Delta i_{L1}} \tag{5}$$

$$L_2 = \frac{DV_{in}}{f \Delta i L_2} \tag{6}$$

The capacitors values are calculated using:

$$C_{1,2} = \frac{DV_{in}}{(1 - D)\Delta v_c Rf} \tag{7}$$

The load profile is 120-V, 2000-W, resistive load. The switching frequency, f , is selected as 50 kHz, the peak-to-peak ripple voltage of the PV module and the peak-to-peak ripple current of the inductor are specified as 0.2 V and 1 A, respectively [13].

3 Maximum Power Point Tracking (MPPT)

In steady state, it is desired to operate the solar PV panel at a single point, where the output voltage and current results in maximum power are called as maximum power point (MPP) Fig. 4. At this point, the slope of PV characteristics curve is zero, i.e., change in power with respect to change in voltage, $\Delta P/\Delta V$, is equal to zero. Various control techniques are implemented to assure that solar PV module operates at MPP, i.e., to keep power (P) at its maximum value and $\Delta P/\Delta V$ equal to zero and is known as maximum power point tracking (MPPT).

In this paper, two MPPT control techniques have been compared: incremental conductance (InCond) and fuzzy logic controller (FLC).

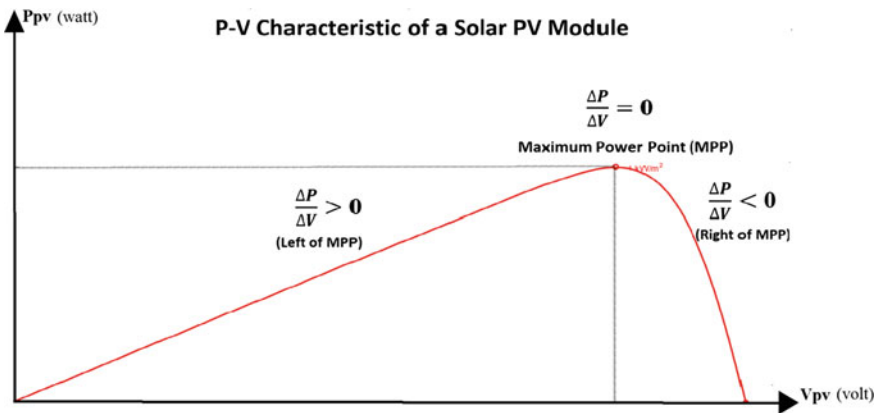


Fig. 4 P–V characteristics

3.1 MPPT Using Incremental Conductance (InCond) Method

The slope of the P–V curve, $\Delta P/\Delta V$, can be written as,

$$\frac{\Delta P}{\Delta V} = \frac{\Delta(VI)}{\Delta V} = \frac{I(\Delta V) + V(\Delta I)}{\Delta V} = \frac{I(\Delta V)}{\Delta V} + \frac{V(\Delta I)}{\Delta V} = I + V \frac{\Delta I}{\Delta V} \tag{8}$$

In InCond method, instantaneous conductance (I/V) is compared with incremental conductance ($\Delta I/\Delta V$), at each sampling time to track maximum power point (MPP) [5]. It is obvious from the curve, that.

- (i) $\Delta P/\Delta V = 0$, zero slope at MPP,
- (ii) $\Delta P/\Delta V > 0$, positive slope at left of MPP,
- (iii) $\Delta P/\Delta V < 0$, negative slope at right of MPP.

Hence,

$$\left. \begin{aligned} \frac{\Delta I}{\Delta V} &= -\frac{I}{V} \text{ at MPP} \\ \frac{\Delta I}{\Delta V} &> -\frac{I}{V}, \text{ at left of MPP} \\ \frac{\Delta I}{\Delta V} &< -\frac{I}{V}, \text{ at right of MPP} \end{aligned} \right\} \tag{9}$$

Thus, an InCond-based controller tracks MPP till $\Delta I/\Delta V = -I/V$, i.e. $\Delta P/\Delta V = 0$.

3.2 MPPT Using Fuzzy Logic Method

In fuzzy logic-based MPPT controller, the controlling action is determined from a set of simple linguistic rules. The rule decision table may be determined in different ways like (i) by trial and error method for simple fuzzy systems, (ii) by using artificial neural network (ANN), or (iii) by using genetic algorithms (GA)-based control techniques for hybrid fuzzy systems making a fuzzy-ANN or a GA-fuzzy system, etc. Hybrid fuzzy systems need high-level computation algorithm which takes relatively more computation time than that for a simple fuzzy logic-based controller. Such type of time-consuming computation algorithm is usually not desired in control system applications. Most of the time simple fuzzy logic controllers (FLCs) are modeled for specific applications and not for a general case. In present study, trial and error method has been adapted [11].

In general, fuzzy logic operation consists of three stages: fuzzification, rule inference, and defuzzification as shown in Fig. 5a.

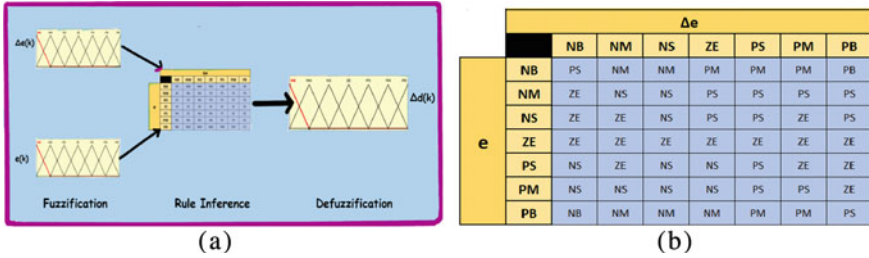


Fig. 5 a Fuzzy logic block diagram rules and b Table for the fuzzy logic controller

3.2.1 Fuzzification

The operation in which crisp numerical values of input variables are converted into a fuzzy variable is known as fuzzification. The values of I_{pv} and V_{pv} are used to calculate the power, P_{pv} from PV array. The error signal $e(k)$ and change in error $\Delta e(k)$ are the input variables and are calculated from (10) and (11), respectively.

$$e(k) = \frac{P_{pv}(k) - P_{pv}(k - 1)}{V_{pv}(k) - V_{pv}(k - 1)} \tag{10}$$

$$\Delta e(k) = e(k) - e(k - 1) \tag{11}$$

3.2.2 Rule Inference

The rule inference is designed and evolved by trial and error method. Rule table for the fuzzy logic controller is shown in Fig. 5b.

3.2.3 Defuzzification

The operation in which fuzzy output variables are converted into a crisp numerical value is known as defuzzification and is made explicit to the external environment, i.e., boost converter. The duty cycle step, $\Delta d(k)$ for the QBC, is the crisp output.

4 Simulations and Results

The simulation model of solar PV-powered quadratic boost converter with MPPT controller on which analysis is done is shown in Fig. 6. The simulation is performed in MATLAB 2016b [14].

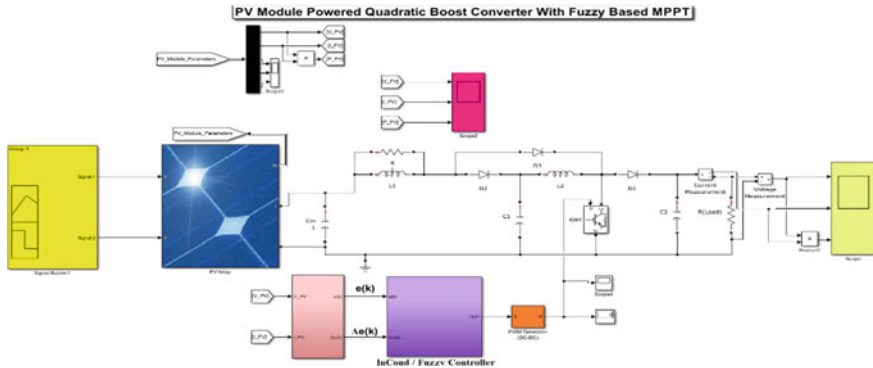


Fig. 6 Simulink model of solar PV system using quadratic boost converter with InCond/fuzzy MPPT controller

Table 1 Characteristics of 1Soltech 1STH-250-WH

Specifications	Values
Maximum power (Pmax)	2000-W
Cells per module	60
Open-circuit voltage (VOC)	37.3 V
Short-circuit current (Isc)	8.66 A
Voltage at maximum power point (VMPP)	30.7 V
Current at maximum power point (IMPP)	8.15 A

The main characteristic of the PV module used (1Soltech 1STH-250-WH) is given in Table 1. The PV array consists of eight parallel strings, i.e., NP = 8 and one series-connected modules per string, i.e., NS = 1.

Simulation and analysis are done for different combinations of solar irradiance and temperature. These values are fed to PV panel using signal builder block in Simulink and the plot is shown in Fig. 7.

4.1 Simulation Results for Solar PV System with InCond MPPT Controller for Solar Irradiance Values: 400, 600, 800, and 1000 W/m² @ T = 25 °C and 1000 W/m² @ T = 35 °C and 45 °C

The output waveforms of solar PV module connected to QBC is shown in Fig. 8. The corresponding waveform from the output of quadratic boost converter is shown in Fig. 9.

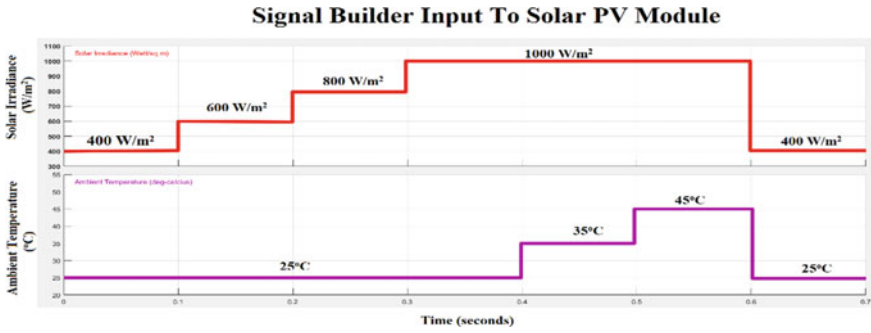


Fig. 7 Signal builder input for solar irradiance values: 400, 600, 800, and 1000 W/m² @ T = 25 °C, and 1000 W/m² @ T = 35 °C and 45 °C

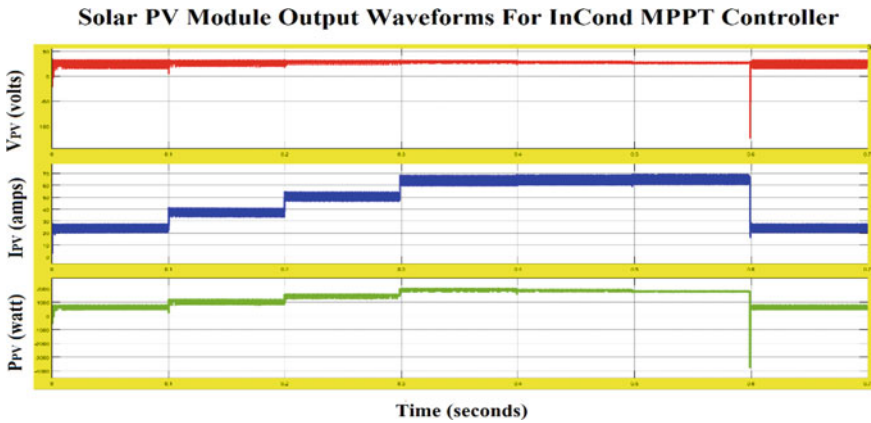


Fig. 8 Solar PV module output waveforms at T = 25 °C and irradiation: 400, 600, 800, and 1000 W/m² @ T = 25 °C, 35 °C, and 45 °C

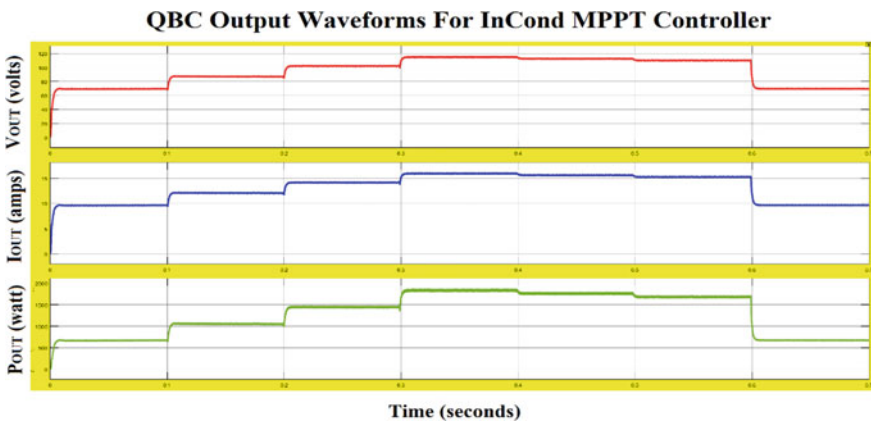


Fig. 9 Output waveforms of quadratic boost converter corresponding to Fig. 8

4.2 Simulation Results for Solar PV system with Fuzzy MPPT Controller for Solar Irradiance values: 400, 600, 800, and 1000 W/m² @ T = 25 °C and 1000 W/m² @ T = 35 °C and 45 °C

The output waveforms of solar PV module connected to QBC are shown in Fig. 10. The corresponding waveform from the output of quadratic boost converter is shown in Fig. 11.

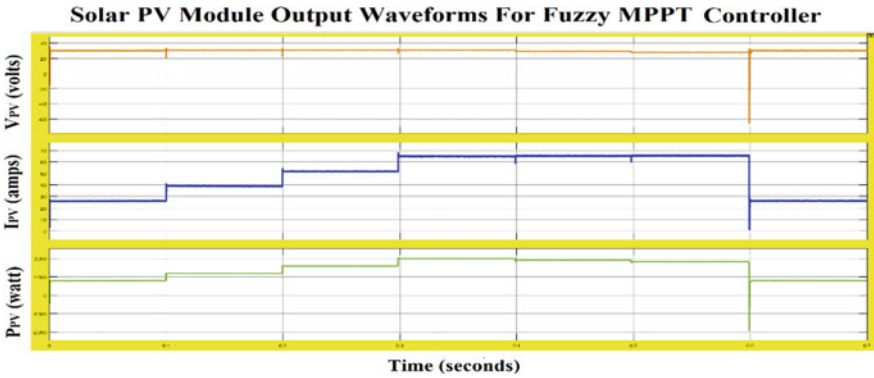


Fig. 10 Solar PV module output waveforms at $T = 25\text{ }^{\circ}\text{C}$ and irradiation: 400, 600, 800, and 1000 W/ m² @ $T = 25\text{ }^{\circ}\text{C}$, 35 °C, and 45 °C

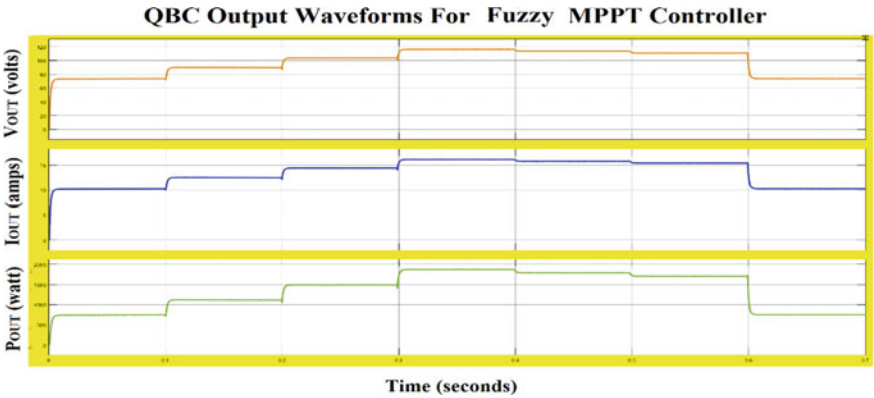


Fig. 11 Output waveforms of quadratic boost converter corresponding to Fig. 10

Table 2 Performance analysis of Solar PV Connected QBC with InCond MPPT Controller

Irradiance/Temp (watt/m ² /°C)	Maximum Power (PV Module), P _{MPP}	PV Module Output Power, P _{PV}	MPPT Efficiency, η_{MPPT} (%)	QBC Output Power, P _{QBC}	QBC Efficiency, η_{QBC} (%)
400/25	792	714.3	90.33	667.8	93.49
600/25	1197	1135	94.82	1062	93.59
800/25	1599	1588	97.44	1458	93.57
1000/25	2000	1964	98.19	1837	93.59
1000/35	1914	1890	98.74	1762	93.26
1000/45	1830	1812	99.02	1685	92.98

Table 3 Performance analysis of Solar PV Connected QBC with Fuzzy MPPT Controller

Irradiance/Temp (W/m ² /°C)	Maximum power (PV module), P _{MPP}	PV module Output power, P _{PV}	MPPT Efficiency, η_{MPPT} (%)	QBC output power, P _{QBC}	QBC Efficiency, η_{QBC} (%)
400/25	792	755.6	95.41	707.2	93.59
600/25	1197	1168	97.58	1095	93.74
800/25	1599	1580	98.84	1482	93.64
1000/25	2000	1980	99.01	1854	93.60
1000/35	1914	1900	99.29	1773	93.31
1000/45	1830	1819	99.39	1691	92.98

5 Analysis and Discussion of the Simulation Results

The performance study of the solar PV system has been evaluated in two aspects as: (i) evaluation of the MPPT efficiency and (ii) evaluation of the QBC efficiency. The results are summarized in Tables 2 and 3.

The MPPT efficiency is 99.01% for fuzzy algorithm and 98.19% for InCond algorithm under standard conditions. The QBC efficiency is about 93.60% in both cases.

6 Conclusions

The fuzzy MPPT controller shows better MPPT efficiency than InCond MPPT controller at all conditions of irradiance and temperature. The converter efficiency is almost same for both controllers. Further, the solar PV system shows faster dynamic

response for fuzzy controller. The InCond MPPT controller exhibits large oscillations at MPP, whereas fuzzy MPPT controller shows almost zero oscillations. Overall, fuzzy MPPT controller shows a superior performance (improved efficiency, fast response time, and negligible oscillation at MPP) in comparison with an InCond MPPT controller implemented for solar PV system.

References

1. Solanki CS (2013) Solar photovoltaic technology and systems: a manual for technicians, trainers and engineers, 2nd edn. PHI Learning Private Limited
2. Selva Kumar R, Gayathri Deivanayaki VP, Vignesh CJ, Naveena P (2016) Design and comparison of quadratic boost converter with boost converter. *IJERT* 5(01)
3. Boujelben N, Masmoudi F, Djemel M, Derbel N (2017) Design and comparison of quadratic boost and double cascade boost converters with boost converter. In: 2017 14th International multi-conference on systems, signals and devices (SSD). Marrakech, pp 245–252. <https://doi.org/10.1109/SSD.2017.8167022>
4. Li Y, Sathiakumar S (2017) Improved quadratic boost converter based on the voltage lift technique. In: 2017 Asia modelling symposium (AMS). Kota Kinabalu, pp 139–144. <https://doi.org/10.1109/AMS.2017.30>
5. Sivaraj D, Arounassalame M (2017) High gain quadratic boost switched capacitor converter for photovoltaic applications. In: 2017 IEEE international conference on power, control, signals and instrumentation engineering (ICPCSI). Chennai, pp 1234–1239. <https://doi.org/10.1109/ICPCSI.2017.8391907>
6. Veerachary M, Kumar N (2018) Analysis and design of quadratic following boost converter. In: 2018 IEEE International conference on power electronics, drives and page 1 82 energy systems (PEDES). Chennai, India, 2018, pp 1–6. <https://doi.org/10.1109/PEDES.2018.8707706>
7. Salas V, Olías E, Barrado A, Lázaro A (2006) Review of the maximum power point tracking algorithms for stand-alone photovoltaic systems. *Solar Energy Mater Solar Cells* 90:1555–1578
8. Subudhi B, Pradhan R (2013) A comparative study on maximum power point tracking techniques for photovoltaic power systems. *IEEE Trans Sustain Energy*, 4(1)
9. Gupta AK, Saxena R (2016) Review on widely-used MPPT techniques for PV applications. In: 2016 International conference on innovation and challenges in cyber security (ICICCS-INBUSH). Noida, pp 270–273. <https://doi.org/10.1109/ICICCS.2016.7542321>
10. Eltamaly AM, Abdelaziz AY (2020) Modern maximum power point tracking techniques for photovoltaic energy systems. Springer Nature Switzerland AG
11. Altaş IH (2017) Fuzzy logic control in energy systems with design applications in MatLab/Simulink. The Institution of Engineering and Technology
12. Priyadarshini J (2018) Modelling and simulation of PV system with Fuzzy MPPT based converter. In: 2018 International conference on recent innovations in electrical, electronics and communication engineering (ICRIEECE). Bhubaneswar, India, pp 1140–1145. <https://doi.org/10.1109/ICRIEECE44171.2018.9009374>
13. Krein PT (1998) Elements of power electronics. Oxford University Press
14. Klee H, Allen R (2018) Simulation of dynamic systems with MATLAB® and Simulink®. Taylor & Francis Group, LLC, ISBN Number-13: 978-1-4987-8777-2 (Hardback)

An Analysis on Frequency Control of Microgrid Including Diverse Renewable Energy Sources



Ritwik Tripathi and Omveer Singh

1 Introduction

The bulk power generation in India (62.8%) and world (67%) is based on fossil fuels mainly coal which are used extensively in thermal power plants. Millions of years before when forests, vegetation, animal remains and other waste got dumped beneath earth's surface, then due to anaerobic conditions, high temperature and pressure, it took thousands of years for formation of coal. The coal which took such long time for its formation has been used by human beings injudiciously in past 400 years with the onset of industrial revolution. As coal is basically made of organic matter so with its usage the carbon content has sharply increased within the atmosphere leading to serious climatic conditions and eventually resulting in global warming and increased earth's temperature.

Being inexhaustible in nature and also overcoming environmental constraints, renewable energy sources (RESs) are getting much importance nowadays [1]. The different RESs that have been used in this work include solar farm and a wind farm. The microgrid thus established can be either of grid-connected or isolated type [2]. Wind farm generates alternating current (AC) which needs to be passed through suitable filters and the frequency should be synchronized with that of grid. While in PV farm, voltage is produced in form of direct current (DC) which needs to be passed through specific rectifiers, then filters in order to reduce harmonic content and finally its frequency too must be in synchronization with microgrid frequency. The resilience can be obtained by using the concept of microgrids instead of earlier power distribution system [3].

R. Tripathi · O. Singh (✉)

Department of Electrical Engineering, Gautam Buddha University, Greater Noida, India

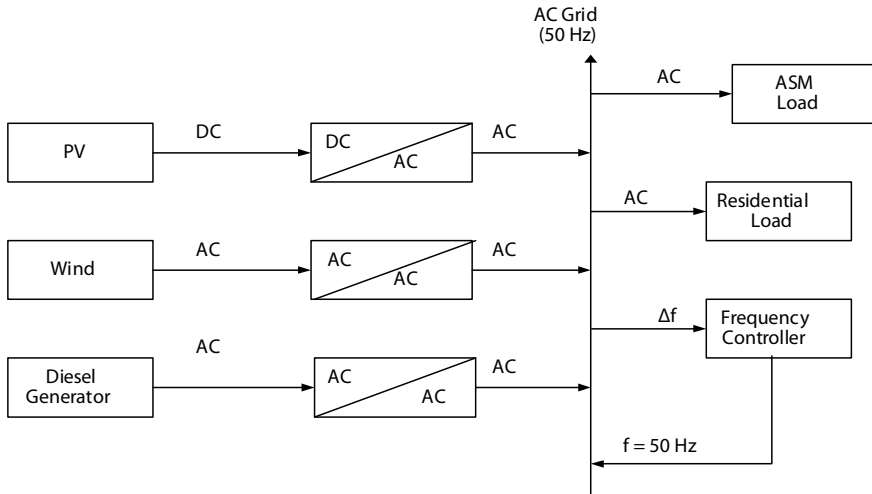


Fig. 1 Proposed microgrid setup

When the microgrid is set up with the above criteria including different loads too then it operates normally but as we know that the wind and solar generation are a function of incident sunlight and wind speed so when there is a cloud cover or shading due to nearby trees, buildings, etc., the solar generation is likely to get affected. Similarly, when there is a dip in wind speed, the wind generation also reduces and it becomes uncertain in nature [4].

So when the abovementioned conditions arise, the total generation tends to fall down for certain duration but during that period, the load in the systems remains the same. This results in a slight reduction in system frequency from 50 Hz (nominal value). In order to meet the demand now, other sources in the system like DG increase their generation during this period. Hence, after some perturbations, the frequency again reaches nominal value of frequency. With the help of frequency control, the power quality of microgrid improves significantly [5].

The proposed setup includes DG, wind farm, PV farm, residential load and an ASM load. Moreover, for frequency control of the above microgrid, the frequency deviation is measured and is applied to specified controllers whose findings are discussed in later sections Fig. 1.

2 Modelling of Diverse Renewable Energy Sources

In total, two RESs have been used in the proposed microgrid. They are modelled mathematically in the following sections.

2.1 Modelling of PV Module/Array

The basic entity that is used to make PV array is a solar cell. PV cells were first time used in 1950 at Bell Laboratory [6]. PV cell [7] is combined to form PV module, then these modules are arranged in series or parallel to form the PV array. So firstly we have modelled PV cell then PV module.

The output of single PV cell is so small that practically it is not feasible to supply loads through it. So in order to increase the magnitude of generated photocurrent (I_{ph}), the cells are grouped together to form a module. Hence, now we created mathematically model the PV module (Fig. 2).

The relationship between module saturation current (I_0) and cell temperature is governed by equation given below [8]:

$$I_0 = I_{rs} \left[\frac{T}{T_r} \right]^3 e^{\left[\frac{q \times E_{g0}}{nk} \left(\frac{1}{T} - \frac{1}{T_r} \right) \right]} \tag{1}$$

where

I_{rs} = Reverse saturation current of module (μA).

T_r = Nominal temperature = 298.15 K.

q = Charge on one electron = 1.6×10^{-19} C.

E_{g0} = Energy band gap of silicon = 0.7 eV.

n = Ideality factor of diode.

k = Boltzmann’s constant = 1.38×10^{-23} J/K.

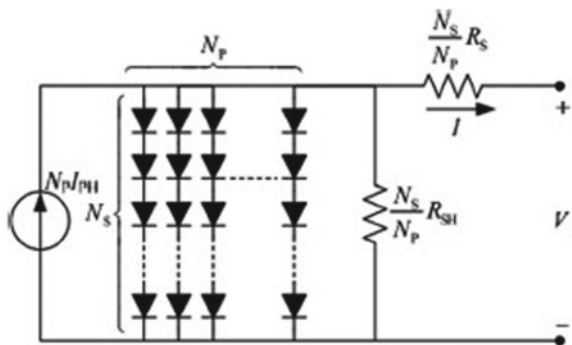
The current output of PV module is given by:

$$I = N_p \times I_{ph} - N_p \times I_0 \times \left[e^{\left(\frac{V/N_s + I R_s/N_p}{n \times V_t} \right)} - 1 \right] - I_{sh} \tag{2}$$

Here,

N_p = No. of PV modules connected in parallel.

Fig. 2 Equivalent circuit of PV module [8]



- N_S = No. of PV modules connected in series.
- V = Operating voltage (V).
- R_S = Series resistance (m Ω).
- V_t = Diode thermal voltage (V).

2.2 Modelling of Wind Farm

When the nonlinearities in the system are neglected, the approximate transfer function of the wind turbine resembling first-order response is given by [9]:

$$G_{WT} = \frac{K_{WT}}{1 + sT_{WT}} \tag{3}$$

The wind turbine model consists of various components like rotor blades, driver train, gear box, induction generator, etc. The wind farm uses pitch control to increase or decrease the output power and ensures that frequency is controlled [10]. The power generated from wind turbine (P_0) is directly proportional to the cube of wind speed (V^3) and is generally given by:

$$P_0 = \frac{1}{2} A \rho C_P V^3 \tag{4}$$

where

- A = Area covered by wind blades (m²).
- ρ = Density of air (kg/m³).
- C_P = Coefficient of power.

Moreover, the wind turbine generator can also be represented by its equivalent circuit as shown [11] (Fig. 3).

In the above circuit,

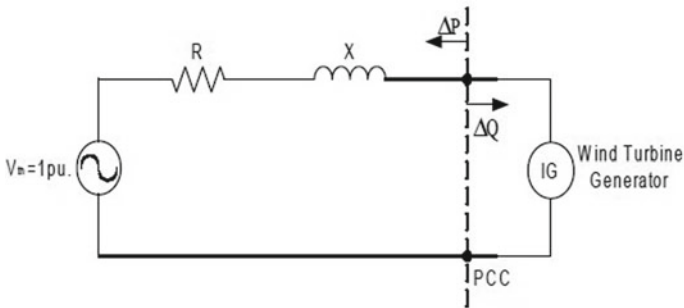


Fig. 3 Equivalent circuit of wind turbine generator [11]

R = Resistance of microgrid (pu).

X = Reactance of microgrid (pu).

ΔP = Variation of active power injected into the microgrid.

ΔQ = Variation of reactive power absorbed from the microgrid.

$\Delta S = \sqrt{\Delta P^2 + \Delta Q^2}$ = Variation in apparent power.

3 Implementation Procedure

Based on the mathematical model developed in the previous section, the desired microgrid is implemented in the MATLAB/Simulink software. The PV farm is implemented using irradiance and partial shading scenarios whose data are fetched with the help of look-up table. The wind farm is implemented by creating a suitable wind profile which aids in the study of frequency control of microgrid. Apart from the main or secondary controller, a primary wind control mechanism is also developed along with the simulation of wind farm. The diesel generator too is simulated along with its excitation system and parametric measurement system. Built-in model of residential load is used which contains asynchronous machine as a prime component. All of the above components are arranged in a specific way to design the microgrid. After the microgrid is set up, various parameters such as active power and reactive power of all the sources and loads are measured.

The dynamics of power system frequency can be easily understood with the help of basic swing equation given below [12]:

$$\frac{2H}{\omega_s} \times \frac{d^2\delta}{dt^2} = (P_m - P_e)_{pu} \quad (5)$$

where

H = Inertia constant of the generator system.

ω_s = Synchronous angular speed (rad/s).

δ = Rotor angle = Angle between rotor m.m.f. and stator m.m.f.

P_m = Mechanical power input to the rotor.

P_e = Electrical power output from the rotor.

Now, the concept of frequency control of microgrid is to adjust the generation in such a way that the mechanical power input to the generator matches with the electrical power output from the generator, i.e. $P_m - P_e = 0$. Generally for the stability of the generators in power systems, power angle characteristics are studied. The system is said to be in stable condition if suppose any small disturbance is introduced in the system, then the synchronous generator will overcome it and again come back to normal after first or second swing. If suppose the generators were stable after first swing but become unstable after second swing, then this situation is neither stable nor unstable instead it is called as instability after surviving the first swing.

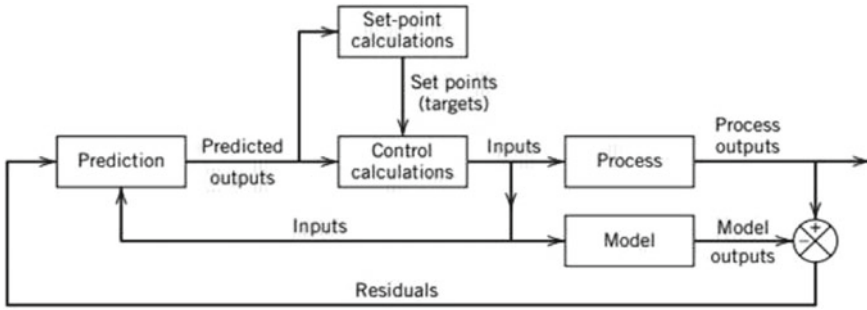


Fig. 4 Block diagram for model predictive controller [14]

In order to obtain above feature, mainly two levels of controllers are placed: primary and secondary. The primary controller has already been placed in the microgrid at wind farm side as mentioned in the previous section. Now we used MPC as secondary controller in the microgrid. Recently, MPC has been preferred for controlling issues in power system that arises due to RES due to its good dynamic performances, high robustness and ability to handle nonlinearity in the systems [13] (Fig. 4).

The basic working of MPC can easily be understood by its block diagram. The predicted outputs from prediction block go as input to both process and model after passing through two types of calculations: set-point calculation and control calculation. The process and model blocks both generate their respective output which is compared and the difference is sent as a residual value to the prediction block again. So in this way, the process outputs are analysed and improved and then finally the optimum results are produced. Moreover, in above method we have used MPC for controlling frequency but the flexibility and economic cost are neglected for easiness in study [14]. By using the abovementioned methods of working of MPC, the frequency control of microgrid was implemented. Finally the implementation of microgrid is depicted using below flowchart in Fig. 5.

4 MATLAB/Simulink Model for the Suggested System

In this section, various models are suggested which were implemented in MATLAB/Simulink.

The model in Fig. 6 measures total active power of load and source. It also compares the difference between the two values and checks if demand and supply are in accordance or not.

In Fig. 7, the model is used to measure total reactive power of load and source. Their difference then needs to be compensated by using suitable equipments such as shunt capacitors and SVC.

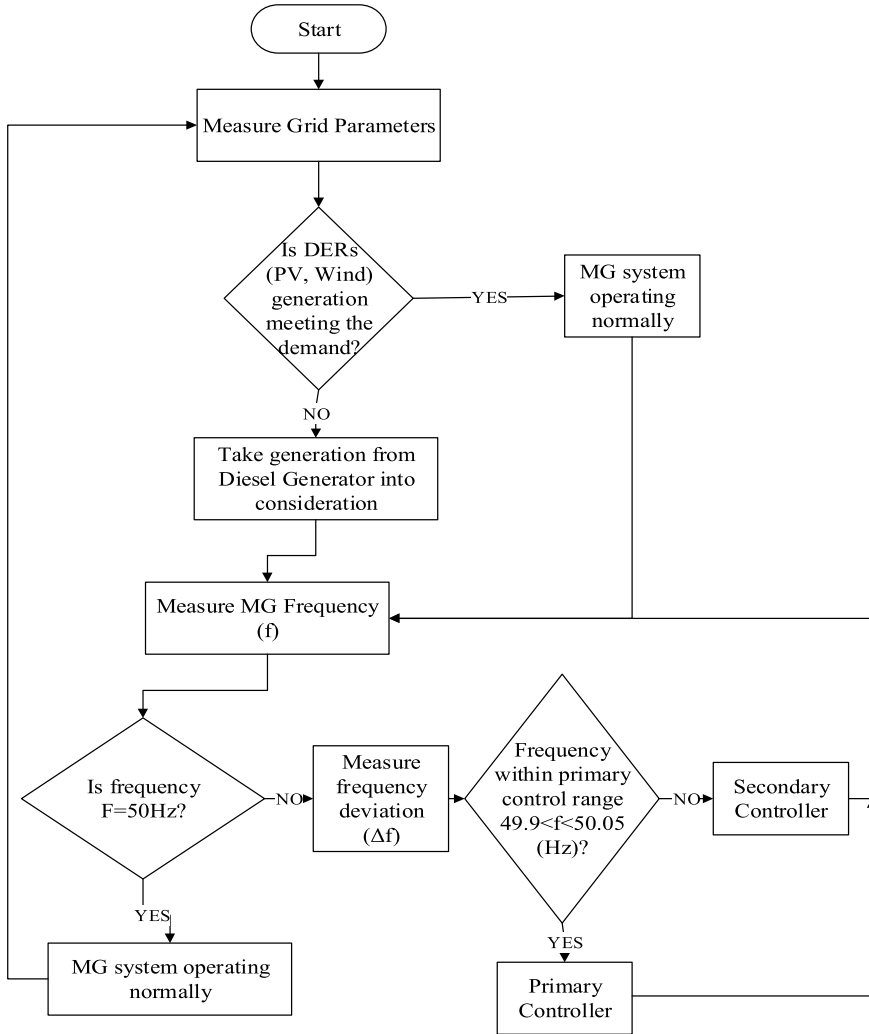


Fig. 5 Flowchart for implementation of microgrid-based system

This setup is used for frequency control of microgrid by using traditional PI controller in Fig. 8. The result obtained is compared with MPC and findings are noted.

Earlier model which has been used above is also shown in Fig. 9 but instead of using PI controller, now we are using MPC, i.e. model predictive controller tool.

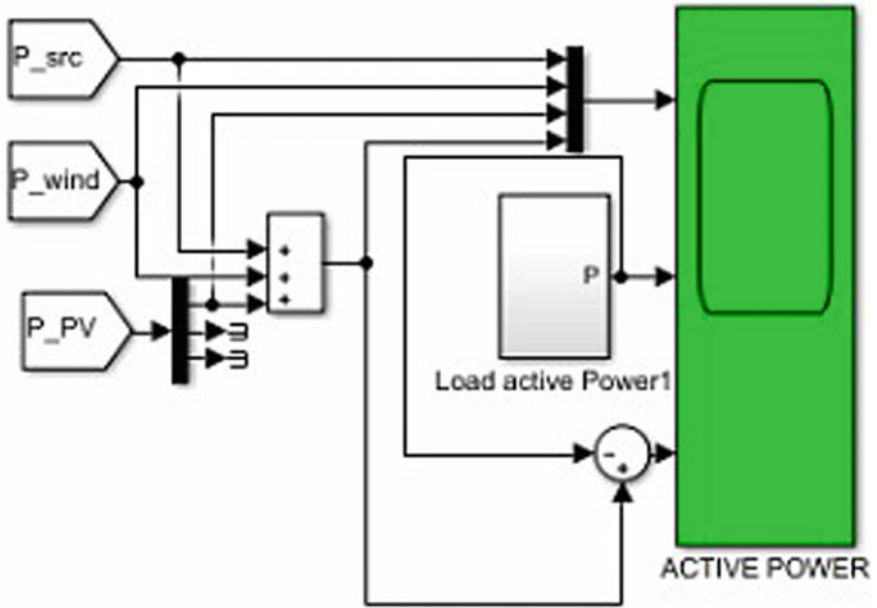


Fig. 6 MATLAB/Simulink model for measuring active power in the microgrid

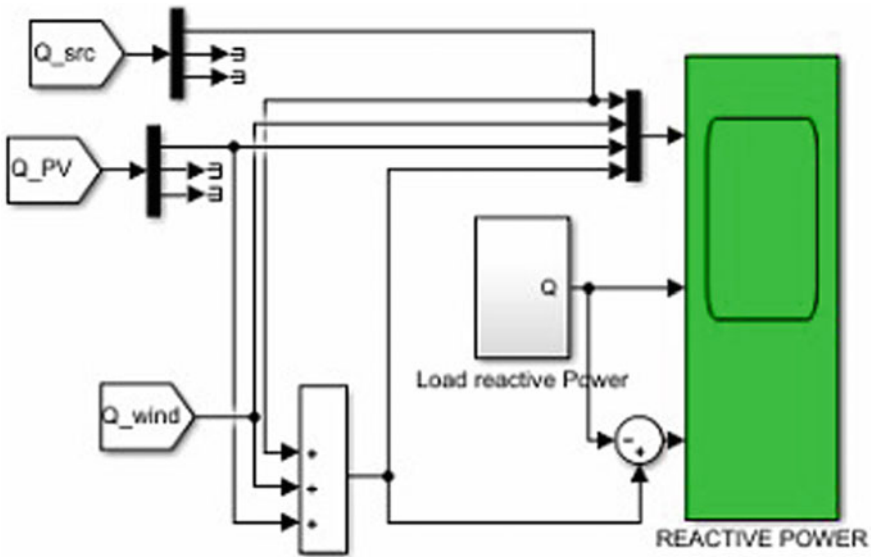


Fig. 7 MATLAB/Simulink model for measuring reactive power in microgrid

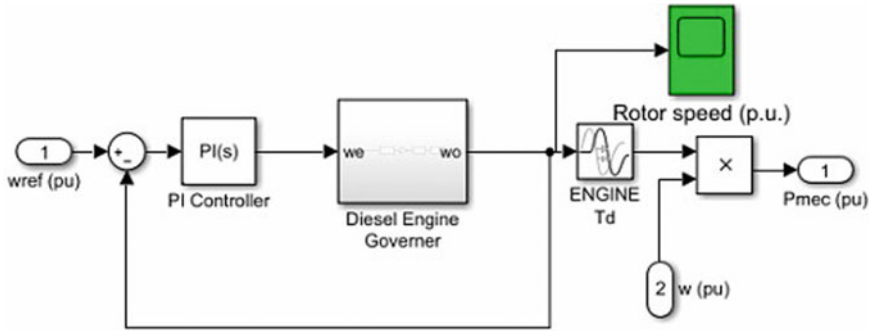


Fig. 8 MATLAB/Simulink model for frequency control of microgrid using PI controller

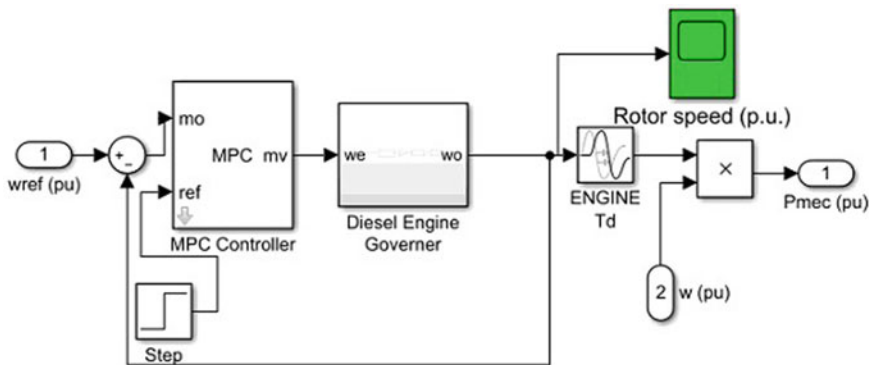


Fig. 9 MATLAB/Simulink model for frequency control of microgrid using MPC scheme

5 Results and Analysis

In this section, the detailed analysis of the results obtained is done.

In Fig. 10, the curve obtained indicates combined power of all sources. On observing graph, we get total active power generated = $[10.5(\text{DG}) + 4.2(\text{PV}) + 4.5(\text{Wind})]\text{MW} = 19.2 \text{ MW}$.

The curve obtained represents the total active power consumed by the loads. Specifically, by observation total active power consumed by load = $[10(\text{Residential}) + 7.8(\text{ASM})] \text{ MW} = 17.8 \text{ MW}$ in Fig. 11.

Figure 12 shows difference between total active power generated and total active power supplied = $[19.2 - 17.8] \text{ MW} = 1.4 \text{ MW}$. Hence, the excess generation is within the 10% limit which can be used as reserve generation for peak load conditions or can also be used for compensating line losses.

As evident DG is handling most amounts as compared to other sources. Mathematically, total reactive power generated = $[6.07(\text{DG}) + 0.15(\text{PV}) + 0.9(\text{Wind})] \text{ MVar} = 7.12 \text{ MVar}$ in Fig. 13.

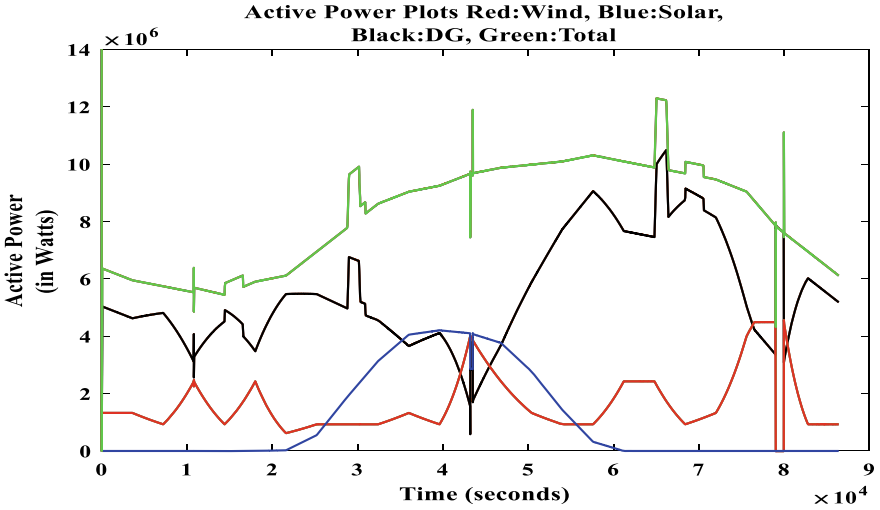


Fig. 10 Active power curve for all sources

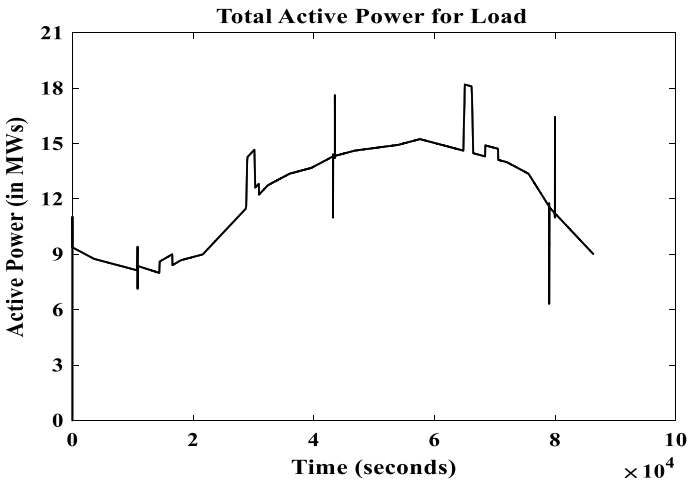


Fig. 11 Active power curve for all loads

In Fig. 14, result shows if sudden increase in load and disturbance occurs then only reactive power requirement is increased, i.e. total reactive power consumed by load = [2 (Residential) + 5.79 (ASM)] MVar = 7.79MVar.

The total reactive power imbalance is of |0.67| MVar {[7.12 – 7.79]MVar}; which can be compensated by placing shunt capacitances of suitable value at the load end as reactive power requirement at load end is more than that being generated at source end in Fig. 15.

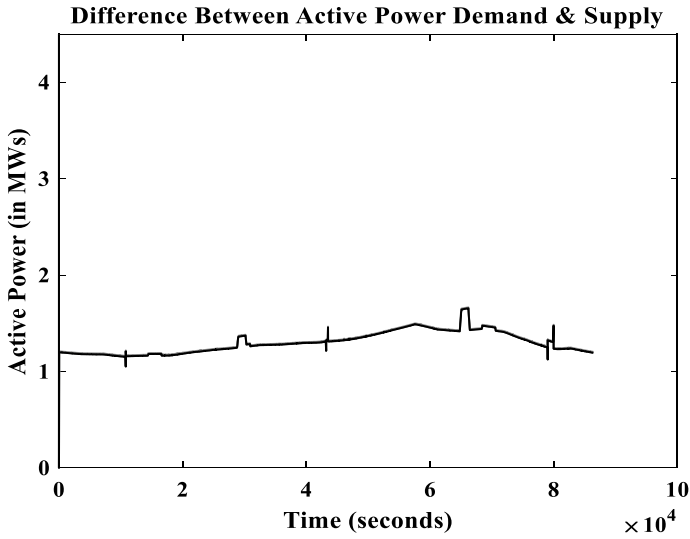


Fig. 12 Curve showing comparison of total active power demand and supply

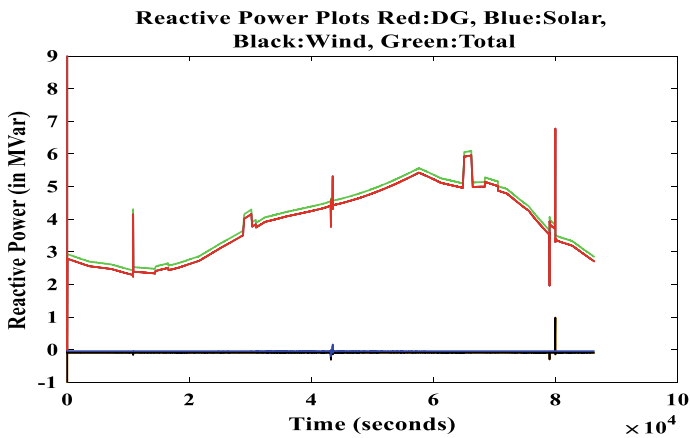


Fig. 13 Reactive power curve (all sources)

Figure 16 is showing the frequency deviation that occurred at the instance of disturbances. The major deviation is due to dip in wind farm generation which occurs because of reduced wind speed.

The Fig. 17 obtained using MPC scheme is shown. Clearly we can see the reduction in peak overshoot, settling time and number of oscillations.

The results obtained above are summarized in Tables 1 and 2.

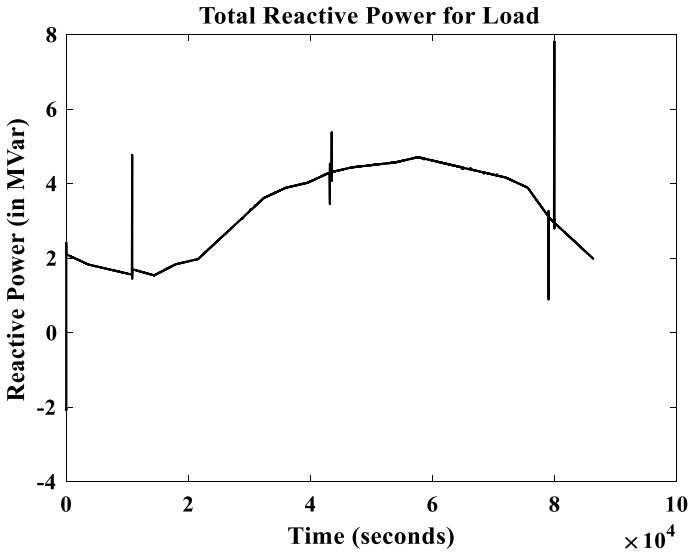


Fig. 14 Reactive power curve for all loads

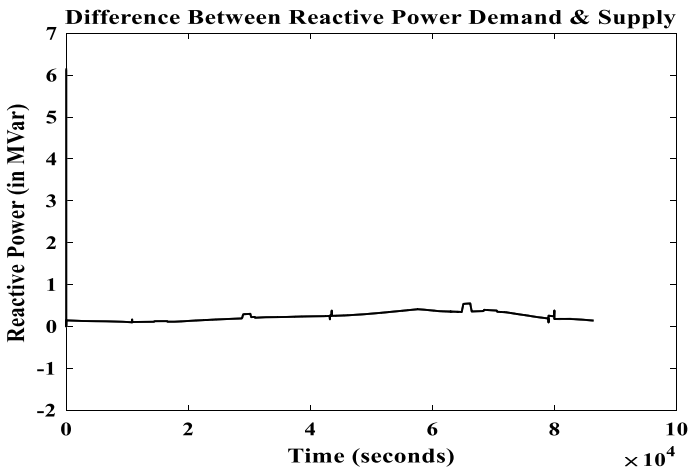


Fig. 15 Curve showing comparison of total reactive power demand and supply

6 Conclusion

The PV and wind units in microgrid are responsible for normal operation but when there is disturbance introduced in the system in the form of partial shading and dip in wind speed, the DG works as a backup supply. Moreover, the dip in frequency due to abovementioned disturbances is handled using PI and MPC-based controllers.

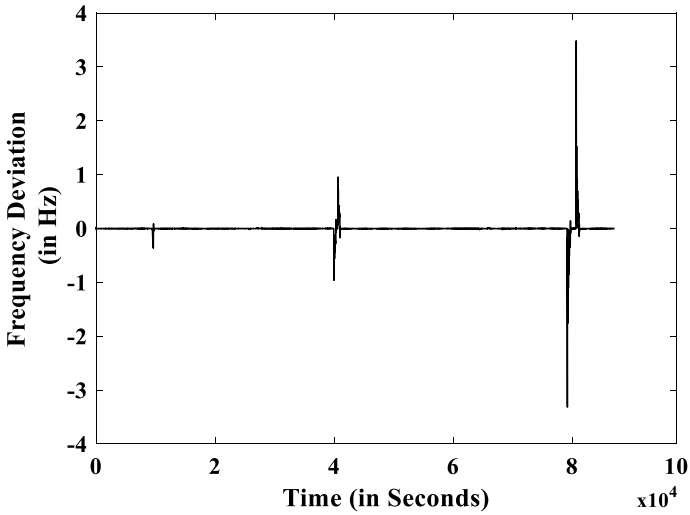


Fig. 16 Frequency deviation curve using PI controller

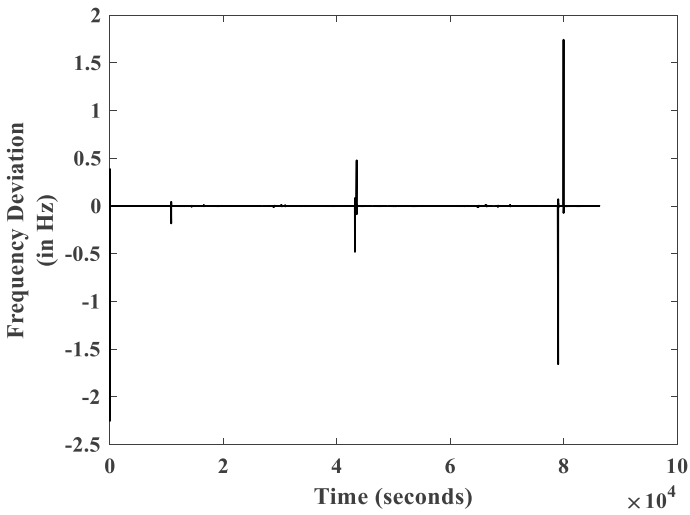


Fig. 17 Frequency deviation curve using MPC

Table 1 Controller response to partial shading

Controllers	Overshoot	Settling time
PI controller	1.02	200
MPC-based controller	0.51	100

Table 2 Controller response to abrupt change in wind speed

Controllers	Overshoot	Settling time
PID controller	3.55	100
MPC-based controller	1.58	50

The results obtained in previous section suggest that the microgrid is capable of meeting its own generation and demand in terms of both active power and reactive power quantities. Based on the tabulated data, it is easy to conclude that MPC not only reduces overshoot but it also reduces settling time in a significant manner as compared to PI controller. Hence, MPC can be used for frequency control of an islanded microgrid having RESs as its prime source.

References

1. Bappy FI et al (2019) Comparison of different hybrid renewable energy systems with optimized pv configuration to realize the effects of multiple schemes. In: 1st International conference on advances in science, engineering and robotics technology. Dhaka, Bangladesh, 3–5 May 2019
2. Aboukheili MG, Shahabi M (2020) Seamless transition of microgrids operation from grid-connected to islanded mode. *IEEE Trans Smart Grid* 11(3)
3. Qadir Z et al (2018) Smart solar micro-grid using ZigBee and related security challenges. In: 18th Mediterranean microwave symposium. Istanbul, Turkey, 31 Oct.–2 Nov. 2018
4. The J et al (2017) Maximization of wind energy utilization through a multi-objective optimization framework. In: IEEE region 10 conference TENCON-2017. Penang, Malaysia, 5–8 Nov. 2017
5. Xu J, Cao X, Hao Z (2019) A droop control strategy based on synchronous rectifier to modulate the frequency and voltage in AC microgrid. In: 22nd International conference on electrical machines and systems. Harbin, China, 11–14 Aug. 2019
6. Zobaa AF, Cecati C (2018) A comprehensive review on distributed power generation. In: International symposium on power electronics, electrical drives, automation and motion. Taormina, Italy, 23–26 May 2018
7. Barik AK, Das DC (2018) Expeditious frequency control of solar photovoltaic/biogas/biodiesel generator based isolated renewable microgrid using grasshopper optimization algorithm. *IET Renew Power Gener* 12(14)
8. Nguyen XH, Nguyen MP (2018) Mathematical modeling of photovoltaic cell/module/arrays with tags in Matlab/Simulink. *Environ Syst Res* 4(24)
9. Ouyang J et al (2019) Active voltage control for DFIG-based wind farm integrated power system by coordinating active and reactive powers under wind speed variations. *IEEE Trans Energy Convers* 34(3)
10. Pengfei L et al (2018) Wind turbines with DFIG participate into primary and secondary frequency control by suboptimal power tracking method. In: IEEE 7th International conference on power and energy (PECon). Kuala Lumpur, Malaysia, 3–4 Dec 2018
11. Hassan H et al (2017) Simulation of directly grid-connected wind turbines for voltage fluctuation evaluation. *Int J Appl Eng Res* 2(1)
12. Teawnarong A, Chirapongsananurak P (2020) Providing frequency response in isolated microgrids using battery energy storage systems. In: 8th International electrical engineering congress. Chiang Mai, Thailand, 4–6 March 2020

13. Bayhan S, Abu-Rub H (2019) Model predictive control for parallel connected three-phase four-leg inverters in islanded AC microgrids. In: IEEE 13th international conference on compatibility, power electronics and power engineering. Sonderborg, Denmark, 23–25 April 2019
14. Xiaobing K et al (2019) Hierarchical distributed model predictive control of standalone wind/solar/battery power system. IEEE Trans Syst Man Cybernet Syst 49(8)

Islanding Detection Scheme for Single-Phase Grid-Connected Solar Photovoltaic System using Support Vector Machine



Jyoti Sagar, Omveer Singh, and Shabana Urooj

1 Introduction

The rapidly falling costs of PV production have led to the development of PV energy production systems in recent decades. This makes PV energy one of the very favorable renewable energy options in distribution generation. As the supply of fossil fuels decreases and greenhouse gases increase, the production of distributed electricity has become increasingly important over the last few years. Distribution generators have greatly contributed to improving the efficiency of clean energy through the use of clean energy, such as solar, wind, and biogas [1]. However, in addition to providing various benefits, DG systems also present certain related problems, such as frequency changes, voltage fluctuations, harmonics distortion, natural islands, or unplanned islands. The DG unit is called voltage control (grid-forming) and current control (grid-following) in the microgrid network. Generally, DG units are operated as grid-following in grid-connected operation, while they are operated as grid-forming in islanded operation [2].

Modern control and security techniques are not enough capable of handling electrical power transfer and controlling multiple parallel operations. By using power distribution, power generation will effectively minimize the impact on the environment, improve power protection, and reduce electrical load during peak hours. However, when using DG, working on the island is the most serious problem. Island mode in a DG situation is once the network is disconnected from the local load, energy will continue to be supplied to the local load [3]. For IEEE 1547, islanding is a situation in which the components of the service system, including power supplies and distributed loads, remain energized even if they are disconnected from the service system.

There are two island modes, intentional or unintentional, also known as planned or unplanned islands. Intentional islands deliberately isolate part of the network during

J. Sagar · O. Singh (✉) · S. Urooj
Electrical Engineering Department, Gautam Buddha University, Greater Noida, India

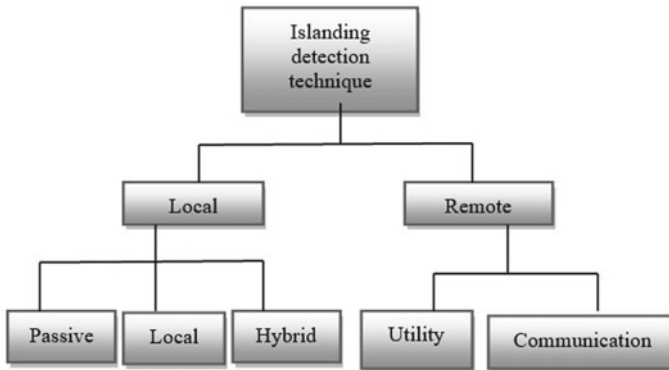


Fig. 1 Block diagram of an islanding detection method

failures and interruptions, and continuous power supply can be designed to meet the load demand [4].

Last decade anti-islanding algorithms and techniques for detection were developed. Such techniques are classified into two groups, namely local and remote islanding detection techniques. The local method is based upon measuring certain parameters or variables (voltage, current, and frequency) on the terminals of the distributed generator. The remote detection method is suitable for communication among the utility grid and the service system.

Several advanced machine learning techniques are introduced to detect islands. Here, we propose a support vector machine pattern recognition approach. The main objective in this paper is to precisely detect and classify the conditions of the islands using support vector machine (SVM).

2 Islanding Detection Method

The methods of detecting islands generally divided into two groups [4–6]: (i) local method and (ii) remote method based on location in the DG system, as shown in Fig. 1. The local method is mainly a traditional method, while the remote method is based on new technology involving technology. The communication and a few additional types of equipment have been implemented.

3 Description of Grid-Connected System

The grid-connected PV systems are a familiar and most prominent component of renewable solar energy. To successfully introduce this technology, there must be

sufficient excellence certification and network standards. These standards have been developed to make PV systems connected to the entire network steady, efficient, and safe to operate.

The different IEEE and IEC standards of the system linked to the network are tabulated in Table 1 [7].

The detection methods for islanding condition have been proposed, and the authors designed a grid-connected distribution network which consists of a PV system using a MATLAB/Simulink platform as shown in Fig. 2.

The proposed system contains PV strings, boost converter inverter, filter transformer, and the grid. The PV energy generation grid interconnection method has the benefit of making extra efficient use of generated power. The PV network grid interconnections are achieved via the inverter, which converted the PV module, generated direct current (DC) into alternating current (AC) by the utilization of ordinary electrical equipment. The technology of inverter is very essential for stable and safe grid interconnection.

Table 1 Standard description for grid-connected system

Standard description	Standard codes
Environmental testing	IEC 60068-2 (1,2,14,30)
Product safety standards	IEC-62109-1 (2010) IEC-62109-2 (2011)
Efficiency measurement	IEC 61683:1999
Grid-connected standards/utility interface	IEC 61727:2004
Test procedures for islanding prevention measures for utility-interconnected PV inverter	IEC 62116:2008 OR IEEE 1547 and IEEE 1547.1
Ingress protection	IP 65(or outdoor)/IP 21(for indoor) As per IEC 529

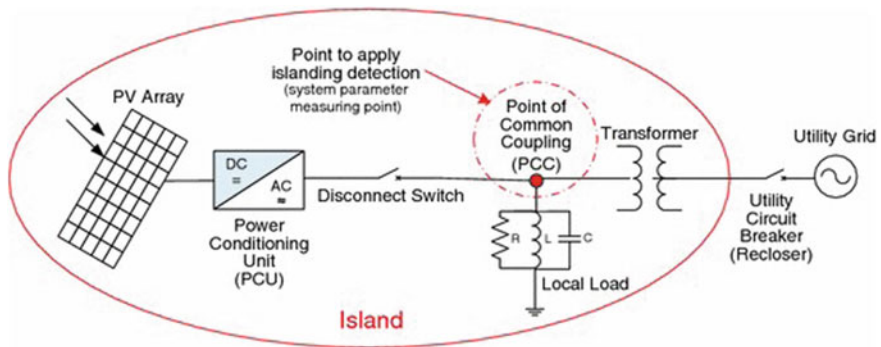


Fig. 2 Grid-connected PV system

To decrease the harmonics of the output current, a filter is necessary between the voltage source inverter (VSI) and the network. Simple inductors in series can be used, but the harmonic attenuation is not very obvious. Similarly, to implement a high voltage drop, the inductance required in the design is very voluminous. Typically, a high-order LCL filter is used in place of the traditional L filter to smooth the output of the VSI. The reduction in the all-inclusive mass and size of the components, LCL filters can be used to achieve greater attenuation and cost savings. LCL filters are used in grid-connected inverters and active pulse width modulation rectifiers, as they can reduce the quantity of current distortion pumped into the distribution network. The higher harmonic attenuation of the LCL filter makes it possible to use lower switching frequencies to fulfill the harmonic limits established by the IEEE-1547 standard.

The PV system faults can be classified into the AC side and the DC side of the network. AC failures include complete power failures, network outages, and inverters, while PV and maximum power point tracking (MPPT) panel failures are DC side failures. The frequency changes, voltage changes, harmonics, and power mismatch are few of the variations that cause the islanding situation in a grid-connected PV system. These changes can be detected using advanced machine learning technology in this paper which is SVM.

4 Islanding Detection in the Microgrid

The current and voltage are measured from different microgrids locations to make sure that the grid was functioning in a protecting situation in Fig. 3.

In this paper, in the incident of a fault that happens on the grid side, the voltage variation will be seen at the common coupling point (PCC) which is the interface

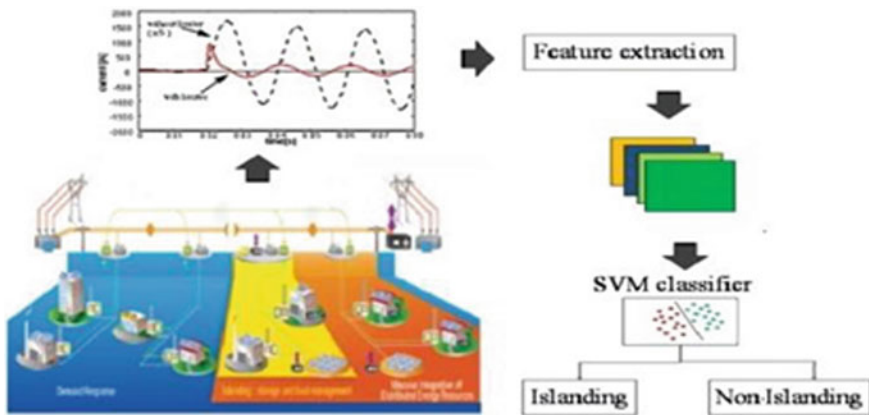


Fig. 3 Basic diagram of the proposed system [8]

among the power supply and the load. The normal operation of systems connected to the grid, fault impedance, frequency variance, grid synchronization, harmonics, power mismatch, and grid-side voltage drop are various types of classes used for the algorithm development. The discrete wavelet transform is utilized to extracting the different features corresponding to the decomposition voltage output of the seven operating conditions and faults. Based on these extracted features, the feature SVM classifier can detect the island conditions and not the island conditions in the microgrid.

4.1 Wavelet Transform

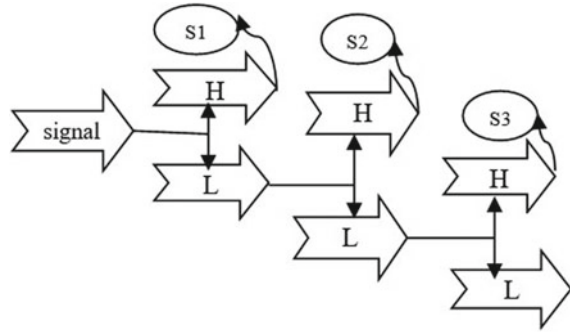
Wavelet-based transformation technology (WT) is used for island detection. By dividing the wavelet into several components, it can be designed to define signals in various frequency bands in a localized time and frequency layout. The WT is an effective and fast way for analyzing transient voltage and current signals. The WT has been used in many power system applications, such as fault detection, feature extraction, noise cancelation, and compression of waveform data. The voltage of the negative signal and the current signal is processed into wavelet transforms. Find out the standard deviation of wavelet coefficients and energy changes to detect island events from non-island events. Generally, for island events, the standard deviation of the negative sequence impedance is observed. The calculated distributed generator power output is applied to the WT and the decomposed signals are used to identify the islands [9].

4.2 Discrete Wavelet Transform

By following the high-pass and low-pass filters, the discrete wavelet transform is utilized to extract features of decomposed signals. Discrete wavelet transform (DWT) analyzes the signal by breaking it down into rough approximations and a detailed coefficient. The approximation coefficient is further subdivided to obtain the specifications for the next step and so on [10]. Figure 4 shows the three-level decomposition of the input signal, resulting in the wavelet coefficients of every level of the input signal. The mathematical expression for the DWT is as follows:

$$X[\emptyset, v] = \frac{1}{\sqrt{v}} = \sum_{t=-\infty}^{\infty} x[t]w\left[\frac{t-\emptyset}{v}\right] \quad (1)$$

Fig. 4 Decomposition of signals



where $x[t]$ = the signal to be analyzed, $w[t]$ = chosen wavelet, and v = velocity and t and are scale and shift parameters, respectively.

Feature Extraction

The output signal is preprocessed by transforming into discrete wavelets. Displays usable characteristics of the decomposed signal, such as energy, entropy, peaks, power, signal-to-noise ratio, harmonic, skewness, and kurtosis that change quickly when disconnection of the DG from the utility grid happens. And, all the listed features support test classifier to detect islands. The transient voltage signal is used to extract the feature vectors necessary for classification. The mentioned features are extracted with the help of mathematical equation which is given below:

The energy of the decomposed signal:

$$E = \int_{-\infty}^{\infty} |S(t)|^2 dt \tag{2}$$

where $S(t)$ = reconstructed signal.

Entropy: it is used to determine the wavelet type which is suitable for decomposing and reconstruction of a given signal.

$$H(s) = - \sum_{i=1}^N p(S) \lim_{i=10} p(S) \tag{3}$$

where $p(s)$ = probability of the voltage signal samples, N = the number of samples, S = reconstructed sample signal.

The peak-to-peak value of the reconstructed signal is given by,

$$S_{PP} = 2\sqrt{2}\sigma \tag{4}$$

where σ is the standard deviation.

The Power of the reconstructed signal is given by,

$$P = \lim_{N \rightarrow \infty} \frac{1}{2T} \int_{-T}^T |S(t)|^2 dt \quad (5)$$

Signal-to-noise ratio (SNR) is defined as a ratio of signal level to the noise level and is given by,

$$\text{SNR} = \frac{\text{Reconstructed Signal}}{\text{Original Signal}} \quad (6)$$

Total harmonic distortion: The equation is given by,

$$y(t) = a_0 + \frac{a_2}{2} + \frac{3a_4}{8} + \left(a_1 + \frac{3a_3}{4} + \frac{10a_5}{16} \right) \sin w_0 t - \left(\frac{a_2}{2} + \frac{a_4}{2} \right) \cos 2w_0 t - \left(\frac{a_3}{4} + \frac{5a_5}{16} \right) \sin 3w_0 t + \frac{a_4}{8} \cos 4w_0 t + \frac{a_5}{16} \sin 5w_0 t \quad (7)$$

where a_i = coefficient of the Taylor's series.

Skewness: It refers to a lack of symmetry, allowing one to define the shape of the distribution data with the help of this function,

$$S = \frac{\frac{1}{N} \sum_{i=0}^N (S_i - \mu)^3}{\left(\sqrt{\frac{1}{N} \sum_{i=0}^N (S_i - \mu)^2} \right)^3} \quad (8)$$

Kurtosis: It refers to the pointedness of a peak in the distribution curve.

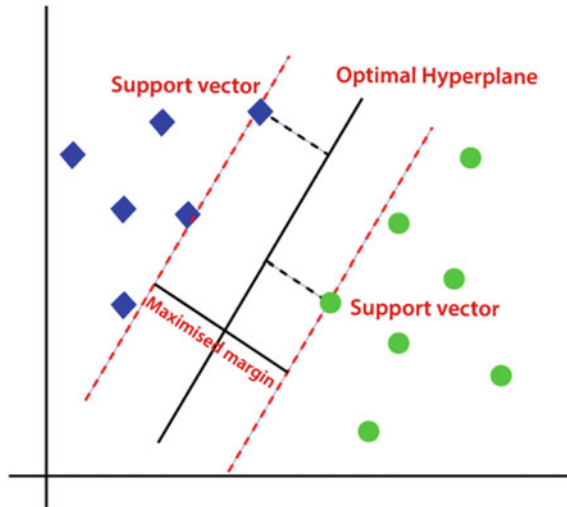
$$K = \frac{\frac{1}{N} \sum_{i=0}^N (S_i - \mu)^4}{\left(\sqrt{\frac{1}{N} \sum_{i=0}^N (S_i - \mu)^2} \right)^4} \quad (9)$$

4.3 Support Vector Machine

SVM is a popular classification method that can be used to analyze signals and systems by building conclusion restrictions to separate the data required for training purposes [11]. The SVM classification technique is utilized to extract the main feature from the calculated point of common coupling voltage and current signals with the help of a DWT [12].

In this case, the hyperplane is called the optimal hyperplane. The SVM classifier is used for the reason of generating a data model during the training process. The model will predict class labels during the testing phase and will only use entity

Fig. 5 Optimal hyperplane of support vectors



attributes as input. The optimal hyperplane is described as a linear decision function and the maxi. The gap between the two types of vectors of different categories is shown in Fig. 5 [8]. It has been found that only a tiny quantity of training data (called support vectors) needs to be taken into account to create these optimal hyperplanes. In general, the higher the margin and lower the general error of the classifier.

4.3.1 SVM Classification Process

The support vector classifier is executed in two phases: the training phase and the test phase.

Figure 6 shows the feature extraction, normalization, and process of classification is performed in our presented SVM technique and parameters are in Table 2.

Every probable feature linked to the faulty circumstances of the simulated model of the PV systems connected to the grid is extracted from the equations. After extracting all the attributes, tab them with their relevant fault categories to generate the trained datasets. First, the SVM classifiers are trained offline to have features related to a variety of island cases and non-island cases. The SVM classifiers distinguish the categories by developing the hyperplane limits between the two categories according to the extracted entities. Contribution to SVM is a matrix of predicators and responses. The response corresponds to the class array specified with labels, and the predicators correspond to the feature extracted from the different conditions of fault. The trained dataset is used to predict or classify the data. At last, trained data is available with a 98% training and validation rate.

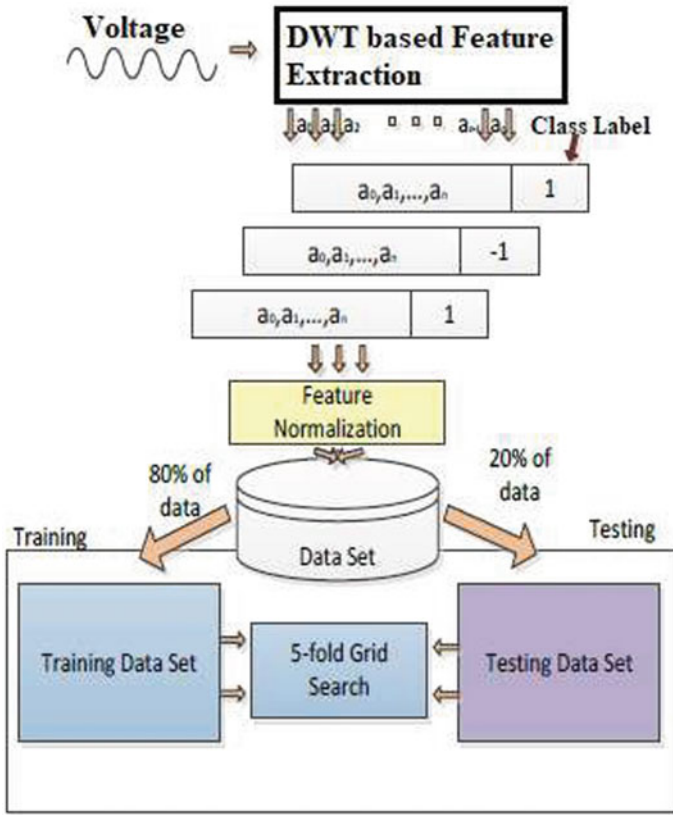


Fig. 6 Process for extracting features and SVM method execution [5]

Table 2 SVM parameters

Model type	Parameters
Preset	Support vector machine
Kernel function	Quadratic
Kernel scale	Automatic
Box constraints level	1
Multiclass method	One-vs-One
Standardized data	True

5 Results and Analysis

A power supply of 432 V, 50 Hz is DG and then attached to the full-bridge insulated gate bipolar transistor (IGBT)-H-based inverter. The inverted voltage is associated with the network and supplied to the load linked to the network. The examination

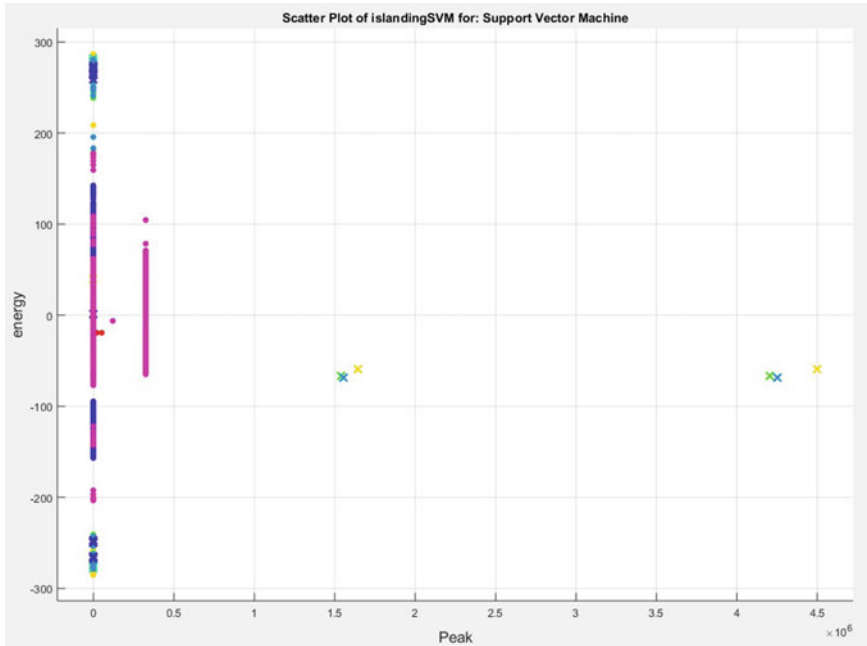


Fig. 7 Scatter plot among several predictor set

of the grid-connected system of the connection line Table 1 is used to produce simulations related to island detection. SVM detection method is proposed by the use of MATLAB/Simulink software.

The quadratic SVM appeared to be the much more appropriate method to trained the table samples of data. Figures 7, 8 and 9 portrayed different plots relating to the training cycle.

A scatter plot utilizes points to symbolize the values of two dissimilar numeric variables. The location of every point on the horizontal and vertical axes denotes the value of a single data point. Scatter plots are used to analyze variable relations. A scatter plot shows to what extent a variable is affected by other variables. Figure 7 shows several interconnections with a confidence period between variable 1 (energy) and variable 2 (peak).

The confusion matrix displays the total number of samples across every cell. Diagonal cells relate to correctly and remaining cells relate to incorrectly classified samples. It helps in determining the classifier’s output in each case. It supports the idea that, whether the classifier is incorrectly performed in the identification of a class or all classes are correctly classified. The confusion matrix is an outline of the estimated result on a dilemma of classification. This graph of the confusion matrix shows the prediction efficiency of various islanding issues.

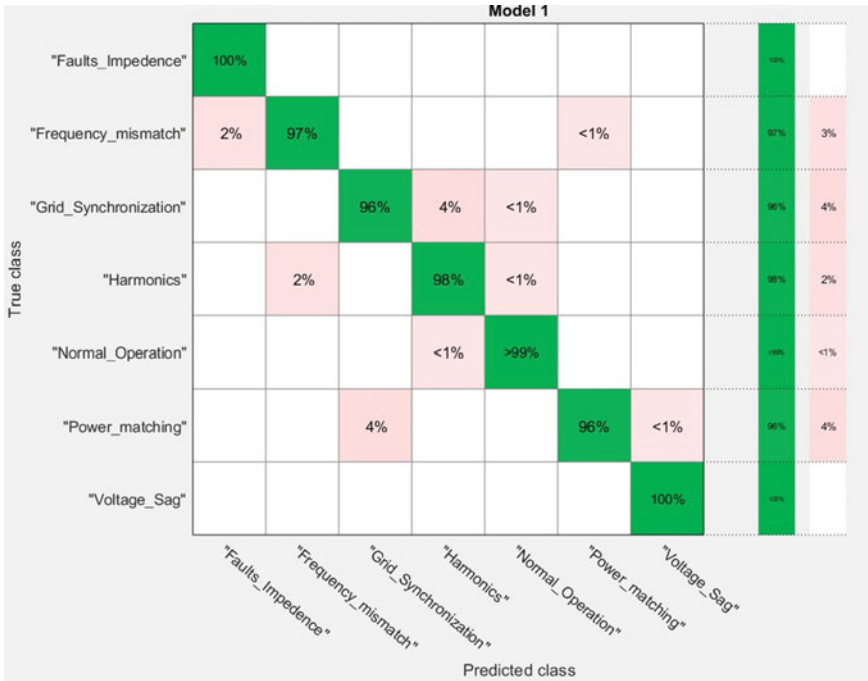


Fig. 8 Confusion matrix for trained classifier and validation procedure

The receiver operating characteristic (ROC) curve is a graphical diagram showing the diagnostic capacity of the binary classifier. The ROC curve is utilized to graphically display the link/compromise between experimental sensitivity and specificity for every achievable wound off value for one test or several tests. It can be seen in Fig. 9 that all categories are closed near the left and upper boundaries of the ROC space, giving the procedure of train and test is the most correct. In a given ROC hardening, a certain category is the fault impedance. In this work, the unknown data is tested for the categorization effectiveness of the proposed scheme. The training speed, predicate velocity, training and test time are listed in Table 3.

6 Conclusion

The major problem of the DG, namely the islanding, is concentrated in this paper and a new efficient detection technique is projected. The identification of the island in the DG is identified by identifying the pattern recognition for the voltage signal calculated in the PCC. WT is used to extract voltage features in various network issues, and then that extracted features are given to the SVM classifier as input to determine if the system is an islanded or not. Since the calculated voltage value is used

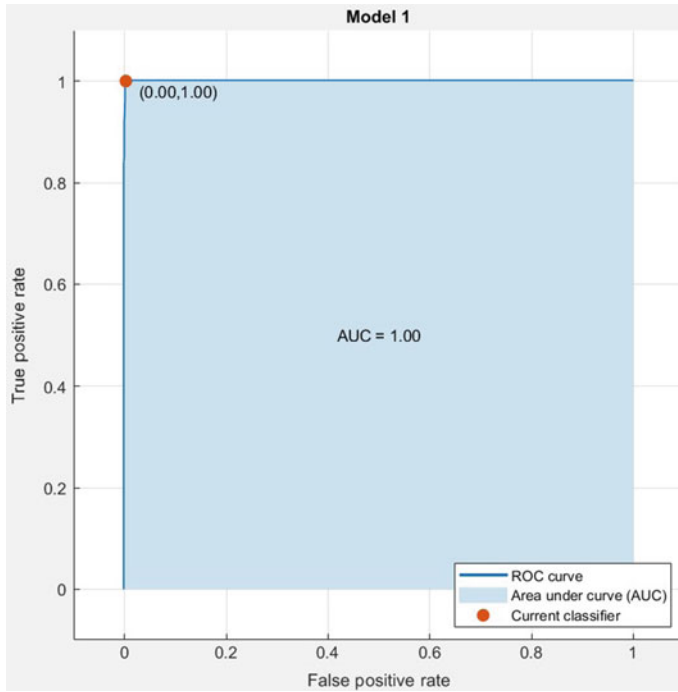


Fig. 9 ROC of the trained classifier

Table 3 Training and testing results of SVM

Parametric status of the system	
No. of samples	4526
Training samples	80% of the total samples
Validation type	Cross-validation
Validation sample	5-fold grid explore from trained samples
Testing samples	20% of the test samples
Overall accuracy	98.6%
Prediction speed	Nearly 25,000 obs/s
Training time	4.5 ms
Testing time	5 ms

to extract the characteristics of the wavelets, it will not affect the quality of the power supply to the inverter. The results of the simulation show that our suggested method successfully detects and classifies the current island state with great robustness and is sensitive to interference from the exterior network, from component switching

malfunction to network malfunction. From the results, it can be determined that the overall accuracy of island detection is 98.6% with is 4.5 ms.

Simulation parameters: PV array: $P_{\max} = 3500$ W, 1 string, 14 series-connected module, $V_{oc} = 37.6$ V, $I_{sc} = 8.55$ A (per module).

Normal grid amplitude: $V_{\text{grid}} = 239.1$ (RMS), $I_{\text{grid}} = 14.34$ (RMS).

Normal grid frequency: $f = 50$ Hz.

LCL filter: $L_1 = 4.366$ mH, $L_2 = 4.366$ mH, $C = 29.42$ μ F.

Sample times: Control system = 26.45 μ s, PWM generator = 1.322 μ s.

DC voltage: $V_{dc} = 432$ V.

Parasitic capacitance: $C_p = 4$ nF.

Filter damping resistor: $R_d = 32.92$ m Ω .

References

1. Guerrero JM et al (2010) Distributed generation: toward a new energy paradigm. *IEEE Ind Electron Mag* 4(1):52–64
2. Han H, Hou X, Yang J, Wu J, Su M, Guerrero JM (2016) Review of power sharing control strategies for islanding operation of AC microgrids. *IEEE Trans Smart Grid* 7:200–215
3. IEEE Application Guide for IEEE Std 1547 (2009) IEEE standard for interconnecting distributed resources with electric power systems. *IEEE Std 1547.2-2008*, pp 1–207
4. Virginia Tech (2007) Consortium in energy restructuring: introduction to DG and intentional islanding. [Online]. Available: <https://www.dg.history.vt.edu/ch3/islanding.html>
5. Lakshmanan SA (2018) Islanding detection for grid connected solar PV system. In: 8th IEEE India international conference on power electronics. NIT Jaipur, 13–15 Dec. 2018
6. Drews et al (2007) Monitoring and remote failure detection of grid-connected PV systems based on satellite observations. *J. Solar Energy* 81(4):548–564
7. BESCL Office (2014) Procedure for empanelment of grid tied inverter manufacturers for implementation of SRTPV electricity generation program in general instructions for empanelment of grid-tied inverter manufacturers
8. Savitha S, Kayalvizhi N (2016) The support vector machine technique for islanding detection in distributed generation. *Int J Adv Res Electr Electron Ind Eng* 5
9. Pigazo M, Liserre R, Mastromauro A, Moreno VM, Aquila AD (2009) Wavelet-based islanding detection in grid-connected PV systems. *IEEE Trans Ind Electron* 56(11)
10. Sharma R, Singh P (2012) Islanding detection and control in grid based system using wavelet transform. In: IEEE 5th power India conference. DCRUT, Murtal, Haryana, 19–22 Dec. 2012
11. Hamidef B, Shekholeslamzadeh M (2012) A novel SVM approach of islanding detection in microgrid. In: IEEE innovative smart grid technologies conference. Washington DC, USA, 16–20 Jan. 2012
12. Matic-Cuka B, Kezunovic M (2014) Islanding detection for inverter based distributed generation using support vector machine method. *IEEE Trans Smart Grid* 5:2676–2686

Thermal Imaging-Based Fault Diagnosis of Electronics Circuit Boards



Laxmi and Rajesh Mehra

1 Introduction

Due to the significant increase in complexity of electronic circuits as the core of modern digital circuits, has substantially improved the semiconductor integration level production by generation. With technology scaling, the very large-scale integrated circuits density has grown exponentially [1, 2]. This leads to increase the manufacturing defects in circuits and as resulted several reliability problems such as instance manufacturing defects, power dissipation limits and parametric variations. These threats can effect correct program execution which is the most significant aspect of any computer system. Therefore, testing of a digital circuit becomes imperative, particularly in integrated circuit technologies [3, 4]. Traditionally, testing approaches for these electronic circuits includes visual inspection, characteristics test, signal analyzer which consume a lot of time-handling issues. Due to voltage drop, the defected components like transistor, diode, and integrated circuits that create a hot spot will stay invisible [5]. To overcome these issues and enhance the quality of circuits, the non-invasive methods like TI come into picture. TI is widely accepted non-destructive testing and evaluation (NDT&E) approach for evaluation and testing of component in the field of integrated circuits technology. Consequently, the overheated components can lead to subsequent failure of electronics boards that create fire hazard and unplanned outages. Moreover, thermal anomalies have been created due to poor component installation poor or loss connections, unbalanced current distribution, short circuits, etc.

Laxmi (✉) · R. Mehra

Department of Electronics and Communication Engineering, National Institute of Technical Teachers Training and Research, Chandigarh 160019, India

2 Thermal Imaging as a Diagnosis Tool

Thermal imaging is very common, and due to its remarkable properties viz. has received significant attention from NDT&E community. It is the method of region inspection which is non-destructive, non-contact, quick, and comprehensive. TI measures the emission of radiant heat across the sample element and monitors fluctuations in temperature and relative humidity using thermal imaging camera TI has a wide range of applications including electrical [6], mechanical [7], agricultural [8], defense [9], aviation [10], geological [11], automotive [12], and medical [13]. IRT is roughly divided into two categories: the passive and active approaches to thermography, taking the measuring methods into account. The passive thermal imaging approach requires no external heating elements, whereas the active thermal imaging includes an external heating element such as physical, hydraulic, gravitational, or other means of excitation to improve the thermal contrast. With the integration of image processing and artificial intelligence techniques, TI is more efficient and can be used to build an autonomous framework for industrial use as discussed in [14]. In [15], a fault detection approach has been implemented for electronics circuit board using vector quantization and Hopfield neural network based on thermal images. Finite element model (FEM) has been applied for analysis of the thermal behavior of circuit boards with variation width of copper and amount of current [16]. ANSYS software is used to enhance the reliability of thermal behavior analysis based on thermal images of circuit boards. Furthermore, thermal images were captured and region of interest was extracted using segmentation, and finally, comparative analysis was done between adaptive neuron-fuzzy inference systems (ANFIS) and SVM [17]. Temperature is the most common parameter used as a parametric test that can be observed for ICs in various scenarios, while thermal imaging is a temperature measurement process that detects invisible infrared radiation and converts energy from visible light into an electrical signal. The thermal imaging technique is a technique which is completely non-contact. Since component images are difficult to access physically, they can be scanned with thermal technique. Thermal test methods may be characterized as a measuring temperature for detecting structural defects in an IC.

3 Experimental Setup and Data Acquisition

The very first task starts at the image acquisition process. The FLIR P-640 thermal imaging camera has been used to capture thermal images of different circuit boards of electronic components. The experimental setup has been shown in Fig. 1, a thermal image of resolution of 640×512 pixels, operating in 8–14 μm range in standalone or PC-controlled mode which can detect temperature differences down to 0.05 $^{\circ}\text{C}$ with an uncooled microbolometer (amorphous silicon, a-Si) features 17- μm pixel pitch

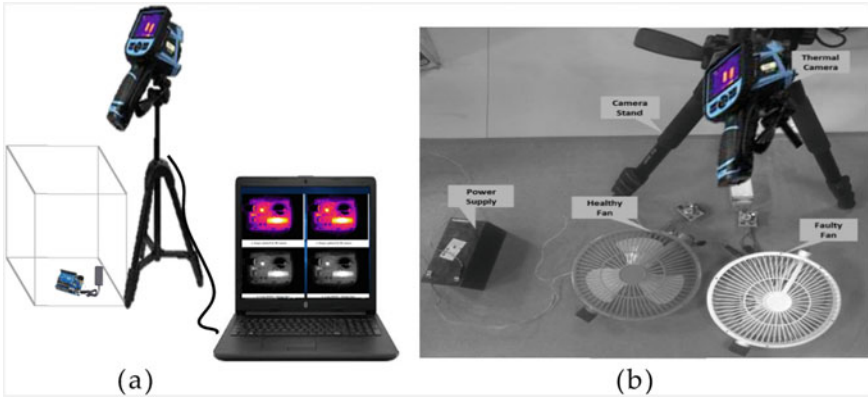


Fig. 1 a Experimental setup with two electrical table fans b thermal image without power supply and c thermal image with power supply

with >99% pixel operability have been used for capturing the thermal response of the electronics components of the fan circuit board. The maximum-rated current of the electronic component was determined in both healthy and faulty conditions. In order to faulty boards, which is overload condition of circuit boards; it was imposed on switch board by increase the input current until it exceed the rated current value. By doing so, the current value reaches at maximum. The experiment has been performed with two circuit boards of DC table fans and Arduino Uno boards in both the conditions, i.e., healthy and faulty.

4 Experimental Setup and Data Acquisition

The failure of any electronics circuit board equipment, such as circuit of DC table fans, Arduino Uno, could be caused by insulation or short-circuit faults or any other component damages. Initially, electronic components damages are by far the highest possibility cause of component failures. Consequently, this study focuses on the detection of electronics components of circuit faults in the circuit boards of fans and Arduino Uno. In both the cases, two electronic circuits of each equipment or boards are used; one is in working (healthy) condition, and another one is non-working (faulty) condition. Experimental setup for proposed methodology is shown in Fig. 1. The proposed methodology has five parts (i) thermal image collection, (ii) preprocessing of raw thermal image, (iii) extracting the RoI, (iv) feature extraction and feature selection, and (v) finally, the optimal features are given to SVM to classify the faulty and healthy condition of circuit board. The flow diagram of proposed methodology is illustrated in Fig. 2.

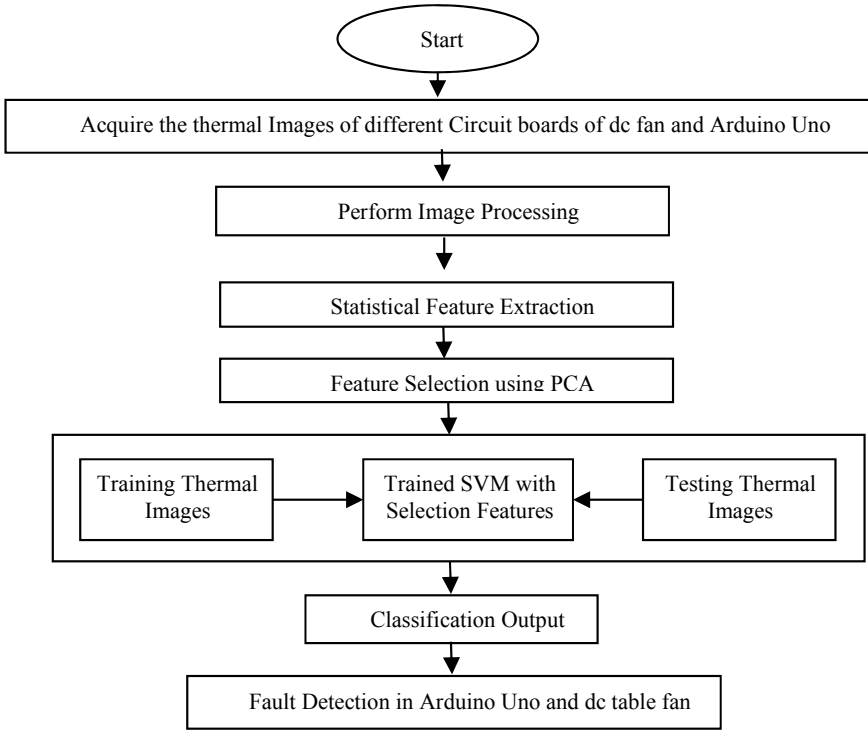


Fig. 2 Flowchart of proposed methodology

4.1 Discrete Wavelet Transform

DWT is a few of the best decomposing processes approach and gives outstanding output [18]. It is able to undertake frequency as well as time domain multi-resolution evaluation. DWT separates information into different frequency bands and analyzes each portion with a comparable resolution of its size. At each step, a two-dimensional DWT decomposes an image and provides four sub-band images consisting of one approximation and three detailed coefficients, as seen in Fig. 4. This procedure explores in both ways, i.e., row and column wise, independently. Next, a high-pass and low-pass filter is implemented for either row information to get the low- and high-frequency information throughout the row and column and instead downsampled by 2. Both the filterings are first added to the column, instead downsampled by 2. Four sub-band images are then replicated: three sub-images of the coefficient (HL, LH, and HH) as well as low-resolution sub-images (LL) (Fig. 3).

Through sub-band picture does have its own feature, because as components of high frequency occur throughout the detailed coefficients, i.e. Bands from HH, HL, and LH. In the LL band, that further decomposed in the same manner during the next step of sub-band image decomposition, that low frequency portion is located. The

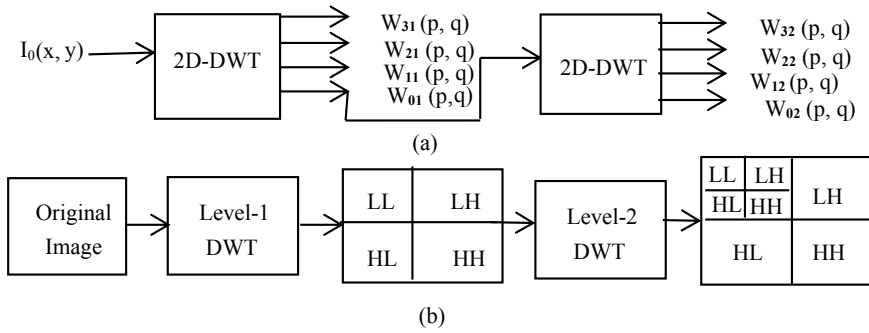


Fig. 3 Two-level 2D DWT **a** sub-bands functional diagram, **b** wavelet sub-bands block diagram

scale of the raw image (I_0) at $k = 0$ can be specified by $2k = 2^0 = 1$. Moreover, the sub-images in the result at $n = 1$ can be computed as

$$w_{01}(p, q) = [L_x * [L_y * I_0] \downarrow_2] \downarrow_2 (p, q) \tag{1}$$

$$w_{11}(p, q) = [L_x * [H_y * I_0] \downarrow_2] \downarrow_2 (p, q) \tag{2}$$

$$w_{21}(p, q) = [H_x * [L_y * I_0] \downarrow_2] \downarrow_2 (p, q) \tag{3}$$

$$w_{31}(p, q) = [H_x * [H_y * I_0] \downarrow_2] \downarrow_2 (p, q) \tag{4}$$

where even the sampling of the convolution instead down is represented by $*$ and \downarrow , respectively. Here, (H_x, H_y) and (L_x, L_y) are high- and low-pass filters, and the downsampling and filtering process for w_{01} can be written as

$$\begin{aligned} Y_{low}(p, q) &= [L_y * I_0] \downarrow_2 (p, q) \\ &= \sum_{k=-2}^1 I_0(p, k) L_y(p, 2q - k), \end{aligned} \tag{5}$$

$$\begin{aligned} w_{01}(p, q) &= [L_x * [L_y * I_0] \downarrow_2] \downarrow_2 (p, q) \\ &= \sum_{k=-2}^1 Y_{low}(k, q) L_x(2p - k, q). \end{aligned} \tag{6}$$

Similar steps are taken to get w_{11} , w_{21} and w_{31} .

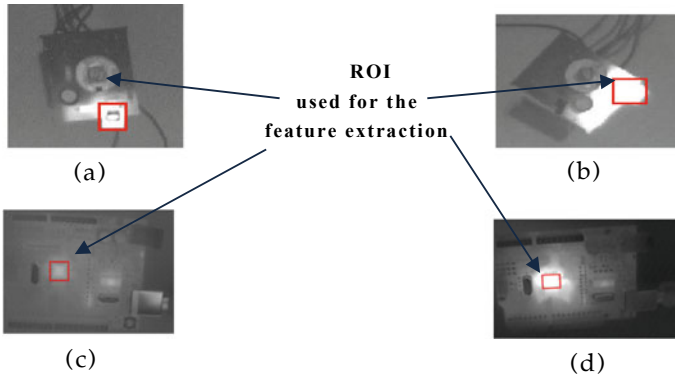


Fig. 4 Area highlighted with red colored rectangular bar is represents the region of in-terest **a** Healthy fan circuit, **b** faulty fan circuit, **c** healthy Arduino Uno, **d** faulty Arduino Uno

4.2 Feature Extraction

A variety of different approaches can decide and extract the image function. These features might include information about pixels, region, boundaries, and texture. Nonetheless, before receiving features, different images are applied to the sampled thermal image by preprocessing techniques such as thresholding, resizing, normalization, binarization, etc. Furthermore, the feature extraction was applied in order to obtain the features that will aid in the classification and diagnosis of thermal images. The first step of the proposed methodology consists of extracting the region of interest (RoI) as shown in Fig. 4. It has been done by using cropping tool in MATLAB; extracting most relevant features is necessary to detect fault using a reliable fault-prediction system. Here, the mean, standard deviation, root mean square, skewness, kurtosis, and variance have been used for the feature extraction. Finally, the extracted feature vectors are then correctly standardized to have zero mean and unity standard deviation to minimize the influence of DC offset and amplitude biases ranged from $[0, 1]$ to the classifier student data.

4.3 Feature Reduction and Selection

The features extracted from the region of interest are suitable features, some may be unrelated to the fault, some may be related to each other, and redundancy could occur. PCA carries out the dimension reduction to reduce linear dependency between features. Because the healthy and faulty machines in the feature space are not linearly separable, more features need to be kept to improve the results of classification. PCA can only eliminate the linear relationship between features and is a powerful tool for extracting features or selecting features by keeping the data at maximum variance.

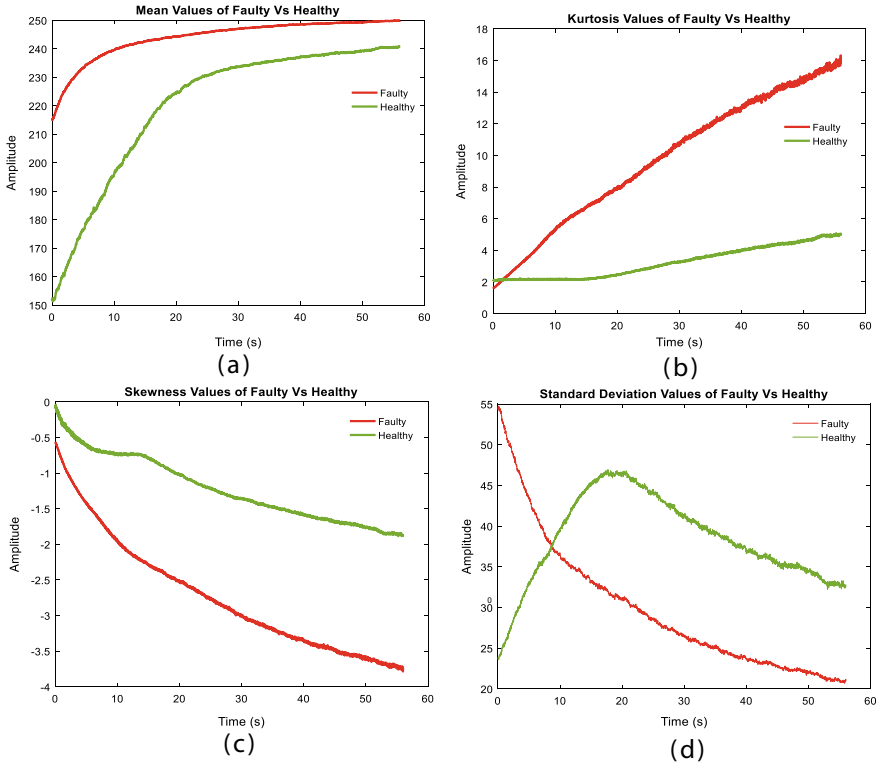


Fig. 5 Most relevant extracted features vs time plots for table fan **a** mean, **b** kurtosis, **c** skewness, and **d** standard deviation

In order to demonstrate the characteristics of the extracted features from circuit boards of DC table fan with respect to time and plotted the most relevant feature vectors (i.e., mean, SD, kurtosis, and skewness) vs time plots as illustrated in Fig. 5. It can be observed among the feature vectors vs time plots that there is an inconsistency in normal and faulty features and also show the noticeable changes in the amplitude of features in rising time.

In order to demonstrate the characteristics of the extracted features of Arduino Uno with respect to time and plotted the most relevant feature vectors (i.e. mean, SD, kurtosis and skewness) vs time plots as illustrate in Fig. 6, it can be observed among the feature vectors versus time plots that there are an inconsistency in normal and faulty features and also shows the noticeable changes in the amplitude of features in rising time.

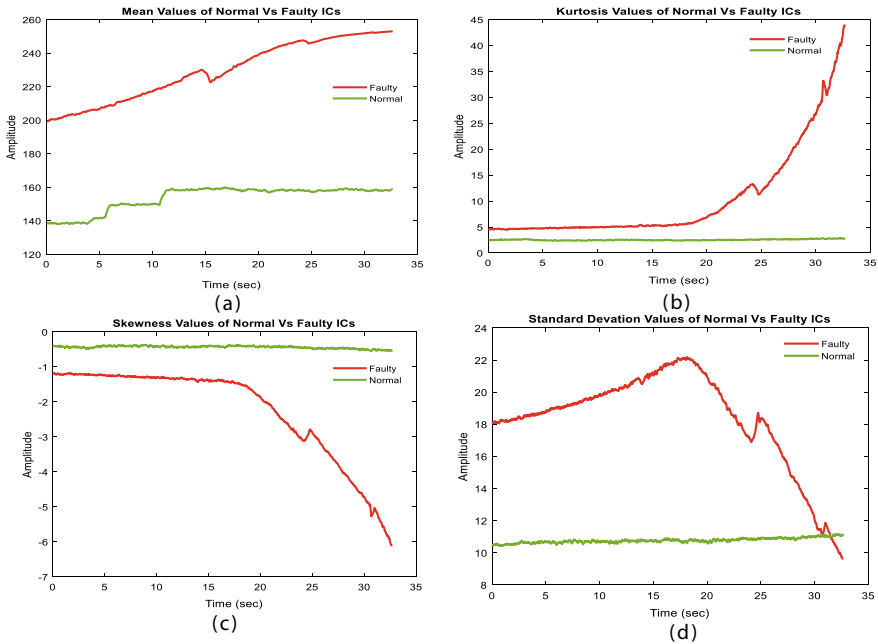


Fig. 6 Most relevant extracted features vs time plots for Arduino Uno **a** mean, **b** kurtosis, **c** skewness, and **d** standard deviation

5 Result and Discussion

SVMs are used as classifiers in this study because they provide better properties than the other models, and with a limited training dataset, they can also offer high classification performance. Nevertheless, when SVM is used for classification, an appropriate base kernel feature needs to be chosen for SVM. Here, the feature vector dataset has been trained and testified for the classification of normal and faulty components in both the circuits of Arduino Uno and DC table fan by various SVM classifiers with different basis kernel functions (i.e., linear, quadratic, cubic, fine Gaussian, medium and coarse Gaussian), and the resultant overall classification accuracy has been analyzed. For the improvement of the classification accuracy, the cross-validation training and testing model have been employed to avoid overfitting and underfitting and to obtain optimize critical parameters of SVM. In n -fold cross-validation system, the whole feature vector dataset is divided into n -groups. Each category is applied to test the trained model, while other categories are being used to train the model. The overall average accuracy of the classifier is an output result, and selected the different base kernel functions of SVMs to the output result with the supreme accuracy to build the final classification model. The classifier with the optimum features has been trained with whole normalized feature vector dataset followed by PCA using different n -fold (fivefold, tenfold, 15-fold, 20-fold, and 25-fold) cross-validation and aforementioned kernel functions of SVMs for evaluating

the classification rate. The mentioned accuracy is reflecting the overall accuracy of the classifier performance and the ability of the classification model to discriminate among the classes (i.e., healthy and faulty). It has been found that among all basis kernels of SVM the fine Gaussian SVM offered highest accuracy of 98.8% for DC table fan, and in the case of Arduino Uno, it is 97.6%, which is improved remarkably. The overall classification accuracy between the various kernel function SVMs with n -fold cross-validation system for the classification of normal and faulty components through the bar chart plotted for the DC table fan and Arduino Uno is illustrated in Fig. 7.

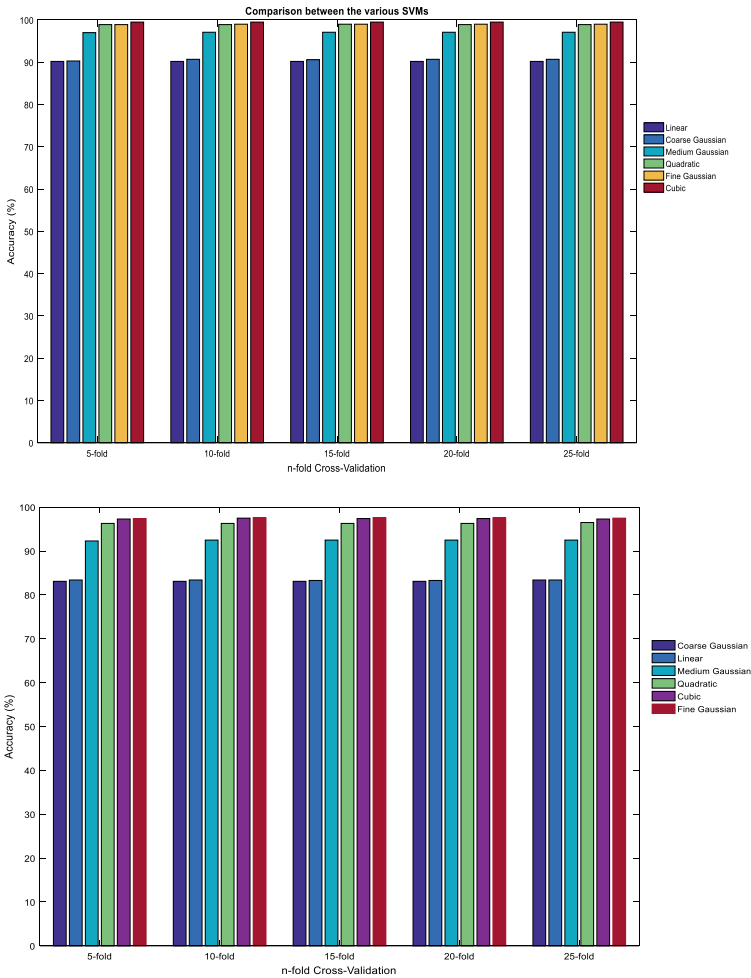


Fig. 7 Bar chart plot of overall classification accuracy between the various kernel function SVMs with n -fold cross-validation system for healthy and faulty component classifications **a** Table fan **b** Arduino Uno

6 Conclusion

In this work, a thermal imaging-based intelligent fault diagnosis approach has been presented. The classification models based on the different SVM kernels have been tested for electronic components fault diagnosis. Using 2D-DWT, the thermal images were preprocessed, followed by the removal of irrelevant characteristics using PCA and the ranking of chosen characteristics was then carried out in order of importance. In addition, for classification and performance assessment evaluation, the feature vectors were forwarded to SVM. It has been observed that SVM fine Gaussian outperformed the other kernel. The result reveals the probable use of SVM-based approach to establish rigorous proactive development fault detection in electronics circuit boards and electrical circuits.

References

1. Wang WL, Zhang H, Xiao JD, Sun YY (2016) PCB-integrated thin film thermocouples for transient temperature measurement. *Electron Lett* 52(13):1140–1141
2. Daniel PP (2014) Software-based self-test techniques for online test and diagnosis of embedded controllers and memories. Doctor of Philosophy Thesis, National Institute of Technology, India (2014)
3. Al-Musawi AK, Anayi F, Packianather M (2020) Three-phase induction motor fault detection based on thermal image segmentation. *Infrared Phys Technol* 104
4. Zhang L, Guo H, Garne CM, Kloster G, Atwood G, Mosley L, Palanduz AC (2005) Challenges for dielectric materials in future integrated circuit technologies. *Microelectron Reliab* 45(5–6):919–924
5. Taib S, Jadin M, Kabir S (2011) Thermal imaging for qualitative-based measurements of thermal anomalies in electrical components. In: *Proceedings of IEEE International Conference on electronic communication*, pp 1–6
6. Lee D-W, Ono T, Abe T, Esashi M (2002) Microprobe array with electrical interconnection for thermal imaging and data storage. *J Microelectromech Syst* 11(3):215–221
7. Schulz R, Verstockt S, Vermeiren J, Loccufier M, Stockman K, Van Hoecke S (2014) Thermal imaging for monitoring rolling element bearings. In: *12th international conference on quantitative infrared thermography*, Bordeaux, France, pp. 7–11
8. Vadivambal R, Jayas DS (2011) Applications of thermal imaging in agriculture and food industry—a review. *Food Bioprocess Technol* 4(2):186–199
9. Grasso RJ (2016) Defence and security applications of quantum cascade lasers. In: *Optical sensing, imaging, and photon counting: nanostructured devices and applications*, vol 9933, pp 99330F. International Society for Optics and Photonics
10. Andoga R, Főző L, Schrötter M, Češkovič M, Szabo S, Breda R, Schreiner M (2019) Intelligent thermal imaging-based diagnostics of turbojet engines. *Appl Sci* 9(11):2253
11. Meng Z, Zhao R, Cai Z, Ping J, Tang Z, Chen Si (2017) Microwave thermal emission at Tycho area and its geological significance. *IEEE J Selected Topics Appl Earth Observ Remote Sens* 10(6):2984–2990
12. Alaviyoun SS, Ziabasharhagh M (2020) Experimental thermal survey of automotive turbocharger. *Int J Engine Res* 21(5):766–780
13. Sousa E, Vardasca R, Teixeira S, Seixas A, Mendes J, Costa-Ferreira A (2017) A review on the application of medical infrared thermal imaging in hands. *Infrared Phys Technol* 85:315–323

14. Moldovan H, Marco M, Vladutiu M (2005) PCB testing using infrared thermal signature. In: Proceedings of IEEE international conference on instrumentation and measurement, vol 3, pp 1970–1974
15. Farrokhi F, Mohammadi FA (2010) Temperature and power measurement of modern dual core processor by infrared thermography. In: Proceedings of IEEE international conference on circuits system (ISCAS2010), Paris, pp 1603–1606, 30 May–2 June 2010
16. Li Bo, Tang M, Yue H, Tang Y, Mao J (2019) Efficient Transient thermal simulation of ICs and packages with laguerre-based finite-element method. *IEEE Trans Components Packaging Manuf Technol* 10(2):203–211
17. Xu S, Li X (2011) Analysis on thermal reliability of key electronic components on PCB board. In: 2011 international conference on quality, reliability, risk, maintenance, and safety engineering, Xi'an, pp 52–54
18. Zhan L, Zhuang Yi, Huang L (2017) Infrared and visible images fusion method based on discrete wavelet transform. *J Comput* 28(2):57–71

Power-Efficient Bidirectional Shift Register Using Conditional Bidirectional Pulsed Latch Circuit



Karan Kumar and Vaithiyathan Dhandapani

1 Introduction

As technology node is reducing day-by-day designers put more emphasis on circuit design with low-power consumption and less area. But miniaturizing of transistors leads to active second-order effect which leads to increase power dissipation. Digital circuit designers focus on power, performance, area (PPA) and trade-off of these three parameters will be considered more while designing any digital circuit. Node power dissipation becomes a crucial parameter with aggressive scaling in CMOS technology. Especially power dissipation in clock networks contributes almost 30–45% of overall dynamic power consumption. The reduction of power consumption in the clock tree circuit is required by reducing dynamic power dissipation. Main sequencing block which is used in clock tree synthesis (CTS) is master–slave flip-flop (MSFF) which can be replaced by pulsed latch circuit to gain benefit of both flip-flop and latch circuit. In pulsed latch circuit, a pulse signal will be given as a clock pulse to latch circuit. Due to small pulse width, latch circuit will behave as a master–slave flip-flop [1].

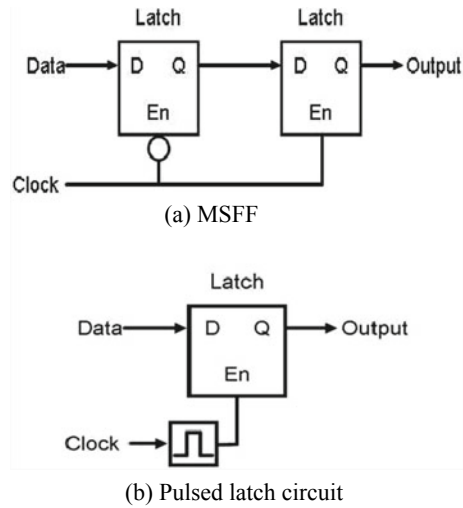
In simple latch circuit due to data transparent nature, verification of static timing analysis (STA) was difficult, but in pulsed latch circuit, we can apply static timing analysis. Therefore, rising edge of pulse is used for setup and falling edge of pulse is used to calculate hold time [3].

The conventional bidirectional shift register uses MSFF and a multiplexer circuit for shifting the data left or right. Bidirectional shift register clock signal left/right is used to shift from right to left but due to transparent nature pulsed latch circuit cannot share same pulse due to which different clock pulse generator is being introduced for

K. Kumar (✉) · V. Dhandapani
National Institute of Technology Delhi, New Delhi 110040, India

V. Dhandapani
e-mail: dvaithiyathan@nitdelhi.ac.in

Fig. 1 a MSFF, b pulsed latch circuit



pulse generator in bidirectional shift register so that race condition can be avoided [2] (Fig. 1).

Outline of this paper is arranged as follows. Section 2 contains description of bidirectional shift register using bidirectional pulsed latch (BDPL) circuits. Sub-section contains one-bit pulsed latch circuit, in which detailed analysis of pulsed latch circuit is described as well as description of BDPL circuit further sub-section entails modified circuit with block diagram. Section 4 contains results and conclusion.

2 Design of 4-Bit Bidirectional Shift Register Using Bidirectional Pulsed Latch circuit

2.1 One-Bit Conditional Clock Generator

Figure 3 has a feedback path from input and output of a latch into the clock generator. In clock generator, there will be a comparison in between input signal and output signal of latch. If both signals are opposite to each other only then a pulse generator; i.e., clock generator will initiate positive signal which will act as a clock signal for latch circuit [1] (Fig. 2).

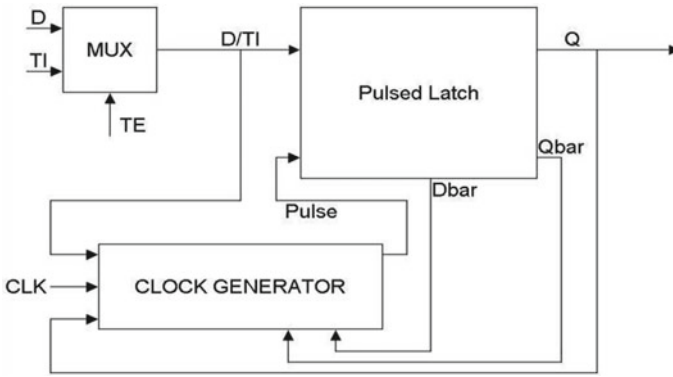


Fig. 2 Block diagram of conditional pulsed latch circuit

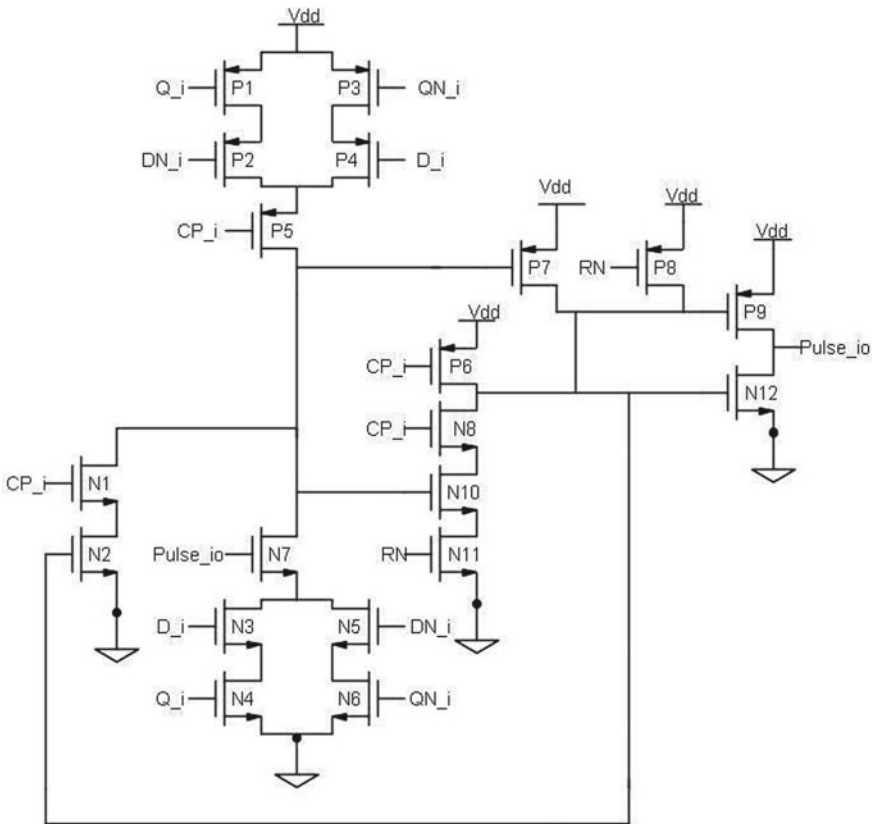
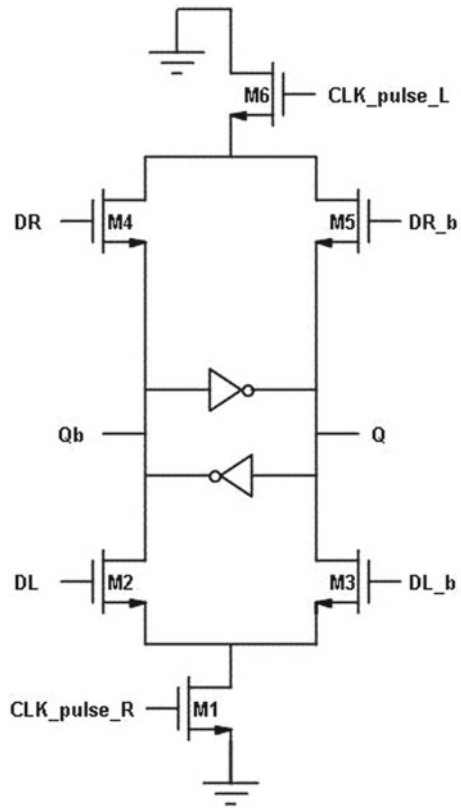


Fig. 3 One-bit conditional clock pulse generator

Fig. 4 Circuit diagram of BDPL



2.2 Bidirectional Pulsed Latch Circuit

Bidirectional shift register is conventionally using flip-flops and a multiplexer for shifting for the power dissipation; we replaced it with BDPL circuit, and the left latch inputs, i.e. DL and DL_b, is connected with data output, i.e. Q and Qb of next bidirectional latch. Likewise input of right latch is connected with data output of right latch, and data is being updated bidirectionally, i.e. left or right [2] (Fig. 4).

2.3 Modified Bidirectional Circuit

This modified bidirectional shift register circuit which uses conditional BDPL with delayed clock pulses to control signal right or left according to the requirement which is used for shifting a bit towards the right or left (Figs. 5, 6 and 7).

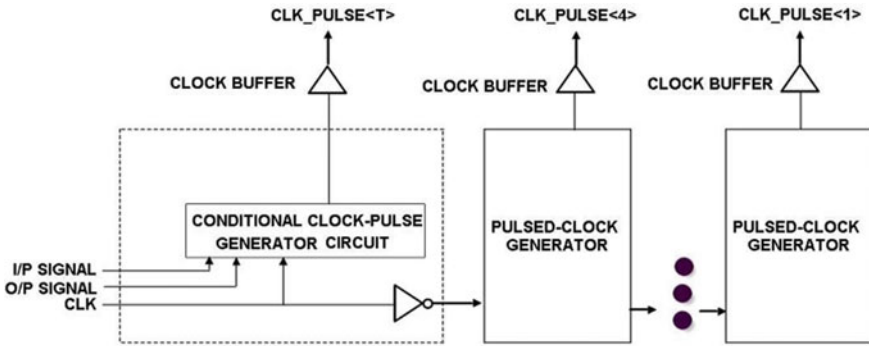


Fig. 5 Block diagram of conditional clock generator

3 Simulation Results

The advantage of modified Bidirectional shift register is that it can be use for low-power applications. The final output of modified bidirectional shift register is using conditional BDPL with 0.75 V Vdd at the typical process corner. In Fig. 8, initial signal is the clock pulse which is connected to pulse generator so that it can generate non-overlapping signal for shifting bit towards right if right is high using BDPL (Table 1).

4 Conclusion

In this paper, we have modified bidirectional shift register with conditional bidirectional pulsed latch circuit. Bidirectional shift register was designed using 28 nm CMOS technology. Simulation result of modified bidirectional shift register using conditional bidirectional pulsed latch circuit shows the power reduction by 38% when we compare it with bidirectional shift register using flip-flops with multiplexer. This modified circuit can be utilized for very low-power devices.

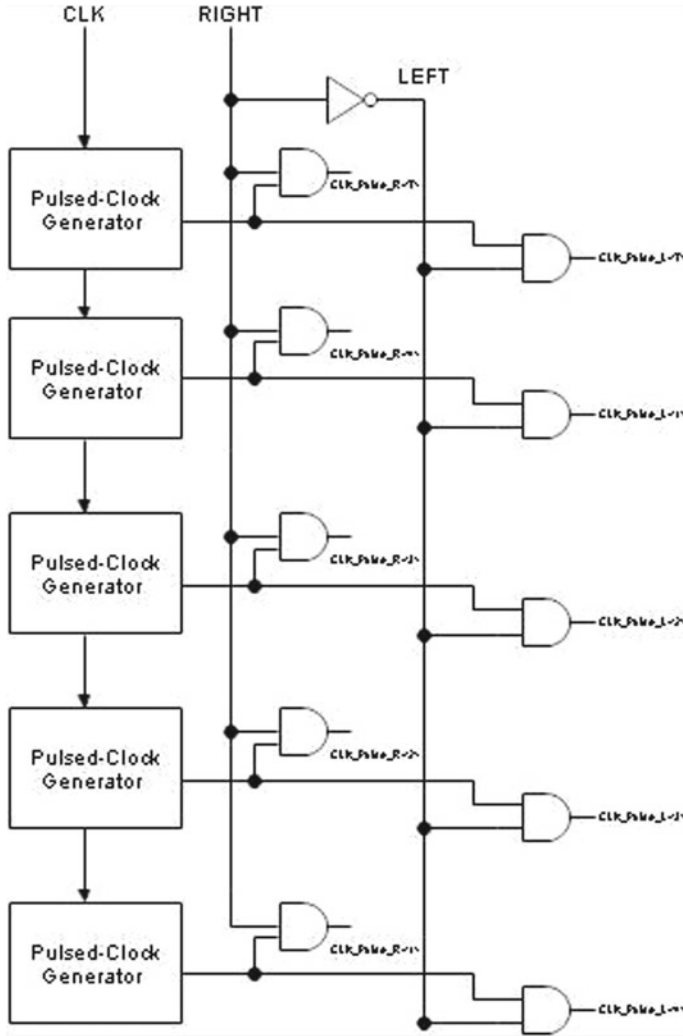


Fig. 6 Bidirectional clock generator

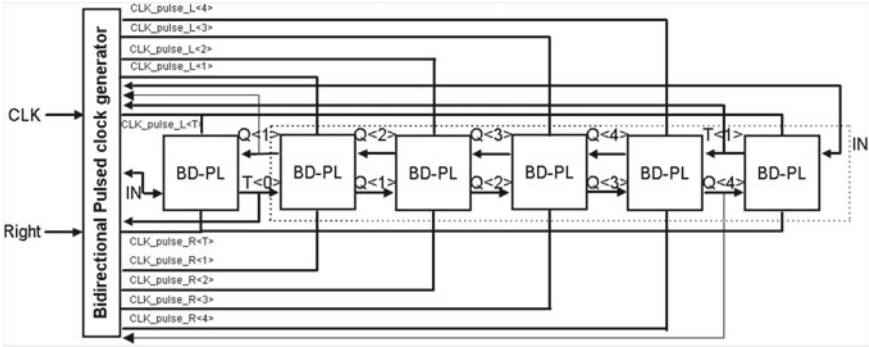


Fig. 7 Modified bidirectional shift register using conditional BDPL

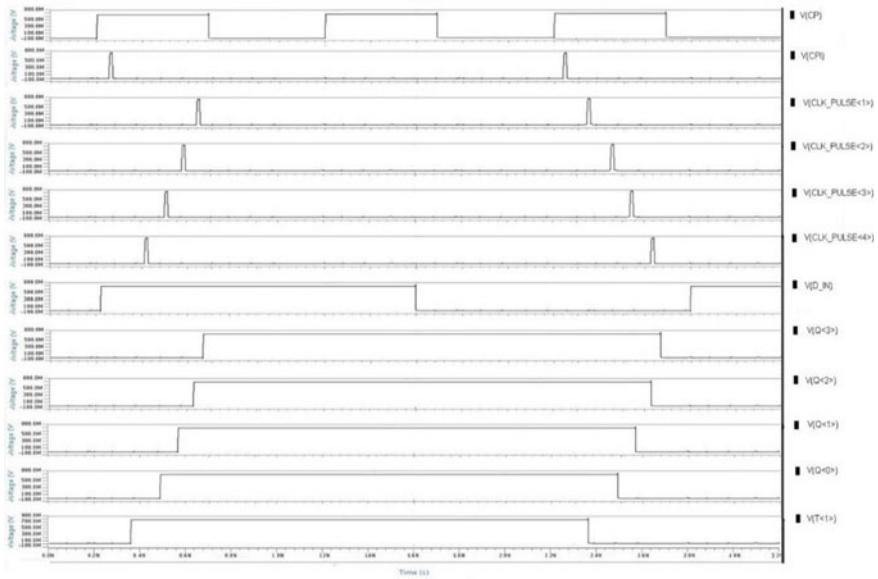


Fig. 8 Bidirectional shift register using conditional BDPL

Table 1 Comparison between 4-bit shift register using flip-flop with 4-bit shift register using BDPL

Circuit parameters	4-bit shift register using flip-flop	4-bit shift register using feedback BDPL
Area [μm^2]	52.24	80.68
Power [μW]@ $f_{\text{clk}} = 0.1 \text{ GHz}$	36.24	22.46 (38%)
Maximum clock frequency [GHz]	5.18	1.8

References

1. Sulthan M, Chowdury S, Garg R, Tripathi A (2019) Design of a power efficient pulse latch circuit as a solution for master slave Flip Flop. https://doi.org/10.1007/978-981-32-9767-8_44
2. Woo K, Kang H, Yang B (2019) Area-efficient bidirectional shift-register using bidirectional pulsed-latches. *IEEE Trans Circuits Syst II Express Briefs* 66(8):1386–1390
3. Yang B (2015) Low-power and area-efficient shift register using pulsed latches. *IEEE Trans Circ Syst I: Regular Pap* 62(6):15641571
4. Jin W, Kim S, He W, Mao Z, Seok M (2017) Near- and sub- Vt pipelines based on wide pulsed-latch design techniques. *IEEE J Solid-State Circ*. 52(9):2475–2487
5. Singh K, Rosas OAR, Jiao H, Huisken J, de Gyvez JP (2018) Multi-bit pulsed latch based low power synchronous circuit design. In: 2018 IEEE international symposium on circuits and systems (ISCAS), Florence, pp. 1–5
6. Chang C-L, Jiang IH-R, Yang Y-M, Tsai E, Chen A (2012) Novel pulsed-latch replacement based on time borrowing and spiral clustering. In: Proceedings of the international symposium on physical design. <https://doi.org/10.1145/2160916.2160944>
7. Paik S, Yu L, Shin Y (2010) Statistical time borrowing for pulsed-latch circuit designs. In: 2010 15th Asia and South pacific design automation conference (ASPDAC), Taipei, pp 675–680. <https://doi.org/10.1109/ASPDAC.2010.5419801>
8. Heo S, Krashinsky R, Asanovic K (2007) Activity-sensitive flip-flop and latch selection for reduced energy. *IEEE Trans Very Large-Scale Integr (VLSI) Syst* 15(9):1060–1064. <https://doi.org/10.1109/TVLSI.2007.902211>
9. Chuang Y, Kim S, Shin Y, Chang Y (2010) Pulsed-latch aware placement for timing integrity optimization. In: Design automation conference, Anaheim, CA pp 280–285
10. Lin H, Chuang Y, Ho T (2011) Pulsed-latch-based clock tree migration for dynamic power reduction. In: IEEE/ACM international symposium on low power electronics and design, Fukuoka, pp 39–44. <https://doi.org/10.1109/ISLPED.2011.5993601>
11. Lin H, Chuang Y, Yang Z, Ho T (2014) Pulsed-latch utilization for clock-tree power optimization. *IEEE Trans Very Large-Scale Integr (VLSI) Syst* 22(4):721–733. <https://doi.org/10.1109/TVLSI.2013.2252211>
12. Dhong S et al. A 0.42V Vccmin ASIC-compatible pulse-latch solution as a replacement for a traditional master-slave flip-flop in a digital SOC, in Proceedings of the IEEE 2014 custom integrated circuits conference, San Jose, CA, pp 1–4. <https://doi.org/10.1109/CICC.2014.6946044>
13. Kim L, Dutton RW (1990) Metastability of CMOS latch/flip-flop. *IEEE J Solid-State Circ*. 25(4):942–951. <https://doi.org/10.1109/4.58286>

A State-of-the-Art Review on LVRT Enhancement Techniques for DFIG-Based Wind Turbines



Priyanka Paliwal

1 Introduction

Environmental impact of electricity generation through conventional resources has been a major concern for countries across the world. Hence, electric power industry is shifting towards large-scale deployment of renewable energy-based technologies owing to their environment friendly nature. Renewable energy sources such as wind have emerged as a strong alternative to conventional sources [1]. In the recent years, significant growth has been witnessed in wind energy generation around the globe from around 7.6 GW in 1997 to over 651 GW at the end of 2019 [2]. Various factors have contributed to the substantial increase in wind power generation; one of the significant factors has been the introduction of efficient WTGs like PMSG and DFIG. Amongst all the WTGs, DFIG offers a variety of advantages [3, 4] over its other counterparts such as

- i. Variable speed operation
- ii. Four quadrant active and reactive power control
- iii. Reduced ratings of power electronics converters
- iv. Better capacity utilization factor

Thus, owing to its superior performance, DFIG is most widely employed wind turbine generator and is surely dominating the production market.

With all the advantages it has to offer, DFIG also has its own share of concerns. As the stator of DFIG is directly connected to grid, even a slight fluctuation in grid affects the performance of DFIG. This characteristic of DFIG has given rise to an attribute known as low voltage ride through (LVRT) capability. LVRT capability is defined [5] as the ability of a wind turbine generator to remain connected to the grid, and in some cases support it, when the grid is experiencing a fault. In other words, it is

P. Paliwal (✉)

Department of Electrical Engineering, Maulana Azad National Institute of Technology, Bhopal, India

the ability of wind turbine generators to ride through grid faults. Earlier, in the event of a fault, the WTGs were disconnected from the grid, as the level of penetration of wind energy in the grid was not significant. However, with substantial wind energy penetration in power sector [6, 7] today, this operation may result in large fluctuations in grid. Hence, to overcome this difficulty, several countries have devised stringent grid codes which have made it obligatory on the part of generators to stay connected to the grid during fault conditions and support it. To comply with such grid codes, it is essential for the generators to have an enhanced LVRT capability. A commendable amount of work has been reported in the literature for improving LVRT capability of DFIG. Nevertheless, it is imperative to analyse different enhancement techniques in detail so as to determine the best fitted solution for a particular situation.

The review papers reported in the literature do not provide adequate categorization of these techniques. Hence, the objective of this paper is to put forward an exhaustive survey on various techniques employed for enhancement of LVRT capability of DFIG. The techniques are systematically classified into following categories: (i) Protection strategies-based techniques (ii) Control strategies-based techniques (iii) FACTS-based techniques (iv) Hybrid techniques. The techniques are critically analysed and compared. Relevant conclusions are drawn on the basis of results reported in various references which can help researchers to identify gaps in this area.

The remainder of the paper is organized as follows: Sect. 2 emphasizes the aspects of LVRT capability. Section 3 presents various LVRT enhancement techniques. These methods have been classified into four major categories as follows, viz.. protection strategies-based techniques, control strategies-based techniques, FACTS-based techniques, and hybrid strategies-based techniques. Different methods under each category have been extensively analysed, and tabular comparison of these methods has been provided in this section. In Sect. 4, relevant conclusions have been drawn based on the literature survey which can help researchers in identifying future research avenues.

2 Aspects of LVRT Capability

With increasing wind energy penetration, it becomes essential to maintain the operation of wind turbines during voltage dips. In order to address this issue, efforts were made to explore the reasons for inability of DFIG to stay connected to a faulty grid and possible solutions to help it do so. Grid codes have been devised in order to provide guidelines for regional wind farms' operation. Figure 1 presents the essential features of LVRT enhancement techniques in accordance with the grid codes.

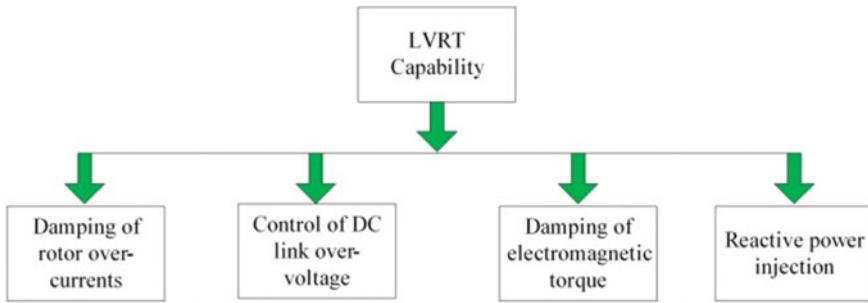


Fig. 1 Aspects of LVRT capability

3 LVRT Capability Enhancement Techniques

In this paper, a systematic classification of LVRT enhancement techniques has been presented. In [8], various techniques including crowbar method, converter control strategy, control strategies based on optimization techniques and employment of FACTS devices have been explained. However, the review does not present adequate categorization of various techniques. In order to take the categorization presented in [9–12] to another level, this paper proposes a fourth category, i.e. hybrid topologies and also allots two sub-categories to the protective circuits. Unlike [9–12], this paper provides a tabular analysis of the various methods. This paper aims at providing more distinct categorization and also compares various methods based on their performance. Figure 2 presents a detailed classification of LVRT enhancement techniques. Based on the classification, various techniques have been discussed in the following subsections.

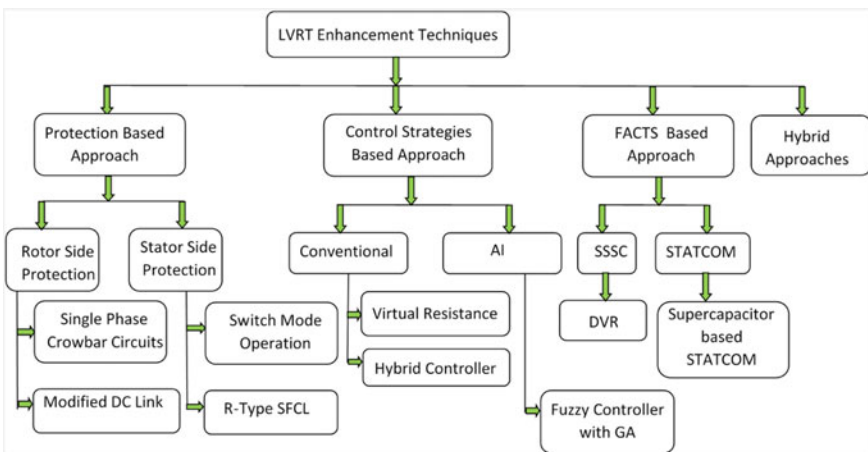


Fig. 2 Classification of LVRT enhancement techniques

3.1 Protection Strategies Based Techniques

The protection strategies-based techniques utilize additional hardware circuitry to protect generator from adverse effects of the voltage dip. The installed hardware may be a crowbar circuit, DC chopper, SFCL, SDBR, etc. These methods incorporate the provisions for suppression of overcurrent, machine torque oscillations and DCC link overvoltage. The crowbar is considered as the most popular method [10, 13–16]. In this method, as soon as the fault is sensed rotor circuit is short-circuited through an arrangement of resistors. Thus, rotor of machine is isolated from converters and machine operates as an induction generator. This prevents any potential damage to the converters. However, to function as an induction generator all the required reactive power is drawn from the grid during fault, which is highly undesirable. Moreover, the controllers are disconnected from rotor, thus making the system uncontrollable. These drawbacks of crowbar circuit have compelled the researchers to look for alternate protection methods for enhancing LVRT capability. Over the years, various topologies have been proposed, and depending on their way of connection, they can be categorized into rotor side protection circuits and stator side protection circuits.

Rotor side protection techniques. The traditional crowbar circuit is connected on the rotor side of DFIG. However, upon its activation, the converters along with controllers are cut off from the machine. This is highly undesirable, as under such circumstances, the system fails to regulate the active and reactive power flow. Thus, all the schemes proposed under this category try to inculcate within themselves the provision for controlled operation of DFIG. Moreover, attention is also given to have provision for limiting excessive reactive power absorption. Critical analysis of rotor side protection strategies has been presented in Table 1.

Stator side protection techniques. Initially, almost all the protective circuits were connected on the rotor side. But this arrangement led to uncontrolled operation of machine and absorption of excessive reactive power during faults. Thus to overcome these problems, initiatives were taken to connect protective circuits on stator side [17–25] and encouraging results have been obtained. A systematic analysis of stator side protection circuits has been presented in Table 2.

3.2 Control Strategies-Based Techniques

The protective circuits-based schemes involve utilization of external auxiliary circuits, thereby making system bulkier, which adversely affects the compactness of system. In order to overcome this problem, control strategies-based methods have been found to be more useful. In these strategies, different controllers of system are suitably designed so as to reject the disturbances in various parameters such as rotor current, DC link voltage and electromagnetic torque during fault conditions. Combined strategy of virtual resistance and demagnetizing control has been

Table 1 Analysis of rotor side protection strategies

Technique	Merits	Demerits	Results inference	Ref.
DC brake chopper with DC link capacitor	<ul style="list-style-type: none"> Prevents the effects of stray inductance 	<ul style="list-style-type: none"> Increase in rating of the anti-parallel diodes in RSC 	<ul style="list-style-type: none"> Simple delayed control method was found to be more efficient 	[13]
Single-phase crowbar circuits	<ul style="list-style-type: none"> Zero current state possible Prevents major overvoltage 	<ul style="list-style-type: none"> Bulky circuit Costly Un-controlled operation 	<ul style="list-style-type: none"> Reduction in duration of uncontrolled operation Better results than crowbar circuit 	[14]
Modified DC link based on polypropylene as well as super-capacitor	<ul style="list-style-type: none"> Economical advantage over methods like DVR Simple, 100% sag mitigation 	<ul style="list-style-type: none"> Bulkier RSC 	<ul style="list-style-type: none"> In both the faults, super-capacitor-based scheme proved superior to both DC chopper and polypropylene-based modified DC link 	[26]
GCSC in series with rotor	<ul style="list-style-type: none"> RSC inrush currents suppressed Controlled operation 	<ul style="list-style-type: none"> Increased size 	<ul style="list-style-type: none"> Inferior DC link voltage profile as compared to crowbar-based scheme for single-phase fault 	[27]
Inductor-type superconducting coil (SC)	<ul style="list-style-type: none"> Damping of power fluctuations in steady state Mitigation of faults near to DFIG 	<ul style="list-style-type: none"> Costlier 	<ul style="list-style-type: none"> The use of optimal SC proved to be better than other auxiliary devices such as battery, STATCOM and non-optimal SC 	[28]

reported in various references [22, 29–31]. AI methods have also been explored because of their ability to handle nonlinear complications effectively. The merits and demerits of control strategies-based techniques and inference drawn from some notable references have been presented in Table 3.

3.3 FACTS-Based Techniques

FACTS devices possess the ability to control transmission systems’ parameters thereby governing its operation. The parameters include current, voltage, phase angle, damping of oscillations at various frequencies, and shunt and series impedance. The static synchronous compensator (STATCOM) and the static synchronous series compensator (SSSC) are highly versatile and effective FACTS controllers that are

Table 2 Analysis of stator side protection strategies

Technique	Merits	Demerits	Inference	Ref.
Switch mode operation of DFIG	<ul style="list-style-type: none"> • Total isolation of stator from the grid 	<ul style="list-style-type: none"> • Absorption of reactive power • Limited power transfer 	<ul style="list-style-type: none"> • MSDFIG offers better results than system with no protection 	[17]
R-type SFCL	<ul style="list-style-type: none"> • Compact • Simple operation 	<ul style="list-style-type: none"> • Reactive power requirement 	<ul style="list-style-type: none"> • Successfully limits quantities to acceptable levels 	[18]
Switch type SFCL	<ul style="list-style-type: none"> • Overvoltage by pass circuit not required • Controllability improved 	<ul style="list-style-type: none"> • Increased cost • Size increased 	<ul style="list-style-type: none"> • Switch type SFCL was found to be superior in all aspects 	[20]
R-type HTSFCL	<ul style="list-style-type: none"> • Provides better voltage and angle stability • Less complex 	<ul style="list-style-type: none"> • Performance deteriorates for 100% sag 	<ul style="list-style-type: none"> • HTSFCL provided fault ride through but DVR system offered more flexibility 	[21]
Low-rated SDBR on stator side	<ul style="list-style-type: none"> • Cheaper than most of the other stator side protection • Rapid synchronization 	<ul style="list-style-type: none"> • Cost varies largely • Parameter determination is tedious 	<ul style="list-style-type: none"> • Provided better results with different values of SDBR than SRC scheme 	[22]

Table 3 Comparison of control strategies-based techniques

Technique	Merits	Demerits	Inference	Ref.
SRC control	<ul style="list-style-type: none"> • Cheaper solution • Simplicity 	<ul style="list-style-type: none"> • Relatively poor performance 	<ul style="list-style-type: none"> • Inferior to SDBR scheme 	[22]
Magnetizing Current Controller	<ul style="list-style-type: none"> • Sag detection not necessary • Faster response 	<ul style="list-style-type: none"> • Adversely affected by high turbine speed 	<ul style="list-style-type: none"> • Successful ride through 	[29]
Modified control action of RSC and GSC	<ul style="list-style-type: none"> • Overvoltage/ Overcurrent protection not required • Cost effective 	<ul style="list-style-type: none"> • Increased mechanical stress 	<ul style="list-style-type: none"> • Proposed scheme proved better 	[30]
GA tuned fuzzy controller	<ul style="list-style-type: none"> • No auxiliary hardware required • Cost effective even for larger dips 	<ul style="list-style-type: none"> • Disturbances may hinder performance • Increased complexity 	<ul style="list-style-type: none"> • Effective enhancement of LVRT capability 	[31]

fast emerging in power systems. These devices have the ability of four-quadrant active and reactive power regulation thus can prove to be effective in assisting DFIG in enhancing its FRT capability. Performance of a dynamic voltage restorer (DVR) and STATCOM [32] has been investigated in various references. DVRs have been

Table 4 Analysis of FACTS-based techniques

Technique	Merits	Demerits	Inference	Remarks	Ref.
Super-capacitor with STATCOM	<ul style="list-style-type: none"> • Damping enhancement 	<ul style="list-style-type: none"> • Increased cost 	<ul style="list-style-type: none"> • Ride through worst scenario 	<ul style="list-style-type: none"> • Expensive 	[32, 39, 40]
DVR	<ul style="list-style-type: none"> • Auxiliary protection devices not needed • Lowers complexity 	<ul style="list-style-type: none"> • Higher cost • Complicated • System size increased 	<ul style="list-style-type: none"> • Superior than crowbar circuit 	<ul style="list-style-type: none"> • Expensive 	[35, 41]

used for compensating deep and shallow symmetric and asymmetric voltage sags to enhance the LVRT capability [33, 34]. A comparative study of these methods has been presented in Table 4.

3.4 Hybrid Strategies-Based Techniques

The references discussed in previous sections have suggested methods which solely rely on a single technique. However, every technique has its own share of difficulties. Thus, the proposed schemes based on these techniques also have some drawbacks. For instance, the crowbar-based schemes faces the problem of excessive reactive power absorption, the DVR-based scheme are uneconomical and the various control strategies-based scheme exhibits complexity and feasibility issues [10].

However, it is witnessed that the desired feature which cannot be provided by one method is contributed by another. So it is possible to eliminate the drawbacks of one method by combining it with another. Thus, the hybrid strategies have come to the floor. The categories of these hybrid strategies comprise of combination of conventional methods and are as follows [36–38]:

- Control strategies and FACTS
- FACTS and protective circuits
- Control strategies and protective circuits

Table 5 presents a comparison of hybrid strategies based on their merits and demerits.

Table 5 Analysis of hybrid strategies-based techniques

Technique	Merits	Demerits	Ref.
Fuzzy controller with crowbar	<ul style="list-style-type: none"> • Mitigation of swell possible • Capable of handling general grid perturbations • Faster convergence 	<ul style="list-style-type: none"> • Upto 50% sags can be mitigated 	[14, 36]
RSC control with SDR	<ul style="list-style-type: none"> • Simpler • Cost effective • Effective damping of negative sequence oscillation 	<ul style="list-style-type: none"> • Conduction losses during normal operation 	[38]
Active compensator with RCL	<ul style="list-style-type: none"> • Mitigation of deep sags • Improved performance 	<ul style="list-style-type: none"> • Inclusion of RCL may induce disturbances 	[37]

4 Conclusion

In this paper, a comprehensive review of various techniques for enhancement of LVRT capability of a DFIG-based WTG has been presented. In order to impart clarity to classification, the techniques have been distinctly segregated into (i) Protection strategies-based techniques; (ii) Control strategies-based techniques; (iii) FACTS-based techniques; (iv) Hybrid strategies-based techniques. Merits/demerits and assessment of effect of various schemes on various performance parameters have been presented, hence portraying the potential of each method. The enhancement of LVRT capability has become an important aspect from power system stability point of view. Inefficient LVRT capability may lead to grid collapse because of increased penetration of wind power in the grid. Based on extensive review carried out in this paper, following inferences have been drawn:

- i. Reactive power support is demanded from the wind farms as per some grid codes, but very few methods are able to provide it effectively.
- ii. Hybrid methods can prove to be a major contributor in LVRT enhancement as one method's shortcoming can be overcome by the other. However, selection of two strategies to be hybridized must be done judiciously.
- iii. Some methods are proposed only for symmetric faults. Although symmetric faults are mentioned in the grid codes, asymmetric faults are more common. Therefore, it is desired that these techniques must be able to handle the asymmetric faults as well.
- iv. Almost all the methods have been devised for a stiff grid. However, the wind farms connected grid is generally weak. Thus, future methodologies must be designed as per the requirement of weak grid.

The review presented in this work is expected to assist researchers to apprehend the extent of work achieved in this field and perform future analysis with better efficiency and efficacy. This review also aims to assist researchers in selecting a

specific technique based upon their requirements, thus facilitating improved system performance.

References

1. Saqib MA, Saleem AZ (2015) Power-quality issues and the need for reactive-power compensation in the grid integration of wind power. *Renew Sustain Energy Rev* 43:51–64
2. <https://gwec.net/global-wind-report-2019/>.
3. Rolan A, Pedra J, Corcoles F (2014) Detailed study of DFIG-based wind turbines to overcome the most severe grid faults. *Electr Power Energy Syst* 62:868–878
4. Nian H, Song Y (2014) Direct power control of doubly fed induction generator under distorted grid voltage. *IEEE Trans Power Electron* 29(2):894–905
5. Rahim AHMA, Nowicki EP (2012) Supercapacitor energy storage system for fault ride-through of a DFIG wind generation system. *Energy Conv Manag* 59:96–102
6. Jadhav HT, Ranjit R (2013) A comprehensive review on the grid integration of doubly fed induction generator. *Electr Power Energy Syst* 49:8–18
7. Rona B, Guler O (2015) Power system integration of wind farms and analysis of grid code requirements. *Renew Sustain Energy Rev* 49:100–107
8. Alsmadi YM et al (2018) Detailed Investigation and Performance improvement of the dynamic behavior of grid-connected DFIG-based wind turbines under LVRT conditions. *IEEE Trans Ind Appl* 54(5):4795–4812. <https://doi.org/10.1109/TIA.2018.2835401>
9. Maga, J., Jadhav, H.T.: Improving fault ride through capability of DFIG connected wind turbine system: a review. In: International conference on power, energy and control, pp 613–618. <https://doi.org/10.1109/ICPEC.2013.6527731>
10. Tohidi S, Mohammadi-ivatloo B (2016) A comprehensive review of low voltage ride through of doubly fed induction wind generators. *Renew Sustain Energy Rev* 57:412–419
11. Jutso JJ, Mwasilu F, Jung JW (2015) Doubly-fed induction generator based wind turbines: a comprehensive review of fault ride-through strategies. *Renew Sustain Energy Rev* 57:447–467
12. Mahela OP, Gupta N, Khosravy M, Patel N (2019) Comprehensive overview of low voltage ride through methods of grid integrated wind generator. *IEEE Access* 7, pp 99299–99326. <https://doi.org/10.1109/ACCESS.2019.2930413>
13. Niu L, Wang X, Wu L, Yan F, Xu M (2019) Review of low voltage ride-through technology of doubly-fed induction generator. *J Eng* 3(16):3106–3108. <https://doi.org/10.1049/joe.2018.8443>
14. Pannell G, Zahawi B, Atkinson DJ, Missailidis P (2013) Evaluation of the performance of a dc-linkbrake chopper as a DFIG low-voltage fault-ride-through device. *IEEE Trans Energy Conv* 28(3):535–542
15. Duong M, Leva S, Mussetta M, Le KH (2018) A Comparative study on controllers for improving transient stability of DFIG wind turbines during large disturbances. *Energies* 11:480. <https://doi.org/10.3390/en11030480>
16. Din Z, Zhang J, Zhu Y, Xu Z, El-Naggar A (2019) Impact of grid impedance on LVRT performance of DFIG system with rotor crowbar technology. *IEEE Access* 7:127999–128008. <https://doi.org/10.1109/ACCESS.2019.2938207>
17. Haidar AMA, Muttaqi KM, Hagh MT (2017) A coordinated control approach for DC link and rotor crowbars to improve fault ride-through of DFIG-based wind turbine. *IEEE Trans Ind Appl* 53(4):4073–4086. <https://doi.org/10.1109/TIA.2017.2686341>
18. Wei F, Vilathgamuwa DM, Shing CS (2015) Design of mode switching scheme for low-voltage ride-through of doubly fed induction generators. *IET Renew Power Gener* 9(2):109–119
19. Elshiekh ME, Mansour DEA, Azmy AM (2013) Improving fault ride-through capability of DFIG-based wind turbine using superconducting fault current limiter. *IEEE Trans Appl Superconductivity* 23(3)

20. Zheng Z, Huang C, Yang R, Xiao X, Li C (2019) A low voltage ride through scheme for DFIG-based wind farm with SFCL and RSC Control. *IEEE Trans Appl Supercond* 29(2):1–5. <https://doi.org/10.1109/TASC.2019.2891687>
21. Guo W, Xiao L, Dai S, Li Y, Xu X, Zhou W, Li L (2015) LVRT capability enhancement of DFIG with switch-type fault current limiter. *IEEE Trans Ind Electron* 62(1):332–342
22. Alaraifi S, Moawwad A, Moursi MSE, Khadkikar V (2013) Voltage booster schemes for fault ride through enhancement of variable speed wind turbines. *IEEE Trans on Sustain Energy* 4(4):1071–1081
23. Okedu KE, Muyeen SM, Takahashi R, Tamura J (2012) Wind farms fault ride through using DFIG with new protection scheme. *IEEE Trans Sustain Energy* 3(2):242–254
24. Rashid G, Ali MH (2017) Nonlinear Control-Based Modified BFCL for LVRT capacity enhancement of DFIG-based wind farm. *IEEE Trans Energy Convers* 32(1):284–295. <https://doi.org/10.1109/TEC.2016.2603967>
25. Hossain ME (2018) Low voltage ride through capability improvement methods for DFIG based wind farm. *J. Electr. Stst. Inform. Tech* 5(3):550–561
26. Zou Z, Liao J, Lei Y, Mu Z, Xiao X (2019) Postfault LVRT Performance enhancement of DFIG using a stage-controlled SSFCL-RSDR. *IEEE Trans Appl Supercond* 29(2):1–6. <https://doi.org/10.1109/TASC.2892821>
27. Mendes VF, Sousa CV, Silva SR, Rabela BC Jr, Holfmann W (2011) Modeling and ride-through control of doubly fed induction generators during symmetrical voltage sags. *IEEE Trans Energy Conv* 26(4):1161–1171
28. Yang L, Xu Z, Ostergaard J, Dong ZY, Wong KP (2012) Advanced control strategy of DFIG wind turbines for power system fault ride through. *IEEE Trans Power Syst* 27(2):713–722
29. Vrionis TD, Koutiva XI, Vovos NA (2014) A genetic algorithm-based low voltage ride-through control strategy for grid connected doubly fed induction wind generators. *IEEE Trans Power Syst* 29(3):1325–1334
30. Wessels C, Gebhardt F, Fuchs FW (2011) Fault ride-through of a DFIG wind turbine using a dynamic voltage restorer during symmetrical and asymmetrical grid faults. *IEEE Trans Power Electron* 26(3):807–815
31. Falehi AD, Rafiee M (2017) Enhancement of DFIG-wind turbine's LVRT capability using novel DVR based odd-nary cascaded asymmetric multi-level inverter. *Int J Eng Sci and Tech* 20:805–824
32. Benali A, Khiat M, Allaoui T, Denai M (2018) Power Quality improvement and low voltage ride through capability in hybrid wind-PV farms grid-connected using dynamic voltage restorer. *IEEE Access* 6:68634–68648. <https://doi.org/10.1109/ACCESS.2878493>
33. Mokryani G, Siano P, Piccolo A, Chen Z (2013) Improving fault ride-through capability of variable speed wind turbines in distribution networks. *IEEE Syst J* 7(4):713–722
34. Mohammadi J, Afsharnia S, Vaez-Zadeh S (2014) Efficient fault-ride-through control strategy of DFIG-based wind turbines during the grid faults. *Energy Convers Manage* 78:88–95
35. Huchel L, Moursi MSE, Zeineldin HH (2015) A parallel capacitor control strategy for enhanced FRT capability of DFIG. *IEEE Trans Sustain Energy* 6(2):303–312
36. Mohammadpour H, Zadeh SG, Tohidi S (2015) Symmetrical and asymmetrical low voltage ride through of doubly fed induction generator wind turbines using gate controlled series capacitor. *IET Renew Power Gener* 9(8):840–846
37. Karaipoom T, Ngamroo I (2015) Optimal superconducting coil integrated into DFIG wind turbine for fault ride through capability enhancement and output power fluctuation suppression. *IEEE Trans Sustain Energy* 6(1):28–42
38. Rahimi M, Parniani M (2014) Low voltage ride-through capability improvement of DFIG based wind turbines under unbalanced voltage dips. *Electr Power Energy Syst* 60:82–95
39. Liu J, Xu Y, Qiu J, Dong ZY, Wong KP (2020) Non-Network solution coordinated voltage stability enhancement with STATCOM and UVLS for wind-penetrated power system. *IEEE Trans Sustain Energy* 11(3):1559–1568. <https://doi.org/10.1109/TSST.2019.2931455>

40. Kamel OM, Diab AAZ, Do TD, Mossa MA (2020) A Novel hybrid ant colony-particle swarm optimization techniques based tuning STATCOM for grid code compliance. *IEEE Access* 8:41566–41587. <https://doi.org/10.1109/ACCESS.2020.2976828>
41. Chen L et al (2017) Comparison of superconducting fault current limiter and dynamic voltage restorer for LVRT improvement of high penetration microgrid. *IEEE Trans Appl Superconductivity* 27(4):1–7. Art no. 3800607. <https://doi.org/10.1109/TASC.2017.2656624>

Design of Traffic Sign Detection Using Hardware and Software Co-design



V. Muthu Ganesh and N. Janakiraman

1 Introduction

Traffic signal detection mandates a vital role in many applications like intelligent driver assistance. Many traffic sign detection system detects the stop sign to reduce the accidents, but other signs like speed limits, no U-turn can also be detected and indicate it to the driver. At times, it may be very difficult-to-recognize traffic signs accurately due to some environmental factors, and in such cases, traffic sign identification system is providing intelligent to the driver. There are various existing systems for the designing traffic sign recognition that includes neural networks and its variants, deep neural networks and convolution neural networks and also support vector machine [1] (SVM). Even, FPGA-based hardware accelerators are designed and achieved 12 frames/sec and energy consumption of 0.041 J/frame [2].

Though machine learning algorithms like DNNs and CNNs provide high detection accuracy, it is complex to implement and it works slowly for real-time traffic sign detection, so we choose cascade classifiers because it is a simple algorithm for designing. Since this CNN-based systems need a dataset of 43 classes of different road sign images of size of 50,000 [3]. With 99.46% exact classification rate with the burden of complex computational complexity. One method of making the detection accuracy more feasible, improved Libra R-CNN method [4] is used which uses the difficult-to-distinguish target in training is proposed and got 3% more accuracy than unimproved Libra R-CNN mean average precision. In pyramidal convolutional networks [5], the Tsinghua-Tencent challenge was solved with 100 K benchmark by adopting deep feature pyramidal architecture, and this architecture makes sensitive semantic features for objects with fewer sizes. In another method, there are various

V. Muthu Ganesh (✉)

K.L.N.College of Engineering, Pottapalayam, Sivagangai, Tamil Nadu, India

N. Janakiraman

Department of ECE, K.L.N.College of Engineering, Pottapalayam, Sivagangai, India

hardware platforms available that includes FPGA [2], system-on-chip (SOC) and graphics processing unit (GPU).

With Cascade classifiers [6] having minimum computation time and high detection accuracy of 15 frames/s in real-world applications. With similar fast detection algorithm such as SURF [7], having SVGA video at 60 fps, it includes parallel architecture and data flow methods to reduce the computational complexity. Other detectors which depend on Haar features and linear classifiers, like Viola–Jones framework [8], are used to benchmark different solutions and still the best detection algorithms are missing. In a novel method [9], it is robust to variations of road signs and this method results in finding different road signs in a single frame, and this method uses both Viola–Jones framework along with deep learning.

Some other discusses FPGA-based FREAK [10], implements faster for SVGA video at 60 fps. Having fast computation and provides high detection accuracy for ten different traffic signs. In a particular method like speed limiting road sign recognition and recognition using MNIST and SVM datasets [11], these architectures have results approximately above 98% and are tested with STS, GTSRB and BTSD datasets, with a processing time of 11 ms. In TI OMAP [1], SVM-based classifiers are implemented with 90% classification and recognition accuracies.

2 Background

Traffic sign detection has three main steps (1) processing, (2) conversion, and (3) implementation (Fig. 1).

2.1 Processing

Processing is done using **model-based design** (MATLAB and Simulink). Processing follows three steps: (a) pre-processing, (b) classification and (c) post-processing (Fig. 2).

Fig. 1 Flow for detecting different traffic sign

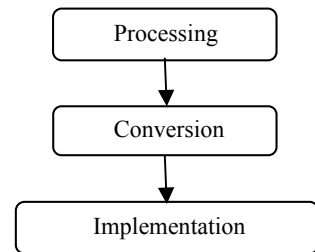
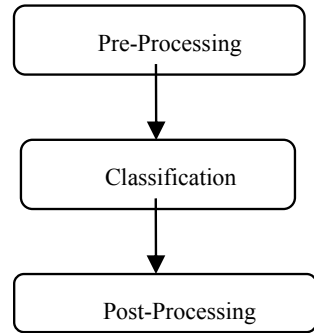


Fig. 2 Flow for traffic sign detection



2.1.1 Pre-processing

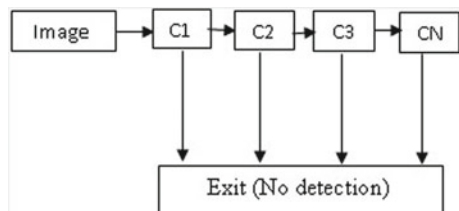
The very first step of pre-processing is image scaling which is followed by image cropping. In this step, the input video is divided into frames and each frames of video input get scaled to multiple levels. Scaling refers to resizing of the frames. Scaling factors which is referred as resizing factors differs from 100 to 0%. The scaled images are then cropped to a fixed level. During image cropping, the images are divided into regions (4 parts or 6 parts). Cropped image block gets evaluated to check whether it contains different sign or not. If size of the traffic sign is too large, adjustments will be done by applying different scaling factors. Scaling factor increases the accuracy.

2.1.2 Classification

Classification is done using cascade classifiers. Several weak stages are combined together in order to get a strong classifier. During classification, the image blocks are passed through each stages of the cascade classifier. Each stage will detect the traffic sign by sliding window which contains Haar feature; it allows the image block to the next stage if it contains the traffic sign and eliminates the blocks of image which does not have the signs of different traffic signals of interest (Fig. 3).

Cascade classifier [6] in this classification few hundred samples of positive and negative examples are trained and also it depends on Haar-like features. Once the classifier is trained, it is given to detector. If detector detects traffic sign, bounding box will bound over the sign. The classifier gives 1 as output if it has a traffic sign

Fig. 3 Flow for detecting different traffic sign



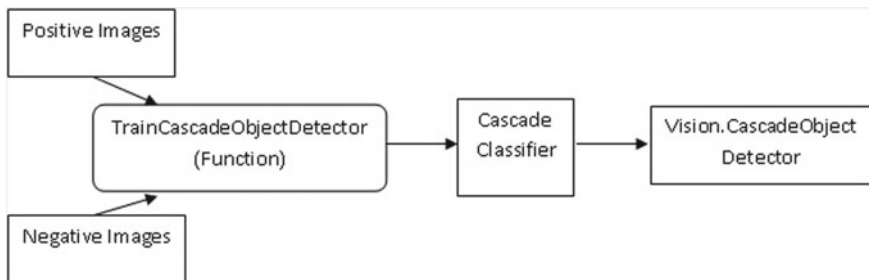


Fig. 4 Training flow for classifier

if not it gives 0 as the output. The classifier checks each and every location of the image (Fig. 4).

The classifiers are built by using basic classifiers and they are at a different stage of cascade is different and complex and using any one of boosting technique. Currently, real AdaBoost, LogitBoost, discrete AdaBoost and real AdaBoost are supported. The features are extracted from each and every stage from a given image block. There are a variety of features, such as scale invariant feature transform, histogram of oriented gradients [6], Haar-like feature [8] and so on. Some other discusses the trade-off between different detectors have been presented [12]. Among that we use Haar-like feature because it provides high accuracy and low computational cost (Fig. 5).

The Haar transform has a nature of symmetric and separable transform which uses Haar function as base format. It exists for $N = 2^n$, where n is an integer. It is the simplest orthonormal wavelet function which can process an odd rectangular pulse pair formats. The scale of the Haar functions may be varied in both width and position. Haar transform contains $2N$ nonzero entries and all other transforms

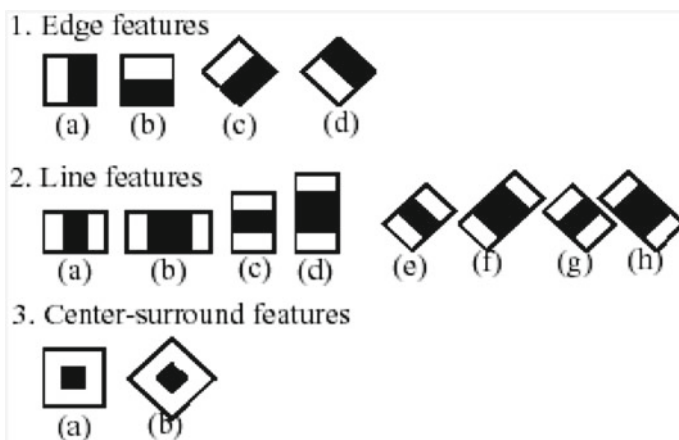


Fig. 5 Haar features

have N^2 nonzero elements. These features are useful in the calculation of spectral coefficients which have zero entries before the next retrieval processes.

For any particular classifier, a feature is specified by its position (1a, 2b, etc.) and shape (1a, 2b, etc.), within the region of interest. For example, for third-line feature (2c), the response is calculated based on the difference between the sum of image pixels under the rectangle covering the two white stripes and two black stripes, which is the whole feature and the sum of the image pixels under the black stripe multiplied by number, 3 to compensate for the differences in the area size. The integral image is used rapidly to calculate the sum of pixel values over rectangular regions. The late stage classifier faces more difficulty than early stages. After all through cascade classifier, the target sign will be contained in surviving image block.

2.1.3 Post-processing

In post-processing step, image block integration is done to merge all the image blocks into the superblock. Image block integration is done to acquire high density blocks of image, using spatial filtering which belongs to the same superblock.

2.2 Conversion

After processing is completed, HDL coder is used to convert it to the portable and synthesizable Verilog and VHDL code. Conversion is very necessary, so that we can perform implementation using a hardware ZC706 board. HDL coder automatically converts floating point to fixed point. HDL coder provides traceability between Simulink model and the generated Verilog and VHDL code. It also used for verification of high-integrity applications.

2.3 Implementation

The implementation of detection and traffic sign recognition is shown in the below figures. RTL simulation and synthesis reports are also attached. Then, the bit stream generated using HDL coder is loaded onto the FPGA board (Figs. 6, 7, 8 and 9).

The performance analysis and synthesis reports are the hardware performance of the proposed system are evaluated in terms of resource utilization and operating frequency.

FPGA = Zynq - 7000 XC7Z012S - 2FFG900C SoC

Maximum operating frequency = 722 MHz (14.027 ns)

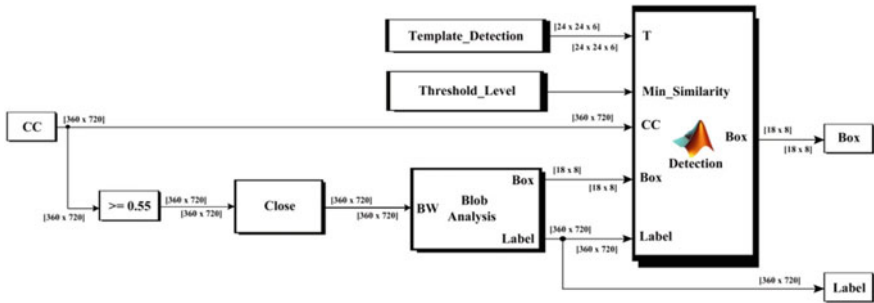


Fig. 6 Simulink detection block

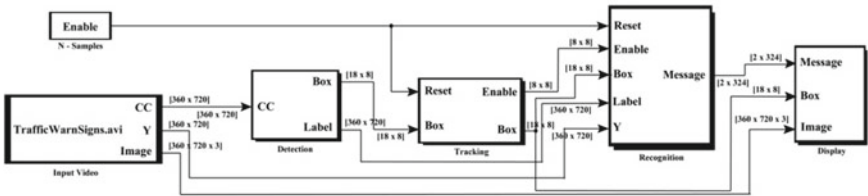


Fig. 7 Simulink traffic sign recognition block

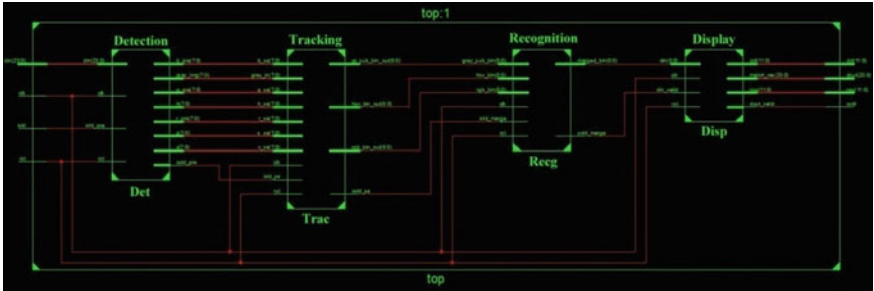


Fig. 8 RTL diagram of the traffic sign recognition

Slice logic utilization	Used	Available	Utilization (%)
Number of slice registers	8499	301,440	2
Number of slice LUTs	7451	150,720	4
Number of LUT flip-flop pairs used	10,545		
Number of RAMB18E1/FIFO18E1s	93	832	11
Number used as memory	49	58,400	1
Number of bonded IOBs	76	720	10
Number of DSP48E1s	11	768	11

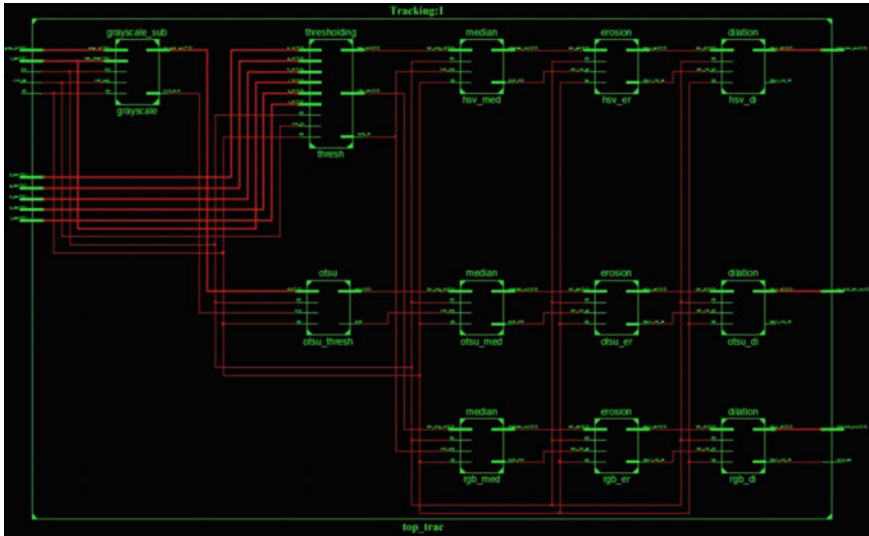


Fig. 9 RTL diagram of tracking

3 Simulation Results

Simulation results show that the hardware and software co-design system identifies the traffic signs categories such as stop sign, speed limit and U-turn. The results are shown as images as a sample for this classification (Fig. 10).

4 Conclusion

In this paper, we proposed a traffic sign detection system using hardware and software co-design. Three types of traffic signs, namely stop sign, speed limit and no U-turn sign are detected. False alarm rate is reduced to less than 1% by this system. True positive rate of about 98% is achieved by using Haar features. Processing frame rate is 120 frames/s. Before HDL conversion floating point to fixed point conversion is performed in order to utilize the resources of FPGA efficiently. Camera can be interfaced with FPGA in real-time applications. Apart from traffic sign detection, other autonomous car technology can be extended with this by using computer vision.



Fig. 10 Simulation results

References

1. Ganapathi PK, Madumbu V, Rajendran R, David S (2013) Design and implementation of an automatic traffic sign recognition system on TI OMAP-L138. In: Proceedings of IEEE international conference on information technology, Feb 2013, pp 1104–1109
2. Shi W, Li X, Yu Z, Overett G (2017) An FPGA-based hardware accelerator for traffic sign detection. IEEE Trans. VLSI 25
3. Stallkamp J, Schlipsing M, Salmen J, Igel C (2012) Man vs. computer: benchmarking machine learning algorithms for traffic sign recognition. Neural Netw. 32:323–332
4. Zijing Zhao, Xuewei Li, Hongzhe Liu, and Cheng Xu, “Improved Target Detection Algorithm based on Libra R-CNN”, in IEEE Access, Vol 8, June 17th 2020
5. Liang Z, Shao J, Zhang D, Gao L (2020) Traffic Sign Detection and Recognition based on pyramidal convolutional networks. Neural Comput Appl 32:6533–6543. <https://doi.org/10.1007/s00521-019-04086-z>

6. Viola P, Jones M (2001) Rapid object detection using a boosted cascade of simple features. In Proceedings of IEEE Conference on Computer Vision and Pattern Recognition, vol 1, pp I-511–I-518
7. Zhao J, Zhu S, Huang X (2013) Real-time traffic sign detection using SURF features on FPGA. In: Proceedings of high performance extreme computing conference, Sep. 2013, pp 1–6
8. Houben S, Stallkamp J, Salmen J, Schlipsing M, Igel C (2013) Detection of traffic signs in real-world images: the German traffic sign detection benchmark. In: Proceedings of international joint conference on neural network, Aug. 2013, pp 1–8
9. Jose A, Thodupunoori H, Nair BB (2019) A novel traffic sign recognition system combining Viiola-Jones framework and deep learning. In: Wang J et al (eds) Soft computing and signal processing, advances in intelligent systems and computing. https://doi.org/10.1007/978-981-13-3600-3_48
10. Zhao J, Huang X, Massoud Y (2014) An efficient real-time FPGAimplementation for object detection. In: Proceedings of IEEE international new circuits system conference, June 2014, pp 313–316
11. Saadna Y, Behloul A, Mezzoudi S (2019) Speed limit Sign detection and recognition system using SVM and MNIST datasets. *Neural Comput Appl* 31(9), pp 5005–5015
12. Timofte R, Mathias M, Benenson R, Van Gool L (2013) Traffic sign recognition—how far are we from the solution. In: Proceedings of international joint conference on neural network, Aug 2013, pp 1–8

Electricity Generation Using Wind Tree



**Yogesh Tomar, Ashutosh Kumar, Pradhan Singh Meena,
Sunil Kumar Yadav, Anshul Agarwal, and Vinay Kumar Jadoun**

1 Introduction

Due to rapid industrialization and technological development, natural resources have been exploited. Renewable and non-renewable are the two types of energy present. As non-renewable energy is limited, it is necessary for us to move toward renewable energy sources. Sunlight, wind, tides and geothermal are some of the renewable energy resources. These resources renew naturally in a human time scale. In most of the places, solar energy is being used as a replacement. But solar power system requires sunlight throughout which make its less efficient. Solar panels have an average efficiency of 15–20%. So we can shift toward wind energy which not only has more efficiency of nearly 50% [1] but also produced less carbon dioxide and can work 24 h a day. Wind energy is one of the fastest-growing energy sources in the world. It is described as the process by which wind is used to generate electricity. In this paper, electrical energy is produced using wind just like windmills but difference is that a tree is designed in which its leaves rotate by the wind and generate electricity. These leaves are called as Aeroleaf. Windmills are considered the only device for wind energy but windmill has its disadvantages as they are very costly and noisy. They can only be installed on selective locations, and also they affect the wildlife such as primarily birds and bats. So wind tree comes as a great alternative to the windmill as it is silent, compact and can be installed irrespective of location.

Y. Tomar (✉) · A. Kumar · P. S. Meena · S. K. Yadav · A. Agarwal
Department of Electrical and Electronics, National Institute of Technology Delhi, New Delhi,
India

A. Agarwal
e-mail: anshul@nitdelhi.ac.in

V. K. Jadoun
Department of Electrical & Electronics Engineering, Manipal Institute of Technology, Manipal
Academy of Higher Education, Manipal, Karnataka, India

2 Literature Review

Since smart cities are becoming center of attraction for the advancement of developing countries, it is very important that these smart cities should have renewable sources of energy. Therefore, large number of projects and research is going on in the area of renewable energies whether its solar, wind or hybrid of both, and to implement such projects, many new technologies are coming up. Gilbert M. Masters, “Renewable and Efficient Electric Power Systems” in, John Wiley and Sons discussed wide range of renewable energy systems [1]. The book mainly focused on wind and solar energy and discussed various management and maintaining procedure within the economic constraints. It is very informative resource for energy engineers and tech-focused individuals. Also, recently, a France’s startup company named “Newwind” [2] has successfully able to design a special product, which can be described as a fake tree having small wind turbines as leaves. The company already started production and has deployed a few units of that trees, which are currently being used for generating electricity in many parts of Paris, and it is now expanding its market in the USA. Similarly, in this paper, production of electrical energy using wind is discussed. This paper represent the optimize use of wind energy by a artificial tree as whenever the wind flows through the tree, its leaves rotate which in turn produce electric energy without any noise or pollution. It can be installed in wide location unlike windmill and can act as a substitute for non-renewable energy resources.

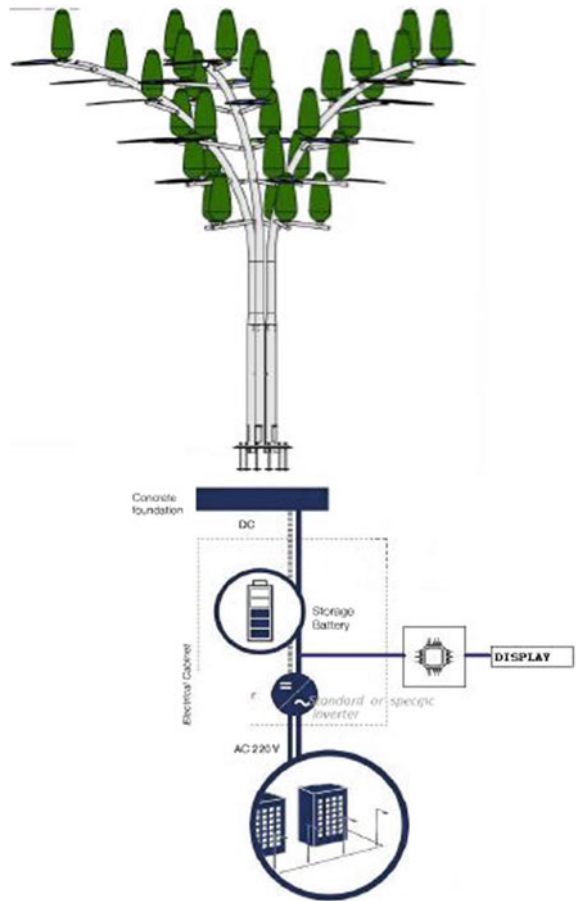
3 Wind Tree

The wind tree is a structure used as electric energy producing platform which is shaped like a tree as shown in Fig. 1. This device is capable of capturing all types of wind in cities or natural environments. Whether the wind flow is turbulent or laminar, strong or light, it is capable of capturing it in all 360°. A small-sized wind tree generally contains of 3–5 branches. Each of the branch carries six micro-wind turbines named as Aeroleaf. Wind tree is proven an interesting alternative to the windmills. It is much smaller, simpler, capable keeping the same design and silent [2–4].

4 Wind Turbines

Wind turbines are used for producing electricity by rotation with the natural wind. Wind energy is considered as renewable energy as it will never run out, and it is also clean and reliable. Wind turbines can be differentiated in two types: horizontal axis and vertical axis turbines [5, 6].

Fig. 1 Wind tree [2]



4.1 Horizontal Axis Turbines

Horizontal turbines are mostly used in windmills. Windmills are installed in the areas of high winds, and their turbines are very different from Aeroleaves as they can work in low-speed wind also. These turbines consist of a rotor that has blade attached to it which deflect with the wind, therefore, creating force on blades which further create torque in the rotor shaft, and rotor rotates on its axis. In windmills, these turbines are horizontal is positioned at the top.

4.2 Vertical Axis Turbines

Vertical axis turbine has advantage as they can catch the wind from all direction so, even a low-speed wind is able to create required torque and generate electricity. Size requirement is also less in vertical axis [7]. The generators in this type of turbine are positioned close to the ground and hence easily accessible. In wind tree, these turbines are used, and it is known as Aeroleaf.

5 Aeroleaf

Aeroleaf is a vertical wind turbine used in wind tree for the production of electricity. Each Aeroleaf is designed such that it is connected to a 12 V DC generator also called dynamo. Aeroleaf is designed in an optimized aerodynamic shape so that it can gather the smallest wind and air movement. In this paper, the design used for Aeroleaf is savonius type as shown in Fig. 2. In this design, turbines have aerofoil standing vertically on a shaft or platform. It is one of the simple design for vertical turbine. It can contain two or three scoop-like foils which appear S-shaped from top view. These are basically drag-type devices, and savonius turbines use much less of the wind's power than any other type of turbines. Because of its structure, it will experience less air drag while moving against the wind than moving with the wind.

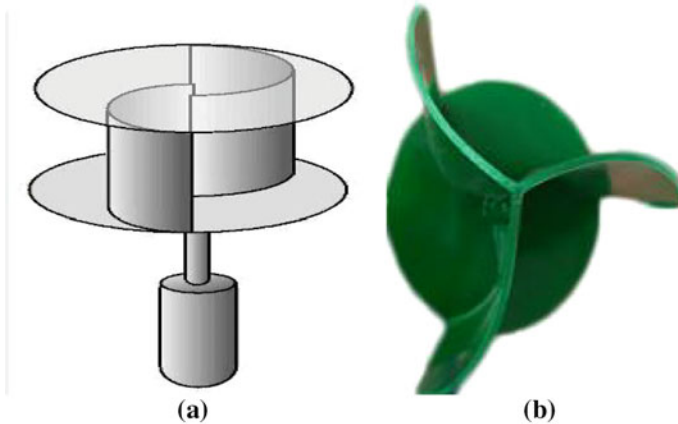


Fig. 2 Savonius-type wind turbine: **a** side view, **b** top view [8]

6 Component Required for Wind Tree

6.1 Plastic Molded Aeroleaves

Each Aeroleaf is made up of plastic material and shaped specifically in savonius type. These catch the winds and act as a propeller for generation action. It is connected to one generator each.

6.2 12 V DC Generator

Instead of using AC generator, a 12 V DC generator is used as to avoid rectification circuit and to make circuit cheap and compact. These generator is connected to a common panel.

6.3 Auto Buck/Boost Converter

LM2577s module is used as a step up/down DC-DC converter for maintaining the output voltage constant as if the wind input is low or high constant output voltage can be delivered to battery. (input voltage: DC 4–35 V; output voltage: DC 1.2–25 V).

6.4 Rechargeable 12 V / 48 V DC Battery

All the output terminals of converters are connected in series so that voltages from all the Aeroleaves get added. Output of all four converters adds up to 48 V which is stored in rechargeable batteries. The load according to the requirement is provided supplied by batteries. If the load demand is AC, with the help of inverter, stored DC is converted to AC.

7 Methodology and Working of Wind Tree

Working of this wind tree is like any other electricity generation system using a turbine. Wind flows through the Aeroleaves and rotates them. The generator action then takes place and emf is created, which is passed to the converters through wire via braches of tree. The terminals of the converters have constant DC voltage. Such converters are connected in series to produce higher output voltage. The resultant voltage id used to charge the DC batteries. Battery can either be connected with a

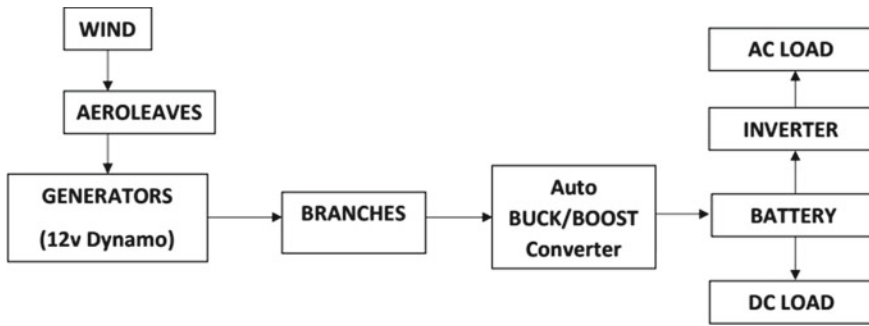


Fig. 3 Flowchart of whole setup of wind tree

DC load or through the inverter with AC load. The flowchart of the whole setup is shown in Fig. 3.

The flowchart in Fig. 3 shows that the wind flows through the Aeroleaves and rotates them. The generator action then takes place and emf is created which is passed to the converters through wire via braches of tree. The terminals of converters have constant DC voltage which is further connected to charge the DC batteries. From battery, one can either connect a DC load or through the inverter, AC load can also be connected.

8 Expected Model of Wind Tree and Its Technical Description

Estimated model is shown in Fig. 4 having four Aeroleaves connected to trunk through branches. All the internal connections are inside these branches. Generator is placed just below the Aeroleaves, and the rest of the components are placed separately in a panel.

Table 1 shows the technical description of wind tree. This table consists of maximum and average power of wind tree. Total number of Aeroleaf and average power per Aeroleaf are also mentioned in this table.

9 Advantages/Disadvantages of Wind Tree

9.1 Advantages

- Complex gear system is not necessary unlike windmills.
- Require less space than solar panels and can be installed on rooftops, balconies or gardens.

Fig. 4 Expected model of wind tree

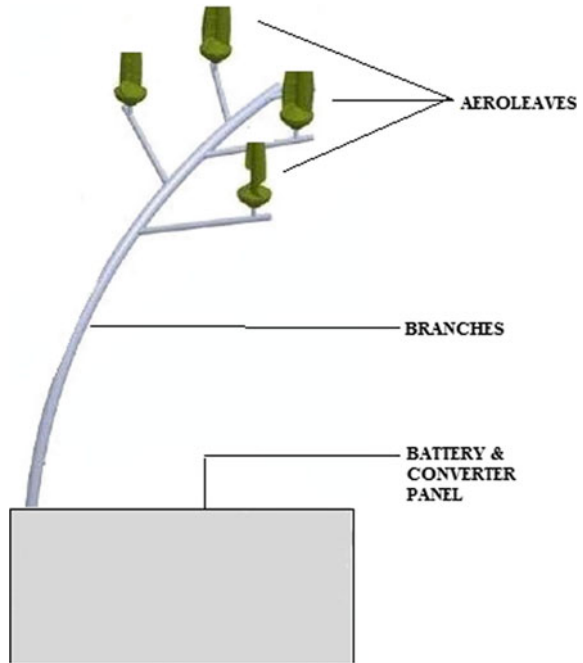


Table 1 Technical description of wind tree

Maximum power	120 W
Average power	100 W
Total no. of Aeroleaf	4
Average power per Aeroleaf	25 W- 30 W

- Work more silently with noise less than 5 dB and produce less CO₂ which help in pollution control.
- Transmission of power from generation to load is easy and cheaper as these are present near to the consumer premises
- Threshold wind for working of its turbine is very less and irrespective of direction; hence, it can produce electricity throughout the year.

9.2 Disadvantages

- Vertical axis turbine are consider less efficient than horizontal axis turbine. Hence, they are not able to produce more electricity out of wind.
- For larger power generation cost of installing, these trees become high and complex

- Wind trees cannot become a complete independent source for a particular office/house.
- As power generated is DC extra cost of converters, devices along with their maintenance are required.

10 Application with Respect to Society

- One of the major advantage of wind trees is that they can work silently with noise level of less than 5 dB, and it has very less wind threshold and irrespective of wind direction. These some properties make wind trees more efficient, and they can be installed at any locations.
- Power can be provided for up to 15 street lamps with these wind tress which in turn reduce the electricity demand.
- As electric vehicles are going to take over, these trees can play a major role in that as it can provide charging stations for vehicles. Also can be used for mobile and laptop charging.
- These tree can also be used in commercial shops, parking lots, schools as it not only provide electricity but also improve the scenic beauty of place due to its tree-like structure.

11 Conclusion

This paper presents a new technique of generating electricity which is totally eco-friendly and is reliable. Non-renewable energy is limited, and it is necessary for us to move toward renewable energy sources. Since the conventional windmills are criticized for large, noisy and selective location therefore this paper provides an alternative for energy generation by wind i.e instead of generating electricity by windmills, artificial trees known as wind trees is discussed in which its leaves will act as horizontal turbine and generate electricity. Wind tree is a new emerging technology in which leaves of the tree are designed such that it can rotate easily irrespective of the direction of wind and with very less threshold air speed. All the leaves are connected to generator and battery through branches. This paper displays the optimize use of wind energy as when the wind flows through the tree, its rotate which in turn produce electric energy without any noise or pollution. It can be installed in wide location unlike windmill and can act as a substitute for non-renewable energy resources. Whole system setup, material required has been discussed along with advantages and application with respect to society.

12 Future Scope

After solar energy, wind energy revolution can also help world to completely shift to the renewable energy source. Wind tree is affordable, efficient and have many application. In the future, we all know electric cars/vehicles going to be on roads so, they will require charging stations. For that, these wind trees can be used. Providing residents an alternative source of electricity can help them in times of power cuts. As these wind trees do not create any kind pollution, it will help to lower down the pollution level especially in cities like Delhi. These trees along with hybrid solar panel can result in a large energy source which will be very beneficial [9]. In the coming future, wind energy will play a vital role in shaping India economically and in sustainable development.

References

1. Masters GM (2004) Renewable and efficient electric power systems. Wiley, New York
2. NewWorldWind.com, "Modular Trees".
3. IJARSET—Generation of Electricity by Wind Tree. In: Chalageri SB, Deshpande AM, Banad MS, Pavate AS, Eresimi S (eds)
4. Chavan DS et al (2017) Tree mounted wind turbine. In: 2017 international conference on energy, communication, data analytics and soft computing (ICECDS), Chennai, pp 3122–3126
5. Luo FL (2010) Design of wind-turbine energy system. In: 2010 conference proceedings IPEC, Singapore, pp 110–115. <https://doi.org/10.1109/IPEC/CON.2010.5697140>
6. Koushik M, Narayana A, Gowtham V, Aziz A (2018) Design and fabrication of small VAWT for turbine tree using PVC Blades (2018).
7. Tullis S, Zaida S. Performance testing of a small vertical-axis wind turbine
8. <https://www.reuk.co.uk/>
9. Devashish, Thakur SA, S. Panigrahi and R. R. Behera, "A review on wind energy conversion system and enabling technology. In: 2016 international conference on electrical power and energy systems (ICEPES), Bhopal, pp 527–532

Reliability-Based Optimal Sizing for an Isolated Wind–Battery Hybrid Power System Using Butterfly PSO



Priyanka Paliwal

1 Introduction

Hybrid power systems [1] using inexhaustible sources of energy like solar and wind have gained a lot of importance in recent years. These are particularly suitable for secluded location where it is not possible to provide grid extension. Wind energy presents an unrestrained and environment friendly alternative to fossil fuel-based generation. As per the statistics presented by World Wind Energy Association, the capacity of wind has reached 650.8 GW toward the end of 2019. India has shown a remarkable growth and holds fourth position worldwide in terms of installed wind capacity [2]. The benefits and shortcomings of wind-based generation are briefly discussed as follows [3]:

Advantages

- Lower operating costs of wind-based technologies results in reduction of total life cycle costs.
- A suitable mix of two independent technologies results in increased reliability of system.
- Reduces environmental impact by decreasing reliance on conventional fossil fuel-based technologies.
- Encourages utilization of locally available resources.

Disadvantages

- Increased expenditure due to higher capital costs.
- Reliability issues due to variable nature of wind.

P. Paliwal (✉)

Maulana Azad National Institute of Technology, Bhopal, India

The key issue in utilization of wind power is the effect of intermittency of wind speed [1, 4]. This becomes further significant if wind power generation is deployed for autonomous applications [5]. Integration of electric energy storage has been seen as a powerful solution in order to deal with intermittency associated with these resources [6, 7]. Thus models for reliability analysis of systems based on wind and storage have been put forward by researchers.

Optimal sizing problem involving wind-based generators and storage has been discussed in several references [1,5,8,9] economic evaluation. The sizing problem has been primarily focused on system reliability, cost, and environmental emissions. Paliwal et.al. [1] have proposed planning considering techno-socioeconomic criteria. Akram et al. [8] have put forward a two level optimization for renewable energy-based generators and storage. Ajlan et al. [10] have conducted a feasibility study for off grid systems. Optimal resource planning has also been done in [6, 11, 12].

Various optimization techniques have been used for solving optimal component sizing problem. Yang et al. [13] have used genetic algorithm for determining component sizing of hybrid system battery. PSO [14] and simulated annealing-Tabu search [15] have also been employed for optimal sizing.

This paper proposes a reliability constrained determination of optimal component sizes for a wind–battery storage-based isolated hybrid power system. The wind speed has been modeled using Weibull probability density function. The battery storage sizing is carried out in conjunction with wind generation to offset the effect of intermittency of wind speed. An efficient metaheuristic called as butterfly particle swarm optimization (BF-PSO) is used to obtain the optimum component size. The results have been analyzed to facilitate a deeper understanding into planning problem. A case study has been carried out for isolated power system sited in Jaisalmer, India.

The organization of paper is as follows: In Sect. 2, the modeling of wind speed and output power has been explained. Section 3 presents the problem formulation. In Sect. 4, the methodology involving implementation of Butterfly PSO has been discussed. Section 5 presents case study and discussion on results. In Sect. 6, conclusion from work has been discussed.

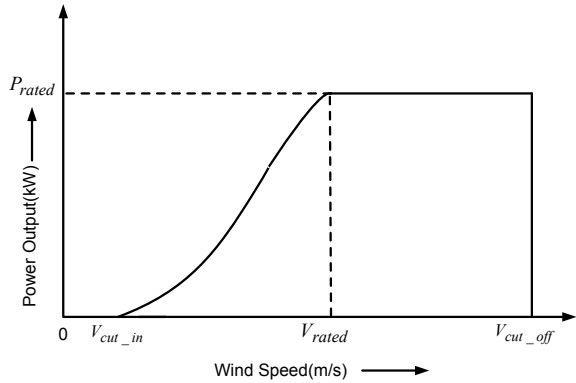
2 Wind Power Modeling

The modeling of wind speed is carried out using Weibull distribution as follows [1]:

$$f_w(v) = \frac{k}{c} \left(\frac{v}{c}\right)^{k-1} e^{-(v/c)^k} \quad \text{for } v > 0, \quad c > 1 \text{ and } k > 0 \quad (1)$$

where v = wind speed in m/s, $f_w(v)$ = Weibull probability density function for wind speed, k and c represent the shape and scale parameters, respectively, of Weibull distribution.

Fig. 1 Power curve of a wind generator



The primary parameters which affect generation of output power are cut-in, rated, and cut-out speed, respectively. This characteristic is typically depicted in power curve as shown in Fig. 1.

The power from wind generators is expressed as [8]:

$$P_w(v) = \begin{cases} 0 & v < v_{cut_in} \\ P_{rated} \times \frac{v-v_{cut_in}}{v_{rated}-v_{cut_in}} & v_{cut_in} \leq v < v_{rated} \\ P_{rated} & v_{rated} \leq v \leq v_{cut_out} \\ 0 & v \geq v_{cut_out} \end{cases} \quad (2)$$

where v_{cut_in} , v_{rated} , v_{cut_out} = cut-in, rated and cut-out speed, respectively of wind generator(m/s), P_{rated} = Rated power of wind generator(kW).

3 Problem Formulation

The optimal component analysis of wind–battery hybrid power system is performed on the basis of objective function as well as constraints which are explained as follows.

3.1 Objective Function

The objective function employed in this paper is Levelized cost of energy, LCOE

$$\text{Minimize LCOE} \quad (3)$$

The different cost components associated in determination of LCOE have been calculated as explained in [1].

3.2 Constraints

The various constraints used in optimal sizing problem are as follows:

Constraint on system reliability

$$EENS \leq EENS_{ref} \quad (4)$$

where $EENS$ = Expected energy not served, kWh, $EENS_{ref}$ = Reference value of $EENS$ used for system planning.

Constraint on capacity of units

The wind generator and battery storage units are restricted by maximum and minimum values

$$C_{W_{min}} \leq C_W \leq C_{W_{max}} \quad (5)$$

$$C_{B_{min}} \leq C_B \leq C_{B_{max}} \quad (6)$$

$C_{W_{min}}$ and $C_{W_{max}}$ is minimum and maximum capacity, respectively, of wind generators, kW.

$C_{B_{min}}$ and $C_{B_{max}}$ is minimum and maximum capacity, respectively, of battery storage, kWh.

Constraint on battery parameters

State of charge (SOC) of battery is to be restricted within minimum and maximum values.

$$SOC_{min} \leq SOC \leq SOC_{max} \quad (7)$$

4 Methodology: Implementation of BF-PSO

The problem of determining optimal component size for of wind–battery system is a constrained discrete combinatorial optimization problem. For solving optimization problem, a modified version of classic PSO called as Butterfly PSO [16] has been used. The BF-PSO mimics the natural intelligence and information sharing mechanism which the butterflies exhibit during nectar search process. The velocity and

position of each particle are calculated as follows:

$$v_{id}(k+1) = w_k v_{id}(k) + S_k(1 - P_k)C_1 r_1 [Pbest_{id}(k) - x_{id}(k)] + P_{kg} C_2 r_2 [gbest_d(k) - x_{id}(k)] \quad (8)$$

$$x_{id}(k+1) = x_{id}(k) + \alpha_k v_{id}(k+1) \quad (9)$$

where x_{id} = Position, v_{id} = velocity, $Pbest_{id}$ = Personal best and $gbest_d$ = global best position of d th dimension of i th particle, w_k = inertia weight for k th iteration, C_1 and C_2 = acceleration coefficients and r_1 and r_2 are random variable (0 to 1), S_k = butterfly sensitivity toward flower and P_k = probability of food for k th iteration, α = time varying probability coefficient.

The values of sensitivity and probability are considered varying between 0.0 and 1.0 and are expressed as a function of iteration as follows:

$$S_k = e^{-(iteration_{max} - iteration_k) / iteration_{max}} \quad (10)$$

where $iteration_{max}$ = maximum number of iterations and $iteration_k$ = k th iteration count.

$$P_k = Fitness_{gbest,k} / \sum Fitness_{pbest,k} \quad (11)$$

where $fitness_{pbest,k}$ and $Fitness_{gbest,k}$ = Fitness of pbest and gbest solutions respectively in k th iteration, P_{kg} = probability of global best (for global solution, $P_{kg} = 1$)

$$\alpha_k = rand * P_k \quad (12)$$

where, $rand$ = random number in the interval [0, 1].

The flowchart depicting implementation of BF-PSO is presented in Fig. 2.

5 Case Study and Results

The optimal sizing study is conducted for isolated hybrid power system situated in Jaisalmer, India. The peak load of system is 70 kW, and the load data has been obtained from [17]. The data for wind speed has been obtained from [18]. As discussed in Sect. 2, wind speed has been modeled using Weibull pdf. Figure 3 shows the wind speed and respective probabilities for time slot 1:00–2:00 pm for a day of each season. Such pdfs are obtained for each time segment. This facilitates the acknowledgment of intermittent nature of wind speed.

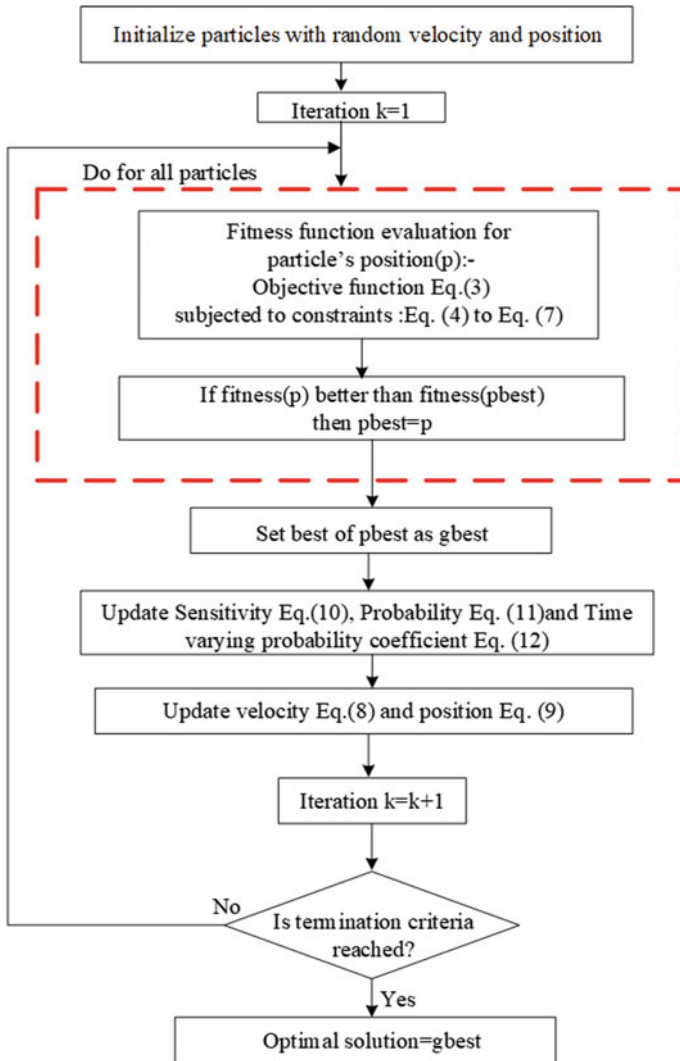


Fig. 2 Implementation of BF-PSO for optimization problem

The technical and economic parameters considered in the analysis have been obtained from [1]. The reliability criterion used for carrying out optimal sizing problem is subjected to following constraint:

$$EENS \leq 0.5\%.$$

The correlation between intermittent wind generators and battery storage is being established by using probabilistic battery state model [19]. The optimal solving

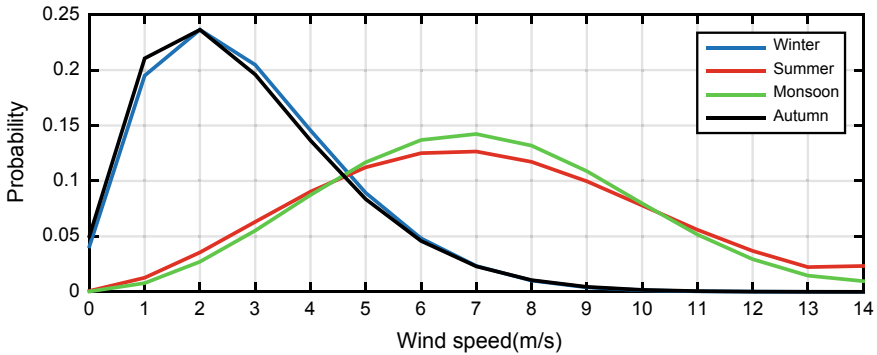


Fig. 3 Wind speed and respective probabilities for time slot 1:00–2:00 pm

problem is solved using Butterfly PSO explained in Sect. 4. The convergence characteristics are presented in Fig. 4. Table 1 presents the result of optimal sizing study.

As shown in Table 1, the optimal wind and battery capacity required to maintain required reliability standard are 250 kW and 712.8 kWh, respectively. This combination presents the lowest LCOE = 0.3891 \$/kWh.

The intermittency associated with wind generators is counteracted effectively by battery storage. Figure 4 presents the curves for load, power supplied by wind generators and battery storage for a particular day of every season. The importance of battery storage in maintaining system reliability is clearly asserted in Fig. 5. This

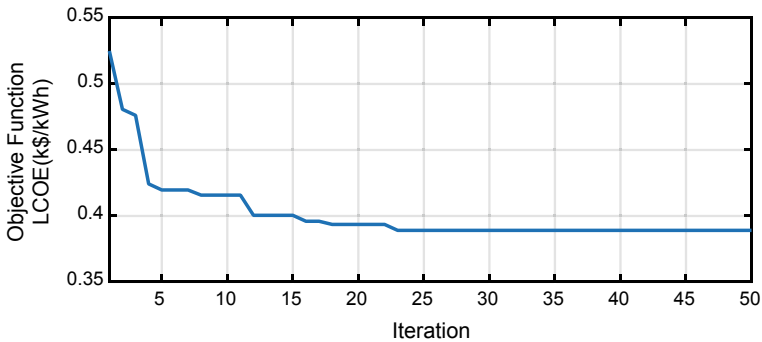


Fig. 4 Convergence characteristics

Table 1 Results of optimal sizing problem

Capacity of wind generators (kW)	Capacity of Battery storage (kWh)	TLCC (k\$)	LCOE (\$/kWh)	EENS (kWh)
250	712.8	1433	0.3891	969.66

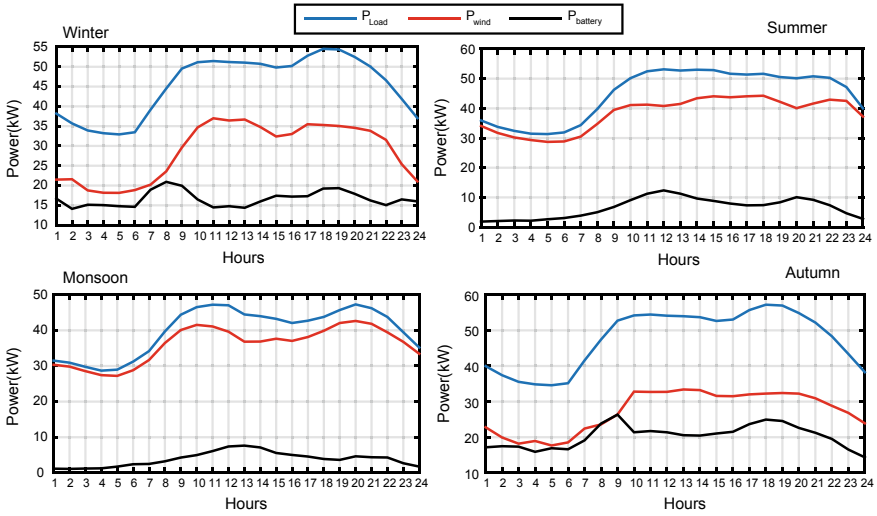


Fig. 5 Power distribution from wind generator and battery storage for a typical day in different seasons

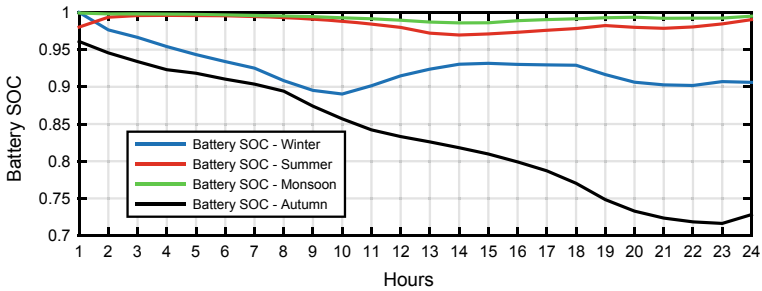


Fig. 6 Variation of battery SOC over 24 h for a typical day in different seasons

is further demonstrated in Fig. 6 which depicts the variation of battery SOC over 24 h.

6 Conclusion

In this paper, optimal sizing of an isolated power system based on wind generators and storage has been presented. The focus of system planning is to determine the optimal component sizes such that system is not only reliable but also cost-effective. The variability inherent with wind power is counteracted by integrating storage in right proportion. In order to adequately address the stochastic behavior, the wind speed

has been modeled using Weibull pdf. Seasonal variations in wind speed have been adequately accounted for. The optimization has been carried out using a very efficient metaheuristic, Butterfly PSO. The *EENS* has been used as a reliability constraint, and *LCOE* has been used for economic evaluation. It has been asserted that storage forms an integral component of isolated power system using renewable energy sources like wind. The formulation presented in this paper can serve as a tool for a well-organized and effective system planning.

References

1. Paliwal P, Patidar NP, Nema RK (2014) Determination of reliability constrained optimal resource mix for an autonomous hybrid power system using particle swarm optimization. *Renew Energy* 63:194–204. <https://doi.org/10.1016/j.renene.2013.09.003>
2. Chaurasiya PK, Warudkar V, Ahmed S (2019) Wind energy development and policy in India: a review. *Energy Strategy Rev* 24:342–357. <https://doi.org/10.1016/j.esr.2019.04.010>
3. Paliwal P, Patidar NP, Nema RK (2014) Planning of grid integrated distributed generators: a review of technology, objectives and techniques. *Renew Sustain Energy Rev* 40:557–570. [10.1016/j.rser.2014.07.200](https://doi.org/10.1016/j.rser.2014.07.200)
4. Bhargava SK, Das SS, Paliwal P (2014) Multi-objective optimization for sizing of solar-wind based hybrid power system: a review. *Int J Innov Res Sci Eng Technol* 3(4):195–201
5. Paliwal P (2020) Reliability constrained planning and sensitivity analysis for solar-wind-battery based isolated power system. *Int J Sustain Energy Planning Manage* 29:109–126. <https://doi.org/10.5278/ijsepm.4599>
6. Paliwal P, Patidar NP, Nema RK (2020) Probabilistic indices for analyzing the impact of DER penetration on system reliability. *IET Renew Power Gener* 14(12):2154–2165. <https://doi.org/10.1049/iet-rpg.2019.1214>
7. Paliwal P, Patidar NP, Nema RK (2012) Fuzzy logic based model for determination of battery state of charge applied to hybrid power system. *J World Acad Eng Sci Technol* 71:1164–1168
8. Akram U, Khalid M, Shafiq S (2018) Optimal sizing of a wind/solar/battery hybrid grid-connected microgrid system. *IET Renew Power Gener* 12(1):72–80. <https://doi.org/10.1049/iet-rpg.2017.0010>
9. Kumar A, Singh AR, Deng Y, He X, Kumar P, Bansal RC (2018) A novel methodological framework for the design of sustainable rural microgrid for developing nations. *IEEE Access* 6:24925–24951. <https://doi.org/10.1109/ACCESS.2018.2832460>
10. Ajlan A, Tan CW, Mohamed Abdilahi A (2017) Assessment of environmental and economic perspectives for renewable-based hybrid power system in Yemen. *Renew Sustain Energy Rev* 75:559–570. <https://doi.org/10.1016/j.rser.2016.11.024>
11. Huanna N, Lu Y, Jingxiang Z, Yuzhu W, Weizhou W, Fuchao L (2018) Flexible-regulation resources planning for distribution networks with a high penetration of renewable energy. *IET Gener Transm Distrib* 12(18):4099–4107. <https://doi.org/10.1049/iet-gtd.2018.5531>
12. Wang L, Singh C (2009) Multicriteria design of hybrid power generation systems based on a modified particle swarm optimization algorithm. *IEEE Trans Energy Convers* 24(1):163–172. <https://doi.org/10.1109/TEC.2008.2005280>
13. Yang H, Lu L, Fang Z (2008) Optimal sizing method for stand-alone hybrid solar–wind system with LPSP technology by using genetic algorithm. *Sol Energy* 82(4):354–367
14. Wang L, Singh C (2007) Compromise between cost and reliability in optimum design of an autonomous hybrid power system using mixed-integer PSO algorithm. *International conference on clean electrical power*, pp 682–689
15. Katsigiannis YA, Georgilakis PS, Karapidakis ES (2012) Hybrid Simulated annealing–Tabu search method for optimal sizing of autonomous power systems with renewables. *IEEE Trans Sustain Energy* 3(3):330–338

16. Kamdar R, Paliwal P, Kumar Y (2019) A hybrid multi-agent based BFPSO algorithm for optimization of benchmark functions. *J Circ Syst Computers*. <https://doi.org/10.1142/S0218126620501121>.
17. Reliability test system task force of the application of probability methods subcommittee (1999). The IEEE reliability test system-1996. *IEEE Trans Power Syst* 14(3):1010-1020
18. Mani A (1992) Wind energy resource survey in India-II. Allied Publishers Limited
19. Paliwal P, Patidar NP, Nema RK (2014) A novel method for reliability assessment of autonomous PV-wind-storage system using probabilistic storage model. *Int J Electr Power Energy Syst* 55:692–703

Analyzation of Temperature Rise in Induction Motor for Electric Vehicles



Sohail Khazi, Anusha Vadde, Krishnan Manickavasagam,
Govind R. Kadambi, Venkat Narayanan, B. M. Lokesh, Swapan Sarkar,
and Jagadeesha

1 Introduction

Induction motors are a common drive for all applications. In the design stage of induction motor, determination of temperature distribution is the crucial problem. The temperature distribution in all the part of the machine depends on the electromagnetic losses. The losses in an induction motor bring about the temperature rise which can cause thermal stresses. Direct temperature measurement, parameter-based temperature estimation and computational approaches are used to monitor the thermal stresses continuously in induction machine for thermal analysis. In direct temperature measurement, thermal monitoring performed using sensors requires constant human interpretation. In parameter-based temperature estimation, stator and rotor resistance are predicted using DC injection, sensor less rotor speed detection and Goertzel algorithm. In this method, sensors are not used and hence accuracy is quite good compared to direct temperature measurement method [1]. Computational approaches for thermal analysis are further classified as lumped parameter thermal network model (LPTNM), computational fluid dynamics (CFD) and finite element analysis (FEA).

LPTNM is an analytical approach which is very fast and low computational time compared to other approaches. The accuracy of this model is highly depends on thermal parameters and the heat transfer coefficients [2]. The difficult level increases with the complexity of the model due to the conversion of network model from the

S. Khazi · A. Vadde (✉) · K. Manickavasagam · G. R. Kadambi
Ramaiah University of Applied Sciences, Bangalore, Karnataka, India
e-mail: anushav.ee.et@msruas.ac.in

K. Manickavasagam
e-mail: manickavasagam.ee.et@msruas.ac.in

V. Narayanan · B. M. Lokesh · S. Sarkar · Jagadeesha
ABB India Pvt Ltd, Bangalore, India

complex geometrical models. In this approach, the accuracy is increased when the complexity of the model is simpler.

CFD is the numerical approach which is used to model any geometry. CFD is mainly utilized to determine the coolant air flow rate, pressure distribution and velocity in the cooling areas or locations around the motor. CFD analyzes the levels of heat transfer on the surface in the active materials and other solid structures. This method can predict the heat flow in complex regions such as around the motor, end windings and within rotor bars. Computation of temperature due to convection is the limitation of FEA [3]. CFD approach is used in 2D and 3D models for analysis depending on the geometry. 3D models require large model setup and more computation time which depends on PC configuration and speed.

FEA is a numerical method for solving the systems of governing equations over a domain of continuous physical system. Thermal analysis is one of the module in FEA and compatible for solving the 2D and 3D models which are presented in [3–5]. In complex geometrical models, FEA plays a vital role for computation of heat transfer, thermal conductivity and power losses accurately. The thermal analysis of the induction motor in different conditions is given in [6–10]. Since the mode of heat transfer is involved with conduction and convection in parts of the motor, the combination of CFD and FEA is accounted for in this work. Effect of loading an induction motor is investigated in terms of temperature rise and is given in [11].

There are few literatures available to predict the temperature rise of induction motors. Change in load causes variation in temperature and resistance which leads to variation in torque. Temperature rise of the SCIM directly affecting the full load torque. Hence, after certain life span of motor, the SCIMs are not able to utilize to maximum rating [10]. As a result, the performance of induction motor in electric vehicle decreases. This leads to make an attempt to predict the temperature in all the parts of the motor using FEA.

Thermal management is required for induction motors which are prominently using in electrical vehicles. Hence, the computation of temperature rise is needed at ambient temperature for the analyzation of performance and reliability of induction machine [13].

In this research work, A 15 kW tightly enclosed fan cooled (TEFC) three-phase squirrel cage induction motor (SCIM) is considered for the thermal analysis. The geometrical model of SCIM is created, and heat distribution is analyzed for rated load under steady-state conditions at 25 °C ambient temperature. An attempt is made to find the temperature rise in all parts of the motor. The main scope of the research is as follows:

- To observe the temperature rise in all parts of the motor without fins and fans
- To observe the temperature rise in all parts of the motor with fins and fans
- To observe the temperature rise reduction in the motor by modification in fins design

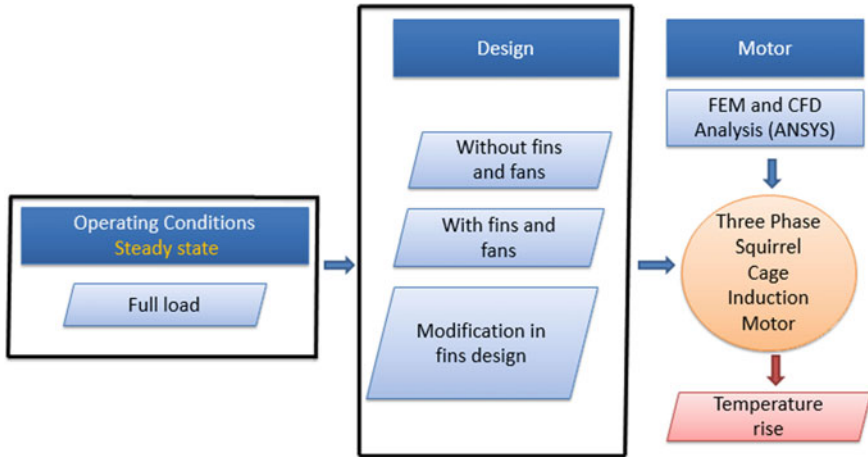


Fig. 1 Proposed approach

2 Proposed Approach for Thermal Analysis

In general, thermal analysis is carried out under different operating conditions such as starting, no load, running, rated load and maximum load at steady-state and transient state [12]. The design aspects of SCIM involve without fins, with fins and modification of fins. In this work, rated load is considered at steady state with all the design aspect. A 15 kW, SCIM of three-phases, TEFC is considered for thermal analysis using FEA and CFD which gives the temperature as output. The proposed approach is given in Fig. 1.

3 Model of TEFC-Type Induction Motor

3.1 Specifications of TEFC Induction Motor

The CFD analysis is initiated by accompanying by the heat sources. This heat sources are computed by the specifications of the SCIM three-phase, 15 kW, TEFC induction motor listed in Table 1.

Table 1 Specifications of 15 kW TEFC-type induction motor

Type	M2BAX160LB4 (IE1)
Voltage	415 V
Rated current	28.18 A
No load current	11.72 A
Power	15 kW
Pole	4 no
Rated speed	1461.8 rpm
No load speed	1498 rpm
Efficiency	90%
Temperature tolerance class and insulation class	B and F

3.2 Calculation of Heat Sources

Heat sources are computed in terms of the power losses per volume and given as input to the CFD analysis. The losses for each part of the machine are provided by ABB India Pvt Ltd. and heat source are given in Table 2.

In meshing, along with the solid domains five fluid domains are created. The fluid domain is created to capture the air flow inside and around the motor, over the fins and near the fan using CFD analysis.

- Two fluid domains are created near the fan; one stationary and one rotating fluid between fan cover and the fan.
- Two fluid domains are created inside the motor; one is stationary fluid domain between inner surface of the outer frame and stator core. Second one is outer frame to rotating fluid domain where there is air gap observed near the end bells, shaft, conductors, rotor core and stator core.
- One fluid domain is the external fluid domain that is rectangular box. The overall meshed model for the induction motor is represented in Fig. 2.
- The created meshed model is exported to the ANSYS CFD tool for analyzing the temperature distribution of SCIM induction motor. Conservative heat transfer flux is assigned to the domain interfaces such that heat transfer takes place among the

Table 2 Calculation of heat sources

Motor components	Losses (W)	Heat Sources (W/m ³)
Stator core	247.14	56,795
Rotor core	204.2	71,148.09
Stator windings	734.2	284,205.77
Rotor bar	5.43	10,053.69
Shaft	83.4	79,061.13
Short circuit ring	203.37	342,431.38

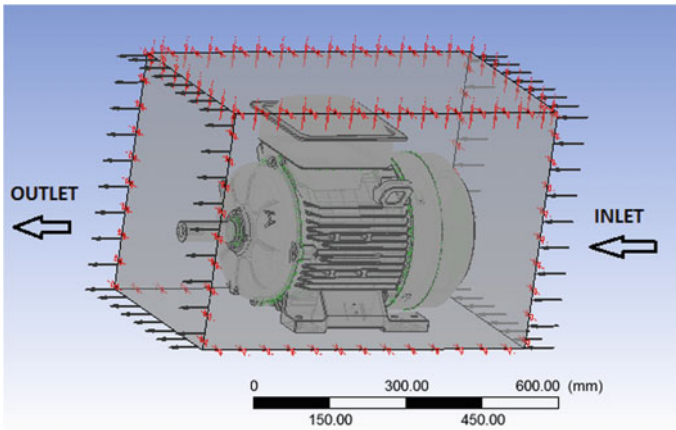


Fig. 2 Overall model setup

domain-domain interfaces or the coupled boundary conditions such as fluid–solid interfaces, solid–solid interfaces or fluid–fluid interfaces.

4 Results for Thermal Analysis of Induction Motor

Thermal analysis is carried out at rated load under steady-state condition of 25 °C ambient temperature.

4.1 Air Flow in Motor

The air flows are captured for two rotating fluid domains inside the motor and one rotating fluid domain that is external domain. Air flow inside the fan casing, near the end bells inside the motor and over the fins are captured in the form of vector plot of ANSYS CFX tool. The air flow velocity and air flow rate of the motor at the rated speed of 1461.8 rpm are in Table 3. Both air flow velocity and speed value decreases as the air flow travels in the axial direction from the non-driving end to driving end of the motor as observed in Table 3. The maximum air flow velocity of 21.45 m/s

Table 3 Details of the air flow inside the motor

Locations	Air flow velocity (m/s)	Air flow rate (m ³ /s)	Speed (rpm)
Over the fins	8–11	0.59–0.82	496–682
Fan casing	8.30–23.57	0.62–1.75	514.6–1461.8
Near end bells	2.77–19.38	0.15–1.08	198.14–1386.3

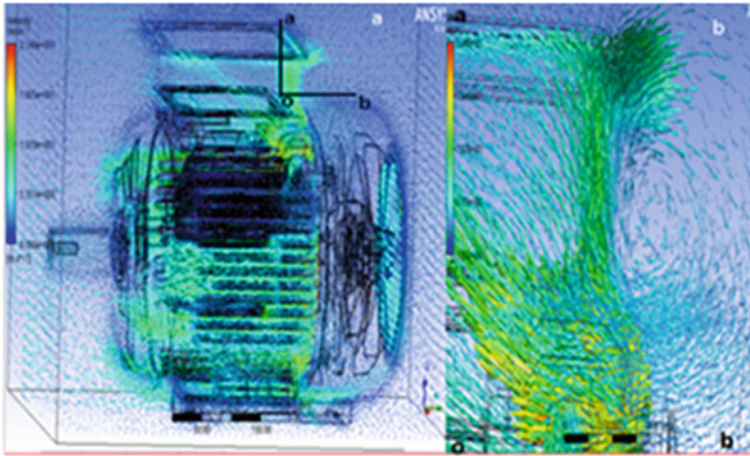


Fig. 3 a Vector plot of air flow over the fins, b air flow near terminal box

at speed of 1461.8 rpm is observed inside the fan casing as shown in Fig. 3a. From Fig. 3b, it is clearly observed that the air hits the top of the terminal box and flows in the backward direction in the section 'aob'.

4.2 Prediction of Temperature Rise in Various Parts of the Motor

In order to examine and analyze the temperature rise in each part of the motor, FEM analysis is performed on the developed mesh model for each part of the motor. Temperature contour plots of rotor core, stator core, shaft, stator windings, rotor bars and squirrel cage at rated load condition are represented in Fig. 4, which gives the prediction of the mean temperature values under steady-state condition for the rated load at 25 °C ambient temperature. From the temperature contour, it can be observed that the temperature at the center of each parts of motor is high compared to its driving end and non-driving end. This can be observed from the color of contour.

Discretization of each part of the motor is analyzed by the computational tool for thermal analysis. In the proposed method, it is possible to observe the temperature of the motor for any number of fins in outer frame. Fins and fans are the main components to dissipate the internal heat of the motor to the atmosphere. In this simulation studies, it is possible to change the number of fins and shape of the fins. In this work, 100% (with fins) and 0% of fins (without fins) with fans are considered for study to observe the temperature rise in the presence and absence of fins. The operating temperature of the motor is influenced by the ambient temperature. The analysis is performed by considering the 25 and 50 °C ambient temperatures. The results are produced in Fig. 5 at 25 °C ambient temperature without fins and with

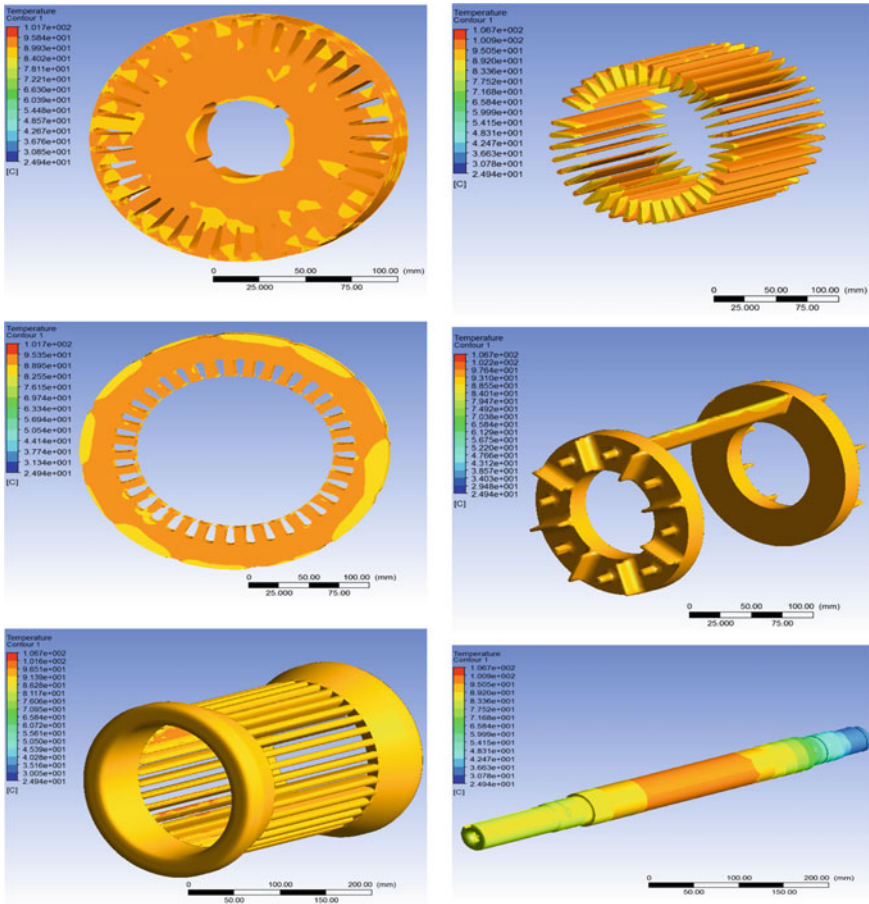


Fig. 4 Distribution of heat in **a** rotor core, **b** stator core, **c** stator windings, **d** rotor bars, **e** squirrel cage and **f** shaft

fans. From Fig. 5, for 0% fins with fan, the temperature of stator winding is reached to 83.55 °C which is maximum and temperature near the fan is 13.66 °C is minimum among all other parts of the motor. Figure 5 indicates that for 100% fins with fan, and the temperature of stator winding is reached to 68.62 °C which is maximum and temperature near the fan is 10.61 °C is minimum among all other parts of the motor. The stator winding draws the rated current and act as main heat source due to copper losses so that the temperature is maximum. The generated heat is dissipated gradually by conduction and convection across various parts of the motor and reaches minimum in the outer frame.

To check the feasibility of the proposed method, the fin is modified from width of 5–10 mm and height is modified from 35 to 37 mm as shown in Fig. 6 so that both width and height increased to a percentage of 2 and 1%.

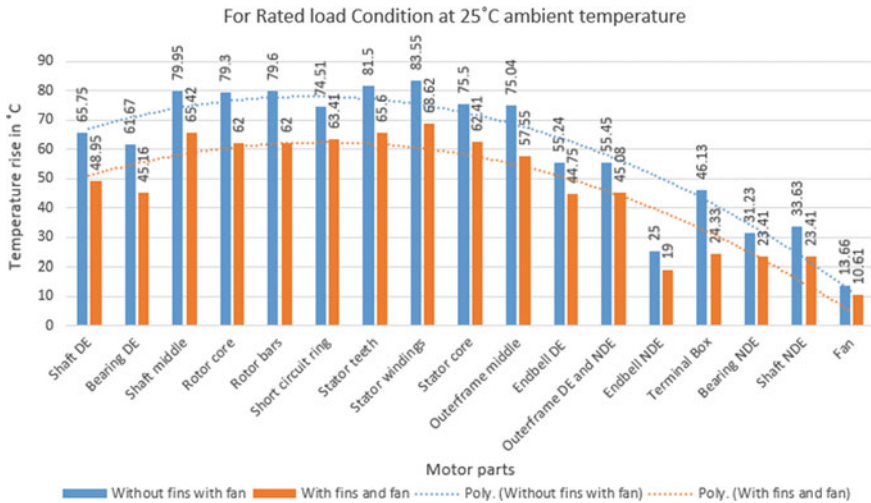
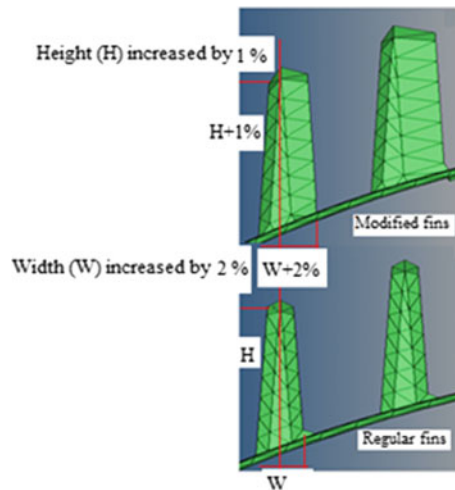


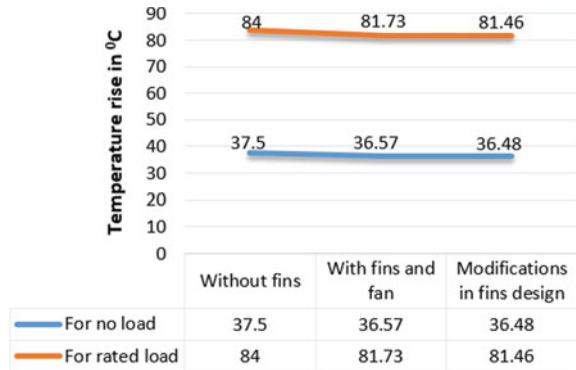
Fig. 5 Temperature rise in all parts of the motor under full load at 25 °C ambient temperature

Fig. 6 Modified fins design



The thermal analysis of 0% of fins, 100% of fins and modified fins are performed using CFD model. The impact of the modified fins on the temperature rise of motor is indicated in Fig. 7. The temperature rise is high for 0% fins under no load and rated load compared to 100% fins and modified fins design of motor. The temperature rise is observed at the 25 °C ambient temperature.

Fig. 7 Temperature rise in the motor with fins, without fins and modified fins



4.3 Validation of Results

The motor is made to run at rated load and allows to reach thermal equilibrium. Thermocouples are placed inside the various parts of the motor and on the motor surface. The temperature rise is predicted experimentally under the steady-state condition at 25 °C ambient temperature. The results are depicted in Fig. 8 represents the temperature rise in stator windings, frame driving end (ED), bearing DE and NDE which are main parts influencing the surrounding environment of motor in electric vehicles. From Fig. 8, it can be observed that the computational results are near to the experimental results provided by ABB India Pvt. Ltd. Temperature rise is been measuring experimentally by the resistance temperature detector on the windings is shown in Fig. 9.

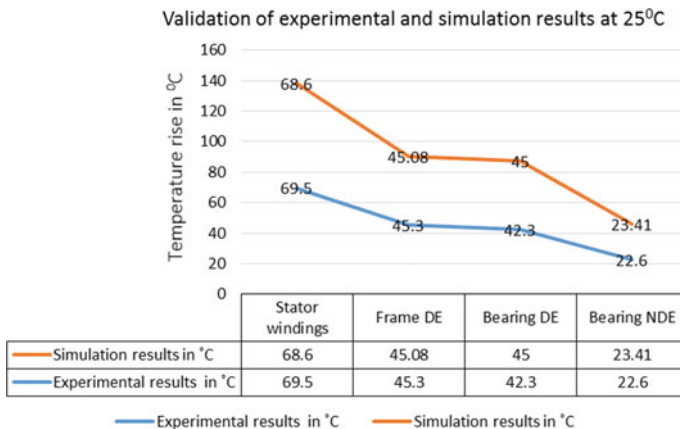


Fig. 8 Validation of experimental and simulation results at 25 °C ambient temperature

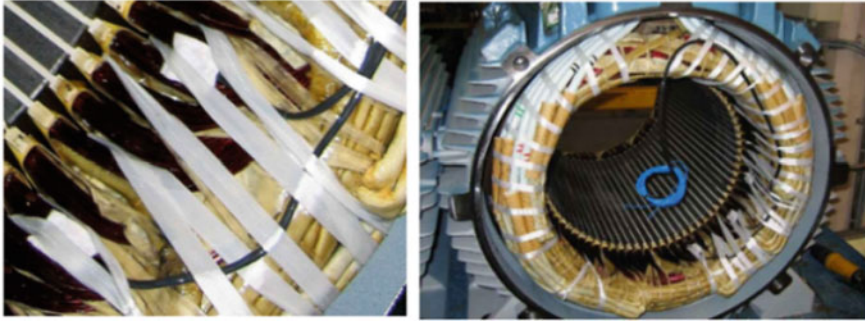


Fig. 9 Mounting the resistance temperature detector (Courtesy by: ABB India Pvt. Ltd.)

5 Conclusion

The thermal analysis of induction motor is beneficial for designing the windings of stator, stator core, rotor bar, stator frame and insulation level. In this work, 15 kW TEFC-type SCIM model is implemented using FEM. Heat source is given as input which results the heat distribution across the various parts of the motor. The proposed method is analyzed for 0% fins, 100% fins and modified design of fins which gives the temperature rise under no load and rated load conditions at 25 °C ambient temperature. The simulation results are compared with the experimental results provided by ABB India Pvt. Ltd. The results show that the temperature can be observed at any part of the machine and even the distribution of temperature can be observed at element wise. This result proves that rise in temperature at each part of machine gradually effect the performance of electric vehicles.

References

1. Boglietti A, Cavagnino A, Staton D, Shanel M, Mueller M, Mejuto C (2009) Evolution and modern approaches for thermal analysis of electrical machines. *IEEE Trans Ind Electron* 56(3):871–882
2. Popescu M, Dorrell DG, Alberti L, Bianchi N, Staton DA, Hawkins D (2013) Thermal analysis of duplex three-phase induction motor under fault operating conditions. *IEEE Trans Ind Appl* 49(4):1523–1530
3. Zhang Y, Ruan J, Huang T, Yang X, Zhu H, Yang G (2012) Calculation of temperature rise in air-cooled induction motors through 3-D coupled electromagnetic fluid-dynamical and thermal finite-element analysis. *IEEE Trans Magn* 48(2):1047–1050
4. Gao Z (2006) Sensor less stator winding temperature estimation for induction machines. Ph.D. dissertation, School of Electrical and Computer Engineering, Georgia Institute of Technology
5. Liu Y, Lee Y, Jung HK, Hahn SY, Youn JH, Kim KW, Kwon JL, Bae D, Lee JI (2000) 3D thermal stress analysis of the rotor of an induction motor. *IEEE Trans Magn* 36(4):1394–1397
6. Kylander G, Thermal modelling of small cage induction motors. Ph.D. dissertation, School of Electrical and Computer Engineering, Chalmers University of Technology

7. Staton D, Boglietti A, Cavagnino A (2005) Solving the more difficult aspects of electric motor thermal analysis in small and medium size industrial induction motors. *IEEE Trans Energy Convers* 20(3):620–628
8. Lee Y, Hahn S-Y, Kauh SK (2000) Thermal analysis of induction motor with forced cooling channels. In: *IEEE Trans Magn* 36(4):1398–1402
9. Seong KH, Hwang J, Shim J, Cho HW (2014) Investigation of temperature rise in an induction motor considering the effect of loading. *IEEE Trans Magn* 50(11):1–4
10. Yang Y, Bilgin B, Kasprzak M, Nalakath S, Sadek H, Preindl M, Cotton J, Schofield N, Emadi A (2016) Thermal management of electric machines. *IET Electrical Syst Transport* 7(2):104–116
11. Khalifa FA, Serry S, Ismail MM, Elhady B (2009) Effect of temperature rise on the performance of induction motors. In: *International conference on computer engineering & systems*, Egypt, pp 549–552
12. Boglietti A, Cavagnino A, Pastorelli M, Staton D, Vagati A (2006) Thermal analysis of induction and synchronous reluctance motors. *IEEE Trans Ind Appl* 42(3):675–680
13. Boglietti A, Cavagnino A, Staton DA (2005) TEFC induction motors thermal models: a parameter sensitivity analysis. *IEEE Trans Ind Appl* 41(3):756–763

Technical Review on Optimal Reactive Power Dispatch with FACTS Devices and Renewable Energy Sources



S. N. V. S. K. Chaitanya, R. Ashok Bakkiyaraj, and B. Venkateswara Rao

1 Introduction

ORPD, in general, is deliberated as a global optimization problem with a nonlinear and non-continuous function. It shows a main role in enlightening the economy and security in the process of the power systems. The ORPD achieves the reactive power flow within the limits of the system. The problem of reactive power is more difficult to solve than the optimal power flow problem due to its additional complex association among variables. Many techniques are implemented to decipher the problem of ORPD. In the conservative methodologies to the ORPD problem, search direction is considered based on the objective function of voltage gradient, with the assumption of voltage and angle changes does not affect the true power and reactive power. But in actual practice, true power losses are affected by true power variation, which is influenced by phase angle. So the gradient methods may not search in proper direction and may not converge if the system is big. This indicates that gradient methods may not be useful to solve ORPD problems. That is why heuristic optimization techniques have been established to elucidate the ORPD problems like genetic algorithm, PSO, ABC method, moth flame optimization, whale optimization technique, ant lion optimizer, HPSO and imperialist competitive algorithms, GSA, improved harmony search algorithm, gray wolf optimizer, PSO in graph theory, chaotic krill herd algorithm, advice genetic algorithm, chaotic artificial bee colony differential evolution, group search optimization, directional bat algorithm, hybridization of PSO with firefly algorithm,

S. N. V. S. K. Chaitanya · B. Venkateswara Rao (✉)

Department of EEE, V R Siddhartha Engineering College (Autonomous), Vijayawada, Andhra Pradesh, India

S. N. V. S. K. Chaitanya

Department of EEE, Annamalai University, Chidambaram, Tamil Nadu, India

R. Ashok Bakkiyaraj

Department of Electrical Engineering, Annamalai University, Chidambaram, Tamil Nadu, India

multiobjective differential evolution, moth flame algorithm, water wave optimization, etc. ORPD shows a main role in efficient optimal economical operation and planning of power system. The power system is the key task of ORPD problem for minimizing the power losses, improving the system stability and voltage deviation. These ORPD problems are applied to different IEEE9, 14, 30, 39, 57, 59, 118, and 300 bus systems.

FACTS devices have been suggested as an active alternate for monitoring power flow and adaptable bus voltage in power systems, resulting in an improved transfer capability, little system losses, and improve stability. In the case of first generation, FACTS devices are utmost modest devices and fewer complexes and less disparity. SVC, TCSC, and TCPST are examples of first era FACTS devices. The second era FACTS device is used in interrelated systems. Interline power flow system which affords better voltage control under variation of load, series-parallel united devices is the second era devices. STATCOM, SSSC, UPFC, IPFC are examples of second era FACTS devices. The deployment of FACTS devices have so many advantages, out of which some of them are environmental assistance, improved stability, enhancement of quality of supply, flexibility and uptime, minimal maintenance cost, etc. This boosts the current authors to practice these FACTS devices in this work. The difficult of reactive power and voltage control by predictable optimization techniques similar to linear programming, nonlinear PPG, mixed integer method, decomposition practice, dynamic encoding were deliberate in last 20 years. Additionally, no. of mathematical optimization procedures such as interior point method, quadratic programming, and Newton's techniques were projected to elucidate the traditional problem of ORPD. However, in preparation, these methods failed to give the solution of ORPD problem consisting FACTS devices because these devices display the order nonlinearity in power system. So these days, meta-heuristic techniques are established to solve ORPD problem consisting FACTS devices. These methods are oppositional krill herd algorithm, TLBO, symbiotic organisms algorithm, quasi-oppositional chemical reaction optimizer, harmony algorithm, glowworm swarm optimization, chaotic krill herd algorithm, etc.

For further enhancing the system performance, incorporate the renewable energy sources like solar, wind, and small-pumped storage plants in power system by using minimizing the fuel cost, minimization emission. These are presented in stochastic multiobjective ORPD, SHADE-EC algorithm, Jaya algorithm, dance bee colony (DBC), cuckoo search algorithm (CSA), etc. The remaining paper is structured as follows: primarily, literature review of most collective mathematical inventions of ORPD achievable with single- and multiobjective optimization methods. In succeeding section, the review related to practices is used to elucidate the ORPD with FACTS devices labeled and ordered. Additionally, numerous comparative studies are obtainable along with non-conventional energy sources. Lastly, particular significant conclusion is pinched to focus potential opportunities in this area.

2 Review on ORPD as a Single- and Multiobjective Optimization Problem

ORPD problem is solved by so many optimization algorithms consisting of different single-objective functions such as decreasing the true loss of power, decline of voltage deviation, improving the voltage profile, voltage stability improvement, minimum operating cost, improvement of voltage stability index, minimization of fuel cost or L-index or emission or combination of economic and environmental cost, and combining two or more objectives as a multiobjective function.

Mukherjee and Mukherjee [1] proposed a new algorithm known as chaotic krill herd algorithm for ORPD employed on IEEE30 and 57 bus systems. For this algorithm, all the three cases like reduction of true power loss and voltage deviation and improvement of voltage stability are taken as the objectives. Pandya and Roy [2] dealt with ORPD with the primary objective of declination of real power loss. This was applied to IEEE—14, 30, 57 and IEEE—39 New England bus test systems by using particle swarm optimization technique and compared with various optimization techniques. Biswas [3] implemented multiobjective function has fuel cost, power losses, emission, voltage deviation for IEEE30 bus system by using multiobjective bi-level programming (MOBLP). Mehdinejad et al. [4] proposed a HPSO and imperialist competitive algorithms applied on IEEE57 and 118 bus systems. This was solved for main objective functions such as reduction of true power loss and total voltage deviation. This hybridization improves its convergence capability and efficiency. Polprasert et al. [5] solve IPG-PSO for solving the ORPD problem for minimizing the true power loss, voltage deviation, and VSI on the IEEE30 and 118-bus systems. Basu [6] solved reduction of cost, emission, and enhancement of voltage profile and voltage stability implemented by group search optimization applied to various bus systems. Jain et al. [7] reduce the losses, improve the voltage deviation, and minimize the cost for IEEE30 bus system by using an evolutionary computational algorithm. Mohseni-Bonab et al. [8] proposed two-point estimate method (TPEM). The proposed approach is used to solve multiobjective ORPD problem valuable to IEEE14, IEEE30 bus systems as the objectives of power losses and voltage deviations. TPEM solution is compared with Monte Carlo simulations (MCS). Basu [9] proposed quasi-oppositional differential evolution for the purpose of ORPD. This method uses QOBL for initialization of population and implemented on various systems to reduce losses, voltage deviation, improve the system performance, and eliminate grid congestion. Basu [10] presents multiobjective differential evolution to explain multiobjective ORPD for IEEE30, IEEE57, and IEEE118 bus systems.

Pradeep et al. [11] implemented hybrid PSO-MVO method for solving the ORPD problem with cost reduction, enhancement of voltage profile and voltage stability. Kaur et al. [12] solved ORPD for the primary objective of voltage security implementing PSO in graph theory. In the case of occurrence of a fault and during isolation graph theory is very useful. To show the efficiency of the projected method, this was implemented on IEEE14 bus systems. Abaci et al. [13] present differential search algorithm (DSA) on IEEE30 bus and IEEE57 system for various objectives. Shaheena

et al. [14] use realistic backtracking search algorithm (BSA) to the IEEE standard 30-bus system to solve ORPD. Ng Shin Mei et al. [15] applied a newly surfaced optimization known as moth flame optimization technique which is addressed to solve the problem of ORPD. This technique makes use of the moment of moths which travels during dark time and is applied to IEEE—30, 57, 118 bus systems. Moth flame optimization technique simulation time is more compared to GWO, PSO, GSA, and CPVEIHBMO. Heidari et al. [16] proposed and utilized the Gaussian bare-bones WCA (NGBWCA) algorithm to tackle ORPD problem in power system. Nuaekaeaw et al. [17] implemented the MGWO algorithm on solving ORPD with different objectives for different systems. Mouassa et al. [18] implemented ant lion optimizer to demonstrated through IEEE30, IEEE118, and IEEE300-bus power systems as the objective of minimizing the power losses and improvement of L-index. Li et al. [19] executed hybridization of chaotic artificial bee colony with differential evolution algorithm to true power loss for IEEE14 and IEEE30 bus system. Ben Oualid Medani et al. [20] applied whale optimization algorithm (WOA) method examined and long-established on the IEEE14 bus, IEEE30 bus, and Algerian 114 bus system for minimization of losses in ORPD problem. Shareef and Rao et al. [21] used ABC-FF algorithms for ORPD, conducted on the IEEE14 and IEEE39 benchmark bus systems. Zhou et al. [22] performed WWO which is pragmatic to give the solution of ORPD problem the objective of minimum losses of active power for IEEE30 bus system and matched through BA, FPA, PSO, SCA, and CSA algorithms. Ravi et al. [23] interface between MATLAB and DigSILENT Power Factory software through genetic algorithm that has been tested on standard IEEE30 bus system to decrease the overall true power losses in transmission lines and the voltage deviation at the load buses. Sravanthi and Karthikaikannan [24] implemented directional bat algorithm solved to reduce true power transmission loss applied for IEEE—14 and 57 buses. Londoño et al. [25] association mean–variance mapping optimization (MVMO) algorithm with the IEEE30 bus test system to minimize system power losses.

Kamel et al. [26] use EGWO to solve the ORPD problem. Pattanaik et al. [27] launch and advised improved real-coded genetic algorithm (IRCGA) investigated on various systems with different objectives. Bhattacharyya and Karmakar [28] apply genetic algorithm (GA) on IEEE30-bus, 57-bus. Nguyen and Vo [29] propose an improved social spider optimization. The results are related to altered optimization algorithms, in IEEE30 bus system. GSA and QOTLBO give better results than ISSO in voltage deviation, and GSA, ALO, ABC, GWO, BA, QOTLBO, IPG-PSO, and DE give better results than ISSO in voltage stabilization index. Prasad et al. [30] crack ORPD by minimizing true power loss and total voltage deviation with modified differential evolution (MDE) algorithm for studied IEEE 30 systems. Indu and Yadav [31] present a gravitational search algorithm (GSA) applied to IEEE14 bus system for minimizing the power loss. Talbi et al. [32] executed trust region-based multiplier method (TRMM) algorithm for solving IEEE 30 bus system which has considered the objective functions for the minimization of cost of the fuel, power losses minimization, and voltage profile improvement. Zhang and Li [33] proposed multi-objective evolutionary algorithm (CPSMOEA) to solve ORPD with multiobjective.

Kunapareddy and Venkateswara Rao [34] suggested and implemented hybridization of PSO with a firefly algorithm solves the multiobjective function as reduction of the power losses and voltage deviation applied to IEEE14 and 30 bus system. The obtained results are compared with PSO and firefly algorithm. From the above literature, it is witnessed that majority of the authors use minimization of total true power loss as an objective function, and many authors applied this to IEEE30 bus system.

3 Review on ORPD Problem with FACTS Devices

Some authors incorporate the FACTS devices into ORPD problem, which enhances the system performance by reducing losses with proper management of reactive power. In the literature, the authors use the FACTS devices alike SVC, TCSC, STATCOM, TCPS, and UPFC out of which incorporation of UPFC into ORPD problem gives better results because of its series and shunt compensation.

Roy et al. [35] advice hybrid biogeography-based optimization (HBBO) for minimization of losses and voltage deviation incorporating FACTS devices like TCSC and TCPS. This method is functional on IEEE30 bus system to demonstrate the usefulness of the projected method and compared to ABC, BBO techniques with diverse mixtures of FACTS devices. Dutta et al. [36] presented the use of chemical reaction optimization (CRO) for optimal distribution of STATCOM to minimize transmission losses, progress voltage profile and voltage stability in a power system on IEEE30 and IEEE57 bus test systems. Battacharya and Raj [37] have functional swarm intelligence-based algorithm for the operative coordination of FACTS devices with other obtainable var sources presented in the grid. SPSO and other two swarm-based intelligence methodologies like APSO and EPSO are used for the optimal location of var sources and FACTS devices. IEEE30 and IEEE57 bus systems are engaged as regular test systems. Mukherjee and Mukherjee [38] proposed oppositional krill herd algorithm (OKHA) projected for solving the OPF problem with FACTS devices on modified IEEE30 bus and modified IEEE57 bus with TCSC and TCPS fitted at fixed considered locations. Prasad and Mukherjee [39] presented symbiotic organisms search (SOS) algorithm proposed for the explanation of OPF problem of power system furnished with FACTS devices. The enactment of SOS algorithm is verified on about the modified IEEE30 and IEEE57 bus test systems integrating with TCSC and TCPS. Mukherjee and Mukherjee [40] presented a recently established meta-heuristic CKHA, for the clarification of ORPD problem with FACTS devices. The suggested CKHA is tested, on IEEE30, IEEE57, and IEEE118 bus systems.

Dutta et al. [41] propose UPFC-based reactive power dispatch oppositional krill herd algorithm on IEEE57 and IEEE118 bus systems. The working efficiency of OKHA is better when associated with other algorithms. Praveen and Rao [42] presented multiobjective flow of optimal power with and without FACTS devices along with PSO, and it is verified on IEEE30 bus system. Dutta et al. [43] present a capable QOCRO method to find achievable optimal solution of multiobjective ORPD problem with FACTS device (with SVC and TCSC devices). The projected method is

tested on IEEE14 and IEEE30 bus systems, and it has outstanding convergence characteristics and is greater to further multiobjective optimization techniques. Nusair and Alomoush [44] proposed the solution of ORPD problem using a TLBO algorithm with considering FACTS devices STATCOM. The projected method is studied on IEEE14 and IEEE30 bus power systems for minimization of transmission losses. Prasad and Mukherjee [45] proposed symbiotic organism search (SOS) algorithm with FACTS devices to the IEEE30 bus system to solve minimize the power losses voltage deviation.

Kannan and Ravi [46] exhausting HSA and improved HSA with FACTS devices minimizes the total active power losses on IEEE14 and 57 bus systems. Shafik et al. [47] proposed an adaptive seeker optimization algorithm (ASOA) to find an optimal solution for the selection of lines to be equipped with TCSC devices that optimize the benefits. That TCSC provided to the transmission system and is tested over IEEE9 bus and IEEE14 bus systems to consider minimization of generation cost, true power loss, voltage deviation, TCSC cost and reactive power loss as objective functions. Banerjee and Bhattacharya [48] applied to IEEE5, IEEE30, and IEEE57 bus systems to minimizing power loss and fuel cost by using differential search algorithm (DSA) with UPFC.

4 Review on ORPD Considering the Impact of Renewable Energy Sources

In recent years, some of the authors include the uncertainties of renewable energy sources in ORPD problem. Some renewable energy sources require the reactive power for their proper operation, which is achieved by the optimization of reactive power. The literature as follows: Masond et al. [49] propose the wind integrated stochastic multiobjective ORPD problem in power system which is studied. The proposed model is employed to multiobjective function on the IEEE57 bus test system to reduce true power loss and voltage stability enhancement index. Hadji et al. [50] executed dance bee colony (DBC) with wind integration for solving IEEE30 bus system to consider the functions as emission, cost, true power loss, and voltage deviation. The results were compared with PSO_TVAC. Sarda and Pandya [51] executed cuckoo search algorithm (CSA) for minimizing the total fuel cost by using two combinations of renewable generators applied to IEEE57 bus system. The results are related to flower pollination algorithm (FPA). Biswas et al. [52] studied the SHADE-EC algorithm for deterministic ORPD by considering IEEE30 bus and 57 bus systems as case studies. Advantage of this is effectiveness, drives quickly toward optimal region and fast convergence to global optima. Amrane et al. [53] presented the autonomous group PSO (AGPSO) optimization employed for solving the ORPF problem to IEEE30 bus system as an objective function of reduction of true power loss, investment cost of wind turbine and investment cost of FACTS devices. Salkuti [54] resolves a glowworm swarm optimization (GSO) algorithm in a wind, thermal power system

is solved on a modified IEEE30 and 300 bus test systems to consider the objective function as a cost of total generation, losses and voltage stability enhancement index. Das et al. [55] implement Jaya algorithm with solar energy sources attempt to minimize transmission line power losses which has been examined for IEEE14 bus and IEEE30 bus test systems. The results are compared with PSO.

For further improving the system performance, FACTS devices are also incorporated into renewable energy sources consisting of ORPD problem. Combination of suitable FACTS device with non-conventional energy sources by using hybrid optimization technique in ORPD problem provides superior results.

5 Conclusion

This review paper discusses the ORPD problem solved by using various heuristic and meta-heuristic techniques with single- and multiobjective functions based on year of publication. In these past 5 years taken for survey, it can be observed that for the first few years, meta-heuristic techniques were commonly applied for the solution of ORPD problem. On the other side, a trend was observed in the past two years is ORPD with FACTS device with soft computing techniques. The chief benefit of each meta-heuristic technique lies in its usefulness to solve multiobjective problems. From this survey, authors conclude that majority of the authors have taken true power losses minimization as an objective function in transmission system to solve the ORPD problem. In the analysis, it is observed that losses are reduced and voltage profile improved by using meta-heuristic optimization methods. Authors finally conclude that by placing the proper FACTS devices, the system performance further enhanced, and lastly, it is also suggested that incorporation of non-conventional energy sources along with FACTS devices in ORPD problem gives better outcome.

References

1. Mukherjee A, Mukherjee V (2015) Solution of optimal reactive power dispatch by chaotic krill herd algorithm. *IET Gener Transm Distrib* 9(15):2351–2362
2. Pandya S, Roy R (2015) Particle swarm optimization based optimal reactive power dispatch. In: *Proceedings of 2015 IEEE ICECCT 2015*
3. Biswas P (2015) Genetic algorithm based multiobjectivebilevel programming for optimal real and reactive power dispatch under uncertainty. In: *Computational intelligence applications in modeling and control, studies in computational intelligence*. Springer International Publishing, Switzerland, pp 171–202
4. Mehdinejad M, Mivatlou B, DBoab R, Zare K (2016) Solution of optimal reactive power dispatch of power systems using hybrid particle swarm optimization and imperialist competitive algorithms. *Int J Electr Power Energy Syst* 83:104–116
5. Polprasert J, Ongsakul W, Dieu VN (2016) Optimal reactive power dispatch using improved pseudo-gradient search particle swarm optimization. *Electr Power Components Syst* 44(5):518–532

6. Basu M (2016) Group search optimization for solution of different optimal power flow problems. *Electr Power Components Syst* 44(6):606–615
7. Jain VK, Prasad U, Gupta AK (2016) Emerging research in computing information, communication and applications. *Emerg Res Comput Inform Commun Appl*
8. Mohseni-Bonab SM, Rabiee A, Mohammadi-Ivatloo B, Jalilzadeh S, Nojavan S (2016) A two-point estimate method for uncertainty modeling in multi-objective optimal reactive power dispatch problem. *Int J Electr Power Energy Syst* 75:194–204
9. Basu M (2016) Quasi-oppositional differential evolution for optimal reactive power dispatch. *Int J Electr Power Energy Syst* 78:29–40
10. Basu M (2016) Multi-objective optimal reactive power dispatch using multi-objective differential evolution. *Int J Electr Power Energy Syst* 82:213–224
11. Jangir P, Parmar SA, Trivedi IN, Bhesdadiya RH (2016) A novel hybrid PSO with multi verse optimizer for global numerical optimization and Optimal Reactive Power Dispatch problem. *Eng Sci Technol Int J* 20(2):570–586
12. Kaur D, Lie TT, Nair NKC, Valles B (2016) An optimal reactive power dispatch (ORPD) for voltage security using particle swarm optimization (PSO) in graph theory. In: *IEEE International conference on sustainable energy technology (ICSET)*, pp 25–30
13. Abaci K, Yamaçlı V (2016) Optimal reactive-power dispatch using differential search algorithm. *Electr Eng* 99(1):213–225
14. Shaheen AM, Sehiemy RA, Farrag SM (2017) Optimal reactive power dispatch using backtracking search algorithm. *Aust J Electr Electron Eng* 13(3):200–210
15. Ng Shin Mei R, Sulaiman MH, Mustaffa Z, Daniyal H (2017) Optimal reactive power dispatch solution by loss minimization using moth-flame optimization technique. *Appl Soft Comput J* 59:210–222
16. Heidari AA, Ali Abbaspour R, Rezaee Jordehi A (2017) Gaussian bare-bones water cycle algorithm for optimal reactive power dispatch in electrical power systems. *Appl Soft Comput J* 57:657–671
17. Nuaekaew K, Artrit P, Pholdee N, Bureerat S (2017) Optimal reactive power dispatch problem using a two-archive multi-objective grey wolf optimizer. *Expert Syst Appl* 87:79–89
18. Mouassa S, Bouktr T, Salhi A (2017) Ant lion optimizer for solving optimal reactive power dispatch problem in power systems. *Eng Sci Technol Int J* 20(3):885–895
19. Li Y, Li X, Li Z (2017) Reactive power optimization using hybrid CABC-DE algorithm. *Electr Power Components Syst* 45(9):980–989
20. ben Oualid Medani K, Sayah S, Bekrar A (2017) Whale optimization algorithm based optimal reactive power dispatch: a case study of the Algerian power system. *Electr Power Syst. Res.* 163:696–705
21. Shareef SM, Rao RS (2018) Optimal reactive power dispatch under unbalanced conditions using hybrid swarm intelligence. *Compt Electr Eng* 69:183–193
22. Zhou Y, Zhang J, Yang X, Ling Y (2018) Optimal reactive power dispatch using water wave optimization algorithm. *Oper Res* 0123456789
23. Ucheniya R, Saraswat A, Siddiqui SA (2018) Optimal reactive power dispatch through minimization of real power loss and voltage deviation. In: *ICTSES 2018*, Springer, pp 421–430
24. Sravanthi CH, Karthikaikannan D (2018) Optimal reactive power dispatch using directional bat algorithm. In: *ICICA 2018*. Springer, Berlin, pp 311–320
25. Londoño DC, JM-L, Villa-Acevedo WM, López-Lezama JM (2018) Assessment of meta-heuristic techniques applied to the optimal reactive power dispatch, vol 1
26. Kamel S, Abdel-Fatah S, Ebeed M, Yu J, Xie K, Zhao C (2019) Solving optimal reactive power dispatch problem considering load uncertainty. In: *2019 IEEE PES innovative smart grid technology Asia (ISGT 2019)*, pp 1335–1340
27. Pattanaik JK, Basu M, Dash DP (2019) Improved real-coded genetic algorithm for reactive power dispatch. *IETE J Res* 1–13
28. Bhattacharyya B, Karmakar N (2019) Optimal reactive power management problem: a solution using evolutionary algorithms. In: *IETE Technical Review (Institution of Electronic and Telecommunication Engineering, India)*, pp 1–9

29. Nguyen TT, Vo DN (2019) Improved social spider optimization algorithm for optimal reactive power dispatch problem with different objectives, vol 4. Springer, London
30. Prasad D, Banerjee A, Singh RP (2019) Optimal reactive power dispatch using modified differential evolution algorithm. In: *Advances in computer, communication and control*, lecture. Springer Nature Singapore Pte Ltd, pp. 275–283
31. Indu B, Yadav A (2019) Optimal reactive power dispatch using gravitational search algorithm to solve IEEE-14 bus system. In: *ICIPDIMS 2019*. Springer, Berlin, pp 463–473
32. Talbi EH, Abaali L, Skouri R (2019) Optimal power flow dispatch using trust region based multiplier method. In: *Advanced intelligent systems for sustainable development applied in energy and electrical engineering*, vol 7. Springer, Berlin, pp 187–199
33. Zhang M, Li Y (2020) Multi-objective optimal reactive power dispatch of power systems by combining classification-based multi-objective evolutionary algorithm and integrated decision making. *IEEE Access* 8:38198–38209
34. Kunapareddy M, Venkateswara Rao B (2020) Hybridization of particle swarm optimization with firefly algorithm for multi-objective optimal reactive power dispatch. In: *Lecture notes in mechanical engineering, innovative product design and intelligent manufacturing systems*. Springer, Singapore, pp 673–682
35. Dutta S, Roy PK, Manna DK (2015) HBBO optimization for optimal reactive power dispatch incorporating TCSC and TCPS devices. *IET Conf Publ* 2015(CP683):156–163
36. Dutta S, Roy PK, Nandi D (2016) Optimal location of STATCOM using chemical reaction optimization for reactive power dispatch problem. *Ain Shams Eng J* 7(1):233–247
37. Bhattacharyya B, Raj S (2016) Swarm intelligence based algorithms for reactive power planning with Flexible AC transmission system devices. *Int J Electr Power Energy Syst* 78:158–164
38. Mukherjee A, Mukherjee V (2016) Solution of optimal power flow with FACTS devices using a novel oppositional krill herd algorithm. *Int J Electr Power Energy Syst* 78:700–714
39. Prasad D, Mukherjee V (2016) A novel symbiotic organisms search algorithm for optimal power flow of power system with FACTS devices. *Eng Sci Technol Int J* 19(1):79–89
40. Mukherjee A, Mukherjee V (2016) Chaotic krill herd algorithm for optimal reactive power dispatch considering FACTS devices. *Appl Soft Comput J* 44:163–190
41. Dutta S, Mukhopadhyay P, Roy PK, Nandi D (2016) Unified power flow controller based reactive power dispatch using oppositional krill herd algorithm. *Int J Electr Power Energy Syst* 80:10–25
42. Praveen J, Rao BS (2016) Multi objective optimization for optimal power flow with IPFC using PSO. In: *3rd International conference on electrical energy systems*. IEEE, pp 85–90
43. Dutta S, Paul S, Roy PK (2016) Optimal allocation of SVC and TCSC using quasi-oppositional chemical reaction optimization for solving multi-objective ORPD problem. *J Electr Syst Inf Technol* 5(1):83–98
44. Nusair KN, Alomoush MI (2017) Optimal reactive power dispatch using teaching learning based optimization algorithm with consideration of FACTS device ‘STATCOM’. In: *2017 10th Jordan international electrical and electronic engineering conference (JIEEEEC)*
45. Prasad D, Mukherjee V (2018) Solution of optimal reactive power dispatch by symbiotic organism search algorithm incorporating FACTS devices. *IETE J Res* 64(1):149–160
46. Kannan D, Ravi G (2018) Optimal reactive power dispatch considering multi-type FACTS devices using harmony search algorithms. *Automatika* 59(3–4):303–314
47. Shafik MB, Rashed GI, Ei-Sehtemy RA, Chen H (2018) Optimal sizing and siting of TCSC devices for multi objective operation of power systems using adaptive seeker optimization algorithm. In: *2018 IEEE region ten symposium (tensymp)*, pp 231–236
48. Banerjee D, Bhattacharya S (2019) Optimal placement of unified power flow controller using differential search algorithm. *Int J Innov Comput Appl* 10(2):69–85
49. Mohseni-Bonab SM, Rabiee A, Mohammadi-Ivatloo B (2016) Voltage stability constrained multi-objective optimal reactive power dispatch under load and wind power uncertainties: a stochastic approach. *Renew Energy* 85:598–609
50. Hadji B, Mahdad B, Srairi K, Mancner N (2018) Optimal power flow solution considering wind integration using dance bee colony with dynamic step. *Int J Energy Technol Policy* 14(2–3):133–152

51. Sarda J, Pandya K (2018) Optimal active–reactive power dispatch considering stochastic behavior of wind, solar and small-hydro generation. In: SIGMA 2018, vol 1. Springer, Berlin, pp 255–263
52. Biswas PP, Suganthan PN, Mallipeddi R, Amaratunga GAJ (2019) Optimal reactive power dispatch with uncertainties in load demand and renewable energy sources adopting scenario-based approach. *Appl Soft Comput J* 75:616–632
53. Amrane Y, Boudour M, Ladjici AA, Elmaouhab A, Belazzoug M, Lamari M (2019) Optimal reactive power flow in the presence of wind power for active power loss minimization. In: Proceedings of 2018 3rd international conference on Electrical Sciences and Technologies in Maghreb (CISTEM), pp 1–6
54. Salkuti SR (2019) Optimal power flow using multi-objective glowworm swarm optimization algorithm in a wind energy integrated power system. *Int J Green Energy* 16(15):1547–1561
55. Das T, Roy R, Mandal KK, Mondal S, Mondal S, Hait P, Das MK (2020) Optimal reactive power dispatch incorporating solar power using Jaya Algorithm. In: Computational advancement in communication. Springer Nature Singapore Pte Ltd., pp. 37–48

A Deep Learning Approach to Recognize Faces After Plastic Surgery



Tanupreet Sabharwal and Rashmi Gupta

1 Introduction

Face is the most accessible trait to prove uniqueness of one's identity, in consideration of which face recognition and identity verification have been gaining attention in almost all fields in the recent decades. Human face preserves the richest information about one's identity such as age, gender, emotion, expression which are unique for everyone, but nowadays, it is relatively easy to impersonate or steal someone's identity using masks or conceal one's identity by covering or obfuscating it. Spoofing attacks have already become a common scenario for many theft-based cases and criminal records. Plastic surgeries are used nowadays to forge one's genuine identity and commit stern crimes [1–4]. Therefore, human identity is subjected to multiple risks and needs to be ensured of its safety, and hence, facial authentication-based biometric techniques are widely employed to authenticate a person and ensure safety as well as uniqueness of his/her identity. Although a multitude of solutions have been proposed for identity verification purposes, deep learning is a technique which makes use of multiple layers of classification and processing to learn from various data representations. All the existing methods for face recognition and verification can be classified into two major sub-divisions, the first of which is the handcrafted techniques, which includes principal component analysis (PCA), local binary patterns (LBP), eigenfaces and many more. In general, all traditional methods aim to recognize faces using only one to two layers of representations. Also, these methods could target only one constraint in an unconstrained environment such as light, pose, illumination and gender. There was no integrated technique for facial recognition until AlexNet won the ImageNet competition in 2012 [5].

T. Sabharwal (✉)
USICT, GGSIPU, New Delhi, India

R. Gupta
Department of Electronics and Communication Engineering, NSUT East Campus (Formerly
AIACT&R), New Delhi, India

The other technique which is deep learning for face detection and verification (commonly known as recognition) consists of innumerable neural networks such as CNN's, generative adversarial networks (GANs). A neural network framework provides many levels of feature extraction which helps the algorithm learn the correctness and authenticity of a face in an image. In recent times in the arena of neural networks, deep learning is being highly explored. A lot of face recognition algorithms have been developed using deep learning techniques, and it has been perceived that they outpaced all other state-of-the-art techniques. Deep models make use of deep neural nets for instance CNN's [6, 7]. Neural networks basically consist of a bunch of "neurons" which are values that start off with input data, and then get multiplied by weights, are summed up, and then passed through an activation function to produce new values, and this process then repeats over however many "layers" the neural net is defined up-to.

Deep models, for example CNN's, use a cascade of several layers of processing units for attribute alteration and abstraction. These models learn multiple levels of demonstrations that relate to diverse abstraction levels. These levels constitute an order of perceptions, presenting robust invariance to the face posture, illumination and countenance changes, as shown in Fig. 1.

CNN approach makes use of back-propagation apart from just being a feed-forward neural network. The concept of back-propagation helps in calculation of loss after each state and then adjusting the parameters of the model to improve its

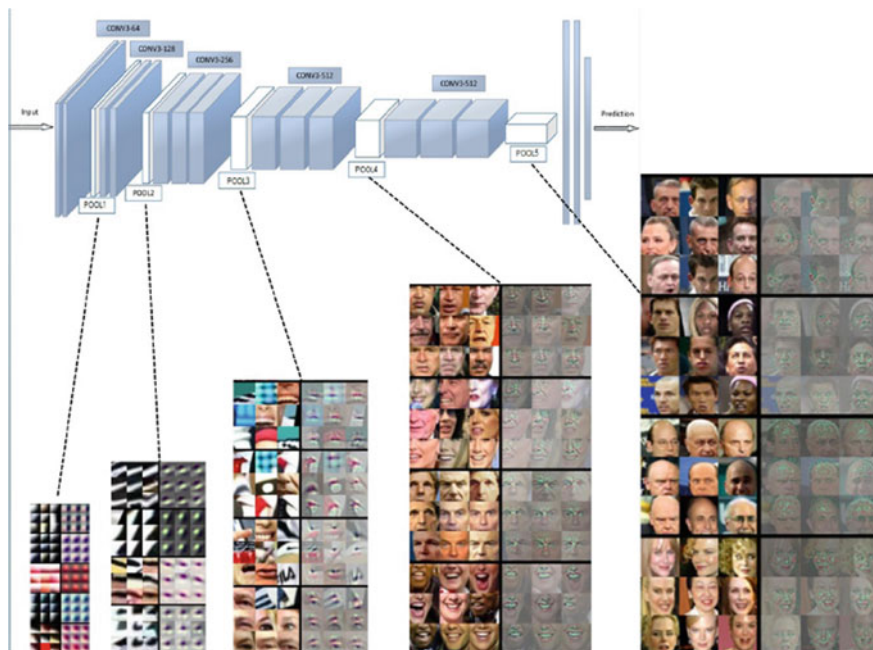


Fig. 1 Deep representation of multiple layers in a convolutional neural network [5]

output using an optimizer. All these steps will be discussed in detail later in Section 3. The output of a CNN is analysed using loss and accuracy after each step. A good recognition system is also characterized by having a greater rate of correct positives and a minor rate of untrue positives. The total number of exact positives is divided by total recognition rate to obtain the accuracy of the model.

In this paper, we have introduced a CNN that aims to recognize images from a plastic surgery dataset and predicts the accuracy of the model. The paper is ordered as follows: after the introduction section, literature survey and associated works have been discussed in Sect. 2, following which the algorithm applied for has been discussed in Sect. 3. Later on, in Sect. 4 the results obtained have been presented and the future scope of the paper has been elaborated in Sect. 5 along with the drawn conclusions.

2 Literature Survey

Farfade et al. [8] projected a deep model based on CNN for facial detection, which contained a total of eight layers, the first five layers being the convolutional layers and the next three layers as fully connected layers. This method resulted into excellent accuracy; however, detection time was not mentioned as an improved parameter. Since it is a deep neural network, the time for detection would be unnecessarily long. Levi et al. [9] also stated that by using the feature extraction method in CNN's, the efficacy of the system can be significantly increased in terms of age and gender-based facial recognition. Taigman et al. [10] performed face alliance by means of explicit three-dimensional modelling and anticipated a nine-layer deep network for learning generic face illustrations in unrestrained scenarios. Wen et al. [11] anticipated a vigorous deep CNN model using softmax loss function with centre loss function to surge the discriminative power of learned attributes for face acknowledgement. Yet, in another work, Li et al. [12] adopted the convolutional neural networks technique in a cascaded pattern. The cascade classifier comprised of six stages, out of which three were used for classification of a face into face and non-face, the other three for the calibration on the windows' scale and position. This approach discards majority of non-face windows in the early stages and pays more consideration to challenging samples in the final stages. This process ominously reaches promising performance and also greatly augments the detection speed, i.e. 14 frames/s on a single CPU and 100 frames/sec with a GPU. A low-power CNN-based recognition system has also been designed by Kyeongryeol et al. [13], which features an always on detector using image sensor and SRAM cell.

3 Proposed Algorithm

In this segment, we first explain the assessment methodology and introduce the deep CNN model that we have built, keeping in mind the necessity to obtain an algorithm with lesser computational requirements and minimal training time, yet achieving accurate and efficient results. We then continue by presenting the database and process used to train the deep models and conclude the section with a detailed explanation of the covariates considered in this research.

3.1 Overall Framework

Although CNN's can deal with huge amounts of data, it is first necessary to divide the data into training/testing sets for training the network and obtaining the validation loss. The dataset we used consisted of images from the plastic surgery dataset (<https://iab-rubric.org/resources.html>), on which the neural network is run and training and validation losses as well as accuracies are obtained. Each pair of images in the dataset corresponds to a before and after image of a surgically altered face. The motivation to use this network architecture is to reduce the GPU and computational requirements for the training process, along with minimal time usage to train the network over CPU. Training data is used to train the CNN over the images which are labelled and the testing set images are used to test the precision of the convolutional neural network with each iteration. The final plots are then obtained for a comparative analysis of accuracy as well as loss of testing and training set over the dataset. For each iteration in the dataset, we grab the features and labels from the current batch, then zero the gradients to pass the data through a layer. After this, the data is passed through the network and the loss is calculated for each epoch. Then, for each iteration, we adjust the weights in the network to minimize the loss further. That is how we obtain a final CNN with minimal loss targeting the required application. Figure 2 gives a pictorial representation of the anticipated scheme.

3.2 Network Architecture

The meekest neural network is fully connected and feed-forward, which means we go from input to output. In one side and out the other in a "forward" manner. But a convolutional neural network is made using some complex layers, which we do by adding convolutional layer. Apart from input and output size, this layer consists of one more parameter, called the kernel size. Kernel size is basically the size of a window of pixels the net computes each time in an iteration. A kernel size of 3 would mean (3×3) convolutions. After the application of convolutional layers, we need to flatten the obtained output, this is done using the linear layers. Convolutional layers

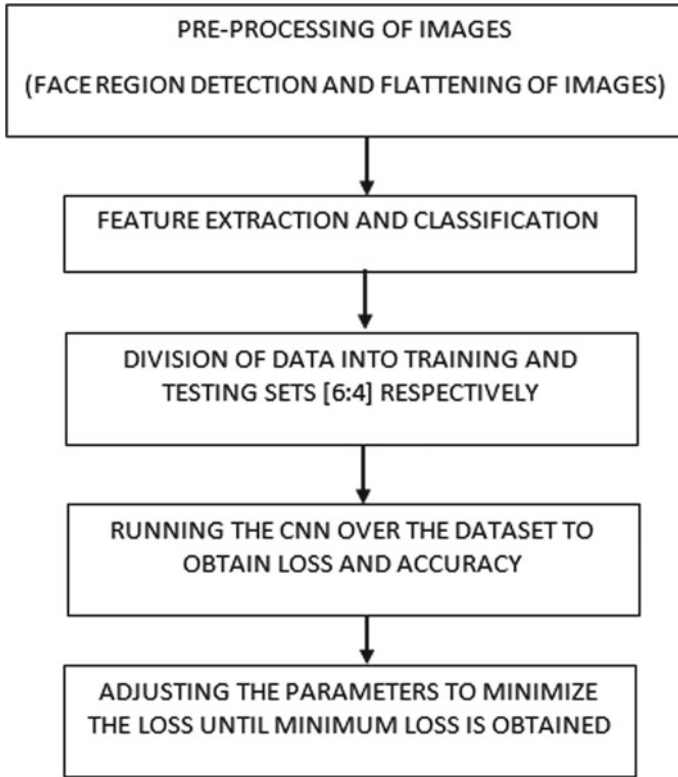


Fig. 2 Flowchart illustration of the projected methodology

perform convolutions by taking in an image and producing an output of multiple images obtained by convolutions, which are not flat. But to pass these images to further layers, we need to first flatten them using linear layers before passing to dense layers. The outcome of linear layer is given as an input to the first fully connected layer of the CNN. Before passing the outcome of last fully connected layer to a regular layer, flattening needs to be done. After applying all the layers to the net, the activation function needs to be invoked. In this network, we have used a rectified linear unit activation function (ReLU) and we run it over the convolutional layer. We use activation functions to keep our data scaled between certain ranges, say, for example, 0 to 1 in our case. Afterwards, we run all of it over a two-dimensional max-pool layer. Finally, we apply the loss function and optimizer to completely build our neural network. The loss function works as the supervision signal to tell about the separation of features and estimate how far-off the obtained result is from accurate and actual desired result (Fig. 3).

We have used softmax loss function in the last layer of the network and mean squared error loss (MSE loss) for the linear layers since they have been used for flattening. The optimizer that we have used is the most commonly used Adam optimizer,

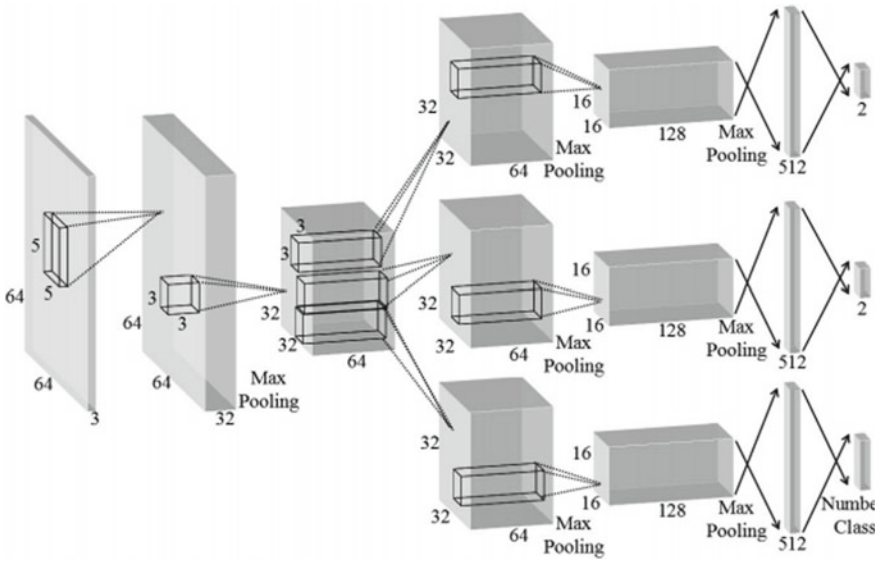


Fig. 3 Layered architecture of CNN

which is adaptive momentum which helps in altering the adjustable parameters in the network to get the model closer to fit the architecture. The first convolutional layer takes 1 as the input and produces 32 channels at the output with a kernel of size five. The second convolutional layer takes the response-normalized and pooled outcome of the first convolutional layer as input and filters images of input size 32, producing 64 output channels after convolution with a kernel size of 5. Then, the third convolutional layer inputs 64 channels and produces 128 channels with the same kernel size.

There are three convolutional layers, followed by flattening and normalization and two fully connected layers. All the three convolutional layers are max pooled over ReLU activation. Now the data obtained needs to get iterated over the neural network architecture, and this is done by diving the training and validation sets further into smaller batches and running the CNN over each batch a specific number of times to run the network. After this, the loss and accuracy after each epoch (iteration) are analysed.

4 Results and Discussion

A variety of techniques have been offered till date for reaching promising precision for recognizing faces ranging from principal component analysis (PCA), linear binary patterns histogram (LBPH), Fisher vector analysis (FV), eigenfaces, local feature analysis (LFA), speeded-up robust features (SURF), local binary patterns

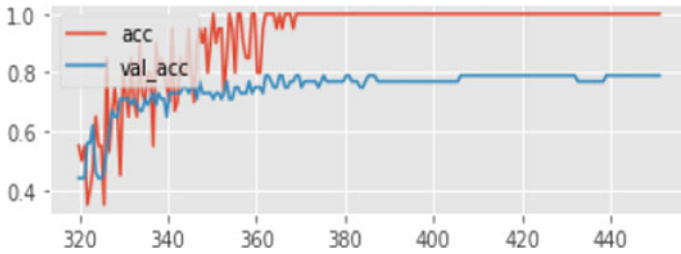


Fig. 4 CNN accuracy plot for training and validation sets

(LBP), geometric features (GF) and neural networks, to lesser used approaches such as evolutionary-genetic algorithm (GA), particle swarm optimization (PSO) and structural similarity image maps (SSIM) [14]. We obtained our results on a convolutional network for facial recognition with a training accuracy of 100% and validation accuracy of 82% over plastic surgery images (Fig. 4).

These results are basically evaluated by counting the number of true matches over the total number of matches (including the false positives). The loss function we have used helps in dropping the number of incorrect positives for each iteration. The accuracy is calculated using the following formula:

$$\text{Accuracy} = \text{len}(\text{True matches}) / \text{len}(\text{total matches}),$$

where the “len” function records the length of matches.

The loss parameter describes how closer the current model is to the accurate model and helps in adjusting the parameters of the model to further decrease the loss in next iteration.

A loss of 0.17 was obtained (Fig. 5) for validation test set over approximately 400 epochs. However, the training time is significantly reduced due to the robust and efficient architecture of the neural network. Also, such a model has reduced the computational requirements and complexities of the system without compromising with the precision (i.e. accuracy).

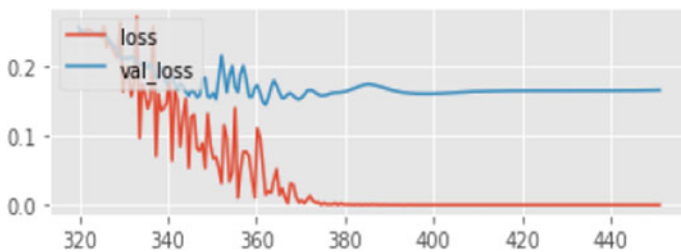


Fig. 5 CNN loss plot for training and validation sets

5 Conclusion

In this work, we have presented a CNN design to perform facial recognition after plastic surgery by extracting features. This model can deal with both normally classified and surgically altered images. Also, the computational complexity of the system has been reduced to such an extent that it can also outperform existing methods in future. Thus, we can conclude that a CNN-based facial recognition model can work over a single CPU with minimal GPU requirement to achieve higher rates of accuracy, which makes the model even more efficient. Establishment of a real-time robust identification system is the need of the day. Such systems can be further implemented by fusing two deep models together to further reduce the space and time complexities of the system. In future, we aim to implement a deep model for facial disguise recognition (camouflaged faces) to recognize samples of faces that are either attacked or impersonated. Various forms of disguise are a threat to facial identity for which robust and efficient face verification systems need to be built.

References

1. Liu X, Shan S, Chen X (2012) Face recognition after plastic surgery: a comprehensive study. In: Asian conference on computer vision, pp 565–576
2. Sabharwal T, Gupta R, Son LH et al (2019) Recognition of surgically altered face images: an empirical analysis on recent advances. *Artif Intell Rev* 52(1009–1040):2019. <https://doi.org/10.1007/s10462-018-9660-0>
3. Sabharwal T, Gupta R (2019) Human identification after plastic surgery using region based score level fusion of local facial features. *J Inform Secur Appl* 48:102373. ISSN 2214-2126. <https://doi.org/10.1016/j.jisa.2019.102373>
4. Mehta H (2009) On innovations in plastic surgery. *J Plastic Reconstr Aesthetic Surg* 62:437–441
5. Mei W, Weihong D (2019) Deep face recognition: a survey. School of Information and Communication Engineering, Beijing University of Posts and Telecommunications, Beijing, China. arXiv: 1804.06655v8 [cs.CV] 12 Feb 2019
6. Krizhevsky A, Sutskever I, Hinton GE (2012) Imagenet classification with deep convolutional neural networks. In: Pereira F, Burges C, Bottou L, Weinberger K (eds) *Advances in neural information processing systems*. Curran Associates, Inc., pp 1097–1105
7. Sabharwal T, Garg T, Singh SV (2019) A Comparative analysis of various deep learning models for facial recognition. In: 6th international conference on computing for sustainable global development (INDIACom), New Delhi, India, pp 966–970
8. Farfade SS, Saberian MJ, Li L-J (2015) Multi-view face detection using deep convolutional neural networks. In: *Proceedings of the 5th ACM on international conference on multimedia retrieval*. ACM, pp 643–650 (2015)
9. Levi G, Hassner T (2015) Age and gender classification using convolutional neural networks. In: *Proceedings of the IEEE conference on computer vision and pattern recognition workshops*, pp 34–42
10. Taigman Y, Yang M, Ranzato MA, Wolf L (2014) Deepface: closing the gap to human-level performance in face verification. In: *Proceedings of the IEEE conference on computer vision and pattern recognition*, p 1701
11. Wen Y, Zhang K, Li Z, Qiao Y (2016) A discriminative feature learning approach for deep face recognition. In: *European conference on computer vision*, p 499

12. Li H, Lin Z, Shen X, Brandt J, Hua G (2015) A convolutional neural network cascade for face detection. In: Proceedings of the IEEE conference on computer vision and pattern recognition, pp 5325–5334
13. Kyeongryeol B, Sungpill Choi C, Changhyeon K, Donghyeon H, Hoi-Jun Y (2018) A low-power convolutional neural network face recognition processor and a CIS integrated with always-on face detector. *IEEE J Solid-State Circ* 53(1)
14. Nappi M, Ricciardi S, Tistarelli M (2016) Deceiving faces: when plastic surgery challenges face recognition. *Image and Vision Computing*
15. Plastic surgery face database, https://iiitd.edu.in/iab/Image_Analysis_and_Biometrics_Group/Resources.html, <https://iab-rubric.org/resources.html>
16. American Society of Plastic Surgeons (ASPS) website: <https://www.plasticsurgery.org/about-asps.html>
17. Ricanek K (2013) The next biometric challenge: medical alterations. *IEEE Computer Society*, pp 94–96

IoT-Based Energy Monitoring and Controlling System for Home Automation



C. S. S. Barath and R. Nirmaladevi

1 Introduction

The Indian electricity sector has a national electric grid installed with a capacity of 370.498 GW as of May 2020 [1]. India is the third largest consumer and producer of electricity in the world after China and the USA with a 5.8% global share [2, 3]. The gross utility electricity generation was 1384 billion kilowatt-hours in 2019–20, and the electricity generation target of conventional sources for the year 2020–21 was fixed at 1,330 billion units [4, 5]. There are significant upgradations in automating various industrial aspects for the reduction of manual efforts with the expeditious development in wireless technology for which it has become significant for the utility companies to devise better, non-intrusive, and user friendly techniques so that proper bills can be generated [6, 7]. Moreover, it has become a mighty task in controlling the power as per the growing requirements. One such example is the recent incident in Chennai where the electricity bills gave the residents a high voltage shock as numerous customers claim that they have been charged 30–40% more than their usual consumption, especially in June 2020. This has mainly occurred due to the COVID-19 pandemic that has restricted the Electricity Board officials (Tamil Nadu Generation and Distribution Corporation Limited) to note the meter readings for a bi-monthly cycle. The unheralded and arbitrary hike has impacted many residents. Therefore, the numerous drawbacks of the conventional electromechanical meters must be resolved by deploying advanced and innovative technological methods.

Internet of Things (IoT), also referred to as the third wave of information technology, is the network of physical devices that enables these objects to acquire and exchange data resulting in minimal human interventions, enhanced accuracy and thus provides economic benefits to the consumer as well as the service provider [8]. One of the most commonly used protocol, Message Queuing Telemetry Transport

C. S. S. Barath (✉) · R. Nirmaladevi

Department of Electronics and Communication Engineering, Meenakshi Sundararajan Engineering College, Kodambakkam, Chennai, Tamil Nadu, India

(MQTT), is a lightweight messaging protocol entirely based on publish/subscribe operations to exchange data between clients and the server [9]. Dammina et al. [10] presented a detailed survey on smart metering and electricity smart meter data analytics. Anitha et al. [11] have proposed an energy monitoring system with the pre-emption of agenda using Arduino microcontroller and a GSM Module. Dileep et al. [12] uniquely addressed and developed a systematic approach to build an integrated power consumption monitoring system through IoT. The potential of 'Full Home Control' using GSM modem for controlling the home appliances via SMS is investigated by Teymourzadeh et al. [13]. A study based on the architecture and elements of IoT along with its different applications was proposed by Tiwary et al. [14]. An Information framework for the realization and creation of smart cities through the Internet of Things (IoT) was provided by Jin et al. [15]. Barsocchi et al. [16] discussed a concept of non-intrusive real-time load monitoring of domestic appliances using a cheap and easy to install a device like Arduino. Das and Saikiya [17] developed a smart energy system and virtual instrumentation for the residential customers to function as In-Home Display (IHD) for Energy Management System (EMS). Zanella et al. [18] analyzed the possible technical solutions currently available for implementing and enabling technologies, protocols, and architecture for an urban IoT. Sun et al. [19] proposed a systematic review of the development and deployment of smart energy meters by inspecting its various functions and insights. Hao et al. [20] presented the algorithm for smart meter deployments to track the switching states of the massive electrical appliances. This algorithm is optimized by using minimal number of smart meters.

Block diagram and the proposed methodology are explained in Section 2. Experimental results and analysis of the proposed system are discussed in Section 3. Conclusion of this paper is described in Section 4.

1.1 Existing System

The measurement of the consumed energy is done using the electromechanical metering system in which its use of the old infrastructure leads to many technical issues such as electric power shortfall, voltage sags, overload transformer, electricity theft, and regular load shedding. The traditional manual meter reading process demands a lot of manpower and material resources as the human operators need to go to the consumer's place for computing the units consumed leading to high labor costs. The conventional metering system is not suitable for longer operating purposes as it lacks an intelligent mechanism for real-time monitoring and controlling of the energy consumption and bill calculation. Besides, the manual calculation performed by the electricity meter readers has numerous flaws in estimating energy consumption. Therefore, the existing metering system cannot be considered as safe and theft-proof from modifications and other tampering methods.

2 Proposed System

The functional block diagram of the proposed system is given in Fig. 1. In the proposed system design, a systematic methodology is deployed to optimize the monitoring and control of real-time information regarding power consumption and the respective cost value. The system gathers the information utilizing the light-dependent resistor (LDR) connected to the analog input of the microcontroller, NodeMCU in order to detect the Calibration (Cal) LED's blinking of the energy meter. The system encompasses a 100 W light bulb as a load for testing. A microcontroller, NodeMCU (Wi-Fi Module), is responsible for processing the input pulses of the blinking of the Cal LED. In the process of computing real-time information, the system monitors and controls the values of the power consumed, in a very short duration of time and provides vital insights regarding the consumer's energy consumption through the Internet of Things (IoT) platform. The consumer and the Electricity Board will acquire the data of the power consumption and the respective amount for the power consumed using an application named Message Queuing Telemetry Transport (MQTT) Dashboard in a real-time basis.

2.1 System Flow Diagram

See Fig. 2.

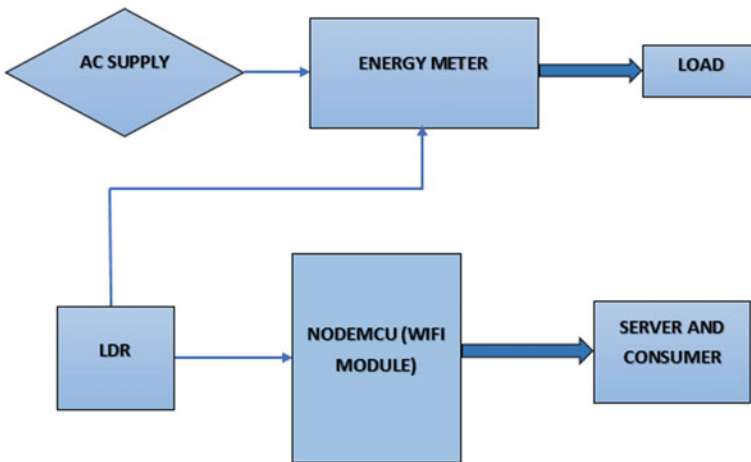
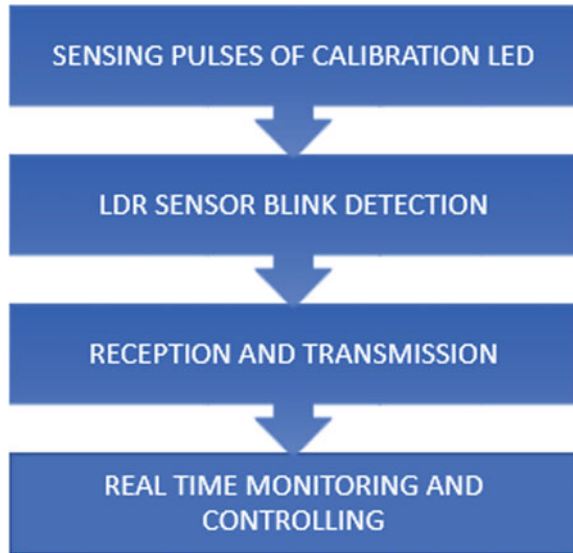


Fig. 1 Functional block diagram of the proposed system

Fig. 2 The four-step process of the proposed system is demonstrated in the form of flow diagram



2.2 Modules and Description

The following four steps outline an effective strategy for determining the real-time values of power and cost.

Sensing Pulses of Calibration LED

Energy meter or watt-hour meter is an instrument that measures the amount of electrical energy consumed by the consumers for domestic, industrial, and agricultural purposes in terms of units. A single-phase two-wire static AC electronic energy meter is used in the proposed system for the calculation of the units consumed. There are four pins in the energy meter, namely Phase, Earth, Reverse Power, and Calibration. The consumed units are manipulated with the assistance of the pulses which is indicated by the Cal LED pin of the energy meter. These pulses are equal to kilowatt-hour (kwh/unit). Usually, the pulse rate is between the range 800 imp/kwh and 3600 imp/kwh. In this case, an energy meter with 3200 impulse/kwh is used. Generally, the energy meter has two input terminals and two output terminals. AC Supply (220 V) is fed to the input terminals of the energy meter. The output terminals are connected to the load used in the system. The pulse rate is determined by sensing the blinks of the Calibration (Cal) LED which forms the first step of the computation process.

LDR Sensor Blink Detection

Light-dependent resistor (LDR) sensor, a light-controlled variable resistor that works on the basic principle of photoconductivity, is mainly used for detecting the presence of the light from the blinks of the Calibration LED of the energy meter. Therefore, the LDR sensor is placed upon the Cal LED. The blinking of the Calibration LED

varies depending on the load used in the system. One significant feature of LDR is that the resistance is inversely proportional to the incident light intensity. Therefore, when a light is incident on the LDR sensor, the output of the module goes high and the resistance value is as low as a few hundred ohms and vice versa when there is an absence of light. An analog voltage is given as the output from the sensor once the presence of light is detected for each blink of the Cal LED. LDR sensor acts as the bridge between the energy meter and the microcontroller as it receives analog input from the Cal LED and gives out an analog voltage as output to the NodeMCU. LDR sensor is powered by connecting the 3 V pin of NodeMCU to the VCC of the LDR sensor. A 100 W light bulb is considered as a load in the proposed system. The number of pulses for a 100 W light bulb is equal to the number of times the Cal LED blinks in a minute.

Reception and Transmission

NodeMCU (Wi-Fi Module) is a microcontroller development board featuring the popular ESP8266 Wi-Fi chip which forms the backbone of the proposed system. Its operating voltage is 3.3 V and has 4 MB of flash memory. It has a total of 11 digital input/output pins and an analog input pin (ADC) as well. NodeMCU is embedded with a 10-bit ADC channel to read the analog voltage from the external device. Hence, every input signal is mapped to a value in a range of 0–1023 as the ADC has a resolution of 2^{10} . Since the LDR sensor gives out an analog voltage, the analog output pin of the LDR (A0) is fed as an input to the analog input pin (ADC) of the microcontroller. Initially, the micro-controller serves as a receiver as it receives the response as an analog voltage from the LDR sensor and then, it converts the analog voltage from (0–5 V) to a digital value ranging between (0–1023) with its built-in ADC. The microcontroller then acts as the transmitter by transmitting the essential information regarding the power consumed and the respective cost to the device through the Wi-Fi network which is achieved with the help of the ESP8266 Wi-Fi chip present in the microcontroller. The power is supplied to the NodeMCU via the on-board MicroB USB connector connected to the laptop. The code written in the software named Arduino IDE is fed to the NodeMCU through the USB connector, and the cost value per unit is computed according to the program written.

Real-Time Monitoring and Controlling

The consumer's device, mobile phone, will receive the real-time information from the microcontroller only when it is present in the range of the data reception. A proper connection is established only when the microcontroller and the device are connected to the same Wi-Fi network. After the connection is established, the details of the power consumption and the respective cost are sent to the MQTT Dashboard application of the consumer's mobile phone through Wi-Fi.

As shown in Sect. 1, the mobile phone is the connected device and the MQTT client as well in this system. There are numerous brokers which implement the MQTT protocol. One of the most common and popular broker is the 'HiveMQ' which is used in this process. The MQTT Dashboard application capitalizes the HiveMQ MQTT broker where any MQTT client or library is used to publish to the broker on specific

topics. The system makes use of the MQTT Dashboard to monitor and control the real-time data passing through MQTT broker and the mobile phone connected to the IoT application ensuring a secure communication medium.

Features of the Proposed System:

1. Reduces the human intervention to note the readings every two months proving the system to be effective in terms of cost as well as time.
2. The transmission of real-time information enables consumers to reduce electricity consumption by comparing the daily usage.
3. The user can monitor the usage remotely as the data is available in digitized form.
4. The controlling option accessible in the proposed system assists the consumers to set threshold value in order to avert the unwanted usage of energy consumption.
5. As the communication medium is secure, tampering of energy meter and unauthorized consumption of electricity can be identified very easily.
6. High accuracy and delivery speed of real-time values in a short duration of time.
7. Reliable and efficient network utilization of the IoT application.

3 Results and Discussion

As a proof-of-concept, the proposed power monitoring and the controlling solution are tested to infer when the resistive load of a 100 W light bulb was switched on. The power consumption of the resistive load was monitored for several minutes. Since the entire process is based on the Internet of Things (IoT), the MQTT Dashboard application is preferred for the client-server interfacing over other applications. Figure 3a shows that the real-time information is received by the consumer's mobile phone (Client) in the MQTT Dashboard application which is connected to the MQTT server (broker) whose website is 'broker.hivemq.com'. MQTT utilizes a unique clientID, username, and password to ensure that the client establishes a proper connection with the server named MQTT broker, which handles data transmission between the clients. The MQTT client will have the major responsibility of coordinating the publishing and subscribing operations based on certain topics. There are two MQTT topics such as power and cost whose friendly names are 'power in kwhr' and 'cost,' respectively as shown in Fig. 3a.

Initially, the MQTT client publishes messages to the MQTT server (broker) based on topics such as power and cost. Later, the mobile phone, which acts as the MQTT client, subscribes to the two topics from the broker after which the real-time information is displayed in the MQTT Dashboard application. The data was transmitted without notable delay which could provide the consumer as well as the server, the essential information regarding the power consumed, and the respective cost. Figure 3b shows the web interface used for publishing the real-time values from the MQTT Dashboard application to the MQTT Websocket client for better viewing

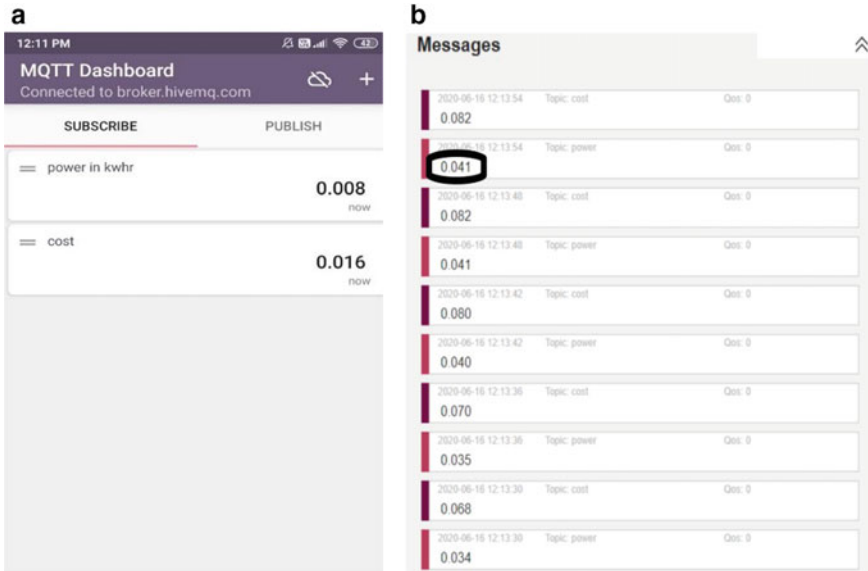


Fig. 3 a Monitoring of real-time values. b Controlling of real-time values

purposes. The system also proves to be efficient in controlling the real-time data by setting a particular threshold value beyond which the readings are not accepted. As shown in Fig. 3b, we have considered the threshold value as 0.041 which is rounded mainly to indicate that the system doesn't receive the real-time values beyond 0.041.

3.1 Features of HiveMQ MQTT Broker

Since the HiveMQ MQTT broker uses the MQTT protocol, there are significant features which are listed below:

- (1) Fast and instant movement of data due to the reduced packet size. Therefore, the amount of data passing through the network is also reduced significantly.
- (2) Reduced network bandwidth due to its optimal use of MQTT protocol as a result of which it consumes less battery power.
- (3) Cost-efficient through the structured use of hardware and network resources.
- (4) Scalable by maintaining extremely fast throughput and minimal latency.
- (5) Reliable and secure transmission of data through the MQTT protocol without any disturbances.
- (6) Real-time data monitoring of the values passing through the MQTT broker and the MQTT clients.

3.2 Comparison of MQTT Protocol and HTTP Protocol

There are many reasons to justify that the MQTT protocol is efficient and reliable as compared to HTTP protocol, and the reasons are listed in the form of Table 1

Even though the free electricity scheme for farmers in the state of Tamil Nadu has proven to be beneficial in numerous ways, there are certain issues concerning the overconsumption of electricity beyond the limit in the agricultural field. The initiated controlling system can assist in the prevention of unauthorized usage of electricity so that penalty can be issued by the government to the person who consumes electricity beyond the threshold limit.

In this case, it has been tested practically that the time duration between the data sent from the microcontroller and the response received by the device does not exceed 500 μ s which is fast enough to detect the incoming message. Therefore, these fundamental reasons prove that the human-intensive work of collecting the data for a bi-monthly cycle can be prevented as the simple visualization enables the consumers to monitor and control the essential real-time information regarding the power consumed and the respective cost.

In future works, the major plan is to fabricate new prototypes and expand the capabilities of the proposed system by testing it in real scenarios with multiple loads

Table 1 Performance comparison of MQTT with HTTP technology

Features	MQTT	HTTP
Architecture	Publish/subscribe	Request/response
Message size	Small, with a compact binary header of 2 bytes in size	Large, because of the ASCII format
Complexity	Simple	More complex
Throughput	93 times faster as compared to HTTP due to small packet size	Slow due to larger packet size
Network traffic	Low network traffic since there is no client polling	High network traffic due to client polling
Battery power	Consumes less power because of the pub/sub model	Consumes more power
Service levels	3 quality of service (QoS) levels ensures the reliability of data	All messages get the same level of service
Encryption	Payload encryption is done before transmission of data	Data is not encrypted before transmission
Bandwidth efficiency	Bandwidth efficient for transmission of fewer metrics	Less bandwidth efficient as compared to MQTT
Connectivity	Ideal even in case of an irregular connectivity	Not ideal in case of irregular connectivity
Applications	Provides options of last will and testament and retained messages	Composes lengthy headers and messages

in a house. Also, future works include modifying the MQTT Dashboard application depending on the added features of the system.

4 Conclusion

The cost-effective framework concept of the energy monitoring and controlling system is proposed in this paper which implements a novel approach for establishing bi-directional communication between the server and the consumer in order to achieve an expeditious development in transmitting real-time information regarding the power consumption and the respective cost securely and accurately through the Internet of Things (IoT) platform using the Message Queuing Telemetry Transport (MQTT) application. Another major contribution of this paper is that it has objectively validated its performance and features against the conventional metering system. The system enables the consumers to economize their energy consumption, prevent human intervention, reduce maintenance costs, avoid miscalculations in billing, and provide remote access to energy usage. The operating speed, which is a crucial factor in determining the effectiveness of the proposed system, does not exceed 500 μ s. By examining the diverse applications and the associated benefits, the proposed system seems a promising alternative to the traditional meter system.

References

1. All India Installed Capacity of Utility Power Stations (PDF). Retrieved 11 June 2020
2. Tripathi B (2018) Now, India is the third largest electricity producer ahead of Russia, Japan. Business Standard India. Retrieved 11 June 2020
3. BP Statistical Review 2019 (PDF). Retrieved 11 June 2020
4. Summary electricity generation report, Mar 2020 (PDF). Retrieved 11 June 2020
5. Power sector at a glance ALL INDIA. Government of India Ministry of Power. Retrieved 11 June 2020
6. Harish G, Preethi V (2016) Design and implementation of smart energy meter. In: IEEE international conference on inventive computation technologies (ICICT)
7. Aruna R, Asha R, Balasaranya K, Divya J (2018) Smart meter for advanced metering and billing alert framework. IJESC 8(3)
8. "Internet of Things (IoT)—Gloify. Gloify. Retrieved 11 June 2020
9. MQTT IoT Protocol complete Tutorial—How it Works with a demo. 1Sheeld. Retrieved 11 June 2020
10. Alahakoon D, Xinghuo Yu (2016) Smart electricity meter data intelligence for future energy systems: a survey. IEEE Trans Industr Inf 12(1):425–436
11. Anitha K, Anitha V, Prathik M (2018) Smart energy meter surveillance using IoT. In: IEEE international conference on power, energy, control and transmission systems, 22–23 Feb 2018
12. Dileep Bind M, Ganesh Sonawane L, Nikhil Patil N, Sumit Khamkar N, Vivek Kurade R (2018) Smart wireless electronic energy meter. IRJET 5(3)
13. Teymourzadeh R, Ahmned SA, Chan KW, Hoong MV, Nasiruzzaman ABM (2013) Smart GSM based home automation system. In: IEEE conference on systems, process & control, pp 306–309

14. Tiwary A, Mahato M, Chidar A, Chandrol MK, Shrivastava M, Tripathi M (2018) Internet of things (IoT): research, architectures and applications. *Int J Future Revol Comput Sci Commun Eng* 4(3)
15. Jin J, Gubbi J, Marusic S, Palaniswami M (2014) An information framework for creating a smart city through internet of things. *IEEE Internet Things J* 1:112–121
16. Barsocchi P, Ferro E, Palumbo F, Potorti F (2014) Smart meter led probe for real time appliance load monitoring. *IEEE Sens* 1451–1454
17. Das H, Saikiya LC (2015) GSM enabled smart energy meter and automation of home appliances. In: *IEEE international conference on energy, power and environment: towards sustainable growth (ICEPE)*, 12–13 June 2015
18. Zanella A, Bui N, Castellani A, Vangelista L, Zorzi M (2014) Internet of things for smart cities. *IEEE Internet Things J* 1(1):22–32
19. Sun Q, Li H, Ma Z, Wang C, Campillo J, Zhang Q, Wallin F, Guo J (2016) A comprehensive review of smart energy meters in intelligent energy networks. *IEEE Internet Things J* 3(4):464–479
20. Hao X, Wang Y, Wu C, Wang AY, Song L, Hu C, Yu L (2012) Smart Meter deployment optimization for efficient electrical appliance state monitoring. In: *IEEE Third international conference on smart grid communications*, 5–8 Nov 2012

Power Transformer Summer Peak Load Prediction Using SCADA and Supervised Learning



Neeraj Kanwar, Divay Bargoti, and Vinay Kumar Jadoun

1 Introduction

Electrical power system planning and operation are important features for electric utilities. Accurate planning can provide a stable and reliable system. Therefore, from planning and operation perspective of electric utilities, load forecasting is considered to be a vital and an integral process [1]. It plays a crucial role to help an electric utility for making vital decisions on distribution system network reconfiguration, voltage control, infrastructure expansion, load switching, etc. For any electric power provider, one of the most crucial task is to plan an electric power system. An important part in this is a power transformer, commonly used for stepping up and stepping down the voltage at different locations of power system. It is required to predict the power needed to meet the demand and supply equilibrium and also its associated peak load.

Several methods are defined in literature for load forecasting. Statistical techniques or artificial Intelligence (AI)-based algorithms are generally used for short-term forecasting. Some of them are regression method [2, 3], neural networks [4], time-series [5] and expert systems [6]. For medium- and long-term forecasting, econometric approach [7] is widely used. In [4], the prediction of peak load on power transformers is done using back propagation-based neural network method. A short-term load forecasting is done in [5] to forecast the power system daily peak load using time-series modeling. Load forecasting model is supported in [6] using a knowledge-based expert system. The forecasting is suggested for power system planning for both medium and long terms.

The main objective of this work is to visualize the growth of the load in future by predicting the peak load on a power transformer. This may be helpful for the

N. Kanwar (✉) · D. Bargoti

Department of Electrical Engineering, Manipal University Jaipur, Jaipur, India

V. K. Jadoun

Department of Electrical and Electronics Engineering, Manipal Institute of Technology, Manipal Academy of Higher Education, Manipal, Karnataka, India

electricity provider company to get a rough idea about the peak load for the future and can make respective changes, if the peak load exceeds the maximum reading. This may ensure the safety of the transformer. In this study, multiple regression technique of supervised learning is used for power transformers peak load forecasting. It is useful for predicting the variable value of dependent feature that is created using two or more other variables of independent feature.

2 Methodology

There are two types of load forecasting, namely quantitative and qualitative forecasting. This work is based on quantitative forecasting. It is categorized under this forecasting because of fulfillment of the following three reasons, availability of the past datasets, the data available have the ability to be converted into numeric form and lastly continuation of aspects of past pattern [4]. In order to successfully get the correct prediction of peak load, two vital steps are required to be executed.

Step-1: The first step is to import the data from SCADA control center. It is performed with the help of features like archiving and logging residing in SCADA application. Afterward, peak load current of 5 MVA, 33/11 kV power transformer of stadium substation, Bikaner district, is collected from SCADA. A view of this transformer is shown in Fig. 1. Human-machine interface (HMI) is shown in Fig. 2 that facilitates



Fig. 1 5-MVA stadium transformer

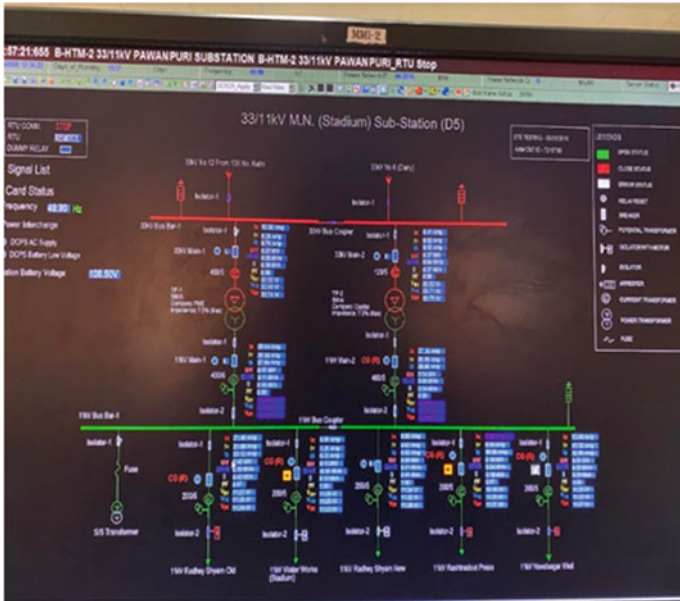
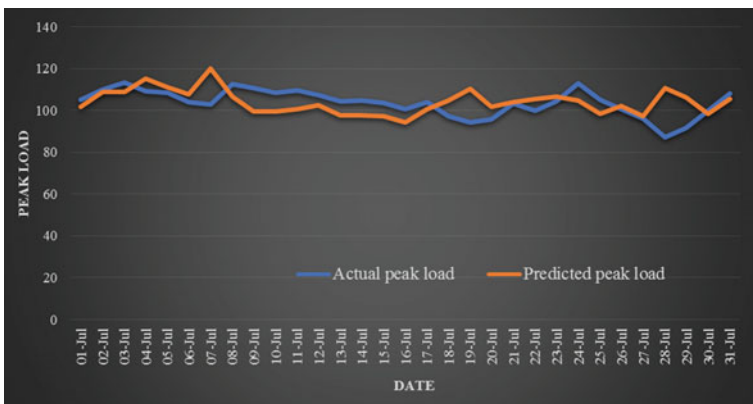


Fig. 2 Human-machine interface

the operating personnel to see the backed up information in tabular as well as graphical way. The data is then noted down in an excel sheet. It is mandatory to perform this step so that Anaconda can read the available data. After importing the dataset to Anaconda, it is transformed and cleaned thereby bracing it for the application of regression model. The code used for it is presented in Listing 1. A part of dataset used for training is presented in Table 1.



Listing 1 Coding for Stage-1

Table 1 Training dataset

Date	Peak load	Temperature	Humidity
1-Apr	60.72	38	11
2-Apr	57.6	39	11
3-Apr	60.96	41	12
4-Apr	72.4	43	8
5-Apr	74.4	39	18
6-Apr	81.28	42	11
7-Apr	76.24	39	17
8-Apr	78.08	40	16
9-Apr	83.04	41	14
10-Apr	84	41	16

After importing the dataset, representation of dataset using variables is done. Temperature and humidity are represented as independent variable x , and peak load is represented as dependent variable y . The code used for it is presented in Listing 1.

Step-2: The second step requires learning and applying multiple regression model to the obtained dataset. This model is an extension of linear regression model which attempts the modeling of relationship between two or more than two features. Along with this, a response is modeled by fitting a linear equation to the observed data extension. After obtaining the linear equation, it is then applied to predict the future readings. This process of obtaining the equation is done with the help of training dataset. For this work, training and testing datasets are in the ratio of 3:1. The peak load data, temperature and humidity data for the month of April, May and June are used as training data, and the temperature and humidity data for July are used as test data which result in predicted peak load for the month of July. After analyzing the results, it is observed that it contains few errors which occurs due to the abrupt shutdown of the transformer. The source code for stage-2 is presented in Listing 2. The entire dataset comprises data generated in the months of April, May, June and July.

3 Results Analysis

After the successful compilation of the code, it is observed that there are four days which do not match with actual value of the peak load. The reason of this deviation is justified due to the abrupt shutdown of the transformer caused due to bad weather conditions. Table 2 presents actual and predicted peak load. It also presents percentage error obtained for each day. A comparison of obtained and predicted peak load is also shown in graphical form in Fig. 3. It can be seen in figure that there are four days, i.e., 7th, 19th, 28th and 29th July on which maximum deviation occurs. It happens due to the rain on all the four days the system faced. The graph in blue

```

#From the sklearn module we will use the LinearRegression() method to create a linear regression object.
"""This object has a method called fit() that takes the independent and dependent values as parameters and fi
lls
the regression object with data that describes the relationship:"""
from sklearn import linear_model
regr = linear_model.LinearRegression()
regr.fit(x, y)
import xlrd
#importing xlrd to read .xls file
file_location = r'C:\Users\Lenovo\Desktop\stadiumtestdata.xlsx'
#opens the excel file to read data
workbook=xlrd.open_workbook(file_location)
sheet=workbook.sheet_by_index(0)
#extracting the number of rows and copying it in l
l=sheet.nrows
i=0
j=0
k=1
#putting i=0,j=0 to extract the values from starting
"""using the for loop upto the range l which is the so to extract full data of the file and
incrementing j by 1 to take full data from a particular row"""
for i in range(l):
    a=sheet.cell(i,j).value
    b=sheet.cell(i,(j+1)).value
    predict = regr.predict([[a,b]])#predicting the value from a and b.
    print(predict),
    k=k+1
#loops will continues till i reaches a value greater than l

```

Listing 2 Coding for Stage-2

represents the actual peak load values, whereas the graph in orange represents the predicted peak load values.

4 Conclusions

Future load forecasting is considered as one of the main parts of power system planning. Based on this load forecasting, peak load on system may be predicted and this may be helpful to determine future load growth. So utility may be prepared for electric loads that may be available on system in future. In this study, the peak load current of power transformer is predicted successfully with an accuracy of 90% and implying the mean absolute percentage error (MAPE) to be equivalent to 6.45% approximately. Further, it is observed that the peak current helps to protect the transformer. It can be concluded that machine learning is of great importance as it not only helps to increase the speed of process but also generates accurate results.

Table 2 Actual and predicted peak load

Date	Actual peak load	Predicted peak load	Percentage error (%)
1-Jul	105.28	101.8389224	-3
2-Jul	110	108.97556	-1
3-Jul	113.2	108.97556	-4
4-Jul	109.36	115.1077181	5
5-Jul	108.32	110.9845191	2
6-Jul	104.08	107.645565	3
7-Jul	102.72	120.015162	17
8-Jul	112.64	106.7560393	-5
9-Jul	110.8	99.61940164	-10
10-Jul	108.56	99.61940164	-8
11-Jul	109.44	100.6238812	-8
12-Jul	107.2	102.5275594	-4
13-Jul	104.24	97.70605039	-6
14-Jul	104.8	97.49548874	-7
15-Jul	103.76	97.3998809	-6
16-Jul	100.48	94.17588063	-6
17-Jul	104.16	100.5186004	-3
18-Jul	97.28	104.6417994	8
19-Jul	94.4	110.2475533	17
20-Jul	95.76	101.7239686	6
21-Jul	103.12	103.8382085	1
22-Jul	99.92	105.6462789	6
23-Jul	104.4	106.6507584	2
24-Jul	112.96	104.7470802	-7
25-Jul	105.2	98.40436045	-6
26-Jul	100.8	102.0011553	1
27-Jul	96.08	97.39020792	1
28-Jul	87.28	110.8212366	27
29-Jul	91.6	106.1243543	16
30-Jul	99.84	98.29907962	-2
31-Jul	108	105.6462789	-2

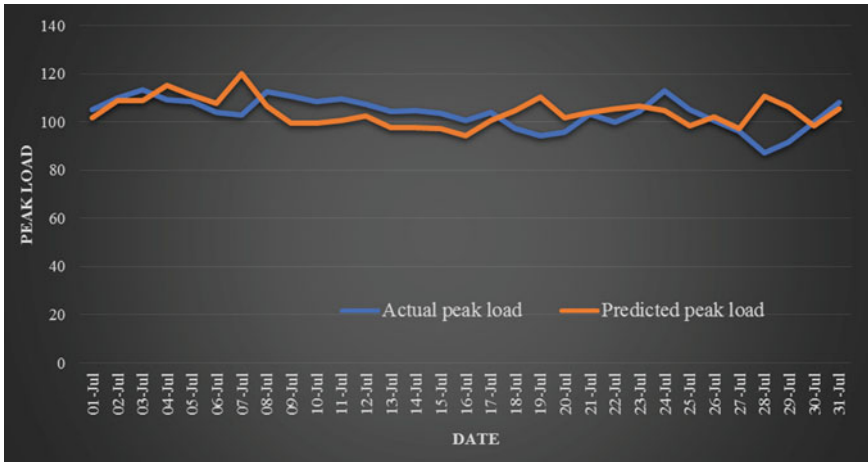


Fig. 3 Comparison of actual and predicted loads

References

1. Gupta V, Pal S (2017) An overview of different types of load forecasting methods and the factors affecting the load forecasting. *Int J Res Appl Sci Eng Technol* 5(4):729–733
2. Charytoniuk W, Chen MS, Olinda PV (1998) Nonparametric regression based short-term load forecasting. *IEEE Trans Power Syst* 13:725–730
3. Haida T, Muto S (1994) Regression based peak load forecasting using a transformation technique. *IEEE Trans Power Syst* 9:1788–1794
4. Syahputra R, Syahfitra FD, Soesanti I (2018) Application of artificial neural network for power transformer peak load prediction. *J Theor Appl Inf Technol* 96(22):7643–7653
5. Amjady N (2001) Short-term hourly load forecasting using time-series modeling with peak load estimation capability. *IEEE Trans Power Syst* 16(3):798–805
6. Kandil MS, El-Debeiky SM, Hasanien NE (2002) Long-term load forecasting for fast developing utility using a knowledge-based expert system. *IEEE Trans Power Syst* 17(2):491–496
7. Mtembo V, Taylor GA, Ekwue A (2014) A novel econometric model for peak demand forecasting. In: 2014 49th international universities power engineering conference (UPEC). IEEE (2014)

Analysis of M-ary QAM-Based OFDM Systems in AWGN Channel



Sarthak Pandey , Manisha Bharti , and Ayush Kumar Agrawal 

1 Introduction

Wireless communication field is ever dynamic and these services have been increasing extensively over time [1]. The constantly booming demand of mobile technologies, wireless local area networks (WLANs) and sudden growth of broadband industry has obligated to explore new methods for constructing higher capacity wireless networks [2]. The operation of transmitting and receiving structures is of immense importance in wireless communication. Contemporary telecommunication system has been able to provide better versatility in data rates, greater capacity and densely incorporated services. The paramount importance of spectral efficiency and higher data rates must be heeded because of the growing congestion due to increasing traffic in wireless networks. This calls for a more bandwidth-efficient scheme because spectral efficiency and higher data rates for transmission are of utmost significance in wireless communication. M-ary modulation techniques provide higher data rates, improved methods for error correction, better data security, high noise immunity and more resistivity. Various modulation techniques utilise different numbers of bits for each symbol to obtain different degrees of throughput and efficiency. Spectral efficiency increases with the increase in the order of modulation. The amount of errors in the message can be varied by changing the modulating order [3]. Data transmission involving very high bit rates is essential for videos, high-quality audios and mobile ISDN services. It is quite possible to achieve these rates of data transmission, but the major hindrance, in this case, is the limitation to the total spectrum availability. An attractive method to overcome this problem is M-ary quadrature amplitude modulation (M-QAM) because of its high spectral efficacy. M-QAM is efficiently employed by encoding wave bits per symbol for a given energy level.

S. Pandey (✉) · M. Bharti · A. K. Agrawal
National Institute of Technology Delhi, New Delhi, Delhi 110040, India
e-mail: 171220043@nitdelhi.ac.in

However, achieving high data rates must also require a careful selection of the available multi-carrier modulation schemes. Orthogonal frequency division multiplexing (OFDM) is a multi-carrier transmission technique which reliably provides the essential improvement in performance efficiency by multiplexing and transmitting at higher data rates and simultaneously improving spectral efficiency [4]. The technique splits up the available spectrum into many frequency bands (or sub-carriers) and employs the transmitter to send a single data stream (i.e. parallelly split out of the serial data) over each one of them, each sub-carrier being modulated at a lower symbol rate, resulting into a signal with a high resistance to interference. This technique is almost identical to frequency division multiple access (FDMA) in the fact, that multiple access, in this case, is obtained by splitting the available spectrum (i.e. total bandwidth of the channel) into multiple channels, that are now assigned to the users. But, OFDM handles the bandwidth much more efficiently because the sub-streams are now much nearer (overlapping) as opposed to FDMA where channels are separated with a significant distance to intercept the inter-carrier interference (ICI) and subsequently aid in minimising bit error rates. This removes the requirement of inter-carrier guard bands employed in FDMA, and hence, simplifying the design of OFDM transceivers by significantly reducing the circuit complexity and cost. All carriers are made orthogonal (i.e. 90° phase shift) to each other to prohibit inter-carrier interference in OFDM. OFDM also presents other benefits like robustness against frequency-selective fading channel, efficient computations through fast Fourier transform and simple equalisation techniques besides the much high-speed rate channelling and improved spectral efficiency [5]. These benefits have endorsed OFDM to be the most credible technique for wideband digital transmission utilised in domains like digital television and audio broadcasting, wireless networks and 4G mobile communication [6].

2 Quadrature Amplitude Modulation (QAM) and M-ary QAM

Wireless communication field is ever dynamic and these services have been increasing extensively over time [1]. QAM can be regarded as both an analog as well as a digital modulation technique. In QAM, the respective data of two different message signals (can be either analog or digital bit streams) gets delivered through the unequal amplitudes of carrier signals. The effective bandwidth becomes double due to the combination of two different signals into one single channel (data stream). Generally, the two carrier waves are typical sinusoids and essentially have a phase difference of 90° between them (i.e. quadrature). Therefore, one of the given carrier signals is denoted by a sine wave, and the other one, by a cosine wave, respectively. Mathematically, the transmitted signal can, hence, be given by,

$$s(t) = x_1(t)A \cos(2\pi f_c t) + x_2(t)A \sin(2\pi f_c t) \quad (1)$$

The signal $s(t)$ consists of two carriers whose phases are in quadrature with each other and also each of the carriers is now modulated by a group of discrete amplitudes, and consequently, the name being given as quadrature amplitude modulation (QAM). Union of the two modulated carriers is done by the transmitter and extraction of the original signal is completed by the receiver when the carriers are separated from the combined modulated signal. The resultant waveforms from the output of the demodulator are the sustained extraction of signals that are fused through the modulation process of simultaneously combining the attributes of both phase shift keying (PSK) and amplitude shift keying (ASK) methods. Digital QAM uses a finite minimum number of at least two phases and two amplitudes are used mandatorily.

Two or more than two bits are joined together to generate symbols in case of M-ary QAM, and during each symbol period T_s , one of the M available signals corresponding to a specific symbol in that duration (T_s) is transmitted. The total number of signals is M (i.e. $= 2^n$) where n is an integer. Mathematically, the general expression of an M-ary QAM signal can be described as

$$S_i(t) = \sqrt{\frac{2E_{mn}}{T_s}} a_j \cos(2\pi f_c t) + \sqrt{\frac{2E_{mn}}{T_s}} b_j \sin(2\pi f_c t);$$

$$0 < t < T_s \text{ and } j = 1, 2, \dots, M \quad (2)$$

where E_{mn} is the energy of the signal with least amplitude, and a_j and b_j are pair of independent integers taken as per the position of a specific symbol, i.e. signal point.

2.1 Modulator and Demodulator in QAM

The QAM modulator is fed with two carrier signals which are 90° out of phase with each other. I (In-phase) and Q (Quadrature) are the separated bit (data) streams that modulate the two carrier signals are in their amplitudes. These modulated data streams (i.e. I-channel and Q-channel) are then summed together by an adder. This merged signal is then employed at the radio-frequency (RF) range, and finally, converted to frequencies suitable for transmission as desired. The structures of modulator and demodulator are represented in Fig. 1.

In M-QAM, there are total M (i.e. 2^n) levels (symbols) available for encoding. This implies each of the n (i.e. $\log_2 M$) symbols of I and Q could be changed from one level to the other in every symbol period. The symbol rate hence becomes $1/n$ times the bit rate. Consequently, QAM modulation enhances the spectral efficiency of the transmission. QAM is commonly used in several areas of digital communication involving digital data radio, cable television, Internet services and also in cellular wireless technology. Different types of QAM are feasible such as 4, 16, 32, 64, 128, 256-QAM, etc. A convenient method of assessing the performance of digital modulation techniques is the constellation diagram. Also known as the signal space plot, it helps in providing a pictorial depiction of the location of the complex envelope

of each of the available symbol states. Figure 2 denotes the combined signal space plot for 4, 16, 32 and 64-QAM.

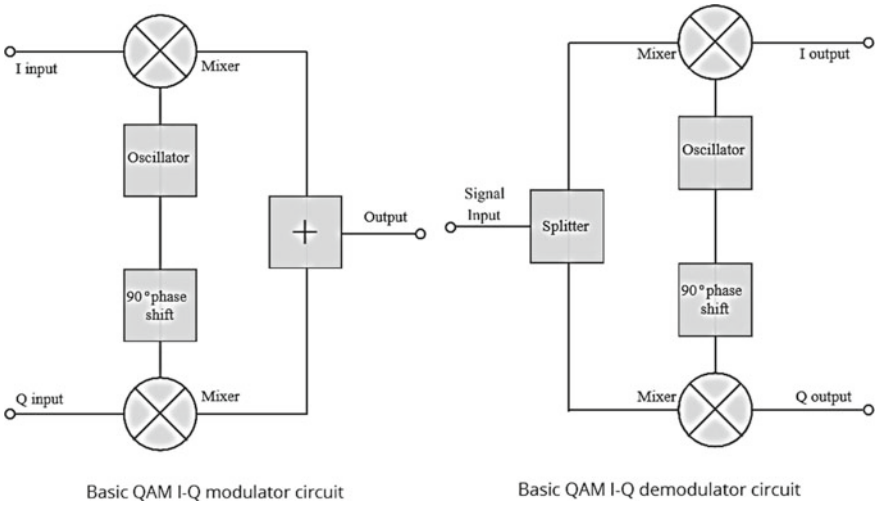
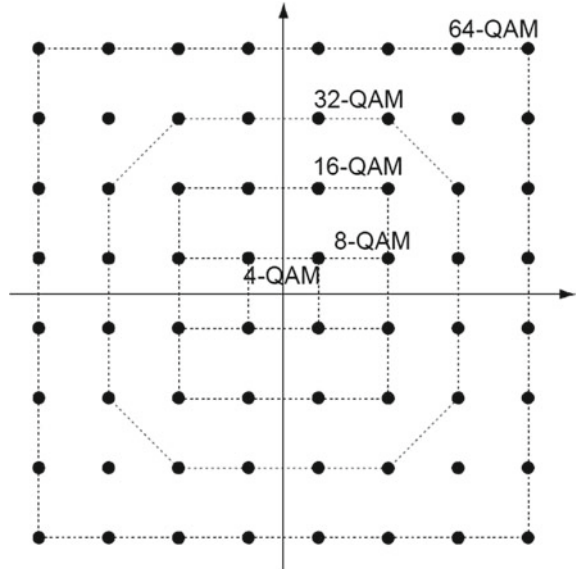


Fig. 1 Modulator and demodulator of QAM

Fig. 2 Constellation diagram of M-QAM



3 OFDM System Design

Concerns about the wastage of bandwidth or unused frequency bands by the guard bands or intervals in frequency division multiplexing (FDM) gave birth to the concept of a novel channelling technique known as orthogonal FDM or OFDM. It is a peculiar multi-carrier transmission method with a prime motive to conserve the channel bandwidth by introducing closely packed sub-carriers having their spectra overlapping to a great extent. It can be thought of as a bandwidth conservation scheme which allows the successful reception of data or information despite the overlapping of sidebands from each carrier. This can be accomplished when the spacing between carriers equals (or matches) the reciprocal of the symbol duration. The primary concept involved in OFDM is to divide a data stream of very high data rate into several streams of much less data rate that are transmitted concurrently over numerous sub-carriers, i.e. a single channel is split into many new sub-channels. Orthogonality is important in this system, as its loss would lead to inter-carrier interference (ICI). The sub-carriers in OFDM are arranged equally and as closely as it is ideally feasible but simultaneously and also not compromising the orthogonality among them [7]. In a multi-carrier channelling method, a stream or frame of data is broken into multiple symbols, and a different sub-carrier is allocated to each symbol or a separate group of symbols. Hence, it can be thought of as a block transmission technique in which each block holds a set of symbols. The generated signals are channelled simultaneously in the same frequency band. Therefore, even if a certain frequency gets distorted by the effects of noise in the channel, then also, only a specific part of data would be lost but not the entire information. To enhance the rigidity against frequency-selective fading and narrowband interference, it is one of the chief motives to use multi-carrier transmission. The orthogonality between the sub-carriers despite their spectral overlapping will ensure their effortless separation at the destination, and thereby, reducing the complexity of the receiver and providing better spectral efficiency in contrast to conventional FDM.

Typically, the OFDM system has three major parts: the transmitter, channel and receiver as can be seen in Fig. 3.

The QAM process of modulation starts in the transmitter where incoming bits are mapped and modulated according to the available modulation scheme (i.e. QAM, in this case). The serial to parallel converter transforms the serially obtained complex data into N (total message length) parallel data streams (i.e. discrete frequency signals). Now, the already modulated parallel bit streams undergo baseband OFDM modulation which is executed using inverse fast Fourier transform (IFFT) process. IFFT translates these parallel data signals in samples of the time-domain as per the sequence of message length (N). The time-domain complex baseband OFDM signal at the output of the IFFT process is described as:

$$x[n] = \frac{1}{N} \sum_{i=0}^{N-1} X(i) e^{j \frac{2\pi ni}{N}} \quad (3)$$

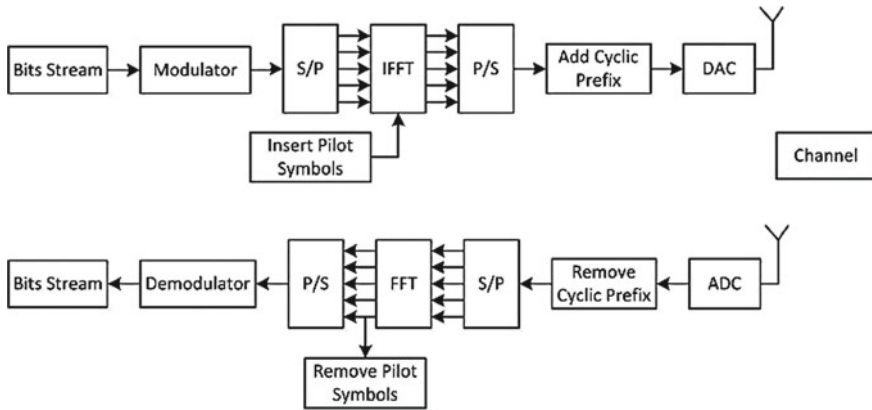


Fig. 3 OFDM system diagram

After that, the parallel bits are serialised by the parallel to series converter. A cyclic prefix (CP), whose length is not more than one-fourth of the OFDM symbol duration, is appended to each data symbol to prevent inter-symbol interference (ISI). The multipath nature of the transmission radio channel introduces ISI in OFDM signals [8]. Multipath transmission leads to an increase in the amount of inter-symbol interference (ISI), in the case, where maximal delay spread of radio channel is more than the guard interval's length. This is the reason why the length of the guard interval must be more than the maximum delay spread. Hence, the guard interval is appended to reduce the ISI effect [9]. Generally, the main purpose to introduce guard interval is to maintain the separation among sub-carriers and ensure the disjunction between the OFDM symbols, when the signal is sent over a multipath channel (Fig. 4).

Cyclic prefix (CP) is just a periodic addendum of the OFDM symbol and is applied to insert the guard interval. The CP is the same as the endmost values of the OFDM symbols and is added at the starting of the symbol. Let us assume that T_G denotes the cyclic prefix length in terms of the sample time. The expanded OFDM symbol has the interval of:

$$T_{sym} = T_{sub} + T_G \tag{4}$$

where T_{sym} is the net symbol duration and T_{sub} is the useful symbol duration. The ISI effect on the next OFDM symbol due to its predecessor is limited to the guard

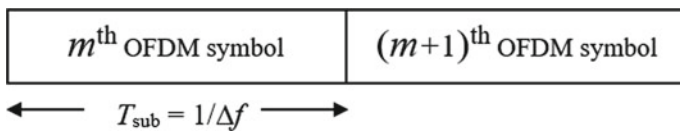


Fig. 4 OFDM symbol without guard interval

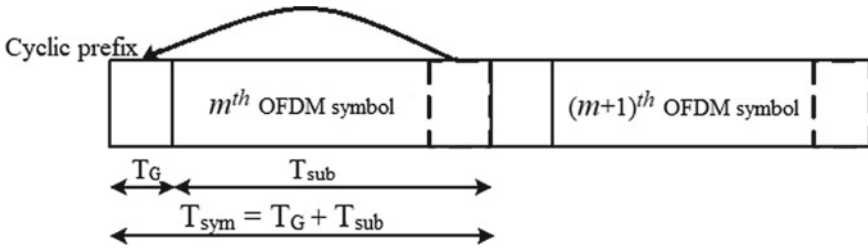


Fig. 5 OFDM symbol with cyclic prefix

interval when the cyclic prefix is more than or equal to the maximum delay of the multipath channel so that the effective part of the next OFDM symbol would not be affected with the duration, T_{sub} (Fig. 5).

The consequence of this is that when the guard interval is larger than the maximum delay of a multipath channel, and the orthogonality amongst the sub-carriers is maintained. Introducing guard interval reduces throughput, hence, it is usually limited to be less than or equal to one-quarter of the useful symbol duration. The data is now sent to the receiver through the channel. At the receiver, the inverse of the transmitter process occurs. The cyclic prefix is removed, after which the serial to parallel converter again reshapes the serialised information into parallel streams. These parallel streams of data are demodulated using fast Fourier transform (FFT) and again converted to a serial stream where they are de-mapped and demodulated to get back the original bits.

3.1 Estimation of AWGN Channel

The undesired electrical signals that consistently persist in electronic systems are termed as noise. Specifically, in communication, noise is described as any undesired energy or voltage that tends to disrupt the performance by inhibiting the accurate reception and regeneration of transmitted signals. Noise produces undesired pulses or probably eliminates the ones required in digital systems. Noise can curtail the range of systems for a given transmission power and also creates grave mathematical errors in the analysis of signals. It may also deteriorate the receivers' sensitivity by having restrictions imposed on the weaker signals to get amplified. [10].

The most prevalent noise which usually influences any and every channel in communication systems is the additive white Gaussian noise (AWGN). It is an elementary noise prototype employed to comprehend the effects of different random processes which happen in a wireless channel. These random processes often stem from some natural sources like thermal noise from the sun or the thermal movement of electrons in all emissive electrical devices, i.e. resistors, wires, etc. [11]. Phenomena or events such as dispersion, interference, frequency selectivity, nonlinearity, fading, etc., are not explained by this model [12, 13]. Instead, it provides simple methods

to give gainful insights into the elementary behaviour of a system before the above-mentioned factors are taken into account. Hence, the model is assumed to be fruitful in imitating the background noise of channel. This model adds a white Gaussian noise in the signal which passes through it for analysis.

Theoretically, AWGN is modelled as a random process following Gaussian (or normal) distribution with a zero-mean in which a random variable z is the sum of the random noise variable n and a direct variable a , i.e. $z = a + n$. Thus, for a transmitted signal $f(t)$, the received signal $r(t)$ is expressed as:

$$r(t) = f(t) + n(t) \quad (5)$$

where $n(t)$ is the additive white Gaussian noise.

The probability density distribution for the Gaussian noise is described as follows

$$p(z) = \frac{1}{\sigma\sqrt{2\pi}} e^{-\frac{1}{2}\left(\frac{z-\mu}{\sigma}\right)^2} \quad (6)$$

where σ is the standard deviation and μ is the mean.

The fluctuation of the received symbols increases with the increase in variance for the signal space diagram and, hence, the greater are the chances to decipher an incorrect symbol and commit errors. The term **white** in AWGN implies that the model for this noise presumes its power spectral density (PSD) $G_n(f)$ to be flat (constant) for all frequencies and is specified as:

$$G_n(f) = N_0/2 \quad (7)$$

The scalar 1/2 in Eq. (7) signifies that one-half of total power links with +ve frequencies and the other half with the -ve frequencies. This kind of noise is commonly employed to emulate the noise parameters in communication systems to evaluate their performance. It is generally used to simulate digital systems that can be restored by some other interference methods.

3.2 Bit Error Rate (BER)

As bits are sent from their source to their destination, some of them get corrupted or destroyed passing through the channel due to several factors. Bit error rate (or BER) is a depiction of accuracy which identifies the total number of such bits. Numerous properties that influence BER involve signal-to-noise ratio (SNR), bandwidth, channelling medium and channelling speed. It is used to estimate the difference between the original transmitted signal and received signal at the receiver.

$$\text{Bit Error } (t) \text{ or } \text{BE}(t) = \text{abs}(a(t) - b(t)) \quad (8)$$

Table 1 Parameters for the simulation of OFDM

Parameters	Values
System	OFDM
Modulation techniques	QAM: 4/16/32/64/128/256
Channel	AWGN
Tx and Rx Antenna	Single input single output (SISO)
FFT/IFFT points	64, 128, 256, 512
Guard type	Cyclic prefix (CP)
Cyclic prefix length	25%

where $a(t)$ is the original signal and $b(t)$ is the received signal.

In other words, the bit error rate (BER) is the total number of bit errors that occur in a given unit time. It can be expressed into a simple formula:

$$\text{BER} = \frac{\text{Number of bit error}}{\text{Total number of bits transmitted}}$$

4 Simulation

In this study, all simulations are implemented through the MATLAB software. It is used to simulate the described OFDM system in the AWGN channelling medium. The efficiency results of a system employing different modulation orders of the QAM scheme are attained employing the OFDM parameters listed in Table 1. The E_b/N_0 parameter of the AWGN channel block parameter was varied from 0 to 25, and the simulation was run to obtain the required plots. The BER of the OFDM system is calculated using in-built MATLAB functions and then is plotted against the SNR values of E_b/N_0 .

5 Results

The results obtained after simulating 4, 16, 32, 64, 128 and 256 QAM under AWGN channel are shown in Fig. 6 for different ranges of SNR values of E_b/N_0 .

Tables 2, 3 and 4 summarise the performance of an OFDM system in an AWGN channel using various digital QAM techniques according to the BER values at different values of SNR.

It is observed that as the value of E_b/N_0 increases for all modulation schemes, the system's performance in terms of error reduction gets considerably better and its efficiency enhances. As the plots displayed similar patterns each time after running the simulation; therefore, it implies that increasing or varying the number of FFT points

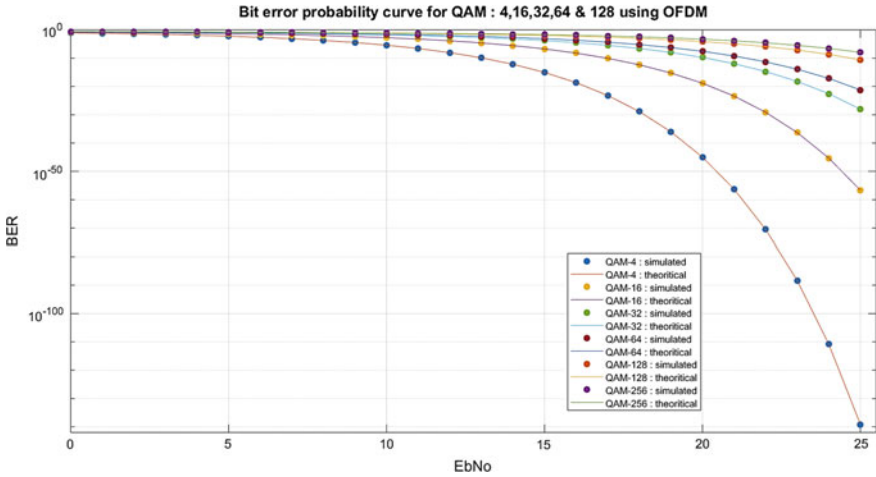


Fig. 6 BER against Eb/No: 0–25 for M-QAM based OFDM system under AWGN channel

Table 2 BER calculation of different QAM schemes at different values of Eb/No

Eb/No	0 db	5 db	10 db	15 db	20 db	25 db
QAM-4	7.865×10^{-2}	5.954×10^{-3}	3.872×10^{-6}	9.124×10^{-16}	1.044×10^{-45}	7.307×10^{-140}
QAM-16	1.411×10^{-1}	4.189×10^{-2}	1.754×10^{-3}	1.842×10^{-7}	1.404×10^{-19}	2.179×10^{-57}
QAM-32	1.895×10^{-1}	8.802×10^{-2}	1.621×10^{-2}	1.585×10^{-4}	1.815×10^{-10}	9.058×10^{-29}
QAM-64	1.998×10^{-1}	1.008×10^{-1}	2.653×10^{-2}	7.725×10^{-4}	2.634×10^{-8}	5.818×10^{-22}
QAM-128	2.477×10^{-1}	1.463×10^{-1}	6.498×10^{-2}	1.061×10^{-2}	7.220×10^{-5}	2.664×10^{-11}
QAM-256	2.546×10^{-1}	1.593×10^{-1}	7.860×10^{-2}	1.980×10^{-2}	5.053×10^{-4}	1.145×10^{-8}

does not influence the performance results. It is also noticed that the higher-order modulation schemes are not able to perform as well as their lower-order counterparts as they have greater BER and low efficiency in terms of error-reduction.

As can be seen from the plots in Fig. 6, by using the 4-QAM scheme, the bit error rate is the least which accounts for a significant reduction in the number of error bits at the receiver. Hence, it can be deduced that 4-QAM modulation process in AWGN channelling medium gives the best performance characteristics as compared to other higher modulation orders of QAM. Similar patterns were produced at other FFT points whilst employing 25% of FFT points as virtual carriers in each case.

Normally, it can be inferred that the performance of the system does not get significantly affected by increasing or reducing the amount of FFT points in OFDM

Table 3 Amount of % increase in BER between successive orders of M-QAM at a given value of SNR

Eb/No (in db)	0 (in %)	5 (in %)	10 (in %)	15 (in %)	20 (in %)	25 (in %)
QAM: 4-16	79.402	603.561	4.520×10^4	2.019×10^{10}	1.345×10^{28}	2.983×10^{84}
QAM: 16-32	27.427	110.122	824.173	8.595×10^4	1.293×10^{11}	4.157×10^{30}
QAM: 32-64	5.435	14.519	63.66	387.382	1.441×10^4	6.423×10^8
QAM: 64-128	23.9	45.139	144.930	1.274×10^4	2.740×10^5	4.579×10^{12}
QAM: 128-256	2.786	8.886	20.960	86.616	599.862	4.197×10^4

Table 4 Amount of % decrease in BER at successive values of SNR for a given modulation order of QAM

Eb/No	QAM-4 (%)	QAM-16 (%)	QAM-32 (%)	QAM-64 (%)	QAM-128 (%)	QAM-256 (%)
(0-5) db	1.221×10^3	236.530	115.280	98.272	69.268	59.784
(5-10) db	1.537×10^5	2.288×10^3	443.153	279.877	125.161	102.739
(10-15) db	4.244×10^{11}	9.523×10^5	1.013×10^4	3.335×10^3	512.315	296.883
(15-20) db	8.737×10^{31}	1.312×10^{14}	8.731×10^7	2.933×10^6	1.460×10^4	3.819×10^3
(20-25) db	1.4291×10^{96}	6.442×10^{39}	2.004×10^{20}	4.527×10^{15}	2.710×10^8	4.415×10^6

system because none of the modulation techniques exhibited superior performance over another in this regard. However, this would invariably affect the energy per bit of the signal.

6 Conclusion

Since M-ary modulation schemes have been able to provide better utilisation of the channel bandwidth as compared to other lower-order modulation schemes, so they are preferred for applications involving the use of a much higher rate of data. In these schemes, the data rate and bandwidth increase along with the value of ‘M’. Another significant parameter besides the high data rate (i.e. speed) is the error rate which must also be considered in communication systems while selecting a

specific modulation scheme. In this work, the performance characteristics of the OFDM system have been evaluated under AWGN channel using different orders of M-ary QAM modulation scheme. The 4, 16, 32, 64, 128 and 256-QAM modulation techniques over AWGN channel have been emulated and the results of the OFDM system performance for these five modulation schemes have been analysed. It is observed that the error rate decreases substantially with the increment in signal power for all modulation schemes. It is also noticed that 4-QAM gives the most efficient performance attributes (i.e. the least BER) when compared to all other higher-order QAMs in this discussion. The results of comparison also convey that a modulation technique in which the constellation points are more closely spaced has better BER attributes due to higher bit rate.

From Table 3, it has been observed that the amount of % increase in BER between successive higher orders of M-QAM shows a decreasing trend (except for the case of QAM: 64–128) for a given particular value of SNR. Also, this amount of % increase in BER further increases with an increase in the value of SNR for a particular difference between successive orders of QAM. In Table 4, the amount of % decrease in BER between successive values of E_b/N_0 (SNR) increases manifold for a particular modulating order (M) of QAM. But, this % decrease in BER decreases with an increase in M value (i.e. the order of modulation) for a particular difference between successive values of SNR. Normally, it can be inferred that, although, techniques with low modulating order exhibit better performance than the techniques with a comparatively higher order of modulation, but this results at the price of declining speed, as lower-order techniques have very low rates of data as compared to their higher-order equivalents. Hence, it can be concluded that the system performance eventually gets better with the decrease in the order of modulation without bothering about the spectral efficiency.

Besides, the study also examined the extent to which the total number of FFT points utilised for computation purposes anyhow influence the overall performance of the system by making similar comparisons among transmissions at various FFT points for the system. When transmitting at a higher number of sub-carriers, there was no noticeable improvement in any of the modulation techniques. Hence, transmitting at more sub-carriers usually does not affect OFDM channelling, although transmit power can be affected.

References

1. Sharma D, Srivastava P (2013) OFDM simulator using MATLAB. *Int J Emerging Technol Adv Eng* 3(9):493–496
2. Gupta R, Parida S (2013) Challenges and opportunities: mobile broadband. *Int J Fut Comput Commun* 2(6):660–664
3. Ghosh S (2014) Performance evaluation on the basis of Bit error rate for different order of Modulation and different length of Sub channels in OFDM system. arXiv preprint [arXiv:1406.7405](https://arxiv.org/abs/1406.7405)

4. John SN, Akinola E, Ibikunle F, Ndujiuba CU, Akinaade B (2012) Modeling of orthogonal frequency division multiplexing (OFDM) for transmission in broadband wireless communications. *J Emerging Trends Comput Informat Sci* 3(4):534–539
5. Kansal L, Kansal A, Singh K (2011) Performance analysis of MIMO-OFDM system using QOSTBC code structure for M-QAM. *Canadian J Signal Process* 2(2):4–15
6. Rohling H (ed) (2011) *OFDM: concepts for future communication systems*. Springer Science & Business Media
7. Kamboj A, Kaushik G (2012) Study & Simulation of OFDM System. *Int J Modern Eng Res (IJMER)* 2(1):235–241
8. Ahmed E, Aziz W, Saleem S, Islam Q (2012) Performance analysis of OFDM system for different channel lengths and multipath channel taps. *Adv Electri Eng Syst* 1(2):124–128
9. Achra N, Mathur G, Yadav RP (2013) Performance analysis of MIMO OFDM system for different modulation schemes under various fading channels. *Int J Adv Res Comput Commun Eng* 2(5):2098–2103
10. Proakis JG, Salehi M (2008) *Digital communications*. 5th edn. McGraw-Hill International
11. Samsuzzannan M, Rahman MA, Masud MA (2010) Bit error rate performance analysis on modulation techniques of wideband code division multiple access. *J Telecommun* 1(2):22–29
12. Gupta S, Sharma H (2012) Performance Investigation for different modulation techniques in WCDMA with multipath fading channels. *Int J Adv Res Comput Sci Softw Eng* 2(7):20–23
13. Anioke CL, Nnamani CO, Ani CI (2016) Review of Wireless MIMO Channel Models. *Niger J Technol* 35(2):381–391

Detection of Imagery Vowel Speech Using Deep Learning



Jigar Patel and Syed Abudhagir Umar

1 Introduction

Vocal speech and physical gestures are typical ways for humans to communicate with each other. However, these normal means of communications are not possible for some individuals due to some special conditions such as advanced stage of amyotrophic lateral sclerosis (ALS) or locked-in syndrome (CIS). Brain–computer interface (BCI) system can translate brain activities into computer commands, and hence, allow an individual to communicate using their brain activities. Recent developments in the area of BCI have resulted in multiple systems that can be helpful to LIS of advanced ALS patients [1–4].

To capture the activity of the brain, electroencephalography (EEG) one of the most popular techniques. EEG records brain activity in the form of electrical signals (which are produced as a result of underlying brain activities) by placing electrodes on the scalp surface. The reasons behind EEG being the most popular technique to be used in the BCI system are its cost-effectiveness and simplicity in the acquisition of data. EEG can monitor minute changes in the brain activity due to high temporal resolution.

The EEG signals vary based on the type of brain activities. These activities can be differentiated into several types such as event-related synchronization/event-related desynchronization (ERD/ERS) [5], steady-state visual evoked potential (SSVEP) [6], mental task [7], and P300 potentials [8]. These types are called paradigms in BCI systems. The BCI systems based on SSVEP and P300 paradigm present visual stimuli to the subject and upon focusing on them, and the brain will produce specific signals

J. Patel (✉) · S. A. Umar

Department of Electronics and Communication Engineering, B V Raju Institute of Technology,
Narsapur, Medak District, Telangana, India

e-mail: jigar.patel@bvrit.ac.in

S. A. Umar

e-mail: syedabudhagir.u@bvrit.ac.in

which can be distinguished. These approaches are mainly used in developing speller systems [9–11]. The ERD/ERS and mental task-based BCI systems require subject to the image or perform some mental activities to produce brain signals which can be detected. The major advantage of this type of paradigm is that any external stimuli are not required and the user can perform a mental activity at his/her pace. These paradigms are mainly used in controlling prosthetics, wheelchairs, etc. [12, 13].

Apart from these four paradigms, there is another paradigm that is based on imagined speech. This paradigm has received comparatively less attention than other paradigms. Earlier studies report that the signals are produced in the motor cortex area of the brain while imagining vowels [14, 15]. These signals can be called speech-related potentials (SAP) and can be used to develop speech prostheses.

An earlier study implemented an imaginary vowel speech paradigm classify imagery vowels ‘u’ and ‘a’ using spatial filters and support vector machines [16]. They reported classification accuracy from 68 to 78%. Similar studies are based on the same dataset reported accuracies of 70–80% [17, 18]. A similar approach was used to classify imagined pronunciations of Chinese characters ‘zuo’ and ‘yi’. They reported average classification accuracies from 74 to 95% across eight subjects [19]. The more recent studies implement detections of imaginary speech of five vowels and words. To detect these imagined activities, features based on the time domain, Mel-frequency cepstral coefficients along with the classifiers such as support vector machine [20–22]. A home automation system was also implemented based on the hybrid approach of imagined speech and event-related potentials [23].

Recently, many researchers focus on developing deep learning methods for classification-based tasks. The most popular architectures for deep learning-based models are convolution neural network (CNN) and long short-term memory (LSTM). Deep learning-based approaches using CNN were also implemented to detect imagery speech with five vowels and six words [24, 25].

In this study, three different approaches based on deep learning architectures using CNN and LSTM are proposed to classify between imagined speech containing two vowels ‘a’ and ‘u’ along with no activity as a control task.

2 Data Acquisition

The EEG data utilized in this study was acquired from the ‘speech imagery dataset’ from ‘<https://www.brainliner.jp>’ and was recorded by Dasalla et al. [16]. The EEG data was collected using BioSemi Active Two system manufactured by BioSemi B. V., Amsterdam, Netherland. The EEG was recorded with a sampling rate of 2048 Hz using Ag–AgCl electrodes. To reduce the size, the data has been down-sampled to 256 Hz of sampling rate. Also, to remove electronic noise and low-frequency baseline shifts, a zero-phase bandpass filter with the range 1–45 Hz was applied to the recorded data. The data was recorded from the locations Fz, C3, C4, and Cz of the international 10–20 system for EEG.

2.1 Subjects

The data was recorded from three subjects, two males and one female (right-handed) with the ages from 26 to 29 years. The subjects did not report any health problems or neurological disorders and were fluent in English.

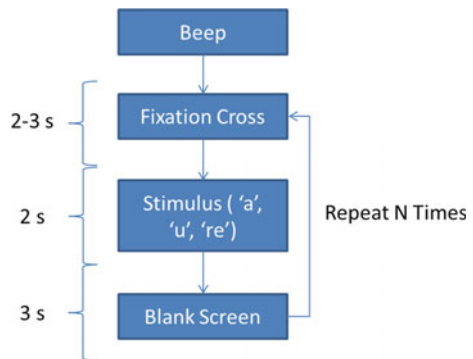
2.2 Experimental Procedure

The subjects were settled in a comfortable chair and asked to perform one of the three tasks based on a visual stimulus. The three tasks were

1. Vowel ‘a’: Imagine vocalization of ‘a’
2. Vowel ‘u’: Imagine vocalization of ‘u’
3. Rest ‘re’: no action, rest.

The subjects were trained beforehand in addition to the rehearsal with real movements to ensure correct task execution. The visual cue will be displayed on the monitor place at approx. 1 m away from the subject. The experiment consists of multiple trials. A fixation cross is placed in the screen for a duration between two to three seconds to help the subject focus on the upcoming tasks on remove any potentials from the previous task. The trial begins with a beep sound followed by a visual cue that is randomly selected. The cue will be displayed for two seconds on the screen followed by a blank screen for three seconds. The participants were instructed to perform appropriate tasks for the duration the cue is displayed on the screen. Each task is repeated 50 times and each task is considered as a trial. So, each subject performed total 150 tasks or trials. The experiment procedure is depicted in Fig. 1.

Fig. 1 Experiment task



3 Methodology

There are three deep learning models implemented in this study. These three models are the CNN model, the LSTM model, and the CNN-LSTM model. The data was not pre-processed apart from the bandpass filter with range 1–45 Hz which was applied on the dataset beforehand. The hyper-parameters β_1 and β_2 were set to 0.9 and 0.999 for all three models. The hyper-parameters learning rate and decay rate were tuned to obtain the best performance from the network. All three networks were trained using Adam optimizer. The 70% of data was used for training the models and remaining 30% data was used for testing. The data was randomized before the split to avoid any training bias.

3.1 CNN Model

Convolution neural networks have been used extensively in implementing image processing methods such as object detection and face recognition. In this study, a similar model is implemented to classify imaginary vowel pronunciations.

The model can be divided into two sections: convolution layers and dense or fully connected layers. The convolution layers are mainly utilized for extracting features from the data while the dense layers will be used to map the patterns and classify the data into distinct groups.

There are three convolution layers in the proposed model, and the one-dimension convolutions are used in this model as the input data consists of EEG data series. A batch normalization layer was inserted after each of the convolution layers. The three dense layers of fully connected layers were connected to the last convolution layer after applying to flatten. Figure 2 illustrates the architecture of the CNN model.

The kernel size for the convolution was set at 10 for all the layers. Reducing or increasing this kernel size resulting in the dropping of the classification accuracy. The number of filters used in the convolution layers is 64, 64, and 128 for the respective convolution layers. The dense layers contain 128 and 32 nodes followed by the output layer with 3 node. The model contains dropout layers with a coefficient of 0.3 after each convolution blocks and dense layer blocks to reduce overfitting.

3.2 LSTM Model

The LSTM model is seen as more effective compared to feed-forward or CNN models in terms of sequence prediction. An LSTM model is usually implemented to process and classify time-series or sequence data. The proposed model contains two LSTM blocks followed by output block. Each LSTM block is followed by the batch normalization block. The diagram in Fig. 3 depicts the model architecture.

Fig. 2 CNN model

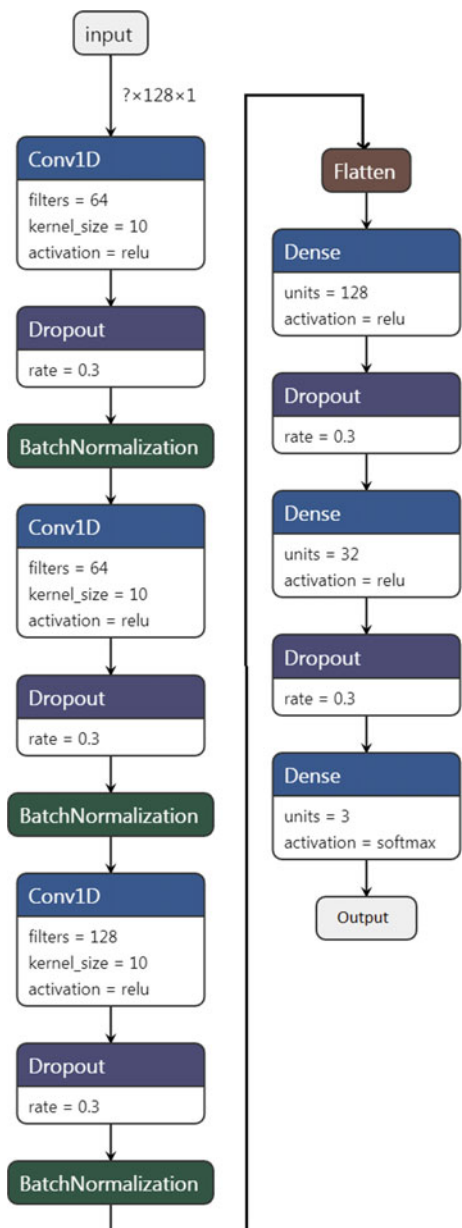
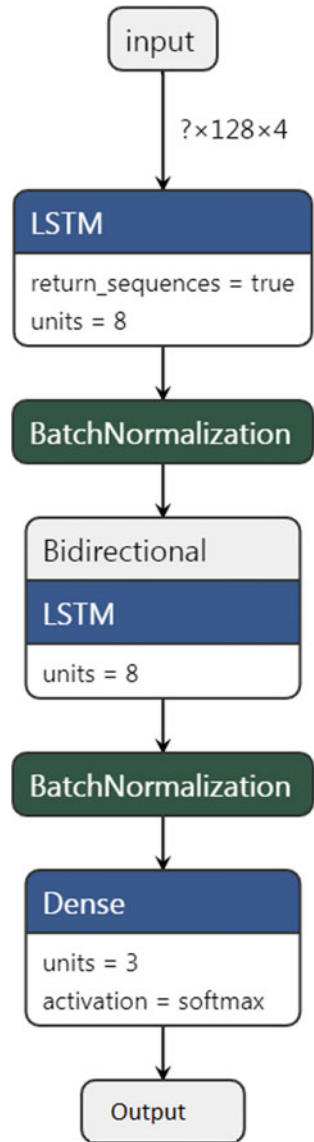


Fig. 3 LSTM model



3.3 CNN + LSTM Model

The proposed model contains a single CNN block followed by batch normalization, a bidirectional LSTM block, and an output layer. The ‘softmax’ activation method was used at the output layer. The convolution layer consists of 32 filters with a kernel size of 16. The LSTM layer is consists of 16 units. Both CNN and LSTM blocks are

followed by batch normalization blocks. Figure 4 illustrates the architecture of the proposed model.

4 Results and Discussion

Here, we report the performance of all three proposed models applied to detect imaginary vowel pronunciations. The first model we trained and evaluated is CNN model. CNN was proved to be very successful in classifying images and detecting objects in images. However, in this scenario, the CNN model performed with the average classification accuracy of 51% across all the subjects. The model was trained with the hyper-parameters learning rate = 0.0001, decay rate = 0.0001, $\beta_1 = 0.9$, and $\beta_2 = 0.999$. The models were trained for 20 epochs. The model was found to be overfitting the data even after adding dropout layers. The training and testing classification accuracies and loss for subject 'S1' are depicted in Fig. 5.

The second model which was trained and evaluate is the LSTM model. The LSTM models have been known to be performing well for the time-series of sequence classification tasks. In this EEG signal classifications, the LSTM model performed better than the CNN model with the average classification accuracy of 63%. The hyper-parameters used to train the model were learning rate of 0.001, β_1 and β_2 values same as CNN model, 0.9 and 0.999, respectively, and decay rate of 0.001. The total number of epochs was 50 with batch size being 10. The classification accuracies and loss for train and test data are illustrated in Fig. 6.

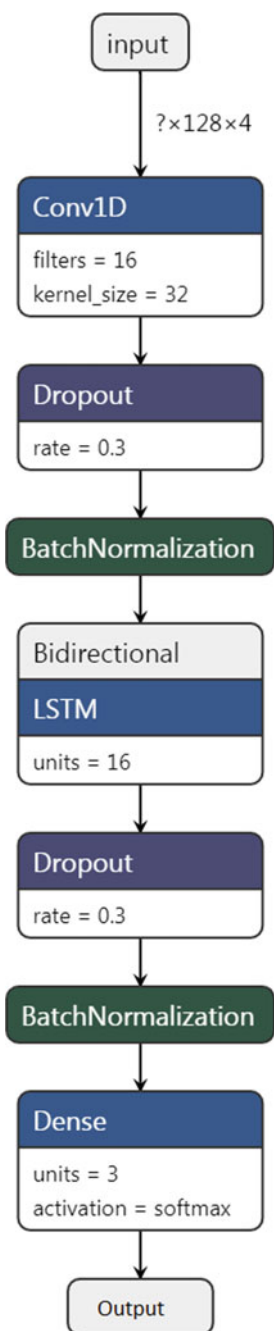
The last model to train and evaluate is the combination of CNN and the LSTM model. The model was trained with the same β_1 and β_2 values as per the previous model. The learning rate and decay rates were set to 0.0001 and 0.001, respectively. The batch size was set to 10 and the number of epochs is set to 50. This model proved to be better performing than the previous models with the average classification accuracy of 84% across three subjects (Fig. 7).

The subject-wise classification accuracies are presented in Table 1. The overall performance of CNN + LSTM was best among all three proposed models as discussed earlier. Among the subjects, the data from the subject 'S3' yielded the best classification accuracy for all the models across subjects.

5 Conclusion

In this study, three deep learning models to classify the EEG data belonging to the imagined activities of pronouncing vowels 'a', 'u', and no activity have been proposed. The multiclass classification models are based on deep learning architectures and that based CNN, LSTM, and the combination of both is implemented to classify brain activity. The data used for the analysis was not pre-processed in any

Fig. 4 CNN + LSTM model



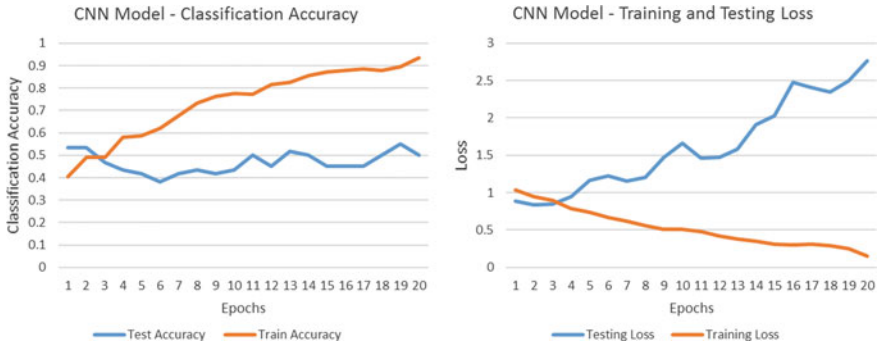


Fig. 5 CNN model—classification accuracy and loss

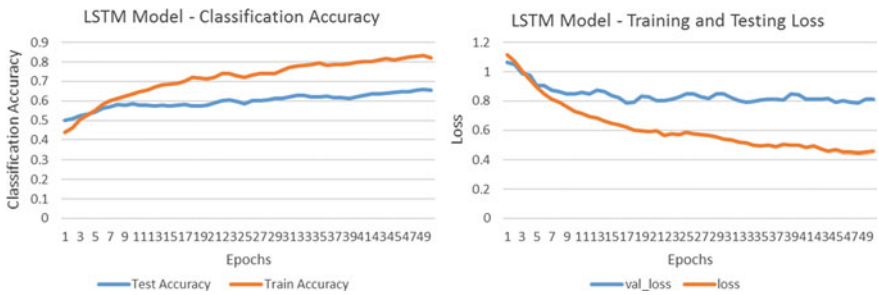


Fig. 6 LSTM model—classification accuracy and loss

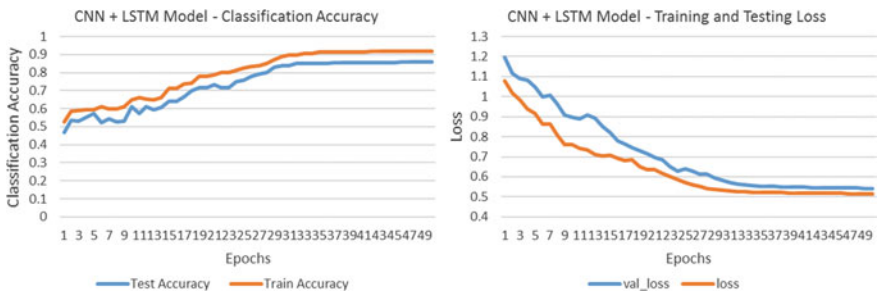


Fig. 7 CNN + LSTM model—classification accuracy and loss

Table 1 Subject-wise classification accuracies

Subject/model	CNN	LSTM	CNN + LSTM
S1	50	65	85
S2	51	60	82
S3	53	64	86
Avg	51	63	84

way other than the bandpass filtering. The models performed with the average classification accuracy of 51% for CNN-based model, 63% for LSTM-based model, and 83% CNN + LSTM model. While the accuracies are comparable to the other studies employing the same dataset [16–18, 26], these studies employ pair-wise classification compared to multiclass classification employed in this study. This study can be extended to classify for more imaginary speech activities.

References

1. Wolpaw JR (2010) Brain–computer interface research comes of age: traditional assumptions meet emerging realities. *J Motor Behav* 42(6):351–353
2. Allison B (2007) The I of BCIs: next generation interfaces for brain–computer interface systems that adapt to individual users. In: *International conference on human–computer interaction*. Springer, Berlin, Heidelberg, pp 558–568
3. Birbaumer N, Cohen LG (2007) Brain–computer interfaces: communication and restoration of movement in paralysis. *J Physiol* 579(3):621–636
4. Hwang HJ, Kim S, Choi S, Im CH (2013) EEG-based brain–computer interfaces: a thorough literature survey. *Int J Hum-Comput Interact* 29(12):814–826
5. Pfurtscheller G, Brunner C, Schlögl A, Da Silva FL (2006) Mu rhythm (de) synchronization and EEG single-trial classification of different motor imagery tasks. *Neuroimage* 31(1):153–159
6. Lee PL, Yeh CL, Cheng JYS, Yang CY, Lan GY (2011) An SSVEP-based BCI using high duty-cycle visual flicker. *IEEE Trans Biomed Eng* 58(12):3350–3359
7. Faradji F, Ward RK, Birch GE (2009) Plausibility assessment of a 2-state self-paced mental task-based BCI using the no-control performance analysis. *J Neurosci Methods* 180(2):330–339
8. Salvaris M, Cinel C, Citi L, Poli R (2011) Novel protocols for P300-based brain–computer interfaces. *IEEE Trans Neural Syst Rehabil Eng* 20(1):8–17
9. Kaper M, Meinicke P, Grossekhoefer U, Lingner T, Ritter H (2004) BCI competition 2003-data set IIb: support vector machines for the P300 speller paradigm. *IEEE Trans Biomed Eng* 51(6):1073–1076
10. Nijboer F, Sellers EW, Mellinger J, Jordan MA, Matuz T, Furdea A, Halder S, Mochty U, Krusienski DJ, Vaughan TM, Wolpaw JR (2008) A P300-based brain–computer interface for people with amyotrophic lateral sclerosis. *Clin Neurophysiol* 119(8):1909–1916
11. Volosyak I, Moor A, Gräser A (2011) A dictionary-driven SSVEP speller with a modified graphical user interface. In: *International work-conference on artificial neural networks*. Springer, Berlin, Heidelberg, pp 353–361
12. Pfurtscheller G, Neuper C (2001) Motor imagery and direct brain–computer communication. *Proc IEEE* 89(7):1123–1134
13. Carlson T, Leeb R, Chavarriaga R, Millán JDR (2012) The birth of the brain-controlled wheelchair. In: *2012 IEEE/RSJ international conference on intelligent robots and systems*. IEEE, pp 5444–5445
14. Callan DE, Callan AM, Honda K, Masaki S (2000) Single-sweep EEG analysis of neural processes underlying perception and production of vowels. *Cogn Brain Res* 10(1–2):173–176
15. Fujimaki N, Takeuchi F, Kobayashi T, Kuriki S, Hasuo S (1994) Event-related potentials in silent speech. *Brain Topogr* 6(4):259–267
16. DaSalla CS, Kambara H, Sato M, Koike Y (2009) Single-trial classification of vowel speech imagery using common spatial patterns. *Neural Netw* 22(9):1334–1339
17. Idrees BM, Farooq O (2016) EEG based vowel classification during speech imagery. In: *2016 3rd international conference on computing for sustainable global development (INDIACom)*. IEEE, pp 1130–1134

18. Patel, J., Pasha, I.A. and Krishna, D.H.: Classification of imagery vowel speech using EEG and cross correlation. *International Journal of Pure and Applied Mathematics*, 118(24) (2018).
19. Wang L, Zhang X, Zhong X, Zhang Y (2013) Analysis and classification of speech imagery EEG for BCI. *Biomed Signal Process Control* 8(6):901–908
20. Min B, Kim J, Park HJ, Lee B (2016) Vowel imagery decoding toward silent speech BCI using extreme learning machine with electroencephalogram. *BioMed Res Int*
21. Riaz A, Akhtar S, Iftikhar S, Khan AA, Salman A (2014) Inter comparison of classification techniques for vowel speech imagery using EEG sensors. In: *The 2014 2nd international conference on systems and informatics (ICSAI 2014)*. IEEE, pp 712–717
22. Watanabe H, Tanaka H, Sakti S, Nakamura S (2019) Synchronization between overt speech envelope and EEG oscillations during imagined speech. *Neurosci Res*
23. Kim HJ, Lee MH, Lee M (2020) A BCI based Smart Home System Combined with Event-related Potentials and Speech Imagery Task. In: *2020 8th international winter conference on brain-computer interface (BCI)*. IEEE, pp 1–6
24. Cooney C, Raffaella F, Coyle D (2019) Optimizing input layers improves CNN generalization and transfer learning for imagined speech decoding from EEG. In: *IEEE international conference on systems, man, and cybernetics, 2019: Industry 4.0*
25. Tamm MO, Muhammad Y, Muhammad N (2020) Classification of vowels from imagined speech with convolutional neural networks. *Computers* 9(2):46
26. Yoshimura N, Satsuma A, DaSalla CS, Hanakawa T, Sato MA, Koike Y (2011) Usability of EEG cortical currents in classification of vowel speech imagery. In: *2011 international conference on virtual rehabilitation*. IEEE, pp 1–2

Optimization of Process Parameters by Application of Adaptive Neuro-Fuzzy Inference System (ANFIS) Model of FFF Process



Imran Siraj and Pushpendra S. Bharti

1 Introduction

Additive manufacturing (AM) technology is a constructive technology that builds products by adding material bit by bit and manufacture part directly from design, thereby eliminating the cost and time incurred in setup. Also, almost all the materials can be processed; hence, AM has got a wide range of applications over conventional manufacturing. Apex body of testing and materials, American Society of Testing and Materials (ASTM) has defined ‘additive manufacturing’ as a process of manufacturing, that propels raw material from a nozzle injector [1]. ASTM released standards ‘ASTM F3187-16,’ for normal functionality and ‘ASTM F3303-2018,’ for critical functionality, metallic parts, ‘ASTM D638-10’ for plastics parts, produced by FFF [2–5]. Fused filament fabrication (FFF) is the main technology that produces layers of material superimposed over each other. FFF has gained broad applicability in select areas of manufacturing, since it produces parts quickly and directly from the design stage [6]. With the exponential growth on its sleeve, FFF has not gained popularity with industrial productions as expected. Manufacturers of machineries, automobiles, and infrastructure have not adopted FFF technology, despite many advantages over other manufacturing technologies, and those who chose, are weaning away. The reasons behind this could be summed up as poor mechanical properties of the process [7]. The hunt for the excellence of quality becomes essential for broader applicability of FFF; hence, exploration of the reasons associated with quality has become the core of research in FFF processes [8]. Researchers have focused on the quality issues associated with FDM and applied several tools and techniques to expedite the actual cause associated with poor quality. Feeding quality in a quick process like FFF becomes a challenging task; hence, optimization of process parameters is the obsession of researchers for perfect performance characteristics.

I. Siraj (✉) · P. S. Bharti

University School of Information ,Communication & Technology, GGS IndraPrastha University, New Delhi, India

Tools and techniques applied to FFF for optimization are summarized in the literature review section.

2 Literature Review

In the recent analysis, Yadav et al. connected the properties with input parameters of 3D printer by applying ANFIS model. The fabric used was PETG, ABS, and multi-material. The error found to be a pair of 6.3% [9]. In his analysis, Negrete stressed the result of method parameters on the half quality and productivity. The conclusion in his study was that the printing plane was the foremost important issue for reducing process time. In dimensional accuracy, the length was full of layer thickness, and dimension was chiefly influenced by the filling pattern [10]. Sood et al. in their analysis argued that any purposeful half is subjected to completely different load conditions in actual observe, leading to numerous fatigue and stresses developed. Principal element analysis (PEA) technique was applied to co-relate, layer thickness, formation dimension, formation angle, orientation, and air gap with tensile, bending, and impact strength. The results indicate that each factor like layer thickness, orientation, formation angle, formation dimension, and air gap and interaction between layer thickness and orientation considerably influence the response [11]. Mohamed et al. reiterated in their analytical analysis the importance of half quality and accuracy, owing to employability in medical implant, natural philosophy, telecommunication, and part missions, that need higher exactness and accuracy. The results of their study stressed that I-optimality criterion model is an up-and-coming technique for improvement [12]. Chohan et al., in their analysis, assessed the feasibility of vapor smoothing technique for surface finishing at a low price and shorter lead times. The result of pre-processing and post-processing parameters studied several, that enclosed dominance, limitations, validity, and reach of varied techniques adopted to enhance surface end their analysis is predicated on a case study. The development of precise, automatic, and controlled surface finishing techniques with low price and time [13] Chadha et al., in their analysis, targeted the result of bed temperature, layer thickness, and infill pattern (rectilinear, honeycomb, triangular) on lastingness and bending strength. They found that with the rise in bed temperature, lastingness, and flexural strength at first will increase then decreases [14]. Schmitt et al. centered on the part's weight and relationship with strength since a load of elements has great results in the automotive business. Their paper bestowed experimental results and style issues for the FDM method of vinyl cyanide hydrocarbon vinyl benzene material. An optimum infill configuration was additionally found; they summarized the causes of deviations within the dimensional accuracy within the kind of Ishikawa fish-bone diagram [15]. Durão et al. studied the results of method parameters; layer thickness, deposition rate, and infill rate, on lastingness and established the quantitative relationship. Their results established the quantitative relationship between parameters, layer thickness, infill rate, and deposition rate with lastingness. The

numerical analysis foresaw a decent model, and results were verified through an experiment [16].

3 Quality Issues in FFF

FFF process is simple, versatile, additive manufacturing technology and has the potential to incorporate the present need of customized and cost-effective manufacturing solutions. However, many drawbacks are also associated with FFF. It has a complex mechanism that does not accurately define the functional relationship between the controlled process parameters and quality and accuracy. Even sectors like organ implants in humans, electronics and telecommunications, and aerospace missions require a high degree of dimensional accuracy as well as surface finish [17]. The poor dimensional accuracy and surface finish are primary hurdles ahead while implementing FFF as rapid prototyping technology [18]. Poor mechanical properties are responsible for slow expansion of this process [19]. Manufacturers are reluctant to adopt FDM as core technologies of their production [20]. Rapid and quick settlement of quality issues will bring back the FDM processes into main stream of manufacturing [21]. By controlling input parameters, output parameters are controlled, that's all we know, but how much will they affect, is a million dollar question [22]. A real-time measurement system of parameters is the urgent need of the hour [23]. Quality issues, surface finish, dimensional accuracy, mechanical properties need to be addressed appropriately and precisely [24].

All established methods of optimizations are applied to find the effect and optimize the factors responsible for quality and accuracy; however, the process requires extensive research to relate and optimize the variables for enhanced performance.

4 Research Gap

A research gap was identified between the available solutions and problem statement. To fill this gap, experimental study was carried out with three objectives:

- (i) To find a functional relationship between process parameters and performance characteristics.
- (ii) To find the effect of process parameters on performance measures.
- (iii) To optimize the level of parameters for better quality.

To fulfill the objectives, six process parameters were considered to relate four performance measures, by developing an optimization model that combines best features of two methods. In order to achieve our objectives, an optimization technique called adaptive neuro-fuzzy inference system (ANFIS) has been applied. This technique is a hybrid between artificial neural network and fuzzy logic. However, this

Table 1 Process parameters, their levels and performance measures

Process Parameters	Levels		Performance measures
i. Infill ratio(A)	40	60 (%)	Ultimate tensile strength(W)
ii. Layer thickness (B)	0.1	0.2 (mm)	Compressive strength (X)
iii. Print speed (C)	100	120(mm/s)	Flexural stress(Y)
iv. Nozzle temperature (D)	200	210 (°C)	Hardness (Z)
v. Bed temperature (E)	60	80 (°C)	
vi. Shell thickness (F)	0.8	1.2 (mm)	

optimization model ANFIS has already been applied successfully by researchers, to train the models and achieve the objects, for finding single mechanical property:

The novelty of this work is implementation of this technique to find four performance measures at a time.

ANFIS is discussed in details in Sect. 6. Before implementing ANFIS, another analysis, principal component analysis (PCA) is performed to find the contribution of each parameter, is discussed in detail in Sect. 5.

Process Parameters considered in this study are given in Table 1.

5 Principal Component Analysis

PCA is a mathematical transformation that linearly combines the input process parameters to create a new set of variables, called principal components (PCs). PCs minutely detail the variation in the original data. PCA explains the complete spectrum of the variation as true as in the original data [25]. The PCA decomposition algorithm has the capability of explaining first PC minutely explains details of the input data. Similarly, the second PC details the maximal leftover data subjected to being non-correlated orthogonal and so on. PCs are basically derived from raw input data (using two covariance matrices) or from standardized data (using correlation matrix) [26].

6 Adaptive Neuro-Fuzzy Inference System (ANFIS) Introduction

ANFIS model is a hybrid cross between ANN and fuzzy logic. Adaptive capacity ANN and qualitative approach of fuzzy been logic have properly tuned into achieve best results. Mathematical properties rule of ANN are synced with rule-based fuzzy system to develop a model that depicts human way of data processing [27]. ANFIS combines the best features fuzzy system and ANN, thereby eliminating their own discrepancies; framework provides the ANFIS modeling highly systematic and little reliant on expert knowledge [28]. Neural networks are applied to predict the future values, based upon the past learnings. The learning is sharp and crisp, and it can predict accurate values, but limitation of this network is its inability to explain the process of decision making. It lacks in transparency [29]. Lotfi-Zadeh, father of neuro-fuzzy systems, could not improve or increase the learning capability of fuzzy systems. Combining these two powerful and popular techniques gave birth to neuro-fuzzy systems, thereby removing the drawbacks of both the systems and producing even more powerful technique. ANFIS model has earlier been applied to FDM by Yadav et al. with five input and one output systems. In this study, it has been applied for six input and four output parameters, one at a time [30]. The ANFIS architecture and model of the system expressing the nonlinear relationships between the input sand outputs of FDM are explained here. The ANFIS structure is a five layers network with a hybrid learning algorithm that is used to adjust the system in accordance with the input and output data structures. An ANFIS having two inputs (α and β) and one output (γ) is known as Takagi–Sugeno–Kang fuzzy interface system, having two membership functions for each input and two set of rules are depicted here;

First-order fuzzy interface systems are based on fuzzy rules ‘If–Then,’ explained as follows:

$$\text{Rule 1 : If } \alpha \text{ is } \alpha_1 \text{ and } \beta \text{ is } \beta_1 \text{ Then } f_1 = p_1 \alpha + q_1 \beta + r_1 \quad (1)$$

$$\text{Rule 2 : If } \alpha \text{ is } \alpha_2 \text{ and } \beta \text{ is } \beta_2 \text{ Then } f_2 = p_2 \alpha + q_2 \beta + r_2 \quad (2)$$

where α_1, α_2 and β_1, β_2 are the parameter for the input functions, p_1, q_1, r_1, p_2, q_2 and r_2 are the parameters for output functions. Input parameters α and β are nonlinear, whereas the output parameters p_1, q_1 and r_1 are linear. Six inputs and one output have been considered to develop the model. The model has five layers: (i) Fuzzy (ii) Production (iii) Normalized (iv) Defuzzy, and (v) Production and total output layer in order [31, 32].

7 Development of ANFIS Model by Application of MATLAB®

The ANFIS model in this problem has been developed using the ANFIS toolbox of MATLAB® R16 of MathWorks Inc. USA, software. The designed network was developed by using six input neurons on input layer, each neuron represented an input parameter, and similarly output layer consisted only one neuron that represented a single output parameter. The hidden layer used the transfer function in this network is *tansig*, and another transfer function *purelin* is applied in the output layers. The two transfer functions used in developing the network are hyperbolic tangent sigmoid transfer function, and the other transfer function, *purelin*, is linear in nature. The outputs in these transfer functions are evaluated as per following equations:

$$\text{tans}(n) = \frac{2}{1 + e^{-2n}} - 1 \quad (3)$$

Purelin (n) = n Where n ; input to the function.

Lavenberg–Marquardt algorithm is deployed to train the network, having two-layer network with six input neurons and one output neuron, with a single hidden layer of five neurons [35]. The selection of the transfer functions and the training algorithm is based on trial-and-error method. The objective was to achieve the find error range in a minimum number of trials in cyclic training. The cyclic functioning of the network was found to deliver better performance with aforesaid conditions. On the basis of this exhaustive study, two critical processes like the transfer functions and training algorithm were selected and applied to the network. Also, the numbers of neuron associated with the hidden layer is decided on functionality.

8 Methodology

The objective of this investigation is to find the deliverance of FDM process in terms of performance measures and to find an optimum level of process parameters for better yield. The experiment was designed applying Taguchi method. Six process parameters were considered each having two levels.

As per full factorial design, the total number of runs would be $2^6 = 64$; to reduce the number of runs; Matrix L32 was applied, since a sample of 32 key runs would represent the whole lot and would be as true as 64 runs (Taguchi design). The six parameters identified on the basis of literature survey and from interaction with professionals from industry are as follows: Similarly the performance characteristics identified, that play key role in design and service of the parts are: total number of specimens printed were $32 \times 5 = 160$, each experimental runs printed 5 specimens together, for the sake of keeping the sanctity, in the same environment. Four

different tests performed to determine six parameters by application of L32 matrix. Experimental setup along with different constituents is discussed in detail as follows:

- (a) **Design of Experiment** Minimum number of runs that are required to achieve significant data in Taguchi method can be calculated on the basis on the degrees of freedom approach.

$$N_{\text{Taguchi}} = 1 + V(L - 1) \quad (4)$$

where V = No. Of variables and L = levels, For this experimentation. Since $V = 6$ and $L = 2$; Hence,

$$N_{\text{Taguchi}} = 1 + 6(2 - 1) = 7[36] \quad (5)$$

Minimum runs required are 7. Hence, Matrix L7 will yield the desired results. However, for more consistency and higher accuracy, Matrix L32 is applied. Design and Analysis Software Minitab® was used to design the experimental runs, and experiment was conducted as per the plan. The experimental run along with results is presented in Table 2:

- (b) **Design of specimen** Design of the test specimens was taken from testing standards apex body; American Standards of Testing Materials, in accordance with the code: ASTM D638-10 (Type: IV), Standards. The testing method of plastics to determine mechanical properties of plastics is given in the abovementioned code in details.
- (c) **Raw Material** The raw material is filament for of a material called polylactic acid (PLA), Manufactured by REVER Industries, with brand name FIBREEL, and India. The specifications of the filament are $\phi 1.75$ mm (diameter) and of wooden color. This color is cool and light and would not play any significant role in determining the properties. Manufacturer and researchers have recommended the nozzle temperature around 210°C and bed temperature 60°C for printing PLA. The optimum level of temperature of fusion is below 200°C for the given material.
- (d) **Machine** Experimentation was performed a machine procured from CADx Technologies Pvt. Ltd., India. Model name of the printer is ARYA-PRO, to print the specimens. The printer ARYA-PRO has following specifications:

Table 2 Experimental runs with results

S. No.	(A)	(B)	(C)	(D)	(E)	(F)	(U)	(V)	(Y)	(Z)
1	40	0.1	100	200	60	0.1	19.37029	34.09091	31.70	62
2	40	0.1	100	200	50	0.2	19.39218	36.02716	32.84	62
3	40	0.1	100	210	60	0.2	19.38641	36.20184	33.16	64
4	40	0.1	100	210	80	0.1	19.38022	35.06032	32.00	62
5	40	0.1	120	200	60	0.2	19.38800	34.80881	31.90	60
6	40	0.2	120	200	80	0.1	21.70388	36.88042	32.68	65
7	40	0.1	120	210	60	0.1	20.37029	36.38044	32.86	64
8	40	0.1	120	210	80	0.2	22.58986	38.72600	36.42	66
9	40	0.2	100	200	60	0.2	20.82066	36.32325	33.38	64
10	40	0.2	100	200	80	0.1	20.00842	36.00233	32.98	62
11	40	0.2	100	210	60	0.1	19.84662	35.20032	32.50	61
12	40	0.2	100	210	80	0.2	20.50102	35.82232	32.80	61
13	40	0.2	120	200	60	0.1	19.58480	34.59008	31.90	62
14	40	0.2	120	200	80	0.2	20.08040	35.00800	32.30	62
15	40	0.2	120	210	60	0.2	20.50822	35.50002	32.70	64
16	40	0.2	120	210	80	0.1	20.20183	35.00282	32.40	62
17	60	0.1	100	200	60	0.2	19.57884	34.45599	32.50	62
18	60	0.1	100	200	80	0.1	19.59227	34.55004	32.20	64
19	60	0.1	100	210	60	0.1	19.47029	34.50090	32.10	65
20	60	0.1	100	210	80	0.2	20.07740	35.01780	32.35	65
21	60	0.1	120	200	60	0.1	19.55850	34.40044	32.25	62
22	60	0.1	120	200	80	0.2	20.15042	35.32482	33.20	64
23	60	0.1	120	210	60	0.2	20.52382	35.84230	33.95	64
24	60	0.1	120	210	80	0.1	20.48222	35.58020	33.00	64
25	60	0.2	100	200	60	0.1	19.52118	36.57102	33.56	64
26	60	0.2	100	200	80	0.2	20.22242	37.00040	34.06	64
27	60	0.2	100	210	60	0.2	20.54233	37.55403	34.54	62
28	60	0.2	100	210	80	0.1	21.02200	38.00250	35.44	62
29	60	0.2	120	200	60	0.2	22.02052	38.10360	36.48	65
30	60	0.2	120	200	80	0.1	21.84822	37.88860	35.86	62
31	60	0.2	120	210	60	0.1	21.48000	36.96960	35.47	65
32	60	0.2	120	210	80	0.2	23.25696	40.06500	38.13	64

Desktop Volume : 390 mm × 360 mm × 490 mm
 Build Volume ; 200 mm × 200 mm × 180 mm
 Print Temperature : 180 – 260°C
 Print Speed : 50 – 220 mm/s
 Layer height : 50 – 300 μ
 Filament : PLA, ABS&Nylon
 Connectivity : SD Card

(e) **Conversion software**

The design of specimen was taken from ASTM Website, in STL Format; the standard form of tessellation language. This design was replicated for five times in the open-source software CURA Version 15.04.6., to create necessary NC Code that guides the printer head. Software used is powerful and compatible with all the machines (Figs. 1 and 2).

(f) **Connectivity ports** An SD card slot is given as the data input system on the printer and data can be transferred by SD card. Code generated in the software CURA has a file format *.nc file can transfer to the machine by SD card.

(g) **Material testing setup** the material testing setup consisted of the following machines:

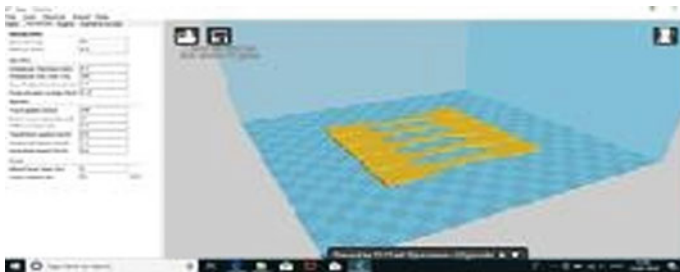


Fig. 1 Software CURA



Fig. 2 Machine display unit

- (i) The specimens produced for tensile and compressive tests were are tested on ultimate tensile machine and hardness tester of the following specifications (Figs. 3 and 4):

Specifications	UTM	Hardness tester
Model and Make	AMT, 5A-5B, HARRISS & TARRISS	HT,3010C
Maximum load	1000(kN)	150 (kgf)
Load range	20–1000 (kN)	60, 100 & 150 (kgf)
Accuracy	±1%	±1%
Test performed	Tensile, compressive and flexural	Rockwell and Brinell

- (h) **Data collection** The printed parts are thus tested on UTM and hardness tester for the six properties, and their readings are presented in tabular form for further processing.
- (i) **Analysis**
 - (A) PCA was performed first to find the contribution of each parameter, and PCs and TPCI were calculated as explain in PCA section. The percent effect of each factor was found.



Fig. 3 FDM printer



Fig. 4 Specimen printing

Fig. 5 Failure in tensile test



Fig. 6 Hardness test



Fig. 7 Design of specimen

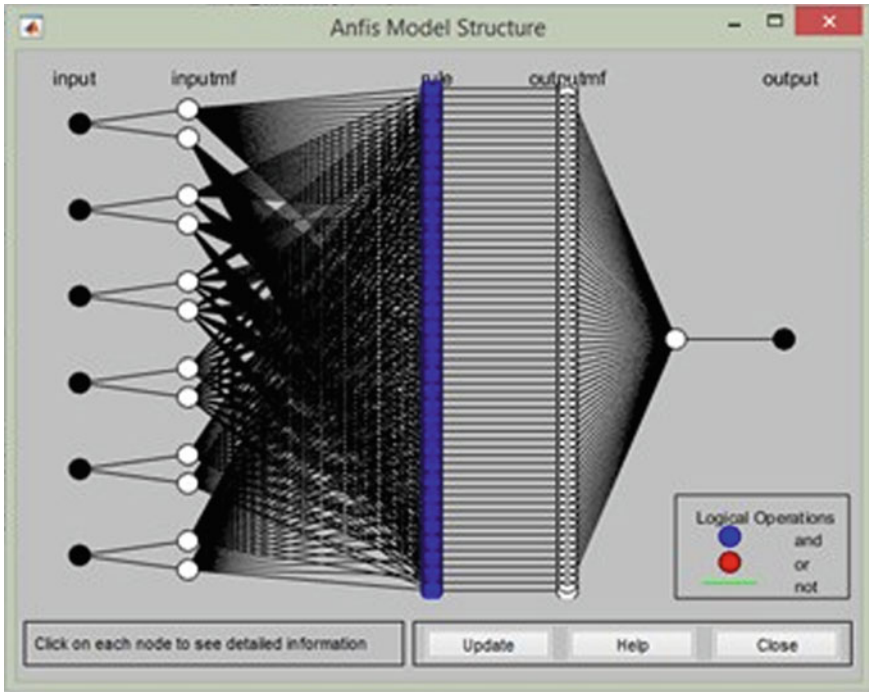
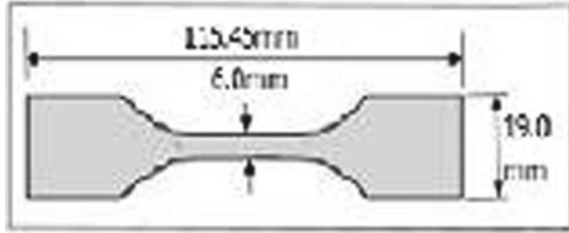


Fig. 8 ANFIS structure

(B) ANFIS model was developed in the software MATLAB® Version: 2016a of MathWorks Inc. USA, using ANFIS tool box: as discussed in Section IV, the procedure is given here:

- (a) **Neuro-Fuzzy Design:** To design the network, neuro-fuzzy designer toolbox is invoked in applications pull-down menu of MATLAB software. Data is loaded by invoking *.dat file from the current directory. Data file has 70% of the data achieved as per data analytics, 30% data is saved for testing. The obtained data is processed with the help of software.

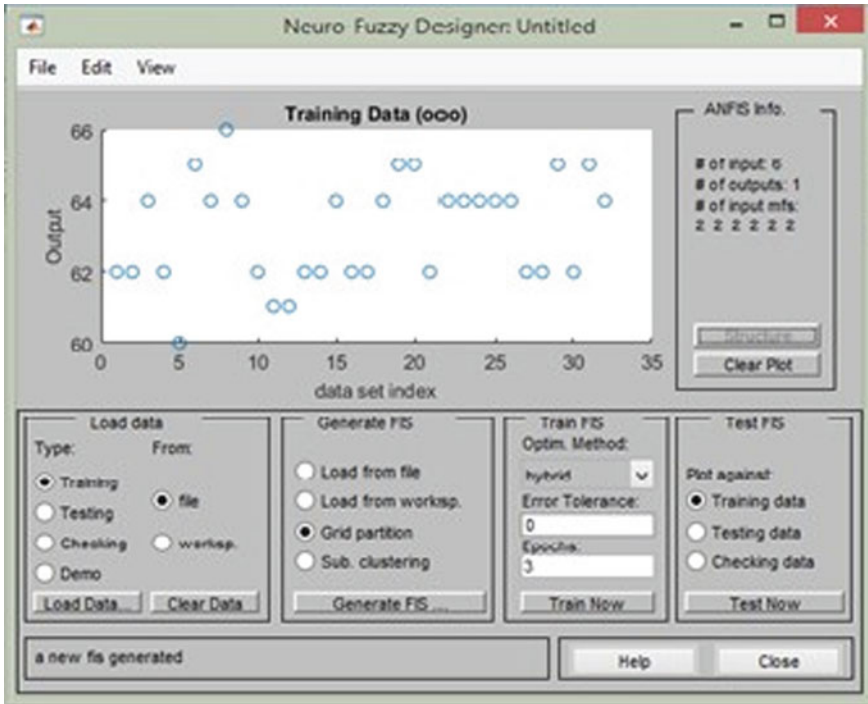


Fig. 9 Training ANFIS

- (b) **Generate Fuzzy Inference System:** To generate FIS, six linguistic variables corresponding to six process inputs and two membership functions corresponding to two levels of inputs are selected. Next step is to check the structure to confirm appropriate model and is invoked, as shown in Figs. 5, 6, 7, 8, and 9.
- (c) **Training Fuzzy Inference System:** To train the system hybrid command is invoked, as it already comprises of backpropagation training. Testing can be performed.
- (d) **Testing Data:** Testing is performed on the remaining 30% data. The testing data is first uploaded, and testing is then performed. The testing gives FIS output in graphical form. The blue dots on the graph show the actual readings recorded during the experimentation, whereas the red stars are the FIS output. The deviation from each point is calculated in mean square error (MSE). An average error of 1.2747 is depicted by the software.

Table 3 Percentage contribution of process parameters

Process parameters:	Contribution (%)	Optimum level
A. Infill ratio	100	60%
B. Layer thickness	85	0.2 mm
C. Print speed	85	100 m/s
D. Nozzle temperature	54	210 °C
E. Bed temperature	54	180 °C
F. Shell thickness	44	0.2 mm

9 Results and Discussions

The experimentation was performed as per the methodology, described in Section 4. ANFIS modeling and subsequent analysis give in-depth knowledge about various parameters, their standalone, and in-combination effects on various properties of material; the results are discussed in detail:

- (1) **Ultimate Tensile Strength:** The mean value of UTS is 20.39002, and the predicted value by FIS is 20.64 MPa; hence, error of 1.2747% is noted by the software. This error is almost negligible. The UTS can be targeted 22 by the following optimal combination of input parameters, given in Table 4:
- (2) **Compressive Strength:** The mean value of compressive strength is 36.04538 MPa. The predicted value by FIS is 32.006 that means the deviation is about 4.4301%. The target value of compressive strength 32 MPa can be achieved by following optimal set of parameters, as shown in Table 5 below:
- (3) **Flexural Strength:** Mean value of FS is 33.42531, whereas predicted value is 35.50. The mean square error is 6.2139, highest among all the errors. The network is not trained sufficiently and hence produced error more than 5%, highest among all the parameters. Optimum values of parameters are given in following Table 6 for achieving 35.5 value of flexural strength.
- (4) **Hardness:** The hardness predicted by FIS is 65.5, and the mean value of observed hardness is 63.15625. A deviation of 3.711%. The optimum values are given in Table 3:

10 Conclusions

The main objectives of this research are:

- (i) To find a functional relationship between process parameters in performance measures.
- (ii) Also to find the contribution of every parameter on performance characteristic.
- (ii) To find the optimal values of all the parameters.

The first objective was achieved by developing ANFIS model in MATLAB software using neuro-fuzzy design toolbox. The second objective was achieved by

applying the PCA. The principal component values were found and that determine the contribution of each parameter on quality measures that are discussed in the above section. The third objective was also achieved by developing the ANFIS model to find the optimum level of all the parameters. Hence, the study is performed successfully for mapping relationship between process parameters and main responses and for the evaluation of quantified relationship between process inputs: layer thickness, infill rate and deposition velocity and mechanical properties, tensile strength, compressive strength, flexural strength, and hardness. The developed model exhibits fine-tuned experimental results, which demonstrates the effectiveness of this predicted model. ANFIS model is used to predict the optimum level of process parameters. The neural network selected for this study has optimized architecture, used to train, test, and simulate the network. Normalization, PCA, feature reduction, and ANFIS tests were performed to predict the desired performances. It is, therefore, can be concluded that, this study has presented the main effects of important process parameters on the performance measures.

References

1. "ISO/ASTM 52900:2015(en), Additive manufacturing - General principles Terminology," International Organization for Standardization (ISO), Geneva, Switzerland, (2015).
2. ASTM ISO 52900–15 Standard Terminology for Additive Manufacturing-General Principles-Terminology. *ASTM International, West Conshohocken, PA, 3(4)*, (2015).
3. ISO/ASTM Standard 52900 (2015) Standard terminology for additive manufacturing general principles terminology. ASTM international. <https://www.astm.org>. (2018).
4. ISO/ASTM Standard 52910 (2017) Standard guidelines for design for additive manufacturing. ASTM International. <https://www.astm.org>. (2018).
5. Gibson, I., Rosen, D. W., & Stucker, B. *Additive manufacturing technologies* (Vol.17)(2014).
6. Frazier WAM (2014) Review. *J Mater Eng* 23(6):1917–1928
7. Wu HC, Chen TCT (2018) Quality control issues in 3D-printing manufacturing: a review. *Rapid Prototyping Journal* 24(3):607–614
8. Pérez, M., Medina-Sánchez, G., García-Collado, A., Surface quality enhancement of fused deposition modeling (FDM) of critical printing parameters. *Materials*, 11(8), 1382(2018).
9. Yadav, Dinesh, et al. "Modeling and analysis of significant process parameters of FDM 3D printer using ANFIS." *Materials Today: Proceedings* 21 (2020).
10. Camposeco-Negrete, "Optimization of FDM parameters for improving quality, productivity and sustainability of the process" *Progress in Additive Manufacturing* 5.1 (2020).
11. Sood, Anoop Kumar, et al. "Optimization of weighted principal component analysis." *Journal of Advanced Manufacturing Systems* 10.02 (2011).
12. Mohamed Ahmed, Syed Masood, and Jahar Lal Bhowmik "Optimization of fused deposition modeling process parameters using I-optimality criterion." *Measurement* 81(2016).
13. Chohan, Jasgurpreet Singh, and Rupinder Singh "Pre and post processing techniques to improve surface characteristics of FDM parts" *Rapid Prototyping Journal* (2017).
14. Chadha, Abhinav "Effect of fused deposition modelling process parameters on mechanical properties." *World Journal of Engineering* 4(3), 291–313 (2019)..
15. Schmitt, Matt, Raj Mattias Mehta, and Il Yong Kim. "Additive manufacturing infill optimization 3D-printed components." *Rapid Prototyping Journal* 12(3), 1291–1313(2019) .
16. Durão LFC, Barkoczy R, Zancul E, Ho LL, Bonnard R (2019) Optimizing additive manufacturing parameters. *Progress in Additive Manufacturing* 4(3):291–313

17. Schirmeister, C. G., Hees, T., Licht, E. H., & Muelhaupt, R. 3D printing of high density polyethylene by fused filament fabrication. *Additive Manufacturing*, 28(2019).
18. Hernandez, D. D. Factors affecting dimensional precision of consumer 3D printing. *International Journal of Aviation, Aeronautics, and Aerospace*, 2(4)(2015).
19. Wu HC, Chen TCT (2018) Quality control issues in 3D-printing manufacturing: a review. *Rapid Prototyping Journal* 24(3):607–614
20. Gomez-Gras, G., Jerez-Mesa, R., Travieso-Rodriguez, J. A., & Lluma-Fuentes, J. Fatigue performance of fused filament fabrication. *Materials & Design*, 140(2018).
21. Kim, H., Lin, Y., & Tseng, T. L. B.A review on quality control in additive manufacturing. *Rapid Prototyping Journal*. 4(3), 291–313(2018).
22. Tanikella, N. G., Wittbrodt, B., & Pearce, J. M. Tensile strength of commercial polymer materials for fused filament fabrication. *Additive Manufacturing*, 15 (2017).
23. Mani, M., Lane, B. M., Donmez, M. A., Feng, S. C., & Moylan, S. P. A review on measurement science needs for real-time control of additive manufacturing. *International Journal of Production Research*, 55(5), 1400–1418(2017).
24. Jin, Y., & He, Y. An approach of high-quality and uniform additive manufacturing. *The International Journal of Advanced Manufacturing Technology*, pp. 651–662 (2017).
25. Bastianoni, S. & Pulselli, Correlations through Principal Components Analysis (PCA) applied to SPIn-Eco Project. *Journal of environmental management*, 86(2), 419–426(2008).
26. Heba, F. E., & Abraham, A. Principle components analysis vector machine based detection system. *10th international conference on intelligent systems design* pp.363 (2010).
27. Tatikonda, R. C & Kumar, V. Control of pendulum adaptive neuro fuzzy inference structure (ANFIS). *Proceedings of International Symposium , Circuits Systems* pp. 1348–1351(2010).
28. Haznedar, B., & Kalinli, A. Training ANFIS structure using simulated annealing algorithm for dynamic systems identification. *Neurocomputing*, 302(2018).
29. Ghomsheh, V. S. & Teshnehlab, M. Training ANFIS structure with modified PSO algorithm. In *2007 Mediterranean Conference on Control & Automation* (pp. 1–6). IEEE(2007).
30. Yadav, D., Chhabra D. & Ahlawat, Modeling and analysis of significant process parameters of FDM 3D printer using ANFIS. *Materials Today: Proceedings*, 21,1592–1604 (2020).
31. Abdulshahed AM, Fletcher S (2015) The application of ANFIS prediction models for thermal error compensation on CNC machine tools. *Applied Soft Computing* 27:158–168
32. Mohan, S. V., & Reddy, M. V., Optimization of critical factors to enhance PHA synthesis by Taguchi design of experimental methodology. *Bioresource technology*, 409–416. (2013).

Skin Lesion Characterization with Ensembles of Machine Learning and Deep Learning Models



D. Abhila, B. Priyanka, A. Aishwariya, S. Nihal Mathew, S. Suriya Kumar,
and Kunaraj Kumarasamy

1 Introduction

In the year 2013, skin-based diseases added 1.79% to the burden of disease among the 306 diseases and injuries worldwide [1]. Some of the common skin lesions include seborrheic keratosis, basal cell carcinoma, actinic keratosis, dermatofibroma, melanoma, pigmented benign keratosis, nevus, squamous cell carcinoma, and vascular lesion. Our paper aims at classifying skin lesions with a simple photograph taken from a standard camera (non-dermoscopic). This can help doctors to assess the skin conditions of patients living in remote areas. Also, the five-year survival rate for melanoma detected in its earliest stages is around 97%, which drops to approximately 14% if it is detected in its later stages. The detection of melanoma in its early stages requires expert dermatologists. But, dermatologists cannot screen every one of their patients for melanoma. Our paper provides a non-invasive method to detect melanoma in its early stages, thereby, saving a load of work for dermatologists. We make a comparison between two different techniques that can be used to classify skin lesions. The first approach consists of five stages, namely, image pre-processing like filtering, segmenting the appropriate regions, extracting the features, training, and testing of a machine learning classifier. The extracted features from the image include both color and texture features out of which color features play a dominant role in classifying the lesion. Machine learning classifiers are trained using supervised learning with the extracted features as predictors. Later, when an unknown lesion is given as input, the proposed solution extracts the features of the image and classifies the lesion. The second approach makes use of transfer learning to train neural networks (AlexNet and GoogLeNet) on clinical images of skin lesions. The trained CNN can then classify the skin lesions automatically. To improve the prediction accuracy, we ensemble the results of the individual networks. The approach

D. Abhila · B. Priyanka · A. Aishwariya · S. Nihal Mathew · S. Suriya Kumar ·
K. Kumarasamy (✉)
Loyola-ICAM College of Engineering and Technology (LICET), Chennai, India

which makes use of deep learning outperformed the other approach using machine learning in terms of accuracy. The ensembled CNN achieved an accuracy of 90.2% which is comparable to the level of trained dermatologists.

2 Artificial Intelligence in Medicine

There is already an incredible amount of technology and automation in play in medicine. Digitized medical records, online scheduled appointments, health wearables, and wireless brain sensors are some of the notable advancements in medical technologies. With the increase in technology usage in all areas of life, how we seek medical care has also changed. AI supports ‘precision medicine’ that improves diagnosis and prognosis and also it reduces the physician’s time. The AI algorithms need to be tested repeatedly to reduce the margin of error.

The diagnosis of skin diseases is an arduous process. The lesion is examined by a dermatologist to determine whether it is benign or fatal. Malignant lesions often appear to be benign in their early stages and such lesions are screened for a pathologist to determine its malignancy. This delays treatment and may put patients in a life-threatening situation.

Automatic diagnosis of skin diseases and various other ailments using machine learning and deep learning algorithms has shown significant results and gaining a lot of momentum, and several pieces of research have been carried out in this regard [2–11]. This can make diagnostics cheaper and more accessible for people living in remote areas. The AI systems cannot replace doctors but it can highlight potentially malignant lesions facilitating early treatment of such lesions.

3 Dataset

A large number of skin lesion images are required to achieve better classification accuracy. Images of nine different skin lesions are collected from the ISIC archive. The ISIC archive [12] is the largest known open-source dataset for skin lesions. It is a widely used dataset for developing automated diagnostic systems. These systems help reduce unnecessary biopsies by improving the accuracy of skin lesion classification. Table 1 depicts the different skin lesions and the number of images collected for each of the skin lesions.

4 Machine Learning Classifiers

Machine learning enables the classification of an unknown skin lesion on the features extracted from an image of the lesion. Before proceeding to the classification of

Table 1 List of skin lesions being classified

Name of the skin lesion	No. of images
Actinic keratosis	132
Basal cell carcinoma	515
Dermatofibroma	122
Melanoma	526
Nevus	396
Pigmented benign keratosis	320
Seborrheic keratosis	419
Squamous cell carcinoma	219
Vascular lesion	142

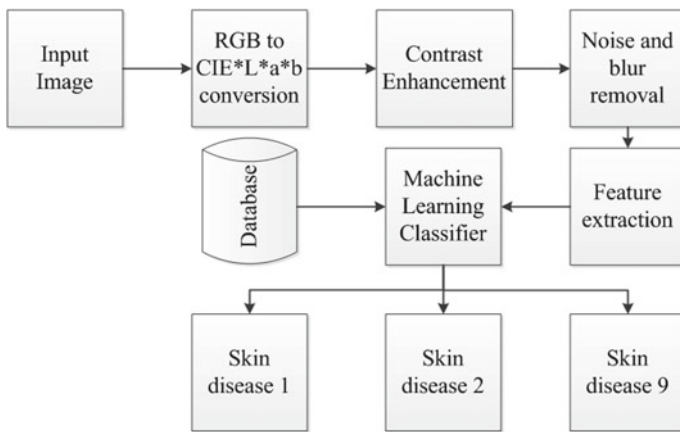


Fig. 1 Steps involved in the classification of skin lesion using machine learning classifier

unknown lesion, the machine learning classifier has to be trained on features extracted from a training dataset. Figure 1 depicts the various steps involved in the classification of skin lesions.

4.1 Image Pre-Processing

This is a significant initial stage in computer-aided skin lesion diagnostics. The images captured may be subjected to noise, blur, and other factors which may lead to misdiagnosis. Pre-processing consists of modifying the pixels in an image to achieve better classification accuracy. Figure 2 shows the different pre-processing stages. The images are read one-by-one from the folders in which they are stored. The images can be processed in the existing RGB color space or even in wavelet domain [13].

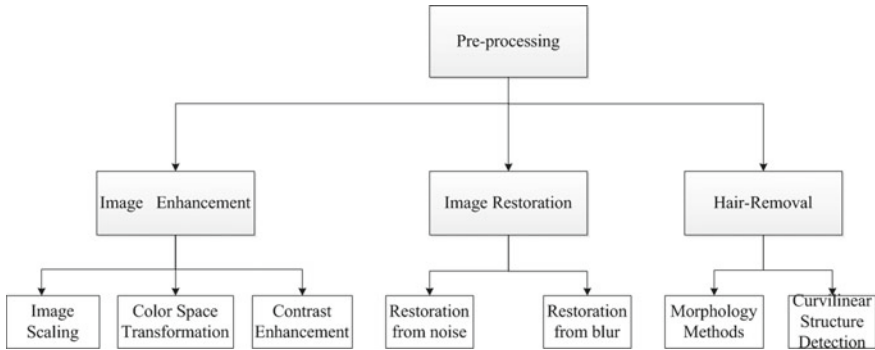


Fig. 2 Steps in image pre-processing

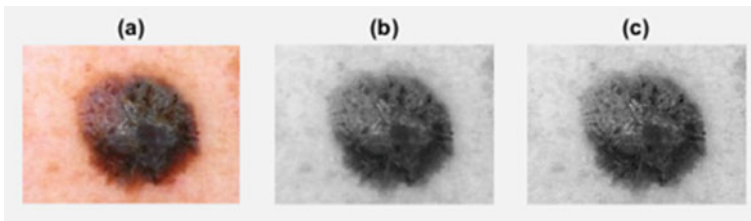


Fig. 3 **a** RGB image of skin lesion, **b** luminance part of the image after transformation from RGB to LAB color space, **c** image after contrast enhancement using unsharp masking

The images are converted to the CIE $*L^*a^*b$ color space as it is the exact way of denoting color and is not dependent on the device. The luminance part of the LAB color space is the grayscale image. Contrast enhancement is performed using unsharp masking to enhance the visual quality of the image by processing its edges. Noise and blur are removed using the Wiener filter. The results of pre-processing an RGB image of the skin lesion are shown in Fig. 3.

4.2 Segmentation

The pre-processed images converted back to RGB format are then given as input to the segmentation algorithm which localizes the region of interests (RoI) by partitioning a digital image into multiple segments. Some of the most common segmentation techniques used for skin lesion segmentation include:

- Edge-based segmentation [14]
- Thresholding-based segmentation [15]
- Region-based segmentation [16]
- Fuzzy C-means-based segmentation [17]

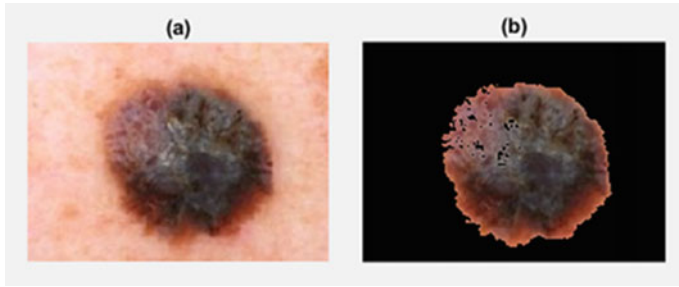


Fig. 4 **a** RGB image of skin lesion before segmentation, **b** RGB image of skin lesion after segmentation

We use Otsu’s algorithm to obtain the threshold of the image. It is based on a normalized histogram of the image.

The normalized histogram sets the optimal threshold value and this value is used to separate the input pixels into two homogeneous classes (C_0 and C_1). The resultant of Otsu’s algorithm is a binary mask.

$$w1 = \Pr(C1) = \sum_{i=k+1}^L Pi = 1 - w(k) \tag{1}$$

$$w0 = \Pr(C0) = \sum_{i=1}^k pi = w(k) \tag{2}$$

An algorithm is then developed to apply the binary mask on the original RGB image of the skin lesion to obtain the segmented image. By the algorithm, the RGB image is read pixel by pixel, and those pixel positions for which the binary mask has value 255 (white) are assigned the value 0 (black) for all three color channels (R, G, and B). The remaining pixels are left unchanged in the RGB image. The resulting RGB image is the segmented image of the skin lesion. The same procedure is repeated for all the images in the dataset, and the segmented images are stored in the corresponding folders. Though this is a robust way of segmenting the lesion, it provides better results for most of the skin lesion images. Figure 4 shows the color image before and after segmentation using Otsu’s thresholding.

4.3 Feature Extraction

Feature extraction plays a major role in machine learning and as the proper choice of features plays an important role in improving the accuracy of classification. Both color and texture features are useful for skin lesion classification out of which the color features have a major impact [5]. The various color and texture features include:

Color features

Mean and standard deviation of every component of CIE*L*a*b and CIE*L*u*v color spaces contribute to 12 color features. When the image is separated into chromaticity and lightness, the role of RGB pixel values has less impact over the color space. Taking this into account, the CIE L*a*b* and CIE L*u*v* color spaces are used in our problem rather than mere RGB pixel values.

Texture features

Raw moments, central moments, scale invariant moments, and Hu's invariant moments are the various texture features used for classification.

Raw moments

$$M_{ij} = \sum_a \sum_b a^i b^j I(a, b) \quad (3)$$

Central moments

$$\mu_{pq} = \sum_a \sum_b (a - \bar{a})^p (b - \bar{b})^q f(a, b) \quad (4)$$

Scale invariant moments

$$k_{ij} = \frac{\mu_{ij}}{\mu_{00}^{(1+\frac{i+j}{2})}} \quad (5)$$

Hu's invariant moments

$$I_1 = k_{20} + k_{02} \quad (6)$$

$$I_2 = (k_{20} - k_{02})^2 + 4k_{11}^2 \quad (7)$$

$$I_3 = (k_{30} - 3k_{12})^2 + (3k_{21} - k_{03})^2 \quad (8)$$

$$I_4 = (k_{30} + k_{12})^2 + (k_{21} + k_{03})^2 \quad (9)$$

$$I_5 = (k_{30} - 3k_{12})(k_{30} + k_{12})[(k_{30} + k_{12})^2 - 3(k_{21} + k_{03})^2] \\ + (3k_{21} - k_{03})(k_{21} + k_{03})[3(k_{30} + k_{12})^2 - (k_{21} + k_{03})^2] \quad (10)$$

$$I_6 = (k_{20} - k_{02})[(k_{30} + k_{12})^2 - (k_{21} + k_{03})^2] + 4k_{11}(k_{03} + k_{12})(k_{12} + k_{03}) \quad (11)$$

$$I_7 = (3k_{21} - k_{03})(k_{30} + k_{12})[(k_{30} + k_{12})^2 - 3(k_{21} + k_{03})^2] \\ - (k_{30} - 3k_{12})(k_{21} + k_{03})[3(k_{30} + k_{12})^2 - (k_{21} + k_{03})^2] \quad (12)$$

4.4 Training the Machine Learning Classifier

The features extracted from the images are used as predictors and the image labels are used as responses. The results are subjected to fivefold cross-validation. The following classifiers are trained using the extracted features:

- Support vector machine
- Boosted decision trees
- Bagged decision trees
- K-nearest neighbor

Support Vector Machine (SVM)

SVM is a supervised learning-based machine learning classifier. Sumithra et al. used SVM and KNN to classify skin lesions in the year 2015 [18]. Support vector machines make use of hyperplanes to classify data. The hyperplanes are decision boundaries which help distinguish between feature vectors of different objects. The best hyperplane is chosen with the help of support vectors which are points that are near the hyperplane. The best hyperplane is the one with the largest margin from the support vectors. The dimensionality of the hyperplane is determined by the number of feature vectors. We use the quadratic kernel function to define the hyperplane.

Boosted decision trees

Decision tree builds classification models in the form of a tree structure where the data is continuously split according to a certain parameter. Boosted decision trees are used in order to produce better predictive performance. It combines several decision trees in series and each decision tree aims at improving the error performance of the previous tree. The main drawback of boosted decision trees is that they take a longer time to train, owing to their series structure.

Bagged decision trees

Bagged decision tree is a type of ensemble technique that provides better accuracy when compared to decision tree classifiers. Bagged decision trees create subspaces of the training data and these subspaces are used to train independent decision trees. An aggregate of the probabilities of the individual decision trees is used to determine the final probability, and this technique has been applied to many imaging tasks line noise pixel classification, etc. [19].

K-nearest neighbor

K-nearest neighbor classifies each element in the dataset based on a similarity measure. It classifies data points on the basis of its 'k' nearest neighbors. The value of k has to be suitably chosen to avoid overfitting and achieve better training and validation error performance.

Table 2 Accuracy of different classifiers

Classifier	Accuracy (%)
Support vector machine	87.2
Bagged decision trees	85.4
K-nearest neighbor	82.5
Boosted decision trees	80.9

4.5 Result

The support vector machine was able to achieve better performance than the other classifiers with an accuracy of 87.2%. It is highly preferred by many as it produces better accuracy with less computation power. The accuracy achieved using the machine learning classifiers is shown in Table. 2.

5 Deep Learning Network

5.1 Pretrained CNN

Pretrained networks have different characteristics that matter when choosing a network to apply to a specific problem. The pretrained CNN may be either trained from scratch making use of the basic architecture of the network or trained using a technique known as transfer learning.

Training the network from scratch consumes a lot of time as the weights need to be adjusted from the initial stage. This would be similar to building the network from scratch. On the other hand, transfer learning allows us to use the network trained on one task for a second task with the replacement of the final pooling and classification layers. Transfer learning has been gaining a lot of importance owing to its speed and simplicity and has been used widely in research involving the automated diagnosis of skin lesion [3, 6].

The most important characteristics that need to be considered are accuracy, speed, and size. Choosing a network is a trade-off between these characteristics. Table 3 depicts the no. of convolutional layers and no. of learnable parameters in widely used pretrained CNNs.

A proper choice of a network would be one with low training and prediction time and an acceptable value of accuracy for the problem at hand.

AlexNet and GoogLeNet

The AlexNet network is 8 layers deep and is pretrained to classify images into 1000 object categories. It was first introduced in the year 2012 by A. Krizhevsky et al. [20]. It has three fully connected layers and five convolutional layers. GoogLeNet is a pretrained neural network which is 22 layers deep and is trained on the ImageNet

Table 3 No. of convolutional layers and no. of learnable parameters in various pretrained CNNs

Name of deep neural network	No. of convolutional layers	No. of learnable parameters (M)
AlexNet	8	60
VGG16	16	138
VGG19	19	144
GoogLeNet	22	4
Resnet50	50	25.6
Resnet101	101	44.5
Resnet152	152	60.2

database to classify 1000 different object categories. It was first introduced in the year 2015 by C. Szeged et.al. [21]. The architecture contains 1×1 convolution in the middle to reduce computation, and instead of fully connected layers, global average pooling is used at the end of the network to improve the accuracy. The input layer of GoogLeNet accepts input images of size 224×224 .

The number of learnable parameters was reduced to 7 million but still the network achieved a top-5 error rate of 6.67%. GoogLeNet achieves better computational efficiency compared to AlexNet.

5.2 Ensemble Approach

The main drawback of CNNs is that the adjustment of weights varies with each training process, and it is not possible to obtain stable results using single CNNs. To overcome this variance in the output of CNN, a method called ensemble is used. Ensemble uses the aggregation of probabilities of individual CNNs to achieve highest possible accuracy. Some of the common aggregation techniques include: majority voting, sum of probabilities, product of probabilities, and sum of the maximum probabilities. We initially trained GoogLeNet and AlexNet networks, and then aggregate the resulting probabilities of the two networks using the sum of probabilities approach to obtain the ensembled result.

The combined probability using the sum of probabilities approach may be written as:

$$p'_i = \frac{\sum_{j=1}^m p_{ij}}{\sum_{i=1}^n \sum_{j=1}^m p_{ij}}, i = 1, \dots, n \tag{13}$$

Here, i denotes the response class and j denotes the individual deep neural networks. We use two deep neural networks in the ensemble, and hence the value of j can be 1 or 2. The total number of response classes is nine, and hence the value of i varies as 1, 2, 3, ..., 9.

Fig. 5 Ensembles of deep CNN using AlexNet and GoogLeNet

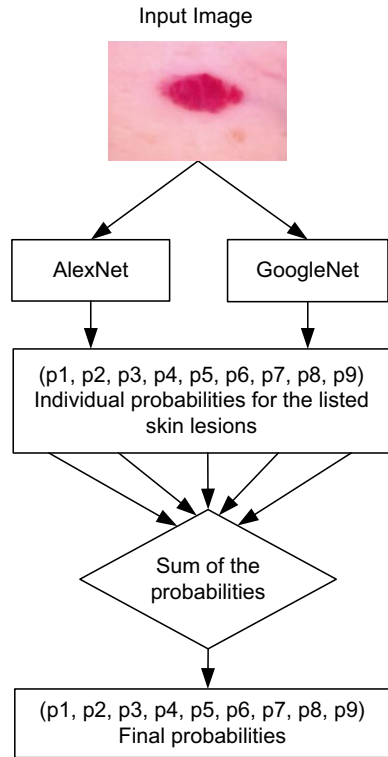


Figure 5 depicts the steps involved in classifying a skin lesion using ensemble approach.

5.3 Result

Training plot

The training plot displays training metrics at each iteration. In every iteration, the network parameters are updated. From the training plot, the smoothed training accuracy, training accuracy, training loss, and smoothed training loss can be found. Figures 6 and 7 depict the training progress of AlexNet and GoogLeNet, respectively.

Accuracy

The ensemble of AlexNet and GoogLeNet achieved better accuracy and error performance compared to the individual deep neural networks. Table 4 depicts the accuracy achieved by the various deep learning models.



Fig. 6 Training plot of AlexNet



Fig. 7 Training plot of GoogLeNet

Table 4 Accuracy of different deep neural networks

Network	Validation accuracy (%)
AlexNet	89.1
GoogLeNet	87.5
Ensemble	90.2

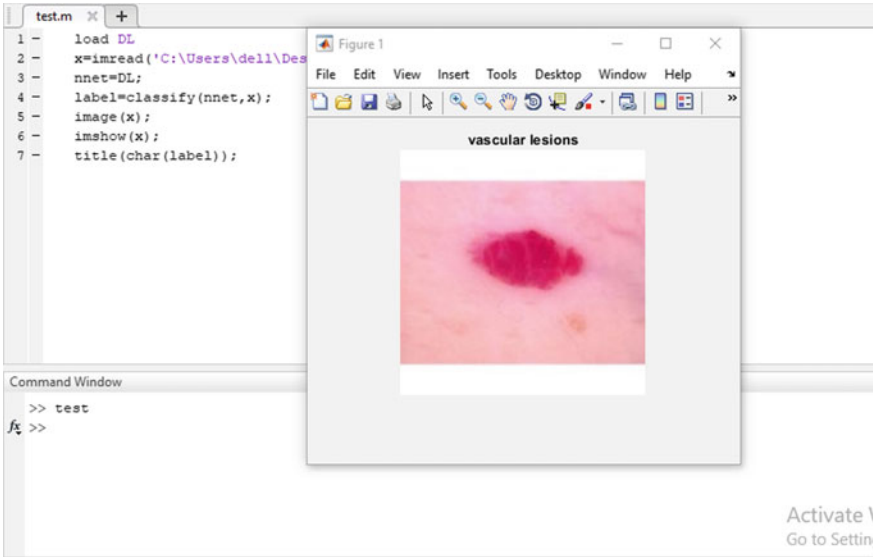


Fig. 8 Output from testing the trained network

5.4 Testing the Trained Network

The saved network is loaded into the workspace. A sample image is given as input for testing the network. An image of a vascular lesion is given as a sample image, and the network was able to classify it accurately. Figure 8 shows the image classified using ensemble approach.

6 Conclusion

A successful comparison between machine learning and deep learning techniques in classifying nine different skin lesions has been made. The dataset collected from the ISIC archive, which is the largest skin lesion database, was used to train both the models. The deep learning model outperformed the machine learning classifier in terms of accuracy and the best DNN model achieved an accuracy of 90.2%.

Detection of malicious lesions at their early stage increases the survival rate of patients. The dermatologist, once he finds a lesion to be suspicious, sends the excised tissue to a pathologist, who then diagnoses the malignancy of the lesion. Remote areas, which do not have such facilities, fail to treat malignant skin lesions in their early stages. This leads to the inevitable death of patients. Using the deep learning model, doctors can assess and treat skin conditions of people living in remote areas with a simple photograph of the lesion. This can also reduce the burden on dermatologists and pathologists by eliminating the need to screen every skin lesion for a malignant one. This paper is limited to classifying only nine skin lesions due to the limited number of images available in the open-source databases. It could be further improved to classify several different skin lesions by collecting real-time image samples from patients who visit dermatologists.

References

1. Karimkhani C, Dellavalle RP, Coffeng LE et al (2017) Global skin disease morbidity and mortality: an update from the global burden of disease study 2013. *JAMA Dermatol* 153(5):406–412
2. Abbas Q, Emre Celebi M, Garcia IF, Ahmad W (2012) Melanoma recognition framework based on expert definition of ABCD for dermoscopic images. *Skin Res Technol* 19(1)
3. Lopez AR, Giró-i-Nieto X, Burdick J, Marques O (2017) Skin lesion classification from dermoscopic images using deep learning techniques. In: Conference on biomedical engineering
4. Mahbod A, Schaefer G, Wang C, Ecker R, Ellinger I (2019) Skin lesion classification using hybrid deep neural networks. In: IEEE international conference on acoustics, speech and signal processing, pp 1229–1233
5. Barata C, Ruela M, Francisco M, Mendonca T, Marques JS (2013) Two systems for the detection of melanomas in dermoscopy images using texture and color features. *IEEE Syst J* 8
6. Esteva A, Kuprel B, Novoa RA, Ko J, Swetter SM, Blau HM, Thrun S (2017) Dermatologist-level classification of skin cancer with deep neural networks. *Nature* 542:115–118
7. Bae Y, Kumarasamy K, Ali IM et al (2018) Differences between schizophrenic and normal subjects using network properties from fMRI. *J Digit Imaging* 31:252–261. <https://doi.org/10.1007/s10278-017-0020-4>
8. Kawahara J, BenTaieb A, Hamarneh G (2016) Deep features to classify skin lesions. In: IEEE 13th international symposium on biomedical imaging (ISBI), Prague, pp 1397–1400
9. Kharazmi P, Kalia S, Lui H, Wang ZJ, Lee TK (2017) A feature fusion system for basal cell carcinoma detection through data-driven feature learning and patient profile. *Skin Res Technol* 24(2)
10. Codella N, Cai J, Abedini M, Garnavi R, Halpern A, Smith JR (2015) Deep learning, sparse coding, and SVM for melanoma recognition in dermoscopy images. In: Proceedings of the 6th international workshop on machine learning in medical imaging, vol 9352, pp 118–126
11. Codella N, Nguyen Q, Pankanti S, Gutman D, Helba B, Halpern A, Smith JR (2016) Deep learning ensembles for melanoma recognition in dermoscopy images. *IBM J Res Develop* 61(4)
12. Barcelos CAZ, Pires VB (2009) An automatic based nonlinear diffusion equations scheme for skin lesion segmentation. *Appl Math Comput* 215(1):251–261
13. Otsu N (1979) A threshold selection method from gray-level histograms. *IEEE Trans Syst Man Cybern* 9:62–66
14. Celebi ME, Kingravi HA, Iyatomi H, Alp Aslandogan Y, Stoecker WV, Moss RH et al (2008) Border detection in dermoscopy images using statistical region merging. *Skin Res Technol* 14:347–353

15. Zhou H, Schaefer G, Sadka AH, Celebi ME (2009) Anisotropic mean shift based fuzzy C-means segmentation of dermoscopy images. *IEEE J Select Topics Signal Process* 3:26–34
16. Sumithra R, Suhil M, Guru DS (2015) Segmentation and classification of skin lesions for disease diagnosis. *Procedia Comput Sci* 45:76–85
17. Krizhevsky A, Sutskever I, Hinton GE (2012) Imagenet classification with deep convolutional neural networks. *Adv Neural Inform Process Syst* 1097–1105
18. Szegedy C, Liu W, Jia Y, Sermanet P, Reed S, Anguelov D, Erhan D, Vanhoucke V, Rabinovich A (2015) Going deeper with convolutions. In: 2015 IEEE conference on computer vision and pattern recognition (CVPR), Boston, MA, pp 1–9
19. Kunaraj K, Maria Wenisch S, Balaji S, Mahimai Don Bosco FP (2020) Impulse noise classification using machine learning classifier and robust statistical features. In: Smys S, Tavares J, Balas V, Iliyasu A (eds) *Computational vision and bio-inspired computing. ICCVBIC 2019. Advances in intelligent systems and computing*, vol 1108. Springer, Cham
20. <https://www.isic-archive.com/#!/onlyHeaderTop/gallery>
21. Vaithyanathan D, Seshasayanan R, Kunaraj K, Keerthiga J (2014) An evolved wavelet library based on genetic algorithm. *Sci World J*

Auto Streetlight Control with Detecting Vehicle Movement



Dinesh Kumar Saini, Sameer Meena, Kamlesh Choudhary, Sheetal Bedia, Anshul Agarwal, and Vinay Kumar Jadoun

1 Introduction

Nowadays, urban communities and industries are being developed very fast with the development of the road lighting frameworks. The important factor is the reduction of the cost and effective utilization's mechanization. To control road lighting systems, the implementation of various types of road light control systems is done. Town's open lighting systems are controlled, and energy utilizations are diminished by different types of effective systems. The design for detecting the vehicle movement on roads to turn on and turned off lights in the street is shown in this paper. IR sensors are used for the detection of vehicle movement. The IR sensor is the sensor which consists of two LEDs: one is the emitter LED and the other one is receiver LED. The emitter LED emits the radiation. Whenever an object comes near the IR sensor, the radiation of the sensor is blocked and reflected back. The reflected rays are received by the receiving LED. The street lights are set accordingly that whenever the transmission of radiation for a particular streetlight's IR sensor is obstructed, few lights ahead of this light should glow. And once the vehicle has left the vicinity, the light be off. It means that the streetlights will be switched on wherever the vehicle will go and will be switched off once there are no vehicles around.

D. Kumar Saini · S. Meena · K. Choudhary · S. Bedia · A. Agarwal (✉)
Department of Electrical and Electronics, National Institute of Technology Delhi, New Delhi, India

V. K. Jadoun
Department of Electrical & Electronics Engineering, Manipal Institute of Technology, Manipal Academy of Higher Education, Manipal, Karnataka, India

2 Review of Literature

A well-controlled plan can be devised for the smart streetlight automatic control project. It is proposed that all streetlights on a side of the road regularly glow for a few seconds, i.e., in the presence of a vehicle or a passenger and switches off when there are no vehicles near the streetlight. When a vehicle is passing by the road, a bunch of streetlights gets switched ON, and when the vehicle goes forward, the corresponding streetlights turn ON while the lights left behind will be turned OFF. The streetlighting systems are becoming major electrical energy consumers in today's world due to the fast development of cities [1]. This referenced paper proposes that the work be done by using an Arduino Uno microcontroller, infrared sensors and a light-dependent resistor. For the starters, it shows that the streetlights can be controlled according to the time of the day, i.e., whether it is a day or night and object's presence. The streetlights are proposed to turn automatically to dim state at nighttime and switch to high-intensity state on obstacle's identification or on dusk's arrival, while during daytime the streetlights shall be off, except for when it is a cloudy day and the visibility is very low. And then, in second section of the paper the system skips dimming of lights and goes straight to turning off on default and turning on at object's detection to further save energy [2]. In any city or town, streetlights put up significantly to the electricity utilization by public systems. This paper scrutinizes different switching schemes to optimally turn on and turn off streetlights on the road according to the extent of ambient darkness in a place, i.e., the lights be turned in night and turned off during the day except for when the day is too dark taking visibility level to very low. This paper proposes a simple, economic automatic turning on/off of street lights [3]. A cost-effective and completely renewable energy-based power generation is performed and utilized to charge electric vehicles (EVs) and streetlights. This paper aims in conservation of energy from speed breaker and solar energy, to later use this energy to store and utilize for automatic street lighting and charging of electric vehicles using wireless power transfer technique [4]. This paper [5] is aimed at design and execution of the advanced level development street lighting systems. Nowadays, we have become far too busy and cannot find time even to turn the lights whenever they are not in use. In the present scenario, it is such that the street lights will be turned on in the evening before the sun sets and they are turned off the next day morning after there is enough light on the roads mainly due to lethargic tendencies of people responsible for the job. This paper provides a solution to prevent electrical power wastage [5]. This paper was conference in Bangladesh where people surviving in the land are facing genuine load shedding because of the generation shortage. The suffering of citizens, however, could be lessened by a well-planned load management system. In this paper, the authors have depicted and built a circuitry which can control the allowance of power supply of a particular region on the basis of daylight intensity in the area. As the intensity of light changes with seasons or any other features, it can be managed. Again, when there is any fault (like short circuit) or if any bulb/tube does not work, it could find out the position of the fault and could provide alarm signal to the operator. The circuit is simple in design, easy to execute and is cheap

[6]. In Internet of things (IoT), the objects communicate and exchange information which provides the used advanced intelligent services. The aim of a smart city is to make a better use of the public administration resources and physical resources. This goal is supposed to be accomplished by the deployment of an urban IoT. Street light system plays a very important role in development of cities as we all know how convenient the presence of streetlights can be. So, in this paper, the focus is on the street light system for the development of the smart city with the help of Internet of things. In the year 2020, the number of Internet connected devices will be increased to 50 billion, it is estimated. In India, central government plans to setup 100 smart cities throughout the nation and for this plan to get executed there needs to be an advanced and developed street lighting system [7]. In this paper [8], the authors propose energy-efficient and economic automatic street lighting system based on low-cost microcontrollers and other sensors. While the control and management of the system are on the basis of amount of traffic and five different stage of street light brightness has been used for lighting up the street and directly proportional to the number of traffic as per the luminous intensity. The system in the proposed paper was programmed to automatically turn the streetlights off in the daytime and only operate during the nighttime and rainstorm or bad weather such as cloudy day. As a result, it is estimated, around $\frac{3}{4}$ of trimming in total power consumption can be gained through this proposed automatic street lighting system for economic and optimal system [8]. In this paper [9], the authors proposed energy-efficient and economic automatic street lighting system based on Arduino Uno. The main intention is to construct economic smart streetlights to conserve energy wasted in streetlights. While the control and management of the model are based on the amount of traffic and the amount of luminosity. The system was devised to automatically switch off the streetlights during the hours of daylight and only operate during the nighttime or when there is little to no light during the day; i.e., the visibility is very low and rainstorm or bad weather [9]. Currently, large amount of electricity is being consumed by street lights, which remain turned ON whole night and sometimes even after the sun has risen due to the laziness of the labor responsible. Because of this large wastage of electricity occurs across the whole cities, it has to be reduced. The main objective of designing automatic street lighting is that lights will remain switched ON with maximum intensity only when there are passengers or vehicles walking by the road and shall remain switched off otherwise. The electricity produced using the pressure exerted by vehicles and footsteps and the jerked energy at road bumps can further be used to light up the streetlights [10–13].

3 Working Topology

The control of streets lights on vehicle detection is shown in Fig. 1. In the circuit diagram of the paper, the 4 ports (pin 2 to 5) in Arduino are connected to IR sensor circuit. The input signals will be sent to Arduino board. And we will connect all IR sensors to GND (ground) port of Arduino. LED's positive terminals are connected



Fig. 1 Flowchart of vehicle movement detection

to Arduino (pin 6 to 10.) And the grounds of the LED's to GND port of Arduino. Whenever a vehicle should cross it works in accordance with that.

In the initial phase, the IR sensors are to be remained in LOW state. Now, when a vehicle passes past an IR sensor, the IR sensor detects it and as per requirement 3 or 4 positive terminals of LEDs are made high through the Arduino output ports, and hence, they start glowing. As soon as the vehicle crosses one streetlight, the LEDs of that street light and behind it are turned off. And when the vehicle goes by the next IR sensor, the next LEDs will glow and the lights left behind are turned off. This process continues as long as there are vehicles on the road. Since the street lights (LEDs) are not turned on all the time, vast amount of electricity will be saved. The flowchart for detection of Vehicle is illustrated in Fig. 1.

3.1 Hardware Design

For the design of this model, 12 light emitting diodes (LEDs), 3 infrared (IR) sensors, and some set of variable resistors are used. All these components are assembled on the Arduino Board as shown in Fig. 2. The IR sensors are set on the opposite side of the street light. These IR sensors are used for obstruction identification and to send the logic signals to Arduino's pins for glowing the LEDs ahead of the vehicle.

3.2 Components

Arduino Uno

Arduino Uno was the first software of the Arduino series. The circuit diagram of Arduino Uno is shown in Fig. 3. It is a microcontroller based on the microchip Atmega328p. It is developed by Arduino, and it is open source. The microcontroller board of the Arduino is equipped with 14 digital pins (i/o pins) in which six are capable for the output of PWM. It can be powered by a USB cable or Arduino charging cable.

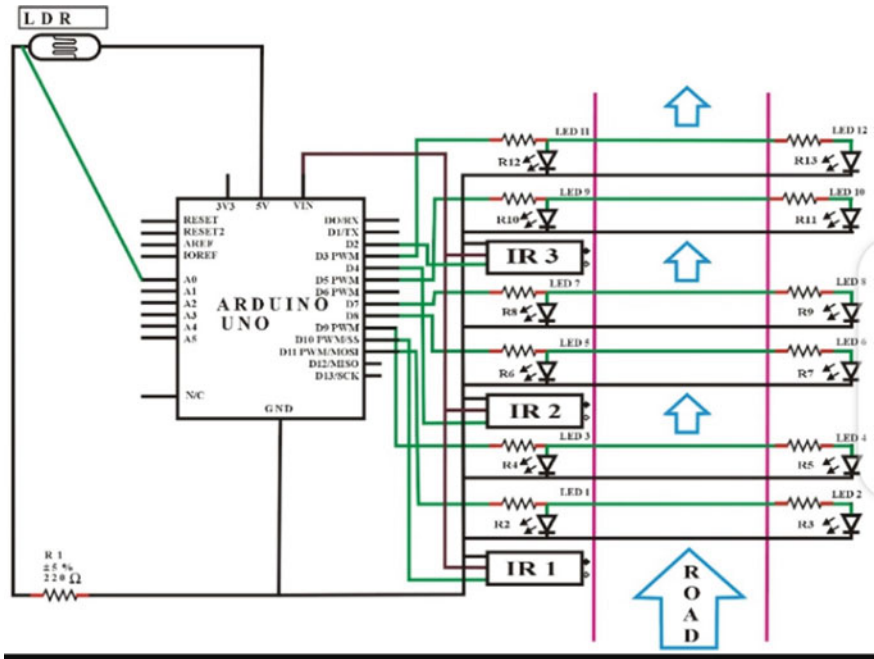


Fig. 2 Circuit diagram of automatic street light control with detecting vehicle movement

IR Sensor

An infrared sensor is an electronic device as shown in Fig. 4. It is used to detect objects. It is done by emitting infrared radiation. It can also be used to measure heat of an object and detect the motion of object also. IR sensors radiate only thermal radiation which cannot be seen by human eyes but an IR sensor can easily detect them. In IR sensor, LED is used as the emitter and infrared photodiode is used as detector which is sensitive to IR LED wavelength. If and when infrared light strikes on the photodiode detector, then resistance will change, and accordingly, the output voltage will change as well.

LDR

Light-dependent resistor is a photoresistor that works according to the light. The resistance of the photoresistor decreases when the incident light intensity is increased. LDR is shown in Fig. 5.

LED

These are the semiconductor devices that emit lights when current is passed through it. To represent the street lights in this paper, LEDs are used as shown in Fig. 6.

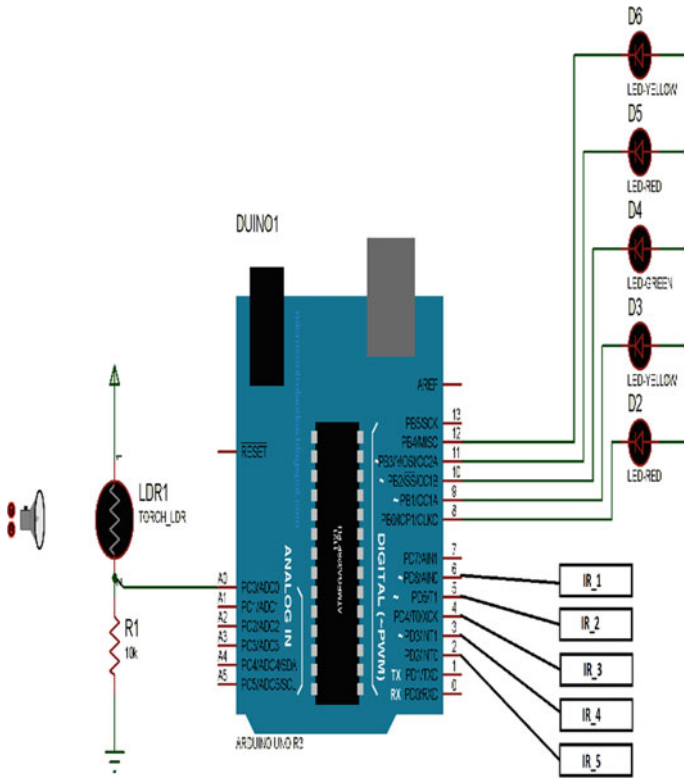


Fig. 3 Circuit diagram of Arduino Uno

Fig. 4 Working principal of IR sensor

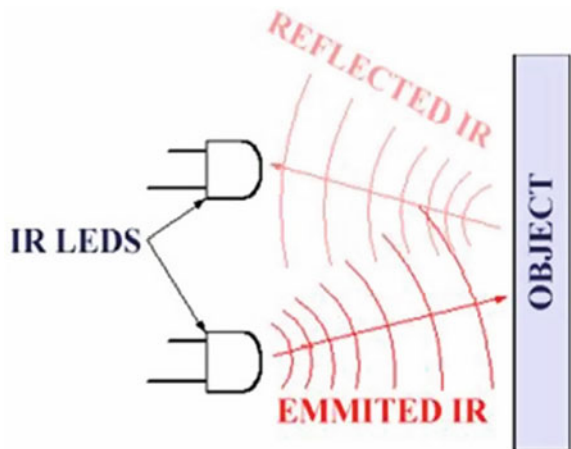


Fig. 5 Light-dependent resistor



Fig. 6 Light emitting diode

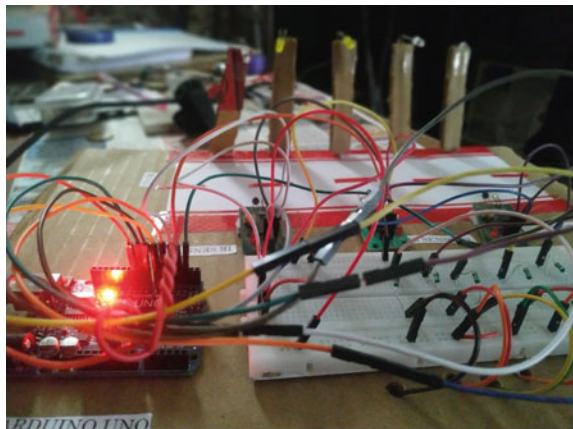


4 Results

The following images show how when a vehicle moves on the road the LEDs turn on and off:

1. When there are no vehicles in the vicinity, transmission between transmitter and receiver will be smooth and there shall be no obstruction in transmission. The Arduino will receive the code to be 1 for all the streetlights and hence none of the street lights will glow as shown in Fig. 7.

Fig. 7 When there are no vehicles on the road



2. When the vehicle comes into contact with first IR sensor, the transmission between the transmitter and the receiver is obstructed, and as a result, the Arduino will receive the code to be 0 for the first street light, and hence, the first 3 LEDs will glow as shown in Fig. 8.
3. When the vehicle has passed through first streetlight and is now in front of second streetlight, the transmission between transmitter and receiver of first streetlight has started again so the Arduino will receive its code to be 1, and hence, first streetlight will be switched off and the transmission between the transmitter and receiver of the second streetlight will be obstructed, and the Arduino will receive its code to be 1 and hence the second, third and fourth streetlights will glow as shown in Fig. 9.
4. Likewise when the vehicle has passed through second streetlight and has come into contact with third one, the Arduino will receive the code for second streetlight to be 1 and that for third streetlight to be 0, resulting in switching off of

Fig. 8 When a vehicle comes into contact with first streetlight

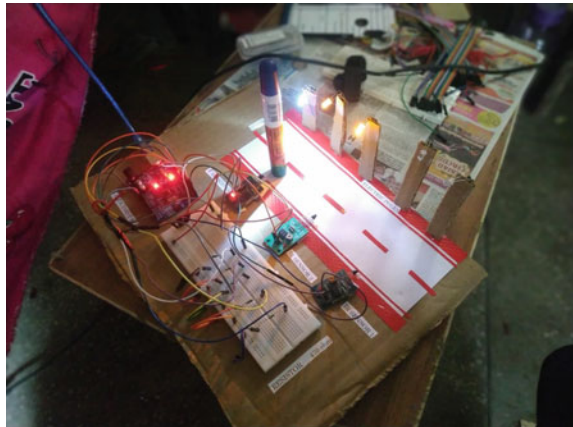


Fig. 9 When vehicle has passed through first streetlight

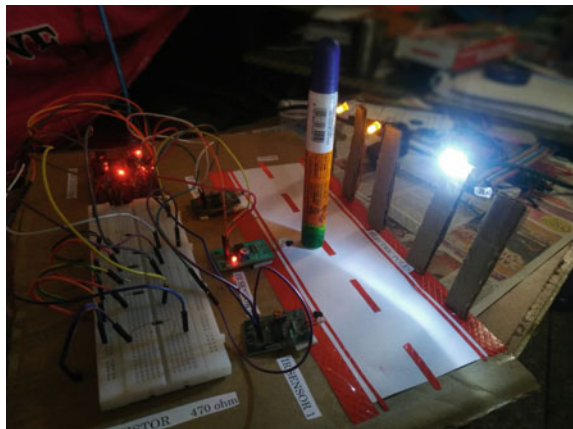


Fig. 10 When vehicle passes through second streetlight

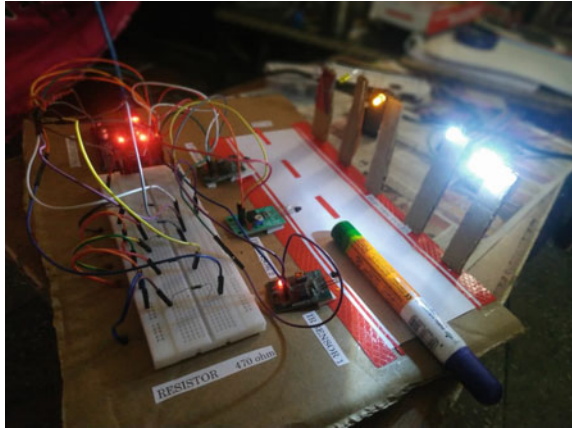


Fig. 11 When there are vehicles in front of all the streetlights at the same time



the second streetlight and switching on of the third, fourth, and fifth streetlight as observed in Fig. 10.

5. When there are vehicles in contact with all the streetlights at the same time, i.e., for all the IR sensors, transmission is obstructed and the Arduino will receive the code to be 0 for all the streetlights, and hence, all the streetlights will glow at the same time as shown in Fig. 11.

5 Conclusion

The designed model is an economic, pragmatic, environment-friendly, and the most secure way to save energy. According to mathematical data, 35–40% of electricity is used by the local street lights, state highways, and national highways. The primary

expenditure cost and fabrication will be the disadvantage, but with the huge production of the module, the total cost of expenditure can be minimized further due to increment in technology and innovation, the cost of this project can be minimized. It has been estimated that this project has the potential to save around 75–78% of electrical energy used by streetlights. The model presented in this paper has scope in various applications, for example, supplying lighting for grounds, buildings, office, parking garages, and walking paths of large shopping malls. This can also be used for security observation in school premises, businesses centers, corporate buildings, etc.

References

1. Kumar P, Raghu N, Nagendra K (2018) Automatic street light control by detecting vehicle movement. In: International conference on recent trends in electronics, information & communication technology, at Bangalore
2. Mumtaz Z, Ullah S, Ilyas Z, Aslam N, Iqbal S, Liu S, Meo JA, Madni HA (2018) An automation system for controlling streetlights and monitoring objects using Arduino. *Sensors* 18(10):3178
3. Karthikeyan M, Saravanan V, Vijayakumar S (2014) Cloud based automatic street light monitoring system. In: 2014 international conference on green computing communication and electrical engineering (ICGCCEE), pp 1–6. IEEE
4. Srinivas M, Naga Siva Ram T, Kanthi Aishwarya P, Priyanka KL (2018) Analysis on IoT based dynamic street light control system. *Int J Eng Technol* 7(2, 7): 622–625
5. Naga Sai NC (2018) Automatic street light system using lora wireless communication. Ph.D. Diss Asian Institute of Technology
6. Wazed MA, Nafis N, Islam MT, Sayem ASM (2010) Design and fabrication of automatic street light control system. *Eng e-Trans* 5(1):27–34
7. Watson IA Oshomah Abdulai Braimah AO (2015) Design and implementation of an automatic street light control system. *Int J Emerging Technol Adv Eng* 5(3)
8. Husin R, Al Junid SAM, Majid ZA, Othman Z, Shariff KKM, Hashim H, Saari MF (2012) Automatic street lighting system for energy efficiency based on low cost microcontroller. *Int J Simul Syst Sci Technol* 13(1):29–34
9. Mangal D, Singhal S, Kumar K, Tiwari S, Singh T (2020) Smart E-Diya: a way to reduce air pollution. In: 2020 international conference on power electronics & IoT applications in renewable energy and its control (PARC). IEEE, pp 263–266
10. Hajra A, Naseer K, Asif M, Alam MF (2019) Smart street light system powered by footsteps. In: 2019 international conference on green and human information technology (ICGHIT). IEEE, pp 122–124
11. Yue W, Shi C, Zhang X, Yang W (2010) Design of new intelligent street light control system. In: IEEE ICCA 2010. IEEE, pp 1423–1427
12. Yashaswini N, Raghu N, Yashaswini S, Prathib Kumar G (2018) Automatic street light control by detecting vehicle movement. In: 2018 3rd IEEE international conference on recent trends in electronics, information & communication technology (RTEICT). IEEE, pp 847–850
13. Zhou J, Gao D, Zhang D (2007) Moving vehicle detection for automatic traffic monitoring. *IEEE Trans Veh Technol* 56(1):51–59

Optimal Automatic Generation Control in Multi-Area Power Systems with Diverse Energy Sources



Ashwini Kumar and Omveer Singh

1 Introduction

1.1 General Study and Motivation

For modern power systems, frequency must be constant. The frequency variation is not acceptable in current power system for world wide. The quality power supply can be achieved for power systems with the help of AGC for more area interconnected with diverse energy sources. As robust power demand is a need of mankind globally, when load penetrates from its defined value with perturbation, the state of the grid system condition may appear abnormal from normal state. AGC must identify the deviation in frequency and maintained it to constant system frequency.

As the operation of interconnected power systems should be balanced between generated powers with total load demand plus system losses. If operating point differ the system frequency can deviates, cumulative cause shows unbalanced power in the exchange of areas, result may undesirable effect [1–3].

1.2 Literature Review

ACE used as a single variable is a combination of two variables one is frequency, another is tie-line power exchange. Many good ideas reflected by researchers for AGC problem, through the design of AGC regulators for uncertainty or variation, load characteristics, excitation control and other link like Alternating Current (AC)/Direct Current (DC) [4–8]. In research article, Singh et al. [8, 9] showed as the load demand for different loading scenarios, the generators are interconnected by power line which

A. Kumar (✉) · O. Singh

Department of Electrical Engineering, School of Engineering, Gautam Buddha University, Uttar Pradesh, Greater Noida 201308, India

increases the complexity of power system. Authors have been categorized the huge power systems with the principle of coherency for different control areas.

In the last decade, the modern concept for AGC like Genetic Algorithm (GA), Artificial Neural Network (ANN), and Fuzzy Logic Algorithm (FLA) are used to make our AGC simple and robust, as thermal power plant associating with solar energy in Photovoltaic (PV) modules, wind turbine, Electric Vehicle (EV), micro-grid, smart grid, and Super Conducting Magnetic Energy Storage (SMES). This research paper [10] gives a brief exploration of recent research articles written by various authors/researchers/technocrats used different techniques of Artificial Intelligence (AI) and Soft Computing (SC) techniques. The modern AI and SC techniques used for AGC in which different algorithms are like Differential Evolution Particle Swarm Optimization (DEPSO) [11], Firefly Algorithm (FA) [12–14], Grey Wolf Optimizer (GOW) Algorithm [15–21], Ant Colony Optimization (ACO) [22]. These algorithms are justified by its authors with certain parameters, acceptability and also with their limitations.

1.3 Contribution to the Present Research Work

- Design and development of mathematical model of diverse energy sources used in multi-area power systems.
- Modify the proposed model with/without parallel EHVAC/DC links.

2 Power System Model (Two Areas)

Mohanty et al. [23] concreted two unequal areas with multiple hybrid-sources interconnected power system. In Fig. 1 shows the model of non-reheat thermal system and PID controller used in power system.

For generator the output frequency Δf and area control error is given by Eq. (1). In this B denotes the parameter of frequency bias.

$$ACE = \Delta P_{Tie} + B \Delta f \quad (1)$$

The transfer function shows the analysis in frequency-domain as it represents each component of the area. The transfer function of turbine is shown in Eq. 2.

$$G_T(s) = \frac{\Delta P_T(s)}{\Delta P_V(s)} = \frac{1}{1 + sT_T} \quad (2)$$

With Elgerd [1], a governor is represented for its transfer function in Eq. (3).

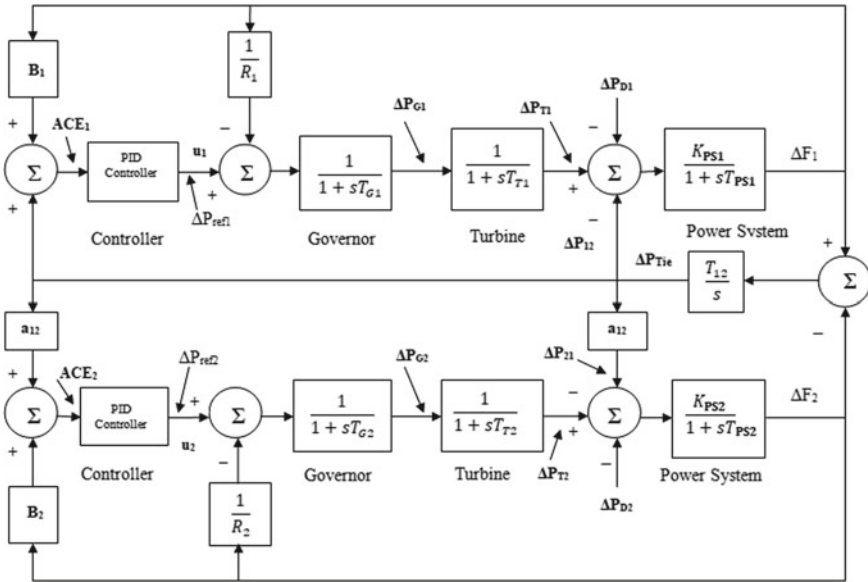


Fig. 1 Transfer function model for power system of 2area non-reheat thermal system ACE with PID controller

$$G_G(s) = \frac{\Delta P_V(s)}{\Delta P_G(s)} = \frac{1}{1 + sT_G} \tag{3}$$

Two inputs used for speed governing system as ΔP_{ref} also Δf for 1 output ΔP_G(s) shown by [2] as following;

$$\Delta P_G(s) = \Delta P_{ref}(s) - \frac{1}{R} \Delta f(s) \tag{4}$$

The representation of generator and load shown by the transfer function as [2], as following;

$$G_p(s) = \frac{K_P}{1 + sT_P} \tag{5}$$

In this notation are $T_P = \frac{2H}{fD}$ and $K_P = \frac{1}{D}$.

The load system for generator show 2 inputs ΔP_D(s) and ΔP_T(s) with 1 output Δf(s) shown by following [2]:

$$\Delta f(s) = [\Delta P_T(s) - \Delta P_D(s)] G_p(s) \tag{6}$$

3 Design Controller Structure of AGC

PI controller is used for development of advanced control. Controller has simple design and reliable operation utilized, also not need of higher skills than others. Proportional and integral are two mode of PI controller, it increases the gain of closed loop also improves the transient phenomenon but steady state error remained. The steady state error reduces to with an integral control. For integral controller the response for a transient period is slow. The dynamic and static accuracy not eliminate by proportional—plus—integral control. For

$$\left| \frac{d(\text{ACE})}{dt} \right| > \Delta$$

$$\Delta P_C = K_P \text{ACE}(t);$$

While ACE stands for area control error.

$$\left| \frac{d(\text{ACE})}{dt} \right| \leq \Delta;$$

$$\Delta P_C = K_I \int \text{ACE}(t)$$

The design a controller is based on constraints and specification. The controller is integral of absolute error (IAE), integral square error (ISE), integral time absolute error (ITAE), and integral time square error (ITSE). Authors [24] considered ITAE as an objective function and parameters of PI controller are optimized using GWO algorithm as given in equation.

$$J = \int (|\Delta f_1| + |\Delta f_2| + |\Delta P_{\text{Tie}}|)$$

The deviations for system frequency are Δf_1 and Δf_2 , also a ΔP_{Tie} is the incremental change for tie line power.

3.1 Dynamic Response Analysis

Rout et al. [25] worked for PI controller with DE algorithm used in AGC. A comparative performance assessment enhanced by Shiva et al. [26], examined for QOHS algorithm and internal model control made for AGC (Tables 1; Fig. 2).

Table 1 Gain of controller, value of objective function, and time of settling

Algorithms	Parameter	ITAE	Settling time (2% Band) Ts, s		
			Δf_1	Δf_2	ΔP_{Tie}
Conventional PI [34]	$K_P = -0.7005$	3.7568	45	45	28
	$K_I = 0.3802$				
GA tuned PI [34]	$K_P = -0.2346$	2.745	10.59	11.39	9.37
	$K_I = 0.2662$				
BFOA tuned PI [34]	$K_P = -0.4207$	1.7975	5.52	7.09	6.35
	$K_I = 0.2795$				
DE tuned PI [35]	$K_P = -0.2146$	0.9991	8.96	8.16	5.75
	$K_I = 0.4335$				
MFO tuned PI [25]	$K_P = -0.3735$	0.9704	6.10	6.5	5.76
	$K_I = 0.3645$				

3.2 System Data

See Tables 2 and 3; Fig. 3.

4 Brief Optimization Techniques Used in AGC

4.1 Particle Swarm Optimization Algorithm

Singh et al. [8, 9] showed as the load demand for different loading scenarios; the generators are interconnected by power line which increases the complexity of power system. Authors have been categorized the huge power systems with the principle of coherency for different control areas. Sahu et al. [11] worked for AGC of interconnected power system, like hDEPSO, FLA based PID controller. Investigations have been shown effectiveness of hybrid DEPSO technique over PSO and DE. Pathak et al. [27] worked for dynamic performance with two area AGC of thermal-thermal system also worked for generation schedule trajectories versus time constant of steam chest time constant and re-heater time constant find for various control strategies of power output.

Arya et al. [28] developed AC/DC parallel links interconnected via with two equal control areas with thermal and hydro generating power sources. Authors made the CRAZYPSO and hBFOA-PSO algorithms for optimal PI regulators in AGC with thermal power system of 2-area non-reheat and GDB nonlinearity. In this article, RES uncertainties with penetration for AGC in power system. Authors [14, 15] implemented hybrid DEPSO optimized fuzzy PID controllers, and 2-area power systems with different energy sources like hydro, thermal and gas sources and genetic

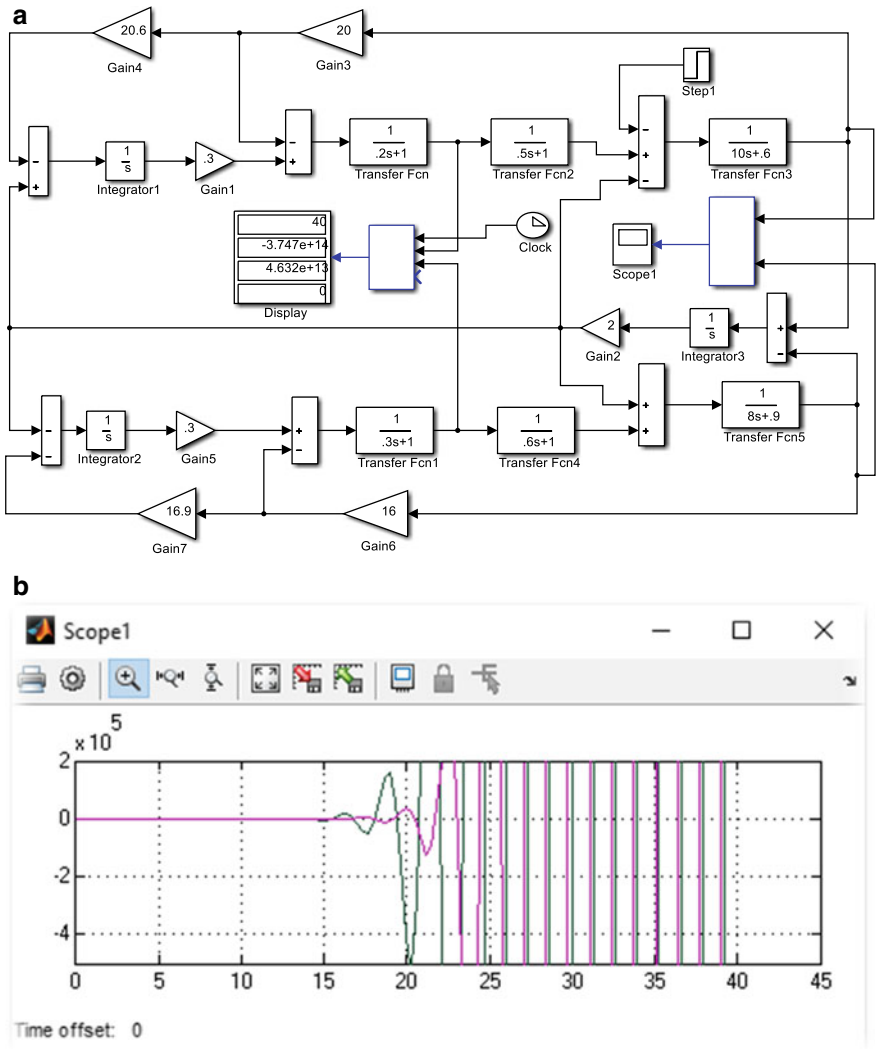


Fig. 2 a Simulation of two-area system, b step response of simulation for two-area system

algorithm has utilized for gain of optimal PID also for various test had been done with cases using ISE plus ITAE performance.

Table 2 The values of the power system constants with steam turbine and hydro turbine

Steam turbine	Hydro turbine	Power system
Time constant of speed governor $T_g = 0.08$ s	Rest time of speed governor TRH = 5.0 s	Rated area capacity $Pr1 = Pr2 = 2000$ MW Inertia constant $H = 5$ MW-s/MVA
Time Constant of Turbine $T_t = 0.3$ s	Time constant of transient droop TGH = 0.2 s	Rated frequency $fr = 60$ Hz Load frequency characteristic, $D = (dPL/df)*(1/Pr)$ pu MW/Hz
Time Constant of re-heater $Tr = 10$ s	Main servo time constant $T_w = 1.0$ s	Gain Constant for Power System $Kps = (1/D)$ Hz/pu MW
Coefficient of re-heat steam turbine $Kr = 0.3$	Speed governor regulation parameter $R_{hy} = 2.4$ Hz/pu MW	Power System Time Constant $Tps = (2H/fr*D)$ s Frequency bias constant $B1 = B2 = 0.425$ puMW/Hz
Regulation parameter for Speed governor $R_{th} = 2.4$ Hz/pu MW		Tie-line: $P12_{max} = 100$ MW $(d1-d2) = 30^\circ$

Table 3 The power system constants of values for different nominal loads and corresponding scheduled power generation

Load (MW) in each area	Area-1 Generation		Ptie,12 (MW) Thermal (MW)	Area-2 Generation		Power system constants	
	Thermal (MW)	Hydro (MW)		Thermal (MW)	Hydro (MW)	Kps (Hz/pu/MW)	Tps (sec)
1600	1000	600	100	1000	600	68	11
1500	900	600	100	1000	500	75	13

4.2 Firefly Algorithm

Pradhan et al. [12] used FA for optimization of PID in AGC where comparison shows the better one over GSA and GA, Authors also mention the impact of unified power flow controller and super conducting magnetic energy storage system. Padhana et al. [13] proposed a FA for LFC of multi-area power systems and compare it with other intelligent technique like BFOA, DE, and hBFOA-PSO optimized PI controller’s performance developed FA-optimized PID controller.

Jagatheesan et al. [14] developed FA for optimizing the PID controller in more than one area power system for reheat thermal and compared with genetic algorithm and particle swarm optimize based PID controller.

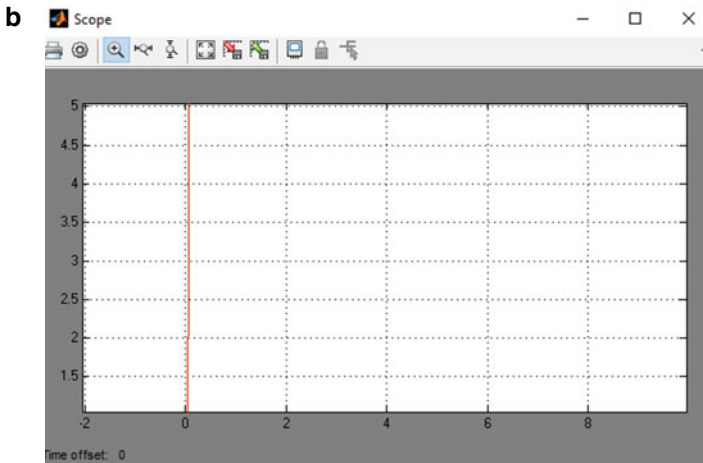
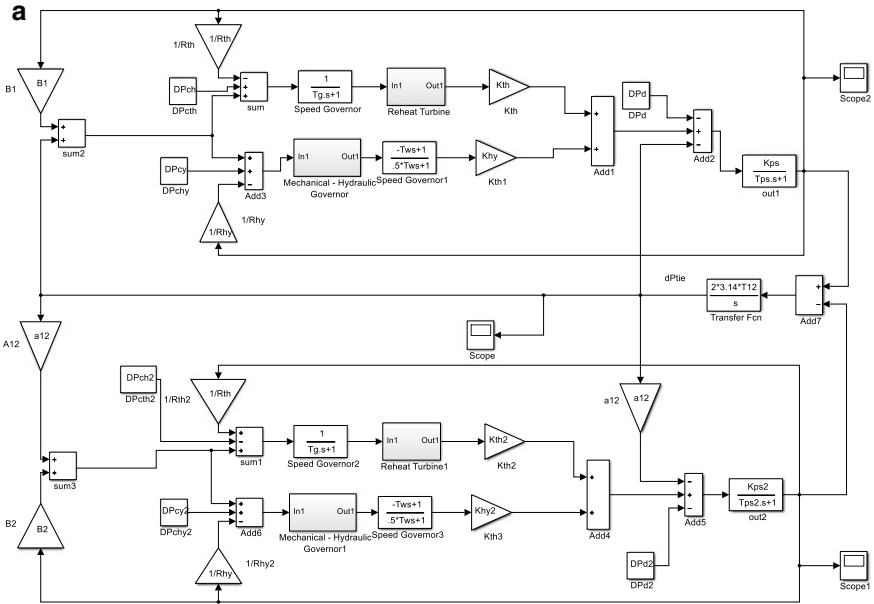


Fig. 3 a Simulation of two-area with diverse energy source, b Simulation result of power system for two-areas with ACE

4.3 Grey Wolf Optimization Algorithms

Y. Sharma et al. [15] made PID controller with GWO optimization also used data like peak overshoot, settling time, and magnitude of oscillations in the system, with or without solar thermal power plant (STPP). Guha et al. validated the QOGWO

Table 4 Diverse Energy Sources in Multi-Area Power Systems with

Area-1	Solar; Thermal
Area-2	Wind; Diesel
Area-3	Hydro; Nuclear
Area-4	Electric Vehicle; SMES; HVDC link

method [16] compared with its simulation with GWO and other AI techniques. Srinivasarathnam et al. [17] analyzed Grey Wolf Optimization (GWO) algorithm for PID controller gains of optimal tuning in secondary frequency control as the multi micro grid system and autonomous micro grid system operates in isolation. Padhy et al. [18] developed Modified GWO based optimal cascade PI-PD controller in plug-in EVs for AGC of power systems also algorithm qualified its superiority. Singh et al. [19] used GWO technique to optimize gains of three unequal area of AGC with reheat thermal system also doubly fed induction generator wind turbine. GWO algorithm used by Lal et al. [20] for interconnected hydro-thermal power system with fuzzy based PID controllers in AGC. Soni et al. [21] represented system robustness of 2DOF-PID controller optimized by varying the parameters with standard test system, operating load, by size and location at unbalanced area (Table 4; Fig. 4).

Extension to Multi-Area Power Systems with Diverse Energy Sources

Arya et al. [28] worked for AC/DC parallel links with 2-equal control areas integrated by thermal and hydro generating power sources. Authors made the CRAZYPSO and hBFOA-PSO algorithms for optimal PI regulators in AGC with 2-area non-reheat

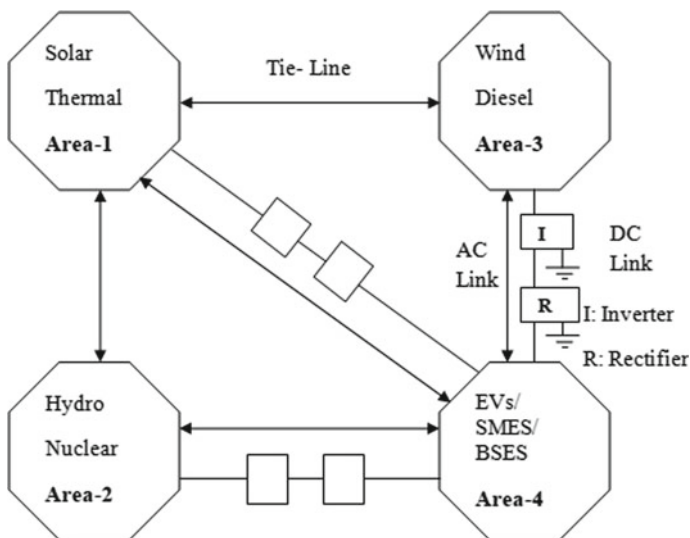


Fig. 4 Power system for 4-area diverse energy. Source with HVAC/DC link

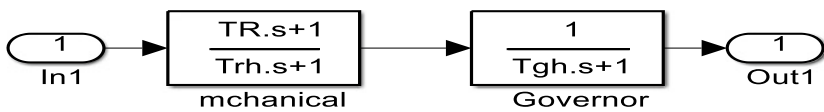
thermal system and the GDB nonlinearity. An equation based AGC regulators developed by Sharma et al. [29] for interconnected for 2-area power system with AC/DC tie-line. McNamara et al. [30] introduced for frequency regulation in AC/Multi-terminal Direct Current (MTDC)-connected grids, proposed article for MPC as a means of implementing AGC, while minimizing DC grid power losses. Almeida et al. [31] worked on EVs to stabilize with AGC. Gaur et al. [32] made a model consisting of a three area system embedded with EVs. The research article [33] Zhang et al. presented a LL algorithm based complementary generation control of integrated power grids for high penetration RESs and EVs. Oshnoei et al. [34] researched for EVs with AGC for perturbation of multi-area. Recently used of EVs with ABCO with tilt ID controller. Mathur et al. [35] explored on integration with wind power and V2G for stable frequency by perturbation. Authors worked for AGC in multi area power system [36–38], so that smooth and stable system developed.

5 Conclusions

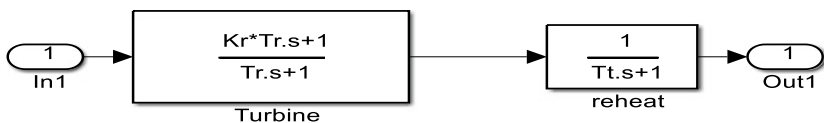
In this research paper investigation has done for PSO, FA, and GWO technique based AGC controllers with diverse energy sources in each areas. Power systems are as thermal, diesel, nuclear, and many more sources interconnected with hybrid resources like solar power, wind energy, hydro power, electric vehicles, micro-grid, and smart grid. The interconnection of different sources with two areas, also for multi area as well as tie-line control with several algorithms and soft computing techniques are shown in brief.

Appendix

Mechanical—Hydraulic Governor



Reheat Turbine



References

1. Elgered OI (2016) *Electric energy system theory-an introduction*, 2nd edn. McGraw Hill Education (India) Pvt Ltd, New Delhi, 46th reprint
2. Kundur P (2009) *Power system stability and control*. Tata McGraw-Hill
3. Ibraheem, Kumar P, Kothari DP (2005) Recent philosophies of automatic generation control strategies in power systems. *IEEE Trans Power Syst* 20(1):346–357
4. Elgerd OI, Fosha C (1970) Optimum megawatt frequency control of multi-area electric energy systems. *IEEE Trans Power App Syst* 89(4):556–563
5. Quazza G (1970) Automatic control in electric power systems. *Automatica* 6:123–150
6. Alhelou HH, Golshan M-HH, Zamani R, Forushani EH, Siano P (2018) Challenges and opportunities of load frequency control in conventional, modern and future smart power systems: a comprehensive review. *Energies*, 11(2497):1–35
7. Bevrani H (2014) *Robust power system frequency control*, 2nd edn. Springer
8. Singh O, Nasiruddin I (2012) Design of particle swarm optimization (PSO) based automatic generation control (AGC) regulator with different cost functions. *J Electri Electron Eng Res* 4(2):33–45
9. Singh O, Nasiruddin I (2016) Optimal AGC regulator for multi-area interconnected power systems with parallel AC/DC links. *Cogent Eng Syst Control* 3
10. Kumar A, Singh O (2019) Recent strategies for automatic generation control of multi-area interconnected power systems. In: *IEEE Xplore, 2019 3rd international conference on recent developments in control, automation & power engineering (RDCAPE)*. NOIDA, India, pp 153–158. <https://doi.org/10.1109/RDCAPE47089.2019.8979071>
11. Sahu BK, Pati S, Panda S (2014) Hybrid differential evolution particle swarm optimisation optimised fuzzy proportional–integral derivative controller for automatic generation control of interconnected power system. *IET Gener Transm Distrib* 8(11):1789–1800
12. Pradhan PC, Sahu RK, Panda S (2016) Firefly algorithm optimized fuzzy PID controller for AGC of multi-area multi-source power systems with UPFC and SMES, Elsevier. *I J Eng Sci Technol Int J* 19:338–354
13. Padhana SR, Sahu K, Panda S (2014) Application of firefly algorithm for load frequency control of multi-area interconnected power system. Elsevier, *Electri Power Energy Syst* 42(13):1419–1430
14. Jagatheesan K, Anand B, Samanta S, Dey N, Ashour AS et al (2017) Design of a proportional-integral-derivative controller for an automatic generation control of multi-area power thermal systems using firefly algorithm. *IEEE/CAA J Automat Sinica* 1–14
15. Sharma Y, Saikia LC (2015) Automatic generation control of a multi-area ST—thermal power system using grey wolf optimizer algorithm based classical controllers. *Int J Electri Power Energy Syst* 73:853–862
16. Guha D, Roy PK, Banerjee S (2016) Load frequency control of large scale power system using quasi-oppositional grey wolf optimization algorithm, Elsevier. *I J Eng Sci Technol Int J* 19:1693–1713
17. Srinivasarathnam C, Yammani C, Maheswarapu S (2019) Load frequency control of multi-microgrid system considering renewable energy sources using grey wolf optimization, Taylor & Francis. <https://doi.org/10.1080/23080477.2019.1630057>
18. Padhy S, Panda S, Mahapatra S (2017) A modified GWO technique based cascade PI-PD controller for AGC of power systems in presence of plug in electric vehicles. *Eng Sci Technol Int J* 20:427–442. <https://doi.org/10.1016/j.jestch.2017.03.004>
19. Singh A, Nautiyal B, Naresh R (2017) Grey wolf optimizer based PI-PD cascade controller for automatic generation control of integrated wind-thermal power system. *J Energy Res Environ Technol* 4(2):139–144
20. Lal DK, Barisal AK, Tripathy M (2016) Grey wolf optimizer algorithm based fuzzy PID controller for AGC of multi-area power system with TCPS, ICC-2016. *Procedia Comput Sci* 92:99–105

21. Soni V, Parmar G, Kumar M, Panda S (2016) Hybrid grey wolf optimization-pattern search (hGWO-PS) optimized 2dof-Pid controllers for load frequency control (LFC) in interconnected thermal power plants. *ICTACT J Soft Comput* 6(3):1244–1256
22. Kaliannan J, Baskaran A, Dey N, Ashour AS (2016) Ant colony optimization algorithm based PID controller for LFC of single area power system with non-linearity and boiler dynamics. *World Academic Press, World Academic Union* 12(1):3–14
23. Mohanty B, Acharyulu BVS, Hota PK (2017) Moth-flame optimization algorithm optimized dual-mode controller for multiarea hybrid sources AGC system. *Optim Control Appl Meth* 1–15
24. Ali ES, Abd-Elazim SM (2011) Bacteria foraging optimization algorithm based load frequency controller for interconnected power system. *Electric Energy Syst.* 33:633–638
25. Rout UK, Sahu RK, Panda S (2012) Design and analysis of differential evolution algorithm based automatic generation control for interconnected power system, Elsevier. *Ain Shams Eng J* 1–13
26. Shiva CK, Mukherjee V (2015) Comparative performance assessment of a novel quasi-oppositional harmony search algorithm and internal model control method for automatic generation control of power systems. *IET Generat Trans Distrib* 9(11)
27. Pathak N, Nasiruddin I (2018) AGC of two area power system based on different power output control strategies of thermal power generation. *IEEE Trans Power Syst* 33(2)
28. Arya Y, Kumar N (2016) AGC of a multi-area multi-source hydrothermal power system interconnected via AC/DC parallel links under deregulated environment. Elsevier, *Electri Power Energy Syst* 75:127–138
29. Sharma G, Nasiruddin I, Niazi KR, Bansal RC (2016) Robust automatic generation control regulators for a two-area power system interconnected via AC/DC tie-lines considering new structures of matrix Q. *IET Generat Trans Distrib* 10(14):3570–3579
30. McNamara P, Milano F (2018) Model predictive control-based AGC for multi-terminal HVDC-connected AC grids. *IEEE Trans Power Syst* 33(1):1036–1048
31. Rocha Almeida PM, Peças Lopes JA, Soares FJ, Vasconcelos MH (2010) Automatic generation control operation with electric vehicles. In: 2010 IREP symposium bulk power system dynamics and control-VIII(IREP), Rio de Janeiro, 1–7. <https://doi.org/10.1109/IREP.2010.5563295>
32. Gaur P, Soren N, Bhowmik D (2018) Secondary frequency regulation of multi-area interconnected hybrid power system with electric vehicle. *Int J Electri Eng Informat* 10(4):738–752. <https://doi.org/10.15676/ijeei.2018.10.4.8>
33. Zhang XS, Yu T (2018) Lifelong learning for complementary generation control of interconnected power grids with high-penetration renewables and EVs. *IEEE Trans Power Syst* 33(4):4097–4110
34. Oshnoei A, Khezri RS, Muyeen M, Oshnoei S, Blaabjerg F (2019) Automatic generation control incorporating electric vehicles. *Electric Power Comp Syst.* <https://doi.org/10.1080/15325008.2019.1579270>
35. Mathur HD, Bhatshvar YK (2016) Frequency regulation with vehicle-to-grid (V2G) option in multi-generation power network. *Energetika* 62:68–77
36. Ramakrishna KSS, Sharma P, Bhatti TS (2010) Automatic generation control of interconnected power system with diverse sources of power generation. *Int J Eng Sci Technol* 2(5):51–65
37. Yu-Qing BAO, Yang L, Wang B, Hu M, Chen P (2017) Demand response for frequency control of multi-area power system. *J Mod Power Syst Clean Energy* 5(1):20–29. <https://doi.org/10.1007/s40565-016-0260-1>
38. Rakhshani E, Remon D (2017) Virtual synchronous power strategy for multiple HVDC interconnections of multi-area AGC power systems. *IEEE Trans Power Syst* 32(3):1665–1677

BLDC Motor Torque Ripple Minimization Technique by Using Isolated Type DC–DC Buck–Boost Converter



Arpit Satta, Jay Prakash Keshri, Harpal Tiwari, and Vishal Jain

1 Introduction

At current scenario, brushless direct current (BLDC) motors are one of the fast gaining popularities among all types of motors. These motors come with cost-effective modules that use specialty software and proven hardware to take away the complexity and difficulty of motor control and design. These motors also called permanent magnet (PM) direct current Synchronous motors. Because of high power density (i.e., the amount of power per unit volume), lack of sparks, decline in electromagnetic interference, extended life span, extraordinary efficiency, lesser energy costs, and reliable operation, these motors are much useful for its switching system, and these motors do not require any mechanical brushes. These motors are used for the automation of industries such as automotive, aerospace, medical, electronics, industrial automation, military applications, toys, and household appliances. This motor is sort of a class of synchronous motor but likewise synchronous motor. Along with this in this motor, there is no slip in the middle of the stator and rotor.

Therefore, due to the many advantages of this BLDC motor, many researchers work in the area of the development of the controlling and designing aspect of this motor. Some of the researcher is using the DC–DC boost conversion circuit (i.e., super-lift Luo converter) to eliminate the switching torque ripple of a BLD motor with rectangular flux distribution approach [1, 2]. These motors switching torque

A. Satta · J. P. Keshri (✉) · H. Tiwari · V. Jain
Malaviya National Institute of Technology, Jaipur, India
e-mail: 2014ree9538@mnit.ac.in

A. Satta
e-mail: 2018ppd5062@mnit.ac.in

H. Tiwari
e-mail: hptiwari.ee@mnit.ac.in

V. Jain
e-mail: 2018ppd5052@mnit.ac.in

depend on the current of the transient line commutation. The reason behind it was noticed that the restriction of the DC link voltage, the commutation torque ripple cannot be suppressed over the maximum speed range [3]. A few research works using a strategy of DC link voltage control during commutation to keeping changing at the same rate with respect to each other of the incoming and outgoing phase currents [4]. In this approach in front of the inverter, there is a DC–DC single-ended primary inductor converter (SEPIC) and a switch selection circuit [4–6]. Some of the researchers proposed the torque ripple suppression circuit which utilized the combination of multilevel inverter with three-level diode clamping, an improved converter using single-ended primary inductor (SEPIC), along with the voltage selector circuit of DC bus is used. According to this approach, the regulation of DC bus voltage selector circuit is using the improved SEPIC for the duration of the switching interval for operative suppression of torque pulsation [6, 7]. Because in low- and high-speed applications, it is necessary to reduce in the ripple of the commutation torque substantially.

For the rectifying of above-mentioned problems, few of the researchers using a diode-based buck–boost inverter. According to this approach, the switching torque ripple is effectively suppressed by unified switching vectors over the full speed range during the switching period, without the need to switch control strategies to speed range [7]. Few researchers try to reduce the voltage stress of switching; due to the parallel connection of capacitor, it is not possible to increase the voltage instantaneously. But series discharge of two capacitors, therefore, requires high rating inverter switches [8]. However, few of the research work uses ideal trapezoidal back emf with many pulse width modulation patterns for commutation torque ripples [9, 10]. Along with this, some of the research work using Laplace transformation and PWM method. These proposed methods in which ripples in torque can be minimized. If the input voltage can be varied as per the requirement, then the DC link voltage could be varied accordingly [10–12]. This paper is mainly proposed a control technique to reduce the torque ripples by using a closed-loop DC–DC isolated buck–boost converter (flyback converter) before inverter and that also overcomes the problem mentioned above the paragraph.

2 Torque Ripples in BLDC Drive System

The drive system of BLDC includes permanent magnet synchronous motor, three-phase inverters to change DC input to AC, and a rotor position sensor. In BLDC motor, normally rotor location is found out by employing Hall effect sensor, an indicator that can sense or detect the position. Hall effect sensor sends high or low signal when magnetic pole of rotor passes near to it, so according to signal switching in inverter controlled. Figure 1 shows three-phase BLDC drive system. Each stator winding in star forms adjusted at 120° interval [12]. In every 60° , interval switching states change or Hall effect sensor sends a signal. Torque ripples in BLDC motors

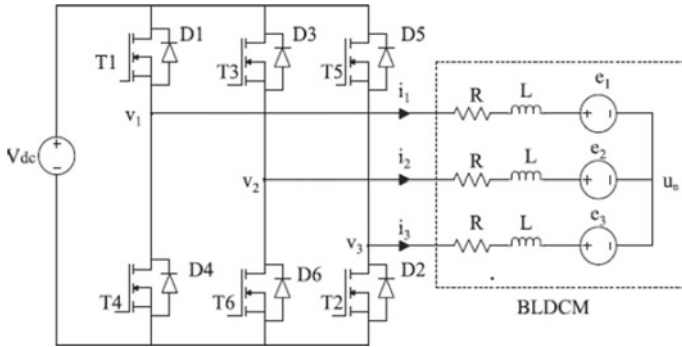


Fig. 1 Circuit model of BLDC motor

are affected by self-inductance of rotor, ideal, or non-ideal back emf form, and phase current of the rotor.

2.1 Mathematical Model of BLDC Motor

Figure 1 shows the circuit model of the BLDC motor. From this model, it contains resistance, inductance, and back emf per phase. Figure 1 shows the ideal current and back emf voltage waveform for the elimination of ripples from torque. The BLDC motor with the mathematical equation form can be written shown in Eq.(1) as:

$$\begin{bmatrix} V_1 \\ V_2 \\ V_3 \end{bmatrix} = \begin{bmatrix} R & 0 & 0 \\ 0 & R & 0 \\ 0 & 0 & R \end{bmatrix} \begin{bmatrix} i_1 \\ i_2 \\ i_3 \end{bmatrix} + \begin{bmatrix} L & 0 & 0 \\ 0 & L & 0 \\ 0 & 0 & L \end{bmatrix} \frac{d}{dt} \begin{bmatrix} i_1 \\ i_2 \\ i_3 \end{bmatrix} + \begin{bmatrix} e_1 \\ e_2 \\ e_3 \end{bmatrix} + \begin{bmatrix} u_1 \\ u_2 \\ u_3 \end{bmatrix} \quad (1)$$

Torque in any motor can be expressed as shown in Eq. (2) as,

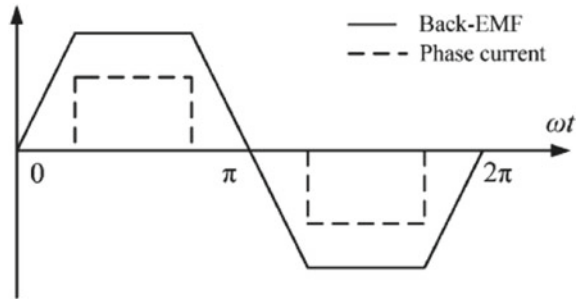
$$T_e = \frac{1}{W_m} e_1 + e_2 + e_3 \quad (2)$$

Phase current and back emf before commutation $i_a = i_c, e_a = e_b$, and $T_{e1} = \frac{2EI}{W_m}$. At the time of commutation, rotor phase current and back emf per phase $e_a = e_b = e_c$ and $i_a + i_b + i_c = 0$. Therefore, at the time of commutation torque generated is shown in Eq. (3) as,

$$T_e = \frac{2E}{W_m} \left(1 + \frac{u_c t}{3L} - \frac{4E}{3L} \right) \quad (3)$$

Ripples in torque at the commutation time are shown in Eq. (4) as

Fig. 2 Ideal waveform of back emf and current



$$\Delta T = \frac{2E}{W_m} u_{dc} - 4E \tag{4}$$

It has been identified that when the torque before and after the commutation remains constant, the power source voltage equals to four times back EMF amplitude. So, the suppression of ripples from the torque is possible only when input voltage applied across inverter is four times of back emf voltage, and for this, there is a need for different types of the DC–DC converter as shown in Fig. 2.

2.2 Simulation of BLDC Motor

From the current waveform and the mathematical torque expression, it is shown that there is the presence of torque ripples at the time of commutation and it can be minimized if we use a DC to DC converter that can change DC input according to the back emf value.

2.3 Flyback Converter

Flyback converters are the control converters that can change either DC or AC to DC. They can make multiple times DC output from AC or DC input. The main difference between buck-boost and flyback converter is that there is isolation between input and output of flyback converter. The advantage of this isolation transformer is that output voltage is a multiple of the input voltage. This flyback converter contains some small parts as output rectifier, output capacitor, couple inductor, input capacitor, and primary switch (MOSFET), etc. The flyback converter is made up of the following components which are mentioned above. Transformer or inductor coils used for isolation and as per the requirement of output voltage turn ratio of transformer coils are designed. If high output voltage requires, then a secondary number of turns is higher than the primary. If it works as a buck converter, then the primary

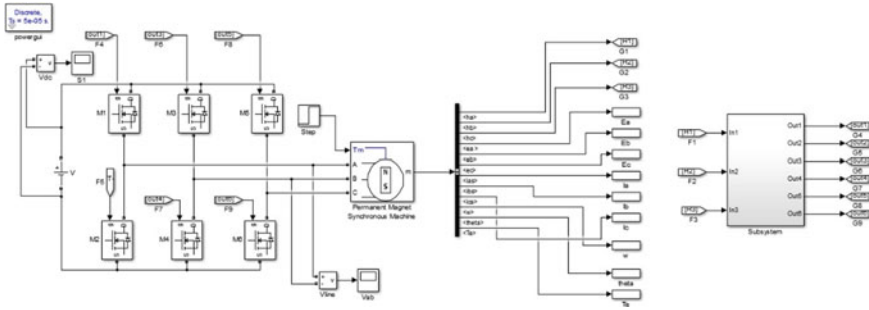


Fig. 3 BLDC motor MATLAB simulation diagram

number of turns is kept higher. Flyback converter for isolation uses a transformer, and transformer coils are made up of inductor coils.

2.4 Operation Principal of Flyback Converter

When the MOSFET switch goes to on position, power delivers by input side DC or AC source. Transformer primary coils store that energy. Energy store by primary coils equals primary source energy then MOSFET switched off. When MOSFET switched off, then primary coil energy transfers to secondary side coils so that diode which connects at load side becomes forward biased or starts conducting via diode energy transfers to load. When MOSFET switch on, then diode is in reverse biased or off condition as shown in Figs. 3, 4, 5, 6 and 7.

MOSFET turns on: The primary side of transformer energies is an input source. The diode connected at the load side is reverse biased so there is no ow of current and in primary-side current rises continue till primary side transformer energy equals source energy. The diode at the load side is a reverse bias by the sum of output voltage and voltage transfer from the input side.

MOSFET turns off: Primary coils transfer its energy to secondary coils, and due to its polarity, diode becomes forward bias and now its conduction. So that energy transfers from secondary to load via a diode. Due to demagnetization current at load side decreases and continues. The voltage across MOSFET switch when it is in off position equals to the sum of input voltage and transferred voltage from the secondary side as shown in Fig. 8.

3 Simulink Model of BLDC Drive with Flyback

Figure 9 shows the simulation model of the BLDC motor with a DC–DC closed-loop flyback converter with PI controller feedback which is used. The voltage applied

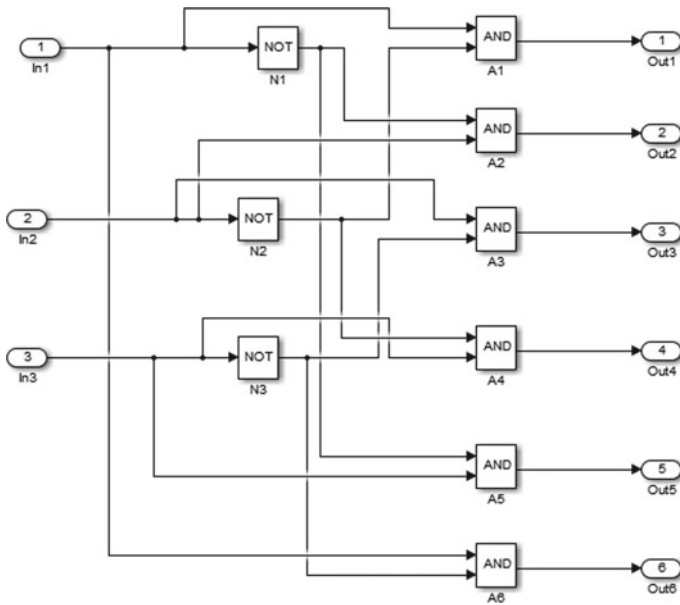
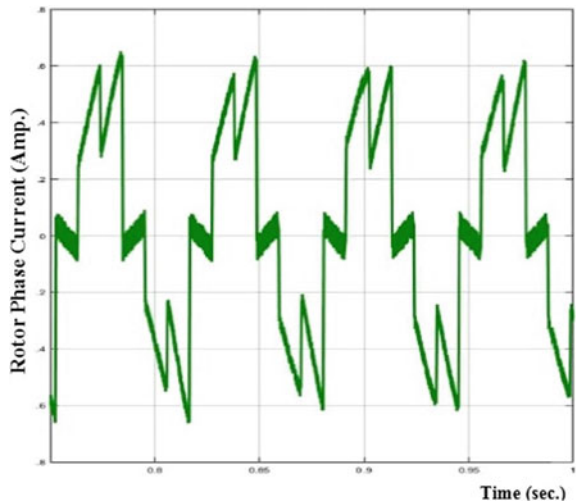


Fig. 4 Hall signals for switching

Fig. 5 Rotor phase current waveform



across the inverter is controlled by the PI controller. The PI controller reduces error that occurs in voltage across inverter [13] as shown in Table 1.

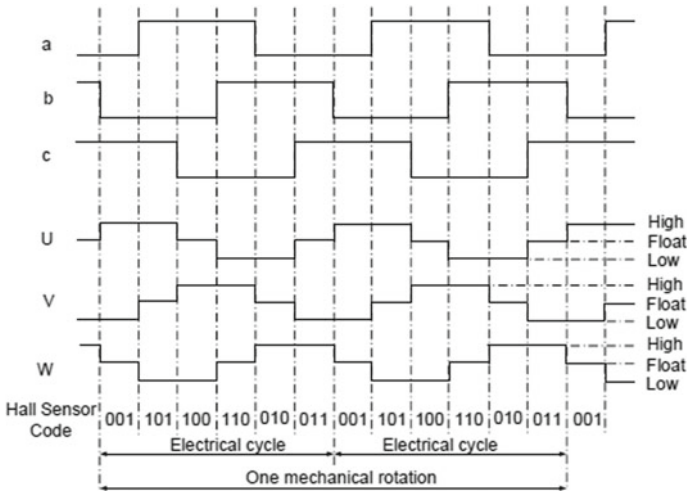
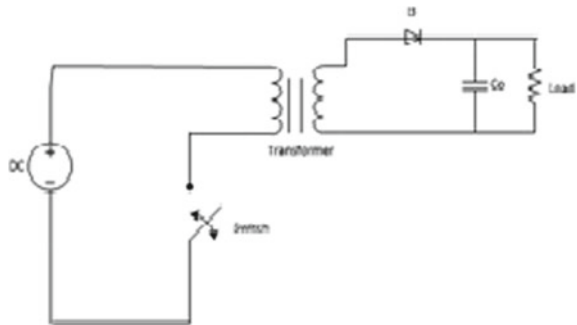


Fig. 6 Hall signal waveform over a cycle

Fig. 7 Flyback converter



4 Simulation Results

For design a simulation model for validating the proposed approach, MATLAB platform is used. At the time of fault, performance of the system model is described in graph as shown in Figs. 10, 11, 12, 13, and 14. Different types of fault or disturbance condition use for the validation of the proposed approach [14, 15]. Whereas, Fig. 10 represents the torque graph of the BLDC motor. In Fig. 11, time in seconds at x -axis and the y -axis represents as torque in joules. Figure 11 represents the rotor current waveform of the BLDC motor. In Fig. 11, time in seconds at x -axis and the y -axis represents as phase current in ampere. Figure 12 represents the back emf per phase of the BLDC motor. In Fig. 12, time in seconds at x -axis and the y -axis represents as beck emf in volts. Figure 13 represents the speed of rotor. Figure 13 time in seconds at x -axis and the y -axis represents as rotor speed in radian per seconds. Figure 14

Fig. 8 MOSFET on state

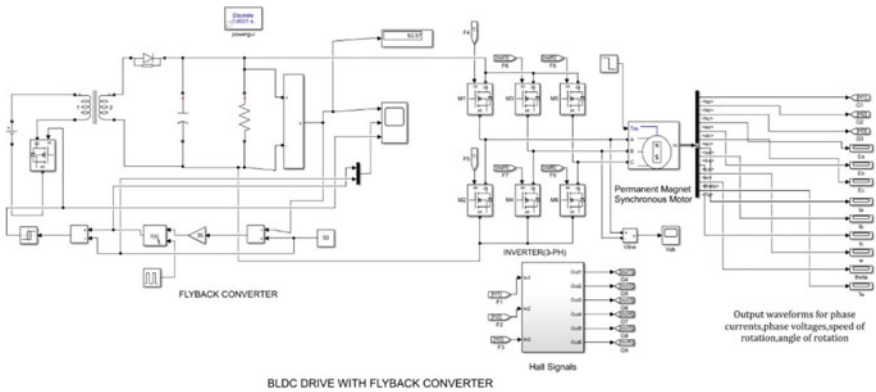
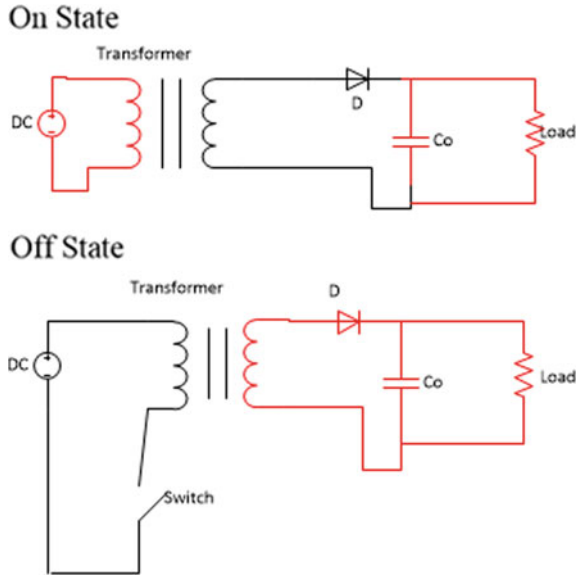


Fig. 9 Simulation diagram of BLDC motor with flyback converter

Table 1 MATLAB circuit parameters used for simulation

Circuit parameters	
V(input voltage)	25 V
Capacitor	68×10^{-6} F
RL	100 Ω
Turns ratio	1:04
Switching frequency	100 kHz
Integral gain(I)	2000
Proportional gain (P)	35

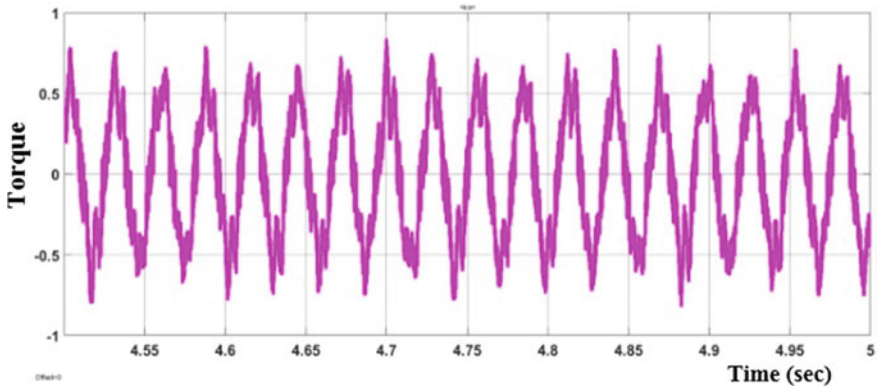


Fig. 10 Torque waveform

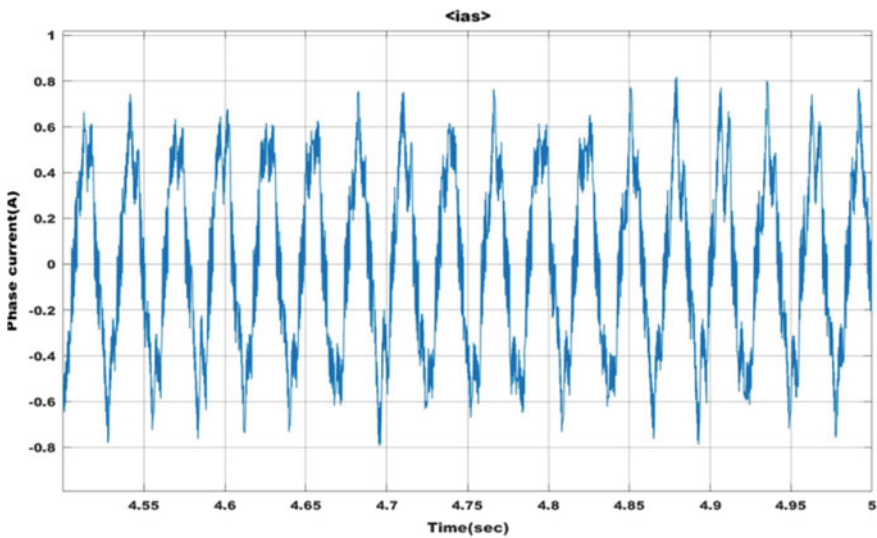


Fig. 11 Rotor phase current waveform

represents the line voltage of inverter. Figure 14 time in seconds at x -axis and the y -axis represents as inverter line voltage in volts.

These figures from Figs. 10, 11, 12, 13, and 14 show that at any fault or disturbance condition system performance not much affected. It can also observed that line voltage, current, torque, rotor speed, and back emf of the inverter with closed-loop flyback converter show enhanced results in terms of the nearly sinusoidal waveform with much small steady-state error. Some harmonics are presents in voltage and current waveform due to fault condition but within the permissible limits. Switching with MOSFET is also good selection for this model for better performance due to

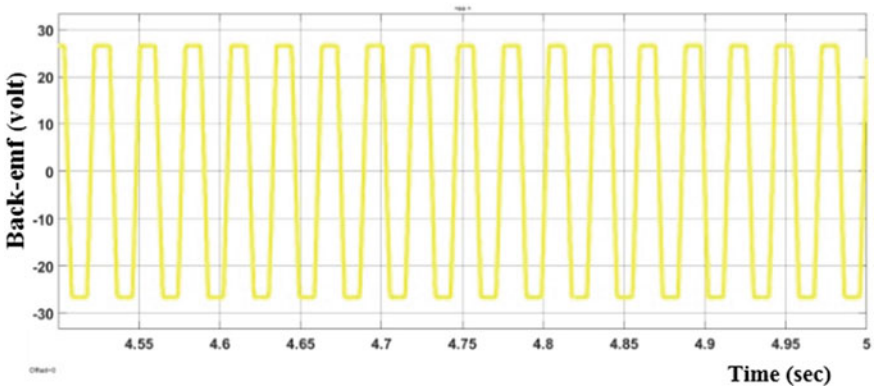


Fig. 12 Back emf waveform

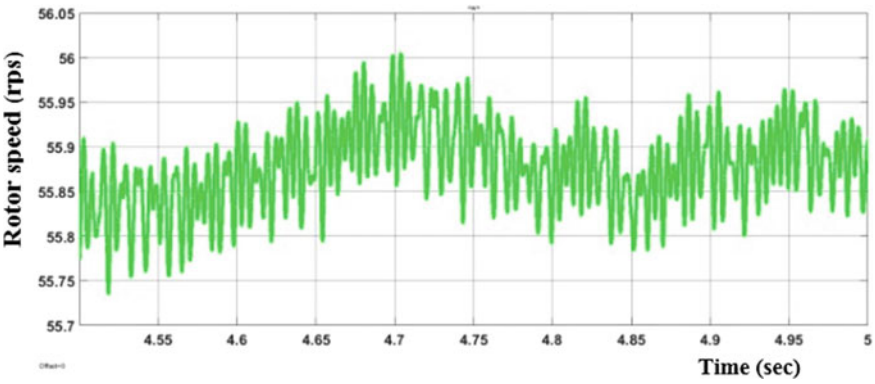


Fig. 13 Rotor speed (RPS)

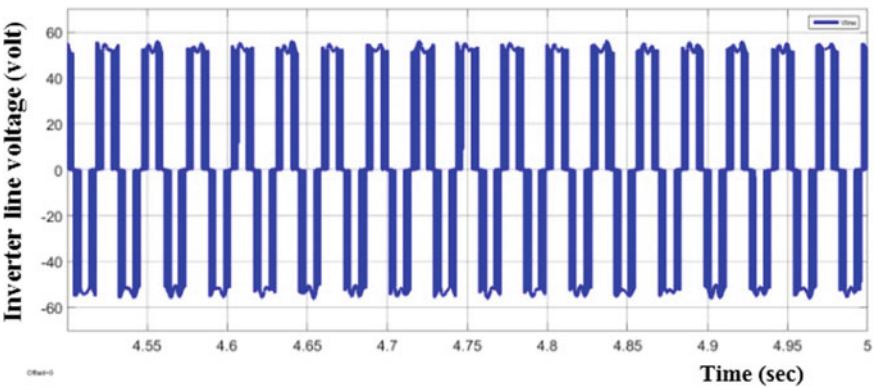


Fig. 14 Inverter line voltage (Volts)

its excellent performance at this disturbed condition. Therefore, it is concluded that proposed approaches works precisely as per our exception that describe with different waveform.

5 Conclusion

This paper proposed an approach that controls the system performance from disturbance or fault conditions and forms the above-described approached and their application at the time of fault that provided a reliable and accurate result within the permissible limits. It can also observed that line voltage, current, torque, rotor speed, and back emf of the inverter with closed-loop flyback converter show enhanced results in terms of the nearly sinusoidal waveform with much small steady-state error. While maintaining high efficiency and low noise emission compared to waveforms without closed-loop flyback converter, some harmonics are presented in voltage and current waveform due to fault condition but within the permissible limits. Therefore, it is concluded that the proposed approaches function precisely in accordance with our exception which describes different waveforms.

References

1. Lee Y A new method to minimize overall torque ripple in the presence of phase current shift error for three-phase BLDC Motor Drive. *Canadian J Electri Comput Eng* 42(4):225–231
2. Chen W, Xia C, Xue M (2008) A torque ripple suppression circuit for brush-less DC motors based on power DC/DC converters. In: 3rd IEEE conference on industrial electronics and application
3. Leitner S, Gruebler H, Muetze A (2019) Cogging torque minimization and performance of the sub-fractional HP BLDC Claw-pole motor . *IEEE Trans Ind Appl* 55(5):4653–4664. <https://doi.org/10.1109/TIA.2019.2923569>,Sept.-Oct
4. Lad CK, Chudamani R (2018) Simple overlap angle control strategy for commutation torque ripple minimisation in BLDC motor drive. *IET Electr Power Appl* 12(6):797–807. <https://doi.org/10.1049/iet-epa.2017.06447>
5. Shi t, Guo Y, Song P, Xia C (2010) A new approach of minimizing commutation torque ripple for brushless dc motor based on DC-DC Converter. *IEEE Trans Ind Electron* 57(10)
6. Viswanathan V, Seenithangom J (2018) Commutation torque ripple reduction in the BLDC motor using Modi_ed SEPIC and three- level NPC inverter. *IEEE Tran Power Electron* 33(1)
7. Cao Y, Shi T, Li X, Chen W, Xia C (2019) A commutation torque ripple suppression strategy for brushless DC motor based on diode- assisted buck-boost inverter. *IEEE Trans Power Electron* 34(6)
8. Fang J, Li H, Han B (2012) Torque ripple reduction in BLDC torque motor with non ideal back EMF. *IEEE Trans Power Electron* 27(11)
9. Ransara HKS, Madawala UK (2015) A torque ripple compensation technique for a low-cost brushless DC motor drive. *IEEE Trans Indust Electron.* 62(10)
10. Jiang G, Xia C, Chen W, Shi T, Li X, Cao Y (2018) Commutation torque ripple suppression strategy for brushless DC motors with a novel non inductive boost front end. *IEEE Trans Power Electron* 33(5)

11. Zhang XF, Lu ZY (2006) A new BLDC motor drives method based on BUCK converter for torque ripple reduction. In: Proceedings of IEEE power electronic motion control conference, pp 1–4
12. Chen W, Xia C, Xue M (2008) A torque ripple suppression circuit for brushless dc motors based on power dc/dc converters. In: Proceedings of IEEE Industrial electronics and applications conference, pp 1453–1457
13. Gupta V, Anjana P, Narayan P, Keshri JP, Tiwari HP (2013) A review on active power filter. In: Proceeding of international conference on advance trends in engineering & technology (ICATET-2013), pp 214–223, 2013
14. Keshri JP, Tiwari H (2017) Fault location in overhead transmission line without using line parameter. In: 4th international conference on engineering and technology (ICSET), pp 11–15
15. Keshri JP, Tiwari H (2017) Parameter-less fault locator using synchronized/un-synchronized data for overhead transmission line. In: international conference on computer, communications and electronics (comptelix), pp 260–264. <https://doi.org/10.1109/COMPTELIX.2017.8003975>

High Gain Converter with Switched Coupled Inductors for Renewable Energy Systems



Pankaj, Jay Prakash Keshri, Harpal Tiwari, and Arpit Sadda

1 Introduction

As population increases, energy demand also increases. To fulfil energy demand, utility uses conventional energy sources like coal, diesel, nuclear and hydroplants. The main concerning aspect is regarding fossil fuel depletion, and their over-exploitation leads to courses many environment problems [1]. To avoid the above problem, utility is moving towards renewable energy sources. Particularly wind and solar energies are more popular and demanding [2, 3]. Most widely used is solar energy, as they are pollution-free. Widely used solar energy can be divided into two types depending upon use (i) solar thermal technologies where solar energy is converted into heat form and (ii) direct conversion of solar energy into electricity [4]. Solar energy system is very popular in industrial applications like electric drives and electric vehicle. But the drawback of the existing system is less efficiency, and output voltage and current depend upon the radiation of sun and temperature of the surrounding. Therefore, a power converter is mandatory to increase the solar PV system output to a required voltage level for industrial application. DC-DC converters are playing very important role to increase the output measurement (V_{out} and I_{out}) and also for increasing the efficiency or performance of the system. In study review, numerous DC-DC converters are discussed

Pankaj · J. P. Keshri (✉) · H. Tiwari · A. Sadda
Malaviya National Institute of Technology, Jaipur, India
e-mail: 2014ree9538@mnit.ac.in

Pankaj
e-mail: 2018PPD5215@mnit.ac.in

H. Tiwari
e-mail: hptiwari.ee@mnit.ac.in

A. Sadda
e-mail: 2018ppd5062@mnit.ac.in

A standard step-up converter and step-up/down converter are having maximum gain of 10 and 9 at duty cycle 90%, respectively. Though using a high rating power device, the drawback of the standard step-up and step-up/down converter is a low gain [5, 6]. The SEPIC and CUK converter give a maximum gain at 90% duty cycle. Compare to standard Boost converter, the number of elements in SEPIC and CUK converter is higher, but advantage of these converters is less ripple in output [7–9].

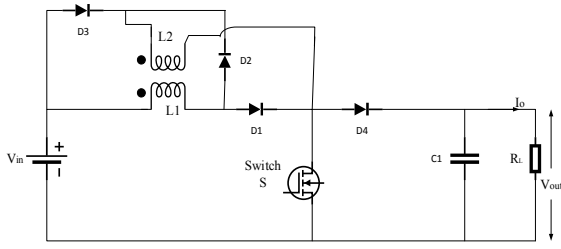
Therefore, a modification should be done in existing converters to boost the solar PV output voltage for industrial need. Recently, many DC–DC converters are developed for large gain on the basis of voltage multipliers, but the main drawback of these converters involves a large number of diodes and capacitors of same rating. The advantages of the multistage multiphase converter are the overall gain, and it is modified but large number of components is required. In switched inductor step-up converter and switched inductor step-up/down converter (SIBBC) are projected whose gain is higher than standard step-up converter [10–14]. Interleaved multilevel boost converter (IMBC) is projected by non-inverting output voltage whose gain is N times of standard step-up converter [15–19]. $2N_x$ and $4N_x$ IMBC with non-inverting output is projected to attain the higher gain. It provides higher gain as compared to N_x IMBC and recently projected DC–DC converter but it required large number of components. Inverting attains high negative gain, and this converter requires more diodes and capacitors at output side [20–26].

Switched coupled inductor boost converter is presented in this paper for using renewable energy systems. SCIBC is amalgamation of couple inductor stack and conventional boost converter for high voltage gain. In SCIBC, input side couple inductor is operated in such a way that they are charging in parallel and discharging in series. The advantage of SCIBC is that voltage gain is increased by $(1 + (2N - 1)D)$ times in N -stacks convention step-up converter. Section 2 describes the fundamentals of SCIBC, working modes, and mathematical analysis describes in detail in the next sections.

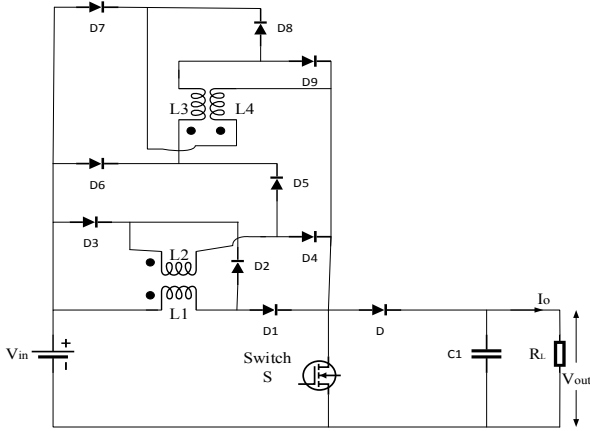
2 Switched Coupled Inductor Boost Converter (SCIBC)

The proposed converter is a combination of the convention boost converter and the stacks of couple inductors. The circuit of standard boost converter with single stack, two stacks and N -stack couple inductors are shown in Fig. 1. In convention boost converter, the input side inductor is replaced by switched coupled inductor stacks to design the SCIBC as shown in Fig. 1. The arrangement couple inductor in stack in such a way that all couple inductors are parallel coupled and charge in parallel from input supply when controlled switch is turn ON. And during OFF state all couple inductors are series couple and discharge through the load in series with supply.

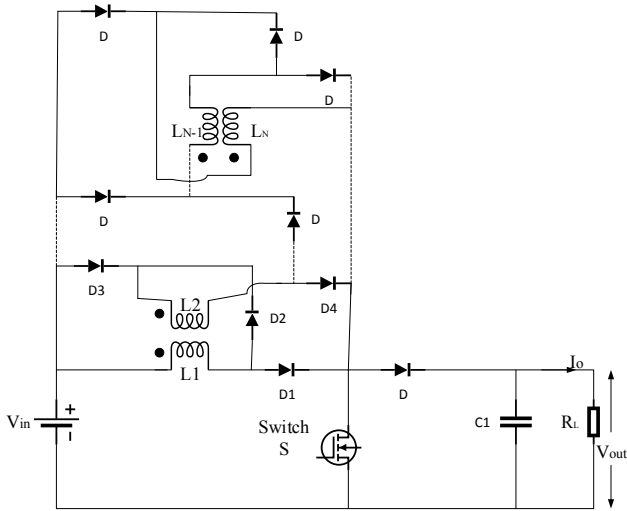
In the stack, the number of coupled inductors is one ($N = 1$) with the number of diodes is four, single-stack SCIBC, as shown in Fig. 1a and increased total gain by $(1 + D)$ conventional boost converter (CBC) times. If number of coupled inductor in the stack is two ($N = 2$), projected converter acts as high gain converter with number



(a) Single stack SCIBC



(b) Two Stack SCIBC



(c) N-stack SCIBC

Fig. 1 Circuit of proposed boost converter

Table 1

Stacks quantity	Couple inductors	Diodes	Capacitors	Switches	Input supply	Gain at 90% duty ratio
Stack-1	1	4	1	1	1	19
Stack-2	2	10	1	1	1	37
Stack-3	3	16	1	1	1	55
Stack-4	4	22	1	1	1	73
Stack-5	5	28	1	1	1	91
Stack-N	N	6N-2	1	1	1	$(1+(2N-1)D)/(1-D)$

of diodes is ten, as shown in Fig. 1b and overall gain is increased by $(1 + 2D)$ times of CBC. If number of couple inductors is increased to N and the diodes to $(6N-2)$, the overall gain is increased to $(1 + (2N-1)D)$ times of CBC. The components count and gain of SCIBC for different number of stacks are given in Table 1 and graphically represented in Fig. 2.

1. Modes of Operations of SCIBC: In this section, we study the working of switched coupled inductor boost converter in detail. To this end, we divide the entire operation into two different modes: one mode operated power switch (switch ON) is closed and coupling inductors store the energy or we may say that inductors are magnetized. In second mode, controlled power switch is open (Turn Off) and couple inductor demagnetize through load. Due to this, we get the high output voltage gain. Here we discussed the single stack SCIBC, and all other configuration is having same behaviour.

- Mode-1: During Switch ON ($0 \leq t \leq DT_s$) At $t = 0$, power controlled switch S is closed. Coupling inductors L_1 and L_2 are connected in parallel to supply voltage V_{in} with the help of diode d_1 and d_3 . In this activity mode, inductors L_1 and L_2 are coupled in parallel, as shown in Fig. 3(b). Parallel coupled

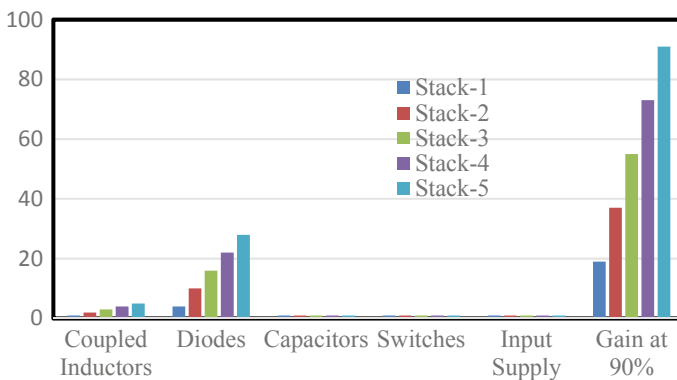
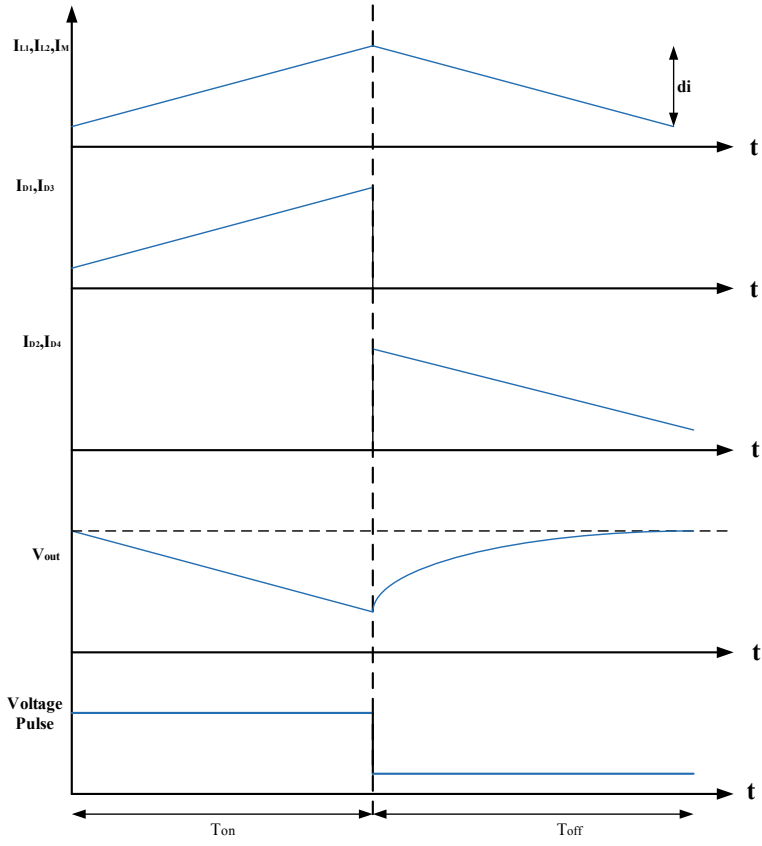
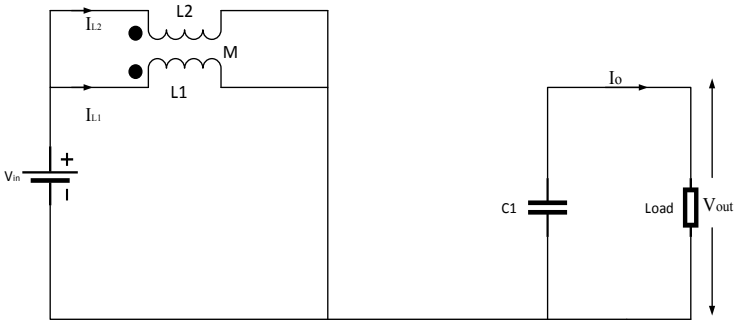


Fig. 2 Requirement of number of components for the proposed converter



(a)



(b)

Fig. 3 Proposed converter equivalent circuit In ON State and OFF State

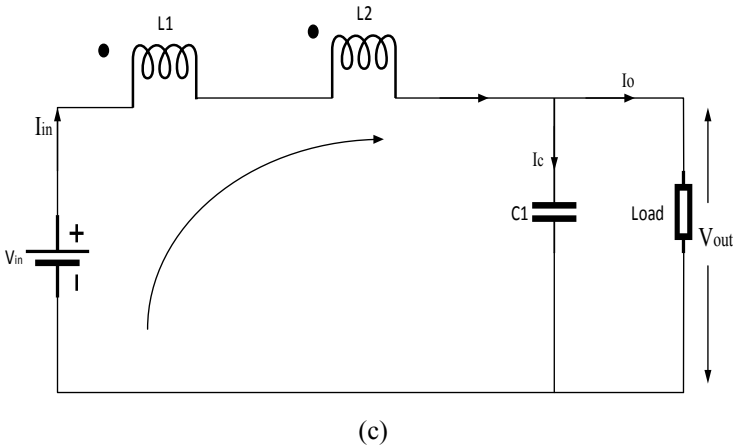


Fig. 3 (continued)

- inductors L_1 and L_2 get magnetized during this process. In this mode, the capacitor is attached parallel to the load and the C_1 capacitor is discharged via load. Coupled inductors are entirely magnetized at the end of this mode.
- Mode-2: During Switch OFF ($DT_s \leq t \leq Ts$) in this mode, power controlled switch is open and diodes D_1 and D_3 are open and diode D_2 is closed. Due to this, inductors L_1 and L_2 are series coupled. These series coupled inductors L_1 and L_2 are connected load through the diode D_4 . Equivalent circuit is shown in Fig. 3c. During this mode, series coupled inductors L_1 and L_2 are demagnetized through the load and capacitor C_1 . So, capacitor is charged in this mode. At the end, inductors are demagnetized and capacitor is charged. After it again mode-1 starts, and this process is repeated.
 - Analysis of SCIBC: The analysis of projected converter is done on the basis of inductor voltage second balance rule and capacitor current second balance rule. The analysis takes into account the drop in the ON state voltage of diodes, couple inductors and the controlled switch. For simplicity, coupling coefficient is unity ($k = 1$) and voltage drop due to diode, couple inductors and controlled switch is taken as V_d .
 - Single Stack SCIBC:
In Fig. 1a, power circuit of single-stack SCIBC is depicted. The power circuit of single stack SCIBC consists of one coupled inductor with four diodes at input side.
During Switch ON ($0 \leq t \leq DT_s$)

$$V_L = V_{L_1} = V_{L_2} = V_{in} - 3V_d = L \frac{di}{dt} + M \frac{di}{dt} \tag{1}$$

$$V_c = V_{out} \tag{2}$$

During Switch OFF ($DT_s \leq t \leq T_s$)

$$V_{in} - V_{L_1} - V_{L_2} - 4V_d - V_c = 0 \quad (3)$$

$$V_{L_1} = V_{L_2} = M \frac{di}{dt} + M \frac{di}{dt} \quad (4)$$

$$2V_L = V_{in} - V_c - 4V_d \quad (5)$$

From above equations and inductor balance rule that is Average $V_L = 0$

$$\frac{V_{out}}{V_{in}} = \frac{1 + D}{1 - D} \quad (\text{let } V_d = 0) \quad (6)$$

- Two Stack SCIBC:

In Fig. 1b, power circuit of two stack SCIBCs is depicted. It consists of two coupled inductors and ten diodes at input side.

During Switch ON ($0 \leq t \leq DT_s$)

$$V_L = V_{L_1} = V_{L_2} = V_3 = V_{in} - 3V_d = L \frac{di}{dt} + M \frac{di}{dt} \quad (7)$$

$$V_c = V_{out} \quad (8)$$

During Switch OFF ($DT_s \leq t \leq T_s$)

$$V_{in} - V_{L_1} - V_{L_2} - V_{L_3} - V_{L_4} - 6V_d - V_c = 0 \quad (9)$$

$$V_{L_1} = V_{L_2} = V_{L_3} = V_{L_4} = M \frac{di}{dt} + M \frac{di}{dt} \quad (10)$$

$$4V_L = V_{in} - V_c - 6V_d \quad (11)$$

From above equations and inductor balance rule that is Average $V_L = 0$

$$\frac{V_{out}}{V_{in}} = \frac{1 + 3D}{1 - D} \quad (\text{let } V_d = 0) \quad (12)$$

- N-Stack SCIBC:

In Fig. 1c, power circuit of N-stack SCIBC is depicted. It consists of N coupled inductors and $(6N-2)$ at input side.

During Switch ON ($0 \leq t \leq DT_s$)

$$V_L = V_{L_1} = V_{L_2} \dots = V_N = V_{in} - 3V_d = L \frac{di}{dt} + M \frac{di}{dt} \quad (13)$$

$$V_c = V_{out} \tag{14}$$

During Switch OFF ($DT_s \leq t \leq T_s$)

$$V_{in} - V_{L1} - V_{L2} \dots - V_{2N} - 2N V_d - V_c = 0 \tag{15}$$

$$V_{L1} = V_{L2} = V_{L3} \dots = V_{L2N} = M \frac{di}{dt} + M \frac{di}{dt} \tag{16}$$

$$2N V_L = V_{in} - V_c - 2N V_d \tag{17}$$

From above equations and inductor balance rule that is Average $V_L = 0$

$$\frac{V_{out}}{V_{in}} = \frac{1 + (2N - 1)D}{1 - D} \quad (\text{let } V_d = 0) \tag{18}$$

3 Result and Discussion

Projected converter is simulated for single stack with power rating of 250 W. The simulation parameter is provided in Table 2. The controlled input DC supply (10 V) is applied to the projected converter to avoid the high starting current and voltage. The projected converter is simulated for 10 MHz switching frequency to decrease L , C value and reduce the ripple in output. The waveforms of output voltage and output current, respectively, are shown in Fig. 4b and c. It is found that output voltage has ripples of 3% and output current ripples of 0.15%. The average output voltage is also 189.5 V, and the current is 1.27A. It is concluded from the measurements that average output power is 240. 67 W. The waveform shown in Fig. 4d is input couple inductor current that supply from the voltage source. It is found that couple inductors store the energy during ON state and during OFF state discharges. Figure 4e describes

Table 2 Simulation specifications of proposed converter

Parameters	Symbol	Values
Supply voltage	V_{in}	10 V DC
Output voltage	V_{out}	190 V
Input coupled inductor	L_1, L_2, M	0.4 mH, 0.4 mH, 0.34 mH
Duty ratio	D	90%
Load	R_L	150 ohm
Switching frequency	f_s	10 MHz
Output capacitor	C_{DC}	0.5 μ F

the waveform around the regulated switch. It indicates that, during off state, voltage around the regulated posed converter output voltage gain for specific stack number versus duty ratio is shown in Fig. 5. It is demonstrated that in ideal cases the voltage gain is maximum ($V_d = 0$), and in practical cases, it is reduced; consider VdIt is stated that in ideal cases, the voltage gain from single stack SCIBC is 19 at a duty ratio of 90%.

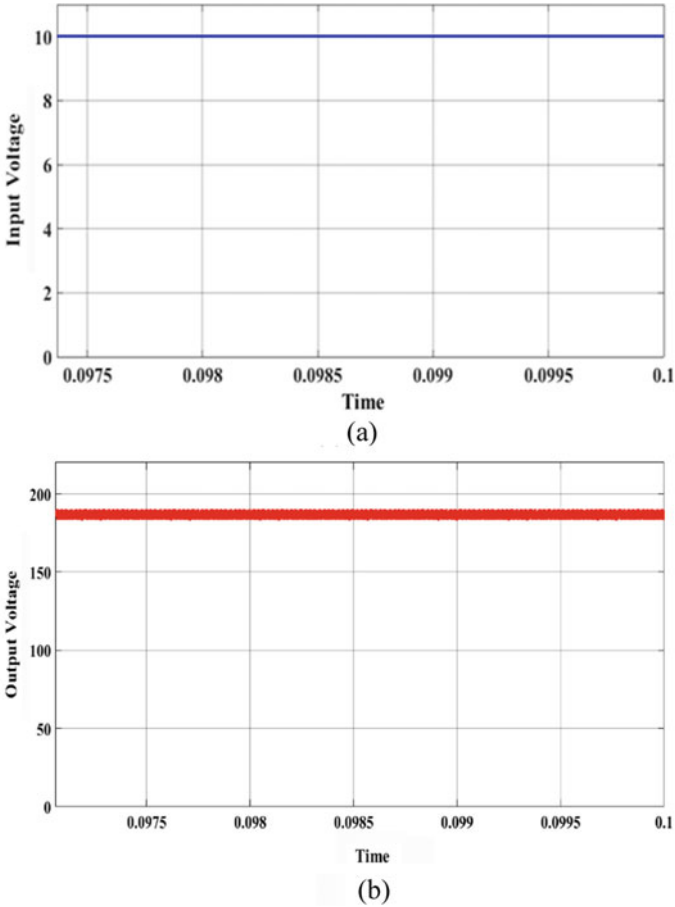


Fig. 4 Simulation performance of single stack SCIBC **a** V_{in} **b** V_{out} at 90% Duty ratio **c** Output current **d** Couple inductor current **e** Switch voltage

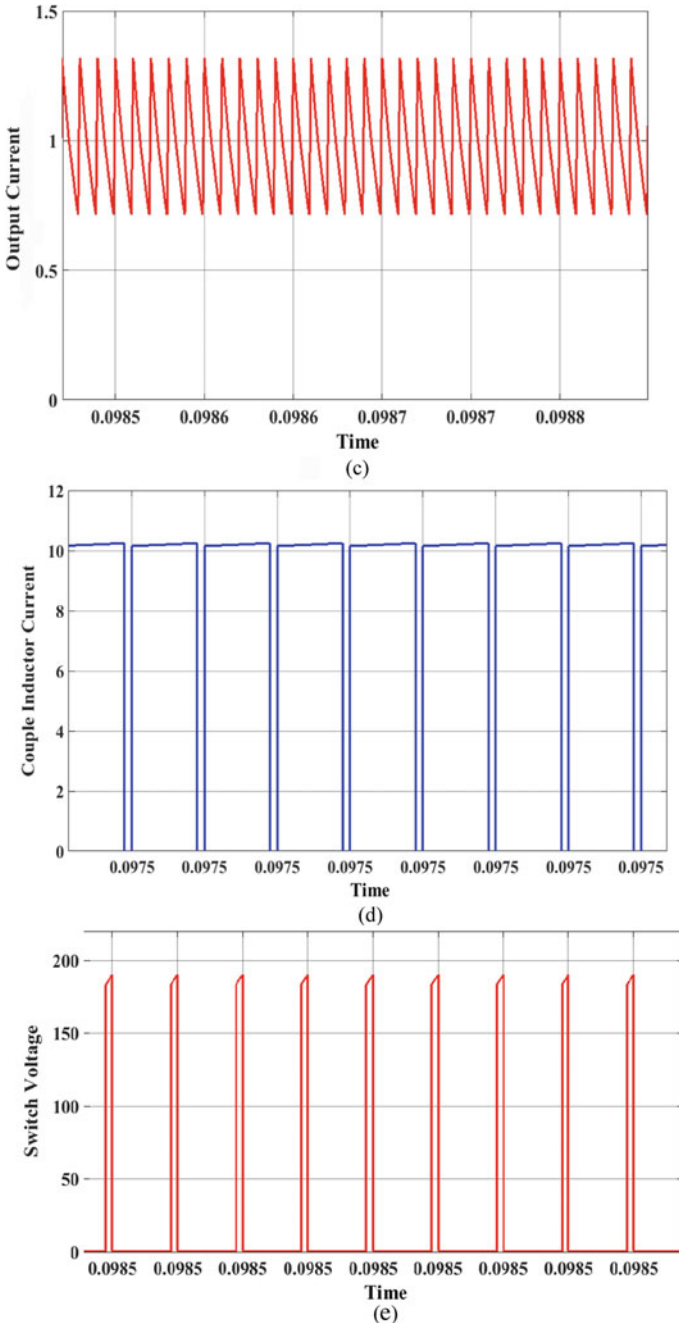
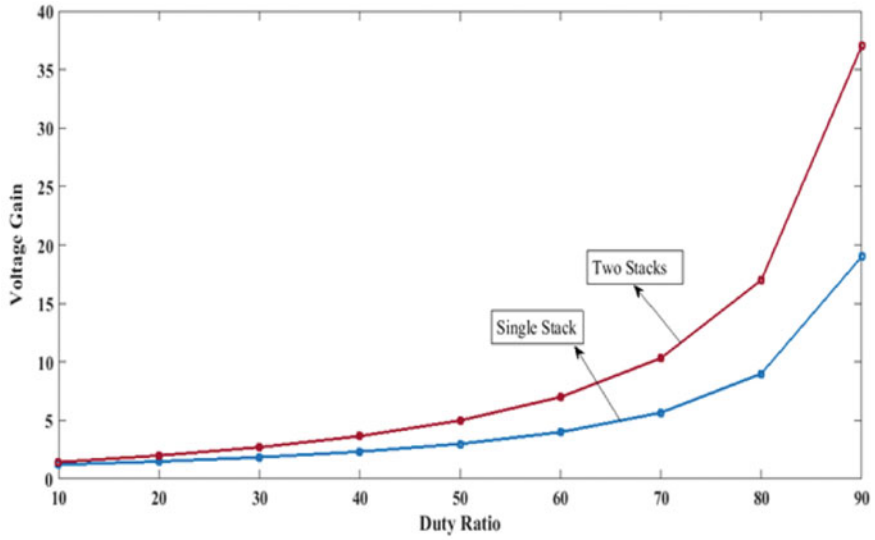
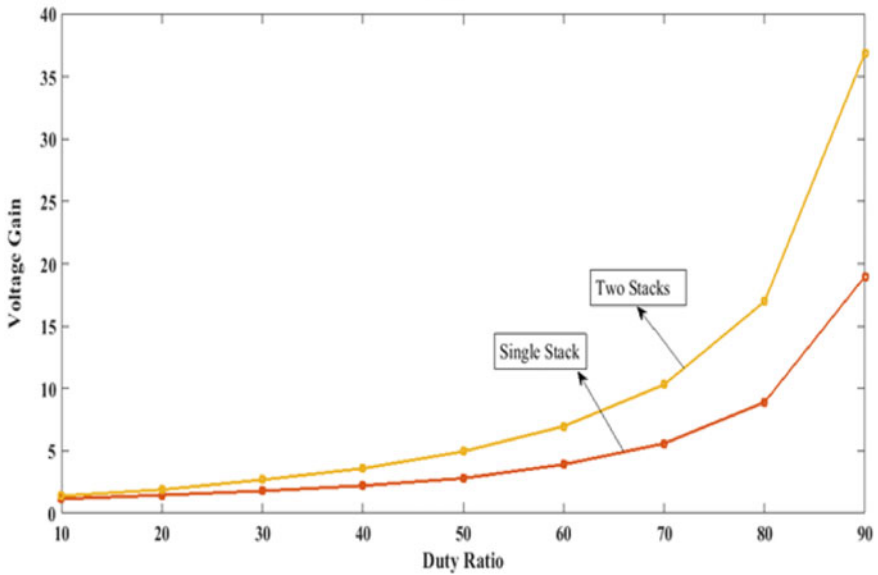


Fig. 4 (continued)



(a)



(b)

Fig. 5 Voltage gain versus duty ratio for ($N = 1$) and ($N = 2$) proposed converters with voltage drop V_d across diode **a** $V_d = 0$ and **b** $V_d = 0.5$

4 Conclusion

A proposed novel SCIBC step-up converter topology for renewable energy systems is being discussed. SCIBC's corresponding power circuit is a mixture of CBC and coupled inductor stacks, which can be increased to N . Compared with other DC-DC converters (step-up converters) and multistage converters, the gain from SCIBC is high. The gain of SCIBC is increasing with increasing in a number of coupled inductor stack. The power circuit operation and gain analysis of SCIBC is discussed in detail. SCIBC is required single power semiconductor switch which results less number of driving circuit required. Therefore, overall cost and size are reduced and work efficiently with better accuracy.

References

1. Fedak V, Siano P, Ramachandramurthy VK (2007) Switched Inductor Boost Converter for Renewable Energy Application. *IEEE Tran Power Electron* 1(17):324–332
2. Vipin D, Sanjeevikumar P, Karthikeyan V, Rajasekar S, Blaabjerg F, Pierluigi S (2017) Recent advances and challenges of fuel cell based power system architectures and control—a review. *Renewable Sustainable Energy Rev* 73:10–18
3. Hu Y, Cao W, Ji B, Si J, Chen X (2015) New multi-stage DC–DC converters for grid-connected photovoltaic systems. *Renewable Energy* 74:247–254
4. Padmanaban S, Blaabjerg F, Wheeler P, Ojo JO, Ertas AH (2017) High-voltage dc-dc converter topology for pv energy utilization—Investigation and implementation. *Electric Power Compon Syst* 45(3):221–232
5. Li W, He X (2011) Review of non-isolated high-step-up DC/DC converters in photovoltaic grid-connected applications. *IEEE Trans Industr Electron* 58(4):1239–1250. <https://doi.org/10.1109/TIE.2010.2049715>, April
6. Moradpour R, Ardi H, Tavakoli A (2017) Design and implementation of a new SEPIC-based high step-up DC/DC converter for renewable energy applications. *IEEE Trans Industrial Electron* 65(2):1290–1297. <https://doi.org/10.1109/TIE.2017.2733421>
7. Bhaskar MS, Kulkarni RM, Padmanaban S, Siano P, Blaabjerg F (2016) Hybrid non-isolated and non-inverting N_x interleaved DC-DC multilevel boost converter for renewable energy applications. In: 2016 IEEE 16th international conference on environment and electrical engineering (EEEIC). Florence, pp 1–6. <https://doi.org/10.1109/EEEIC.2016.7555827>
8. Bhaskar MS, Sanjeevikumar P, Blaabjerg F, Fedák V, Cernat M, Kulkarni RM (2016) Non isolated and non-inverting Cockcroft-Walton multiplier based hybrid $2N_x$ interleaved boost converter for renewable energy applications. In: 2016 IEEE international power electronics and motion control conference (PEMC). Varna, pp 146–151. <https://doi.org/10.1109/EPEPEMC.2016.7751989>
9. Bhaskar MS, Padmanaban S, Blaabjerg F, Norum LE, Ertas AH (2016) $4N_x$ non-isolated and non-inverting hybrid interleaved multilevel boost converter based on VLSIm cell and cockcroft walton voltage multiplier for renewable energy applications. In: 2016 IEEE international conference on power electronics, drives and energy systems (PEDES). Trivandrum, pp1–6. <https://doi.org/10.1109/PEDES.2016.7914529>
10. Bhaskar MS, Padmanaban S, Kulkarni R, Blaabjerg F, Seshagiri S, Hajizadeh A (2016). Novel LY converter topologies for high gain transfer ratio—a new breed of XY family. In: 4th IET clean energy and technology conferenace, (CEAT 2016). Malaysia, pp 4(8)

11. Mahajan SB, Padmanaban S, Blaabjerg F (2017) A multistage DC-DC step-up self-balanced and magnetic component-free converter for photovoltaic applications: hardware implementation. *Energies J MDPI Publicat Switzerland*10(5):719
12. Forouzes M, Siwakoti YP, Gorji SA, Blaabjerg F, Lehman B (2017) Step-Up DC-DC converters: a comprehensive review of voltage-boosting techniques, topologies, and applications. *IEEE Trans Power Electron* 32(12):9143–9178. <https://doi.org/10.1109/TPEL.2017.2652318>, Dec
13. Rosas-Caro JC, Mayo-Maldonado JC, Cabrera RS, Rodriguez AG, Nacu SCE, Castillo-Ibarra R (2011) A Family of DC-DC multiplier converters, Avanc line publication. *Eng Lett*
14. Maroti PK, Ranjana MSB Prabhakar DK (2014) A novel high gain switched inductor multilevel buck-boost DC-DC converter for solar applications. In: 2014 IEEE 2nd international conference on electrical energy systems (ICEES). Chennai, pp 152–156. <https://doi.org/10.1109/ICEES.2014.6924159>
15. Mousa M, Ahmed M, Orabi M (2010) A switched inductor multilevel boost converter. In: 2010 IEEE international conference on power and energy. Kuala Lumpur, pp 819–823. <https://doi.org/10.1109/PECON.2010.5697692>
16. Balakrishnan S, Sreethumol MV (2014) An interleaved soft wwitched two inductor boost converter with improved load regulation. In: 2014 international conference on computation of power, energy, information and communication (ICCPEIC). IEEE, pp 164–167
17. Parsa L (2007) A novel high efficiency high power interleaved coupled-inductor boost DC converter for hybrid and fuel eell electric vehicle. In: 2007 IEEE vehicle power and propulsion conference
18. Sun J (2006) Dynamics characterization of coupled-inductor boost DC-DC converters. In: 2006 IEEE workshops on computers in power electronics
19. Wang J, Dunford WG, Mauch K (1997) Analysis of a ripple-free input-current boost converter with discontinuous conduction characteristics. In: IEEE transactions on power electronics
20. Axelrod B, Beck Y, Berkovich Y (2015) High step-up DC–DC converter based on the switched-coupled-inductor boost converter and diode-capacitor multiplier: steady state and dynamics. *IET Power Electron* 8(8):1420–1428
21. Nakamura Y, Yamamoto M (2011) Optimal control design method for trans-linked type multi-phase boost converter. In: 2011 IEEE ninth international conference on power electronics and drive systems
22. Suraj S, Soman S, Jijesh JJ (2016) Implementation of interleaved dual boost converter utilizing FPGA for PWM. In: 2016 IEEE international conference on recent trends in electronics, information & communication technology (RTEICT)
23. Chai Y, Li X (2017) A novel boost conversion with high voltage ratio. In: MATEC web of conferences
24. Gupta V, Anjana P, Narayan PP, Keshri JP, Tiwari HP (2013) A review on active power filter. In: Proceeding of international conference on advance trends in engineering & technology (ICATET-2013), pp 214–223
25. Keshri JP, Tiwari H (2017) Parameter-less fault locator using synchronized/un-synchronized data for overhead transmission line. In: 2017 international conference on computer, communications and electronics (comptelix), pp 260–264. <https://doi.org/10.1109/COMPTELIX.2017.8003975>
26. Keshri JP, Tiwari HP (2017) Fault location in overhead transmission line without using line parameter. In: 4th international conference on engineering and technology (ICSET), pp 11–15

Five-Level Single-Phase Converter Using SiC with Reduced Switched Voltage Stress



Vishal Jain, Jay Prakash Keshri, Harpal Tiwari, and Pankaj

1 Introduction

Multilevel converters (MLCs) present superior advantages which are characterized by improvement in output waveforms, reduction in harmonics, lower switching losses. MLC uses medium power devices and provide applications in field where high power is utilized. MLCs are prior options in field where bulk amount of power with low and medium range of voltage is used. MLCs have effective footprints in fields such as FACTS, uninterrupted power supplies, line conditioners, active filters (UAPF), electric traction, drives for AC motors and electric and hybrid vehicle technology [1–5]. AC-AC MLCs find applications in industries to provide sine-wave input currents with unity power factor in regulators and guard the sensitive appliances like computers, medical instruments and communication setups from poor quality supplies. DC-AC MLCs are used in gas, oil, mining and marine industries. In renewable energy low-power applications, these MLCs are treated as effective solutions for efficiency problems [6].

Various MLC topologies available in literature are shown in Fig. 1. Mainly, they are of three types: flying capacitor (FC), neutral-point-clamped (NPC) and cascaded H-bridge.

V. Jain · J. P. Keshri (✉) · H. Tiwari · Pankaj
Malaviya National Institute of Technology, Jaipur, India
e-mail: 2014ree9538@mnit.ac.in

V. Jain
e-mail: 2018ppd5052@mnit.ac.in

H. Tiwari
e-mail: hptiwari.ee@mnit.ac.in

Pankaj
e-mail: 2018PPD5215@mnit.ac.in

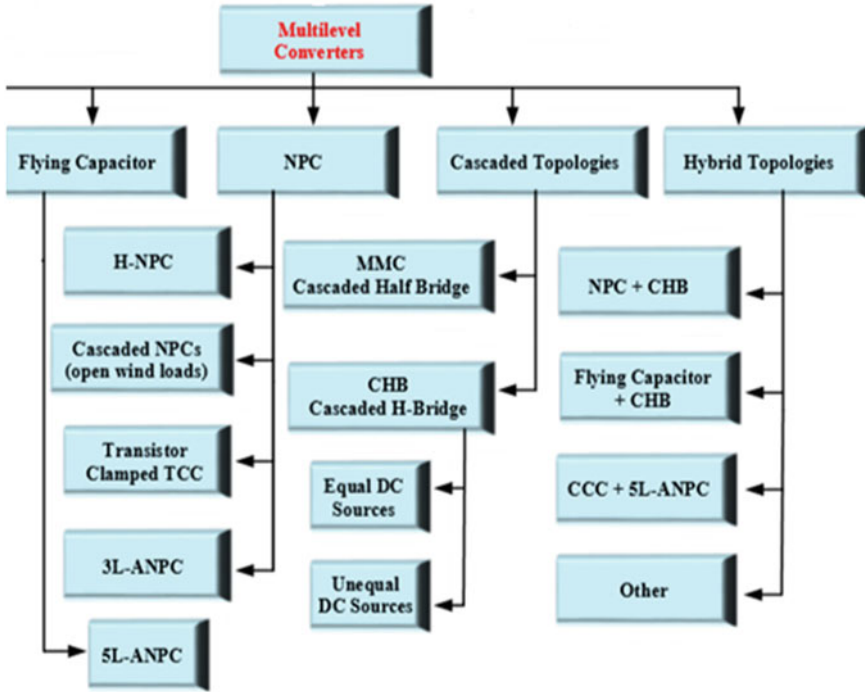


Fig. 1 Multilevel converters classifications

CHB and other converter architectures are derived using these. Despite of their superior nature and attention they are gaining in research and development, MLCs exhibit:

- Huge number of power electronics switches.
- Complex nature of system; responsible for reliability reduction.
- Supporting circuits: driver units, protection circuits, heat dissipation system, etc., lead to problem of additional cost and bulky system.
- Ambiguous control circuitry: complex controlling.

For MLC results, performance and efficiency are superior at the cost of above-mentioned points; therefore, primary concern is to minimize the counting of power electronics devices, replacing conventional switching devices with advance featured modern switches and simplifying driver and control circuits with cost optimization, and hence, researchers are paying attention toward above-mentioned factors [7]. In [8], authors presented a novel converter topology by modifying active (ANPC)-type converter and named it T-type topology because its shape is similar to English letter “T”. This topology claims the reduction in two clamping diodes per bridge and reduction in conduction losses which is drawback of NPC-topology, but T-type suffers from high switching losses. In [9–11], the authors modified the T-type leg

and presented a five-level just by modifying three-level T-type with minimization in switch voltage stress. So, it contains all the benefits of T-type with the improvisation in wave shape and reduction in harmonics. In [11, 12], authors focused on high switching losses and presented a T-type highly efficient converter in which outer switches are replaced by SiC MOSFET which is superior.

In this paper, conventional T-type topology is modified and outer switch used by previous authors is replaced by highly advanced and superior SiC switch. Two novel T-type legs are used in voltage source inverters (VSIs) which can be an option against other five-level topologies, including NPC, FC and CHB shown in Fig. 2, and T-type circuit is depicted in Fig. 3. In modified T-type leg, the number of devices is equal to devices in conventional T-type leg with an achievement of reducing voltage stress and low switching losses. Apart from this, other benefits being less quantity of clamping switches and deduction in bi-directional switches with respect to typical T-type. It is further can be used to extent the voltages level, and poly-phase system can be formed using modified legs. Concept formulation, modulation of topology

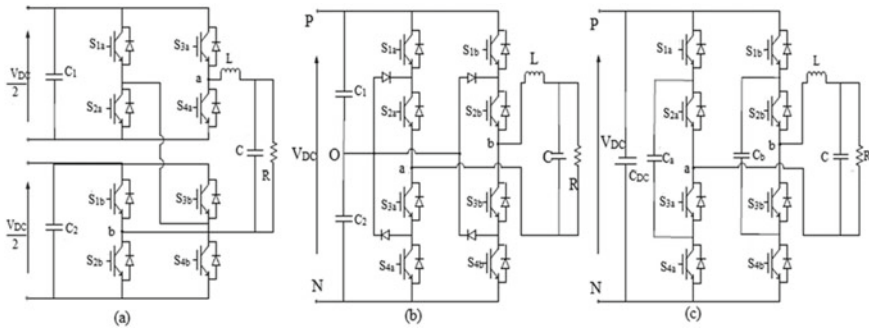


Fig. 2 Five-level topology a cascaded-half-bridge, b neutral-point-clamped and c flying-capacitor

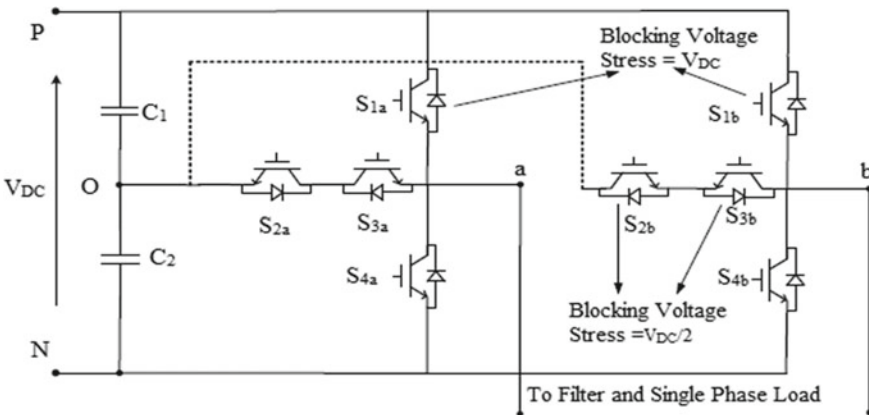


Fig. 3 Five-level T-type inverter from three-level legs

and comparison are presented comprehensively using MATLAB simulations in next sections.

2 Formation of Topology

2.1 Topology Synthesis

The typical single-phase converter formed by three-level T-type legs is given in Fig. 3. This comprises totally eight power devices $S_{1x} - S_{4x}$ ($x = a, b$) and anti-parallel diodes. There are two possible configurations of three-level legs, either common emitter (CE) or common collector (CC) as delineated in Fig. 4.

Using these, two novel legs are introduced using two SiC MOSFET switch in outer and two Si MOSFET of lower rating as bidirectional switches as depicted in Fig. 5a, b.

In Fig. 5a one modified leg (*leg A*) is formed by connecting terminal of S_{1a} , collector terminal of switch S_{2a} and collector terminal of S_{3a} at point “x” and this configuration is common collector configuration of bidirectional switch. In same manner, other modified leg (*leg B*) is formed using S_{4a} , emitter terminal of switch S_{2a} and emitter terminal of S_{3a} at point “y” and this configuration is common emitter (CE) arrangement of bi-directional switches shown in Fig. 5b.

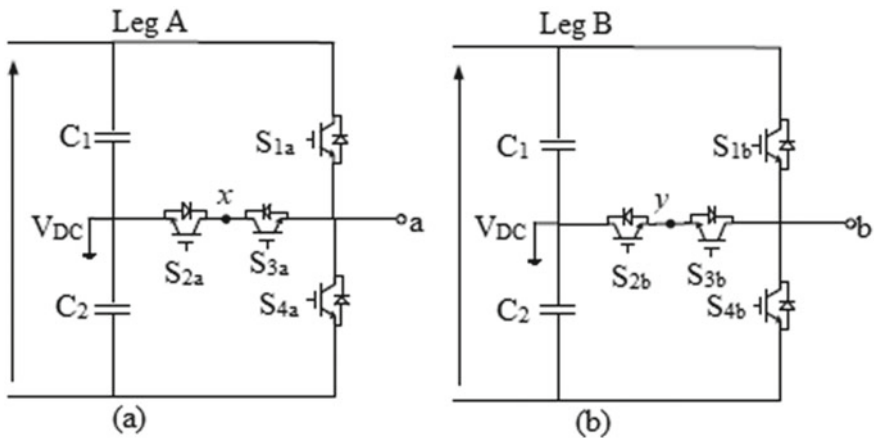


Fig. 4 T-type legs a CC, b CE configuration

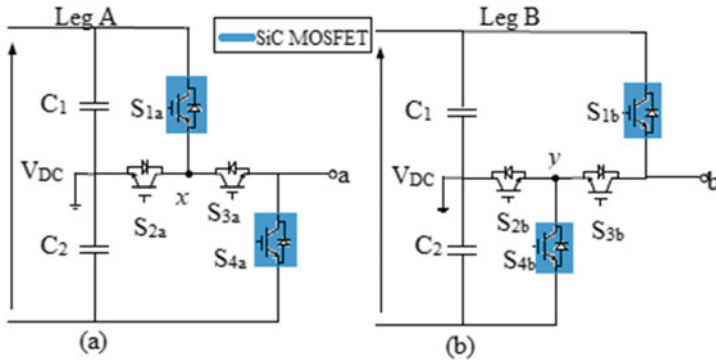


Fig. 5 Novel T-type legs a CC, b CE configuration

2.2 Operating Principles and Circuit Analysis

The novel inverter circuit is presented in Fig. 6, a five-level single-phase T-type inverter which comprises two advanced modified three-level T-type leg. Circuit is simplified as there is no clamping diode. Voltage level obtained at \$V_{a0}\$ and \$V_{b0}\$ has three voltage levels, and voltage obtained as output has five-level which is evaluated by, $V_{ab} = V_{a0} - V_{b0}$.

For easy controlling, symmetry is obtained for which Complementary logic is required which is achieved by choosing suitable switch numbering. To stop conduction at same time, switching limits are defined. So, $Q_{xy} + \overline{Q_{xy}} = 1$ where $x = 1, 2$ and $y = a, b$.

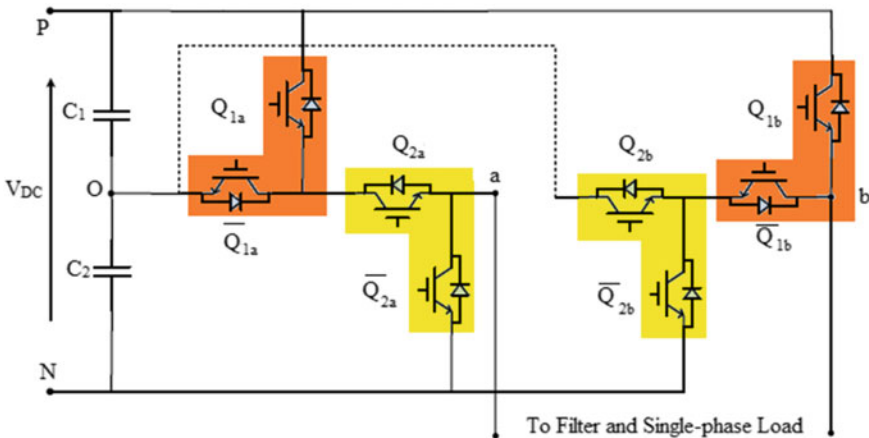


Fig. 6 Inverter formed using novel T-type legs using SiC

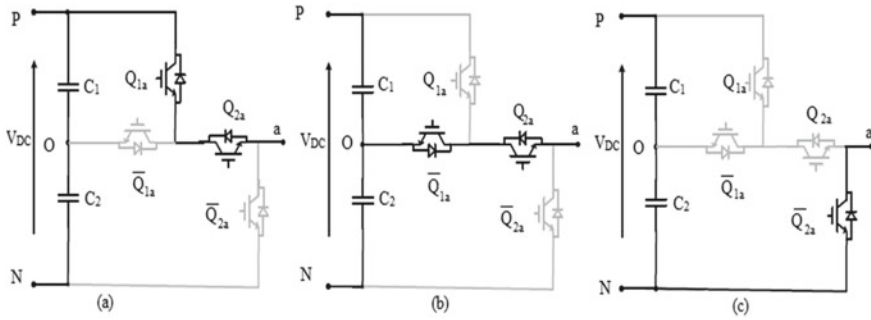


Fig. 7 Operating modes and current path circuits

Table 1 Switching patterns and respective voltages of novel T-type three-level inverter *leg A*

V_{a0}	Q_{1a}	$\overline{Q_{1a}}$	Q_{2a}	$\overline{Q_{2a}}$
V_{C1}	1	0	1	0
0	0	1	1	0
$-V_{C2}$	0	1	0	1

Table 2 Switching patterns and respective voltages of novel T-type three-level inverter *leg B*

V_{b0}	Q_{1b}	$\overline{Q_{1b}}$	Q_{2b}	$\overline{Q_{2b}}$
V_{C1}	1	0	1	0
0	0	1	1	0
$-V_{C2}$	0	1	0	1

Switching state circuit of novel inverter *leg A* is described in Fig. 7. Possible switching patterns to get voltages level are given in Table 1. In a same way, switching state patterns for *leg B* are listed in Table 2. Q_{xy} is 1 if respective switch is close and 0 if switch is open. Phase voltages V_{a0} , V_{b0} are also given. Phase current flow from one of the node point of DC-link. Depending on switching state, respective capacitor voltage will come out on AC side.

In further analysis, it can be observed that novel T-type inverter facilitates suppression in total voltage stress on switch of inverter *leg A* and *leg B*. Another positive aspect is that the *leg A* and *leg B* are independent to each other and can be used in forming poly-phase converter.

3 Control Scheme and Simulation Results

Nature of proposed converter is asymmetrical, pulse width modulation (PWM) schemes used for other topologies such as NPC and T-type can be used for proposed converter also. From various modulation techniques, phase disposition (PD) modulation displayed in Fig. 8 is used here. By using wave 1 and wave 2 as carrier wave, switching signals are generated for $(Q_{1y}, \overline{Q_{1y}})$ and $(Q_{2y}, \overline{Q_{2y}})$ respectively. Sinusoidal modulation wave is out of phase by 180° . A novel T-type five-level single-phase converter is simulated in MATLAB. The control scheme used is phase disposition (PD) modulation, and results are obtained and analyzed. Load of 125 V, 1 kVA, 0.8 lag pf, 50 Hz is connected at output side. DC-link voltage is 200 V.

Figure 8 describes the modulation scheme based on phase disposition that completely follow the desire proposed scheme. And Fig. 9 shows the desire outputs from one leg and voltage output of novel converter. Along with Fig. 10 describes the stress and output voltage of leg A, and in the similar way, Fig. 11 shows the stress and output voltage of leg B. From results from Figs. 8, 9, 10 and 11, it is observed that during positive voltage from leg A, full DC-link voltage stress appeared only across (Q_{2a}) and similarly, for leg B, during negative output, full DC-link voltage stress appeared only across Q_{1b} . From the described results, it shows the applicability of the proposed topology within desired permissible limits. Therefore, it is observed that this scheme is much useful for the converter topology.

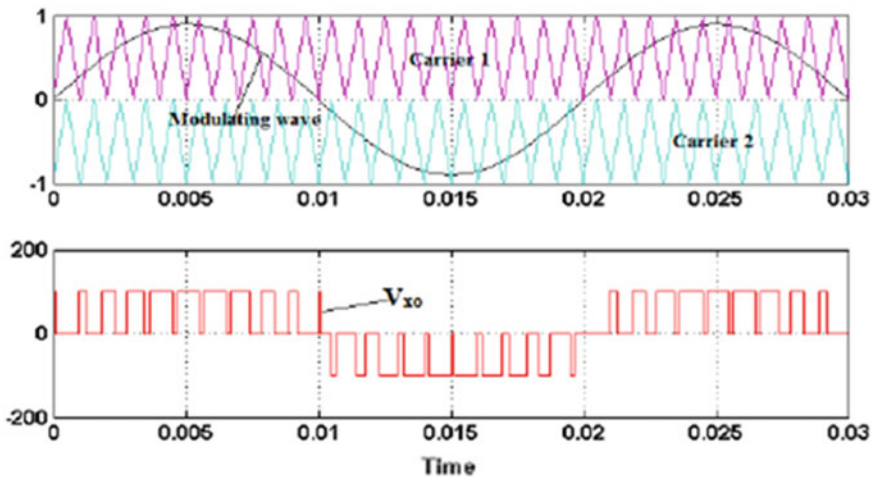


Fig. 8 Modulation scheme based on phase disposition (PD)

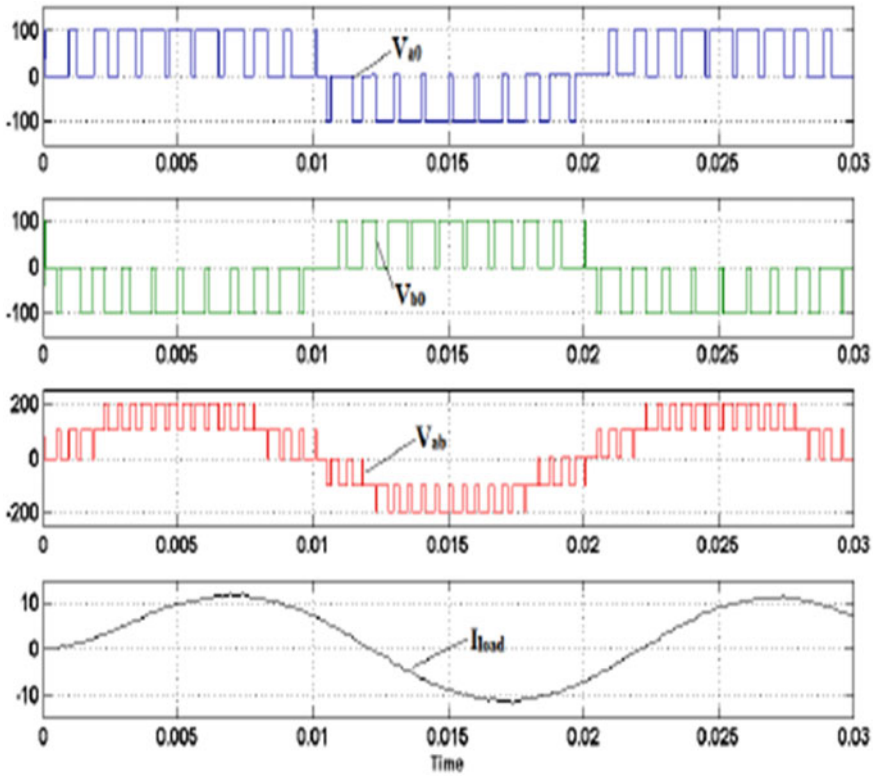


Fig. 9 Outputs from one leg and voltage output of novel converter

4 Comparison Among Different Five-Level Topologies

The proposed topology is compared against conventional T-type, NPC, FC and CHB topologies. Various factors like component required, isolated supplies, clamping diodes requirements, etc. are listed in Table 3. As the number of main switches is nearly equal or comparable but clamping diodes and capacitors are eliminated in few topologies, this proposed topology also focused on reduction in voltage stress and replacing conventional Si switch with advantageous SiC switch. So along with reducing stress and minimizing switch count switching frequency for same losses can be increased and efficiency and reliability converter is improved. Therefore, it is concluded that proposed topology fulfills our desire requirement within the permissible limits.

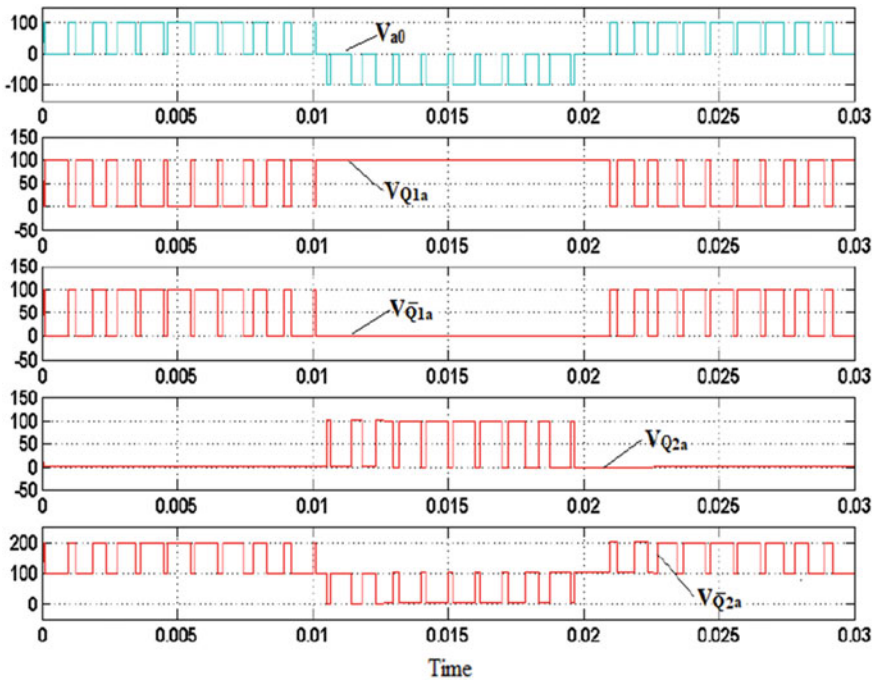


Fig. 10 Stress and output voltage of leg A

5 Conclusive Remarks and Future Scope

In this paper, two novel T-type legs are proposed which are modified from actual three-level T-type legs topology in which advanced SiC MOSFET is used as outer switch in derived legs. Novel T-type legs topology exhibits a switching voltage stress fewer than conventional T-type. Poly-phase system can be realized using these independent legs, and higher voltages level can be achieved with the help of H-bridge cells. Five-level single-phase inverter is formed using novel T-type legs using SiC MOSFET. PD carrier-based modulation is used. Three-level PWM output voltage is obtained at three-level legs, and five-level output voltage is obtained as output voltage. Further in this paper, the losses can be calculated and compared with conventional topologies and highly efficient inverter and AC-DC-AC converter can be proposed. Therefore, these researches could be done to reduce the voltage impact on switch which is still facing full voltage stress.

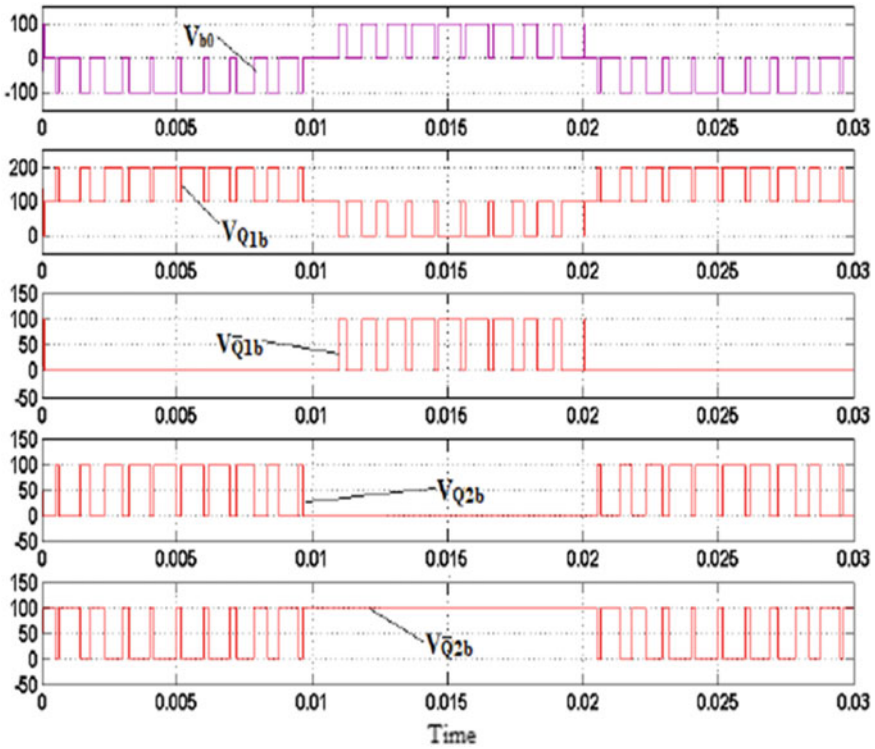


Fig. 11 Stress and output voltage of leg B

Table 3 Comparison between different five-level topology

Factors	FC	CHB	T-type	NPC	Novel T-type
Voltages level	5	5	5	5	5
Switch count in a leg	4	4	4	4	4
Clamping diode	0	0	0	2	0
Flying capacitors	1	0	0	0	0
Isolated supply	1	2	1	1	1
Total elements	13	10	9	13	9

References

1. Kolhatkar YY, Das SP (2007) Experimental investigation of a single phase UPQC with minimum VA loading. *IEEE Trans Power Deliv* 22(1):373–380
2. de Azpeitia MAP, Fernandez A, Lamar DG, Rodriguez M, Hernando MM (2008) Simplified voltage-sag filler for line-interactive uninterruptible power supplies. *IEEE Trans Ind Electron* 55(8):3005–3011

3. Bento AA, da Silva ER, Praga PP (2008) Integrated one-cycle control for three-leg universal active power filter. In: Proceedings of IEEE power electronics specialists conference, pp 3974–3980
4. Kim T, Choi J, Kwon B (2004) High-performance line conditioner with output voltage regulation and power factor correction. *IEEE Proc Electr Power Appl* 151(1):91–97
5. Franquelo LG, Leon JI, Kouro S, Portillo R, Prats MA (2008) The age of multilevel converters arrives. *IEEE Ind Electron Mag* 2(2):28–39
6. Steimer PK (2010) Enabled by high power electronics—energy efficiency renewable and smart grids. In: International power electronics conference, pp 11–15
7. Elasser A, Chow TP (2002) Silicon carbide benefits and advantages for power electronics circuits and systems. *Proc IEEE* 90(6):969–986
8. Keshri JP, Tiwari H (2017) Fault location in overhead transmission line without using line parameter. In: 4th international conference on engineering and technology (ICSET), pp 11–15
9. Somasekhar VT, Gopakumar K (2003) Three-level inverter configuration cascading two two-level inverters. *IEEE Proc Electr Power Appl* 150(3):245–254
10. Narendrababu A, Yalla N (2018) A modified T-type single phase inverter with reduced switch voltage stress. In: IEEE conference on power electronics, IIT Roorkee. 978-1-5386-2462-3
11. Kwon O, Kwom JM (2018) A highly efficient single-phase three-level three-leg converter using SiC for AC-AC applications. *IEEE Trans Ind Electron* 66(9):08
12. Keshri JP, Tiwari H (2017) Parameter-less fault locator using synchronized/un-synchronized data for overhead transmission line. In: International conference on computer, communications and electronics

Chassis Design with Integrated Battery Pack Space for Electric Motorcycle



Mohammad Irfan Ahmad and Pankaj Dorlikar

1 Introduction

The automobile industry has continuously worked on weight reduction attributed to several benefits such as material cost reduction, performance improvement, etc. For several years now, the automotive industry has been utilizing optimization algorithms to reduce the weight of its products [1, 2]. This has seen a major boom due to increased non-conventional machining processes such as additive manufacturing and 3D printing. The advancement in the additive manufacturing techniques has unveiled the freedom to design complex shapes and geometries, thereby broadening the ambit of topology optimization. The complex shapes obtained using this technique can now be realized through the advanced additive manufacturing method, thereby enabling designers to think and configure beyond conventional shapes and geometries based on interesting optimal results. AM techniques can handle complex optimized shapes and geometries at an efficient cost as compared to conventional manufacturing techniques, viz., casting, stamping, forging, etc. [3].

Topology Optimization (TO) is a tool with the help of which, a creator can get the expected completion using a proper structural arrangement. First of all, the restricted material volume is stipulated which is also known as the design domain. The choice of simple geometry is vital to realize a mesh of appropriate quality [4]. Certain area in the design space has various ergonomic and functional characteristics and has to be excluded from the removed from the optimization process. Such areas should be restricted geometrically in order to save them from getting optimized (in this case, the battery pack space, front forks, and swing-arm pivot hole). Topology optimization problems deal with structural response of the system and their load path within the

M. I. Ahmad (✉) · P. Dorlikar

Department of Mechanical Engineering, Army Institute of Technology, Pune 411015, India

e-mail: irfanahmad_18987@aitpune.edu.in

P. Dorlikar

e-mail: pvdorlikar@aitpune.edu.in

control volume constraint and boundary condition. Two targets are being used in this study, the first one being mass reduction by 30, 20, and 10% that of the design domain and the second one being stiffness maximization.

TO has seen significant recognition in the past few years. Various techniques have been developed, viz., homogenization method [5], the solid isotropic element with penalization SIMP [6–8], level set [9, 10], evolutionary structural optimization ESO [11, 12], and a few others [13–15]. The ESO method has its basis on an easy theory that unfit material shall be regularly eliminated from the study area so that the topology's result converges alongside the optimum. In bi-directional ESO, element removal and addition to inefficient and efficient regions take place simultaneously. This leads to the generation of reliable shapes concerning optimization obstacles with restrictions such as stiffness [16], pulse [17], or power consumption [18–20].

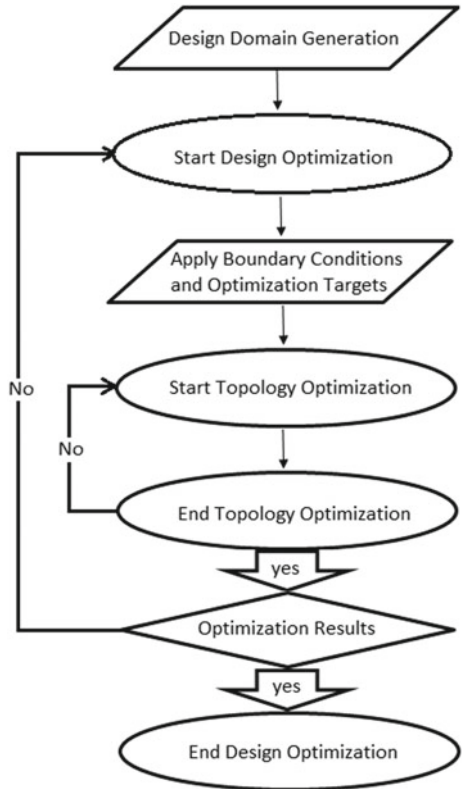
This work has been undertaken to design a chassis for an electric motorcycle that can cater to commuter segment. The control volume has been designed out of dimensions such as average wheelbase, seat height, width, and ground clearance. Castor angle for the front forks has been taken 25° . While performing topology optimization on the control volume, various regions such as front fork, battery pack space, and pivot hole of swing arm were geometrically restricted to prevent any material removal from them. Load calculations have been done primarily for 4 cases, i.e., maximum acceleration, maximum braking to the head axle, highest braking to the rear axle, and during the bike is the interior arch with adherence border of pneumatics. TO is performed for three iterations of volume reduction, i.e., for 70, 80, and 90% and the 90% volume reduction model has been used to build the roll-cage that can be manufactured.

The topology optimization process used in this work has been depicted in Fig. 1. The design domain was generated using SolidWorks2019[®] and the topology optimization was performed using Autodesk's Fusion 360[™] software. The process begins by building the CAD of the design domain and further optimizing it by adjusting the battery pack volume inside it in such a way that maximum material surrounds the battery pack space. During the first phase, the optimization targets are fixed for 30% target volume and maximum stiffness to extract the desired mass required to carry the applied loads. In the subsequent iterations, the target volume is reduced to 20% and 10%, respectively. After the completion of each iteration, the objective function and constraints are evaluated and the control volume is again subjected to the TO algorithm for the subsequent iterations until convergence for satisfactory levels is achieved for the development of the optimized shape.

2 Survey on Design Domain Generation

TO approach points to material order in the study region in such a way that the composition can display the production constraint. There are various advantages of having a lightweight vehicle, for example, it performs better in acceleration, braking, and turning as compared to heavy vehicles [21]. Also, safety improves significantly

Fig. 1 Flowchart of optimization process



[22] due to KE of vehicle reducing mass and thus maximizing crashworthiness during collision. TO techniques gained significance in past two decades. Initially, it focused on light weighting of automotive components, for example, in truck frames, deck lids, etc. [23]. Its application started evolving from simple forms to complicated ones, for example, those used in performance chassis [21, 22]. The evolution also inculcated in itself the desired performance standards in torsion, bending, mode shapes, crash, etc.

Recently, Airbus AP Works light rider has been developed using TO [24]. It weighs 35 kg where the frame itself weighs just 6 kg and comes entirely from a 3D printer. The parts were modeled using a patented aluminum alloy of the aerospace industry which is as light as Al but almost as strong as Ti.

For the purpose of generating a design domain, various motorcycle segments presently manufactured in India were studied for their geometric specifications such as wheelbase, seat height, length, width, and ground clearance. With the GOI’s plans to replace existing 150 cc and lesser capacity motorcycles before 2025 with all electric motorcycles, the research has been oriented toward developing chassis for the commuter segment based out of information from existing motorcycles. The

Table 1 18650 lithium-ion cell and battery pack specification

Parameter	18650 lithium-ion cell	Battery pack
Voltage (V)	3.6	150
Capacity (Ah)	3.4	40
Mass (g)	47.5	23.940
Volume (l)	1.6E-02	10.84

commuter segment is the workhorse. The characteristics pertaining to this segment include frugal nature, minimal maintenance, and ruggedness.

Another challenge faced in such development was locating the space required for accommodating battery pack. Calculations regarding the battery pack volume [25] and capacity have been shown in Table 1.

It has been shown in [25] that ~504 (18650 Lithium-Ion) cells are required to suffice the energy requirements, and hence for computational purposes, the range within which the battery pack needs to be constrained is

$$10.5l \leq V_{\text{battery pack}} \leq 11l \tag{1}$$

The volume has been calculated from the six design variables using the following formula:

$$V_{\text{battery pack}} = \sqrt{\left[(x_i - x_j)^2 + (y_i - y_j)^2 + (z_i - z_j)^2 \right]} \tag{2}$$

The batteries constitute the major cost in an e-vehicle and have to be placed symmetrically along the major axis of the vehicle in order to provide stability to it. Thus, the batteries must be placed strategically within the design domain in order to secure the location.

Nodes n_i and n_j (Fig. 2b) determine the bounds within which the square parallelepiped battery pack space is placed.

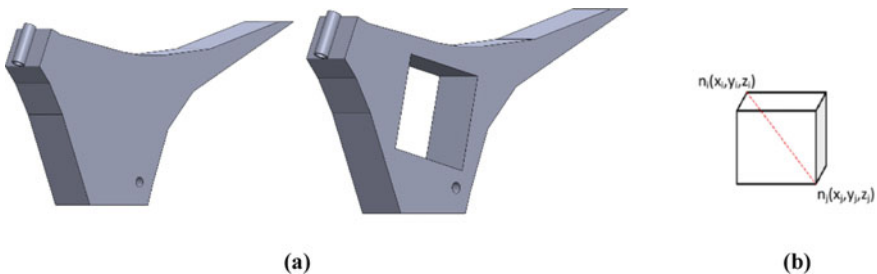


Fig. 2 Design domain for topology optimization including space for battery pack

3 Methodology and Model Setup

For a TO problem, we need to define the design space and the output parameters, viz., objectives and limitations of the optimization. The dimensions for the design domain have been obtained from measurements of commuter segment motorcycles as shown in Fig. 3.

To optimize the design space, the design domain must be as large as possible to accommodate the volumetric space occupied by the commuter segment's chassis. It must be congruous with the design constraints. Thus, the opening position in this research is a 3D steel volume-occupying utmost of the space inside a postulated motorcycle built throughout the skeleton as shown in Fig. 2a. The place for the principal vehicle divisions such as engine, gearbox, and fuel tank has not been considered for leaving maximum freedom for the optimization algorithm. The design space can constantly be adjusted posterior and optimization process repeated. For the study, the wheelbase has been fixed and chassis has been considered as a spatial structure made up of four rigid bodies, i.e., front assembly, rear assembly, front wheel and rear wheel, suspension is rigid, and FOS of 3 has been used for load application.

The study region has meshed with roughly 1.083 million tetrahedral elements that are of the first order (4 nodes each), and the size is 5 mm (see Fig. 4). The suspensions, engine, gearbox, and various other components are neglected in design space and in succeeding iterations, and the same constraints have been repeated. The optimization constraints and objectives used here are not too different from the ones used in [25], though this work addresses the optimization of the chassis from a control volume of frame space for initial stages of product development.

By implementing TO, a multidisciplinary optimization problem can be addressed by letting the optimizing tool select the optimal design from scratch.

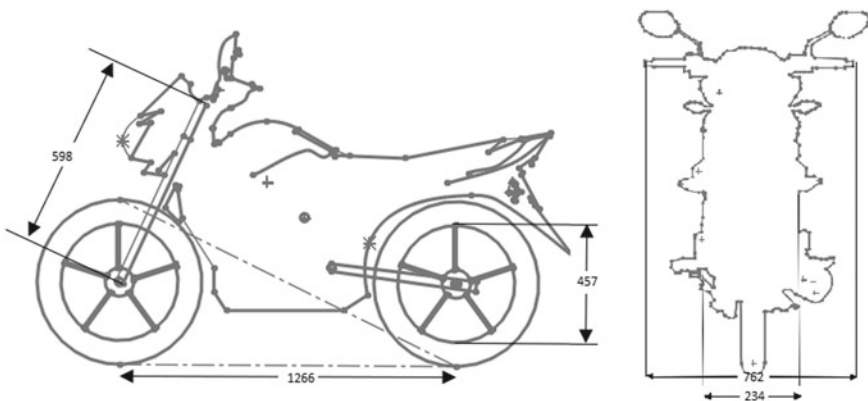


Fig. 3 Measurement of dimensions for design domain extraction from the commuter segment motorcycle

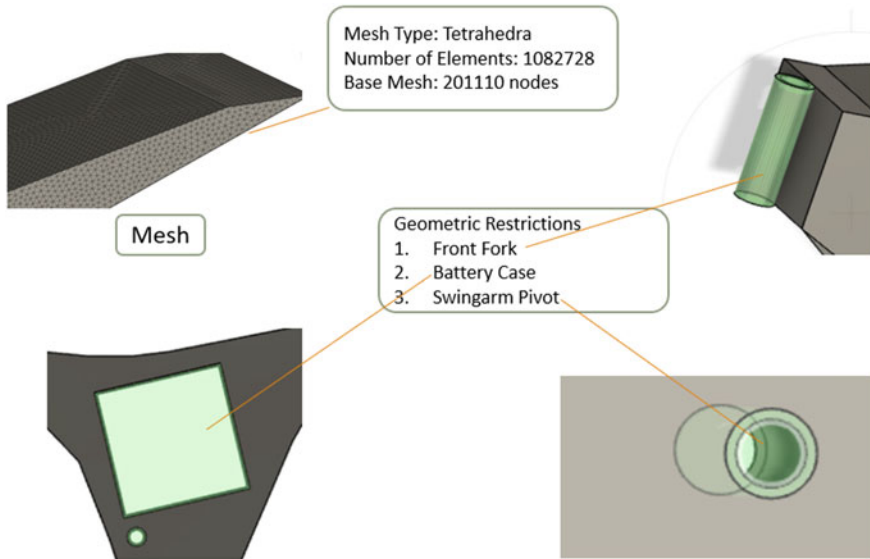


Fig. 4 Mesh and geometric restrictions

4 The Optimization Process

As mentioned earlier, loads have been calculated for four situations. However, for the purpose of topology optimization, the forces acting due to extreme braking have been used as the magnitude of such forces is larger than the ones in other cases. In case of extreme braking, the rear wheel gets lifted just above the surface and net downward force becomes equal to weight of the rider, and the motorcycle acting downwards at the front wheels. The loads F_1 and F_2 are the internal forces that act on the fork (steering) due to the braking on the front wheels whose values have been calculated by using Newton’s second law and equating moments about the axle (B) and topmost point of fork (C) to zero [26] (Fig. 5).

So, the condition will be:

$$N_r = mg \times \frac{b}{p} - F \times \frac{h}{p} = 0$$

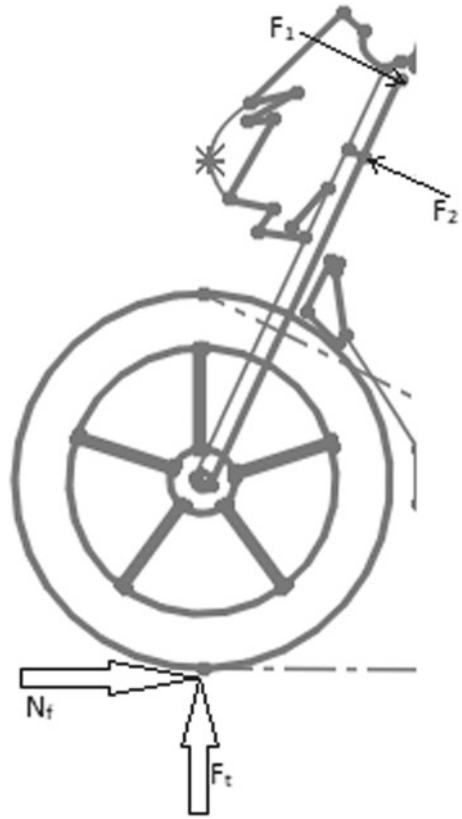
$$N_f = mg = 140 \times 9.81 = 1373.4 \text{ N}$$

$$F_t = mg \times \frac{b}{h} = 140 \times 9.81 \times \frac{760.5}{503.84} = 2073.02 \text{ N}$$

where

N_r is the normal reaction on the rear wheel,

Fig. 5 Forces in extreme braking



- N_f is the normal reaction on the front wheel,
- F_t is the tangential force acting at the front wheel,
- $\frac{b}{h}$ is the ratio of distance between cog to front axle and distance of cog from the ground,
- $\frac{b}{p}$ is the ratio of distance between cog to front axle and the wheelbase,
- $\frac{h}{p}$ is the ratio of distance of cog from the ground to the wheelbase.

$$\sum M_B = 0, \sum M_C = 0.$$

$$F_1 = 5864.512 \text{ N}, F_2 = 3534.226 \text{ N}.$$

Considering the factor of safety (FOS) value of 3, values of F_1 and F_2 are 17,593.53 N and 10,602.78 N, respectively. The depiction of load case along with geometric constraints has been shown in Fig. 6.

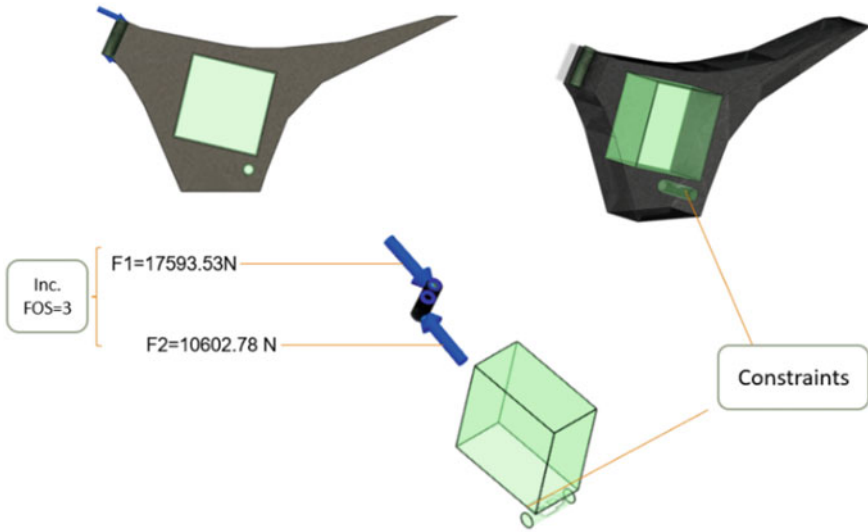


Fig. 6 Forces on the frame and constraints

5 Conclusion

An optimization technique for developing a motorcycle chassis is presented. The method helped reform the design space through TO by achieving an optimum design, keeping in consideration the acceptable stiffness and mass. The shapes obtained from the TO are depicted in Figs. 7, 8, and 9 and tabulated for the results in Table 2 Also, Fig. 10 depicts the conversion of topology optimized shape into roll-cage model

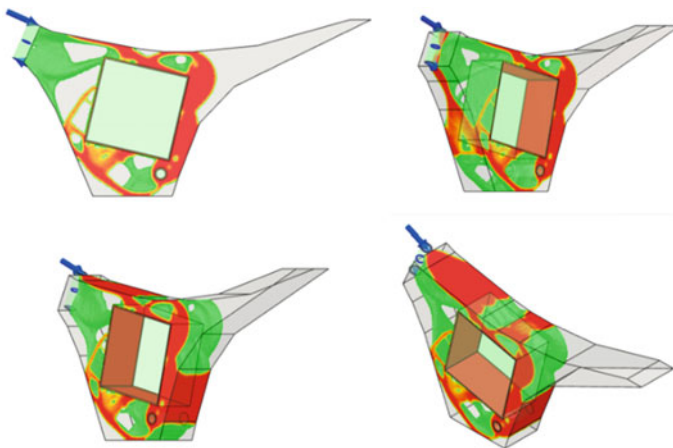


Fig. 7 Topology optimization with mass reduction target of 30%

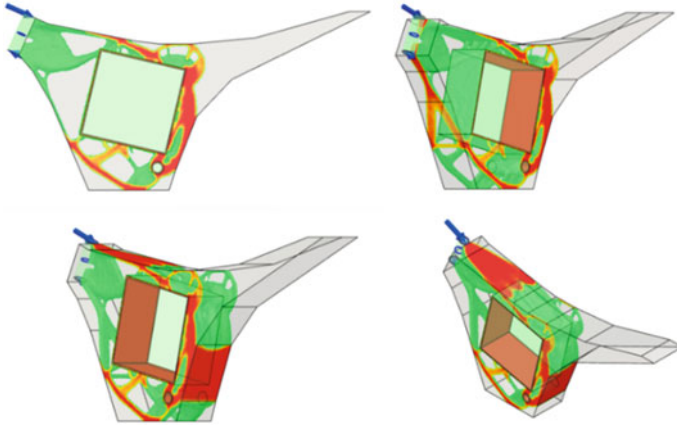


Fig. 8 Topology optimization with mass reduction target of 20%

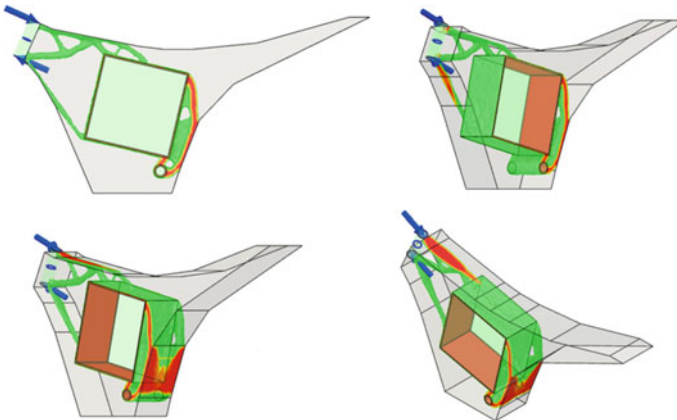


Fig. 9 Topology optimization with mass reduction target of 10%

Table 2 Topology optimization results

Formulation	Stage	CV mass	Target mass (%)	Reduced mass (%)	Final mass of chassis
Min mass and max stiffness	1	220.736 kg	≤ 30	38.11	62.049
Min mass and max stiffness	2	220.736 kg	≤ 20	18.54	40.921
Min mass and max stiffness	3	220.736	≤ 10	10.38	20.71

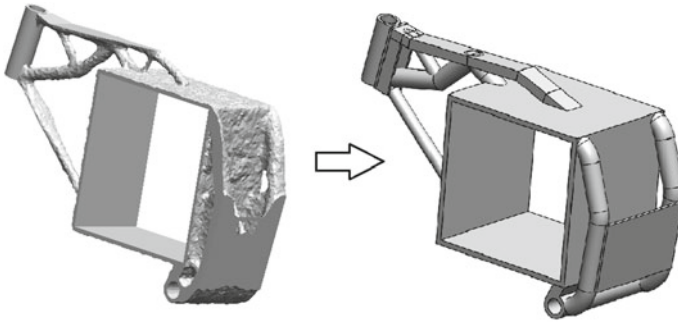


Fig. 10 Topology optimized geometry CAD conversion for physical realization

from the manufacturability point of view, and for that purpose, 90% volume/mass reduction model is taken as reference. The applicability of the technique lies in a much broader domain and can easily be extended in designing optimal-sized components and mechanisms. For example, TO can be used to design cladding, mountings, crank, piston, etc.

References

1. Lagaros ND (2014) A general purpose real-world structural design optimization computing platform. *Struct Multidiscip Optim* 49:1047–1066
2. Lagaros ND (2018) The environmental and economic impact of structural optimization. *Struct Multidiscip Optim* 58:1751–1768
3. Gibson I, Rosen DW, Strucker B (2010) *Additive manufacturing technologies: rapid prototyping to direct digital*. Springer, Boston
4. Barbieri SG, Giacomini M, Mangeruga V, Mantovani S (2017) A design strategy based on topology optimization techniques for an additive manufactured high performance engine piston. *Proc Manuf* 11:641–649
5. Bendsøe MP, Kikuchi N (1988) Generating optimal topologies in structural design using a homogenization method. *Comput Methods Appl Mech Eng* 71:197–224
6. Bendsøe MP (1989) Optimal shape design as a material distribution problem. *Struct Opt* 1:193–202
7. Zhou M, Rozvany GIN (1992) DCOC—an optimality criteria method for large systems, Part I: theory. *Struct Opt* 5:12–25
8. Bendsøe MP, Sigmund O (2003) *Topology optimization: theory, methods and applications*. Springer-Verlag, Berlin
9. Sethian JA, Wiegmann A (2000) Structural boundary design via level set and immersed interface methods. *J Comput Phys* 163(2):489–528
10. Wang MY, Wang XM, Guo DM (2003) A level set method for structural topology optimization. *Comput Methods Appl Mech Eng* 192:227–246
11. Xie YM, Steven GP (1993) A simple evolutionary procedure for structural optimization. *Comput Struct* 49:885–896
12. Xie YM, Steven GP (1997) *Evolutionary structural optimization*. Springer, London
13. Rong JH, Tang ZL, Xie YM, Li FY (2013) Topological optimization design of structures under random excitations using SQP method. *Eng Struct* 56:2098–2106

14. Kaveh A, Hassani B, Shojaee S, Tavakkoli SM (2008) Structural topology optimization using ant colony methodology. *Eng Struct* 30(9):2559–2565
15. Tovar A, Khandelwal K (2013) Topology optimization for minimum compliance using a control strategy. *Eng Struct* 48:674–682
16. Huang X, Xie YM (2009) Bi-directional evolutionary topology optimization of continuum structures with one or multiple materials. *Comput Mech* 43(3):393–401
17. Huang X, Zuo ZH, Xie YM (2010) Evolutionary topology optimization of vibrating continuum structures for natural frequencies. *Comput Struct* 88:357–364
18. Huang X, Xie YM, Lu G (2007) Topology optimization of energy absorption structures. *Int J Crashworthiness* 12(6):663–675
19. Huang X, Xie YM (2008) Topology optimization of nonlinear structures under displacement loading. *Eng Struct* 30(7):2057–2068
20. Ghabraie K, Chan R, Huang X, Xie YM (2010) Shape optimization of metallic yielding devices for passive mitigation of seismic energy. *Eng Struct* 32(8):2258–2267
21. Cavazzuti M, Baldini A, Bertocchi E, Costi D, Torricelli E, Moruzzi P (2011) High performance automotive chassis design: a topology optimization based approach. *Struct Multidiscip Optim* 44:45–56. <https://doi.org/10.1007/s00158-010-0578-7>
22. Cavazzuti M, Splendi L (2012) Structural optimization of automotive chassis: theory, set up, design. In: Conference on Problèmes Inverses, Contrôle et Optimisation de Formes 2012, Paris
23. Sudin M, Tahir M, Ramli F, Anuar Shamsuddin S (2014) Topology optimization in automotive brake pedal redesign. *Int J Eng Technol* 6:398–402
24. APWorks (2018) APWorks by Airbus Group, inspired by nature: electric motorcycle goes 3D—combining topology optimization, new materials, and additive manufacturing in the development of the Airbus APWorks light rider results in a revolutionary lightweight design. Altair. Available online at: <https://altair-india.in/RelatedCaseStudy.aspx?id=8707>
25. Stefanos EM, Lagaros ND, Nassiopoulos E (2019) Nested topology optimization methodology for designing two-wheel chassis front. *Built Environ* 5:34. <https://doi.org/10.3389/fbuil.2019.00034>
26. Cossalter V (2006) *Motorcycle dynamics*, 2nd edn, pp 119–122

Extraction of Maximum Electrical Power from Solar Photovoltaic-Based Grid-Tied System



Dhairya Karna, Aditya Vikram, Astitva Kumar, and M. Rizwan

1 Introduction

A majority of residential complexes nowadays include renewable energy resources in integration with a grid of low voltage which are connected to individual receivers in association with a dedicated transmission and distribution network. Therefore, the optimal utilization of renewable energy sources (RES) is gradually becoming a matter of extreme importance so that the increased energy consumption demands can be met and the usage of fossil fuel can be restricted. Taking into notice the variety of RES, each with its own set of boon and bane, one of the major drawbacks of various forms of RES is the uncertainty or fluctuations in the energy generation process which can lead to wearing and tearing of electrical components [1].

Solar photovoltaic (PV) is an influential technology where the PV process of energy generation is completely silent due to absence of movable parts and the energy from the sunlight is directly converted into electrical energy. The PV technology can be used either as an autonomous system in itself or a grid-tied system. In an autonomous system, there is a requirement of battery bank for storage purposes which is sufficient for a low-voltage system but in this scenario of the grid-tied-type system, the extra energy is directly transferred to the grid for external use or other useful purposes. The PV energy generation is highly dependent on quantities like temperature and solar irradiance [1]. Due to various factors, the most challenging hurdle for PV is the irregularities faced during energy generation which has led to its incapability to contest in today's market and this has further led to limit in their use for large-scale grid operations.

D. Karna (✉) · A. Vikram · A. Kumar · M. Rizwan
Department of Electrical Engineering, Delhi Technological University, Delhi, India
e-mail: dhairya_bt2k16@dtu.ac.in

M. Rizwan
Department of Electrical Engineering, College of Engineering, Qassim University, Buraidah,
Kingdom of Saudi Arabia

The difficulty of uncertain and irregular power generated by RES can be solved with the help of a grid-tied system with smart management system. A grid-tied RES system is a type of an electrical system in which one or more than one renewable energy resources are used in association with a storage device and an electric grid. In a global scenario, a country's energy grid network is deliberated similar to a hybrid PV system. Numerous literary articles present a concept of handling a hybrid, autonomous, and grid-tied system with a storage device [2, 3], with use of energy management (EM) and optimization in real-time scenario [1, 4].

This paper suggests the employment of PSO-based fuzzy algorithm for MPPT control to draw out the maximum power that is available at the PV terminals in a grid-tied RES electrical system. In [3, 5], the authors present the concept of smart power extraction for an autonomous PV system, where MATLAB and Simulink were used to create a model for the same, whereas in [2, 6], the authors present an AI-based demand-side management structure for the autonomous PV system. Hence, the primary goal of this paper is implementation and literary overview of the AI optimization via PSO-based fuzzy algorithm in a grid-tied PV system and the use of the optimization method explained as "PSO Fuzzy" for the purpose of balancing irregularities on the generation side of the system and consumption side of the system.

The paper entails five different sections. The effects, use, and advantages of grid-tied system and fuzzy logic and PSO are concisely elucidated in Sect. 2 of this paper. The mathematical modeling of the suggested algorithm for EM is proposed in Sect. 3. Section 4 provides the data for the concurrent testing outcomes, while Sect. 5 comprises of the conclusion of the paper.

2 Grid-Tied PV System

In the current scenario, the grid-tied PV systems consist of a PV array connected to a storage device which is further connected to the local grid which can be utilized for transferring power to the local residential facilities surrounding the test site by trading it directly to the electricity provider in that particular region. Various components that comprise the grid-tied system like the PV panel and the DC-DC boost converter are further explained (Fig. 1).

2.1 PV Panel

The equivalent model for the PV array is shown in Fig. 2, which shows a p-n semiconductor junction, that is essentially the building block of a solar cell [7, 8]. The voltage and current equation for the solar cell for the model presented in Fig. 2 is as follows:

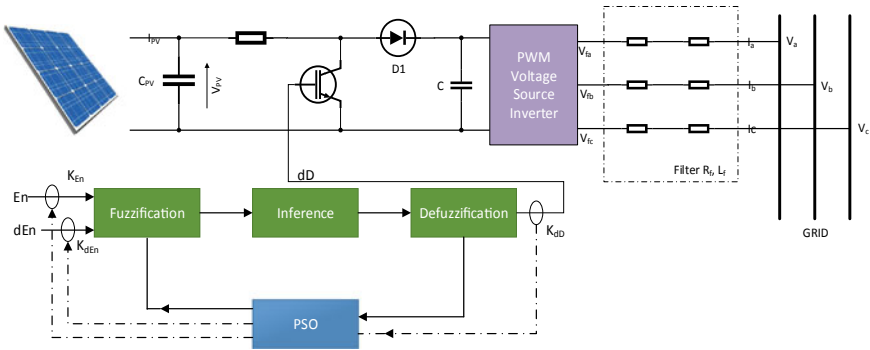


Fig. 1 Grid-tied solar photovoltaic-based system

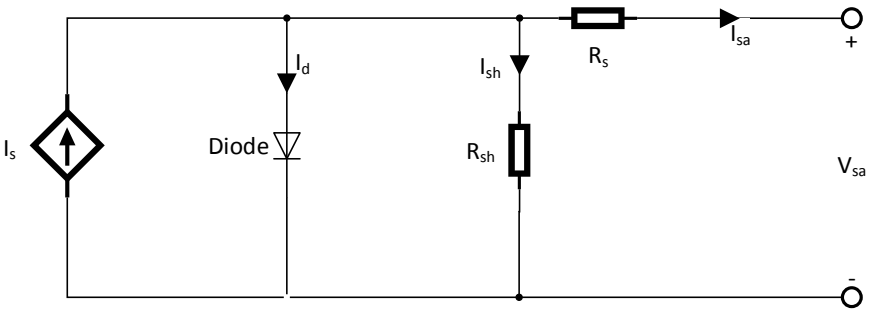


Fig. 2 Equivalent model for a PV cell

$$I_{sa} = I_s - I_o \times \left\{ e^{\left(\frac{V_{sa} + R_s I_{sa}}{m V_T} \right)} - 1 \right\} - \frac{V_s + R_s I_{sa}}{R_{sh}} \tag{1}$$

here the model comprises of I_s and V_s is the current and voltage of the source, respectively, a diode and a resistance R_s , the shunt resistance R_{sh} , the diode current I_o (dependent on temperature), V_{sa} and I_{sa} are the voltage and current being fed to the DC-DC boost converter, m is the ideal factor (ideally $m = 1$, real $m > 1$) and V_T is the thermal potential which is characterized as:

$$V_T = \frac{KT}{q} \tag{2}$$

T is the temperature in Kelvin, K signifies Boltzmann constant ($K = 1.38 \times 10^{-23}$ J/K), and q is electrical charge of an electron ($q = 1.6 \times 10^{-19}$ C). The net voltage V_{sa} and the net current I_{sa} are given by the following formulae:

$$I_{sa} = I_s - I_D \tag{3}$$

Taking into consideration of Fig. 2, it is possible to determine the I-V characteristics of the PV array with N cells in series and M cells in parallel.

$$V_{sa} = \varphi \times V_T \times \ln \left\{ \frac{I_s - I_{sa}}{M \times I_O} + 1 \right\} - R_s I_{sa} \tag{4}$$

where

$$\varphi = M \times N \tag{5}$$

The real solar cell in simple terms can be described by the elementary parameter of the open-circuit voltage and short-circuit current I_{sc} which correlates to the voltage drop across the diode when it is traversed by the diode current I_D which are mentioned in Eqs. (1), (2), (3), (4), and (5). At the test site, $M = 2$ and $N = 2$.

2.2 DC-DC Boost Converter

The dynamic model for the DC-DC boost converter displayed in Fig. 3 can be expressed in terms of current and voltage between output and input as follows:

$$\begin{bmatrix} \frac{di_L}{dt} \\ \frac{dV_{bus}}{dt} \end{bmatrix} = \begin{bmatrix} 0 & -\frac{1-D}{L} \\ \frac{1-D}{C} & -\frac{1}{RC} \end{bmatrix} \begin{bmatrix} i_L \\ V_{bus} \end{bmatrix} + \begin{bmatrix} \frac{1}{L} \\ 0 \end{bmatrix} \cdot V_{in} \tag{6}$$

where I_s is the infused current in the boost converter, L is inductance, and C is capacitance as seen in Fig. 3, D signifies the duty cycle, V_{Bus} is voltage across the bus bar and V_{in} is input voltage. The values of the electrical parameter (L and C) is assumed to be high enough so that the switching device chosen has a smooth current (due to L) and smooth output voltage (due to C).

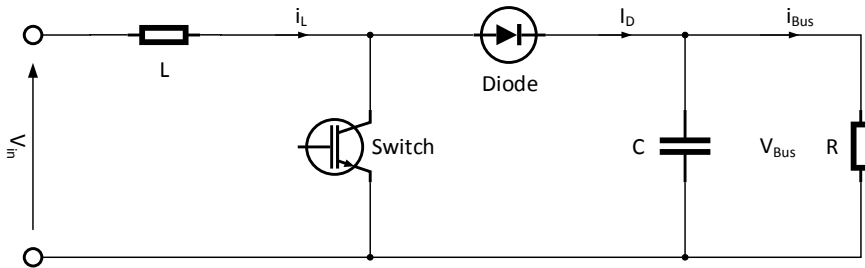


Fig. 3 Simplified DC-DC boost converter

3 Mathematical Model and Flowchart

3.1 Fuzzy Logic for MPPT Controller

Fuzzy logic can be defined as a Boolean logic with further bifurcations in order to take into account a real-time scenario which cannot be represented by normal Boolean logic. The actualization of fuzzy controllers is done in three stages: fuzzification, inference, and defuzzification, respectively [9, 10]. The suggested fuzzy algorithm has been given two inputs (change of error and error) and a single output (duty cycle for the converter). The equations for the two inputs are as follows:

$$E_n(K) = \frac{P_s(K + 1) - P_s(K)}{V_s(K + 1) - V_s(K)} \tag{7}$$

$$dE_n(K) = E(K + 1) - E(K) \tag{8}$$

where the instantaneous power of the solar generator is P_s , the instantaneous voltage of the solar generator is V_s , $E_n(K)$ is the error and $dE_n(K)$ is the change in error input parameter. The output parameter of duty cycle D is given as:

$$dD = \frac{\sum_{i=1}^n \mu(D_i) - D_i}{\sum_{i=1}^n \mu(D_i)} \tag{9}$$

Due to the presence of a single output, Mamdani method for fuzzy logic inference is preferred as well as the defuzzification process employs the center of gravity approach to determine the value of duty cycle D (the output in this scenario) which is computed from Eq. (9). There are various methods for automatic tracking of MPPT. However, fuzzy logic is very convenient to operate upon and is significantly robust than its peers, hence fuzzy logic was used.

The fuzzy inference rules table is given in Table 1 while the membership function graph for the input E_n/dE_n and output dD is represented in Fig. 4 [11].

Table 1 Fuzzy inference rule table

E_n dE_n	Negative big (NB)	Negative small (NS)	Zero (Z)	Positive small (PS)	Positive big (PB)
NB	Z	Z	PB	PB	PB
NS	Z	Z	PB	PB	PB
Z	PS	Z	Z	Z	NS
PS	NS	NS	NS	Z	Z
PB	NB	NB	NB	Z	Z

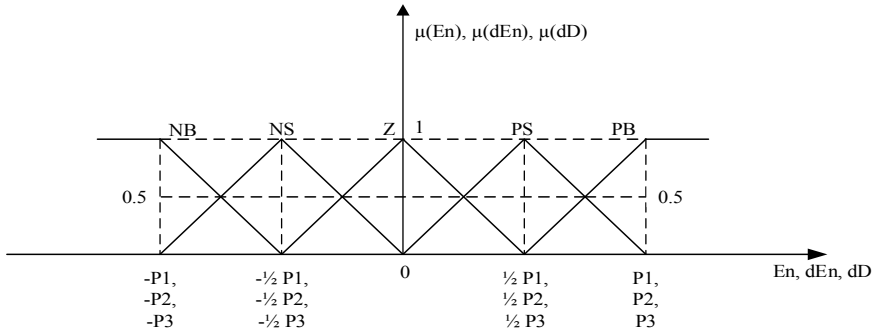


Fig. 4 Membership function for input E_n/dE_n and output dD

3.2 Particle Swarm Optimization

Developed by Kennedy and Eberhart in 1995 [10], PSO is an evolutionary technique used for computation. It is highly efficient for problems related to optimization, specifically related to multiple dimensions, non-differentiable and nonlinear-related problems [11]. N particles are considered in a search space D for the purpose of minimization of the objective function f . Every particle is initialized with a value of position and velocity which can be calculated by the following equations.

$$v_{i,j}^{k+1} = w \left\{ v_{i,j}^k + c_1 \text{rand}_1 \left(x_{\text{pbest},i,j}^k - x_{i,j}^k \right) + c_2 \text{rand}_2 \left(x_{\text{gbest},j}^k - x_{i,j}^k \right) \right\} \quad (10)$$

$$x_{i,j}^{k+1} = x_{i,j}^k + v_{i,j}^{k+1} \quad (11)$$

$$w = \frac{2}{\left| 2 - C - \sqrt{C^2 - 4C} \right|} \quad (12)$$

$$C = C_1 + C_2 \quad (13)$$

where x_i is the position vector, v_i is the position vector, $x_{\text{pbest},i}$ is the local best position vector, x_{gbest} is the global best position vector, rand_1 and rand_2 are random constants between $[0, 1]$ which are evenly distributed after each update in velocity, c_1 and c_2 are the positive learning rate constants between $(0, 2.05]$, [12] w is the constriction factor, D is the search space, and j is a number where $j \in \{1, \dots, D\}$. The values of $x_{\text{pbest},i}$ and x_{gbest} are computed after every iteration by the following equations:

$$x_{\text{Pbest},i}^{k+1} = \begin{cases} x_{\text{pbest},i}^k & \text{if } f(x_i^{k+1}) \geq x_{\text{pbest},i}^k \\ x_i^k & \text{otherwise} \end{cases} \quad (14)$$

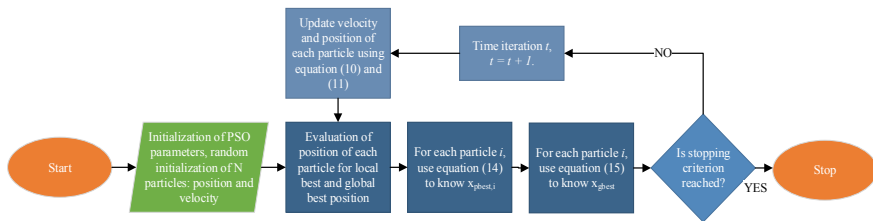


Fig. 5 Algorithm for PSO

$$x_{gbest}^{k+1} = \min_{pbest,i} f(x_{pbest,i}^{k+1}), \quad 1 \leq i \leq N \tag{15}$$

After every iteration, the value of k is restricted between $[x_{min}, x_{max}]$, in the case of violation in values of the limits as specified the following equation forces the proper values into place [10].

$$x_i = \begin{cases} x_{min} & \text{if } x_i < x_{min} \\ x_i & \text{if } x_{min} < x_i < x_{max} \\ x_{max} & \text{if } x_i > x_{max} \end{cases} \tag{16}$$

When such changes in the position vector are implemented then the i th particle is forced to hunt for its global best and its local best, i.e., x_{gbest} and $x_{pbest,i}$ respectively (Fig. 5).

3.3 Fuzzy PSO Tuning

The practical application of the fuzzy controller logic in real-time scenario is only plausible when the parameter of the controller is properly regulated. Additionally, a risk is involved by early allocation of a randomly selected parameter which can lead to instability in the system. Therefore, during the time of simulation as well as during practical application, a close to real model of the grid-tied PV system is absolutely necessary for the successful completion of the procedure. Hence, the design for the fuzzy tuning before going online is presented in Fig. 1, where the controllers $P_1, P_2, P_3, K_{E_n}, K_{dE_n}$ and K_{dD} are used for the purpose of minimizing the fitness function whose equation is as follows:

$$f(k) = \sum_{i=1}^N |e(i)| \tag{17}$$

$$e(i) = P_{max} - P_s \tag{18}$$

where $f(k)$ is the fitness function, the maximum power for the solar generator is P_{\max} , total amount of samples is N , k is iterations. For the initial population, the regulated parameter set is distributed according to the limits as follows for every particle.

$$0.01 < P_1, P_2, P_3 < 1 \text{ and } 0.001 < K_{E_n}, K_{dE_n}, K_{dD} < 100 \quad (19)$$

4 Results and Discussion

The implementation of the PSO-based fuzzy algorithm is performed on a PC in Python, while the simulations were performed on the MATLAB/Simulink system. The scheduled timeline for simulation data, as well as for practical implementation, was of 15 days from mid-December 2019 to January 2020. The simulation and practical applications were carried out in irradiance level changing from 120 to 500 W/m². The grid-tied PV system is optimized with $c_1 = c_2 = 2.05$ and starting with a population size of 40 particles with 40 iterations using PSO-based fuzzy algorithm. The PV panel rating (for 1000 W/m², 25 °C) is given in Table 2. The data received after the PSO-based fuzzy process successful implementation is shown in Table 3. The graphs of irradiance (in W/m²), temperature (in °C), power and current from the PV generator of the PSO-based fuzzy algorithm for MPPT control for the grid-tied PV system are displayed in Figs. 6, 7, 8, and 9, respectively. The graphs for PV power and current are the values of 1 out of the 4 panels installed at the test site whereas Table 2 contains the data for all of the 4 panels ($M = 2$ and $N = 2$ as seen in Eq. (5)).

Table 2 Specifications of solar PV module (PM-0250 photon energy systems)

Description	Value
Type	Polycrystalline
Maximum power of module	250 Wp
Open-circuit voltage of module	37.05 V
Short-circuit current of module	8.58 A
Maximum power voltage of module	30.74 V
Maximum power current of module	8.15 A
Output tolerance of module	±2%

Table 3 Data after successful implementation (all the 4 modules)

Date	Voltage (V)	Current (A)	Radiation (W/m ²)	E-generated (KJ)	E-loss (KJ)	Consumption (W)
16/12	237.273	1.197	414	227.388	42.28	467.075
17/12	238.720	1.194	294	231.703	42.28	468.539
18/12	239.365	1.192	900	237.549	42.20	468.226
19/12	237.326	1.203	616	243.336	42.08	470.452
20/12	235.608	1.204	630	249.954	41.94	467.227
23/12	230.306	1.227	422	255.802	41.74	469.514
24/12	238.507	1.196	748	262.771	41.70	467.894
26/12	233.104	1.221	432	267.572	41.64	471.490
27/12	231.685	1.223	606	274.21	41.60	470.200
30/12	238.895	1.198	234	279.834	41.55	470.358
31/12	234.622	1.219	440	284.255	41.54	473.553
01/01	247.102	1.183	550	290.714	41.54	474.814

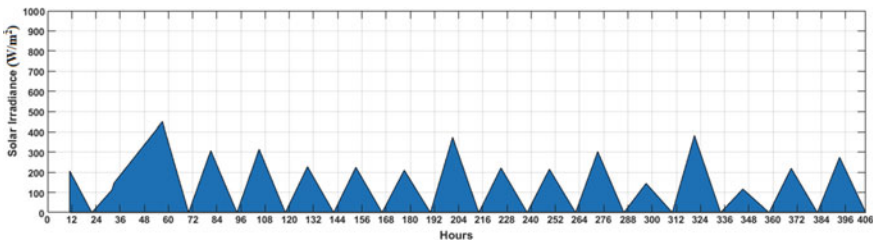


Fig. 6 Graph of solar irradiance (W/m²) in the scheduled period

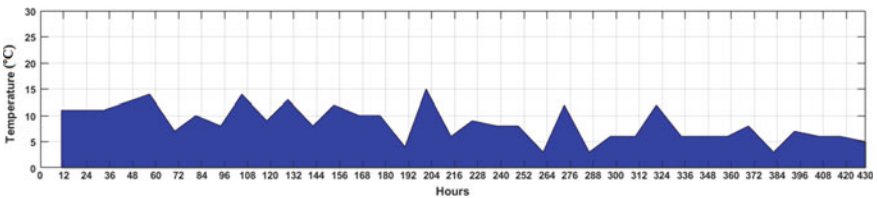


Fig. 7 Graph of temperature (in °C) in the scheduled period

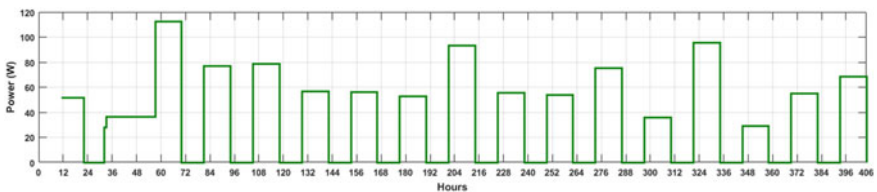


Fig. 8 Graph for photovoltaic generator power in the scheduled period (1 of the 4 modules)

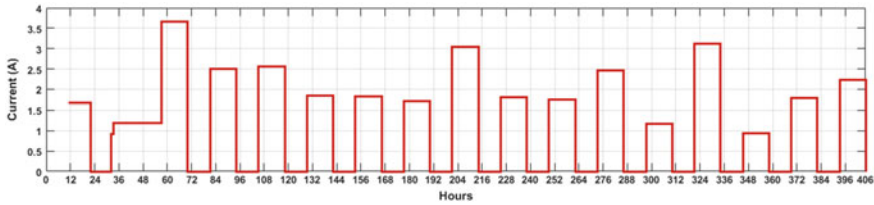


Fig. 9 Graph for photovoltaic generator current in the scheduled period (1 of the 4 modules)

5 Conclusion

In this paper, a PSO-based fuzzy algorithm was used for the purpose of MPPT control to draw out the maximum power that is available at the PV terminals of a grid-tied PV system at the testing facility in Delhi with integration of a storage device as well as local electricity grid. The findings clearly state that the aim of smart control of MPPT in the partially shaded condition and optimization of generated and consumed data was successfully achieved. The simulation in MATLAB/Simulink and practical application via Python/MATLAB provides the verification about the capabilities of the proposed structure for SEM. The results of various MPPT algorithms vary drastically in a situation where partial shading is present and the PV module does not receive a uniform solar irradiance. Due to the partial shading, the PV characteristics for the complete PV array turn more complicated having numerous peaks. Hence, a necessity arises for efficient tracking for the global maximum point and the need for an improved MPPT algorithm. To overcome these challenges, the use of fuzzy PSO takes into account variables like irradiance and temperature (of cell) which assisted in MPPT even in partial shading conditions. This can be seen from extreme variations in irradiance and temperature values and its slight effect on generated and consumed energy. The data was received using a smart energy meter having functionality of automatic data logging at programmable interval of time. From the observed partially shaded PV array, it can be easily stated that the power as well as current for the PV generator are not only dependent on irradiance and temperature but also dependent on array arrangement and pattern of shading. Furthermore, utilization of the same resource in a large-scale controller and system as well as integration into specified software library of the programming language (microgrid PSO Master Python library) is proposed.

References

1. Singh AK, Idrisi AH (2020) Evolution of renewable energy in India: wind and solar. *J Inst Eng India Ser C* 101:415–427
2. Karna D, Vikram A, Kumar A, Rizwan M (2020) A novel fuzzy based intelligent demand side management for automated load scheduling. In: 2020 4th international conference on green energy and applications (ICGEA), Singapore, pp 171–175

3. Kumar A, Rizwan M, Nangia U (2020) A hybrid intelligent approach for solar photovoltaic power forecasting: impact of aerosol data. *Arab J Sci Eng* 45:1715–1732
4. Vikram A et al (2020) *IOP Conf Ser Mater Sci Eng* 946:012007
5. Jagadish, Ray A (2015) Multi-objective optimization of green EDM: an integrated theory. *J Inst Eng India Ser C* 96:41–47
6. Wai R-J, Jhung S-J, Liaw J-J, Chang Y-R (2013) Intelligent optimal energy management system for hybrid power sources including fuel cell and battery. *IEEE Trans Power Electron*
7. Menadi A, Abdeddaim S, Ghamri A, Betka A (2015) Implementation of fuzzy-sliding mode based control of a grid connected photovoltaic system. *ISA Trans* 586–594
8. Boumaaraf H, Talha A, Bouhali O (2015) A three-phase NPC grid-connected inverter for photovoltaic applications using neural network MPPT. *Renew Sustain Energy Rev* 1171–1179
9. Eberhart RC, Kennedy J (1995) A new optimizer using particle swarm theory. In: *The sixth international symposium on micro machine and human science, Nagoya*, pp 39–43
10. Chang W-D, Shih S-P (2010) PID controller design of nonlinear systems using an improved particle swarm optimization approach. *Commun Nonlinear Sci Numer Simul* 15:3632–3639
11. Borni A, Abdelkrim T, Zaghba L, Bouchakour A, Lakhdari A, Zarour L (2017) Fuzzy logic, PSO based fuzzy logic algorithm and current controls comparative for grid-connected hybrid system. *AIP Conf Proc* 1814
12. Bingül Z, Karahan O (2011) A fuzzy logic controller tuned with PSO for 2 DOF robot trajectory control. *Expert Syst Appl* 38:1017–1031

Power System Service Restoration Methods—A Study



Prapti Rastogi, Neeraj Kanwar, and Samarendra Pratap Singh

1 Introduction

The infrastructure of the power system is changing worldwide. As we can see the increasing bulkiness and intricacy of the distribution system, it has become a necessity to automate it for legitimate checking and controlling. Among the various strategies, service restoration is the method utilized to provide the power to the faulty region of the system which gets separated after an event of fault. The strategies have been varying widely to adapt the varying nature of the power system. With the implementation of the advanced metering, infrastructure as well as distribution automation (DA), self-recuperating is a fundamental aspect to improve the flexibility of distribution systems. After occurrence of a fault, the network operator of distribution system executes a self-healing plan itself to find and limit the fault and to re-establish power supply to out-of-service segments. Self-healing of the distribution systems is an idea that enables identification and isolation of the faulty part of the system and the restoration of service to the end-users provided by healthy parts of the system. This process might be led with practically no human involvement and has the goal of limiting interferences of the service and keeping the system away from further degradation of system quality. Power systems self-healing is directed through DA that limits the affected clients during contingency situations by automatic isolation of faulty region and connecting clients to an alternate supply when their regular source has been disoriented.

An extensive difference has been found in different methods used for service restoration. With reference to communication configuration, the different service restoration approaches are broadly classified in:

P. Rastogi · N. Kanwar (✉) · S. P. Singh
Department of Electrical Engineering, Manipal University, Jaipur, India

S. P. Singh
e-mail: samarendra.singh@jaipur.manipal.edu

1. Centralized approach
2. Distributed approach
3. Hierarchical approach

In these approaches, various methods are used to obtain solutions for restoration which include metaheuristic algorithms, mathematical programming, expert systems (ES), heuristic rules, multi-agent systems (MAS), and graph theory. Each of these methods has its benefits and limitations. In this paper, different techniques that are available for restoration of service are reviewed and presented.

2 Methods of Service Restoration

When the out-of-service portion is brought in isolation, the areas which are not functioning beyond the portion in fault are re-established promptly. These areas are restored using following techniques of restoration [1]:

- (1) Centralized approach: The decision-making is done by the agents through proper communication with a central controller with the help of overall system information.
- (2) Decentralized approach: The decision-making is done by the agent on the basis of local information, and no communication happens among them.
- (3) Distributed approach: The decision-making is done without central controller by the agents through proper communication with neighbors.
- (4) Hierarchical approach: The decision-making is completed in hierarchical way by the agents.

Service restoration can be performed in two ways which can be categorized as service restoration with communication system and service restoration without communication system. Methods of service restoration with communication system proposed by different authors are as follows.

2.1 Expert System

ES has three main parts [2]

- Information base
- Database
- Inference engine

The domain knowledge is included in information base that is used to solve the problem. It is interpreted as rules, e.g., if (condition) and then (action) rules. The database includes factual information to match the rules with the information base.

In [3], authors created an information base which had 180 guidelines obtained from the literature and by meeting with different power engineers. These guidelines can be implemented by the operators of system for planning a restoration scheme. The system can re-establish the service with single-zone or multi-zone restoration plans. To make the system more resilient, the guidelines for reduction in line losses are included in the system. An ES is created in [4] utilizing object-oriented programming procedure which arranges feeder design information into a chain of command form and enhances the execution of the inference. In [5], an ES is created on the basis of colored Petri Net (CPN) model. The elements of the system like switches are modeled using CPN and rules which are used on the network are used to create strategies for restoration. As the CPN possess parallel like inference qualities, it helps in finding strategies to restore the service in case of multiple fault occurrences. In [6], objectives such as detection of fault, restoration, and three inference engines are used by proposed ES.

2.2 *Heuristic Algorithm*

The methodology is dependent on heuristic algorithms additionally utilizes heuristics to acquire solutions. The heuristics are changed into algorithms to control searching of solution. The heuristic restoration strategy is converted into an algorithm in [7] where loads which get de-energized are restored right off by supporting feeders. It is followed by corresponding supporting laterals so as to decrease switching action. In [8] every single available switch, aside from those switches open for fault isolation are shut to create a meshed network. The switch passing on the least current is eliminated with one network loop with the objective that the power flow disturbance is limited. This procedure is repeated until a radial network with healthy operating conditions is obtained and a multi-tier heuristic algorithm is created.

To manage expressions which are not precise of heuristic standards and, uncertainty of load, the fuzzy set theory is utilized. In [9], fuzzy cause-effect networks are proposed for service restoration of distribution systems. In [10], fuzzy variables are utilized to model the uncertain nature of the load with the help of previous patterns of load of different consumers and days. After that, the procedures mentioned in [7] are utilized to find restoration solutions.

2.3 *Graph Theory*

A distribution network includes substations and load zones interconnected with each other using switches. If these substations and load areas are considered as vertices and the switches are considered as edges, the system can be presented as a graph. Therefore, service restoration issue is assumed to be a problem in searching for spanning trees which represents a radial network while fulfilling operation constraints.

In [11], new configurations are created on the basis of a graph theory-based heuristic method. To obtain spanning tree, a single edge can be eliminated from the fundamental loop. The feasibility of all acquired configurations is checked using power flow study while satisfying all operational constraints. It is likewise led to locate the best configuration according to the specific criteria. Heuristic algorithms dependent on decision trees are also proposed for service restoration in [12], and it develops the solution area as a tree and utilizes various searching strategies for looking through the tree. A theory based on the cut set concept for spanning tree searching calculation was given in [13], in that switch pairs are worked on to produce a new tree and flow of power calculations are performed to access every newly obtained tree. In [14], an “interested tree” concept is proposed to represent a tree in which every load is delivered by substations. An algorithm is created to search for all such trees from spanning trees which satisfies the operational constraint.

2.4 Mathematical Programming

This method has been utilized in [15–17] to take care of restoration issues as indicated by the solution requirements, i.e., the optimality and computation time. The restoration issue can be figured as mixed integer (MI) type models such as MI nonlinear programming model, MI linear programming model, and MI second-order cone programming model.

In [18], a two-phase plan is presented in which the target configuration is found using genetic algorithm (GA) in the first phase and the optimal switching operation sequence is determined by using dynamic programming (DP) method in the second phase. In [19], the DP is utilized to decide the arrangement of feeders in out-of-service regions for reducing the energy which could not be provided during the time of restoration. The mathematical programming-based methodologies can give a point by point presentation of the restoration issue in detail.

2.5 Metaheuristic Algorithms

The service restoration problem can likewise be resolved using metaheuristic techniques. These techniques use knowledge perceived from natural phenomena to infer solutions. These are comparable techniques with different searching and encoding procedures. Several metaheuristic algorithms are explored for service restoration problem like GA, particle swarm optimization, tube search, and parallel simulated annealing. Some meta-technique algorithms were compared in [20] for average time of calculation and solution quality. From the comparative analysis, the reactive TS algorithm is found to be best choice as it gives optimal solution with less time taken for computation. In [21], an interactive fuzzy fulfilling technique combined with the theory of fuzzy sets and GA to manage multifaceted nature of service restoration was

Table 1 Comparison of different centralized approaches

Centralized approaches	Features
ES	Maintenance at large scale when applied for practical ES is costly, and it is not easy to construct a huge knowledge base
Heuristics	Difficult to maintain the system because of the software being large and intricate
Graph theory	Difficult to maintain the system because of the extensive searching, the trees numbers might be very large for a huge network, subsequently creating the method complex
Mathematical programming	This may have substantial calculation and maintenance burdens because of the expanding size and the intricacy of the system. Often the time taken for finding the solution exceeds the allotted computational time when it is used for large scale
Metaheuristics	It requires extensive computational time when applied on large system. To calculate the objective function numerical values and to satisfy different constraints, a power flow engine is required

proposed. The multiple aspect values are assigned by their membership functions and then decisions-maker assigns the [0, 1] value for every target. At that point, GA is utilized to discover the solutions whose values nearly match the present values. At last, as indicated by level of satisfaction of the obtained solution, the satisfied values can be put again by the decision maker to obtain other solutions.

2.6 Hybrid Approaches

Several research proposed hybrid techniques to influence the benefits of various combined strategies. In [22], the ES first divides the entire system into a few sub-networks, and at last, each one is planned as a MILP model. The strategy created with a combination of fuzzy logic and heuristic rules with optimization technique gives a better competence and powerful results as shown in [23].

A comparison of different centralized approaches is presented in Table 1.

2.7 Decentralized Method

The centralized techniques take care of the service restoration issue from a centralized perspective. They require a controlling core that has an expensive processing ability and can transfer a lot of information. Moreover, centralized strategies endure a risk of failure, even a single failure will cause severe power outages and will give heavy computational burdens. A MAS has three kinds of agents such as switch, load,

and generator agents in [24]. The agents can access the local information and then communicate it with other nearby agents.

MAS coordinates and communicates to tackle the issues as per determined heuristic-based rules. Every agent can get and respond to changes in its environment independently. Other than service restoration, MASs are also been utilized in the literature for other applications. As given in [25], strategy for restoration is considering the vehicle-to-grid (V2G) feature of electric vehicle. It has some agents, which are load, aggregator, DG, etc. After accepting restoration demands from the load agents, the accessible V2G power will be utilized by the aggregator agents to re-establish service locally.

The methodologies based on MAS can realize distributed execution and obtain optimal solutions. However, the process of decision-making is based on certain basic heuristic guidelines, which do not ensure the solution optimality.

3 Conclusions

This paper presents a literature review on different approaches used for service restoration of distribution networks. Two techniques are generally referred to solve this problem, i.e., without and with communication framework. The restoration approaches without communication frameworks include smart switches-dependent feeder automation, relay protection, automatic control for reclosing, automatic backup switching control. These methodologies can promptly re-establish the connection to the end-users based on the predefined operation logic but it is not easy to coordinate in intricate circumstances. The restoration techniques with communication systems can be arranged as centralized, distributed, and hierarchical approach. Among them, various strategies are utilized to acquire restoration including expert system, heuristic, mathematical programming, metaheuristic techniques, graph theory, etc.

There is a huge change in the approaches utilized for restoration of power from conventional strategies to artificial intelligence-based strategies. The utilization of the intelligence in restoration of service has given us results like resilience enhancement, reduction in losses, and less time requirement to restore services. The successful implementation of restoration plans depends also on the different hardware components used in the system. The devices utilized presently should be upgraded to manage up with algorithms of restoration. Moreover, efficient and a resilient two-way data communication is required for a reliable delivery of communication information.

References

1. Molzahn DK, Dorfler F, Sandberg H et al (2017) A survey of distributed optimization and control algorithm for electric power systems. *IEEE Trans Smart Grid* 8(6):2491–2962

2. Srivastava S, Butler-Burry KL (2006) Expert-system method for automatic reconfiguration for restoration of shipboard power systems. *IEE Proc Gener Transm Distrib* 153(3)
3. Liu CC, Lee SJ, Venkata SS (1988) An expert system operational aid for restoration and loss reduction of distribution systems. *IEEE Trans Power Syst* 3(2)
4. Tsai MS (2008) Development of an object-oriented service restoration expert system with load variations. *IEEE Trans Power Syst* 23(1)
5. Chen C, Lin C, Tsai HY (2011) A rule-based expert system with colored petri net models for distribution system service restoration. *IEEE Trans Power Syst* 17(4)
6. Hotta K, Nomura H, Takemoto H et al (1990) Implementation of a real-time expert system for a restoration guide in a dispatching center. *IEEE Trans Power Syst* 23(4)
7. Hsu Y, Huang H, Kuo H et al (1992) Distribution system service restoration using a heuristic search approach. *IEEE Trans Power Delivery* 7
8. Shirmohammadi D (1992) Service restoration in distribution networks via network reconfiguration. *IEEE Trans Power Delivery* 7(2):952–958
9. Huang CM (2003) Multi-objective service restoration of distribution systems using fuzzy cause-effect networks. *IEEE Trans Power Syst* 18
10. Kuo H, Hsu YY (1993) Distribution system load estimation and service restoration using a fuzzy set approach. *IEEE Trans Power Delivery* 8(4)
11. Drayer E, Kechagia N, Hegemann J et al (2018) Distributed self-healing for distribution grids with evolving search space. *IEEE Trans Power Delivery* 33(4):1755–1764
12. Wu J, Tomsovic KL, Chen C (1991) A heuristic search approach to feeder switching operations for overload, faults, unbalanced flow and maintenance. *IEEE Trans Power Delivery* 6
13. Liu J, Cheng H, Li Q (2003) Feeder automation based on recloser and voltage-current mode pole-mounted switches. *Autom Electr Power Syst* 27
14. Sarma NDR, Prasad VC, Rao KSP et al (1994) A new network reconfiguration technique for service restoration in distribution networks. *IEEE Trans Power Delivery* 9
15. Romero R, Franco JF, Leão FB et al (2016) A new mathematical model for the restoration problem in balanced radial distribution systems. *IEEE Trans Power Syst* 31
16. Lopez JC, Franco JF, Rider MJ et al (2018) Optimal restoration/maintenance switching sequence of unbalanced three-phase distribution systems. *IEEE Trans Smart Grid* 9(6)
17. Cavalcante PL, Lopez JC, Franco JF et al (2016) Centralized self-healing scheme for electrical distribution systems. *IEEE Trans Smart Grid* 7(1):145–155
18. Carvalho PMS, Ferreira LAFM, Barruncho LMF (2007) Optimization approach to dynamic restoration of distribution systems. *Electr Power Energy Syst* 29
19. Perez-Guerrero R, Heydt GT, Jack NJ, Keel BK, Castelhana AR (2008) Optimal restoration of distribution systems using dynamic programming. *IEEE Trans Power Delivery* 23(3)
20. Toune S, Fudo H, Genji T et al (2002) Comparative study of modern heuristic algorithms to service restoration in distribution systems. *IEEE Trans Power Delivery* 17(1)
21. Hsiao YT, Chien CY (2000) Enhancement of restoration service in distribution systems using a combination fuzzy-GA method. *IEEE Trans Power Syst* 15(4)
22. Nagata T, Sasaki H, Yokoyama R (1995) Power system restoration by joint usage of expert system and mathematical programming approach. *IEEE Trans Power Syst* 10(3)
23. Zhou Q, Shirmohammadi D, Liu WHE (1997) Distribution feeder reconfiguration for service restoration and load balancing. *IEEE Trans Power Syst* 12(2)
24. Solanki JM, Khushalani S, Schulz NN (2007) A multi-agent solution to distribution systems restoration. *IEEE Trans Power Syst* 22(3)
25. Sanches DS, London Jr JBA, Delbem ACB (2014) Multiobjective evolutionary algorithm for single and multiple fault service restoration in large-scale distribution systems. *Electr Power Syst Res* 110

A Study on Implementation of Various Approaches for Shop Floor Management



Varun Tripathi, Suvandan Saraswat, and Girish Dutt Gautam

1 Introduction

In today's competitive environment, developing a quality, effective product has become a challenging task. At present, several methods are used by industries to reduce the cost of production and production time. These methods are known as the process optimization approaches in technical language. These mainly include lean manufacturing (LM), kaizen (K), total quality management (TQM), and six sigma (SS) [1, 2]. These approaches are implemented to optimize the production processes in the industries and eliminate wastes. From the research work done so far, it was concluded that all these wastes were generated for some reason. Due to which the efficiency of the production system was adversely affected, and as a result, productivity decreased, and production cost increased. Process optimization techniques were implemented to identify and eliminate these causes. The result of research works revealed that improvements in productivity and product quality were achieved, as well as a reduction in production costs. Figure 1 shows the objectives of shop floor management.

2 Literature Review

Shop floor management approaches are used for maximization of productivity level within limited constraints [3–7]. LM, K, TQM, and SS have been implemented as

V. Tripathi

Accurate Institute of Management and Technology, Greater Noida, India

S. Saraswat

JSS Academy of Technical Education, Noida, India

G. D. Gautam (✉)

Mangalmay Institute of Engineering and Technology, Greater Noida, India



Fig. 1 Aim of shop floor management

shop floor management approaches in worldwide industries. This approach includes several techniques as shown in Fig. 1. It has revealed in previous research work that the selection of shop floor management approaches mainly depended on the type of problem in the industry. The literature review found that of discussed optimization techniques, lean is a technique that has been mostly favoured by the industry’s shop floor management system as it is competent in improving any production situation, and its implementation has led to a high level of improvement in production. Lean and other optimization techniques have been implemented to eliminate the waste present in production [2]. The selection of shop floor management approaches depends on several factors. The significant factors are shown in Fig. 2.

In the present study, an analysis was conducted on the causes of waste generated in the production and the appropriate approach for their elimination, and the results obtained from the analysis are shown in Table 1.

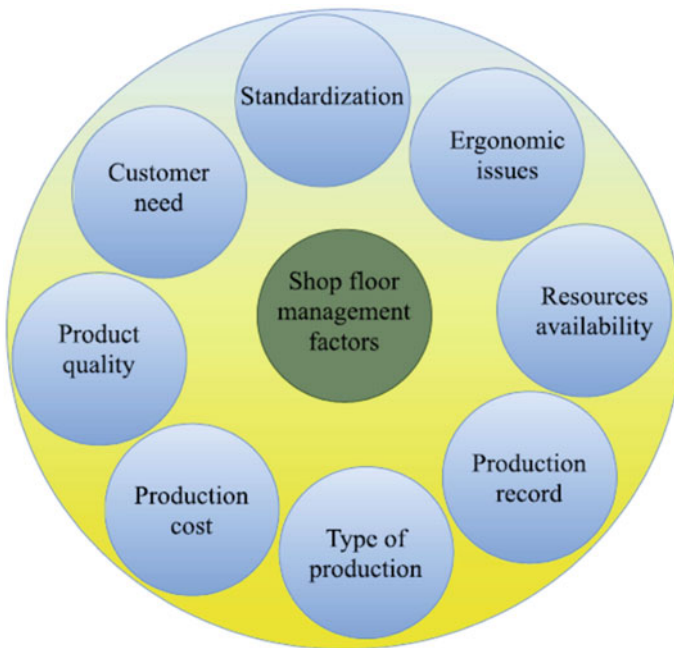


Fig. 2 Factors required in the selection of shop floor management approaches

Table 1 Selection of approaches according to the reason of wastes

S. No.	Reason of non-value-added activities	A suitable approach for shop floor management			
		LM	K	TQM	SS
1	Lack of production record	✓			
2	Uncertainty in objective	✓			
3	Lack in quality control	✓	✓	✓	✓
4	Excess inventory	✓	✓		
5	Defects in product design				✓
6	Lack in standard	✓			
7	Communication gap	✓		✓	
8	Automation failure	✓		✓	✓
9	Careless worker		✓	✓	
10	Unplanned work	✓	✓		
11	Absentees	✓		✓	
12	Higher downtime	✓		✓	
13	High setup time	✓	✓		
14	Unskilled worker			✓	
15	Poor layout	✓			
16	More distance between work stations	✓			
17	Disorganized machineries	✓	✓		
18	Human error	✓	✓		✓
19	Non standardized working			✓	✓
20	Ineffective production control system	✓		✓	✓
21	Improper work load distribution	✓		✓	
22	Lack of training			✓	
23	Lack in resources utilization	✓	✓	✓	

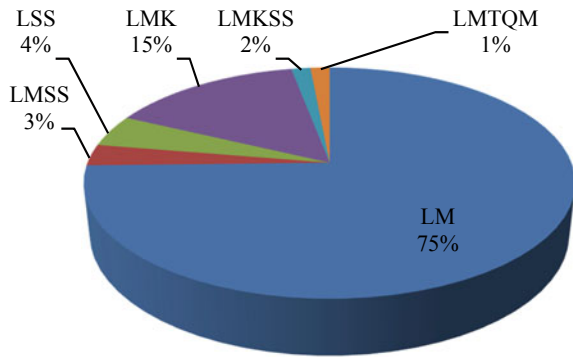
2.1 Implementation of Approaches for Shop Floor Management

A total of 70 papers are analyzed to identify approaches that have implemented for shop floor management. These approaches implementation are categorized in six forms. Table 2 shows the implementation of the shop floor management approaches in previous research work. Figure 3 shows the number of papers according to approach implementation.

Table 2 Shop floor management approaches and previous research works

S. No.	Shop floor management approach	References
1.	LM	[4–50]
2.	LM, six sigma (LMSS)	[3, 11]
3.	Lean six sigma (LSS)	[51–53]
4.	LM, kaizen (LMK)	[5, 54–62]
5.	LM, kaizen, six sigma (LMKSS)	[63]
6.	LM, total quality management (LMTQM)	[64]

Fig. 3 Approaches implementation in research work



2.2 Improvement Achieved in Factors of Shop Floor

To get rid of production problems, the production team is discussed the production planning before production starting and an efficient approach are chosen [8–10, 54, 64, 65]. By analyzing previous research work, it was found which factors were improved by implementing approaches in the industry and which approach has been most effective in improving shop floor management. The results obtained from the shop floor management approach were analyzed from a comprehensive review and described in Table 3.

3 Result and Discussion

From an extensive review, it has been revealed that the selection of the approaches for improvement in shop floor management has been the subject of research over the past several decades. The purpose of this paper is to provide an approach to shop floor management as demand for an efficient approach is increasing in world-wide industries. Table 1 shows a summary of implemented approaches according to the reason for non-value-added activities. Table 2 shows the implementation of

Table 3 Improvement in factors by implementation of shop floor management approaches (Y means improvement and X means reduction)

S. No.	Author and references	Improved factors						Shop floor	Resource utilization	Productivity	Setup time	Work in progress
		Ergonomic issues	Product quality	Production parameter (cycle time, takt time, lead time, idle time, non-value-added time)	Production cost							
1	Alhuraish et al. [3]	Y	Y	X	X			Y				
2	Esa et al. [4]			X	X			Y				
3	Rohani and Zahraee [5]			X	X			Y				
4	Mwanza and Mbohwa [6]			X	X			Y				
5	Choomlucksana et al. [7]	Y		X	X			Y				
6	dos Santos et al. [8]	Y	Y	X	X		X	Y		X	Y	
7	Rahani and Al-Ashraf [54]		Y	X	X			Y				
8	Noor et al. [64]			X	X			Y				
9	Rahman et al. [9]			X	X							
10	Dotoli et al. [10]			X	X							
11	Gupta et al. [65]	Y		X	X			Y		X		

(continued)

Table 3 (continued)

S. No.	Author and references	Improved factors												
		Ergonomic issues	Product quality	Production parameter (cycle time, takt time, lead time, idle time, non-value-added time)	Production cost	Shop floor	Resource utilization	Productivity	Setup time	Work in progress				
12	Timans et al. [11]			X	X									
13	Östlin and Ekholm [12]			X	X				Y					
14	Motwani [13]			X	X									
15	Vinodh et al. [14]			X	X						Y			
16	Solding and Gullander [15]			X	X						Y			
17	Singh and Sharma [16]	Y		X	X						Y			
18	Tripathi and Sarswat [17]	Y	Y	X	X				Y		Y			
19	Tripathi and Sarswat [18]	Y	Y	X	X				Y		Y			
20	Masuti and Dabade [19]			X	X						Y			
21	Deshkar et al. [20]			X	X				Y		Y			

(continued)

Table 3 (continued)

S. No.	Author and references	Improved factors								
		Ergonomic issues	Product quality	Production parameter (cycle time, takt time, lead time, idle time, non-value-added time)	Production cost	Shop floor	Resource utilization	Productivity	Setup time	Work in progress
22	Roriz et al. [21]			X	X	Y	Y		X	
23	Antosz and Stadnicka [22]		Y	X	X					Y
24	Gupta et al. [23]	Y	Y				Y			Y
25	Garre et al. [24]			X	X	Y	Y		X	
26	Morales Méndez and Rodríguez [25]				X		Y			Y
27	Ferreira et al. [26]									
28	Srimivasan et al. [27]	Y		X		Y				Y
29	Ali Naqvi et al. [28]			X	X	Y	Y			
30	Thomas et al. [51]		Y	X	X	Y				
31	Tripathi et al. [29]			X	X		Y			Y

(continued)

Table 3 (continued)

S. No.	Author and references	Improved factors							Work in progress	
		Ergonomic issues	Product quality	Production parameter (cycle time, takt time, lead time, idle time, non-value-added time)	Production cost	Shop floor	Resource utilization	Productivity		Setup time
32	Venkat Jayanth et al. [30]		Y	X		Y	Y	Y		
33	Shou et al. [31]									
34	Sivaraman et al. [55]	Y			X		Y	Y		
35	Amrani and Dueq [32]		Y	X	X					Y
36	Sutharsan et al. [33]		Y	X	X			Y		
37	Mohan Prasad et al. [56]			X		Y		Y		Y
38	Balamurugan et al. [34]			X		Y	Y	Y		
39	Gopi et al. [35]			X				Y		Y
40	Masuti and Dabade [57]			X	X		Y			Y

(continued)

Table 3 (continued)

S. No.	Author and references	Improved factors									
		Ergonomic issues	Product quality	Production parameter (cycle time, takt time, lead time, idle time, non-value-added time)	Production cost	Shop floor	Resource utilization	Productivity	Setup time	Work in progress	
41	Mundra and Mishra [52]				X				Y		
42	Suhardi et al. [58]			X					Y		
43	Gonzalez et al. [36]			X	X				Y		
44	Ur Rehman et al. [59]			X		Y	Y	Y	Y	X	
45	Singh et al. [37]		Y	X	X	Y					Y
46	Gurumurthy and Kodali [38]			X		Y	Y	Y	Y		Y
47	Singh and Sharma [16]			X			Y	Y			Y
48	Vinodh et al. [14]		Y	X							Y
49	Sahoo et al. [39]		Y	X	X				Y	X	Y
50	Storch et al. [40]								Y		Y

(continued)

Table 3 (continued)

S. No.	Author and references	Improved factors									
		Ergonomic issues	Product quality	Production parameter (cycle time, takt time, lead time, idle time, non-value-added time)	Production cost	Shop floor	Resource utilization	Productivity	Setup time	Work in progress	
51	Pattanaik and Sharma [41]			X		Y	Y		X		Y
52	Jiménez et al. [42]			X						Y	Y
53	Schaeffer et al. [60]									Y	
54	Hodge et al. [63]						Y			Y	
55	Bertolini and Romagnoli [43]		Y	X	X	Y	Y			Y	
56	Jeyaraj et al. [44]			X			Y			Y	
57	Ismail et al. [53]		Y	X	X	Y				Y	
58	Singh Amin et al. [45]				X					Y	
59	Al Askari et al. [46]		Y	X	X				X		Y
60	Eswaramoorthi et al. [47]									Y	

(continued)

Table 3 (continued)

S. No.	Author and references	Improved factors									
		Ergonomic issues	Product quality	Production parameter (cycle time, takt time, lead time, idle time, non-value-added time)	Production cost	Shop floor	Resource utilization	Productivity	Setup time	Work in progress	
61	Jasti and Sharma [61]		Y	X	X		Y			Y	
62	Kumar et al. [48]		Y	X	X	Y	Y		X	Y	
63	Kumar et al. [62]		Y	X							
64	Storck and Lindberg [66]				X						
65	Chitturi et al. [67]			X							
66	Braglia et al. [68]			X	X				X	Y	
67	Bonavia and Marin [69]			X					X		
68	Seth and Gupta [70]			X			Y			Y	
69	McDonald and Van Aken [49]			X						Y	
70	Brunt [50]			X						Y	

shop floor management approach in previous research work. Suitable approaches to improving factors for shop floor management are suggested in Table 4.

4 Future Work

A robust shop floor management system is a basic need of the present industries. To fulfill this need to identify an efficient approach for shop floor management, various approaches for production planning on the shop floor are implemented by researchers and production teams for the achievement of higher productivity need and product quality as well as cost-saving within limited resources. Implementation of approaches to process optimization in industries around the world has led to the improvement in production levels; therefore, the implementation of approaches in the area of shop floor management has received the attention of researchers. At the present time, four approaches are used for shop floor management in industries, including LM, K, TQM, and SS. These approaches enhance overall production by eliminating non-value-added activities. The integrated approach is an emerging better option for shop floor management. An integrated approach is able to understand and rectify the shortcomings of the production system better and effectively. Lean six sigma and lean kaizen have been identified in these approaches because the results obtained from integrated approaches were much better than those obtained from other single approaches such as LM, SS, K, TQM.

5 Conclusions

In this article, the reasons for non-value-added activities have been analyzed and identified a suitable approach for shop floor management. The main conclusions obtained from the present article are discussed below:

1. An efficient approach is needed to achieve a robust production system on the shop floor so that productivity can be effectively increased.
2. This study paper describes which approach may provide higher productivity. To do this, analyzed how non-value-added activities reason could be eliminated from different approaches.
3. Approaches selection for shop floor management may have improved from some activities like documentation, feedback, meeting, training, and direct observation of the shop floor.
4. In this paper, from extensive review, it was found that lean manufacturing is a prevalent approach for shop floor management in industries that can provide higher improvement levels in production.

Table 4 Suitable approaches for improvement in factors

Approaches for shop floor management	Improved factors									
	Ergonomic issues	Product quality	Production parameter (cycle time, takt time, lead time, idle time, non-value-added time)	Production cost	Shop floor	Resource utilization	Productivity	Setup time	Work in progress	
LM	X	X	X	X	X	X	X	X	X	X
LMSS		X	X	X			X		X	X
LSS		X	X	X		X	X		X	X
LMK	X	X	X	X	X	X	X	X	X	X
LMKSS	X	X	X	X	X	X	X	X	X	X
LMTQM			X	X		X	X			X

5. Other approaches like kaizen, total quality management, and six sigma were implemented rarely because they can only be implemented in limited production circumstances.

References

1. Womack J, Jones DT, Roos D (1990) *The machine that changed the world*. Macmillan, New York
2. Monden Y (1993) *Toyota production system: an integrated approach to Just in time*, 2nd edn. Industrial Engineering and Management, Norcross
3. Alhuraish I, Robledo C, Kobi A (2016) The effective of lean manufacturing and six sigma implementation. In: *Proceedings of 2015 international conference on industrial engineering and systems management*. IEEE IESM 2015, Oct, pp 453–460
4. Esa MM, Rahman NAA, Jamaludin M (2015) Reducing high setup time in assembly line: a case study of automotive manufacturing company in Malaysia. *Procedia Soc Behav Sci* 211:215–220
5. Rohani JM, Zahraee SM (2015) Production line analysis via value stream mapping: a lean manufacturing process of color industry. *Procedia Manuf* 2:6–10
6. Mwanza BG, Mbohwa C (2015) Design of a total productive maintenance model for effective implementation: case study of a chemical manufacturing company. *Procedia Manuf* 4:461–470
7. Choomlucksana J, Ongsaranakorn M, Suksabai P (2015) Improving the productivity of sheet metal stamping subassembly area using the application of lean manufacturing principles. *Procedia Manuf* 2:102–107
8. dos Santos ZG, Vieira L, Balbinotti G (2015) Lean manufacturing and ergonomic working conditions in the automotive industry. *Procedia Manuf* 3:5947–5954
9. Rahman NAA, Sharif SM, Esa MM (2013) Lean manufacturing case study with Kanban system implementation. *Procedia Econ Financ* 7:174–180
10. Dotoli M, Epicoco N, Falagario M, Costantino N, Bari P (2013) A lean warehousing integrated approach: a case study. In: *18th conference on emerging technologies & factory automation (ETF A)*. IEEE
11. Timans W, Antony J, Ahaus K, Van Solingen R (2012) Implementation of lean six sigma in small- and medium-sized manufacturing enterprises in the Netherlands. *J Oper Res Soc* 63(3):339–353
12. Östlin J, Ekholm H (2007) Lean production principles in remanufacturing—a case study at a toner cartridge remanufacturer. In: *IEEE international symposium on electronics and the environment*, pp 216–221
13. Motwani J (2003) A business process change framework for examining lean manufacturing: a case study. *Ind Manag Data Syst* 103(5):339–346
14. Vinodh S, Arvind KR, Somanaathan M (2010) Application of value stream mapping in an Indian camshaft manufacturing organisation. *J Manuf Technol Manag* 21(7):888–900
15. Solding P, Gullander P (2009) Concepts for simulation based value stream mapping. In: *Winter simulation conference*, pp 2231–2237
16. Singh B, Sharma SK (2009) Value stream mapping as a versatile tool for lean implementation: an Indian case study of a manufacturing firm. *Meas Bus Excell* 13(3):58–68
17. Tripathi V, Sarswat S (2018) Lean manufacturing for shop floor of automotive industries: a study. *J Exp Appl Mech* 9(2):58–65
18. Tripathi V, Saraswat S (2018) Lean management implementation in mining equipment manufacturing shop floor. In: *National conference on mining equipment: new technologies, challenges & applications*, Dhanbad, pp 7–10

19. Masuti PM, Dabade UA (2019) Lean manufacturing implementation using value stream mapping at excavator manufacturing company. *Mater Today Proc* 19(Part 2):606–610
20. Deshkar A, Kamle S, Giri J, Korde V (2018) Design and evaluation of a lean manufacturing framework using value stream mapping (VSM) for a plastic bag manufacturing unit. *Mater Today Proc* 5(2, Part 2):7668–7677
21. Roriz C, Nunes E, Sousa S (2017) Application of lean production principles and tools for quality improvement of production processes in a Carton Company. *Procedia Manuf* 11:1069–1076
22. Antosz K, Stadnicka D (2017) Lean philosophy implementation in SMEs—study results. *Procedia Eng* 182:25–32
23. Gupta V, Narayanamurthy G, Acharya P (2018) Can lean lead to green? Assessment of radial tyre manufacturing processes using system dynamics modelling, vol 89. Elsevier Ltd
24. Garre P, Nikhil Bharadwaj VVS, Shiva Shashank P, Harish M, Sai Dheeraj M (2017) Applying lean in aerospace manufacturing. *Mater Today Proc* 4(8):8439–8446
25. Morales Méndez JD, Rodríguez RS (2017) Total productive maintenance (TPM) as a tool for improving productivity: a case study of application in the bottleneck of an auto-parts machining line. *Int J Adv Manuf Technol* 92(1–4):1013–1026
26. Ferreira T, Baptista AA, Azevedo SG, Santos FC (2016) Lean manufacturing implementation in intermittent environments: a framework. In: Ao S, Yang GC, Gelman L (eds) *Transactions on engineering technologies*. Springer, Singapore. https://doi.org/10.1007/978-981-10-1088-0_18
27. Srinivasan S, Ikuma L, Shakouri M, Nahmens I, Harvey C (2016) 5S impact on safety climate of manufacturing workers. *J Manuf Technol Manag* 27:364–378. <https://doi.org/10.1108/JMTM-07-2015-0053>
28. Ali Naqvi SA, Fahad M, Atir M, Zubair M, Shehzad MM (2016) Productivity improvement of a manufacturing facility using systematic layout planning. *Cogent Eng* 3(1)
29. Tripathi V, Gautam GD, Saraswat S (2020) Process optimization methods for shop floor planning: a study. *Int J Eng Res* 8(10):244–247
30. Venkat Jayanth B, Prathap P, Sivaraman P, Yogesh S, Madhu S (2020) Implementation of lean manufacturing in electronics industry. *Mater Today Proc*
31. Shou W, Wang J, Wu P, Wang X (2020) Lean management framework for improving maintenance operation: development and application in the oil and gas industry. *Prod Plan Control* 1–18
32. Amrani A, Ducq Y (2020) Lean practices implementation in aerospace based on sector characteristics: methodology and case study. *Prod Plan Control* 1–23
33. Sutharsan SM, Mohan Prasad M, Vijay S (2020) Productivity enhancement and waste management through lean philosophy in Indian manufacturing industry. *Mater Today Proc*
34. Balamurugan R, Kirubagharan R, Ramesh C (2020) Implementation of lean tools and techniques in a connecting rod manufacturing industry. *Mater Today Proc*
35. Gopi S, Suresh A, John A (2020) Value stream mapping & manufacturing process design for elements in an auto-ancillary unit—a case study. *Mater Today Proc* 22:2839–2848
36. Gonzalez ME, Quesada G, Mora-Monge CA, Barton ME (2019) An empirical study of the application of lean tools in U.S. industry. *Qual Manag J* 26(4):174–190
37. Singh RK, Kumar S, Choudhury AK, Tiwari MK (2006) Lean tool selection in a die casting unit: a fuzzy-based decision support heuristic. *Int J Prod Res* 44(7):1399–1429
38. Gurumurthy A, Kodali R (2011) Design of lean manufacturing systems using value stream mapping with simulation. *J Manuf Technol Manag* 22(4):444–473
39. Sahoo AK, Singh NK, Shankar R, Tiwari MK (2008) Lean philosophy: implementation in a forging company. *Int J Adv Manuf Technol* 36(5–6):451–462
40. Storch RL, Lim S, Williamson M (1998) Evaluating value streams to achieve lean production in large assembly manufacturing systems utilizing virtual enterprise relationships. In: Bititci US, Carrie AS (eds) *Strategic management of the manufacturing value chain*. IFIP—the international federation for information processing, vol 2. Springer, Boston. https://doi.org/10.1007/978-0-387-35321-0_26

41. Pattanaik LN, Sharma BP (2009) Implementing lean manufacturing with cellular layout: a case study. *Int J Adv Manuf Technol* 42(7–8):772–779
42. Jiménez E, Tejada A, Pérez M, Blanco J, Martínez E (2012) Applicability of lean production with VSM to the Rioja wine sector. *Int J Prod Res* 50(7):1890–1904
43. Bertolini M, Romagnoli G (2013) Lean manufacturing in the valve pre-assembly area of a bottling lines production plant: an Italian case study. In: *Proceedings of 2013 international conference on industrial engineering and systems management (IESM)*, Rabat, pp 1–8
44. Jeyaraj KL, Muralidharan C, Mahalingam R, Deshmukh SG (2013) Applying value stream mapping technique for production improvement in a manufacturing company: a case study. *J Inst Eng Ser C* 94(1):43–52
45. Singh Amin S, Atre R, Vardia A, Sebastian B (2014) Lean machine manufacturing at Munjal Showa limited. *Int J Prod Perform Manag* 63(5):644–664
46. Al Askari O, Ahmad M, Pinedo-Cuenca R (2016) Development of a methodology to assist manufacturing SMEs in the selection of appropriate lean tools. *Int J Lean Six Sigma* 7:62–84. <https://doi.org/10.1108/IJLSS-02-2015-0005>
47. Eswaremoorthi M, Kathiresan GR, Prasad PSS, Mohanram PV (2011) A survey on lean practices in Indian machine tool industries. *Int J Adv Manuf Technol* 52(9–12):1091–1101
48. Kumar MK, Rajan AJ, Navas RKB, Rubinson SS (2014) Application of lean manufacturing in mass production system a case study in Indian manufacturing unit. *Ind Eng Manag* 702–706
49. McDonald T, Van Aken EM (2002) Utilising simulation to enhance value stream mapping: a manufacturing case application. *Int J Logist Res Appl* 5(2):213–232
50. Brunt D (2000) From current state to future state: mapping the steel to component supply chain. *Int J Logist Res Appl* 3(3):259–271
51. Thomas AJ, Francis M, Fisher R, Byard P (2016) Implementing lean six sigma to overcome the production challenges in an aerospace company. *Prod Plan Control* 27(7–8):591–603
52. Mundra N, Mishra RP (2020) Impediments to lean six sigma and agile implementation: an interpretive structural modeling. *Mater Today Proc*
53. Ismail A, Ghani JA, Ab Rahman MN, Md Deros B, Che Haron CH (2014) Application of lean six sigma tools for cycle time reduction in manufacturing: case study in biopharmaceutical industry. *Arab J Sci Eng* 39(2):1449–1463
54. Rahani AR, Al-Ashraf M (2012) Production flow analysis through value stream mapping: a lean manufacturing process case study. *Procedia Eng* 41:1727–1734
55. Sivaraman P, Nithyanandhan T, Lakshminarasimhan S, Manikandan S, Saifudheen M (2020) Productivity enhancement in engine assembly using lean tools and techniques. *Mater Today Proc*
56. Mohan Prasad M, Dhiyaneswari JM, Ridzwanul Jamaan J, Mythreyan S, Sutharsan SM (2020) A framework for lean manufacturing implementation in Indian textile industry. *Mater Today Proc*
57. Masuti PM, Dabade UA (2019) Lean manufacturing implementation using value stream mapping at excavator manufacturing company. *Mater Today Proc* 19:606–610
58. Suhardi B, Anisa N, Laksono PW (2019) Minimizing waste using lean manufacturing and ECRS principle in Indonesian furniture industry. *Cogent Eng* 6(1):1–13
59. Ur Rehman A, Usmani YS, Umer U, Alkahtani M (2020) Lean approach to enhance manufacturing productivity: a case study of Saudi Arabian factory. *Arab J Sci Eng* 45(3):2263–2280
60. Schaeffer JA, Cadavid J, Backström T (2010) Spatial design for continuous improvement: the case study of three manufacturing companies. *Int J Comput Integr Manuf* 23(8–9):791–805
61. Jasti NVK, Sharma A (2011) Lean manufacturing implementation using value stream mapping as a tool: a case study from auto components industry. *Int J Lean Six Sigma* 5(1)
62. Kumar S, Dhingra A, Singh B (2018) Lean-Kaizen implementation: a roadmap for identifying continuous improvement opportunities in Indian small and medium sized enterprise. *J Eng Des Technol* 16(1):143–160
63. Hodge GL, Goforth Ross K, Joines JA, Thoney K (2011) Adapting lean manufacturing principles to the textile industry. *Prod Plan Control* 22(3):237–247

64. Noor NA, Kasolang S, Jaffar A (2012) Simulation of integrated total quality management (TQM) with lean manufacturing (LM) practices in forming process using Delmia Quest. *Procedia Eng* 41:1702–1707
65. Gupta V, Acharya P, Patwardhan M (2013) A strategic and operational approach to assess the lean performance in radial tyre manufacturing in India. *Int J Prod Perform Manag* 62(6):634–651
66. Storck J, Lindberg B (2007) A lean production strategy for hot charge operation of a steel mill. In: IET international conference on agile manufacturing (ICAM 2007), vol 2007, no 528 CP, pp 158–167
67. Chitturi RM, Glew DJ, Paulle A (2007) Value stream mapping in a jobshop. In: IET international conference on agile manufacturing (ICAM 2007), pp 142–147
68. Braglia M, Carmignani G, Zammori F (2006) A new value stream mapping approach for complex production systems. *Int J Prod Res* 44(18–19):3929–3952
69. Bonavia T, Marin JA (2006) An empirical study of lean production in the ceramic tile industry in Spain. *Int J Oper Prod Manag* 26(5):505–531
70. Seth D, Gupta V (2005) Application of value stream mapping for lean operations and cycle time reduction: an Indian case study. *Prod Plan Control* 16(1):44–59

An Analysis on Cyber Security Issues in the Smart Grid



Shikha Kuchhal, Ikbal Ali, and Ibraheem

1 Introduction

Many types of cyber-attacks in the smart grid can lead to extensive energy black-outs and devastating damage to power resources. Also, it may weaken the cyber security purposes and requirements. The actual cyber security cases and correlated occurrences illustrate that the modern grid is not reliable. Furthermore, thanks to the increasing usage of ICT tools, the grid is becoming smarter and the numbers of users (e.g. Service providers, advertisers etc.) are increasing rapidly. This is adding new risks thus methods to cope with them, should be well identified.

Incidents opposed to the framework can legitimately affect people's lifestyle. Open areas and C-level team of the services working the dispersion and communication systems, just as power advertisers and age associations ought to know about this circumstance. Without them, it is unworkable to set up the fundamental instruments to enhance the protection stance of their present systems and to incorporate cyber security as an essential target of the intelligent frameworks.

The smart matrix utilizes shrewd transmission and dispersion systems to convey power. The purpose of the smart matrix methodology is to improve the electric framework's dependability, security, and effectiveness through the two-route correspondence of utilization information and dynamic enhancement of electric framework activities, support, and arranging (Fig. 1).

The shrewd framework fuses numerous assets, applications, and empowering advancements to influence supply, burden, or framework conditions and also including conveyance infrastructure, data systems, end use frameworks, and related disseminated vitality assets. Applications are operational techniques that utilization assets to make advantages or worth. Empowering innovations incorporate basic, crosscutting components of the smart matrix. The smart framework is ready to change a unified, maker regulated system to a decentralized, customer intelligent system that

S. Kuchhal (✉) · I. Ali · Ibraheem
Jamia Millia Islamia University, New Delhi, India

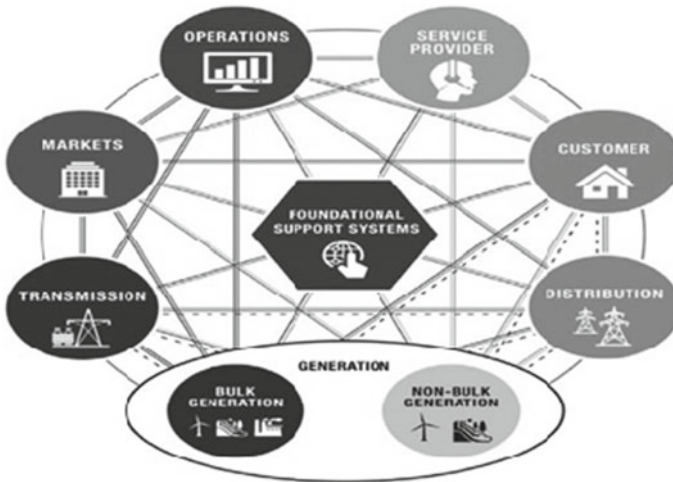


Fig. 1 Modified NIST conceptual model of SG architecture

is upheld by fine-grained observing. For instance, customers respond to value flags (i.e., supply) including the assistance of smart meters to accomplish dynamic burden the board (Fig. 2).

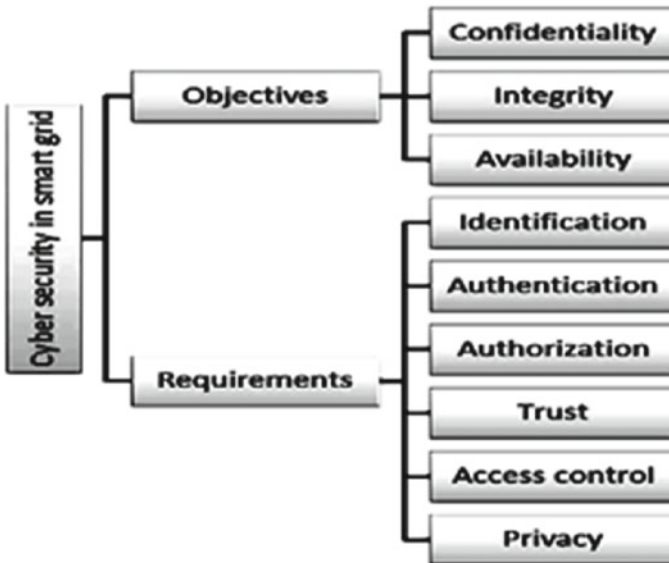


Fig. 2 Cyber security objectives

On the checking side, old metering information recorded hourly or month to month is supplanted by a smart meter that gathers information consistently. Additionally, current supervisory control and data acquisition (SCADA) frameworks gather one information direct every 1 toward 2 s, while phasor estimation units gather 30–60 information that focuses every second.

2 Literature Survey

The shrewd grid can be viewed as a “network of frameworks” that will extend its flow abilities of age, transmission, and circulation to conveyed age, electric vehicles (EV), and sustainable power sources [1]. Smart grid conveys power among providers and considers utilizing two-way data and correspondence innovation (ICT), and trading close to ongoing data regarding the framework affirms to empower control and computerization of smart gadgets. This permits the performer to spare vitality and decrease power bills while expanding the dependability, proficiency, heartiness, and straightforwardness of the framework. It is empowered by various innovative advances in detecting, estimating, and control gadgets. Dissimilar to the inheritance power frameworks, the smart grid gives better situational mindfulness for the condition of the framework [2–4]. Thusly, top burden the administration (PLM) and request reaction (DR) can be actualized to straighten the pinnacle request. The smart grid likewise performs prescient examination so as to keep the force adjusted. Similarly, the combination of new stockpiling advancements will enhance smart request expectations [5]. The intelligent grid is imagined to homogenizing rapid and two-way correspondence innovation with different force and control hardware. In any case, such a considerable reliance on data and correspondence organizing builds the danger of inherent issues in the smart grid. The extraordinarily lessens each effectiveness and unwavering quality of the force framework, which, regardless, does a definitive objective.

Yu et al. [6] have indicated that network invasion by foes may prompt genuine outcomes in the smart grid system. As per the report of the electric power research institute (EPRI), the difficulties that the current shrewd grid will face the expanding plausibility of cyber security attacks and occurrences as an expanding number of gadgets are becoming interrelated.

Cyber security becomes much all the further testing when the measure and intricacy of the shrewd matrix increments. Different scientists and approved organizations have created exhaustive systems to handle cyber menaces and give systematic design to forestall such cyber threats [7–9]. Weakness evaluation of electric force utilities additionally helps in finding the ideal network [10]. It is that as it may important to break down and measure the significance of the effects of cyber threats before any assessment. This challenge recognizing powerless connections inside the cyber infrastructure. This justification for cyber-attacks on the smart grid system may run from financial purposes, tricks, displeased workers, mechanical undercover work, and right to psychological oppression. A weak cyber infrastructure permits

an attacker to penetrate safety during the feeble connections. Afterward, it accesses control programming, modifies charging data, and burdens situations to destabilize the framework prompting a significant financial unsettling influence. Moreover, an enemy may attack purchasers' security by gathering individual data. The wide size of the smart matrix makes it difficult to give resistance to every single segment of such a mindboggling system. To exacerbate things, complex control engineering, element evaluation, and calculations manifold the danger of attacks. Administration framework malware similar to Stuxnet focusing on helpless SCADA frameworks constrained the advantages to re-examine around their current force matrix surety [11]. The services, in this manner, must make choices on each decision of scientific networks while dispatching another SCADA framework or ensuring a current unit. Cyber security should likewise discuss accidental trade-offs of the data framework because of client blunders, gear disappointments, and catastrophic events [12]. The present IT states strategies, for example, open key infrastructure (PKIs), virtual private systems (VPNs), firewall, interruption discovery frameworks (IDSs), hostile to infection, and so forth might be grafted into the smart grid system; however, because of their inalienable contrasts, it despite everything cannot be made powerful with no improvements [13]. The time criticalness of the system traffic is an essential distinction in the smart framework. The exploration of shrewd framework cyber security is in the early stages, which propels us to completely look at these framework segments and recognize completely conceivable security menaces and surviving issues in the cyber infrastructure of the smart grid system [14].

This work presents around hazard review methods wherever cyber security resources are recognized, monitored for any weakness in the framework, and following investigated as the effect of particular cyber threats of the smart grid system in the framework activity. That will help the intelligent framework cyber security scientists in the planning of fitting cyber security engineering and system frameworks to send proper countermeasures to forestall, distinguish, and relieve cyber-attacks of the smart grid in the shrewd matrix [15, 16].

3 Issues and Risk Factors

The smart grid is based on ICT, and ICT will assume a fundamental job in the dependability and protection of intensity frameworks, and along these lines, the assurance of flow and innovative ICT innovations has to be tended by the power area. This is not just an errand of matrix administrators yet additionally of open bodies, institutionalization associations, the scholarly world, new specialist organizations, and some other partner (Fig. 3).

In all the areas and time period of the smart framework, cyber security has to be studied from the structure stage to neutralize, via improvement, organization, upkeep, and so on. Moreover, cyber security must address not just conscious attacks propelled by disappointed representatives, operators of modern secret activities, or fear mongers. As we previously talked about in the past area, incidental trade-offs



Fig. 3 Risk evaluation process

of the data infrastructure because of client mistakes, gear disappointments, and cataclysmic events ought to likewise be considered.

Accomplishing a safe smart matrix would not be a simple assignment. There are progressions of issues/shortcomings that must be recognized and investigated first and afterward attempt to get comprehended through hazard the management forms. Nonetheless, there are various difficulties, for example, mechanical holes, authoritative issues, or mindfulness gives that must be explained to accomplish this goal.

4 Cyber Security Threats in Smart Grid

It is exceedingly vital to understand the forthcoming helplessness threats in the smart matrix. Right now, hazard appraisal philosophy that gives a premise to abusing the conceivable section focuses which are helpless to vindictive attacks has been illustrated. How these attacks permit an enemy to take undesirable activities, and thusly, influence the whole smart grid infrastructure has likewise been featured.

4.1 Technical Sources of Smart Grids Threats

This grouping as introduced depends on the recognized threats which can be followed to the technical parts of SGs. Three key parts of the technical sources of these threats are recognized, and these are infrastructural security, technical operational security, and frameworks' information the management security (Fig. 4).

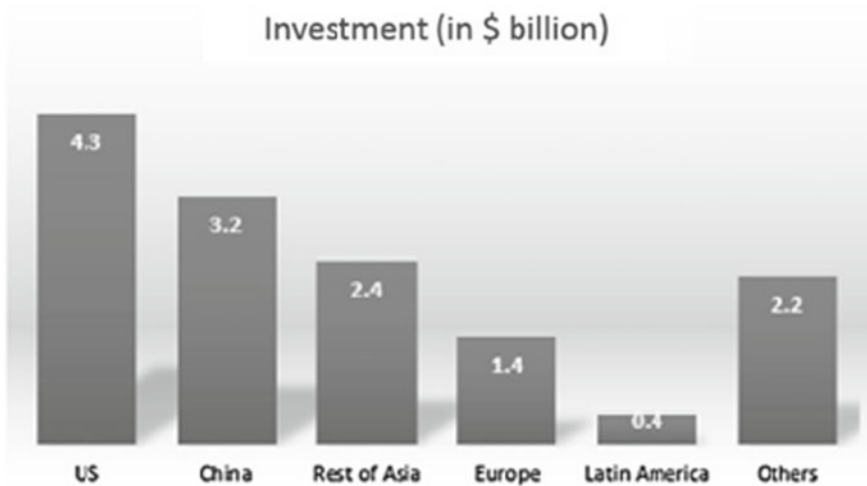


Fig. 4 SGs investment by region as at 2012

The infrastructural security. SGs infrastructure is an exceptionally perplexing framework which is geologically, intelligently, and financially disseminated, inter-connecting clients, power plants, utilities, transmissions, conveyances, substations, transformers, and so forth.

Technical operational security. The intricacy of the matrix requires made sure about operational plans. This is on the grounds that disappointments may almost certainly have more noteworthy impact since basic infrastructures rely upon made sure about and solid power tasks and supplies for vitality and control.

Systems' data management security. This perspective covers continuous chronicle, observing and putting away of vital information and data, security of information against attacks, rules, and guidelines controlling information network, protection adherence by working staff, clients' fulfillment regarding security affirmation, and so on.

4.2 Non-technical Sources of Smart Grids Threats

Environmental security. Network of environmental security is pivotal in SGs execution as it helps control and stay away from potential disastrous impacts on the frameworks because of any of the common or counterfeit caused natural threats, for example, floods, tremors, quakes, avalanches, falling of trees, consuming of hedges, and so forth by articulating smart reaction.

Government strategies. As circumstances augment in SGs advances and administrations, the regular utility progressively faces difficulties all because of the prerequisite of new advances, strategies, expanding requests, and plans of action associated with changing to SGs time.

5 Data Privacy and Consumer Protection

Information security and shopper insurance stay top worry for the dissemination utilities just as customers. Shoppers need to pick up certainty to share their own information to the outsider specialist organizations or the utilities so as to improve the operational proficiency of the smart framework. Right now, brief diagram of the threats with respect to protection of the purchasers has been given. Smart meters introduced at the buyers' end trade data with the home area network (HAN) or building area network (BAN) in regard to the information utilization of the customers just as impart control signs to the smart apparatuses introduced at the shoppers' premises. These systems in any case might be helpless against information spillage or spying that could uncover exercises of the buyers and touchy data like record numbers. For residential shoppers, such information spillage could likewise uncover data with respect to the shrewd apparatuses, electric vehicles, and long-range interpersonal communication action which thusly displays customers' very own conduct. Likewise, constant data of vitality utilization may unveil whether a home or office is involved, where individuals are in the structure, what is going on with them, etc. For mechanical and business shoppers, such information spillages can uncover exceptionally touchy data, for instance, the advancements utilized, fabricating yield, deal occasions, and so forth. This raises the possibility of modern undercover work among different contenders. Then again, utilities and outsider specialist co-op total vitality use information of various customers for better interest gage and pinnacle load the management. Nonetheless, it is of developing worry that such close to home data can be serenely gotten to by any approved staff at the control community making information protection and shopper insurance a strenuous activity for cyber security scientists and designers.

6 Conclusions

Cyber protection in smart systems is still undergoing fundamental improvement process. This paper introduces cyber infrastructure smart brace device with analysis bearings inside and out. The anonymity, integrity, and transparency of the network must be improved by creating a comfortable and efficient cyber-infrastructure for the smart grid. Recognition of threats, mitigation, verification, and core is an administration between all remaining research problems. The countermeasure plans should

be made, tried out, and sent with conventions for issues. Having stable convention by administrative framework is prescribed.

References

1. Quinn EL (2009) Smart metering and privacy: existing laws and competing policies. SSRN eLibrary
2. Vijayan J (2010) Stuxnet renews power grid security concerns. *Computerworld*, 26 July 2010
3. Kerckhoffs A (1883) *La cryptographie militaire*. *J Sci Milit* IX:5–38
4. Mo Y, Kim TH, Brancik K, Dickinson D, Lee H, Perrig A, Sinopoli B (2012) Cyber-physical security of a smart grid infrastructure. *Proc IEEE* 100(1):195–209
5. Electric Power Research Institute (2009) Report to NIST on smart grid interoperability standards roadmap
6. Yu J, Mao A, Guo Z (2006) Vulnerability assessment of cyber security in power industry. In: *Proceedings of IEEE power and energy society general meeting (PES'06)*, pp 2200–2205
7. Huang Y, Esmalifalak M, Nguyen H, Zheng R, Han Z, Li H, Song L (2013) Bad data injection in smart grid: attack and defense mechanisms. *IEEE Commun Mag* 27–33
8. Bou-Harb E, Fachkha C, Pourzandi M, Debbabi M, Assi C (2013) Communication security for smart grid distribution grids. *IEEE Commun Mag* 42–49
9. Mohajerin Esfahani P, Vrakopoulou M, Margellos K, Lygeros J, Andersson G (2010) Cyber attack in a two-area power system: impact identification using reachability. In: *Proceedings of American control conference*, July 2010, pp 962–967
10. Liu Y, Ning P, Reiter MK (2009) False data injection attacks against state estimation in electric power grids. In: *Proceedings of the 16th ACM conference on computer and communications security*. ACM, New York, pp 21–32
11. Liu J, Xiao Y, Li S, Lian W, Philip Chen CL (2012) Cyber security and privacy issues in smart grids. *IEEE Commun Surv Tutor* 14(4):981–997, fourth quarter
12. Anderson R, Fuloria S (2010) Who controls the off switch? In: *Proceedings of 1st IEEE SmartGridComm 2010*, Gaithersburg, Oct 2010, pp 96–101
13. McDaniel P, McLaughlin S (2009) Security and privacy challenges in the smart grid. *IEEE Secur Priv* 7(3):75–77
14. Bennett C, Wicker SB (2010) Decreased time delay and security enhancement recommendations for AMI smart meter grids. In: *Innovative smart grid technologies (ISGT 2010)*, Gaithersburg, Jan 2010, pp 1–6
15. Sun Z, Huo S, Ma Y, Sun F (2010) Security mechanism for smart distribution grid using ethernet passive optical grid. In: *2nd international conference on advanced computer control (ICACC 2010)*, vol 3, Shenyang, China, Mar 2010, pp 246–250
16. Kosut O, Jia L, Thomas RJ, Tong L (2010) Malicious data attacks on smart grid state estimation: attack strategies and countermeasures. In: *Proceedings of 1st IEEE SmartGridComm 2010*, Gaithersburg, Oct 2010, pp 220–225

Optimal Planning of EV Fast-Charging Station with DG in Distribution System Using PSO



Dhiraj Kumar Singh and Aashish Kumar Bohre

1 Introduction

Concern of global warming, climate change, urban air pollution and dependence on ambiguous and costly supplies of foreign oil have advance research and policymakers management to explore alternatives. The optimal charging schedule of electric vehicles at battery swapping stations in a smart distribution is presented in [1]. The reliability assessment-based approach for integrated transportation and electrical powers systems incorporating electric vehicles is reported in [2]. Electric-operated vehicles have the lowest or negligible greenhouse gases and urban air pollutant [3, 4]. Two environmental impacts are accounted for travelling from one place to another which are air pollution and greenhouse gases (GHGs) emission. The greenhouse gases are carbon dioxide (CO_2), methane (CH_4), nitrous oxide (N_2O) and sulphur hexafluoride (SF_6) which have greenhouse gases impact weighing coefficient relative to CO_2 of 1, 21, 310 and 24,900, respectively [5, 6]. Air pollutants like carbon monoxide (CO), nitrogen oxides (NO_x), sulphur oxides (SO_x) and volatile organic compounds (VOCs) impact weighing coefficient 0.017, 1, 1.3 and 0.64, respectively. With the availability the electric vehicle in the present scenario, the overall requirement of electrical power increases with a large ratio [7]. To overcome this problem, power generation must be increased in the same ratio.

As the pie chart in Fig. 1 represents that the dependence of power generation in India is on fossil fuel should change complete before the implementation EVs, because the objective will not meet the requirement [8–10]. It will only reduce the pollution of certain cities but globally the scenario remains the same. After the major change the next step milestone is the life cycle of the batteries of EVs, the cost of

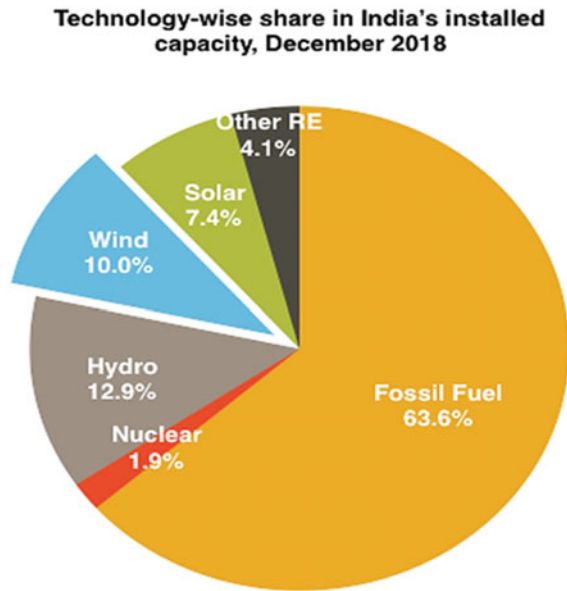
D. K. Singh (✉) · A. K. Bohre

Electrical Engineering Department, National Institute of Technology, Durgapur, Durgapur, India

A. K. Bohre

e-mail: aashishkumar.bohre@ee.nitdgp.ac.in

Fig. 1 Pie chart of power generation in India



the EVs manufacturing and anxiety of charging station as well as the charging [11–13]. All the above-mentioned challenges are the areas of research these days. In this paper, focus is on the charging station and the charging time that is allocation of fast-charging station (FCS) and also deals with present scenario of the power system configuration to handle the requirement of power by EVs [14]. Depending upon the power level, there are four different modes of charging time and charging speed are as [1–3, 8–10]:

- Mode 1: This is simply an extension cord that plugs into a standard domestic 16 A socket. Max power is limited to 16 A/2 kW.
- Mode 2: Charging is a smart extension cord that has electronics in line to communicate with the car under charge and associated safety features. Better than Mode 1, but still very limited charging capacity for larger batteries.
- Mode 3: Mode 3 is single or three phase AC fast charging up to 22 kW.
- Mode 4: DC fast or fast chargers. They are also the most expensive.

This paper considers the IEEE 33 bus distribution system [15–17] to be capable to handle the load increased in the system due to the rising EVs load in the power system. Zones are created depending range anxiety. Different zone has specific areas where there is need of charging station. The EVs are encouraged because it reduces environmental pollution as well as it has energy-efficient benefits. But, EVs enhance the upstream emission in fuel production, that is generation, transmission and distribution of electric power. Upstream emission analysis became a major concern after the adoption of EV was viewed as an option [18, 19]. The distribution generation has similar advantages as the EV station as it decreases the emission of carbon dioxide

and NO_x , it also rectifies the voltage profile and voltage stability in the distribution system. It intensifies the reliability and power quality of the distribution feeder. But, inappropriate planning of DGs will not meet the above-mentioned advantages related to the power system that is voltage stability, reliability and other safety issues. So, to meet the demand DGs optimal sizing must be considered [20–23]. The microgrid is a localized generating unit that is centralized with the national grid and ably to operate after localizing the network which means it can be able operated independently. DGs are the part of the micro-grid which can be able to operate independently as well as with the central grid. Independent operation means if the EV stations are being in operation at its full load of EV charging, whereas if the EV station is on under loaded condition then the extra power can be transmitted to the central grid [1–3, 24].

2 Station Development

2.1 EV Station

Economical aspects of EV station are also the important content of concern for the EV station owner. Equipment related to charging station has their certain cost and requirements must be observed before the implementation. This paper has considered the different requirements including land requirements. Electrical equipment includes the bus bars, transformers, etc. The infrastructure of FCS consists of a sub-station via a dedicated overhead line. Sub-station consists of LV and HV bus bar and having two parallel transformers [1–3]. Station infrastructure development requires equipment and land area. The linear variation of equipment cost is considered which has a dependence on the capacity and number of the connector to be installed. Each connector requires at least 9 ft. width and 18 ft. in length, and clearance between each connector is considered to be 3 ft. Area required for each connector to be assumed being 25 m^2 . For station, the infrastructure cost (SIC_i) is then calculated as:

$$\text{SIC}_i = C_{\text{ini}} + 25 * C_{\text{land}} * S_i + \text{RP} * C_{\text{con}} * (S_i - 1) \quad (1)$$

where RP—connector rated power, kW; C_{con} —connector infrastructure cost, \$/kW; C_{ini} —fixed-cost, \$; C_{land} —rental cost of land per annum, \$/m²; and S_i —number of connectors. The capacity of station (in KW) SC_i :

$$\text{SC}_i = \text{RP} * S_i \quad (2)$$

Table 1 DG station cost

Parameter	Unit	Value
Investment cost	\$/MW	15,900
Operational cost	\$/MW	29
Maintenance cost	\$/MW	7

2.2 DG Station

The cost of DG depends largely upon the MW rating. Before implementation, we have optimized the size of the DG at the EV station. Similarly, as the EV stations we have to consider the economic aspects of the DG before being into operation. The size of the DG is used in the optimization technique which reduces the cost as well achieved the objective that is voltage stability, reduced power losses, improved reliability and enhanced voltage profile [17–20]. The cost of DG Station depends on the parameter that is investment cost, operational cost and maintenance cost are tabulated in Table 1.

3 Defining Problem

In this paper, we have tried to configure EV zones with uniform distribution of EV in each zone and also try to maintain the minimum distance of two consecutive EV stations which are within the anxiety limit of the EV user and also calculate the objective function and index functions for the optimization of the EV station at a particular location with minimum power loss and voltage deviation and maximization of reliability. From the DG point of view, the cost of DG is to be minimized through the optimization technique. In this work, we have used the size of DG for the economical consideration for the EV station owner. Size of the DG is used in the optimization technique which reduces the cost as well achieved the objective that is voltage stability, reduced power losses, improved reliability and enhanced voltage profile.

3.1 With EV FCS and DGs Both

Our objective is to locate the EV charging station and DGs; there must be a charging station of EV considering the technical and economical aspects. We try to find a fast-charging station in all the four zones of IEEE 33 distribution system. The locations of DGs obtained after the EVs FCS optimization are implemented. The location is being fixed now the size is to be calculated through PSO optimization with a similar objective function as given in Eq. 4. Considered the Durgapur map having 33 bus configurations (modified IEEE 33 bus system) as shown in Fig. 2, where four different

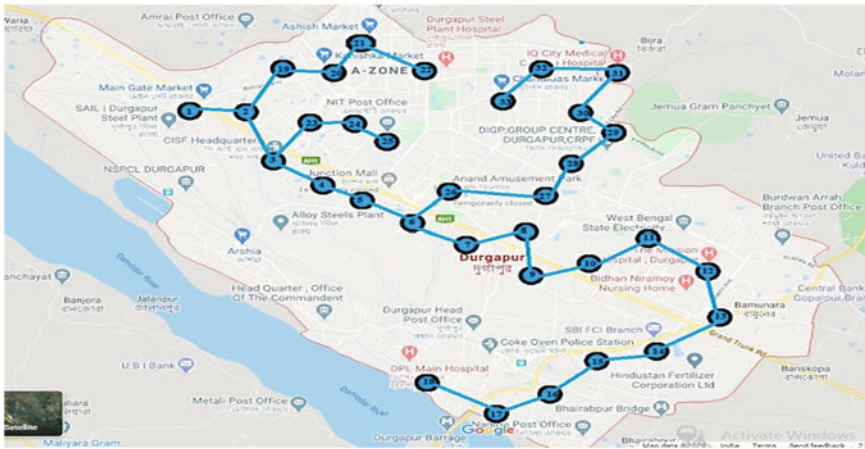


Fig. 2 Durgapur network with the FCS placement

FCSs are to be placed in different zones. Evaluation is done by considering the area in four different zones as Z_1, Z_2, Z_3 and Z_4 . Each zone has a uniformly distributed EV population.

- Z_1 have bus number 19, 20, 21 and 22.
- Z_2 have bus number 23, 24 and 25.
- Z_3 have bus number 27, 28, 29, 30, 31, 32 and 33.
- Z_4 have bus number 9–18.

So, the first goal is to place the fast-charging stations (FCS) after that allocation of DGs, where the power loss is minimum which reduces the cost and also the voltage deviation. We have also considered the reliability parameter which is to be maximized.

Decision Variable: Locating the fast-charging stations in all the four zones considers the variable as mentioned above.

Objective Function: As mentioned before, the optimization problem consists of cost as well as the power loss of the system including the EV station.

$$Z_{li} = \min\{(PL + S_1 + S_2 + S_3 + S_4) * pri\} \tag{3}$$

Objective function including the EV station and DGs

$$Z_{li} = \min\{(PL + S_1 + S_2 + S_3 + S_4 + DG_1 + DG_2 + DG_3 + DG_4) * pri\} \tag{4}$$

where, P_{loss} = Power loss of overall System, S_1 = EV Charging Station no. 1, S_2 = EV Charging Station no. 2, S_3 = EV Charging Station no. 3, S_4 = EV Charging Station no. 4, Pri = Cost of charging, DG_1 = EV Charging Station cum DG Station

no. 1, DG₂ = EV Charging Station cum DG Station no. 2, DG₃ = EV Charging Station cum DG Station no. 3, DG₄ = EV Charging Station cum DG Station no. 4.

Constraints: The constraints are the voltage deviation which considers the stability of the bus voltage. Due to the increase in demand, these parameters are disturbed throughout the area.

These constraints are as follows:

$$V_i^{Min} \leq V_i^t \leq V_i^{Max} \tag{5}$$

where $\forall i \in \{1, 2, \dots, N_b\}$.

Penalty function in the objective function:

$$PVC_i = [\max(V_{i,t}, V, Max) - V_i^{Max}] + [V_i^{Min} - \min(V_{i,t}, V_i^{Min})] \tag{6}$$

The second constraint is the reliability [20, 25] which must be maximized.

$$Z_{2i} = 1/Reliability \tag{7}$$

Index function:

$$Index_{1i} = Z_1/Z_{10} \tag{8}$$

$$Index_{2i} = \max(PVC) / \max(PVC_0) \tag{9}$$

$$Index_{3i} = Z_{20}/Z_2 \tag{10}$$

The overall objective function is:

$$O_i = \min\{a * (Index_{1i}) + b * (Index_{2i}) + c * (Index_{3i})\} \tag{11}$$

where a = coefficient of Cost and Power Loss (0.4); b = coefficient of penalty factor (0.3); c = coefficient of Reliability (0.3); i = denotes the function with EV station only; and 0 = denotes the initial condition that is without EV and DG station (specific in second term underlined like Z_{20}). The a , b and c are selected based on the priority of system parameters in such away so the sum should be unity [16].

4 Particle Swarm Optimization (PSO)

PSO which means particle swarm optimization was firstly suggested in 1995 by experts Eberhart Russell and Kennedy James, which was basically driven through the birds and fishes social behaviour. It is an optimization technique based on the

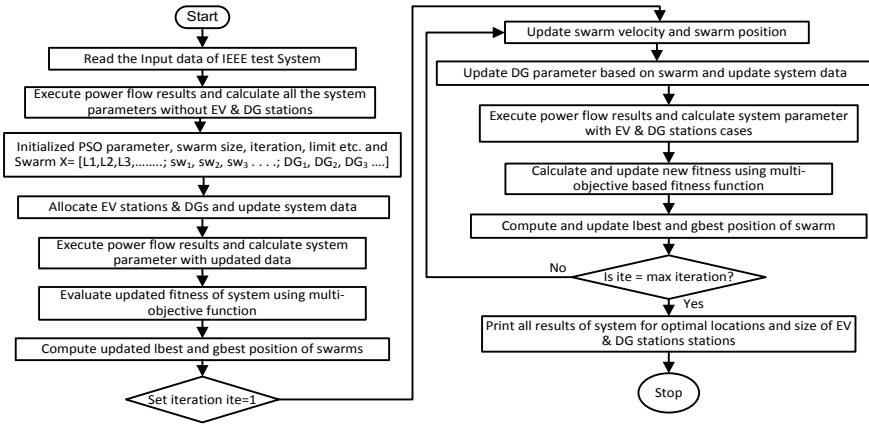


Fig. 3 Flowchart for optimal planning of EV stations with DGs using PSO

movement and intelligence of swarms [20–23]. It uses the concept of social interaction to search for food (problem-solving). Each swarm is considered as a particle in N-dimensional space which changes its speed and flying technique as per own experience and also the experience of other swarms [20, 21]. It uses the number of swarms (particle) moving in the search space for the best solution. Each swarm keeps the record of its solution space which helps to obtain the fitness (best solution) that has obtained till now. This is termed as personal best (pbest). PSO keeps the track of another best value obtained till now by any swarm (particle) in the neighbourhood of that swarm. This is termed as global best (gbest). PSO basic concept lies in accelerating each particle towards its personal best (pbest) and global best (gbest) locations, with a random weighted factor in every step time. The different PSO parameters consider for case study are such as $c_1 = c_2 = 2$, inertia weight (w) range 0.95–0.4 and the random variables in the range of 0–1. Also, the total number of trials are 30, and the total number of iterations are 50 correspondingly defined here. The flowchart for optimal planning of EV stations with DGs using PSO is given in Fig. 3. The PSO technique implementation steps for optimal allocation EV FCS with DGs are as:

- Step 1:* Read input data of IEEE 33 bus System.
- Step 2:* Execute power flow and calculate all the system parameter without EV FCS Station and with EV FCS Station.
- Step 3:* Updating of some parameter in the test system.
- Step 4:* Initialization of the EV FCS and DGs size and location for all four zone.
- Step 5:* Execute power flow and calculate all the system parameters.
- Step 6:* Evaluating initial fitness function using multi-objective function.
- Step 7:* Compute local best and global best solutions.
- Step 8:* Update swarm velocity and swarm position.
- Step 9:* Update EV FCS Station location based on the swarm and updated system data.
- Step 10:* Calculate and update fitness using multi-objective function.

Step 11: Compute and update local best and global best.

Step 12: Check for maximum iteration limit or converging criteria if achieved move next step *else go to Step 7*.

Step 13: Print the EV FCS station and DGs size and locations.

5 Case Study

This paper presents the case study of city Durgapur, WB, by considering the modified IEEE 33 bus distribution system with some assumptions required for the implementation. The study considering the Tesla Model S (released in 2014) having an efficiency of 92% and having a battery capacity of 85 kWh. In this study, the IEEE 33 bus system is modified based on different system parameters. The overall load of the system is raised from 3.75 to 11.1 MW. So, the active as well the reactive power load is also raised in the same ratio that is $11.1/3.75$, and to meet the load demand, the alteration of different parameters is also done like the overall voltage of the system is raised from 12 to 20 kV [1, 20]. As well as the parameter like resistance and inductance of the line to be reduced with a factor that is $(2/3)$. Maximum and minimum voltage deviations are maintained from 1.05 to 0.95 p.u.

6 Results and Discussions

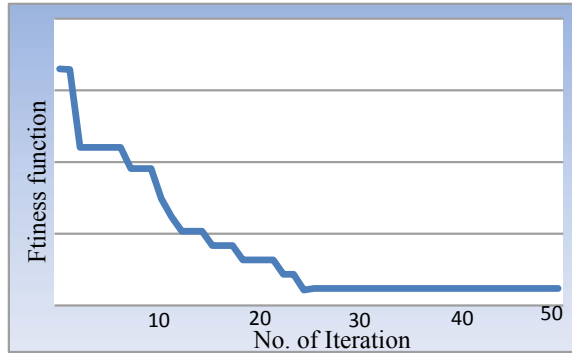
6.1 With EV Station Only

To evaluate the PSO algorithm, we have used the 30 trial and 50 iterations for evaluating the accuracy of the result. Best trial having a minimum value of the objective function is considered as the result. Table 2 represents the minimum value of the objective function that is about 4.92644, and the EV FCS location obtained are 9, 28, 25 and 22 buses, respectively. Figure 2 displays the overall bus configuration in Durgapur City which has four different zones as Z_1 , Z_2 , Z_3 and Z_4 . Each zone has a uniformly distributed EV population as discussed above. The results of different zone buses are Z_1 FCS is at 22, Z_2 FCS is at 25, Z_3 FCS is at 28 and Z_4 FCS is at 9

Table 2 EV FCS location, DG station size and objective function values

Objective function with EV FCS only	4.926440795	Objective function with EV FCS and DGs	3.5618
EV station no. 1 location	9th bus	DG station no. 1 size	0.001 MW
EV station no. 2 location	28th bus	DG station no. 2 size	4.1830 MW
EV station no. 3 location	25th bus	DG station no. 3 size	3.7992 MW
EV station no. 4 location	22nd bus	DG station no. 4 size	2.9510 MW

Fig. 4 Fitness convergence with EV and DG stations



bus. Zone 1 has its EV FCS at bus number 22 from the collection set of bus sets that is 19, 20, 21 and 22. Zone 2 has its EV FCS at bus number 25 from the collection set of buses that is 23, 24 and 25. Zone 3 has its EV FCS at bus number 28 from the collection set that is 26, 27, 28, 29, 30, 31, 32 and 33. Zone 4 has its EV FCS at bus number 9 from the collection set that is from bus number 9 to 18 buses. And the best fitness value obtained is about 4.9244 which is the lowest value of all the ten trials executed in the program.

6.2 With EV Station and DGs

The result is expressed in this section to evaluate the PSO algorithm, and we have used the 10 trial and 50 iterations for evaluating the accuracy of the result. Figure 4 represents that the fitness function converges at 26th iteration of the best trial. And the best fitness value obtained is about 3.5618 which is the lowest value of all the ten trials executed in the program. Fitness value is obtained by the objective function as mentioned in Eq. 4. Table 2 represents the DG Station size which are located the different EV station that is bus number 9, 28, 25 and 22, respectively. Each EV station will have its generating unit of different size obtained after optimization is 0.001 MW, 4.183 MW, 3.7992 MW and 2.951 MW, respectively. The overall station development cost (SDC) with EV station and DGs is 2,747,900\$. Pie chart in Fig. 4 represents the cost of EV station and DG station. The system's voltage profile for the arrangement of minimum and maximum values for the system at buses is shown in Fig. 5. Voltage profile is shown on different buses, as we know that the voltage profile improves with the increased generation. DG generation changes the voltage profile as shown in Fig. 5. Both EV and DG Stations combined have a positive impact on voltage profile. Minimum voltage is 0.9 p.u. at the extreme end bus number 33, which is better than the initially test system. Figure 5 represents voltage profile which was having a negative impact after the implementation of EV station only is also being improved with DGs. With the increased load reliability of the system

Fig. 5 Pie chart of cost

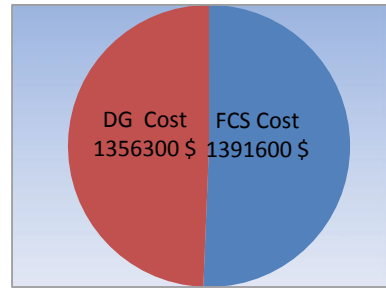
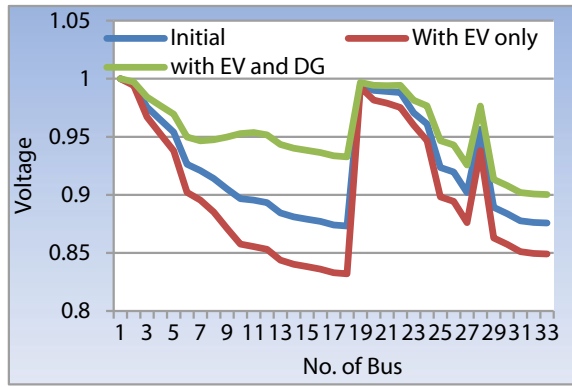


Fig. 6 Overall voltage profile at different buses

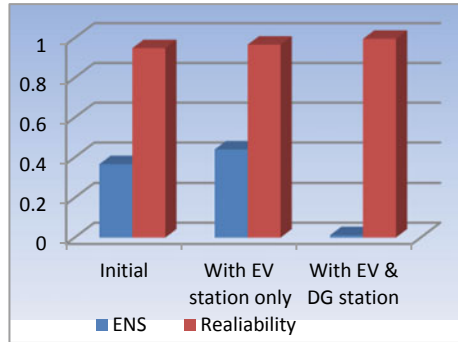


must decreased, but the objective function is designed in such a manner that the reliability improves. Figure 6 represents the reliability of the system, which is initial was 94.93% which improved up to appox 99% after the implementation of EV as well as DG station simultaneously. As the load is increased in the system, the value of current is increased in the system which leads to the increase in power losses. With the implementation of the DG, the generation of power is localized which reduces the power losses in the system. Table 3 represents the impact of system power losses for all three cases, i.e. initial, with EV only and with EV and DG, respectively. Hence with EV stations and DGs, the losses are reduced significantly as shown in Fig. 7.

Table 3 System power losses comparison

Losses	Initial case	With EV station only	With EV and DG stations
P loss (in MW)	0.667867	1.139965624	0.418907724
Q loss (in Mvar)	0.445989	0.760827628	0.280953995

Fig. 7 Bar graph of ENS and reliability



7 Conclusion

The optimum location of fast-charging station (FCS) including DGs in different four zones of the Durgapur City which covers the overall requirements of the EV distribution in the city using PSO is reported in this work. The PSO is used for minimization of problem objective function by minimizing the power losses, minimization of voltage deviation and maximizing the reliability of the system and also calculated the station infrastructure cost (SIC), which is fixed as per the land area requirement as well as the electrical equipment like connector and transformer. And the station development cost (SDC) of EV FCS station without DGs is 1,391,600\$. The placement of FCS at different location is bus number 9, 22, 25 and 28. Each location FCS is the best location as per the concern of this paper that is its dependence on cost, voltage and reliability. After optimal allocation of EV FCS station, DGs are also placed at that particular location by the FCS station owner. Each FCS station is having the DG station of different sizes that is 1 kW, 2.591 MW, 3.7992 MW and 4.183 MW at bus number 9, 28, 25 and 22, respectively. The station development cost (SDC) of DGs is 1,356,300\$. The reliability of the system is improved to approx 99% after the implementation of DG station on the same FCS station. Voltage profile which was having a negative impact after the implementation of EV station only is also being improved with DGs allocation. And power losses are reduced by approx 37% then initial test system. Reliability is improved up to 6% of the initial test system, and the voltage deviation is reduced which is maintained at buses upto 0.9 per unit.

References

1. Amiri SS, Jadid S (2017) Optimal charging schedule of electric vehicles at battery swapping stations in a smart distribution network. In: IEEE smart grid conference (SGC), 20 Dec 2017, pp 1–8
2. Hou K, Xu X, Jia H, Yu X, Jiang T, Zhang K, Shu B (2016) A reliability assessment approach for integrated transportation and electrical power systems incorporating electric vehicles. IEEE Trans Smart Grid

3. You P, Yang Z, Zhang Y, Low SH, Sun Y (2016) Optimal charging schedule for a battery switching station serving electric buses. *IEEE Trans Power Syst* 31(5):3473–3483
4. Sadeghi-Barzani P, Rajabi-Ghahnavieh A, Kazemi-Karegar H (2014) Optimal fast charging station placing and sizing. *Appl Energy* 15(125):289–299
5. Sawle Y, Gupta SC, Bohre AK (2018) Review of hybrid renewable energy systems with comparative analysis of off-grid hybrid system. *Renew Sustain Energy Rev* 81:2217–2235
6. Rani KS, Sannigrahi S, Acharjee P, Bohre AK (2019) Determining optimal size and placement of renewable DG considering variation of load. *Int J Recent Technol Eng (IJRTE)* 8(2S7):310–315
7. Granovskii M, Dincer I, Rosen MA (2006) Economic and environmental comparison of conventional, hybrid, electric and hydrogen fuel cell vehicles. *J Power Sources* 159(2):1186–1193
8. Ren X, Zhang H, Hu R, Qiu Y (2019) Location of electric vehicle charging stations: a perspective using the grey decision-making model. *Energy* 173:548–553
9. Liu Z, Wen F, Ledwich G (2012) Optimal planning of electric-vehicles charging stations in distribution systems. *IEEE Trans Power Delivery* 28(1):102–110
10. Luo L, Gu W, Zhou S, Huang H, Gao S, Han J, Wu Z, Dou X (2018) Optimal planning of electric vehicle charging stations comprising multi-types of charging facilities. *Appl Energy* 226:1087–1099
11. Zhang Y, Zhang Q, Farnoosh A, Chen S, Li Y (2019) GIS-based multi-objective particle swarm optimization of charging stations for electric vehicles. *Energy* 169:844–853
12. Battapothula G, Yammani C, Maheswarapu S (2019) Multi-objective simultaneous optimal planning of electrical vehicle fast charging stations and DGs in distribution system. *J Mod Power Syst Clean Energy* 7(4):923–934
13. Pang C, Dutta P, Kezunovic M (2012) BEVs/PHEVs as dispersed energy storage for V2B uses in the smart grid. *IEEE Trans Smart Grid* 3(1):473–482
14. Cheng L, Chang Y, Lin J, Singh C (2013) Power system reliability assessment with electric vehicle integration using battery exchange mode. *IEEE Trans Sustain Energy* 4(4):1034–1042
15. Zimmerman RD, Murillo-Sánchez C. MATPOWER user's manual
16. Bohre AK, Agnihotri G, Dubey M (2016) Optimal sizing and siting of DG with load models using soft computing techniques in practical distribution system. *IET Gener Trans Distrib* 10(11):2606–2621
17. Kalambe S, Agnihotri G, Bohre AK (2013) An analytical approach for multiple Dg allocation in distribution system. *Electr Electron Eng Int J (ELELIJ)* 2(3):39–48
18. Sedghi M, Ahmadian A, Aliakbar-Golkar M (2015) Optimal storage planning in active distribution network considering uncertainty of wind power distributed generation. *IEEE Trans Power Syst* 31(1):304–316
19. Ameli A, Bahrami S, Khazaeli F, Haghifam MR (2014) A multiobjective particle swarm optimization for sizing and placement of DGs from DG owner's and distribution company's viewpoints. *IEEE Trans Power Delivery* 29(4):1831–1840
20. Bohre AK, Agnihotri G, Dubey M (2015) The optimal distributed generation placement and sizing using novel optimization technique. *Middle-East J Sci Res* 10:1228–1236
21. Bohre AK, Agnihotri G, Dubey M (2015) Impacts of the load models on optimal sizing and siting of distributed generation in distribution system. *World Appl Sci J* 33(7):1197–1205
22. Bohre AK, Agnihotri G, Dubey M (2015) The OPF and butterfly-PSO (BF-PSO) technique based optimal location and sizing of distributed generation in mesh system. *Electr Electron Eng Int J* 4(2):127–141
23. Bohre AK, Agnihotri G, Dubey M (2015) The butterfly-particle swarm optimization (Butterfly-PSO/BF-PSO) technique and its variables. *Int J Soft Comput Math Control* 4:23–39
24. Chadha M (2019) India's wind capacity crosses 10% share in overall installed base. *CleanTechnica*, 30 July 2019. cleantechica.com/2019/01/21/indias-wind-capacity-crosses-10-share-in-overall-installed-base/
25. Medjoudj R, Bediaf H, Aissani D (2017) Power system reliability: mathematical models and applications. *Syst Reliab* 279

Congestion Management of System with N-1 Contingency by Optimal Placement of TCSC Using PSO



Ashish Singh and Aashish Kumar Bohre

1 Introduction

Power industry in India is undergoing a significant transformation and more competitive with the entry of private player. With the increasing load demand and to meet the electricity at affordable price, restructuring and deregulation are a must. In India, the ownership of the power sector is government controlled, which has led to supply shortages, inability to add the generating capacity, and the electricity supply is treated as social services rather than a market commodity. In a restructured power market system, private organization and government organization both operate in all the sectors of GENCOs, TRANSCO, DISCO, and the whole revenue collection is changed. Independent system operator (ISO) maintains the coordination between all the deregulated power system models. Due to deregulation, the electricity price goes down, and the consumer has a choice to select the retailer according to load and tariff, and the market has more innovation in term of cost and profit. Construction of a new transmission line takes a long period, and massive investment is involved [1]. Overload and outage of the line caused congestion in a transmission line of a deregulated power systems. Congestion occurs when the power flow is higher than the operating limits, which cause violation of system constraints such as thermal limits of the line, voltage limit and stability of the system. It not only results in the equipment failure but also results in poor power quality. Congestion management is essential for relieving the congestion to maintain optimal power flow, improving the power quality, preventing any equipment damage and avoiding the condition for the blackout [2]. Congestion has to be relieved properly and timely, if not, then the cost needed to relieve the congestion, and the damage that occurs due to the congestion

A. Singh (✉) · A. K. Bohre

Department of Electrical Engineering, National Institute of Technology, Durgapur, Durgapur, India

A. K. Bohre

e-mail: aashishkumar.bohre@ee.nitdgp.ac.in

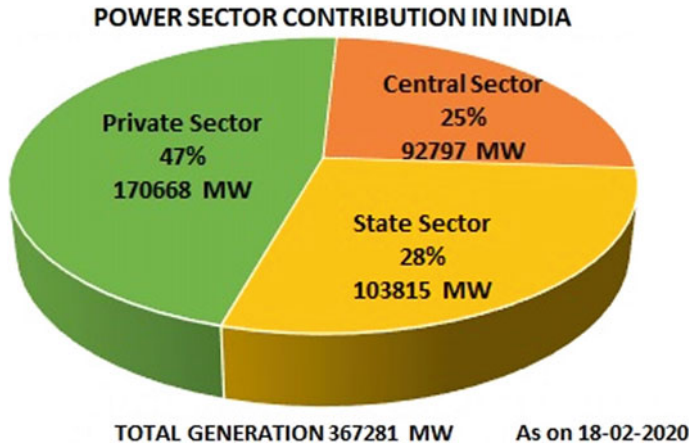


Fig. 1 Deregulated power market sharing

is much more for the electricity trading. Congestion is a major threat to optimal the power flow, which consequently affects the voltage, led to power loss and therefore, economic losses. Therefore, there is a high risk of stability and transmission security [3]. FACTS devices help to relieve the congestion considering all the violation constraints. TCSC a series FACTS device used to remove the congestion also in mitigating sub-synchronous resonance. The deregulated power market sharing related to Indian power sector is shown in Fig. 1.

India is vast abundant amount of coal and lasting for more than 200 years. India has potentially used these coals for the energy generation and strengthens the economy. Thermal power plant contributes more than 70% of the total power generation as of 2020. Coal deposits are abundant in south-central and eastern parts of the India. Jharkhand had the maximum coal reserve of around 26.16%. In India, leveled electricity generation cost from thermal power plant is at around \$44.5/MWh (Rs. 3.05/kWh), from solar power generation is at around \$38.2/MWh (Rs. 2.62/kWh), and onshore wind power generation is at \$48.9/MWh (Rs. 3.36/kWh) which is low from many nations as represented in Fig. 2 and Table 1 respectively.

This paper consists of two sections. Firstly, the optimal location of TCSC due to N-1 contingency using PSO. Secondly, the environmental effect due to gases produced in a thermal power plant. Following which environmental cost is calculated using CO₂, NO₂, SO₂ and is added to the generation cost. This environmental cost is for the damage done due to air pollution. This paper discussed the environmental impact of the different power plant and its market tariff analysis.

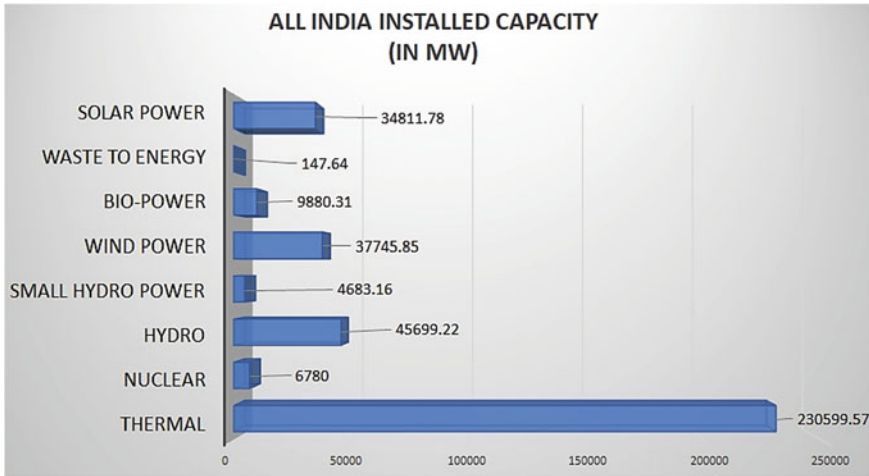


Fig. 2 Electricity production by different sources (April/2020) [4]

Table 1 Thermal power plant sub-category (in MW)

Coal	Lignite	Gas	Diesel	Total
198,524.5	6610	24,955.36	509.71	230,599.6

2 TCSC and congestion

2.1 Thyristor-Controlled Series Capacitor (TCSC)

TCSC includes the series compensating capacitors shunted by a thyristor-controlled reactor (TCR) for providing a smoothly variable series capacitive reactance. TCSC is used in the operation and control of power systems such as enhancing power flow and is used for increasing the power transmission capability, system stability is improved, system losses are reduced and improvement in the voltage profile of the lines [5–7]. Thus, TCSC reactance characteristics show that operations in both inductive and capacitive region by changing the firing angle (α) are shown in Fig. 3.

TCSC devices reduce the line reactance in a branch of a transmission line those enhancing the active power in the line and compensating reactive power flow. The related schematic diagram of TCSC is given in Fig. 4.

Fig. 3 Characteristic curve of reactance versus firing angle

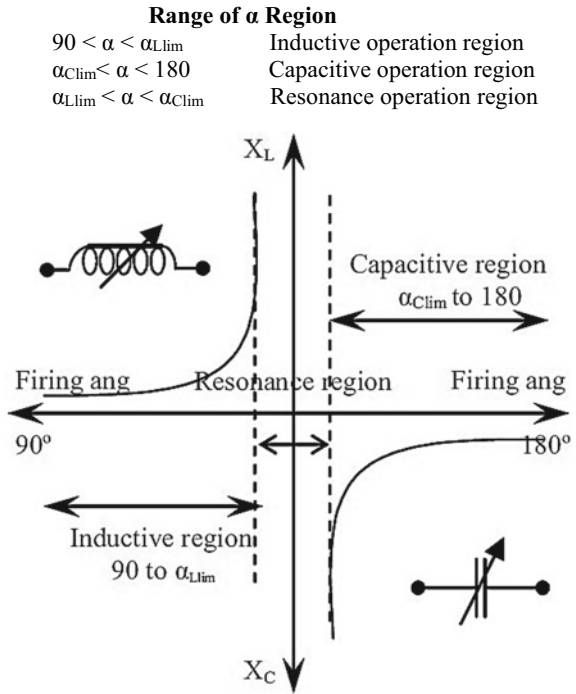
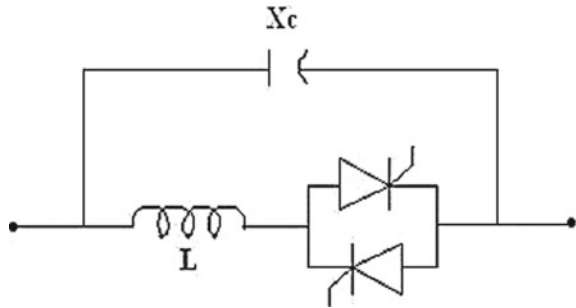


Fig. 4 Schematic diagram of TCSC



2.2 Creation of Congestion

Transmission congestion occurs mainly due to generation outages, line outages and higher load demands. Congestion is created arbitrarily by outage of any branch [8, 9].

3 Problem Function and System Index

The primary objective of the presented work is to determine the optimal placement of TCSC device in a network while satisfying the thermal limits. The cost of TCSC devices is very high. The objective is to find the location while minimizing the cost of the TCSC device, voltage deviation, power loss and maximizing the reliability. The multi-objective function is addressed here by weighting each objective function properly.

3.1 Cost Index

Generally, TCSC is a series reactance with the operating reactance limits as:

$$-0.8x_1 < x_c < 0.7x_1$$

Cost function for the TCSC:

$$C_{\text{TCSC}} = 0.0015S^2 - 0.713S + 153.75 \quad (1)$$

$$S = |Q_2 - Q_1| \quad (2)$$

$$C_{\text{index}} = \frac{(C_t + C_{\text{TCSC}})}{C_t} \quad (3)$$

where x_1 : Transmission line reactance where TCSC is placed, x_c : TCSC reactance, C_{TCSC} : TCSC investment cost in \$/kVaR, Q_1 and Q_2 are the reactive power flow of the considered line before and after the placement of TCSC.

3.2 Voltage Deviation Index

Voltage profile of a system must be within the limit.

$$V_{\text{index}} = \frac{(V_{\text{ref}} - V_{\text{new}})}{V_{\text{ref}}} \quad (4)$$

where V_{ref} = voltage after outage (slack bus), V_{new} : voltage after each iteration.

3.3 Loss Index

Here, total losses are calculated in MVA.

$$S_{\text{loss}} = P_{\text{loss}} + jQ_{\text{loss}}$$

$$S_{\text{index}} = \frac{S_{\text{loss new}}}{S_{\text{loss base}}} \quad (5)$$

where $S_{\text{loss}} = P + jQ$, $S_{\text{loss new}}$ = losses after each iteration, $S_{\text{loss base}}$ = loss after outage.

3.4 Reliability

The reliability is significant used to access the system performance. Here, the reliability is considered based on the energy not served (ENS) or energy not supplied to the network [10]. The ENS can be calculated by Eq. (6):

$$\text{ENS} = \alpha d \sum_{k=1}^N \lambda_k |I_{kp}| * V_{\text{rated}} \quad (6)$$

where I_{kp} is branch peak load current, λ_k is k th branch or line failure rate, and V_{rated} is system rated voltage. The d and α are repair duration and load factor, respectively. Also, system reliability can be given in Eq. (7):

$$\text{Reliability } (R) = \left(1 - \frac{\text{ENS}}{\text{PD}} \right) \quad (7)$$

where PD is total power demand by customer, and ENS is total energy not supplied/served. Here, the objective is to maximize the reliability.

3.5 Multi-objective Functions

The objective function (f) can be given as:

$$f = 0.2C_{\text{index}} + 0.5V_{\text{index}} + 0.3S_{\text{index}} + 0.1R^{-1} \quad (8)$$

All the above objective function is considered in a single multi-objective function to make the fitness function used for PSO. Highest weighting factor is considered for

the voltage deviation, then loss index. Minimize fitness function is primary objective to obtain optimal placement of TCSC in a 14-bus system.

4 Particle Swarm Optimization (PSO)

Particle swarm optimization (PSO) is a heuristic method inspired by the social behavior of fish schooling and bird swarms. Kennedy and Eberhart developed PSO in 1995 for the solution of nonlinear problems with continuous variables. Location the FACTS devices is obtained with the help of the PSO algorithm. In PSO, particles fly throughout the search area via flowing current optimal particles. Each particle flies with a velocity in search area, and these particles get updated each time through their own flying experiences and other particles flying experiences. The best solution (fitness) is associated by keeping track of each individual so far, and this best solution value is P_{best} . Finally, the best value determined throughout the population is known as G_{best} [11, 12]. The velocity and position updates of a particle are by the following equations:

$$V_{ik+1} = W * V_{ik} + C_1 * rand * (P_{best}_i - S_{ik}) + C_2 * rand * (G_{best}_i - S_{ik}) \quad (9)$$

$$S_{ik+1} = S_{ik} + V_{ik+1} \quad (10)$$

where V_{ik} = Agent i velocity at k th iteration, V_{ik+1} = Agent i velocity at $(k + 1)$ th iteration, W = inertia weight, S_{ik} = Present position of agent i at k th iteration, S_{ik+1} = Present position of agent i at $(k + 1)$ th iteration, W_{max} = Inertia weight initial value, W_{min} = Inertia weight final value, P_{best}_i = agent i best position, G_{best}_i = group best position.

4.1 Algorithm of Proposed Methodology

1. Run the optimal power flow for the N-1 contingency to identify the overloaded lines.
2. Define inputs of system like TCSC data, line data and load data.
3. Maximum number of iterations and PSO parameters are specified.
4. Initialize the random population with random position and velocity of particles.
5. Define the minimum (equals to 1) and maximum iterations.
6. Estimate the problem objective function value based on Eq. (8).
7. Run optimal power flow to assess active power, line flows, reactive power rescheduling, system losses and voltage magnitude of all buses. The total power loss of system is calculated with TCSC in the system.

8. Update particles and calculated objective function value and if more than individual Pbest, assign it as current Pbest and update in current position.
9. Update Gbest based on the minimum Pbest value among all particles.
10. Updates all particles position and velocity.
11. Check for termination criteria, i.e., if reached maximum iterations, then get optimal solution by Gbest solution. Else, iteration = iteration + 1 and repeat process from step 4.
12. Find the optimal solution for TCSC location in the system.

The different PSO parameter considered in this work such as number of particles are 30, $c_1 = c_2 = 2$ and the random variables in the range of 0–1. Also, the total number of trials and iterations are 30 and 50, respectively.

5 Environmental Effect

For removing the congestion, a conventional approach is to establish a new transmission line in the system. Establishing a new transmission line needed year of planning and also results in a vast amount of capital is also needed non-technical hurdles is also there like land acquisition, market loans, biological impacts and the public interest. TCSC helps in removal of congestion and thus avoiding the chance of land acquisition and other environmental hazards. In this paper, all generating plant is assumed as a thermal power plant. A proposed method is given considering the hazardous gases in terms of additional market cost with the generation cost. This is an attempt to impose a new tariff on the thermal power plant for environmental damage and also for boosting the new era of energy generation by shifting toward renewable energy generation. This new tariff is known as environmental cost. The thermal power plant produces a lot of pollution. In Sushil et al. [13], heavy metal concentrations of Cr, Pb, Mn, Zn, Cu, Ni and Co are present in the in-fly ashes and bottom ashes produced by the thermal power plant. The wet disposal technique using ash pond makes the heavy metal to contaminate. In Raghuvanshi et al. [14], the paper discussed the CO₂ emission from coal power generation and other energy indicator on which GHG emission is dependent. In Indian power plant, it has been found that 0.8–0.9 kg per unit carbon dioxide is emitted. Best option for disposal of CO₂ is into sinks. Carbon dioxide sink is biosphere sink, geosphere sink and sequestration (oil reserve, coal bed and deep ocean) and material sink.

An environmental cost is added to the generation cost for the impact of gases produced so that stress is there for producing harmful gases. This environmental cost collected, separated and rewarded to the renewable energy sector. An environmental cost calculated through the following Eqs. (11)–(14):

$$C_{CO_2} = a_{CO_2} P_g^3 + b_{CO_2} P_g^2 + c_{CO_2} P_g + d_{CO_2} \quad (11)$$

$$C_{\text{NO}_2} = a_{\text{NO}_2} P_g^3 + b_{\text{NO}_2} P_g^2 + c_{\text{NO}_2} P_g + d_{\text{NO}_2} \quad (12)$$

$$C_{\text{SO}_2} = a_{\text{SO}_2} P_g^3 + b_{\text{SO}_2} P_g^2 + c_{\text{SO}_2} P_g + d_{\text{SO}_2} \quad (13)$$

$$C_{\text{env}} = C_{\text{CO}_2} + C_{\text{NO}_2} + C_{\text{SO}_2} \quad (14)$$

where C_{CO_2} = Cost due to production of CO_2 , C_{NO_2} = Cost due to production of NO_2 , C_{SO_2} = Cost due to production of SO_2 , C_{env} = Environmental cost.

a_{CO_2} , b_{CO_2} , c_{CO_2} , d_{CO_2} , a_{NO_2} , b_{NO_2} , c_{NO_2} , d_{NO_2} , a_{SO_2} , b_{SO_2} , c_{SO_2} , d_{SO_2} are coefficient depends on plant and vary according to plant. The variation depends on the step taken through the plant in term of particulate gases, and the quality of coal used varies from plant to plant. These parameters enhance the efficient of a thermal power plant.

Cost function of each plant:

$$C_i = a + bP_g + cP_g^2 \quad (15)$$

$$C_{\text{gen}} = \sum_{i=1}^n C_i \quad (16)$$

where P_g = Generation of active power, C_{gen} = Total generator cost.

Total cost is calculated in Eq. 17:

$$C_{\text{TOTAL}} = C_{\text{gen}} + C_{\text{CO}_2} + C_{\text{NO}_2} + C_{\text{SO}_2} \quad (17)$$

The objective is to calculate the tariff for the production of harmful gases. These equations are a direct relation of harmful gases produce in term of tariff. And the tariff is imposed to the thermal power plant which finally reflects in the total cost of energy generated by the thermal power plant. In thermal power plant [15], coal usage is less than 0.7–0.8 kg per unit. NO_2 emissions per unit is 4.34 g/kWh. CO_2 emissions per unit is 0.94 kg/kWh of electricity generation.

6 Results and Discussion

The projected method is applied on 14-bus system. Optimal power flow results are obtained for the base case, and then, N-1 outage is created arbitrary. In this paper, branch no. 13 (in between bus 6 and 13) is outage, and then, optimal power flow results are obtained. PSO technique is used to obtain optimal location considering multi-objective function. Through PSO, TCSC is placed at each branch except the outage branch corresponding to which the minimum fitness function branch is obtained, and

Table 2 Voltage profile with base case, N-1 case and with TCSC case

Bus no.	Base case	Outage case	TCSC case	Bus no.	Base case	Outage case	TCSC case
1	1.0600	1.0600	1.0600	8	1.0600	1.0600	1.0600
2	1.0408	1.0409	1.0409	9	1.0437	1.0360	1.0366
3	1.0156	1.0155	1.0156	10	1.0391	1.0326	1.0332
4	1.0145	1.0135	1.0139	11	1.0460	1.0425	1.0429
5	1.0164	1.0161	1.0162	12	1.0448	1.0222	1.0324
6	1.0600	1.0600	1.0600	13	1.0399	0.9870	0.9921
7	1.0463	1.0424	1.0428	14	1.0239	0.9959	0.9986

TCSC setting value is obtained. TCSC optimal location is at branch 12 (in between bus 6 and 12). Environmental cost is obtained at a thermal power plant according to generation capacity.

6.1 Voltage Profile

Voltage at all 14 bus is obtained for the base case, N-1 outage case, with TCSC. Voltage profile of the base cases at within the specified limit, with N-1 outage the voltage profile, gets deteriorated, i.e., poor voltage profile and including TCSC, the voltage profile is enhanced. A detailed comparison of the voltage profiles for all case as given in Table 2.

Here, bus 1 is considered slack bus at 1.06 p.u. With outage the voltage profile is very low, thus threatening the system. N-1 outage at branch 13 results in poor voltage at bus 12, 13. With TCSC at branch 12 voltage at bus 12, 13 is improved to a greater extent.

6.2 Losses

Due to N-1 contingency, congestion occurs in the system; as a result, the line reaches its thermal limits (I^2R), and the current also reaches at its limits, hence the more losses in the system. With TCSC, reactive power compensation is done and congestion is removed, thereby results in less losses in the system. In this paper, losses of all branches are added to get the total losses. A detailed total losses comparison is revealed in Table 3.

Table 3 Comparison of losses with base case, N-1 case and with TCSC case

Base case (MVA)	Outage case (MVA)	TCSC case (MVA)
40.2470	41.6528	40.7045

Table 4 Reactance value in the outage branch and TCSC setting value

Cases	Reactance of branch 13 (between bus no. 6 and 13)	Reactance of branch 12 (between bus no. 6 and 12)	TCSC setting value
Base case (p.u)	0.13027	0.25581	–
Outage case (p.u)	Outage	0.25581	–
TCSC case (p.u)	Outage	0.051162	–0.204648 (capacitive region)

Due to outage, the system total losses are increased by 1.4058 MVA from base case, and with the placement of TCSC, the losses are reduced in the contingency system. The dispatch time for calculation is considered 1 h. A saving of 0.9483 MVA is achieved. Annually, 8307.108 MVA is saved.

6.3 Outage

Reactance value of a branch considered for outage and reactance of branch before and after TCSC is given in Table 4. With the placement of TCSC, the p.u. value of the branch overall is decreased due to TCSC (series capacitance). TCSC prevents the condition of sub-synchronous resonance which arises in case of series capacitance.

The optimal TCSC allocation using PSO in this system after N-1 contingency is at branch 12. The TCSC set value is in capacitive region here.

6.4 Reactive Power Flow

Reactive power is more when the difference in the voltage is more in between the respective two buses. Due to outage, the whole active power and reactive flow from different branch by optimal power flow method as the load consumption is same. In the most congested line, the reactive power hits the upper limit. A reactive power compensation in a branch is obtained with the help of TCSC. The reactive power flow in the outage branch and in branch where TCSC is placed is tabulated in Table 5.

Table 5 Reactive power flow in the outage branch and in branch where TCSC is placed

Parameter	Base case	Outage case	TCSC case
Reactive power in branch 13 (MVar)	7.7265	Outage	Outage
Reactive power in branch 12 (MVar)	2.6604	6.8162	5.4299

Table 6 Generation cost and environmental cost estimation

Generator no.	Generation (MW)	Base case cost (\$/h)	CO ₂ cost (\$/h)	NO ₂ cost (\$/h)	SO ₂ cost (\$/h)	Total (\$/h)
1	194.3302	5511.6	984.83	125.48	846.83	7468.74
2	36.7192	1071.5	046.85	5.54	48.61	1172.5
3	28.7426	1158.0	038.65	2.60	43.80	1243.05
4	0.0003	0.0000	-02.45	-0.34	-7.40	-10.19
5	8.4949	0340.5	12.10	1.72	1.37	355.69
Total	268.2872	8081.6	1079.98	135	933.21	10,229.79

Due to N-1 outage, the voltage profile is deteriorated so the reactive power in a branch is increased to a greater extent. Here, the upper limit of the branch 12 is of 6 MVA, and after outage, it exceeds the upper limits. With TCSC, the voltage profile is improved due to reactive power compensation and the reactive power is within the limits. TCSC also enhances the active power in a branch. Thus, with TCSC, the branch is a transmission line which is within the thermal limits.

6.5 Environmental Cost Estimation

Linear polynomial method is used for getting the market cost of the generator. Generation cost and environmental cost tariff are calculated for a duration of 1 h in Table 6. Credits are given to those inactive generators. All the co-efficient parameter of different plant varies according to plant. The revenue penalizing the plant for producing harmful gases and resulting in the improvement in term of environmental.

With the addition of environmental cost in the generation cost, the total market cost of the thermal power plant is increased in a significant value. Also, the generator inactive (negative value) in the region is given benefit in term of environmental cost tariff, and environmental cost is levied on the active generator.

6.6 Environmental Effect

The amount of coal consumed and the harmful gases produced by a thermal power is shown in Table 7. This study is conducted for base case considering thermal power plant.

An estimation of coal consumed by a thermal power plant and the harmful gases produce are reduced with TCSC. Also with the use of TCSC, 0.9483 MVA is saved. Thus, a significant amount of coal is saved and reduction in the harmful gases.

Table 7 Amount of coal consumed in thermal power plant and gases produced

Generator no.	Generation (MW)	Coal consumed (ton)	CO ₂ produced (ton)	NO ₂ produced (kg)
1	194.3302	1360.3	1826.70	843.393
2	36.7192	257.0344	345.16048	159.361
3	28.7426	201.1982	270.18044	124.74
4	0.0003	0.0021	0.00282	0.001302
5	8.4949	59.4643	79.85206	36.867866
Total	268.2872	1878.0104	2521.89968	1294.566

7 Conclusion

The PSO is used to locate optimal placement of TCSC in the presented work. Through the proposed method, the optimal location was found out considering the multi-objective function. The result is obtained of standard 14-bus system. TCSC value and its optimal location on the branch are obtained through PSO. With the N-1 outage, the voltage profile of the system is very severe, and also the losses in the system were increased, thus threatening the system. The voltage profile is enhanced and losses are less by optimal location of TCSC as compared with the N-1 outage. This paper discusses the techno-economical–environmental aspect in a system. Cost of installation of the new transmission lines is saved with the help of TCSC, and the installation of new transmission line saves crore of INR. Environmental cost tariff is calculated with relation with the harmful gases. This paper discussed the future of the energy market, restructured power market. Results show that the ton of harmful gases is produced. The environmental cost is a new way of rewarding the energy generation unit. Moreover, the gases co-efficient will make a significant improvement in the measure taken by the thermal power plant. With the help of TCSC, the losses are reduced by 0.9483 MVA (for a dispatch time of one hour), thus saving the significant amount of coal used and reducing the harmful gases produced by the thermal power plant. TCSC secures the system, and this security also ensures the reduction of environmental tariff. This paper presents the technical approach and control of TCSC and environmental approach with direct relation in term of market in a restructured power system. This paper proposed a new form of environmental pollution trading and also securing the system with the help of TCSC, also accountability of environmental protection. This paper presents the border objective of using FACTS device both in term of network security and environment.

References

1. Kishore TS, Singal SK (2014) Optimal economic planning of power transmission lines: a review. *Renew Sustain Energy Rev* 39:949–974

2. Pillay A, Prabhakar Karthikeyan S, Kothari DP (2015) Congestion management in power systems—a review. *Int J Electr Power Energy Syst* 70:83–90
3. Narain A, Srivastava SK, Singh SN (2020) Congestion management approaches in restructured power system: key issues and challenges. *Electr J* 33(3):106715
4. All India installed capacity. Central Electricity Authority. https://www.cea.nic.in/reports/monthly/installedcapacity/2020/installed_capacity-04.pdf
5. Shivashankar S (2013) Optimal location of TCSC in transmission lines using contingency severity index and performance index methods for single contingency using PSO. In: 2013 international conference on power, energy and control (ICPEC). IEEE
6. Manganuri Y, Choudekar P, Asija D (2016) Optimal location of TCSC using sensitivity and stability indices for reduction in losses and improving the voltage profile. In: 2016 IEEE 1st international conference on power electronics, intelligent control and energy systems (ICPEICES). IEEE
7. Singh A, Bohre AK (2020) Market analysis in a restructured power system with TCSC by LMP calculation. In: IEEE international conference on computational intelligence for smart power system and sustainable energy (CISPSSE), pp 1–7
8. Zimmerman RD, Murillo-Sanchez CE (2013) MATPOWER 7.0 user's manual, 2019
9. Paul K, Kumar N (2017) Application of MATPOWER for the analysis of congestion in power system network and determination of generator sensitivity factor. *Int J Appl Eng Res* 12(6):969–975
10. Bohre AK, Agnihotri G, Dubey M (2016) Optimal sizing and sitting of DG with load models using soft computing techniques in practical distribution system. *IET Gener Transm Distrib* 10(11):2606–2621
11. Hashemzadeh H, Hosseini SH (2009) Locating series FACTS devices using line outage sensitivity factors and particle swarm optimization for congestion management. In: 2009 IEEE power & energy society general meeting. IEEE
12. Sheth A, Kotwal CD, Pujara S (2015) Optimal placement of TCSC for improvement of static voltage stability. In: 2015 5th Nirma University international conference on engineering (NUiCONE). IEEE
13. Sushil S, Batra VS (2006) Analysis of fly ash heavy metal content and disposal in three thermal power plants in India. *Fuel* 85(17–18):2676–2679
14. Raghuvanshi SP, Chandra A, Raghav AK (2006) Carbon dioxide emissions from coal based power generation in India. *Energy Convers Manag* 47(4):427–441
15. Mittal ML, Sharma C, Singh R (2012) Estimates of emissions from coal fired thermal power plants in India. In: 2012 international emission inventory conference

Optimal Reactive Power Dispatch Under Load Uncertainty Incorporating Solar Power Using Firefly Algorithm



P. Ramkee, S. N. V. S. K. Chaitanya, B. Venkateswara Rao,
and R. Ashok Bakkiyaraj

1 Introduction

An ORPD problem is also a big challenge in power system. ORPD means control the apparatus to optimize reactive power flow to reduces active power, losses and improve voltage quality [1, 2]. There are several challenges faced in power systems in which some of them are voltage instability and optimal reactive power flow. To overcome the operating necessities of a consistent power system is to retain the voltage inside the allowable range [3, 4]. Power balance equations are the equality constraints, and generator voltages, transformer tap settings and shunt capacitors are the inequality constraints, respectively. Minimize the active power loss and voltage deviation through the optimal modifications in control variables of the power system, at the same time fulfilling different constraints detected by the electrical network. This problem requires the finest use of the obtainable voltage magnitude of the generator, tapings of the transformer and the output of capacitor banks to reduce the losses and voltage deviation of the system [5]. The uncertainty of loads and solar power in [6] is simplified by a scenario reduction approach [7, 8].

In power system, economical operation is to run the network at low cost by maintaining reliability and security of the power system, and it also studied the estimation of active power loss. Real power regulation as well as imaginary power dispatch is the goals of the economic operation in power system. The way to regulate real power and distribute the reactive power is to introduce the renewable source. The sustainable sources show a vital role in the electrical power systems. By incorporation of renewable source into power system, the cost of generation is reduced, and system performance is also enhanced [9]. The uncertainty at different solar power outputs

P. Ramkee · S. N. V. S. K. Chaitanya · B. Venkateswara Rao (✉)
Department of Electrical and Electronics Engineering, V R Siddhartha Engineering College
(Autonomous), Vijayawada, Andhra Pradesh, India

S. N. V. S. K. Chaitanya · R. Ashok Bakkiyaraj
Department of Electrical Engineering, Annamalai University, Chidambaram, Tamil Nadu, India

and different loading conditions is observed by considering the renewable energy source.

Here, the firefly algorithm is engaged for the solution of the ORPD problem, and it effectively tests on IEEE 14-bus test system. The remaining of this paper listed as follows: The problem formulation is depicting in Sect. 2; the procedure of the firefly algorithm is illustrated in Sect. 3. The simulation outcomes that initiate the firefly algorithm designed for ORPD are exposed in Sect. 4. To end with, the paper conclusions are programmed in Sect. 5.

2 Problem Formulation

2.1 Objective Functions

2.1.1 Real Power Loss

The aim of these function remains minimizing losses of real power (P_{loss}) in the network is calculated as

$$F_1 = \text{Min}\{P_{\text{Loss}}(x, y)\} = \sum_{m=1}^{N_1} P_{\text{loss}} \quad (2.1)$$

where N_1 stands transmission line number, and P_{loss} represents real power loss usually expressed in MW.

2.1.2 Voltage Deviation

For improvement of the profile of voltage, the additional objective be situated to diminish voltage deviation in any way load buses, and it is calculated as

$$F_2 = \text{Min}\{V_{\text{deviation}}(x, y)\} = \sum_{n=1}^{N_b} |V_n - V_{\text{spec}}| \quad (2.2)$$

where N_b is quantity of load bus, and V_{spec} is a pre-specified voltage amount at load bus.

For multi-objective function, above-stated two functions in Eqs. (2.1) and (2.2) are given equal weight such that

$$F_3 = 0.5 * F_1 + 0.5 * F_2 \quad (2.3)$$

2.2 Constraints

To minimize the objective functions of the ORPD problem is subjected to the following constraints, one is equality, and another is inequality constraints.

2.2.1 Equality Constraints

The active power and reactive power balance equations are given by

$$P_{Ga} - P_{Da} - V_a \sum_{b=1}^{NB} V_b [G_{ab} \cos(\delta_{ab}) + B_{ab} \sin(\delta_{ab})] = 0 \quad (2.4)$$

$$Q_{Ga} - Q_{Da} - V_a \sum_{b=1}^{NB} V_b [G_{ab} \sin(\delta_{ab}) - B_{ab} \cos(\delta_{ab})] = 0 \quad (2.5)$$

2.2.2 Inequality Constraints

$$V_{Gm,\min} \leq V_{Gm} \leq V_{Gm,\max}; \quad m \in N_g \quad (2.6)$$

$$Q_{Gm,\min} \leq Q_{Gm} \leq Q_{Gm,\max}; \quad m \in N_g \quad (2.7)$$

$$T_{m,\min} \leq T_m \leq T_{m,\max}; \quad m \in N_t \quad (2.8)$$

$$Q_{cm,\min} \leq Q_{cm} \leq Q_{cm,\max}; \quad m \in N_c \quad (2.9)$$

where

- N_g number of generators,
- N_t number of transformers,
- N_c number of capacitors.

2.3 PV Array Output

The calculation of the PV power output requires the some significant electrical characteristics which are open-circuit voltage, short-circuit current and fill factor. The open-circuit voltage is obtained by number of cell connected in series, and short-circuit current is calculated by number of cells connected in parallel. The fill factor is formulated by using the following expression.

$$P_{\max} = FF \times V_{oc} \times I_{sc} \quad (2.10)$$

The power output of array can be calculated using the product of number of PV modules arranged in series as well as in parallel, and module output power can be given below

$$P_A = N_p \times N_s \times P_M \quad (2.11)$$

The PV array power output is calculated by using different parameters are given in [10, 11]. In given reference paper, total 20 units are considered to generate 6.967 MW, and every unit is having 10 modules both in series and parallel. The output power of one PV module is 348.35 kW. The total power generated from PV system is given to the load bus 14.

2.4 Uncertainty of Load and Solar

PDF means that probability density function and lognormal probability density are the methods to model the load uncertainty and solar irradiance, respectively. Different loading conditions are considered randomly as 25, 50, 75, 100 and 105%. Solar irradiance is available only 12 h in a day. The generation from solar PV system is zero during night-time. Zero irradiance is set through 50% possibility, and the leftover 50% possibility protects the conditions of solar irradiance generate by lognormal distribution function.

3 Firefly Algorithm

The firefly algorithm (FA) is an advanced optimization technique implemented by Yang in 2008 [12], and FA is motivated by the flashing performance of fireflies. FA is simple, flexible and easy to implement. The three main rules of firefly algorithm are given in [13–15]. The light intensity varies according to the inverse square law for a particular distance.

$$I_0 \propto \frac{1}{r^2} \quad (3.1)$$

The brightness I of a firefly at an exacting position x preserve stay selected as $I(x) \propto f(x)$. The distance between the fireflies is directly proportional to the light intensity which is given as

$$I(r) = I_0 \exp(-\gamma r^2) \quad (3.2)$$

The attractiveness denoted with β of a firefly is defined through following expression

$$\beta = \beta_0 \exp(-\gamma r^2) \quad (3.3)$$

where β_0 is the attractiveness at $r = 0$.

In general, the values of α , β , γ are considered in between 0 and 1.

The distance between the two fireflies located at m and n is given as

$$r_{mn} = \sqrt{\sum_{k=1}^d (x_{m,k} - x_{n,k})^2} \quad (3.4)$$

The faction of a firefly m is involved to one more attractive firefly, and n is resolute by

$$x_m = x_m + [\beta_n(r)](x_n - x_m) + \alpha(\text{rand}) \quad (3.5)$$

3.1 Implementation of FA for ORPD

Step 1: Initialize

Number of fireflies

Amount of iterations

Set the standards of α , β , and γ

In this, the standards of α , β and γ are considered as 0.2, 0.1 and 1, respectively.

Step 2: Set the iteration count $i = 0$ and increase the iteration by $i = i + 1$.

Step 3: Determine the fitness result of each firefly by substituting in the objective function stated in Eqs. (2.1), (2.2) and (2.3).

Step 4: Sort the fireflies depending on their light intensities and for every iteration find the best firefly. Light intensity is varied based on top of the space involving them.

Step 5: Progress fireflies (control variables) derived from their light intensity.

Step 6: Continue the process until stopping criteria is reached.

4 Simulation Results

IEEE 14-bus system contains five generator buses in which bus number 1 represented as reference bus, and remaining buses stay generator buses. In between buses, 20 branches are connected and also have three tap-changing transformers. The real power output of solar PV system is additional to load bus 14, without changing

Table 1 Limits of control variables

Variables	Minimum in p.u.	Maximum in p.u.
Voltages of generator	0.9	1.1
Transformer tap changing's	0.95	1.05
Shunt capacitors	0	0.20

limits of the control variables. Total generation from PV system is 6.967 MW, and it is given to the load bus, i.e. at the 14th bus. In the 14-bus system, the control variables are 11, after including PV array at the 14th bus and their restrictions are scheduled in Table 1.

Uncertainty of Load and Solar Power Output

Initially, the load data is calculated as some particular value in percentages, and similarly, the availability of solar PV power is also divided in percentages as 0%, 25%, 50%, 75% and 100%, respectively. For each percentage of solar power output, different loading conditions like 25, 50, 75, 100 and 105% are given a total of 25 scenarios. For each time, the firefly optimization is applied and tabulated the optimal values of objective functions which are loss minimization and minimization of deviancy of voltage. The minimization of real power losses for random loads and solar power (PV) output is shown in Table 2, minimization of voltage deviation for random loads and solar power output is presented in Table 3, and minimization

Table 2 Minimization of losses for random loads and solar power output

PV power	0%	25%	50%	75%	100%
25% load	0.6760	0.3730	0.5249	1.0496	1.7659
50% load	2.5363	1.9836	1.7635	1.8556	2.2343
75% load	6.4273	5.4616	4.8351	4.5083	4.4838
100% load	12.273	10.882	9.8030	9.0869	8.6624
105% load	13.829	12.313	11.1484	10.3079	9.7894

Source: Bold indicates the minimum and maximum values

Table 3 Minimization of voltage deviation for random loads and solar power output

PV power	0%	25%	50%	75%	100%
25% load	0.0251	0.0351	0.0303	0.0228	0.0411
50% load	0.0343	0.0401	0.0382	0.0364	0.0466
75% load	0.0446	0.0490	0.0406	0.0444	0.0417
100% load	0.0640	0.0570	0.0581	0.0614	0.0560
105% load	0.0623	0.0650	0.0647	0.0525	0.0694

Source: Bold indicates the minimum and maximum values

Table 4 Minimization of multi-objective function for random loads and solar power output

PV power	0%	25%	50%	75%	100%
25% load	0.0196	0.0181	0.0240	0.0268	0.0340
50% load	0.0329	0.0347	0.0351	0.0333	0.0317
75% load	0.0648	0.0573	0.0560	0.0532	0.0505
100% load	0.1107	0.1008	0.1010	0.0965	0.0999
105% load	0.1218	0.1041	0.0992	0.0915	0.0966

Source: Bold indicates the minimum and maximum values

of multi-objective function for random loads and solar power output is given in Table 4. From the tabular columns 2, 3 and 4, it is observed that for different cases of objectives, the values are low after incorporating full solar power into the system compared to other cases. After increasing load, also the increase in losses is less after incorporating solar power into the system.

Case 1—Minimizing Real Power Loss

The first and foremost objective is to minimize the total transmission line active power losses, and the main goal of dispatch problem is reducing loss in transmission line. In this case, we only consider the real power loss minimization as objective. The firefly algorithm is run for both with solar and without solar and tabulated the parameters represented in Table 5. Optimal values of control variables corresponding to different objectives and its meeting characteristics are exposed in Fig. 1.

Table 5 Parameters of control variables and power loss

Control variables	FA without solar	FA with solar
VG 1	1.1000	1.1
VG 2	1.0878	1.086
VG 3	1.0637	1.0558
VG 6	1.1000	1.0563
VG 8	1.0709	1.058
VG14 (solar)	–	0.9
T4-7	0.9500	1.0397
T4-9	1.0057	0.9668
T5-6	1.0161	1.0121
QC9 in MVAR	14.3777	9.9612
QC14 in MVAR	5.1587	14.4415
RPL	12.5837	11.46883
VD	0.7234	0.858075

Source: Bold indicates objective function values of FA with solar

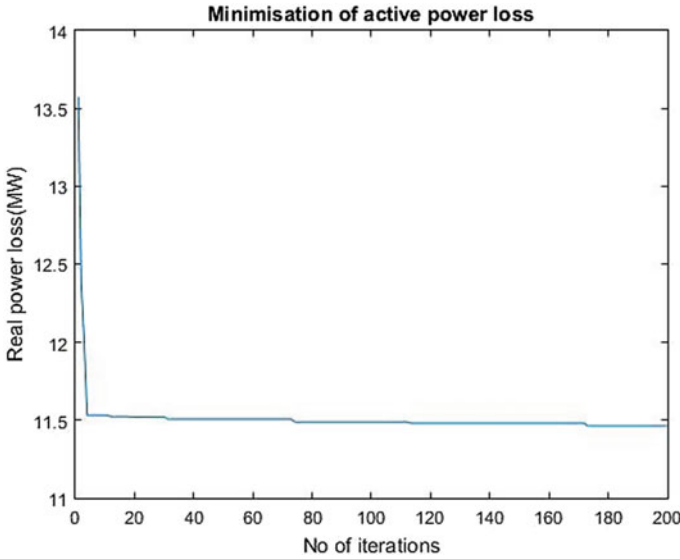


Fig. 1 Convergence characteristics of losses

Table 6 Mean and standard deviation

Technique	Minimum value (MW)	Maximum value (MW)	Mean value (MW)	Standard deviation
FA	11.4420	11.5138	11.4688	0.01782

The average value along with standard deviation value is calculated for the given IEEE 14-bus system is exposed in Table 6.

Case 2—Minimizing Voltage Deviation

The control variables here are tuning such so as to the whole voltage deviation is minimized. The voltage deviations are listed in Table 7 with its convergence characteristics are shown in Fig. 2.

Case 3—Multi-objective Function

Nothing like the two earlier cases, this case reflects equally both objective functions given which are real power loss then voltage deviation all at once. This technique is utmost appropriate for optimizing the all parameters of reactive power involved. FA performs excellently in optimizing equally the both objective functions.

From Table 8, it is clear that real power loss is 14.381 MW, and the voltage deviation is 0.06533 p.u. Since equal weight is given to both the objectives, the optimal value is shown in Fig. 3. Comparison of results for three different cases without and with solar is presented in Table 9.

$$\text{Optimal value} = 0.5 * 0.14381 + 0.5 * 0.06533 = 0.10457 \text{ p.u.}$$

Table 7 Optimal values of bus voltage deviation

Bus	Voltage deviation (p.u) without solar	Voltage deviation (p.u) with solar
1	0.0070	0.0024
2	0.0146	0.0031
3	0.0027	0.0013
4	0.0057	0.0120
5	0.0017	0.0081
6	0.0135	0.0149
7	0.0002	0.0035
8	0.0011	0.0033
9	0.0018	0.0010
10	0.0069	0.0060
11	0.0004	0.0007
12	0.0009	0.0010
13	0.0019	0.0000
14	0.0016	0.0019
VD	0.0600	0.0592
RPL	15.574	14.5554

Source: Bold indicates objective function values of FA with solar

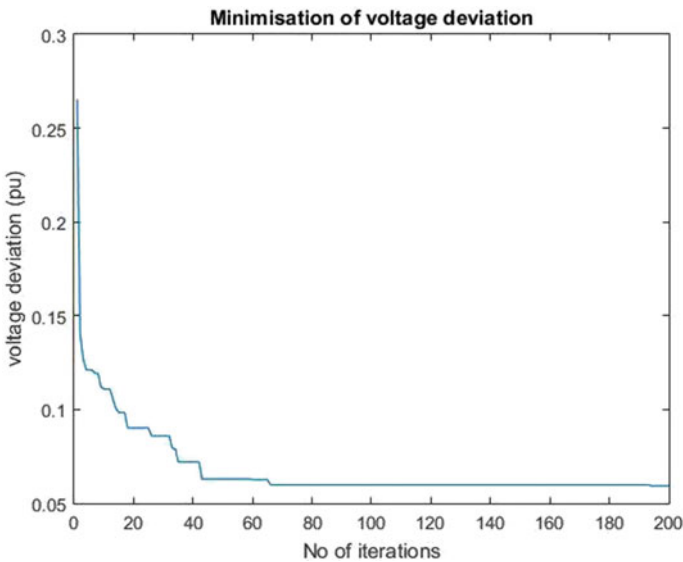


Fig. 2 Convergence characteristics of voltage deviation

Table 8 Optimal values of multi-objective function

Control variables	FA without solar	FA with solar
VG 1	1.0193	1.0082
VG 2	1.0101	1.0088
VG 3	1.0044	1.0017
VG 6	1.0157	1.0137
VG 8	1.0000	0.9981
VG14 (solar)	–	1.0711
T4-7	1.0001	1.0013
T4-9	0.9771	0.9961
T5-6	1.0267	1.0418
QC9 in MVAR	18.5362	15.3078
QC14 in MVAR	10.6494	5.0979
RPL	14.69	14.381
VD	0.0680	0.06533

Source: Bold indicates objective function values of FA with solar

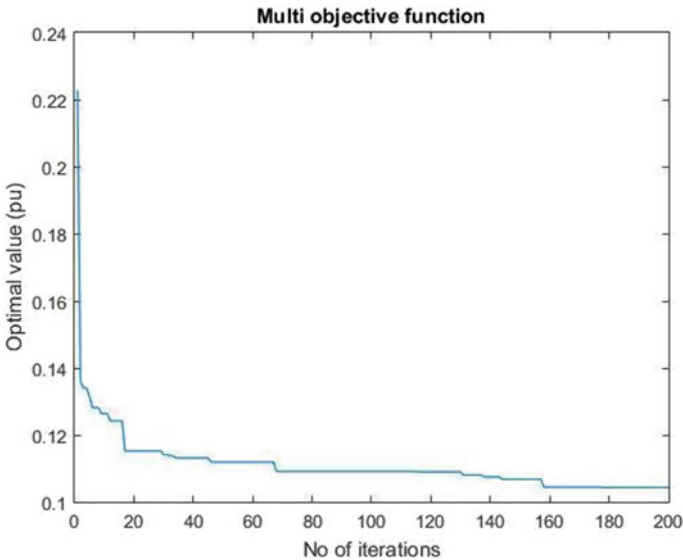


Fig. 3 Convergence characteristics of multi-objective function

5 Conclusion

In this paper, the objective functions aimed at the minimizing real power losses; also voltage deviation is performed on IEEE 14-bus system using FA. The algorithm gives the best results for both with solar and without solar in three cases. When comparing

Table 9 Comparison of results

	FA without solar		FA with solar	
	RPL (MW)	VD (p.u.)	RPL (MW)	VD (p.u.)
Case 1	12.583	0.723	11.468	0.8580
Case 2	15.574	0.0600	14.555	0.0592
Case 3	14.690	0.068	14.381	0.0653

the results, losses are less when solar power is added at load bus. Uncertainty at different loading conditions and different solar power outputs also gives better results when integrated with solar power. Therefore, the access of further sustainable power in network produces less loss in ORPD problem.

References

1. Mouassa S, Bouktir T, Salhi A (2017) Ant lion optimizer for solving optimal reactive power dispatch problem in power systems. *Eng Sci Technol Int J* 20(3):885–895
2. Bhattacharyya B, Karmakar N (2019) Optimal reactive power management problem: a solution using evolutionary algorithms. *IETE Tech Rev (Inst Electron Telecommun Eng India)* 1–9
3. Dutta S, Roy PK, Nandi D (2016) Optimal location of STATCOM using chemical reaction optimization for reactive power dispatch problem. *Ain Shams Eng J* 7(1):233–247
4. Praveen J, Rao BS (2016) Multi objective optimization for optimal power flow with IPFC using PSO. In: 3rd international conference on electrical energy systems. IEEE, pp 85–90
5. Das T, Roy R, Mandal KK, Mondal S, Mondal S, Hait P, Das MK (2020) Optimal reactive power dispatch incorporating solar power using Jaya algorithm. In: Computational advancement in communication. Springer Nature Singapore Pte Ltd, pp 37–48
6. Biswas PP, Suganthan PN, Mallipeddi R, Amaratunga GAJ (2019) Optimal reactive power dispatch with uncertainties in load demand and renewable energy sources adopting scenario-based approach. *Appl Soft Comput J* 75:616–632
7. Mukherjee A, Mukherjee V (2015) Solution of optimal reactive power dispatch by chaotic krill herd algorithm. *IET Gener Transm Distrib* 9(15):2351–2362
8. Biswas P (2015) Genetic algorithm based multiobjective bilevel programming for optimal real and reactive power dispatch under uncertainty. In: Computational intelligence applications in modeling and control. Studies in computational intelligence. Springer International Publishing, Switzerland, pp 171–202
9. Basu M (2016) Multi-objective optimal reactive power dispatch using multi-objective differential evolution. *Int J Electr Power Energy Syst* 82:213–224
10. Kunapreddy M, Venkateswara Rao B (2020) Hybridization of particle swarm optimization with firefly algorithm for multi-objective optimal reactive power dispatch. In: Innovative product design and intelligent manufacturing systems. Lecture notes in mechanical engineering. Springer, Singapore, pp 673–682
11. Zhou W, Yang H, Fang Z (2007) A novel model for photovoltaic array performance prediction. *Appl Energy* 84:1187–1198
12. Yang X-S (2013) Firefly algorithm recent advances and applications. *Int J Swarm Intell* 1:36–50
13. Venkateswara Rao B, Nagesh Kumar GV (2015) Thyristor controlled series capacitor for generation reallocation using firefly algorithm to avoid voltage instability. *Majlesi J Electr Eng* 9(2):1–9

14. Venkateswara Rao B, Nagesh Kumar GV (2014) Firefly algorithm based optimal power flow with static VAR compensator for improvement of power system security under network contingency. *Int Electr Eng J (IEEJ)* 5(12):1639–1648
15. Venkateswara Rao B, Nagesh Kumar GV (2016) Firefly algorithm based optimal power flow for sizing of thyristor controlled series capacitor to enhance line based voltage stability. *J Electr Eng* 16(1):269–280

Power Quality Improvement Using Harmonic Passive Filter in Distribution System



Arjun Baliyan, Majid Jamil, and M. Rizwan

1 Introduction

Due to the rapid increase of power demand, nowadays there has been an increase in the nonlinear loads in the system such as drivers, rectifiers, and the power appliances. These nonlinear loads generally offer high nonlinear characteristics in the system and decrease the power quality of the supply. Since these loads have the characteristics to draw non-sinusoidal currents and voltage from the mains and therefore resulting in distortion in the current and voltage waveform which is commonly referred as harmonics [1].

These harmonics led to severe complications in the supply system and the domestic appliances that are further attached with the system, and some of these problems are overheating, reduced power factor, transformer excessive heating and disrupted current and voltage waveforms [2–4].

Till now, the implementation of the active power filter was too costly that it was generally avoided in the system. Although the passive filters were widely used to improve the harmonics in the demand side or in the distribution system, the cost of passive filters is not too much but their performance is not as satisfactory as expected due to the presence of nonlinear loads. Hence, the active filter is a future option available for the harmonic refinement in the distribution system due to its superb peculiarity. A filter that is a merger of both the passive filter and the active power filter is recommended to solve the issue of power quality on the demand side. There are two types of frequency component available in the system, and therefore, the fixed components are removed or deaden by the passive filters and the remaining frequency components from the load are removed by the active power filters [5]. There were several control schemes that were available in the past to determine

A. Baliyan (✉) · M. Jamil
Jamia Millia Islamia, New Delhi, India

M. Rizwan
Delhi Technological University, New Delhi, India

the compensating current which were easy to implement because they use the line current as the input parameter [6–8]. The voltage source converters have also been used in the past and provide a feasible solution [9–11].

It must be noted that the nonlinear loads that create harmonics in the system are non-avoidable in the power system network. Therefore, only two ways are available by which harmonics can be eliminated one is at the starting stage and we can separate out the loads that can disturb the power quality by using the isolation transformer [12]. But in order to eliminate the harmonics from the already running systems, we have to go for different reactors as well as active, passive, and hybrid filters. The passive filters were also used in the past to minimize the distortion in the existing supply systems. Since the problem of resonance exists in the passive filters, therefore the active power filters together with the combination of passive filters are used nowadays in order to overcome the resonance problem and to improve the total harmonic distortion (THD) further to a desired level of 5% as per the IEEE recommendations [13, 14].

The paper is distributed as follows. In Sect. 2, a brief description about the active power filter, reference current generation technique, and the proposed PID control strategy has been discussed. In Sect. 3, an overall idea about harmonic passive filters is given. In Sect. 4, experimental results obtained from simulation are presented and Sect. 5, concludes the paper.

2 Active Power Filter

2.1 Basic Working Principle

The above figure explains the working principle of the filter. A pulse width modulation converter along with the combination of passive elements is used widely as an active power filter. Its function is to impart the necessary reactive and harmonic current so that it nullifies the reactive and harmonic current required by the nonlinear loads such that as a result of it we get the input current from the source to be almost sinusoidal. We can even say that in ideal condition the active filter just produces sufficient harmonic and reactive current so that it exactly compensates the nonlinear load requirement in the system [15]. The block diagram describing the above combination is shown in Fig. 1.

2.2 Proposed Method Representation

The proposed scheme here is proportional plus integral plus derivative controller that is used to generate the reference current. The block diagram describing the basic principle of APF is shown in Fig. 2.

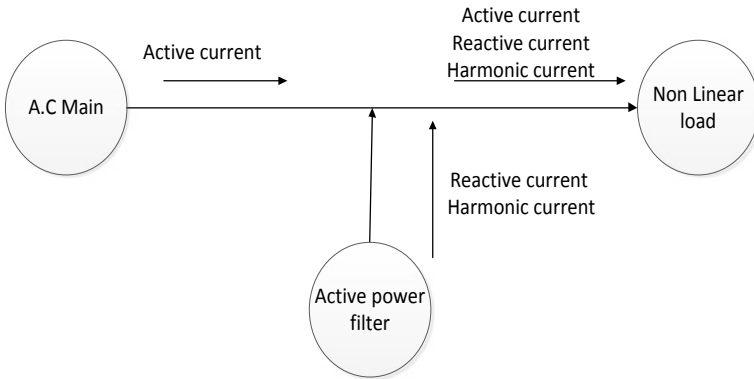


Fig. 1 Basic principle of active power filter

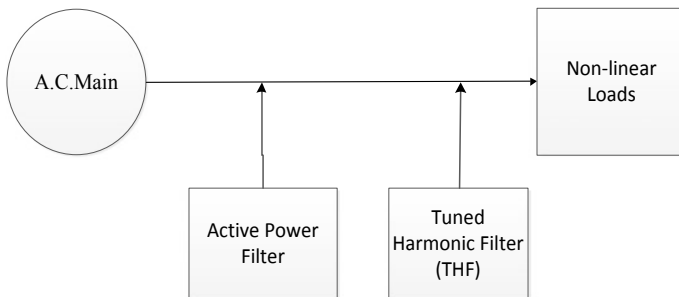


Fig. 2 Proposed method representation

The incorporation of both active power filter and tuned harmonic passive filter is needed for the reduction of harmonics to a desired level. Since the THD without using active power filter is not up to the desired level, therefore the hybrid combination of both serves the purpose to eradicate the harmonics generated by the various nonlinear loads. Hence, the simulation results prove that the APF is highly significant in order to achieve the goal of harmonic elimination from the system [16].

2.3 Reference Current Generation

The basic working phenomenon of the shunt active filter has been shown in Fig. 3. It explains that the active filter is designed to work in such a fashion that it draws/supply a current i_c , that cancels the harmonics present on the supply side and forces the current to be sinusoidal. The equation describing the relation is written below:

$$i_s(t) = i_l(t) + i_c(t) \tag{1}$$

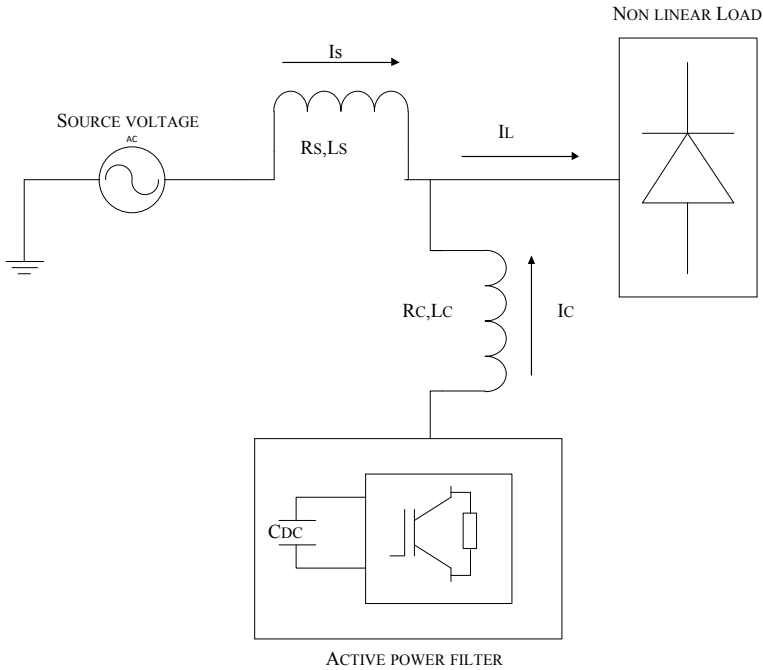


Fig. 3 Configuration of shunt power filter

Value of source voltage can be defined as:

$$V_s = V_m \sin \omega t \tag{2}$$

The equation describing the load current having the fundamental frequency component and the harmonics can be expressed as:

$$i_1(t) = \sum_2^{\infty} I_n \sin(n\omega t + \theta_n) \tag{3}$$

The load power is determined mathematically as the product of the voltage and the current so therefore it can be written as:

$$P_1(t) = V_s(t) * I_1(t) \tag{4}$$

Apart from the power drawn by the load, there are some switching losses in the system, and therefore, they must also be supplied by the system, and these include the PWM converter switching losses and the capacitance leakage losses. Hence, the total value of peak current must be equal to the peak value of the source current and the peak value of the component of loss current. This is given by the relation below:

$$I_{sp} = I_{sm} + I_{sl} \tag{5}$$

where I_{sl} contributes to the max value of loss current.

The maximum value of the reference current is obtained by varying the capacitor voltage on the DC side. Ideally, the job of the compensating current is to remove the harmonics present in the system and to make the supply current and voltage to be in phase with each other. The expected value of source current to be obtained after compensation must be:

$$I_{sa}^* = I_{sp} \sin \omega t \tag{6}$$

$$I_{sb}^* = I_{sp} \sin(\omega t - 120) \tag{7}$$

$$I_{sc}^* = I_{sp} \sin(\omega t + 120) \tag{8}$$

Here I_{sp} represents the peak value of required supply current. To determine this maximum value, we have to vary the capacitor voltage on the DC side of the PWM converter. The value of the capacitor voltage is passed through the comparator where it gets compared with the reference value, and the error obtained is given to the PID controller. The result obtained from PID controller is treated as the magnitude of source current for the purpose of our analysis.

2.4 Proposed PID Control Strategy

Proportional plus integral plus derivative controller is considered to be the most precise and accurate since it combines the advantages of PI, PD, and Proportional controller. It reduces the error of the system as well as increases the stability of the system.

Figure 4 describes the PID control strategy to generate the gate pulses required by the system. Figure 5 represents the active filter compensation scheme that has been used in the system.

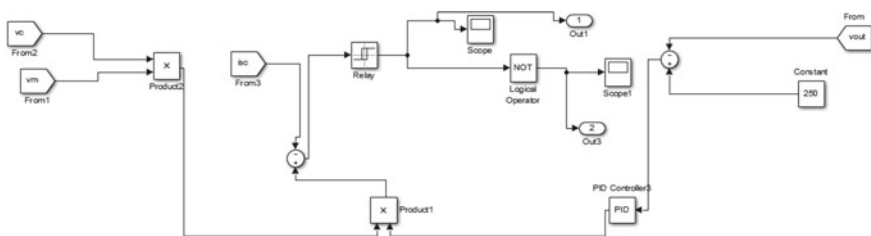


Fig. 4 Control circuit design

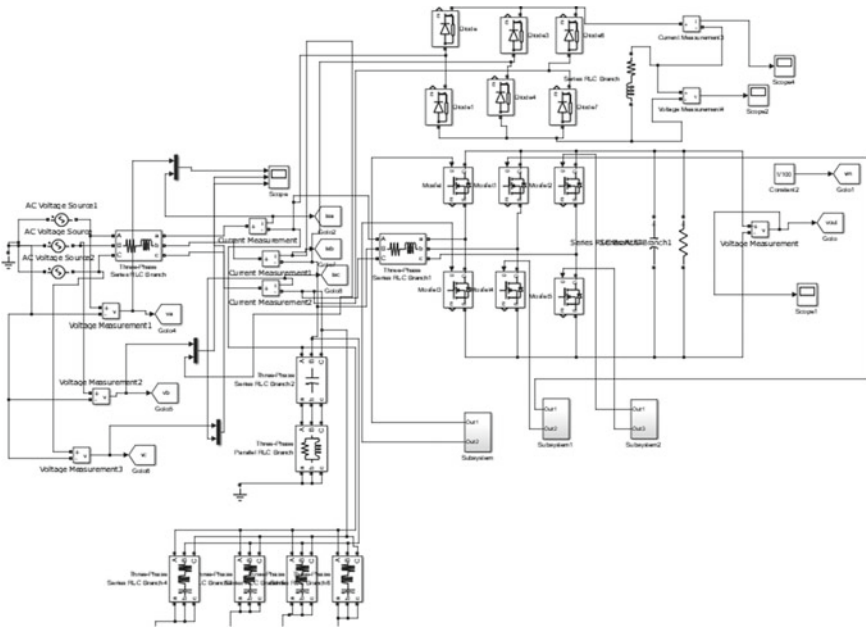


Fig. 5 Active filter compensation scheme

To implement the control strategy in a closed loop, we have to first sense the DC voltage at the converter end and then it has to be compared with the value of reference voltage. Error of the both the values will be given as a input to the PID controller, and therefore, the resultant value after the limiter is selected to be considered as the magnitude of the maximum value of reference current (I_{max}). The gate signal needed by the PWM converter is derived by the comparison of actual value of source current and the reference current as mentioned in Eqs. (6), (7), and (8) in the hysteresis controller. The output from the hysteresis controller is given as a firing pulse to the devices of pulse width modulation converter [17].

3 Harmonic Passive Filter

These filters are used to enhance the quality of the voltage waveform by diverting the current other than the fundamental current or we can say the high-frequency component current into the low impedance path. They are usually connected in shunt and fulfill the necessary reactive power demand of the load for the purpose of power factor improvement.

In this system, we are using four harmonic passive filters in order to eliminate the 5, 7, 11, and 13th order harmonics. To remove the high-frequency component, we are also using the high pass branch in the circuit. Using the technique recommended

in the paper [18], we have calculated the value of elements R, L, and C in such way that it optimize the performance of the filter. Also, in order to remove the resonance problem the filter is tuned at the frequency which is less than the harmonic frequency as we know most of the power systems are inductive in nature [19]. Figure 6 describes the passive harmonic filter, and Fig. 7 represents the high-pass filter or the damped filter.

Fig. 6 Harmonic passive filter

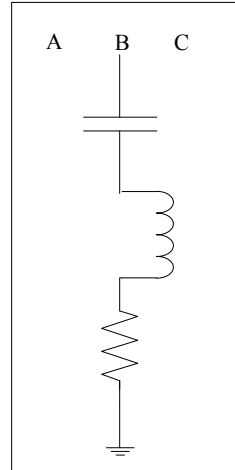
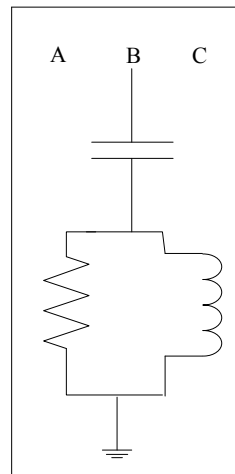


Fig. 7 Damped filter



4 Simulink Outcome

To assess the working of the system, the value of active and harmonic passive filter components have been given in Tables 1 and 2. The values of K_p and K_i that have been taken are 0.75 and 9.15 to obtain the desired results. A source current waveform of one of the phases has been represented in Fig. 8, and a load with nonlinear peculiarity has been taken into consideration for the purpose of study.

It must be acclaimed that the load and source current would have the same peculiarity whenever the active filter is not present in the above configuration. Since the passive filters are connected to examine the system so the overall THD without connecting the active filter has been reduced from 23.85 to 14.75%. Figure 9 represents the THD of the supply current without filter. Figure 10 represents the THD when passive filter is connected alone and Fig. 11 shows the THD with active power filter and finally the Fig. 12 shows the % harmonics when both the filters are connected together.

It is clear from figure that when both the filters are connected in the system, the THD has been reduced to a significant low level that is 0.74%.

Table 1 Different parameter value for passive filter

C (μF)	L (mH)	R (Ω)	Q
$C_5 = 56$	$L_5 = 8$	$R_5 = 0.03$	50
$C_7 = 56$	$L_7 = 3.7$	$R_7 = 0.05$	50
$C_{11} = 56$	$L_{11} = 1.5$	$R_{11} = 0.1$	50
$C_{13} = 56$	$L_{13} = 1.07$	$R_{13} = 0.08$	50
$C_H = 56$	$L_H = 10$	$R_H = 1.2$	5

Table 2 System parameter value

Parameters	Values
Supply voltage	100 V
Supply frequency	50 Hz
Source parameter	0.1 Ω , 0.15 mH
Filter parameter	0.1 Ω , 0.66 mH
Load parameter	7 Ω , 20 mH

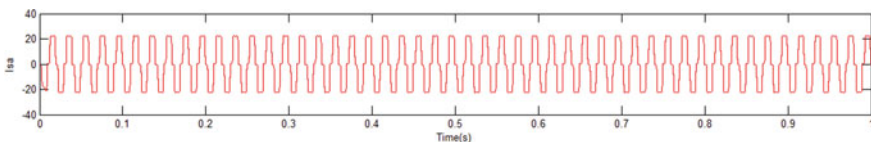


Fig. 8 Supply current waveform for phase a (without filter)

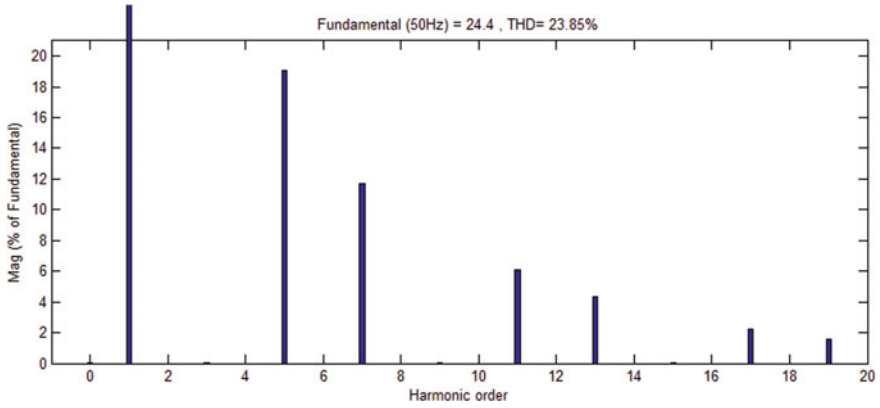


Fig. 9 THD without filter

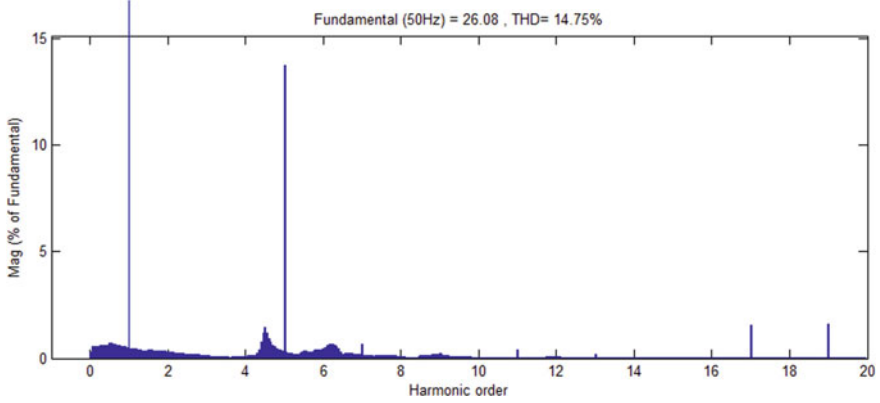


Fig. 10 THD with passive filters is connected in the system

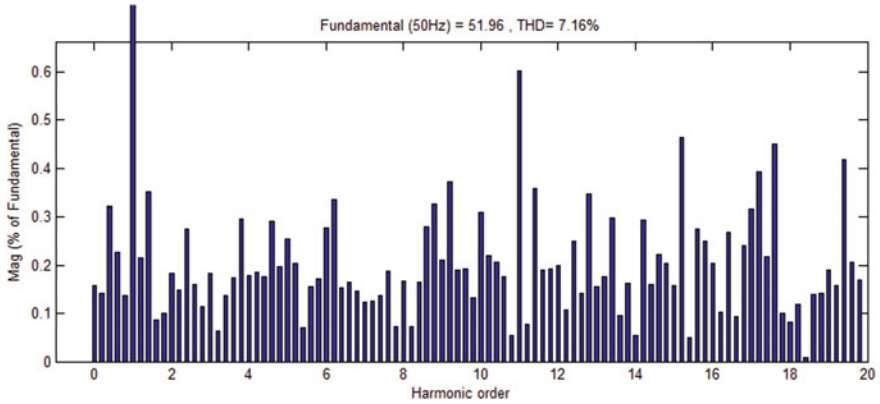


Fig. 11 THD when APF is connected in the system

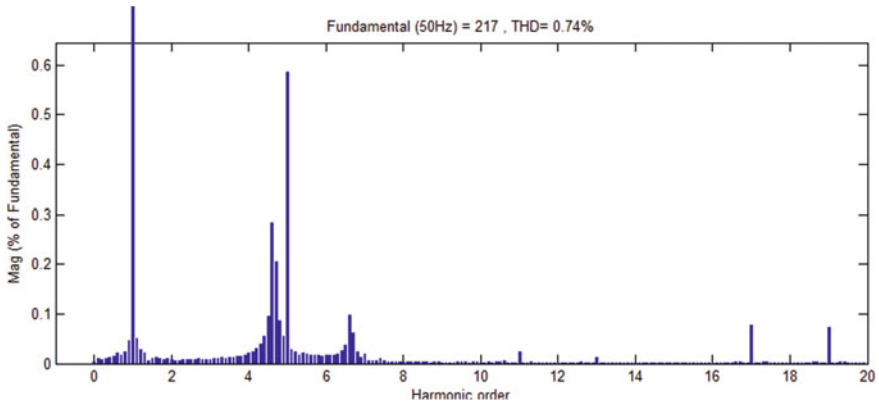


Fig. 12 THD when both the filters is connected in the system

5 Conclusion

In this paper, an amalgamation of active power filter and the shunt passive filter has been proposed to remove the distortion in the waveform and to improve the transient as well as the steady-state performance. The simulation results prove that the THD obtained as per the proposed combination of filters is less than 0.8%. Its value is well accepted for the power system network, and the combination responds well to the load variations in the system. Apart from this, the passive filters that have been connected in the system are not too much costly so it further adds advantage to the system overall cost.

References

1. Mack Grady W, Santoso S (2001) Understanding power system harmonics. *IEEE Power Eng Rev* 21(11):8–11
2. Subjek JS, Mcquilkin JS (1990) Harmonics-causes, effects, measurements and analysis. *IEEE Trans Ind Appl* 26(6):1034–1041
3. Duarte LHS, Alves MF (2002) The degradation of power capacitors under the influence of harmonics. In: *Proceedings of 10th international conference on harmonics and quality of power*, vol 1, Oct 2002, pp 334–339
4. Wagner VE, Balda JC, Griffith DC, McEachern A, Barnes TM, Hartmann DP, Philleggi DJ, Emmanuel AE, Hortion WF, Reid WE, Ferraro RJ, Jewell WT (1993) Effects of harmonics on equipments. *IEEE Trans Power Delivery* 8(2):672–680
5. Su W-F, Lin CE, Huang C-L (1998) Hybrid filter application for power quality improvement. *Electr Power Syst Res* 47:165–171
6. Akagi H, Kanazawa Y, Nabae A (1984) Instantaneous reactive power compensators comprising switching devices without energy storage components. *IEEE Trans Ind Appl* IA-20(3):625–630
7. Peng FZ, Akagi H, Nabae A (1990) Study of active power filters using quad series voltage source PWM converters for harmonic compensation. *IEEE Trans Power Electron* 5(1):9–15

8. Grady WM, Samotyj MJ, Noyola AH (1990) Survey of active power line conditioning methodologies. *IEEE Trans Power Delivery* 5(3):1536–1542
9. Singh B, Chandra A, Al-Haddad K (1999) Computer-aided modeling and simulation of active power filters. *Electr Mach Power Syst* 27:1227–1241
10. Chatterjee K, Fernandes BG, Dubey GK (1999) An instantaneous reactive volt-ampere compensator and harmonic suppressor system. *IEEE Trans Power Electron* 14(2):381–392
11. Jain S, Agarwal P, Gupta HO (2003) Design simulation and experimental investigations on a shunt active power filter for harmonics and reactive power compensation. *Electr Power Compon Syst* 32(7):671–692
12. Abdelaziz AY, Mekhamer SF, Ismael SM (2013) Technical considerations in harmonic mitigation techniques applied to the industrial electrical power systems. Presented at the 22nd international conference on electrical distribution
13. Obulesu Y, Reddy MV, Kusumalatha Y (2014) A% THD analysis of industrial power distribution systems with active power filter-case studies. *Int J Electr Power Energy Syst* 60:107–120
14. Tarnini M, Abdallah A (2015) Analytical estimation in APF sizing for networks of analogous loads (estimation of overall THD). In: 2015 international conference on renewable energy research and applications (ICRERA), pp 124–128
15. Singh GK, Singh AK, Mitra R (2006) A simple fuzzy logic based robust active power filter for harmonics minimization under random load variation. *Electr Power Syst Res* 77(8):1101–1111
16. Aissa O, Moulahoum S, Colak I, Babes B, Kabache N (2016) Analysis, design and real-time implementation of shunt active power filter for power quality improvement based on predictive direct power control. In: 2016 IEEE international conference on renewable energy research and applications (ICRERA), pp 79–84
17. Bhende CN, Mishra S, Jain SK (2006) TS-fuzzy-controlled active power filter for load compensation. *IEEE Trans Power Delivery* 21(3):1459–1465
18. Joorabian M, Seyfossadat SGH, Zamani MA (2006) An algorithm to design harmonic filters based on power factor correction for HVDC systems. In: IEEE international conference on power electronics, Dec 2006
19. Dos JC (2004) Passive filters—potentialities and limitations. *IEEE Trans Ind Appl* 40(1):232–241

Implementation and Performance Measurement of Q -Varying and r -Varying IIR Notch Filter for Bio-medical Application



Kunal Kumar, Sandeep Kumar , and Upendra Kumar Acharya

1 Introduction

Filter is used to select the useful signal or remove unwanted signal of a particular range of frequencies that means filter is a frequency selective circuit. Notch filter has transient response of short duration and very large selective magnitude [1]. In most of the application, very large selective magnitude notch filters are being used [1–4]. In any type of filter response, there is some transient occurs at the beginning of the signal.

Usually, the transient response duration depends on the order of the filter [5]. It creates some issues when a small duration of signals is being filtered or whenever initial part of the signal contains some important and unavoidable information [1]. Due to this problem, lower order filters are generally used. Since for the same specification of the magnitude response of a filter, structure can be designed by using the lesser order of IIR filter than FIR filter [6]. That is why, we are using IIR notch filter. Selectivity of any type of filter should be high. It depends upon the quality factor (Q) and pole radius (r) of the system [5]. For any filter, we required high selectivity with less transient duration. But, when both Q and r are increased, then both selectivity and transient duration of the system are also increased. To overcome these situations, the different concepts of digital IIR notch filters were introduced which are based on quality factor and pole radius variation with time [5, 7].

In some applications of notch filter, high quality factor and short transient duration are required simultaneously. So, hyperbolic tangent sigmoid (HTS) function has been utilized to achieve both the both the requirements [8]. Two-notch and three-notch filters have been presented in [9], and it is also based on HTS function. The author

K. Kumar · S. Kumar (✉) · U. K. Acharya
Department of ECE, National Institute of Technology Delhi, New Delhi, India
e-mail: sandeep@nitdelhi.ac.in

of this paper claimed that the proposed MNFs are efficient designs for removing harmonics from sinusoids and ECG signals. The concept of the second order digital infinite impulse response narrow band-reject filter with reduced transient response is presented in [10]. In this paper, Bézier parametric curve is used to vary the pole radius temporarily which is needed to suppress the transient response of the considered infinite impulse response (IIR) notch filter. Including the above, some other designs are presented in [11–13] which are also based on IIR notch filter and biomedical applications.

In this paper, we have implemented the Q -varying and r -varying IIR notch filters that have been reported earlier. Further, these Q and r varying notch filters were used for the biomedical application, i.e., filtering of these ECG signals which are corrupted by fixed power line interference. The performance of these filters has been compared with tradition IIR notch filters having constant Q and r . From the comparison results, we have observed that, due to Q -varying and r -varying, the IIR notch filter has a lesser transient time duration as compared with traditional notch filters [5]. Moreover, the filtered ECG signals with to Q -varying and r -varying IIR notch filters are more accurate as compared to the traditional notch filters. That means these types of filters (Q -varying or r -varying) suppress the duration of transient of the system. Hence, when the interference of the noise occurs initially to the useful signal, then due to less transient time duration of the filter, error in the reading of the data is more accurate than the case of traditional filter. So, these types of digital filter are more suitable for the biomedical applications.

The rest part of the paper is arranged in following order: Sect. 2 includes the details of IIR notch filters. Implementation and discussion on Q -varying and r -varying IIR notch filters are discussed in Sects. 3 and 4, respectively. Performance measurement of Q -varying and r -varying IIR notch filters in filtering of ECG signal is presented in Sects. 5 and 6 is allocated for concluding the paper.

2 Notch Filter

The digital notch filter frequency response [5] can be represented as

$$H(e^{j\Omega}) = \begin{cases} 0, & \Omega = \Omega_0 \\ 1, & \Omega \neq \Omega_0 \end{cases} \quad (1)$$

where $\Omega = 2\pi f/f_s$ is the normalized frequency of digital filter with respect to sampling frequency f_s and notch frequency of digital filter is given by

$$\Omega_0 = \frac{2\pi f_0}{f_s} \quad (2)$$

Here, f_0 is the notch frequency of analog filter. Digital bandwidth is given by

$$\Delta\Omega = \frac{2\pi\Delta f}{f_s} \quad (3)$$

where Δf = bandwidth of the analog notch filter.

2.1 Q -Constant IIR Notch Filter

By the method of bilinear transformation (BLT), a second order IIR notch filter transfer function (TF) with constant quality factor (Q) [5] is depicted as

$$H_N(z) = \frac{1}{1+C} \cdot \frac{z^2 - 2\beta z + 1}{z^2 - \frac{2\beta}{1+C}z + 1 - \frac{2}{1+C}} \quad (4)$$

where β and quality factor Q are mathematically represented as

$$\beta = \cos(\Omega_0), \quad C = \tan(0.5\Delta\Omega) \quad (5)$$

$$Q = \frac{f_0}{\Delta f} \quad (6)$$

Figure 1 shows the response of the IIR notch filter by taking quality factor, $Q = 10, 30,$ and 50 . From Fig. 1, it has been noticed that transient performance of the IIR notch filter becomes superior by decreasing values of quality factor (Q).

Therefore, for better transient performance of the above-discussed filter, quality factor (Q) should be a decreasing function of time. However, the enhancement of

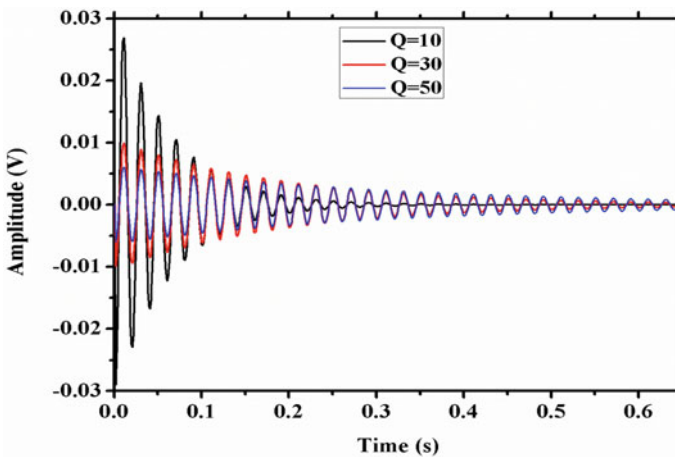


Fig. 1 Notch filter response for different values of Q

quality factor causes swelling the transient process duration, after excitation process. So, there is a back-and-forth between the width of the rejection band and transient response.

2.2 Constant Pole Radius (r) IIR Notch Filter

This filter is also modeled by taking constant pole radius and pole-zero arrangement. The pole radius of such filter is taken as [14]

$$r = 1 - \frac{\Delta f}{f_s} \tag{7}$$

Here, the sampled frequency is represented by f_s , Δf is bandwidth of the stop-band, and location of pole of such filter is depicted as

$$\phi_0 = \frac{2\pi f_0}{f_s} \tag{8}$$

According to pole radius and location of pole-zero, the TF of this filter [6] is described as

$$H(z) = \frac{z^2 - 2\cos(\phi_0)z + 1}{z^2 - 2r\cos(\phi_0)z + r^2} \tag{9}$$

Figure 2 represents the response of this filter with quality factor $r = 0.85, 0.92,$ and 0.98 . From Fig. 2, it has been noticed that when pole radius of notch filter

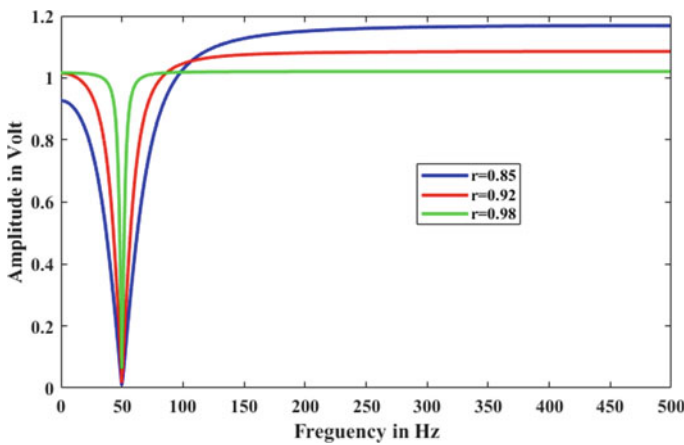


Fig. 2 IIR notch filter frequency response for different values of r

is increased, then the bandwidth of notch filter becomes tampered and frequency response becomes better. Pole radius r can have maximum value 1. If pole radius r is greater than 1, then it loses its characteristics as shown in Fig. 3.

From Fig. 4, it is observed that the transient performance of such filter can be improved with decreasing values of the pole radius of the notch filter. However, with increasing the pole radius, the durability of transient process after the process of the excitation is also increased. Hence, a trade-off is noticed in between the rejection bandwidth and filter transient response.

So, the different concept of Q -varying and r -varying aided with notch filters is implemented in this paper, whose quality factor is a time depended function [1, 5, 14, 15].

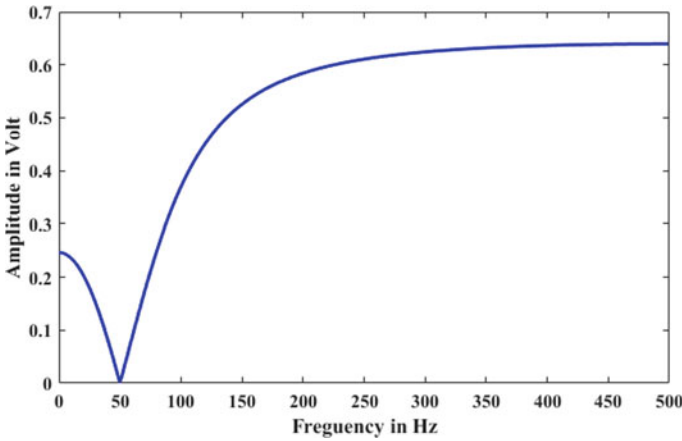
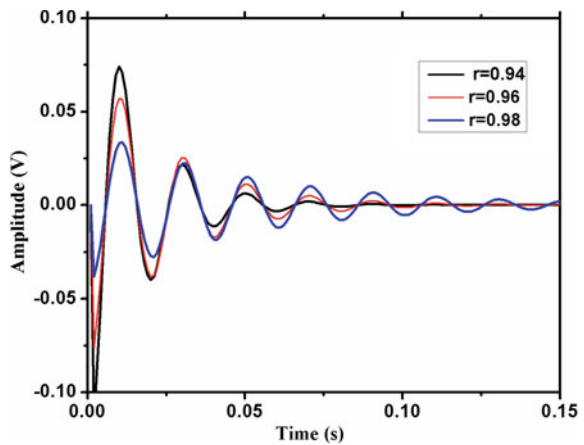


Fig. 3 Frequency response of IIR notch filter for $r > 1$

Fig. 4 Response of notch filter for different r value



3 Q -Varying IIR Notch Filter

The time difference equation of the digital IIR notch filter by varying quality factor [3] is represented by

$$[1 + C(n)]y(n) = 2\beta y(n-1) - [1 - C(n)]y(n-2) + x(n) - 2\beta x(n-1) + x(n-2) \quad (10)$$

where $C(n)$ is represented as

$$C(n) = \tan(0.5\omega_0 Q^{-1}(n)) \quad (11)$$

Here, the variation in quality factor is due to $Q(n)$, which is defined as

$$Q(n) = \bar{Q} \cdot \left[1 + (d_Q - 1) \cdot e^{-\frac{nr}{r'}} \right], \quad n \geq 0 \quad (12)$$

where \bar{Q} and d_Q (variation rate) can be found as

$$\bar{Q} = \lim_{n \rightarrow \infty} Q(n) \quad (13)$$

$$d_Q = \frac{Q(0)}{\bar{Q}} \quad (14)$$

The transfer function is given as

$$H_N(z) = \frac{1}{1 + C(n)} \cdot \frac{z^2 - 2\beta z + 1}{z^2 - \frac{2\beta}{1+C(n)}z + 1 - \frac{2}{1+C(n)}} \quad (15)$$

The Simulink model for realization of $C(n)$ function is shown in Fig. 5, and the model of digital IIR notch filter with varying Q is presented in Fig. 6. Here, d_Q is variation range, and r' is the exponential variation rate of the quality factor $Q(n)$. We have chosen d_Q as 0.25, i.e., before the start of the variation process the initial value $Q(0)$ is 5 for the final approximated $\bar{Q} = 20$. Figure 7 shows the variation of quality factor with time.

Figure 8 shows the comparison plot between transient response of traditional IIR notch filter and IIR notch filter with variable Q . It has been observed that Q -varying filter has better transient suppression as compared to traditional Q -constant notch filter.

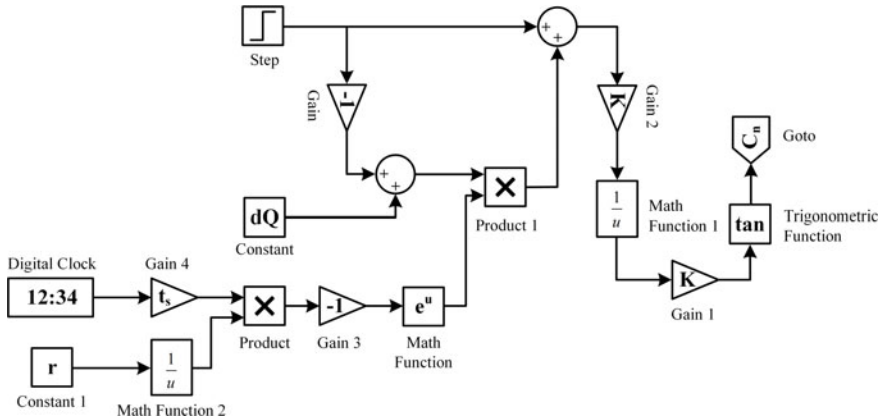


Fig. 5 Simulink model for realization of $C(n)$ function

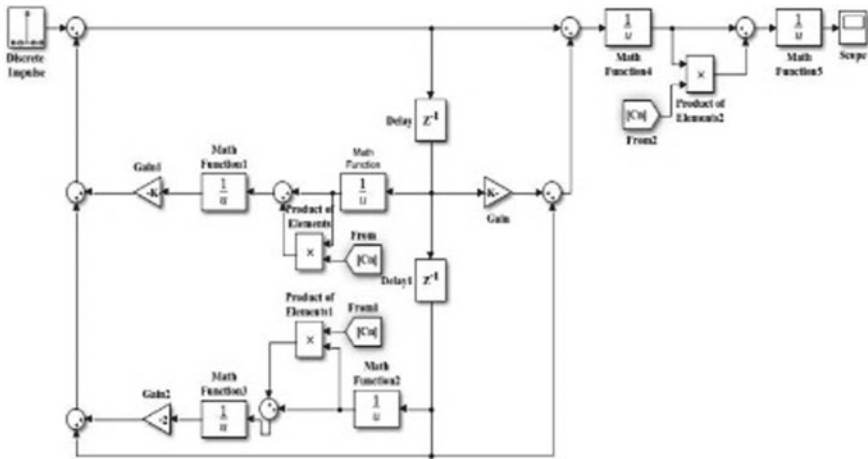


Fig. 6 Simulink model for realization of IIR notch filter

4 r -Varying IIR Notch Filter

The difference equation of IIR notch filter by varying pole radius (r) [6] is represented by

$$y(n) = \sum_{k=0}^N b_k x(n - k) - \sum_{k=1}^N r^k(n) a_k y(n - k) \tag{16}$$

Here, the time-varying pole radius is taken as $r(n)$, input to the filter is $x(n)$, and response of filter is taken as $y(n)$. The TF of r varying IIR notch filter of second order

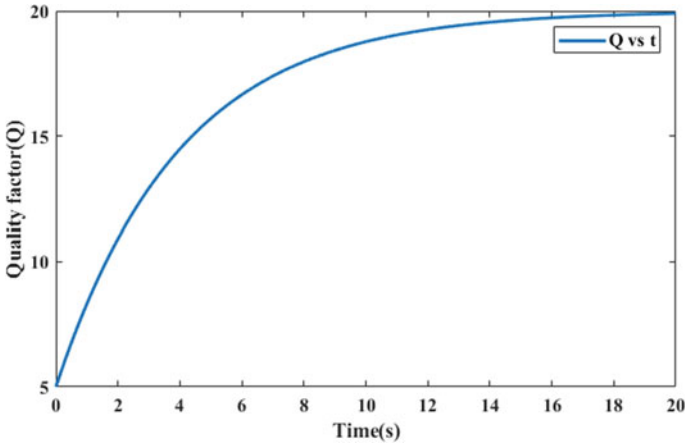
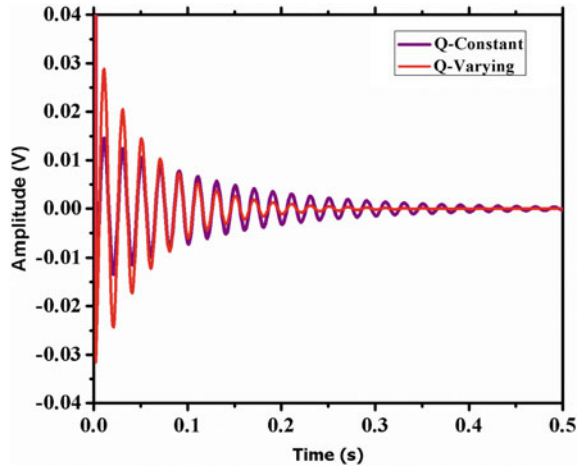


Fig. 7 Quality factor as function of time

Fig. 8 Response of notch filter for constant Q and variable Q



is represented by

$$H(z) = \frac{z^2 - 2 \cos(\phi_0)z + 1}{z^2 - 2r(n) \cos(\phi_0)z + r^2(n)} \tag{17}$$

Since transient performance of notch filter is made better by varying the pole radius of the filter. Hence, function responsible to vary the pole radius is given by

$$r(n) = \bar{r} \left\{ 1 + (\beta - 1) \exp\left(\frac{-n}{\alpha f_s}\right) \right\}, \quad n \geq 0 \tag{18}$$

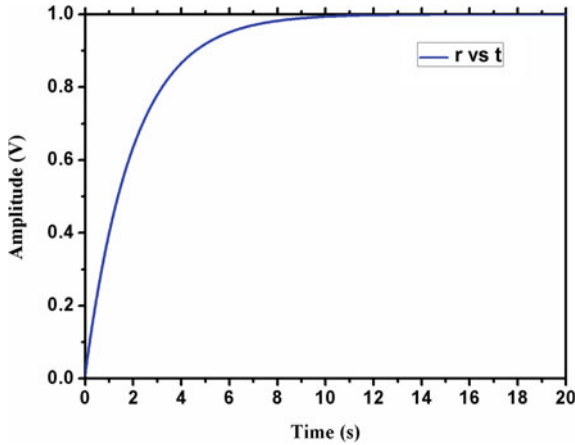


Fig. 9 Pole radius as function of time

where α = pole radius damping rate

$$\beta = \frac{r(0)}{\bar{r}} \quad \text{and} \quad \bar{r} = \lim_{n \rightarrow \infty} r(n) \tag{19}$$

Here, $r(0)$ and \bar{r} are the initial and final value of the pole radius, respectively. The r -varying IIR notch filter is implemented in this paper by using Matlab-2017a (.m file). For implementation, parameter values are taken as follows: \bar{r} as 0.98, α as 2.8, β as 0.9 and f_s as 1500 Hz [14]. Figure 9 shows the variation of pole radius r with time. Figure 10 shows the comparison of notch filter response with constant r and variable r . From Fig. 10, it is observed that the notch filter with varying r is able to settle the transient response effectively and faster than the traditional notch filter. Therefore, the usefulness of r -varying IIR notch filter can be increased instead of a traditional notch filter.

5 Performance Measurement of Q -Varying and r -Varying IIR Notch Filter in Biomedical Application

The Q -varying and r -varying IIR notch filter are used in this paper, for filtering of corrupted electrocardiogram (ECG) signal with unwanted power line interference of 50 Hz signal. The ECG is a time-varying signal reflecting the ionic current flow, which causes the cardiac fibers to contract and subsequently relax. The primary problem found in the recording of ECGs is that the measured signal is debased by a power line interference. Such problems can be resolved by using notch filter having a unit gain except notch frequency. The real ECG signals are taken from MIT-BIH database [7] for our experimental work.

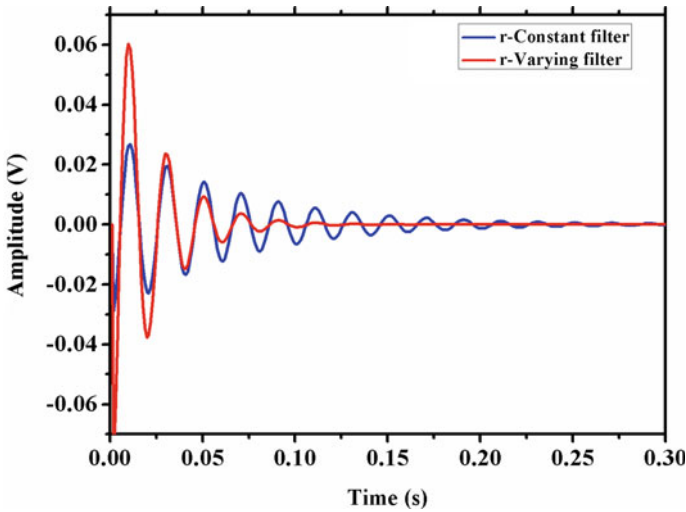


Fig. 10 Notch filter response for constant r and variable r

Figure 11 shows the real ECG signal for 10 s time duration, and Fig. 12 shows the ECG signal corrupted with 50 Hz noise. The major problem of the correct reading of ECG signal is interference with 50 Hz power frequency.

An ECG signal which is corrupted by 50 Hz interference is shown in Figs. 13 and 14 represents the filtered ECG signal using Q -constant filter for too low Q and too high Q , respectively. Figure 15 shows the comparison of filtering result Q -varying and traditional IIR notch filter using ECG signal. From Fig. 15, it is easy to observe that an acceptable level transient duration and the selectivity are obtained by using Q -varying IIR notch filter.

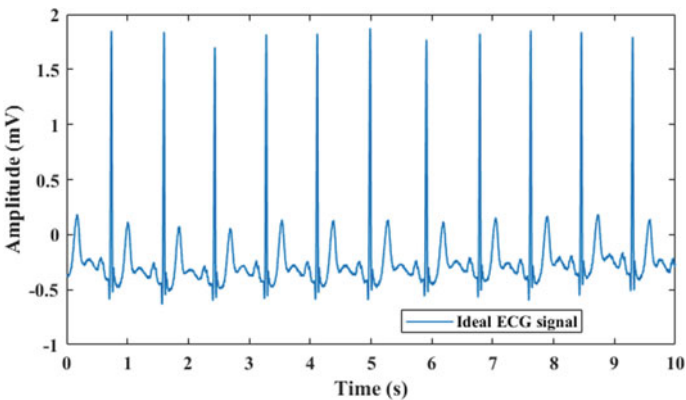


Fig. 11 Real ECG signal

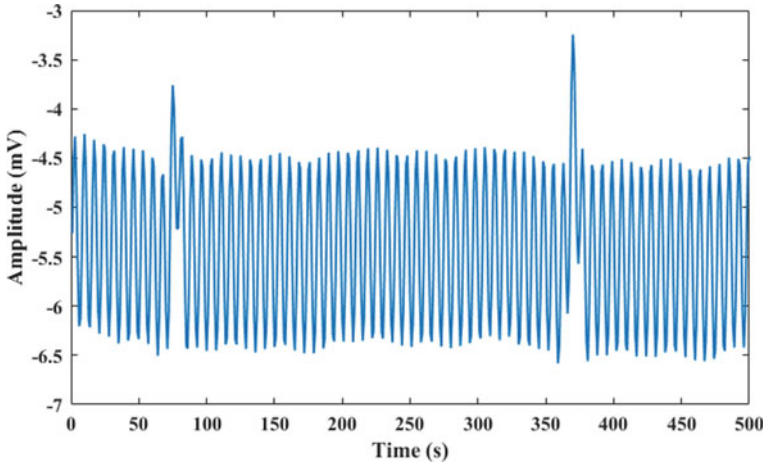
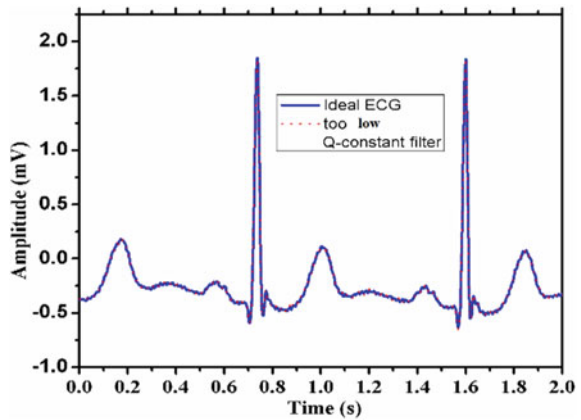


Fig. 12 ECG signal corrupted by 50 Hz interference

Fig. 13 Filtering result of ECG signal with too low Q traditional notch filter



Figures 16 and 17 represent the filtering results of ECG signal using r -constant traditional IIR notch filter with too low r and too high r . Figure 18 represents the comparison of filtering result of varying- Q and traditional IIR notch filter by taking ECG signal. From this figure, it is easy to notice that selectivity and transient suppression both are more effective than traditional IIR notch filter.

6 Conclusion

In conclusion, Q -varying and r -varying IIR notch filters have been studied and implemented in this paper. It was observed that the transient duration with the Q -varying

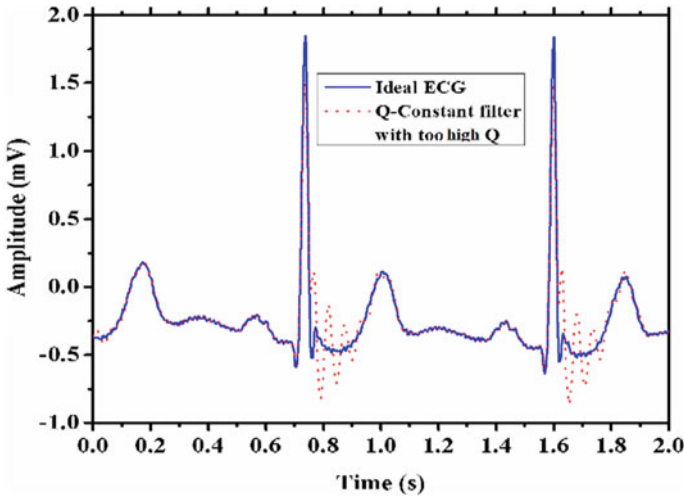


Fig. 14 Filtering result of ECG signal using too high Q traditional notch filter

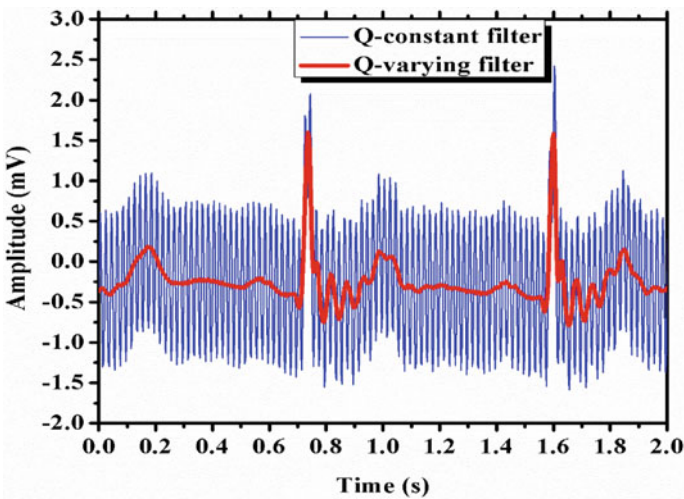


Fig. 15 Comparison of filtering result of ECG signal using Q varying and traditional IIR notch filter

and r -varying IIR notch filters has been reduced as compared to the conventional IIR notch filters having fixed Q and r . Further, the performance of these Q -varying and r -varying IIR notch filters was evaluated for filtering of the noisy ECG signal (corrupted by the fixed frequency noise). From the results, it was observed that the IIR notch filters with variable Q and r parameters performs better as compared to the conventional IIR notch filters.

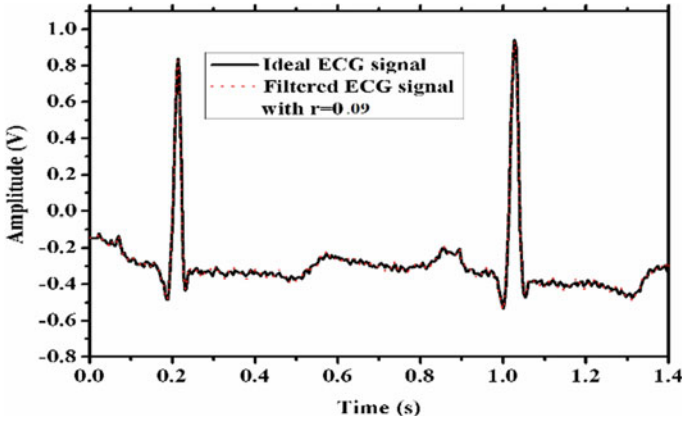


Fig. 16 Filtering result of ECG signal using very low r traditional notch filter

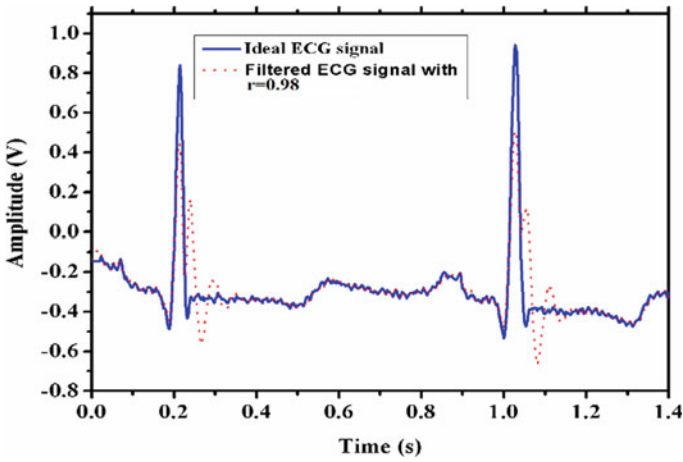


Fig. 17 Filtering result of ECG signal using very high r traditional notch filter

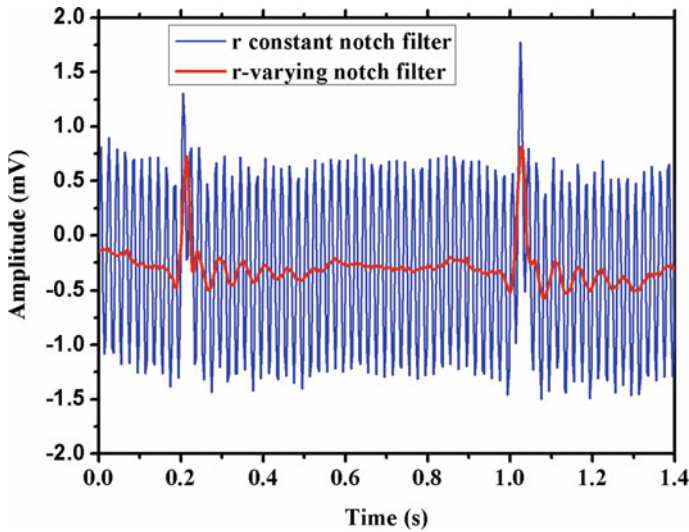


Fig. 18 Comparison of filtering result of ECG signals using r -varying and traditional IIR notch filter

References

1. Piskorowski J (2010) Digital notch filter with time-varying quality factor for the reduction of powerline interference. In: Proceedings of 2010 IEEE international symposium on circuits and systems, pp 2706–2709
2. Ziarani AK, Konrad A (2002) A nonlinear adaptive method of elimination of power line interference in ECG signals. IEEE Trans Biomed Eng 49:540–547
3. Pei SC, Tseng CC (1995) Elimination of AC interference in electrocardiogram using IIR notch filter with transient suppression. IEEE Trans Biomed Eng 42(11):1128–1132
4. Guilani MN, Ardeshir G (2018) A new analog-based LO harmonic rejection technique with tunable notch frequency. Int J Eng Trans B: Appl 31(11):1893–1902
5. Piskorowski J (2009) Digital Q -varying notch IIR filter with transient suppression. IEEE Trans Instrum Meas 59(4):866–872
6. Sharifi M, Mojallali H (2013) Design of IIR digital filter using modified chaotic orthogonal imperialist competitive algorithm. Int J Eng Trans A: Basics 27(7):1033–1040
7. Moody GB, Mark RG (2001) The impact of the MIT-BIH arrhythmia database. IEEE Eng Med Biol Mag 20(3):45–50
8. Rana KPS, Kumar V, Gupta A (2017) A pole-radius-varying IIR notch filter with enhanced post-transient performance. Biomed Signal Process Control 33:379–391
9. Rana KPS, Kumar V, Singhal A, Chandel A, Pahuja D, Vashisht A (2019) Time-varying pole-radius IIR multi-notch filters with improved performance. Arab J Sci Eng 44(8):7101–7120
10. Kocoń S, Piskorowski J (2019) Time-varying IIR notch filter with reduced transient response based on the Bézier curve pole radius variability. Appl Sci 9(7):1309
11. Prashar N, Sood M, Jain S (2019) Design and performance analysis of cascade digital filter for ECG signal processing. Int J Innov Technol Explor Eng 8(8):2659
12. Sohel MA, Naaz M, Raheem MA, Munaaf MA (2017) Design of discrete time notch filter for biomedical applications. In: 2017 Devices for integrated circuit (DevIC), pp 487–490

13. Sharma D, Kaur R (2015) Design and analysis of IIR notch filter using LabVIEW. In: 2015 IEEE international conference on computational intelligence & communication technology, pp 612–616
14. Rajagopalan R, Dahlstrom A (2014) A pole radius varying notch filter with transient suppression for electrocardiogram. *Int J Electron Commun Eng* 8(3):134–138
15. Piskorowski J, Kaszynski R (2010) A concept of Q -varying digital IIR narrow band pass filter with improved dynamic behavior. In: 15th IEEE mediterranean electro technical conference, pp 1402–1405

Advanced Optimization Scheme to Improve Photon Management to Increase Solar Cell Efficiency



Dilip Yadav and Nidhi Singh

1 Introduction

The possibility of the boundless selection of sun-based vitality era from photovoltaic is in a span. A steady increase in material performance, cell, and assembly scaling has driven to increased productivity, which has decreased costs in many kinds of sun-oriented cells, with fall rates for both silicon and cadmium telluride modules. Absorbing much light could be expected into solar cells, it is vital in accomplishing consolidate photon management elements, including antireflection coatings, back-reflectors, furthermore, surface texturing, to diminish optical discrepancies. A reduction in thickness might likewise be joined by incomplete retention of photons and a comparing diminish inefficiency. Besides, sunlight-based cells advance into diverse sorts of systems and designs, including following frameworks, concentrator systems, and building-underground frameworks, new optical prerequisites, etc. In this paper, we concentrate on the optimized structures that empower PV cells, to work efficiently even at low intensity to produce higher yields.

In sun-rich regions with direct normal irradiance (DNI) levels of more than 2000 kWh/m²a (kilowatt-hours per square meter per year), concentrator photovoltaic (CPV) is used for power generations. The central idea of using the CPV technology is that it can be used as cost-effective concentrating optics that significantly decrease the cell area, facilitating the use of more expensive high-efficiency cells and a leveled electricity cost (LCOE) that is easily comparable with conventional flat-plate PV technology in some areas [1]. The paper by N. Pandiarajan, Mathematical Modeling of PV module [2] explains the step-by-step procedure of converting an equivalent

D. Yadav (✉) · N. Singh

Department of Electrical Engineering, Gautam Buddha University, Greater Noida, India

N. Singh

e-mail: nidhi@gbu.ac.in

circuit into a PV module into a Simulink model for 36 W solar module. The material and the reflective angles of a sunray reflector are important in calculating the physical dimensions of the dish [3]. The applications of a reflective dish can be used in such a way that the total concentrated sunlight can be increased many folds. For assuming the net useful area of a parabolic dish, we need to know the main factors governing the physical nature of the dish [4]. These factors include height, focus, beamwidth, wind loading, and other conditions. As far as the factors are involved, the dishes are frequency-independent, the shape of these dishes is different in shape too. The main factors, which are kept in mind to construct a dish, are its feed ratio and the diameter. The dish we have used is PL12-59E [5]. The texturing of a honeycomb is a pivotal part of how good or bad a honeycomb can be used as a filter structure. This is explained in the paper by Anne-Kristin Volk [6]. The electrical properties are also governed by the honeycomb structure as compared to the parabolic dish. Since it is important to keep in mind the electrical properties while optimizing the efficiency, it is advised that the architecture of the honeycomb be carefully monitored. With growing research in the improvisation of PV modules, the efficiency of these solar cells also started to increase [7]. The development of photovoltaic cells was in abundance and millions of investments are done at the research level [8]. With this, major advancements in the tendency to increase the efficiency and lower the costs begin which would allow the common man to dwelling upon and relying on using solar energy more. Applications of solar energy are increased by using different conversion systems which were marked in [9], in the applications of conversion systems in solar energy. These conversion systems allow increasing the applications many folds by combining the solar, electrical, and mechanical forms as forming pillars. Faria Kamal et al. stated in [10] that by increasing the incident photon to current conversion efficiency of the intrinsic layer of a silicon solar cell, performance can be improved and if the tandem (or multijunction) cell is chosen then it can provide almost three times maximum power compared to the conventional PV cell [11].

In the following Sect. 2, the methodology of the PV module which is taken as a base is explained with the help of the formulas used. The section also defines the saturation current, the reverse saturation current, and other guiding parameters. Section 3.1 explains the PV module in combination with the parabolic reflector. By plotting graphs, an increase in irradiance is observed and power is measured. The change in I-V characteristics can also be noted down as with the change in irradiance the increase in I_{out} and V_{out} can be recorded and shown through graphs. In the Sect. 3.2 honeycomb structure is used as a filter so that the small electrical properties which are I_{sol} (deformation in parabolic lens surface) in parabolic reflectors can be reinstated and the efficiency can be monitored keeping in mind the overall feasibility. In the end, the paper shows an efficiency assessment between the cases. Section 4 discusses the Simulink models and their corresponding graphs of irradiance and power for different cases. Thus, by analyzing graphs, the efficiency assessment can be done closely.

2 Methodology

This section of the paper discusses the photovoltaic module with its equations and input irradiance and output power, voltage, and current. The PV module mainly comprises PV cells grouped into large units. The module which is taken from mathematical modeling of PV module with Simulink, Natrajan Pandiarajan [2], comprises four main parameters, namely module photocurrent (I_{ph}), module reverse saturation current (I_{rs}), module saturation current (I_o), and the current output of PV module (I_{pv}). The model equations are as follows (1)–(4) [12–14].

$$\text{Module photo-current } (I_{ph}) = [I_{scr} + K_i(T - 298)] * \frac{\lambda}{1000} \tag{1}$$

where in this equation I_{scr} is rated solar current at nominal weather conditions (25 °C and 1000 W/m²), k_i is short-circuit temperature coefficient. λ is solar irradiance in W/m² and 1000 is nominal irradiance in normal weather conditions (25 °C and 1000 W/m²), $\Delta T = (T - 298)$ is the difference between the operating temperature and nominal temperature ($T - T_r$).

$$\text{Module reverses saturation current } (I_{rs}) = \frac{I_{scr}}{\left[\exp\left(\frac{qV_{oc}}{N_s k A T}\right) - 1 \right]} \tag{2}$$

where I_{rs} is the reverse saturation current of the cell for nominal temperature and irradiance values and E_{go} is band-gap energy of the material that is used. The values of I_{ph} and I_o will expand the value of I and it will be as follows

$$I_o = I_{rs} [T/T_r^3] \exp\left[\frac{q * E_{go}}{AK} \left\{ \frac{1}{T_r} - \frac{1}{T} \right\} \right] \tag{3}$$

Configuration of PV modules depends on the required rated voltage and current. I_{pv} can be expressed as:

$$I_{PV} = N_p * I_{ph} - N_p * I_o \left[\exp\left\{ q * \frac{(V_{PV} + I_{PV} R_s)}{N_s A k T} \right\} - 1 \right]. \tag{4}$$

N_s and N_p are the Numbers of cells connected in series and parallel. For Design purposes, V_{pv} is equal to the V_{oc} , $N_p = 1$, and $N_s = 36$ in numbers.

Figure 1 represents the block diagram of the photovoltaic solar module, which shows that with the input of voltage, irradiance, and temperature, the solar module gives the output in terms of power and current. The function block parameters of the photovoltaic module used for PV module are shown in Table 1.

When the above PV module is run for a time period of 4.5 s, the maximum peak irradiance obtained is 390 W/m². At the same time, the power recorded is 13.5 W.

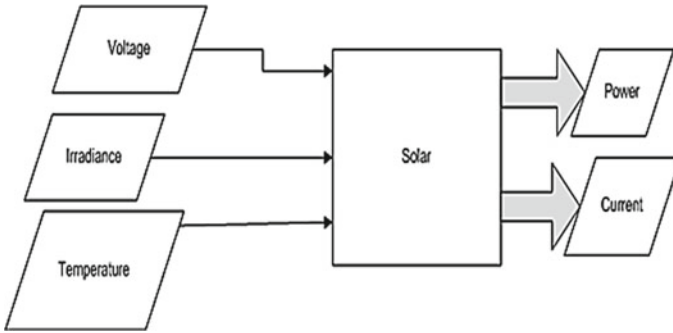


Fig. 1 Block diagram of photovoltaic solar module

Table 1 Function block parameters (PVM)

Parameters	Units
Number of cells connected in series	10
Number of cells connected in parallel	1
Current coefficient	0.0017
Open-source voltage	16.27
Short-circuit current	2.55
Temperature	25
Irradiance	Datasheet

Each second on the Simulink represents 2 h of actual daytime. Thus, the time at which we get the peak irradiance is around 10 am.

3 Study of Photon Management

3.1 Parabolic Reflector

The parabolic reflector plays an important role in concentrating the sun rays that are falling on a particular area to converge it at a particular point i.e. the focus of that specified parabolic reflector [3]. Since all the sunlight falling on the parabolic reflector will not be concentrated and some would reflect and scatter, those rays are not taken into account. The area of the parabolic dish that would reflect the sunlight is considered as (A) . The irradiance (I) at that moment before falling on the parabolic reflector. Thus,

Table 2 Antenna dimensions

Antenna	PL12-59E
Diameter	12 feet
Feed ratio	0.333

Before parabolic dish: Irradiance = I Watt/m²

After parabolic dish: Irradiance = $(A * I)$ Watt/m²

It can be said from this that the irradiance increases “A” times after reflection from the parabolic reflector. The irradiance formula from Jurgita Grigoniene [3], is given by

$$W = -9.874t^2 + 236.9t - 900.4 \tag{5}$$

It is seen that the irradiance varies to time as per Eq. (5) and with different time inputs we get different irradiances. The quantity of solar energy is an integral multiple of the area under the curve having the limit $[a b]$ and $W = f(t)$, which shows that W is a function of time for that duration. The segment $[a b]$ describes the duration of solar radiation energy falling into a solar collector; here, a is the start point and b is the endpoint. So, the total irradiance at a time is the integration of the formula within given time intervals-

$$W = \int_a^b W = -9.874t^2 + 236.9t - 900.4 \tag{6}$$

For a particular parabolic dish, we would have a fixed set of physical parameters. The basic parameters are diameter, focus, height, feed ratio, and area. The antenna we have taken for acquiring the physical parameters is the PL12-59E [5]. The dimensions of the antenna are given in Table 2.

$$\text{Feed Ratio} = \frac{\text{Focus}}{\text{Diameter}} = \frac{F}{D} \tag{7}$$

So, the formula used for the calculation of focus height and diameter is as follows [4].

Diameter = 12 feet = 3.6 m

Focus = Feed ratio * diameter *therefore*, $\text{Focus (F)} = 3.6 * 0.333 = 1.1988 \text{ m}$;
 $F = 1.1988 \text{ m}$

$$\text{Height} = \frac{D^2}{16F}$$

$$\therefore H = \frac{(3.6)^2}{(16 * 1.1988)} \quad H = 2.43 \text{ m}$$

$$Area = \frac{2}{3} * D * H$$

$$\therefore A = \frac{2}{3} * 3.6 * 2.43 \quad Area = 165.722 \text{ m}^2$$

Thus, irradiance after parabolic reflector is

$$I_{\text{new}} = I * 165.722 \text{ Watt/m}^2$$

3.2 Honeycomb Structure

Man-made honeycomb structural materials are typically created by layering a honeycomb material between two thin layers to provide tensile strength. Honeycomb materials are commonly used where smooth or gently curved surfaces are used and where high specific strength is appropriate. Since with ample amount of increase in irradiance the model may lose its electrical properties to some extent, the paper introduces honeycomb structure as a filter for retaining the electrical properties. The honeycomb structure is mainly columnar and hexagonal. They are hollow and act as filters; we use them in our model as filters for passing 30% of the radiations and refracting or scattering the rest of them.

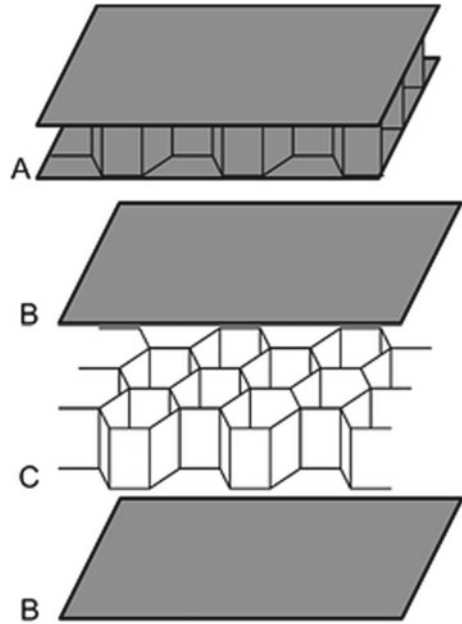
Figure 2 shows the sandwich structure of honeycomb. In nature, we find the honeycomb structure in beehives, tripe, and honeycomb weathering in rocks. They are made from different materials for different purposes and roles intended to be used. There are three basic techniques of production of honeycomb, namely expansion, corrugation, and molding, and these techniques were basically for non-sandwich applications [6].

3.3 Artificial Bee Colony (ABC) Algorithm

The ABC model mainly consists of three kinds of bees—employed bees, onlookers, scouts. ABC is a population-based algorithm that runs as a loop. It is a very efficient optimization technique and gives out the best results. The basic algorithm is used for food sites and here in this paper, food sites have been replaced with sites having varying irradiances. The algorithm follows some steps given:

Employed bees produce food sources initially. The work of the employed bee is to go to a food source in her memory and a neighbor source is determined, and the nectar amount is evaluated and subsequently dances in the hive. The onlooker watches the

Fig. 2 Sandwich structure
honeycomb structure



moves and chooses a source depending on that dance and moves toward the source. The scouts discover new food sources and replace the abandoned food sources. Best food sources found till now are registered. In this manner, the algorithm chooses the best sites and calculates their fitness. The fit sites are given preference. Thus, if we compare this phenomenon with our model, the fittest sites will be the sites where we will be getting the maximum irradiance levels, e.g., if there are a total of 150 sites then after the ABC algorithm is run these 150 sites would be enhanced and sort in decreasing order. These 150 enhanced sites would be fed into the PV module as input that would give power and current as output and efficiency assessment can be carried out.

4 Results

4.1 Simulink Model with Parabolic Reflector

Figure 3 is the Simulink model with a parabolic reflector. This model shows the comparison between the change in behavior in irradiance and power with the introduction of the parabolic reflector. The corresponding graphs are given in Figs. 4 and 5 for Table 3 values.

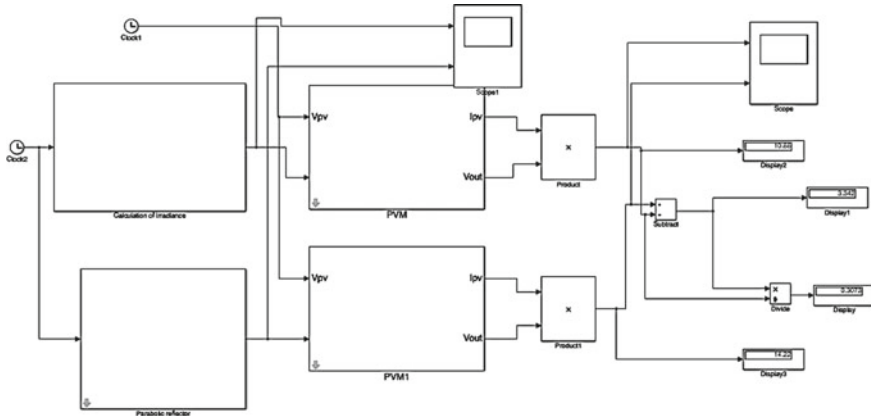


Fig. 3 Simulink model with parabolic reflector

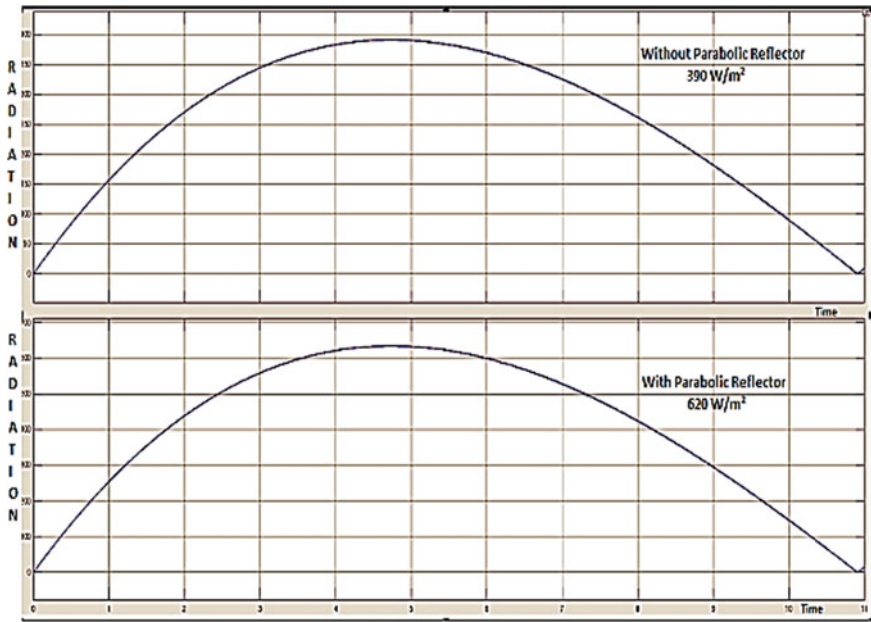


Fig. 4 Variation in irradiance after using parabolic reflector

According to the simulation result obtained from Fig. 3, the percentage increase in efficiency is about 30.0923%. If we look at the power curve obtained in Fig. 5, the output power has increased after using the parabolic reflector in terms of the normal PV module. In Table 4 a comparison is between the two modules having different power for different radiation and temperature, after using the parabolic reflector the

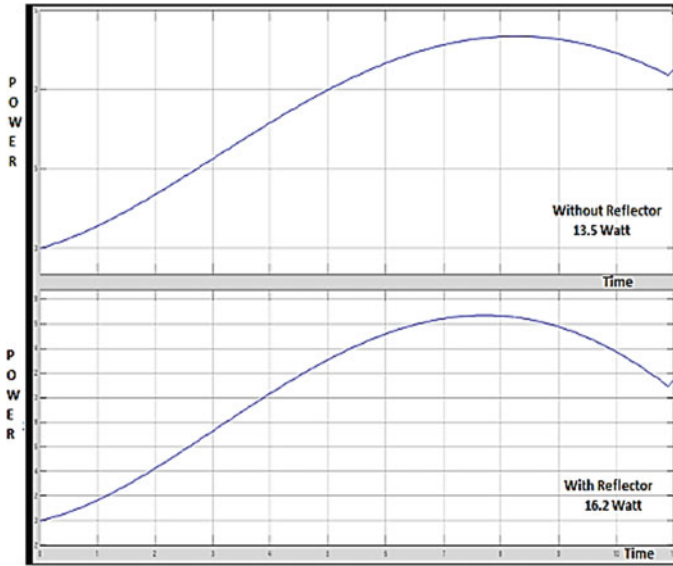


Fig. 5 Variation in power after using parabolic reflector

Table 3 Comparison of irradiation characteristics

Irradiation without parabolic reflector	Irradiation with parabolic reflector
390 W/m ²	620 W/m ²

Table 4 Comparison of power characteristics

Module	Power without parabolic reflector (W)	Power with parabolic reflector (W)	Difference in power (W)	Efficiency increased (%)
Module 1	13.5	16.2	2.7	16.66
Module 2	10.8472	14.20148	3.35428	30.0923

efficiency of the modules has been increased by 16.66% and 30.0923% for the other modules.

4.2 Simulink Model with Honeycomb Structure

This Simulink model in Fig. 6 takes the dataset received from the ABC algorithm and injects it into the Simulink. There is a comparison shown between the original dataset

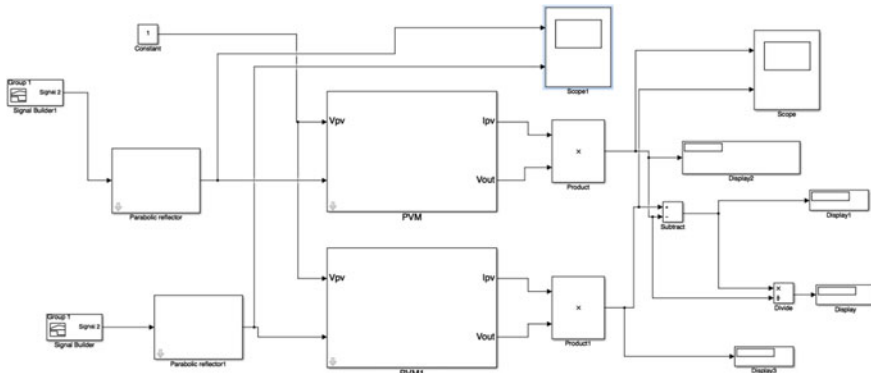


Fig. 6 Simulink model with honeycomb structure

and the refined dataset that is obtained by filtering through the ABC algorithm. For the irradiance characteristic graph, the values are:

PV module radiation **457 W/m²**

After parabolic reflector radiation **726 W/m²**

After HC with parabolic **730 W/m²**

For power characteristic values are:

Before using HC structure with parabolic reflector Power **2.833 W**

After applying HC with parabolic reflector **2.860 W**

Figure 7 shows the irradiance in the parabolic reflector after using the honeycomb structure. It was found that after using the honeycomb structure on parabolic reflector the irradiance comes out to be 730 W/m² which was earlier 726 W/m² for the module. In Fig. 8, the output power of the system has increased by 0.95% after using the honeycomb structure with a parabolic reflector. The advantage of using the reflector with the HC method is it improves the performance and efficiency of the module.

5 Conclusion

In this paper, the efficiency improvement in the PV solar module has been shown after using the parabolic reflector and ABC algorithm with the help of a simulation model, designed in Matlab/Simulation software. This paper proposes a novel improvement in the efficiency of the PV module by using a parabolic reflector and honeycomb structure which can improve the performance up to 31.01%. The experimental data have been taken around 10 AM, by using the mathematical equation of PV. Different simulation models were developed and efficiency was calculated with and without a

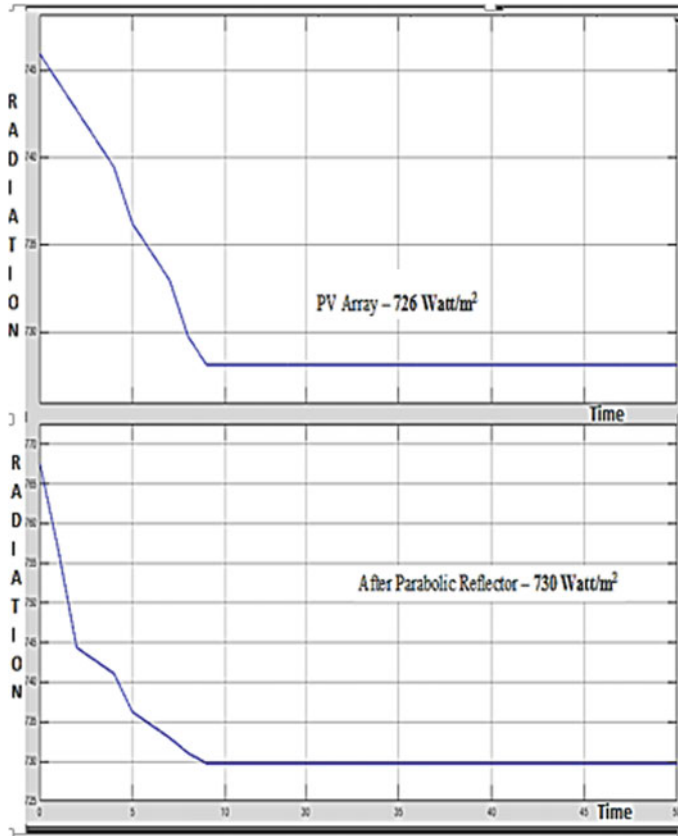


Fig. 7 Irradiance with HC structure

parabolic reflector. The PV module operates at a certain irradiation level, by using a parabolic reflector, the efficiency of the PV module can be increased to 30.092%. In the next case, honeycomb structure was used as a filter on the dish, and observations were recorded, by using the parabolic reflector and HC structure for the particular time the efficiency has been improved by 0.95%, overall efficiency comes out to be 31.01%.

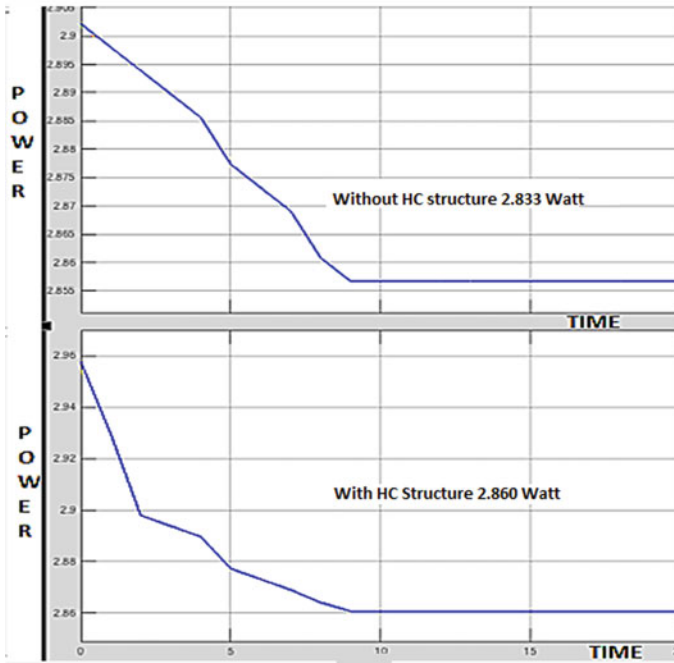


Fig. 8 Power after HC structure

References

1. Fraunhofer ISE (2017) NRL, Current status of concentrator photovoltaic technology
2. Pandiarajan N, Muthu R (2011) Mathematical modeling of a photovoltaic module with Simulink. IEEE 1st International Conference on Electrical Energy Systems, 258–263
3. Grigonienė J, Karnauskas M (2009) Mathematical modeling of optimal tilt angles of solar collector and sunray reflector. *Energetic*, pp 1–46
4. Comly D (2017) N3AOG, parabolic antennas and their feeds
5. Knop CM, Senior Member, Ieee (1976) On the front to back ratio of a parabolic dish antenna. *IEEE Trans Antennas Propag* 109–111
6. Volk A-K, Tucher N, Seiffe J, Hauser H, Zimmer M, Bläsi B, Hofmann M, Rentsch J (2014) Honeycomb structure on multi-crystalline silicon Al-BSF solar cell with 17.8% efficiency. *IEEE J PV*
7. Ago, Manning CD (1999) Development of a PV array model for use in power-electronics simulation studies. *IEEE Proc-Electra Power Appl* 146(2)
8. Green MA, Emery K, Hishikawa Y, Warta W, Dunlop ED (2016) Solar cell efficiency tables (version 47). *Prog Photovolt Res Appl* 24(1):3–11
9. Pandiarajan N, Ramaprabha R, Muthu R (2012) Application of circuit model for photovoltaic energy conversion system. *Int J Photo Energy*, Article ID410401, 14 p
10. Kamal F, Zaman UT, Sayeed KA, Momen A (2013) Improved quantum efficiency with increasing number of quantum dot sizes in silicon-based solar cell. In: 2nd International conference on advances in electrical engineering, pp 19–21
11. Wongsodihardjo H (2013) Photovoltaic cell modeling For MPPT using MATLAB/Simulink to improve the conversion efficiency. <https://doi.org/10.1109/pesmg.2013.6672819>

12. Chowdhury S, Chowdhury SP, Taylor GA, Song YH (2008) Mathematical modeling and performance evaluation of a stand-alone polycrystalline PV plant with MPPT facility. IEEE power and energy society general meeting—conversion and delivery of electrical energy in the 21st century, Pittsburg, USA, 20–24 July 2008
13. Jung J-H, Ahmed S (2010) Model construction of single-crystalline photovoltaic panels for real-time simulation. IEEE Energy Conversion Congress & Expo, 12–16 Sept, Atlanta, USA
14. Singh GK (2013) Solar power generation by PV (photovoltaic) technology: a review. *Energy* 53:1–13. ISSN 0360-5442

Music Generation Using Supervised Learning and LSTM



Suman Maria Tony and S. Sasikumar

1 Introduction

Music composing is one of the finest arts where the imagination of the music composer plays a major role in the outcome. Automating this music generation for a given scenario is a complex task where no scientific community had achieved results on par with the human composition. The idea is to generate a melody or a polyphony without any chords or patterns. The digitized song is converted to the *musical instrument digital interface* (MIDI) format for ease of processing and synthesizing music data.

Automatic music generation can be done using algorithms that follow grammar and rules [1, 2], but the learning algorithms such as machine learning (ML) or deep learning (DL) can suit to generate music of varieties of genres. DL and ML have found several applications in a variety of fields including music generation and medical image processing [3, 4]. Various LSTM architectures for speech processing were explored which includes deep long short-term memory (DLSTM), long short-term memory projected (LSTMP), and deep long short-term memory projected (DLSTMP) architectures [5]. Many researchers have attempted to generate music that involves chord sequences [6] and melodies [7].

Section 1 introduces the music synthesis using an artificial network by supervised learning. Section 2 highlights the related work in music synthesis available in the literature. Section 3 explores the LSTM architecture and its variants. Section 4 has the materials and methods involved in the experiment which is explained in Sect. 5. The concluding remarks are given in Sect. 6.

S. M. Tony (✉) · S. Sasikumar
Department of Electronics and Communication Engineering, Hindustan Institute of Technology and Science, Chennai, India
e-mail: sumanmariatony@licet.ac.in

S. M. Tony
Loyola-ICAM College of Engineering and Technology (LICET), Chennai, India

2 Related Work in Music Generation

With the development of artificial neural network (ANN) and several learning algorithms introduced using ANN, the music generating models created by such supervised learning algorithms play a significant role in music synthesis [8–13]. The usage of LSTM in the music generation of Bach’s music style was implemented using a trained neural network by considering arbitrary datasets [14]. Aiva IA, an AI-based automatic music synthesizer, has its own copyrighted audio tracks [15]. Jazz guitar music is synthesized by Sergio [16] using machine learning algorithms and also it is tuned using ornamentations to be similar to natural musical performances. Also, machine learning algorithms like the random forest were used to evaluate the parameters in music [17]. Manipulation of loudness to properly convey the emotion involved in the music was attempted using ML algorithms from the dynamic markings [18]. Also, the generation of melody sequences was attempted using the genetic algorithm by modeling each sequence like a chromosome and having multi-objective optimization and fitness function [19]. Though a lot of research is on the anvil, the limitations of generating music using deep learning algorithms still exist and the music composer has a prominent role in composing music [20].

3 Architecture of Long Short-Term Memory (LSTM) and Its Variants

LSTM has been used to synthesize music and for works related to natural language processing (NLP). LSTM is a recurrent neural network that can process and remember time series data and can be used to predict the chain for a defined period.

3.1 Conventional LSTM

Conventional LSTM in Fig. 1 consists of an input gate, a memory cell, multiplicative units, and an output gate. The input gate processes the input data and the memory cell stores the temporal data, while the output gate controls the flow of output activations (Eq. 1). A forget gate is added to the architecture to let the unit discard the unwanted time series data which need not be considered as part of the series.

3.2 Peephole LSTM

LSTM network with peephole connection is shown in Fig. 2. The mathematical equations (Eq. 2) governing the peephole LSTM and peephole convolutional LSTM are

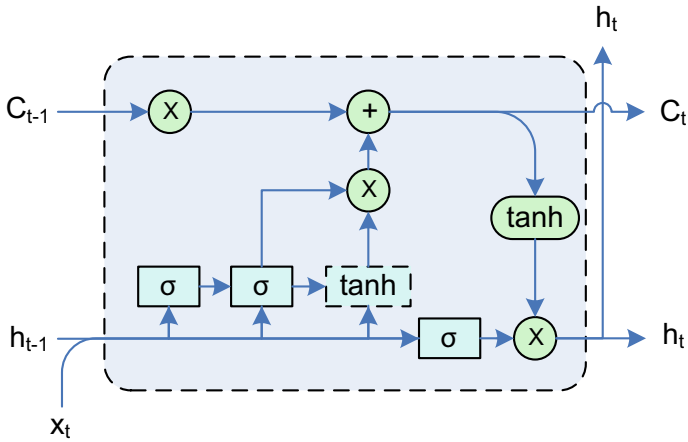


Fig. 1 LSTM architecture

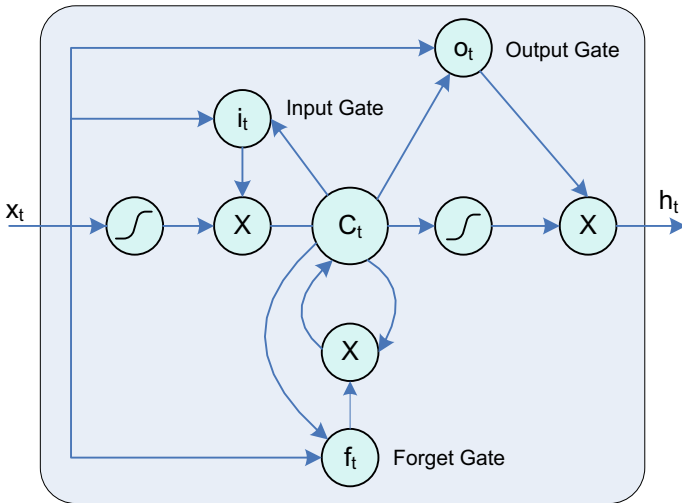


Fig. 2 Peephole LSTM architecture

also highlighted to understand the dataflow and weight optimization. The Constant Error Carousel (CEC) avoids speedy decaying of error by adding a constant error to the units, thereby addressing the vanishing gradient problem.

The LSTM network maps the input and output using various activation units inside the cell. The following equations are iterated for $t = 1$ to T .

$$f_t = \sigma_g(W_f * x_t + U_f * h_{t-1} + V_f \circ c_{t-1} + b_f)$$



$$i_t = \sigma_g(W_i * x_t + U_i * h_{t-1} + V_i \circ c_{t-1} + b_i)$$

$$\begin{aligned}
c_t &= f_t \circ c_{t-1} + i_t \circ \sigma_c(W_c * x_t + U_c * h_{t-1} + b_c) \\
o_t &= \sigma_g(W_o * x_t + U_o * h_{t-1} + V_o \circ c_t + b_o) \\
h_t &= o_t \circ \sigma_g(c_t)
\end{aligned} \tag{1}$$

(i input gate, o output gate, f forget gate, c memory cell).

Peephole convolutional LSTM is defined by the following expressions:

$$\begin{aligned}
f_t &= \sigma_g(W_f x_t + U_f C_{t-1} + b_f) \\
i_t &= \sigma_g(W_i x_t + U_i C_{t-1} + b_i) \\
c_t &= f_t \circ c_{t-1} + i_t \circ \sigma_c(W_c x_t + b_c) \\
o_t &= \sigma_g(W_o x_t + U_o C_{t-1} + b_o) \\
h_t &= \sigma_h(o_t \circ c_t)
\end{aligned} \tag{2}$$

 is the element-wise multiplication and  is the differentiable function.

The other variants of LSTM are deep LSTM where the architecture is deeper and it was used for some speech recognition tasks [21, 22].

4 Materials and Methods

4.1 Music Background and File Formats

MIDI format is widely used by electronic instruments and software drivers, and it has notes and blanks. The note has a channel number, MIDI note number, velocity, etc. The main drawback of MIDI is in encoding multiple tracks and saving the intention of multiple notes which reduces the effectiveness in terms of usage. Another format that overcomes this difficulty is the piano roll which comes from the automatic piano that uses a perforated roll of papers.

4.2 LSTM Topologies

Several LSTM implementation topologies are shown in Fig. 3. These topologies include DLSTM, LSTMP, and DLSTMP.

Various deep LSTM recurrent neural networks (RNN) are shown in Fig. 3. These deep LSTM topologies which vary in depth have already been used for audio processing tasks in speech modeling [22, 23]. These deep LSTMs are constructed by stacking LSTM RNNs and thus increasing the depth further. Thus, the input travels through the stacked LSTM RNNs and facilitates learning at different times.

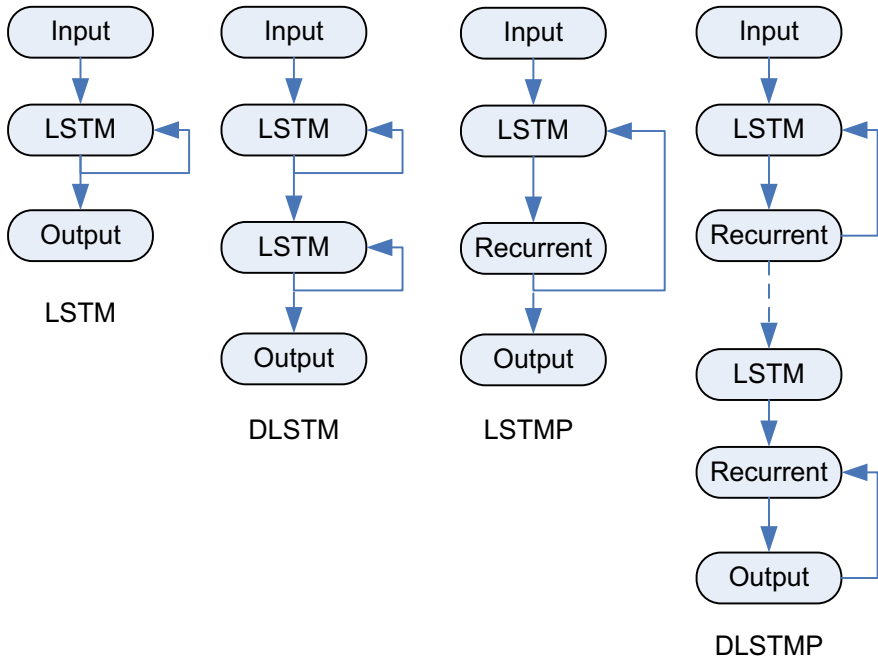


Fig. 3 LSTM architectures [3]

4.3 Workflow

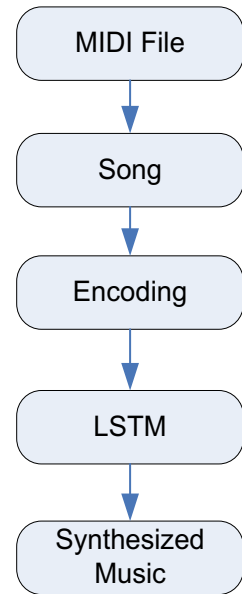
As shown in Fig. 4, the workflow is carried out. The MIDI file is encoded to the proper format, and the LSTM network is trained with that. The model created is used to synthesize music. The MIDI file from the dataset is converted into song format for a more natural way of learning and synthesizing music based on the learned model. The music file is then encoded into a format suitable for the LSTM network to recognize the sequence. Here, the music file is converted into a two-dimensional matrix of samples generated by the music data. The output of LSTM after few epochs of training represents the synthesized music which is converted to a “wav” or encoded to “mp3” format to make the output compatible with a conventional audio player.

5 Experiments and Results

5.1 Dataset and Tools

A lot of open-source music files of different genres and instruments are available on the Internet. These files of different formats are converted to a single format (MIDI)

Fig. 4 Workflow of music synthesis

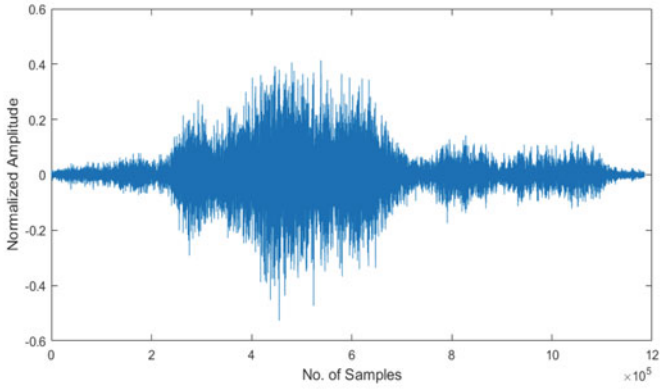


for creating a database called “training library.” The MIDI music files in a particular library belong to a particular instrument like piano, drum, violin, etc. Before training the LSTM network, we have chosen one such training library as we wanted to create unique LSTM networks for each instrument.

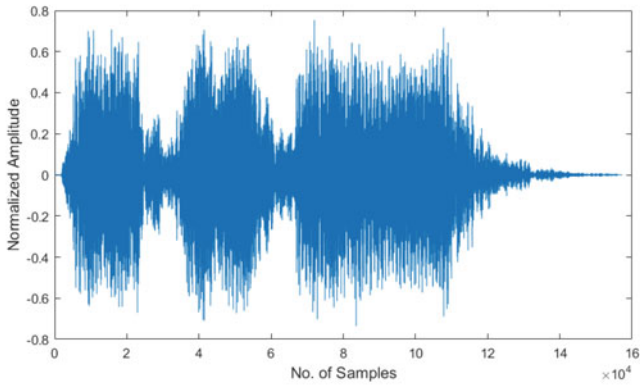
5.2 *Simulation Results*

The LSTM network is trained with a set of music files collected and compiled as a separate training library discussed in the previous section. The next step in this experiment is to train the LSTM network with the music files available in the library and following the training of the network with a few epochs, the model is stored. This model is then used to synthesize music files with random initial seed and the output files obtained are compared with the music files in the training library.

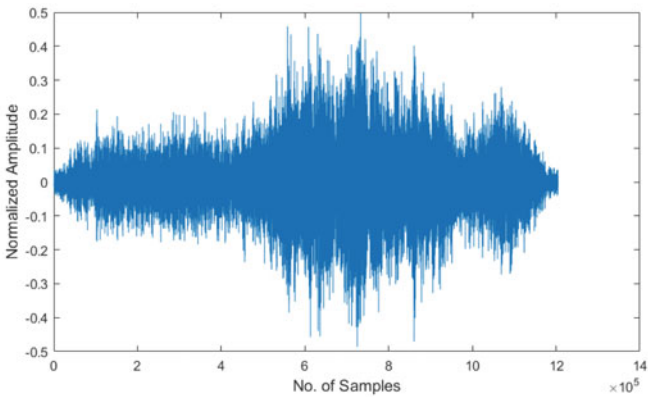
At this moment, quantitative analysis of the synthesized music file is not a major concern as we focused on an acceptable music file which has good harmony that is in sync with the training library. We have generated as many as music files available in the training library. Figure 5 shows some of the best music file synthesized which is on par with the music available in the library.



(a) Synthesized music sample-1



(b) Synthesized music sample-2



(c) Synthesized music sample-3

Fig. 5 Music files synthesized by LSTM Network

6 Conclusion

The LSTM-based model created by supervised training using a set of music files is discussed in this paper. The created model after training for a few epochs works satisfactorily based on the music file synthesized by the trained network. Though the trained network generated an arbitrary note, it is comparable with the existing music files when analyzed qualitatively. The structure of the LSTM and its topology also plays a significant role in generating music file. By using the deep LSTM network, we could generate music files in a short time, but could not predict its efficiency from the conducted experiment as we focused on generating music on par with the training library. The synthesized music file is similar in harmony when compared with the training library created. Further, we are looking ahead to assess the synthesized music quantitatively by extracting statistical features and to improve the discontinuity in some music files. Also, the deep LSTM architecture can be optimized and implemented for this application thereby improving the efficiency of the training.

References

1. Ebcioğlu K (1988) An expert system for harmonizing four-part chorales. *Comput Music J (CMJ)* 2(3):43–51
2. Steedman M (1984) A generative grammar for Jazz chord sequences. *Music Percept* 2(1):52–77
3. Kunaraj K, Maria Wenisch S, Balaji S, Mahimai Don Bosco FP (2020) Impulse noise classification using machine learning classifier and robust statistical features. In: Smys S, Tavares J, Balas V, Ilyasu A (eds) *Computational vision and bio-inspired computing, ICCVBIC 2019. Advances in Intelligent Systems and Computing*, vol 1108. Springer, Cham. https://doi.org/10.1007/978-3-030-37218-7_72
4. Bae Y, Kumarasamy K, Ali IM et al (2018) Differences between schizophrenic and normal subjects using network properties from fMRI. *J Digit Imaging* 31:252–261. <https://doi.org/10.1007/s10278-017-0020-4>
5. Sak H, Senior A, Beaufays F, Long short-term memory recurrent neural network architectures for large scale acoustic modeling. 15th Annual Conference of the International Speech Communication Association, Singapore, 2014:14–18. Google, USA
6. Conklin D (2016) Chord sequence generation with semiotic patterns. *J Math Music* 10(2):92–106. <https://doi.org/10.1080/17459737.2016.118172>
7. de León P, Pedro J, Iñesta JM, Calvo-Zaragoza J, Rizo D (2016) Data-based melody generation through multi-objective evolutionary computation. *J Math Music* 10(2):173–192. <https://doi.org/10.1080/17459737.2016.118171>
8. Laden B, Keefe DH (1989) The representation of pitch in a neural net model for chord classification. *Comput Music J* 13(4)
9. Chen CCJ, Miikkulainen R (2001) Creating melodies with evolving recurrent neural network. In: *Proceedings of the international joint conference on neural networks, IJCNN'01*, pp 2241–2246
10. Eck D, Schmidhuber J (2002) A first look at music composition using LSTM recurrent neural networks. Technical Report: IDSIA-07-02
11. Franklin JA (2006) Recurrent neural networks for music computation. *INFORMS J Comput* 18(3):321–338
12. Mozer MC (1994) Neural network music composition by prediction: exploring the benefits of psychoacoustic constraints and multiscale processing. *Connect Sci* 6(2–3):247–280

13. Carpinteiro OAS (2001) A neural model to segment musical pieces. In: Proceedings of the second Brazilian symposium on computer music. Fifteenth congress of the Brazilian Computer Society, pp 114–120
14. Hewahi N, AlSaigal S, AlJanahi S (2019) Generation of music pieces using machine learning: long short-term memory neural networks approach. *Arab J Basic Appl Sci* 26(1):397–413
15. Travers J (2018) Can I write music well? *J Technology* (online). LabRoots. Retrieved from <https://www.labroots.com/trending/technology/8810/listen-ai-writing-music-decide>
16. Giraldo S, Ramírez R (2016) A machine learning approach to ornamentation modeling and synthesis in jazz guitar. *J Math Music* 10(2):107–126. <https://doi.org/10.1080/17459737.2016.1207814>
17. Phillip B, Kirlin, Yust J (2016) Analysis of analysis: using machine learning to evaluate the importance of music parameters for Schenkerian analysis. *J Math Music* 10(2):127–148. <https://doi.org/10.1080/17459737.2016.1209588>
18. Kosta K, Ramírez R, Bandtlow OF, Chew E (2016) Mapping between dynamic markings and performed loudness: a machine learning approach. *J Math Music* 10(2):149–172. <https://doi.org/10.1080/17459737.2016.1193237>
19. Iñesta JM, Conklin D, Ramírez R (2016) Machine learning and music generation. *J Math Music* 10(2):87–91. <https://doi.org/10.1080/17459737.2016.1216369>
20. Casini L, Marfia G, Rocchetti M (2018) Some reflections on the potential and limitations of deep learning for automated music generation. In: IEEE 29th annual international symposium on personal, indoor and mobile radio communications (PIMRC), Bologna, 2018, pp 27–31. <https://doi.org/10.1109/pimrc.2018.8581038>
21. Eyben F, Wollmer M, Schuller B, Graves A (2009) From speech to letters using a novel neural network architecture for grapheme based ASR. In: IEEE workshop on automatic speech recognition & understanding: ASRU. IEEE, pp 376–380
22. Graves A, Mohamed A, Hinton G (2013) Speech recognition with deep recurrent neural networks. In: Proceedings of ICASSP
23. Eyben F, Wollmer M, Schuller B, Graves A (2009) From speech to letters using a novel neural network architecture for grapheme based ASR. In: IEEE workshop on automatic speech recognition & understanding, 2009. ASRU 2009. IEEE, pp 376–380

Controlling an SSB-SC Amplitude Modulator Using a Second-Order Control System



Manisha Bharti, Aditya Joshi, and Tanvika Garg

1 Introduction

1.1 Theory

Second-Order Control System. A system designed such that it can control other system(s) and device(s) is called a control system. The characteristic equation of the overall transfer function/gain of a control system decides its order. The degree of the characteristic equation in a first-order control system is 1, in a second-order system is 2 and so on. In this paper, we shall be using a second-order control system because it is one of the most practically feasible control systems and also because it provides us with a parameter that can further be manipulated in order to obtain the desired output or, as in this case can influence another system/set of devices (the modulator). That parameter is the “damping ratio” which changes the amplitude along with the damped frequency of the time response of the system, which in turn is the message signal itself, the details of which have been explained in the paper.

SSB Amplitude Modulation. Modulating the amplitude of the carrier wave with respect to the message signal in such a way that the frequency response of the final modulated signal contains only a single side band without any carrier wave is called “SSB Amplitude Modulation” and is carried by an SSB Amplitude Modulator. The side band involved can either be the lower side band or the upper side band.

M. Bharti · A. Joshi (✉) · T. Garg
National Institute of Technology Narela, New Delhi, India

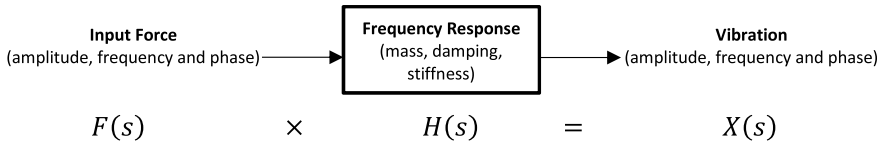


Fig. 1 Frequency response of an LTI system

1.2 Objective

The objective here is to externally operate an SSB amplitude modulator using a second-order control system. A relationship between the parameters of both the components needs to be formulated in order to make sure we get the desired output. A second-order control system can be reduced to a simple block diagram with the transfer function as the gain. In frequency domain, the input simply gets multiplied by the transfer function to give the output (Fig. 1).

1.3 Method

A second-order control system has a second-order characteristic equation, and hence, simple mathematics shows us that the time response of a sinusoidal signal when passed through an LTI second-order system (which is the transfer function of the control system in this case) is a steady-state sinusoidal output with a phase angle of -90 degrees [1–4].

We have,

$$x(t) = \frac{1}{\sqrt{(1 - \mu^2)^2 + (2\xi\mu)^2}} \sin\left(\omega t - \tan^{-1} \frac{2\xi\mu}{(1 - \mu^2)}\right);$$

$\xi \Rightarrow$ damping ratio

$$\mu = \frac{\omega}{\omega_n}; \therefore \mu \geq 0$$

$x(t)$ is also the message signal.

We know that the phase is -90 degrees, so,

$$\begin{aligned} \tan^{-1} \frac{2\xi\mu}{(1 - \mu^2)} &= -90 \\ \Rightarrow (1 - \mu^2) &= 0 \end{aligned}$$

$$\Rightarrow \mu = 1$$

$\omega \rightarrow$ damped frequency, $\omega_n \rightarrow$ natural frequency, $\omega_m \rightarrow$ message frequency

$$\frac{\omega}{\omega_n} = 1 \Rightarrow \omega = \omega_n = \omega_m$$

$$x(t) = \frac{\cos(\omega_m t)}{2\xi} \tag{1}$$

$$c(t) = A_c \cos(\omega_c t); s_{SSB} \Rightarrow \text{Modulated signal}$$

Considering the lower side band

$$S_{SSB}(t) = \frac{1}{4\xi} \cos((\omega_c - \omega_m)t) \tag{2}$$

modulation index $\rightarrow m = \frac{A_m}{A_c}$ [5]

$$\text{Amplitude}_{SSB} \propto \frac{1}{\xi} \tag{3}$$

Block Diagram. The steady-state output obtained and the carrier signal are then passed through the ‘‘Balanced Modulator’’ for DSB-SC amplitude modulation. The output from that is then passed through a ‘‘Side band Suppression filter’’ which removes one of the side bands. The next step which involves the ‘‘Mixer’’ is used if the obtained SSB signal is to be transmitted and hence raises its frequency to the value desired for transmission [5] (Fig. 2).

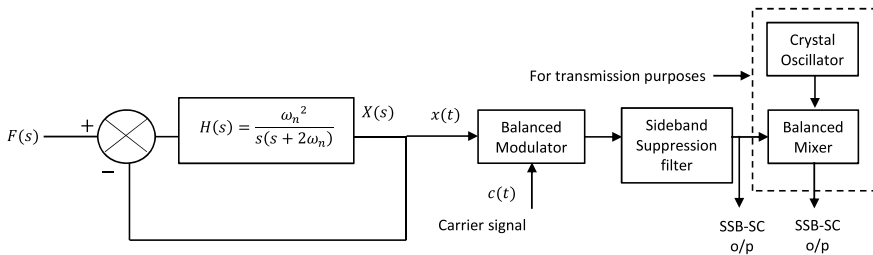


Fig. 2 Entire arrangement of a second-order control system attached to an SSB-SC amplitude modulator

Table 1 Mathematical relations obtained

S. No.	Parameter	Mathematical expression
1	Current (I_t)	$I_t = I_c \sqrt{1 + \frac{k_a^2}{8\xi^2}}$
2	Voltage (V_t)	$V_t = V_c \sqrt{1 + \frac{k_a^2}{8\xi^2}}$
3	Efficiency (η)	$\eta = \frac{k_a^2}{k_a^2 + 8\xi^2}$
4	Total Power (P_t)	$P_t = P_c \left(1 + \frac{k_a^2}{8\xi^2}\right)$

$I_c \rightarrow$ Carrier current; $V_c \rightarrow$ Carrier voltage; $P_c \rightarrow$ Carrier power

2 Literature Survey

2.1 State of the Art

A design for amplitude modulation using frequency analysis of a second-order control system was proposed in [6], and its modulated signal was obtained as follows:

$$S_{AM}(t) = A_c \cos(\omega_c t) + \frac{A_c m}{2} \cos((\omega_c + \omega_n)t) + \frac{A_c m}{2} \cos((\omega_c - \omega_n)t)$$

$$m = \frac{1}{2\xi A_c} = \frac{k_a}{2\xi}$$

$\frac{1}{A_c} = k_a \rightarrow$ amplitude sensitivity.

Further, depending on the modulation index and the damping ratio nine possible cases emerge that highlight the level of manipulation which can be done using the control system. Using the mathematical relations established above, the current, power, voltage, and efficiency expressions are derived as follows [6] (Table 1).

3 Controlling the Modulator’s Input–Output and Their Parameters

3.1 The Message Signal

The message signal is the time response of the second-order control system, so naturally the damped frequency becomes the message frequency. The damped frequency

on the other hand can be controlled by adjusting the damping ratio of the control system.

Since

$$\omega_m = \omega$$

and

$$\omega = \omega_n \sqrt{1 - \xi^2}$$

So, increasing the damping ratio will decrease [5] the message frequency and vice versa. Similarly, the amplitude of the message signal can also be controlled by adjusting the damping ratio.

From (1) we have,

$$\text{Amplitude}_{\text{message}} = \frac{1}{2\xi}$$

So, increasing the damping ratio will decrease the amplitude of the message signal and vice versa.

3.2 Amplitude of the Modulated Signal (Voltage)

The amplitude of the modulated signal is inversely proportional to the damping ratio of the second-order control system. From (3), we have:

$$\text{Amplitude}_{\text{SSB}} \propto \frac{1}{\xi}$$

The variation in damping ratio can be done in the following three ways in Table 2.

The amplitude of the sinusoidal graph changes with any changes made to the damping ratio of the control system (Fig. 3).

Table 2 Nature of the system corresponding to the damping ratio

S. No.	Condition	Nature of the system
1	$1 > \xi > 0$	Under-damped
2	$\xi = 1$	Critically damped
3	$\xi > 1$	Over-damped

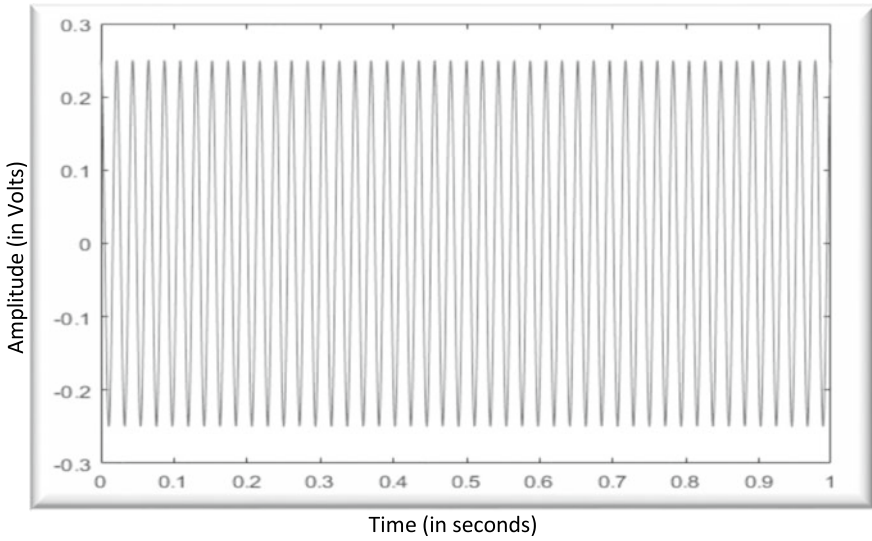


Fig. 3 Graph for the modulated signal when the control system is critically damped, obtained using MATLAB

3.3 Power Dissipated by the Modulated Signal

The mathematical expression for the average power is:

$$P_{\text{avg}} = \frac{V_{\text{rms}}^2}{R} \quad (4)$$

From (2) and (4), we get

$$P_{\text{AM-SSB}} = \frac{1}{32\xi^2 R} \quad (5)$$

So, the power dissipated by the modulated signal is inversely proportional to the square of the damping ratio.

3.4 Current Due to the Modulated Signal

The current relation is as follows:

From (5)

$$I_{\text{SSB}} = \frac{1}{4\sqrt{2}\xi R}$$

So, in order to ensure lesser current and prevent the [5, 7–12] devices before the power amplifier stage from sustaining damage due to overheat (power dissipation in the form of heat loss) the damping ratio has to be increased.

4 Evaluation

We have compared the design proposed in this paper and the one proposed in [6] on the basis of parameters like power consumption, SNR, and the level of independence from modulation parameters.

4.1 SNR

SNR stands for “signal-to-noise ratio”, and it is used to describe the proportion of actual information [5] signal to undesirable signal also called noise. Mathematically, it is the ratio of signal power (P_S) to noise power (P_N). Since it is a ratio it does not have any unit, due to having large values it is expressed in decibels by taking log to the base 10 and then multiplying it by 10.

$$\text{SNR}_{(\text{dB})} = 10 \log_{10} \frac{P_S}{P_N}$$

The most prominent type of noise present in practical circuits is the “White Gaussian Noise”. The noise is so-called because it contains all spectral frequencies [5] equally on an average. The average or mean white noise voltage across a conductor is zero, but the root mean square (RMS) value is finite and can be easily measured. This voltage is proportional to the resistance of the conductor, its absolute temperature and the frequency bandwidth. The average white noise [5] power P_N in watt is:

$$P_N = KTB$$

$K = 1.38 \times 10^{-23}$ J/K (Boltzmann’s constant)

T = absolute temperature in kelvin.

B = bandwidth in Hz.

It is apparent from Figs. 4a–c that the proposed method gives a far better SNR in under-damped systems than AM-DSB. While it is true that the SNR for the proposed method is lesser than AM-DSB for critically damped and over-damped systems, the fact that critically damped systems are practically impossible to make and over-damped systems never reach a steady state has ensured that almost all of the practical control systems are “Under-damped” in nature (Tables 3, 4 and 5).

This argument proves that the proposed method will offer way better SNR than AM-DSB in practical circuits.

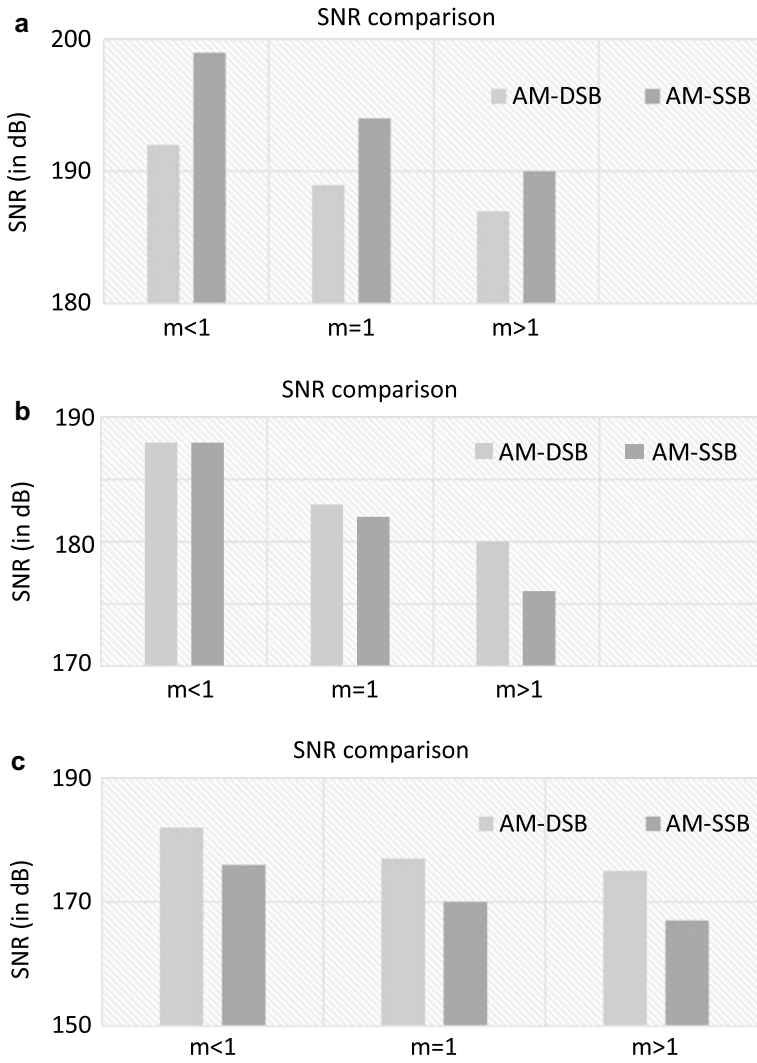


Fig. 4 **a** Graph comparing the SNR of both the methods for $\xi < 1$. **b** Graph comparing the SNR of both the methods for $\xi = 1$. **c** Graph comparing the SNR of both the methods for $\xi > 1$

Table 3 SNR values in $\xi < 1$

Under-damped system			
S. No.	Type of modulation	SNR (in dB)	
		AM-DSB	AM-SSB
1	Normal modulation	192	199
2	Critical modulation	189	194
3	Over modulation	187	190

Table 4 SNR values in $\xi = 1$

Critically damped system			
S. No.	Type of modulation	SNR (in dB)	
		AM-DSB	AM-SSB
1	Normal modulation	188	188
2	Critical modulation	183	182
3	Over modulation	180	176

Table 5 SNR Values in $\xi > 1$

Over-damped system			
S. No.	Type of modulation	SNR (in dB)	
		AM-DSB	AM-SSB
1	Normal modulation	182	176
2	Critical modulation	177	170
3	Over modulation	175	167

4.2 Power Consumption

As expected, the average power consumption/dissipation was drastically lower in the proposed method as compared to the method used in [6] for all the 9 possible cases as mentioned in [6]. Lower power dissipation in turn makes sure that the circuit elements have a longer life time. Mathematically, the power dissipated in AM-DSB [6] and AM-SSB is as follows:

From (4)

$$P_c = \frac{V_{c-rms}^2}{R}$$

From [6]

$$P_{AM-DSB} = P_c \left(1 + \frac{k_a^2}{8\xi^2} \right)$$

From (5)

$$P_{AM-SSB} = \frac{1}{32\xi^2 R}$$

$$R = 1\Omega$$

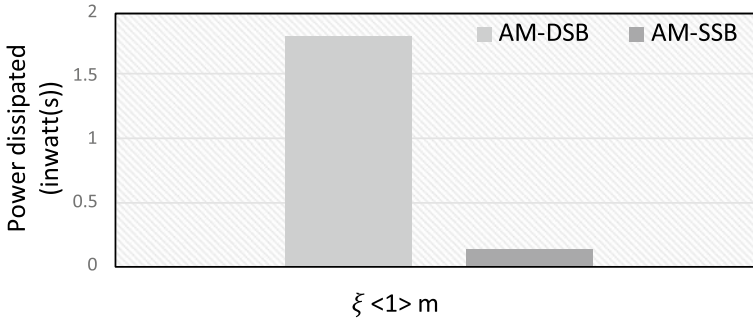


Fig. 5 Graph showing the power dissipated in both the methods in one of the practically possible cases of an under-damped control system

The power dissipation was calculated using these formulas for a unit circuit resistance and in none of the 9 cases did the proposed method dissipate more power than AM-DSB (Fig. 5).

4.3 Level of Independence from Modulation Parameters

The expressions for the final output signals for both the designs are [6]:

$$S_{AM}(t) = A_c \cos(\omega_c t) + \frac{A_c m}{2} \cos((\omega_c + \omega_n)t) + \frac{A_c m}{2} \cos((\omega_c - \omega_n)t)$$

$$S_{SSB}(t) = \frac{1}{4\xi} \cos((\omega_c - \omega_m)t) \tag{6}$$

It is apparent that the message signal frequency can be externally controlled ($\because \omega_m = \omega$) in both, using the damping ratio and the natural frequency of the control system but when it comes to deciding the amplitude of the final signal, the method proposed in [6] falls short, since from its expression we can see that its amplitude is directly proportional to either the carrier amplitude or the modulation index (depends on what the variable parameters of the modulation apparatus involved are), whereas the amplitude in case of the proposed method is completely independent of any modulation parameters whatsoever.

Hence, it can be said that the level of independence in the proposed method is higher as compared to AM-DSB, and it can thus be controlled externally with a comparatively greater ease.

5 Conclusion

We proposed a control system design that externally controls an SSB amplitude modulator by directly influencing its parameters and components like the message signal, the amplitude of the modulating signal, the voltage, power, and current. The extent to which the components of the modulator depend on its parameters is very low and the only part of the entire design that the modulator has a little control over is the carrier signal and indirectly the modulation index. Even though the latter does not have much significance in case of SSB amplitude modulation, controlling the carrier is the next important step that we will take and, hence in a way, finalize the design. We also intend to design a frequency modulator that is externally controlled by a second-order control system.

References

1. Liu Y, Du W, Xiao L, Wang H, Cao J (2015) A method for sizing energy storage system to increase wind penetration as limited by grid frequency deviations. *IEEE Trans Power Syst* 31(1):729–737
2. Bidadfar A, Nee HP, Zhang L, Harnefors L, Namayantavana S, Abedi M, Karrari M, Gharehpetian GB (2015) Power system stability analysis using feedback control system modeling including HVDC transmission links. *IEEE Trans Power Syst* 31(1):116–124
3. Wang J, Yan JD, Jiang L, Zou J (2015) Delay-dependent stability of single-loop controlled grid-connected inverters with LCL filters. *IEEE Trans Power Electron* 31(1):743–757
4. Podlubny I (1999) Fractional-order systems and PI/sup/spl lambda/D/sup/spl mu/-controllers. *IEEE Trans Autom Control* 44(1):208–214
5. Kennedy G, Davis B (1985) *Electronic communication systems*. Tata McGraw-Hill Publishing Co., Ltd., New Delhi
6. Kumar A, Arya N (2017) Design amplitude modulation using frequency analysis second order control system. In: 2017 International conference of electronics, communication and aerospace technology (ICECA), 20 Apr 2017, vol 2. IEEE, pp 148–151
7. Yao X, Liu Y, Lin G (1999) Evolutionary programming made faster. *IEEE Trans Evol Comput* 3(2):82–102
8. Walsh GC, Ye H, Bushnell LG (2002) Stability analysis of networked control systems. *IEEE Trans Control Syst Technol* 10(3):438–446
9. Oriolo G, De Luca A, Vendittelli M (2002) WMR control via dynamic feedback linearization: design, implementation, and experimental validation. *IEEE Trans Control Syst Technol* 10(6):835–852
10. Ogata K, Yang Y (2002) *Modern control engineering*. Prentice Hall, India
11. Agurto C, Murray V, Barriga E, Murillo S, Pattichis M, Davis H, Russell S, Abràmoff M, Soliz P (2010) Multiscale AM-FM methods for diabetic retinopathy lesion detection. *IEEE Trans Med Imaging* 29(2):502–512
12. Bain JR, Lengden M, Stewart G, Johnstone W (2015) Recovery of absolute absorption line shapes in tunable diode laser spectroscopy using external amplitude modulation with balanced detection. *IEEE Sens J* 16(3):675–680

Simultaneous Frequency and SSB Modulation for Ultrasonic Speakers



Manisha Bharti, Meghav Shukla, Aditya Joshi, and Tanvika Garg

1 Introduction

Most speakers are designed to emit sound as far and wide as they can. But ultrasonic speakers are designed to function more like a laser beam where sound is focused at relatively smaller area. The directivity is such that two people standing only a meter apart would notice different results, one would hear it and the other might not [1] (see Fig. 1). Those modulated waves become demodulated when they interact with air [2]. Ultrasonic speakers do a good job of demonstrating the propagation of sound in air. But all that directivity comes at a price, i.e., the sound quality. At low frequencies, the sound quality is genuinely bad. On top of that, demodulation of AM waves results in harmonic distortions. There has not been much research done on FM as a substitute, even then we know that FM demodulation produces even higher harmonic distortion than AM. But the sound pressure level that we got in FM is much better than in AM. So in this paper, we will try to overcome the shortcomings of the modulation techniques mentioned before by trying to combine them. We would also like to try the same combined technique with SSB instead of AM.

2 Relation to Prior Work

The current modulation method that we used for ultrasonic methods is AM-DSB [3]. The formula for the envelope of DSB modulated wave is:

M. Bharti · M. Shukla (✉) · A. Joshi · T. Garg
National Institute of Technology Delhi, New Delhi, Delhi 110040, India

M. Bharti
e-mail: manishabharti@nitdelhi.ac.in

T. Garg
e-mail: 192220010@nitdelhi.ac.in

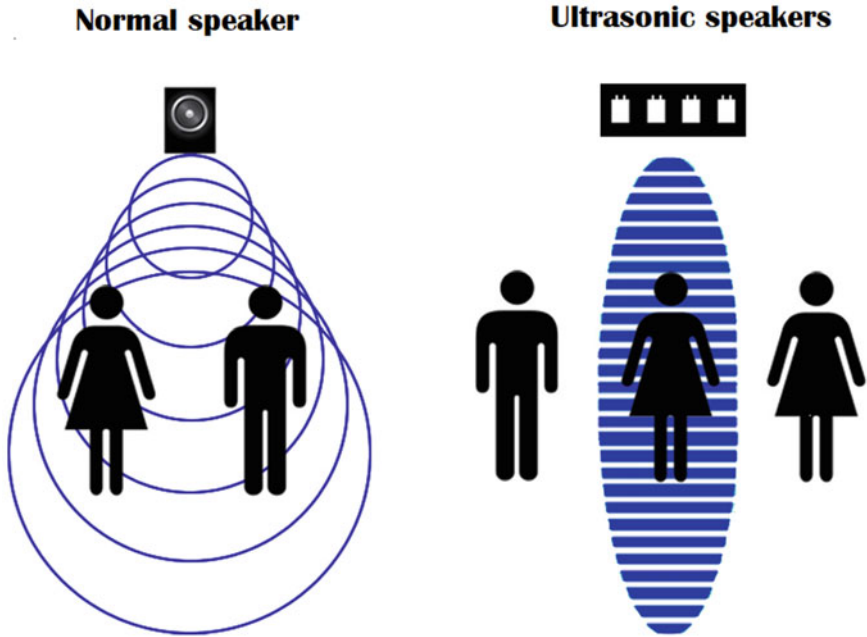


Fig. 1 Demonstration of the directivity of the ultrasonic loudspeaker

$$Env_{DSB}(t^r) = 1 + \mu x_m(t^r)$$

Here, $t^r = t - (z/s)$.

$t \rightarrow$ time, $z \rightarrow$ distance b/w ultrasonic speaker and the point of observation.

$s \rightarrow$ speed of sound, $\mu \rightarrow$ modulation index.

This method can provide better sound pressure level than normal AM modulation. But the harmonic distortion is even more evident.

So square root AM was used [4-7] the envelope for which can be given by the following formula:

$$Env_{SR-AM}(t^r) = \sqrt{1 + \mu x_m(t^r)}$$

To reduce the power consumption, even more SSB was proposed.

AM as the modulation method for ultrasonic speaker can be given by [8]:

$$\begin{aligned}
 AM_{DSB}(t) &= (C_0 + s(t))C(t) \\
 &= C_0 \left(1 + \int_{f_{low}}^{f_{high}} \mu_f^{AM} \cos(2\pi f t - \phi_f) df \right) C(t) \\
 C(t) &= C_0 \cos(2\pi f_0 t)
 \end{aligned}$$

$$s(t) = \int_{f_{low}}^{f_{high}} S_f \cos(2\pi f t - \phi_f) df$$

where

$AM_{DSB}(t) \rightarrow$ AM-DSB modulated wave.

$C(t) \rightarrow$ carrier wave.

$s(t) \rightarrow$ audible sound wave.

$f_{low} \rightarrow$ lower frequency limit of the audible sound wave.

$f_{high} \rightarrow$ higher frequency limit of the audible sound wave.

$S_f \rightarrow$ amplitude of the ‘frequency component with frequency f ’ of the audible sound wave.

$\phi_f \rightarrow$ phase of the ‘frequency component with frequency f ’ of the audible sound wave.

$\mu_f^{AM} \rightarrow$ amplitude modulation index of the ‘frequency component with frequency f ’ of the audible sound wave.

Using FM to modulate the carrier, we get the expression as [8]:

$$\begin{aligned} x_{FM}(t) &= C_0 \sin \left(\int_0^t \left(2\pi f_0 + 2\pi \Delta f \int_{f_{low}}^{f_{high}} \cos(2\pi f t - \phi_f) df \right) dt \right) \\ &= C_0 \sin \left(2\pi f_0 t + \int_{f_{low}}^{f_{high}} \mu_f^{FM} \sin(2\pi f t - \phi_f) df \right) \end{aligned}$$

where $\Delta f \rightarrow$ max. frequency deviation.

$\mu_f^{FM} \rightarrow$ frequency modulation index of the ‘frequency component with frequency f ’ of the audible sound wave.

3 Suggested Modulation Method Combining AM DSB and FM

Using the findings of various researches who tried to combine AM DSB and FM [8], we have this envelop function (Figs. 2 and 3)

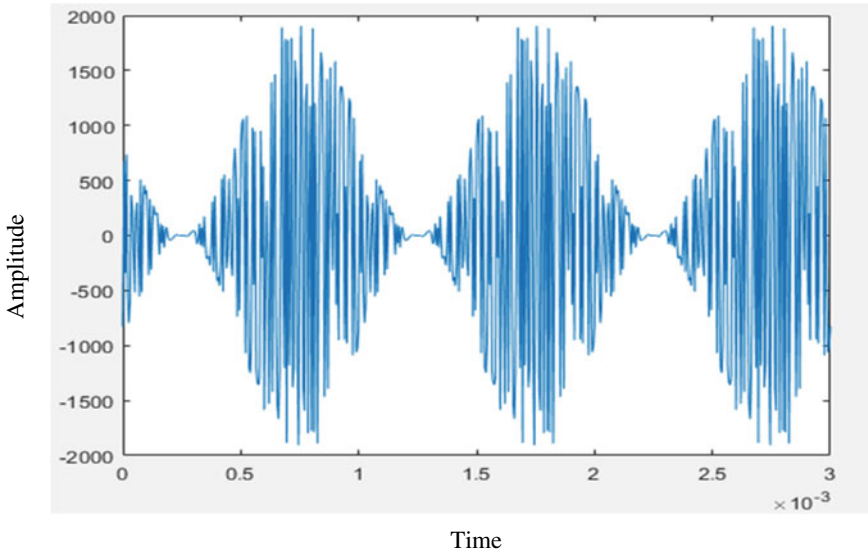


Fig. 2 Envelope function of the AM DSB + FM

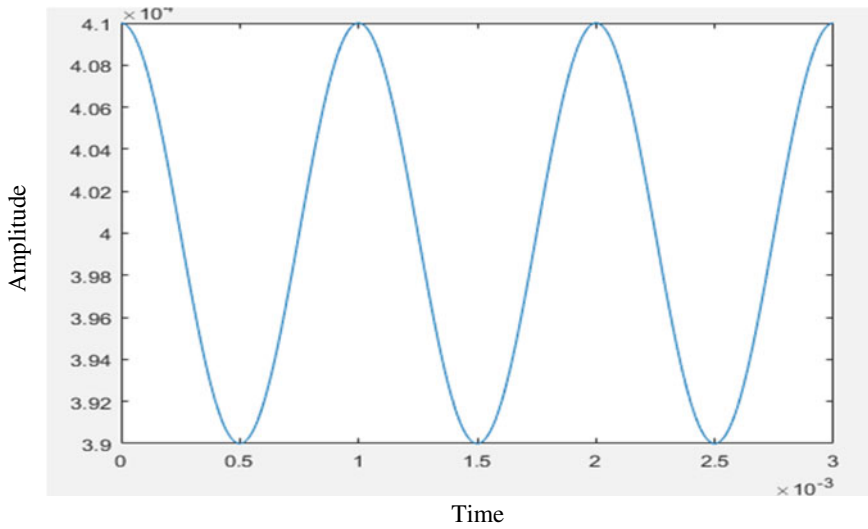


Fig. 3 Time versus amplitude of frequency of the signal

$$d = 1000 \cos(2\pi ft)$$

$$x_p = \mu_c^{\text{FM}} \cdot (1 - \sin(2\pi ft)) \cdot \sin(2\pi f_c t - d)$$

4 Suggested Modulation Method Combining AM SSB and FM

Here is the suggested method to combine AM SSB and FM.

We have this envelop function:

$$f_{SSB} = ms \cos((2\pi f_c t) - \mu^{FM} \cos(2\pi f_m t))$$

$$f_{FM} = \text{im}(\widehat{ms} \cdot (\sin((2\pi f_c t) - ms f_c \cos(2\pi f_m t))))$$

where

f_{SSB} is the SSB modulated part of the suggested method.

f_{FM} is the FM modulated part of the suggested method.

f_m is the message signal frequency.

f_c is the carrier signal frequency.

ms is the message signal.

\widehat{ms} is the Hilbert transform of the message signal.

Figure 4 shows the envelope function that we get after combining the aforementioned methods. This method was suggested as a power conserving version of the last one (i.e., DSB + FM).

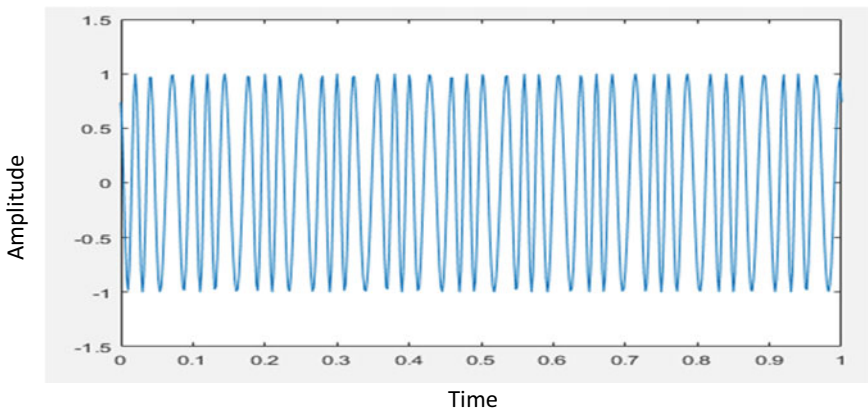


Fig. 4 Envelope function for AM SSB + FM

5 Evaluation

5.1 SNR

We compared various modulation methods namely AM DSB, FM, AM SSB, AM DSB + FM, and AM SSB + FM. We used the same message and carrier signals to keep the comparison fair. We are using SNR as the measurement parameter to compare the desired levels of signal to levels of the noise. SNR is the ratio of signal power to the noise power. We are using this as a measure of quality because if the desired signal has essential data with low tolerance for noise, then even a little disruption could cause the signal to lose data or at the very least make the task of demodulation a little more challenging. That is why it is important to have a high signal-to-noise ratio. A better SNR would mean better quality of the signal. The noise used is white noise because that is the most common type of noise.

$$\text{SNR} = 10s \log_{10} \frac{P_S}{P_N}$$

where P_S is the power of message signal and P_N is the power of noise.

$$P_N = K \times T \times B$$

where

K is the Boltzmann's constant.

T is temperature in Kelvin.

B is the bandwidth in Hz.

Using the above-mentioned formula we get the following data.

5.2 Power Consumption

As we can see in Fig. 5 that the AM DSB + FM has the best SNR, followed by AM DSB. The suggested method of AM SSB + FM has comparatively low SNR but when compared to normal SSB we can see a clear increase in SNR value, and this trend of increase in SNR when coupled with FM is very noticeable as the same thing happened in DSB.

So we can say that on its own SNR does not tell the whole story, so we are going to compare their power consumption because the method that gives the best quality at the least power is the most practical solution.

So here is the power comparison of the aforementioned methods.

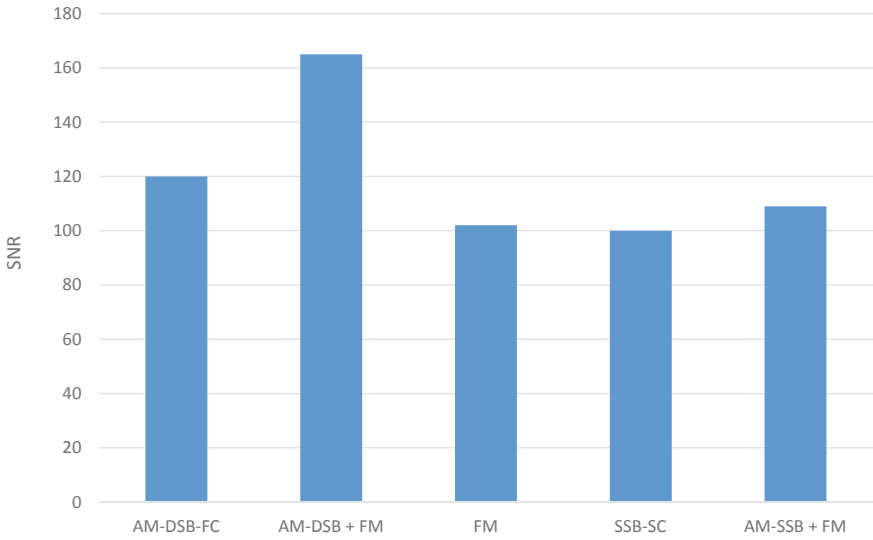


Fig. 5 SNR values of various methods

Figure 6 shows even though the SNR of AM DSB + FM was the best, its power consumption is also the highest. On the other hand, our AM SSB + FM has the least power consumption. Other thing to notice is the trend of having the same power as their non-FM coupled counterparts, AM DSB + FM has the same power consumption as AM DSB and AM SSB + FM has the same power consumption as AM SSB. So

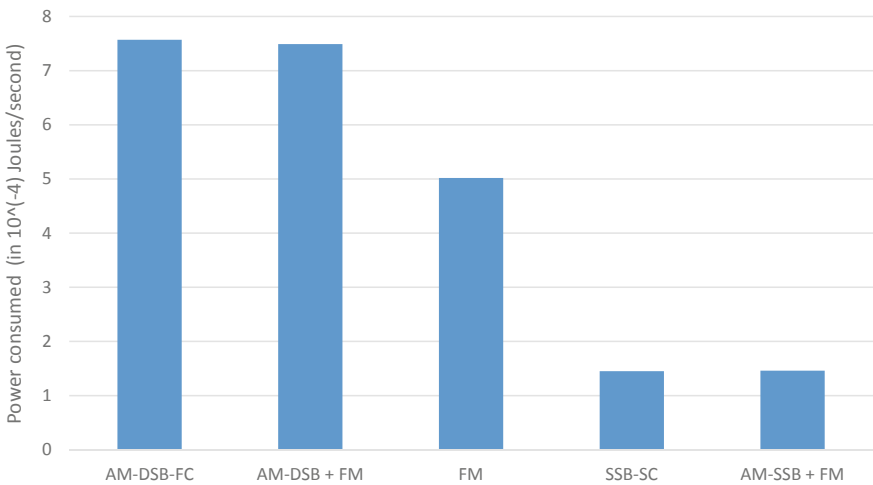


Fig. 6 Power consumption of various methods

we can assume that the method of simultaneous AM and FM gives better SNR for almost no increase in power consumption.

6 Conclusion

The main objective of this experiment was to find a method that can give high-quality sound for an ultrasonic loudspeaker and we wanted to reduce the power consumed as well. We devised two methods that work by simultaneous AM and FM of a signal. The two methods were AM DSB + FM and AM SSB + FM. We compared them with normal modulation methods such as FM, SSB, and DSB. In the SNR category, the method that was most effective was AM DSB + FM. But other than that we noticed a trend that the SNR values of normal AM-DSB and AM-SSB increased when they were coupled with FM. So even though AM-SSB + FM had comparatively low value of SNR, it was still an improvement over the normal AM-SSB and the fact that AM-SSB + FM had the lowest power consumption compels us to say it is a viable power saving option.

References

1. Shi C, Gan WS (2010) Development of parametric loudspeaker: a novel directional sound generation technology. *IEEE Potentials* 29:20–24
2. Chen M, Xu L, Cao Y, Xu L, Wang X, Li X, Ma J (2008) Research on an improved amplitude modulation method of audio directional loudspeaker. In: *ICALIP*. IEEE, pp 5–9
3. Yoneyama M, Fujimoto J, Kawamo Y, Sasabe S (1983) The audio spotlight: an application of non linear interaction of sound waves to a new type of loudspeaker design. *J Acoust Soc Am* 73:1532–1536
4. Kamakura T, Yoneyama M, Ikegaya K (1984) Development of a parametric loudspeaker for practical use. In: *10th International symposium on nonlinear acoustics*, pp 147–150
5. Kamakura T, Yoneyama M, Ikegaya K (1985) A study for the realization of a parametric loudspeaker. *J Acoust Soc Jpn* 1–18
6. Pompei FJ (1999) The use of airborne ultrasonics for generating audible sound beam. *J Audio Eng Soc* 47:726–731
7. Kite TD, Post JT, Hamilton MF (1998) Parametric array in air: 726 distortion reduction by preprocessing. In: *Proceedings of 16th ICA and 135th meeting of the ASA*, vol 2, pp 1091–1092
8. Nakayama M, Nishiura T (2017) Synchronized amplitude-and-frequency modulation for a parametric loudspeaker. In: *APSIPA annual summit and conference 2017*, 12–15 Dec 2017, Malaysia, pp 130–135

Opportunities and Challenges in Solar Photovoltaic-Based Electric Vehicles Charging Stations: A Step Toward Smart Cities Development



Mohammad Bilal and M. Rizwan

1 Introduction

A serious threat is encountered by transport sector throughout the world due to increasing concentration of particulate matter (PM) in the atmosphere. The polluting agents like carbon monoxide, nitrogen dioxide, sulfur dioxide, etc., have deteriorating effects on human health. Keeping in view, the government of countries all over the world are trying to provide a sustainable and eco-friendly nature of environment. The combustion engines based on non-renewable sources of energy produce greenhouse gases in large quantities which have negative impact on environment. Also, the optimal location of charging station (CS) is of utmost importance for charging electric vehicles (EVs) [1]. EVs do not produce any harmful end product. Thus, there is an increasing demand of EVs in transportation industry. However, the power required for recharging the batteries of EVs directly from the power grid will create an additional load, especially during peak hours, i.e., during day time [2]. For the sake of minimizing the overload on grid network due to charging of EVs, many alternative solutions have been developed. One of the solutions is to employ solar PV for charging EVs.

Due to recent developments in the area of PV modules, they are becoming cost-effective and gained popularity in EV charging application [3]. Application of PV modules in EV charging has many advantageous such as low maintenance cost and no fuel wastage. [4]. The PV application for charging EV can be upgraded by new developments in conversion technologies, battery management system (BMS), and their installation practices [5]. During day time, EV can be charged directly using solar power, and this method of charging is popularly known as “charging while parking” [6]. EVs can be charged conveniently by parking them below the PV-based parking lot as shown in Fig. 1. This approach of PV-based charging of EVs proves to be eco-friendly and cost-effective in nature, which is generally employed

M. Bilal (✉) · M. Rizwan

Department of Electrical Engineering, Delhi Technological University, Delhi, India



Fig. 1 PV-based parking lot for EV charging [6]

at workplaces, such as near big malls and offices, and parking firms [7]. This method of overhead PV-based charging system protects EVs from direct sun and rain, which is common in hot and humid climatic conditions.

Over the past few years, many methods have been proposed related to PV-EV charging. The most feasible method is the PV-grid combination to charge EVs. In PV-EV charging, initially, solar PV is utilized for charging EVs and shifts to grid system when power from solar PV is unavailable or insufficient. Whereas in standalone type, charging process is carried out using solar PV only [8]. This approach of charging EV is predominant in areas where power grid is unavailable. There are certain modifications for standalone approach, such as the inclusion of fuel cell and battery bank as power source.

During last few years, many review and research papers have been published on recent trends and developments in the area of solar PV-based EV charging. In this paper, techno-economic feasibilities of charging EV using the combination of PV and grid as well as PV-standalone are discussed and compared with grid only system.

This paper presented the feasibility analysis and some of the important aspects of different modes of operation of PV-based EVs charging. Several PV-based approaches for charging EV such as PV-grid charging and PV-standalone are described in this paper. Furthermore, the inclusion of energy storage unit (ESU) for storing the energy obtained from solar PV and grid, especially when there are no EVs required for charging is mentioned which is rarely available in the literature.

2 PV-EV Charging Approaches

Electric vehicle (EV) takes a large amount of current from utility system during charging, which imposes an extra load on the system [9]. Moreover, if charging of electric vehicle (EV) is carried out during peak hours, i.e., day time, the EV owner has to pay a high tariff.

Renewable energy system (RES) should be used for EV charging for reducing the overload on grid and to enhance its stability [10]. At present, the most common charging approaches which involve PV are PV-grid charging and PV-standalone. In former case, it is possible to charge electric vehicle (EV) even during inadequate irradiance level by taking power utility grid [11].

It is also more advantageous because the power obtained from solar PV can be supplied to the grid when EV is not available for charging. While in latter one, i.e., PV-standalone is well suited in those areas where the availability of utility grid either very low or it is quite expensive [12]. Its setup is simpler due to fewer conversion stages are required.

2.1 PV-Grid Charging

A specific configuration of PV-grid charging mechanism is shown in Fig. 2. It comprises three major sections (1) DC-DC converter with MPPT capability, (2) bi-directional inverter, and (3) bi-directional DC charger. For the stabilization of the voltage of DC bus, the energy storage unit (ESU) has also been recommended. It also provides compensation for the fluctuating behavior of RES [13]. Regardless of these advantages, the initial cost, operating cost, and maintenance cost of energy storage unit (ESU) are high. However, the reduction in initial investment can be made using lead-acid battery. Furthermore, for safety issues, BMS is introduced which also maintains the battery life of EV and ESU. All main components are integrated conveniently at the DC common bus [14]. The voltage of DC bus is variable in nature, but typically its value ranges between 200 and 400 V. The DC bus acts as a medium for signaling, i.e., transfer the signal within the system [15]. A central controller is introduced which decides the flow of power and activates the converter. It operates on the basis of some decision-making algorithm. It is mainly designed based on some objectives, i.e., charging cost minimization, maximizing profit, etc.

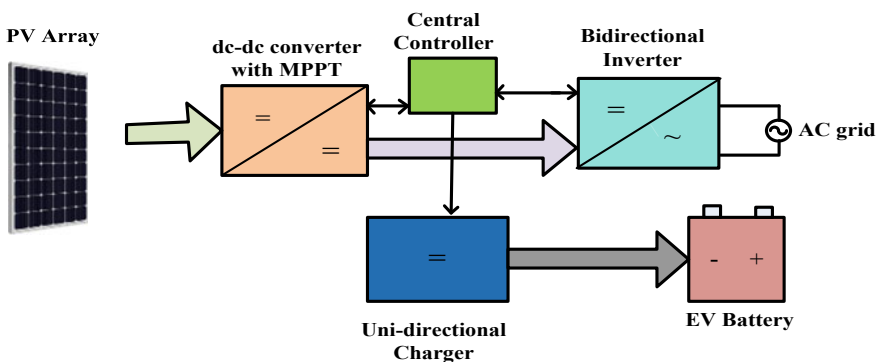


Fig. 2 Typical block diagram of PV-grid for EV charging mechanism [14, 15]

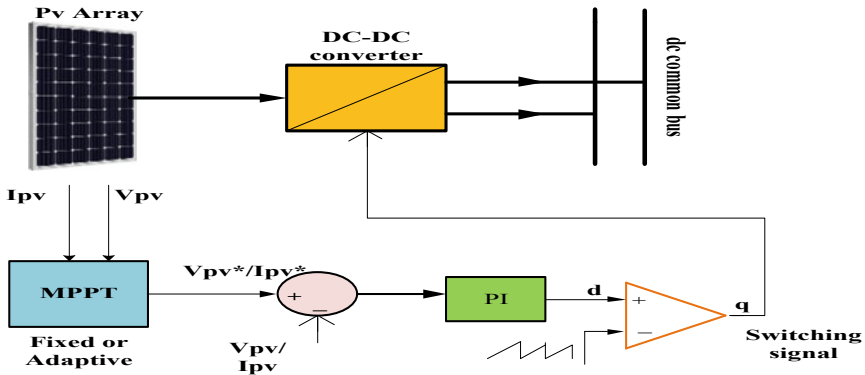


Fig. 3 MPPT-based DC-DC converter

2.1.1 DC-DC Converter with Capability of MPPT

The primary goal of MPPT-based DC-DC converter is to take out large amount of power from the PV panel. Usually, this converter is operated either in boost or buck-boost mode. In Fig. 3, the working of MPPT has been described. At a specific sampling cycle, sensors are employed for sensing the voltage and current obtained from the solar panel [16]. Magnitude of both voltage and current is injected into MPPT which determines MPP. Once determined, it generates the reference value of current, i.e., I_{pv}^* .

I_{pv}^* and voltage V_{pv}^* . These values should be comparable to the DC-DC converter. After this, measured value of power is compared with MPP value. If there is mismatch between the two values, duty cycle is adjusted to decrease the difference. PI controller or hysteresis controller are used for adjustment process. When the two power values, i.e., measured power and reference power becomes equal, the array will deliver the maximum power.

2.1.2 DC-AC Bi-Directional Inverter

The bi-directional DC-AC inverter operates in the entire four portions of current/voltage regime [17]. Therefore, it either work as an inverter, i.e., DC bus power is injected into the grid or as a rectifier, i.e., power can be taken out from the grid for the charging of DC bus. It acts as boost converter in rectification mode and as buck converter in inversion mode. Moreover, it must operate at controllable power factor during inversion process.

2.1.3 Bi-directional DC-DC Charger

The DC charger is employed for controlling the current and voltage to a level such that it matches with EV which is being charged. It needs to be directional, i.e., power flows in both directions for full power control. In discharging, it acts as a boost converter, while in charging, it acts as a buck converter. It can be assumed as current controlled source which supplies current to the battery, estimated by the variation between the battery voltage and set reference value.

2.1.4 Charging Operation

Initially, when EV connected with the grid battery has a state of charge (SOC) lesser than 100%. In PV-grid network without incorporating ESU, vehicle to grid (V2G), and vehicle to vehicle (V2V) operations, the charging process sequence is as stated [11].

Case 1: If power supplied by solar PV is higher than what EV requires, than in this case additional power is generally provided to the grid and grid energy does not play any role in EV charging.

Case 2: In this case, charging of EV takes place only due to the grid power because of unavailability of PV power either due to bad climatic condition or during night hours.

Case 3: In this case, EV is initially charged by PV power. But due to low irradiance, the remaining charging is carried out by grid power.

Case 4: If there is no requirement of charging EV, power delivered by solar PV is injected into the utility grid directly; providing financial benefit to the owner.

Mode 1: EV connected to PV only

If power delivered by solar PV is enough for charging EV, then EV charging is done completely by solar PV. Schematics of charger and converter used for charging process are shown in Fig. 4a [18]. System is connected partially to the grid in this particular mode and alone PV perform the charging activity. The charger is employed for regulating the DC voltage so that it matches with the EV.

Mode 2: EV connected to grid only

On the other hand, if PV is not capable of providing power to EV, the EV charging takes place using grid power only. Bi-directional inverter is used to convert AC grid power to DC and the obtained DC voltage is conditioned using charger as shown in Fig. 4b [18].

Mode 3: PV and grid-based charging of EV

In certain special cases, where PV generated power is not enough to charge vehicle than grid connected PV could be utilized. Schematic for grid connected PV is as shown in Fig. 4c [18]. The quantity of power output delivered by solar PV decides the energy to be taken from grid. The remaining energy is provided by the grid.

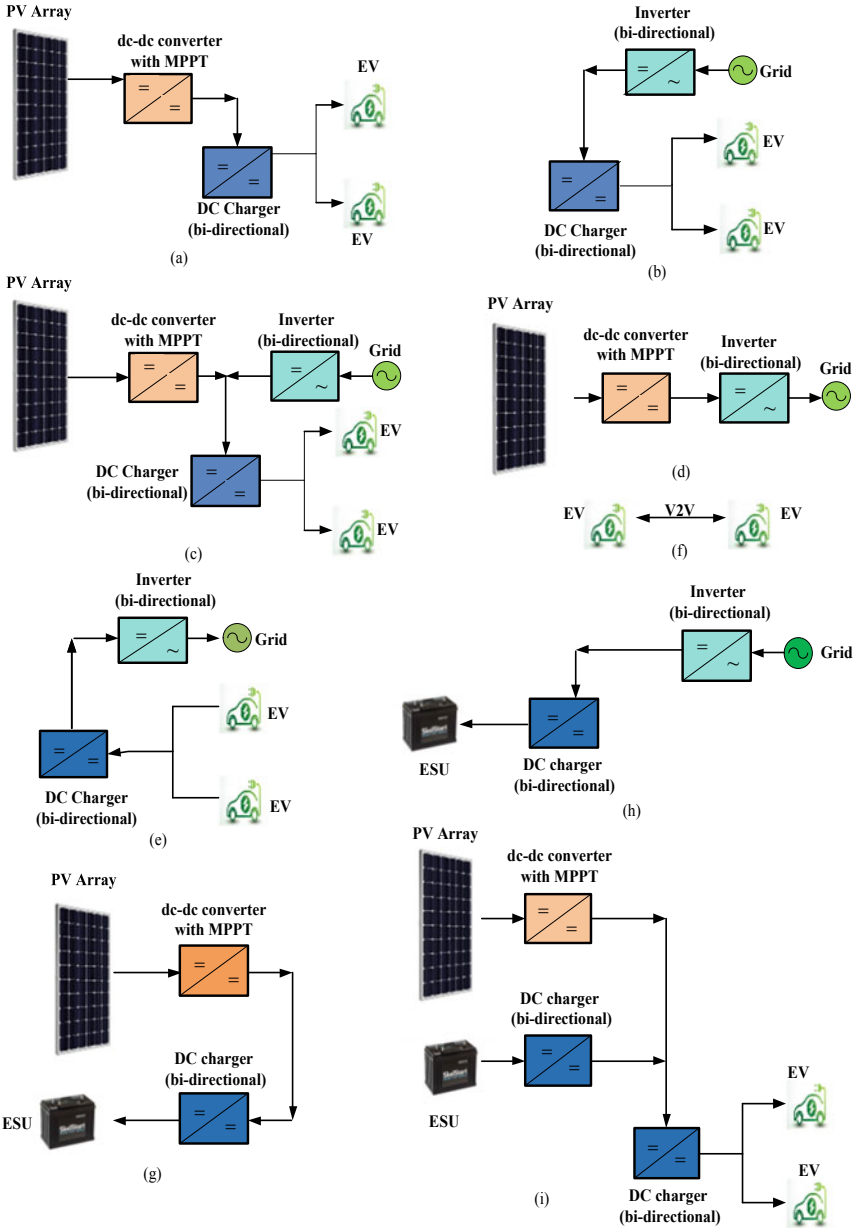


Fig. 4 Possible modes of operation. **a** Mode 1: charging of EV by PV only; **b** Mode 2: charging from grid only; **c** Mode 3: combination of energy from PV as well as grid; **d** Mode 4: EV is not available and solar power is fed to the grid; **e** Mode 5: V2G mode; **f** Mode 6: V2V mode; **g** Mode 7: PV power is fed to the ESU when EV is not available; **h** Mode 8: EV and PV not available and grid is charging ESU in case of low SOC; **i** Mode 9: PV is not available and ESU is supplying energy to EV

Because of irregular irradiance condition, the power taken from the solar PV must be continuously monitored and accordingly make some adjustment for taking grid power for maintaining the EV charging profile.

Mode 4: Grid inversion mode

In this mode, there is no EV need to be recharged and solar PV is continuously producing power, all the power will be supplied to the grid by means of DC-DC converter and bi-directional inverter as shown in Fig. 4d [18].

Mode 5: Vehicle to grid (V2G) mode

In this mode of operation [19], power flow takes place from vehicle to grid. The tariff is high during some specific hours of a day. Thus, additional energy stored in EV parked in a lot is fed to the grid. Such type of charging is performed via bi-directional inverter and bi-directional DC-DC charger as illustrated in Fig. 4e.

Mode 6: Vehicle to Vehicle (V2V) mode

This mode deals with the flow of power/energy between the two vehicles as illustrated in Fig. 4f [19]. In some hours of the day, energy is transferred from the EV which has surplus energy to the vehicle which is assumed to depart from the parking lot earlier or does not have enough SOC. This process also affects the life of battery. That is why it is practically uncommon in practice.

Mode 7: Power transfer from PV to ESU

In some cases, when no EV need to be charged either due to unavailability of EV or they are fully charged then ESU are employed to store the power taken from solar PV to meet the future requirement. This charging mode minimizes the dependence on grid because energy stored in ESU will be utilized.

Mode 8: Power transfer from grid to ESU

When grid is lightly loaded and electricity prices are low, i.e., night time and there is a need to charge ESU, then energy can be transferred from grid to ESU in order to maintain its charging profile as shown in Fig. 4h [18]. This mode has the advantage of low grid tariff to be utilized for CS benefit.

Mode 9: Power transfer from PV and ESU to EV

PV power and ESU are combined to charge EV as shown in Fig. 4i [18]. This mode becomes active when PV power is insufficient to charge EV and ESU has enough SOC. This operation mode reduces the burden on grid for EV charging.

2.2 PV-Standalone Charging

In PV-standalone, charging of EV takes place completely by solar PV without involving grid as illustrated in Fig. 5 [20]. This approach of EV charging is more

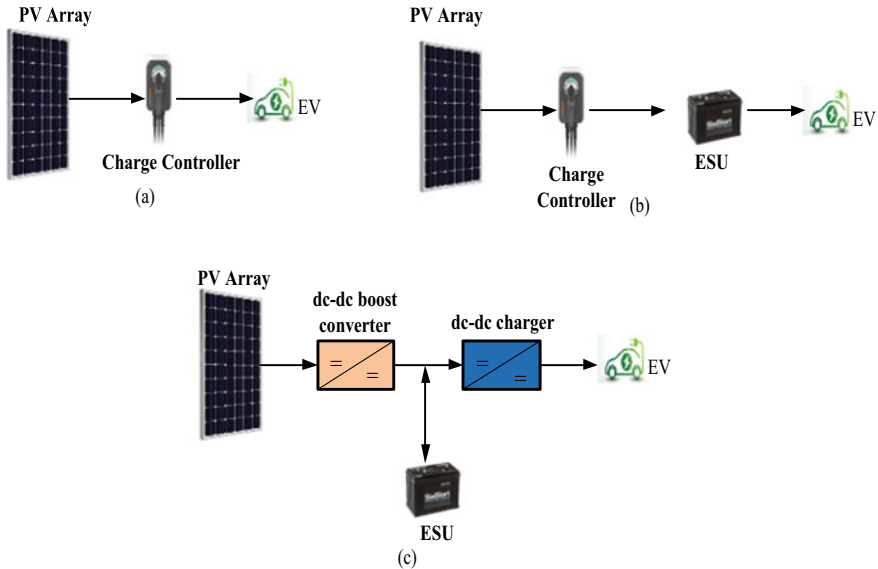


Fig. 5 PV-standalone charging mechanism: **a** without a battery, **b** with battery, **c** with battery

reliable as the less power conversion steps are required. The PV modules should be sized such that the charging demand of specified number of EVs must be met. Due to the fluctuations in irradiance level, this method is unpopular in comparison with former charging approach.

Two charging approaches are existed on PV-standalone system (a) EV are directly connected to PV as illustrated in Fig. 5a, (b) EV and PV are connected via intermediate ESU, i.e., battery bank as shown in Fig. 5b, c [21]. In addition to this, there are various methods which involve hybrid solution. However, the limitation of direct charging of EV is inadequate and fluctuating nature of solar power. While ESU stores extra energy and to be used during the non-availability of PV power [22]. Also, ESU flatten the sudden changes in output power form solar PV [22]. The EV charger controller has a significant effect on this process. DC-DC converter has the capability of tracking MPP. It is employed for regulating the PV voltage in a way such that the charging current must be an optimized value.

3 Future Research Directions

The higher the penetration of EVs on the electric grid, the more complicated would be the grid integration of solar PV alongside with charger. It is expected that a proper and robust battery management system will be needed for managing the charging system for charging considerable number of EVs at the same instant of time. The main

problem arises when several electric vehicles are plugged into the grid simultaneously which causes grid interruptions.

These are some research topics that need to be explored in the area of solar PV-based charging stations.

- One more research area includes the improvement in control strategy for charging, i.e., the optimized EV charging on the basis of availability of power obtained from solar PV.
- For ensuring life span of EV batteries, the charging patterns using BMS must be maintained.
- The incorporation of PV power prediction model and grid energy on the basis of tariff structures is one of the worth research area needs to be examined.
- Apart from solar PV, there are various options are available for the integration of renewable sources. There would be an interesting opportunity to integrate such as fuel cell, wind turbines, supercapacitors with PV-EV charging in a smart grid network.
- Through the enhancement of the BMS the life span of the battery can be increased.
- The V2V and V2G are the future research areas even if feasibilities are uncertain.

4 Conclusion

This paper highlights about the technology, performance, and current scenario of PV-EV charging systems. The paper presents several PV-based approaches for charging EV such as PV-grid charging and PV-standalone. PV-standalone type might not be financially viable due to some technical limitations and limited battery capacity. Furthermore, the variability of solar energy due to intermittent nature and energy demand could not be met. The trend of the cost for solar PV is declining which would be the catalyst for the growth of PV-based electric vehicles (EV). Moreover, the proposed approach is eco-friendly and cost-effective as well in the long term. In addition, the proposed system would provide an effective, reliable, and sustainable grid management which is an important aspect for making any technology sustainable in nature. Finally, the paper offers a number of recommendations and suggests future studies need to be explored in this domain.

References

1. Bilal M, Rizwan M (2020) Electric vehicles in a smart grid: a comprehensive survey on optimal location of charging station. *IET Smart Grid* 3(3):267–279
2. Kelman C (2010) Supporting increasing renewable energy penetration in Australia the potential contribution of electric vehicles. In: *Proceedings of 20th Australasian universities power engineering conference (AUPEC)*, pp 1–6
3. Barker PP, Bing JM (2005) Advances in solar photovoltaic technology: an applications perspective. *Proc Power Eng Soc Gen Meet* 2:1955–1960

4. Kadar P, Varga A (2013) Photovoltaic EV charge station. In: Proceedings of IEEE 11th international symposium on applied machine intelligence and informatics (SAMII), pp 57–60
5. Branker K, Pathak MJM, Pearce JM (2011) A review of solar photovoltaic levelized cost of electricity. *Renew Sustain Energy Rev* 15:4470–4482
6. VanRoy J, Leemput N, Geth F, Salenbien R, Buscher J, Driesen J (2013) Apartment building electricity system impact of operational electric vehicle charging strategies. *IEEE Trans Sustain Energy* 5:264–272
7. Gamboa G, Hamilton C, Kerley R, Elmes S, Arias A, Shen J (2011) Control strategy of a multi-port, grid connected, direct-DC PV charging station for plug-in electric vehicles. In: Proceedings of IEEE energy conversion congress and exposition (ECCE), pp 1173–1177
8. Chiang SJ, Hsin-Jang S, Ming-Chieh C (2009) Modeling and Control of PV charger system with SEPIC converter. *IEEE Trans Ind Electron* 56:4344–4353
9. Galus MD, Andersson G (2008) Demand management of grid connected plug-in hybrid electric vehicles (PHEV). In: Proceedings of IEEE energy 2030 conference, Energy, pp 1–8
10. Hawaii (2012) Natural energy institute school of ocean and earth science and technology university of Hawaii, Organization UoHiER. Statewide and electricity-sector models for economic assessments of Hawaii clean energy policies. Hawaii distributed energy resource technologies for energy security, Award No DE-FC26-06NT42847
11. Preetham G, Shireen W (2012) Photovoltaic charging station for plug-in hybrid electric vehicles in a smart grid environment. In: Proceedings of IEEE PES innovative smart grid technologies (ISGT), pp 1–8
12. Tong SJ, Same A, Kootstra MA, Park JW (2013) Off-grid photovoltaic vehicle charge using second life lithium batteries: an experimental and numerical investigation. *Appl Energy* 104:740–750
13. Ibrahim H, Ilinca A, Perron J (2008) Energy storage systems—characteristics and comparisons. *Renew Sustain Energy Rev* 12(5):1221–1250
14. Traube J, Fenglong L, Maksimovic D (2012) Electric vehicle DC charger integrated within a photovoltaic power system. In: Twenty-seventh annual applied power electronics conference and exposition (APEC). IEEE, pp 352–358. <https://doi.org/10.1109/apec.2012.6165843>
15. Traube J (2013) Mitigation of solar irradiance intermittency in photovoltaic power systems with integrated electric-vehicle charging functionality. *IEEE Trans Power Electron* 28(6):3058–3067
16. Salam Z, Ahmed J, Merugu BS (2013) The application of soft computing methods for MPPT of PV system: a technological and status review. *Appl Energy* 107:135–148
17. Wu TF, Hsieh H-C (2013) Digital control for a three-phase transformer less bi-directional photovoltaic inverter with wide inductance variation. In: Proceedings of future energy electronics conference (IFEEC), pp 658–662
18. Goli P, Shireen W (2014) PV powered smart charging station for PHEVs. *Renew Energy* 66:280–287
19. Ma T, Mohammed O (2014) Optimal charging of plug-in electric vehicles for a car park infrastructure. *IEEE Trans Ind Appl* 50(4):2323–2330
20. Abu-jasser AA (2010) Stand-alone photovoltaic system, case study: a residence in Gaza. *J Appl Sci Environ Sanit* 5(1):81–91
21. Sharaf AM, Sahin ME (2011) A novel photovoltaic PV powered battery charging scheme for electric vehicles. In: 2011 International conference on energy, automation, and signal (ICEAS)
22. Mossoba J, Kromer M, Faill P, Katz S, Borowy B, Nichols S (2012) Analysis of solar irradiance intermittency mitigation using constant DC voltage PV and EV battery storage. In: Proceedings of IEEE transportation electrification conference and expo (ITEC), pp 1–6

Role of IoT in Industry 4.0



Ankita Sharma , Vibha Burman , and Shipra Aggarwal

1 Introduction

The smart processing arrangement has immense potential to create highly productive, as well as established companies among the various commands of scale superior potential in manufacturing, financial system and civilization. For proposing cyberspaces, as of their intense, complicated, it requires en route to employ distant additional all-purpose modeling approach than individuals broadly used so to facilitate utilize influential, smart processing arrangements scheduled set of connections workstation support taking place on cellular spatial arrangements [1].

Real-time monitoring is supervising the outside gadgetry and transmits real-time images and examines the values for forecasting and diagnosis. The remote monitoring system is an efficacious medium for inspecting, conveying, governing and taking responses of the remote last judgment. It is a point to point utilization of computer software, advanced communication, electronics, instrumentation and many more disciplines. Smart plants in Industry 4.0 that localized management, production and manufacturing are done across the wireless networking. Under smart factories, the modules like RFIDs are used as an intelligent barcode to accumulate all the data and gather synchronized data with complete factory [2].

Technology plays a versatile influence on an accustomed industry. With the integration of Internet with various devices and gadgets, the solution becomes very simplified to our day-to-day problems. IoT technology provides new innovative ideas and growth to enhance the living standards of life. With the involvement of IoTs in the work environment and coming wireless technologies provides help in monitoring and controlling the gadgets remotely [3].

Industrial Internet of things (IIoT) specifies the IoT crosswise various manufacturing companies, namely logistic services, shipping, power utilization, chemical,

A. Sharma (✉) · V. Burman · S. Aggarwal
Department of Mechanical and Automation Engineering, Indira Gandhi Delhi Technical University for Women, New Delhi, India

navigation and further industrial regions. It is generally utilized in the Industry 4.0 area. Industry 4.0 focuses on the latest industrial revolution with focusing on mechanization, modernization, information, cyberphysical systems, procedures and human [4].

The changeover in the direction of current fresh certainty of the digital engineering is on the top move back and forth every part of the globe [5]. The execution of Industry 4.0 using IoT is on the edge to turn out to be the subsequently giant craze within the IT sector. Nevertheless, the exercises of IoT technology necessitate a cooperative attempt [6]. The profit and amenity offered through the IoT are innumerable. The employment of intelligent sensors within an isolated and tricky environment wherever aforesaid apparatuses are cooperating further effortlessly [7]. The domains of accomplishment of IoT support lying on existing tools in progress all over the globe are intelligent metropolitan, manufacturing, shipping, agriculture, health care, intelligent energy, intelligent home, wearable gadgets and appliances [8].

This survey provides the following objectives, specifically,

- Anatomy of diverse research sectors of non-identical scientific communities where research still has to overlook.
- Explore the entitled technical knowledge and exhibits notable gain of this criterion in usual day-to-day life.
- Administers the research workers with the representation of the varied perception of IoTs criterion defined varies scientific communities.
- Exchange of data signals and connecting machines and their product.
- Exchange of data signals interconnecting machines entangled in the operations of productions.
- Exchange of data signals integrated with machines and the outside world for interacting with the production system.

2 Literature Review

The process of industrialization started toward the end of the eighteenth century. Transformation about Industry 4.0 as follows [9] is shown below in Fig. 1.

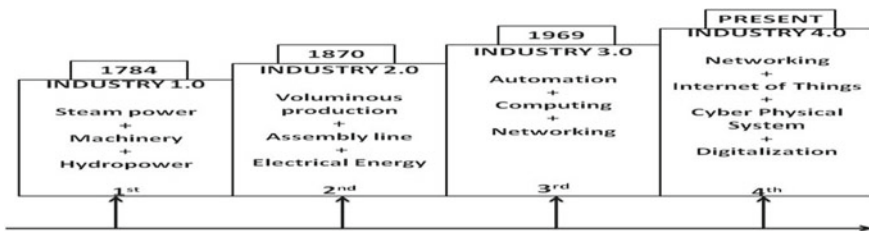


Fig. 1 Levels of industrial revolutions

- Industry 1.0. The First Industrial Revolution is converted of hydropower and steam power to mechanization. The usage of liquid and vapor power engine is required for automation of manufacturing industry.
- Industry 2.0. The Second Industrial Revolution considers automated technicalities in production that absorbs electric energy (i.e., mass production). Mass manufacture through electrically powered.
- Industry 3.0. The Third Industrial Revolution simulates the involvement of intelligent systems, namely, industrial robotics [1]. The electronic signal changes acquired from the Digital Acquisition System connect Electronics and IT sector for additionally mechanizing the manufacturing process.
- Industry 4.0. The arrangement of industry, automation, digitization and IoT is named as a 4th revolution in the industry. Industry 4.0 choose the accomplishment of interconnect smart as well as controlled structures of procedures in addition to arrangements. Industry 4.0 integrates a number of technologies; namely, machine learning, big data, cloud computing and IoT. It also includes industrial wireless networks, augmented reality and cybersecurity.

For smart plants under Industry 4.0, new IoT-based technologies and market demands are switching manufacturing industries to smart industries. The basic concept of an IoT arrangement is an embedded system where physical items are merged with the electronic gadgets and at the end they are interfaced with the Internet [10]. The IoT framework grants network between the various systems (namely, individual beings, locomotive robots, wireless sensors, etc.), with distinct but practical communication protocol and generate a progressive multimodal network. The framework consists of systems termed as “things” and has the expertise to identify and explore in system, build, equip to pass on data to IoT. The “things” are categorized, namely, people, machinery and information.

The IoT has diverse applications irrespective of their field of the work. The main applications of the IoT are in the automation industry, software development and logistic control. These fields are being reviewed and the main contributions in their field of work are listed in the paragraphs to appear. The hardware components acquired in the various fields are also discussed.

2.1 Autonomous Field Applications

In autonomous applications, the majority of fields lies in this section is manufactured, autonomous robot, automotive factory, smart factory, re-manufacturing and process-related re-manufacturing. These applications are tabulated below in Table 1.

In manufacturing applications, there is a vast application of IoT as there is a need of communication and exchange of information among the various components. Optimization of various phases of product development can be achieved using IoT. However, there is the issue of reliability of information exchange among various sub-systems of the industrial system. In robotics system, security, adaptability and

Table 1 Autonomous field applications

Authors	Applications	Limitations	Findings
Sadiku et al. [11]	Manufacturing	Difficult to guarantee high quality, diverse data entities and reliability of the information recorded from an industry system	Enormous IIoT market consists of large connected industrial systems and communicate with each other
Stăncioiu [5]	Automotive industry		Steady increase in automotive industry
	Digital factory		Optimization of each and every segment inside the product life cycle
Vaidya et al. [12]	Autonomous robot		Perform autonomous production with security, elasticity, adaptability and collaboratively
Rholam et al. [13]	Smart factory	The IWN signals cannot supply sufficient bandwidth for intense connection and huge amount of information, but it is greater to the wired network in an industry [14]	The real-time dynamics applied to industry are data analytics
Kerin and Pham [15]	Re-manufacturing		Additive manufacturing for renovate and replacement
	Process-related re-manufacturing		Maintenance Real-time monitoring Core supply

collaborative development can be achieved. In smart factories, there are issues with secure transmission of huge amounts of data over the network.

2.2 Applications in Software Industries

IoT possesses its wide range applications in the domains of core software domains. These provide higher standards of security, remote monitoring data and performing analyses of data values specified. These are illustrated under Table 2.

These applications include data mining, big data analytics, cloud, cyberphysical system (CPS) research for cloud computing, fog computing, fog-enabled industrial

Table 2 Applications in software field

Authors	Applications	Limitations	Findings
Kerin and Pham [15]	Data carrying devices (DCD)		Sustainable monitoring and allocation of resources
	Equipment-based (Web-based, virtual re-manufacturing)		Technology Techniques Algorithms
Tang et al. [16]	Data mining		Early prediction of Bayesian reliability
Thames and Schaefer [17]	Software distinct cloud development		Software distinct systems software representation cloud industrialized designs
Kim [18]	Cyberphysical system (CPS) for cloud computing	With increased connectivity, cybersafety threats have increased significantly	Integrated communication along set of connections Organizing administration and safety of CPS
Kim [18], Aazam et al. [19]	Big data analytics	The big data is not appropriate for offline process resolution	Integrated big data with 4.0, quantity and assortment of information
Kim [18], Cheng et al. [20], Aazam et al. [19]	Cybersecurity and cyberphysical system (CPS)	Physical objects are added to raise flexible mechanization and improving integrated industrialized systems	A secured system of calculation, communication and control systems (cyberspace)
Aazam et al. [19]	Cloud	A reviving is achieved to integrate dissimilar information for superior data analytics [21]	“Digital production” concept provides technical strength for the interfacing and communication
Trappey et al. [22]	Fog computing	Decreased effective comparison and control representation need to designed as a self-contained system [14]	Localized WSNs, controlling and managing CPS, virtual sensing and sensor networking and Web of things for the industry
	Fog-enabled industrial IoT		Mining, smart grid power plant, transportation, waste management industry, food industry and agriculture

IoT, data carrying devices, software distinct cloud development and cybersecurity and CPS.

2.3 Core IoT and Logistics Field Applications

This section identifies the scope of IoT in their core technical areas as well as their applications in the field of logistics and listed under Table 3. The logistics applications stated are transportation and smart logistic service, whereas, the core, it technical areas stated are technical standard for IoT, lack of open IoT middleware, Industry 4.0 and smart industrialization and Industrial IoT.

2.4 Microcontrollers Involved in IoT Applications

The IoT incorporates many hardware controllers for different projects. Therefore, the hardware controllers are listed below in Table 4. A microcontroller can be fixed as the computer attached on a single integrated circuit consisting of computer storage, a CPU and input/output peripherals that can be programmed. They are specifically designed for applications of embedded varieties. The various microcontrollers are utilized by different researchers, according to their requirements. Mostly consumed microcontrollers families are Arduino and Raspberry Pi due to their flexible working and easy human-friendly architecture.

PIC microcontroller family is suitable for the cost-sensitive and consumer applications [8]. Arduino microcontroller family is suitable for cost-effective, easily programmed and less complex configuration applications. The Raspberry Pi microcontroller is utilized with employing camera interfacing, visual navigation and are expensive in comparison with aforesaid microcontrollers.

3 Limitations

There are various advantages of IoT include the integration of distributed data anywhere which results in saving time. However, there are certain limitations in the execution of Industry 4.0 in the existing production industries is the investment issues. Investment issue is a quite universal matter for mainly of fresh technology and reliable lead in industrialization. The important asset is needed for executing Industry 4.0 be an SME primary. The executions of support of industry 4.0 need a vast quantity of investment in an industry [13].

Table 3 Core IoT and logistics field applications

Authors	Applications	Limitations	Findings
Sadiku et al. [11]	Transportation	Require compatible and smart transmission division that reforms manufacturing path [14].	Second-largest IIoT market. Combined enormous information to validate operations
Rholam et al. [13]	IIoT		Wireless sensor network (WSN), cyberphysical systems (CPS)
Thames and Schaefer [17]	Industry 4.0 and smart industrialization	The system requires self-sufficiency as a major aspect of the enclosed arrangement [14]	IIoT, cloud-based development, public manufactured good and improving
Trappey et al. [22]	Smart logistic service		Logistic service solutions The outlook structure empowers elegant logistics Patent study
Salazar et al. [23]	Technical standard for IoT	Distributivity, interoperability, scalability	ITU, ISO, IEC
	Lack of open IoT middleware	Low-consumption model, security	Real-time information and applications, collection and analysis
Nayyar et al. [24]	Military, entertainment, medical, home automation, manufacturing and systems maintenance		Hardware and application layer, Internet connectivity/IoT protocols, robotic platform support, big data services, IoT business cloud services and robotics transportation

4 Conclusions

Industry 4.0 obtains the research to interconnect among the data mining and decision maintain systems to prepare the product planning software much proficiently with clarity in information to compose of additional segments of the supply chain and phases in a product’s life cycle. IoT in Industry 4.0 possess a lot of IoT frameworks and are equipped with core IoT technologies.

Table 4 Diverse IoT controllers utilized

Microcontrollers	Authors
ATMEGA-16/32/328/2560/89C51	Singh et al., Sundaram et al., Rajwade and Gawali, Badre et al., Sarkar et al., Vishaal et al., Joge and Nagtode, Nedumaran et al. [25–31], Shukla and Shimi [32], Gonzalez et al. [33]
P PIC-16/18F	Gidansky and Sudano, Vaussard et al. [34, 35], Rathod et al., Ilyas et al. [36, 37], Patil and Iyer [38]
ARM 7	Sunitha and Pratyusha, Karthi et al., Pawar and Deosarkar, Zouka, Kadam et al., Patil and Iyer, Fan et al., Evangelin and Lenin [38–45]
Arduino-UNO/Mega/Nano	Badre et al. [27], Nedumaran et al., Ong and Azir [31, 46], Pawar and Deosarkar, Zouka, Kadam et al., Patil and Iyer [38, 41–43], Dey et al., Singh et al., Pol and Murugan, Rashid et al., Sivasankari et al., Vippalapalli et al., Suresh, Kanade et al., Raj and Srivani, Memon et al., Mittal et al., Gondalia et al., Bhingare et al., Garud et al., Nasiri et al., Dutt et al., Mohalkar et al., Archana and Suma, Ali et al. [47–65], Sarathkumar et al., Abdullahi et al., Parmar et al., Das et al., Indra and Yang [66–70], Gonzalez et al. [33]
Raspberry Pi	Sundaram et al. [25], Pawar and Deosarkar [41], Raj and Srivani [55], Das et al. [69], Hassan et al., Shaikh and Chitre, Garprabhu and Gopalan, Pardeshi et al., Soppimath et al., Kamble and Bhutad, Kavitha and Niranjana, Jansi and Amutha, Gayathri et al. [71–79], Al-Kuwari et al. [80]
NodeMCU	Ong and Azir [46], Khan et al., Al-Kuwari et al., Bakar et al., Jayaraman et al. [80–83]
AT89C51	Vishaal et al. [29], Deepika et al., Shukla and Shimi [32, 84]
Beagle Bone Black	Kadam et al. [85]
Intel Galileo Generation 2	Kodali et al. [86]
CC3200	Gonzalez et al. [33]

With the help of IIoT, real-time data is available for tracking both the products and slowdown together in the industry. By integrating sensor, devices and embedded system, a whole new model or an existing model of the organization can be improved.

References

1. Kunii TL (1997) The 3^d industrial revolution through integrated intelligent processing systems. In: IEEE international conference on intelligent processing systems. IEEE, pp 1–6
2. Peijiang C, Xuehua J (2008) Design and implementation of remote monitoring system based on GSM. In: IEEE Pacific-Asia workshop on computational intelligence and industrial application. IEEE
3. Shrouf F, Ordieres J, Miragliotta G (2014) Smart factories in Industry 4.0: a review of the concept and of energy management approached in production based on the Internet of Things Paradigm. IEEE

4. Pavitra D, Ranjith Balakrishnan (2015) IoT based monitoring and control system for home automation. 2015 Global Conference on Communication Technologies (GCCT), 169–173
5. Stăncioiu A (2017) The fourth industrial revolution Industry 4.0. *Fiabilitate Și Durabilitate* 1:74–78
6. Zawra LM, Mansour HA, Eldin AT, Messiha NW (2017) Utilizing the Internet of Things (IoT) technologies in the implementation of Industry 4.0. In: *Proceedings of the international conference on advanced intelligent systems and informatics 2017*, pp 798–808
7. Anwar RW, Zainal A, Abdullah T, Iqbal S (2020) Security threats and challenges to IoT and its applications: a review. In: *2020 Fifth international conference on fog and mobile edge computing (FMEC)*, pp 301–305
8. Nižetić S, Šolić P, González-de DL, Patrono L (2020) Internet of Things (IoT): opportunities, issues and challenges towards a smart and sustainable future. *J Clean Prod* 1–77
9. Adebayo AO, Chaubey MS, Numbu LP (2019) Industry 4.0: the fourth industrial revolution and how it relates to the application of Internet of Things (IoT). *J Multidiscip Eng Sci Stud (JMESS)* 5:2477–2482
10. De Silva PCP, De Silva PCA (2016) Ipanera: an Industry 4.0 based architecture for distributed soil-less food production systems. In: *Proceedings of the 1st manufacturing & industrial engineering symposium. IEEE*
11. Sadiku MNO, Wang Y, Cui S, Musa SM (2017) Industrial Internet of Things. *Int J Adv Sci Res Eng (IJASRE)* 3:1–5
12. Vaidya S, Ambad P, Bhosle S (2018) Industry 4.0—a glimpse. *Procedia Manuf* 20:233–238
13. Rholam O, Tabaa M, Monterio F (2019) Smart device for multi-band industrial IoT communications. *Procedia Comput Sci*
14. Singh HP, Mahajan A, Sukavanam N, Budhraja V, Singh S, Kumar A, Vashisht A (2014) Control of an autonomous industrial fire fighting mobile robot. *DU J Undergrad Res Innov* 124–130
15. Kerin M, Pham DT (2019) A review of emerging industry 4.0 technologies in remanufacturing. *J Clean Prod*
16. Tang TJ, Chung A, Zhao A, Kang R, Zhang M, Chien K, Yang J, Zhang J (2016) An IoT inspired semiconductor reliability test system integrated with data-mining applications. In: *International conference on cloud computing and Internet of Things (CCIoT)*. IEEE, pp 111–114
17. Thames L, Schaefer D (2016) Software defined cloud manufacturing for Industry 4.0. *Procedia CIRP* 12–17
18. Kim JH (2017) A review of cyber-physical system research relevant to the emerging IT trends: Industry 4.0, IoT, big data, and cloud computing. *J Ind Integr Manage* 2(3):1–22
19. Aazam M, Zeadally S, Harras KA (2018) Deploying Fog computing in industrial Internet of Things and Industry 4. In: *IEEE Trans Ind Inform* 1–9
20. Cheng J, Xu LD, Chen W, Tao F, Lin C-L (2018) Industrial IoT in 5G environment towards smart manufacturing. *J Ind Inf Integr*
21. Thoben KD, Wiesner S, Wuest T (2017) Industrie 4.0 and smart manufacturing—a review of research issues and application examples. *Int J Autom Technol* 11(1):4–16
22. Trappey AJC, Trappey CV, Fan C-Y, Hsu APT, Li XK, Le IJY (2017) IoT patent roadmap for smart logistic service provision in the context of Industry 4.0. *J Chin Inst Eng* 1–10
23. Salazar GDC, Venegas C, Baca M, Rodriguez I, Marrone L (2018) Open middleware proposal for IoT focused on Industry 4.0. IEEE
24. Nayyar A, Bath RS, Nagpal A (2018) Internet of robotic things: driving intelligent robotics of future-concept, architecture, applications and technologies. In: *International conference on computing sciences*. IEEE, pp 151–160
25. Shanmuga Sundaram P, Raj Pradeesh T, Aravind Raj S, Jaya Krishna K (2016) A case study on investigation of fire accident analysis in cotton mills. 14th International Conference on Humanizing Work and Work Environment HWWE-2016 At: NIT Jalandhar
26. Rajwade KC, Gawali DH (2016) Wearable sensors based pilgrim tracking and health monitoring system. 2016 International Conference on Computing Communication Control and automation (ICCUBEA), 1–5

27. Badre V, Agarwal P, Chavan S, Kabra P (2017) Smart fire fighting robot. *Int J Sci Res Comput Sci Eng Inf Technol* 2:96–100
28. Sarkar K, Mukherjee M, Saha A, Saha P, Paul A, Sarkar S (2018) A review on heart beat sensor using Arduino Atmega 328. *Int J Recent Innov Microelectron Microcontrol Appl* 1(1):1–10
29. Vishal R, Raghavan P, Rajesh R, Michael S, Elara MR (2018) Design of dual purpose cleaning robot. *Procedia Comput Sci* 133:518–525. In: *International conference on robotics and smart manufacturing (RoSma2018)*
30. Joge PD, Nagtode SA (2018) Home assist robot by using e-Yantra and IOT. *IJSRSET: Eng Technol* 4(7):19–22
31. Nedumaran AM, Silvakumaran K, Tan N, Pathmakumar T, Mohan RE, Suganya SK (2018) Towards robot-aided visual sampling of floor dust in indoor settings. In: *3rd international conference on advanced robotics and mechatronics (ICARM)*, pp 805–811
32. Shukla P, Shimi SL (2014) Design of inspection and cleaning robot. *Int J Sci Res Eng Technol (IJSRET)* 3:970–975
33. Gonzalez R, Chandler S, Apostolopoulos D (2019) Characterization of machine learning algorithms for slippage estimation in planetary exploration rovers. *J Terramech* 82:23–34
34. Harwayne-Gidansky J, Sudano M (2007) A low-complexity navigation algorithm for a scalable autonomous fire fighting vehicle. In: *The 5th student conference on research and development*. IEEE
35. Vaussard F, Fink J, Bauwens V, Retornaz P, Hamel D, Dillenbourg P, Mondada F (2014) Lessons learnt from robotic vacuum cleaners entering home ecosystem. *Robot Auton Syst* 62:376–391
36. Rathod PD, Wandile PV, Mohitkar KS, Jiwtode PG (2018) Multipurpose smart floor cleaning system by using android device. *Int J Sci Res Sci Eng Technol Eng Technol (IJSRSET)* 4:12–18
37. Ilyas M, Yuyao S, Mohan RE, Devarassu M, Kalimuthu M (2018) Design of sTetro: a modular, reconfigurable, and autonomous staircase cleaning robot. *J Sens* 1–16. Hindawi
38. Patil N, Iyer B (2017) Health monitoring and tracking system for soldiers using Internet of Things (IoT). In: *International conference on computing, communication and automation (ICCCA2017)*, pp 1347–1352
39. Sunitha R, Prathyusha K (2014) Microcontroller based heartbeat, blood pressure, and body temperature monitoring and alerting system using GSM modem. *IOSR J Electron Commun Eng* 9(6):100–104
40. Karthi A, Rajendran R, Mathiarasan P (2017) Smart health surveillance with automated database using android mobile device. *Braz Arch Biol Technol* 60:1–14
41. Pawar RR, Deosarkar SB (2017) Health condition monitoring system for distribution transformer using Internet of Things (IoT). In: *Proceedings of the IEEE 2017 international conference on computing methodologies and communication (ICCMC)*. IEEE, pp 117–122
42. Zouka HA (2017) An authentication scheme for wireless healthcare monitoring sensor network. IEEE, pp 68–73
43. Kadam DD, Patil SC, Bormane DS (2017) Wireless healthcare monitoring system. *Techno-Societal* 135–145. Springer International Publishing AG
44. Fan C, Liu X, Ling R, Si B (2018) Application of proteus in experimental teaching and research of medical electronic circuit. *Adv Soc Sci Educ Human Res* 215:512–515. In: *3rd International conference on modern management, education, technology, and social science (MMETSS 2018)*
45. Suganthi Evangeline C, Lenin A (2019) Human health monitoring using wearable sensor. *Sensor Rev*. Emerland Publishing Limited
46. Ong RJ, Ku Azir KNF (2020) Low cost autonomous robot cleaner using mapping algorithm based on Internet of Things (IoT). *IOP Conf Ser: Mater Sci Eng* 767:1–10. In: *1st International symposium on engineering and technology (ISETech)*
47. Dey A, Pal A, Nandi S, Roy L (2015) Three way controlled android Smartphone based robotic vehicle via Bluetooth. *Int J Appl Sci Eng Manage*
48. Singh R, Kuchhal P, Choudhury S, Gehlot A (2015) Implementation and evaluation of heating system using PID with genetic algorithm. *Indian J Sci Technol* 8:413–418

49. Pol RS, Murugan M (2015) A review on indoor human aware autonomous mobile robot navigation through a dynamic environment. Survey of different path planning algorithm and methods. In: International conference on industrial instrumentation and control (IIC). IEEE, pp 1339–1344
50. Rashid H, Ahmed IU, Ullah A, Newaz F, Robin MSR, Taslim Reza SM (2016) Multiple sensors based fire extinguisher robot based on DTMF, Bluetooth and GSM technology with multiple mode of operation. In: International workshop on computational intelligence (IWCI). IEEE, pp 41–46
51. Sivasankari P, Anbarasan M, Moses M (2016) Arduino based human health care monitoring and control system. IOSR J Electr Electron Eng 11(3):9–18
52. Vippalapalli V, Ananthula S (2016) Internet of things (IoT) based smart health care system. In: International conference on signal processing, communication, power and embedded system (SCOPEs)—2016. IEEE, pp 1229–1233
53. Suresh J (2017) Fire-fighting robot. In: International conference on computational intelligence in data science (ICCIDIS). IEEE
54. Kanade AV, Selvakumar A, Jalamkar D, Sengodan P, Jbara YHF (2017) Development of IoT controlled agri-rover for automatic seeding. Int J Pure Appl Math 114(11):241–251
55. Anantha Raj P, Srivani M (2018) Internet of robotic things based autonomous fire fighting mobile robot. In: IEEE international conference on computational intelligence and computing research. IEEE
56. Memon AW, Du J, Abro AH, Shah SI, Bhutto MA (2018) Design and implementation of fire extinguisher robot with robotic arm. In: MATEC web of conferences. EECR, pp 1–5
57. Mittal S, Rana MK, Bhardwaj M, Mataray M, Mittal S (2018) Cease fire: the fire fighting robot. In: International conference on advances in computing, communication, control and networking (ICACCCN2018). IEEE, pp 1143–1146
58. Gondalia A, Dixit D, Parashar S, Raghava V, Sengupta A (2018) IoT-based healthcare monitoring system for war soldiers using machine learning. Procedia Comput Sci 133:1005–1013. In: International conference on robotics and smart manufacturing (RoSma2018)
59. Bhingare KM, Ransing VS, Palve AB, Misal HM (2018) Vacuum cleaner using microcontroller. Open Access Int J Sci Eng (OAIJSE) 3:15–17
60. Garud MJ, Shinde VR, Dudkekar VS, Thorat SS, Aldar KM (2018) A review wireless floor cleaning robot. Int J Sci Res Comput Sci Eng Inf Technol 3:648–652
61. Mir-Nasiri N, Hudyjaya Siswoyo J, Hazrat Alia M (2018) Portable autonomous window cleaning robot. Procedia Computer Science 133:197–204. In: International conference on robotics and smart manufacturing (RoSma2018)
62. Jothi Sreeram Dutt AN, Rahul A, Sarkar A, Rani N, Dilna U (2019) Autonomous lavatory cleaning robot. Int J Sci Res Rev 7:2053–2057
63. Mohalkar S, Arote M, Khoje T, Pansare P (2019) An automated fire fighter robot. IJARIII 5:1626–1633
64. Archana BT, Suma K (2019) Design and fabrication of an autonomous fire fighting robot with obstacle detection and fire detection using Arduino. Int Res J Eng Technol (IRJET) 6:331–333
65. Ali MM, Haxha S, Alam MM, Nwibor C, Sakel M (2019) Design of Internet of Things (IoT) and android based low-cost health monitoring, embedded system wearable sensor for measuring SpO2, heart rate, and body temperature simultaneously. In: Wireless personal communications. Springer, pp 1–15
66. Sarathkumar B, Periyazhagar D, Sivasakthi S (2019) Live health care monitoring system using Arduino. Int Res J Eng Technol (IRJET) 2:688–694
67. Abdullahi U, Oladimeji SA, Audu WM, Saidu M, Wayo M (2019) Implementation of remote patient monitoring system using GSM/GPS technology. In: 3rd international engineering conference (IEC 2019), pp 521–527
68. Parmar HS, Meena A, Bhovaniya J, Priyadarshi M (2019) Automatic smart mop for floor cleaning. Int R J Eng Technol (IRJET) 6(4):3159–3165
69. Das NR, Daga R, Avte S, Mhatre K (2019) Robotic automated floor cleaner. Int Res J Eng Technol (IRJET) 6(3):4715–4721

70. Indra WA, Yang CJ (2019) Development of multi-controlled floor vacuum cleaner using RF energy harvesting. *ARPN J Eng Appl Sci* 14(21):3738–3742
71. Hassan AH, Awad A-FY, El-Amin AH, Hameed RA (2015) Smart home: home monitoring & control system using simple mobile app. Sudan University of Science and Technology, College of Engineering, School of Electronics Engineering, pp 1–75
72. Shaikh S, Chitre V (2017) Healthcare monitoring system using IoT. In: International conference on trends in electronics and informatics, pp 374–377
73. Garbhapu VV, Gopalan S (2017) IoT based low cost single sensor node remote health monitoring system. *Procedia Comput Sci* 113:408–415. In: The 7th international conference on current and future trends of information and communication technologies in healthcare (ICTH 2017)
74. Pardeshi V, Sagar S, Murmurwar S, Hage P (2017) Health monitoring systems using IoT and Raspberry Pi—a review. In: International conference on innovative mechanisms for industry applications, pp 134–137
75. Soppimath VM, Google A, Kolachal S, Kalal P, Baligar D (2018) Human health monitoring system using IoT and cloud technology—review. *Int J Adv Sci Eng* 5(2):924–930
76. Kamble A, Bhutad S (2018) IoT based patient health monitoring system with nested cloud security. In: 4th International conference on computing, communication and automation (ICCCA), pp 1–5
77. Kavitha R, Niranjana C (2018) Smart health care monitoring system. *Int J Innov Technol Explor Eng (IJITEE)* 8(2):413–416
78. Jansi R, Amutha R (2018) A novel chaotic map based compressive classification scheme for human activity recognition using a tri-axial accelerometer. *Multim Tools Appl* 77(23):31261–31280
79. Gayathri C, Venkatanarayanan S, Karpaga Priya R, Kannan M (2018) Internet of Things based health monitoring system using microelectromechanical systems sensor. *Asian J Appl Res* 4(10):44–55
80. Al-Kuwari M, Ramadan A, Ismael Y, Al-Sughair L, Gastli A, Benammar M (2018) Smart-home automation using IoT-based sensing and monitoring platform, pp 1–6
81. Khan A, Aesha AA, Aka JS, Faisal Rahman SM, Jamil-Ur Rahman M (2018) An IoT based intelligent fire evacuation system. In: 21st International conference of computer and information technology (ICCIT), pp 21–23
82. Bakar MAFBA, Nasir LABA, Ali NAB, Chek WAKBW (2018) Cloud controlled watering system using Blynk application. *Electr Eng Innov Compet Exhib 2018 (EEICE 2018)* 1:7–8
83. Jayaraman G, Muthukumaran N, Vanaja A, Santhamariam R (2019) Design and analysis the fire fighting robot. *Int J Emerg Technol Innov Eng* 5:690–695
84. Deepika NS, Singh M (2006) Designing a microcontroller based temperature data logger. In: Department of electrical and instrumentation engineering Thapar Institute of Engineering & Technology, pp 1–76
85. Kadam DD, Patil SC, Bormane DS (2017) Wireless healthcare monitoring system. In: *Techno-Societal*. Springer International Publishing AG, pp 135–145
86. Kodali RK, Swamy G, Lakshmi B (2015) An implementation of IoT for health care. In: *IEEE recent advances in intelligent computational systems (RAICS)*, pp 411–416

Three-Level Modified Capacitor-Assisted Extended Boost Z-Source Multilevel Inverter for Photovoltaic Applications



S. Nagaraja Rao , B. M. Kiran Kumar , and Swathy Nair 

1 Introduction

The potential of worldwide installed solar PV is increasing rapidly. This is due in large part to the depletion of fossil fuels, low capital cost, free and clean energy, and technology advancement [1–4]. The energy generated from solar photovoltaic is in the form of DC and can be used for both on-grid and off-grid applications such as lightings and load requirement by household applications. In most of the cases, the energy generated from solar PV is integrated to grid with the help of various power electronics converters [5–7]. As the solar photovoltaic output is irregular in nature, it turns into the challenging task of integrating solar PV into the utility grid network [8]. In order to integrate the solar PV with grid/load, various power converters with their advantages and disadvantages have been studied in the literature [8–11].

Among all available power converters, Z-source or impedance source inverters are gaining importance day by day and are also considered to be the most prominent converter in power electronic for DC-to-AC conversion. Z-source inverters eliminates the DC-DC conversion stage, which makes it a single/one-stage converter, and does buck and boost task in single-stage conversion. Furthermore, for all kinds of power conversion, such as AC-DC, AC-AC, and DC-DC, the idea of Z-source inverter can be applied. Z-source inverters provide a proficient way to convert power between DC source and load. Z-source inverters are reliable, less cost, reduced volume due to lesser use of switches [12]. A typical Z-source inverter is defined as a two-port

S. Nagaraja Rao (✉) · B. M. Kiran Kumar · S. Nair
Department of Electrical Engineering, M S Ramaiah University of Applied Sciences, Bangalore,
Karnataka 560058, India
e-mail: nagarajarao.ee.et@msruas.ac.in

B. M. Kiran Kumar
e-mail: kirankumar.ee.et@msruas.ac.in

S. Nair
e-mail: swathynair.ee.et@msruas.ac.in

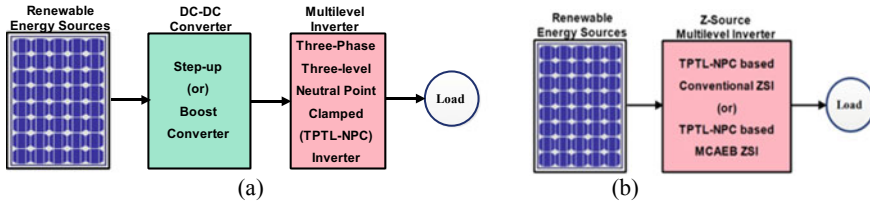


Fig. 1 RES integrated with **a** DC-DC converter and TPTL-NPC inverter (two-stage converter) **b** TPTL-NPC-based MCAEB ZSI (single-stage converter)

network containing of pairs of cross-connected inductors and capacitors [12, 13]. These inverters are introduced to overcome the drawbacks associated with voltage-fed and current-fed inverters, which are used as the most common power electronic converters [13–15]. The voltage-fed inverters output is often smaller than the voltage from the input. An extra boost converter is therefore needed to get the anticipated output voltage, which results in a two-stage conversion of higher cost and lower efficiency. Also, dual switches of the similar leg in voltage-fed inverters can never be switched on simultaneously, that leads to a leg short circuit and damages the inverter [16]. Likewise, the output of the current-fed inverters is always higher compared with input voltage. It therefore needs an added buck converter to get the voltage of the desired output. This further makes the converter bulky, costly, and less efficient. The conventional two-stage multilevel inverter and ZSMLIs are depicted in Fig. 1a, b, respectively. The Z-source inverter takes advantage of ST condition by switching on the top and bottom leg switches to raise the input voltage. Therefore, Z-source inverter will increase the voltage available for the DC bus to the desired output voltage.

Various switching designs are implemented to exploit the Z-source network property and are modulated with various control methods to meet particular application specifications. Possible switch configurations have been discussed, ranging from basic switch configurations to multifaceted regulated multilevel and matrix configurations [15, 16].

This paper presents the performance analysis of TPTL-NPC inverter with MCAEB Z-source network for photovoltaic applications.

2 ZSMLI

ZSMLIs are more efficient to overpower current and voltage ripples since the impedance network does the function of a second-order filter. It has smaller inductance and capacitance requirement when compared to an inverter interfaced with a conventional boost converter. The circuit also provides buck–boost action. These types of inverters are a better choice for renewable energy integration. In this paper,

performance analysis of a TPTL-NPC with MCAEB Z-source network is carried out and compared with a conventional TPTL-NPC with Z-source network.

2.1 Three-Phase Three-Level Neutral Point Clamped ZSMLI

A conventional TPTL-NPC with Z-source network is shown in Fig. 2 [15]. This topology has two cascaded Z-source networks named as upper and lower Z-network that interfaces the PV voltage V_{dc} with the TPTL-NPC inverter. A NPC multilevel inverter topology with ‘ m ’ levels possesses $6(m - 1)$ power switches, $3(m - 1)(m - 2)$ diodes, and $(m - 1)$ DC bus capacitors. The configuration splits the input DC voltage to three levels with the help of cascaded networks. Based on the clamping of diodes, output voltage levels of V_{PV1} and V_{PV2} are obtained. The capacitor voltage (V_C) and output voltage (V_O) of this topology are given by:

$$V_C = \frac{1 - k}{1 - 2k} V_{dc} \tag{1}$$

$$V_o = \frac{V_{dc}}{1 - 2k} \tag{2}$$

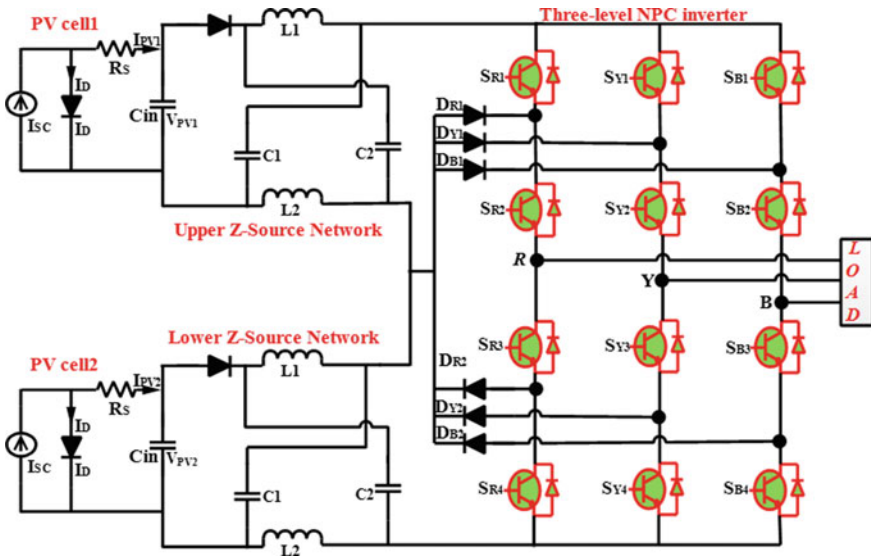


Fig. 2 TPTL-NPC inverter with conventional Z-source network

where V_{dc} is the total input voltage ($V_{PV1} + V_{PV2}$) and k is the ST ratio of the inverter. The boost factor of the topology is given by, $B = \frac{1}{1-2k}$. The boost factor of Z-source inverter can be increased by various topologies of Z-source networks [16].

3 Suggested TPTL-NPC Inverter with MCAEB Z-Source Network

The proposed TPTL-NPC inverter with MCAEB Z-source network is shown in Fig. 3. Like any general ZSI, this network also has two stages, ST and non-ST [16]. The topology gives higher voltage gain and reduced capacitor stress in comparison with the conventional topology discussed in Sect. 2.1. The configuration also provides low total harmonic distortion (THD) and a lesser amount of electromagnetic interference (EMI) which makes it a better configuration for PV integration. The network is a quasi-Z-source network which provides continuous conduction.

3.1 Steady-State Analysis

The MCAEB Z-source network comprises four capacitors, three inductors, and two diodes. The simplified circuit supplants the inverter circuit with a current source and parallel switch. In NST state, the switch is open and the diodes, D_1 and D_2 , are in conductive mode. During this interval, the inductors discharge and capacitors charge, the corresponding circuit is indicated in Fig. 4a. This interval can be denoted

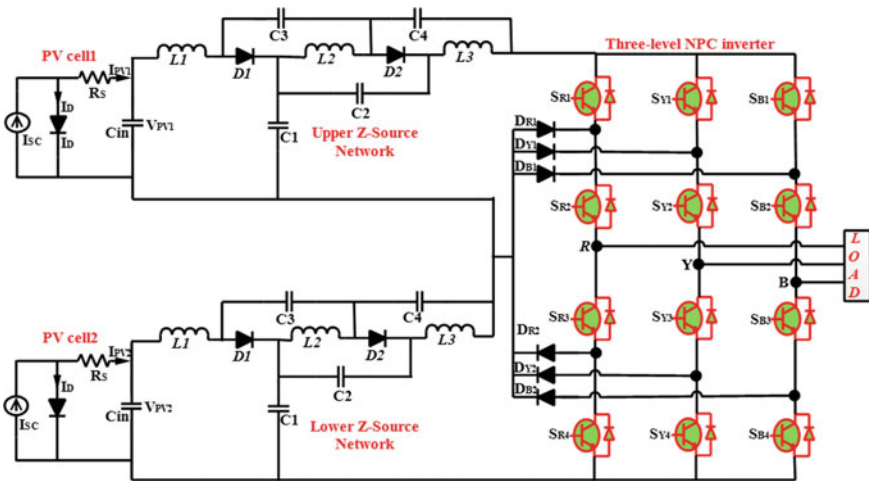


Fig. 3 TPTL-NPC inverter with MCAEB Z-source network

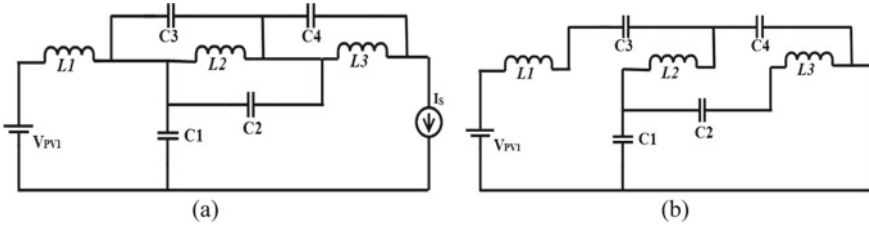


Fig. 4 MCAEB Z-source network equivalent circuit for **a** NST mode and **b** ST mode

as $(1 - k)T$, where T is time period. During this period, the voltage equations can be written as: $V_{dc} + v_{L1} = V_{C1}$, $V_{L2} = V_{C3} = V_{C2}$, $V_{L3} = V_{C4}$ and $V_S = V_{C1} + V_{C2} + V_{C3}$. During ST period (kT), the inverter switches act as short circuit and fuels boost action. The corresponding circuit is indicated in Fig. 4b, the diodes D_1 and D_2 are in blocking mode, the capacitors discharge and inductor stores energy. Voltage equations can be written as: $V_{L1} = V_{dc} + V_{C3} + V_{C4}$, $V_{L2} = V_{C1} + V_{C4}$, $V_{L3} = V_{C1} + V_{C2}$ and $V_S = 0$. Considering lossless conduction, the mean voltage over the inductors is zero and can be written as:

$$(1 - k)(V_{C1} - V_{dc}) = k(V_{dc} + V_{C3} + V_{C4}) \tag{3}$$

$$(1 - k)(V_{C2}) = k(V_{C1} + V_{C4}) \tag{4}$$

$$(1 - k)V_{C4} = k(V_{C1} + V_{C2}) \tag{5}$$

Solving Eqs. 4 and 5, the voltages across the capacitors are obtained as:

$$V_{C1} = \frac{1 - 2k}{1 - 3k} V_{dc} \tag{6}$$

$$V_{C2} = V_{C3} = V_{C4} = \frac{k}{1 - 3k} \tag{7}$$

The output voltage of the capacitance-assisted extended boost Z-source network is given by:

$$V_S = \frac{V_{dc}}{1 - 3k} \tag{8}$$

The increased boost factor of the modified topology, $B = \frac{1}{1 - 3k}$.

The boosted output voltage from the Z-source network is given to the neutral point clamped three-phase, three-level inverter. The sine reference-based modulation technique used for simple boost control (SBC) is shown in Fig. 5. The modulation index is given by, $M = \frac{A_{ref}}{A_{carrier}}$ where A_{ref} and $A_{carrier}$ are amplitude of reference and

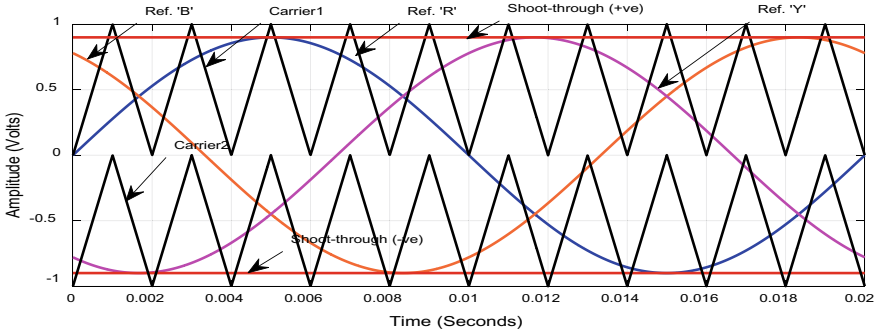


Fig. 5 SBC method-based on sine reference

carrier waves, respectively. The expression of k for the three-level SBC is defined by the equation:

$$k = 1 - M \tag{9}$$

The voltage gain of the circuit is given by:

$$G = MB = \frac{M}{3M - 2} \tag{10}$$

The switching sequence of the inverter for single phase is shown in Table 1. Full ST in a single phase leads to short circuit of the phase which is not preferable. So during the preferred full ST, the switching of single-phase switches along with other phase switches is shown in the table.

Table 1 Switching sequence for single phase

S. No.	Switches in conduction	Diodes in conduction	Voltage	State
1	S_{R1}, S_{R2}	D_1, D_2	$+V_{dc}$	Active
2	S_{R2}, S_{R3}	D_1, D_2 (or) D_{R1}, D_{R2}	0	Active
3	S_{R3}, S_{R4}	D_1, D_2	$-V_{dc}$	Active
4	S_{R1}, S_{R2}, S_{R3}	D_{R2}, D_1	0	Upper-ST
5	S_{R2}, S_{R3}, S_{R4}	D_{R1}, D_2	0	Lower-ST
6	$S_{R1}, S_{R2}, S_{R3}, S_{B2}, S_{B3}, S_{B4}$	D_{R2}, D_{B1}	0	Full-ST (preferred)
7	$S_{R1}, S_{R2}, S_{R3}, S_{R4}$	-	0	Full-ST (not preferred)

4 Simulation Results of TPTL-NPC Inverter with Conventional Z-Source Network and MCAEB Z-Source Network

The proposed topology in Fig. 2 is simulated using MATLAB/Simulink and the results are compared with conventional TPTL-NPC ZSI. The chosen simulation parameters of MCAEB-ZSI and conventional-ZSI are given in Table 2.

The input from PV module into the Z-source network is shown in Fig. 6a. The line-to-line output wave form for TPTLNPC conventional ZSI for ST ratios 0.1 and 0 is shown in Fig. 6b, c, respectively. For a ST ratio, $k = 0.1$ the peak output voltage is enhanced to 103.8 V and for $k = 0$, the peak output voltage raised up to 82.7 V. The FFT analysis of the waveform for $k = 0.1$ is shown in Fig. 6d. For the line-to-line output voltage without filter, the THD is observed as 39.37%.

Similar analysis for the proposed TPTL MCAEB Z-source inverter shows that the peak-to-peak, line-to-line output voltages are increased to 118.38 V and 83.2 V for $k = 0.1$ and 0, respectively (see Fig. 7a, b). The voltages across the capacitors show reduced capacitance stress in the proposed topology (see Fig. 7c, d). The inverter gain of the proposed topology is boosted to 59.19 V and THD without filter is observed as 39.34 for $k = 0.1$ (see Fig. 7e, f).

The comparison of theoretical and simulation results for conventional and proposed topologies for different values of M and k in terms of output voltage, boost factor, and THD is presented in Table 3.

The boost factor that corresponds to different values of M and k for proposed and conventional topologies is tabulated in Table 3. ST ratio, k , is limited to 0.3 because that is the maximum possible value for proposed topology. The results show that the boost factor is more for MCAEB ZSI compared to conventional ZSI for any values of M and k . It is also observed that the difference is more as the values of M and k increase as exhibited in Fig. 8a, b. The voltage gain of the two topologies for different values of M , based on Eq. (10), is plotted and the result is obtained as shown in Fig. 9.

Table 2 Simulation parameters

Parameters	Value/range
Output of PV1/PV2	41.8 V
Switching frequency	5 kHz
L ₁ , L ₂ , L ₃ , and L ₄ of MCAEB-ZSI	2 mH
L ₁ , L ₂ and L ₃ of conventional-ZSI	3600 μF
C ₁ and C ₂ of MCAEB-ZSI and conventional ZSI	3600 μF
M	0–1
K (ST-ratio)	0–0.5
Three-phase resistive load	10 Ω/phase

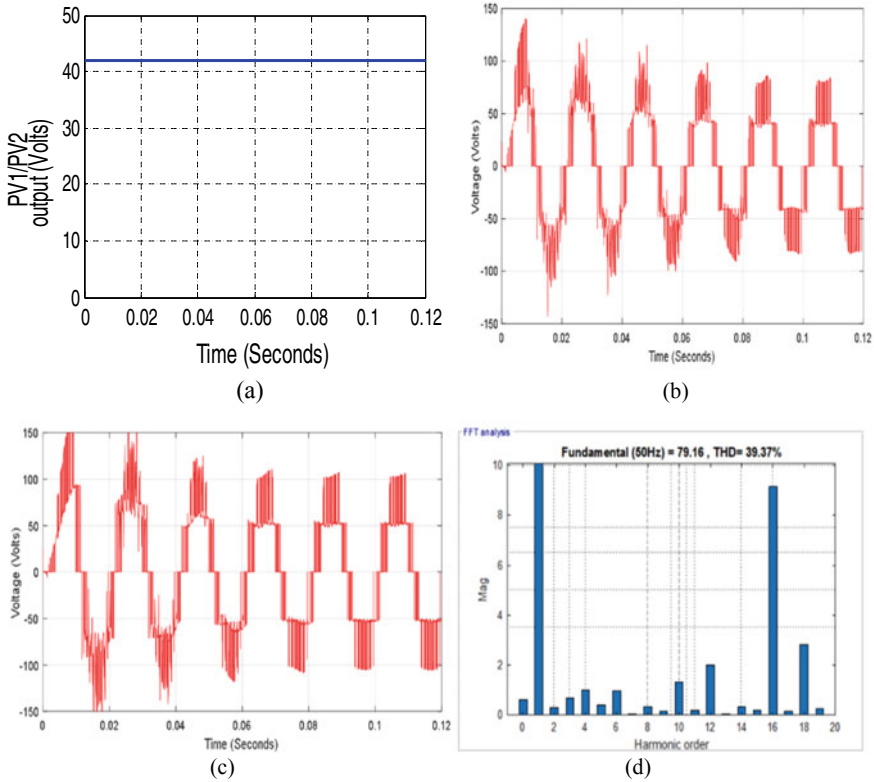


Fig. 6 **a** PV output voltage, line-to-line output voltage of a TPTL conventional ZSI for **b** $k = 0.1$, **c** $k = 0$ and **d** FFT analysis of the output waveform for $k = 0.1$

5 Conclusion

The performance of proposed TPTL-NPC inverter with MCAEB Z-source network for PV integration is analyzed and compared with conventional TPTL-NPC Z-source network. The sine reference SBC modulation technique is used for switching. Analysis is done for distinct values of ST ratio and modulation index. From the results, it is apparent that the boost factor and hence the voltage gain of the inverter improved with MCAEB Z-source network compared to conventional Z-source network. The proposed topology also has the advantage of reduced capacitance stress. With three levels, the THD without filter is still not in the acceptable limit and can be further decreased by higher number of levels. The performance analysis can also be done for different modulation schemes.

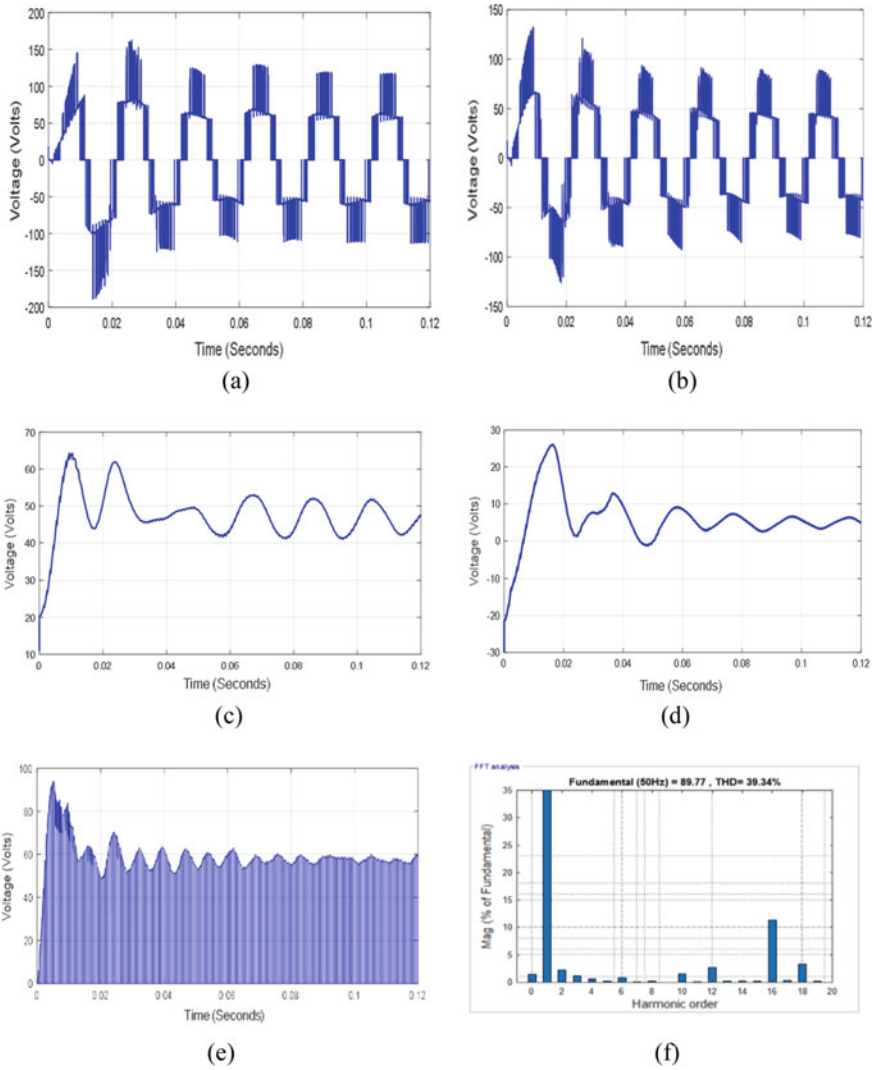


Fig. 7 Line-to-line output voltage of a TPTL-NPC MCAEB ZSI for **a** $k = 0.1$, **b** $k = 0$, **c** voltage across capacitor C_1 for $k = 0.1$, **d** voltage across capacitor C_2 and C_3 for $k = 0.1$, **e** inverter gain output voltage for $k = 0.1$ and **f** FFT analysis of the output waveform for $k = 0.1$

Table 3 Comparison of conventional-ZSI and MCAEB ZSI topologies

S. No.	k	M	TPTL-NPC conventional ZSI				%THD	TPTL-NPC MCAEB ZSI				%THD
			Theoretical V_o	Simulated V_o	B	Theoretical V_o		Simulated V_o	B			
1	0	1	83.6	82.7	1	39.34	83.6	83.2	1	39.22		
2	0.1	0.9	104.5	103.8	1.25	39.37	119.42	118.38	1.42	39.34		
3	0.2	0.8	139.33	138.31	1.66	39.51	209	207.82	2.5	39.48		
4	0.3	0.7	209	206.52	2.5	39.92	836	833.41	10	39.83		

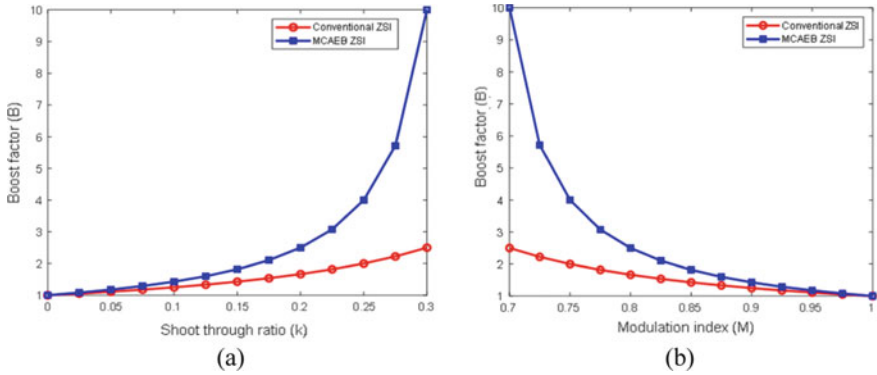
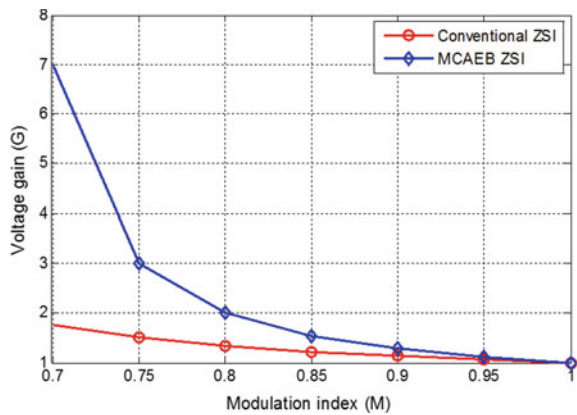


Fig. 8 Comparison of boost factor for conventional and MCAEB ZSIs for different values of **a** ST ratio and **b** modulation index

Fig. 9 Comparison of voltage gain for conventional and MCAEB ZSIs for different modulation indices



References

1. Shahsavari A, Akbari M (2018) Potential of solar energy in developing countries for reducing energy-related emissions. *Renew Sustain Energy Rev* 90:275–291
2. Kabir E, Kumar P, Kumar S, Adelodun AA, Kim KH (2018) Solar energy: potential and future prospects. *Renew Sustain Energy Rev* 82:894–900
3. Brockway PE, Owen A, Brand-Correa LI, Hardt L (2019) Estimation of global final-stage energy-return-on-investment for fossil fuels with comparison to renewable energy sources. *Nat Energy* 4(7):612–621
4. Ebhota WS, Jen TC (2020) Fossil fuels environmental challenges and the role of solar photovoltaic technology advances in fast tracking hybrid renewable energy system. *Int J Precis Eng Manuf-Green Technol* 7(1):97–117
5. Kumar V, Pandey AS, Sinha SK (2016) Grid integration and power quality issues of wind and solar energy system: a review. In: 2016 International conference on emerging trends in electrical electronics & sustainable energy systems (ICETEESES). IEEE, pp 71–80
6. Badwawi RA, Abusara M, Mallick T (2015) A review of hybrid solar PV and wind energy system. *Smart Sci* 3(3):127–138

7. Wang G, Konstantinou G, Townsend CD, Pou J, Vazquez S, Demetriades GD, Agelidis VG (2016) A review of power electronics for grid connection of utility-scale battery energy storage systems. *IEEE Trans Sustain Energy* 7(4):1778–1790
8. Blaabjerg F, Yang Y, Ma K, Wang X (2015) Power electronics—the key technology for renewable energy system integration. In: 2015 International conference on renewable energy research and applications (ICRERA). IEEE, pp 1618–1626
9. Sandhu M, Thakur T (2014) Issues, challenges, causes, impacts and utilization of renewable energy sources-grid integration. *Int J Eng Res Appl* 4(3):636–643
10. Monfared M, Golestan S (2012) Control strategies for single-phase grid integration of small-scale renewable energy sources: a review. *Renew Sustain Energy Rev* 16(7):4982–4993
11. Colak I, Kabalci E, Fulli G, Lazarou S (2015) A survey on the contributions of power electronics to smart grid systems. *Renew Sustain Energy Rev* 47:562–579
12. Ellabban O, Abu-Rub H (2016) Z-source inverter: topology improvements review. *IEEE Ind Electron Mag* 10(1):6–24
13. Siwakoti YP, Peng FZ, Blaabjerg F, Loh PC, Town GE (2014) Impedance-source networks for electric power conversion part I: a topological review. *IEEE Trans Power Electron* 30(2):699–716
14. Peng FZ, Yuan X, Fang X, Qian Z (2003) Z-source inverter for adjustable speed drives. *IEEE Power Electron Lett* 1(2):33–35
15. Shults TE, Husev OO, Zakis JG (2015) Overview of impedance source networks for voltage source inverters. In: 16th International conference of young specialists on micro/nanotechnologies and electron devices, Erlagol, pp 514–520. <https://doi.org/10.1109/edm.2015.7184596>
16. Misal S, Rao SN (2015) Comparative analysis of a 3-phase, 3-level diode clamped ZSI based on modified shoot through PWM techniques. In: IEEE international conference on signal processing, informatics, communication and energy systems (SPICES), Kozhikode, pp 1–5. <https://doi.org/10.1109/spices.2015.7091409>

An Overview on the Topologies and Control Strategies for Solar Photovoltaic Emulators



K. R. Jeswanth Kumar, S. Kamatchi Rajeswari, S. Sridharan,
and K. Sundararaman

1 Introduction

The rapid depletion of fossil fuels and the consequent apprehensions on energy security have sent the governments of the world scurrying towards finding alternate forms of energy which would be everlasting. This coupled with the concerns on global warming and pollution have made solar and wind energy systems popular. The Government of India has planned a stiff target of generating 100 GW of power through solar energy by 2022. Research and development into the issues connected with solar energy have also kept pace, and the cost of generation for every unit of solar energy is now even less than traditional forms of energy.

However, solar energy has its own issues, the major one being intermittency. Hence, it has to be necessarily used along with other forms of energy or in parallel with the grid or would need substantial storage options. A researcher intending to test a new design of an inverter or a battery charger or a new control algorithm would be handicapped by the fact that the solar power is intermittent and is also highly fluctuating due to climatic conditions or due to shading of the panels. A photovoltaic emulator would help to carry out experiments without depending on the solar power and without bothering about climatic variations. They require much less area than actual solar panels and the testing cost is substantially less. They are also portable and programmable and can be incorporated with protection features.

A photovoltaic emulator, as the name suggests, emulates the actual performance of solar photovoltaic panels in that it is able to produce the same current–voltage characteristics for a given load and for different climatic conditions as that of the chosen solar panels. Photovoltaic panels are connected in arrays in series or parallel or series–parallel or in many other different configurations and the emulator should be able to show the same output characteristics as that of the array.

K. R. Jeswanth Kumar · S. Kamatchi Rajeswari · S. Sridharan · K. Sundararaman (✉)
Rajalakshmi Institute of Technology, Chennai, India

A photovoltaic emulator would be very useful during the design and development phase for building a stand-alone or a grid-connected inverter system and for trying out new control algorithms like maximum power tracking. It could also be used to estimate the amount of energy production during the operational phase.

An ideal emulator should not only be able to closely reproduce the static nonlinear I-V characteristics of a solar panel array under varying climatic and shading conditions but also have a good transient response and match the dynamic characteristics of the panel array. Since the emulator may have to work with converters of different topologies and of different manufacturers, it has to be flexible in terms of compatibility. It would do well to have a low power consumption while being cheap, compact and efficient.

Existing papers which review the photovoltaic emulators described in the literature are given in [1–3]. This paper endeavours to give a general overview to research scholars and working professionals who wish to build a PV emulator in the laboratory for further experimental work. The paper briefly describes the major topologies and control strategies in the literature that have been used for building PV emulators and the issues associated with them.

2 Approaches to Emulation

Seo et al. [4] outline clearly the two approaches towards configuring a photovoltaic emulator with a power electronic converter, as shown in Fig. 1. The climatic conditions in the form of temperature, irradiance and even wind should be obtained as input parameters. The solar array simulator engine emulates a photovoltaic panel by generating a suitable reference which takes into account these climatic conditions. This reference drives the power electronic converter to generate the physical output. The engine could be a microcomputer or a digital signal processor or a field-programmable gate array (FPGA) or a hardware-in-loop (HIL) system. It could even be a software in a computer, like LabView. MATLAB has been used very often but occasionally other softwares like PSIM have also been used [5].

In the first approach, the engine could use a lookup table which is generated offline through experiments conducted on real PV panels or on PV models. During operation, the data has to be simply picked up from the tables which could be very fast. However depending on the number of points stored in the memory, some interpolation may be required to fetch the specific values and there could be a little loss of accuracy. Also, the lookup table data is panel specific and has to be regenerated if the panel is changed.

The second approach uses a PV model like 1D2R or 2D2R, and the reference is determined in real time from the governing equations of the model. The parameters of the model have to be extracted based on the climatic conditions using iterative methods like Newton–Raphson method or by techniques like evolutionary computing. Seo et al. [4] suggest an optimisation method known as conjugate gradient

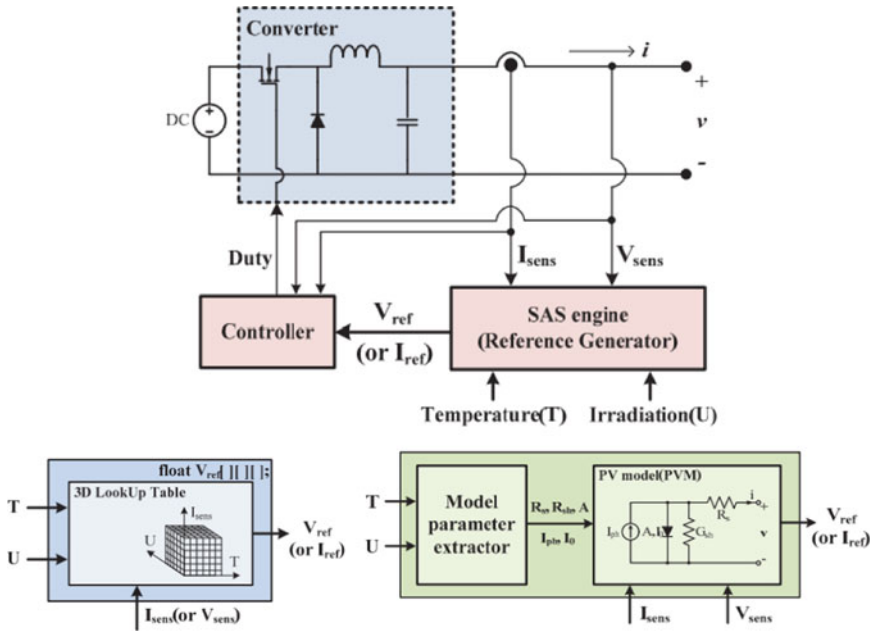


Fig. 1 Simulator engine and the two approaches for the emulator [4]

that uses the gradient of an error function. The memory requirement is less but calculations have to be fast. With the three known operating points, namely current at short circuit, voltage at open circuit and maximum power point, any suitable algorithm can be used to determine the other points. The reference generated by the controller is input to a power electronic converter which actually brings about the operating point in terms of load current and voltage, which should be identical to that of a real PV array.

3 Photovoltaic Models

To determine the points on the current–voltage (I-V) characteristics of a PV cell at different temperature and irradiance conditions, a model of the photovoltaic cell is required. Some of the models often used by researchers are summarised in Figs. 2, 3 and 4. In all the cases, the PV output is modelled with a current source. In the 1D2R model, a diode is in parallel with the current source and additional series and shunt resistances are represented. In the double diode model, two diodes are placed in parallel instead of one. Both the above models are known as DC models. In the AC model, a capacitance is inserted in parallel to the diode which becomes important to study transient conditions [A7]. The 1D2R model is simplest to analyse while the

Fig. 2 1D2R model

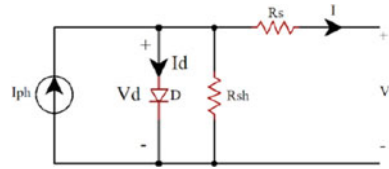


Fig. 3 2D2R model

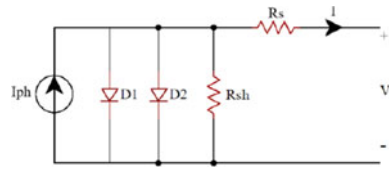
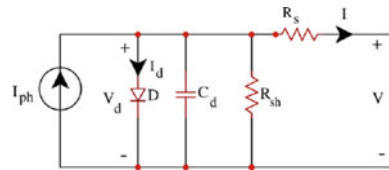


Fig. 4 AC model of a PV cell



other two models have more computational overheads, while being more accurate during variations in irradiances.

The parameters of the model are extracted from datasheets of the PV panels by an iterative process like Newton–Raphson method. Once the parameters are extracted for a set of climatic conditions, the operating points on the I-V curve can be determined for any load condition. Normally, the climatic conditions that are considered are only temperature and irradiance. But since wind speed and its direction also have the effect of influencing the temperature, wind effects have also been considered recently [6]. Abdelghani and Sethom [7] present an approach to estimate the parameters of a 1D2R model of a PV array. The array could have a series–parallel combination, and a part of the array could also be partially shaded.

As an alternative to the PV model + converter combination, Park et al. [8] propose a topology which consists of a PV module in parallel with a power supply and a resistor R_{add} in addition, as shown in Fig. 5. The model is claimed to be accurate near the maximum power point. Zhou and Macaulay [9] use a current source without the resistor to represent the power supply. The bypass diode of the PV panel which prevents hotspots during partial shading conditions is incorporated in the model.

Leaving out the knee region, the I-V curve for a PV panel has a region where the current is more or less constant and a region where the voltage is almost constant as shown in Fig. 6. Effectively, it behaves as a nonlinear current source. Nousiainen et al. [10] define the necessary properties for a source to satisfy the emulation requirements of a photovoltaic generator. PV emulation can broadly be done either by artificial illumination of a PV panel with a light source or by using a power electronic converter which derives its reference from a controller driven by a PV model.

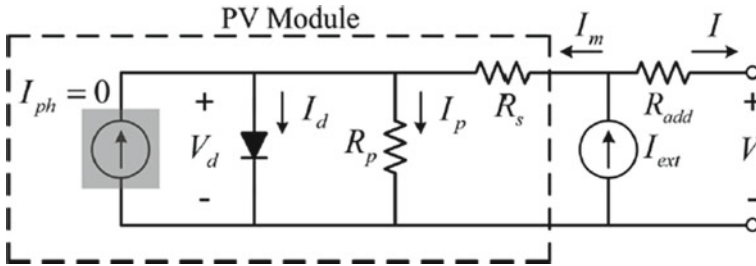
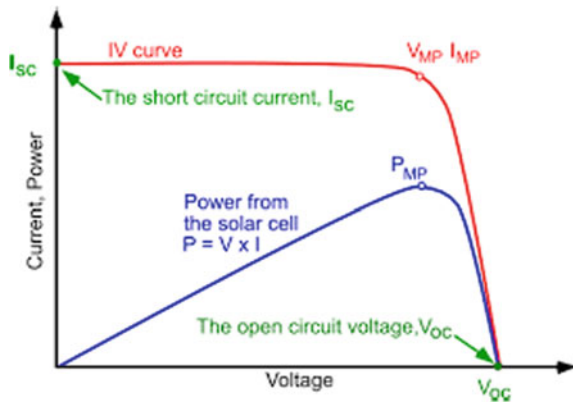


Fig. 5 PV panel with a power supply in parallel [8]

Fig. 6 P-V and I-V characteristics of a solar cell



3.1 PV Panels Illumined by Light Sources

One way to construct an emulator would be to use a light source whose intensity and spectrum can be varied. This method does not require a reliable model for the PV panel. For the light source, halogen lamps would be economical but they do not match exactly with the solar spectrum. They also generate a lot of heat. A combination of LED and halogen bulbs or halogen in combination with Xenon bulbs gives a better performance.

Buso et al. [11–13] outline the design of photovoltaic emulators where a modulated light source comprising LED, Xenon or halogen bulbs or a combination thereof is used to illuminate PV panels and thereby generate the required I-V characteristics. The light source illuminates the PV module and causes photogeneration. The light source should match the spectral radiation distribution of the sun for higher accuracy. To have fast response to load and climatic variations, the bandwidth of the driver circuit should be large.

4 Power Electronic Converters

Linear regulators have fast response but are no longer preferred due to their low efficiencies. The power electronic converter that is most commonly used for generating the physical output from the reference generated by the controller is the pulse width modulated buck converter. The output voltage of the photovoltaic panel is the open-circuit voltage (V_{oc}) of the panel when no load is connected and is zero when the panel is short-circuited. Hence, the voltage has to vary from 0 to ' V_{oc} ' and a buck converter is ideally suited for the application. But other non-isolated converters have also been used sporadically. A multiplier SEPIC converter with a Dickson charge pump for a higher gain has been used in [14] along with dSPACE 1104 power-hardware-in-the-loop (PHIL) controller. A PHIL controller has also been used in [15]. A boost converter and a buck converter in cascade with a double current mode controller have been outlined in [16] based on the lookup table principle and uses a TMS320 DSP.

At operating points close to open-circuit voltage the current is low and the converter may go into discontinuous mode and voltage may rise. This may call for a dummy load to be connected in shunt. Similarly at low duty cycles which typically happen when the operating point is close to short-circuit condition, the current pulses may be spiky and current limiting resistances may be called for. These resistances tend to reduce the efficiency. Moreover, a simple buck converter is hard switched and has more switching losses at higher frequencies besides causing electromagnetic interference.

Some of these issues could be solved by going for isolated converters, albeit at higher expense. Wandhare and Agarwal [17] discuss a flyback topology for the power electronic converter and controlled with a dsPIC microcontroller as shown in Fig. 7.

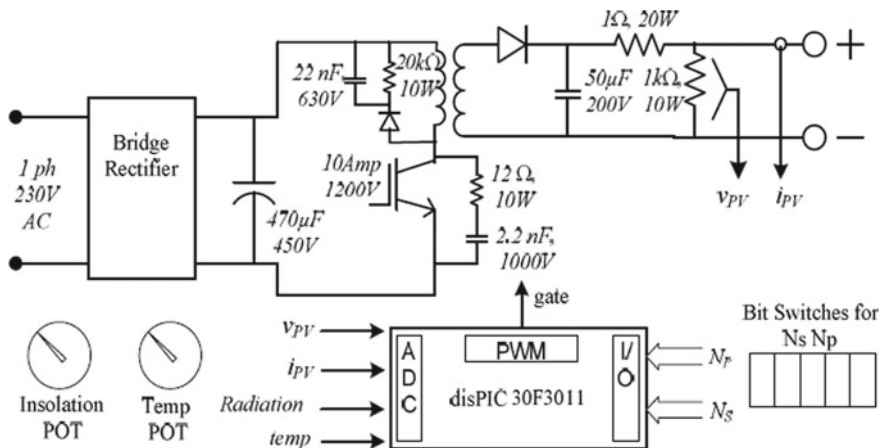


Fig. 7 Schematic of the flyback converter-based emulator in [17]

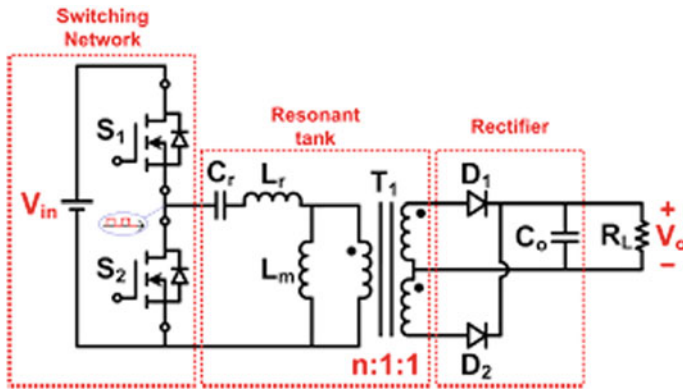


Fig. 8 Half-bridge LLC resonant converter

Due to isolation with a high-frequency transformer and operation at a high switching frequency, the converter is compact.

Load resonant converters like series or parallel resonant converters can be varied over the full range by frequency modulation. They have zero voltage switching of the main switches, and the rectifier diodes are also zero current switched. Hence, they have lesser switching losses and higher efficiency. The resonant capacitor in series with the transformer prevents it from getting saturated. The converter could also have a front-end power factor controller.

Among the isolated resonant converters, LLC resonant converter is the converter of choice. A series resonant converter has an issue with no load regulation and parallel or series-parallel resonant converters have more circulating energy than LLC resonant converters at low output voltages. D’Cruz and Rajesh [18–21] discuss topologies with LLC resonant DC-DC converters. A typical schematic of a half-bridge LLC resonant converter is shown in Fig. 8. However, it may be noted that under changing climatic conditions, the switching frequency may have to vary widely. Additionally, because of the transformer such converters may be bulky, heavy and costly.

A PV array in conjunction with a two-stage converter has been emulated together to study a converter system connected to the grid in [22]. In [23], an additional LCL filter is introduced at the output of the simulator to minimise current ripples at the output. A three-phase galvanically isolated DC-DC converter has been used in [24] with a TMS320 DSP for controller.

5 Control Methodologies

Control of the power electronic converters can be done using analog controllers or with microcontrollers or digital signal processors. The nonlinear I-V characteristic of a PV panel necessitates a high control bandwidth for stable operation, and if digital

control is used, it has to be fast-acting. Schofield et al. [25] use an analog controller but in many other papers, digital control has also been employed. An operational amplifier-based analog controller which implements an emulator on a logarithmic approximation of the 1D2R PV model is described in [26]. A linear regulator is used for the power part. Koran et al. [27] describe a simulator which has the merits of both analog and digital controllers. The analog extraction strategy for the I-V characteristics uses a controlled illumination on a PV cell. A digital signal processor is used for processing the curve information and generating the reference for the power section which constitutes a three-phase interleaved DC-DC converter which has a front-end active rectifier.

Gadelovits et al. [28] suggest a method by which an existing power supply can be modified to obtain the programmable power supply required for the emulator rather than building a converter from the scratch. This helps to achieve rapid prototyping. This is done by injecting a variable analog signal into the feedback loop of the existing power supply. The method is generic and suitable for any AC/DC power supply.

Kapoor et al. [29] suggest an adaptive strategy for control of the PV panel at different load conditions. The emulator output voltage is changed based on the deviation between the expected and the actual current of the PV module. The controller gains are changed based on the circuit conditions.

5.1 LabView-Based Implementation

Dolan et al. [30–33] discuss the implementation of a PV emulator using LabView. The PV panel parameters are generated through several analytical models. The model of the photovoltaic system is implemented in LabView, and it is interfaced with the external sensors and converter using a data acquisition system. The climatic conditions are input to the system by suitable input voltages. The details of the PV array can be suitably parameterised in LabView. Effects of partial shading and sometimes effects of panel degradation are also incorporated. The maximum power point tracking algorithm is built into the LabView interface. The PV model in LabView is executed in real time, the dynamic resistance of the panel corresponding to the operating point in I-V characteristics is tracked and the required reference is output to the converter for physical realisation. The converter is a buck or boost converter in combination with a voltage source inverter. A schematic of the emulator in [31] is shown in Fig. 9, and the front panel of the emulator in [33] is shown in Fig. 10.

5.2 FPGA-Based Implementation

Tornez-Xavier et al. [34–38] discuss implementation of emulators which make use of field-programmable gate arrays (FPGAs). FPGA enables rapid system prototyping, and due to its high clock frequency, the switching frequency of the converter can be

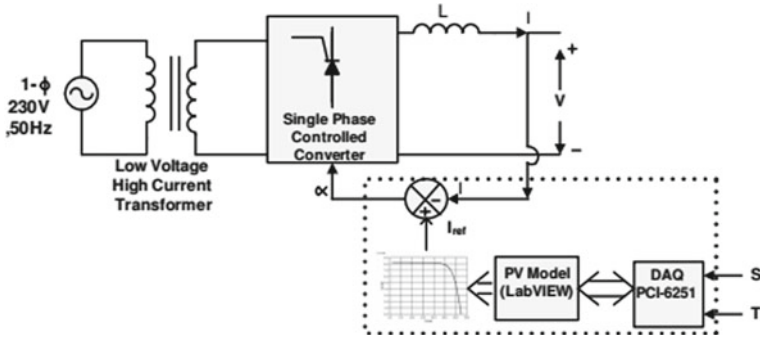


Fig. 9 Schematic model of the emulator [31]

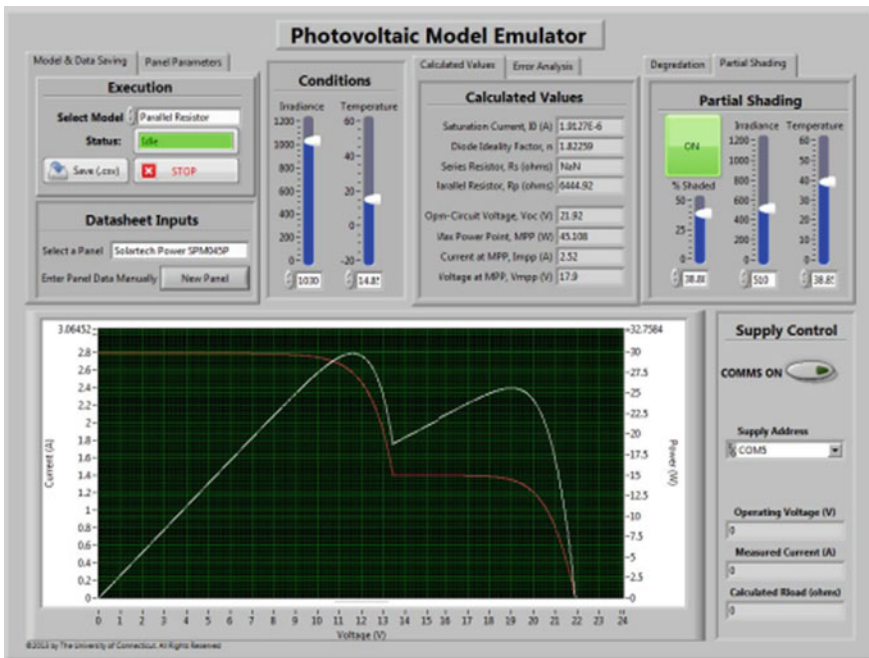


Fig. 10 Front panel of the emulator [33]

high enabling a reduction in the size of the converter. In [34], an analog model of the solar panel is created using the framework of Mentor Graphics. The temperature and irradiance are fed as inputs, and open-circuit voltage and short-circuit current values of the PV panels are generated. Using these values, an artificial neural network is trained in MATLAB and its optimised output is implemented with FPGA. Ickilli et al. [35] use an Altera Cyclone-III FPGA board, the reference signal from which drives a buck converter to generate the physical output of the emulator. In [37], the PV

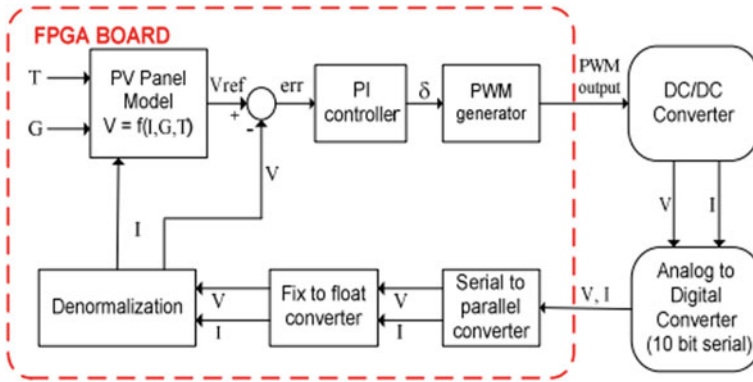


Fig. 11 Control schematic of emulator in [35]

characteristics are modelled with the Xilinx System Generator (XSG) platform based on FPGA, which has the advantage that the VHDL code is automatically generated using HDL co-simulation. Jin and Zhang [38] propose a FPGA-based space solar array simulator in combination with a linear power regulator for fast response. A control schematic of the emulator in [35] is shown in Fig. 11.

5.3 Dual Mode Controls

Escobar et al. [39] propose a controller which is a combination of a proportional-derivative voltage mode controller (VMC) and a passivity-based current mode controller (CMC). By introducing an additional variable, the location of the operating point is determined, and the appropriate mode of control is chosen with some hysteresis. A dual-mode control has also been suggested in [40] to avoid the stability problems in the constant current zone or constant voltage zone. A hysteresis-based controller based on dsPIC33F is proposed for stable operation. Since the PV controller normally operates at maximum power point, small disturbances can make it oscillate between the modes which are avoided by the hysteresis. The hysteresis controller takes the difference between the actual PV voltage and the voltage at maximum power point and decides the switch between voltage mode and current mode vide Fig. 12.

5.4 Other Controls

Sliding mode controllers have been proposed for control of PV emulators in [41–44]. Such controllers show a robust response to parametric variations and to disturbance

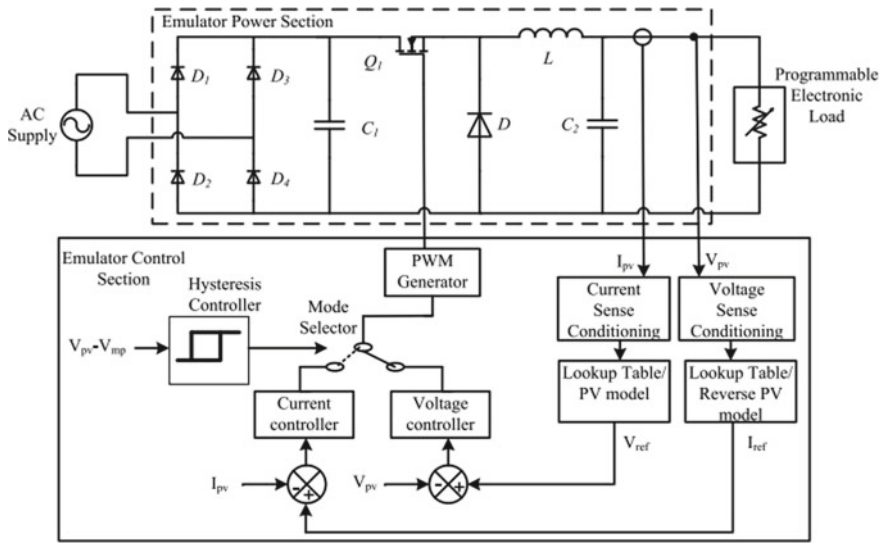


Fig. 12 Schematic of the emulator in [40]

inputs and possess a high control bandwidth. Mahmud et al. [41] use a three-phase interleaved buck converter for the power section which reduces the ripple current considerably. Mahmud and Zhao [44] use a differential mode phase current signal which helps to make the circuit more robust to errors in measurement and makes use of a current balancing algorithm. A fractional order sliding mode control which replicates the I-V characteristics of a PV array more robustly has been suggested in [45].

Cupertino et al. [46] propose a two-stage emulator connected to the grid. A front-end PWM voltage source rectifier fixes the DC voltage while ensuring a high source power factor. Grid synchronisation is done using PLL techniques, and space vector modulation is used for control. The second stage bidirectional DC-DC converter enables rapid response with stable operation down till no load. It can operate either in open-circuit control mode during unloaded conditions or in array control mode where current reference is obtained from I-V characteristics embedded in lookup tables. The control schematic is shown in Fig. 13.

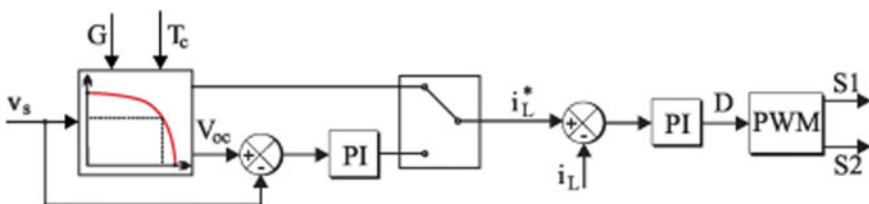


Fig. 13 A control schematic of emulator in [46]

A buck converter-based emulator with a front-end power factor controller has also been discussed in [47]. The emulator makes use of the 2D2R PV model. Chariag and Sbita [48] use an average current mode control for the current loop. [49] is proposed an emulator which is modular in nature. Any series–parallel combination of PV panels can be taken care of by one emulator, and many such emulators can again be connected in series/parallel. A DC bench power supply is made use of and control is with a DSP. The inductor current of the buck converter of each emulator is controlled based on the PV model. The emulator can also take care of partial shading due to the modular nature of the emulator. A distributed MPPT-based approach has also been described in [50] based on a dynamic boost converter and implemented with a low-cost Arduino board.

A cloud-connected virtual PV emulator has been outlined in [51]. An emulator with a combination of fractional order PID control and fuzzy control has been suggested in [52]. An emulator capable of emulating accurately even under partial shading conditions has been analysed in [53]. The emulator makes use of the lookup table principle and uses an adaptive PI controller as the control strategy. Since dynamic response is an important requirement of an emulator and since this is closely related to stability aspects, a nonlinear Lyapunov controller with a hybrid referencing technique has been proposed in [54]. The mode transitions between voltage and current modes that occur in a normal emulator are regulated by the Lyapunov controller.

A hybrid damping injection controller has been suggested in [55] which is based on the 1D2R model and makes use of a look up table generated offline. The controller takes care of the instabilities in the constant current and constant voltage regions by suitable damping. Apart from series/parallel configurations, the emulator can also take care of honeycomb, bridge-link and total-cross-tied configurations and track the I-V characteristics even under partial shading.

A PV system is vulnerable to changing climatic conditions, and the power generation can swing rapidly under passing cloud conditions. Wild variations are not acceptable to the utility authorities who prescribe an acceptable power ramping rate. This aspect has been analysed, and an emulator which can take care of such variations has been incorporated in the emulator described in [56].

6 Conclusion and Future Scope

This paper has presented a detailed summary of the different topologies and control strategies used to configure solar photovoltaic emulators. The issues involved and the relative merits have been outlined. It is foreseen that this would give an overview of the technology and push people to explore new avenues in configuring solar simulators. As a further extension of this, the optimisation techniques used in emulators can be further explored and new techniques like grey wolf optimisation and teacher–learner-based optimisation can be pursued [57, 58].

References

1. Shahabuddin M, Riyaz A, Asim M, Shadab MM, Sarwar A, Anees A (2018) Performance based analysis of solar PV emulators: a review. In: 2018 Proceedings of the IEEE international conference on computational and characterization techniques in engineering & sciences (CCTES), Integral University, Lucknow, India, 14–15 Sept 2018
2. Prasanth Rama J, Manghania H, Pillaia DS, Sudhakar Babua T, Miyatakeb M, Rajasekar N (2018) Analysis on solar PV emulators: a review. *Renew Sustain Energy Rev* 81:149–160
3. Ayop R, Tan CW (2017) A comprehensive review on photovoltaic emulator. *Renew Sustain Energy Rev* 80:430–452
4. Seo Y-T, Park J-Y, Choi S-J (2016) A rapid I-V curve generation for PV model-based solar array simulators. In: Proceedings of the 2016 IEEE Energy Conversion Congress and Exposition (ECCE), 1–5
5. Salman A, Williams A, Amjad H, Kamran Liaqat Bhatti M, Saad M (2015) Simplified modeling of a PV panel by using PSIM and its comparison with laboratory test results. In: Proceedings of the IEEE
6. Esfandiari S, Montazeri SH, Milimonfared J (2020) Improvement of a high-accuracy photovoltaic emulator by considering wind effect. In: Proceedings of the IEEE
7. Abdelghani AB-B, Sethom HBA (2020) Modeling PV installations under partial shading conditions. *SN Appl Sci* 2:627
8. Park S, Kim M, Jung J-H (2020) Effective in-laboratory test method for PV power generation with enhanced PV emulation accuracy. *J Power Electron Online* in May 2020
9. Zhou Z, Macaulay J (2017) An emulated PV source based on an unilluminated solar panel and DC power supply. *Energies* 10(2017):1–20
10. Nousiainen L, Puukko J, Maki A, Messo T, Huusari J (2013) Photovoltaic generator as an input source for power electronic converters. *IEEE Trans Power Electron* 28(6)
11. Buso S, Spiazzi G, Meneghini M (2013) Laboratory PV generator for MPPT dynamic response testing. In: Proceedings of the IEEE
12. Dafalla Y, Osman M (2016) A solar simulator for the renewable energy instruction laboratory. In: 2016 Proceedings of the IEEE conference on technologies for sustainability
13. Kuisis T, Aswat M, Nixon K, Cronje W (2020) Design of a 90 W low cost solar emulator for testing MPPT algorithms on PV based energy systems. In: Proceedings of the IEEE
14. Martínez JR, Rengifo HR, Córdoba JS, Palacios J, Posada J (2019) Design and implementation of a multiplier SEPIC converter to emulate a photovoltaic system using power HIL. In: Proceedings of the IEEE
15. Jayawardana I, Ho CNM, Pokharel M (2019) Design and implementation of switch-mode solar photovoltaic emulator using power-hardware-in-the-loop simulations for grid integration studies. In: Proceedings of the IEEE
16. Zhao J, Kimball JW (2012) A digitally implemented photovoltaic simulator with a double current mode controller. In: Proceedings of the IEEE
17. Wandhare RG, Agarwal V (2011) A low cost, lightweight and accurate photovoltaic emulator. In: Proceedings of the IEEE
18. D’Cruz R, Rajesh M (2015) Half bridge LLC resonant DC-DC converter for solar array simulator application. In: Proceedings of the IEEE
19. Chang C-H, Cheng C-A, Cheng H-L (2014) Modeling and design of the LLC resonant converter used as a solar-array simulator. *IEEE J Emerg Sel Top Power Electron*
20. Chang C-H, Chang E-C, Cheng H-L (2013) A high-efficiency solar array simulator implemented by an LLC resonant DC–DC converter. *IEEE Trans Power Electron* 28(6):3039–3046
21. Chang C-H, Lin C, Ku C-W (2010) A high efficiency solar array simulator implemented by an LLC resonant DC/DC converter. In: Proceedings of the IEEE international power electronics conference
22. Cao W, Ma Y, Wang J, Yang L, Wang J, Wang F, Tolbert LM (2013) Two-stage PV inverter system emulator in converter based power grid emulation system. In: Proceedings of the IEEE

23. Freitas SP, Fernandes NAC, Mendes VF, Cupertino AF, Pereira HA (2017) An improved solar array simulator topology based on LCL filter. In: Proceedings of the IEEE
24. Viglus FJ, Casaro MM (2016) Photovoltaic array emulation using a three-phase DC-DC converter with galvanic isolation. In: 2016 12th proceedings of the IEEE international conference on industry applications (INDUSCON), Curitiba, pp 1–8
25. Schofield DMK, Foster MP, Stone DA (2011) Low-cost solar emulator for evaluation of maximum power point tracking methods. *Electron Lett* 47(3)
26. Moussa I, Khedher A, Bouallegue A (2019) Design of a low-cost PV emulator applied for PVECS. *Electronics* 8:232
27. Koran A, LaBella T, Lai J-S (2014) High efficiency photovoltaic source simulator with fast response time for solar power conditioning systems evaluation. *IEEE Trans Power Electron* 29(3):1285–1297
28. Gadelovits S, Sitbon M, Kuperman A (2014) Rapid prototyping of a low-cost solar array simulator using an off-the-shelf DC power supply. *IEEE Trans Power Electron* 29(10)
29. Kapoor D, Sodhi P, Deb D (2012) Solar panel simulation using adaptive control. In: 2012 Proceedings of the IEEE international conference on control applications (CCA) Part of 2012 IEEE Multi-conference on systems and control, 3–5 Oct 2012
30. Dolan DSL, Durago J, Taufik (2011) Development of a photovoltaic panel emulator using Labview. In: Proceedings of the IEEE
31. Agrawal J, Aware M (2012) Photovoltaic system emulator. In: 2012 Proceedings of the IEEE international conference on power electronics, drives and energy systems, 16–19 Dec 2012, Bengaluru, India
32. Altin N, Yildirimogluglu T (2013) LabVIEW/MATLAB based simulator for grid connected PV system. In: 4th international conference on power engineering, energy and electrical drives, Istanbul, Turkey, 13–17 May 2013
33. Xenophontos A, Rarey J, Trombetta A, Bazzi AM (2014) A flexible low-cost photovoltaic solar panel emulation platform. In: Proceedings of the IEEE
34. Tornez-Xavier GM, Gómez-Castañeda F, Moreno-Cadenas JA, Flores-Nava LM (2013) FPGA development and implementation of a solar panel emulator. In: Proceedings of the IEEE 10th international conference on electrical engineering, computing science and automatic control (CCE) Mexico City, Mexico. 30 Sept–4 Oct 2013
35. Ickilli D, Can H, Parlak KS (2011) Development of a FPGA-based photovoltaic panel emulator based on a DC/DC converter. In: Proceedings of the IEEE
36. Koutroulis E, Kalaitzakis K, Tzitzilonis V (2006) Development of an FPGA-based system for real-time simulation of photovoltaic modules. In: Proceedings of the seventeenth IEEE international workshop on rapid system prototyping
37. Moussa I, Bouallegue A, Khedher A (2017) Development of a low cost PV simulator based on FPGA technology. In: Proceedings of the IEEE
38. Jin S, Zhang D (2016) A simple control method of open-circuit voltage for the FPGA-based solar array simulator. In: 2016 Proceedings of the IEEE international conference on power and renewable energy
39. Escobar G, Lopez-Sanchez MJ, Llenez IE, Ordonez EE, Hernandez-Gomez M (2014) A combined controller for a PV simulator. In: Proceedings of the IEEE
40. Shinde UK, Kadwane SG, Keshri RK, Gawande SP (2017) Dual mode controller-based solar photovoltaic simulator for true PV characteristics. *Can J Electr Comput Eng* 40(3):237–245
41. Mahmud MH, Zhao Y, Wang L (2017) A high-bandwidth PV source simulator using a sliding mode controlled interleaved buck converter. In: Proceedings of the IEEE
42. Shinde UK, Kadwane SG, Gawande SP, Keshri R (2016) Solar PV emulator for realizing PV characteristics under rapidly varying environmental conditions. In: Proceedings of the IEEE
43. Cordeiro A, Foito D, Fernão Pires V (2015) A PV panel simulator based on a two quadrant DC/DC power converter with a sliding mode controller. In: Proceedings of the IEEE international conference on renewable energy research and applications, Palermo, Italy
44. Mahmud MH, Zhao Y (2018) Sliding mode duty cycle control with current balancing algorithm for an interleaved buck converter-based PV source simulator. *IET Power Electron*

45. Ullah N, Nisar F, Alahmadi AA (2020) Closed loop control of photovoltaic emulator using fractional calculus. *IEEE Access* 8
46. Cupertino AF, Santos GV, Cardoso EN, Pereira HA, Mendes VF (2015) Modeling and design of a flexible solar array simulator. In: *Proceedings of the IEEE*
47. Garg P, Priyanshi, Bhuvaneshwari G (2018) Power electronic circuit based implementation of a solar PV emulator using a power factor corrected buck converter. In: *Proceedings of the IEEE*
48. Chariag D, Sbita L (2017) Design and simulation of photovoltaic emulator. In: *Proceedings of the IEEE*
49. Mishra S, Raju S, Kshirsagar A, Mohan N (2018) An extremely low-cost multi-panel PV emulator for research and education. In: *Proceedings of the IEEE*
50. Balato M, Liccardo A, Petrarca C (2020) Dynamic boost based DMPPT emulator. *Energies* 13:2921
51. Suresh Babu G, Sai Varun NR (2020) A novel technique to observe the performance of virtual solar PV module system. In: *Innovations in electrical and electronics engineering, Lecture Notes in Electrical Engineering*, pp 653–661
52. Sharma S, Joshi D (2020) Analysis of designed PV Emulator using FOPID controller and fuzzy logic controller by load variation. *J Inf Optim Sci* 41(1):283–292
53. Alaoui M, Maker H, Mouhsen A (2019) Solar photovoltaic emulation under partial shading conditions. In: *International meeting on advanced technologies in energy and electrical engineering*
54. Alaoui M, Maker H, Mouhsen A (2020) A new PV source emulator based on modified hybrid referencing technique with nonlinear Lyapunov controller. In: *Proceedings of the IEEE*
55. Alaoui M, Maker H, Mouhsen A, Hihhi H (2020) Photovoltaic emulator of different solar array configurations under partial shading conditions using damping injection controller. *Int J Power Electron Drive Syst (IJPEDS)* 11(2):1019–1030
56. Chen X, Yang D, Lim E, Wen H, Yan K, Kirtley J (2020) Power ramp-rates of utility-scale PV systems under passing clouds: Module level emulation with cloud shadow modeling. *Appl Energy* 268:
57. Rathore NS, Singh VP, Kumar B (2018) Controller design for doha water treatment plant using grey wolf optimization. *J Intell Fuzzy Syst* 5329–5336
58. Singh SP, Singh V, Singh VP (2019) Analytic hierarchy process based approximation of high-order continuous systems using TLBO algorithm. *Int J Dyn Control* 7:53–60

An Enhanced Boost Z-Source Inverter Topology for Electrical Vehicle Applications



S. Nagaraja Rao , V. Praveen Kumar , and Veerabhadra 

1 Introduction

The universal motive to reduce the carbon emissions has given thrive for the emergence of electric vehicles with optimum fuel efficiency, ultra-low emissions, and excellent performance. Despite of many operational challenges, the EVs are promising potential solution for emissionless transportation [1]. The heart of EV is drive system which comprises of a motor for torque production and a power electronic controller for controlling [2–6]. To achieve smooth and accurate control of the motor, the converter circuit must be selected optimally.

The converter with single-stage conversion capability and high fault tolerance and high efficiency must be used as controller. The Z-source inverters will encompass all the above features and able to sustain large input variations. The problems with discontinuous input current such as degradation in battery life have been addressed in the SL-IqZSI topology. The reliability of the SL-IqZSI topology is increased by an extra shoot-through states, during which the converter operates in boost mode by storing the energy in the inductors [7–11].

In [9, 12–15], SL-qZSI has few demerits like increased voltage stress across the switches and capacitors, enormous inrush current, and low boost factor (B). The various control techniques were used to minimize the drawbacks of SL-qZSI topology and the value of B is enhanced with less component ratings, SL-IqZSI topology is proposed.

S. Nagaraja Rao (✉) · V. Praveen Kumar · Veerabhadra
Department of Electrical Engineering, Ramaiah University of Applied Sciences, Bangalore,
Karnataka, India
e-mail: nagarajarao.ee.et@msruas.ac.in

V. Praveen Kumar
e-mail: praveen.ee.et@msruas.ac.in

Veerabhadra
e-mail: veerabhadra.ee.et@msruas.ac.in

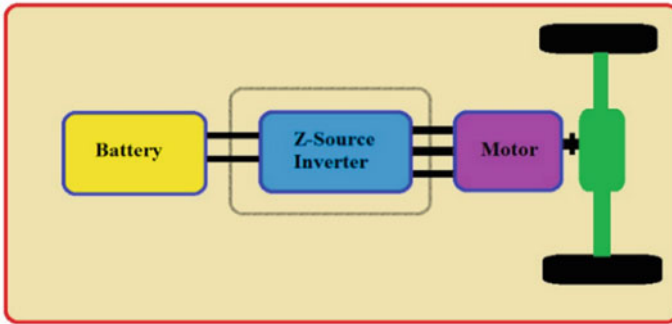


Fig. 1 Block diagram

During the start-up, existing SL-qZSIs can limit the inrush current, thereby protecting the switches. With the same ‘K’, the SL-IqZSI topology possesses additional boost ability and it limits the voltage stress on devices and it also minimizes inductor input current ripple. Additionally, the efficiency of the SL-IqZSI topology is improved. These features ideally make the application of SL-IqZSI in EV. Figure 1 shows the block diagram wherein the proposed SL-IqZSI is feeding a motor from the battery pack. SL-IqZSI topology is analyzed and compared with the existing SL-qZSI topology in detail. Hence, from the analytical study and the simulated result of the SL-IqZSI topology, it is proved that in comparison with the existing SL-qZSI topology, boost capability is enhanced considerably and the efficiency of the converter is also improved.

2 Structure and Mathematical Analysis of the Existing SL-qZSI Topology

The topology of SL-qZSI is represented in Fig. 2. It has single SL cell constituted by two inductors ($L2, L3$) and three diodes ($D1, D2,$ and $D3$), in addition to this it has an inductor $L1$, two capacitors ($C1$ and $C2$), and diode Din . The merits of this topology are reduction in device count and suppression of inrush current.

The voltage across capacitors are given by

$$V_{c1} = \left(\frac{1 - K}{1 - 2K - K^2} \right) * V_{dc} \tag{1}$$

$$V_{c2} = \left(\frac{2K}{1 - 2K - K^2} \right) * V_{dc} \tag{2}$$

The DC-link voltage obtained in (3) by adding V_{c1} and V_{c2}

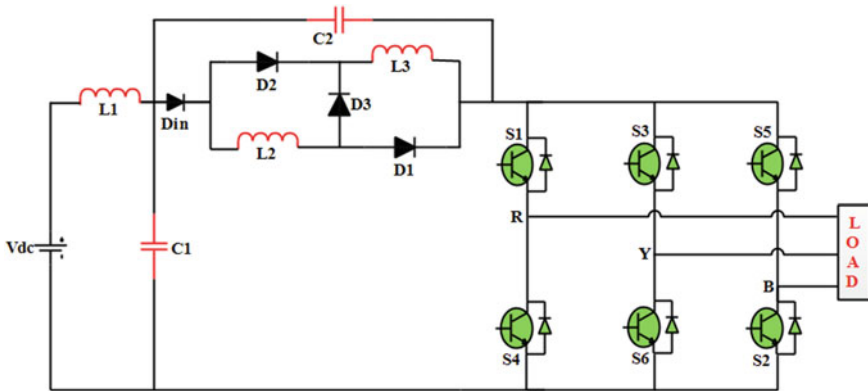


Fig. 2 Topology of SL-qZSI

$$V_{dc - link} = \left(\frac{1 + K}{1 - 2K - K^2} \right) V_{dc} \tag{3}$$

$$V_{dc - link} = B V_{dc} \tag{4}$$

The SL-qZSI boost factor is given by

$$B = \frac{1 + K}{1 - 2K - K^2}, \quad \text{where } K = \frac{T_{on}}{T} \tag{5}$$

3 Theoretical Analysis of the Proposed SL-IqZSI Topology

3.1 Operation

Introducing trivial changes in the existing SL-qZSI, a new topology emerges with improved boost factor. The SL-IqZSI topology is depicted in Fig. 3. The diode in the SL cell is interchanged by a capacitor which provides boots trapping. The suggested topology has operating principle and operating states alike to existing SL-qZSI. The circuits given in Fig. 4a, b describe the modes of operation. In shoot-through state, the $L2-C3-L3$ will become parallel, $C3$ alone charged and remaining capacitors will be discharged. And all the inductors charged simultaneously. This process is depicted in Fig. 4a.

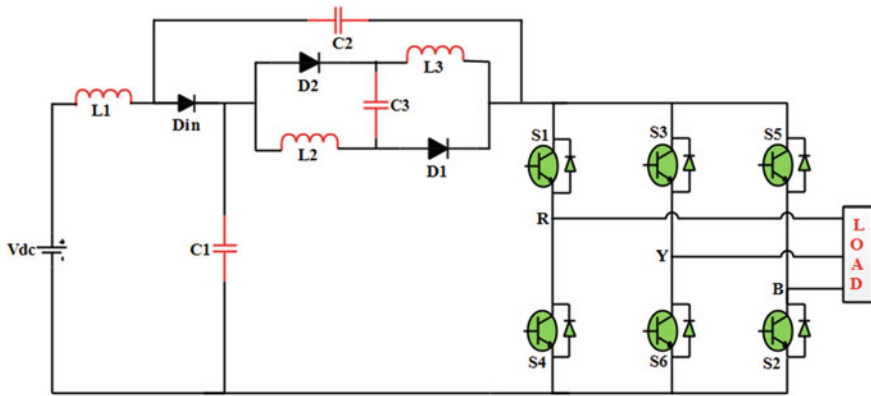


Fig. 3 SL-IqZSI topology

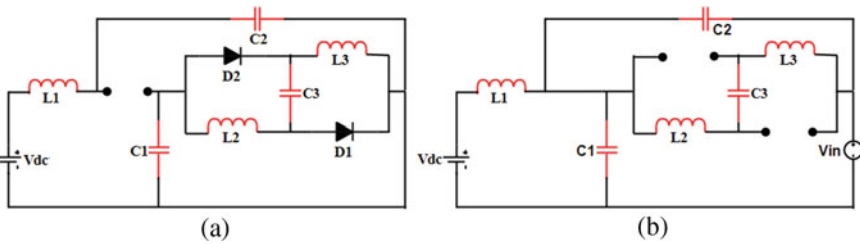


Fig. 4 SL-IqZSI topology, a shoot-through state, b non-shoot-through state

3.2 Mathematical Analysis

The equations governing this state are

$$V_{in} + V_{C2} = V_{L1} \tag{6}$$

$$V_{C1} = V_{C3} = V_{L2} = V_{L3} \tag{7}$$

During non-shoot-through state, the complementary operation takes place wherein the energy stored in the inductors is retrieved to DC-link, C_3 discharges and remaining capacitors will be charged. The equations for this state are

$$V_{in} + V_{L1} = V_{C1} \tag{8}$$

$$V_{C2} = V_{C3} + V_{L2} + V_{L3} \tag{9}$$

$$V_{dc-link} = V_{C1} + V_{C2} \tag{10}$$

Boost Factor Analysis: For the simplicity of analysis, all components are assumed to be ideal and all the capacitors ($C_1, C_2, C_3 = C$) and inductors ($L_1, L_2, L_3 = L$) have the same value. The period in which inductors store energy is KT and release energy in the period $(1 - K) * T$. Applying the volt-sec balance principle at the inductor at L_1 .

$$KT * (V_{in} + V_{C2}) = (1 - K)T * (V_{C1} - V_{in}) \tag{11}$$

From (8)–(10).

$$V_{C1} = \frac{1}{1 - K} V_{in} + \frac{K}{1 - K} V_{C2} \tag{12}$$

The voltages of L_2 and L_3 are equal in shoot-through state because of the symmetry of the bridge network (i.e., $V_{L1} = V_{L2} = V_{C3}$), in non-shoot-through state

$$V_{L1} = V_{L2} = \frac{V_{C2} - V_{C3}}{2} \tag{13}$$

Again applying principle of volt-sec balancing at L_2 we get

$$DTV_{C3} = \frac{1}{2}(V_{C2} - V_{C3})(1 - K)T \tag{14}$$

The above equation can be rewritten as

$$V_{C3} = \frac{1 - K}{1 + K} V_{C2} \tag{15}$$

In one complete cycle, the capacitor voltage does not alter and thus it can be viewed as a source of voltage, and this gives rise to

$$V_{C1} = V_{C3}. \tag{16}$$

Further mathematical simplification produces

$$\frac{1}{1 - K} V_{in} + \frac{K}{1 - K} V_{C2} = \frac{1 - K}{1 + K} V_{C2} \tag{17}$$

Therefore, V_{C2} is given as

$$V_{C2} = \frac{1 + K}{1 - 3K} V_{in} \tag{18}$$

Substituting V_{C2} in V_{C3} gives rise to

$$V_{C1} = V_{C3} = \frac{1 - K}{1 - 3K} V_{in} \tag{19}$$

Hence, the DC-link voltage is given as,

$$V_{dc-link} = \frac{2}{1 - 3K} V_{in} \tag{20}$$

The boost factor as, $B = \frac{2}{1-3K}$.

4 SBC Technique

The switching pulses are produced in comparison with the reference signal with 5 kHz triangular wave. In the present work, sine-based and THI-based reference signals were used. To control over shoot-through ratio ‘K’, a constant signal of equal or greater magnitude with the reference signal is used; this technique is called as SBCT. The switching pulse using SBCT methodology for both sine and third harmonic reference signals is shown in Fig. 5.

The mathematical equation governing the third harmonic injection-based reference signal is given by

$$V_{THI_REF} = \frac{2}{3\sqrt{3}} \sin \theta + \frac{1}{3\sqrt{3}} \sin 3\theta \tag{21}$$

The modulation index is given as

$$M = \frac{\text{Magnitude of reference signal}}{\text{Magnitude of carrier Signal}} \tag{22}$$

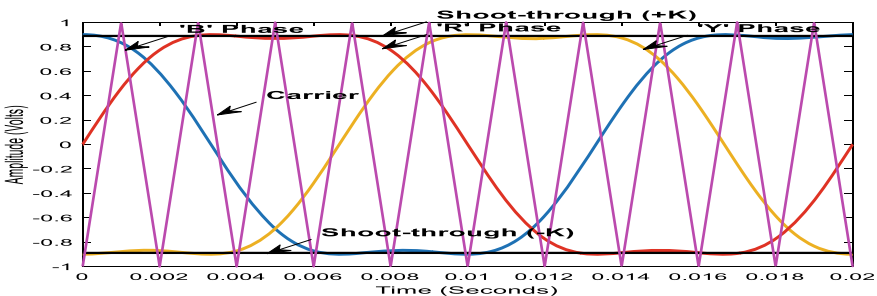


Fig. 5 THI reference wave-based shoot-through modulation technique

From the above (21), it is evident that the modulation index value M can be taken up to 1.154 in THI-based reference, whereas in sine-based reference M value is constrained for a maximum value of 1.

5 Simulation Results

5.1 Simulation Results of SL-qZSI

Figures 6 and 7 depict the simulated results of the SL-qZSI using SBC technique for two combinations of K and M . The sine-based and THI-based reference signals are used to generate PWM pulses. From Figs. 6b and 7b, it is observed that the voltages of $C1$ (V_{c1}) and $C2$ (V_{c2}) are 27 V, 6 V and 36.5 V, 20.6 V are in good agreement with theoretical values as per the equation given in (1) and (2) for both the sine and THI reference signals, respectively. In Fig. 6a, the DC-link voltage is raised to 33.4 V. In Fig. 6c, the output voltage is raised to 33.4 V for 24 V input with a B value of 1.39 for sine reference. The input and output voltages of SL-qZSI at $K = 0.22$ and $M = 0.9$ for THI reference have been represented in Fig. 7. The obtained results through simulation are matching with the theoretical values.

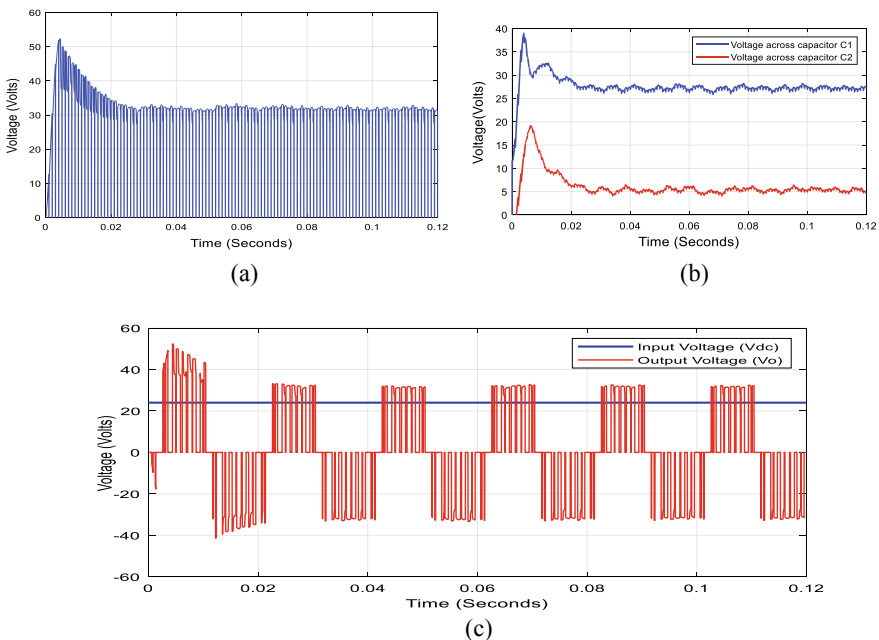


Fig. 6 Simulation results of SL-qZSI at $K = 0.1$ and $M = 0.9$, **a** DC-link voltage, **b** capacitor voltages and **c** input and output voltages

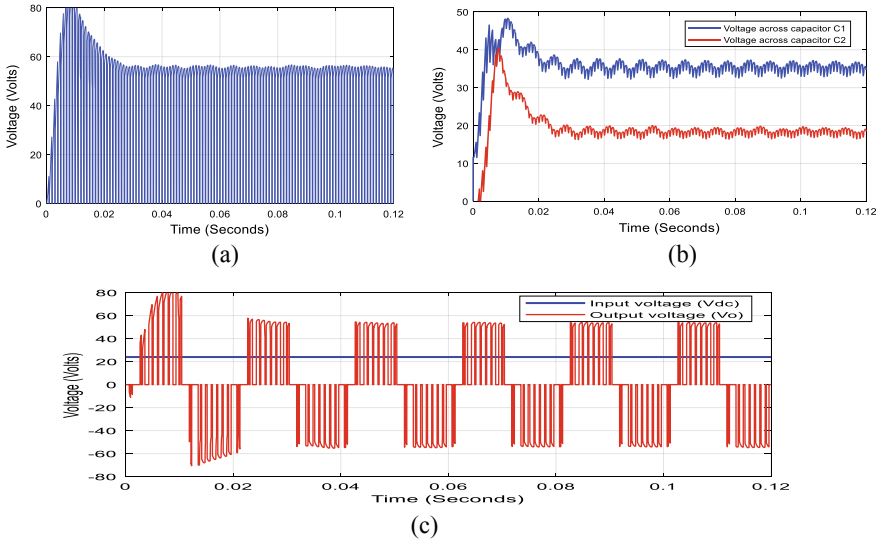


Fig. 7 Simulation results of SL-qZSI at $K = 0.22$ and $M = 0.9$, **a** DC-link voltage, **b** capacitor voltages and **c** input and output voltages

5.2 Simulation Results of SL-IqZSI

Figures 8 and 9 show the simulation results of SL-qZSI using SBC technique for two combinations of K and M . From Figs. 8b and 9b, it is observed that the voltages across C_1 and C_2 are 30.8 V, 37 V and 55 V, 77 V are in good agreement with theoretical values as per the equation given in (1) and (2) for both the sine and THI reference signals, respectively. The DC-link voltage shown in Fig. 8a is raised to 68.5 V. In Fig. 8c, the output voltage is raised to 68.5 V for 24 V input with a B value of 2.85 for sine reference. In addition, the input and output voltages of SL-IqZSI at $K = 0.22$ and $M = 0.9$ for THI reference have been represented in Fig. 9c. The obtained results through simulation are matching with the theoretical values.

6 Comparison of SL-qZSI and SL-IqZSI Topologies

Table 1 represents the comparative analysis of SL-qZSI and SL-IqZSI topologies using sine reference-based SBC technique with theoretical and simulation results. The comparative analysis is made on output voltage, voltage gain, and boost factor for different ‘ K ’ and ‘ M ’ values. It is evident that, for 24 V input, the simulated output of 52.92 V is obtained with a boost factor of 2.14 using SL-qZSI for ‘ K ’ and ‘ M ’ values of 0.3 and 0.7, respectively, using sine reference-based SBC technique. Similarly, the output voltage of 119.22 V is obtained with a boost factor of 5 using

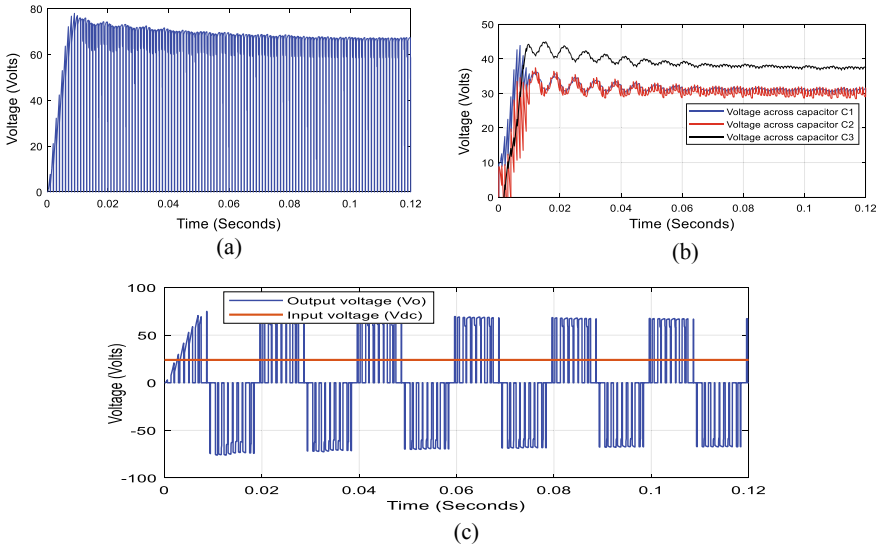


Fig. 8 Simulation results of SL-IqZSI at $K = 0.1$ and $M = 0.9$ **a** DC-link voltage, **b** capacitor voltages, and **c** input and output voltages

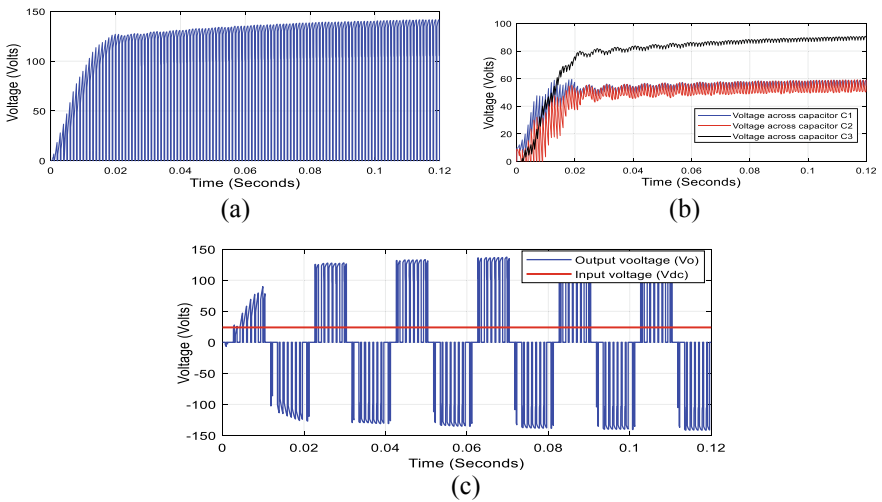


Fig. 9 Simulation results of SL-IqZSI at $K = 0.22$ and $M = 0.9$ **a** DC-link voltage, **b** capacitor voltages and **c** input and output voltages

Table 1 Analysis of SL-qZSI and SL-IqZSI topologies using sine reference-based SBC

S. No.	M	K	SL-qZSI topology				SL-IqZSI topology			
			Expected V_o	Obtained V_o	B	Voltage gain	Expected V_o	Obtained V_o	B	Voltage gain
1	1	0	24	23.95	1	1	24	23.95	2	2
2	0.9	0.1	33.36	32.91	1.39	1.25	68.4	67.68	2.85	2.56
3	0.8	0.2	51.36	52.92	2.14	1.71	120	119.22	5	4

SL-IqZSI for the same ' K ' and ' M '. Therefore, the value of B of SL-qZSI is quite high in comparison with the SL-IqZSI.

Table 2 represents the comparative analysis of SL-qZSI and SL-IqZSI topologies using THI reference-based SBC technique with theoretical and simulation results. The comparative analysis is made on output voltage, voltage gain, and boost factor for different ' K ' and ' M ' values. It is evident that, for an input of 24 V, the simulated output of 99.64 V is obtained with a boost factor of 4.19 using SL-qZSI for ' K ' and ' M ' values of 0.3 and 0.7, respectively, using THI reference-based SBC technique. Similarly, the output voltage of 478.11 is obtained with a boost factor of 20 using SL-IqZSI for the same ' K ' and ' M ' values. Therefore, the value of B of SL-qZSI is quite high when compared to SL-IqZSI and also a higher output voltage can be obtained with THI-based SBC when compared to sine reference-based SBC for the same ' M '.

Further, from Tables 1 and 2, the simulation results of SL-qZSI and SL-IqZSI confirm the theoretical values with an acceptable error of 1%. Figure 10a shows the boost factor analysis of SL-qZSI and SL-IqZSI topologies with a variation of ' K ' from 0 to 0.3. It can be concluded that the boost factor of both the topologies is increased by varying ' K ' and the SL-IqZSI is having the highest boost factor in comparison with SL-qZSI with both shoot-through and non-shoot-through conditions. Figure 10b indicates the voltage gain of SL-qZSI and SL-IqZSI topologies with a variation of ' M ' from 0.7 to 1. Hence, it can be concluded that the voltage gain of both the topologies is decreased by varying ' M ' and the SL-IqZSI is having the highest voltage gain when compared with SL-qZSI with both shoot-through and non-shoot-through conditions.

7 Conclusion

In this paper, three-phase, two-level SL-IqZSI topology is proposed for EV applications with an enhanced boost ability in comparison with the existing SL-qZSI topology. The proposed SL-IqZSI topology verifies with theoretical analysis and simulated result that it enhances the high boost voltage inversion ability and improves the high efficiency of the conversion. Simulation results are verified with SBCT with sine- and THI-based reference signals. Further, a three-phase, two-level SL-IqZSI topology has been compared with an existing SL-qZSI. From the analytical and simulation studies, it is concluded that the proposed SL-IqZSI topology has enhanced boost factor and voltage gain when compared to existing SL-qZSI.

Table 2 Analysis of SL-qZSI and SL-IqZSI topologies using THI reference-based SBC

S. No.	M	K	SL-qZSI topology				SL-IqZSI topology			
			Expected V_o	Obtained V_o	B	Voltage gain	Expected V_o	Obtained V_o	B	Voltage gain
1	1	0	24	23.95	1	1	24	23.95	2	2
2	0.9	0.22	56.16	55.23	2.34	2.1	141.12	140.54	5.88	5.29
3	0.8	0.3	100.56	99.64	4.19	3.3	480	478.11	20	16

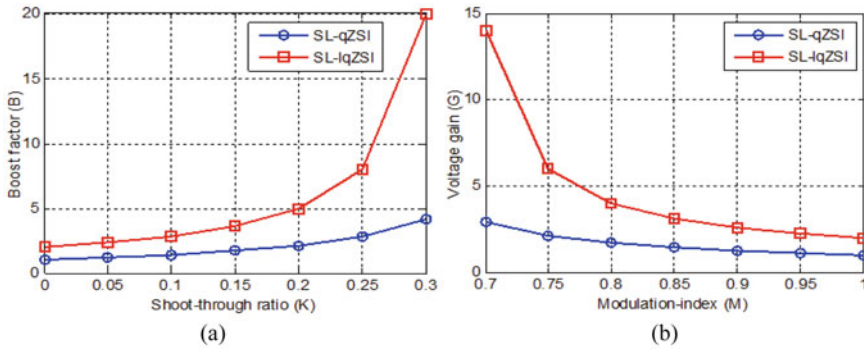


Fig. 10 Analysis of SL-qZSI and SL-lqZSI topologies, **a** boost factor versus shoot-through ratio, **b** voltage gain versus modulation index

References

1. Srijeeth J, Thiagarajan VC, Mohanrajan SR (2018) Z-source dual active bridge bidirectional AC-DC converter for electric vehicle applications. In: 2018 IEEE international conference on power electronics, drives and energy systems (PEDES). IEEE, pp 1–4
2. Senanayake T, Iijima R, Isobe T, Tadano H (2018) Quasi Z-source with single pulse drive inverter for hybrid/electric vehicles. In: 2018 20th European conference on power electronics and applications (EPE'18 ECCE Europe). IEEE, pp P-1
3. Na T, Zhang Q, Dong S, Raheemihaja HJ, Chuai G, Wang J (2019) A soft-switched modulation for a single-phase quasi-Z-source-integrated charger in electric vehicle application. *IEEE Trans Power Electron* 35(5):4602–4612
4. Chauhan AK, Singh SK (2018) Integrated dual-output LZ source inverter for hybrid electric vehicle. *IEEE Trans Transp Electrif* 4(3):732–743
5. Ismeil MA, Kouzou A, Kennel R, Abu-Rub H, Orabi M (2012) A new switched-inductor quasi-Z-source inverter topology. *IEEE*, 978-1-4673-1972-0/12
6. Kai D, Jun M, Jianyong Z, Wei H, Huping B (2013) An improved switched-inductor quasi-Z-source inverter. *IEEE*, 978-1-4799-0073-2/13
7. Deng K, Zheng J, Mei J (2014) Novel switched-inductor quasi-Z-source Inverter. *J Power Electron* 14(1):11–21
8. Yuan J, Yang Y, Blaabjerg F (2020) A switched quasi-Z-source inverter with continuous input currents. *Energies* 13:1390
9. Zhu H, Yu D, Zhu W, Zhou Z (2016) DC-link voltage regulation of bidirectional quasi-Z-source inverter for electric vehicle applications. *IEEE*, 978-1-5090-3528-1/16
10. Chowdhury VR, Saritha B (2014) Comparative analysis of quasi Z-source inverter and active bidirectional converter for hybrid electric vehicle application. *IEEE*, 978-1-4799-6373-7/14
11. Chub A, Husev O, Zakis J, Rabkowski J (2014) Switched-capacitor current-fed quasi-Z-source inverter. *IEEE*, 978-1-4673-9539-7/14
12. Jagan V, Das S (2017) Switched impedance enhanced-boost quasi-Z-source inverter. *IEEE*, 978-1-5386-4318-1/17
13. Singh SA, Carli G, Azeez NA (2017) Modelling, design, control, and implementation of a modified Z-source integrated PV/Grid/EV DC charger/inverter. *IEEE Trans Ind Electron*

14. Misal S, Nagaraj Rao S (2015) Comparative analysis of a 3-phase, 3-level diode clamped ZSI based on modified shoot through PWM techniques. In: International conference on SPICES. IEEE, pp 1–5
15. Nagaraja Rao S, Veerabhadra, Praveen Kumar V (2020) Performance analysis of Z-source inverter topologies for renewable energy sources and fuel cell applications. In: IEEE fourth international conference on distributed computing, VLSI, Electrical Circuits and Robotics

Study of Human Body Temperature and Different Modes of Heat Transfer Using Steady-State Energy Balance Model



Shashikant Das and Sudhakar Subudhi

Abbreviations

CSIG	Cold signals from the body
f_{cl}	Ratio of body area with cloth to without cloth
h_{cv}	Convective heat transfer coefficient
h_{rd}	Radiation heat transfer coefficient ($W/m^2 K$)
I_{cl}	Insulating factor due to clothing ($W/m^2 K$)
LR	Lewis ratio (clo)
m_{bl}	Blood flow per unit of skin area between core and skin (g/sm^2)
m_{rsw}	Sweat production rate per unit skin area (W/m^2)
M	Metabolic rate
Q_{st}	Rate of heat stored inside the body (W/m^2)
Q_{cv}	Convection heat transfer ($^{\circ}C$)
Q_{evp}	Evaporation heat transfer (W/m^2)
Q_{rd}	Radiation heat transfer (W/m^2)
Q_{res}	Respiration heat exchange (W/m^2)
$Q_{e,sk}$	Heat loss by evaporation (W/m^2)
RH	Relative humidity (%)
T_{cl}	Mean outer clothing temperature ($^{\circ}C$)
T_a	Air temperature ($^{\circ}C$)
T_b	Mean body temperature ($^{\circ}C$)
T_{cr}	Body core temperature ($^{\circ}C$)
T_{cr}	Core temperature ($^{\circ}C$)
T_{mrt}	Mean radiation temperature ($^{\circ}C$)
T_{sk}	Skin temperature ($^{\circ}C$)
T_{mrt}	Mean radiant temperature (W/m^2)

S. Das (✉) · S. Subudhi

Department of Mechanical and Industrial Engineering, IIT Roorkee, Roorkee 247667, India

e-mail: sdas@me.iitr.ac.in

W	Work acquire (W/m^2)
WSIG	Warm signals from the body
w_{rsW}	Skin wittedness due to regulatory sweating
ε	Emission coefficient at the body surface
σ	Stefan Boltzmann's constant
α	Fraction of total body mass concentrated in skin compartment

1 Introduction

It is important to study thermoregulatory mechanisms of human body under different conditions and suggest practical ways for providing thermal comforts to the human body. Analytical study helps to predict the behavior and comfort of human, which may not be found through experiments. Moreover, there are conditions for which experiments are difficult to perform or are too expensive. Under those situations, theoretical study becomes a handy tool, which may not give exact results but predicts results close to the actual results. It can help to estimate energy efficiency, safety and tolerance limits in the design of indoor air-conditioning, mines applications, military applications, aerospace, etc. [1, 2].

Several authors have given different models for this kind of study. Fanger [3] has established a steady-state mathematical energy balance model, and this model assumes no energy is stored inside the body. Kilic et al. [4] have derived a steady-state mathematical model of the human body, in which their primary work is to find the core temperature. This study combined the relationship of the heat balance of the human body with thermoregulatory at steady state. They also compare their results with ISO-7730. Cheng et al. [5] have numerically examined the behavior of the human body with surrounding. In their study, they found the interactions of the body with surrounding and self-regulation of the body by different thermoregulatory mechanisms in the change in climatic condition. Stolwijk and Hardy [6] divided the normal man body parts into three sections: head, trunk and extremities along with the central blood compartment. Each cylinder was further divided into two or more concentric layers. In this model, physiological variables as a function of time were calculated by heat transfer equations at core and skin (also muscle for trunk), and the nodes are used for all three compartments along with central blood. Li et al. [7] studied the validation of mean skin temperature by measured and predicted average skin temperature in a warm environment, which includes 21 typical conditions. They also evaluate the efficiency of evaporation of sweat, relations of blood flow and heat loss due to evaporation. Their new predicted modal was compared with two-node model experimentally. For warm environments, they found that their model was statistically precise in determining mean skin temperature.

In this study, a steady-state energy balance model is developed which investigates body temperature and heat transfer. Different modes of heat transfer through the

human body are examined with increase of ambient temperatures. Different physiological parameters like core temperature, mean body temperature, evaporative heat transfer, respiration heat transfer and fractions of body mass concentrate in the skin are investigated with the increase of metabolic rate.

2 Mathematical Modeling

2.1 Steady-State Energy Balance Modal

Human body can be considered as a control volume, and energy balance can be applied on it. A mathematical modeling considering steady-state energy balance modal assumes that no energy is stored inside the body per unit area which is given by

$$(Q_{\text{res}} + Q_{\text{rd}} + Q_{\text{evp}} + Q_{\text{cv}}) = (M - W) \quad (1)$$

where M is metabolic rate, Q_{rd} is radiation heat transfer, Q_{cv} is convective heat exchange, Q_{evp} is evaporation heat loss, Q_{res} represents respiration heat transfer, W is work obtained, and for light activity, work obtain is taken as zero [8, 9].

Considering clothing into account, the heat transfer by radiation is given by Stefan Boltzmann's law [4, 4]. The corresponding equation is expressed by:

$$Q_{\text{rd}} = h_{\text{rd}}(T_{\text{cl}} - T_{\text{mrt}})f_{\text{cl}} \quad (2)$$

$$h_{\text{rd}} = 4\sigma(0.72)\varepsilon(273.15 + ((T_{\text{cl}} + T_{\text{mrt}})/2))^3 \quad (3)$$

where σ represents Stefan Boltzmann's constant, ε represents emission coefficient of outer body part, T_{cl} is the average outer clothing temperature, and T_{mrt} is mean radiation temperature.

The mean radiant temperature (T_{mrt}) is an significant environment parameter, which contributes to the radiation [10]. T_{mrt} cannot be measured directly. Globe thermometer is used to measure T_{mrt} in °C with the help Eq. (4). In this equation, T_{g} refers to the temperature measured by the globe in °C, D represents globe diameter in meter, V is air velocity in m/s, ε is black globe emissivity, and T_{a} is air temperature in °C.

$$T_{\text{mrt}} = -273.1 + \left[(273.15 + T_{\text{g}})^4 + \frac{v_{\text{a}}^{0.6} \times 1.1 \times 10^8}{D^{0.4} \varepsilon} (T_{\text{g}} - T_{\text{a}}) \right]^{0.25} \quad (4)$$

The convection heat transfer from the surface of the body (considering cloths into account) to the surrounding can be expressed by [4]

$$Q_{cv} = (T_{cl} - T_a) f_{cl} h_{cv} \quad (5)$$

h_{cv} represents the convective heat transfer coefficient in $W/m^2 \text{ } ^\circ C$ and can be determined as the maximum value of the following three equations [11]:

$$h_{cv} = (P_B/760)^{0.53} \times 3 \quad (6)$$

$$h_{cv} = (P_B V/760)^{0.53} \times 3 \quad (7)$$

$$h_{cv} = [(M/58.2) - 0.85]^{0.53} 5.66 \quad (8)$$

where P_B represents barometric pressure in mmHg. f_{cl} represents cloth area factor, which is the ratio of whole body area with cloth to without cloth, and it can be estimated by [7]

$$f_{cl} = 0.3I_{cl} + 1 \quad (9)$$

The mean outer surface temperature of clothing (T_{cl}) can be estimated by [4]

$$\begin{aligned} T_{cl} = & -(M - W) \times 0.0275 - R_{cl}[(M - W) - 0.42 \times (-58.2 + (M - W)) \\ & - 3.05(5.73 - P_a - 0.007(M - W)) - 0.0014(34 - T_a)M \\ & - 0.0173(5.87 - P_a)M] + 35.7 \end{aligned} \quad (10)$$

The respiration heat exchange is the sum of dry heat exchange (sensible) and evaporative heat transfer (latent), and it can be estimated by [12]

$$Q_{res} = [0.0023(44 - P_a) + 0.0014(34 - T_a)]M \quad (11)$$

Evaporative heat loss ($Q_{e,sk}$) is the sum of heat transfer due to diffusion of water from the skin ($Q_{e,dif}$) and evaporation of sweat secretion because of thermoregulation ($Q_{e,rsw}$), which is controlled by sweat gland, and it can be estimated by [13]

$$Q_{e,rsw} = h_{fg} \times m_{rsw} \quad (12)$$

$$Q_{e,dif} = 0.06(1 - w_{rsw})Q_{e,max} \quad (13)$$

w_{rsw} denotes skin wittedness, and it can be estimated by

$$w_{rsw} = \frac{Q_{e,rsw}}{Q_{e,max}} \quad (14)$$

$Q_{e,max}$ denotes maximum evaporation potential, and it is determined by [13]

$$Q_{e,\max} = \frac{P_{sk,s} - P_a}{\frac{R_{cl}}{LR} + \frac{1}{f_{cl}h_{cv}LR}} \quad (15)$$

LR represents Lewis ratio, which is the function of skin temperature, and it can be estimated by [13]

$$LR = \frac{(273.15 + T_{sk}) \times 15.15}{273.15} \quad (16)$$

m_{rsw} represents sweat mass flow rate per unit skin area, and it can be determined by [4]

$$Q_{rsw} = 4.7 \times 10^{-5} \times \exp\left(\frac{WSIG_{sk}}{10.7}\right) \times WSIG_b \quad (17)$$

$$WSIG_b = -36.49 + T_b \quad (18)$$

$$WG_{sk} = -33.7 + T_{sk} \quad (19)$$

where T_b represents average body temperature which is the weighted average of skin and core temperature of the body. The skin temperature, which delivers thermal comfort, is determined by [4]

$$T_{sk,req} = -0.0275(M - W) + 35.7 \quad (20)$$

$$Q_{rsw,req} = 0.42 \times (M - 58.15 - W) \quad (21)$$

$$T_b = T_{sk} \times \alpha + T_{cr} \times (1 - \alpha) \quad (22)$$

Equation (23) α represents fractions of mass concentrate in the skin section of the body. m_{bl} defines the blood flow per unit of skin area between core and skin. $CSIG$ and $WSIG$ are body cold and warm thermoregulatory signals, respectively, [12].

$$\alpha = \frac{0.745}{0.585 + (3600 \times m_{bl})} + 0.0418 \quad (23)$$

$$m_{bl} = \frac{200WSIG_{cr} + 6.3}{3600(0.5CSIG_{sk} + 1)} \quad (24)$$

3 Flow Chat of the Calculation

Steady-state energy model is solved using simulation shown in Fig. 1. Following are steps which have been used to solve this mathematical model. In first step, input parameters required are metabolic rate, core temperature, air temperature, air velocity, relative humidity, work obtained, clothing insulation and mean radiant temperature. The core temperature is considered as initial guess. In next step of the simulation, using input parameters, sensible heat transfer through the skin and respiratory heat transfer are determined. Further core temperature is determined using $T_{sk,req}$, $Q_{e,rsw}$ and $Q_{res,req}$. Core temperature is the only unknown in this steady-state energy balance model, which can be solve using present simulation. Lastly, evaporative heat transfer and all desired parameters are determined.

3.1 Validation of Present Model

Firstly, the present simulated model is solved for 21 °C and 50% RH, and then, it is compared with results of Hoppe and Martinac [14]. For the validation, the input parameters of the present model are taken as follows: $M = 80 \text{ W/m}^2$, $V = 0.05 \text{ m/s}$, $RH = 50\%$, $T_a = T_{rd} = 21 \text{ }^\circ\text{C}$, $I_{cl} = 1 \text{ Clo}$. Table 1 shows the present model which is found to give results, which is in close agreement with Hoppe and Martinac. Therefore, it is used for further study.

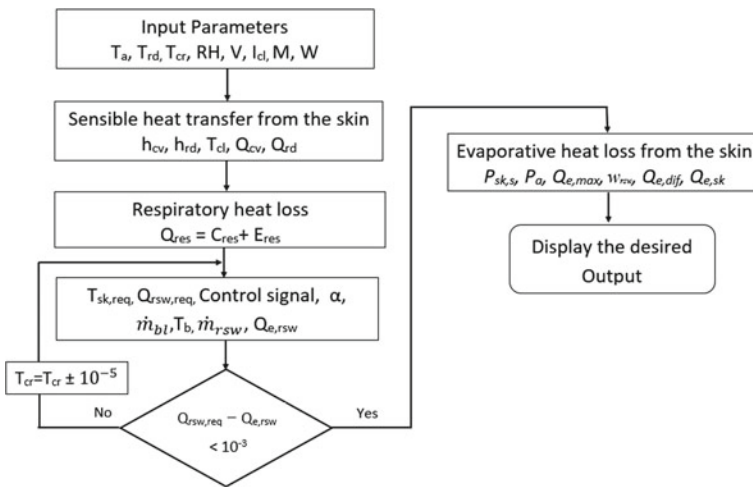


Fig. 1 Simulation of present model

Table 1 Validation of present model with Hoppe and Martinac

	Q_{res} (W/m ²)	$Q_{e,sk}$ (W/m ²)	Q_{cv} (W/m ²)	Q_{rd} (W/m ²)	Q_{total} (W/m ²)
Hoppe and Martinac [14]	6.67	18.46	24.62	30.26	80.01
Present modal	7.86	15.78	26.39	29.38	79.42

4 Results and Discussion

4.1 Effect on the Body Due to the Change of Metabolic Rate

The variations of mean body temperature, core temperature and skin temperature that deliver comfort, with an increase in activity level, are shown in Fig. 2. The fixed input parameters used to find body temperature with increase in activity level are as follows: $T_a = T_{mrt} = 24\text{ }^\circ\text{C}$, $V = 0.05\text{ m/s}$, $RH = 40\%$, $I_{cl} = 0.5\text{ Clo}$. The required skin temperature, which delivers comfort, is calculated from Eq. 20. The graph shows a decrease in required skin temperature with an increase in activity level. In order to achieve thermal comfort when metabolic rate increases, skin temperature should reduce. Figure 2 shows that with an increase of activity level, body core temperature increases, and to compensate this increase of core temperature to attain thermal comfort, skin temperature is supposed to decrease. The mean body temperature (calculated from Eq. 22) also increases with increase in metabolic rate and follow similar path that of core temperature. However, mean body temperature is found lower than body core temperature. The possible reason may be that for the calculation of mean body temperature, it takes higher weightage of core temperature than that of skin temperature.

With the increase of metabolic rate from 60 to 120 W/m², the variations of heat transfer due to respiration and evaporation are shown in Fig. 3. The fixed input

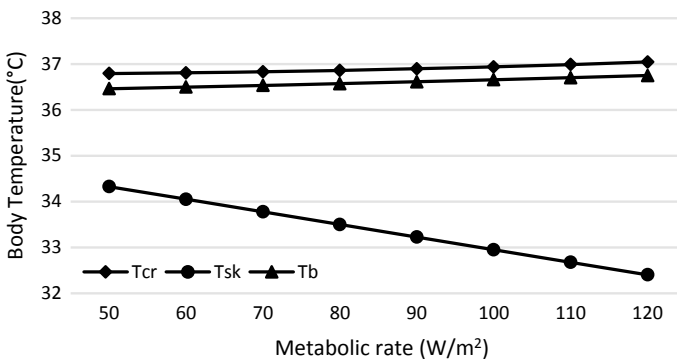


Fig. 2 Body temperature variations with different metabolic rate ($T_a = T_{mrt} = 24\text{ }^\circ\text{C}$, $V = 0.05\text{ m/s}$, $RH = 40\%$, $I_{cl} = 0.5\text{ clo}$)

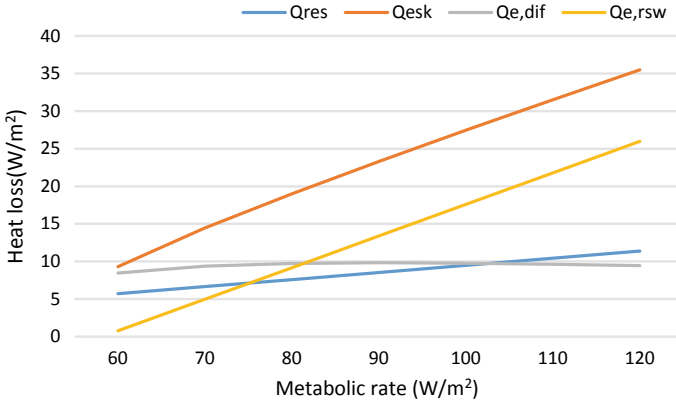


Fig. 3 Required heat transfer variations with metabolic rate ($T_a = T_{mrt} = 24\text{ }^\circ\text{C}$, $V = 0.05\text{ m/s}$, $I_{cl} = 0.5\text{ clo}$, $RH = 40\%$)

parameters used here are as follows: $T_a = T_{mrt} = 24\text{ }^\circ\text{C}$, $V = 0.05\text{ m/s}$, $I_{cl} = 0.5\text{ clo}$, $RH = 40\%$. Heat loss due to respiration heat transfer (Q_{res}) increases from 5.7 to 11.4 W/m^2 but this increase is very less compare to heat loss due to evaporation. The heat loss due to evaporation from the skin ($Q_{e,sk}$) increases from 9.3 to 35.5 W/m^2 . Evaporative heat transfer ($Q_{e,sk}$) is the sum of heat transfer due to natural diffusion of water from the skin to the environment ($Q_{e,dif}$) and evaporation of sweat secretion ($Q_{e,rsw}$). In this condition, the contribution of $Q_{e,rsw}$ is more compared to that of $Q_{e,dif}$. $Q_{e,rsw}$ increases from 0.78 to 25.98 W/m^2 and $Q_{e,dif}$ increases from 8.46 to 9.43 W/m^2 .

The variations of some physiological parameters with increase of metabolic rate from 50 to 120 W/m^2 are shown in Table 2. With increase of metabolic rate, body start accumulating heat inside the body. For proper functioning of body, this heat must release to the environment. Through the vasodilation, the blood vessels are dilated, which results in increase of blood flow and heat release increases. This increase of

Table 2 Variations of some physiological parameters with increase of metabolic rate ($T_a = T_{mrt} = 24\text{ }^\circ\text{C}$, $V = 0.05\text{ m/s}$, $I_{cl} = 0.5\text{ clo}$, $RH = 40\%$)

M (W/m^2)	T_{cr} ($^\circ\text{C}$)	T_{sk} ($^\circ\text{C}$)	T_b ($^\circ\text{C}$)	m_{bl} (g/sm^2)	α	Q_{res} (W/m^2)	Q_{esk} (W/m^2)
50	36.79	34.33	36.46	2.07	0.135	4.75	0.51
60	36.81	34.05	36.50	2.74	0.113	5.69	9.31
70	36.83	33.78	36.53	3.58	0.097	6.64	14.45
80	36.86	33.50	36.57	4.59	0.085	7.59	19.00
90	36.90	33.23	36.61	5.72	0.077	8.54	23.29
100	36.94	32.95	36.66	6.91	0.071	9.49	27.45
110	36.99	32.68	36.70	8.10	0.067	10.44	31.51
120	37.04	32.40	36.75	9.27	0.064	11.39	35.50

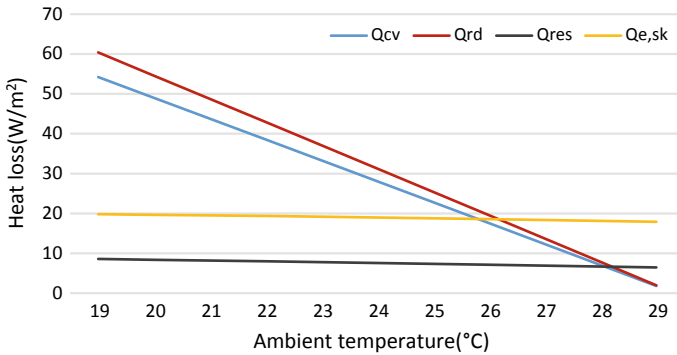


Fig. 4 Required heat transfer variations with air temperature ($M = 80 \text{ W/m}^2$, $V = 0.05 \text{ m/s}$, $I_{cl} = 0.5 \text{ clo}$, $\text{RH} = 40\%$)

blood flow rate with increase of metabolic rate is observed in Table 2. The blood flow rate is found increasing from 2.07 to 9.27 g/sm^2 . Sensible heat releasing to the environment is not enough when metabolic rate inside body is higher. At this stage, majority of the heat loss is through the evaporative mechanism. There is an increase of evaporative heat loss from skin observed with increase of metabolic rate from 0.51 to 35.5 W/m^2 . The much variation in respiration heat loss is not observed in this condition. The relations between core and skin layer become closer when blood flow rate increases, and hence, there is decrease of α from 0.135 to 0.064 .

4.2 Effect on the Body Due to the Change in Air Temperature

With increase of temperature from 23 to $29 \text{ }^\circ\text{C}$, the variations of different modes of heat transfer are shown in Fig. 4. In this calculation, the input parameters used are as follows: $T_a = T_{mrt} = 24 \text{ }^\circ\text{C}$, $\text{RH} = 40\%$, $M = 80 \text{ W/m}^2$, $V = 0.05 \text{ m/s}$, $I_{cl} = 0.5$. From the graph, it is observed that the radiative heat transfer is maximum, and respiration heat transfer is minimum at $19 \text{ }^\circ\text{C}$. With the increase of ambient temperature, the sensible heat transfer (radiation and convection) takes place from the environment to the body. Hence, radiation and convective heat loss from the body is decreasing in Fig. 4 and become low value at $29 \text{ }^\circ\text{C}$. However, decrement of radiative heat loss is faster than convective heat loss. For stable metabolic rate, evaporative heat loss from skin is not varied much in this temperature range. The average heat loss from skin is approximately 18.9 W/m^2 . The respiration heat loss shows a decrease in the pattern as shown in the graph. As the temperature increases, the difference between the body core and environment temperature also decreases, and this result in decrease in respiration heat loss. The decrease of respiration heat loss was found from 8.5 to 6.4 W/m^2 .

5 Conclusions

Thermal comfort study is the area that the researchers explore extensively to enhance human performance. Here, analytical study is carried out on the human body's physiological behavior. The research focuses on the concept of a steady-state energy model, where no energy is retained within the body. This energy balance is solved by considering various modes of heat transfer; radiation, convection, respiration and evaporation. The transfer of respiration heat is measured as the amount of the transfer of dry heat (sensible) and the transfer of evaporative heat (latent). The flow of evaporation heat is measured as the amount of evaporation sweat secretion due to thermoregulation ($Q_{e, rsw}$) that is regulated by sweat gland and natural water diffusion from the skin ($Q_{e, dif}$).

With the variations of metabolic rate from 50 to 120 W/m², the impact on the body is studied by fixing all other parameters of the climate. It is found that the core temperature increases with increase of body activity rates. To account for this core temperature change and achieve thermal comfort, the necessary skin temperature should be needed. The mean body temperature also rises with the metabolic rate. With increase of metabolic rate, the blood flow rate found increases from 2.07 to 9.27 g/sm². With increase of metabolic rate, evaporative heat also found increase from 0.51 to 35.5 W/m². However, α found decrease from 0.135 to 0.064 with increase of metabolic rate. The contribution of evaporative heat loss because of sweat secretion ($Q_{e, rsw}$) is found more compare to that of heat loss due to natural diffusion ($Q_{e, dif}$).

By fixing all other parameters, the impact on the body attributable to a raise of the atmospheric temperature from 19 to 29 °C is studied. With the rise in air temperature, the radiation and convection heat transfer reduces and becomes a weak value at 29 °C. The rate of decrement of radiative heat loss found higher than convective heat loss. For same metabolic rate, evaporative heat loss from skin found not varied much with increase of ambient temperature. The respiration heat loss reductions from 8.5 to 6.4 W/m². Further, with rise of air temperature the core temperature and mean body temperature increases, which indicates immediate prevention is required at higher ambient temperatures.

References

1. Zhou X, Lian Z, Lan L (2013) An individualized human thermoregulation model for Chinese adults. *Build Environ* 70:257–265
2. Das S, Upadhyay K, Subudhi S, Elangovan R (2019) Study of physiological thermoregulation of human body at extreme thermal condition. In: *Proceedings of the 25th national and 3rd international ISHMT-ASTFE heat and mass transfer conference (IHMTTC-2019)*. Begel House Inc.
3. Fanger PO, Toftum J (2002) Extension of the PMV model to non-air-conditioned buildings in warm climates. *Energy Build* 34:533–536

4. Kilic M, Kaynakli O, Yamankaradeniz R (2006) Determination of required core temperature for thermal comfort with steady-state energy balance method. *Int Commun Heat Mass Transf* 33:199–210. <https://doi.org/10.1016/j.icheatmasstransfer.2005.10.003>
5. Cheng Y, Niu J, Gao N (2012) Thermal comfort models: A review and numerical investigation. *Build. Environ.* 47:13–22
6. Stolwijk JAJ, Hardy JD (1966) Temperature regulation in man—A theoretical study. *Pflüger's Arch. für die gesamte Physiol. des Menschen und der Tiere.* 291:129–162
7. Li B, Yang Y, Yao R, Liu H, Li Y (2017) A simplified thermoregulation model of the human body in warm conditions. *Appl Ergon* 59:387–400
8. ASHRAE Standard (2013) Standard 55-2013 thermal environmental conditions for human occupancy. ASHRAE, Atlanta, 30329
9. Fanger PO (1970) Thermal comfort. Analysis and applications in environmental engineering. *Therm Comf Anal Appl Environ Eng*
10. Thorsson S, Lindberg F, Eliasson I, Holmér B (2007) Different methods for estimating the mean radiant temperature in an outdoor urban setting. *Int J Climatol A J R Meteorol Soc* 27:1983–1993
11. Doherty T, Arens EA (1988) Evaluation of the physiological bases of thermal comfort models. *ASHRAE Trans* 94
12. Prek M (2005) Thermodynamic analysis of human heat and mass transfer and their impact on thermal comfort. *Int J Heat Mass Transf* 48:731–739
13. Pala U, Oz HR (2015) An investigation of thermal comfort inside a bus during heating period within a climatic chamber. *Appl Ergon* 48:164–176
14. Höppe P, Martinac I (1998) Indoor climate and air quality. *Int J Biometeorol* 42:1–7

Power Quality Analysis and Enhancement Using DSTATCOM for Three-Phase Variable Load



Shamshad Ali, Majid Jamil, and M. A. Khan

1 Introduction

DSTATCOM is known as distribution STATCOM or distribution static compensator. STATCOM technology has a significant aspect in the field of power quality improvement. The advantages of DSTATCOM technology are the advent of fast, solid-state device, self-communicating device [1]. In 1976, the notion of DSTATCOM was given by Gyugyi. To reduce the value, dimensions, losses with light mass of DSTATCOM, PWM-based VSCs are preferred. For the improvement of voltage profile and the elimination of higher order harmonics, a small ripple filter is used at PCC of DSTATCOM. AC distribution network is making availability compensation for reactive power, balance load, neutral and harmonic currents compensation. DSTATCOM topology includes a VSI having capacitor of direct current as energy saving material [2]. The load basically depends on current (load current) a system demand current as nature of load to improve power factor the load current can be minimized and also improve the share of load current, that is why quality of power factor will improve. Poor power factor system draws more load current and shows poor power quality. DSTATCOM is a device which provides reactive power compensation, can compensate harmonics in current, suppresses the voltage flicker in AC network system. The DSTATCOM technology one of the most popular technologies to compensate reactive power, reduction of harmonics, improve pf, regulation of voltage, improve the voltage balance in three-phase system and correction of reactive power. With the development of

S. Ali (✉)

Department of Electrical and Electronics Engineering, Mewat Engineering College, Nuh, Haryana, India

M. Jamil

Department of Electrical Engineering, Jamia Millia Islamia, New Delhi, India

M. A. Khan

Electrical Engineering Section, University Polytechnic, Jamia Millia Islamia, New Delhi, India

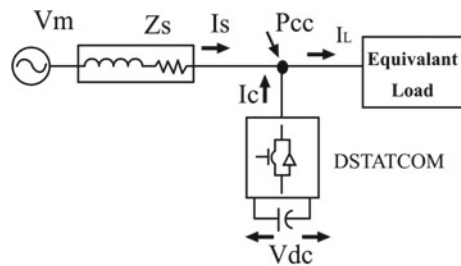
solid-state devices, DSTATCOM starts playing a vital role in power system application. In AC distribution system, power quality problem has been faced for long time in terms of poor pf and poor VR, disbalancing of load and enhanced load current. DSTATCOM technology is a best technology to mitigate the entire current-based power quality problem. Thyristor-controlled reactor (TCRs) and thyristor-switched capacitor (TSCs) used for power system application as reactive VAR composition and as a switching device. Flexible AC transition system is an important tool which gives solution of problems of power system and application with the help power electronics-based control for reactive power. FACTS is referred as the flexible AC transmission system incorporate with power electronics-based controller [3, 4]. To enhance the capacity to control and uplift the accomplishment of power transfer, it makes power system protective and more controllable. Thus, line capacity increased which improve reliability of power system [5–7]. Static VAR controller (SVC) can control only voltage, impedance and phase angle to determine AC flow of power in power system. It is a synchronous condenser feasible with the use of GTO.

2 Literature Review

Power quality plays an important role at every moment of power system. Consumer required supply from AC substation is all about power quality, power quality issues deal with harmonics in power system, power factor, voltage stability. The IEEE standard coordination committee 22 has great contribution in the USA to support the level of power quality.

The groups of IEC classification are done at low-level frequency criteria harmonics, voltage fluctuation, down voltage and fluctuation in voltage imbalance, power frequency alternation, induce low-frequency voltage. Redial low-frequency phenomena (magnetic field and electric field), uplifted frequency criteria, issue of high-frequency criteria, electro-static discharge criteria, nuclear electromagnetic pulse. DSTATCOM should be connected in transition line as shown in Fig. 1. I_L is load current sending end current Z_s is transition line impedance and I_c is the DSTATCOM current DSTATCOM can be delivered current or take current as requirement of transitions line (reactive power, leading, lagging) [8, 9].

Fig. 1 Single line diagram of a DSTATCOM



3 Methodology

3.1 Unit Template- or PI Controller-Based Algorithm

Unit template or PI controller-based algorithm is a simple control algorithm for active compensating devices such as DSTATCOMs for AC VR at load side at PCC and balance of load of unbalanced loads. This can be stated that the control algorithm of DSTATCOM is made adaptable and can be improved either for pf correction say UPF at PCC or for voltage control (zero voltage regulation at PCC) to compensate reactive power along with balancing of load of unbalanced loads. This algorithm fundamentally gives a self-supporting direct current bus of voltage source compensator used as a DSTATCOM. It can be used for the DC control of VSC currents of the DSTATCOM and provides an estimation of reference compensator currents. However, an indirect current control of supply currents is preferred to attain pulse width modulation giving signals for devices which is utilized in the CC-VSC functioning as a DSTATCOM. This ancillary current control of DSTATCOM offers advantages for fast control, reduced burden on the processor (DSP used for implementation), inherent elimination of sharp notches in currents and so on. For this purpose, 3- Φ reference currents of supply are taken using sensed AC voltages (at PCC) and DC bus voltage of the DSTATCOM as the signals of feedback. 2 PI voltage controllers, one to regulate the DC bus of the VSC used as a DSTATCOM and other for amplitude regulation for PCC voltages. These are utilized to evaluate the amplitudes of in-phase and quadrature components of reference currents of supply [10–12].

VSC-sensitive load interface distribution and DSTATCOM are functioning in the mode of captivity. If the voltage of grid has higher intensity than the DSTATCOM voltage, it consumes reactive power from the grid and it operates in inductive mode. And if the grid voltage and DSTATCOM voltage are not different in the magnitude, then there will be no exchange of reactive power between the grid and STATCOM and also DSTATCOM operates in smooth way. The operation of DSTACOM can be utilized to exchange real power with the grid by controlling the phase angle of its output voltage. As for the operation of DSTACOM is concerned, it is used as reactive power compensation on mode only and no difference can be observed between the DSTACOM output voltages and grid voltages. Therefore, it is clear that DSTACOM neither provides nor takes real power [13–15].

3.2 System Modelling

Designing of the model has been done by using MATLAB/Simulink.

Model configuration.

Alternating Current Source three-phase, 415 V (LL), 50 Hz;

Impedance Source.

R_s 0.07 Ω ;

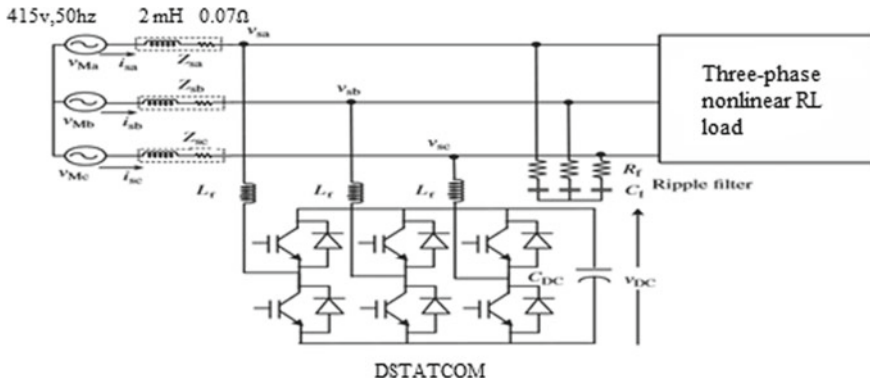


Fig. 2 System model for DSTATCOM with three-phase nonlinear load

L_s 2 mH;
 3- Φ full bridge rectifier (uncontrolled).
 R_1 10 Ω ;
 L_1 90 mH;
 Ripple filter.

R_f 5 Ω ;
 C_f 15 microfarad;
 Bus capacitance (DC) 3500 microfarad;
 Bus voltage (DC) 700 V;

By using an interfacing reactor of value 1 mH at 0.5 s DSTATCO is connected to the system.

- The time period from 0 to 0.5 s shows the system behaviour when DSTATCOM is not connected.
- DSTATCOM not connected in the period from 0.5 s onwards shows the system behaviour.

The system is operated in both power factor correction as well as zero voltage regulation mode (Fig. 2).

4 Results and Discussion

4.1 Power Factor Correction

In Fig. 3 Phase-A wave form of source voltage current is shown. During the period 0.4–0.5 s, when DSTATCOM is not connected the waveforms V and I are highly distorted also source current lags source voltage. From the period, 0.5 s onwards when

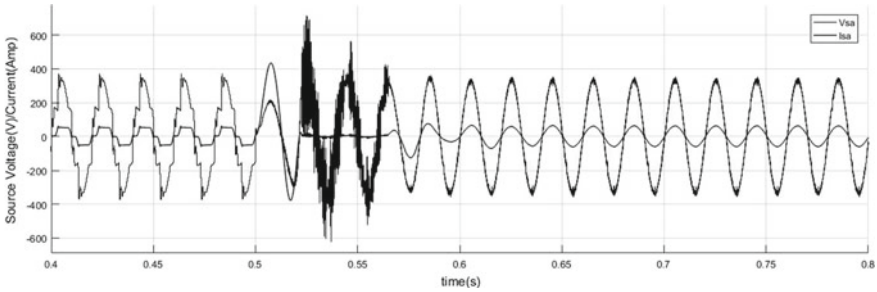


Fig. 3 Phase-A waveform for source voltage and current

DSTATCOM is connected unity power factor is achieved and the THD reduces to satisfy IEEE 519 standard.

Figures 4 and 5 show the variation of voltage and FFT analysis of voltage (source) waveform. The time period from 0.4 to 0.5 s shows the variation of source voltage when DSTATCOM is not connected. During this period, the waveform has a peak value of 326.9 V and THD of 18.57%. The time period from 0.5 s onwards shows the variation of source voltage when DSTATCOM is connected. The peak value of

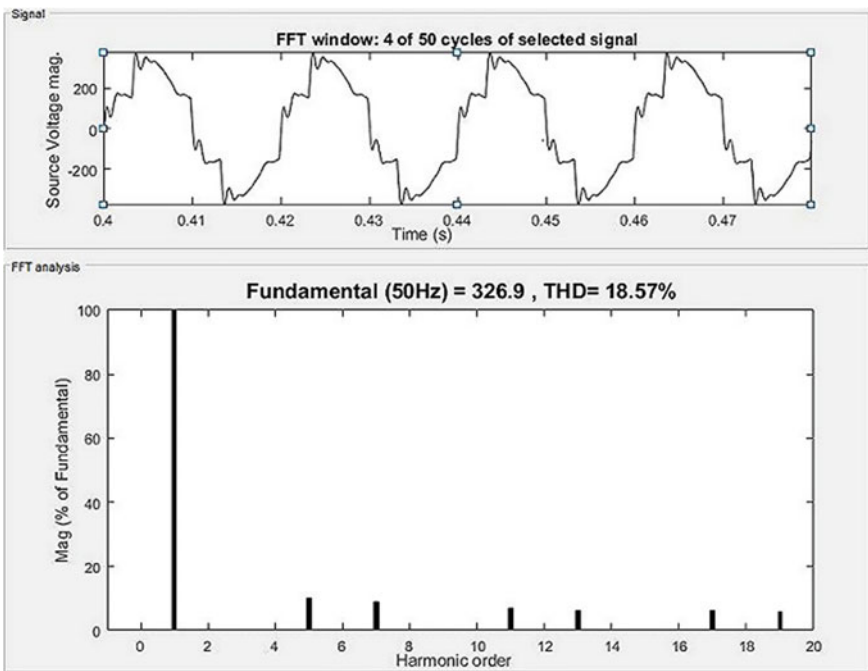


Fig. 4 FFT analysis of voltage (source) waveform when DSTATCOM is not connected

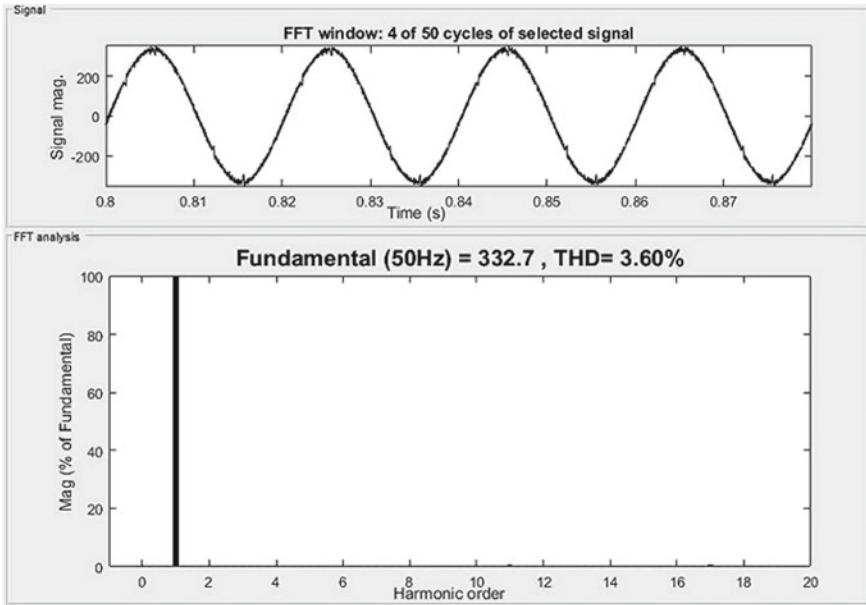


Fig. 5 FFT analysis of voltage (source) waveform when DSTATCOM is connected

source voltage increases to 332.7 V, and the THD of the waveform reduces to 3.6% satisfying IEEE 519 standard.

Figures 6 and 7 show variation of current and FFT analysis of waveform of current. Time period from 0.4 to 0.5 s shows the variation of current (source) when DSTATCOM not connected. During this period, current waveform has a peak value of 57.02 A and THD of 23.19%. The time period from 0.5 s onwards shows the variation of source current when DSTATCOM is connected. The peak value of source current is 61.31 A, and the THD of the waveform reduces to 1.14% satisfying IEEE 519 standard.

Figures 8, 9 and 10 show the reactive power injected by the source, reactive power injected by DSTATCOM and bus voltage of DSTATCOM across capacitor. Period from 0.4 to 0.5 s shows the behaviour of uncompensated system. DC bus voltage rises and attains a constant value after connecting the DSTATCOM to the system at 0.5 s.

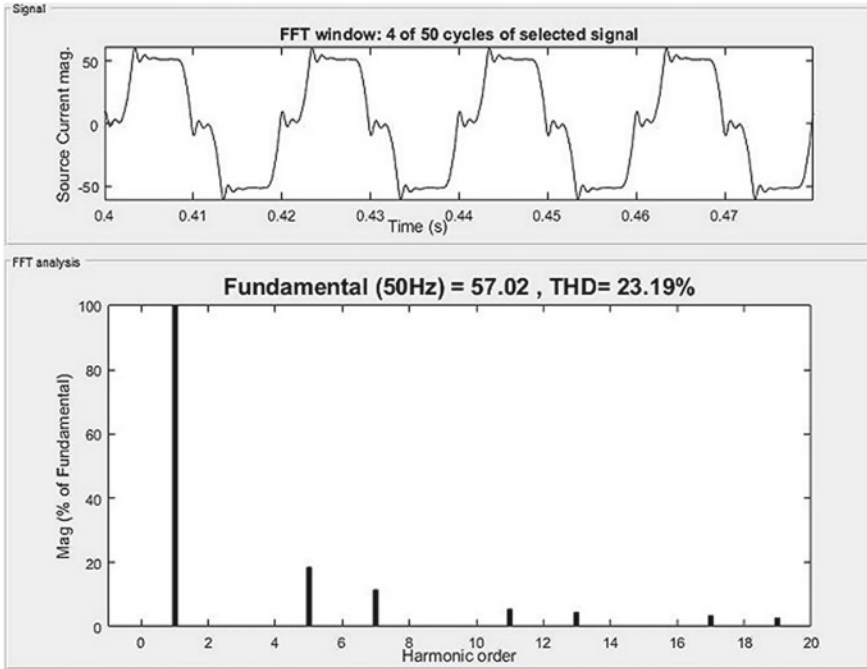


Fig. 6 FFT analysis of current (source) waveform once DSTATCOM not connected

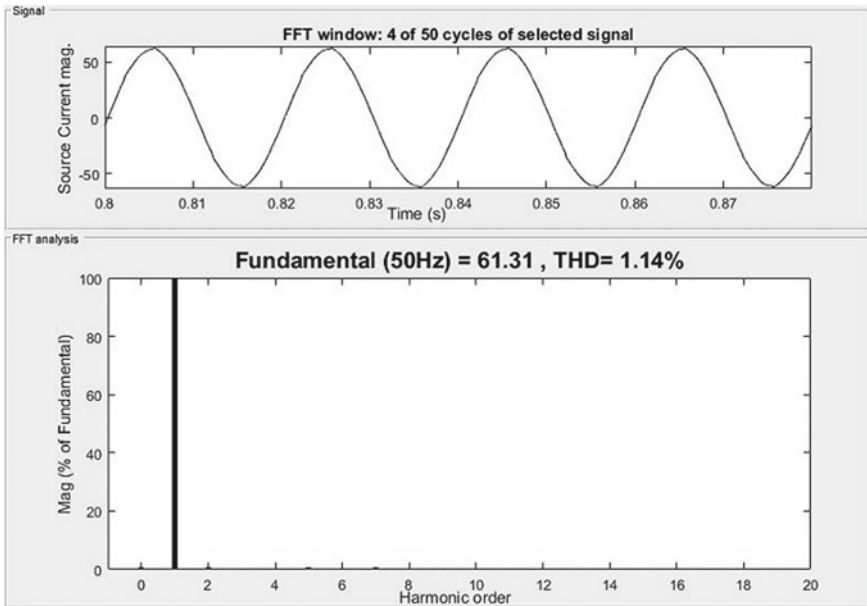


Fig. 7 FFT analysis of current (source) waveform when DSTATCOM connected

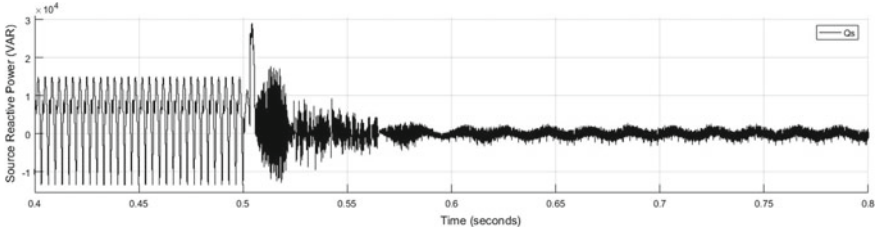


Fig. 8 Source reactive power

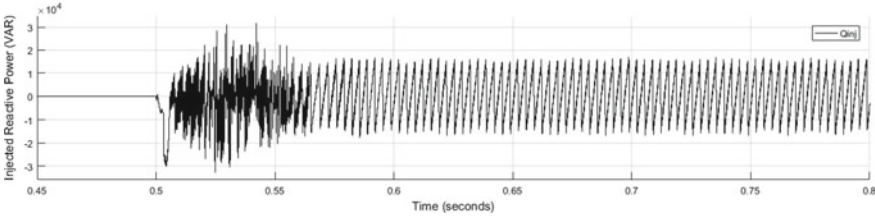


Fig. 9 Injected reactive power by the DSTATCOM

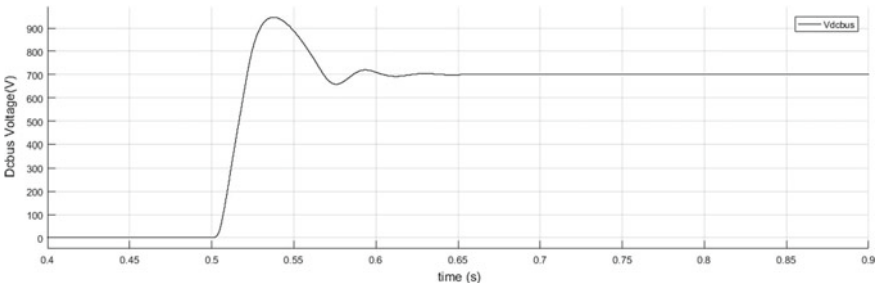


Fig. 10 Bus voltage (DC)

4.2 Zero Voltage Regulation

To achieve zero voltage regulation, the supply current should lead the voltage which is achieved by the DSTATCOM by operating it in zero voltage regulation mode.

Figure 11 shows variation of source voltage during ZVR mode of DSTATCOM. During no load conditions, DSTATCOM not connected to system up to this point the source voltage is 338.8 V (peak value) at 0.25 s the nonlinear load is connected due to which the voltage drops to 326.9 V (peak value).

At 0.5 s, DSTATCOM connected leading to zero voltage regulation. The voltage is restored preload conditions, i.e. 338.8 V.

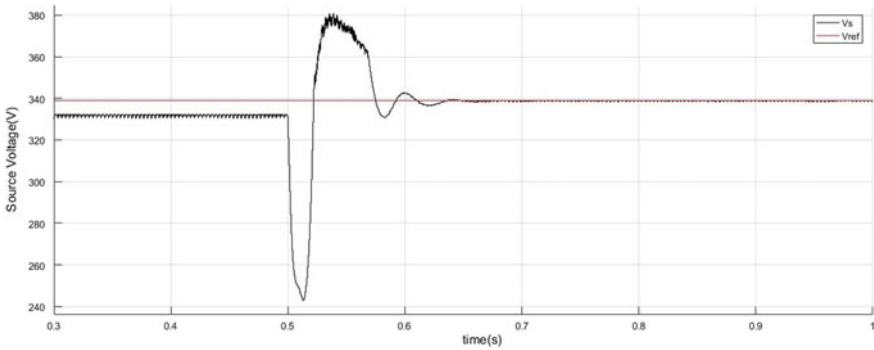


Fig. 11 Variation of source voltage during ZVR mode of DSTATCOM

Figures 12 and 13 show the variation of source voltage and FFT analysis of voltage (source) waveform. The time period from 0.4 to 0.5 s shows the variation of source voltage when DSTATCOM is not connected. During this period, the waveform has a peak value of 326.9 V and THD of 18.56%. The time period from 0.5 s onwards shows the variation of source voltage when DSTATCOM is connected. The peak

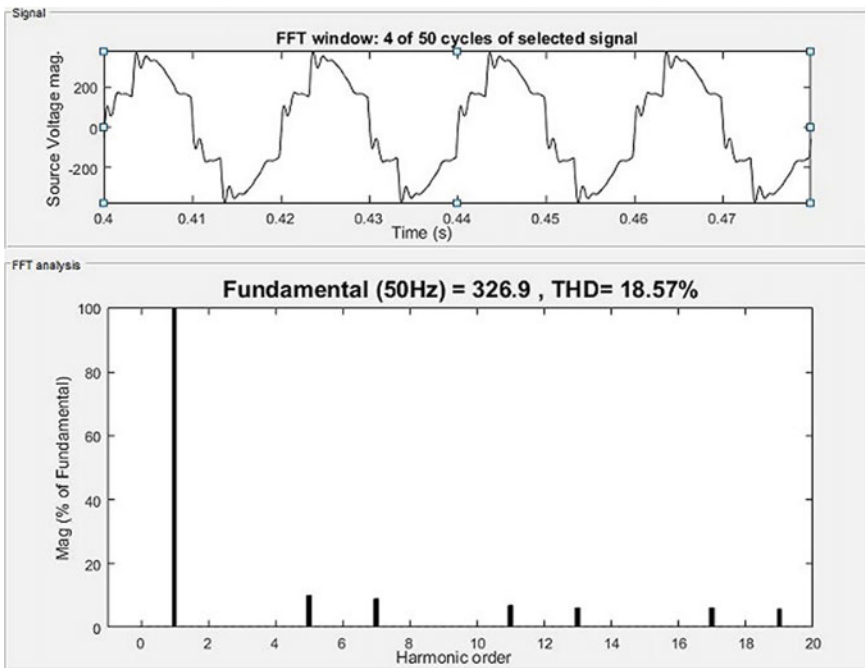


Fig. 12 FFT analysis of voltage (source) waveform when DSTATCOM is not connected

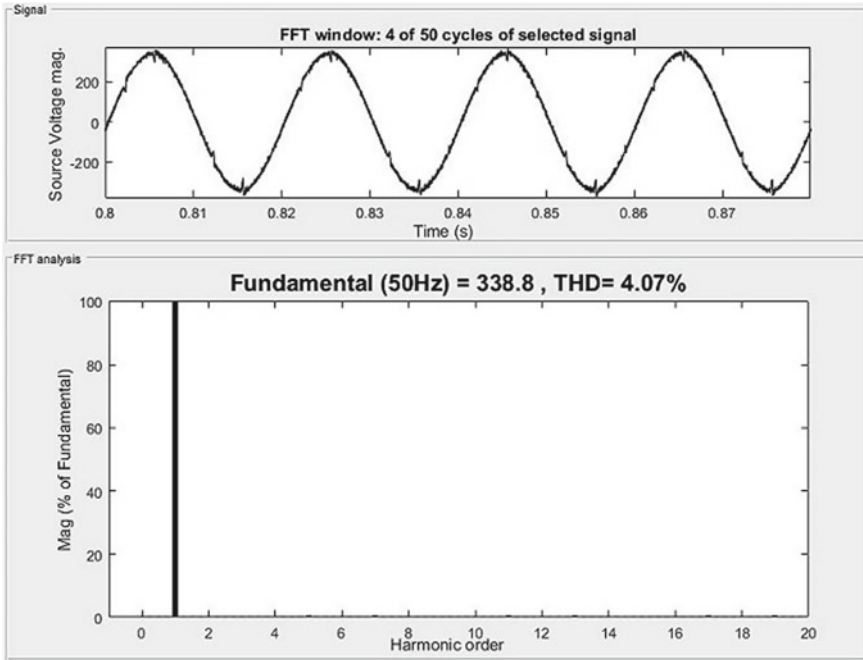


Fig. 13 FFT analysis of voltage (source) waveform when DSTATCOM is connected

value of source voltage increases to 338.8 V, and the THD of the waveform reduces to 4.07% satisfying IEEE 519 standard.

Figures 14 and 15 show the variation of source current and FFT analysis of current (source) waveform. Time period from 0.4 to 0.5 s shows the variation of current when DSTATCOM not connected. During this period, current waveform has a peak value of 57.02 A and THD of 23.19%.

The time period from 0.5 s onwards shows the variation of source current when DSTATCOM is connected. The peak value of source current is 63.23 A, and the THD of the waveform reduces to 1.32% satisfying IEEE 519 standard.

Figures 16 and 17 show the difference of load voltage and current waveforms with time. Time period from 0 to 0.5 s shows the system behaviour when DSTATCOM not connected. Load voltages and currents are highly distorted.

The period from 0.5 s onwards express system behaviour once DSTATCOM connected to system. The THD of load voltage reduces to satisfy IEEE 519 standard (Tables 1 and 2).

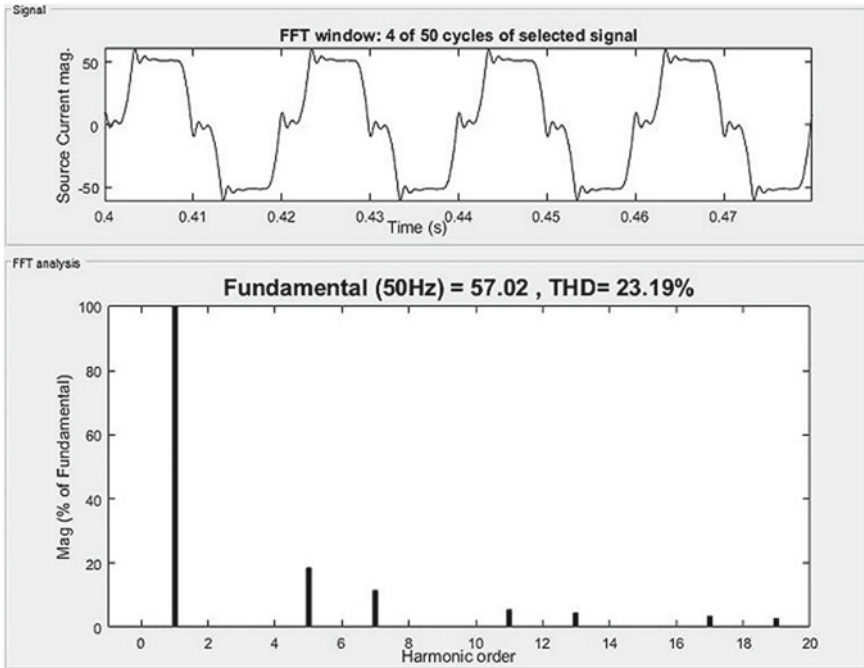


Fig. 14 FFT analysis of current (source) waveform when DSTATCOM is not connected

5 Conclusion

This paper presents the enhancement in quality of power using DSTATCOM for variable load by unit template technique/PI controller-based technique. From results undoubtedly it is seen that there is a significant reduction in THD in voltage and current also improvement in power factor from lagging to unity. Zero voltage regulation is also achieved efficiently using this method. From results obtained above, it is concluded that using the PI-based unit template technique DSTATCOM works satisfactorily to correct power factor correction as well as achieve zero voltage regulation in addition to reducing harmonic content at the PCC/source voltages and currents. Further, research can be done by using artificial intelligence-based control technique, which improves the characteristics of DSTATCOMs for power quality of variable load.

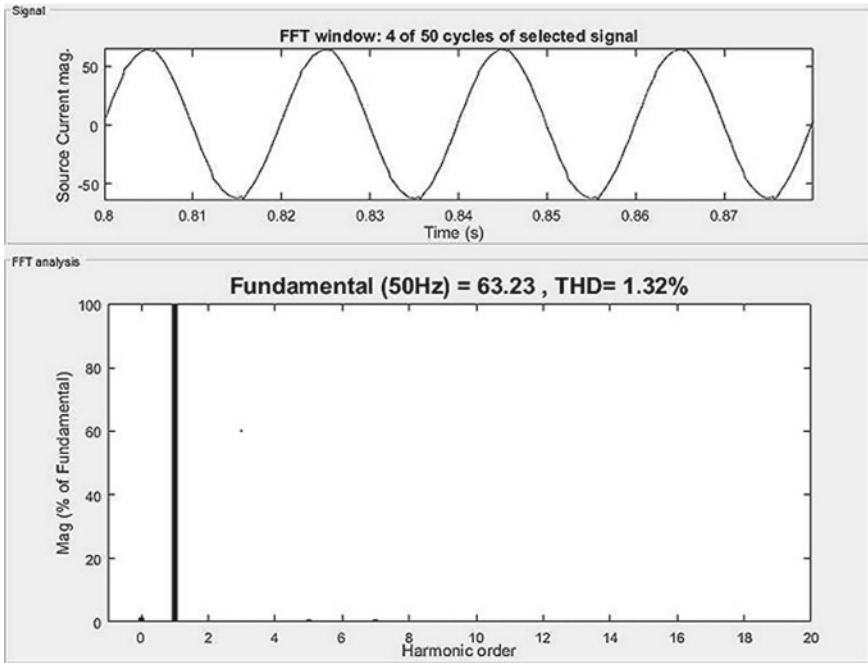


Fig.15 FFT analysis of current (source) waveform when DSTATCOM connected

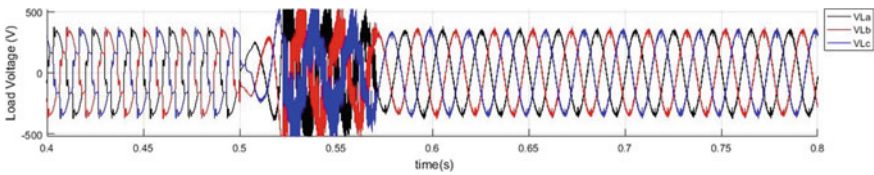


Fig. 16 3-phase load voltage waveform

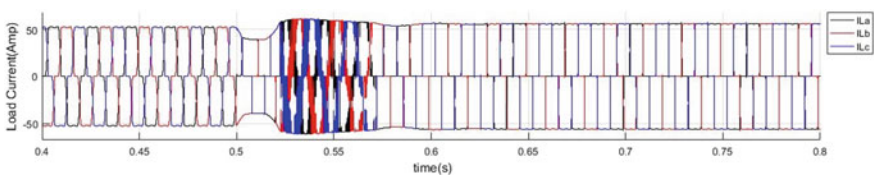


Fig. 17 3-phase load current waveform

Table 1 Comparative analysis in power factor correction mode for three-phase nonlinear RL load

Phase-A voltage and current	V_{sa} and I_{sa} magnitude and THD before compensation		Unit template	
	Magnitude	THD (%)	Magnitude	THD (%)
V_{sa} (V)	326.9	18.56	332.7	3.6
I_{sa} (A)	57.02	23.19	61.31	1.14
	Lagging power factor		UPF achieved	

Table 2 Comparative analysis in ZVR mode for three-phase nonlinear RL load

Phase-A voltage and current	V_{sa} and I_{sa} magnitude and THD before compensation		Unit template	
	Magnitude	THD (%)	Magnitude	THD (%)
V_{sa} (V)	326.9	18.56	338.8	3.6
I_{sa} (A)	57.02	23.19	63.23	1.32
	Low voltage and high THD		ZVR achieved	

References

1. Energy Sector Power Transmission Division Power Transmission Solutions. Published by Siemens AG 2016 Energy Management Division Freyeslebenstrasse1 91058 Erlangen, Germany
2. McGranaghan M, Roettger B (2002) Economic evaluation of power quality. *IEEE Power Eng Rev* 22:8–12
3. Singh B, Chandra A, Al-Haddad K (2015) Power quality problems and mitigation techniques. Wiley, New York
4. Nguyen PT, Saha TK (2004) DVR against balanced and unbalanced voltage sags: modeling and simulation. In: *IEEE-School of Information Technology and Electrical Engineering*, University of Queensland, Australia
5. Shi J, Noshadi A, Kalam A, Shi P (2015) Fuzzy logic control of DSTATCOM for improving power quality and dynamic performance
6. Prajapati R, Sharma S (2014) Fuzzy logic controller based distribution static compensator. In: 2014 IEEE students’ conference on electrical, electronics and computer science. Shi J, Kalam A, Noshadi A, Shi P (2014) Genetic algorithm optimised fuzzy control of DSTATCOM for improving power quality. In: *Australasian universities power engineering conference, AUPEC 2014*. Curtin University, Perth, Australia, 28 Sept–1 Oct 2014, pp 1–6
7. Hingorani NG (1995) Introducing custom power. *IEEE Spectr* 32(6):41–48
8. Arya SR, Niwas R, Bhalla KK, Singh B, Chandra A, Al-Haddad K (2015) Power quality improvement in isolated distributed power generating system using DSTATCOM. *IEEE Trans Ind Appl* 51(6)
9. Shuhong K, Zhongdong Y, Renzhong S, Weidong S (2009) A survey on the principle and control of dynamic voltage restorer. In: *International conference on energy and environment technology*, 2009. ICEET ‘09, vol 2, pp 57, 60, 16–18 Oct 2009
10. Elango S, Chandra Sekaran E (2011) Mitigation of voltage sag by using distribution static compensator (D-STATCOM). In: 2011 International conference on process automation, control and computing (PACC), pp 1, 6, 20–22 July 2011

11. Sharma R, Nijhawan P (2013) Effectiveness of DSTATCOM to compensate the load current harmonics in distribution networks under various operating conditions. *Int J Sci Eng Technol* 2(7):713718
12. Nijhawan P, Bhatia RS, Jain DK (2013) Improved performance of multi-level inverter-based distribution static synchronous compensator with induction furnace load. *IET Power Electron* 6(9):1939–1947
13. Singh B, Senior Member, IEEE, Solanki J (2009) A comparison of control algorithms for DSTATCOM. *IEEE Trans Ind Electron* 56(7)
14. Eltamaly AM, Elghaffar ANA, Sayed Y, El-Sayed A-HM (2018) Enhancement of power system quality using static synchronous compensation (STATCOM). *Int J Mechatron Electr Comput Technol (IJMEC)* 8(30):3966–3974
15. Varma RK, Siavashi EM (2019) Enhancement of solar farm connectivity with smart PV inverter PV-STATCOM. *IEEE Trans Sustain Energy* 10(3):1161–1171

A Dopingless Tunnel FET and MOSFET-Based Comparative Study of a Simple Current Mirror



Harihar Nath, Suruchi Sharma, Abhishek Verma, and Baljit Kaur

1 Introduction

The rapid downscaling of MOSFET technology helps one to scale down the source voltage, thereby increasing the current driving capacity with a reduced power supply. However, the higher leakage by the off-state has always been detrimental to MOSFET technology. Nonetheless, MOSFET limitations include restriction to a subthreshold swing (SS) of 60 mV/dec, random dopant fluctuation (RDF), drain-induced barrier lowering (DIBL), and short channel effects (SCE) [1–4]. Therefore, in order to ease such MOSFET limitation, conventional doped TFET with the low off-state current is adopted, the whole problem of SCE, DIBL is neutralized, and subthreshold swing is reduced, but the result of the weak band-to-band tunneling (BTBT) the on-state current is boosted by a small fraction [5–7]. Dopingless TFET has been introduced to produce large current on-state and neutralize doping-related spontaneous doping variability. The DLTFET has a low thermal budget [8–10].

1.1 Dopingless Tunnel FET

Many papers were published within the last few years regarding the tunnel FET. Tunnel FET was implemented to lift the limitations of the MOSFETs like SCEs and SS. The on-current of the tunnel FET was very low because of the RDF due to the physical doping of atoms. Kumar and Janardhanan utilized the charge plasma principle to establish the source and the drain of the tunnel FET [8] (which is known as dopingless tunnel FET), and now, the ion implantation technique is not required for the tunnel FET. He also improved the BTBT to increase the on-current. Sharma

H. Nath · S. Sharma · A. Verma · B. Kaur (✉)
National Institute of Technology Delhi, New Delhi, India
e-mail: baljitkaur@nitdelhi.ac.in

et al. proposed another DLTFET [11] in which work function engineering was also added which means the source and the drain were created with the help of two different metals of different work functions. Nigam et al. [12] proposed the novel DLTEFT with the control gate of dual material; holes were induced in the source with the help of platinum metal of work function 5.93 eV and electrons were induced in the drain with the help of hafnium metal of work function 3.9 eV. Yadav et al. [13] proposed another DLTFET to replace the conventional TFET, in which he used InAs material (heteromaterial) which is a narrow bandgap material in place Si in th source region to reduce the source-channel lateral tunneling distance which helped in increase in the on-current by improving BTBT rate. Harris et al. [14] proposed heterostructure DLTFET in which GaAs material was used for the drain region to reduce the off-current without affecting the on-current. Raad et al. improved the conventional DLTFET by introducing the metallic layer between the gate oxide and the source interface which lowered the SS and increased the on-current. Verma et al. [15] proposed another DLTFET which is used in this paper for the circuit. The sectional cross-view of DLTFET is shown in Fig. 1. The charge plasma concept was used on the source region with p+ and drain region with n+ platinum was used to produce the holes in the source region and hafnium was used to produce electrons in the drain region. A strip of GaAs is inserted between the channel and the source to increase the on-current because its electron mobility is $8500 \text{ cm}^2/\text{Vs}$ which improves the tunneling of electrons at the channel and the source interface. The electron of the valence band (VB) of the drain cannot pass to the conduction band (CB) of the source during the off-state because the bands do not get aligned whereas they get aligned during the on the state; so, the electron can easily pass from the VB of the source to the CB of the drain by BTBT [8].

The channel length of DLTFET is only 20 nm, which means it covers the lesser area on a chip than the other three NMOS technologies. SCE is lesser in DLTFET than the NMOS technologies. The slope of the curve of the drain current in the output characteristic of DLTFET is almost zero. Subthreshold swing (SS) of DLTFET is

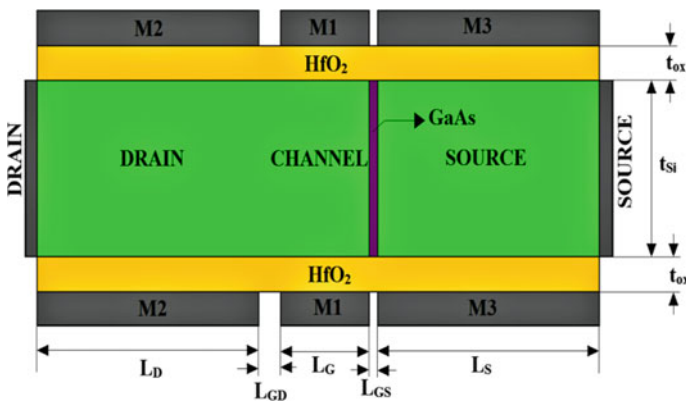


Fig. 1 Sectional cross-view of DLTFET

Table 1 Some critical parameters of DLTFET

Parameters	Values
Channel length (nm)	20
I_{ON} (A/um)	10^{-4}
I_{OFF} (A/um)	10^{-19}
I_{ON}/I_{OFF}	10^{15}
Subthreshold swing (SS) (mV/dec)	~ 10.25

~ 10.25 mV/dec at $V_{ds} = 0.6$ V [15], whereas it is above 60 mV/dec for the NMOS technologies. Therefore, DLTFET should be preferred over NMOS technologies for SCM due to the above reasons.

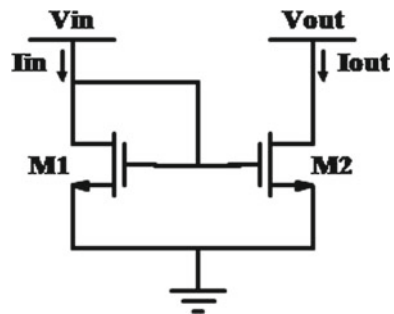
The following procedure is followed for the simulation of SCM by using the NMOS technologies and DLTFET:

- GaAs DLTFET is modeled with the conditions mentioned in [15] using TCAD Silvaco. Table 1 shows the results for the DLTFET.
- I_d , C_{gs} and C_{gd} lookup tables are created for DLTFET by using the same software.
- DLTFET is called in HSPICE with the help of Verilog-A and lookup tables.
- DLTFET SCM circuit is simulated on HSPICE.
- All three NMOS technologies BPTM models are used for the gate dielectric of SiO_2 to simulate the SCM circuit on HSPICE.
- All the results of all the four transistors SCM circuits are compared.

1.2 Simple Current Mirror

The current mirror can be called as a current amplifier with a current gain equal to 1, which means it is a circuit in which output current must be equal to the input current. Figure 2 shows the SCM circuit. CM is one of the most critical building blocks used to improve the performance of many analog ICs. It is used as a current amplifier, dynamic load, and biased in many circuits like op-amp, ADC, DAC, etc. [16, 17]. It is used as a dynamic load to improve the gain without increasing the

Fig. 2 Simple current mirror circuit using NMOS



supply voltage and the chip area [16, 17]. It copies DC current from one branch to another branch of the circuit, which can detect the alteration in the given voltage. Thus, it is used to replace an external resistor of a chip [16]. It is also used as a current amplifier by calibrating the width of the transistors [16–18]. Hence, the performance of the ICs depends on the performance of the CM. Some circuits require an ideal CM like biomedical circuit, bioamplifiers, etc. [19, 20]. Perfect CM is also needed as the current source for the differential amplifier to advance the CMRR [16, 17]. There are billions of transistors in a computer that require a constant current source to perform most of the logic functions. Even signal processing, such as audio amplifiers are based on the current source. But a constant current source does not exist in this world. So, transistors were used to make a constant current source by using an SCM. SCM circuit was made using the MOSFETs and a CNTFET [21]. Current errors for different technologies SCM were compared in the paper. It was found that current error increases as the MOSFETs scale down from 45 to 22 nm, and it was negligible the CNTFET SCM. But input resistance was found high which should be as low as possible. Researchers made many CMs like Wilson CM, Cascode CM, Advance CM, etc., to improve the accuracy. But they were also a little inaccurate and were complex. So, the main motive of the work in the paper is to make a CM with the least error, high output resistance and not very complex.

It is almost impossible to get the output current similar to the input current in MOSFET SCM because according to the drain current equation in the saturation region,

$$I_d = \frac{1}{2} \mu_n C_{ox} \frac{W}{L} (V_{gs} - V_t)^2 (1 + \lambda V_{ds}) \quad (1)$$

where

I_d = Drain current

μ_n = Electron mobility

C_{ox} = Gate to oxide capacitance

W = Width of the MOSFET

L = Length of the channel

V_{gs} = Gate to source voltage

V_{th} = Threshold voltage.

λ = channel length modulation constant

V_{ds} = Drain to source voltage.

Generally, the value λ is considered 0 for the ideal MOSFET, but there is no such MOSFET exist. λ always has some value greater than 0 due to which drain current alters linearly with V_{ds} even in the saturation mode. Input voltage in the SCM is set to a voltage more significant than the threshold voltage of both the transistors because they are similar to each other and put them in the saturation region and vary the output voltage ($>V_{gs} - V_{th}$), M_2 will not give constant current instead, and the output current will vary linearly with output voltage. So, we can say that due to the channel length modulation effect, we do not get the equal currents in the MOSFET SCM.

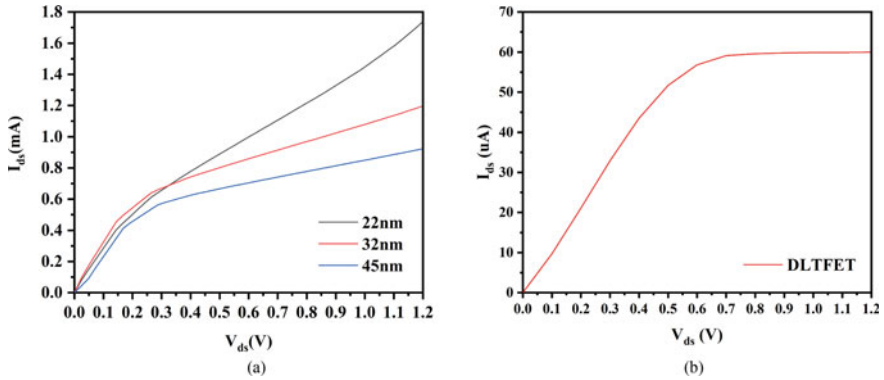


Fig. 3 Output characteristics at $V_{gs} = 0.8$ V of **a** different NMOS and **b** DLTFET

2 Simulation Results and Discussion

There are two main parameters that describe the SCM. First is the current error, i.e., the difference of the output current and the input current should be 0. Second is its AC output resistance, which should be high for an extended frequency band. It helps us to determine how variable I_{out} is with the voltage applied to the SCM. There are some more parameters that describe the SCM, like input resistance, transient response, leakage current. So, the MOSFET SCMs are compared with the DLTFET SCM on the basis of these parameters in this section.

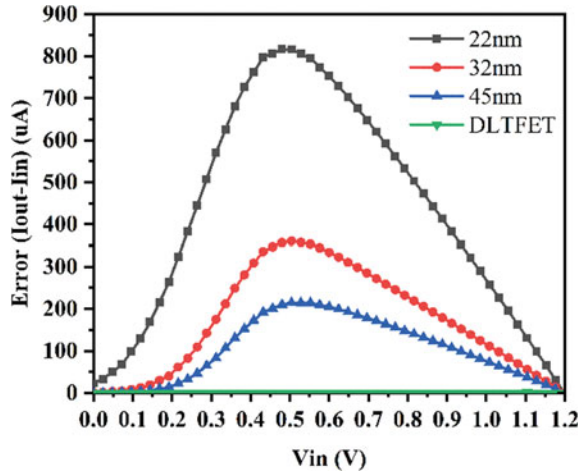
2.1 Output Characteristics Comparison of the Devices

V_{gs} for all the devices is kept constant at 0.8 V, and the drain to source is swiped from 0 to 1.2 V to plot output characteristics of the four devices. Figure 3a shows the output characteristic of the three NMOS, and Fig. 3b shows the output characteristic of the DLTFET, and it can be observed that the current becomes constant for the DLTFET in the saturation region, whereas currents for the other devices keep on increasing in the saturation region. It means that the DLTFET is a more stable device than the others.

2.2 Variation in the Output Current (I_{out}) W.R.T. the Input Voltage (V_{in})

The stability of the output current should be maintained in the SCM. Input current changes with the input voltage, which must give rise to a similar change in the output

Fig. 4 Error ($\Delta I = I_{out} - I_{in}$) is shown in the plot when V_{in} is altered from 0 to 1.2 V. DLTfET is showing the ideal behavior with negligible error



current. SCM must show the minimum current error ($\Delta I = I_{out} - I_{in}$). The output voltage is altered from 0 to 1.2 V, and the input voltage is remained steady at 1.2 V to see the current error for the four technologies. From Fig. 4, it can be observed that the current error is maximum in 22 nm NMOS SCM and minimum in DLTfET SCM. DLTfET SCM exhibits a typical behavior with the negligible current error. It is all because of the less effect of channel length modulation on DLTfET.

2.3 Variation in the Output Current (I_{out}) W.R.T. the Output Voltage (V_{out})

The production of the input current in SCM relies on the input voltage applied, and the achievement of the output current equal to the input current relies on the output voltage. Input voltage is kept constant at 1.2 V, and the output voltage is altered from 0 to 1.2 V for the analysis. Input voltage drawn in DLTfET SCM is minimum, which can be observed from Fig. 5a. It is a disadvantage of DLTfET. Leakage current is minimum in DLTfET SCM among all the four transistors SCM which can be observed from Fig. 5b.

The proportion of the output current to the input current is known as the normalized output current. The normalized output current should be equal to 1, and it is the necessary condition that should be fulfilled by the SCM. DLTfET SCM reaches the condition first, which can be observed from Fig. 6.

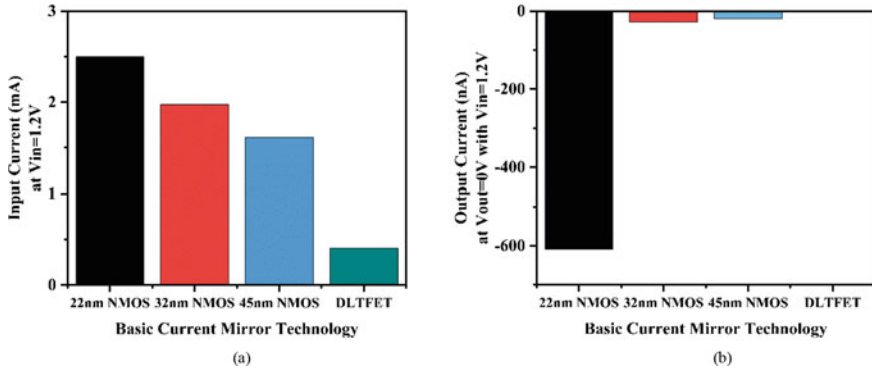
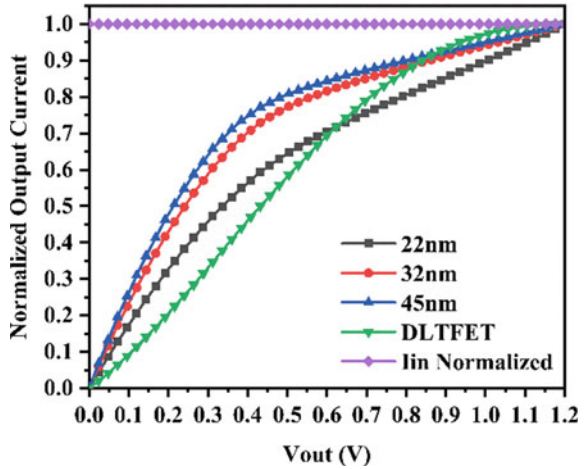


Fig. 5 a I_{in} produced at $V_{in} = 1.2 V$. b leakage current obtained at $V_{in} = 1.2 V$ and $V_{out} = 0 V$

Fig. 6 Normalized I_{out} is plotted with V_{out} varying from 0 to 1.2 V



2.4 Transient Response to the Square Wave Input

The pulse voltage supply is applied to V_{out} with initial voltage = 0 V, final voltage = 1.2 V, delay time = 100 ps, rise time = 100 ps, fall time = 100 ps, pulse width = 2 ns and time period = 4 ns. V_{in} is kept constant at 1.2 V. Figure 7 shows the current transient response of all the four transistors SCM. From Table 2, it can be observed that delay time is maximum in DLTFET SCM, but power consumption is minimum, so PDP is not too high among the four transistors SCM.

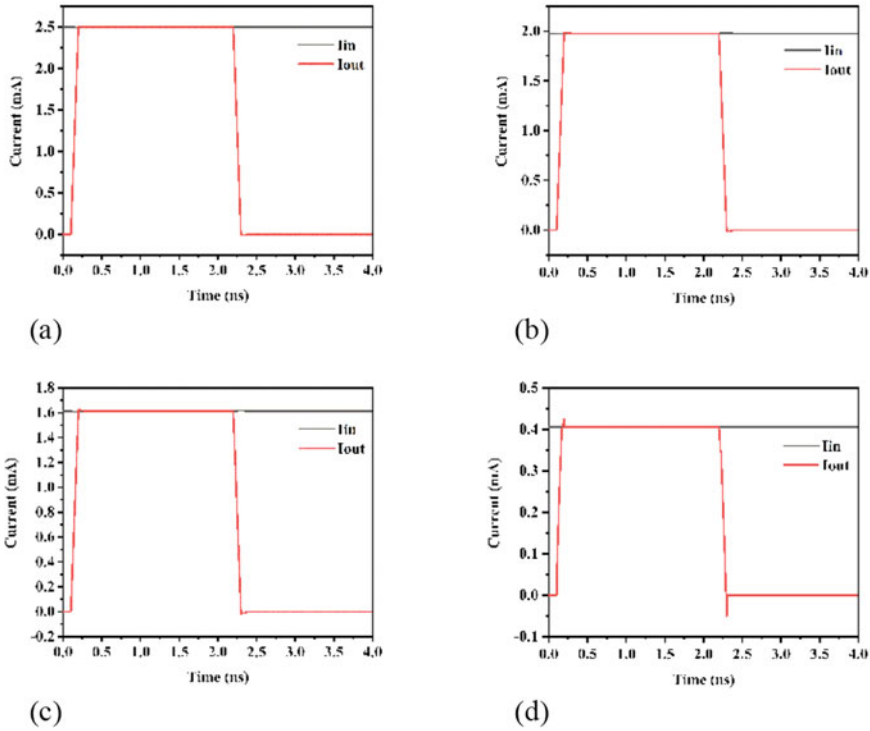


Fig. 7 Transient response of I_{in} and I_{out} of the SCM using different technologies. **a** 22 nm NMOS, **b** 32 nm NMOS, **c** 45 nm NMOS, **d** DLTFET

Table 2 Compared parameters for current transient response of I_{in} and I_{out} of BCM technologies at $V_{in} = 1.2$ V and pulse V_{out}

Parameters	Unit	22 nm NMOS	32 nm NMOS	45 nm NMOS	DLTFET <i>n</i> -type
Output current	mA	2.498	1.976	1.613	0.406
Rise time	ps	77.43	66.91	63.84	62.95
Fall time	ps	77.66	68.22	64.91	71.77
Negative overshoot	μ A	12.5	13.69	14.9	51.48
Positive overshoot	μ A	11	11.7	12	24.84
Delay 50% (low to high)	ps	11	12	11	80
Delay 50% (high to low)	ps	20	2	7	80
Total delay	ps	31	14	18	160
Power	mW	3.835	3.04	2.48	0.62
Power delay product	fJ	118.88	42.56	44.64	99.2

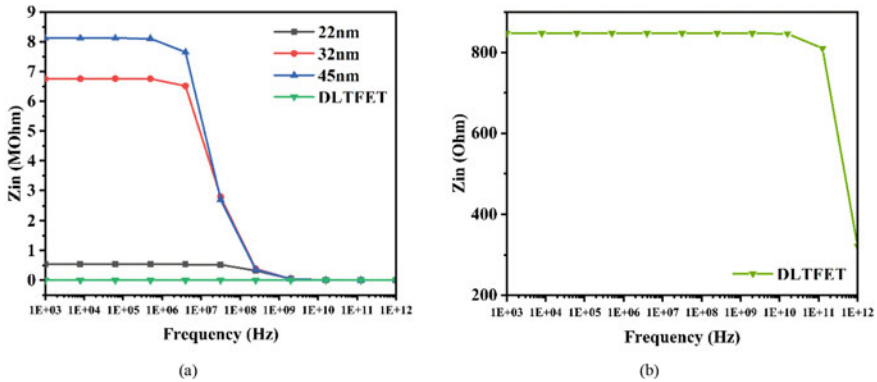


Fig. 8 a Z_{in} versus frequency plot of the SCM for different technologies. b Z_{in} versus frequency plot of the SCM for DLTFET

2.5 Input Resistance (Z_{in}) Alter with Frequency

The input resistance of SCM must be as low as possible and must be stable for an extended frequency band. From Fig. 8a, it can be detected that the input resistance of DLTFET SCM is the lowest among the four transistors SCM. But it is not possible to make it clear that input resistance is stable for an extended frequency band, so another graph is plotted for the same, i.e., Fig. 8b.

2.6 Output Resistance (Z_{out}) Alter with Frequency

The output resistance of SCM must be as high as possible for an extended frequency band. From Fig. 9, it can be concluded that the output resistance of DLTFET SCM is highest among the four transistors SCM for the frequency up to 10 GHz.

2.7 AC Analysis

Input voltage and output voltage are set to 1.2 V DC each for biasing and set both the transistors in the saturation mode. Furthermore, 1 mV, 1 kHz sinusoidal signal is applied over the DC supply. To evaluate the input current response, the output current response, and the gain concerning frequency for the SCM for the different technologies, AC sweep is applied up to 1 PHz. From Fig. 10a, it can be observed that SCM of all the four transistors has shown nearly the same input current response. From Fig. 10b, the output current becomes constant for all the frequencies. From Fig. 10c -3 DB gain is 0 for the frequency up to 100 GHz for DLTFET. It is difficult

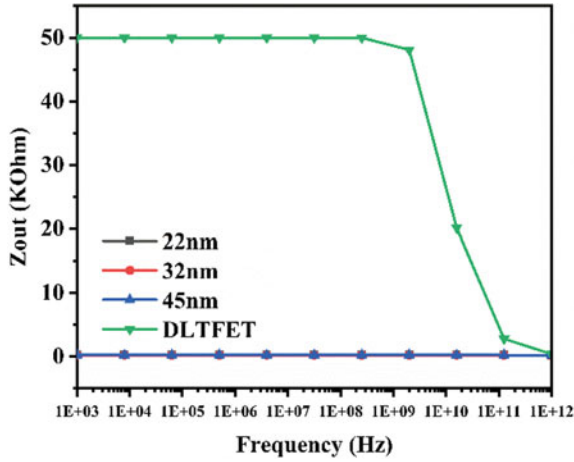


Fig. 9 Z_{out} versus frequency plot of the BCM for different technologies

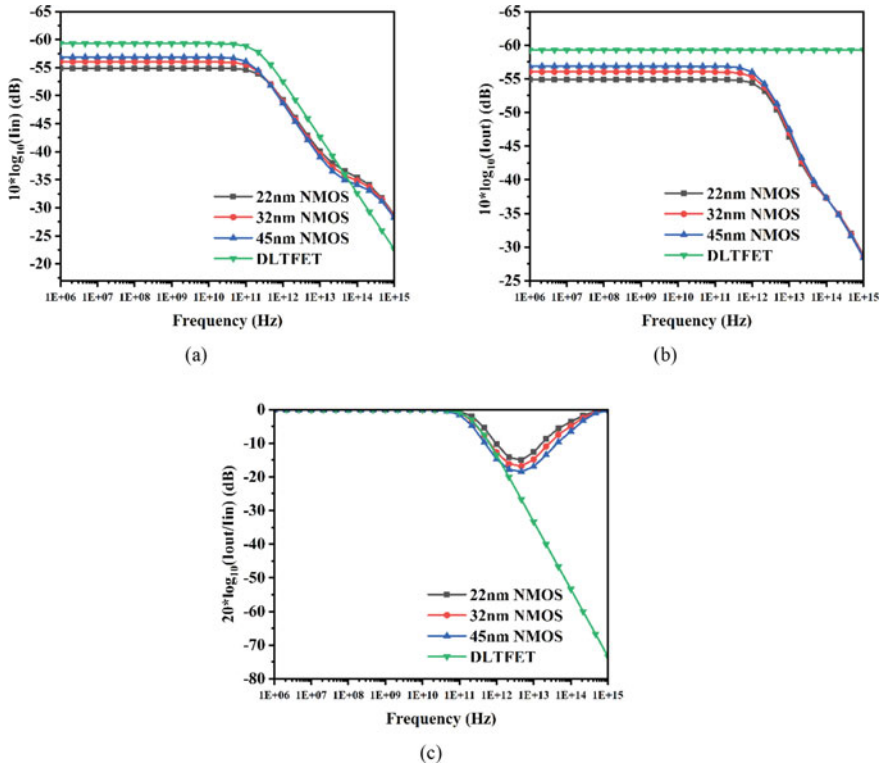


Fig. 10 SCM a I_{in} b I_{out} c -3 dB gain versus frequency response for different technologies

to understand the response of gain for the DLTFET for the frequency higher than 100 GHz.

3 Conclusion

This manuscript investigates a DLTFET-based simple current mirror using numerical simulations. It is found that 20 nm DLTFET can be used as a better substitute for NMOS technologies at and beyond the 45 nm technology node for the analog applications such as current mirror because of its low threshold voltage (V_{th}), high transconductance (g_m), high output impedance (Z_{out}), and low input impedance (Z_{in}), symmetrical response, stable bandwidth response over frequency, and negligible leakage. This paper compares the 20 nm DLTFET technology because it works better in the SCM over 45, 32, and 22 nm NMOS technologies by considering several comparative parameters. Furthermore, a small length of transistors is desired for the accumulation of a higher number of transistors in an IC. Additionally, the analysis can also be done for more complicated circuits such as cascaded current mirrors, differential amplifiers, and operational amplifiers in the future.

Acknowledgements SMDP-C2SD has supported the work as per the reference letter no. 9(1)2014-MDD (NIT Delhi, INDIA).

References

1. Choi WY, Park B, Lee JD, Liu TK (2007) Tunneling field-effect transistors (tfets) with subthreshold swing (ss) less than 60 mV/dec. *IEEE Electron Device Lett* 28(8):743–745. <https://doi.org/10.1109/LED.2007.901273>
2. Wang F, Hilsenbeck K, Nirschl T, Oswald M, Stepper C, Weis M, Schmitt-Landsiedel D, Hansch W (2004) Complementary tunneling transistor for low power application. *Solid-state Electron* 48(12):2281–2286. <https://doi.org/10.1016/j.sse.2004.04.006>
3. Asenov A, Brown AR, Davies JH, Kaya S, Slavcheva G (2003) Simulation of intrinsic parameter fluctuations in decananometer and nanometer-scale MOSFETs. *IEEE Trans Electron Devices* 50(9):1837–1852. <https://doi.org/10.1109/TED.2003.815862>
4. Shin C, Sun X, Liu TK (2009) Study of random-dopant-fluctuation (RDF) effects for the trigate bulk MOSFET. *IEEE Trans Electron Devices* 56(7):1538–1542. <https://doi.org/10.1109/TED.2009.2020321>
5. Jhaveri R, Nagavarapu V, Woo JCS (2011) Effect of pocket doping and annealing schemes on the source-pocket tunnel field-effect transistor. *IEEE Trans Electron Devices* 58(1):80–86. <https://doi.org/10.1109/TED.2010.2089525>
6. Le Royer C, Mayer F (2009) Exhaustive experimental study of tunnel field effect transistors (TFETs): from materials to architecture. In: 2009 10th international conference on ultimate integration of Silicon, Aachen, pp 53–56. <https://doi.org/10.1109/ULIS.2009.4897537>
7. Leonelli D, Vandooren A, Rooyackers R, De Gendt S, Heyns MM, Groeseneken G (2010) Optimization of tunnel FETs: impact of gate oxide thickness, implantation, and annealing conditions. In: 2010 Proceedings of the European solid-state device research conference, Sevilla, pp 170–173. <https://doi.org/10.1109/ESSDERC.2010.5618408>

8. Kumar MJ, Janardhanan S (2013) Doping-less tunnel field effect transistor: design and investigation. *IEEE Trans Electron Devices* 60(10):3285–3290. <https://doi.org/10.1109/TED.2013.2276888>
9. Damrongplait N, Shin C, Kim SH, Vega RA, King Liu T (2011) Study of random dopant fluctuation effects in germanium-source Tunnel FETs. *IEEE Trans Electron Devices* 58(10):3541–3548. <https://doi.org/10.1109/TED.2011.2161990>
10. Damrongplait N, Kim SH, Liu TK (2013) Study of random dopant fluctuation induced variability in the raised-Ge-source TFET. *IEEE Electron Device Lett* 34(2):184–186. <https://doi.org/10.1109/LED.2012.2235404>
11. Sharma N, Chauhan SS (2017) Dual metal drain Ge-source dopingless TFET with enhanced turn-ON steep subthreshold swing and high ON-current. *Electron Lett* 53(14):960–962. <https://doi.org/10.1049/el.2017.0157>
12. Nigam K, Pandey S, Kondekar PN, Sharma D, Kumar Parte P (2017) A barrier controlled charge plasma-based TFET with gate engineering for ambipolar suppression and RF/linearity performance improvement. *IEEE Trans Electron Dev* 64(6):2751–2757. <https://doi.org/10.1109/TED.2017.2693679>
13. Yadav DS et al (2017) Performance investigation of hetero material (InAs/Si)-based charge plasma TFET. In: *Micro Nano Lett* 12(6):358–363. <https://doi.org/10.1049/mnl.2016.0688>
14. Haris M, Loan SA, Mainuddin (2017) An ambipolar immune Si/GaAs hetero-junction doping-less TFET. In: 2017 International conference on microelectronic devices, circuits and systems (ICMDCS), Vellore, pp 1–4. <https://doi.org/10.1109/ICMDCS.2017.8211539>
15. Verma A, Sharma S, Bharti S, Bharti M, Kaur B (2020) Design of tunnel junction engineered dopingless TFET for low power application. In: *The 21st International symposium on quality electronic design*, pp 1–6
16. Sedra S, Smith KC (2009) *Microelectronics circuits theory and applications*, 5th edn. Oxford University Press, New York
17. Jaeger RC, Blalock TN (2011) *Microelectronic circuit design*. McGraw-Hill, New York
18. Allen PE, Holberg DR (2011) *CMOS analog circuit design*, 2nd edn. Oxford University Press, United Kingdom
19. Laskovski AN (2011) *Biomedical engineering trends in electronics, communications, and software*. Published by InTech, Rijeka
20. Tanguay L, Sawan M, Savaria Y (2008) A very-high output impedance current mirror for very-low voltage biomedical analog circuits. *APCCAS 2008–2008 IEEE Asia Pacific conference on circuits and systems*, Macao, pp 642–645. <https://doi.org/10.1109/APCCAS.2008.4746105>
21. Gupta R, Rana AK (2013) Study of CNTFET based basic current mirror in comparison with NMOS technologies. In: 2013 International conference on advanced computing and communication systems, Coimbatore, pp 1–6. <https://doi.org/10.1109/ICACCS.2013.6938695>
22. Sharma S, Kaur B (2020) Performance investigation of asymmetric double gate doping less tunnel FET with Si/Ge heterojunction. *IET Circuits Devices Syst* 14(5):695–701. <https://doi.org/10.1049/iet-cds.2019.0290>

Energy Harvesting Techniques for Self-sustainable Energy Systems



Bishal Nahak , Yogesh Dewang , and Vipin Sharma 

1 Introduction

Energy demand of the world is increasing due to technological advancement and increasing population, whereas fossil fuels are depleting at a faster rate [1–4]. According to energy researchers, it was estimated that 30 trillion watts more energy will be needed by 2050 due to global population growth [3]. The majority of energy being produced depends on fossil fuels like gas, coal and oil. Unfortunately, the use of these resources leads to degradation of human health and raises environmental concern, and extensive use of these products causes scarcity of the fossil fuels [4]. In order to overcome this, the concept of renewable energy has been established. It represents a way to produce clean and safe energy from the eco-friendly sources present in the environment.

Reduction in weight usually in turn enhances the versatility in performance of electronic devices. Manually operated devices with compactness are commercially available which can operate large operations and can communicate wirelessly. These devices are driven by battery supply which offers a finite amount of energy [5, 6]. Apart from that these batteries occupy a large amount of space, and sometimes, it becomes economically expensive which ultimately affects the price hike of the device. Energy crisis and global warming are some of the major concerning issues that are increasingly discussed worldwide. With the passage of time, electronic devices

B. Nahak

Department of Electronics and Communication Engineering, National Institute of Science and Technology, Berhampur, Odisha, India

Y. Dewang

Department of Mechanical Engineering, Lakshmi Narain College of Technology, Bhopal, MP, India

V. Sharma (✉)

Department of Mechanical Engineering, Sagar Institute of Research & Technology, Bhopal, MP, India

are becoming smaller, thus, requiring a very small amount of energy. There is continuous research being carried out to increase the energy density of batteries, but the amount of power available in batteries is limited, which ultimately affects the lifetime of devices [5–7]. Therefore, it becomes necessary to extend the life of the device, especially in the areas where instruments present in a manufacturing plant are used to synthesize chemical processes in hazardous conditions. It requires a source supply independent of the limited energy available in batteries.

Currently, several developed ideas and options exist, to provide new ways to harvest energy. In upcoming years, there is possibility of dependency on ambient energy resources which may remove present constraints. The aim of this work is to review the various types of materials that emerged as an advance for energy applications.

2 Various Aspects of Energy Harvesting

Energy harvesting is the technique to recover lost energy or to tap the ambient energy on a smaller scale. The lost energy can be utilized to create a self-sustaining energy system [5–7]. It is similar in concept to renewable energy generation, like solar or wind power. The renewable energy power generation is concerned with megawatts of power, whereas energy harvesting is limited to micro to milliwatts. The energy harvesting can be a better alternative for batteries. As batteries contain a fixed supply of energy and require periodic recharging. In remote or unreachable locations and medical devices which reside in the human body, the energy harvesting technique is the promising solution [5–10].

In the last decades, the energy harvesting concept gained a boost and explosive research and development were carried out by researchers in the past. The basic aim is to deliver power from the sources that are available in the environment [5]. This concept can also be related to capturing the energy coming out as by-product of an automated process.

The use of this energy promotes wireless devices and also reduces the battery maintenance problem [6]. The output of the harvesting system can take in form of voltage and current, depending on the nature of the harvester. Then, the output from the harvester is supplied to the energy management system, where it modifies the output to desired excitation so that it can be fed into subsystems (sensors). It is always not possible to generate continuous energy from the harvester. Considering the example of solar energy, in which the maximum power will be generated from PV cells in day time which also depends on the position of sun at sky, and it is obvious that there will be no power generated during night. Therefore, it becomes necessary to store the generated power on a temporary basis so that it can be delivered in a controlled fashion to the subsystem [7]. Figure 1 shows the generalized block diagram of the energy harvesting system attached with subsystems. Examples of various energy harvesting techniques involve electromagnetic energy in the form of light energy, radio frequency energy, mechanical energy, vibration energy, piezoelectric

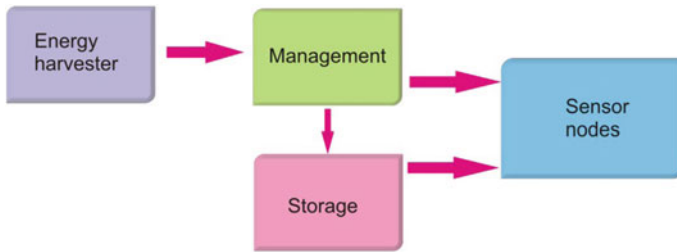


Fig. 1 Basic energy harvesting system

energy, energy generated by human motions and thermal energy. These energies are stored and converted into useful electrical energy with the aid of different sensors. On the other hand, recently, triboelectric has come to be known for its competitive energy harvesting approach [8–10]. Though this process of energy harvesting is efficient, there is a need for proper research to bring it in commercial use [11–17]. Such renewable energy systems can increase the life span and capability of the devices and also lessen the environmental concern caused by disposal of batteries.

3 Energy Harvesting Techniques

3.1 Thermoelectric Energy Harvesting

The most abundant form of energy present in the environment is thermal energy after solar energy. Devices working on the basis of thermal energy get their input from different sources such as humans, animals and heat produced by machines. In order to harvest, the energy thermoelectric effect or pyroelectric effect can be used. In the thermoelectric generator, different materials junctions are kept at hot and cold temperature to generate electricity. The schematic presentation of a thermoelectric generator is shown in Fig. 2.

3.2 Piezoelectric Energy Harvesting

Out of all other energy harvesting techniques, piezoelectric materials-based energy harvesting techniques are the most studied once because of its high efficiency and applicability. It converts the available mechanical energy into electrical energy. The piezoelectric generators work on the piezoelectric effect exhibited by the piezoelectric materials. The piezoelectric generator is presented schematically in Fig. 3. Worthington et al. [18] designed a model which accounts for the amount of energy

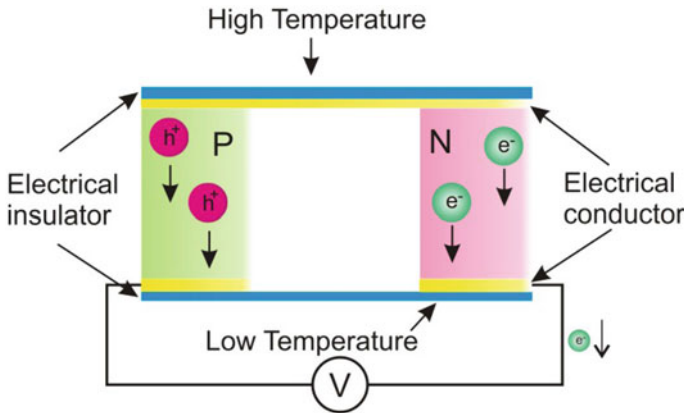


Fig. 2 Schematic illustration of thermoelectric generator

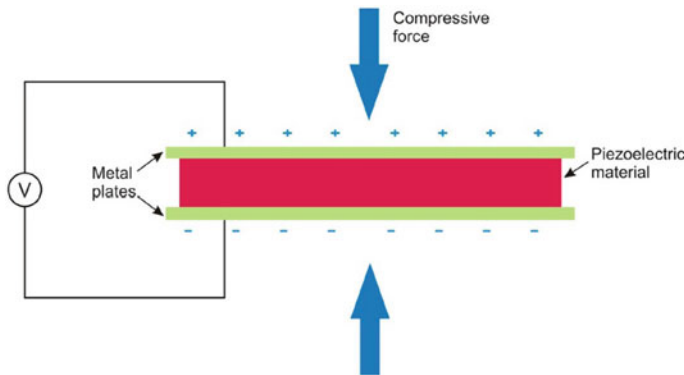


Fig. 3 Schematic illustration of the piezoelectric generator

generation via vibration of cantilever beam that are connected to piezoelectric transducer elements. They found that model to be efficient through experiments and do not depend upon load resistance. This experiment proved to be the base in several other experiments. Further, Hagood et al. [19] developed this model by using PZT shunt damping circuits to control passive vibration. Such types of advanced technologies are utilized in order to eradicate problems in concern to wearable electronics and health monitoring.

Thermoelectric effect consists of Seebeck effect, Thomson effect and Peltier effect [20]. Heat source is vital for generation of energy via using these effects. The efficiency depends mainly on the temperature gradient. More is the temperature difference, better will be the energy transfer. Spontaneous polarization of anisotropic solids due to instantaneous temperature variation is responsible for generation of

pyroelectric effect. It can be used when there is availability of uniform temperature gradient in the environment [21]. The output generated varies from $10 \mu\text{W}/\text{cm}^2$ and can go up to $60 \text{W}/\text{cm}^2$. Though this technology is good to use, durable and scalable, it does not provide much output or efficiency due to low temperature gradient. Therefore, a subsequent research is needed to use human activity for thermal energy harvesting. Piezo-thermo-fluidic and piezo-thermo-mechanic are the alternative conversion methods that are also implemented for thermal energy generation, and these methods can be used to run appliances [22].

Humans are the reservoir of energy, since human body stores the chemical energy and use it to do work, i.e., converting the chemical energy to mechanical energy. Energy can be harvested from everyday activities of the human being. The related devices must be wearable and consist of a sensor and based on wireless technology. Implantable sensors are being used to monitor the activity; energy can be generated from the body movement (kinetic). Research is going on to combine human movement and piezoelectric materials to maximize the output [23, 24]. It has been observed that human actions such as exhalation and inhalation produce less than 1 W, body heat produces around 2.1–4.8 W, finger movement produces <60 W or football (heel strike) produces 67 W [25].

3.3 Triboelectric Energy Harvesting

With the growing advanced technology and electronics, it is necessary to explore renewable and portable energy sources. The environment is a rich source of energy, mechanical, wind, solar, thermal and chemical energy [26–29]. The traditional systems could not meet the energy requirement with high efficiency and also in a sustainable manner. The triboelectric generator harvest energy due to electrostatic charge developed on contact materials. Schematic presentation of the triboelectric generator is displayed in Fig. 4.

In a study, Wang et al. [30] had developed a triboelectric nanogenerator (TENG). The TENG converts mechanical input into electrical output. These devices are low cost, simple fabrication and highly efficient. Till now, there have been some TENGs fabricated which are able to generate power up to $500 \text{W}/\text{m}^2$ with an efficiency of 85% [31, 32]. With the fast growing of flexible technology, the flexible TENGs have been

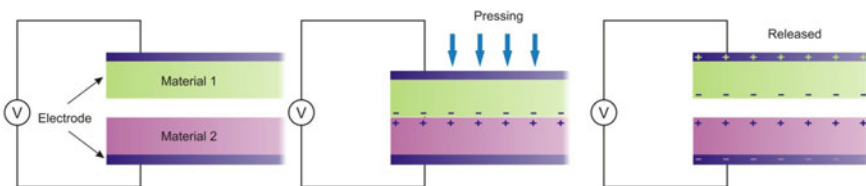


Fig. 4 Schematic illustration of triboelectric generator

extensively studied. One of the main principles on which TENGs work, it contains two different contact materials that are arranged in a face to face fashion. It is well known that when two materials are placed close to each other, opposite static charges appear to the surface, owing to contact electrification. To enhance the performance of TENGs, different methods have been investigated. Materials such as polyamide, polytetrafluoroethylene, polyvinylidene fluoride and silk are found to be the most favorable one, due to their lower cost, portable and disposable characteristics.

Recently, several investigations have been performed to increase output of TENGs by using carbon nanotubes, nano-Ag ink and graphene [33]. Also, the interchange of TENGs can be done with other types of generators, and the output performance can be increased dramatically.

4 Applications

The concept of energy storage has made wide range of products to work through without wire fashion. Use of energy harvesting techniques helps in reducing traditional battery-based systems and also enhances the lifetime of the sensors. Jason et al. [34] presented a “duty cycle algorithm which is adaptive in nature, i.e., the sensor nodes can autonomously adjust their duty cycle as per the energy availability in the environment.”

4.1 *Biomedical Applications*

With the extensive research on energy harvesting, a lot of effort is being invested in the development of medical applications. Portable medical devices have attracted major concern because these devices need to be small in size, lightweight and either wearable or implanted in the body. These devices require very less amount of energy consumption. To meet this requirement, small size batteries would be enough, but due to technological issues, these batteries have not gone undersize evolution. This limits the lifetime of the portable devices. Replacement of the battery after every 8 years is essential for smooth functioning of the pacemaker. Implantable neuro-stimulator has a battery life of nearly five years. In order to overcome this, ZnO nanogenerators [21] based on piezoelectric effects are used inside the human body. Thus, there is a need for low powered medical equipment and research is being carried out.

4.2 *Biomedical Applications*

Apart from biomedical applications, energy harvesting techniques are also prominently used in the field of industrial applications. Piezoelectric material (PFCB) is

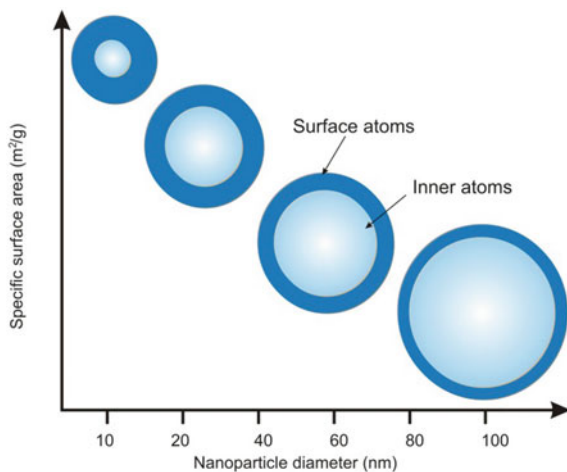
utilized for making piezoelectric shoes [35]. A sensor senses the motion created on PFCB, and then it converts it into electrical energy which is further used to power small appliances. This process can be adopted by everybody as it is easy to use and it also does not require any additional care. Another example, in 2009, few Harvard undergraduates designed a prototype “power ball” [35]. It has an induction coil inside the ball which detects when it is kicked or any motion occurs. Further, they enhanced the prototype in which other electronic gadgets can be charged by connecting it through the USB port. Energy harvesting trees are based on advanced nanotechnology which has a cable to convert solar and wind energy into usable electrical energy.

5 Materials for Energy Harvesting

Exceptional characteristics of nanoparticles make them appropriate candidates for energy storage applications. The properties of nanoparticles are significantly different from their bulk owing to an increase in fraction of surface atom and higher surface area [1, 2]. The fraction of surface atoms in the nanoparticles increases with the reduction in size as shown in Fig. 5.

Carbon is one of the most abundant elements that are being present in the environment and its allotropes like fullerenes, carbon nanotubes, graphene, etc., have been known as good sources for energy harvesting and storing materials [36, 37]. One of such prominent applications of carbon nanotubes is in the fuel cell devices. These devices convert the chemical energy into direct electricity instead of heating it to get energy. It consists of an anode, cathode and electrode. In the typical mechanism of the fuel cell involved, hydrogen is being supplied at the anode which further gets split into its constituent’s electrons and protons. The generated protons get diffused

Fig. 5 Increase in surface atoms of nanoparticles on decreasing the diameter



at cathode and electrons flow out of anode providing electricity. At the end electron and proton, both combine to form water [36]. Since the early 1960s, considerable research has been conducted to increase the proton exchange membrane fuel cell (PEMFC). In order to increase the performance, carbon nanomaterials have been used. For instance, carbon blacks like Acetylene black, Ketjen Black, Vulcan XC-72, etc., are commonly used materials for PEMFC. They support large surface area to ensure high activity. Carbon nanomaterials are also used in making improvised electrolyte materials for fuel cells. Kannan et al. [37] in their experiment he had added functionalized single wall nanotubes into nafion matrix. This provides a network for proton mobility and also improved the mechanical stability of membranes in H_2/O_2 cells.

In recent years, conducting polymers have emerged as a prominent candidate for thermal energy harvesting [15]. In comparison with traditional inorganic semiconductors or semiconducting polymers having relatively lower thermal conductivity, while their electrical conductivity is as high as ~ 1000 s/cm. This distinctive combinational property of these materials makes it a favorable condition for energy harvesting. Additionally, these polymers have advantages like printable, flexible and moldable. In order to increase its properties, doping is also performed. For example, poly (3, 4-ethylenedioxythiophene) turned dark blue to transparent when it turned from undoped state to heavily doped state [16, 17].

During the 1880s, piezoelectric materials are used to be naturally occurring substances (quartz). After 140 years, researchers were able to develop piezoelectric materials bearing outstanding characteristics which are similar with those naturally made quartz. Piezoelectric ceramics and piezoelectric crystals are the two major forms of inorganic materials which are majorly applied in mechanical energy storage [38–40]. ZnO nanowires and quartz films are piezoelectric crystals which exhibit single crystal structure. In contrast to piezoelectric crystals, piezoelectric ceramics have shown multiple crystal structures. These piezoelectric ceramics show the piezoelectricity under application of a high electric field for arranging orientations of crystals. $Pb[Zr_xTi_{1-x}]O_3$, AlN and barium titanate ($BaTiO_3$) are examples of piezoelectric ceramics [40].

Polymers, for example, poly (vinylidene fluoride-co-tri-fluoroethylene) (PVDF) offers superior characteristics such as easy fabrication, sufficiently mechanically tough and flexible as compared to inorganic materials [41–47]. PVDF polymers found to be more appropriate for piezoelectric energy harvesting applications. PVDF exhibits five semi-crystalline different phases, namely as α , β , γ , δ and ϵ . β phase found to be most strong among all five phases [47].

It is noteworthy that biological tissues or microorganisms like bone, virus and silk demonstrate property of piezoelectricity [48–50]. With the advancement of biotechnology, these materials offer an eco-friendly approach to energy harvesting. Lee et al. [51] have demonstrated that M13 bacteriophage shows piezoelectric behavior and can be utilized for energy storage purpose. It exhibits strength up to 7.8 pm/V. Further, studies show that the generator of piezoelectric based on M13 bacteriophage shows a voltage of about 400 mV and current intensity up to 6 nA. Gosh and Mandal [52]

have designed a nanogenerator bio-based nanogenerator piezoelectrically driven-based through the swim bladder of Catla fish. It showed open circuit voltage up to 10 V and short circuit current up to 51 nA at a stress of ~ 1.4 MPa.

Solar cells as a sustainable source of energy have gained an intensive research interest [53]. One of the major problems associated with this is the recombination rate of electron and hole pairs [54–56], in which the use of graphene materials has significantly enhanced the efficiency of the solar cell [57–61]. It has magnificent electrical and optical properties. It provides a large interface for efficient exciton and dissociation of charge carriers in solar cells and also it acts as a buffer layer and slows down the charge recombination rate [62]. Thus, novel nanostructure fabrication of graphene is very significant research to further improve the device efficiency.

6 Conclusions

Energy harvesting techniques, materials used in energy harvesting and their applications were briefly summarized. The energy harvesting techniques become increasingly important to address technological advancement in the field of Internet of things, wireless sensor, biomedical equipment and self-sustained systems. Conventional battery technology in remote or in biomedical applications was successfully replaced by energy harvesters. Flexibility of energy harvesters makes them suitable for wearable energy devices. Recent research focuses on increasing the efficiency of energy harvesters and hybridization. The hybrid energy harvesters, i.e., harvesting energy from multiple sources are gaining importance owing to high efficiency and higher energy output.

Acknowledgements Authors gratefully acknowledges virtual internship program of science leadership.

References

1. Khan S, Dewang Y, Raghuwanshi J, Sharma V (2019) Nanoparticles exceptional properties: applications in internal combustion engines. In: AIP conference proceedings, vol 2100, no. 1, pp 020146. AIP Publishing LLC
2. Khan S, Dewang Y, Raghuwanshi J, Shrivastava A, Sharma V (2016) Nanoparticles as fuel additive for improving performance and reducing exhaust emissions of internal combustion engines. *Int J Environ Anal Chem* 1–23
3. Gilbert G (1999) World population: a reference handbook. ABC-CLIO
4. Notarianni M, Liu J, Vernon K, Motta N (2016) Synthesis and applications of carbon nanomaterials for energy generation and storage. *Beilstein J Nanotechnol* 7(1):149–196
5. Nozariasbmarz A, Collins H, Dsouza K, Polash MH, Hosseini M, Hyland M et al (2020) Review of wearable thermoelectric energy harvesting: from body temperature to electronic systems. *Appl Energy* 258:114069

6. Gholikhani M, Roshani H, Dessouky S, Papagiannakis AT (2020) A critical review of roadway energy harvesting technologies. *Appl Energy* 261:114388
7. Beeby S, White NM (eds) (2010) Energy harvesting for autonomous systems. Artech House
8. Wang S, Lin L, Wang ZL (2010) Nanoscale triboelectric-effect-enabled energy conversion for sustainably powering portable electronics. *Nano Lett* 12(12):6339–6346
9. Jiang W, Li H, Liu Z, Li Z, Tian J, Shi B, Zou Y, Ouyang H, Zhao C, Zhao L, Sun R (2010) Fully bioabsorbable natural materials based triboelectric nanogenerators. *Adv Mater* 30(32):1801895
10. Chen L, Shi Q, Sun Y, Nguyen T, Lee C, Soh S (2018) Controlling surface charge generated by contact electrification: Strategies and applications. *Adv Mater* 30(47):1802405
11. Shaikh FK, Zeadally S (2016) Energy harvesting in wireless sensor networks: A comprehensive review. *Renew Sustain Energy Rev* 55:1041–1054
12. Bai Y, Jantunen H, Juuti J (2019) Ferroelectric oxides for solar energy conversion, multi-source energy harvesting/sensing, and opto-ferroelectric applications. *Chem Sus Chem* 12(12):2540
13. Starner T, Paradiso JA (2004) Human generated power for mobile electronics. *Low-Power Electron Design* 45:1–35
14. Moll F, Rubio A (2000) An approach to the analysis of wearable body-powered systems. In: *Proceedings of the MIXDES*
15. Russ B, Glauddell A, Urban JJ, Chabiny ML, Segalman RA (2016) Organic thermoelectric materials for energy harvesting and temperature control. *Nat Rev Mater* 1(10):1–14
16. Bredas JL, Street GB (1985) Polarons, bipolarons, and solitons in conducting polymers. *Acc Chem Res* 18(10):309–315
17. Chance RR, Bredas JL, Silbey R (1984) Bipolaron transport in doped conjugated polymers. *Phys Rev B* 29(8):4491
18. Sodano HA, Park G, Inman DJ (2004) Estimation of electric charge output for piezoelectric energy harvesting. *Strain* 40(2):49–58
19. Hagood NW, Chung WH, Flotow AV (1990) Modelling of piezoelectric actuator dynamics for active structural control. *J Intell Mater Syst Struct* 1(3):327–354
20. Yildiz F, Coogler, K.L. (2017) Low power energy harvesting with a thermoelectric generator through an air conditioning condenser. *J Eng Technol* 34(1):8–16
21. Yang Y, Guo W, Pradel KC, Zhu G, Zhou Y, Zhang Y, Hu Y, Lin L, Wang ZL (2012) Pyroelectric nanogenerators for harvesting thermoelectric energy. *Nano Lett* 12(6):2833–2838
22. Monfray S, Puscasu O, Savelli G, Soupremanian U, Ollier E, Guerin C, Frechette LG, Leveille E, Mirshekari G, Maitre C, Coronel P (2012) Innovative thermal energy harvesting for zero power electronics. In: *IEEE Silicon Nanoelectronics Workshop (SNW)*, pp 1–4
23. Mitcheson PD, Yeatman EM, Rao GK, Holmes AS, Green TC (2008) Energy harvesting from human and machine motion for wireless electronic devices. *Proc IEEE* 96(9):1457–1486
24. Shenck NS, Paradiso JA (2013) Energy scavenging with shoe-mounted piezoelectrics. *IEEE Micro* 21(3):30–42
25. Yildiz F (2004) Energy harvesting from passive human power. *J Appl Sci Eng Technol* 4
26. Lewis NS (2007) Toward Cost-Effective Solar Energy Use. *Science* 315(5813):798–801
27. Himmel ME, Ding SY, Johnson DK, Adney WS, Nimlos MR, Brady JW, Foust TD (2007) Biomass recalcitrance: engineering plants and enzymes for biofuels production. *Science* 315(5813):804–807
28. Wen X, Yang W, Jing Q, Wang ZL (2014) Harvesting broadband kinetic impact energy from mechanical triggering/vibration and water waves. *ACS Nano* 8(7):7405–7412
29. Dagdeviren C, Joe P, Tuzman OL, Park KI, Lee KJ, Shi Y, Huang Y, Rogers JA (2016) Recent progress in flexible and stretchable piezoelectric devices for mechanical energy harvesting, sensing and actuation. *Extreme Mech Lett* 9:269–281
30. Fan FR, Tian ZQ, Wang ZL (2012) Flexible Triboelectric Generator. *Nano Energy* 1(2):328–334
31. Zhu G, Zhou YS, Bai P, Meng XS, Jing Q, Chen J, Wang ZL (2014) A shape adaptive thin film based approach for 50% high efficiency energy generation through micro grating sliding electrification. *Adv Mater* 26(23):3788–3796
32. Xie Y, Wang S, Niu S, Lin L, Jing Q, Yang J, Wu Z, Wang ZL (2014) Grating structured freestanding triboelectric layer nanogenerator for harvesting mechanical energy at 85% total conversion efficiency. *Adv Mater* 26(38):6599–6607

33. Fan X, Chen J, Yang J, Bai P, Li Z, Wang ZL (2015) Ultrathin, rollable, paper-based triboelectric nanogenerator for acoustic energy harvesting and self-powered sound recording. *ACS Nano* 9(4):4236–4243
34. Hsu J, Zahedi S, Kansal A, Srivastava M, Raghunathan V (2006) Adaptive duty cycling for energy harvesting systems. In: *Proceedings of the 2006 international symposium on Low power electronics and design*, Oct 2006, pp 180–185
35. Shenck NS, Paradiso JA (2001) Energy scavenging with shoe-mounted piezoelectrics. *IEEE Micro* 21(3):30–42
36. Gupta S, Meek R (2020) Highly efficient thermo-electrochemical energy harvesting from graphene-carbon nanotube ‘hybrid’ aerogels. *Appl Phys A* 126(9):1–12
37. Kannan R, Kakade BA, Pillai VK (2008) Polymer electrolyte fuel cells using Nafion based composite membranes with functionalized carbon nanotubes. *Angew Chem Int Ed* 47(14):2653–2656
38. Mattiat OE (2013) *Ultrasonic transducer materials*. Springer Science & Business Media
39. Tan T, Yan Z, Hajj M (2016) Electromechanical decoupled model for cantilever-beam piezoelectric energy harvesters. *Appl Phys Lett* 109(10):101908
40. Kim HS, Kim JH, Kim J (2011) A review of piezoelectric energy harvesting based on vibration. *Int J Precis Eng Manuf* 12(6):1129–1141
41. Hwang GT, Annapureddy V, Han JH, Joe DJ, Baek C, Park DY, Kim DH, Park JH, Jeong CK, Park KI, Choi JJ (2016) Self powered wireless sensor node enabled by an aerosol deposited PZT flexible energy harvester. *Adv Energy Mater* 6(13):1600237
42. Jeong CK, Park KI, Son JH, Hwang GT, Lee SH, Park DY, Lee HE, Lee HK, Byun M, Lee KJ (2014) Self-powered fully-flexible light-emitting system enabled by flexible energy harvester. *Energy Environ Sci* 7(12):4035–4043
43. Misra V, Bozkurt A, Calhoun B, Jackson T, Jur JS, Lach J, Lee B, Muth J, Oralkan Ö, Öztürk M, Trolier-McKinstry S (2015) Flexible technologies for self-powered wearable health and environmental sensing. *Proc IEEE* 103(4):665–681
44. Fang J, Wang X, Lin T (2011) Electrical power generator from randomly oriented electrospun poly (vinylidene fluoride) nanofibre membranes. *J Mater Chem* 21(30):11088–11091
45. Pan CT, Yen CK, Wang SY, Lai YC, Lin L, Huang JC, Kuo SW (2015) Near-field electrospinning enhances the energy harvesting of hollow PVDF piezoelectric fibers. *RSC Adv* 5(103):85073–85081
46. Liu H, Zhong J, Lee C, Lee SW, Lin L (2018) A comprehensive review on piezoelectric energy harvesting technology: Materials, mechanisms, and applications. *Appl Phys Rev* 5(4):041306
47. Zhu G, Zeng Z, Zhang L, Yan X (2008) Piezoelectricity in β -phase PVDF crystals: a molecular simulation study. *Comput Mater Sci* 44(2):224–229
48. Yucel T, Cebe P, Kaplan DL (2011) Structural origins of silk piezoelectricity. *Adv Func Mater* 21(4):779–785
49. Otter M, Shoening J, Williams WS (1985) Evidence for different sources of stress generated potentials in wet and dry bone. *J Orthop Res* 3(3):321–324
50. Wei H, Wang H, Xia Y, Cui D, Shi Y, Dong M, Liu C, Ding T, Zhang J, Ma Y, Wang N (2018) An overview of lead-free piezoelectric materials and devices. *J Mater Chem C* 6(46):12446–12467
51. Lee BY, Zhang J, Zueger C, Chung WJ, Yoo SY, Wang E, Meyer J, Ramesh R, Lee SW (2012) Virus-based piezoelectric energy generation. *Nat Nanotechnol* 7(6):351
52. Ghosh SK, Mandal D (2016) High-performance bio-piezoelectric nanogenerator made with fish scale. *Appl Phys Lett* 109(10):103701
53. Yu D, Yang Y, Durstock M, Baek JB, Dai L (2010) Soluble P3HT-grafted graphene for efficient bilayer– heterojunction photovoltaic devices. *ACS Nano* 4(10):5633–5640
54. Teichler A, Eckardt R, Hoepfener S, Friebe C, Perelaer J, Senes A, Morana M, Brabec CJ, Schubert US (2011) Combinatorial screening of polymer: fullerene blends for organic solar cells by inkjet printing. *Adv Energy Mater* 1(1):105–114
55. Ding IK, Zhu J, Cai W, Moon SJ, Cai N, Wang P, Zakeeruddin SM, Grätzel M, Brongersma ML, Cui Y, McGehee MD (2011) Plasmonic dye sensitized solar cells. *Adv Energy Mater* 1(1):52–57

56. Song QL, Yang HB, Gan Y, Gong C, Ming Li C (2010) Evidence of harvesting electricity by exciton recombination in an n–n type solar cell. *J Am Chem Soc* 132(13):4554–4555
57. Treat ND, Brady MA, Smith G, Toney MF, Kramer EJ, Hawker CJ, Chabinyc ML (2011) Interdiffusion of PCBM and P3HT reveals miscibility in a photovoltaically active blend. *Adv Energy Mater* 1(1):82–89
58. Guai GH, Song QL, Guo CX, Lu ZS, Chen T, Ng CM, Li CM (2012) Graphene-Pt ITO counter electrode to significantly reduce Pt loading and enhance charge transfer for high performance dye-sensitized solar cell. *Sol Energy* 86(7):2041–2048
59. Scharber MC, Mühlbacher D, Koppe M, Denk P, Waldauf C, Heeger AJ, Brabec CJ (2006) Design rules for donors in bulk-heterojunction solar cells-Towards 10% energy-conversion efficiency. *Adv Mater* 18(6):789–794
60. Mastroianni S, Asghar I, Miettunen K, Halme J, Lanuti A, Brown TM, Lund P (2014) Effect of electrolyte bleaching on the stability and performance of dye solar cells. *Phys Chem Chem Phys* 16(13):6092–6100
61. Park S, Ruoff RS (2009) Chemical methods for the production of graphenes. *Nat Nanotechnol* 4(4):217–224
62. Wu YH, Yu T, Shen ZX (2010) Two-dimensional carbon nanostructures: fundamental properties, synthesis, characterization, and potential applications. *J Appl Phys* 108(7):10

A Novel Color-Coded Light-Based Communication for Autonomous Swarm Robotics Research



Abhishek Kaushal and Anuj Kumar Sharma

1 Introduction

A system with several autonomous robots operating together severe difficulties on the design of control schemes when using the traditional approach to accomplish the given task. Inspired from the natural swarm systems (bees, ants, and other social animals), swarm robotics in conjunction with swam intelligence aims at providing solution to control such large multi-robot system. The individual robots of a swarm robotic system are relatively simple and can only perform some basic operations on their own. Swarm robots accomplish the given task by interacting and cooperating with each other and with the environment they are in. Thus, communication between the agents of the artificial swarm system plays an important role in the completion of the given task [1].

The control in swarm robotic system is generally decentralized [2, 3] which gives the system self-organizing feature, thus making the system highly robust, scalable, and self-reliant [4]. While using swarm system, a complex task can be distributed among the agents of the swarm, and hence, various tasks can be performed simultaneously [5]. The robots of the swarm can be interconnected over a network over which they can share the information among other agents of the swarm and to the human operator as well [6].

The robots of the swarm can communicate with each other using three ways [7] to accomplish some collective behavior. Firstly, by interacting with the environment they are in, the robots communicate with each other by changing or modifying certain characteristics of their surrounding like placing markers or by moving objects in certain order. This mode of communication involving the environment for indirect coordination is referred as *stigmergy*. Secondly, the robots can communicate via

A. Kaushal (✉) · A. K. Sharma
Centre for Advanced Studies, A.K.T.U, Lucknow, India

A. K. Sharma
e-mail: anujksharma@cas.res.in

Table 1 Wireless communication technologies

Communication technologies	System accuracy ^a (m)	Advantages	Limitations
Cellular	20–50	Global coverage	Base station synchronization
ZigBee	1–10	Low power and cost	Low data speed, insecure
Wi-Fi	1–5	Low cost	Environment dependent
Bluetooth	1–5	Low power and cost	Low accuracy, short range
RFID	1–2	Low power and cost, easy to implement	High response time, mobility limitations
Infrared	1–2	Low power requirements	Short range, affected by environment
Ultra-Wideband (UWB)	0.1–1	Low power, high data rates, noise immunity	High cost, interference to other radio technologies
Ultrasonic	0.03–1	Less expensive, quick startup	Environment sensitive

^aCan be found in [9–12]

sensing by utilizing the on board sensing and actuation system. By using this mode of communication, robot can easily detect the presence of neighboring robots and obstacles. Lastly, robots can interact with each other via direct wireless communication, exchanging data with nearby robots over a network. In this mode of communication, the robot can either communicate to its closest neighbor referred as local communication or to the whole swarm via broadcast known as global communication [8]. Table 1 shows a comparison of various communication technologies that are typically used in multi-robot systems.

Several communication modes have been studied for swarm system. Image processing technique has been used by some researchers for swarm system [13–15], such systems tend to be complex and require more computation resources. Conventional radio communication is also used which allows for long distance communication and comes with its own limitations [16, 17]. Based on low power long range wide area network protocol, LoRa can be used for efficient long range inter-robot communication [18], limited by low bandwidth availability, small network size, and network latency.

As the robots in the swarm robotic system are very simple in design so as to maintain easy scalability of the system and hence are severely limited in computation power making them unable to handle multi-channel radio communication networks. Moreover, due to their mobility it becomes challenging for distance and location estimation. Thus, making the local sensing-based communication the most suitable for multi-robot swarm systems [19]. Table 2 shows various swarm robotic platforms developed earlier and communication technology used by them.

Table 2 Some swarm robotic platform communication technologies

Robot	Communication
Alice [20]	Infrared
S-bot [21]	Infrared, Wi-Fi
E-puck [22]	Infrared, Bluetooth, Serial
Kilobot [23]	Infrared
Thymio II [24]	Infrared, Wi-Fi
Droplet [25]	Infrared
Pheeno [26]	Wi-Fi, Bluetooth, Serial
Mona [27]	RF, XBee

This paper presents a novel communication technique based on the local sensing utilizing color-coded light signals for information and command transfer from one agent of the swarm to another. This communication technique can be very helpful for swarm behavior studies. As color light signal can be easily observed, the performance and activity of every agent of the swarm can be monitored with ease. Thus, impact of individual robot on the emergent behavior of the swarm can be studied giving more insight into swarm behaviors.

The rest of the paper is divided into following sections, and Sect. 2 describes the hardware implementation of the color-coded light communication system. Section 3 describes the experiments using the communication. Section 4 concludes the work and discusses in brief about the future scope of the current work.

2 Hardware Implementation

2.1 Color Light Receiver

The main work of the receiver is to capture the color-coded light signals from the transmitter and convert them into digital signals, and these signals will then be processed by a microcontroller to generate actuation commands. As the signals used in the current work are mostly within the visible range, with wave length ranging from approximately 400 nm to approximately 700 nm (see Fig. 1), therefore, the IR and UV noise needed to be filtered.

Broadcom APDS 9960 RGBC (red, green, blue, clear) digital sensor (see Fig. 2) was chosen as receiving light sensor. The sensor has integrated optical lens collimating the incoming light and thereby improves the sensitivity of the sensor. The sensor gives red ‘R’, blue ‘B’, green ‘G’, and clear ‘C’ light data in terms of the respective intensity. Each of the channels has individual data converters producing 16-bit data simultaneously, making the sensor very quick. The sensor also has a programmable gain amplifier which contributes to its high sensitivity. The sensor uses I^2C communication protocol for interfacing with the microcontroller.

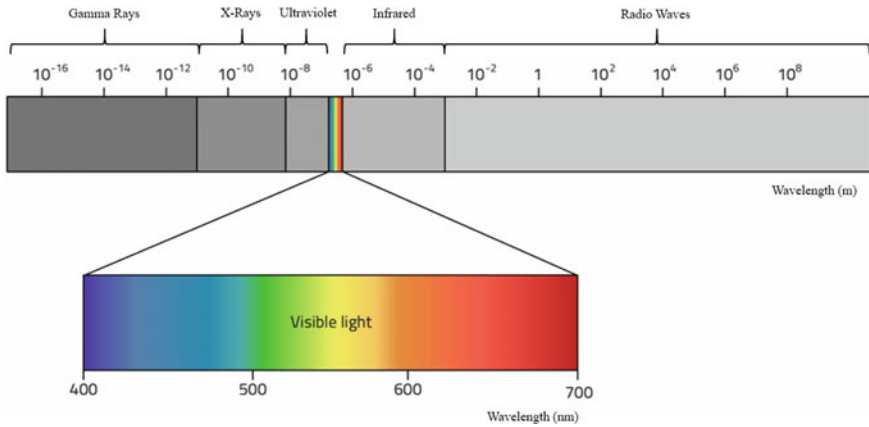


Fig. 1 Part of electromagnetic spectrum used for communication

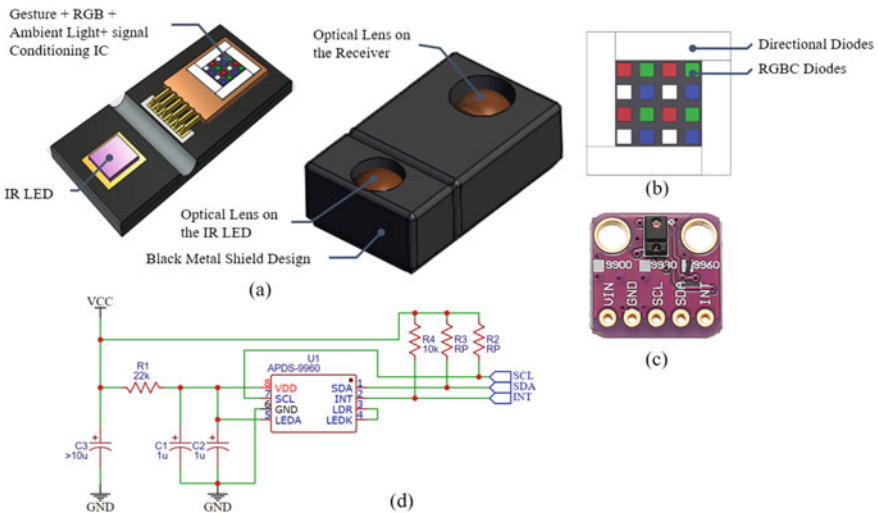
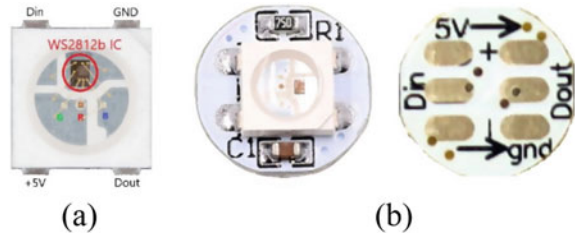


Fig. 2 RGBC color sensor; a APDS9960 sensor, b APDS9960 photodiodes, c APDS9960 breakout module, d circuit diagram

2.2 RGB Transmitter

The transmitter converts the digital signals from the microcontroller into color-coded light signals and sends it to the receiver. For transmitter WS2812B intelligent RGB LED is used. The transmitter LED comes in 5050 SMD package making it easy to implement. The LED can emit the three-primary color with brightness ranging from 0 to 255 and therefore can be used to display complete 16777216 color.

Fig. 3 RGB Transmitter;
a 5050 SMD Package,
b WS2812B breakout



The LED has built in control chip (see Fig. 3), which enables the control of the full color via single input. The LED can also be connected serially and individual LED from the series can be controlled to emit any color combination.

3 Validation Experiments and Results

3.1 Transmitter LED Performance Analysis

The transmitter LED WS2812B was tested for current consumption at various intensities and for RGB colors, and the test was performed in order to determine the power consumption, which plays a significant role in case of miniature swarm robot with small battery. The LED was connected to a 3.3 V power supply, controlled via Arduino Uno current measurements were taken with the help of a digital multimeter (see Fig. 4).

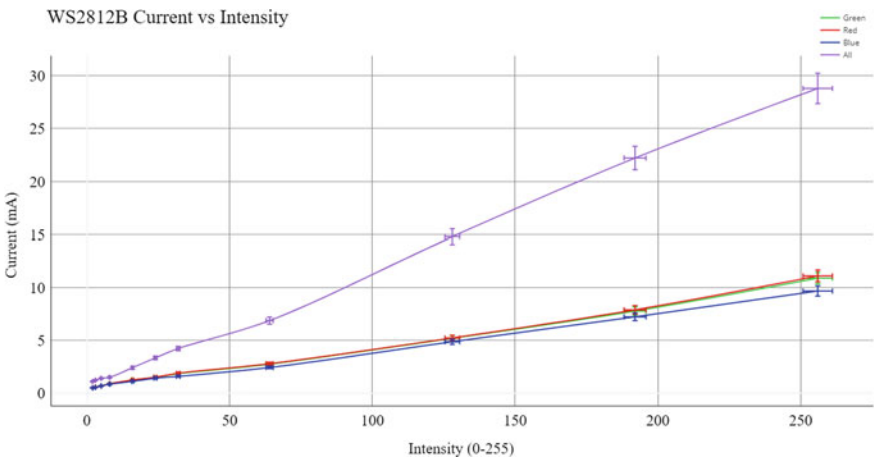


Fig. 4 WS2812B current versus light intensity

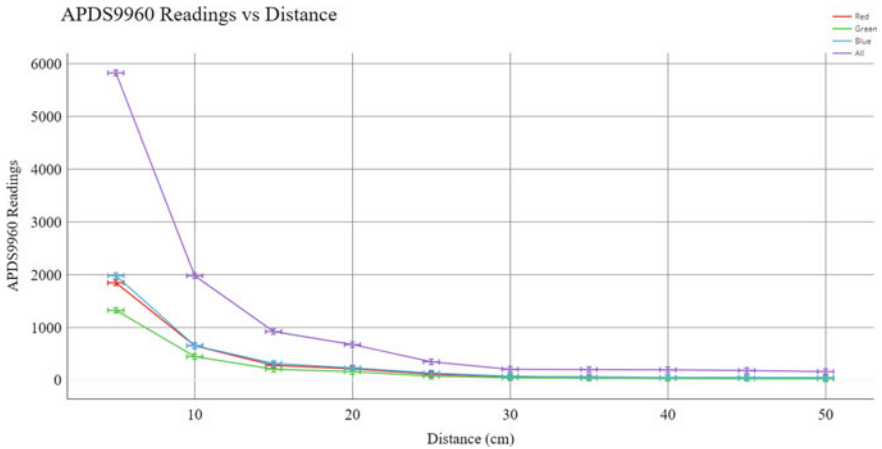


Fig. 5 APDS9960 readings versus distance

3.2 Color-Coded Communication

The WS2812B LED was connected to Arduino Uno (Atmega328P) for giving color control commands and was supplied with 3.3 V supply of the Arduino Uno. The APDS9960 sensor was connected to another Arduino control board and was fixed at one point; while the transmitter LED was moved, the readings of the sensor were recorded with the changing distance of the transmitter LED (see Fig. 5). The sensor readings were calibrated by subtracting the ambient light reading from the useful data.

It was observed that a reliable and distinguishable data reception takes place at around 25–30 cm distance from the sensor, thus making the sensor suitable for communicating with neighboring robots in multi-robot configuration. The information can be encoded in form of colors and data can be distinguished at the receiver based on the percentage of the RGB values in the received signal. Received light intensity can be used to determine the approximate distance between the transmitter and the receiver.

The data can also be sent in form of color-coded pulses; thus, more complex data can be sent. At the receiving end, pulse-on time and color are used to decode the data. A combination of different color and different duration pulses can also be used encode the data (see Fig. 6).

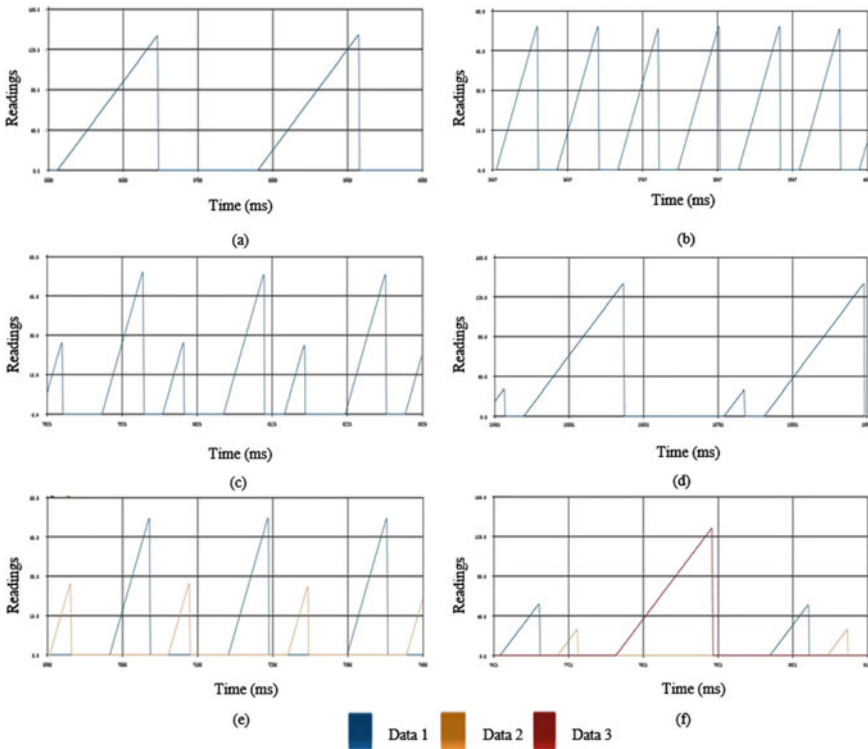


Fig. 6 Different types of data received. **a** One color slow pulse, **b** one color fast pulse, **c** one color fast variable pulses, **d** one color slow variable pulses, **e** two color fast pulses, **f** three color pulses

4 Conclusions and Future Scope

Communication using the color-coded signals with the help of RGB LED and APDS9960 color sensor is efficient, cost-effective, and easy to implement. The current work can be concluded as follows:

- Characteristic analysis of the transmitting LED WS2812B at various intensities was conducted in order to determine the power consumption by the transmitting system.
- Reception range of communication system at which received data can be distinguished from the environmental noise was determined.
- Various light pulsing techniques for the data transfer and its reception were developed.
- The developed system is compact and can be easily controlled using low computing power system, making it suitable for local communication in miniature swarm robotic systems.

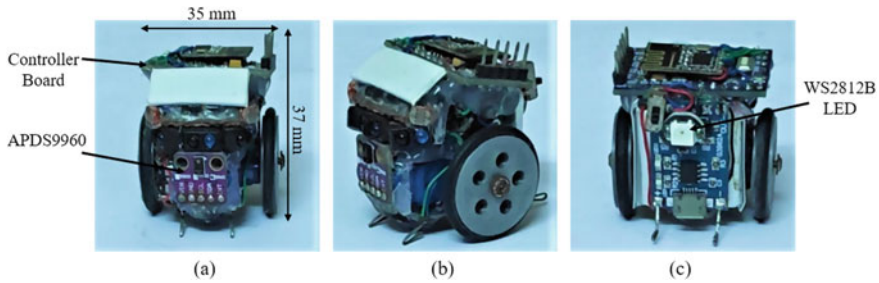


Fig. 7 Miniature robot prototype using color-coded communication system

In the future, further investigation can be made in order to develop more modulation technique for the fast and efficient communication. A miniature robot (see Fig. 7) equipped with this communication system for swarm robotics system is under development.

Moreover, multiple color sensors can also be implemented in order to capture light signals from multiple directions. Similarly, multiple WS2812B LEDs connected in series can be placed around the robot body giving it the ability to transmit directionally constrained data.

References

- Balch T, Arkin RC (1994) Communication in reactive multiagent robotic systems. *Auton Robots* 1:27–52
- Hauert S, Leven S, Zufferey JC, Floreano D (2010) Communication-based leashing of real flying robots. In: Proceedings of IEEE international conference on robotics and automation, pp 15–20. <https://doi.org/10.1109/ROBOT.2010.5509421>
- Garattoni L, Birattari M (2018) Autonomous task sequencing in a robot swarm. *Sci Robot* 3
- Brambilla M, Ferrante E, Birattari M, Dorigo M (2013) Swarm robotics: a review from the swarm engineering perspective. *Swarm Intell* 7:1–41
- Khalidi B, Cherif F (2015) An overview of swarm robotics: swarm intelligence applied to multi-robotics. *Int J Comput Appl* 126:31–37
- Kolling A, Walker P, Chakraborty N, Sycara K, Lewis M (2016) Human interaction with robot swarms: a survey. *IEEE Trans Hum Mach Syst* 46:9–26
- Cao YU, Fukunaga AS, Kahng AB (1997) Cooperative mobile robotics: antecedents and directions. *Auton Robots* 4:7–27
- Nedjah N, Junior LS (2019) Review of methodologies and tasks in swarm robotics towards standardization. *Swarm Evol Comput* 50:100565
- Yasir M, Ho SW, Vellambi BN (2016) Indoor position tracking using multiple optical receivers. *J Light Technol* 34:1166–1176
- Dardari D, Closas P, Djuric PM (2015) Indoor tracking: theory, methods, and technologies. *IEEE Trans Veh Technol* 64:1263–1278
- Yazici A, Yayan U, Yücel H (2011) An ultrasonic based indoor positioning system. In: INISTA 2011—2011 international symposium on innovations in intelligent systems and applications, pp 585–589. <https://doi.org/10.1109/INISTA.2011.5946154>

12. Arrue N, Losada M, Zamora-Cadenas L, Jiménez-Iratorza A, Vélez I (2010) Design of an IR-UWB indoor localization system based on a novel RTT ranging estimator. In: Proceedings of 1st International Conference Sensor Device Technologies and Applications. *SENSORDEVICES 2010*, pp 52–57. <https://doi.org/10.1109/SENSORDEVICES.2010.17>
13. Se S, Lowe DG, Little JJ (2005) Vision-based global localization and mapping for mobile robots. *IEEE Trans Robot* 21:364–375
14. Adorni G et al (2001) Vision-based localization for mobile robots. *Rob Auton Syst* 36:103–119
15. Mateos LA (2020) AprilTags 3D: dynamic fiducial markers for robust pose estimation in highly reflective environments and indirect communication in swarm robotics. arXiv preprint [arXiv: 2001.08622](https://arxiv.org/abs/2001.08622)
16. Thompson EA, Harmison E, Carper R, Martin R, Isaacs J (2006) Robot teleoperation featuring commercially available wireless network cards. *J Netw Comput Appl* 29:11–24
17. González J et al (2009) Mobile robot localization based on Ultra-Wide-Band ranging: a particle filter approach. *Rob Auton Syst* 57:496–507
18. Maneekittichote T, Chanthasopeephan T (2020) Mobile robot swarm navigation and communication using LoRaWan. In: 2020 6th International conference on mechatronics and robotics engineering. *ICMRE 2020*, pp 22–25. <https://doi.org/10.1109/ICMRE49073.2020.9064973>
19. Labrador MA (2006) Communication-assisted topology control of semi-autonomous robots. In: Proceedings of conference on local computer networks, *LCN*, pp 563–564. <https://doi.org/10.1109/LCN.2006.322170>
20. Estier T, Caprari G, Siegwart R (2001) Fascination of down scaling—Alice the sugar cube robot. *J. Micromechatron* 1, 177–189
21. Mondada F et al (2003) SWARM-BOT: from concept to implementation. In: IEEE international conference on intelligent robots and system, vol 2, pp 1626–1631
22. Mondada F et al (2009) The e-puck, a robot designed for education in engineering. In: Proceedings of 9th conference on autonomous robot systems and competitions 1:59–65
23. Rubenstein M, Ahler C, Nagpal R (2012) Kilobot: a low cost scalable robot system for collective behaviors. In: proceedings of international conference on robotics and automation, pp 3293–3298. <https://doi.org/10.1109/ICRA.2012.6224638>
24. Riedo F, Chevalier M, Magnenat S, Mondada F (2013) Thymio II, a robot that grows wiser with children. In: IEEE international workshop on advanced robotics and its social impacts, *ARSO*, pp 187–193. <https://doi.org/10.1109/ARSO.2013.6705527>
25. Farrow N, Klingner J, Reishus D, Correll N (2014) Miniature six-channel range and bearing system: Algorithm, analysis and experimental validation. In: Proceedings of IEEE international conference on robotics and automation, pp 6180–6185. <https://doi.org/10.1109/ICRA.2014.6907770>
26. Wilson S et al (2016) Pheeno, a versatile swarm robotic research and education platform. *IEEE Robot Autom Lett* 1:884–891
27. Arvin F et al (2019) Mona: an affordable open-source mobile robot for education and research. *J Intell Robot Syst Theory Appl* 94:761–775

Recent Advancement of Weed Detection in Crops Using Artificial Intelligence and Deep Learning: A Review



Puneet Saini

1 Introduction

With the continuously increasing world population, the global hunger index has also increased rapidly. This can be dealt with the means of digital farming which in turn will help in production of disease free crops and can provide high nutritional food [32]. By 2050, the global population will reach 9 billion according to reports by the United Nations. So automating the farming techniques can help in feeding the human population in the near future [33]. Climate crisis is also impacting the agriculture, and with extreme rainfall to severe shortage of rains in the past few years have also degraded the agriculture output. Extreme rainfall leads to plant diseases and threats from pests and weeds [18]. Researchers and farmers for past many years have been trying to overcome the provocations posed by the weeds, initially by introducing herbicides and then using mechanical means to remove weeds.

Weeds can appear anywhere in the field, and they compete for essential nutrients with crops, if not controlled, it could result in lower crop yield and quality [22]. Numerous techniques were tried to control weeds, and some of them includes manual weeding with hands or by simple hand tools. These methods were used for many years and still being used in small fields [31]. Herbicides used for weeds management may destroy weeds but are mistrusted for being problematic to the environment. For example, arsenical-based herbicides like monosodium methyl arsenate (MSMA) may be the reason for groundwater contamination [21]. Mechanical way of removing weeds is efficient and cost-effective but they are not able to remove intra-row weeds and may damage the crops, though efforts are being made to design mechanical hoes [34]. Intra-row weeding is still a challenging task which needs different assisting methods, like using real-time kinematic GPS (RTKGPS) for measurement of diameter and height of agriculture crops.

P. Saini (✉)

Department of Mechanical Engineering, Delhi Technological University, Rohini, Delhi 110042, India

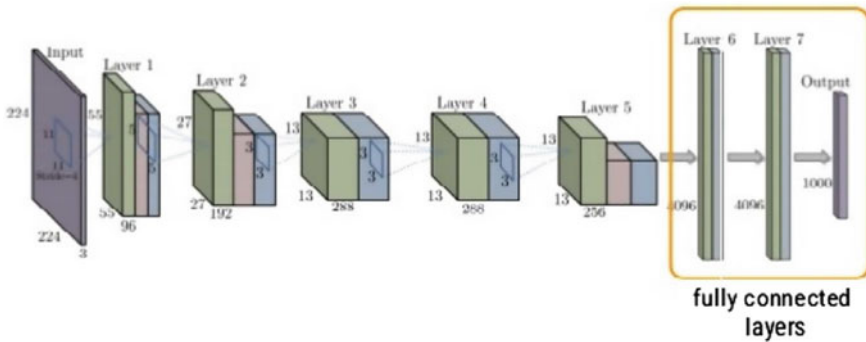


Fig. 1 An example of CNN architecture: CaffeNet. *Source* caffe.berkeleyvision.org [15]

Agriculture ecosystem is complex, unpredictable, and multivariate and can be understood in a greater way by constant observation and analyzing various traits related to it. This means need of big agriculture data and obtaining new information from it [3]. Data can be collected from satellites, unmanned aerial vehicles (UAV), airplanes, drones, field robots, providing large dataset of images of the agriculture environment. Raw images provide variety of challenges and need to be passed through various image processing techniques for decision-making purposes [12]. There are various techniques used for analyzing images, some popular techniques include machine learning (ML) (artificial neural networks (ANN), K -means clustering, support vector machines (SVM) amongst others) [38].

Besides the above-mentioned techniques, deep learning is gaining momentum in the past few years [29]. DL belongs to machine learning class and is similar to artificial neural network (ANN). However, it differs from conventional neural networks as they are deeper and have complex layers of interconnection with the requirements of strong computational power for extraction of desired parameters [27]. There are various network architectures used in deep learning (i.e., recursive neural networks (RNN), pre-trained networks, recurrent neural network, convolutional neural network (CNN) [15] (Fig. 1).

2 Methodology

The review presented aims to identify weeds in crops using artificial intelligence and deep learning methods. A procedure was established to interpret and compare the results relevant to the research using a systematic literature analysis. As deep learning in agriculture is relatively new, focus was on the research papers published from 2015 to 2020 with areas related to removal of weeds. The papers were selected from databases like ScienceDirect, Springer, IEEE Xplore, and Google Scholar. An expression-based research was initiated with keyword: (“weed detection” OR



Fig. 2 Images from Grass–Broadleaf dataset. Upper row shows images of broadleaf weeds and lower row shows images of soil class. Adapted with permission from Elsevier, Copyright 2019. *Source* [5]



Fig. 3 Images from DeepWeeds dataset showing two examples of each weed species. Adapted with permission from Elsevier, Copyright 2019. *Source* [5]

“deep learning in agriculture”) and (“deepweeds”). For each study, information was obtained and classified into: year of publication, problems described, architecture of the deep learning framework used, labels, classes, and data used (Figs. 2 and 3; Table 1).

3 Deep Learning

DL learning is an extension of classical ML with more depth and complexity in the neural network which allows data to be represented in hierarchical way, through abstraction at several levels [27]. Feature learning is the biggest advantage of deep learning in comparison with ML. In ML, the input image has to go through preprocessing, segmentation, and feature extraction steps, in which normalization, size reduction, spectral property, etc., are done and the image is then fed to a machine learning model [33]. In DL due to the hierarchical representation, the features at higher level are formed by the lower level features.

The papers reviewed showed convolutional neural network (CNN) used as a class of deep learning framework to identify weeds from crops. CNN layers represent data with general features at the first layer, then becoming more specific going to the deeper layer [17]. Maxpooling was used to reduce the dimensionality of the layers,

Table 1 Deep learning methodology used by authors for weed detection

S. No.	References	Problem description	Data used	DL model used
1	[13]	Classify weeds from RGB images	Dataset of 17,509 images taken from DeepWeeds dataset	Graph weeds net (GWN), author defined
2	[14]	Classify weeds from four different weed dataset	Cornweed—4200 images Lettuceweed—560 Radishweed—280 Mixed—5040 images	Graph convolutional network (GCN), author defined
3	[9]	Combining pre-trained CNN with SVM and XGBoost	2 crops, tomatoes and cotton and two weed species	Inception-ResNet with SVM classifier
4	[10]	Improving neural network pre-trained on agriculture datasets instead of ImageNet	504 RGB images of four different species	VGG-19, ResNet
5	[16]	Calculation flow in real time for neural network	Dataset of images collected in carrot farm	Author defined
6	[36]	Several DCNNs were constructed to identify weed in perennial grass	15,486 negative images (no weeds) and 17,600 images (with weeds)	Comparison between VGGNet, GoogleNet
7	[1]	Methodology was developed to accelerate labeling of pixels	906 images from canola fields	Comparison between VGG-16 and ResNet-50

and fully connected layers were placed near the output of the network which acts as a classifier to classify input image or to make predictions.

3.1 DL Architectures and Frameworks

There are various prevalent architectures which were used by researchers reviewed in this paper either for using as pre-trained weights or for comparison of accuracy with their own DL model. AlexNet, VGG, CaffeNet (Fig. 1), GoogleNet among others were used for comparison. Various tools which researchers have utilized to experiment with their model were TensorFlow, Py-Torch, Caffe, Theano, Keras (programming interface which is integrated with TensorFlow 2.0), and DL MATLAB Toolbox.

4 Deep Learning in Weeds

The papers presented in the review were classified according to the problem they addressed, sources of data with classes and labels, DL architecture implemented, whether data segmentation or preprocessing done, performance according to metrics chosen and comparison with other DL architectures.

4.1 Data Sources

DL model works best when fed with lots of image data containing thousands of images either captured through a camera, UAV, satellite, or mounted on a movable platform [25]. Some authors have synthetically increased the number of images by altering the images through various operations [2, 12]. Some researchers have used publically available dataset for weeds identification purpose like DeepWeeds [5, 14, 23], while other have generated their own dataset for their required research [35]. Papers dealing with weed identification who generated their own dataset used small dataset of images to be fed into DL model [25]. In general, problems in which large number of weeds species were to be identified required large number of data [26]. Many researchers have used camera mounted on a moving platform to catch images of weeds, and it turned to be most economical way to collect data [24, 26].

4.2 Data Preprocessing and Augmentation

Many researchers opted to do some image preprocessing or segmentation steps, before the specific features of the image were fed as input to the deep learning model. The most common was image resize, mostly converting into an image of smaller sizes of 128×128 or of 60×60 pixels [15]. Image segmentation was done to alter the size of the dataset or for expediting the learning process by feature enhancement [4, 8]. Pixel extraction [2, 12], background removal [26, 29] of images were done. The work under study utilized data augmentation to synthetically increase the dataset of training images. This was done when the datasets available were smaller in size and to increase the performance and the learning procedure of the deep learning model [9]. This process became important for authors who trained their model on artificial images and tested them on original ones.

4.3 Technical Details

Many researchers employed faith in CNN architectures like Inception-ResNet, GoogleNet, VGG16, and AlexNet, and some also developed their own architecture to compare their performance metrics with them [8, 13, 16]. Some of the research work also compared deep learning models with traditional machine learning models like support vector machines (SVM), artificial neural networks (ANN) [19] to evaluate performance between them.

Regarding deep learning framework used, papers published from 2015 to 2019 have employed Caffe followed by TensorFlow. Some authors also developed their own framework on top of Keras/Theano, Keras/TensorFlow. In [32], TensorFlow 2.0 was released which used Keras as API this prompted authors to use this as their programming framework [14]. Many studies divided their dataset into training/cross-validation and testing in the ratio of 90–10 or 95–5, respectively, with learning rate varying from 0.001 and 0.005 up to 0.01 [15]. Moreover, many authors used pre-trained weights as transfer learning to influence the learning efficiency [20].

4.4 Overall Performance

Measuring the performance of the deep learning model is to check with what percentage of accuracy the weeds have been correctly identified [19]. Authors have used different performance metrics related to their study. Kounalakis et al. [6] dos Santos Ferreira et al. [17] used precision and recall as their performance metrics with accuracy more than 90% indicating good performance. Jiang et al. [14] compared *F1* score of their self-developed CNN architecture with other deep learning architectures. In nearly all of the cases reviewed DL approach outperformed the traditional ML approach (SVM, ANN, *K*-Means) when comparison was done to identify weed [29].

5 Discussion

The analysis of the research published in last five years shows the superiority of Deep learning in identifying weeds. It offered better accuracy and performance when compared to other ML approaches. Traditional ML approach required various preprocessing steps for feature extraction from the image such as histogram, scale-invariant feature transform (SIFT), texture- and shape-based algorithms and many more, whereas in DL, the hierarchical representation helps the features to get automatically extracted. Many of the author's preferred CNN models to perform classification and some modified their model for complex problems like plant disease detection. Dyrmann et al. [7] used DetectNet CNN to detect weeds in cereal crops

Table 2 Performance comparison of deep learning models with different framework used

S. No.	Framework used	Error estimation method used	Measure of error in (%)	CNN architecture and comparison	Reference
1	Caffe	CA	98%	Modified VGG-16 used (no more details)	[8]
2	Keras	Intersection over union (IOU), <i>F1</i>	IOU—(99.05%), <i>F1</i> —99.52%)	VGG-16, ResNet-50	[32]
3	MATLAB, DL Toolbox	CA	94.72%	N/A	[11]
4	Machine Vision	CA	98.93%	CNN and DCNN	[28]
5	N/A	CA	90.19%	N/A	[3]
6	Keras	Precision, recall, <i>F-1</i>	99.25% for <i>F1</i>	AlexNet, VGG-16, and ResNet-101	[14]
7	Caffe	CA with probability distribution	98%	Compared with SVM, Adaboost	[6]
8	Keras	Precision and recall	3.3 ± 0.2 (Precision), 78.5 ± 2.5 (Recall)	CNN with SVM and logistic regression classifiers	[17]

using bounding boxes. This establishes a very promising future in the research to identify weeds in real time as it will be helpful for an automated machine or a robot to detect and remove weeds (Table 2).

The biggest advantage of using deep learning to identify weed was the reduced effort to extract features from the images as it can be very time-consuming and requires considerable time to put the images in a shape that can be fed into a traditional machine learning algorithm [37]. A considerable shortcoming in using DL is that it needs large amount of data for training purpose and even longer time to train the model than ML approaches. There is an immense potential for the application of DL in agriculture and specifically in weed identification.

6 Conclusions

In this paper, a review of weed detection in crops using artificial intelligence and deep learning was summarized. Papers were identified with the technical details of the DL models employed, DL framework used, data preprocessing and augmentation techniques utilized, performance of the model according to the classification accuracy and comparison with other ML models were done. The finding indicates that DL deals with better classification accuracy, performance and offers better confidence

in finding weeds than other image processing techniques. For future work, DL could be applied to complex agriculture problems like plant disease detection and weeds removal. AI and DL can significantly improve farming practices and could lead to smarter and sustainable farming.

References

1. Asad MH, Bais A (2019) Weed detection in canola fields using maximum likelihood classification and deep convolutional neural network. *Inf Process Agric.* <https://doi.org/10.1016/j.inpa.2019.12.002>
2. Bakhshipour A, Jafari A, Nassiri SM, Zare D (2017) ScienceDirect Weed segmentation using texture features extracted from wavelet sub-images. *Biosyst Eng* 157:1–12. <https://doi.org/10.1016/j.biosystemseng.2017.02.002>
3. Bechar A, Vigneault C (2016) Agricultural robots for field operations: Concepts and components. *Biosyst Eng* 149:94–111. <https://doi.org/10.1016/j.biosystemseng.2016.06.014>
4. Dian Bah M, Hafiane A, Canals R (2018) Deep learning with unsupervised data labeling for weed detection in line crops in UAV images. *Remote Sens* 10:1–22. <https://doi.org/10.3390/rs10111690>
5. dos Santos FA, Freitas DM, da Silva GG et al (2019) Unsupervised deep learning and semi-automatic data labeling in weed discrimination. *Comput Electron Agric* 165:104963. <https://doi.org/10.1016/j.compag.2019.104963>
6. dos Santos FA, Matte Freitas D, Gonçalves da Silva G et al (2017) Weed detection in soybean crops using ConvNets. *Comput Electron Agric* 143:314–324. <https://doi.org/10.1016/j.compag.2017.10.027>
7. Dyrmann M, Jørgensen RN, Midtiby HS (2017) RoboWeedSupport—Detection of weed locations in leaf occluded cereal crops using a fully convolutional neural network. *Adv Anim Biosci* 8:842–847. <https://doi.org/10.1017/s2040470017000206>
8. Dyrmann M, Mortensen AK, Midtiby HS, Jørgensen RN (2016) Pixel-wise classification of weeds and crops in images by using a Fully Convolutional neural network. *Int Conf Agric Eng*, 6 p
9. Espejo-Garcia B, Mylonas N, Athanasakos L et al (2020) Towards weeds identification assistance through transfer learning. *Comput Electron Agric* 171:105306. <https://doi.org/10.1016/j.compag.2020.105306>
10. Espejo-Garcia B, Mylonas N, Athanasakos L, Fountas S (2020) Improving weeds identification with a repository of agricultural pre-trained deep neural networks. *Comput Electron Agric* 175:105593. <https://doi.org/10.1016/j.compag.2020.105593>
11. Farooq A, Hu J, Jia X (2019) Analysis of spectral bands and spatial resolutions for weed classification via deep convolutional neural network. *IEEE Geosci Remote Sens Lett* 16:183–187. <https://doi.org/10.1109/LGRS.2018.2869879>
12. Hall D, Dayoub F, Perez T, McCool C (2018) A rapidly deployable classification system using visual data for the application of precision weed management. *Comput Electron Agric* 148:107–120. <https://doi.org/10.1016/j.compag.2018.02.023>
13. Hu K, Coleman G, Zeng S et al (2020) Graph weeds net: a graph-based deep learning method for weed recognition. *Comput Electron Agric* 174:105520. <https://doi.org/10.1016/j.compag.2020.105520>
14. Jiang H, Zhang C, Qiao Y et al (2020) CNN feature based graph convolutional network for weed and crop recognition in smart farming. *Comput Electron Agric* 174:105450. <https://doi.org/10.1016/j.compag.2020.105450>
15. Kamilaris A, Prenafeta-Boldú FX (2018) Deep learning in agriculture: A survey. *Comput Electron Agric* 147:70–90. <https://doi.org/10.1016/j.compag.2018.02.016>

16. Knoll FJ, Czymmek V, Harders LO, Hussmann S (2019) Real-time classification of weeds in organic carrot production using deep learning algorithms. *Comput Electron Agric* 167:105097. <https://doi.org/10.1016/j.compag.2019.105097>
17. Kounalakis T, Triantafyllidis GA, Nalpantidis L (2019) Deep learning-based visual recognition of rumex for robotic precision farming. *Comput Electron Agric* 165:104973. <https://doi.org/10.1016/j.compag.2019.104973>
18. Lee WS, Alchanatis V, Yang C et al (2010) Sensing technologies for precision specialty crop production. *Comput Electron Agric* 74:2–33. <https://doi.org/10.1016/j.compag.2010.08.005>
19. Liakos KG, Busato P, Moshou D et al (2018) Machine learning in agriculture: a review. *Sensors (Switzerland)* 18:1–29. <https://doi.org/10.3390/s18082674>
20. Liu F, Yang Y, Zeng Y, Liu Z (2020) Bending diagnosis of rice seedling lines and guidance line extraction of automatic weeding equipment in paddy field. *Mech Syst Signal Process* 142:106791. <https://doi.org/10.1016/j.ymssp.2020.106791>
21. Mahoney DJ, Gannon TW, Jeffries MD et al (2015) Management considerations to minimize environmental impacts of arsenic following monosodium methylarsenate (MSMA) applications to turfgrass. *J Environ Manage* 150:444–450. <https://doi.org/10.1016/j.jenvman.2014.12.027>
22. Marinoudi V, Sørensen CG, Pearson S, Bochtis D (2019) Robotics and labour in agriculture. A context consideration. *Biosyst Eng* 184:111–121. <https://doi.org/10.1016/j.biosystemseng.2019.06.013>
23. Olsen A, Konovalov DA, Philippa B et al (2019) DeepWeeds: a multiclass weed species image dataset for deep learning. *Sci Rep* 9:1–12. <https://doi.org/10.1038/s41598-018-38343-3>
24. Pantazi XE, Moshou D, Bravo C (2016) Active learning system for weed species recognition based on hyperspectral sensing. *Biosyst Eng* 146:193–202. <https://doi.org/10.1016/j.biosystemeng.2016.01.014>
25. Pantazi XE, Tamouridou AA, Alexandridis TK et al (2017) Evaluation of hierarchical self-organising maps for weed mapping using UAS multispectral imagery. *Comput Electron Agric* 139:224–230. <https://doi.org/10.1016/j.compag.2017.05.026>
26. Partel V, Charan Kakarla S, Ampatzidis Y (2019) Development and evaluation of a low-cost and smart technology for precision weed management utilizing artificial intelligence. *Comput Electron Agric* 157:339–350. <https://doi.org/10.1016/j.compag.2018.12.048>
27. Patrício DI, Rieder R (2018) Computer vision and artificial intelligence in precision agriculture for grain crops: a systematic review. *Comput Electron Agric* 153:69–81. <https://doi.org/10.1016/j.compag.2018.08.001>
28. Raja R, Nguyen TT, Slaughter DC, Fennimore SA (2020) Real-time weed-crop classification and localisation technique for robotic weed control in lettuce. *Biosyst Eng* 192:257–274. <https://doi.org/10.1016/j.biosystemseng.2020.02.002>
29. Rehman TU, Mahmud MS, Chang YK et al (2019) Current and future applications of statistical machine learning algorithms for agricultural machine vision systems. *Comput Electron Agric* 156:585–605. <https://doi.org/10.1016/j.compag.2018.12.006>
30. Rehman TU, Zaman QU, Chang YK et al (2019) Development and field evaluation of a machine vision based in-season weed detection system for wild blueberry. *Comput Electron Agric* 162:1–13. <https://doi.org/10.1016/j.compag.2019.03.023>
31. Rueda-Ayala V, Rasmussen J, Gerhards R (2010) Mechanical weed control. Elsevier Inc.
32. United Nations (2019) Wpp2019_Pop_F01_1_Total_Population_Both_Sexes
33. Wang A, Zhang W, Wei X (2019) A review on weed detection using ground-based machine vision and image processing techniques. *Comput Electron Agric* 158:226–240. <https://doi.org/10.1016/j.compag.2019.02.005>
34. Wu X, Xu W, Song Y, Cai M (2011) A detection method of weed in wheat field on machine vision. *Procedia Eng* 15:1998–2003. <https://doi.org/10.1016/j.proeng.2011.08.373>
35. Yu J, Schumann AW, Cao Z et al (2019) Weed detection in Perennial Ryegrass with deep learning convolutional neural network. *Front Plant Sci* 10:1–9. <https://doi.org/10.3389/fpls.2019.01422>
36. Yu J, Sharpe SM, Schumann AW, Boyd NS (2019) Deep learning for image-based weed detection in turfgrass. *Eur J Agron* 104:78–84. <https://doi.org/10.1016/j.eja.2019.01.004>

37. Zhai Z, Zhu Z, Du Y et al (2016) Multi-crop-row detection algorithm based on binocular vision. *Biosyst Eng* 150:89–103. <https://doi.org/10.1016/j.biosystemseng.2016.07.009>
38. Zhao Y, Gong L, Huang Y, Liu C (2016) A review of key techniques of vision-based control for harvesting robot. *Comput Electron Agric* 127:311–323. <https://doi.org/10.1016/j.compag.2016.06.022>
39. Zheng Y, Zhu Q, Huang M et al (2017) Maize and weed classification using color indices with support vector data description in outdoor fields. *Comput Electron Agric* 141:215–222. <https://doi.org/10.1016/j.compag.2017.07.028>

A Review of Performance of Solar Photovoltaic Refrigeration System



Shailendra Kasera, Rajlakshmi Nayak, and Shishir Chandra Bhaduri

1 Introduction

Refrigeration technology is required for the preservation of food and vaccine cold chains in hospitals but many villages are still not connected to the grid. Many far-flung areas of India have an uneven power supply. Without electricity, the low temperature cannot be achieved. Kattakayam and Srinivasan [1] explained that solar energy appears to be a good solution to this problem, especially in countries where high solar irradiations are available; therefore, solar refrigerators may be considered as an optimal solution for storing the vaccines and life drugs. Secondly, conventional fossil fuel-based power plants are used in order to supply electricity that causes global warming. Consequently, the use of new and renewable energy has become the center of attention for all researchers around the world. Ekren et al. [2] told that technologies related to DC compressors are more useful as compared to AC compressors. It is especially suitable for a renewable type of energy sources. DC compressors do not require the power inverter. Opoku et al. [3] discussed that during the refrigeration cycle, DC compressors have low surge power as compared to AC compressors. Khan et al. [4] told that VRF technology coupled with solar refrigeration brings additional advantages. A variable speed solar DC refrigerator can reduce the size of the solar PV array and reduce the overall cost.

S. Kasera (✉) · R. Nayak
Department of Mechanical Engineering, JK Lakshmi Pat University, Jaipur, India

R. Nayak
e-mail: rajlakshmi.nayak@jklu.edu.in

S. C. Bhaduri
Faculty of RAC, Automotive, Electrical Skills, Bhartiya Skill Development University, Jaipur, India

2 Studies of Solar Photovoltaic Refrigerator

The studies on solar photovoltaic refrigerator are divided into two sections. The first section consists of the researches based on the DC compressor, and the later section reviews the researches of AC compressors. A brief summary of the same is also shown in Tables 1 and 2 for DC and AC compressor, respectively.

2.1 Studies Related to DC Compressors

Su et al. [5] proposed a variable speed solar DC refrigerator. It is directly run by solar PV without any help of batteries and inverter. The speed of the compressor changed as per the change in solar radiation. They have presented a dynamic model for simulation of variable speed DC milk refrigerator and performed the various tests to validate the models. They have studied the surrounding temperature, solar radiation intensity and compressor speed. They have published that cooling capacity and average PV utilization efficiency for variable speed refrigerator are increased by 32.76 and 45.69%, respectively, as compared to fixed speed. They concluded that the average cooling capacity decreases with increment in surrounding temperature but the surrounding temperature has less effect on power consumption.

Khan et al. [4] designed the milk chilling system using VRF technology. The main aim of this work is to minimize the torque load of the solar-driven milk chilling system. VRF system can also reduce the peak power of the solar array. They coupled the 200 L milk chilling tank with one ton of a refrigeration system which is powered by 2 kW. They conducted the experiments using the batch size of 50, 100, 150 and 200 L to decrease the raw milk refrigerator from 30 to 4 °C. Three different types of compressor, i.e., reciprocating, rotary with compressor and VRF-based rotary compressor are utilized for the study. The power required to run all the three compressors was 1.8 kW, 1.2 kW and 0.8 kW, respectively, and the torque loads were 3.3 kW, 1.6 kW and zero kW for, respectively. They concluded that the less than one kW power is required to chill the 200 L milk with zero torque load.

Salilih and Birhane [6] studied solar PV refrigerator equipped with R134a variable speed DC compressor for the purpose of simulation and analysis. It is done with the help of datasheets of the compressor and solar PV under the condition of real weather. Solar PV of capacity 175 was connected with the DC compressor. They reported that the COP of the system was 2.25 and 1.85, respectively for low and high speed. They indicated that the minimum solar radiation required for running the compressor is 700 and 350 W/m² for 4200 RPM and 1800 RPM, respectively. They concluded that such a method can be successfully utilized to know the performance of a variable speed DC compressor coupled with solar PV.

Daffallah [7] studied the effect of surrounding temperature on 12 and 24 V refrigerator solar PV DC refrigerator with and without load. He chose the surrounding temperature between the 25 and 35 °C. He performed the experiment under different

Table 1 Studies related to DC compressors

Researcher	Refrigerant	Evaluation
Su et al. [5]	R-134a	Proposed a dynamic model of variable speed solar milk refrigerator and validate using experimentation work
Khan et al. [4]	R22, R410A	Designed the solar milk chilling system using VRF technology. 1 kW power is sufficient to chill the 200 L milk with zero torque load
Salilih et al. [6]	R-134a	Simulation of solar PV refrigerator fitted with variable speed compressor using the data sheets of compressor and solar PV
Daffallah [7]	R-134a	Experimental performance evaluation of 12 and 24 V refrigerator under various loading condition and effect of surrounding temperature
Daffallah et al. [8]	R-134a	Experimental performance analysis of solar direct current refrigerator for various thermostat conditions
Opoku et al. [3]	R-134a	Comparative techno-economic study of solar powered both AC and DC refrigerator
Toledo et al. [9]	R-134a	Designed the solar DC ice-maker and its adaptive control unit
El-Bahloul et al. [10]	R-134a	Designed and developed the solar-driven refrigerator with thermal energy storage
Tina and Grasso [11]	R-134a	Developed a web-based remote monitoring system for solar refrigerator for energy performance
Ekren et al. [2]	R-134a	Experimental performance evaluation of a variable speed direct current compressor
Kaplanis and Papanastasiou [12]	R-134a	Energy-efficient refrigerator was developed by using insulation, DC compressor and its variable speed
Toure and Fassinou [13]	R-12	Design and development of solar refrigerator for vaccine storage
Tom et al. [14]	R-12	Performance analysis test of solar PV refrigerator in the tropical climate of Sudan

thermostat settings and calculated the energy consumption on both monthly and annual basis. They investigated the operation time of compressor per day from 25 to 35 °C. The maximum and minimum values were found as 0.912 h/°C and 0.216 h/°C, respectively, for 12 V. Similarly, he calculated 1.079 and 0.317 h/°C for 24 V for various thermostat setting. He reported 91.7 and the 76.9 Wh/L energy consumption

Table 2 Studies related to AC compressors

Researcher	Refrigerant	Evaluation
Verma and Dondapati [15]	R134a	Designed the solar PV plant to run the domestic refrigerator
Oualiet et al. [16]	R134a	Studied the effect of thermal influence in domestic 160 L refrigeration on energy efficiency
Gupta et al. [17]	R134a	Determine the optimum size of solar PV, battery and insulation thickness for 50 L refrigerator
Kattakayam and Srinivasan [18]	R-12	Reported the performance analysis of a lead–acid battery system as a part of a refrigerator
Modi et al. [19]	R134a	Carried out the experimental performance analysis of 165 L capacity domestic refrigerator working with R134a
Cherif and Dhoub [20]	–	Demonstrated the simulation responses of a solar photovoltaic refrigeration system with energy storage system
Kattakayam and Srinivasan [21]	R-12	Determined the thermal performance of a solar photovoltaic refrigerator
Kattakayam and Srinivasan [1]	R-12	Described the major characteristics of a small refrigerator driven by solar PV and backed up small generator
Taha [22]	–	Demonstrated the over sizing and mismatching in solar photovoltaic refrigerators

per day, respectively, for 24 for 12 V. He concluded that the 12 V operation is more efficient than 24 V operation.

Daffallah et al. [8] carried out the experimental performance evaluation of solar PV refrigerator under different loading conditions. They connected the 158 L refrigerator with 12 V, 150 Ah gel battery, charge controller and 150 W solar PV. The refrigerator was incorporated with R134a DC compressor with an AC/DC converter. The temperature inside can be maintained using a thermostat. They investigated the performance of the refrigerator under different thermostat settings. They reported that the ampere hour of refrigerator changed between 25–88 Ah and 55–110 Ah for no loading and loading conditions, respectively. They also tested the refrigerator without photovoltaic and reported that the battery can operate the refrigerator for 36 h.

Opoku et al. [3] did the comparative study of both DC and AC refrigerator driven by solar PV on the basis of techno-economic analysis. They selected the two 92 L identical refrigerators for study. AC refrigerator is connected with 250 W solar panel, 100 A-hour battery, 500 W inverter and 25 A charge controller. DC refrigerator is equipped with a BD35F DC compressor which is manufactured by Danfoss. DC

refrigerator is connected with 200 W solar panel, 100 A-hour battery and charge controller of 20 A. They experimentally reported that the evaporator and cabinet temperatures for both the refrigerators attain temperatures of 2 °C and 10 °C, respectively, at 3000 rpm. They told that DC compressor has a very less power surge of 75 W as in comparison with 250–425 W of AC compressor during the cycle. They concluded that the DC refrigerator can bring down the total installation cost of about 18% as compare to the AC refrigerator.

Toledo et al. [9] designed the solar DC ice-maker and evaluated its performance using an adaptive thermal unit in Tunisia. They presented the design methodology to optimize the supply system of solar energy for producing 12 kg of ice per day. They connected 600 W solar PV array and 65 Ah battery to the ice-maker. They further developed the new control unit so that the compressor can adapt the suitable operation as the availability of solar energy. They reported through the simulation results that ice-maker is able to produce the ice for 89% of the year. Thereafter, they experimentally studied the two weather profile of warm and hot day with low solar radiations using climate chamber, test bench and PV simulator. They concluded the autonomy of 5 days under the low solar irradiance.

El-Bahloul et al. [10] carried out the functioning of a solar-driven vapor compression refrigerator in high ambient conditions with thermal storage using R134a. The experimental facility consists of a solar module, UPS and battery. The solar module has 130 W nominal power and 13% efficiency. Like a refrigerator, a portable compressor cooler of 50 L capacity was used in this process. It has a average input power of about 52 W. It has the temperature range of +10 to -22 °C which could be insulated with polyurethane foam. Outer frame and lid were from polypropylene. The temperature in the refrigerator was put at 5 °C without PCM condition. Similarly, -10 °C was set with PCM condition. During sunset time, PCM, which was employed as thermal storage for the covering of cooling demand, is rubbermaid reusable blue ice at around the evaporator's inner surface. In this experiment, they informed the following: For without PCM at no load indoor condition, the overall COP was noticed at 2.51 during working these three working days. Maximum tilted solar radiation was 670 W/m² and the ambient temperature reached 26.5 °C on the third day. The refrigerator was loaded with a full capacity of 21 L of water for without PCM. The COP was 2.28 during four working days for indoor conditions. For PCM at no load condition, the COP was 1.25 during five working days. Maximum tilted solar radiation was 716 W/m² and the ambient temperature reached 30.4 °C. For PCM at full load condition and indoor test, the COP was 1.32 during six working days. The COP for the outdoor test was 1.22. The storage temperature of 5 °C and 0 °C was attained on the third and sixth day, respectively. The results showed that it could be successfully used for hot arid areas for refrigeration.

Tina and Grasso [11] focused on the online monitoring system to check the performance of the solar stand-alone PV plant with the help of a refrigerator. Renewable sources of energy should be monitored for ensuring consistent operation. Early fault detection is necessary to save money and reliable operation. Their system incorporated refrigerator, DC compressor, 50-W solar PV, two batteries of each 18 Ah in

parallel and boost MPPT charge controller. They have chosen one commercial refrigerator of 70 W for the study and mounted the solar panel on its vertical and horizontal surface. They developed the web-based data acquisition system and distributed the data over the Internet. It was helpful to detect problems like high temperatures of battery, refrigerator, compressor and soiling of solar PV. They identified the critical operating conditions for applications like vaccines. Experimentally evaluated data of prototype were further utilized for an outdoor refrigerator which is equipped with horizontal solar panels. They concluded that the refrigerator worked successfully, and such type of monitoring system can be successfully adopted.

Ekren et al. [2] had done the experimental performance analysis of a variable speed direct current compressor. They compared the performance of the same direct current compressor with reference to cooling capacity, COP and energy efficiency in two modes, namely constant speed and variable speed during ON and ON/OFF. Experiments were carried out on 79-L refrigerator using R134a refrigerants. In this study, the Danfoss BD35 DC compressor of semi-hermetic reciprocating type was utilized. This resulted in the efficiency of the variable speed of DC compressor more than the constant speed of compressor at higher speeds.

Kaplanis and Papanastasiou [12] converted the conventional refrigerator into a solar-powered system. They introduced some changes like polyurethane insulation for the refrigerator which was increased by 25 mm. Refrigerator double door glass was replaced by insulation to reduce the heat loss. Danfoss DC compressor was used. It was compatible with R134a refrigerant. In this experimental setup, 255 W capacity of solar PV was used to generate electricity. These panels were not suitable for refrigeration. 190 Ah lead–acid battery with 80% depth of discharge was connected in series to provide the backup power. The thermostat was connected to the compressor for the controlling of variable speed. They determine the constant ratio of V/f for the compressor. Motor speed increased from 2000 to 3500 rpm for resistance values 0, 277, 692, 1523 Ω and V/f value equal to 0.35 ± 0.01 were also reported during this experiment. They performed the pull-down test to find out the power consumed versus time. A maximum of 102 W was recorded during the pull-down test and 84 W at 3000 rpm for steady-state operation. The energy consumption of a solar photovoltaic powered refrigerator was 1.53 kWh for 15 h of operation, and for conservation, the load was 1.7 kWh for 24 h of operation. The DC compressor increased the transferring of power up to 92% with a speed ratio of 2.5. They have reduced the distance between the components to minimize the power losses in cables.

The results of the solar refrigerator utilized for storage of vaccine, freezing chamber and personal use of medical employees were noticed by Toure and Fassinou [13]. They coupled the 335 W solar PV with R12 refrigerator through 150 Ah-12 V battery. They made cold storage around the evaporator for increasing the autonomy of the system. They analyzed the thermal performance of the refrigerator. The inner temperatures stayed for about three days as per WHO norms showing the significance of water solidification when the compressor was off. They further showed that superior insulation of the refrigerator would enhance the cold autonomy without any thermal loss. In exergy analysis, exergetic efficiency was 17%. They reported that the maximum losses were at the compressor and evaporators which may be reduced by

minimizing the magnetic and mechanical losses. Practical COP and thermal losses were 1.63 and 11 W, respectively.

Tom et al. [14] done the performance analysis test of solar PV refrigerator in the tropical climate of Sudan. The experimental setup consisted of the solar PV array, two batteries, charge controller and 180 L refrigerator based on R12 refrigerant. It had six photovoltaic modules of 40 W each with the connection of three modules in parallel. It formed the two main branches, which have an open-circuit voltage of 18 V. 12 V and 105 Ah capacities of two batteries that were utilized in order to store the energy. A 24 V DC motor compressor was utilized for the refrigerator. After conducting the test, they concluded that the electricity produced by solar PV was not sufficient to charge the batteries fully, especially for overnight operation. They calculated the refrigerator efficiency that was 77 and 64% for low cooling and maximum cooling, respectively. They found that 0 °C temperature can be achieved within 2–3 days, in order to freeze the sufficient ice in the compartment. They further reported that the low evaporation temperature could also be achieved for 40 °C.

2.2 *Studies Related to AC Compressors*

Verma and Dondapati [15] designed the solar PV system to run the domestic air conditioner in order to utilize the renewable source of energy. They calculated the power required to operate the solar refrigerator which was 356 Wh/day. They told that 1.3 modules of 100 W are required for power the refrigerator. Similarly, the size of the battery and inverter is 58 A-h and 462.3 W, respectively. They reported that the solar PV generates 41,760.67 kWh/day in 25 years using the degradation factor of 0.05%. They justified the levelized cost of energy with 0.0870 in 25 years.

Ouali et al. [16] studied the effect of thermal control in 160 L domestic refrigerator using R134a. Energy use was affected by room temperature, thermostat position and door closing and opening. The refrigerator is connected with 450 W solar PV, 100 A-hour battery and 750 W inverter. They revealed the temperature difference between the evaporator and thermostat due to mechanical error in thermostat, the thermal inertia of thermostat and poor contact between the surface of the evaporator and bulb of the thermostat. They calculated the estimated loss which was 2 min/periodic cycle and 1107 h yearly. They revealed that Algeria can save up to 72 million euros per year. Finally, they concluded that this energy efficiency brings down the cost of solar PV refrigerator so one firm energy policy is required.

Gupta et al. [17] focused on the problem of vaccine preservation in the absence of electricity for rural areas and tried to solve the problem with the help of a solar PV refrigerator. They determined the optimum size of solar PV, battery and insulation thickness for 50 L refrigerator. They simulate the solar refrigerator with the help of TRNSYS—transient simulation software and validate through experimental study. They connected the 50 L refrigerator with 24 V battery, solar PV, 1 kVA inverter and charge controller. They reported that the refrigerator of 25 mm thickness insulation

required 320 W solar PV and 50 Ah capacities of batteries. They further reported that 200 W solar PV is required if insulation thickness is doubled to 50 mm.

Kattakayam and Srinivasan [18] reported the performance analysis of a lead–acid battery system. It was the part of a refrigerator. Their experimental setup had a 165 L refrigerator with a cooling capacity of 100 W. They fitted refrigerator with 240 W capacity of AC hermetic compressor and 180 Ah lead–acid batteries of deep discharge type along with the invertors. These batteries will be operated at $0.5 < \text{SOC} < 0.8$ where SOC is the state of charging. The refrigerator was operated with the help of battery invertors during the charging process and observed that the battery temperature increased swiftly which being a no load opens circuit voltage at 27 V. Charging current should be reduced manually after about 500 min so that temperature can be maintained within the limits. They reported that the heating effects would significant for $\text{SOC} > 0.8$ and the requirement of reduction of charging current after 13 continuous days. They showed charging characteristics of battery with mains and 1 kVA generator (two-stroke air-cooled kerosene engine) via a rectifier. The voltage increased steadily with the charging from the mains, but open-circuit voltage decreased exponentially in the case of the generator set. The engine reached the steady-state operating conditions after a long time. Further, they reported that initially, the battery open-circuit voltage was 26 V corresponding to SOC greater than 0.7 which decreased to 25 V. Due to this mismatch, power loss was more than 4%. That is why they operated the battery at $0.5 < \text{SOC} < 0.8$ without the use of maximum power point tracking. It generally consumes 7% of the power generated.

Modi et al. [19]) carried out the experimental performance analysis of 165 L capacity domestic refrigerator working with R134a. It is driven by 140 W solar photovoltaic arrays. The power of the compressor which was rated at 110 W had electricity on 50 Hz. Two lead–acid batteries 12 V-135 Ah were coupled in series in order to provide the backup power. The battery bank was connected to the inverter-transformer system. Its function is to convert the direct current into alternating current. The charge controller had its link with the battery bank and solar panels. The function of the charge controller is to regulate the amount of charge coming from the panel and avoid overcharging of batteries. Their results showed that 140 W solar PV capacity and 135 Ah batteries were the least possible configurable to work the system with satisfactory. They reported that the maximum COP was 2.012 at 7:00 AM, and it was decreased from morning to afternoon. They further informed that the larger PV module and larger battery bank are essential.

Cherif and Dhouib [20] demonstrated the simulation responses of a solar photovoltaic refrigeration system. They utilized the latent energy storage, which was referred to as less battery storage system (LBSS). The LBSS refrigeration plant consists of solar photovoltaic panels, dc/ac converter, dc/dc converter, refrigerator and data acquisition system. There were two sections of the refrigerator; one exists for latent storage and last for the conservation of product which was separated by a controlled flap. When sufficient solar radiations were available, the compressor worked in order to accumulate the ice and maintains the required temperature. The latent storage can be utilized in the night or bad weather conditions. They reported that for good climatic conditions, the storage energy was 705 Wh/day that ensures

the autonomy of 1 day. The energy consumption and storage were 179 kWh/year and 115 kWh/year, respectively, for both the solar plant of 200 W and a load of 1000 Wh/day. They further concluded that the door opening and closing increase the thermal loss but there is no effect on the process of storage temperature. The LBSS parameters decreased with solar irradiation perturbation.

Kattakayam and Srinivasan [21] determined the thermal performance of a solar PV refrigerator. They chose 100 W cooling capacities, 165 L domestic refrigerator working with R12. Experiments were performed with mains and inverter as a power source. For different voltage, they showed the variations in compressor body temperature. The lowest surface temperatures were obtained at 200 V with the least power consumption. The current drawn was larger due to copper losses at a voltage above and below the optimum without any benefit to the cooling capacity. They showed the influence of the refrigerator door opening when it got power from the inverter. The performance of the refrigerator was checked for the 30 s at 30 min interval when the door was opened. Due to this, the left wall of the cabinet touched the level beyond 8 °C which is unhygienic for the purpose of storing the vaccines. They further elaborated on the capacity of the refrigerator in terms of icing. They loaded 5 kg of water into the freezer that took 6 h to freeze it. During this transient condition, the compressor inlet and outlet had no same temperature and indicated that the pressure equalization had not been there. It was found that the inverter might not be suitable for such large cooling loads, and the refrigerators utilized for vaccine operation could not be suitable for ice making. They further identified that the heat which was gained through the panels was the reason for the loss in the refrigerator. Vacuum insulated panels should be utilized instead of conventional insulation. In the case of inverter operation, losses in the inverter can be minimized with the help of a robust controller.

Kattakayam and Srinivasan [21] described the major characteristics of a small refrigerator that is mechanized by solar PV. It got backing through a 1 kVA petrol start, a portable generator set which is run by kerosene. The main source of electrical energy was 280 W capacity of solar PV, which can maximum generate 1450 Wh of electrical energy against the actual demand of 1300 Wh per day. The storage system had deep discharge type four lead–acid batteries each of 6 V × 180 Ah. Fully charged batteries are sufficient for 3 days backup. Another important component was inverter, a pulse width which had a modulated square wave. As the compressor motor was induction start, it required a voltage of 230–250 V when starting and 200–220 V for normal running conditions. It can be done using the transformer and the power transistors. Due to the continuous operation of the inverter, parasitic consumption resulted in a loss of inverter. To overcome this, the inverter had to put in taken off condition from the circuit during the system “off-cycle” with the help of a relay. They noticed that the 8–12 min of the delay were needed during the “off-cycle” of the refrigerator in order to equalize the pressure across the compressor, and time delay circuit was introduced. During their tests, they concluded that the 10 min delay did not affect the inside temperature. They observed that the cycle time is increased in the case of inverter operation using time delay which resulted in considerable energy saving. The inverter discharge current was fairly steady. To simulate the monsoon period, they allowed running the system PV with the help of batteries only. They observed

that the batteries voltage decreased most of the time except for a steep fall during low discharge rate. They showed that the steady temperature inside of the refrigerator could be maintained during the whole time, and there was a backup of 3 days. It took 3600 min to a generator for charging the battery fully.

Taha [22] demonstrated the oversizing and mismatching in solar photovoltaic refrigerators. The experimental setup consisted of a refrigerator compartment, PV array, charger controller and batteries. Refrigerator-1 had two PV modules in series and three parallel strings. Similarly, refrigerator-2 had three photovoltaic modules in series and two parallel strings. He calculated the load mismatch and oversizing. The average mismatch losses were 2.26% and 2.5% for refrigerator-1 and refrigerator-2, respectively, which resulted into a reduction in the overall efficiency of PV arrays. He further showed that for refrigerator-1, photovoltaic modules were adequate to run the system in all operating condition but refrigerator-2 was not suitable for higher cooling levels. The oversizing concept justified the surplus which was being supplied by the solar PV modules. The climatic working conditions made the PV modules oversized with 40%.

3 Conclusion

This review study focused on a detailed overview of the solar photovoltaic refrigeration system. Refrigeration technologies are required for food preservation and storage of vaccines. Electricity is not available in all rural areas, especially in developing countries. Solar energy is a proper solution to this problem. DC compressor is more energy-efficient than AC compressor as it avoids the use of inverter and hence improves the overall performance. It also reduces the cost of components. The cost of equipment can also be reduced by inculcating VRF technology. It can reduce the overall size of the solar photovoltaic array by reducing the peak power. Various studies show that the solar refrigeration system can be successfully utilized for high ambient temperature. Researchers have shown that it is possible that solar refrigeration can be achieved without the use of any battery and inverter. However, it also imposes the minimum solar radiation required to run the DC compressor. Proper utilization of insulation can reduce heat loss and enhance performance. Performance can also be improved by utilizing the solar tracking system and thermal storage. Solar refrigeration requires comparatively higher time to achieve the temperature 0 °C or lower. Therefore, optimum design conditions are required for better performance.

References

1. Kattakayam T, Srinivasan K (1998) Uninterrupted power supply for autonomous small refrigerators. *Energy Conserv Manag* 39:21–26
2. Ekren O, Celik S, Noble B, Krauss R (2013) Performance evaluation of a variable speed DC compressor. *Int J Refrig* 36:745–757
3. Opoku R, Anane S, Edwin IA, Adaramola MS, Seidu R (2016) Comparative techno-economic assessment of a converted DC refrigerator and a conventional AC refrigerator both powered by solar PV. *Int J Refrig* 72:1–11
4. Khan KS, Amjad W, Munir A, Hensel O (2020) Improved solar milk chilling system using variable refrigerant flow technology (VRF). *Solar Energy* 197:317–325
5. Su P, Ji J, Cai J, Gao Y, Han K (2020) Dynamic simulation and experimental study of a variable speed photovoltaic DC refrigerator. *Renew Energy* 152:155–164
6. Salilih EM, Birhane YT (2019) Modelling and performance analysis of directly coupled vapor compression solar refrigeration system. *Solar Energy* 190:228–238
7. Daffallah KO (2018) Experimental study of 12V and 24V photovoltaic DC refrigerator at different operating conditions. *Phys B* 545:237–244
8. Daffallah KO, Benganem M, Alamri SN, Joraid AA, Al-Mashaqri AA (2017) Experimental evaluation of photovoltaic DC refrigerator under different thermostat settings. *Renew Energy* 113:1150–1159
9. Torres-Toledo V, Meissner K, Täschner P, Martinez-Ballester S, Müller J (2016) Design and performance of a small-scale solar ice-maker based on a DC-freezer and an adaptive control unit *Sol Energy* 139:433–443
10. El-Bahloul AAM, Hamza AH, Ookawara S (2015) Performance and sizing of solar driven dc motor vapor compression refrigerator with thermal storage in hot arid remote areas. *Energy Procedia* 70:634–643
11. Tina GM, Grasso AD (2014) Remote monitoring system for stand-alone photovoltaic power plants: the case study of a PV-powered outdoor refrigerator. *Energy Conver Manag* 78:862–871
12. Kaplanis S, Papanastasiou N (2006) The study and performance of a modified conventional refrigerator to serve as a PV powered one. *Renew Energy* 31:771–780
13. Toure S, Fassinou WF (1999) Cold storage and autonomy in a three compartments photovoltaic solar refrigerator experimental and thermodynamic study. *Renew Energy* 17:587–602
14. El Tom OMM, Omer SA, Taha AZ, Sayigh AAM (1991) Performance of a photovoltaic solar refrigerator in tropical climate conditions. *Renew Energy* 1:199–205
15. Verma JK, Dondapati RS (2017) Techno-economic sizing analysis of solar PV system for domestic refrigerators. *Energy Procedia* 109:286–292
16. Ouali M, Djebiret MA, Ouali R, Mokrane M, Merzouk NK, Bouabdallah A (2017) Thermal control influence on energy efficiency indomestic refrigerator powered by photovoltaic. *Int J Hydrogen Energy* 42:8955–8961
17. Gupta BL, Bhatnagar M, Mathur J (2014) Optimum sizing of PV panel, battery capacity and insulation thickness for a photovoltaic operated domestic refrigerator. *Sustain Energy Technol Assess* 7:55–67
18. Kattakayam T, Srinivasan K (2004) Lead acid batteries in solar refrigeration systems. *Renew Energy* 29:1243–1250
19. Modi A, Chaudhuri A, Vijay B, Mathur J (2009) Performance analysis of a solar photovoltaic operated domestic refrigerator. *Appl Energy* 86:2583–2591
20. Cherif A, Dhouib A (2002) Dynamic modelling and simulation of a photovoltaic refrigeration plant. *Renew Energy* 26:143–153
21. Kattakayam T, Srinivasan K (2000) Thermal performance characterization of a photovoltaic driven domestic refrigerator. *Int J Refrig* 23:190–196
22. Taha AZ (1995) The oversizing method of estimation in PV systems. *Renew energy* 6:487–490

A New Design Based on Grid Integrated Solar PV Array Using Vector Control



Jaya Singh  and Vineet Kumar Tiwari

1 Introduction

This paper shows the effective utilization of renewable energy towards fulfilling the load requirement. In current era of 2020–2021, the continuous increment of population of the country demands more load power from generating source. As it could be seen that conventional generating sources are limited, and with lot of restrictions, these are unable to meet the excessive load requirement. Photovoltaic solar residential (PV) technology is becoming an even more critical part of green energy in the country. Usually, PV array at home is connected with the grid at distribution side using single-phase inverter. PV single-phase power unit will optimize PV array power production while ensuring overall electricity grid interface performance, safety, reliability and controllability [1–6]. The photovoltaic solar connected grid (PV) network is one of the electricity pools transforming DC power produced in an AC capacity. The primary function of grid interconnected solar photovoltaic network is to pass solar limit array electricity of cohesion capacity component via system. The structure is tied together through solar inverter which is a type of DC converter which supports if full power is derived from solar PV panels When the device is switched on it is fired appropriately. Delivering quality control is the main problem for photovoltaic (PV) solar-driven grid network. The quality control of the system suggested is determined by the transient existence of photovoltaic control, using electronic converters and the related nonlinear changes to grasp and evaluate the device correctly [7–10]. A significant consideration in the deployment of single-phase PV inverter which is integrated with grid is the introduction of harmonics current is very less in the integrated grid system. Particularly a linear current control scheme along with a resonating Harmonic compensator is connected in cascaded

J. Singh (✉)

ABES Engineering College, Ghaziabad, Uttar Pradesh, India

V. K. Tiwari

United College of Engineering and Research, Allahabad, Uttar Pradesh, India

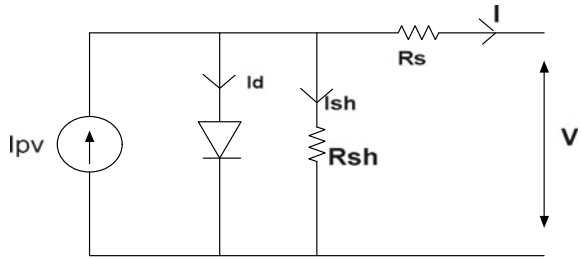
series connection type of tracking regulator (normal harmonic compensation is shunt to tracking regulator). The series cascaded partnership gives an efficient avoidance of voltage connected with grid background intervention, a consistent synchronization with grid voltage and also low response time relative to the traditional control scheme [11, 12]. The sliding control mode (SMC) is known as robust high-stability controller in a large variety of operating environments, even though it suffers from chattering problem. Furthermore, it cannot be extended explicitly to power converters from multi-switches. A good efficiency, set switching frequency for a single-phase unipolar inverter is suggested with sliding mode switch through smoothing eradicates the chattering issue of SMC. The control rule in a thin boundary layer as well as pulse width modulator provides the inverter with a fixed frequency switching regulation. The smoothing technique is based on reducing the modulator's pulse width [13, 14]. In today's situation, despite the sudden transition increasing energy competition and regional climate change resources like fuel, wind and solar distributed generation (DG) society that switches to traditional energy such as sun and wind. Alternate sources like solar panels are required for compensating the surplus demand. In this case, a significant issue is ensuring everything is emission-free, healthy, fair and unrestricted. Microgrid concept is planned which is used in the boost converter to use PV module. Essentially this layout is applicable in remote or island charging schemes [15–19]. The study provides the output of universal active power filter integrated with solar PV battery which is linked in both grid and shielded modes of service. The device consists of a right uniform shunting active control filter where the system's PV array has been connected to DC bus. The battery is attached to the DC-bridge converter through a bidirectional interface. Photovoltaic grid-connected electricity system was introduced. Two FOV MPPT controllers and FSC solutions were developed and used in deduction. The optimum point of activity needed and configured for the maximum full power. A DC-to-DC boost-type converter with PI controller is connected to the first one to raise and stabilize performance DC [20–23]. In this paper, integration of grid with solar PV array and conventional done. After that switching of the boost converter is assessed by using P&O vector control in order to harness the maximum power out of the PV array. It is observed that load requirement is fulfill by using solar PV array.

2 Structure of Solar PV Array

It can be observed that there is continuous fall of irradiation on solar PV array which allow producing certain level of power which is used to store in battery. The basic structure of solar PV array is shown by Fig. 1. In this figure, solar PV array is combination of current source and diode with internal resistance. It is represented by voltage and current. From Fig. 1, it can be drawn that

$$I = I_{pv} - I_d - I_{sh} \quad (1)$$

Fig. 1 Structure of solar PV array



$$I_d = I_o(e^{V/\eta V_t} - 1) \tag{2}$$

where $V_t = KT/q$

$$I_{sh} = (V - IR_s)/R_{sh} \tag{3}$$

from Eq. (1) it can be obtained as

$$I_{pv} = I + I_o(e^{V/\eta V_t} - 1) + (V - IR_s)/R_{sh} \tag{4}$$

Maximum power extracted from PV array is dependent on relationship between O.C voltage and S.C current

$$P_{max} = V_{max} I_{max} \tag{5}$$

From Fig. 2, characteristics between current and voltage, power and voltage are drawn for different set of irradianations. It is observed that P_{max} and current are extracted from PV array at irradiation of 1 kW/m².

3 Design of Boost Converter

The purpose of boost-type converter is to increase magnitude of input voltage. It is observed that output of solar PV array is stored in battery, and this voltage is not sufficient to provide adequate power back to grid terminal. The PV array output acts as input for boost converter. With the help of firing angle, output voltage (V_o) can be adjusted on higher side with respect to input voltage (V_i).

$$V_o = V_i/(1 - \alpha) \tag{6}$$

The structure of boost converter has been shown in Fig. 3. In Fig. 3, switching of switch is done by using vector control and maintain voltage constant due to the presence of capacitance which resist the change in voltage. From Fig. 3, it can be

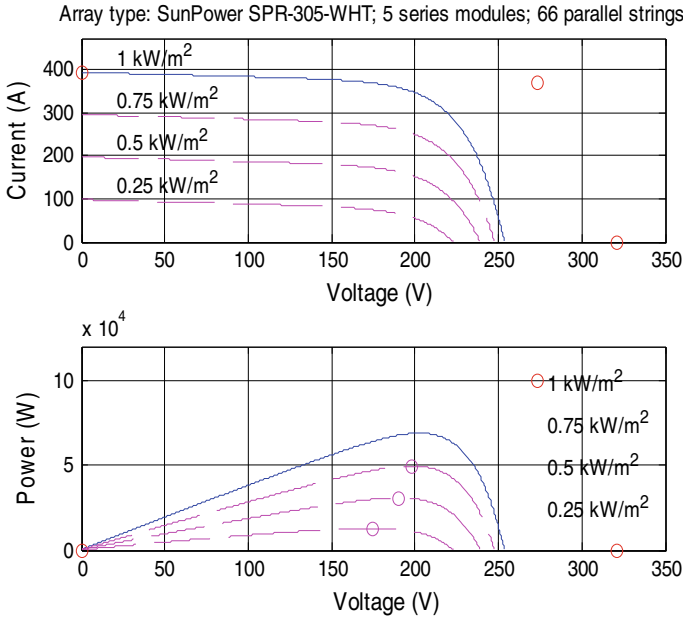
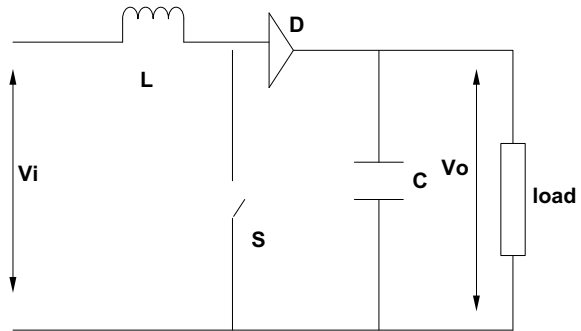


Fig. 2 Current and voltage, power and voltage characteristic of solar PV array

Fig. 3 Structure of boost converter



depicted that selection of inductance and capacitor value always play a significant role. Its value can be given as

$$L = V_i * \alpha / f * \Delta I_o \tag{7}$$

$$C = I_o * \alpha / f * \Delta V_o \tag{8}$$

These values of L and C also calculated the power loss of switching converter which is given by

$$P_{\text{loss}} = V_{\text{gs}}^2/R \tag{9}$$

V_{gs} is voltage appear across switch terminal.

4 Design of Proposed System

The structure of proposed topic is described in Fig. 4, in which it is observed that both solar PV array and AC source are connected directly to DC grid via converter. The design aspect of solar PV array is already discussed above. It is observed that P_{max} is fetched from PV array using P&O method which is discussed in [24]. After this output voltage is stored in battery, this voltage is not sufficient in order to provide adequate amount of power. This is being possible by using boost converter only. Both of conventional source and solar PV array fulfill the load demand. The maximum contribution of load is shared by solar PV array. The switching of boost converter is done by using vector control only which is discussed in Fig. 5. The brief discussion of Fig. 5 is discussed in Sect. 4.1.

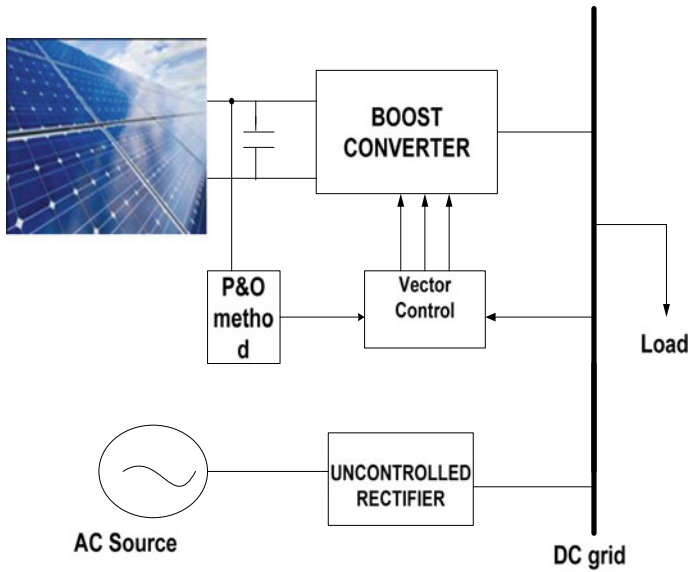


Fig. 4 Layout of the proposed topic

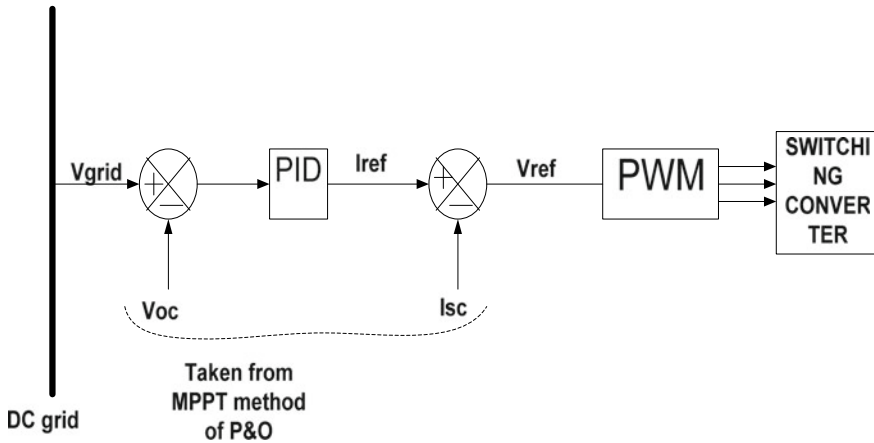


Fig. 5 Vector control scheme

4.1 Vector Control

In order to switch the converters, vector control is used in which grid voltage is compared with open-circuit voltage from P&O method and difference between two passes to PID controller which gives reference value of current as shown in Eq. 10

$$I_{ref} = (K_p + sK_d + K_i/s)(V_{grid} - V_{oc}) \tag{10}$$

$$K_p = 0.23, K_i = 1.32, K_d = 2.32$$

Further, reference value of current compared with short-circuit current and give reference voltage for PWM converter in order to generate pulse for switching the converters. In PWM converter. reference voltage is compared with carrier voltage in order to give pulses for switching.

4.2 Conventional Source

It can seen from Fig. 4, conventional AC source is also connected to DC grid via uncontrolled converter. It is connected in parallel with solar PV array. In this case, 400 AC source is given as input to uncontrolled rectifier. The output of rectifier is the input of DC grid.

The output of the rectifier is V_o which is shown in Eq. (11)

$$V_o = 3V_m/\pi$$

$$V_m = 400\sqrt{2} \tag{11}$$

Power flow to DC grid is P_o which is shown in Eq. (12)

$$P_o = V_o * I_o \tag{12}$$

The total load of 200 MW is connected at DC grid

After switching the boost converter through vector, certain amount of power is obtained. Now it has to realize that how the solar PV array and conventional AC source combined to meet the load demand. The role of contribution of each source varies on day-to-day basis.

It is better observed in Table 1.

It can be concluded that contribution of solar PV array and conventional method varies time to time on each day. It is observed that during morning time contribution of conventional method is more than solar PV array, while in afternoon contribution of solar PV array is more than conventional. In evening time, there is almost equal contribution of both sources to meet the load demand. By using vector control for switching boost converter, it is observed from Fig. 6 that o/p voltage of boost converter is quite smooth and it has lesser THD which is somewhat around 6.42 as shown in Fig. 7.

Table 1 Power flow effect

Time	Load (MW)	Solar (MW)	Conventional (MW)
Morning	100	30	50
Afternoon	400	250	100
Evening	300	100	102

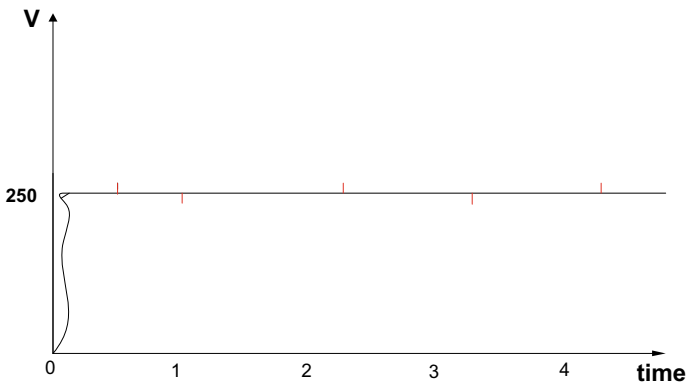


Fig. 6 O/P voltage of boost converter

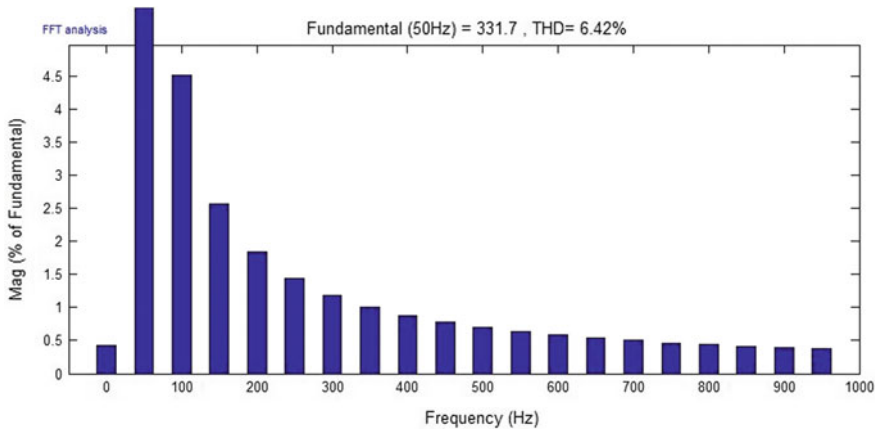


Fig. 7 THD of boost converter output voltage

5 Conclusion

This paper shows the integration of grid with solar PV array and conventional AC sources. The solar PV array has been connected to grid via boost converter. Boost converter switching is assessed by using P&O method with vector control. The boost converter is connected to grid via uncontrolled rectifier. It is observed that performance parameter output of solar PV array gives better reliable solution with better power quality waveform like lesser THD.

References

1. Karanayil B, Agelidis VG, Pou J (2014) Performance evaluation of three-phase grid-connected photovoltaic inverters using electrolytic or polypropylene film capacitors. *IEEE Trans Sustain Energy* 5(4):1297–1306
2. Bahrani B, Rufer A, Kenzelmann S, Lopes LAC (2011) Vector control of single-phase voltage-source converters based on fictive-axis emulation. *IEEE Trans Ind Appl* 47(2):831–840
3. Castilla M, Miret J, Matas J, Vicuna LG, Guerrero JM (2008) Linear current control scheme with series resonant harmonic compensator for single-phase grid-connected photovoltaic inverters. *IEEE Trans Ind Electron* 55(7):2724–2733
4. Abrishamifar A, Ahmad AA, Mohamadian M (2012) Fixed switching frequency sliding mode control for single-phase unipolar inverters. *IEEE Trans Power Electron* 27(5):2507–2514
5. El-Habrouk M, Darwish MK, Mehta P (2000) Active power filters: A review. *IEE Proc Electric Power Appl* 147(5):403–413
6. Lettl J, Bauer J, Linhart L (2011) Comparison of different filter types for grid connected inverter. In: *Proceedings of progress in electromagnetics research symposium, Marrakesh, Morocco*, pp 1426–1429 (2011)
7. Wessels DC, Fuchs FW (2009) Limitations of voltage-oriented PI current control of grid-connected PWM rectifiers with LCL filters. *IEEE Trans Ind Electron* 56(2):380–388

8. Xin Z, Loh PC, Wang X, Blaabjerg F, Tang Y (2016) Highly accurate derivatives for LCL-filtered grid converter with capacitor voltage active damping. *IEEE Trans Power Electron* 31(5):3612–3625
9. Arritt H (2015) Protection practices for an integrated grid. Panel Presentation. In: Proceedings of IEEE Power Energy Society General Meeting, Denver CO, USA
10. Veerachary M, Senjyu T, Uezato K (2003) Neural-network-based maximum-power-point tracking of coupled-inductor interleaved-boostconverter-supplied PV system using fuzzy controller. *IEEE Trans Ind Electron* 50(4):749–758
11. Syafaruddin, Karatepe E, Hiyama T (2009) Artificial neural network-polar coordinated fuzzy controller based maximum power point tracking control under partially shaded conditions. *IET Renew Power Gener* 3(2):239–253
12. Nandurkar SR, Ranjeev M (2012) Design and simulation of three phase inverter for grid connected photovoltaic system. In: Proceedings of Third Biennial National Conference, NCNTE, 24–25 Feb 2012, pp 80–83
13. Tafticht T, Agbossou K (2004) Development of a MPPT method for photovoltaic systems. In: Canadian Conference on Electrical and Computer Engineering, 2004, pp 1123–1126
14. Kulkarni A, John V (2016) Design of a fast response time single-phase PLL and DC offset rejection capability. In: Applied power electronics conference and exposition (APEC), Mar 2016
15. Nthontho MP, Chowdhury SP, Winberg S, Chowdhury S (2014) Protection of domestic solar photovoltaic based microgrid. In: IEEE PES Conference USA
16. Abdel Hady R (2017) Modeling and simulation of a micro grid-connected solar PV system. National Research Center, Ministry of Water Resources and Irrigation, April 2017
17. Chattopadhyay TK, Banerjee S, Maity D, Chanda CK (2016) Microgrid: planning of active and reactive power loss reduction in distribution network. In: 3rd International conference on electrical, electronics, engineering trend, communication optimization and science (EEECOS), p 5
18. Tavakoli A, Negnevitsky M, Lyden S, Haruni O, Member, IEEE (2014) Decentralized control strategy for multiple distributed generation in islanded mode. In: 2014 IEEE PES General Meeting, Conference & Exposition, National Harbor, MD, pp 1–5
19. Hamzah A, Nordin M, Omar AM (2011) Modeling and simulation of photovoltaic (PV) array and maximum power point tracker (MPPT) for grid-connected PV system. In: 3rd International Symposium & Exhibition in Sustainable Energy & Environment, Melaka, Malaysia, 1–3 June 2011
20. Atallah AM, Abdelaziz AY, Jumaah RS (2014) Implementation of perturb and observe MPPT of PV system with direct control method using buck and buckboost converters. *Emerg Trends Electr Electron Instrum Eng Int J (EEIEJ)* 1(1)
21. Yazdani A, Iravani R (2010) Voltage-sourced converters in power systems. In: Modeling, control, and applications. IEEE Press A John Wiley Sons, Inc., pp 204–269
22. Jie L, Ziran C (2011) Research on the MPPT algorithms of photovoltaic system based on PV neural network. In: Chinese control and decision conference (CCDC), pp 1851–1854, Mianyang
23. Sharma V, Fatima M, Prakash A (2017) Performance analysis of grid connected and islanded mode photovoltaic system. In: 2017 4th IEEE Uttar Pradesh Section International Conference on Electrical, Computer and Electronics (UPCON) GLA University, Mathura, pp 145–149, 26–28 Oct 2017
24. Jaldeep, Bhuvnesh, Prakash (2018) Fuzzy and P&O MPPT techniques for stabilized the efficiency of solar PV system. In: International conference on computing, power and communication technologies (GUCON) Galgotias University, Greater Noida, UP, India, 28–29 Sept 2018

Performance-Based Study of HFC134A, HC600A, and HFO1234YF in a VCR System



Sunil Kumar Gupta, B. B. Arora, and Akhilesh Arora

1 Introduction

To fulfill both energetic and environmental requirements, it is necessary to develop new energy-efficient and environment-friendly refrigerants. Global warming produced by high GWP refrigerants has driven the efforts to search for replacement refrigerants which reduce the negative impact on the environment besides producing energy-efficient operations. Many alternative refrigerants have been applied to replace the conventional ones but still, there is a want of refrigerants which have shorter atmospheric life to reduce the impact of global warming.

The very important consideration of introducing any substitute refrigerant is the energetic and exergetic optimization of the system. The energy and exergy are influenced to a great extent by the ambient temperature [10]. The exergy efficiency is incredibly affected by modifying the evaporator and condenser temperature [15]. Exergetic efficiency would be enhanced by reforming different components and including the effect of dead state temperature [1]. A modified VCERS used a heat exchanger as a superheater in the primary loop and a condenser in the secondary loop. It was found that the modified system gave better results on energy and exergy analysis than separate systems [13]. HFO1234yf used in air conditioning found more exergy efficient than HFC134a. The compressor produced the highest exergy destruction [4]. The compressor's exergy destruction rate obtained with HFO1234yf was found lower than that calculated for HFC134a [11].

With low specific volume achieving the same cooling capacity as with HFC134a, the HC600a compressor would require larger displacement [14]. HC600a required 66% lower mass than HFC134a [6]. Navarro et al. concluded that HFO1234yf resulted in lower cooling capacity by approximately 9% and COP by 19% compared

S. K. Gupta (✉)

Aryabhatt Institute of Technology, G.T. Karnal Road, New Delhi 110033, India

B. B. Arora · A. Arora

Delhi Technological University, Bawana Road, New Delhi 110042, India

to the HFC134a [9]. According to Daviran et al., HFO-1234yf produced lower COP as compared to HFC-134a for fixed cooling volume, and the COP was higher for the fixed refrigerant mass flow rate [4]. The COP of the VCRS employing HFO1234yf was 4–8% lower and also cooling capacity about 4–7% lower than that obtained using HFC134a [12]. Through experimental work, it was shown that isobutene (HC600a) increased the refrigeration capacity of a VCRS with the refrigeration loads [8]. Jarall concluded that refrigerating capacity, COP, and compressor efficiency were reduced with HFO1234yf [5].

HFO1234yf was recommended as a major substitute to HFC134a as regards the energy intake, the cooling scope of the refrigeration, and the corresponding safety requirements [3]. HFO1234yf was found as a good alternative for HFC134a in a thermodynamical sense. However, safety requirements have to be taken care of [11].

Going through the literature review, it is concluded that very few works are available on the performance of HC600a and HFO1234yf in an air conditioning system. The authors investigate these refrigerants as a potential alternative to HFC134a based on energy and exergy criteria. The refrigerants used in this study with their thermophysical properties are listed in Table 1.

2 Materials and Methods

A vapor compression cycle (VCC) was employed for the analysis of refrigerants HFC134a, HC600a, and HFO1234yf. Diagrams representing schematic and p–h curves of the VCC are shown in Fig. 1a, b. The evaporator, condenser, and passenger cabin temperatures were used as input variables.

2.1 Energy Analysis

The coefficient of performance (COP) gives the measure of energetic performance of the VCC as:

$$\text{COP} = \frac{\dot{Q}_e}{\dot{W}_c} \tag{1}$$

where \dot{Q}_e is the heat abstracted from the evaporator and \dot{W}_c is the compressor work input during a cycle.

S. No.	Component	Heat/work transfer	Equation
1	Evaporator	$\dot{Q}_e = \dot{m}_r(h_4 - h_1)$	(2)
2	Compressor	$\dot{W}_{cs} = \dot{m}_r(h_{2s} - h_1)$	(3)

(continued)

(continued)

S. No.	Component	Heat/work transfer	Equation
		$\dot{W}_c = \frac{\dot{W}_{ex}}{\eta_s}$	(4)
3	Condenser	$\dot{Q}_r = \dot{m}_r(h_3 - h_2)$	(5)

where \dot{m}_r = refrigerant mass flow rate (kg s⁻¹)

\dot{W}_{cs} = isentropic (ideal) work input to the compressor

\dot{W}_c = actual work input to the compressor

η_s = isentropic efficiency of the compressor

2.2 Exergy Analysis

Exergy is represented by the upper limit of possible work which a system can deliver by reaching the state of the environment through a reversible process. Exergy shows dependence on the system as well as the environment [2]. Therefore, any change in the system or environment will lead to a change in the exergy potential.

Applying the exergy balance, the expressions for component exergy destruction per unit refrigerant mass can be represented as follows:

Component	Exergy destruction	Equation
Evaporator	$\dot{E}_{D,e} = [(h_4 - h_1) - T_0(s_4 - s_1)] + \dot{Q}_e(1 - T_0/T_r)$	(6)
Compressor	$\dot{E}_{D,c} = W_c + [(h_1 - h_2) - T_0(s_1 - s_2)] = T_0(s_2 - s_1)$	(7)
Condenser	$\dot{E}_{D,k} = [(h_2 - h_3) - T_0(s_2 - s_3)]$	(8)
Expansion valve	$\dot{E}_{D,v} = (h_3 - h_4) - T(s_3 - s_4) = T_0(s_4 - s_3)$	(9)
Total	$\dot{E}_{D,t} = \dot{E}_{D,c} + \dot{E}_{D,k} + \dot{E}_{D,e} + \dot{E}_{D,v}$	(10)

The following assumptions have been made for this analysis:

$\dot{Q}_e = 3.5167$ kW.

Isentropic efficiency of the compressor, $\eta_s = 75\%$,

Evaporator Efficiency, $\eta_e = 80\%$

Evaporator Coil Temperature, $T_e = 2$ to 8 °C.

Condenser Temperature, $T_k = 40$ to 60 °C (in steps of 5 °C).

Cold Room Temperature, $T_r = 20$ to 26 °C.

Ambient or environment temperature, $T_0 = 35$ °C.

Refrigerants: HFC134a, HC600a, and HFO1234yf.

Superheating in evaporator = 2° .

Subcooling in the condenser and pressure losses in the evaporator and the condenser have been neglected. A model has been developed for performing energetic and exergetic analysis run on engineering equation solver (EES) software [7].

Table 1 Thermophysical properties of refrigerants (Ref: EES software, Klein et al. [7])

Fluid (chemical formula)	P_{cr} (MPa)	T_{cr} ($^{\circ}$ C)	MW (kg k mol^{-1})	NBP ($^{\circ}$ C)	$V_{sat,v}$ (NBP) ($\text{m}^3 \text{kg}^{-1}$)	h_g (kJ kg^{-1})	Safety group	GWP (100 years)
HFC134a (C2H2F4)	4.059	101.06	102.03	-26.07	0.0693	198.6	A1	1301
HC600a (C4H10)	3.629	134.66	58.12	-11.75	0.2349	354.34	A3	4
HFO1234yf (C3H2F4)	3.382	94.7	114.04	-29.45	0.0567	163.29	A2L	<1

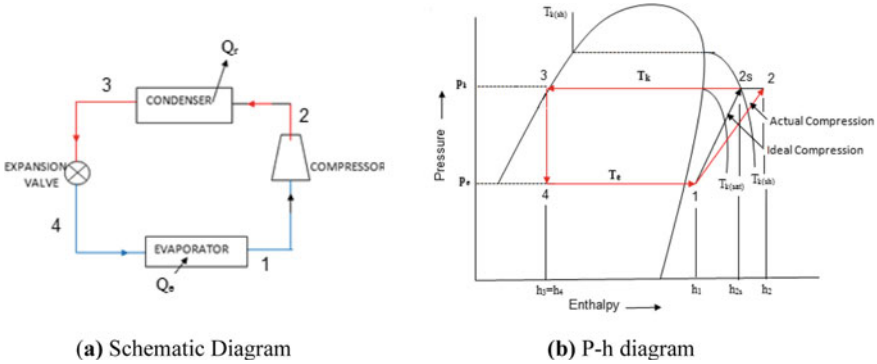


Fig. 1 Simple vapor compression cycle (VCC)

3 Results and Discussion

For a fixed cooling capacity, the refrigerant requiring less power will have more COP. The increasing evaporation temperature would reduce the pressure ratio and, consequently, lower the compressor power requirement. The variations due to changes in condenser temperature are also noteworthy. The outcomes of the different evaporator and condenser temperatures are discussed below.

3.1 Effect on Exergy Destruction

Figure 2a shows exergy destruction in components at condensing temperatures of 40 and 60 °C while the evaporator temperature is fixed at 5 °C. Exergy destruction in the condenser is highest at higher condensing temperature, whereas it is the lowest at lower condensing temperature. The exergy destruction increases in all the components except the evaporator with increasing condensing temperature. It is also found that exergy destruction in the evaporator is unaffected by variation in condensing temperature. This is because in the case of the evaporator the exergy flow involves evaporator temperature only, while exergy flow in other components has interaction with both evaporator and condenser temperatures. HFO1234yf shows the highest exergy destruction in all components except the evaporator.

Referring to Fig. 2b, total exergy destruction ($\dot{E}_{D,t}$) in the system is found to be lowest for HC600a, whereas it is slightly higher for HFC134a and HFO1234yf at different condenser temperatures. The total exergy destruction is more at a higher condensing temperature. The figure also depicts the reduction in total exergy destruction with the increase in the evaporator temperature, and the rising trend is shown with an increase in the condenser temperature. Hence, to minimize exergy destruction, it is desired to bring both these temperatures close to each other, in other words,

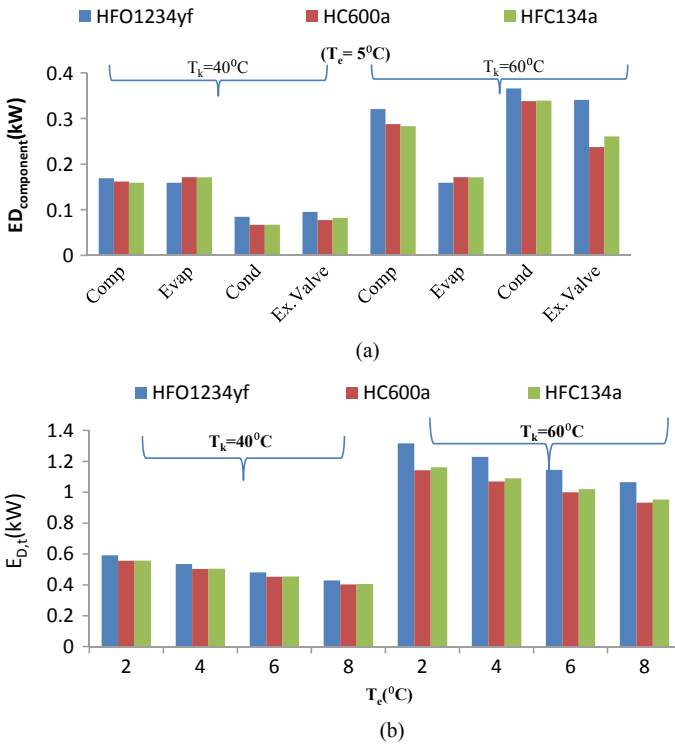


Fig. 2 Effect of T_k and T_e on a) ED component b) $\dot{E}_{D,t}$

keeping the evaporator temperature higher and the condenser temperature lower as much as possible within the specific requirement of the refrigeration system.

3.2 Effect on Compressor Work (\dot{W}_c)

\dot{W}_c decreases with an increase in the evaporator temperature and it increases with increment in the condenser temperature. The effect of evaporator temperature on \dot{W}_c is presented in Table 2a, b. The largest work is consumed by HFO1234yf, whereas HC600a consumes the least work.

3.3 Effect on COP

COP weighs the cooling effect produced in the evaporator against energy input to the compressor. For the fixed cooling effect, the COP varies according to the energy

Table 2 a \dot{W}_c (in kW) at $T_k = 40\text{ }^\circ\text{C}$ (varying T_e), b \dot{W}_c (in kW) at $T_k = 60\text{ }^\circ\text{C}$ (varying T_e)

(a)							
$T_k = 40\text{ }^\circ\text{C}$	$T_e\text{ (}^\circ\text{C)}$						
	2	3	4	5	6	7	8
HFC134a	0.7425	0.716	0.6898	0.664	0.6387	0.6137	0.5891
HC600a	0.7363	0.7097	0.6835	0.6577	0.6324	0.6075	0.5829
HFO1234yf	0.773	0.7444	0.7163	0.6888	0.6617	0.6351	0.609
(b)							
$T_k = 60\text{ }^\circ\text{C}$	$T_e\text{ (}^\circ\text{C)}$						
	2	3	4	5	6	7	8
HFC134a	1.376	1.338	1.301	1.265	1.23	1.195	1.161
HC600a	1.343	1.306	1.269	1.233	1.198	1.163	1.129
HFO1234yf	1.523	1.479	1.435	1.392	1.35	1.308	1.268

supplied to the compressor. As anticipated, since energy consumption for HC600a is the lowest, it shows the highest COP at all condenser and evaporator temperatures. HFC134a has lower COP than HC600a, whereas the COP of HFO1234yf is the lowest. It is also seen in Fig. 3a, b that the COP increases at higher evaporator temperatures and decreases at elevated condenser temperatures.

3.4 Effect on Mass Flow (\dot{m}_r)

Figure 4a represents \dot{m}_r of refrigerants at different condensing temperatures keeping the evaporator temperature fixed ($5\text{ }^\circ\text{C}$). For the same refrigerating effect, the mass of refrigerant HC600a circulated is almost 40% and 60% less than that required for HFC134a and HFO1234yf, respectively. The \dot{m}_r increases at higher condensing temperatures. HFO1234yf shows a slightly steeper rise in \dot{m}_r at higher condensing temperatures. As anticipated, the required \dot{m}_r is more for producing higher cooling effects, as shown in Fig. 4b.

4 Conclusions

Based on the above study, the concluding points are summarized as follows:

1. $\dot{E}_{D,i}$ in the system turns out lowest for HC600a (0.403 at $T_k = 40\text{ }^\circ\text{C}$ and $T_e = 8\text{ }^\circ\text{C}$), whereas it is the largest for HFO1234yf (1.316 at $T_k = 60\text{ }^\circ\text{C}$ and $T_e = 2\text{ }^\circ\text{C}$). Exergy destruction reduces as the evaporator temperature approaches condenser temperature.

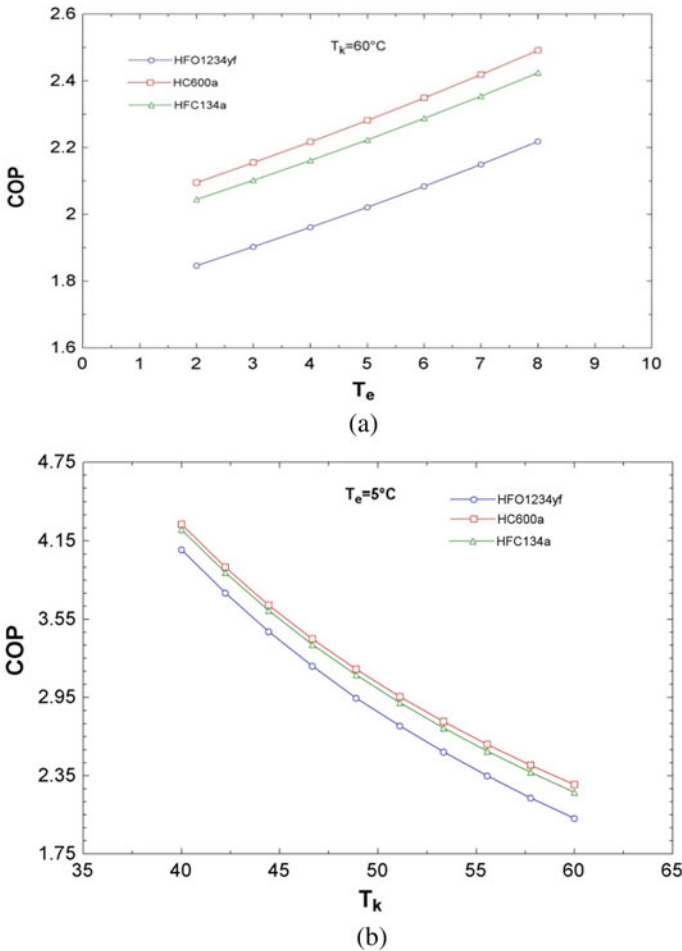


Fig. 3 COP variation **a** at $T_k = 60^\circ\text{C}$, **b** at $T_e = 5^\circ\text{C}$

2. The compressor work required to run the system for HC600a is lowest (0.583 kW at $T_k = 40^\circ\text{C}$ and $T_e = 8^\circ\text{C}$), and it is highest for HFO1234yf (1.523 kW at $T_k = 60^\circ\text{C}$ and $T_e = 2^\circ\text{C}$). The compressor work decreases at elevated evaporator temperatures but increases as the condenser temperature increases.
3. The COP of HC600a is the highest (ranging from 2.1 to 4.2), whereas the COP of HFO1234yf is found to be the lowest (ranging from 1.83 to 4.05) at the corresponding condenser and evaporator temperatures. The COP at higher evaporating temperature is more, and it gets lower at the higher condensing temperature.
4. For the same refrigerating effect, the amounts of charge with HC600a are 40 and 60% less than that required for HFC134a and HFO1234yf, respectively.

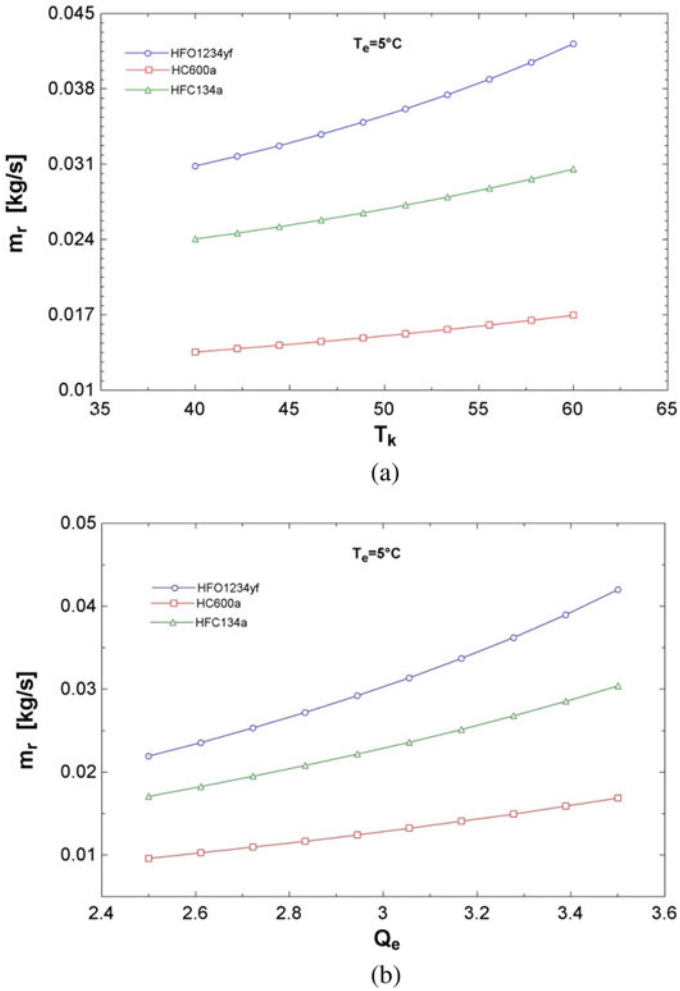


Fig. 4 Effect on \dot{m}_r at $T_e = 5^\circ\text{C}$ a varying T_k , b varying Q_e

Finally, it is concluded that HC600a can be a promising substitute to replace HFC134a.

References

1. Arora A, Arora BB, Pathak BD, Sachdev HL, Arora A (2007) Exergy analysis of vapour compression refrigeration system with R-22, R-407C and R-410A. *Int J Exergy* 4(4)
2. Boles YAÇ, Boles MA (2006) *Thermodynamics: an engineering approach* (5th edn). McGraw-Hill

3. Calleja-Anta D, Nebot-Andrés L, Catalán-Gil J, Sánchez D, Cabello R, Llopis R (2020) Thermodynamic screening of alternative refrigerants for R290 and R600a. *Results Eng* 5. <https://doi.org/10.1016/j.rineng.2019.100081>
4. Daviran S, Kasaeian A, Golzari S, Mahian O, Nasirivatan S, Wongwises S (2017) A comparative study on the performance of HFO-1234yf and HFC-134a as an alternative in automotive air conditioning systems. *Appl Therm Eng* 110:1091–1100. <https://doi.org/10.1016/j.applthermeng.2016.09.034>
5. Jarall S (2012) Study of refrigeration system with HFO-1234yf as a working fluid Etude sur un système frigorifique utilisant le HFO-1234yf comme fluide actif. *Int J Refrig* 35(6):1668–1677. <https://doi.org/10.1016/j.ijrefrig.2012.03.007>
6. Joybari MM, Hatamipour MS, Rahimi A, Modarres FG (2013) Exergy analysis and optimization of R600a as a replacement of R134a in a domestic refrigerator system. *Int J Refrig* 36(4):1233–1242. <https://doi.org/10.1016/j.ijrefrig.2013.02.012>
7. Klein SA, Alvarado F (2012) Engineering equation solver, Version 9.224–3D, F-Chart Software, Middleton, WI
8. Lee YS, Su CC (2002) Experimental studies of isobutane (R600a) as the refrigerant in domestic refrigeration system. *Appl Therm Eng* 22(5):507–519. [https://doi.org/10.1016/S1359-4311\(01\)00106-5](https://doi.org/10.1016/S1359-4311(01)00106-5)
9. Navarro-Esbrí J, Mendoza-Miranda JM, Mota-Babiloni A, Barragán-Cervera A, Belman-Flores JM (2013) Experimental analysis of R1234yf as a drop-in replacement for R134a in a vapor compression system. *Int J Refrig* 36(3):870–880. <https://doi.org/10.1016/j.ijrefrig.2012.12.014>
10. Oruç V, Devecioğlu AG (2015) Thermodynamic performance of air conditioners working with R417A and R424A as alternatives to R22. *Int J Refrig* 55:120–128. <https://doi.org/10.1016/j.ijrefrig.2015.03.021>
11. Özgür AE, Kabul A, Kizilkan Ö (2014) Exergy analysis of refrigeration systems using an alternative refrigerant (HFO-1234yF) to R-134a. *Int J Low-Carbon Technol* 9(1):56–62. <https://doi.org/10.1093/ijlct/cts054>
12. Pottker G, Hrnjak P (2015) Experimental investigation of the effect of condenser subcooling in R134a and R1234yf air-conditioning systems with and without internal heat exchanger. *Int J Refrig* 50:104–113. <https://doi.org/10.1016/j.ijrefrig.2014.10.023>
13. Roy R, Mandal BK (2017) Thermodynamic analysis of modified vapour compression refrigeration system using R-134a. *Energy Procedia* 109:227–234. <https://doi.org/10.1016/j.egypro.2017.03.050>
14. Sánchez D, Cabello R, Llopis R, Arauzo I, Catalán-Gil J, Torrella E (2017) Évaluation de la performance énergétique du R1234yf, du R1234ze(E), du R600a, du R290 et du R152a comme alternatives à faible GWP au R134a. *Int J Refrig* 74(2017):267–280. <https://doi.org/10.1016/j.ijrefrig.2016.09.020>
15. Yataganbaba A, Kilicarslan A, Kurtbaş I (2015) Exergy analysis of R1234yf and R1234ze as R134a replacements in a two evaporator vapour compression refrigeration system. *Int J Refrig* 60:26–37. <https://doi.org/10.1016/j.ijrefrig.2015.08.010>

STT-MRAM A Universal Memory from Device to Circuit



Jyoti Garg and Subodh Wairya

1 Introduction

In a mobile or computer system, memory is a central element. Earlier, we use those systems that have very little memory, and the device size was also significant. According to new technology, the requirement of a small area with high speed has increased. Due to that, memory has a very vital role in any device esp. computers, mobile phones. The existence of smartphones is due to only memory. Any technology depends mainly on these three parameters: area, power, and speed. If any technology can reduce any parameter significantly, the same can replace all. Due to changes in technology, scaling of devices occurs, resulting in a decrease in channel length and an increase in leakage current that impacts device performance, power consumption, battery life, and many other parameters.

A nonvolatile memory consumes less power as compared to volatile memory. For a decade, a search for nonvolatile memory is going on. Spintronics-based memory MRAM has become the excellent memory because of its properties of persistence, energy-efficient (consumes little power). Spintronics devices deal with the swapping of electron spin, matching of magnetic properties, and different magnetic materials are used for the top and bottom layers as ferromagnetic material. Many materials are compatible with the CMOS processes [1–3].

In the upcoming sections, we discuss the history of MRAM, then MRAM device that includes STT-MRAM, its write and read operation. After that, reliability issues, challenges in MRAM, its future aspects have been discussed.

J. Garg (✉)

Department of Electronics Engineering, Dr. A.P.J. Abdul Kalam Technical University, Lucknow, Uttar Pradesh, India

S. Wairya

Department of Electronics and Communication Engineering, IET, Lucknow, Uttar Pradesh, India

2 Background

In the early 1950s, magnetic memories were used in which magnetic rings as an array form were used to store the information [4]. Later in 1968, dynamic random access memory (DRAM) was introduced that was based on semiconductor technology, and it was also compatible with the electronic components. Due to that, DRAM emerged as standard memory for usage [5]. DRAM has the option of mass manufacturing. The existence of MRAM started to come into the picture in late 1960. MRAM has the advantages of non-volatility, low power consumption [6]. Later in the early 2000s, it was experienced that with the usage of Spintronics to switch the magnetization in MRAM, and it can be a future perspective memory [7–10]. MRAM devices work on the principle of Spintronics. In Spintronics, state of a transistor can be changed by only flipping the spin of electrons. There is no movement of charge (electrons), so there is not any flow of current (I^2R avoidable Power dissipation). Due to that, MRAM has an essential feature of low power [11]. In MRAM, magnetic tunnel junction (MTJ) is also formed that uses a ferromagnetic material. These types of materials have magneto resistance property, which means variable resistance due to magnetization. In MTJ, there are two types of layers one is fixed, and the other is the reference layer. Both layers use ferromagnetic material (Co is mostly used). Different materials can be used for better performance [12].

3 Magneto Resistive Random Access Memory

In the early 1980s, MRAM was promoted. This is the first technology that uses a magnetic element as storage. MRAM works on the principle of magnetoresistance (MR) means it changes its resistance with the change in magnetization means magnetization direction is used to encode a binary value. MRAM cell has two layers—one is the anisotropic magnetoresistive layer, and the other is non-magneto resistive layer. The upper layer (AMR layer) is a ferromagnetic layer, while the bottom one is a permanent magnetic material. In the upper layer, polarity can be changed through polarized current. MR of a single cell is the angle between the path of magnetization and the flow of current in the anisotropic magnetoresistive layer. The higher the value of MR shows the more significant changes in the anisotropic magnetoresistive layer. In the late 1980s, changes in MRAM were proposed with a new concept of GMR [13], PSV [14]. Later, in the 1990s, tunnel magnetoresistance (TMR) was discovered in magnetic tunnel junction (MTJ) materials [15], and after that, MTJ became a vital part of MRAM devices.

The magnetic tunnel junction is the central key element in MRAM (MTJ). In MTJ, there are two layers: one that is free and the other that is reference. Ferromagnetic material is used to create both layers. There is an oxide layer between these two layers for tunnelling purposes. The magnetization of the free layer with respect to the magnetization of the reference layer stores information in a bit type of '0' (low

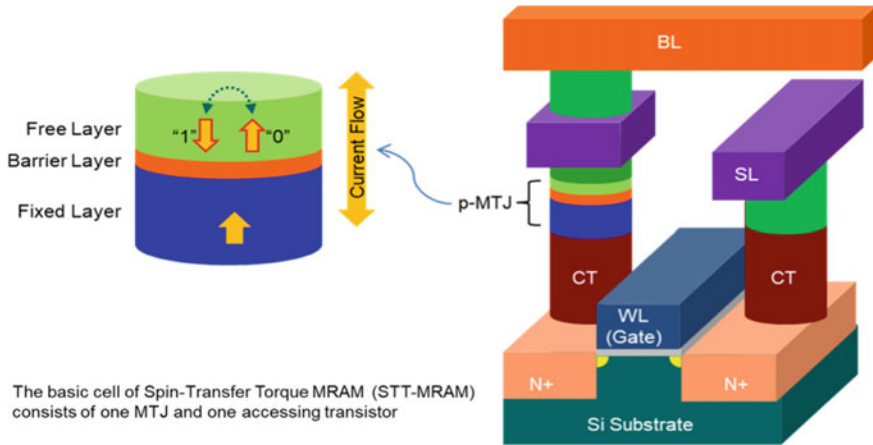


Fig. 1 Representation of magnetic tunnel junction [17]

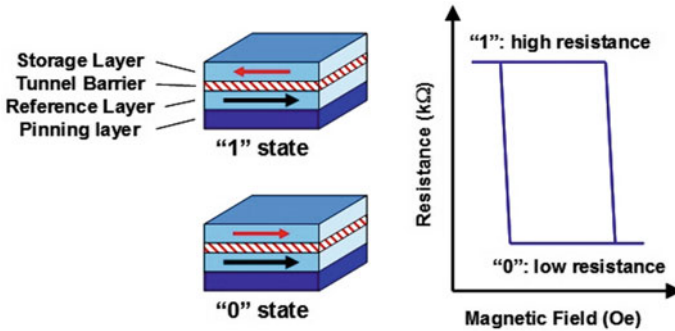


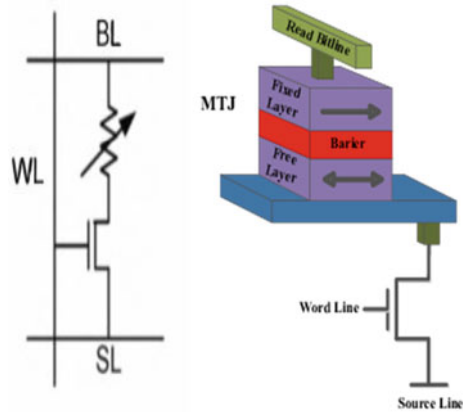
Fig. 2 States of MTJ—'0' low resistance state, '1' high resistance state [18]

resistance state) or '1' (high resistance state). If the magnetic moments of the free layer and the reference layer are in the opposite directions, the MTJ is in a high resistance state, and it is referred to as '1.' The condition of MTJ is called low resistance when the free layer magnetic moment is in the same direction as the reference layer magnetic moment, and it can be read as '0' [16]. The representation of MTJ is shown in Fig. 1, and the low and high resistance states of MTJ are shown in Fig. 2.

3.1 Spin Torque Transfer MRAM (STT-MRAM)

This version of magneto RAM came into existence in late 1996s. In the previous section, MTJ is discussed. It can be inferred that writing current in MTJ is inversely

Fig. 3 Structure of 1T1MTJ model and schematic

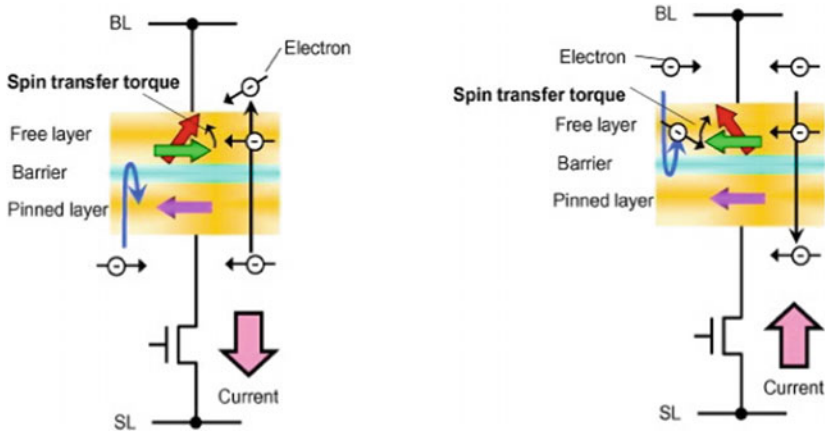


proportional to MTJ size, i.e., as MTJ size decreases, write current increases, and vice versa. To design a small size MTJ, a large amount of current is needed. MRAM's biggest bottleneck was this. STT-MRAM was created in order to solve this problem. The basic structure of STT-MRAM is 1T1MTJ, which has one transistor and one MTJ. Figure 3 depicts the 1T1MTJ [19] concept and schematic.

In the STT mechanism, spin polarization of current is used to change the magnetization, and due to this, required voltage and current can be supplied by minimum no. of transistors. The minimum no. of transistors is a significant advantage in terms of scalability. As per the semiconductor technology roadmap, CMOS logic technology is going to be scaled down in the coming years. Suppose technology scales down, then switching current will increase. This current is the biggest drawback of conventional MRAM, and STT-MRAM is used to avoid this problem. In STT-MRAM, the current is applied vertically through the magnetic tunnel junction, so when scaling of CMOS technology occurs, the area of magnetic tunnel junction decreases, and the total current also decreases [19]. STT-MRAM has better writing methods than earlier ones. In STT-MRAM, two models that are used—(a) iMTJ (b) perpendicular magnetic anisotropy PMA (pMTJ). Compared to iMTJ, pMTJ has a lower switching current because in pMTJs, due to spin torque transfer (STT), the reversal of magnetization occurs and in the same high energy state, thermal radiation takes place and because of that high efficient switching takes place [20].

3.2 Write Current

In memory, there are two crucial operations—read and write. In the previous sections, it is already discussed that write current should be minimum. Many approaches have been used to minimize the write current. One of the oldest methods to store data in memory is using a magnetic field generated by a current-carrying wire [21]. Other



(a) Anti-Parallel (AP) to Parallel(P) Switching

(b) Parallel (P) to Anti-Parallel(AP) Switching

Fig. 4 Electrons flow in STT-MRAM [12]

researches were also done in MRAM, but it was not successful. After that, STT-based switching writes current came into existence; it was also an exciting area of researchers [22]. In the spin torque transfer method, the external magnetic field is not required to change the magnetization state because magnetization is produced with the help of current that is sent in the device [23]. In STT-MRAM, the polarized current is used to write in the cells in that there is the only requirement of state change rather than the electric field. STT magnetization takes place due to the movement of angular momentum and the flow of electrons in the magnetic tunnel junction. Figure 4 shows the movement of electrons from parallel to antiparallel state and vice versa.

3.3 Read Current

The read operation is also a fundamental criterion in memory. The magnetoresistance is one of the critical terms regarding reading operation. In MRAM, low resistance and high resistance difference should be more than 0.2 V for reliable information. A higher value of TMR is essential for reliable read function. This MR effect has risen due to spin-orbit coupling [24]. While doing the scaling of STT-MRAM, the size of the bit and pitch shrink, the width of resistance distribution increases; however, their optimization can be done [25, 26]. Few materials can help to achieve higher MR [27].

4 STT-MRAM Products

Spin torque transfer switching has an attractive solution for scaling. As cell size decreases, writing current also decreases. The iMTJ, as shown in Fig. 5 [28], has the solution for higher writing capacity, due to iMTJ has been used in commercial products, and till now, it is in use.

Tables 1 and 2 compare the feature of conventional memory with the emerging memory [29].

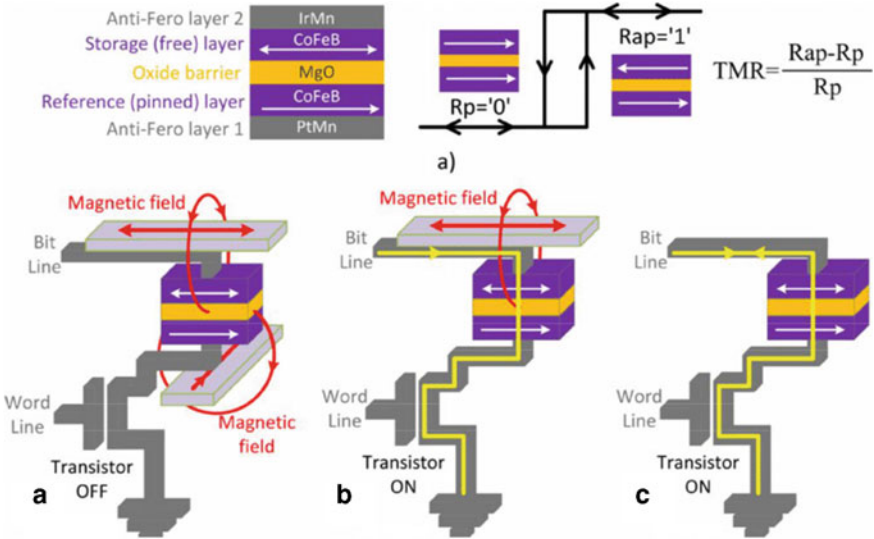


Fig. 5 Three generations of MRAM. a FIMS, b TAS, c STT [28]

Table 1 Features of conventional memory

	DRAM	SRAM	3D NAND flash	eFlash (NOR)	Toggle—MRAM
Non-volatile	No	No	Yes	Yes	Yes
Endurance	Unlimited	Unlimited	10 ³ –10 ⁵	10 ⁴ –10 ⁷	Unlimited
Capacity	Medium	Small–medium	Large	Small	Small
Speed writing	1–10	<1	10 ⁵ –10 ⁶	10 ⁵	1–10
Power consumption	High	Low	Low	Lowest	Low

Table 2 Features of emerging memory

	PCM	ReRAM	FeFET	NRAM (CNT)	STT-RAM
Non-volatile	Yes	Yes	Yes	Yes	Yes
Endurance	10^6 – 10^9	10^5 – 10^9	10^4 – 10^5	10^{15}	10^9 – 10^{12}
Capacity	100 – 10^4	10 – 10^5	10	10	1–100
Speed writing	Medium	Medium	Medium	Medium	Medium
Power consumption	High	Medium	Low	Substantial low	Low

5 Reliability Issues in STT-MRAM

Reliability plays an essential role in memory. Memory devices should show stable behavior in different environments like thermal stability, MTJ stability, write current stability. Two types of errors temper the reliability of STT-MRAM—soft error and hard error. Soft errors are that can be corrected, but it is complicated to correct hard errors. Soft errors are mainly caused by thermal instability, stochastic switching, while hard errors are due to magnetic tunnel junction thickness, TMR ratio [30].

Sometimes in the read operation of STT-MRAM, read current changes the stored data erroneously. So it leads to soft error [30]. Thermal stability leads the data retention. If there is an error due to thermal instability, the orientation of magnetization can change. The value of temperature should be as low as electrons in the free layer should not change their spin. Because of temperature, switching in MTJ takes place randomly. The solution to the above problem is to raise the temperature of MTJ and include the circuits to the design so that errors can be corrected [31].

Magnetic tunnel junction errors lead to hard error. MTJ resistance depends on the oxide layer thickness between ferromagnetic layers. If oxide layer thickness changes slightly, it shows a considerable change in TMR. So this is an important criterion to be considered for the reliability of STT-MRAM [32]. TMR also affects the structure of the cell due to the performance of STT-MRAM is affected. Ferromagnetic materials have the orientation of magnetizations in the plane of the film to evade magnetic poles of the surface. pMTJ has reduced the demagnetized field.

6 Future Aspects of STT-MRAM

In STT-MRAM, write current is low, and size is also small as compared to MRAM. In STT-MRAM, there is no need for current, only the spin of the electron is changed, and it needs very low voltage for reading and writing information. As STT-MRAM has many advantages, it has many future aspects. Many other new technologies have also come into the picture as spin Hall effect (SHE) MRAM, spin-orbit torque (SOT) MRAM, voltage control of magnetic anisotropy (VCMA).

SOT interaction takes place between the heavy metal film and the oxide layer. For heavy metal, we use Pt/W or Ta. Now, MTJ is in direct contact with metal. Due to

this, write current flows directly in heavy metal, not in a magnetic tunnel junction. There is less stress voltage across the magnetic tunnel junction that results in higher endurance [33].

VCMA is an approach that can manipulate the magnetization direction. This approach provides precision control of switching [34].

7 Conclusion

In this paper, Spintronics-based memory has been discussed. Mostly everywhere, MRAM memory is used, but as technology is scaling down and due to that increase of leakage current makes STT-MRAM more critical. STT-MRAM has the properties of non-volatility (NVM), low power, and unlimited endurance, very low write current as there is no movement of charges, and the only spin takes place. Magnetic tunnel junction takes place a vital role in STT-MRAM. MTJ properties can be changed with the use of different materials for ferromagnetic layers. Usually, MgO is used. Write current also has a vital role in the use of STT-MRAM. We have discussed some approaches to write information. The selection of the process of writing information should be appropriate. There are some reliability issues associated with STT-MRAM like thermal instability, TMR stochastically data change. However, these errors can overcome with the help of circuit designing. STT-MRAM has its broad future applications. STT-MRAM can replace all the existing memories if the reliability-related issues could be addressed.

References

1. Zutic I, Fabian J, Sarma SD (2004) Spintronics: fundamentals and applications. *Rev Mod Phys* 323:76
2. Wolf S et al (2001) Spintronics: a spin-based electronics vision for the future science. *Science* 294(5546):1488–1495
3. Wolf S et al (2011) The promise of nanomagnetism and spintronics for future logic and universal memory, vol. 98, no. 12, pp 2155–2168. IEEE Press
4. Williams FC et al (1951) Universal high-speed digital computers: a small-scale experimental machine, vol 98, Issue 61, pp 13–28. IET Press
5. Mittal S (2012) A survey of architectural techniques for dram power management. *Int J High Perform Syst Archit* 4(2):110–119
6. Raffel J, Crowther T (1964) A proposal for an associative memory using magnetic films DTIC document
7. Katine J et al (2000) Current-driven magnetization reversal and spin-wave excitations in Co/Cu/Co pillars. *Phys Rev Lett* 84:3149
8. Kim W et al (2011) Extended scalability of perpendicular STT-MRAM towards sub-20 nm MTJ node. *Electron Devices Meeting (IEDM)*. IEEE
9. Gajek M et al (2012) Spin torque switching of 20 nm magnetic tunnel junctions with perpendicular anisotropy. *Appl Phys Lett* 100:132408
10. Khvalkovskiy A et al (2013) Basic principles of STT-MRAM cell operation in memory arrays. *J Phys D Appl Phys* 46(7):074001

11. Kultursay E et al (2013) Evaluating STT-RAM as an energy-efficient main memory alternative. In: IEEE International symposium on performance analysis of systems and software (ISPASS), pp. 256–267. IEEE Press (2013)
12. Sopaia Li A (2015) Spin transfer torque—RAM devices as a future non volatile memory solution. Corpus ID: 31165598
13. Baibich MN et al (1988) Giant magnetoresistance of (001)Fe/(001) Cr magnetic superlattices Phys. Rev Lett 61(21):2472–2475
14. Chen EY, Tehrani S, Zhu T, Durlam M, Goronkin H (1997) Submicron spin valve magnetoresistive random access memory cell. J Appl Phys 81(8):3992–3994
15. Moodera JS, Kinder LR, Wong TM, Meservey R (1995) Large magnetoresistance at room-temperature in ferromagnetic thin-film tunnel-junctions. Phys Rev Lett 74(16):3273–3276
16. Sumio I, Mancoff FB, Janesky J, Aggarwal S (2020) Magnetoresistive random access memory: present and future. IEEE Trans Electron Dev 67(4)
17. Materion (2015) STT RAM materials. <https://materion.com/-/media/files/advanced-materials-group/me/stt-ram-1-15-final.pdf>. Accessed 22 Sept 2020
18. Thomas GP (2013) Samsung open innovation program for STT-MRAM technology. <https://www.azom.com/>. Accessed 22 Sept 2020
19. Wolf SA et al (2016) Spintronics technology: past, present and future. Int Mater Rev 61(7):456–472
20. Kishi T et al (2008) Low current and fast switching of a perpendicular TMR for high speed and high density spin-transfer-torque MRAM. IEDM Tech Dig 309–312
21. Parkin S et al (1999) Exchange-biased magnetic tunnel junctions and application to nonvolatile magnetic random access memory. J Appl Phys 85(8):5828–5833
22. Parkin S et al (2003) Magnetically engineered spintronic sensors and memory. Proceeding IEEE, vol 91, Issue 5, pp 661–680
23. Yang T et al (2007) Manipulating spin current the magnetic nanopillar. J Nanosci Nanotechnol 7(1):259–264
24. Thomson W (1586) On the electro-dynamic qualities of metals: effect of magnetization on the electric conductivity of nickel and iron: Proc R Soc Lond 8:546–550
25. Lee K et al (2018) 22-nm FD-SOI embedded MRAM technology for low power automotive-grade-1 MCU applications. IEDM Tech Dig 27.1.1–27.1.4
26. Song YJ et al (2018) Demonstration of highly manufacturable STTMRAM embedded in 28 nm logic. In: IEDM Tech Dig 18.2.1–18.2.4
27. Golonzka O et al (2018) MRAM as embedded nonvolatile memory solution for 22FFL finFET technology. IEDM Tech Dig 18.1.1–18.1.4
28. Andre T et al (2013) ST-MRAM fundamentals, challenges, and applications. In: IEEE custom integrated circuits conference (CICC). IEEE Press, USA, Sept 2013, pp 1–8
29. Chen A (2016) A review of emerging non-volatile memory (NVM) technologies and applications. Solid State Electron 125:25–38
30. Zhao WS et al (2012) Failure and reliability analysis of STT-MRAM. J Microelectron Reliab 52(9–10):1848–1852
31. Zhang Y et al (2011) STT-RAM cell design optimization for persistent and non-persistent error rate reduction: a statistical design view. In: International conference on computer-aided design, pp 471–477. IEEE Press, USA
32. Tehrani S et al (2000) Recent developments in magnetic tunnel junction MRAM. IEEE Trans Magn 36:2752–2757
33. Liu L et al (2012) Spin-torque switching with the giant spin Hall effect of tantalum. Science 336(6051):555–558
34. Nozaki T et al (2019) Recent progress in the voltage-controlled magnetic anisotropy effect and the challenges faced in developing voltage-torque MRAM. J Micromach 10(5):327

Designing and Analysis of Dynamic Model for Robotic Manipulator



Aditi Saxena , Jitendra Kumar, Kamal Sharma, and Debanik Roy

1 Introduction

Robotics is very much needed in industrial world; there are various factors which vouch for the need of robotics. Skilled labor shortage is also one of the main factors as it is very tough for human to learn and perform certain works with perfect accuracy in comparison with a robot. Second factor is improved quality product; the products that are being manufactured by machines like robot have very high quality which is impossible to achieve by a human. Third factor is competition which is present in market; there is a huge amount of pressure to increase production rates, and to fulfill this demand, robotics is very necessary. Fourth factor is less preparation time and increased productivity; with the help of a robot, we can manufacture products in large quantity with lesser period of time and also with high quality; the waste produced after production with the help of robots is very less and we could achieve lower rejects and less waste than labor intensive production. In past few years, robots have started working with real-life applications and also provide a ease to human being. Robotics itself is an interdisciplinary branch which involves many different technical topics like designing, modeling, innovation, programming and robotics has itself a wide range of application in almost every field; for example production, painting, welding, pick and place, underwater robots are also widely using. Nowadays, even in medical field robots are now being used as a replacement of care-taking staff in hospitals. In almost every aspect of real life we are using robotics. The term robot is basically a Czech word which means slaved laborer, and it came into existence in 1920. Robot basically acts like a machine and is controlled by a controller; in a robot, human body parts are being replicated especially three H: human hand, heart, and head; this human hand in terms of robotics is known as a robotic manipulator. We can move, grip things with the help of it; we could operate it through various

A. Saxena (✉) · J. Kumar · K. Sharma · D. Roy
IET Department of Electronics and Communication Engineering, GLA University, Mathura
281406, India

programmed motions as it is programmable as well as multifunctional device [1]. Robotics itself is a combination of two branches [2, 3], that is electronics through the field of control and mechanical through the field of manufacturing, designing and kinematics which help in positioning, and orientation of the manipulator devices having multidegree freedom can be positioned with the help of these manipulator, we require high and improved control strategies to achieve accuracy in the trajectory tracking of the manipulator, dynamic model of a robotic manipulator also plays a very important role and it is responsible for the performance of a robotic manipulator, we need to design an accurate mathematical model and after this we need to apply various control strategies to get precise trajectory tracking [4]. For industry purpose, the manipulators that are being used are highly nonlinear and coupled, second-order nonlinear differential equation is being used to design mathematical model [5]. As the number of links increased, complexity also increased; the position and velocity of the manipulator are being controlled using a separate control system and thus it became a challenging task for control engineers to control such manipulator system [6], especially after designing a dynamic model it is very tough to attach a precise and powerful controller to the plant which could deal with nonlinearities and uncertainties, and then to make it adaptable, we need to perform optimization in today's scenario as the world is moving toward automation so we should be very careful while choosing the tuning algorithm. There are many tuning that are present today for optimization like cuckoo search algorithm (CSA), PSO, optimization method of ant colony, genetic algorithm; here we have used genetic algorithm for optimization.

2 Literature Review

Because most practical systems are nonlinear and dynamic in design, it is a difficult task for control engineers to control rigid robotic manipulators with multiple connections and payloads. In today's production industry scenario, the use of artificial intelligence with classical control techniques is helpful for efficient operation. In order to control the nonlinear complexities in this job, tuned fuzzy PID controller is used to control the two-link manipulator that controller can also perform well for monitoring the trajectories..

Sharma et al. conducted several tests on robustness, uncertainties, noise rejection in [7] and as a result found that the fractional order fuzzy PID controller is better among the remaining four controllers. Implementation of fractional order fuzzy PID controller (FOFPID) and for tuning CSA is being used, she also concluded that PID controller was performing better for LINK 1 in comparison with FPID in the presence of noise, and on the contrary, FPID has contributed a lot in achieving perfect trajectory tracking for the two-link manipulator.

A fractional order Fuzzy P + Fuzzy I + Fuzzy D was investigated in [8], Kumar et al., which demonstrates the nonlinear and uncertain system's self-tuning function. And as a result, a comparative analysis of Fuzzy p + Fuzzy I + Fuzzy D was also conducted. Fractional order Fuzzy p + Fuzzy I + Fuzzy D was found to be superior

in all performance parameters compared to basic Fuzzy P + Fuzzy I + Fuzzy D controller. Genetic algorithm is being used for optimization and the controllers are also being evaluated for regulatory and servo problems by taking all aspects.

In [9], for the two-link manipulator system, V. Kumar investigated nonlinear adaptive fractional order fuzzy PID, finding that fractional order has enhanced architecture flexibility and trajectory monitoring has also improved with this controller. The main aim for which this controller is being designed is to control nonlinear system. This industrial environment is being created by injecting disturbances and as a result found that this controller was robust in handling all the nonlinearities adaptively.

In [10], Kumar et al. have proposed fractional order fuzzy PD + I to control an electrically driven robotic manipulator to step and sinusoidal signal are being inserted at the output of the controller; its robustness can be tested for the analysis of uncertainty; the mass and length of the links are being increased by some factor. And after all simulation results the above proposed controller found superior among the rest.

In [11], Weile et al have applied genetic algorithm optimization to electromagnetics because GA can easily optimize multimodal problems; they show excellent results in electromagnetic device design.

In [12], Kong et al., for normal parameter reduction in soft set, the used particle swarm optimization algorithm (PSO) saves the optimization time as it gives optimized result in a very short period of time and also efficiency has been increased; dispensable core-related normal parameters reduction is being done using PSO, and the reduction of these parameters is being carried out very fastly.

In [13], Ghanbari et al. used fuzzy control and ant colony optimization; this algorithm provides flexibility, adaptability, and a very fast response. This algorithm also helps in improving the accuracy and stability in the outcomes.

In [14], Jagatheesan et al. design a PID controller for an automatic generation. The three gains, that are proportional gain, controller gain, derivative gain, are tuned by firefly; this algorithm provides less settling time and less overshoot with more number of iterations; the performance of this algorithm is being increased but on the contrary the settling time is also increased.

In [15], Yang et al. used cuckoo search algorithm and then compared the result with the rest of the algorithm like GA and PSO; as a result observed that parameters are being finely tuned by CSA; it can also help to solve NP problems and the combination of cuckoo with other algorithm can also be very fruitful.

In [16], Yang et al. used the help of the echolocation effects of bats by using bat algorithm found better in comparison with other algorithms.

In [17], Ohtani et al. have used the concept of sliding mode the with the help of fuzzy controller to control the manipulator; this method acts as a learning method.

In [18], A. Hazzab has proposed a hybrid fuzzy controller and a traditional PI controller and the combination provides it with FLC-PI controller as a result overshoot was completely removed rise time was minimum disturbance rejection was also very best.

In [19], Sharma et al. have proposed fuzzy logic combination with fractional order PID and also inserted switching-based scheme; this controller has the advantage of flexibility with fuzzy controller.

In [20], Lin gave equations that are mathematical and can be used for designing a dynamic model.

In [21], George Thuruthel, Thomas et al. have described the various control strategies that we can use for soft robotic manipulator by writing a review paper. In [22], Zhang et al. have used adaptive neural control for controlling of robotic manipulators.

In [23], Bing et al. have done work in tracking the control of robotic manipulator having uncertain kinematics and dynamics. In [24], Khairudin et al. have done research on how to control flexible robotic manipulator as it is tough to control flexible robotic manipulator in comparison with rigid robotic manipulator. In [25], Rus et al. have done research on designing fabricating and controlling of soft robot; these robots are designed by soft material and also provides us with flexibility. In [26], Good et al. have designed a controller for integrated robot and drive system. In [27], Gravagne et al. have done analysis on planar continuum robot. In [28], Xiao has used neural network for controlling robotic manipulator. In [29], Islam et al. have compared the control strategies on multi-degree of freedom robotic manipulator. In [30], Yanga et al. have used a PDE model for observing the design for a flexible link manipulator. In [31], Wu et al. have done dynamic modeling on design and optimization of spherical parallel manipulator. In [32], Sun et al. have used fuzzy neural network for controlling a flexible robotic manipulator. In [33], Mohammed et al. have used advance control techniques for trajectory tracking. In [34], Ajwad et al. have designed a controller for multi-degree of freedom manipulator. In [35], Noohoji et al. have designed constrained neural adaptive PID control. In [36], Shabana et al. have done analysis on dynamics of multibody system. In [37], Ardeshiri et al. have implemented fuzzy logic and fractional order PID collaboration.

3 Dynamical Model for Two-Link Manipulator

By the help of the equations given below, a dynamic model has been developed (Table 1; Fig. 1)

$$\begin{bmatrix} S_{11} & S_{12} \\ S_{21} & S_{22} \end{bmatrix} \begin{bmatrix} \ddot{\theta}_{11} \\ \ddot{\theta}_{22} \end{bmatrix} + \begin{bmatrix} P_{11} \\ P_{21} \end{bmatrix} + \begin{bmatrix} f_{r1} \\ f_{r2} \end{bmatrix} + \begin{bmatrix} fn_{1p} \\ fn_{2p} \end{bmatrix} = \begin{bmatrix} \tau f_{1p} \\ \tau f_{2p} \end{bmatrix} \tag{1}$$

where

$$\begin{aligned} S_{11} = & I_{1p} + I_{2p} + m_{11}l_{c1}^2 + m_{22}l_{c2}^2 + 2m_{22}l_{11}l_{c2} \cos \theta_{22} \\ & + m_v pl_{11}^2 + m_v pl_{22}^2 + 2m_v pl_{11}l_{22} \cos \theta_{22} \end{aligned} \tag{2}$$

$$S_{12} = I_{2p} + m_{22}l_{c2}^2 + m_{22}l_{11}l_{c2} \cos \theta_{22} + m_{vp}l_{22}^2 + m_{vp}l_{11}l_{c2} \cos \theta_{22} \tag{3}$$

Table 1 Representing the value of specific parameters

Parameters for link 1	Values for link 1	Parameters for link 2	Values for link 2
m_{11}	0.392924 kg	m_{22}	0.094403 kg
l_{c1}	0.104648 m	l_{c2}	0.081788 m
l_{11}	0.2032 m	l_{22}	0.1524 m
I_{1P}	0.0011411 kg m ²	I_{2P}	0.0020247 kg m ²
b_{1vp}	0.141231 N-m/radian/s	b_{2vp}	0.3530776 N-m/radian/s
m_{vp}	0.56699 kg		
g	9.81 m		

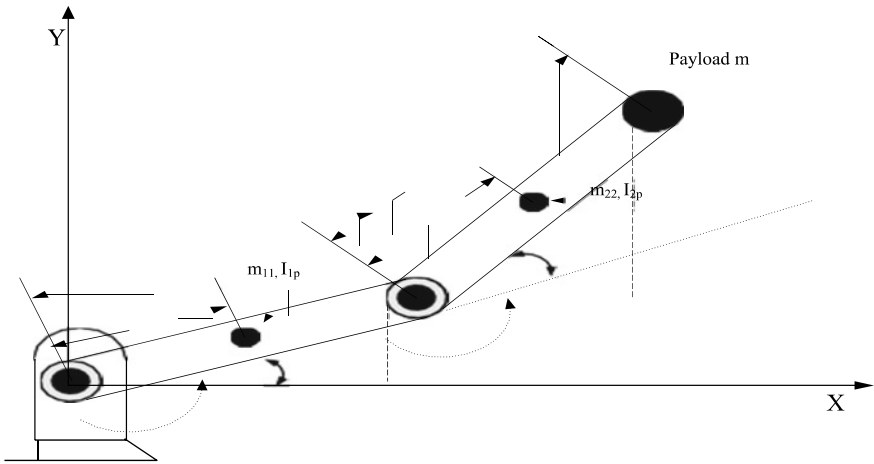


Fig. 1 Two-link manipulator diagram

$$S_{21} = S_{12} \tag{4}$$

$$S_{22} = I_{2P} + m_{22}l_{c2}^2 + m_{vp}l_{22}^2 \tag{5}$$

$$P_{11} = -m_{22}l_{11}l_{c2}(2\theta_{11} + \theta_{22})\theta_{22}\sin\theta_{22} - m_{vp}l_{11}l_{22}(2\theta_{11} + \theta_{22})\theta_{22}\sin\theta_{22} \tag{6}$$

$$P_{21} = m_{22}l_{11}\theta_{11}^2l_{c2}\sin\theta_{22} + m_{vp}l_{11}\theta_{11}^2l_2\sin\theta_{22} \tag{7}$$

$$f_{r1} = b_{1vp}\dot{\theta}_{11} \tag{8}$$

$$f_{r2} = b_{2vp}\dot{\theta}_{22} \tag{9}$$

$$f_{n1p} = m_{11}l_{c1}g \cos \theta_{11} + m_{22}g(l_{c2} \cos(\theta_{11} + \theta_{22}) + l_{11} \cos \theta_{11} + m_{vp}g(l_{22} \cos(\theta_{11} + \theta_{22}) + l_{11} \cos \theta_{11} \tag{10}$$

$$f_{n2p} = m_{22}l_{c2}g \cos(\theta_{11} + \theta_{22}) + m_{vp}l_2g \cos(\theta_{11} + \theta_{22}) \tag{11}$$

Final equations

$$\ddot{\theta}_{11} = \frac{\tau f_{1p} - f_{n1p} - f_{r1} - P_{11} - S_{12} * \theta_{22}}{S_{11}} \tag{12}$$

$$\ddot{\theta}_{22} = \frac{(\tau f_{2p} - f_{n2p} - f_{r2} - P_{21} - S_{12} * \theta_{11})}{S_{22}} \tag{13}$$

4 Dynamical Manipulator Model Deigning in Simulink

For designing this dynamic model, the software which we are seeking for help is MATLAB/Simulink as this software has large library by the help of which we can design the dynamic model; its library has small blocks of adder/subtractor/and many more operators. Firstly, we have to simplify the equations and arrange these equation in terms of theta and hence we obtained two final equations in the form of theta after getting those an individual dynamic model of each block has been made (Figs. 2, 3, and 4).

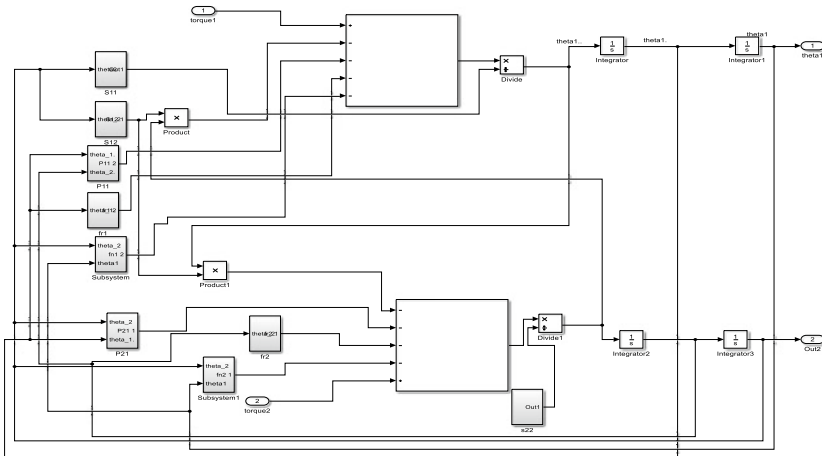


Fig. 2 Dynamic model design in Simulink

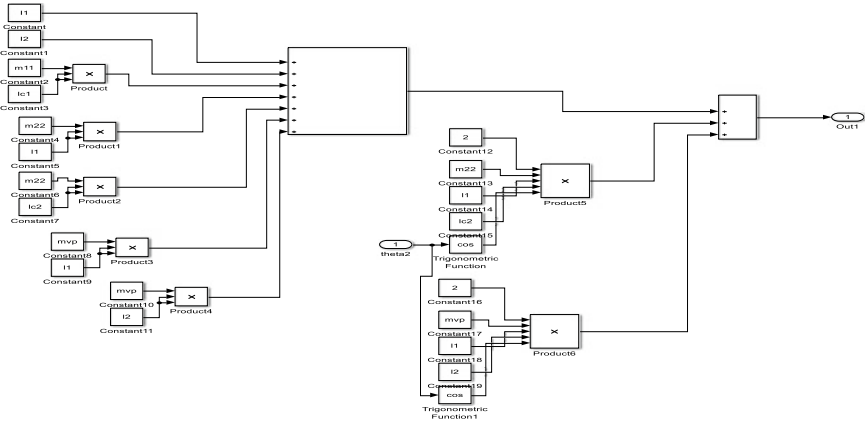
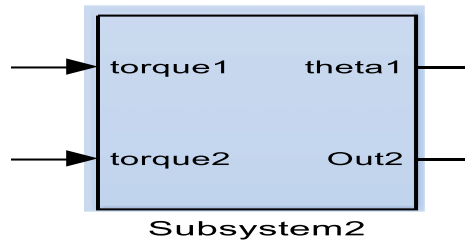


Fig. 3 Dynamic model subsystem structure

Fig. 4 Subsystem of the whole dynamic model



5 Conclusion

In this article, we studied the formulation and mathematics involved in the creation of the dynamic robotic manipulator model; we also understand the kinematics inverse kinematics, the manipulator’s orientation and positioning after extensively studying it, the dynamic model of two-link rigid robotic manipulator on Simulink was developed to handle this dynamic model.

References

1. Spong, MW, Vidyasagar M (2004) Robot dynamics and control, 2nd edn. Wiley, Hoboken
2. Gopal M (2009) Digital control and state variable methods, 3rd edn. Tata McGraw Hill, New York
3. Manseur R (2007) Robot modeling and kinematics. Firewall Media, pp 96–100
4. Spong MW, Hutchinson S, Vidyasagar M, Robot modeling and control, 1st edn. Wiley, Hoboken
5. Loudini M (2013) Modeling and intelligence control of an elastic link robot manipulator. Int J Adv Robot Syst 10:1–18

6. Amer AF, Sallam EA, Elawady WM (2011) Adaptive fuzzy sliding mode control using supervisory fuzzy control for 3 DOF planer Robot manipulators. *Appl Soft Compt* 11:4943–4953
7. Sharma R, Rana KPS, Kumar V (2019) Performance analysis of fractional order fuzzy PID controllers applied to a robotic manipulator. *Exp Syst Appl* 73(9):4274–4289
8. Kumar V, Rana KPS, Mishra JK, Nair SS (2017) A robust fractional order fuzzy P + fuzzy I + fuzzy D controller for nonlinear and uncertain system. *Int J Autom Comput* 14(4):474–488
9. Kumar V, Rana KPS (2017) Nonlinear adaptive fractional order fuzzy PID control of a 2-link planar rigid manipulator with payload. *J Franklin Inst* 354(2):993–1022
10. Kumar J, Kumar V, Rana KPS (2018) A fractional order fuzzy PD+I controller for three link electrically driven rigid robotic manipulator system. *J Intel Fuzzy Syst* 35(5):5287–5299
11. Weile DS, Michielssen E (1997) Genetic algorithm optimization applied to electromagnetics: a review. *IEEE Trans Anten Propag* 45(3); Chuan CI, Jeng-Rern Y (2010) 2–13 GHz broadband CMOS low voltage mixer with active balun designed for UWB systems. In: IEEE international conference on electron devices and solid-state circuits, pp 1–4, 15–17 Dec 2010
12. Kong Z, Wenhua J, Guodong Z, Lifu W (2015) Normal parameter reduction in soft set based on particle swarm optimization algorithm. *Appl Math Model* 39(16)
13. Ghanbari A, Kazemi SMR, Mehmanpazir F, Nakhostin (MM) A cooperative ant colony optimization-genetic algorithm approach for construction of energy demand forecasting knowledge based expert systems. *Knowl Based Syst* 39(2013)
14. Jagatheesan K, Anand B, Samanta S, Dey N, Ashour AS, Balas VE (2019) Design of a proportional-integral-derivative controller for an automatic generation control of multi-area power thermal systems using firefly algorithm. *IEEE/CAA J Autom Sinica* 6(2)
15. Yang XS, Deb S (2009) Cuckoo search via Lévy flights. In: Proceedings world congress on nature & biologically inspired computing, India. 978-1-4244-5053-4
16. Yang XS, Gandomi AH (2012) Bat-algorithm: a novel approach for global engineering optimization. *Eng Comput* 29(5):464–483
17. Ohtani Y, Yoshimura T (1996) Fuzzy control of a manipulator using the concept of sliding mode. *Int J Syst Sci* 27(2):179–186
18. Hazzab A, Bousserhane IK, Zerbo M, Sicard P (2006) Real-time implementation of fuzzy gain scheduling of PI controller for induction motor machine control. *Neural Process Lett* 24:203–215
19. Sharma R, Bhasin S, Gaur P, Joshi D (2019) A switching-based collaborative fractional order fuzzy logic controllers for robotic manipulators. *Appl Math Model* 73:228–246
20. Lin F (2007) Robust control design: an optimal control approach. Wiley, England
21. Thuruthel TG et al (2018) Control strategies for soft robotic manipulators: a survey. *Soft Rob* 5(2):149–163.
22. Zhang S et al (2018) Adaptive neural control for robotic manipulators with output constraints and uncertainties. *IEEE Trans Neural Netw Learn Syst* 29(11):5554–5564
23. Xiao B, Yin S, Kaynak O (2016) Tracking control of robotic manipulators with uncertain kinematics and dynamics. *IEEE Trans Industr Electron* 63(10):6439–6449
24. Khairudin M, Mohamed Z, Husain AR (2011) Dynamic model and robust control of flexible link robot manipulator. *Telkonnika* 9(2):279
25. Rus D, Tolley MT (2015) Design, fabrication and control of soft robots. *Nature* 521(7553):467–475
26. Good MC, Sweet LM, Strobel KL (1985) Dynamic models for control system design of integrated robot and drive systems 53–59
27. Gravagne IA, Rahn CD, Walker ID (2003) Large deflection dynamics and control for planar continuum robots. *IEEE/ASME Trans Mechatron* 8(2):299–307
28. Xiao L et al (2018) Design, verification and robotic application of a novel recurrent neural network for computing dynamic Sylvester equation. *Neural Netw* 105:185–196
29. ul Islam R, Iqbal J, Khan Q (2014) Design and comparison of two control strategies for multi-DOF articulated robotic arm manipulator. *J Control Eng Appl Inform* 16(2):28–39
30. Yang H, Liu J, Lan Xu (2015) Observer design for a flexible-link manipulator with PDE model. *J Sound Vib* 341:237–245

31. Wu G et al (2014) Dynamic modeling and design optimization of a 3-DOF spherical parallel manipulator. *Rob Auton Syst* 62(10):1377–1386
32. Sun C et al (2018) Fuzzy neural network control of a flexible robotic manipulator using assumed mode method. *IEEE Trans Neural Netw Learn Syst* 29(11):5214–5227
33. Mohammed RH et al (2018) Trajectory tracking control and robustness analysis of a robotic manipulator using advanced control techniques. *Int J Eng Manuf (IJEM)* 8(6):42–54
34. Ajwad SA et al (2018) Optimal and robust control of multi DOF robotic manipulator: design and hardware realization. *Cybern Syst* 49(1):77–93
35. Nohooji HR (2020) Constrained neural adaptive PID control for robot manipulators. *J Franklin Inst*
36. Shabana A (2020) Dynamics of multibody systems. Cambridge University Press, Cambridge
37. Ardeshiri RR et al (2020) Robotic manipulator control based on an optimal fractional-order fuzzy PID approach: SiL real-time simulation. *Soft Comput* 24(5):3849–3860

Design and Implementation of Energy Efficiency Augmentation Using Renewable Energy Source for Small-Scaled Residential Micro-grid



Ikbal Ali and Swati Sharma

1 Introduction

Nowadays, renewable energy sources are the chronic technical advance which has caused a significant decline in the price of electrical generating system. The handiness of the technology has helped in obtaining the best efficiency in small-scaled generating stations. The discharge of the electricity market has endorsed the combination of the distributed generation (DG). The non-renewable sources such as fossil fuels, natural gas, coal and nuclear energy are not sufficient to bump into supply needs. Thus, renewable energy sources such as solar, wind, tidal and wave energy come in light to fulfil the supply needs of distribution grid [1]. The scientific advancement, policies and the motivation to report the climatic changes have retained renewable at the key centre of the universal energy revolution [2]. For electric power DG, the renewable energy source has taken an elementary state. The solar energy plays a crucial role in improving the efficiency of the grids. The integration of renewable energy sources restores electrical distribution networks and provides various remuneration and opportunity. For protection, control and operation of the electrical networks bring new challenges due to integration of the renewable energy sources [3]. The most important challenge, the renewable DG systems faces at the time of the integration are intermittent power generation, i.e. weather conditions. The Indian Department of Energy such as PGCIL and power grid defines micro-grid a set of organized loads and DER's which defines the electrical limitations that act as the particular unit with respect to the grid. A micro-grid operates in both grid connected mode and islanding mode and disconnect from the grid as per the requirement. Some organizations define micro-grid as the point of common coupling (PCC) of distributed generation and various controllable loads [4]. In India, the generation of electricity through coal-based generation, hydro-based generation, solar generation and wind generation is described in Fig. 1.

I. Ali · S. Sharma (✉)

Faculty of Engineering and Technology, Jamia Millia Islamia, New Delhi, India

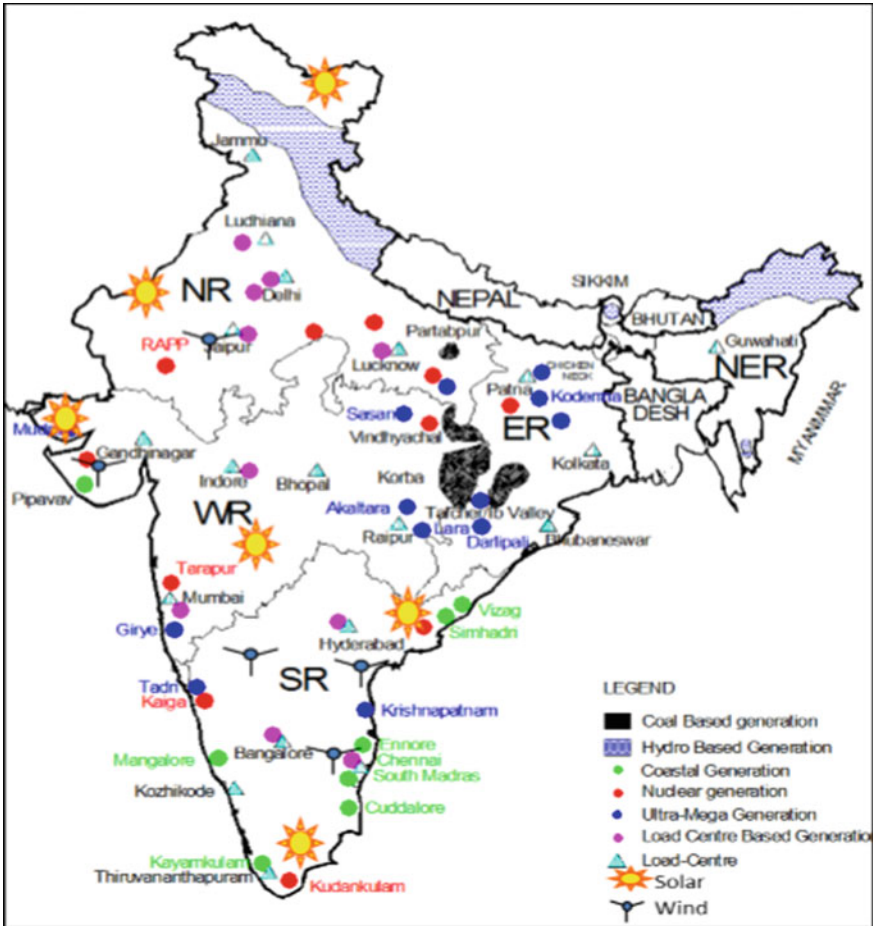


Fig. 1 Distribution of electricity all over India through solar

According to the above-mentioned description, a micro-grid has two operations: grid connected and islanding. In grid connected mode, the main network to a low or medium voltage level is connected through PCC [5]. In islanding mode, the micro-grid works devoid of any interconnection of leading grid. The grids are controlled on the basis of the three hierarchical levels: primary, secondary, and the tertiary control levels. Thus, control levels help in energy management within a micro-grid. Nowadays, the renewable energy sources play a crucial role in managing the micro-grids, and it is the topic which is widely dealt in the world. This work focuses on recuperating the energy efficiency of the micro-grid with the help of renewable energy source, i.e. solar energy. The model explains the phasor solution in order to accelerate the simulation speed. The work completely works on the tertiary control

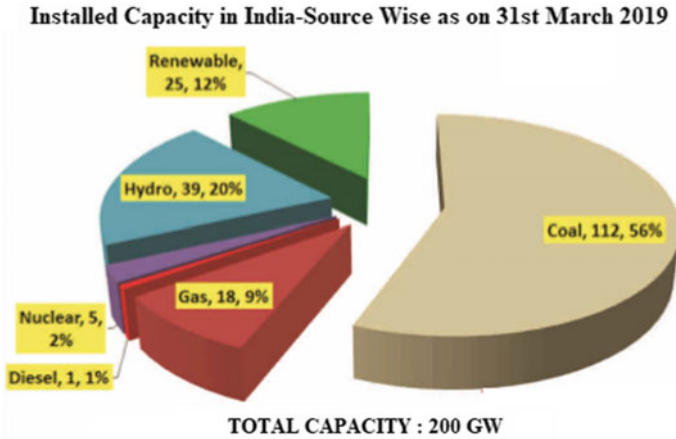


Fig. 2 The share of different types of general capacity (source CEA monthly review of power sector, March 2019)

level. Figure 2 explains about share of varied types of common capacity (SourceCEA monthly review of power sector, March 2019).

The tertiary control level in grid connected mode explains about power flow between micro-grid to the central grid. For this purpose, the power flow and the energy efficiency within the grid is improved. In context of tertiary control, the energy efficiency within the micro-grid is improved [6–9].

Other work focussed on several micro-grid is focussed on the coordination of micro-grids using optimization-based scheduling strategies, mixed integer linear programming, lyapunov programming and algorithms such as particle swarm optimization, ant-colony optimization technique, PID and MPC [10].

In this work, the model of small-scaled micro-grid for residential area is based on improving the energy efficiency of the micro-grid using renewable energy source, i.e. solar energy. The micro-grid was formed by solar panels, battery controllers, power grid, three ordinary houses and battery. The model is formulated in such a way that maximum generation will help in reducing the number of losses, and energy will be distributed as per the load. They are simulated through the simulation toolbox in MATLAB®. The performance of the micro-grid is tested using real data from the Power Grid India Limited.

This paper comprises four sections: Sect. 2 micro-grid components, Sect. 3 operation strategy and modelling of small-scaled micro-grid, Sect. 4 results and discussion and Sect. 5 conclusions followed with acknowledgement and references.

2 Micro-grid Components

Micro-grid components comprise of a power network of single phase AC, storage battery, pole mounted transformer, solar panel and battery controllers.

2.1 Power Grid

Power grid is the composition of three phase source, three phase transformer, three series RLC load and voltage measurement mask. The three phase source has following values: Voltage—66,000 kV, Frequency—50 Hz, Transformation ratio—7, Bus-type—PV, Q_{\min} — $(-\infty)$ and Q_{\max} — $(+\infty)$. The three phase transformer consists of $L_m = 500$ and $R_m = 500$. The RLC load has following data: Nominal Voltage—1000, Nominal Frequency—50 Hz, Active Power—10,000, Inductive Power—100, and Capacitive Power—100.

2.2 Pole Mounted Transformer

The pole mounted transformer having Primary Voltage—6.6 kV and Secondary Voltage—200 V which decreases voltage from 6.6 KV to 200 V.

2.3 Battery Storage

The battery storage has 150 V, 13 Ah. Battery controller controls the storage of the battery. If there is power shortage in micro-grid, it supplies insufficient power; otherwise, it absorbs surplus power in the micro-grid.

2.4 Solar Panel

The renewable energy source which helps in solar generation with the help of solar panel, i.e. maximum 5 KW generation. The single phase AC converts DC power sources in battery storage and generates solar power. It is assumed in control scheme that the micro-grid does not depend on the system for power consumption. For solar power generation, the required power is provided to the system.

2.5 Ordinary Houses

The ordinary houses consume maximum power, i.e. 2.5 KW as electric loads.

3 Operation Strategy and Modelling of Small-Scaled Micro-grid

In most parts of Indian districts, efficiency tests and the electricity prices have been executed. To maximize, the energy efficiency of the system by solar energy is based on the peak shaving strategy and minimizing energy loss. Battery controllers have been used for reducing the consumption of electricity and estimating the lower electricity cost.

3.1 Scenario 1: Analysis of On-Grid Installed Capacity of Solar Energy

Out of some districts of India, the total amount of solar energy installed capacity was 941 MW till March 2012. Later, it was improved to 4995 MW till March 2017. Similarly, the modelling of small-scaled micro-grid for three ordinary houses works on the transmission of solar energy. As 13th plan of the government, the generation of solar energy till 2022 will be 20,000 MW, and the total capacity at the end of the 13th plan will be 72,400 MW from other renewable sources as shown in Table 1 [7, 11].

Table 1 Renewable capacity addition programme (MNRE)

Resource	12th plan projection for RE addition	Total projected capacity by end of 12th plan (2017)	13th plan projection for RE addition	Total projected capacity by end of 13th plan (2022)
Wind power	11,200	27,300	11,200	38,500
Small hydro power	1600	5000	1600	6600
Biomass	500	1525	1000	2525
Bagasse cogen	1400	3216	700	3916
Waste to energy	200	324	500	824
<i>Solar power</i>	<i>3800</i>	<i>4000</i>	<i>16,000</i>	<i>20,000</i>
Total	18,700	41,400	31,000	72,400

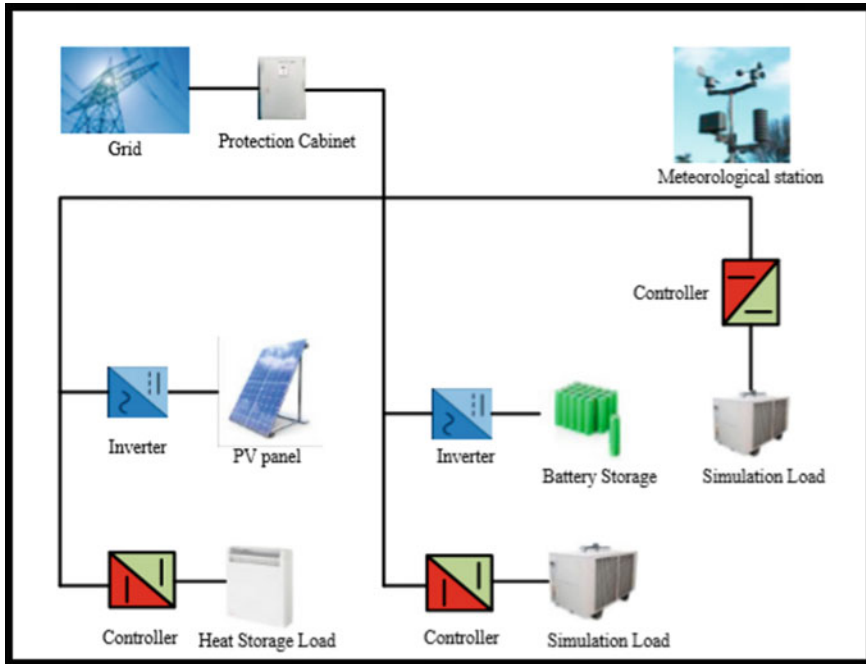


Fig. 3 Layout of small-scaled micro-grid systems

3.2 Scenario 2: Modelling of the Small-Scaled Micro-grid

The small-scaled micro-grid acts as a single phase A.C power network (200 V). The solar power generated by the system is about 5 kW. The battery controller controls storage battery and surplus power absorbed by the system. If the surplus power so absorbed is unsatisfactory, then the power will directly transfer to the micro-grid. The micro-grid is connected with the pole mounted transformer voltage source (66 kV) of three phase alternating current which is connected primary side of the transformer (66 kV) to the secondary side of the transformer 6.6 kV (when voltage decreases). But it changes the voltage 6.6–200 kV from primary to the secondary side. Thus, the power is provided by solar power generation. Figure 3 explains the schematic layout of small-scaled micro-grid systems.

4 Results and Discussion

The results according to small-scaled micro-grid for residential load determine that the battery controller controls the battery storage for 00–08 h and the current traced by the battery controller which is set to zero(0), so that the active power start flowing from the secondary side of the pole transformer. Figure 4 determines the battery storage

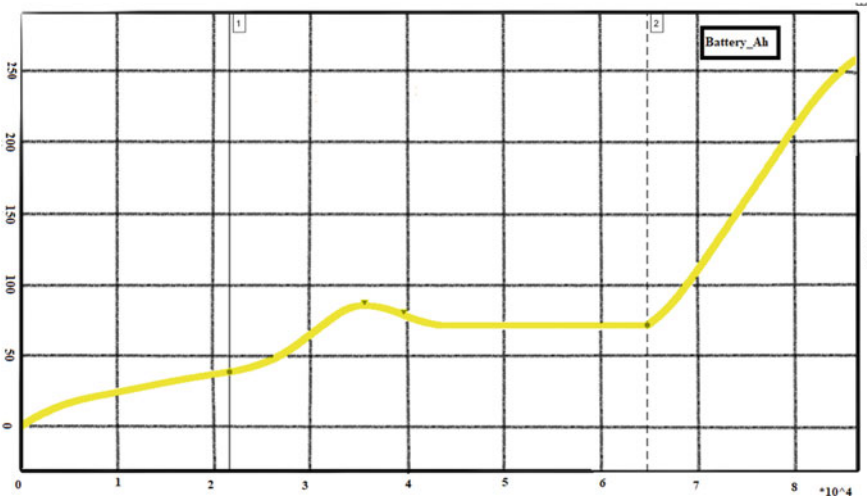


Fig. 4 Operational battery storage curve for battery management system

data for three ordinary houses through solar energy generation. Figure 5 determines Haryana typical solar energy generation month wise from January 2018 to December 2018. Figure 6 determines the small-scaled micro-grid solar Power_PV variations, Power_secondary, Power_Load, Power_battery, state of charge (SOC) and total no. of hours. The state of charge determines the amount of charge stored in the battery after solar energy generation for the three ordinary houses, so that there will be better energy efficiency and low losses. Figure 7 determines the solar energy voltage and current output of three ordinary houses. Table 2 shows the data FY 2017–2018 solar energy-based capacity addition Programme (Fig. 8).

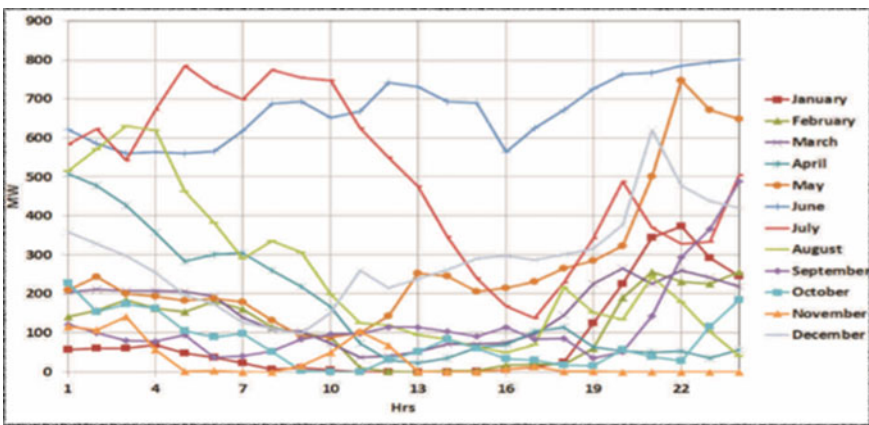


Fig. 5 Haryana typical solar generation pattern month wise (source POSOCO-PGCIL)

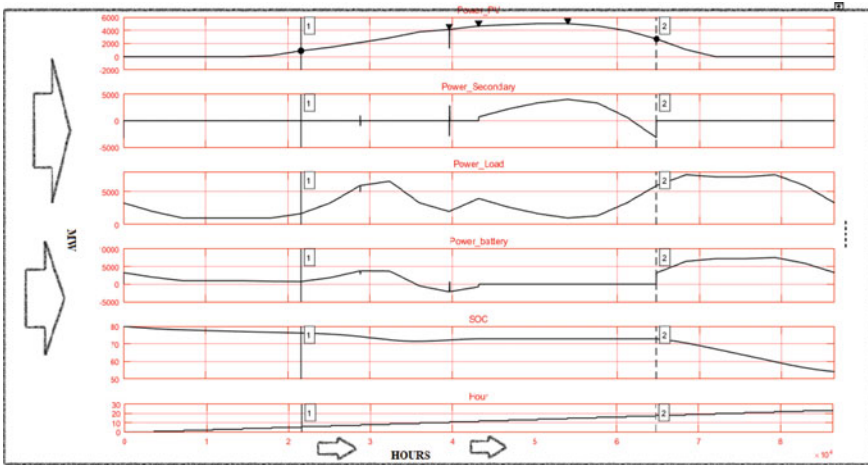


Fig. 6 PV power efficiency w.r.t. the time

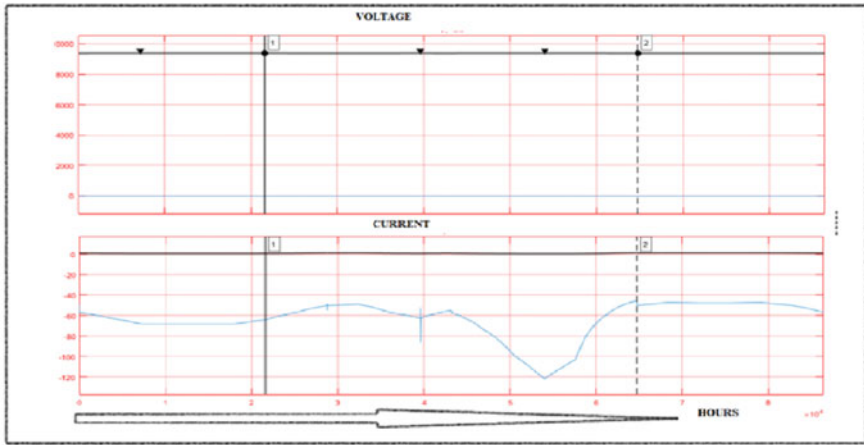


Fig. 7 Voltage and the current value of the solar PV panel per hour for three ordinary houses

Table 2 Solar-based capacity addition Programme

State/year	2015–2016	2016–2017	2017–2018
Haryana	350	300	405
Delhi (NCT)	125	150	200
J&K	1	101	0
Rajasthan	500	1000	900
Total	976	1551	1505

Source Powergrid

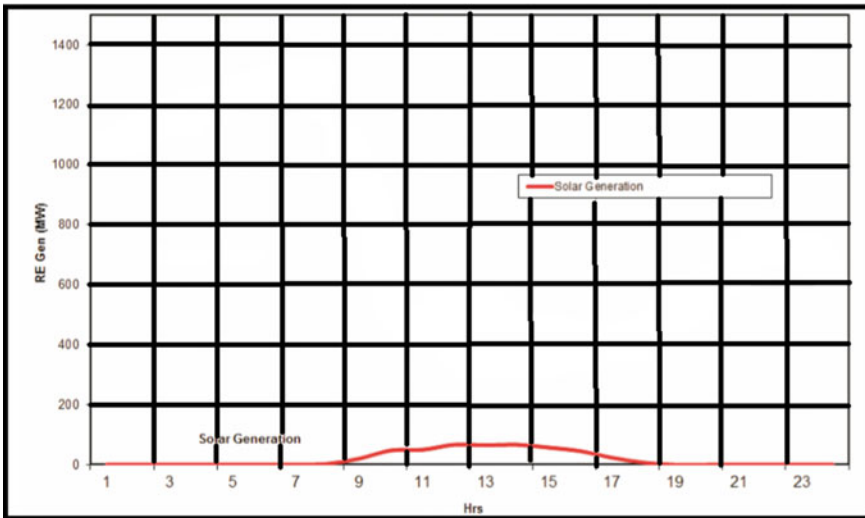


Fig. 8 Solar generation pattern of Haryana Dec’ 2017 (source GETCO/Haryana Power grid)

5 Conclusions

Micro-grid has the ability to provide energy efficiency improvement for residential or regional buildings by profile matching. In this paper, the battery controller controls the battery storage and the amount of solar energy generation. Battery control tracks the current such that the active power of pole transformer is set to zero. Thus, the number of losses will be minimized by keeping battery storage state of charge (SOC) constant such that the efficiency of the system improves. The maximum amount of solar energy is stored in day time and the low price of the electricity at night. The phasor measurement in steady-state condition and initial condition has been calculated for three bus types. The battery management system has peak-to-peak value, i.e. $2.583e + 02$; Rise time: 15.199 ks; Slew rate: 9.654 (/ks). The value of peak-to-peak values of power_PV so obtained is $5.029e + 03$; Rise time: 22.385 ks; Slew rate: 177.923 (/ks); fall time: 11.832 ks; slew rate: $-336.614 (/ks)$ and voltage peak-to-peak value is $1.698e-01$; fall time: 2.959 ks; slew rate: $-23.408(/Ms)$. The real data provided by power grid for the consumption and generation of solar energy in the area of Haryana has been shown. The integral part of the future includes the demand response challenges and their effects on demand curve using renewable energy sources.

Acknowledgements This work is supported by FIST Programme by Department of Science and Technology, Government of India.

References

1. Ackermann T, Andersson G, Söder L (2001) Distributed generation: a definition. *Electr Power Syst Res* 57:195–204
2. International Renewable Energy Agency. Renewable Power Generation Costs in 2017. Available online: <https://www.irena.org/publications/2018/Jan/Renewable-power-generation-costs-in-2017>. Accessed on 14 July 2018
3. Wang J, Costa LM, Cisse BM (2016) From distribution feeder to microgrid: an insight on opportunities and challenges. In: Proceedings of the IEEE international conference on power system technology (POWERCON 2016), Wollongong, Australia, 28 September–1 October 2016
4. Zhang Y, Lundblad A, Campana PE et al (2017) Battery sizing and rule-based operation of grid-connected photovoltaic-battery system: a case study in Sweden. *Energy Convers Manage* 133:249–263
5. Polanco Vasquez LO, Carreño Meneses CA, Pizano Martínez A, López Redondo J, García MP, Álvarez Hervás JD (2018) Optimal energy management within a microgrid: a comparative study, *energies* MDPI, Published: 19 August 2018, pp 1–22
6. Amrollahi MH, Bathaee SMT (2017) Techno-economic optimization of hybrid photovoltaic/wind generation together with energy storage system in a stand-alone micro-grid subjected to demand response. *Appl Energy* 202:66–77
7. Central Electricity Authority, Government of India (1994) Manual on transmission planning criteria, June 1994
8. Lee EK, Gadh R, Gerla M (2013) Energy service interface: accessing to customer energy resources for smart grid interoperation. *IEEE J Sel Areas Commun* 31:1195–1204
9. Zhu T, Mishra AK, Irwin D, Sharma N, Shenoy P, Towsley D (2011) The case for efficient renewable energy management in smart homes. In: Proceedings of the 3rd ACM workshop on embedded sensing systems for energy-efficiency in buildings, Seattle, WA, USA, 1 November 2011
10. Yan J, Zhai Y, Wijayatunga P et al (2017) Renewable energy integration with mini/micro-grids. *Appl Energy* 201:241–244
11. Dudurych IM, Rogers A, Aherne R, Wang L, Howell F, Lin X (2012) Safety in numbers. In: *IEEE Power & Energy Magazine* March/April 2012

Application of Modified Clonal PSO in Distributed Generator Placement for Enhancement of Efficiency and Voltage Stability in Distribution System



Vikas Singh Bhadoria, Shiva Pujan Jaiswal, Nidhi Singh Pal,
and Vivek Shrivastava

1 Introduction

Nowadays, living standard of people has increased, which increases the power demand. Industrialization is also one of the main reasons for the rise in power demand. This rise in power demand has created an unbalance in the generation and demand. To fulfil this gap, installation of DG may be one of the solutions. Several advantages of DG have motivated utility, government and researchers towards this solution. Installation of DG has encouraging effects only if optimal capacity of DG is installed at optimal location in a distribution network. Various types of DG technologies are available in literature. A few DG and their effects in the distribution network are summarized [1, 2]. The effect of DG may be broadly categorized into three groups: technical, economical and operational [3]. These effects of DG on the system mainly depend on the location and capacity of it in distribution system. If it is installed at any bus of distribution network, then it may result in the worst effects also. Due to this reason, some optimization technique has to apply for best assignment of DG in distribution system [4]. Authors have discussed different conventional and other advanced techniques for the best possible assignment of DG with single and multi-objective function. These techniques are categorized as analytical, numerical, heuristic and hybrid [5].

V. S. Bhadoria
ABES Engineering College, Ghaziabad 201009, UP, India

S. P. Jaiswal (✉)
Department of EECE, SET, Sharda University, Greater Noida, India

N. S. Pal
GBU, Greater Noida 201308, UP, India

V. Shrivastava
National Institute of Technology Delhi, New Delhi 110040, India

Optimization methods discussed in the literature have considered different objective functions and different test systems [6–8]. Modified clonal particle swarm optimization (MCPSO) algorithm is applied in this paper for optimum placement of DG in IEEE 30-bus and IEEE 14-bus distribution system. The objectives of the optimization problem are curtailment of cost involved in the power generation and power losses and enhancement of voltage profile of the system. Main contributions of the article are:

- a. Formulation of a multi-objective function including generation cost, power losses and equivalent voltage profile index.
- b. Incorporate the AIS conception in traditional PSO to make a proficient algorithm.

In this article, Sect. 1 discusses a brief introduction and literature review related to the optimum placement of DG. Section 2 is devoted to the formulation of objective function which is formed considering different indices. Different forms of PSO are discussed in Sect. 3. Results of the MCPSO are discussed and compared in Sect. 4. Conclusion of the paper is given in Sect. 5.

2 Formulation of Objective Function

Every optimization process has an objective function. It may be single or multi-objective. A multi-objective function is developed in this paper. It consists of generation cost, bus voltage and line losses. These three parameters are used to indices, considered as cost index (C_i), power loss index (P_i) and voltage profile Index (V_i). Detailed discussion of these indices follows:

2.1 Cost Index (C_i)

Augment in the percentage of the DG in a distribution network has created a challenge to power system planners to reduce capital expenditure (CAPEX) and operational expenditure (OPEX) of DG [9]. This reduction should consider different equality and inequality constraints also. The fixed cost and maintenance cost of DG are the main factors to fix the electricity tariff. These costs are the main factors in determination of the proficiency of the DG. The total cost of power plant consists of three parts: INSCO, MAINCO and RUNCO.

INSCO incorporates the cost included common developments, cost of various types of gear of the plant and other cost identified with instrumentation and control. With increase in the capacity of DG, INSCO also increases. MAINCO included the expenses engaged in the care of equipment of power plant and DG. It incorporates the yearly upkeep cost, wages to the persons involved in the operation of the plant and other different expenses. MAINCO is straightforwardly corresponding to the

capacity and uptime of the generating plant. RUNCO incorporates the expense of consumed fuel and other material required for the generation, expenses involved in waste management, the pay of the personal involved in the running of the plant. It relies upon the energy production and the operational long stretches of DG. By consolidating every one of these costs, a single cost index can be formed, which can be written as (1).

$$TC = N_{DG} \times \left[\sum_{p=1}^{cap} INSCO + \sum_{t=1}^T \sum_{p=1}^{cap} MAINCO + \sum_{t=1}^T \sum_{p=1}^{cap} RUNCO \right] \tag{1}$$

where TC: overall cost; INSCO, MAINCO and RUNCO: installation cost, maintenance cost and operational cost per unit capacity, respectively; N_{DG} : total number of DGs; T : uptime of DG. Generally cost function of a thermal power plant is quadratic in nature and can be given by Eq. (2) [10].

$$C_k = a + bP_{dgk} + cP_{dgk}^2 \tag{2}$$

In this equation, k = serial number of generators; C_k = expenses involved in operation of k th generator; P_{dgk} = output power of k th generator; a , b and c = fuel cost coefficients of k th generator.

Above cost function and generating capacity of generator are utilized in the formation of a cost index which is formed and can be written as Eq. (3).

$$C_i = \frac{C_k}{P_{dgk}} \tag{3}$$

2.2 Power Loss Index (P_i)

Power losses in every network depend to real and reactive power injection in the system at different buses. A generalized formula in N -bus system can be written as Eq. (4) [10]. This equation is also known as exact loss formula.

$$P_L = \sum_{i=1}^N \sum_{j=1}^N [\alpha_{ij}(P_i P_j + Q_i Q_j) + \beta_{ij}(Q_i P_j - P_i Q_j)] \tag{4}$$

where α_{ij} and β_{ij} are given as:

$$\alpha_{ij} = \frac{R_{ij}}{V_i V_j} \cos(\delta_i - \delta_j),$$

$$\beta_{ij} = \frac{R_{ij}}{V_i V_j} \sin(\delta_i - \delta_j),$$

Q_i and P_i are the amount reactive power and active power injection at i th node, respectively,

V_i and δ_i are the magnitude and the angle of the voltage at i th node, and $Z_{ij} = R_{ij} + jX_{ij}$ is the ij th element of $[Z_{BUS}] = [Y_{BUS}]^{-1}$.

For formulation of P_i , line losses in the network are determined before and after integration of DG at each node. Mathematically P_i can be expressed as Eq. (5).

$$P_i = \frac{\text{Losses with DG}}{\text{Losses without DG}} \quad (5)$$

2.3 Index of Voltage Profile (VP_i)

Objective of the optimization problem is to get better profile of the bus voltage. For this purpose, a voltage profile index is formed which is written as Eq. (6). Minimum voltage of i th bus in proposed objective function supports the voltage profile enhancement.

$$VP_i = \frac{\sqrt{(1 - V_{i \min})^2}}{V_{i \min}} \quad (6)$$

2.4 Objective Function (OF)

The purpose of the optimization process is to reduce production costs, as well as line losses and bus voltage profile improvement. To achieve the preferred goals, an objective function is constructed by mingling $VP_i C_i$ and P_i . Selection of weights x , y and z is done in a manner that their sum is one [11]. Thus, combining all the elements, a multi-objective function can be constructed, which can be written as an Eq. (7).

$$OF = xC_i + yP_i + zVP_i \quad (7)$$

The constraints are stated below:

The bus voltage and active power generation at each bus are limited as mentioned in Eqs. (8) and (9):

$$V_{i \min} < V_i < V_{i \max} \quad (8)$$

$$P_{DG}^{\min} \leq P_{DG} < P_{DG}^{\max} \quad (9)$$

Reactive power generation is 20% of active power generation:

$$Q_{DG} = 0.2P_{DG} \quad (10)$$

The power balance is given by Eq. (11)

$$\sum P_G + \sum P_{DG} = P_d + TL \quad (11)$$

3 Evolutionary Algorithms

Evolutionary algorithms belong to set of heuristic algorithms. Nowadays, these meta-heuristic algorithms are becoming very popular due to their advantages over other conventional optimization method. In this article basics of PSO, clonal PSO and modified clonal PSO are discussed.

3.1 Particle Swarm Optimization (PSO)

PSO is good practice that is promoted by the social behaviour of the migration of birds or fish in hunt of the foodstuff. Eberhart and Kennedy developed this algorithm [12]. Food search process by birds or fishes is initiated in group. This group is known as swarm and each bird/fish can be considered as particle. Each member of the swarm has little bit information about location of food. The search process is based on individual data and shared information between group members. Each time the iteration particle examines the gap between its position and the food in relation to the previous location and the excellent herd of the herd closest to the food area.

Initially in PSO random value is assigned to the velocity $v_i(t)$ and position $x_i(t)$. In the next iteration, these particles shift in the search space to search the superlative position. Its movement in next iteration is influenced by the best location of each individual (P_{best}) and its best location in the swarm (G_{best}). During the search process, its position and velocity are given by Eqs. (12) and (13), respectively. The process is repeated till achievement of the target.

$$V_i^n = w \times V_i^{n-1} + c_1 \times R_1 \times (P_{best_i}^{n-1} - X_i^{n-1}) + c_2 \times R_2 \times (G_{best_i}^{n-1} - X_i^{n-1}) \quad (12)$$

$$X_i^n = X_i^{n-1} + V_i^n \quad (13)$$

where

w	The inertia weight
c_1 and c_2	Acceleration coefficients
R_1 and R_2	random numbers between 0 and 1
X_i and V_i	Position and velocity of i th particle
P_{besti}	Best position of the i th particle
G_{best}	Achieved best position.

The velocity Eq. (12) has three mathematical terms. The first term in velocity equation is the local particle speed, the second and third terms are cognitive and social component, respectively. Particle velocity is affected by the inertia weight (w) [11] which is kept in the range of 0.4–0.95.

Usually speed of PSO is fast but sometimes it may be trapped locally in complex optimization process. Reasons for the local trapping can be explained as follows:

- Initialization of inertia weight affects the particle speed throughout the optimization process. This inertia weight has to be selected very carefully. If value of inertia weight is low, then optimization problem may trap in local optimum solution, and if inertia weight is high, then it will result in faster movement of particles and this can lead to skipping the global solution.
- Social component velocity is responsible for sharing information of G_{best} to all particles in the swarm which decides the movement of the swarm. This results in a decline in swarm diversity.

The PSO directs the herd to find a single result to the optimization process through particle position information. The position of the G_{best} particle serves as a guide for other particles. However, the identification of this G_{best} particle is problematic. This problem will only get worse if the search space has too many local optimum solutions. This may be evaded by inserting AIS's clonal selection policy into the PSO. This leads to better interactions within particles trying to reach global optima as the chances of finding a global solution are much higher for G_{best} particles compared to all other search sites. Therefore, the chances of being caught around a small area are very low. Therefore, the CPSO speeds up the process of efficiency and avoid any premature mergers.

In general, the PSO is self-improving but can be caught around the local optima while the clonal selection process protects that problem. Therefore, the integration of AIS and PSO will give better investigate potential.

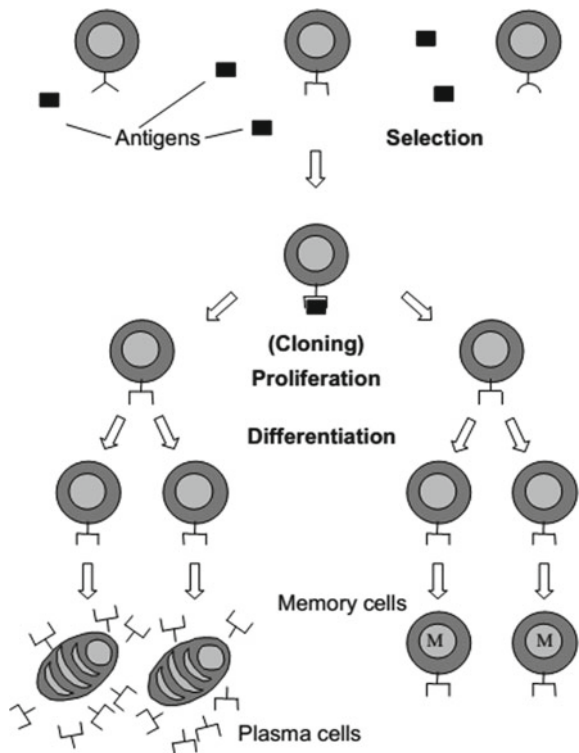
3.2 Clonal Particle Swarm Optimization (CPSO)

In PSO, G_{best} works as a guide for all particles in swarm, though it may be located far away from different particles. In each iteration, movement of all particles is towards the G_{best} . There are some particles in the swarm, which will never achieve the position of G_{best} . This may result in wastage of computational asset. Such issues can be kept

away by consolidating correlative highlights of clonal selection principle and PSO. CPSO is a combination of the idea of logical hypothesis of immune system and the PSO. Hypothesis of the immune system clarifies the reaction cycle of antibodies during any disease. As per the hypothesis, lymphocytes existing in the body are delicate to a unique sort of antigen. If antigen ties with the lymphocyte, then this phenomenon results in formation of plasma and memory cells. Plasma cells stay for very short duration but memory cells will stay alive for expanded time frame fully expecting future attacking of same antigen. This cycle of clonal determination can be clarified by Fig. 1 [13].

By and large in CPSO fundamental administrator of clonal determination, cloning, mutation and reselection are combined in PSO. PSO is performed to refresh speed and places of particles after cloning, transformation and reselection. All particles are chosen for cloning and all clones will be transformed which creates new population in search space. During reselection liking is assessed and arranged in rising request. Low proclivity particles are supplanted by the new randomly produced particles for keeping up assorted variety in the populace. Because of this, an appropriate correspondence stays between particles in a multitude, which helps in their development towards the G_{best} . Consequently, fuse of clonal determination supplements the local

Fig. 1 Clonal selection principle [13]



trapping of PSO and henceforth making CPSO a superior a proficient method than PSO.

3.3 Modified Clonal Particle Swarm Optimization (MCPSO)

For improvement of the performance of CPSO, some modification is done in MCPSO. In CPSO, all particles are selected for cloning at their individual positions. In modified version of CPSO, a slight modification is done in this procedure, and consequently, particle having G_{best} location in the swarm is selected for cloning. After cloning of this particle ‘ n ’ new particles will be created at G_{best} location in search space. After this, movement of cloned particle will be towards the ideal situation.

During the movement, all particles will move with their individual speeds from the location of G_{best} . For MCPSO, values for velocity and position are given by Eqs. (14) and (15).

$$V_i^{n'} = w \times V_i^{n'-1} \quad (14)$$

$$X_i^{n'} = X_i^{n'-1} + V_i^{n'} \quad (15)$$

In velocity Eq. (14), inertia weight is a significant factor. In this condition, new velocity can be obtained by multiplying the inertia weight. It implies that there will be direct increment or reduction in velocity which is relying upon the estimation of inertia weight. CPSO proposed by [14] utilized inertia weight which is changing with time. If this type of inertia weight is used, then due to continuous decrease in the velocity, towards the convergence of the optimization problem the particles velocity will be very low. This low speed of particles restricts the convergence of the optimization problem during dynamics. To keep away from such incidences, inertia weight ought to be chosen cautiously. To beat the disadvantage of the CPSO, another modified clonal particle swarm optimization is proposed by making some alteration in the inertia weight of the speed of the particles. Various strategies for determination of inertia weight are available in literature. Fifteen distinctive inertia weight methodology evaluation concludes that random inertia weight procedure has better efficiency [15]. Hence, this feature is incorporated in clonal PSO and a modified clonal PSO is proposed which beat the disadvantage of CPSO. Random inertia weight is given by equation (16).

$$w = 0.5 + \frac{\text{Rand}()}{2} \quad (16)$$

Above condition produces an irregular weight somewhere in the range of 0.5 and 1 with a mean estimation of 0.75. This evades the issue of constantly diminishing

velocity. Steps of MCPSO are similar to the PSO except position update equation. Detailed description of steps is given below:

1. Input the framework information (bus, line, load and generation data, etc.).
2. Determine power losses using power flow analysis without DG.
3. Find the value of objective function.
4. Initialize parameters of MCPSO randomly for size and location of DG.
5. *for* bus=2 to n (exclude the slack bus).
6. Start iteration.
7. Update particle speed and position as Eqs. (14) and (15) individually and check for limits.
8. Determine the fitness of all particles positions by considering multi-objective function.
9. Do comparison of P_{best} and G_{best} in complete population.
10. Calculate the best value of the fitness function.
11. Check termination criteria, otherwise go to step 3.
12. Record all information and print optimum result.

4 Results and Discussion

Outcomes of the MCPSO strategy are authenticated by comparing results of some existing techniques for two test systems. These two test networks are IEEE-30 bus and IEEE 14-bus distribution systems. Based on two test systems, two different cases are considered: IEEE 30-bus system (Case-I) and IEEE 14-bus distribution system (case-II). IEEE 30-bus system consists of six synchronous generators, four transformers. Load of 283.4 MW and 126.2 MVAR is divided into 21 load points. The information for the test system is taken from [16]. Generator coefficients are considered from [17]. Total active and reactive losses in the system are 17.594 MW and 22.233 MVAR, respectively.

4.1 Case-I

For IEEE 30-bus system, parameters of MCPSO are: swarm size: 25 and number of iterations: 50. Results for the case-I are compared with the analytical [8], Modified Differential Evolution (MDE) [18] and PSO [19] techniques and shown in Table 1. Comparison shows that except MDE and PSO all techniques consider real and reactive power injection both and value of injected reactive power is 0.2 times of injected active power while MDE and PSO consider only active power injection. In analytical technique and MDE, objective function of the optimization problem considers active losses and cost of DG, in PSO only active losses are considered as objective function. CPSO and proposed MCPSO are applied to reduce active losses, cost of DG and voltage profile enhancement. The obtained results confirm that the

Table 1 Results and comparison of MCPSO in case-I

Name of technique	OF	Capacity of DG (MW)	Bus No.	Losses (MW)	DG power injection
Analytical [8]	Active losses and cost of DG	35	11	13.61	P_{inj} and $Q_{inj} = 0.2 * P_{inj}$
MDE [18]	Active losses and cost of DG	49.96	5	13.32	P_{inj}
PSO [19]	Active losses	14.80	6	15.519	P_{inj}
CPSO	Active losses, cost of DG and VPI	45	21	12.982	P_{inj} and $Q_{inj} = 0.2 * P_{inj}$
MCPSO	Active losses, cost of DG and VPI	46.95	23	12.93	P_{inj} and $Q_{inj} = 0.2 * P_{inj}$

proposed size by the MCPSO gives maximum loss reduction. In compared methods, although size proposed by the PSO is less but losses in that case are maximum as 15.519 MW. Proposed MCPSO method suggests higher size with minimum losses in the system. In case of MCPSO size is 46.95 MW and this size gives minimum losses of 12.93 MW. This size is less than that of MDE with lesser losses. Although analytical and CPSO gives lesser size than that of MCPSO as 35 and 45 MW, respectively, but in these cases, losses are more than that of MCPSO. Active and reactive line loss comparison of base case and optimum results with MCPSO are demonstrated in Figs. 2 and 3, respectively. These figures also show that the optimal placement of DG reduces the line losses in the system.

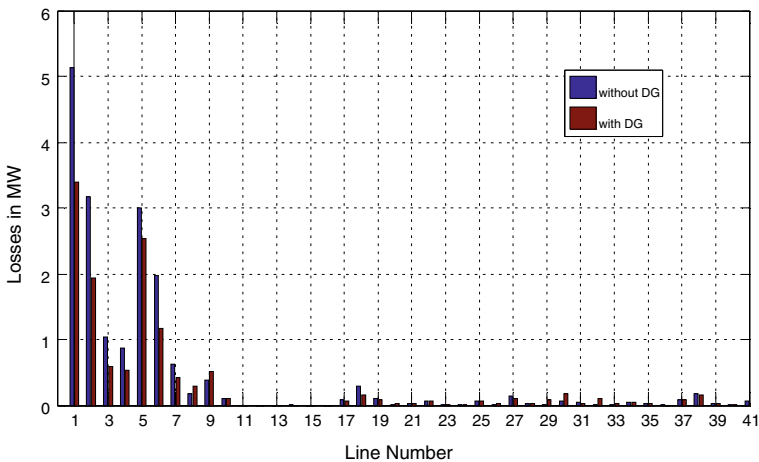


Fig. 2 Active line losses comparison in case-I

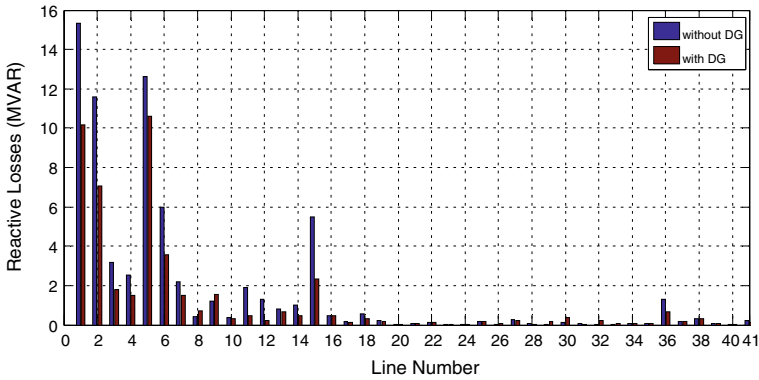


Fig. 3 Reactive line losses comparison in case-I

Table 2 Variation in different indices in case-I

	C_i	VP_i	P_i	OF
Base case	–	0.0266	4.066	–
CPSO	2.168	0.0221	2.7488	1.6301
MCPSO	2.1761	0.0229	2.7211	1.6236

Variation in different indices in case-I with CPSO and MCPSO is shown in Table 2. Table shows that C_i and VP_i in case of MCPSO are slightly higher than that of the CPSO but MCPSO results in minimum objective function. Due to minimum objective function, it can be concluded that MCPSO results in optimum size DG for multi-objective optimization. With the first test system the voltage profile in base case and with optimally placed DG is shown in Fig. 4. Voltage profile is compared for the base case and for the best case as suggested by MCPSO. Figure 4 shows that

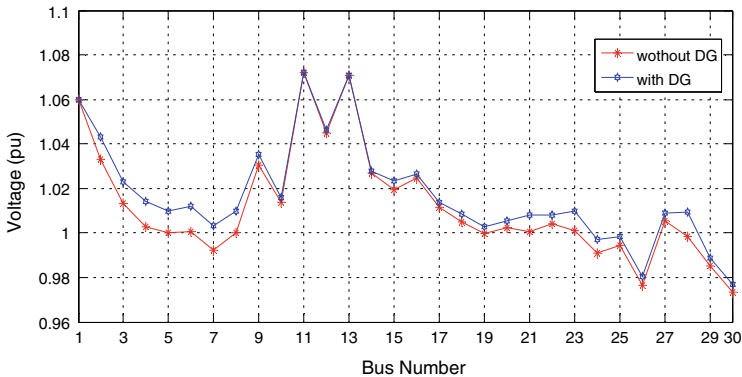


Fig. 4 Voltage profile comparison in case-I

if optimal size DG (46.95 MW) is installed at optimum location (bus #23) then it also supports profile bus voltage.

4.2 Case-II

In case-II, IEEE 14-bus network is considered. In this the proposed MCP SO is judged against other existing approach as analytical [8] and MDE [18], PSO and CPSO. For PSO, CPSO and MCP SO number of particles are 12 and number of iterations are 25. Comparative results of MCP SO with other methods in case-II are shown in Table 3. For optimization using PSO, CPSO and MCP SO a objective function is considered as given in Eq. 7, whereas analytical and MDE techniques consider bi-objective function. Bi-objective function takes the real losses and cost of DG and multi-objective function is a combination of the real losses, cost of DG and voltage profile index. Except MDE, in all other techniques, DG may provide both active and reactive power support. The reactive power provided by DG is related to the active power capacity and is only 20%. According to analytical method, most suitable place for the DG is 8th bus and optimal capacity is 16 MW. With installation of it at bus no. 8, losses in the system are 11.70 MW. According to the MDE, a DG with a capacity of 34.12 MW should be installed at bus number 3. This installation generated losses of 11.54 MW. In the same system with same conditions PSO, CPSO and proposed MCP SO are also applied.

According to PSO, size of DG is 32.45 MW and its place is 6th bus. In this approach, loss is 10.914 MW. This loss is lesser than that of MDE. CPSO suggests the 33.95 MW DG 6th bus. This size results loss of 10.811 MW and these losses are lesser than that of PSO. Size suggested by the MCP SO is in the order of as proposed

Table 3 Results and comparison of MCP SO in case-II

Name of technique	OF	Capacity of DG (MW)	Bus No.	Losses (MW)	DG power injection
Analytical [8]	Active losses and cost of DG	16	8	11.70	P_{inj} and $Q_{inj} = 0.2 * P_{inj}$
MDE [18]	Active losses and cost of DG	34.12	3	11.54	P_{inj}
PSO	Active losses, cost of DG and VPI	32.45	6	10.914	P_{inj} and $Q_{inj} = 0.2 * P_{inj}$
CPSO	Active losses, cost of DG and VPI	33.95	6	10.811	P_{inj} and $Q_{inj} = 0.2 * P_{inj}$
MCP SO	Active losses, cost of DG and VPI	34	14	10.093	P_{inj} and $Q_{inj} = 0.2 * P_{inj}$

Table 4 Variation in different indices in case-II

	C_i	VP_i	P_i	OF
Base case	–	0.01	4.3054	–
PSO	2.1217	0.01	3.2051	1.5058
CPSO	2.1273	0.01	3.1639	1.4974
MCPSO	2.1275	0.01	3.0143	1.4600

by the CPSO but this size results in the maximum loss reduction in IEEE 14-bus system. According to MCPSO optimal capacity of DG is 34 MW at bus number 14. This installation results in 10.093 MW losses only. These losses are least among the compared techniques. Although size suggested by MCPSO is higher than analytical and approximately equal to MDE and CPSO but this size gives minimum losses in the system. These results show that results of the MCPSO are best among the compared methodologies. Variation in different indices in case-II for PSO, CPSO and MCPSO is shown in Table 4. This tables shows that CI is increased in case of size suggested by the MCPSO but overall objective function is lowest in case of MCPSO.

Active and reactive line losses comparison for base case and optimum case proposed by MCPSO are shown in Figs. 5 and 6, respectively. These figures also prove that optimum size suggested by the MCPSO is able to reduce active as well as reactive line losses although in objective function only active losses are considered. Voltage profile of the IEEE 14-bus system without DG and with optimum DG is shown in Fig. 7. Figure shows that optimum installation suggested by the proposed MCPSO improves the overall voltage profile of the system.

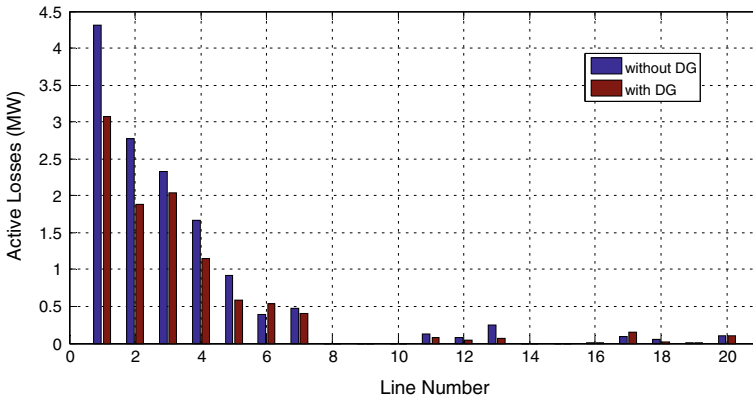


Fig. 5 Active line losses comparison in case-II

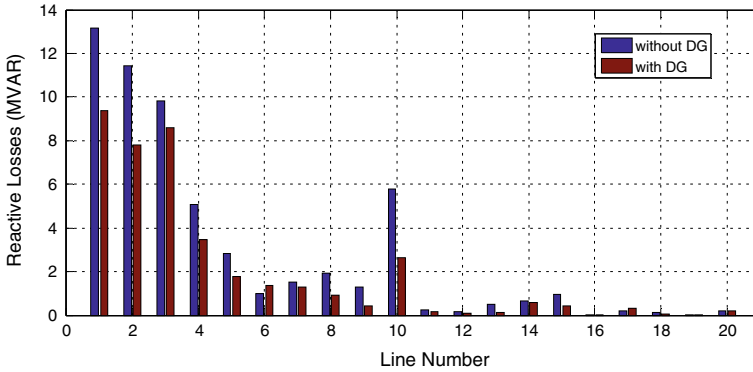


Fig. 6 Reactive line losses comparison in case-II

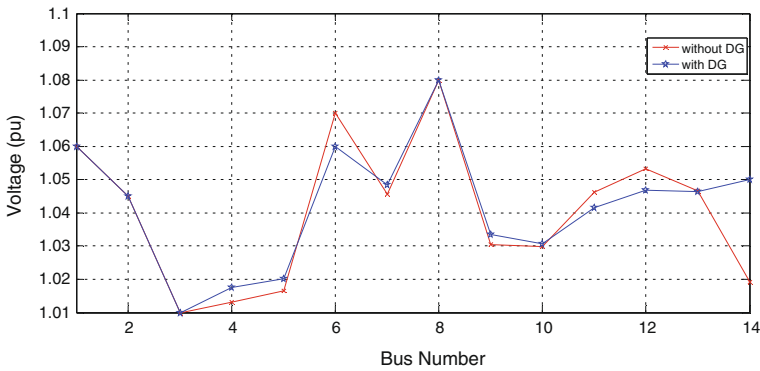


Fig. 7 Voltage profile comparison in case-II

5 Conclusion

In this paper, a principle of clonal selection is combined with the PSO and a new modified clonal PSO is proposed. Selection of inertia weight strategy is also discussed for proposed MCP SO. It also used to optimize a multi-objective function to find the optimal location of DG in IEEE 30-bus and IEEE 14-bus distribution system. Objective of the proposed objective function is to minimization of generation cost and line loss and enhancement of voltage profile. In both cases, results of MCP SO are compared with other existing methodologies. Results are found better than the compared methods in multi-objective optimization.

As a future scope, this MCP SO can be implemented in other types of distribution networks. The proposed work can be extended by considering placement of multiple and different types of DGs. Time varying load can also be considered during optimization.

References

1. Bhadoria VS, Pal NS, Shrivastava V (2016) Comparison of analytical and heuristic techniques for multiobjective optimization in power system. In: Problem solving and uncertainty modeling through optimization and soft computing, pp 264–291. <https://doi.org/10.4018/978-1-4666-9885-7.ch013>
2. Ramavat SR, Jaiswal SP, Goel N, Shrivastava V (2019) Optimal location and sizing of DG in distribution system and its cost–benefit analysis. In: Applications of artificial intelligence techniques in engineering. Advances in intelligent systems and computing, vol 698. Springer, Singapore. https://doi.org/10.1007/978-981-13-1819-1_11
3. Bhadoria VS, Pal NS, Shrivastava V (2013) A review on distributed generation definitions and DG impacts on distribution system. In: International conference on advanced computing and communication technologies (ICACCTM-2013), Panipat, pp 1–7. <https://doi.org/10.13140/RG.2.1.4439.4328>
4. Bhadoria VS, Pal NS, Shrivastava V (2014) Installation of DG for optimal demand compensation. In: 2014 international conference on issues and challenges in intelligent computing techniques (ICICT). IEEE, pp 816–819. <https://doi.org/10.1109/ICICT.2014.6781385>
5. Maurya H, Pal NS, Bhadoria VS (2020) Performance analysis of optimal placement of multiple DGs using PSO. In: Decision analytics applications in industry. Springer, Singapore, pp 239–247. https://doi.org/10.1007/978-981-15-3643-4_18
6. Bhadoria VS, Pal NS, Shrivastava V, Jaiswal SP (2017) Reliability improvement of distribution system by optimal siting and sizing of disperse generation. Int J Reliab Qual Saf Eng. <https://doi.org/10.1142/S021853931740006X>
7. Bhadoria VS, Pal NS, Shrivastava V, Jaiswal SP (2018) Optimal siting and sizing of capacitor using iterative search method for enhancement of reliability of distribution system. Lect Notes Electr Eng 508:123–129. https://doi.org/10.1007/978-981-13-0662-4_11
8. Ghosh S, Ghoshal SP, Ghosh S (2010) Optimal sizing and placement of distributed generation in a network system. Int J Electr Power Energy Syst 32:849–856. <https://doi.org/10.1016/j.ijepes.2010.01.029>
9. Jaiswal SP, Shrivastava V, Singh S (2019) Economic viability solar PV power plant in distribution system. IOP Conf Ser Mater Sci Eng 594:012010. <https://doi.org/10.1088/1757-899X/594/1/012010>
10. Elgerd O (1971) Electric energy systems theory: an introduction. McGraw-Hill, New York
11. Maurya H, Bohra VK, Pal NS, Bhadoria VS (2019, August) Effect of inertia weight of PSO on optimal placement of DG. In: IOP Conference Series: Materials Science and Engineering, vol 594, no 1. IOP Publishing, p 012011. <https://doi.org/10.1088/1757-899X/594/1/012011>
12. Kennedy J, Eberhart R (1995) Particle swarm optimization. In: Proceedings of ICNN'95—international conference on neural networks. IEEE, Perth, WA, Australia, pp 1942–1948. <https://doi.org/10.1109/ICNN.1995.488968>
13. Castro LND, Zuben FJV (2002) Learning and optimization using the clonal selection principle. IEEE Trans Evol Comput 6:239–251
14. Nanda SJ, Panda G (2009) Artificial immune systems: principle, algorithms and applications
15. Bansal JC, Singh PK, Saraswat M, Verma A, Jadon SS, Abraham A (2011) Inertia weight strategies in particle swarm optimization. In: 2011 third world congress on nature and biologically inspired computing, pp 633–640. IEEE, Salamanca, Spain. <https://doi.org/10.1109/NaBIC.2011.6089659>
16. Pai MA (2006) Techniques in power system analysis. Tata McGraw-Hill Publishing Company Limited, New Delhi
17. Gautam D, Mithulananthan N (2007) Optimal DG placement in deregulated electricity market. Electr Power Syst Res 77:1627–1636. <https://doi.org/10.1016/j.epr.2006.11.014>
18. Kumar S, Pal D, Mandal KK, Chakraborty N (2013) Performance study of a new modified differential evolution technique applied for optimal placement and sizing of distributed generation. In: Lecture notes in computer science (including subseries lecture notes in artificial

- intelligence (LNAI) and lecture notes bioinformatics), vol 8297. LNCS, pp 189–198. https://doi.org/10.1007/978-3-319-03753-0_18
19. Haidar AMA (2011) Optimal location of distributed generation using intelligent optimization. In: Proceedings of international conference tools with artificial intelligence ICTAI, pp 891–893. <https://doi.org/10.1109/ICTAI.2011.143>

Performance of an L-shaped Duct Oscillating Water Column Wave Energy Converter Device Under Irregular Incident Waves



Kshma Trivedi and Santanu Koley

1 Introduction

The importance and significance of renewable energy resources increase in the energy production industry due to their expeditious and long-term accessibility. Moreover, renewable energy sources are classified as clean energy because there is no consequence of environmental issues during the process of producing electricity. In this regard, wave energy will play a crucial role in the upcoming future. Out of various wave power generation techniques, the OWC-WEC is the long-established technique to transform the wave power into the electricity. This OWC-WEC comprises a collector chamber which is partly submerged into the water and the PTO system [1]. Thiruvenkatasamy and Neelamani [2] used a 1:50 scale model to analyze the performance of multi-resonant OWC placed in arrays. In this research, the following conclusions are obtained: (i) the efficiency of an OWC-WEC is inversely proportional to the wave steepness, (ii) the energy reflection rate of the device increases as the relative water depth decreases. Tseng [3] developed a multi-resonant OWC model, and it was found that the structural configurations of the OWC-WEC enhance the amplification factor and the energy extraction rate for small wave heights. Wang et al. [4] used the 3D BEM method to develop the numerical model to analyze the efficiency of a bottom-mounted OWC-WEC placed in the nearshore region. It was reported that the capture-width ratio and wave-amplification factor strongly depend on the slope of the bottom bed. Rapaka et al. [5] analyzed the performance of a floating

K. Trivedi (✉) · S. Koley

Department of Mathematics, Birla Institute of Technology and Science-Pilani, Hyderabad Campus, Hyderabad 500078, India

e-mail: p20190439@hyderabad.bits-pilani.ac.in

S. Koley

e-mail: santanu@hyderabad.bits-pilani.ac.in

multi-resonant OWC device experimentally and found that at a lower frequency range, there was no effect of wave steepness on the RAO of sway, heave, and roll motions. Bhattacharjee and Guedes Soares [6] used the semi-analytical method to analyze the working mechanism of the floating OWC-WEC over the stepped bottom. It was reported that the horizontal wave force increases and the vertical wave force decreases with an increase in submergence depth. Sheng et al. [7] developed the physical modeling and scaling for the OWC-WEC, and it was reported that the large Reynolds number guarantees the existence of turbulent flow. Kuo et al. [8] developed a numerical model to investigate the efficiency of breakwater-integrated OWC-WEC using FLOW-3D software. It was concluded that the production of average power by the air strongly depends on the size of the caissons. Mahnamfar and Altunkaynak [9] analyzed the working mechanism of an OWC-WEC experimentally under the action of regular wave series, and it was concluded that the geometrical configuration of the OWC-WEC contributes significantly to enhance the performance of an OWC-WEC. Ning et al. [10] studied the performance of a double chamber cylindrical-shaped OWC-WEC. In this research, the following conclusions are obtained: (i) the wider chamber length and smaller shell thickness enhance the efficiency of the OWC-WEC, and (ii) chamber volume and rotational speed of turbine are important factors for energy conversion. Elhanafi et al. [11] investigated the performance of single-chamber OWC-WEC and double chamber OWC-WEC using 2D and 3D CFD models, and it was reported that the capture-width ratio of the double chamber OWC-WEC is higher than the single-chamber OWC-WEC. Zheng et al. [12] studied the hydrodynamic characteristics of multi-OWC using the eigenfunction expansion method, and the following conclusions are obtained: (i) multiple chambers in the OWC-WEC increase the wave energy extraction from the device platform, and (ii) the smaller submergence depth of the sea side wall and larger draft of the back wall of an OWC-WEC significantly enhances the performance of an OWC-WEC. In the above-mentioned research works, the performance of an OWC-WEC is analyzed under the regular incoming waves.

Nevertheless, in the real sea environment, the incoming waves are highly irregular in nature. Therefore, it is relevant to analyze the performance of an OWC-WEC under random incident waves. Gouaud et al. [13] developed the experimental study to analyze the performance of an OWC-WEC placed over an underwater mound. Ashlin et al. [14] studied the working mechanism of an OWC-WEC over the various bottom profiles such as flat, sloping, and curved shaped and the following conclusions are obtained: (i) due to the shape of the bottom profiles and higher amount of wave reflection from the front wall, the efficiency of OWC-WEC increases as the wave steepness decreases, (ii) due to the higher amount of fluid flow, the efficiency of OWC-WEC increases as the relative water depth increases. Rezanejad and Soares [15] developed the dual-mass system to determine the hydrodynamic performance of an OWC-WEC. It was reported that the existence of stepped bottom in the OWC-WEC configuration enhances the efficiency of an OWC-WEC in the presence of regular and irregular incoming waves. Rezanejad et al. [16] examined the performance of an L-shaped OWC-WEC under random incoming waves. The amplification factor and the hydrodynamic efficiency of an OWC-WEC strongly depend on the submergence depth of

the OWC-WEC. Zabihi et al. [17] used the 1:15 model to analyze the performance of an OWC-WEC experimentally under random waves. It was reported that within the OWC-WEC chamber, the shape of the spectrum is influenced by the form of the wave spectrum. Zhang et al. [18] investigated the performance of breakwater-integrated floating-WEC under the assumption of potential theory. It was concluded that the seaside wall plays a vital role in enhancing the hydrodynamic performance of floating-WEC. Recently, Chen et al. [19] studied the performances of an OWC device integrated with a cylindrical shape caisson breakwater experimentally. It was shown that the peak efficiency of this OWC-WEC could be reached up to 81% for certain optimized designs.

The structure of this study consists of the following sections: Sect. 2 contains the detailed BVP and the solution technique, Sect. 3 represents the parameters related to the performance of an OWC-WEC under the irregular incident waves. Results and conclusions are discussed in Sects. 4 and 5.

2 Solution Methodology Using BEM

The present study yields the mathematical modeling of an L-shaped duct type OWC-WEC. For the modeling of an OWC-WEC, the 2D Cartesian coordinate system is used with the alignment of axes are shown in Fig. 1. An OWC-WEC comprises a rigid and impermeable seaside wall of uniform thickness d and situated at $x = L - b$. Moreover, the rigid backside wall of the OWC device is placed at $x = L$ and b is the chamber length. The draft of the front wall of the OWC-WEC is a and the length of protrusion of the L-shaped duct from its chamber is c . An OWC-WEC is situated at $z = -h$. Internal free surface Γ_4 and external free surface Γ_6 are two components of the free surface (Fig. 1). For the sake of BEM, a fictitious boundary Γ_1 is situated at the origin. Further, the submerged boundaries and the L-shaped

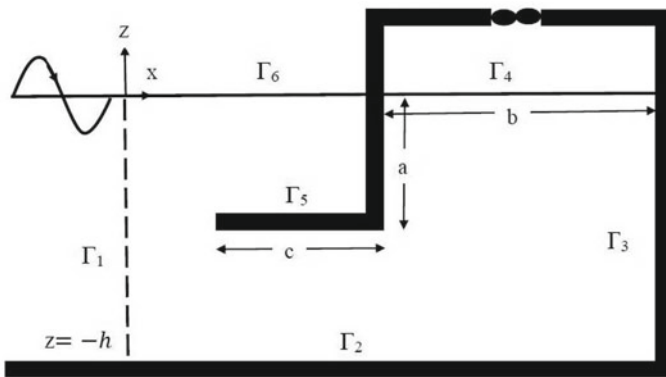


Fig. 1 Schematic of the physical problem

front wall are represented by Γ_5 Moreover, the bottom boundary and back wall of the OWC-WEC are denoted by Γ_2 and Γ_3 , respectively. The mathematical modeling is similar as mentioned in [20]. The expression for the velocity potential is given as $\Phi(x, z, t) = Re\{\phi(x, z)e^{-i\omega t}\}$. Here, we choose governing equation is given by

$$\nabla^2\phi(x, z) = 0 \tag{1}$$

ϕ contains the ϕ^S and ϕ^R (see [21] for details). Now, ϕ^S and ϕ^R satisfy the bc at $z = 0$ and is provided as,

$$\frac{\partial\phi^{S,R}}{\partial n} - K\phi^{S,R} = \begin{cases} \gamma, & \text{on } \Gamma_4, \\ 0, & \text{on } \Gamma_6. \end{cases} \tag{2}$$

Here, we choose $\gamma = 0$ for ϕ^S and $\gamma = 1$ for ϕ^R , respectively, and $K = \omega^2g$. Derivative in the normal direction is represented by $\partial/\partial n$. Now, the boundary conditions on the impenetrable boundaries $\Gamma_2 \cup \Gamma_3 \cup \Gamma_5$ are given by

$$\frac{\partial\phi^{S,R}}{\partial n} = 0, \text{ on } \Gamma_2 \cup \Gamma_3 \cup \Gamma_5 \tag{3}$$

Now, the radiation boundary condition on auxiliary boundary Γ_1 is given by

$$\frac{\partial\phi^{S,R}}{\partial n} - ik_0\phi^{R,S} = \gamma\left(\frac{\partial\phi^I}{\partial n} - ik_0\phi^{S,R}\right), \text{ on } \Gamma_1 \tag{4}$$

Here, k_0 satisfies $\omega^2 = gk\tanh(kh)$ and the expression for ϕ^I is given as $\phi^I(x, z) = \left(\frac{-igH}{2\omega}\right)\frac{\cosh k_0(h+z)}{\cosh(k_0h)}e^{ik_0x}$ and H is termed as incident wave height. In Eq. (4), for $\gamma = 1$ for ϕ^S and $\gamma = 0$ for ϕ^R , respectively.

The solution methodology for the above-mentioned BVP is discussed using the BEM. In this method, firstly, the BVP related to the ϕ^S and ϕ^R is converted into the Fredholm integral equations. Now, the BEM is used to transform these integral equations into number of algebraic equations. The Green’s function $G(x, z; x_0, z_0)$ is given as (see [20] for detailed derivations).

$$G(x, z; x_0, z_0) = -4\pi i \frac{\cosh k_0(h+z_0)\cosh k_0(h+z)}{(2k_0h + \sinh 2k_0h)}e^{ik_0|x-x_0|} - 4\pi \sum_{n=1}^{\infty} \frac{\cos k_n(h+z_0)\cos k_n(h+z)}{(2k_nh + \sin 2k_nh)}e^{-k_n|x-x_0|} \tag{5}$$

Now, applying Green’s theorem on $\phi^{R,S}$ and $G(x, z; x_0, z_0)$ and using the bcs (2), (3), and (4), the following integral equations for ϕ^S and ϕ^R are obtained as

$$\begin{aligned}
 & -\frac{1}{2}\phi^S + \int_{\Gamma_1} \phi^S \left(\frac{\partial G}{\partial n} - ik_0 G \right) d\Gamma + \int_{\Gamma_2+\Gamma_3+\Gamma_5} \phi^S \frac{\partial G}{\partial n} d\Gamma \\
 & + \int_{\Gamma_4} \phi^S \left(\frac{\partial G}{\partial n} - KG \right) d\Gamma + \int_{\Gamma_6} \phi^S \left(\frac{\partial G}{\partial n} - KG \right) d\Gamma = \int_{\Gamma_1} G \left(\frac{\partial \phi^I}{\partial n} - ik_0 \phi^I \right) d\Gamma
 \end{aligned} \tag{6}$$

$$\begin{aligned}
 & -\frac{1}{2}\phi^R + \int_{\Gamma_1} \phi^R \left(\frac{\partial G}{\partial n} - ik_0 G \right) d\Gamma + \int_{\Gamma_2+\Gamma_3+\Gamma_5} \phi^R \frac{\partial G}{\partial n} d\Gamma \\
 & + \int_{\Gamma_4} \phi^R \left(\frac{\partial G}{\partial n} - KG \right) d\Gamma + \int_{\Gamma_6} \phi^R \left(\frac{\partial G}{\partial n} - KG \right) d\Gamma = \int_{\Gamma_4} G d\Gamma
 \end{aligned} \tag{7}$$

Now, Eqs. (6) and (7) are transformed into a number of algebraic equations using the BEM method. The detailed procedure is available in [21]. Finally, the discrete values of ϕ and $\partial\phi/\partial n$ are obtained over each boundary of the domain.

3 Performance of the OWC-WEC in Real Sea Environment

For random incident waves, the concept of wave spectrum along with a number of sea states are used. In the present analysis, the Pierson–Moskowitz spectrum [22] is used, and the form for the same is given by

$$S_{inc}(\omega) = 263H_s^2 T_e^{-4} \omega^{-5} \exp(-1054T_e^{-4} \omega^{-4}) \tag{8}$$

where H_s and T_e are termed as SWH and the energy period, respectively. The chamber pressure standard deviation β_p is given by (see [22] for details)

$$\beta_p^2 = \int_0^\infty S_{inc}(\omega) \left| \frac{Pr(\omega)}{amp(\omega)} \right|^2 d\omega \tag{9}$$

where $amp(\omega) = \sqrt{2S_{inc}(\bar{\omega})_i \delta\omega_i}$ is the incident wave amplitude for each regular wave component. Here, S_{inc} represents the incident wave spectrum. Now, the average efficiency of an OWC device is obtained as

$$\eta_A = \frac{W_A}{P_A}, \tag{10}$$

where P_A and W_A are termed as average incident wave energy flux, and the averaged available power to the Wells turbine, respectively. The expressions for P_A and W_A are given by

$$P_A = \rho g w \int_0^\infty S_{\text{inc}}(\omega) C_g(\omega) d\omega, \tag{11}$$

$$W_A = \epsilon \beta_p^2. \tag{12}$$

Here, w and C_g are the width of the chamber and the group velocity of the incoming waves. Further, ϵ is the turbine damping coefficient.

4 Results

In this section, the OWC device performance is analyzed under the irregular incoming waves environment. The parameters associated with the OWC device and the incoming waves are the following: $h = 10$ m, $\rho = 1025$ kg/m³, $g = 9.81$ m/s², $L = 3h$, $b = h$, $d = 0.05h$, $c = 0.5h$, $a = 0.5h$ unless mentioned explicitly. The characteristics of two different most occurrence sea states for the incoming wave spectrum as in Eq. (8) are the following (see [22] for details): the significant wave heights $H_s = 1.18$ m, 1.96 m and the corresponding energy periods $T_e = 6.50$ s, 7.97 s.

Figure 2a, b depicts the change of the free surface elevation ζ for different (a) chamber length b/h and draft a/h , respectively. Figure 2a illustrates that the amplitude of ζ increases outside the chamber as b/h increases. Moreover, the amplitude of the ζ inside the device chamber becomes lower for higher b/h . Further, certain phase change occurs in the free surface elevation ζ for various b/h . Similarly, in Fig. 2b, it is observed that the amplitude of the ζ increases as the a/h decreases. Moreover, certain phase changes are also observed for various a/h .

Figure 3a shows the variation of ζ for various c/h . It is noticed that ζ decreases as c/h increases. Moreover, the amplitude of ζ decreases significantly within the

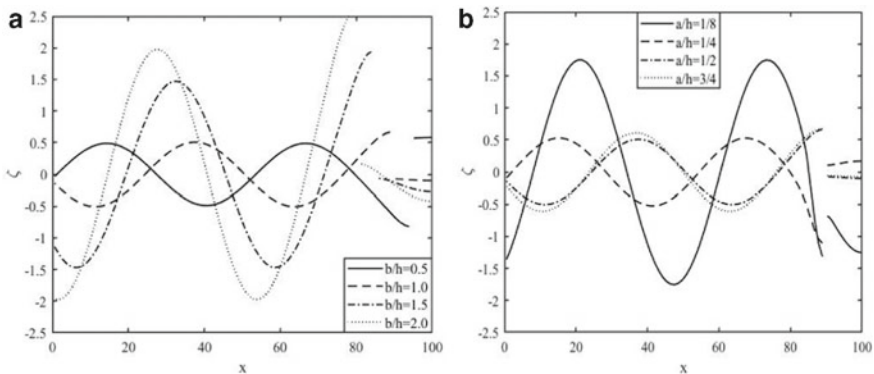


Fig. 2 ζ for a variety of **a** b/h , and **b** a/h with $Kh = 1.0$

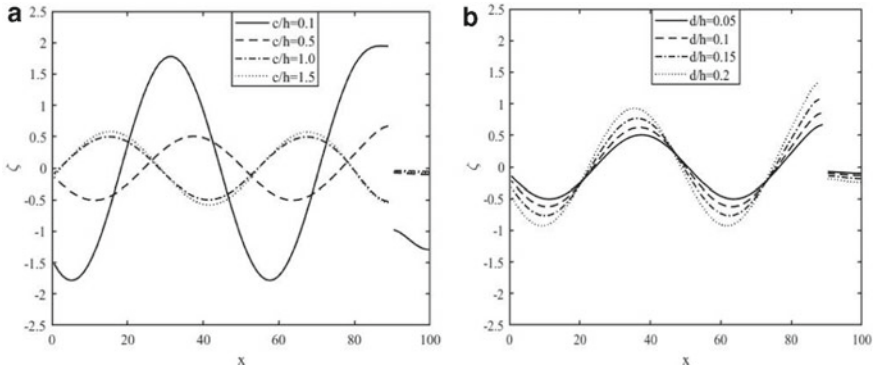


Fig. 3 ζ for a variety of **a** c/h , and **b** d/h with $Kh = 1.0$

chamber as c/h takes higher values. This happens as c/h increases, the front wall of the OWC-WEC obstructs the incoming wave more to enter into the chamber. Further, change in phase also occurs with the variation in c/h . On the other hand, the amplitude of ζ increases as the front wall thickness d/h becomes higher. This happens as more wave energy is reflected back as the thickness d/h increases.

In Fig. 4a, b, the variation of the average efficiency η_A is plotted for various b/h with $H_s = 1.18$ m, $T_e = 6.50$ s and $H_s = 1.96$ m, $T_e = 7.97$ s, respectively. It is observed in Fig. 4a that η_A decreases as the chamber length b/h increases. Further, η_A attains maximum for moderate values of ϵ and thereafter decreases for larger ϵ . In addition, Fig. 4b reveals that the η_A becomes lower for smaller and larger values of $b/h=0.5, 2.0$, whereas for transitional values of $b/h = 1.0, 1.5$, the efficiency η_A becomes higher. In summary, it is concluded that the incident wave characteristics perform a vital role to determine the efficiency of the OWC-WEC.

Figure 5a, b show the variation of average efficiency η_A versus ϵ for various a/h

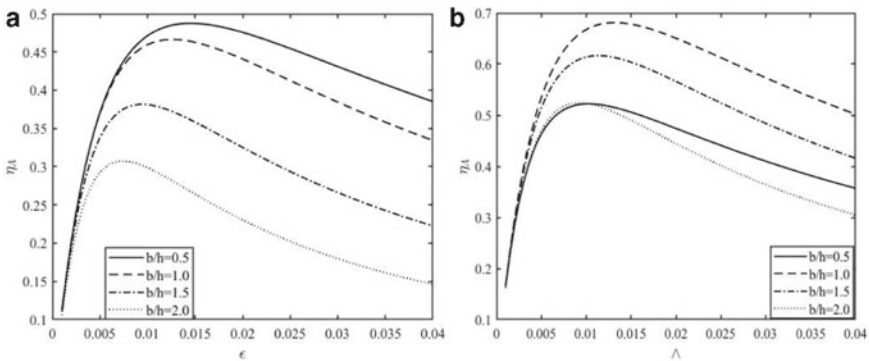


Fig. 4 η_A versus ϵ for various b/h with **a** $H_s = 1.18$, $T_e = 6.50$ and **b** $H_s = 1.96$, $T_e = 7.97$

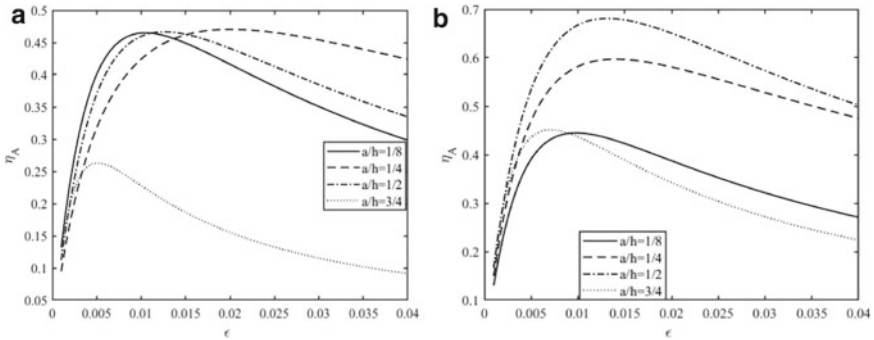


Fig. 5 η_A versus ϵ for various a/h . **a** $H_s = 1.18$, $T_e = 6.50$ and **b** $H_s = 1.96$, $T_e = 7.97$

With $H_s = 1.18$ m, $T_e = 6.50$ s and $H_s = 1.96$ m, $T_e = 7.97$ s, respectively. Figure 5a depicts that η_A becomes higher for smaller and moderate values of a/h . However, the efficiency η_A significantly decreases for very higher values of a/h . This happens as a/h becomes higher, the gap between the OWC device’s front wall and the bottom decreases. Therefore, water flow cannot enter the OWC device chamber. Figure 5b reveals that the η_A becomes lower for smaller and larger values of $a/h = 1/8, 3/4$, whereas for intermediate values of $a/h = 1/4, 1/2$, the efficiency η_A takes higher values. In summary, it is concluded that the incoming wave’s sea states perform a vital role in determining the efficiency of the OWC-WEC. Similar observations were reported in Fig. 4.

Figure 6a, b show the variation of average efficiency η_A versus ϵ for various c/h with $H_s = 1.18$, $T_e = 6.50$, and $H_s = 1.96$, $T_e = 7.97$, respectively. It is observed in Fig. 6a, b that η_A decreases as the c/h increases. Further, average efficiency η_A reaches its maximum value for intermediate values of ϵ . Similar patterns of η_A with the change in ϵ are observed in Figs. 4 and 5.

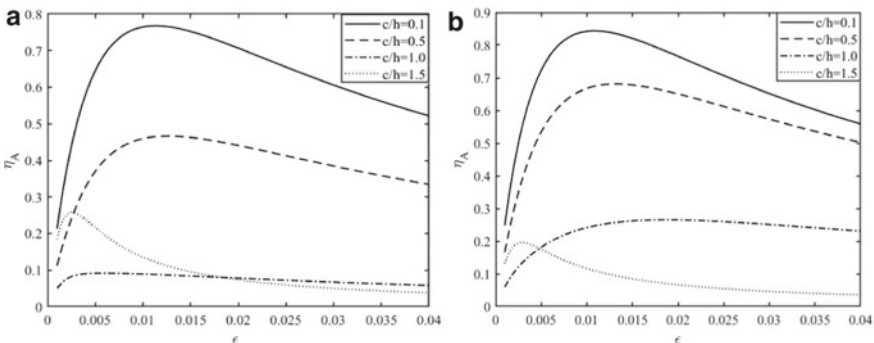


Fig. 6 η_A versus ϵ for various c/h . **a** $H_s = 1.18$, $T_e = 6.50$ and **b** $H_s = 1.96$, $T_e = 7.97$

5 Conclusions

In this work, the average efficiency of an L-shaped duct OWC device is investigated in real sea conditions. For the present study, the Pierson–Moskowitz spectrum is considered as the incoming wave spectrum. To solve the associate BVP, the BEM is used. It is observed that the free surface elevation decreases for higher values of submergence depth and the length of protrusion of the L-shaped OWC-WEC, and an opposite pattern is observed for higher values of the thickness of the seaside wall and the chamber length. Further, it is seen that for $H_s = 1.18$, $T_e = 6.50$, the average efficiency increases with a decrease in chamber length, submergence depth, and length of the protrusion of the L-shaped duct. On the other hand, for $H_s = 1.96$, $T_e = 7.97$, the average efficiency of OWC-WEC is higher for the moderate values of chamber length and submergence depth.

Acknowledgements KT and SK acknowledge the funding provided through the DST Project: DST/INSPIRE/04/2017/002460. Further, SK acknowledges RIG project: BITS/GAU/RIG/2019/H0631 and Additional Competitive Research Grant: BITS/GAU/ACRG/2019/H0631.

References

1. Heath TV (2012) A review of oscillating water columns. *Philos Trans R Soc Math Phys Eng Sci* 370(1959):235–245
2. Thiruvenkatasamy K, Neelamani S (1997) On the efficiency of wave energy caissons in array. *Appl Ocean Res* 19(1):61–72
3. Tseng RS, Wu RH, Huang CC (2000) Model study of a shoreline wave-power system. *Ocean Eng* 27(8):801–821
4. Wang DJ, Katory M, Li YS (2002) Analytical and experimental investigation on the hydrodynamic performance of onshore wave-power devices. *Ocean Eng* 29(8):871–885
5. Rapaka EV, Natarajan R, Neelamani S (2004) Experimental investigation on the dynamic response of a moored wave energy device under regular sea waves. *Ocean Eng* 31(5–6):725–743
6. Bhattacharjee J, Guedes Soares C (2011) Oblique wave interaction with a floating structure near a wall with stepped bottom. *Ocean Eng* 38(13):1528–1544
7. Sheng W, Alcorn R, Lewis T (2014) Physical modelling of wave energy converters. *Ocean Eng* 84:29–36
8. Kuo YS, Chung CY, Hsiao SC, Wang YK.: Hydrodynamic characteristics of oscillating water column caisson breakwaters. *Renew Energy* 103:439–447
9. Mahnamfar F, Altunkaynak A (2017) Comparison of numerical and experimental analyses for optimizing the geometry of OWC systems. *Ocean Eng* 130:10–24
10. Ning D, Zhou Y, Zhang C (2018) Hydrodynamic modeling of a novel dual-chamber OWC wave energy converter. *Appl Ocean Res* 78:180–191
11. Elhanafi A, Macfarlane G, Ning D (2018) Hydrodynamic performance of single–chamber and dual–chamber offshore–stationary Oscillating Water Column devices using CFD. *Appl Energy* 228:82–96
12. Zheng S, Antonini A, Zhang Y, Miles J, Greaves D, Zhu G, Iglesias G (2020) Hydrodynamic performance of a multi-oscillating water column (OWC) platform. *Appl Ocean Res* 99:102168

13. Gouaud F, Rey V, Piazzola J, Van Hooff R (2010) Experimental study of the hydrodynamic performance of an onshore wave power device in the presence of an underwater mound. *Coast Eng* 11–12:996–1005
14. Ashlin SJ, Sundar V, Sannasiraj SA (2016) Effects of bottom profile of an oscillating water column device on its hydrodynamic characteristics. *Renew Energy* 96:341–353
15. Rezanejad K, Soares CG (2018) Enhancing the primary efficiency of an oscillating water column wave energy converter based on a dual-mass system analogy. *Renew Energy* 123:730–747
16. Rezanejad K, Souto-Iglesias A, Soares CG (2019) Experimental investigation on the hydrodynamic performance of an L-shaped duct oscillating water column wave energy converter. *Ocean Eng* 173:388–398
17. Zabihi M, Mazaheri S, Namin MM (2019) Experimental hydrodynamic investigation of a fixed offshore oscillating water column device. *Appl Ocean Res* 85:20–33
18. Zhang Y, Li M, Zhao X, Chen L (2020) The effect of the coastal reflection on the performance of a floating breakwater-WEC system. *Appl Ocean Res* 100:102117
19. Chen J, Wen H, Wang Y, Ren B (2020) Experimental Investigation of an annular sector OWC device incorporated into a dual cylindrical caisson breakwater. *Energy* 211:118681
20. Koley S, Kaligatla RB, Sahoo T (2015) Oblique wave scattering by a vertical flexible porous plate. *Stud Appl Math* 135(1):1–34
21. Koley S, Trivedi K (2020) Mathematical modeling of oscillating water column wave energy converter devices over the undulated sea bed. *Eng Anal Boundary Elem* 117:26–40
22. Gomes RPF, Henriques JCC, Gato LMC, Falcao ADO (2012) Hydrodynamic optimization of an axisymmetric floating oscillating water column for wave energy conversion. *Renew Energy* 44:328–339

Study of Human Behaviour During Lockdown Owing to Corona Epidemic



Brijesh Singh

1 Introduction

Outbreaks of epidemics account for a great number of deaths [1]. Across the globe, with more than 370 million patients and more than one million deaths, the Corona virus epidemic has brought the world to standstill like not even large scale conflicts or world wars could do. It has proved the power of the unknown, unfamiliar and small over the big, powerful and bulky countries, businesses and systems while attacking and ravaging and killing people and animals in different parts of the world. It has also made humans feel helpless and insignificant. Movements have been restricted for everyone, and all of these are confined to their homes.

Almost all the countries imposed lockdown and social distancing, just to reduce spread of Corona virus. Owing to this, citizens are residing at their present home location and abiding the rules and guidelines suggested by all concerned and competent authorities. Work from home, devoting time with family members and uncertainty about the Corona epidemic are influencing the obvious behaviour and attitude of human beings. Thus, during this ongoing period, it is important to know whether the public is really aware about Corona epidemic and is there any shift in their attitude/behaviour and time devoted to various regular activities? With these questions in mind or objectives, this study has been planned to be conducted.

B. Singh (✉)

Department of Mechanical Engineering, Galgotias College of Engineering and Technology,
Greater Noida 201306, India

e-mail: brijesh.singh@galgotiacollege.edu

2 Review of Literature

Corona virus that belongs to the genus Corona virus with its high mutation rate in the Corona viridae [2] causes respiratory infections that included common cold, Middle East respiratory syndrome, severe acute respiratory syndrome and COVID-19 [3]. World Health Organization (WHO), in the beginning of ongoing year, owing to high risk of spreading of Corona virus, declared COVID-19 as pandemic, and thus, the stress is being generated throughout the global population [4]. Spreading of Corona virus is a global public health emergency [5] that necessitates immediate actions to reduce spreading of COVID-19 and, thus, [6] insisted that learning of lessons for future is also very important. The epidemiology of the disease can be understood with the information of public behaviours/attitudes towards COVID-19 which is vital in its control and in reducing its spread [7, 8]. Spreading of Corona virus can be reduced by exercising lockdown and social distancing, and thus, these can be considered as defensive public health strategies [9], which is supported by [10]. West et al. [11] added isolation as measure and quoted that these measures offer huge cost to individuals and society [11].

According to a report published by [12], during this global crisis which is evolving at unprecedented speed and scale, governments and organizations have to take urgent actions to save the life of their citizens. This is changing human attitudes and behaviours at present. Human behaviour may be affected by a large numbers of factors that varies from media to person-to-person communication [13]. Additionally, behavioural responses are also affected by religious and cultural beliefs and norms that can be clustered both spatially and socially. Families play an important role in the development of individuals as the findings of [14] indicated that a significant positive relationship exists between family conflict, psychological needs and externalizing behaviour of preadolescents. Further, stay at home restrictions and other measures restricting the movement of people contribute to an increase in gender-based violence, a finding confirmed by media reports official statements and information received from human rights defenders in many countries [15].

In a research, [16], found that participants were reflecting a mile stressful state, the majority of participants (53.3%) did not feel helpless due to the pandemic; while on the other hand, about 52% of participants felt horrified and apprehensive due to the pandemic. Additionally, the majority of participants received increased support from friends and family members, increased shared feeling and caring with family. Even for households free from the virus, the pandemic is likely to function as a major stressor, especially in terms of chronic anxiety and economic difficulties. Such effects may be exacerbated by self-isolation policies that can increase social isolation and relationship difficulties [17]. Distress, boredom, social isolation and frustration are directly related to confinement, abnormally reduced social/physical contact with others and loss of usual habits [18]. Further, to understand the implications of the pandemic on the mental health and psychosocial well-being of children including the increased risk of violence and abuse and to provide resources for caregivers to help engage with children positively and effectively, a manual for parents and caregivers

entitled 'Psychosocial Support for Children during COVID-19' has been published by UNICEF [19].

3 Methodology

An online survey, in English language, was conducted through a questionnaire during April, 2020. Initial findings are discussed on the basis of descriptive statistics that uses mean, standard deviation (SD) and frequency distribution, using MS Excel. The Cronbach's Alpha is being computed for reliability analysis. Further, to establish a relationship among few identified variables, correlation analysis is being done. The bivariate correlation procedure computes Pearson's correlation coefficient (a measure of linear association), with its significance levels, that generally varies from -1 to $+1$ through 0 for acceptable results. To elaborate further, figures and tables are introduced at suitable places.

A total of 274 respondents (211—male and 63—female) participated in this online survey, out of which about 129 (47%) were of upto 20 years, 25 (9%) were of 20–30 years, 56 (21%) were of 30–40 years, 53 (19%) were of 40–50 years and 11 (about 4%) were of more than 50 years age. Further, a total of 148 students, 49 business/self-employed/professional personnel and 76 service-related personnel participated (1 respondent belongs to not-working category). About 152 respondents have their qualification upto under-graduation level, while 122 respondents have their qualification of post-graduation and above (57 respondents possessed PhD and above qualification). The respondents who were residing in villages were 55, in town were 37 and in cities were 182 respondents (that majorly included 79 respondents who were residing in flats/apartments and 72 respondents who were residing in open houses/posh colonies).

4 Findings of the Survey

4.1 *Present Health, Exercise Habit and Awareness Regarding Corona Epidemic*

In the reply of a question related to suffering of any prolonged disease and routine habit of doing exercise, 117 (42.7%) respondents quoted that they were neither suffering from any prolonged disease nor doing routine exercise, while 123 (44.9%) respondents replied that they were not suffering from any prolonged disease, but doing routine exercise. In its continuation, eight (2.9%) respondents replied that they were suffering from some minor disease, and in spite of this, they were not doing routine exercise, while 19 (6.9%) respondents reported that they were suffering from

Table 1 Awareness regarding Corona epidemic, symptoms and safety measures

S. No.	Parameter	Number of respondents	Per cent of respondents
1	Not aware about Corona epidemic	1	0.4
2	Little bit aware about Corona epidemic	5	1.8
3	Well aware about Corona epidemic	45	16.4
4	Well aware about Corona epidemic and symptoms of Corona infected people	36	13.1
5	Well aware about Corona epidemic, symptoms of Corona infected people and safety measure/care to be taken	187	68.2

some minor disease and were doing routine exercise. The seven (2.6%) respondents reported that they were suffering from major disease and taking utmost care. With this, it can be said that majority of people (142 respondents) whether suffering from any minor disease or not, doing routine exercises. Then, a question related to their awareness regarding prevailing Corona epidemic, symptoms of Corona infected people and care to be taken to avoid Corona infection were asked. Refer Table 1 for outcomes.

With this data, except six (2.4%) respondents, all were well aware about Corona epidemic. So, it can be inferred here that almost all the people are aware about Corona epidemic and symptoms and safety measures concerned with Covid 19.

4.2 Opening of Shops/Schools/Business Entities, etc.

The present situation related to opening of shops/schools/business entities, etc., at respondents residing location was enquired. In its reply, none reported for having situation (fully open and operational) similar to prior to lockdown. Only 17 (6.2%) respondents reported that shops/schools/business entities, etc., are operational with minor restrictions. In its continuation, 32 (11.7%) respondents reported that significant restrictions have been imposed on the shops/schools/business entities to be operational, and these have very limited freedom. A larger population, 201 (73.4%) respondents reported that there is complete lockdown, having availability of daily needs items like milk, grocery, etc., in their localities, while 24 (8.8%) respondents reported that there is curfew like situation in their residing locations. With this, it can be inferred that nearly 94% respondents reported that there is state of lockdown, and shops/schools/business entities, etc., are not operational with full pace. They are

following the imposed/requested restrictions just to safeguard from prevention and spreading of Corona.

4.3 Obedience of Social Distancing and Willingness to Participate in the Fight

A question related to obedience of social distancing and other measures suggested by government/competent authorities was asked from the respondents. In its reply, only one respondent reported for not having awareness about social distancing and other suggested measures and none reported that they are not following these restrictions. However, only eight (2.9%) respondents reported that they are following these rules and measures little bit, while 56 (20.4%) respondents reported that they are following these to a satisfactory level. A larger proportion, 209 (76.3%) respondents reported that they are following social distancing and taking utmost care in following all suitable measures to avoid spreading of Corona infection, as suggested by various competent authorities and government.

In its continuation, respondents were enquired about their willingness to participate in the fight against Corona by obeying further notified rules, measures and social distancing, etc. Only one respondent reported that he/she will not follow, and only one respondent reported that he will provoke others not to follow the rules, measures and social distancing. Out of total 274 respondents, 21 (7.7%) respondents reported that they will follow all such rules in future also, while 47 (17.2%) respondents reported that they will follow all of these rules and measures strictly. And, a larger portion of population, 204 (74.5%) respondents show their strict willing to obey all concerned rules, measures and social distancing and will request others to follow.

Here, it can be stated that almost all the people are following social distancing and taking care of other prescribed measures to avoid infection/spreading of Corona and shown their affirmation for such obedience in near future also.

4.4 Time Devoted to Various Activities

In prevailing situation of restrictions/lockdown, almost all the persons (except those who are involved in security like police, taking care of patients like doctors and health-workers, involved in essential services like bank, LPG distribution, sweeping/cleaning, shops of grocery, etc., distribution/supply of vegetables, fruits, milk, etc., and other related ones who are serving for society) are at home and indulged in the various activities, listed below, from present residing location. With this, the time devoted to these activities get increased/decreased/not affected. So, a questions, having multiple tick options, were asked from the respondents to state whether time devoted to these activities have been increased significantly, decreased significantly

Table 2 Effect on time spent in activities during ongoing lockdown state

S. No.	Activities on which change in time spent has been noticed (permitted for multiple entry)	Numbers of respondents (out of total 274) who reported for devoted time get ---		
		Increased	Reduced	No change
1	Work from home	149	38	42
2	Interaction with family members	173	36	61
3	Usages of Internet/online contents/chat/Whatsapp, etc.	177	42	54
4	TV	114	50	68
5	Indoor and outdoor games/playing with kids	77	112	39
6	Kitchen/cooking	116	30	63
7	Telephonic or mobile calls	76	75	83
8	Reading books, newspapers, novels, etc.	105	90	66
9	Skill learning/online courses/regular studies/trying or doing new knowledge gaining things	161	56	53

or not affected during prevailing situation. The outcomes are summarized in below mentioned Table 2.

With the help of Table 2, it can be seen that majority of respondent reported that the time devoted to ‘work from home’, ‘interaction with family members’, ‘usages of Internet, accessing online contents, chat, whatsapp, etc.’, ‘TV’, ‘Cooking/Kitchen’ and in ‘Skill Learning/Online Courses/Regular Studies/Trying or doing new knowledge gaining things’ has been increased significantly. Further, there is no change in the time spent in telephonic/mobile call. However, time devoted for indoor/outdoor games/playing with kids has been reduced in prevailing lockdown state.

4.5 Behaviour Towards Family Members

In prevailing restricted situations, the attitude/behaviour towards the family members may change. In this respect, 168 (61.3%) respondents reported for no change in their behaviour during ongoing lockdown. However, 45 (16.4%) respondents reported that their behaviour towards their family members became somewhat compromising, while 40 (14.6%) respondents reported for significantly compromising behaviour. In its extent, 14 (5.1%) respondents reported that their behaviour became somewhat rude, irritating and arguing, while seven (2.6%) respondents reported that their behaviour became significantly rude, irritating and arguing.

Table 3 Performance of local, district, state government and central government level authorities (numbers of responses, out of 274 total responses)

Level of authorities	Mean	Standard deviation	Very good (5)	Good (4)	Satisfactory (3)	Poor (2)	Very poor (1)
Local/district-level authorities	3.91	0.97	86	102	66	15	5
State level authorities (state government-related works)	4.11	0.90	106	111	44	8	5
Country level authorities (central government-related works)	4.26	0.88	132	96	36	6	4

In this way, during the lockdown, the change in human behaviour can be noticed for about 39% respondents, including about 8% respondents who were becoming rude and irritating. In contrary, about 31% respondents adopted compromising habit.

4.6 Support Provided by/Performance of Authorities

Overall performance of various authorities in the fight against Corona epidemic (in present scenario), as mentioned in Table 3, was enquired from the respondents. The value of Cronbach's Alpha is 0.790 that shows that outcomes are reliable.

With this data, it can be said that there are only little few respondents who are not satisfied with government support. Only ten (3.7%) respondents are not satisfied with central government, while 13 (4.7%) respondents are not satisfied with state level government/authorities, followed by 20 (7.3%) respondents who are not satisfied with local/district-level authorities. However, most of the people are appreciating the efforts of all the government authorities in the fight against Corona in prevailing situations. The support provided and performance of central government is well appreciated, followed by state government and then followed by district/local level authorities.

4.7 Correlation Among Age, Profession, Qualification, Awareness, Obedience and Behaviour

The correlation among various parameters that included age, profession, qualification and 'awareness regarding Corona Epidemic, its symptoms and safety measures', 'Obedience of Social Distancing and other prescribed measures', 'attitude/behaviour

Table 4 Pearson correlation values (Sig.—2-tailed)

Parameters	Age	Profession	Qualification	Awareness Corona epidemic	Obeying social distancing and other measures	Attitude towards family members
Age	1	0.817** (0.000)	0.825** (0.000)	0.032 (0.598)	0.136* (0.024)	0.065 (0.289)
Profession	0.817** (0.000)	1	0.750** (0.000)	0.033 (0.587)	0.122* (0.044)	0.090 (0.142)
Qualification	0.825** (0.000)	0.750** (0.000)	1	0.079 (0.190)	0.128* (0.034)	0.108 (0.078)
Awareness Corona epidemic	0.032 (0.598)	0.033 (0.587)	0.079 (0.190)	1	0.366** (0.000)	0.042 (0.494)
Obeying social distancing and other measures	0.136* (0.024)	0.122* (0.044)	0.128* (0.034)	0.366** (0.000)	1	0.033 (0.591)
Attitude towards family members	0.065 (0.289)	0.090 (0.142)	0.108 (0.078)	0.042 (0.494)	0.033 (0.591)	1

Correlation is significant at the 0.01 level** (2-tailed) and at the 0.05 level* (2-tailed)

towards family members' have been computed by using bivariate analysis that computed Pearson's correlation coefficient. The outcomes are presented in Table 4.

With Table 4, it can be inferred that there is strong correlation (significant correlation at 0.01 level) between age and profession, between age and qualification, between profession and qualification and between 'obeying social distancing and other prescribed measures' and 'awareness regarding Corona Epidemic', etc. Further, there is significant correlation at 0.05 level between age and obeying social distancing and other prescribed measures, between profession and obeying social distancing and other prescribed measures, between qualification and obeying social distancing and other prescribed measures. Thus, it can be inferred here that the age, profession and qualification influence obedience of social distancing and other prescribed measures concerned with Corona epidemic. In the same line, this can also be inferred that the awareness regarding Corona epidemic influences greatly the obedience of social distancing and other prescribed measures concerned with Corona epidemic.

Hence, it can be concluded that the obedience of social distancing and other prescribed measures concerned with Corona epidemic is influenced by age, profession, qualification and awareness regarding Corona epidemic.

5 Discussion

In prevailing situations, each nation is taking all suitable measures to safeguard their citizens from Corona infection and curing the Covid 19 infected patients. The suggested measures which are being adopted by almost all the nations include social distancing and lockdown. During lockdown state, outdoor and collective activities are banned, and citizens are being forced to stay at home, just to make them safe. Majority of people whether suffering from any minor disease or not, doing routine exercises as they want to remain fit. Immunity may also get better with routine small exercises.

People, in a majority, are well aware regarding Corona epidemic, ways through which people get infected and measures to be taken when any symptom similar to Covid infection is being noticed. In the lockdown state, everyone is following the restriction by their own as everyone feel that these restrictions are just to save their lives. People are staying at home and doing all regular activities in presence of their family members. With this, interaction time with family members gets increased, and in some cases, conflicting/arguing behaviour has been reported. However, there are many people who are following compromising behaviour just to avoid stress feeling and to ensure healthy and entertaining environment at home places. Work from home is the need for most of the personnel, and they are devoting much more time. In this respect, usages of Internet, accessing online contents, chat, whatsapp, etc., and in 'Skill Learning/Online Courses/Regular Studies/Trying or doing new knowledge gaining things has been increased significantly. However, time devoted for indoor/outdoor games/playing with kids has been reduced in prevailing lockdown state because of restrictions imposed by competent authorities. Citizens are well aware about Corona epidemic and appreciating the respective efforts of central government, state government and local/district-level authorities. Everyone must do all his own sincere efforts, in accordance with the instructions of government, so that we can remain safe from the Corona virus infection.

6 Conclusions

In this research, a total of 274 responses were collected through an online survey that was conducted in English language during April, 2020. In prevailing situations, every country is fighting with infection, spreading and deaths owing to Corona virus. In almost all the countries, the adopted measures include awareness programs, social distancing and lockdown. In this scenario, the outcome of this study shows that almost all the people are aware about Corona epidemic, and larger population is well aware about its symptoms and concerned safety measures. During the lockdown, shops/schools/business entities, etc., are not operational and following the imposed/requested restrictions just to safeguard from prevention and spreading of Corona. Almost all the people are following social distancing and taking care of

other prescribed measures to avoid infection/spreading of Corona and shown their affirmation for such obedience in near future also.

In its continuation, this has been identified that the behaviour of more than one-third respondents gets changed owing to prevailing lockdown state and nearly one-tenth respondents becoming rude and irritating, while nearly one-third respondents reported for adopting compromising behaviour with their family members. Indians are showing great faith in their government, and the performance of central government is anonymously well appreciated, followed by state government and district/local-level authorities’.

References

1. Dasaklis TK, Pappis CP, achaniotis N (2012) Epidemics control and logistics operations: a review. *Int J Prod Econ* 139(2):393–410. <https://doi.org/10.1016/j.ijpe.2012.05.023>
2. Sahin AR, Erdogan A, Agaoglu PM, Dineri Y, Cakirci AY, Senel ME, Okyay RA, Tasdogan AM (2019) Novel Corona virus (COVID-19) outbreak: a review of the current literature. *EJMO* 4(1):17. <https://doi.org/10.14744/ejmo.2020.12220>
3. Government of India (2020) Frequently asked questions on Corona, issued by Government of India. Available at <https://www.mohfw.gov.in/>. Accessed on 22 Apr 2020
4. Publication of World Health Organization (2020) Mental health and psychosocial considerations during the COVID-19 outbreak. Available at <https://www.who.int/docs/default-source/coronaviruse/mental-health-considerations.pdf>. Accessed on 22 Apr 2020
5. Zhang Y, Jiang B, Yuan J, Tao Y (2020) The impact of social distancing and epicenter lockdown on the COVID-19 epidemic in mainland China: A data-driven SEIQR model study. <https://doi.org/10.1101/2020.03.04.20031187>
6. Gates B (2020) Responding to Covid-19—A once-in-a-century pandemic? *New Engl J Med* 18:1677–1679. <https://doi.org/10.1056/nejmp2003762>
7. Lipsitch M, Swerdlow L, Finelli L (2020) Defining the epidemiology of Covid-19—studies needed. *N Engl J Med*. <https://doi.org/10.1056/NEJMp2002125>
8. Thelwall M, Thelwall S (2020) Retweeting for COVID-19: consensus building, information sharing, dissent, and lockdown life. Available at <https://arxiv.org/ftp/arxiv/papers/2004/2004.02793.pdf>. Accessed on 22 Apr 2020
9. Jribri S, Ismail HB, Doggui D, Debbabi H (2020) COVID-19 virus outbreak lockdown: what impacts on household food wastage. *Environ Dev Sustain* 22:3939–3955. <https://doi.org/10.1007/s10668-020-00740-y>
10. Tian H, Liu Y, Li Y, Wu CH, Chen B, Kraemer MU, Wang B (2020) The impact of transmission control measures during the first 50 days of the COVID-19 epidemic in China. <https://doi.org/10.1101/2020.01.30.20019844>
11. West R, Michie S, James RG, Amlot R (2020) Applying principles of behaviour change to reduce SARS-CoV-2 transmission. *Nat Hum Behav* 4:451–459. <https://doi.org/10.1038/s41562-020-0887-9>
12. Publication of Accenture (2020): COVID-19: 5 new human truths that experiences need to address. Available at https://www.accenture.com/_acnmedia/Thought-Leadership-Assets/PDF-2/Accenture-COVID-19-New-Human-Truths-That-Experiences-Need-To-Address.pdf. Accessed on 22 Apr 2020
13. Funk S, Bansal S, Bouch CT, Eames KTD, Edmunds WJ, Galvani AP, Klepac P (2015) Nine challenges in incorporating the dynamics of behaviour in infectious diseases models. *Epidemics* 10:21–25. <https://doi.org/10.1016/j.epidem.2014.09.005>
14. Kader Z, Roman N (2018) The effects of family conflict on the psychological needs and externalising behaviour of preadolescents. *Social Work* 54(1):613

15. Publication of United Nations Human Rights (2020) COVID-19 and women's human rights: guidance Available at https://www.ohchr.org/Documents/Issues/Women/COVID-19_and_Womens_Human_Rights.pdf. Accessed on 22 Apr 2020
16. Zhang Y, Ma ZF (2020) Impact of the COVID-19 pandemic on mental health and quality of life among local residents in Liaoning Province, China: a cross-sectional study. *Int J Environ Res Publ Health* 17:2381. <https://doi.org/10.3390/ijerph17072381>
17. Van Bavel JJ et al (2020) Using social and behavioural science to support COVID-19 pandemic response. *Nat Hum Behav* 4:460471. <https://doi.org/10.1038/s41562-020-0884-z>
18. Serafini G, Parmigiani B, Amerio A, Aguglia A, Sher L, Amore M (2020) The psychological impact of COVID-19 on the mental health in the general population. *QJM: Int J Med* 113(8):529–535. <https://doi.org/10.1093/qjmed/hcaa201>
19. A manual published by UNICEF: Psychosocial Support for Children during COVID-19. Available at <https://www.unicef.org/india/media/3401/file/PSS-COVID19-Manual-ChildLine.pdf>. Accessed on 09 Sept 2020

Numerical Investigation of Electro-osmotic Flow of Fluid in Tapered Microchannel



Ravinder Jhorar, Shashi Bhushan, RaviKumar Sharma,
and Dharmendra Tripathi

1 Introduction

Electrokinetic is the study of flow of ionic fluid induced with the application of static or alternating electric fields [1]. Electrokinetic flow process is vital in movement of fluids when electrically charged particle is there in ionic fluid. The development of nano- and micro-scaled channel in bioengineering played an important part in electrokinetics. This miniaturization of lab-on-a-chip created revolution in microfluidics. The microfluidic systems application is limited to a vast research field such as immunology, drug delivery, lab-on-a-chip development, and biomedical diagnostics [2].

Currently, computational as well as mathematical models are important means for the experimental studies. Moreover, they amplify the novel designs, and those are problematic for persistent execution in diverse domain of medicine, aerospace, and other field of engineering. Paul et al. [3] considered the use of electrokinetic pump in micro-total investigation systems. He studied the fluid flow via a porous medium and offered the model and experimental outcomes for the frequency response for this pump.

Kang et al. [4] examined the installation of electrokinetic micro-pumps and flow characteristics. Sayed et al. [5] and tripathi et al. [6] studied the electro hydrodynamic upshots on the peristaltic movement of dielectric oldroyd fluid which shows elastic and viscous behavior during deformation while transmitting from a flexible microchannel. Sinha and Shit [7] have taken in account the electro magneto hydrodynamic results with heat transfer by radiation on flow of blood through capillary. Electro magneto hydrodynamic and heat transfer consequences on the model of non-Newtonian fluid through two microchannel were examined by Wang et al. [8].

R. Jhorar · S. Bhushan · R. Sharma
Manipal University Jaipur, Jaipur, India

D. Tripathi (✉)
National Institute of Technology, Srinagar, Utarakhand, India

In recent times, Oh [9] presented the mathematical study by applying magnetic field in transverse direction on a peristaltic wave with electrical double layer effects.

Shuaib et al. [10] study viscous fluid rotating through disk, and electric field is applied across the disk. In this paper, the governing equations were solved numerically by means of parametric continuation method.

Mahbub et al. [11] studied electrokinetic fluid flow in wavy channel. The numerical solution of electro-osmotic flow in wavy channel is with the help of COMSOL.

Duffle et al. [12] have done CFD modeling of microscale mixing of conductive fluids driven by applying electric field externally and predicted that velocity is increasing with increase in electric field.

Zhao et al. [13] have studied flow of non-Newtonian fluid actuated with the help of electric field in a rectangular microchannel. Authors presented that the flow with a higher value of behavior index ‘n’ responds more quickly to the external applied DC electric field and reaches the steady state more quickly.

Some past studies are presented in tabulated form. Apart from duffer et al. and Zhao et al., all other papers tabulated here had solved governing equations mathematically.

Author (year)	Physiological flows	Electoosmosis	Nano fluids	Power law fluids
Chakraborty et al. (2008)	N	Y	Y	N
Murshed et al. (2008)	N	Y	Y	N
Xuan (2008)	N	Y	N	N
Choi et al. (2011)	N	Y	Y	N
Mao et al. (2015)	Y	Y	N	N
Prasad et al. (2015)	N	Y	Y	N
Shirsavar et al. (2015)	N	Y	N	N
Tripathi et al. (2016)	Y	Y	N	N
Chakraborty et al. (2016)	Y	Y	Y	Y
Rokni et al. (2016)	N	Y	Y	N
Tripathi et al. (2016)	N	N	N	N
Duffle et al. (2018)	N	Y	N	N
Zhao et al. (2017)	N	Y	N	Y

Based on the above applications and discussion, the main emphasis of the current study is to study the electrokinetic transfer through tapered medium with Newtonian fluid. This induced electro-osmotic flow in tapered nano-channel is governed by physics involved in laminar flow, electric current, and transport of diluted species.

This multiphysics phenomenon is solved with the help of COMSOL. The effect of various parameters such as zeta potential and applied potential field is discussed for velocity profile, pressure variation along the axis, trapping phenomenon, and flow rate. This study is helpful in development of organ on a chip and for drug delivery applications.

2 Methodology

COMSOL (5.3) multiphysics divides a large numerical problem having nonlinear equations into smaller parts (small meshing element) for the outcome of approximate solutions to boundary value problems for nonlinear governing equations. The workflow is stated in given Fig. 1.

A tapered channel generated with the help of bezier curve in COMSOL. The fluid considered in channel is ionic fluid, and flow is taking place with the application of fluid. To govern this flow, electric current, creeping flow, and transport of diluted species have been selected.

Electric Current: The governing equations in electric current physics is

$$\nabla \cdot J = Q_i$$
$$J = \sigma E + J_e$$

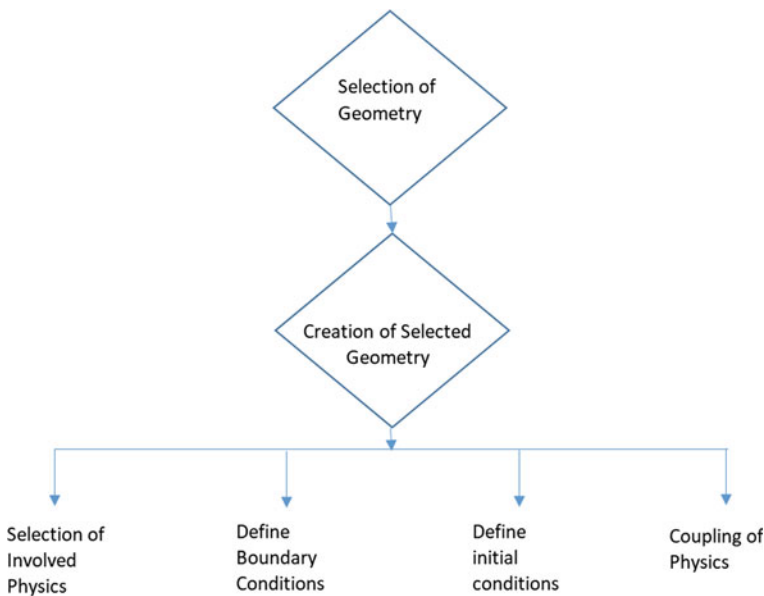


Fig. 1 Workflow for the problem

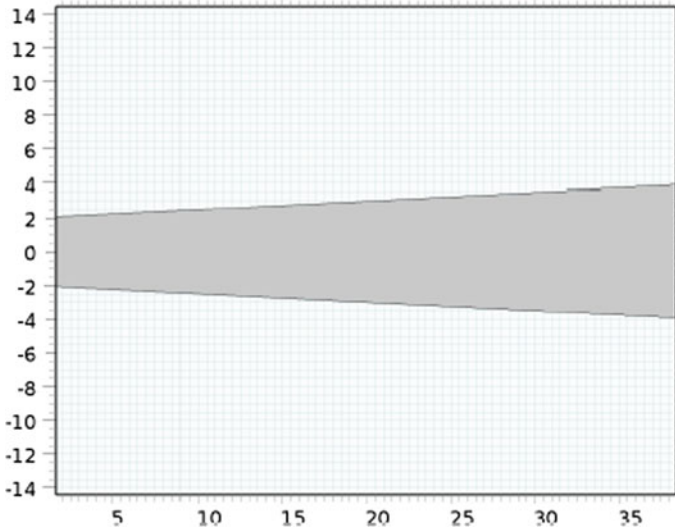


Fig. 2 Geometry of tapered channel

$$E = -\nabla V$$

The inlet boundary provided electric potential of 100 V and outlet boundary grounded. Walls of channel have been given zeta potential (Fig. 2).

Creeping flow: To govern fluid flow, naviers stocks equation is used with equation of continuity. Since flow is taking place, only due to application of electric field so at inlet and outlet boundary, zero pressure is provided.

$$\rho \frac{\partial u}{\partial t} = \nabla[-PL + \mu(\nabla u + (\nabla u)^T)] + F$$

$$\frac{\partial \rho}{\partial t} + \rho \nabla \cdot (u) = 0$$

Transport of Diluted Species: In COMSOL, we have selected physics of transport of diluted species to govern the ionic distribution. At inlet, initial concentration was provided, and outlet was selected.

$$\frac{\partial c_i}{\partial t} + \nabla \cdot (-D_i \nabla c_i) + u \cdot \nabla c_i = R_i$$

$$N_i = -D_i \nabla c_i + u c_i$$

3 Result and Discussion

This part offers the graphical results of the parameters associated in the modeled fluid flow issue. The results are generated at different applied voltage of 100, 200, and 300 V to envision the nature of volume flow rate Q , potential function Φ , pressure rise Δp , and velocity profile u in tapered microchannel.

In Fig. 3, generated velocity profile at applied voltage of 200 V in tapered channel is shown. This flow is plug type of flow at initial section and converted into fully developed flow at the end of section.

Figure 4 presents variation of velocity at different applied voltage. It is evident from the figure that velocity magnitude is increasing with increase in potential value. The flow profile generated in channel is plug profile which one is characteristics of electro-osmotic flow [3].

Figure 5 presents pressure variation along the axis of channel with applied voltage. It is clearly evident that high pressure is being generated at higher voltage. Pressure decrease along the axis as voltage decrease.

From Fig. 6, it can be deduce that velocity is increasing with increase in zeta potential. Velocity profile is drawn for zeta potential -10 , -20 , and -30 mV at applied voltage of 100 V.

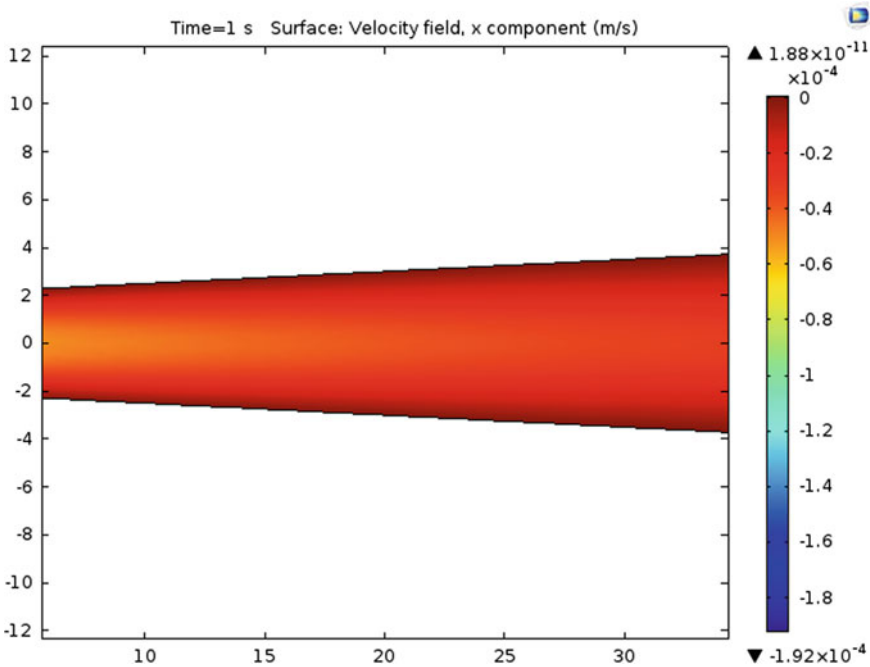


Fig. 3 Velocity profile in tapered channel at 200 V

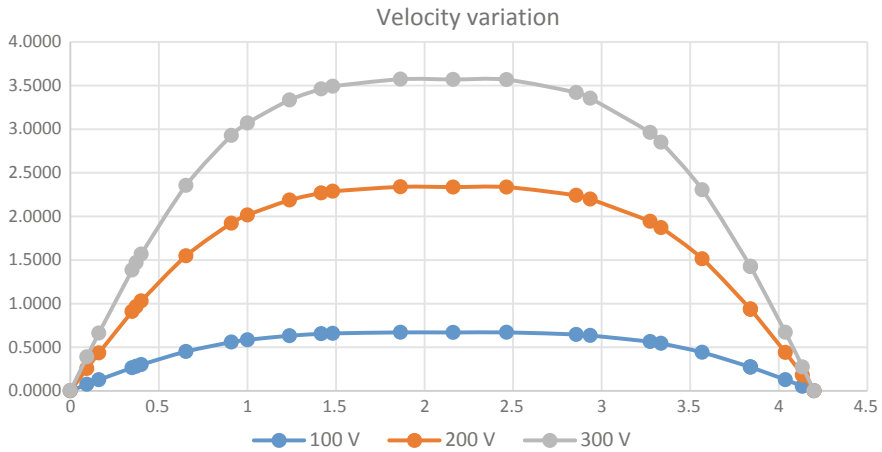


Fig. 4 Velocity variation with different applied voltage 100, 200, and 300 V

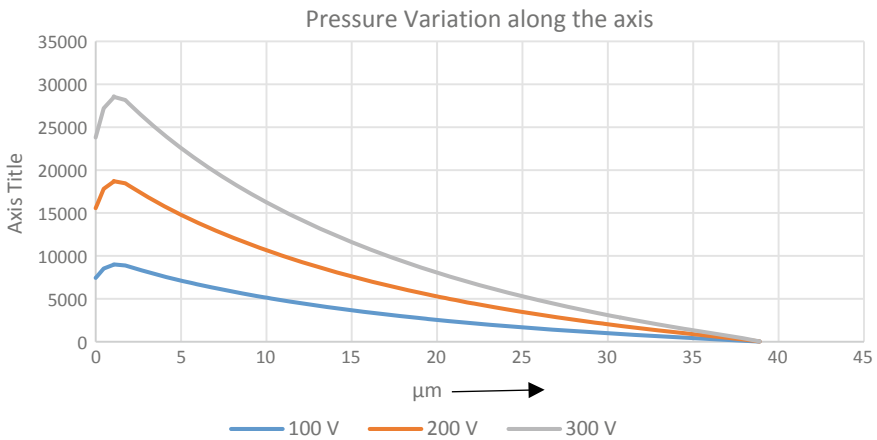


Fig. 5 Pressure variation at different applied voltage 100, 200 and 300 V

4 Conclusion

The present numerical results may provide deep understanding into electrokinetic flow mechanisms for the applications which involves microscale channels including lab-on-a-chip devices for drug delivery, various fluid flow mixing, cell manipulation, etc. Since lot of work related to electrokinetic flow reported is solved analytically, we need to use lubrication approximation and low Reynold number assumption to convert nonlinear governing equation into linear one [4]. This numerical method by COMSOL will avoid such approximation, and published results can be compared. The current work has been limited to a one-fluid model and has overlooked slip

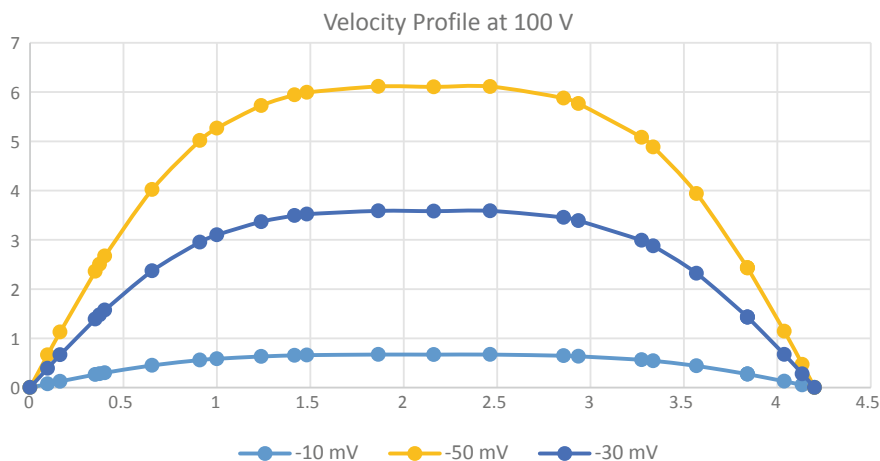


Fig. 6 Velocity variation with zeta potential -10 , -30 and -50 V

effects at the walls, and geometry considered is simple tapered conduit. The non-Newtonian fluid with complex geometry may institute interesting ways for spreading the current work and will be addressed in future.

References

1. Chang CC, Yang RJ (2007) Electrokinetic mixing in microfluidic systems. *Microfluid Nanofluid* 3:501–525
2. Jiwanrao MV (2016) Modeling of electrokinetic mixing in lab on chip microfluidic devices. Doctoral dissertation, Indian Institute of Technology Hyderabad
3. Paul PH, Arnold DW, Neyer DW, Smith KB (2000) Electrokinetic pump application in micro-total analysis systems mechanical actuation to HPLC. In: *Micro total analysis systems 2000*. Springer, Netherlands, pp 583–590
4. Kang Y, Tan SC, Yang C, Huang X (2007) Electrokinetic pumping using packed microcapillary. *Sens Actuat* 133:375–382
5. El-Sayed MF, Haroun MH, Mostapha DR (2014) Electrohydrodynamic peristaltic flow of a dielectric Oldroydian viscoelastic fluid in a flexible channel with heat transfer. *J Appl Mech Tech Phys* 55(4):565–577
6. Tripathi D, Jhorar R, Bég, OA, Shaw S (2018) Electroosmosis modulated peristaltic bio-rheological flow through an asymmetric microchannel: mathematical model. *Meccanica* 53(8):20792090
7. Sinha A, Shit GC (2015) Electromagnetohydrodynamic flow of blood and heat transfer in a capillary with thermal radiation. *J Magn Magn Mater* 378:143–151
8. Wang L, Jian Y, Liu Q, Li F, Chang L (2016) Electromagnetohydrodynamic flow and heat transfer of third grade fluids between two micro-parallel plates. *Colloids Surf* 494:87–94
9. Oh KW (2012) Lab-on-chip (LOC) devices and microfluidics for biomedical applications. In: *MEMS for biomedical applications*, pp 150–171. Woodhead Publishing
10. Shuaib M, Shah RA, Durrani I, Bilal M (2020) Electrokinetic viscous rotating disk flow of Poisson-Nernst-Planck equation for ion transport. *J Molecul Liq* 113412

11. Adamek J, Fromme L. Numerical analysis of electroosmotic flow through capillaries
12. Duffie WL, Lemley EC (2018) Electrokinetically forced turbulence in microfluidic flow
13. Zhao C, Zhang W, Yang C (2017) Dynamic electroosmotic flows of power-law fluids in rectangular microchannels. *Micromachines* 8(2):34
14. Chakraborty S, Das S (2008) Streaming-field-induced convective transport and its influence on the electroviscous effects in narrow fluidic confinement beyond the Debye-Hückel limit. *Phys Rev E* 77(3):037303

Optimal Placement of Distributed Generators in Power System Using Sensitivity Analysis



Anoop Arya , Swatantra Singh Verma, Shweta Mehroliya, Shilpi Tomar, and C. S. Rajeshwari

1 Introduction

Electricity is the most popular and clean form of energy, being utilized in the world, today. The electrical power is the major source of the world today. Due to economics of scale and environmental concerns, generation facilities have been favoring for large power plants, which are of the order of hundreds of mega-watts and located in non-populated areas away from the loads. The generation plants that operate on coal or nuclear fuel cause a lot of pollution. The energy available from sun and wind are absolutely clean and do not produce any pollutants that can damage the atmosphere. Solar cells and windmills can be installed, and electricity can be produced from them. DG cost has recently decreased because of introduction of new technologies, which are more viable. It is hard to add new transmission lines due to its high cost and problem of right of way considering the fact that the existing lines are getting overloaded, and there is a need to add the new generation closer to the load centers. This requires new technologies and distributed generation to be adopted.

Distributed generation uses small electrical power generations by its definition and nearly less than 30 MW located near to the load centers. Deployment of distributed energy system on the consumer side acts as a supplement to the micro-grid that enhances reliability of the power system and provides continuity of power supply to critical loads in case of grid collapse and natural disasters such as earthquake

A. Arya (✉) · S. Mehroliya
Maulana Azad National Institute of Technology, Bhopal, India

S. S. Verma
Chhattisgarh Swami Vivekanand Technical University, Bhilai, India

S. Tomar
SATI, Vidisha, India

C. S. Rajeshwari
NITTTR, Bhopal, India

and war [1]. There are many solar system, micro-turbine and wind turbine system that can be distributed generation. Basically, a DG is a small electric power system, which is placed near to the consumer side and satisfies end user demand. A distributed energy system satisfies end user load demand and also solves the difficulties of power transmission system over long distances [2].

Sizing and proper location allotment plays an important role in distributed generation. Once proper allotment of location is done, then the system has lower losses [3, 4]. Sensitivity factors obtained from sensitivity analysis are applied to find the candidate bus locations for best installment of DG units in the radial system [1]. Several optimization programming like linear, nonlinear programming, and mixed integer linear programming have done for best siting of DG [5]. Optimal DG placement improves system performance and voltage stability [6], and thus, it enhances the system reliability. Multiple DG allocation in the distribution system reduces the loss factor [7]. Various computational techniques have been seamlessly applied to solve the optimization and performance evaluation in power system [8, 9]. The optimal locator index factor has introduced in obtaining the best siting and sizing of distributed generation [10, 11]. A new methodology has been developed for optimization and coordination of the placement of dispersed generators [12, 13]. MATLAB [14] has been used as a tool for the analysis of the algorithm.

2 Research Methodology

2.1 Network Losses

Distribution network in the electric power system having high R/X ratio of lines suffers from the significant power loss. The losses are dependent on the line resistances and current flows in the lines. While the line resistances are fixed, the current flows in the lines are dependent on the network parameters and the loading [15]. The complex power injection (S_i) at any bus I can be expressed as

$$S_i = P_i + jQ_i \quad (1)$$

where P_i and Q_i are the real and reactive power injection at bus i . The power flow equations describing power balance at bus i can be shown as,

$$P_i = V_i \sum_{j=1}^n Y_{ij} V_j \cos(\delta_i - \delta_j - \theta_{ij}) \quad (2)$$

where various notations have their usual meaning as described in [3]. The system loss is defined as

$$P_L = \sum_{i=1}^n P_{G_i} - \sum_{i=1}^n P_{D_i} \tag{3}$$

where P_L is total real power loss; P_{G_i} and P_{D_i} have their usual meaning at node- i . The losses in the above equation may perhaps be difficult to calculate investigative. For this reason, a method known as ‘‘Exact loss formula’’ is employed for loss calculation.

The loss formula is expressed as,

$$P_L = \sum_{j=1}^n \sum_{i=1}^n \alpha_{ij}(P_i P_j + Q_i Q_j) + \beta_{ij}(Q_i P_j - P_i Q_j) \tag{4}$$

where n defines number of buses; α_{ij} and β_{ij} are loss coefficients. The expressions for loss coefficients are given as [16]

$$\alpha_{ij} = \frac{r_{ij}}{V_i V_j} \cos(\delta_i - \delta_j) \tag{5}$$

$$\beta_{ij} = \frac{r_{ij}}{V_i V_j} \sin(\delta_i - \delta_j) \tag{6}$$

where r_{ij} is the real part of the ij th element of Z_{Bus} matrix.

2.2 Optimal Placement of DG

In this work, a set of loss sensitivity factors, utilizing the load flow equations, has been used to establish the optimal location for placement of dispersed generators. A sensitivity index (SI) has been used to discover and rank the nodes, within the network, with respect to adding new generation. From the expression of exact loss formula as given in Eqs. (5) and (6), the loss sensitivity factors with respect to real and reactive power injections are derived as,

$$C_{pi} = \frac{\partial P_L}{\partial P_i} = 2 \sum_{j=1}^n (\alpha_{ij} P_j - \beta_{ij} Q_j) \tag{7}$$

$$C_{qi} = \frac{\partial P_L}{\partial Q_i} = 2 \sum_{j=1}^n (\alpha_{ij} Q_j + \beta_{ij} P_j) \tag{8}$$

Since the distributed generation is used to supply mainly real power, only real power sensitivity factor (C_{pi}) for placement of DGs has been considered. Ranking of buses for DG placement has been done on the basis of decreasing order of absolute

sensitivity values. The optimal locations, according to the number of DGs to be placed, have been chosen starting from the highest sensitive bus.

3 Test System

The efficacy of the projected method has been demonstrated on a 15-bus test system. To evaluate the system performance under different conditions, a computer program in MATLAB was developed for distribution load flow (DLF) [5, 6] having multiple sources. The loss sensitivities were evaluated for the 15-bus system, and the impact of the installation of the DGs was studied, as given below. Figure 1 shows you the line diagram of the 15-bus test arrangement; the line and load data are given in Table 1. The distribution feeder is emanating from a 132/11 kV grid substation. The grid substation (bus number one) is considered to be slack bus. The total real and reactive power loads in the network are 1226 KW and 1251.07 KVAR correspondingly (p.f of load is 0.7).

For this system, two cases were considered.

- Case 1: base case
- Case 2: outage of line 3–11 and interconnector between bus 8–13 switched on

The resistance and reactance of the interconnectors were taken as 0.32530Ω and 0.42360Ω , respectively.

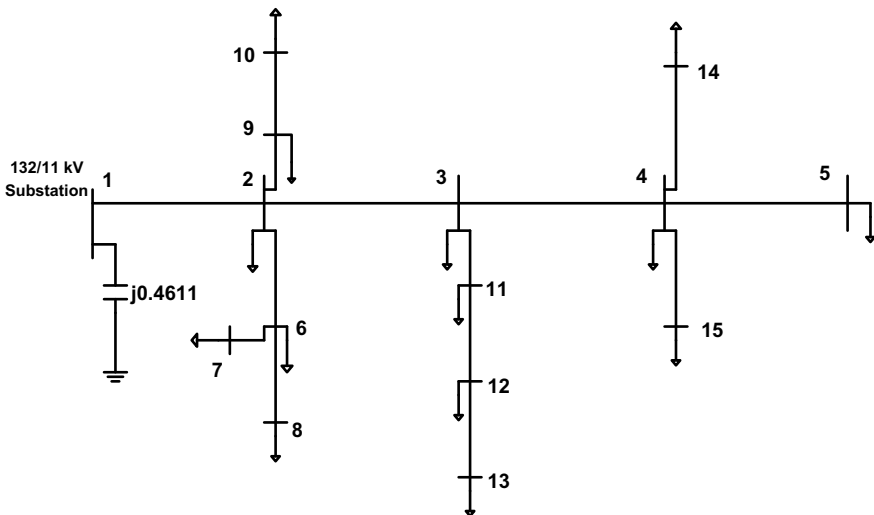


Fig. 1 Line diagram of 15-bus test arrangement

Table 1 Line and load data

Line data					Load data		
Branch no.	Sending node	Receiving node	Line impedance		Bus no.	Real power in kW	Reactive power in kVAR
			R (in ohm)	X (in ohm)			
1	1	2	1.35309	1.32349	1	0	0
2	2	3	1.17024	1.14464	2	44	44.98
3	3	4	0.84111	0.82271	3	70	71.41
4	4	5	1.52348	1.02760	4	140	142.82
5	2	9	2.01317	1.35790	5	44	44.98
6	9	10	1.68671	1.13770	6	140	142.82
7	2	6	2.55727	1.72490	7	140	142.82
8	6	7	1.08820	0.73400	8	70	71.41
9	6	8	1.25143	0.84410	9	70	71.41
10	3	11	1.79553	1.21110	10	44	44.98
11	11	12	2.44845	1.65150	11	140	142.82
12	12	13	2.01317	1.35790	12	70	71.41
13	4	14	2.23081	1.50470	13	44	44.98
14	4	15	1.19702	0.80740	14	70	71.41
-	-	-	-	-	15	140	142.82

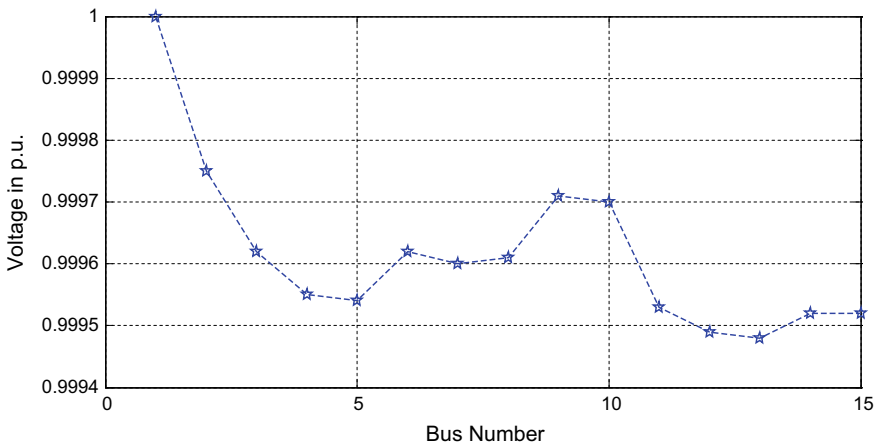


Fig. 2 Voltage summary for 15-bus test system (case 2)

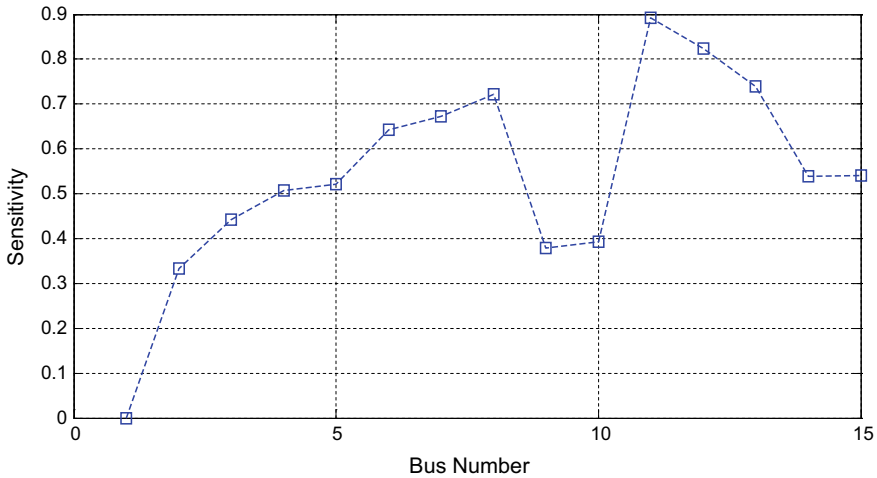


Fig. 3 Real power sensitivity of 15-bus test system (base case)

3.1 Case 1: Base Case

The voltage magnitudes at all the buses are shown in Fig. 2. The real power loss sensitivities at all the buses are presented in Fig. 3. For sensitivity calculation, one needs non-singular Z-bus matrix, but for any radial distribution network, Z-bus matrix is singular. Thus, to make Z-bus non-singular, a shunt of value 0.4611 p.u. was considered to be connected at the slack bus.

From Fig. 2, it is seen that the voltage is the lowest at bus-13, followed by bus 14 and 15. The maximum value of loss sensitivity is 0.66525 at bus-13. Thus, it is the most appropriate location for DG placement. Bus-12 is the next choice, as it has second highest loss sensitivity factor. Table 2 shows the value of voltages, sensitivity factors, and ranking for all the buses.

3.2 Case 2: Outage of Line 3–11 and Inter Connector Between Bus 8–13 Switched On

In this case, interconnector between bus-8 and bus-13 was switched on, and outage of line between bus-3 and bus-11 was considered as shown in Fig. 4. For case-2, the system real and reactive powers loss are 70.15 kW and 61.27 KVAR. The voltage magnitudes at all the buses are publicized in Fig. 5. The real power loss sensitivities at all the buses are presented in Fig. 6.

From Fig. 5, it is clear that voltage is lowest at bus-11, followed by bus 12 and 13. The maximum value of loss sensitivity is 0.8925 at bus-11. Thus, it is the most appropriate location for installment of DG. Bus-12 is the next choice, as it has second

Table 2 Voltage and sensitivity factor for 15-bus system (case-1)

Bus no.	Voltage (magnitude in p.u.)	Sensitivity factor	Rank of bus
1	1.00000	0.00000	15
2	0.99975	0.33205	14
3	0.99962	0.50030	11
4	0.99955	0.56667	7
5	0.99954	0.58008	6
6	0.99962	0.51125	10
7	0.99960	0.54175	8
8	0.99961	0.52878	9
9	0.99971	0.37799	13
10	0.99970	0.39283	12
11	0.99953	0.59161	5
12	0.99949	0.64751	2
13	0.99948	0.66525	1
14	0.99952	0.59792	4
15	0.99952	0.60022	3

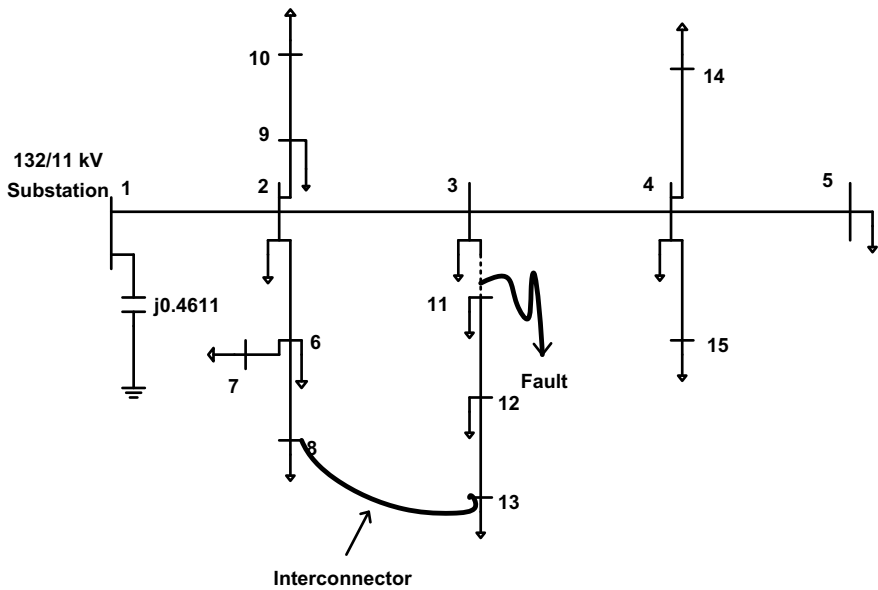


Fig. 4 Line diagram of 15-bus arrangement (case 2)

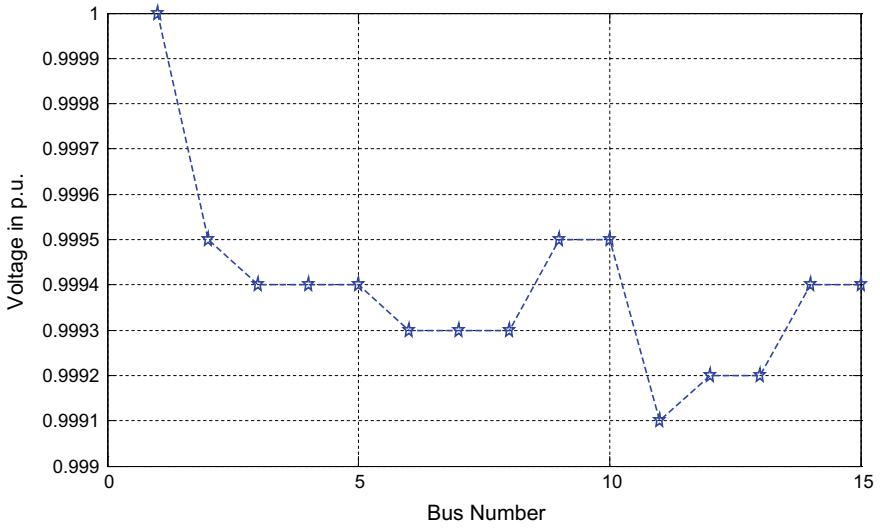


Fig. 5 Voltage profile for 15 bus test system (case 2)

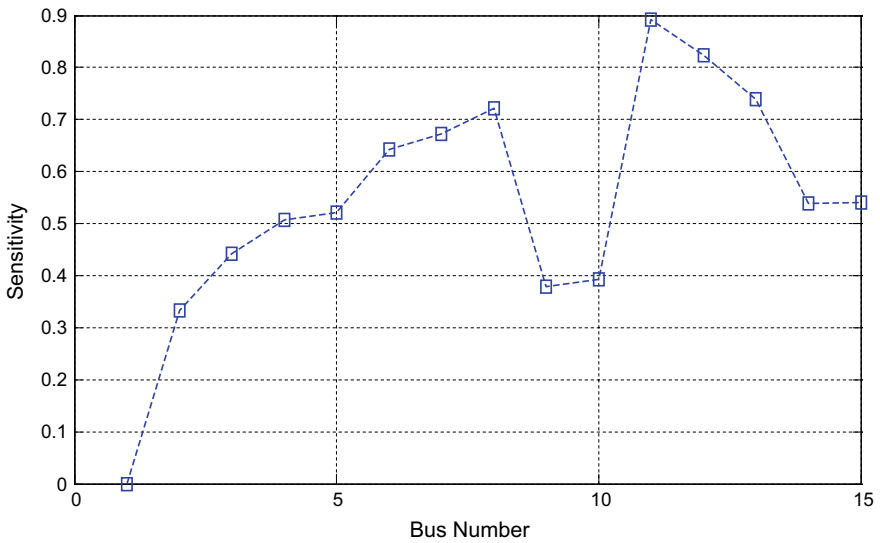


Fig. 6 Real power sensitivity of 15-bus test system (case-2)

highest loss sensitivity factor. Table 3 shows the value of voltages, sensitivity factors, and ranking for all the buses.

Table 3 Voltage and sensitivity factors for 15-bus system

Bus no.	Voltage magnitude (p. u.)	Sensitivity factor	Rank of bus
1	1.0000	0.0000	15
2	0.9995	0.3325	14
3	0.9994	0.4413	11
4	0.9994	0.5070	10
5	0.9994	0.5208	9
6	0.9993	0.6419	6
7	0.9993	0.6723	5
8	0.9993	0.7223	4
9	0.9995	0.3785	13
10	0.9995	0.3924	12
11	0.9991	0.8924	1
12	0.9992	0.8239	2
13	0.9992	0.7394	3
14	0.9994	0.5386	8
15	0.9994	0.5408	7

4 Results

Results presented in Table 4 shows the ranking of buses for DG placement in the below two different cases. It is observed that in case-2, only three out of five ranked buses (in other cases) appear viz. bus-11, bus-12, and bus-13. Hence, as a compromise between the cases, the bus-12 and bus-13 have been selected for DG placement.

An efficient set of sensitivity factors has been suggested in this paper, for locating the optimal location of DGs in the system. A load flow program was developed for distribution network with multiple sources to study the impact of DGs. For 15-bus system, sensitivities at the base case and reconfigured cases were determined, and the best locations for DG placement were found to be at bus-13 and bus-11.

Table 4 Ranking of buses for 15-bus system

Rank of buses	Case 1 (Bus no.)	Case 2 (Bus no.)
1	13	11
2	12	12
3	15	13
4	14	8
5	11	7

5 Conclusion

On-site generation allows for the use of new renewable technologies, such as micro-turbines and combined heat and power (CHP), fuel cells which are having better efficiencies. Dispersed generation will also lower the emissions of pollutants and minimize operating costs through reducing losses and increased efficiencies.

A sincere attempt has been made in this paper, to find the most suitable location for DG placement, in order to minimize the system loss. In addition, it has also focused on evolving strategies for finding the optimum output of DGs. The most important and vital contribution of this paper is to suggest a loss sensitivity factor of dispersed generation for its suitable deployment and evolves an optimal power flow-based formulation to determine the optimal settings of DGs.

In this paper, several case studies for different configuration of the network were performed to find the appropriate site for DG assignment. The most optimum locations for the DG placement were found, where the loss sensitivity was maximum in most of the cases. Accordingly, few buses were ranked based on decreasing order of the loss sensitivity magnitude, and several combinations of DG placements were studied on 15-bus distribution networks. The results of the case studies reveal that in all the combinations of DGs considered, the system loss has considerably reduced. Thus, the proposed loss sensitivity factors can be effectively used for the DG placement.

Acknowledgements This research work was supported by the research project under the YFRF, Visvesvaraya PhD scheme of MeITy, Govt. of India, implemented by D.I.C. (Previously Media Lab Asia). We are furthermore immensely grateful to MANIT, Bhopal for extending us the requisite amenities during the span of this project.

References

1. Sridevi J, Usha Rani V, Rao BL (2020) Integration of renewable DGs to radial distribution system for loss reduction and voltage profile improvement. In: International Conference on Electrical, Control and Instrumentation Engineering
2. Gopiya Naik S, Khatod D, Sharma M (2013) Optimal allocation of combined DG and capacitor for real power loss minimization in distribution networks. *Int J Electr Power Energy Syst* 53:967–973
3. Usha Rani V, Sridevi J (2017) Loss minimization and voltage profile improvement with network reconfiguration and distributed generation. *Int J Comput Eng Res Trends* 4(10):449–455
4. Jain N, Singh SN, Srivastava SC (2010) Particle swarm optimization based method for optimal siting and sizing of multiple distributed generators. In: 16th national power systems conference, Hyderabad
5. Pesaran M, Huy PD, Ramachandara Murthy VK (2017) A review of the optimal allocation of distributed generation: objectives, constraints, methods, and algorithms. *Renew Sustain Energy Rev* 75:293–312
6. Georgilakis PS, Hatziargyriou ND (2013) Optimal distributed generation placement in power distribution networks: models, methods, and future research. *IEEE Trans Power Syst* 28(3):3420–3428

7. Hung Q, Mithulananthan N (2013) Multiple distributed generator placement in primary distribution networks for loss reduction. *IEEE Trans Industr Electron* 60(4):1700–1708
8. Arya A, Mathur SPS, Dubey M (2020) Optimal generator side bidding with carbon emission trading and risk management. *CSIT, Springer Nature* 8:235–240
9. Priyadarshi R, Thakur T, Arya A (2019) Performance evaluation in rural electrification sector of India. In: 8th international conference on power systems (ICPS), Jaipur, India, pp 1–6
10. Lee SH, Park J-W (2013) Optimal placement and sizing of multiple DGs in a practical distribution system by considering power loss. *IEEE Trans Indus Appl* 49(5)
11. Carpinelli G, Celli G, Pilo F, Russo A (2001) Distributed generation siting and sizing under uncertainty. *IEEE Porto power tech proceedings (Cat. No.01EX502)*, Porto, Portugal, p 7, vol 4
12. Keane A, O'malley M (2005) Optimal allocation of embedded generation on distribution networks. *IEEE Trans Power Syst* 20(3):1640–1646
13. Acharya N, Mahat P, Mithulananthan N (2006) An analytical approach for DG allocation in primary distribution network. *Int J Electr Power Energy Syst* 28:669–678
14. MATLAB Primer R2018a, Math works. <https://www.mathworks.com>
15. Yammani C, Naresh S, Sydulu M, Matam SK (2011) Optimal placement and sizing of the DER in distribution systems using shuffled frog leap algorithm. In: *IEEE recent advances in intelligent computational systems*, 22–24 September 2011, Trivandrum, India
16. Hung DQ, Mithulananthan N, Bansal RC (2010) Analytical expression for DG allocation in primary distribution networks. *IEEE Trans Energy Convers* 25(3)

A Review on Performance of Electric Motor Vehicle



Gagandeep Singh, Harshit Manchanda, and Sunny Bhatia

1 Introduction

The increase in pollution is a major problem in today's life. So many automotive industries are focusing more on electric vehicle technology. Electric vehicles are eco-friendly and have a big hand in reducing global environmental pollution because transportation sectors are responsible for approximately 25% of global CO₂ emission [1]. These vehicles enjoy a lot of benefits over IC engines and reduce dependence on petroleum depletion. It has high efficiency, zero-emission, quiet operation, and cost-saving operation. Electric motor vehicle has better over the gasoline vehicle, but it has one major drawback. Electric motor vehicles are facing a major problem nowadays like the range and charging time of the vehicle. Studies have shown that weather control loads will significantly range reduction in both winter and summer seasons [2]. Manufacturers are trying to scale back this problem by using various cooling or heating systems for battery packs [3]. Manufacturers of electrical motor-cars sometimes make use of an electrical pre-heat function to warm up the battery during charging [4]. Through this paper, we will discuss some ways to extend electric vehicle performance and range. We have got and shown some factors which influence the electrical vehicle range and check out to beat it by make use of suitable battery charging system. On the opposite hand, battery size affects the vehicle curbs weight and price [5]. The proper size of the battery pack also can extend the range of the vehicle [6]. If your vehicle is running less distance not more than 50 km in a day only for the office purpose with a 24 kWh battery pack but 50 km distance electric vehicle can be used with half battery capacity means 12 kWh or 8 kWh. The charging of EV influences the scattering grid because these vehicles require a large amount of energy, and this demand for electrical energy can lead to the consumption of more electricity. The batteries of EV can be charged at petrol pumps or at our houses.

G. Singh (✉) · H. Manchanda · S. Bhatia
Department of Automobile Engineering, Manav Rachna International Institute of Research and Studies, Faridabad, India

The alternate of conventional vehicles by EVs also will need a particular or specific charging infrastructure. Several solutions may arise to suit different EV owners' needs, namely charging stations dedicated to fleets of EVs, fast chargers at petrol pumps, battery charging stations, charging facilities at homes. Battery and electric cell EVs only run on electrical power while current hybrid EVs have also an inside combustion engine. Since the hybrid, EVs require high-capacity batteries and with big voltage capacity, this results in create an enormous impact on electrical power system design and operation but will allow using the non-polluting energy resources [7, 8]. In this present paper, we are proceeding to discuss the methods that how to increase the range of vehicles and making it more convenient for the customers and can they use it without any major problem. We must need to enhance the range of the electric motor vehicle by using suitable methods. We need to enhance the range of the electric motor vehicle because EV's average range is very shorter, and it is around 200 miles, and it is very lower as compared to the conventional vehicles for the long-distance routes. Electric vehicle recharging stations are also very few and located very far from each other. So, in this case, if our battery is discharged between the stations, we cannot do anything. So, here we proposed some ways to increase the EV range to make electric vehicles more efficient.

2 Factors Influencing the Electric Vehicle Range

There are mainly three factors that influence the vehicle range the vehicle design, driver driving style, and external environment.

2.1 Vehicle Design

The effect of the maker or manufacturer and design of electric automobile has also may impact on the range. In-vehicle design, generally, we focused on the overall dimension of the vehicle, passenger space, body type, luggage space, type of tire, and the construction of the vehicle should be kept in view of all the forces acting on it. It should be mentioned that the body of an electrical automobile influence the air pull resistance through the precise front area generally with major influence for speeds beyond 36 km/h [9], and this suggested that it is necessary that the development of the vehicle design contains a lower aerodynamic coefficient. Research studies have shown that important parameter of EVs which may directly affect the range characteristics is their weight [10, 11]. But the current situation is our most of the automotive manufacturer's industries use the existing design or body shape for the electric vehicle which is not aerodynamically correct for the electric vehicle.

2.2 Driver Driving Style

The aggressive result of the driver driving style also may reduce the range of the electric motor vehicle. It all depends upon the driver's aggressiveness at that time. The driver's aggressiveness mainly indicates how the driver uses the accelerator pedal, and research has found that an EV's range is not only influenced by vehicle design, but it also may influence by the driver [10]. Another direct factor of influence of the driver's behavior how is he use the vehicle in heavy traffic conditions. But this is impossible to design a specific algorithm that precisely determines the effect of the driver driving style on the range. Because every driver has their own style to drive a vehicle. Some have driven accordingly to traffic conditions and rules and regulations, but some have driven rudely.

2.3 External Environment

The range of the electric vehicle has also been affected by the outside environment (outside ambient temperature). Climate control loads will significantly range reduction in both seasons winter and summer, respectively. In summers, the battery temperature will also increase along with the outside temperature and that may change the battery chemical composition and battery charging efficiency, and specific energy may also change. Similarly, in winters, temperature plays an important role to reduce the electric motor vehicle range because the chemical composition of the battery will also change in this season. In summers, the cooling load will reduce the range from 17.1 to 37.1% while this reduction in range further reduces to about 17.1–54.1% in winters owing to heating load [2]. Hence, it becomes difficult to carry out the charging operation, especially at lower temperatures due to lower diffusion rates of lithium ions in the electrodes [12, 13].

3 Methods to Increase the Range of Electric Vehicle

There are few methods to increase the range.

3.1 Dual Inverter Drive System

In this system, a dual inverter drive system with an open winding motor is an alluring system to supply a higher voltage current to a motor for run an electric vehicle. In this method, we are using two batteries that one is primary, and another one is a secondary battery. A primary battery is the main battery for the electric vehicle which is directly

connected to a motor which runs the vehicle, whenever the primary battery means that the main battery is fully discharged, then it will change to a secondary battery, and now, this battery will deliver power to the motor for run an electric vehicle. On the other hand, the primary battery is charging simultaneously by the charging sources like an alternator, dynamo, or other sources. When the secondary battery starts discharging its charge from the main battery through the motor, whether it is at standby and moving. The shifting from the primary battery to the secondary battery on discharging the primary battery via sensors. These sensors sense the battery discharge level. When the battery gets fully discharged, there is some mechanism that uses a sensor to change the power supply from primary battery to secondary battery. This method is feasible but due to the dual battery system, the weight of the vehicle has somehow increased that will may impact the motor. To compensate for this increase in the weight, the vehicle body weight should be kept minimum. Usually, in a year, an automobile is driven for about 250 h [14] which is approximately equal to 115 h of air-conditioning operation [15] and corresponds to around 45% of the vehicle usage. Further, air-conditioning usage generally results in a decrease of about 33% in the range of EVs [14].

Figure 1 shows that the four different battery packs corresponding to capacity, weight, and EV weight. According to this graph, the 24 kWh battery pack the capacity is 300 Ah, weight is 240 kg, and EV weight is 540 kg. The 20.8 kWh battery pack the capacity is 260 Ah, weight is 225 kg, and the 485 kg. The 16 kWh battery pack the capacity is 200 Ah, weight is 182.5, and EV weight is 382.5 kg. The 18 kWh battery pack the capacity is 100 Ah, weight is 80 kg, and EV weight is 180 kg.

Figure 2 shows that the four different vehicle weights corresponding to range, and these ranges are approximate, because the range is not only depending upon vehicle weight but also it depends on lots of factors. This shows that the effect of increasing the electric vehicle weight on the range. EV with an 8 kWh battery pack having approximately 75 km range in the city traffic with a 24 kWh battery pack having approximately 200 km range in the city traffic. Only these two battery packs are clearly visible from the graph which are most efficient than the other two. But,

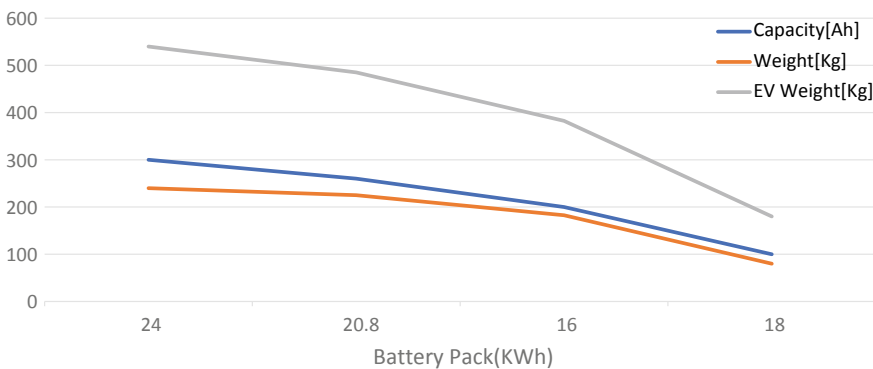


Fig. 1 Different battery pack with capacity, weight, and EV weight [16]

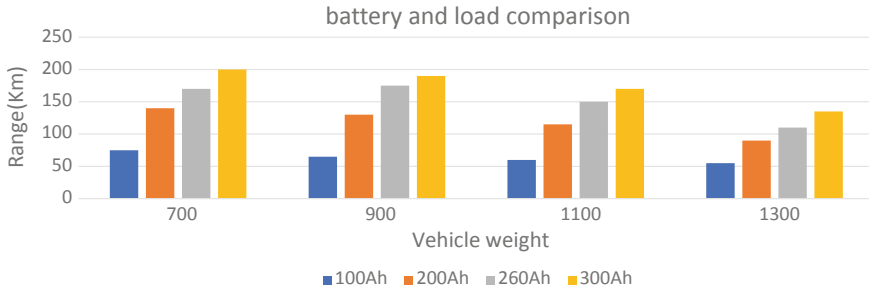


Fig. 2 Battery and load comparison [17]

Table 1 Different battery pack with range per km [16]

Battery pack KWh	Range km/kWh
24	8.333
20.8	8.173
16	8.75
8	9.375

for the daily routine for 70 km in a day, the 24 kWh is less efficient than the 8 kWh battery pack, because the lower battery pack is having less weight and low cost. For showing a better comparison, we will take a range of electric vehicle in a 1 kWh of energy for a 700 kg weight of the vehicle.

According to this Table 1 and the above graph, it is clearly shown that a battery pack with 8 kWh is the highest range than the others.

3.2 Dynamic Wireless Charging System

For high-power applications, a superior wireless charging systems (WCS) has been anticipated, including plug-in electric vehicle and EVs in stationary applications [18–20]. Stationary charging is one of the major constraints of using a wireless charging system as such vehicles can only be charged when they are parked [20]. Bulky structures, limited power transfer, electromagnetic compatibility (EMC) problems, shorter range, and lower efficiency are some other challenges in using stationary WCS [21–23]. Authors [24, 25] have discussed the dynamic WCS, to overcome the problems associated with the stationary WCS. The dynamic WCS method allows the operation of the battery charging while the vehicle is in motion [26]. Infrastructure of this system is quite difficult and more expensive. In this system, wireless charging of electric vehicles is done by an inductive power transmission. It is the technology that allows power transfer between two mutually coupled inductors across a large air gap. In an inductive power transmission system, there is a transmission of electric

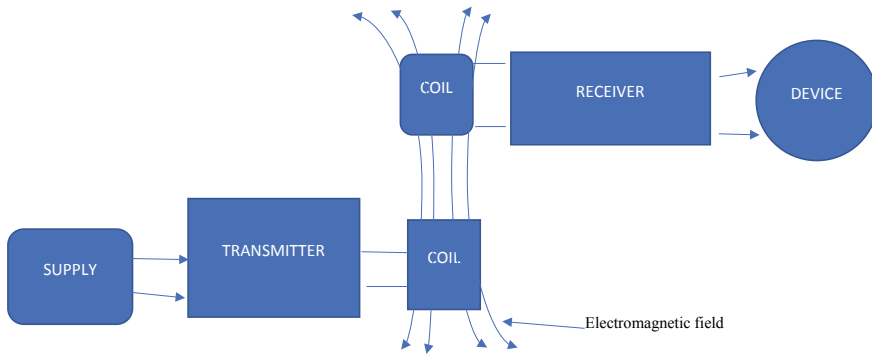


Fig. 3 Block diagram of wireless charging system

energy through air and without wires. The general illustration of the wireless charging system is Fig. 3.

In this system, a transmitter device is driven by electric power from a power source, and this transmitter device is embedded on the ground and generates an electromagnetic field in the primary coil of the transmitter and transmits power across the air gap to a receiver device through which the magnetic field is induced in the secondary coil of the receiver device by mutual induction which is fitted below our vehicle and which received the power and convert it back into DC electric current, and this current is used for charging the battery. A circular pad device which acts as a secondary coil or receiver which is mounted below the vehicle and transmitter device on the one pathway of the highway. So, if the battery is going to discharge, the driver must move its vehicle to this lane, and by this system embedded on the ground, the battery will charge without any wire or without stopping the vehicle. It will also charge the battery while the vehicle is in motion. We use this method at the parking lots and office parking area, while working in the office, we utilized that time for charging our vehicle. But there are a lot of losses in transmitting the power wirelessly. It harms the surrounding species badly, and this transmitting power is not enough to charge the battery because due to the losses, the efficiency of the system has decreased. So, preventing these losses, we use magnetic shielding to prevent this interference or losses. With ferrite material, it is possible to manage or thereby improve the efficiency of power transfer. Material like ferrite has a greater permeability to the magnetic field than the air around them. By using this material, we concentrate these magnetic fields, and further, it improves efficiency and reduces the coupling effect. The dynamic wireless charging system is an agreeable technology, which could reduce the complication linked with the range and cost of EVs. It is also known as a “roadway powered” [27]. Since the establishment of wireless charging systems for electric motor vehicle, there are four techniques of the wireless charging system are using: inductive power transfer, capacitive wireless power transfer, magnetic gear wireless power transfer, and resonant inductive power transfer. The assorted graphs

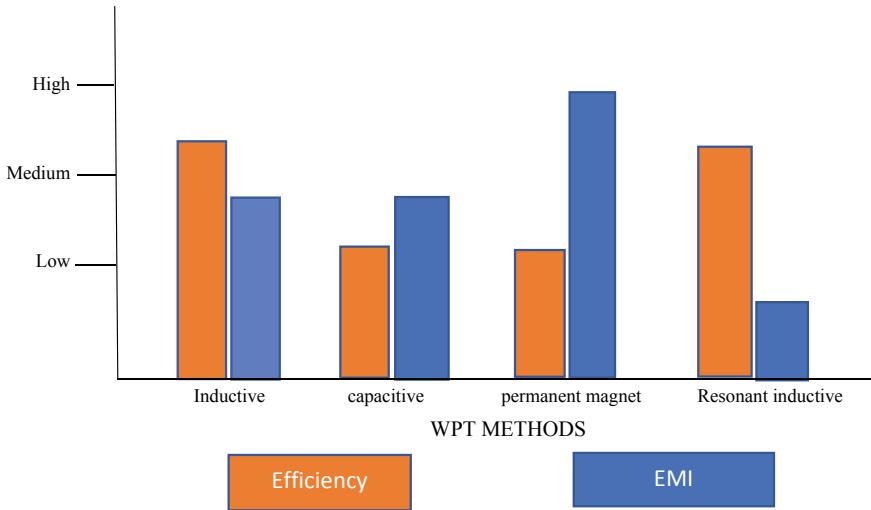


Fig. 4 Different WPT methods with efficiency and EMI [18, 20, 22, 28]

present the summary of obtainable wireless power transfer technologies for battery operated in electric motor vehicles (BEVs).

Figure 4 shows that the WPT METHODS corresponding to the efficiency, EMI of the WPT technologies. In this graph, it shows the WPT METHODS like inductive, capacitive, permanent magnet, and resonant inductive. In inductive wireless power transfer, the graph shows that the efficiency of this method is medium to high, and EMI is medium. In capacitive wireless power transfer, the efficiency of this method is between low to medium, and the EMI of this method is medium. In permanent wireless power transfer, the efficiency is from low to medium, and EMI is high. In resonant inductive wireless power transfer, the efficiency is medium to high, and EMI is low.

Figure 5 shows that the WPT METHODS, like Inductive, capacitive, permanent magnet, and resonant inductive WPT technologies corresponding to price, size, and complexity of the design. In the inductive WPT method, the price of this method is to medium to high, size is medium, and design is medium. In capacitive WPT technologies the price is low, and the size is also low, and the complexity of design is medium. In permanent WPT technologies, the price is high, and the size is high, and the complexity of design is high this means that it is difficult to design or set up the system. In the resonant inductive WPT method, the price of this method is medium to high, and the size is medium, and the complexity of design is medium.

Figure 6 shows us the WPT METHODS, like inductive, capacitive, permanent magnet, resonant inductive corresponding to the power level, and suitability of WEVCS of WPT technologies. In the inductive WPT method, the power level is medium to high, and the suitability for WEVCS is high. In the capacitive WPT method, the power level is low, and the suitability for WEVCS is low to medium. In

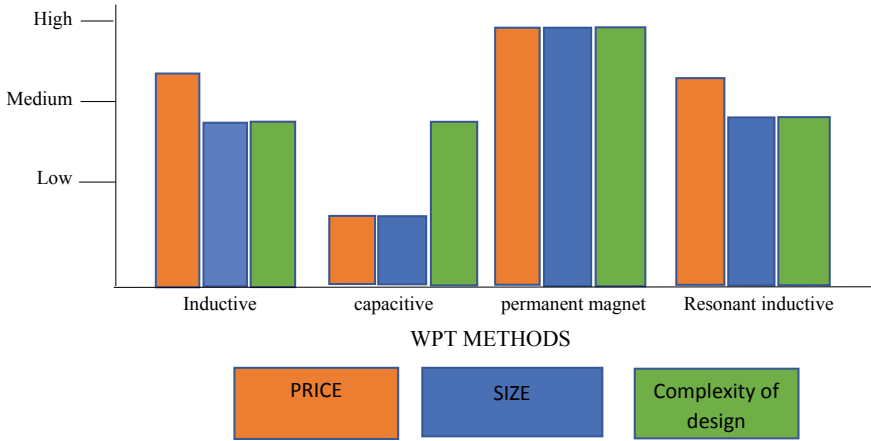


Fig. 5 Different WPT methods with price, size, and design [18, 20, 22, 28]

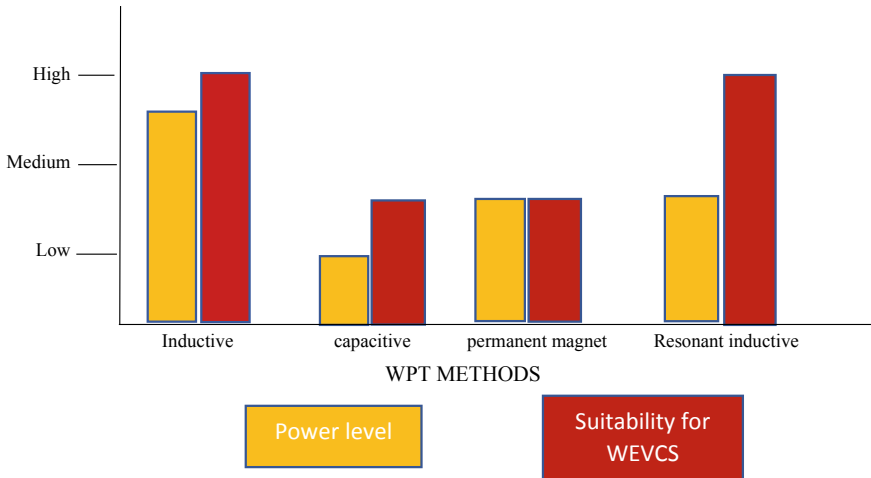


Fig. 6 Different WPT methods with power level and suitability for WEVCS [18, 20, 22, 28]

the permanent magnet WPT method, the power level is low to medium, and the suitability for WEVCS is also low to medium. In the resonant inductive WPT method, the power level is low to medium, and the suitability for WEVCS is high.

Figure 7 shows that the frequency range in kHz corresponding to the WPT methods, like inductive, capacitive, permanent magnet, and resonant inductive. In the inductive WPT method, the frequency range is between 0 and 50. In the capacitive WPT method, the frequency range is between 0 and 450. In a permanent magnet, the frequency range is 0–10. In the resonant inductive WPT method, the frequency range is 0–150.

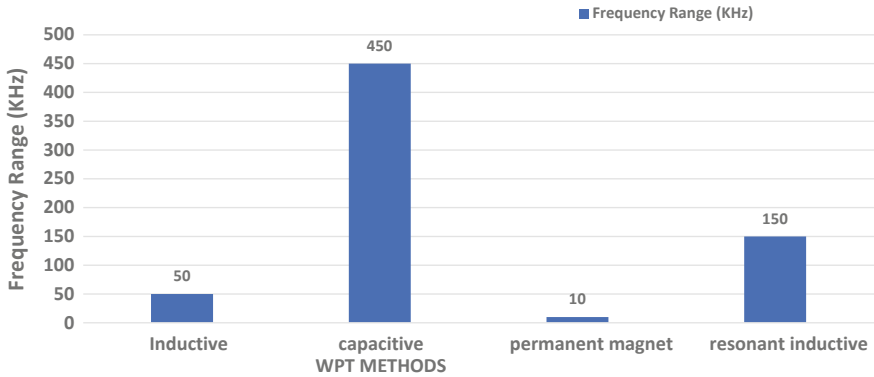


Fig. 7 Different WPT methods with frequency range [18, 20, 22, 28]

3.3 Solar Panel Charging System

In this system, solar panel is operated to charge the battery pack of an electric motor vehicle. The solar panel is a device that is used to charge or run the other electrical appliances. As day by day renewable resources are decreasing, then this system is useful for charging the electric vehicle’s battery. The solar panel uses the sunlight for its working, and this sunlight is available in a vast amount in the atmosphere. Everyday enough amount of sunlight reaches to our ground to meet the energy demand for the humans, but we are wasting this source of energy. It is easily available in the atmosphere, and there is no cost for it and light drawn from the sun is also very easy. Solar energy is an infinite source of energy, and it is accessible at no cost [29, 30]. This technique is extremely efficient and helps the environment to create it pollution-free. The best good thing about alternative energy over the opposite conventional power generators is that the daylight may be directly transformed or converting into alternative energy with the employment of small photovoltaic solar cells [31, 32]. Because no pollutants substances are emitted from this system. The solar system is used everywhere like industrial, residential, and commercial areas. In solar panel, photovoltaic cell converts light energy which is coming from the sun directly into direct electrical energy using a small photovoltaic cell. It converts light energy into DC electric current, and therefore, this DC current is passed through the solar inverter which converts this DC current in AC current. Now, this AC current is used to run or charge the other home electrical appliances and other electrical devices. In an automobile, we have mounted this system at the rooftop of the vehicle, so that there is no other new space which is required for establishing the system. The solar system has many advantages like the easy installation of a solar panel system and does not require any wire, eco-friendly, and it is re-use resource. It has no working parts and does not require any other thing than sunlight. The disadvantages are the initial setup cost is high. The major drawback is no generation of energy when the

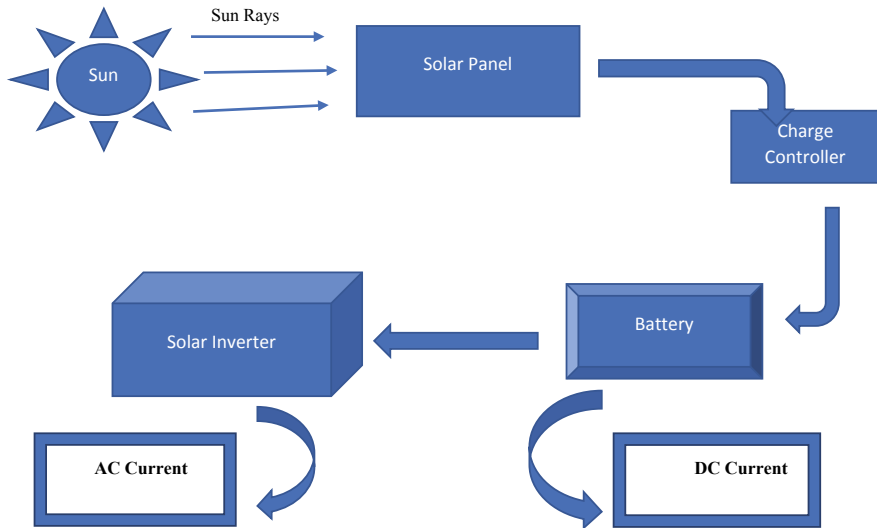


Fig. 8 General block diagram of solar panel charging system [33, 34]

sunlight is not shining or less generation when the clouds are in an atmosphere. But overall, this system is very useful for us to increase the electric motor range (Fig. 8).

3.4 Changing Battery Chemical Composition

We are using various types of batteries for our automobiles. In which commonly we are using a lead–acid battery, nickel-metal hydride (NiMH), and lithium-ion battery. These kinds of the battery were used in the earliest automobile for running the electrical component but now for the electric vehicle, the battery is used as a primary component or the main source for supplying the current to the DC motor. Lead–acid batteries are seen in conventional vehicles like diesel or petrol vehicles. Although, such batteries include a substandard specific energy (34 Wh/kg) [35]. But lead–acid battery incorporates a plus that it is inexpensive. NiMH batteries are superior, as they have up to double the precise energy (68 Wh/kg) compared with lead–acid batteries [35]. Due to this high energy density, NiMH is employed in an electrical vehicle compared to a lead–acid battery. NiMH battery includes a significant advantage which is lower in weight, because of this reduction in weight of the battery our vehicle weight has also reduced, which ends up in less power consumption and energy cost for propelling the vehicle. But it is one major drawback which is auto discharging of the battery. There is also a significant problem with this battery that is self-discharge (up to 12.5%) that is exacerbated when the batteries are in an exceedingly high-temperature environment [36]. This makes that NiMH battery is not carrying there where the atmospheric temperature remains always

Table 2 List of batteries in the market and their interrelating capacity [37]

EV make	Battery (Wh)	Range meter (mi)	Wh/m (mi)	Energy cost/m (mi)
BMW i3	22,000	135,000 (85)	165,000 (260)	₹2.42 (₹3.82)
Chevy bolt	60,000	383,000 (238)	255,000 (411)	₹2.28 (₹3.68)
Fiat 500e	24,000	135,000 (85)	180,000 (290)	₹2.65 (₹4.26)
Ford focus	23,000	110,000 (75)	200,000 (320)	₹2.94 (₹4.85)
GM spark	21,000	120,000 (75)	175,000 (280)	₹2.57 (₹4.12)
Honda fit	20,000	112,000 (70)	180,000 (290)	₹2.65 (₹4.26)
Mitsubishi MiEV	16,000	85,000 (55)	190,000 (300)	₹2.79 (₹4.41)
Mercedes B	28,000	136,000 (85)	205,000 (330)	₹2.94 (₹4.85)
Nissan leaf	30,000	160,000 (100)	190,000 (300)	₹2.79 (₹4.41)
Smart ED	16,500	90,000 (55)	200,000 (320)	₹2.94 (₹4.85)
Tesla S60	60,000	275,000 (170)	220,000 (350)	₹3.23 (₹5.15)
Tesla S85	90,000	360,000 (225)	240,000 (380)	₹3.53 (₹5.59)

high. Lithium-ion batteries are now considered because the most useful in without fuel using vehicles, i.e., an electrical vehicle. These types of batteries are used for a long period and for high-range efficiencies. There are many sorts of lithium-ion batteries. Some of our lithium cobalt oxide, lithium manganese oxide, and lithium iron phosphate each type has their different characteristics and chemical properties. If we compare lithium-ion battery over other types of battery, then lithium-ion battery has several advantages. They tend to have a higher energy density, voltage capacity, and lower self-discharging rate. It has superior energy density and specific energy (140 Wh/kg), making it perfect for electric vehicles [35]. It can retain its energy with a self-discharging issue. But as well as on the other hand, it has a few disadvantages. Firstly, its cost is too much or expensive than the other batteries. Secondly, it has a problem with overcharging and overheating. The battery is too much overheat when it is charging for a long period or where the temperature is quite high. There had been assorted cases where the Tesla Model S, which uses the Li-ion batteries, had outrageous caught fire due to problems with oscillate charging and damage to the battery [36]. But there has been a lot of work on it for its better performance and to fix this overheating and overcharging problem. Because mostly, this type of battery only delivers a large amount of energy, and it is best for our electric vehicle (Table 2).

3.5 Regenerative Braking System

Regenerative braking is a braking technique that makes use of the mechanical energy from the motor by transforming the kinetic energy (K.E) into electrical energy and

returns it back to the battery. Theoretically, the regenerative braking system can convert a good fraction of its K.E to charge up the electric motor vehicle battery, using the same principle as of an alternator. The regenerative braking system uses vehicle's speed and changing its kinetic energy into a form of heat, and that form of energy is being used by this system to charge the battery. This highlights with conventional braking systems, where the inordinate K.E. is changed to undesired and squandered warmth because of scraped area inside the brakes, or with dynamic brakes, any place the energy is recuperated by utilizing an electrical engine as a generator; however, it is promptly scattered as warmth in resistors. In regenerative slowing down, the electric vehicle engine works like a generator to energize the battery [38]. It will improve the efficiency of electric vehicles by reducing the waste of energy. In a regenerative braking system, the K.E of the wheels is transforming into electricity and stored back into a battery or a capacitor. Some existing systems can store as much as 70% of the energy. This method has been enhanced by using flywheels, DC-DC converters, and supercapacitors. Moreover, to improving in general efficiency of an electric motor vehicle, regeneration can significantly increase the viability of the braking system, and the mechanical parts of the braking system will not wear out as quickly. The regenerative braking system makes use of an electric vehicle's DC motor as a generator for transforming the greatest amount of the K.E lost when de-accelerate back into stored energy in an electric vehicle's battery. Then, after whiles when the car accelerates, it uses this maximum energy of the previous energy keeps from the regenerative braking system. It is important to realize that the regenerative braking system is a superior system for increasing the range booster for electric vehicles, and it makes electric vehicles more efficient and economical. In the early "70s," the researchers have studied the feasibility and practicality of apply hybrid power trains incorporating regenerative braking which have the potential to increase the fuel economy of vehicles operating under metropolitan driving conditions [39–41]. However, the main aim behind this system is to lower fuel consumption, thus reduced the emissions of greenhouse gases and many expenses [42–45]. The regenerative braking system is significant for the city driving because in metropolitan cities, there is a lot of braking systems which are used while driving the vehicle because of the traffic and road conditions. Due to this, lot of energy is wasted as heat. If totally all the brake energy is often regenerated with no loss within the regenerative system, fuel consumption would be improved by 33% [46]. A vehicle weighing 1 ton may reach savings (theoretical) of fifteen percent. Research by Volkswagen has indicated that hybrid electric motor vehicle with both electric drive and ICE provides potential fuel saving of over 20%. Electrical vehicles can give a sparing of energy if it is with all appropriate control hardware, they will convert all energy to control for capacity and re-use for the vehicle. An electrical transport to be utilized as public transportation in New York has additionally been created, and this is operated on Nickel–Cadmium batteries and highlights the regenerative braking system. It is a virtuous step taken by New York, and a ton of fuel and energy is saved from this way (Fig. 9).

This block diagram shows the energy flow in the regenerative braking system. The diagram determines the path in which the energy flow and the losses along the

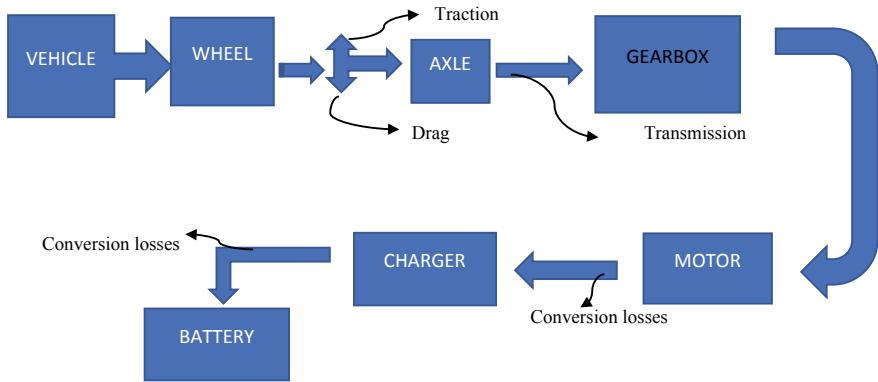


Fig. 9 Energy flow diagram [46]

energy flow pathway. These major losses are traction force, drag, or in transmission and mostly in conversion losses.

3.6 List of Various Advantages and Disadvantages of the Charging Methods

In Table 3, it is showing the list of advantages and disadvantages of the methods that help us to figure out the best and suitable method for charging our electric vehicle battery, according to our need.

4 Conclusion

There are many methods which affect the performance of the electric vehicles in terms of the range. The main factors that have major influence on the range of the EVs are driver driving style and vehicle body shape. Effects of these factors were reviewed, and methods for enhancing the range of the electric vehicles were discussed. The dynamic wireless charging and solar panel charging were reported to be the most efficient and successful methods for the electric vehicles. The dual battery charging system can also be employed for enhancing the range of the vehicles, but the weight of the vehicle will be increased due to additional battery. Therefore, methods focusing on reduction of the vehicle’s weight should be given importance in the research for increasing the vehicle’s range which will lead to the increased application of such vehicles.

Table 3 List of advantages and disadvantages of methods

Methods for increase the range	Advantages	Disadvantages
Dual inverter drive system	<ul style="list-style-type: none"> • It has high efficiency • Due to dual battery, weight of the EV will be increased 	<ul style="list-style-type: none"> • Due to dual battery system, the range will be increased
Dynamics wireless charging system	<ul style="list-style-type: none"> • Without stopping the EV, we can charge our vehicle in motion • No excessive wire is use 	<ul style="list-style-type: none"> • Charging efficiency is low as compared to other methods • Cost is very high • There are lot of losses in transmitting
Solar panel charging system	<ul style="list-style-type: none"> • Free source of sunlight energy which we use for charging our EV • No excessive wire is use 	<ul style="list-style-type: none"> • The major demerit of this system is that the energy is available for charging the battery is 12 h in a day when the sunlight shining
Changing battery chemical composition	<ul style="list-style-type: none"> • By changing battery chemical composition, we can make our battery more efficient and increase the range for EV battery and specific energy 	<ul style="list-style-type: none"> • By the changing chemical composition, the price of the battery will be increased, but it is depending on the chemical composition use in battery
Regenerative braking system	<ul style="list-style-type: none"> • Utilized the wasted heat due to friction on applying brake to charge the EV battery 	<ul style="list-style-type: none"> • Cost of component, manufacturing, and installation is high

References

1. IEA (2010) Sustainable production of second-generation biofuels. IEA Information Paper, Paris
2. Zhang Z, Li W, Zhang C, Chen J (2017) Climate control loads prediction of electric vehicles. *Appl Therm Eng* 110:1183–1188
3. Jaguemont J, Boulon L, Dubé Y (2016) A comprehensive review of lithium-ion batteries used in hybrid and electric vehicles at cold temperatures. *Appl Energy* 164:99–114
4. Bi J, Wanga Y, Shaoa S, Cheng Y (2018) Residual range estimation for battery electric vehicle based on radial basis T function neural network. *Measurement* 128:197–203
5. Redelbach M, Özdemir ED, Friedrich HE (2014) optimizing battery sizes of plug-in hybrid and extended-range electric vehicles for different user types. *Energy Policy* 73:158–168
6. Münster M, Schäffer M, Kopp G, Kopp G, Friedrich HE (2016) New approach for a comprehensive method for urban vehicle concepts with electric powertrain and their necessary vehicle structures. *Transp Res Procedia* 14:3686–3695
7. Kinter-Meyer M, Schneider K, Pratt R (2007) Impacts assessment of plug-in hybrid electric vehicles on electric utilities and regional U.S. power grids. Part IV technical analysis, Pacific North West National Lab., Richland, WA, PNNL-SA-61669
8. EPRI & NRDC (2007) Environmental assessment of plug-in hybrid electric vehicles. Volume 1: Nationwide greenhouse gas emissions, Final Report. 1015 325, pp 1–56
9. Hucho H (1998) Aerodynamics of road vehicles, 4th edn. SAE International, Warrendale, PA, USA
10. Mruzek M, Gajdác I, Kučera L, Barta D (2016) Analysis of parameters influencing electric vehicle range. *Procedia Eng* 134:165–174

11. Berjoza D, Jurgen I (2017) Effects of change in the weight of electric vehicles on their performance characteristics. *Agron Res* 15:952–963
12. Liu H, Wei Z, He W, Zhao J (2017) Thermal issues about Li-ion batteries and recent progress in battery thermal management systems: a review. *Energy Convers Manag* 150:304–330
13. Zhang SS, Xu K, Jow TR (2003) The low-temperature performance of Li-ion batteries. *J Power Sources* 115:137–140
14. Fischer S, Sand J (1997) Total environmental warming impact (TEWI) calculations for alternative automotive air-conditioning systems. In: Proceedings of the SAE international congress and exposition, Detroit, Mich, USA
15. Fischer SK (1995) Comparison of global warming impacts of automobile air-conditioning concepts. In: Proceedings of the international CFC and Halons alternative conference, Washington, DC, USA
16. Lee JT, Kwon S, Lim Y, Chon MS, Kim D (2013) Effect of air-conditioning on driving range of electric vehicle for various driving modes. SAE Technical Paper 2013-01-0040
17. Mruzek M, Gajdáč I, Kučera L, Barta D. Analysis of parameters influencing electric vehicle range. University of Zilina, Univerzita 1, 01026 Žilina, Slovakia
18. Analysis of Parameters Influencing Electric Vehicle Range—Scientific Figure on ResearchGate. Available from: https://www.researchgate.net/figure/Battery-and-load-comparison-on-Zilina-cycle_fig2_293195098. Accessed 7 Sep 2020
19. Kalwar KA, Aamir M, Mekhilef S (2015) Inductively coupled power transfer (ICPT) for electric vehicle charging—a review. *Renew Sustain Energy Rev* 47:462–475
20. Ombach G (2013) Design considerations for wireless charging system for electric and plug-in hybrid vehicles. *Hybrid Electr Veh Conf* 1–4
21. Leskarac D, Panchal C, Stegen S, Lu J (2015) PEV charging technologies and V2G on distributed systems and utility interfaces. In: Lu J, Hossain J (eds) *Vehicle-to-grid: linking electric vehicles to the smart grid*. The Institution of Engineering and Technology (IET), London, pp 157–209
22. Sang Cheol M, Bong-Chul K, Shin-Young C, Chi-Hyung A, Gun-Woo M (2014) Analysis and design of a wireless power transfer system with an intermediate coil for high efficiency. *Indust Electr IEEE Trans* 61:5861–5870
23. Covic GA, Boys JT (2013) Inductive power transfer. *Proc IEEE* 101:1276–1289
24. Covic GA, Boys JT (2013) Modern trends in inductive power transfer for transportation applications. *Emerging and selected topics in power electronics*. IEEE J 1:28–41
25. Lukic S, Pantic Z (2013) Cutting the cord: static and dynamic inductive wireless charging of electric vehicles. *Electr Mag IEEE* 1:57–64
26. Eghtesadi M (1990) Inductive power transfer to an electric vehicle-analytical model. In: Vehicular technology conference, IEEE 40th, pp 100–104
27. Fuller M (2016) Wireless charging in California: range, recharge, and vehicle electrification. *Trans Res Part C: Emerg Technol* 67:343–356
28. Mi CC, Buja G, Choi SY, Rim CT (2016) Modern advances in wireless power transfer systems for roadway powered electric vehicles. *IEEE Trans Ind Electron* 63:6533–6545
29. Hui SYR, Wenxing Z, Lee CK (2014) A critical review of recent progress in mid-range wireless power transfer power. *Electr IEEE Trans* 29:4500–4511
30. Chu Y, Meisen P (2011) Review and comparison of different solar energy technologies. Report of Global Energy Network Institute (GENI), Diego
31. Choubey PC, Oudhia A, Dewangan R (2012) A review: solar cell current scenario and future trends. *Recent Res Sci Technol* 4:99–101
32. McEvoy A, Castaner L, Markvart T (2012) *Solar cells: materials, manufacture, and operation*, 2nd edn. Elsevier Ltd., Oxford, pp 3–25
33. Design and Economic Analysis of a Photovoltaic System: A Case Study. Scientific Figure on ResearchGate. Available from: https://www.researchgate.net/figure/Configuration-of-the-Stand-Alone-PV-System_fig3_233953637. Accessed 12 Sep 2020
34. Fahren Bruch AL, Bube RH (1983) *Fundamentals of solar cells*. Academic Press Inc, New York

35. Burke AF (2007) Batteries and ultra capacitors for electric, hybrid, and fuel cell vehicles. Proc IEEE 95:606
36. Klayman B (2013) Tesla grapples with impact of battery fire in the U.S. Reuters, 3 Oct 13
37. BU-1003 (2019) Electric Vehicle (EV), Mar. 2019
38. Unnewehr LE, Nasar SA (1982) Electric vehicle technology. Wiley, Hoboken
39. Electric Transit Vehicle Institute Current, Fall (1995)
40. WyczalekM FA, Earle DE, Sloan F, Standish JT (1992) Autom Eng 100(7):29–33
41. Metz D (1983) Mechan Eng 105(1):80
42. Cooper-Reade M (1992) Seminar “EV technology”. Motor Industry Research Association, Nuneaton, 29 April 1992
43. Towards Clean and Efficient Automobiles (1993) Proceedings of an international conference, Berlin, 25 March 1991, pp 206–213
44. Energy Technology Support Unit (1991) AEA environment, and energy report, AEA-m-0211, Harwell Laboratory, Oxfordsh’ue
45. Bentley JM, Teagan WP. Parts of the conference “Next generation technologies for efficient energy end uses and the switching”. International Energy Agency/Bundesministerium fur Forschung und Technologie, Dortmund, Germany
46. Ford Motor Company (1981) Energy: ford energy report, vol 1

Comparison of SVM and ARIMA Model in Time-Series Forecasting of Ambient Noise Levels



S. K. Tiwari, L. A. Kumaraswamidhas, and N. Garg

1 Introduction

Noise pollution has become a major apprehension in developing countries like India. Population growth, urban development and migration of people from rural areas to cities have led to a heavy motorization in metropolitan cities. The increase in noise pollution has an adverse effect on human health like mental disturbances and irritation [1, 2]. It is observed that high-intensity noise creates more annoyance as compared to low-intensity noise. Today, in world growing economy, it is very complicated task to setup noise monitoring stations at each site of the metropolitan cities due to its nonlinear behaviour.

Thus, there have been few studies on long-term noise monitoring strategy versus short-term noise monitoring strategy like temporal sampling and time-series modelling [3, 4]. Time-series technique can be succour as suitable substitute to continuous long-term noise monitoring for prediction and forecasting of ambient day and night noise levels. It helps us to discover the series with some margin of error. Several studies have been done by researchers to analyse long-term noise monitoring data using time-series models. Kumar et al. [5] predicted traffic noise using NN model such as FHWA, CORTN, STOP and GO at all identified location in Lucknow. Garg et al. [6] analysed continuous long-term noise data using ARIMA model to calculate equivalent noise level, L_{day} and L_{night} , for a period of 6 months. Again, Garg et al. [7] compared time-series models ANN and ARIMA to evaluate L_{day} and L_{night} in which ANN outperforms ARIMA model in prediction and forecasting.

However, due to high nonlinearity in the noise monitored data, it is imperative to investigate the suitability and applicability of various time-series modelling technique. One such technique is support vector machine (SVM). SVM is widely used

S. K. Tiwari (✉) · L. A. Kumaraswamidhas
Indian Institute of Technology (ISM), Dhanbad 826001, India

N. Garg
National Physical Laboratory, CSIR, New Delhi 110012, India

for time-series forecasting, data mining, regression, classification and financial-based modelling like banking data analysis and forecasting, credit scoring [8–10]. In some studies, support vector machine (SVM) is compared with other traditional neural network (NN) models and concluded that SVM has better performance in comparison with the other NN models based on the prediction of data [11, 12]. In statistical learning, SVM is an adaptable technique for the prediction of air pollution and noise pollution due to its high dimensional tuning ability for processing a long-term assessed data. The Kernel parameters (C , γ) affect the performance of support vector regression (SVR) forecasting [13, 14]. The increasing exponential value of cost (C) and gamma (γ) is an optimized way to get optimal parameter using grid search method which is a time consuming method [15]. Pazakawambwa et al. [16] studied about time-series forecasting of Windhoek rainfall up to 2047. ARIMA model has been considered despite irregular fluctuation in rainfall from year 1891–2011.

The continuous long-term noise monitoring strategy is a cumbersome and expensive process. Thus, it is necessary to conduct noise monitoring study at various sites of major cities in terms of four zones, i.e. commercial, industrial, residential and silence zone. The present study utilizes SVM and ARIMA technique to compare ambient day and night noise levels, L_{day} and L_{night} . The main focus of the paper is to succour the best time-series approach as an alternative of continuous noise monitoring strategy for commercial zone in Indian perspective.

The rest of work is arranged as follows. Section 1 gives a glimpse of introduction about health issues due to noise pollution and various time-series models used by researchers. In Sect. 2, collection of noise data and brief description of site opted for noise modelling is described. In Sect. 3, support vector machine (SVM) is described. Section 4 demonstrates autoregressive integrated moving average (ARIMA) method. In Sect. 5, a statistical comparison of applied models has been performed. In Sect. 6, we finally draw a conclusion substantially.

2 Long-Term Noise Level Analysis

The study primarily focuses on noise data collected under the National Ambient Noise Monitoring Network (NANMN) project by Central Pollution Control Board (CPCB) in seven major cities of India [17–22]. A case study of a commercial zone of continuous day and night noise levels (3 yr \times 365 days \times 24 h) is analysed. The day levels were measured from 6.00 a.m. to 10.00 p.m., while night levels were measured from 10.00 p.m. to 6.00 a.m. in the study Marathali site of Bangalore city which was considered for developing time-series models, namely SVM and ARIMA technique. The 24-h ambient day and night noise data were obtained from the CPCB reports. Figure 1a shows the time-series plot of day equivalent level, L_{day} in dB(A) for 3 years, i.e. January 2015 to December 2018. Figure 1b shows the time-series plot of day equivalent level, L_{night} in dB(A) for 3 years from January 2015 to December 2018.

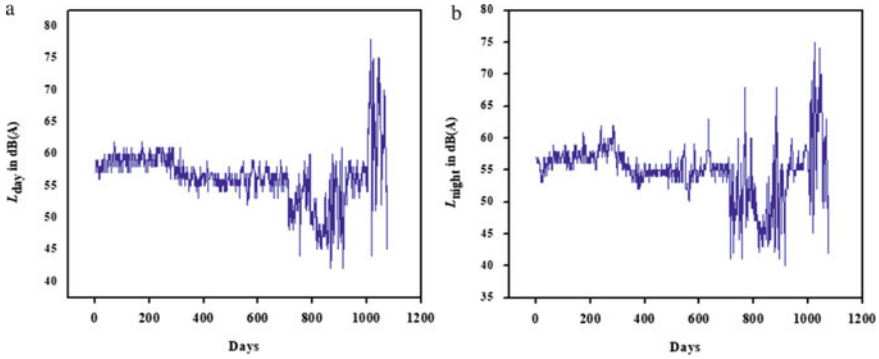


Fig. 1 Measured values of noise levels in commercial zone in dB (A): **a** day, **b** night

2.1 Parameters Defining Accuracy of Model

The statistical parameters used to acknowledge the performance and accuracy of models are root mean squared error (RMSE), mean average error (MAE), mean square error (MSE) and coefficient of determination (R^2). The formula used for these parameters is:

$$RMSE = \sqrt{\frac{1}{N} \sum_{i=1}^N (P_i - O_i)^2} \tag{1}$$

$$MAE = \frac{1}{n} \sum_{i=1}^n |P_i - O_i| \tag{2}$$

$$R = \frac{\frac{1}{n} \sum_{i=1}^n (P_i - \bar{P})(O_i - \bar{O})}{\left(\sqrt{\frac{1}{n} \sum_{i=1}^n (P_i - \bar{P})^2}\right) \left(\sqrt{\frac{1}{n} \sum_{i=1}^n (O_i - \bar{O})^2}\right)} \tag{3}$$

where P_i is the set of predicted values, and O_i is the set of observed values.

3 Support Vector Machine (SVM) Model

3.1 Methodology

SVM is a time-series modelling technique developed by Vapnik [13] based on structural risk minimization (SRM) concept [14] that make it perform better than other NN methods. The basic idea of SVM is mapping the input data x from lower-dimensional

space to higher- dimensional space. The hyper-plane classifies into positive and negative classes.

Suppose X_i is the set of input data, where $\{i = 1, 2, \dots n\}$, then the hyper-plane is formulated as [13]:

$$g(x) = w^t X_i + b \tag{4}$$

where vector (w) represents the direction of hyper-plane, and b is constant term that determines the position of hyper-plane. The mapping of data from lower-dimensional space to higher-dimensional space is possible with Kernel functions. Suppose Y and Y' are two vectors in feature space $\Phi(y)$ and $\Phi(y')$. The dot product of Y and Y' is called Kernel functions [13]. The study focuses on radial basis Kernel function which is demonstrated as:

$$\text{RBF Kernel Function: } K(y, y') = \exp(-\gamma \|y - y'\|^2), \gamma > 0 \tag{5}$$

3.2 Statistical Analysis of SVM Model

The SVM modelling focuses on three stages mainly: Preparing the data, 80% of the input data was used as training dataset and rest of the 20% as testing dataset. The second stage involved the selection of hyper-parameters, i.e. gamma, Epsilon and cost (γ, ϵ, C). The third stage involves simulation of data corresponding to training and testing data.

The present study utilizes the combination of three hyper-parameters gamma, Epsilon and cost (γ, ϵ, C) where ϵ (Epsilon) is the accuracy approximation, C is the penalty factor, and γ defines the distance of single training data from classifier [13]. Hit and trial approach is followed to implement the range of hyper-parameter. It may be noted here that the current work considered the cost and gamma function in $2^{(-5: 5)}$ range on the similar lines as had been discussed by Peña et al. [23], while the value of epsilon is kept constant at 0.4. Table 1 shows the statistical performance of a SVM model in commercial zone.

Table 1 SVM model statistic

SVM parameters	γ	E	C	RMSE	MSE	MAE	R ²
L_{day}	2^5	0.4	2^5	1.3	1.8	1.2	0.7
L_{night}	2^5	0.4	2^5	1.6	2.4	0.9	0.6

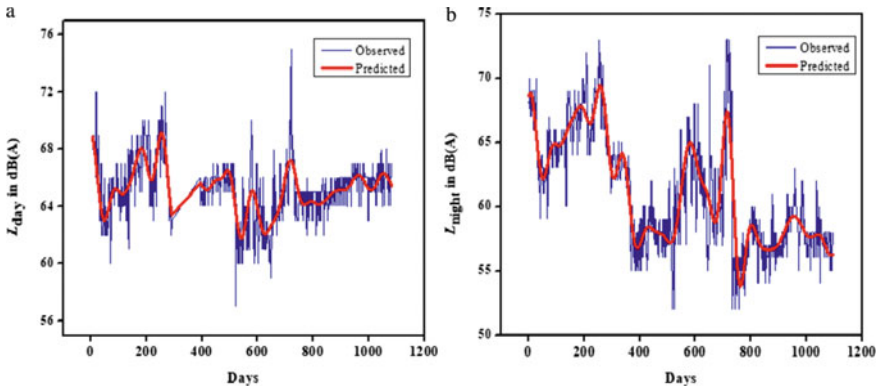


Fig. 2 Comparison of measured (blue line) and predicted (red line) values of commercial zone in dB(A) using SVM: **a** L_{day} , **b** L_{night}

3.3 10-Fold Cross-Validation

Ten-fold cross-validation was used for grid search that divide the sample data into ten subsets for further iteration. The optimum value of hyper-parametric combination for minimum RMSE was $(2^5, 0.4, 2^5)$.

Figure 2a represents the time-series plot of observed and predicted day noise levels (L_{day}) in commercial zone. The RMSE in training data was observed to be 1.3 dB(A) while R^2 was observed to be 0.7 for commercial zone. Figure 2b represents the time-series plot of observed and predicted night noise levels (L_{night}) in commercial. The RMSE in training data was observed to be 1.6 dB(A) while R^2 was observed to be 0.6 for commercial zone.

4 Autoregressive Integrated Moving Average (ARIMA) Approach

4.1 Methodology

ARIMA is a composite time-series model that combines two processes: 1. autoregressive (AR) and 2. moving average (MA) process. The ARIMA is represented as, ARIMA (p, d, q). The key elements of ARIMA model are as follows:

- Autoregressive process (AR): A process that is dependent between an observed sample value and number of lagged observation (p).
- Integrated (I): Difference between the observed values at different instant of time (d) to make the model stationary.

- Moving average (MA): A process that is dependent between an observed sample data and residual error (q).

ARIMA models can predict and forecast both stationary and non-stationary data variables. Box-Jenkins methodology is often used to build ARIMA models [24]. The model involves three stages: (1) model identification stage, (2) model parameters estimation stage and (3) model diagnostic stage.

4.2 Statistical Analysis of ARIMA Model

The first stage is to verify the stationarity of the variable data, i.e. values does not change with respect to time under constant values of mean and variance. In order to make series stationary, difference (d) is used. The study starts with the lowest value of $d = 1$ and is further increased until the series become stationary. The stationary of time-series data was analysed with Dickey- Fuller test. The augmented Dickey-Fuller test results is as follows:

$$\text{Dickey-Fuller} = -6.7385, \text{ lag order} = 3, \text{ p-values} = 0.03$$

The second stage is the model estimation stage in which p and q values are ascertain to determine ARIMA (p, d, q) model. Based on the parametric conditions, ARIMA models, mainly $(0,0,13)$, $(0,0,14)$, $(0,1,12)$ and $(0,1,10)$ were used. The best model will have low Bayesian information criteria (BIC) and Akaike information criteria (AIC) values.

Figure 3a represents the time-series plotation of measured value and predicted value of day noise levels (L_{day}) in commercial zone. The RMSE in training data

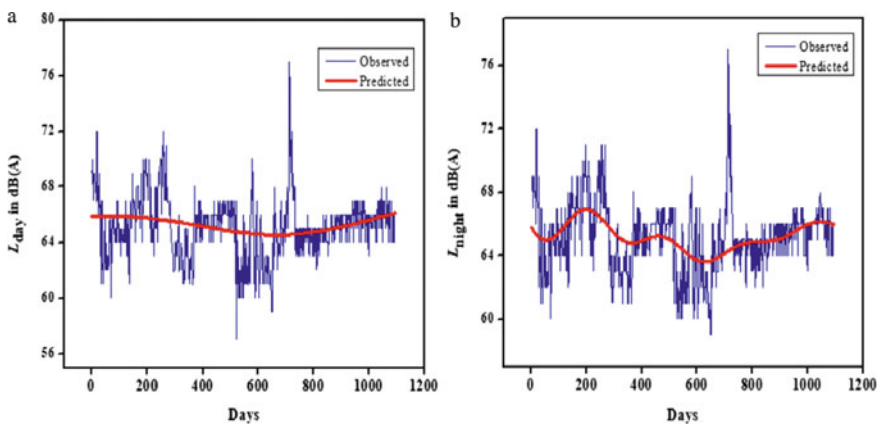


Fig. 3 Comparison of measured (blue line) and predicted (red line) values of commercial zone in dB(A) using ARIMA: **a** L_{day} , **b** L_{night}

was observed to be 1.9 dB (A) while R^2 was observed to be 0.2 for commercial zone. Figure 3b represents the time-series plotation of measured value and predicted value night noise levels (L_{night}) in commercial zone. The RMSE in training data was observed to be 2.3 dB(A) while R^2 was observed to be 0.9 for commercial zone. Table 2 shows the statistical analysis of a ARIMA model in commercial zone. The statistic for L_{day} has been 24.52 while for L_{night} 18.28 that signifies the model validity and compatibility, a low value of $\text{BIC} \leq 1$ was determined for noise levels, i.e. 0.6 and 0.9. The statistic for L_{day} has been 27.88 while for L_{night} 21.89, a low value of $\text{BIC} \leq 1$ was determined for noise levels, i.e. 0.7 and 0.8.

5 Comparison of SVM and ARIMA Model

However, ARIMA approach is quite capable to predict and forecast time-series data for both stationary and non-stationary data. Table 3 shows the comparison of all the two models of ambient day and night noise levels for a period of three years. The mean squared error (MSE), root mean squared error (RMSE) and coefficient of determination (R^2) were observed to compare the time-series models for training and testing data. It can be determined from Table 3 that the RMSE and MSE are quite less in SVM model as compared with ARIMA model for ambient day and night sound level parameter. The coefficient of determination (R^2) has been higher in SVM model for both day and night noise levels for the time-series approach developed by using SVM model.

6 Conclusion

The study focuses on time-series modelling using conventional SVM and ARIMA approach on a statistical performance of 3 years continuous long-term noise monitoring data in an interval of January 2015 to December 2017. The quantification has been done for commercial that including ambient day and night noise levels. A SVM model has been developed with tenfold cross-validation with optimum value of hyper-parameters as a forecasting technique for prediction and forecasting of ambient day and night noise levels. The ARIMA models, mainly (0,1,12) and (0,1,10) for commercial zone, have been classified for predicting ambient day and night equivalent levels. The performance of SVM and ARIMA model is ascertained at various stages. To be specific, the observed and predicted noise levels have been profoundly to match. The statistical parameters like mean square error (MSE), mean average error (MAE), root mean squared error (RMSE) and coefficient of determination (R^2) have been validated to estimate the performance of the model developed using SVM and ARIMA models for prediction and forecasting. Furthermore, it can be concluded from the present study that ambient day and night levels can be a suitable substitute to continuous long-term noise monitoring strategy and is even cost saving also.

Table 2 ARIMA model statistic for commercial zone

Statistical parameter	RMSE	MAE	Normalised BIC	Model fit stationary		Ljung-Box			Model type
				Stationary R^2	R^2	Statistics	df	Sig	
L_{day}	1.9	3.6	0.6	0.3	0.2	24.52	16	0.08	(0,1,12)
L_{night}	2.3	5.2	0.9	0.5	0.3	18.28	18	0.17	(0,1,10)

Table 3 Parametrical comparison of time-series models for L_{day} and L_{night}

Parameters	L_{day}		L_{night}	
	SVM	ARIMA	SVM	ARIMA
MAE in dB(A)	1.2	1.8	0.9	1.8
MSE in dB(A) ²	1.8	3.6	2.4	5.2
RMSE in dB(A)	1.3	1.9	1.6	2.3
R^2	0.7	0.2	0.6	0.3

The study also compared the performance of radial basis function SVM model in comparison to Box-Jerkin ARIMA model. The statistical analysis revealed that SVM model outperforms ARIMA model. The characteristics that demonstrates the superiority of SVM model over ARIMA model are as follows: maximal marginal concept, tenfold cross-validation and adaptability towards nonlinearity. SVM model can be a suitable substitute for forecasting ambient noise levels irrespective of continuous long-term noise monitoring strategy.

Acknowledgements Authors are thankful to Director, CSIR-NPL, New Delhi and Head, Physico-Mechanical Metrology department, and Head Acoustics and Vibration standards for allowing to work in Acoustics and Vibration Metrology division and the Head of Mining Machinery department IIT(ISM), Dhanbad for the support throughout the study.

References

1. Prakash AP, Joute K, Jain VK (2006) An estimation of annoyance due to various public modes of transport in Delhi. *Noise Health* 8:101–107
2. Madhu S, Ravicharan C (1999) Occupational health hazards in industries due to noise pollution. *Indian J Environ Prot* 19:504–507
3. Gozalo GR, Morillas JMB, Escobar VG, Vílchez R, Sierra JAM, del Río FJC, Gajardo CP (2013) Study of the categorisation method using long-term measurements. *Arch Acoust* 38(3):397–405
4. DeVor RE, Schomer PD, Kline WA, Neathamer RD (1979) Development of temporal sampling strategies for monitoring noise. *J Acoust Soc Am* 66(3):763–771
5. Kumar K, Parida M, Katiyar VK (2012) Artificial neural network modeling for road traffic noise prediction. In: 2012 third international conference on computing, communication and networking technologies (ICCCNT'12). pp. 1–5. IEEE
6. Garg N, Soni K, Saxena TK, Maji S (2015) Applications of autoregressive integrated moving average (ARIMA) approach in time-series prediction of traffic noise pollution. *Noise Control Eng J* 63(2):182–194
7. Garg N, Sharma MK, Parmar KS, Soni K, Singh RK, Maji S (2016) Comparison of ARIMA and ANN approaches in time-series predictions of traffic noise. *Noise Control Eng J* 64(4):522–531
8. Flake GW, Lawrence S (2002) Efficient SVM regression training with SMO. *Mach Learn* 46(1–3):271–290
9. Akande KO, Owolabi TO, Twaha S, Olatunji SO (2014) Performance comparison of SVM and ANN in predicting compressive strength of concrete. *IOSR J Comput Eng* 16(5):88–94

10. Shao Y, Lunetta RS (2012) Comparison of support vector machine, neural network, and CART algorithms for the land-cover classification using limited training data points. *ISPRS J Photogram Remote Sens* 70:78–87
11. Tay FE, Cao L (2001) Application of support vector machines in financial time-series forecasting. *Omega* 29(4):309–317
12. Kim KJ (2003) Financial time-series forecasting using support vector machines. *Neurocomputing* 55(1–2):307–319
13. Vapnik V (2013) *The nature of statistical learning theory*. Springer Science & Business Media
14. Samsudin R, Shabri A, Saad P (2010) A comparison of time-series forecasting using support vector machine and artificial neural network model. *J Appl Sci* 10(11):950–958
15. Ding Y, Song X, Zen Y (2008) Forecasting financial condition of Chinese listed companies based on support vector machine. *Exp Syst Appl* 34(4):3081–3089
16. Pazvakawambwa GT (2017) A time-series forecasting model for Windhoek Rainfall, Namibia
17. Garg N, Sinha AK, Gandhi V, Bhardwaj RM, Akolkar AB (2016) A pilot study on the establishment of national ambient noise monitoring network across the major cities of India. *Appl Acoust* 103:20–29
18. Garg N, Sinha AK, Sharma MK, Gandhi V, Bhardwaj RM, Akolkar AB, Singh RK (2017) Study on the establishment of a diversified National Ambient Noise Monitoring Network in seven major cities of India. *Current Sci* 113(7)
19. Garg N, Sinha AK, Dahiya M, Gandhi V, Bhardwaj RM, Akolkar AB (2017) Evaluation and analysis of environmental noise pollution in seven major cities of India. *Arch Acoust* 42(2):175–188
20. Central Pollution Control Board (2015) Status of Ambient noise level in Indian in 2015. CPCB report, NANMN/05/2015
21. Central Pollution Control Board (2016) Status of Ambient noise level in Indian in 2016. CPCB report, NANMN/05/2016
22. Central Pollution Control Board (2017) Status of Ambient noise level in Indian in 2017. CPCB report, NANMN/05/2017
23. Benítez S, Blanquero R, Carrizosa E, Ramírez-Cobo P (2019) Cost-sensitive feature selection for support vector machines. *Comput Oper Res* 106:169–178
24. Babu CN, Reddy BE (2014) A moving-average filter based hybrid ARIMA–ANN model for forecasting time series data. *Appl Soft Comput* 23:27–38

Circuit Theory Base Loss Allocation Methods for Contemporary Distribution System: A Comparative Study



Pankaj Kumar, Nikhil Gupta, K. R. Niazi, and Anil Swarnkar

1 Introduction

The deregulation in electric power industry leads to the formation of generation, transmission and distribution companies. The deregulation wants competition at each level. Earlier, the network usage charges are done on heuristics basis, but now their correct allocation has become very important. Substantial shares of these charges are holds by system power losses. These power losses are occurred while delivering power to the consumer. Therefore, these losses are disbursed among the network users.

From last two decades, the problem of loss allocation (LA) is discussed for transmission and distribution systems. The prime difficulty in LA is that power losses are nonlinear function of branch currents. In fact, there is no unique or ideal procedure exists for LA but it must have these properties [1]: The method must be consistent with the power flow results, take care of energy produced or consumed, topological dependent, can to avoid arbitrariness in result, easy to understand and implement. In addition, method must ponder load power factor (pf) while allocating losses.

Initially, the LA method has gained popularity in transmission system. There are many methods for LA like pro-rata [2], proportional sharing [3], quadratic sharing [4], geometric [4, 5], marginal loss coefficient (MLC) [6]. Pro-rata method is easy to understand and implemented but does not consider network topology. This limitation is overcome in proportional and quadratic method but it does not provide any theoretical foundation. Geometric loss allocation method considers logarithmic scheme for allocating losses. This method may not suitable to distribution system with wide variety of load. MLC methods suffer from the issues like slack bus dependency, cross-subsidies and over recovery. In addition to these methods, there is one

P. Kumar (✉)

Baba Ghulam Shah Badshah University, Rajouri 185234, J&K, India

N. Gupta · K. R. Niazi · A. Swarnkar

Malaviya National Institute of Technology, Jaipur 302017, Rajasthan, India

more category which has gained popularity that is game theory-based method [7, 8] for loss allocation. The conventional game theory-based method has the problem of combinatorial explosion.

In past few years, LA for distribution system is getting equal attention. For this system, majority of methods are based upon circuit theory. These methods are based upon system structures which are expressed by bus impedance matrix and power flow results [9]. These methods are Succinct method [10], power summation method for loss allocation (PSMLA) [11], energy summation method for loss allocation, branch current decomposition loss allocation (BCDLA) [9], etc. Succinct’s method [10] has a paradox according to which it is unable to provide meaningful LA for certain type of reactive loads [9]. BCDLA [9] method removes the paradox in [10] by ignoring the line reactance. This method is further improved by branch current decomposition method (BCDM) [12] which allocates losses by tasking projection of the load currents over constrained branch voltage drop. The PSMLA [11] allocates losses in quadratic way. In [13], it presented a cross-term decomposition method (CTDM) where loss allocation factor (LAF) is derived analytically. Exact cross-term decomposition method (ECTDM) [14] allocates losses by bifurcating load current in active and reactive component, and their loss allocation factor is derived analytically.

The contemporary distribution system can be seen with large number of distributed generation (DGs). DG further complicates the problem of LA by changing line flows from unidirectional to bidirectional. This paper presents a comparative study for active distribution system.

2 Circuit Theory-Based Loss Allocation Methods

In circuit theory-based LA method, losses can be seen as either I^2R or projection based. Let us consider losses by I^2R means. Let a branch ij as shown in Fig. 1. The current in the branch ij is phasor sum of the contributing load current. The real power loss in branch ij can be calculated as [13].

$$ploss(ij) = \sum_{k \in CN(ij)} ploss(ij, k) = R(ij) [\Re(I(ij))^2 + \text{Im}(I(ij))^2] \quad (1)$$

Fig. 1 Single line diagram of a distribution feeder

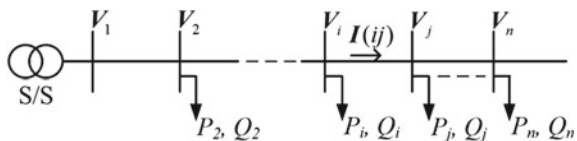


Table 1 Table for loss allocation factor used for different methods

Methods	Loss allocation factor (LAF)	
Quadratic(PSMLA)	$\frac{P_k^2}{P_k^2 + P_q^2}$	
Geometric	$1 + \frac{1}{2} \ln \frac{P_k}{P_q}$	
CTDM	$\frac{I(i,j,k)}{\sum_{k \in CN(ij)} I(i,j,k)}$	
ECTDM	Active: $\frac{\Re\{I(i,j,k)\}}{\Re\{I(i,j,k)\} + \Re\{I(i,j,q)\}}$	Reactive: $\frac{\Im\{I(i,j,k)\}}{\Im\{I(i,j,k)\} + \Im\{I(i,j,q)\}}$

P_k : Active Power of k th node, $I(ij, k)$: contributing current of k th node in branch ij

$$= R(ij) \left[\left(\sum_{k \in CN(ij)} I(ij, k) \cos \phi(ij, k) \right)^2 + \left(\sum_{k \in CN(ij)} I(ij, k) \sin \phi(ij, k) \right)^2 \right] \tag{2}$$

$$= R(ij) \sum_{k \in CN(ij)} (I(ij, k))^2 + R(ij) \sum_{k \in CN(ij)} \sum_{\substack{q \in CN(ij) \\ q \neq k}} I(ij, k) I(ij, q) \cos\{\phi(ij, k) - \phi(ij, q)\} \tag{3}$$

$$= ST(ij) + CT(ij) \tag{4}$$

Equation (4) has two terms, namely squared-term (ST) and crossed-term (CT). The allocation of ST is straightforward; however, CT needs bifurcation. The bifurcation of CT is done by employing LAF which must have the aforementioned properties and should be derived analytically. There are many methods available in the literature which provides loss allocation using different LAFs. Some of them are listed in Table 1. The table shows the methods and their corresponding LAF.

The projection-based approach employed the projection of the load currents over branch voltage drop. These methods are Succinct’s method [10], BCDLA [9] and BCDM [12]. BCDM is extension of BCDLA method. These methods may be expressed as

$$ploss(ij, k) = \Delta\gamma(ij)[\Re\{I(ij, k)\} \cos \psi(ij) + \Im\{I(ij, k)\} \sin \psi(ij)] \tag{5}$$

where $\Delta\gamma$ = branch voltage drop (Succinct’s method)/virtual branch voltage(BCDLA)/constraint branch voltage drop (BCDM).

$\psi(ij)$ = angle between $\Delta\gamma$ and contributing load currents.

3 Simulation Results

In order to compare these methods, results obtained in [5, 12–14] are considered for 33-bus distribution system. The results are presented in Tables 2 and 3. The DGs are chosen from [5], i.e. DG1 is placed at node 6 with 2058.71 kW and 997.10 kVAr rating, DG2 is placed at node 25 with 738.39 kW and 457.60 kVAr rating, and DG3 is placed at node 32 with 499.55 kW rating. Table 2 shows that for system without DG (WODG), all the methods are giving at par LA at almost all the node, except at few nodes (like 30) owing to load pf. Node 30 is having poor pf (0.32 pf lag.), and therefore, loss allocated must be high which is obtained using [11, 13, 14]. This proves that these methods are effectively considering pf for LA. The total system losses under this condition will be 202.67 kW. However, when the DGs are considered, the total system losses are reduced to 43.44 kW. With this, a reduction in LAs to load points has been observed for all method except [12–14]. Table 3 shows the comparison of remuneration allocation (–ve LA) using various methods. Since the DG1 is feeding highest reactive power to system for loss reduction, it deserves higher remuneration, as allocated by [13, 14]. Moreover, for the same value of NRU (43.44 kW), all the methods allocate different LA to load points and DG owners (DGOs). Since the losses are reduced by DGOs, complete benefit, i.e. (202.67–44.44) kW equal to 159.23 kW (as indicated by TRDG in table) should to be given to DGOs but not to consumers who are playing no role in loss reduction. Methods of [12–14] allocate complete benefits to DGOs for their contribution in loss reduction.

4 Conclusion and Future Scope

The paper presents a comparative study of circuit theory-based LA method for contemporary distribution system. For the system without DG, method of [11, 13, 14] is found to be more sensitive to load pf for LA. However, with DG, every method behaves differently. Moreover, the methods of [5, 9, 11] allocate lesser benefits to DG owners by diverting benefits towards load points, whereas [12–14] allocate fair amount of loss reduction benefits (TRDG) to DG owners. In addition, [13, 14] give due consideration to reactive power flow while allocating remuneration to DGOs. This work can be further be extended by incorporating battery energy storage systems (BESSs) and electric vehicle (EV) as a stake holder in distribution system.

Table 2 Comparison results (in kW)

Methods Node	BCDLA [9]		BCDM [12]		PSMLA [11]		Method [5]		CTDM [13]		ECTDM [14]	
	WODG	DG	WODG	DG	WODG	DG	WODG	DG	WODG	DG	WODG	DG
1	0	0	0	0	0	0	0	0	0	0	0	0
2	0.31	0.06	0.31	0.31	0.21	0.21	0.28	0.17	0.29	0.24	0.24	0.24
3	1.51	0.13	1.46	1.46	0.87	0.82	1.28	0.73	1.39	1.07	1.07	1.07
4	3.25	0.27	3.26	3.26	2.68	2.51	3.04	1.68	2.98	2.86	2.86	2.86
5	1.97	0.08	1.92	1.92	0.82	0.78	1.54	0.98	1.77	1.18	1.18	1.18
6	2.77	-0.07	2.58	2.58	1.15	1.06	2.14	1.34	2.5	1.66	1.66	1.66
7	10.34	0.35	10.09	10.09	12.55	11.02	10.92	5.52	9.79	11.61	11.61	11.61
8	11.49	1.35	11.25	11.25	14.42	12.68	12.28	6.84	11.06	13.19	13.19	13.19
9	3.53	0.62	3.36	3.36	1.72	1.57	2.89	2.06	3.27	2.33	2.33	2.33
10	3.88	0.91	3.69	3.69	1.99	1.81	3.22	2.39	3.6	2.64	2.64	2.64
11	3.46	0.95	3.51	3.51	1.39	1.27	2.72	2.11	3.11	2.08	2.08	2.08
12	4.56	1.29	4.56	4.56	2.55	2.32	3.86	2.9	4.14	3.23	3.23	3.23
13	4.96	1.63	4.98	4.98	2.86	2.6	4.24	3.27	4.52	3.59	3.59	3.59
14	10.72	3.66	10.77	10.77	11.62	10.4	10.7	7.74	10.26	10.95	10.95	10.95
15	4.24	1.35	3.86	3.86	2.35	2.12	3.58	2.79	4.12	3.04	3.04	3.04
16	4.7	1.61	4.49	4.49	2.61	2.36	3.99	3.14	4.37	3.36	3.36	3.36
17	4.81	1.7	4.6	4.6	2.69	2.43	4.1	3.24	4.46	3.46	3.46	3.46
18	7.67	2.8	7.52	7.52	6.68	6	7.24	5.5	7.28	6.92	6.92	6.92
19	0.3	0.08	0.29	0.29	0.2	0.19	0.26	0.18	0.28	0.23	0.23	0.23
20	0.58	0.36	0.57	0.57	0.47	0.47	0.54	0.46	0.56	0.51	0.51	0.51

(continued)

Table 2 (continued)

Methods	BCDLA [9]		BCDM [12]		PSMLA [11]		Method [5]		CTDM [13]		ECTDM [14]	
	WODG	DG	WODG	DG	WODG	DG	WODG	DG	WODG	DG	WODG	DG
21	0.63	0.41	0.62	0.62	0.53	0.52	0.59	0.51	0.61	0.61	0.56	0.56
22	0.67	0.45	0.66	0.66	0.57	0.56	0.64	0.55	0.65	0.65	0.6	0.6
23	1.92	0.2	1.9	1.9	1	0.94	1.58	0.86	1.68	1.68	1.28	1.28
24	11.25	1.02	11.05	11.05	15.01	11.17	12.61	4.85	11.35	11.35	13.85	13.85
25	12.58	-0.02	12.38	12.38	16.37	11.35	13.95	4.14	12.68	12.68	15.2	15.2
26	2.98	0.03	2.86	2.86	1.25	1.16	2.34	1.48	2.66	2.66	1.81	1.81
27	3.14	0.11	3.03	3.03	1.3	1.2	2.45	1.56	2.78	2.78	1.89	1.89
28	3.33	0.3	3.4	3.4	1.37	1.25	2.72	1.72	3.12	3.12	2.08	2.08
29	9.11	1.59	9.07	9.07	7.21	6.37	8.4	4.89	7.86	7.86	7.83	7.83
30	37.87	14.78	40.75	40.75	55.54	43.13	45.45	29.52	48.91	48.91	50.7	50.7
31	11.88	1.86	11.74	11.74	10.97	9.4	11.44	6.19	10.55	10.55	11.2	11.2
32	16.89	2.58	16.72	16.72	19.65	16.18	17.52	9.01	15.71	15.71	18.36	18.36
33	5.38	1.05	5.41	5.41	2.08	1.88	4.17	2.64	4.35	4.35	3.16	3.16
Total LA to load points	202.68	43.49	202.66	202.66	202.68	167.73	202.68	120.96	202.66	202.66	202.67	202.67

Table 3 Comparison of remuneration allocation

Indices	BCDLA [9]	BCDM [12]	PSMLA [11]	Method [5]	CTDM [13]	ECTDM [14]
RDG1	-0.04	-105.11	-71.9	-56.28	-118.09	-118.84
RDG2	-0.05	-24.27	-20.05	-8.37	-21.14	-20.89
RDG3	0.04	-29.85	-32.34	-12.87	-20.01	-19.49
NRU	43.44	43.44	43.44	43.44	43.44	43.44
TRDG	-0.05	-159.23	-124.29	-77.52	-159.23	-159.23

RDG Remuneration to DG owners, *NRU* Net revenue to utility, *TRDG* Total revenue to DGO

References

1. Conejo AJ, Arroyo JM, Alguacil N, Guizarro AL (2002) Transmission loss allocation: a comparison of different practical algorithms. *IEEE Trans Power Syst* 17(3):66–66
2. Bialek JW, Ziemianek S, Abi-Samra N (1999) Tracking-based allocation and economic dispatch. In: *Proceedings of 13th PSCC, Trondheim, Norway*, pp 375–381
3. Kashyap SS, De M (2017) Loss allocation and loss minimisation for radial distribution system including DGs. *IET Renew Power Gener* 11(6):806–818
4. Expósito AG, Santos JMR, García TG, Velasco EAR (2000) Fair allocation of transmission power losses. *IEEE Trans Power Syst* 15(1):184–188
5. Jagtap KM, Khatod DK (2017) Novel approach for loss allocation of distribution networks with DGs. *Elect Power Syst Res* 143:303–311
6. Belati EA, da Costa GRM (2008) Transmission loss allocation based on optimal power flow and sensitivity analysis. *Int J Electr Power Energy Syst* 30(4):291–295
7. Molina YP, Saavedra OR, Amarís H (2013) Transmission network cost allocation based on circuit theory and the Aumann-Shapley method. *IEEE Trans Power Syst* 28(4):4568–4577
8. Yu Q, Xie J, Chen X, Yu K, Gan L, Chen L (2019) Loss allocation for radial distribution networks including DGs using Shapley value sampling estimation. *IET Gener Transm Distrib* 13(8):1382–1390
9. Carpaneto E, Chicco G, Akilimali JS (2006) Branch current decomposition method for loss allocation in radial distribution systems with distributed generation. *IEEE Trans Power Syst* 21(3):1170–1179
10. Fang WL, Ngan HW (2002) Succinct method for allocation of network losses. *IEE Proc Gen Transm Distrib* 149(2):171–174
11. Atanasovski M, Taleski R (2011) Power summation method for loss allocation in radial distribution networks with DG. *IEEE Trans Power Syst* 26(4):2491–2499
12. Kumar P, Gupta N, Niazi KR, Swarnkar A (2017) Current decomposition method for loss allocation in distribution systems. *IETGen Transm Distrib* 11(18):4599–4607
13. Kumar P, Gupta N, Niazi KR, Swarnkar A (2019) A circuit theory-based loss allocation method for active distribution systems. *IEEE Trans Smart Grid* 10(1):1005–1012
14. Kumar P, Gupta N, Niazi KR, Swarnkar A (2019) Exact cross-term decomposition method for loss allocation in contemporary distribution systems. *Arab J Sci Eng* 44:1977–1988

A Comparative Study on the Performance of Energy Storage Systems for Hybrid Electric Vehicles



Kanchan Yadav and Sanjay Maurya

1 Introduction

We are very clear with the fact that the energy storage system is not the new thing, as we are using batteries since the early 1800. The various emerging concepts in the transportation and the increase in the usage for various hybrid, all-electric or plug-in vehicles are the main reasons behind the significant role of ESS [1]. The demand for the construction of new energy storage systems has been increased significantly when the more dynamic and cleaner grid requirement has come into existence, and thus, it led the policymakers to think about new and better solutions for the energy storage applications.

Basically, the purpose behind the storage of energy is to capture it and deliver this stored energy for the future usage. For the sustainable use of resources, the concern should be focused on environmental impacts of fossil fuels and various solutions for the energy storage systems. Thus, the various characteristics of the ESS contribute to the performance of the hybrid vehicles [2]. With the involvement of energy storage, the intermittency of solar power and wind power has also been addressed and it can also be effective in reducing the need for building backup power plants. With the change in demand, how quickly the energy storage is able to respond shows the effectiveness of this facility. It is also dependent on several other factors which involve the rate at which energy loss occurs during the process of storage, the overall capacity of the energy storage systems and also on its quicker action during recharging.

Generally, the fossil fuel is the most used form of the energy. Their transportability and the practicality in stored form allow the control in energy supplied. If we look at the energy generation of other resources like solar and wind, then it clearly shows that

K. Yadav (✉) · S. Maurya
Department of Electrical Engineering, GLA University, Mathura, India
e-mail: kanchan.yadav@gla.ac.in

S. Maurya
e-mail: Sanjay.maurya@gla.ac.in

they are intermittent sources and relied on the seasonal changes and environmental factors. In order to achieve improved efficiency and better power quality, these energy storage systems become the viable solution [3].

2 Selected ESS and SOC Estimation

There are many ways to store the energy and each of them has their own pros and cons. The energy storage systems are looked upon with various view points by the researchers. These consideration points can be the use of ESS in power systems or the automotive applications. There is a debate in the automotive industry to select the ESS option for the HEV which is best suitable. There are a number of research practices happening so that these storage devices can be made available with the reduced cost, increased lifetime and the improved energy density [4, 5]. In the automotive applications energy storage systems are used in combination which can be applied in only battery electric vehicles, hybrid electric vehicles, fuel cell electric vehicles etc. If we look at different technologies, then it covers various chemistries like lithium ion, nickel metal hydride, lead acid, nickel cadmium, Ni-Zn, fuel cell, ultra-capacitors or flywheels. In the current scenario, the developments are going on for the various battery technologies, some are already available commercially in the market, while some are in the study struggling in the experimental observations [6]. For the sustainable energy generation taking long term in the view, the three important parameters that are generation, conversion and storage play a crucial role. The clean and efficient energy storage can be used as the strategy if we want to tackle this immense problem of sustainable energy economy [7].

The different storage technologies and their characteristics are observed so that it will serve the purpose to categorize and compare various ESS and it can help in selecting the most appropriate type of ESS for the particular application [8]. Here is the schematic block diagram of the system's configuration model. This block models the ESS as an SOC-dependent voltage in series with the SOC and current direction-dependent internal resistance. By assuming constant current A-h capacity, SOC is computed but limited in a way so that it can never exceed the minimum voltage level of the given ESS.

The most important parameter for the battery pack is its SOC which is defined as the ratio of current capacity $Q(t)$ to the nominal capacity Q_n . The maximum charge that can be stored is given by the nominal capacity and is given by the manufacturer itself and thus we can define SOC as

$$\text{SOC}(t) = \frac{Q(t)}{Q_n} \quad (1)$$

The estimation of state of charge for different battery technologies is discussed in this paper and various methods are illustrated systematically [9]. There are various

SOC estimation methods as well that include direct, book keeping, adaptive or the hybrid methods.

- (A) *Open Circuit Voltage Method* For this method, the OCV value at 0% SOC and 100% SOC needs to be known, and then, we can predict the SOC by estimating its open circuit voltage and then the battery OCV is calculated as

$$V_{OC}(t) = a_1 * SOC(t) + a_0 \tag{2}$$

- (B) *Terminal Voltage Method* During battery discharging, the terminal voltage drops due to internal impedance and thus its emf is taken as proportional to SOC.
- (C) *Coulomb Counting Method* This method is most common for the SOC estimation. With the initial SOC value, the state of charge at different time instants (t) is calculated by the following integration

$$SOC(t) = SOC_i + \frac{1}{3600} \frac{\eta_{bat}(i(t), T)}{Cap(T)} \int_{t_0}^t i(t) dt \tag{3}$$

where $Cap(T)$ is the capacity and $\eta_{bat}(i(t), T)$ is the columbic efficiency of the battery.

3 System Configuration and Description

In the energy storage block, the charge reservoir is the battery pack, and then, we will make the equivalent circuit by considering the remaining charge of reservoir as the parameters of this circuit. The battery model is R_{int} which considers the charge contained by the ESS as the constant value and it is subjected to the minimum voltage limit. After discharging, the battery replenishment gets affected by the columbic efficiency. In order to evaluate the performance and state of health for the battery, internal resistance can be used to get the information. If there is a need to estimate the battery SOC, its open circuit voltage can play an important role by considering the intrinsic characteristics of the battery technology [10]. The power which is given by the battery is limited to the maximum value which can be delivered by the equivalent circuit or which the controller is able to accept subjected to the minimum voltage requirements. After obtaining these values, the comparison is done in order to find that the changes occurred in the beginning and ending of cycle are not too large; thus, in ADVISOR, two methods are offered for this SOC balancing as it is very necessary during vehicle analysis [11] (Fig. 1).

ESS block represents the energy storage unit which contains the onboard energy for the modeled vehicle. With the power requests, this block provides the output battery power. During modeling, the charge gets reserved and the equivalent circuit accounts for the circuit parameters and the minimum voltage limit is subjected to the

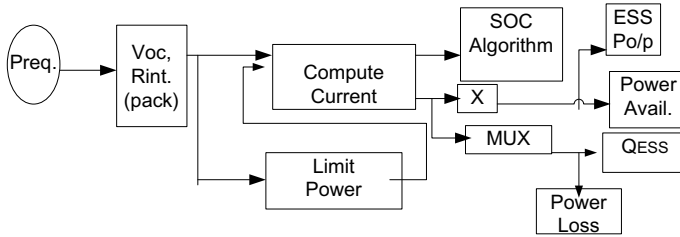


Fig. 1 Schematic block diagram of ESS model

ESS. The charging parameters are limited to maximum voltage level and the charge replenished in the ESS gets affected by the columbic efficiency.

With the response of the SOC requirements, the ESS is modeled to fulfill the requirements of output available power. For computing the power loss, the i^2R and the columbic efficiency losses are included. For the equivalent circuit, the V_{oc} and the R_{int} are taken as the linear functions of SOC. As the total power available is limited in the allowable range thus in addition to V_{oc} , R_{int} actual power available is also taken as the variables for solving the quadratic equation. This quadratic equation is used for obtaining the circuit. The ESS current is used to update the effective SOC. Taking an example, we can say that if the incorrect SOC estimation takes place it can lead to the overcharged or the over-discharged battery and it will in turn damage the battery technology [12].

Maximum power available is also limited to certain parameters; the maximum power limit is obtained by

$$P = V_{bus} * \frac{V_{oc} - V_{bus}}{R} \tag{4}$$

where V_{bus} is either $V_{OC}/2$ or minimum battery voltage.

Power is given as

$$P = V * I \tag{5}$$

$$V = \frac{P}{I} \tag{6}$$

When we combine this power equation with the KVL, then it will yield

$$\frac{P}{I} = V_{OC} - (R * I) \tag{7}$$

By multiplying with I on both sides, the equation becomes

$$P = (V_{OC} * I) - RI^2 \tag{8}$$

Now, the equation is solved in the block diagram

$$RI^2 - (V_{OC} * I) + P = 0 \quad (9)$$

The solution with lower voltage requirement is taken to produce the same amount of power. On charging, the maximum allowable voltage limit should not be exceeded and then the minimum raw current is calculated by

$$I = \frac{V_{OC} - V_{max}}{R} \quad (10)$$

For the prediction of the state of charge values for different battery technologies, the new SOC-based algorithm is proposed in the research which is based upon the back-stepping method by using the partial differential equations [13].

In order to estimate the SOC value with the coulombic efficiency, the discharging current is integrated over time. By investigating $SOC(t)$ from $i(t)$ integration and with the already estimated SOC values $SOC(t - 1)$, we can obtain the state of charge by

$$SOC(t) = SOC(t - 1) + i(t)Q_n \Delta t \quad (11)$$

In ADVISOR, the SOC algorithm determines the residual capacity in Amp-hr charge unit. With the series of steps, this value is approximated, and during this estimation, the coulombic efficiency and the maximum capacity remain the functions of temperature. The model used has the open circuit voltage source and internal resistance. These parameters are proportional to the changes in the state of charge, temperature and current direction [14]. With the average coulombic efficiency estimation, the total effective Amp-hr change is determined. For the initial SOC, non-zero Ah is used, and then, it is calculated by

$$SOC = \frac{C_{max} - Ah}{C_{max}} \quad (12)$$

where C_{max} —Maximum capacity, Ah —Amp-hr used.

Now, the SOC is computed according to the power bus requirements and the output has the available power. Thus, here the battery modeling is done with controlled voltage source which is taken in series with the constant resistance value [15].

4 Result and Discussion

In this section, we are going to present the schematic diagram of the model used for analysis and the comparison based on different attributes of the ESS. This analysis is done on ADVISOR with the following vehicle parameters (Table 1).

Table 1 Parameters for the analysis

Component	Parameter	Value
Vehicle	Veh_Cargo mass	136 kg
	Veh_Glider mass	592 kg
ESS Vnom	ESS_Pb	308
	ESS_Li-ion	267
	ESS_Ni-Mh	335
	ESS_Ni-Zn	307
	ESS_Ni-Cad	159
	ESS_Ultra-cap	44

On the basis of above parameters, the different specifications for the selected ESS are tabulated and the analysis is also presented with their obtained characteristics (Table 2).

The analysis based on different characteristics is shown and illustrated with the following figures. The characteristic variation with state of charge is shown for four different ESS technologies, i.e., valve-regulated lead-acid battery, li-ion battery, nickel metal hydride and nickel cadmium. In the result figures, the different characteristics like the SOC variation of the given ESS with the variation in the model parameters like internal resistance, and the efficiency, are analyzed by taking the four different ESS technologies. From Fig. 2a–d, the curves are shown for the internal resistance variation with the SOC. In Fig. 3a–d, the curves are given for the efficiency illustration.

In these figures, resistance variation with SOC is shown and we can notice that the larger changes are noticed in the nickel-based batteries. For nickel metal hydride battery, the resistance level is highest when SOC is at lower level. We can say that just after the full charge, the higher battery performance cannot be achieved. Low internal resistance is the important factor needs to be noticed as it determines the run time in the large extent. During delivery, the power spikes require the lower resistance value and import the less restriction on the battery itself. The internal resistance value varies widely with the lower value for nickel cadmium, the higher value for nickel metal hydride and the moderate value for li-ion battery.

The critical factor defining the usefulness of the battery storage technology is the roundtrip efficiency which is illustrated in the above figures. In the charge efficiency

Table 2 Obtained ESS specifications

Parameters/ESS	VRLA	Li-ion	Ni-MH	NiCad
Voltage (max)	16.5	11.7	15.67	6.9
Voltage (min)	9.5	6	9.13	5.9
Capacitive module	660	795	830	770
Effective res (off)	0.645	7.81	1.59	0.845
Effective res (on)	0.364	1.12	0.53	0.38

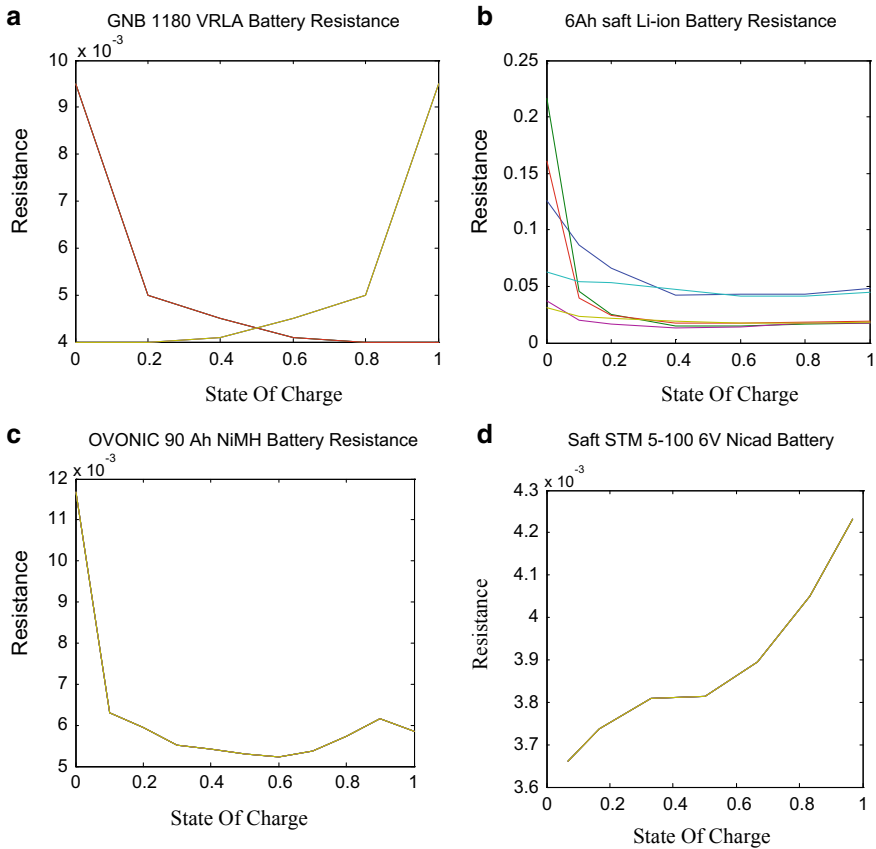


Fig. 2 State of charge variation with resistance

characteristic, the Ni-Mh battery is similar to Ni-cad one, as the efficiency is higher for 70% SOC and then it drops. The batteries' ability to absorb charge is shown with the charge efficiency and has similarities with columbic efficiency. Comparing with lead-acid or li-ion batteries, nickel-based batteries are more complex to charge. For li-ion battery, during a roundtrip, it lost approximately 5% of energy; that is, we can say that it has 95% roundtrip energy efficient when compared with the lead-acid batteries in which the energy lost is approximately 20–25%. The technological and very innovative advancements are happening nowadays to boost the energy efficiency for the li-ion battery storage. Thus, li-ion batteries are often preferred more as compared to lead acid due to their higher energy and power density. We can say that the storage with the higher roundtrip efficiency has the capability to retain more energy and be able to provide more power.

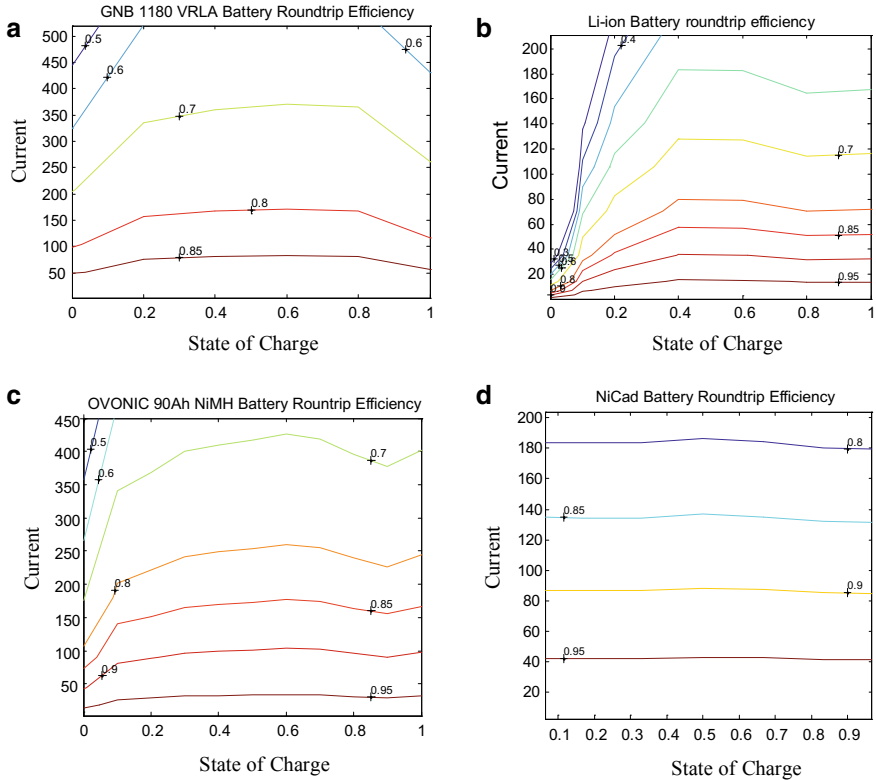


Fig. 3 State of charge variation with current

5 Conclusion

The energy storage technologies came in varieties and the vehicles rely on them so it would be the fair perspective to select the best for the required application. The conventional lead-acid batteries are also proved for extreme reliability with low maintenance and have higher efficiency. NiCad battery chemistry requires high charging rate and has low value of internal resistance, but at the same time it has higher level of discharge cycle. The advantageous attribute of longer cycle life and lower maintenance requirements makes it more suitable. It can be analyzed that its cycle life is dependent on the depth of discharge and has energy efficiency greater than 70%. Li-Ion battery chemistry stores high amount of energy and makes the hybrid vehicles more attractive for them who have high horse power demand. Their use is newer but due to their popular attributes like longer lifetime, quick recharging process, cost and weight effective, thus becomes the best choice, and with the development of science and technology, they have gained the mainstream. By analyzing the different ESS, it can be concluded that in some or the other way if one ESS proves to be superior to the

other but at the same time it does not contain the sufficient attributes to completely replace the existing one. Thus, the combination of ESS proves to be better way to use them effectively and take the automotive technologies to the viable mode.

References

1. Alahakoon S, Leksell M (2015) Emerging energy storage solutions for transportation—a review: An insight into road, rail, sea and air transportation applications. In: 2015 international conference on electrical systems for aircraft, railway, ship propulsion and road vehicles (ESARS), pp. 1–6. IEEE
2. Kim B-H, Lee B-H, Jeong J-B, Shin D-H, Song H-S, Kim H-J (2009) A study on the performance of the improved energy storage system for mild hybrid vehicles. In INTELEC 2009–31st international telecommunications energy conference, pp. 1–6. IEEE
3. Farhadi M, Mohammed O (2015) Energy storage technologies for high-power applications. IEEE Trans Ind Appl 52(3):1953–1961
4. Williamson SS, Khaligh A, Oh SC, Emadi A (2005) Impact of energy storage device selection on the overall drive train efficiency and performance of heavy-duty hybrid vehicles. In: 2005 IEEE vehicle power and propulsion conference, p 10. IEEE
5. Chemali E, Preindl M, Malysz P, Emadi A (2016) Electrochemical and electrostatic energy storage and management systems for electric drive vehicles: State-of-the-art review and future trends. IEEE J Emerg Select Top Power Electron 4(3):1117–1134
6. Divya KC, Østergaard J (2009) Battery energy storage technology for power systems—an overview. Electr Power Syst Res 79(4):511–520
7. Placke T, Kloepsch R, Dühnen S, Winter M (2017) Lithium ion, lithium metal, and alternative rechargeable battery technologies: the odyssey for high energy density. J Solid State Electrochem 21(7):1939–1964
8. Ibrahim H, Ilinca A, Perron J (2008) Energy storage systems—characteristics and comparisons. Renew Sustain Energy Rev 12(5):1221–1250
9. Xiong R, Cao J, Quanqing Yu, He H, Sun F (2017) Critical review on the battery state of charge estimation methods for electric vehicles. IEEE Access 6:1832–1843
10. He H, Xiong R, Guo H (2012) Online estimation of model parameters and state-of-charge of LiFePO4 batteries in electric vehicles. Appl Energy 89(1):413–420
11. Markel T, Brooker A, Hendricks T, Johnson V, Kelly K, Kramer B, O’Keefe M, Sprick S, Wipke K (2002) ADVISOR: a systems analysis tool for advanced vehicle modeling. J Power Sources 110(2):255–266
12. Peng S, Chen C, Shi H, Yao Z (2017) State of charge estimation of battery energy storage systems based on adaptive unscented Kalman filter with a noise statistics estimator. IEEE Access 5:13202–13212
13. Moura SJ, Chaturvedi NA, Krstic M (2012) PDE estimation techniques for advanced battery management systems—Part I: SOC estimation. In: 2012 American Control Conference (ACC), pp 559–565. IEEE
14. Johnson VH (2002) Battery performance models in ADVISOR. J Power Sources 110(2):321–329
15. Tremblay O, Dessaint LA, Dekkiche A-I (2007) A generic battery model for the dynamic simulation of hybrid electric vehicles. In: 2007 IEEE Vehicle Power and Propulsion Conference, pp. 284–289. IEEE